NASA-CR-192103

PART 2, VOLUME I

The Joint NASA/Geosat Test Case Project

Final Report

Michael J. Abrams
James E. Conel
Harold R. Lang
Jet Propulsion Laboratory
California Institute of Technology
Pasadena, California

Editor
Helen N. Paley
Jet Propulsion Laboratory

(NASA-CR-192103) THE JOINT NASA/GEOSAT TEST CASE PROJECT, PART 2, VOLUME 1 Final Report (JPL)
N93-72310
Unclas
Z9/43 0152656

October 1984

AAPG BOOKSTORE
P.O. Box 979
Tulsa, OK 74101, USA

The research described in this publication was carried out jointly by the Jet Propulsion Laboratory, California Institute of Technology, under a contract with the National Aeronautics and Space Administration, and by The Geosat Committee, Inc., and its members.

Reference herein to any specific commercial product, process, or service by trade name, trademark, manufacturer, or otherwise, does not constitute or imply its endorsement by the United States Government, The Geosat Committee, Inc., and its members, or the Jet Propulsion Laboratory, California Institute of Technology.

Published by
The American Association of Petroleum Geologists
Tulsa, Oklahoma 74101, USA

Copyright © 1985 by
The American Association of Petroleum Geologists
All Rights Reserved
ISBN: 0-89181-654-2
Library of Congress Cataloging in Publication Data

Abrams, Michael J.
The Joint NASA/Geosat Test Case Project.

Sponsored by NASA, Jet Propulsion Laboratory, and Geosat
October 1984
Includes bibliographies
1. Joint NASA/Geosat Test Case Project. 2. Geology—Remote sensing. 3. Petroleum—Geology—Remote sensing. 4. Mines and mineral resources—Remote sensing. I. Conel, James E. II. Lang, Harold R. III. Paley, Helen N. IV. United States. National Aeronautics and Space Administration. V. Jet Propulsion Laboratory (U.S.) VI. Geosat Committee. VII. Title.
QE33.2.R4A27 1985 622'.1 85-1381

Contributing Authors

Willis H. Alderman
AMOCO Production Co.
Denver, Colorado

Ronald E. Alley
Jet Propulsion Laboratory

M. Lee Allison
University of Massachusetts
Amherst, Massachusetts

Joe R. Applegate
AMOCO Production Co.
Denver, Colorado

Kathleen W. Baird
Jet Propulsion Laboratory

Gary I. Ballew
Phillips Petroleum Co.
Bartlesville, Oklahoma

Anthony R. Barringer
Barringer Resources Inc.
Golden, Colorado

David Brown
Texasgulf Inc.
Tucson, Arizona

Gary A. Cooke
Gulf Science and Technology Co.
Pittsburgh, Pennsylvania

Aderbal C. Correa
CONOCO Exploration Research Div.
Ponca City, Oklahoma

John B. Curtis
Columbia Gas System Service Corp.
Columbus, Ohio

Michael I. Dailey
Jet Propulsion Laboratory

John B. Davis
Mobil Research and Development Co.
Dallas, Texas

Aurelio A. DeGasparis
Gulf Science and Technology Co.
Pittsburgh, Pennsylvania

James A. Drahovzal
Gulf Science and Technology Co.
Pittsburgh, Pennsylvania

John P. Ford
Jet Propulsion Laboratory

John W. Gabelman
Utah International, Inc.
San Francisco, California

Rhonda Gaylord
University of Wyoming
Laramie, Wyoming

Alexander F.H. Goetz
Jet Propulsion Laboratory

Paul G. Harrison
Cities Service Co.
Tulsa, Oklahoma

H. Robert Hopkins
EXXON Production and Research Co.
Houston, Texas

John S. Kovacs
Columbia Gas System Service Corp.
Columbus, Ohio

Larry Lepley
Tucson, Arizona

Catherine J. LeVine
Jet Propulsion Laboratory

PRECEDING PAGE BLANK NOT FILMED

Leslie L. Lundell
Atlantic Richfield Corp.
Dallas, Texas

Ronald W. Marrs
University of Wyoming
Laramie, Wyoming

Matt D. Matthews
Gulf Science and Technology Co.
Pittsburgh, Pennsylvania

John B. McKeon
Gulf Science and Technology Co.
Pittsburgh, Pennsylvania

Pamela H. Muller
University of Texas, Permian Basin
Odessa, Texas

Paul H. Nadeau
The Geosat Committee, Inc.
San Francisco, California

Steve M. Nicolais
Superior Oil Co.
Denver, Colorado

Gary L. Prost
AMOCO Production Co.
Denver, Colorado

Leigh Readdy
Tucson, Arizona

Robert J. Reed
Cities Service Co.
Tulsa, Oklahoma

David M. Richers
Cities Service Co.
Tulsa, Oklahoma

Barrett N. Rock
Jet Propulsion Laboratory

Floyd F. Sabins, Jr.
Chevron Oil Field Research Company
La Habra, California

Ray Sadowski
AMAX Exploration, Inc.
Tucson, Arizona

Mark Settle
National Aeronautics and
Space Administration

James M. Soha
Jet Propulsion Laboratory

Harry E. Stewart
Sunmark Exploration
Dallas, Texas

Kevin R. Sundberg
Phillips Petroleum Co.
Bartlesville, Oklahoma

James V. Taranik
National Aeronautics and
Space Administration

Robert D. Watson
U.S. Geological Survey
Flagstaff, Arizona

Edward M. Wingo
University of Texas, Permian Basin
Odessa, Texas

Donald U. Wise
University of Massachusetts
Amherst, Massachusetts

IEEE	Institute of Electrical and Electronics Engineering
IFOV	Instantaneous field of view
IGARSS	International Geoscience and Remote Sensing Symposium
IPL	JPL's Image Processing Laboratory
IR	Infrared
JPL	Jet Propulsion Laboratory
JSC	Johnson Space Center
LP	Low-pass; a contrast subduing filter
MCF	Thousand cubic feet
MFMR	The aircraft Multifrequency Microwave Radiometer
M^2S	The aircraft Modular Multispectral Scanner
MSS	Multispectral Scanner; a system on Landsat satellites
NASA	National Aeronautics and Space Administration
NS-001	The aircraft Thematic Mapper Simulator
NURE	National Uranium Resource Evaluation
PC	Principal component
PCA	Principal components analysis
PDB	Pee Dee belemnite
PFRS	Portable Field Reflectance Spectrometer
pixel	Picture element
PMIS	The aircraft Passive Microwave Imaging System
RME	Rocky Mountain Energy
SAR	Synthetic Aperture Radar
SCS	Soil Conservation Service
SEG	Society of Exploration Geophysicists
SLAR	Side-looking airborne (aircraft) radar
SLR	Side-looking radar
SMIRR	Shuttle Multispectral Infrared Radiometer
SMOW	Standard mean ocean water
SPIE	Society of Photo-Optical Instrumentation Engineers
SPOT	Système Probatoire d'Observation de la Terre; a French multispectral satellite terrestrial remote sensing system
TC	True color
TI	Thermal inertia
TIR	Thermal infrared
TM	Thematic Mapper; a multispectral scanner system on Landsat 4
USDA	United States Department of Agriculture
USGS	United States Geological Survey
VH	Cross polarized; vertically transmitted and horizontally received radar signal
VNIR	Visible and near infrared
XRD	X-ray diffraction

Figure Credits

The following figures were reprinted with permission of the copyright holders: Figures 2-5, 5-47, 6-34, and 7-12 by permission of Economic Geology, New Haven; Figure 5-4 by permission of the University of Arizona, National Cooperative Soil Survey, Phoenix; Figures 5-5 and 5-35 by permission of the Arizona Bureau of Geology and Mineral Technology, Tucson; Figures 5-32, 5-33, and 6-5 by permission of the Arizona Geological Society, Tucson; Figure 6-8 by permission of Kennecott Corporation, Cleveland; Figure 7-11 by permission of the Bureau of Mineral Resources, Geology and Geophysics, Canberra City, Australia; and Figure 8-50 by permission of Robert M. Garrels.

Selected Acronyms and Abbreviations

AAPG	American Association of Petroleum Geologists
ACSM	American Congress on Surveying and Mapping
AEC	Atomic Energy Commission
AIME	American Institute of Mining Engineers
ANAMAX	Mining company owned by AMAX and Anaconda mining companies
ASARCO	American Smelting and Refining Company
ASP	American Society of Photogrammetry
ATI	Apparent thermal inertia
BCF	Billion cubic feet
BLM	Bureau of Land Management
BMD	Biomedical Computer Program Series; a set of statistical computer programs developed by the University of California at Los Angeles
CCT	Computer-compatible magnetic tapes
CIR	Color infrared
CRC	Color ratio composite
CSD	Cross-strike discontinuity
CT	Canonical transformation
DEC	Digital Equipment Corporation
DN	Digital number
DOE	Department of Energy
ERIM	Environmental Research Institute of Michigan
EROS	Earth Resources Observation Systems
FLD	Fraunhofer Line Discriminator
FOV	Field of view
Geosat	The Geosat Committee, Inc.
GSA	Geological Society of America
HCMM	Heat Capacity Mapping Mission
HH	Parallel polarized; horizontally transmitted and horizontally received radar signal
HP	High-pass; a contrast enhancing filter
HSI	Hue, saturation, and intensity
HV	Cross polarized; horizontally transmitted and vertically received radar signal

Contents

Selected Acronyms and Abbreviations A-1

1. Project Description 1-i
2. Sensor Assessment Report 2-i
3. Porphyry Copper Commodity Report 3-i
4. Silver Bell, Arizona, Porphyry Copper Test Site Report 4-i
5. Helvetia, Arizona, Porphyry Copper Test Site Report 5-i
6. Safford, Arizona, Porphyry Copper Test Site Report 6-i
7. Uranium Commodity Report 7-i
8. Lisbon Valley, Utah, Uranium Test Site Report 8-i
9. Copper Mountain, Wyoming, Uranium Test Site Report 9-i

Section 1

Project Description

Mark Settle
James V. Taranik
National Aeronautics and Space Administration

Alexander F.H. Goetz
Michael J. Abrams
James E. Conel
Harold R. Lang
Jet Propulsion Laboratory

Section 1
Project Description

Contents

I. Introduction 1-1

II. Project Participants 1-1

A. National Aeronautics and Space Administration 1-1

B. Geosat Committee, Incorporated 1-2

C. Motivation of the Participants 1-2

III. Purpose and Objectives 1-3

IV. Methodology 1-3

A. Site Selection 1-3

B. Data Acquisition and Analysis 1-4

C. Organization and Management 1-6

Appendixes 1-9

A. History of the Project 1-9

B. Publications and Presentations 1-10

Figures

1-1. NASA/Geosat test site locations 1-4

1-2. Organizational chart 1-8

Tables

1-1. Test site locations and characteristics 1-5

1-2. Airborne sensor coverage of test sites 1-6

1-3. Major team and project meetings 1-7

PRECEDING PAGE BLANK NOT FILMED

Acknowledgments

The *Joint NASA/Geosat Test Case Project Final Report* could not have been created without the support of large numbers of individuals in industry and government, many of whom are not included in the Contributing Authors' list. Fred B. Henderson III played a key role in the founding of The Geosat Committee, Inc., and later, as its president, convinced NASA officials that a cooperative industry-government research program in remote sensing was worthwhile. DG Park ably assisted him. The first Board of Directors of the Geosat Committee was made up of R. Anthony Barker, AMAX Exploration, Inc.; Arthur Brant, Newmont Mining Ltd.; Richard Brown, ASARCO Inc.; Jon Davidson, Superior Oil Co.; R. Tom Fetters, EXXON Production and Research Co.; Michel Halbouty, Halbouty Energy Co.; John Havard, Kaiser Engineers; Don Matthews, Superior Oil Co.; Leo Miller, Texasgulf Inc.; and William Trollinger, Trollinger Geological Associates, Inc. The stature and leadership of these members convinced industry management to contribute substantial resources to this study.

Christopher Craft, Director of the Johnson Space Center, was the first to suggest a Geosat/NASA collaborative program to evaluate remote sensing techniques. Bruton Schardt, Chief of the Non-Renewable Resources Branch, was instrumental in developing the first program plan and in initally funding the effort at the Jet Propulsion Laboratory. James Taranik followed B. Schardt as Branch Chief and developed the final Memorandum of Understanding between NASA and the Geosat Committee. He enthusiastically supported the Project and took an active part in developing the outline and scope of the report. In NASA management, Pitt Thome, Director, Earth Observation Division, and Anthony Calio, Associate Administrator, Space and Terrestrial Applications, maintained active interest and support throughout the research phase of the Project.

The production of the *Test Case Project Final Report* at JPL was a lengthy, difficult process not only for the authors but also for the editorial staff. Thanks go to the many employees of the Documentation Section and in particular to Andrea Stein who provided editorial support and continuity throughout the report writing phase. Lori Fry oversaw the artwork, Robert Chandler was responsible for the layout and publication coordination, Michele Kelly-Bozora was responsible for page makeup, and Paulette Cali and Paula Kelly provided additional editorial support.

The long-term commitment of the Geosat Committee, its members, and the NASA and JPL management made possible the preparation of this report and is gratefully acknowledged.

Preface

This volume of the *Joint NASA/Geosat Test Case Project Final Report* contains the results from the porphyry copper and uranium studies as well as the Project Description and Sensor Assessment Report. Part 2, Volume II, contains the results from the petroleum studies and the Technical Appendix. A key to the bandpasses of the multispectral scanners used in this study is included in the Map Envelope, Part 3. Part 1 is a summary of the entire Joint NASA/Geosat Test Case Project.

Section 1
Project Description

I. Introduction

The Joint NASA/Geosat Test Case Project was a research endeavor conducted by the National Aeronautics and Space Administration (NASA)—a public agency of the U.S. Government—and a group of private companies represented by the Geosat Committee, Incorporated. Responsibility for the implementation of the Project resided at the Jet Propulsion Laboratory (JPL), which is operated for NASA by the California Institute of Technology. Geosat is a nonprofit organization that represents the collective interests of a wide variety of private firms in the future development of aerospace technology for global geological investigations. The Project was conducted on a cooperative basis and funds were not exchanged between the participants.

The purpose of the Project was to evaluate the geologic utility of state-of-the-art remote sensing techniques. Joint participation by NASA and industry in a research project of this nature was motivated by very different institutional interests. NASA's overall goal was to obtain greater insight into the capabilities and limitations of remote sensing technology for geological mapping. The results of the Project will assist NASA in establishing the requirements for and measurement characteristics of future space sensor systems. Industry's goal was to obtain greater insight into the potential usefulness of remote sensing technology for resource evaluation. From industry's perspective, the results of the Project may lead to expanded use of remote sensing techniques in mineral and energy exploration.

The Project was initiated in 1977 with the decision to investigate a series of experimental test sites in areas containing known deposits of copper, uranium, and petroleum. Existing remote sensing data collected by Earth-orbiting spacecraft were identified and obtained for each site. In addition, NASA performed a series of airborne remote sensing surveys employing state-of-the-art sensor systems. Geosat companies contributed ancillary geological site information, which had been obtained through ground-based exploration and development efforts. Remote sensing data and conventional types of geological information were analyzed jointly by JPL and industry investigators. The final results of the Project are presented in this document in the following form:

(1) Test site reports containing detailed descriptions of site characteristics and site-specific results.

(2) Commodity reports containing a comparative analysis of results obtained at test sites that contain similar types of mineral deposits.

(3) Sensor evaluation report containing an assessment of sensor systems employed by the Project, and recommendations for future sensor development.

This section describes the goals and interests of the Project participants, the technical objectives and methodology of the Project, and the history, organization, and management of this joint research endeavor.

II. Project Participants

A. National Aeronautics and Space Administration

NASA is the agency of the United States Federal Government with the responsibility of maintaining U.S. leadership in the development and utilization of space technology. The National Aeronautics and Space Act of 1958 specifically empowers NASA to conduct advanced research to determine "the potential benefits to be gained from, the opportunities for, and the problems involved in

the utilization of aeronautical and space activities for peaceful and scientific purposes." NASA has historically sponsored a variety of research programs to determine the utility of advanced forms of aerospace technology for basic and applied studies of the Earth.

The principal objective of earth applications research has been to determine how the measurement capabilities of orbital sensor systems (e.g., accuracy, precision, and resolution) affect the quality and usefulness of information derived from data acquired in space. In the area of geological remote sensing, NASA-sponsored research has concentrated upon developing an improved understanding of the fundamental physical processes involved in the reflection, absorption, and emission of electromagnetic radiation at the Earth's surface. NASA has constructed a variety of ground-based, aerial, and orbital instruments to obtain multispectral measurements of geological materials under laboratory and field conditions. Comparative analysis of measurements acquired at different scales and accuracies has provided insight into the inherent capabilities and limitations of orbital remote sensing measurements for geological applications. This expanding base of fundamental knowledge has, in turn, been employed by NASA in determining the direction and pace of future technology development efforts.

NASA-sponsored research in geological remote sensing has primarily been conducted by the Geology Group within the Earth and Space Sciences Division of JPL. Since 1973, the Geology Group has performed pioneering research in instrument development, computerized data processing, and data analysis and interpretation. JPL scientists have served as principal investigators on a variety of NASA flight programs, including Landsat, Skylab, the Heat Capacity Mapping Mission, Seasat, and, most recently, the experiments conducted during the second flight of the Space Shuttle. Past research at JPL has contributed substantially to present remote sensing capabilities and has historically played a critical role in defining the geological requirements for future sensor systems.

B. Geosat Committee, Incorporated

Geosat is a nonprofit organization that represents the interests of a wide variety of private companies in the future development of space technology for global geological investigations. The majority of Geosat member companies are involved in the search for mineral and energy resources, either through direct leasing and development of specific properties or through the provision of prospecting services to other companies. Private industry generally views remote sensing as a promising technique that can potentially be used as an additional tool in global resource exploration. Industry recognizes that new types of information concerning the composition, structure, and distribution of crustal materials can be obtained through the analysis of remotely sensed data. This information may contribute to improved methods of geologic mapping which, in turn, will lead to more accurate identification of areas of high resource potential.

Private-industry research related to the development and application of geological remote sensing techniques differs significantly from government-sponsored research. Private firms do not generally engage in long-term, high-risk research and development of unproven aerospace technology for geological applications. Instead, industry efforts concentrate mainly on the use and adaptation of data collected by existing technological systems, such as the Landsat Multispectral Scanner and the return-beam vidicon camera. Private investment in remote sensing research and development is motivated by an anticipated near-term return on investment. Consequently, private-industry research tends to be focused upon applications of remote sensing methods for detecting particular geologic features (e.g., rock types, clay minerals, fractures, etc.) that can be used as exploration guides in prospecting for mineral and hydrocarbon deposits.

Mineral and energy companies have used conventional geologic mapping techniques in their worldwide exploration efforts. Exploration firms have conducted pioneering research in the development of geophysical measurement techniques that permit detailed characterization of subsurface structure. In addition, private companies have acquired conventional geologic data for specific districts considered to be possible sites of economic mineralization. Many companies have proprietary geological data for particular areas that are not publicly available.

C. Motivation of the Participants

Joint participation by NASA and private-industry Geosat companies in the Test Case Project was motivated by very different interests. From NASA's perspective, the Project represented a unique opportunity to involve highly skilled geological practitioners with access to detailed ground-based information in the analysis and interpretation of remote sensing data. The results of the Project were expected to contribute to improved understanding of the geological information that can be extracted from remotely sensed data. From industry's perspective, the Project represented a unique opportunity to gain insight into the technical capabilities of state-of-the-art remote sensing instrumentation and access to experimental data acquired

by prototype sensor systems. The results of the Project were expected to permit individual companies, and the exploration industry in general, to better evaluate the practical utility of remote sensing methods for nonrenewable resource exploration.

In summary, the Project has been viewed from the outset as being mutually beneficial to both participants for quite different reasons. Each participant possessed certain types of expertise and easy access to data bases that were of direct interest to the other participant. This expertise and data formed the conceptual basis of this unique joint project between government and industry. A description of the historical development of the Project is provided in Appendix A.

III. Purpose and Objectives

The purpose of the Test Case Project was to evaluate the utility of remote sensing techniques for geologic mapping and resource evaluation by conducting a series of experimental mapping projects in geologically well-studied areas containing known mineral and hydrocarbon deposits. Individual test site studies were performed for research purposes to evaluate the generic capabilities of remote sensing methods for geologic mapping in different geological and environmental settings. The discovery of new deposits and the targeting of new areas for ground-based exploration were never considered to be appropriate goals for the Project.

In the broadest sense, a geologic map is a two-dimensional representation of information concerning the composition, lithology, and structure of crustal materials. The goal of the Project was not necessarily to re-create existing geologic maps using remotely sensed data, but rather to learn what new geological information could be extracted from remote sensing data applicable to geologic mapping relevant to exploration problems. The utility of geological information derived from remote sensing data was evaluated with respect to conventional types of geological information obtained by standard methods (e.g., field mapping, sample collection and analysis, geophysical surveys, etc.). Technical objectives were as follows:

(1) To determine the types, scales, accuracies, and formats of geological information that can be obtained through analysis of data collected by state-of-the-art remote sensing instruments aboard Landsat and Seasat, airborne data acquired by prototype multispectral scanners and microwave systems, and ground-based data acquired by portable field spectrometers. Data analysis concentrated on extracting information pertaining to the composition of rocks and soils exposed in the study areas; assessing the discriminability of alteration phenomena; identifying structural features through the analysis of regional topographic relief and site-specific terrain characteristics; and detecting variations in the density, species distributions, and vigor of vegetation that could be correlated with the lithology and/or composition of substrate materials.

(2) To evaluate the usefulness of geological information derived from remotely sensed data compared to geological information derived from other, conventional sources. Specific questions addressed by the individual test site studies included: To what extent does information derived from remote sensing duplicate information obtained by conventional methods? To what degree is the information obtained by remote sensing methods new and different? To what degree does the combined use of geological information derived from remote sensing and conventional methods lead to improvements compared to conventional mapping capabilities?

IV. Methodology

The Test Case Project consisted of eight separate test site studies that were conducted simultaneously from 1978 to 1981. Remote sensing methods were applied to mapping problems in different localities to assess site-specific results. The results of the overall Project are based on the comparative analysis and synthesis of the results obtained at the individual test sites to obtain a general evaluation of the utility of the techniques. This section provides a brief tabular description of each test site, a discussion of the general factors involved in site selection, and a summary of data acquisition and analysis activities.

A. Site Selection

Test site areas that were to serve as the prime focus of the Project were selected jointly by NASA–JPL and Geosat. The goal of the site selection process was to identify areas that would provide challenging new environments for experimental application of remote sensing techniques. Industry representatives developed an initial list of potential test site areas. Candidate sites were areas of known mineralization that had been extensively studied in the past, using conventional mapping techniques. The types of commodities present at the various sites reflected the interests of the exploration industry at the time the Project was initiated. The initial list of candidate sites was subsequently

reviewed by JPL, and individual sites were jointly agreed upon. The scope of the Project was largely determined by the availability of NASA resources, specifically the availability of people, research funds, and aircraft flight hours for airborne data acquisition.

Site selection was based on a variety of technical considerations related to the surface characteristics and geology of specific areas. Logistical and legal factors were also important in site selection. The criteria used in identifying potential test site areas are summarized below.

(1) *Geological significance.* Sites were chosen in regions of known mineralization to better assess the utility of the techniques for nonrenewable resource exploration in more poorly explored regions.

(2) *Technical feasibility.* The feasibility of using remote sensing methods within particular areas was determined primarily on the basis of prior experience (e.g., earlier remote sensing studies, laboratory measurements of mineral and rock spectra, etc.) and general knowledge of the geological characteristics and physiography of candidate areas. Sites were largely restricted to areas where rock and soil materials were well exposed.

(3) *Availability of ancillary geological information.* Sites were chosen in areas where earlier work by industry, the U.S. Geological Survey, and others had produced extensive information on the surface and subsurface geology that would be accessible to JPL/Geosat investigators.

(4) *Accessibility.* Sites were restricted to areas in the conterminous United States. Furthermore, access to the sites for purposes of field checking and ground-based mapping was to be guaranteed by individual Geosat companies.

(5) *Historical exploration activity.* Sites were restricted to areas that had been thoroughly explored to avoid legal problems that might ensue if the remote sensing techniques actually led to the identification of new mineral deposits.

(6) *Size.* As a general guideline, sites were restricted in size to areas of 500 km^2 or less.

(7) *Surface disturbance.* Sites were largely restricted to areas that were not extensively disturbed or modified by human activity.

Eight test sites were finally selected. The majority of the sites are located in the western United States, although one study site is situated in the central Appalachian Mountains (see site location map, Figure 1-1). The characteristics of the eight sites are presented in summary form in Table 1-1. A more detailed discussion of site characteristics is provided in the individual test site reports that form a part of this document.

COPPER

1. SILVER BELL, ARIZONA
2. HELVETIA, ARIZONA
3. SAFFORD, ARIZONA

URANIUM

4. LISBON VALLEY, UTAH
5. COPPER MTN., WYOMING

PETROLEUM

6. PATRICK DRAW, WYOMING
7. LOST RIVER, W. VIRGINIA
8. COYANOSA, TEXAS

Figure 1-1. NASA/Geosat test site locations

B. Data Acquisition and Analysis

Study teams consisting of JPL and industry investigators were organized for each test site at the outset of the Project. These teams compiled background geological information, including existing geologic maps and information on surface geochemistry, soil type and distribution, vegetation characteristics, and subsurface geology. In addition, a thorough literature search was conducted to survey current models of mineral occurrence and genesis for the specific types of deposits that exist at the various sites. At each site, particular geological features were identified that could potentially be detected and mapped through the use of remote sensing techniques. These features included terrain and cover-type parameters such as lineaments, specific types of minerals and rocks, anomalous distribution of surface vegetation, and weathering characteristics (i.e., surface roughness) of particular rock types. Identification of site characteristics that were potentially amenable to remote sensing analysis guided the selection of appropriate measurement techniques, airborne instrumentation, and data processing techniques. Orbital remote sensing data that had been previously acquired over the test sites were collected.

Table 1-1. Test site locations and characteristics

Site/Staging Location	Commodity/ Operator	Lat/Long Area, km^2	Geologic Setting	Nature of Occurrence	Vegetation Cover Type
Copper Mountain, WY Thermopolis, WY	Uranium Rocky Mountain Energy	43°23'N/107°53'W 400	At base of thrust-faulted Archean Owl Creek Mountains.	Supergene (?) Tertiary age deposits in fractured Archean granitic host rock.	Western Interior pinon-juniper and sage-grass communities; vegetation cover 0 – 30%.
Coyanosa, TX Pecos, TX	Petroleum Exxon & others	31°18'N/103°12'W 1400	Delaware subbasin of the Permian Basin.	Oil and gas production depth from 1200-6000 m. Structural and stratigraphic traps, Permian to Ordovician. Sandstone and carbonate reservoirs, primary and secondary porosity.	Southwestern Sonoran desert and mesquite communities; mesquite, sage, cactus, grass; 30% cultivated; vegetation cover 10 – 60%.
Helvetia, AZ Tucson, AZ	Copper ANAMAX	31°46'N/110°45'W 200	Basin and Range Province, Southern Arizona.	Disseminated copper in Paleozoic limestones.	Sonoran desert community; sage, cactus, pinon-jupiter; vegetation cover 10 – 40%.
Lisbon Valley, UT Moab, UT	Uranium Atlas Minerals Division of Atlas Corp.	38°12'N/109°15'W 200	SW flank of Lisbon Anticline.	Tabular stratabound uranium deposits in sandstone of the Moss Back Member, Chinle Formation.	Great Basin pinon-juniper and sage-grass communities; vegetation cover 0 – 60%.
Lost River, WV Lost River, WV	Petroleum Columbia Gas	39°00'N/78°50'W 200	Valley and Ridge Province of the east-central Appalachian Basin.	Gas production depth of approximately 2100 m. Anticlinal trap, Devonian sandstone reservoir, fracture porosity.	Appalachian pine-hardwood communities; 20% cultivated; vegetation cover 100%.
Patrick Draw, WY Rock Springs, WY	Petroleum Champlin & others	41°30'N/108°31'W 350	Washakie subbasin of the Green River Basin.	Oil production depth of approximately 1400 m. Stratigraphic trap, Cretaceous sandstone reservoir, primary porosity.	Western Interior shrub-grassland and salt desert sage communities; vegetation cover 10 – 60%.
Safford, AZ Tucson, AZ	Copper Phelps Dodge Kennecott	32°55'N/109°40'W 200	Basin and Range Province, Southwest Arizona.	Disseminated copper in Laramide intrusives.	Sonoran desert community; sage, cactus, and pinon juniper; vegetation cover 10 – 40%.
Silver Bell, AZ Tucson, AZ	Copper ASARCO	32°25'N/111°30'W 200	Basin and Range Province, Southern Arizona.	Disseminated copper in Laramide intrusives and skarns.	Sonoran desert community; sage, cactus and pinon juniper; vegetation cover 10 40%.

These included data obtained by Landsat (multispectral scanner), Seasat (synthetic aperture radar), and Skylab (photography). These data sets were obtained in digital form, where possible, for computer processing and enhancement.

Aerial remote sensing surveys were subsequently conducted over each site, using a variety of prototype instruments including the Modular Multispectral Scanner (M^2S), the NS-001 Thematic Mapper Simulator, and the Fraunhofer Line Discriminator (FLD). Microwave data were obtained using both active and passive radar systems (the X- and L-band imaging radars, the Passive Microwave Imaging System [PMIS], and the Multifrequency Microwave Radiometer [MFMR], respectively). A complete description of individual aircraft sensors is included in the Technical Appendix, Section 14. Airborne surveys were repeated over some sites to investigate seasonal variations in the spectral characteristics of surface vegetation. In addition, thermal infrared surveys were performed at selected sites under both daytime and nighttime conditions to determine the thermal inertia of surficial materials.

Coverage of the test sites by different airborne sensors varied because of constraints on available flight hours, logistical problems encountered during the Project, and technical assessment of the utility of certain types of aerial data. Certain sensors, such as the NS-001 Thematic Mapper Simulator and the Modular Multispectral Scanner, were deployed over all of the test sites. Other sensors, such as the X- and L-band radars and the FLD, were selectively flown over a limited number of the sites (Table 1-2).

Table 1-2. Airborne sensor coverage of test sites

Commodity	Test Site	Airborne Sensor									
		NS-001	M^2S	Bendix 24-Channel Scanner	X-Band Radar	L-Band Radar	FLD	Aeromagnetics	Radiometrics	MFMR	PMIS
Porphyry copper	Helvetia	■	■		■					■	
	Safford	■	■		■					■	■
	Silver Bell	■	■		■					■	
Uranium	Copper Mountain	■	■							■	
	Lisbon Valley	■	■	■	■		■			■	
Petroleum	Patrick Draw	■	■				■	■	■	■	
	Lost River	■	■		■					■	
	Coyanosa	■	■		■	■				■	■

Both during and after the aerial remote sensing surveys, a series of field studies were performed to acquire additional ground-based data. Portable field spectrometers were deployed at all sites to obtain *in situ* measurements of surface reflectance. These measurements were used to calibrate and interpret aerial and orbital data sets. Ground-based mapping activities in support of the Project varied greatly from site to site, but individual areas were singled out for more detailed soil geochemical surveys, soil and vegetation mapping, and soil gas measurements (petroleum sites only). Rock and soil samples were collected in the field and returned to the laboratory for spectral and geochemical analyses.

Remotely sensed data were reduced and computer processed at JPL. JPL's Image Processing Laboratory possesses a substantial library of computer programs that have been specifically developed for display and analysis of digital image data. This library includes programs for reformatting aircraft and satellite data, geometric rectification and coregistration of multiple data sets, statistical analysis of multivariate data, and image enhancement. Detailed descriptions of individual computer programs employed by the Project are provided in the Technical Appendix, Section 14.

Image products generated from orbital, aerial, and ground-based data were distributed to team members for joint analysis and interpretation. Preliminary analysis of remote sensing image data was used in planning ground-based surveys of surface reflectance, and in targeting specific areas for sample collection and/or detailed field mapping. The results of these ground-based activities, considered together with information obtained by conventional techniques, were used in devising new methods of displaying and analyzing the remote sensing data. In other instances, interim results established the need for additional field mapping or airborne data collection.

Analysis and interpretation generally proceeded on an informal basis among test site team members. Team meetings were commonly held in conjunction with trips to the field or travel to professional conferences. Periods of informal communication among members of the separate teams were supplemented by collective meetings of all Project participants. These meetings provided an opportunity to assess the relative progress of the individual teams and to exchange information about measurement techniques and data analysis methods.

A chronological record of significant team meetings and major Project presentations is provided in Table 1-3. Interim project results were presented at the 1980 Pecora Conference held in Sioux Falls, South Dakota, and at the 1981 International Geoscience and Remote Sensing Symposium (IEEE) held in Washington, D.C. In addition, interim progress reports were prepared on an annual basis and distributed to Project investigators. A complete listing of papers and abstracts published over the course of the Project is included in Appendix B.

C. Organization and Management

The Test Case Project was a joint effort between a single government agency and a collection of industrial firms represented by the Geosat Committee. Independent lines of control and responsibility were established at the outset of the Project to separately manage public and private sector activities. An organization chart is presented in Figure 1-2.

NASA Headquarters and Geosat established the overall procedural guidelines for the conduct of the Project. A for-

Table 1-3. Major team and project meetings

Topic	Date	Location
	Team Meetings	
Petroleum	June 1978	Pasadena
	July 1978	Houston
	October 1978	Denver
	November 1978	Lost River
	January 1979	Denver
	February 1979	Pasadena
	April 1979	Houston
	May 1979	Tulsa
	December 1979	Tulsa
	March 1980	Pasadena
	June 1980	Denver
	October 1980	Denver
	December 1980	Pasadena
	February 1981	Los Angeles
	March 1981	Pittsburgh
	March 1981	Pasadena
	June 1981	Lost River
	October 1981	Pasadena
Porphyry copper	October 1977	Salt Lake City
	January 1979	Denver
	October 1979	Tucson
	March 1980	Tucson
	January 1981	Tucson
Uranium	April 1978	Denver
	September 1978	Pasadena
	April 1979	Moab
	June 1979	Thermopolis
	July 1980	Thermopolis
	Project Meetings	
Site selections	October 1977	Salt Lake City
Joint presentations	May 1979	Denver
Review	December 1979	Washington, D.C.
Pecora meeting	April 1980	Sioux Falls
IEEE meeting	June 1981	Washington, D.C.

mal memorandum of understanding between NASA and Geosat was adopted in July 1981, which delineated the reporting responsibilities of the Project participants.

NASA implemented its Project-related responsibilities through JPL. The Non-Renewable Resources Branch within NASA's former Office of Space and Terrestrial Applications was responsible for establishing schedules and major milestones, evaluating progress and accomplishments, determining appropriate levels of research funding on an annual basis, and allocating NASA aircraft flight hours in support of data acquisition activities. JPL established the position of Project Manager to manage all technical aspects of Project implementation including preparation of annual budgets, allocation of available resources, and evaluation of technical progress. The JPL Project Manager reported directly to NASA Headquarters.

Three JPL researchers served as Principal Investigators. Each Principal Investigator was responsible for those test sites containing the same type of mineral commodity. The Principal Investigators (1) established plans for airborne data acquisition over individual sites, (2) developed methods of processing and displaying the remote sensing data, and (3) had responsibility for data analysis and interpretation, interaction with industry investigators, and reporting of technical results.

A similar three-tiered organizational structure was created by Geosat to implement the Project. However, the Geosat Committee did not have direct management control over its member companies. Geosat coordinated the activities of industrial investigators and served as an institutional interface between NASA and private industry.

Geosat created a Test Case Panel chaired by two individuals to monitor and coordinate the total range of private-industry activities conducted in support of the Project. These cochairmen interacted directly with the JPL Project Manager in evaluating technical progress. Interaction at this level also provided a mechanism for resolving institutional issues as they arose. The Geosat Test Case Panel, in turn, created three Subpanels for each commodity to coordinate private-industry efforts at the individual test sites. The Subpanel chairmen worked directly with the JPL Principal Investigators on data analysis and interpretation problems and on reporting research results.

Both NASA and Geosat identified individuals who served as team leaders for each test site. These individuals served as principal points of contact in exchanging data, organizing team meetings, and planning ground-truth data collection activities.

Review and evaluation of Project accomplishments were conducted in several different ways. NASA evaluated the progress of its research efforts on a semiannual basis for internal budgeting and program development purposes. Geosat formally reviewed interim Project results at quarterly meetings of its Board of Directors. In addition to these formal evaluations, research results were reviewed by the management of individual companies participating in the Project. Final reviews of the Test Case Project were conducted independently by NASA and Geosat prior to the publication of the final report.

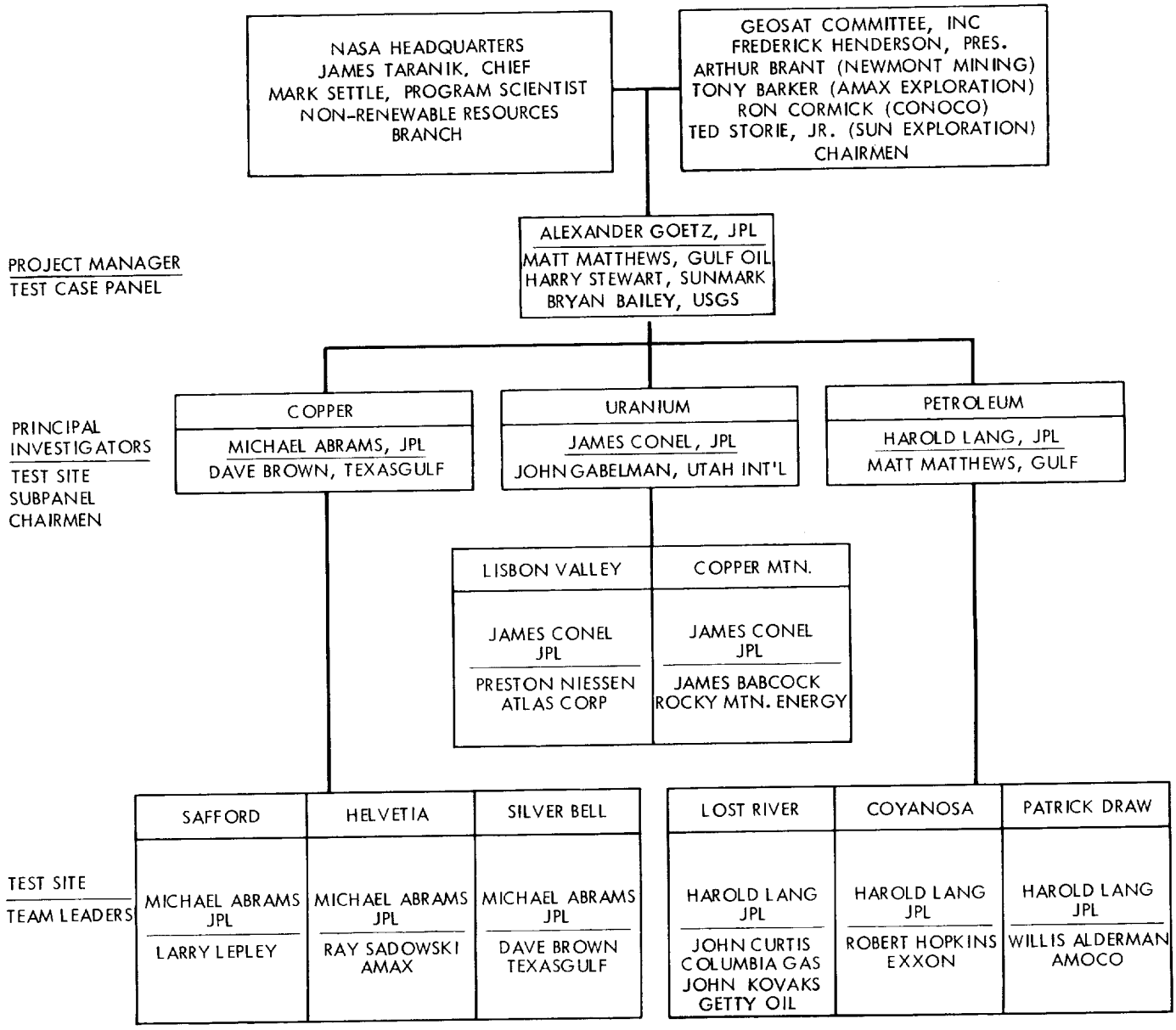

Figure 1-2. Organizational chart

Appendix A
History of the Project

The Geosat Committee was incorporated as a nonprofit organization in December 1976 to represent the interests of the mineral and energy resource industries in the development of space technology for global geological investigations. The Geosat Committee was an outgrowth of an industry-sponsored workshop held in Flagstaff, Arizona, in May 1976. The workshop developed specific recommendations concerning future orbital sensors that would be of greatest use to the geological community.

The Geosat Committee was originally formed to advance the recommendations of the Flagstaff workshop. Geosat initially conceived of an experimental test site program as a means of developing the necessary technical justification for the future development of specific sensor systems. At about the same time, NASA was attempting to evaluate the utility of certain prototype remote sensing instruments from a geological perspective. NASA had experienced great difficulty in identifying and gaining access to areas that were characterized in sufficient geological detail to be used for sensor testing and evaluation.

Both industry and NASA viewed the proposed mapping project as an opportunity to gain access to expertise and data possessed by each institution. In 1977, NASA's Earth Resources program office agreed in principle to a joint Test Case Project to evaluate the geologic utility of state-of-the-art remote sensing techniques. Discussions were held between industry representatives and JPL researchers concerning potential test sites. Mutually agreeable test sites were selected in 1977, and aerial remote sensing data were initially collected by NASA in 1978. A formal memorandum of understanding was executed between NASA and Geosat in 1981, describing the responsibilities of the Project participants in preparing a final report.

Appendix B
Publications and Presentations

Abrams, M. J. (1981). Remote sensing for geology. *Landsat '81 Proceedings of the 2nd Australian Landsat Conference,* 1.1.1–1.1.8. Canberra, Australia, September 1981.

Abrams, M. J. (1982). *Summary of NASA-Geosat copper test sites, Silver Bell, Safford and Helvetia, Arizona.* Paper presented at the 1982 ACSM–ASP Convention, 48th Annual Meeting, Denver, Colorado, March 14–20, 1982.

Abrams, M. J., and D. Brown (1980a). Potential uses of Landsat-D for porphyry copper exploration. *26th International Geological Congress Abstracts.* Paris, France, July 7–17, 1980.

Abrams, M. J., and D. Brown (1980b). *Remote sensing techniques for porphyry copper exploration at Silver Bell Mining District, Arizona.* Paper presented at the 6th Annual Pecora Symposium, Sioux Falls, South Dakota, April 13–17, 1980.

Abrams, M. J., D. Brown, L. Lepley, and R. Sadowski (1982). Landsat-D TM application of porphyry copper exploration. *1982 International Geoscience and Remote Sensing Symposium (IGARSS '82) Digest, I,* WA-3, 4.1–4.3. IEEE Geoscience and Remote Sensing Society, Munich, Germany, June 1–4, 1982.

Abrams, M. J., D. Brown, L. Lepley, and R. Sadowski (1983). Remote sensing for porphyry copper deposits in southern Arizona. *Econ. Geol., 78*(4), June–July.

Abrams, M. J., D. Brown, R. Sadowski, and L. Lepley (1981). Applications of remote sensing to porphyry copper exploration with emphasis on the proposed Landsat-D Thematic Mapper. *1981 International Geoscience and Remote Sensing Symposium (IGARSS '81) Digest, I,* 331–336. IEEE Geoscience and Remote Sensing Society, Washington, D.C., June 8–10, 1981.

Abrams, M. J., and J. Conel (1981). Remote sensing applied to copper and uranium exploration. *Landsat '81 Proceedings of the 2nd Australian Landsat Conference,* 5.1.1–5.1.5. Canberra, Australia, September 1981.

Abrams, M. J., and A. F. H. Goetz (1982). *Clay mineral identification by remote sensing.* Paper presented at the AAPG: Role of Clays in Hydrocarbon Exploration Conference, Santa Fe, New Mexico, October 11–14, 1982, and Abstract published in the *AAPG Bull., 66,* 1442.

Abrams, M. J., and L. Lepley (1980). *Porphyry copper exploration using remote sensing at Safford Mining District, Arizona.* Paper presented at the 6th Annual Pecora Symposium, Sioux Falls, South Dakota, April 13–17, 1980.

Abrams, M. J., and G. Prost (1980). *Helvetia, Arizona porphyry copper deposit: A progress report on the NASA/Geosat Test Case Study.* Paper presented at the 6th Annual Pecora Symposium, Sioux Falls, South Dakota, April 13–17, 1980.

Alderman, W., A. Correa, L. Lundell, R. Reed, F. Sabins, and H. Stewart (1980a). *Patrick Draw, Brady Petroleum Test Case Site: An interim report.* Paper presented at the 6th Annual Pecora Symposium, Sioux Falls, South Dakota, April 13–17, 1980.

Alderman, W., A. Correa, L. Lundell, R. Reed, F. Sabins, and H. Stewart (1980b). *The Geosat Patrick Draw, Brady Petroleum Test Program: An overview of results.* Paper presented at the 6th Annual Pecora Symposium, Integration Techniques Workshop, Sioux Falls, South Dakota, April 13–17, 1980.

Ballew, G., A. Correa, J. Drahouzal, P. Harrison, B. Hopkins, G. Prost, and H. Stewart (1980). *Coyanosa Petroleum Test Site: An interim NASA/Geosat Test Case Study Report.* Paper presented at the 6th Annual Pecora Symposium, Sioux Falls, South Dakota, April 13–17, 1980.

Conel, J. E. (1982). *Summary of NASA-Geosat uranium test sites, Lisbon Valley, Utah, and Copper Mountain, Wyoming.* Paper presented at the 1982 ACSM–ASP Convention, 48th Annual Meeting, Denver, Colorado, March 14–20, 1982.

Conel, J. E., M. J. Abrams, and P. L. Niesen (1979). *Uranium exploration: Analysis of multispectral scanner images at Lisbon Valley, Utah.* Paper presented at the American Society of Photogrammetry Annual Meeting, Washington, D.C., March 20, 1979.

Conel, J. E., and P. L. Niesen (1980). *Analysis of bleaching effects in Wingate Sandstone by aircraft scanner imagery and relations to ore, Lisbon Valley, Utah.* Paper presented at the 6th Annual Pecora Symposium, Sioux Falls, South Dakota, April 13–17, 1980.

Conel, J. E., and P. L. Niesen (1981). Remote sensing and uranium exploration at Lisbon Valley, Utah. *1981 International Geoscience and Remote Sensing Symposium (IGARSS '81) Digest, I,* 318–324. IEEE Geoscience and Remote Sensing Society, Washington, D.C., June 8–10, 1981.

Conel, J. E., S. Reyher, and G. Southard (1980). *Application of remote sensing methods in uranium exploration, Copper Mountain, Wyoming.* Paper presented at the 6th Annual Pecora Symposium, Sioux Falls, South Dakota, April 13–17, 1980.

Conel, J. E., and G. Southard (1980). *Application of remote sensing methods in uranium exploration: Copper Mountain, Wyoming, USA.* Paper presented at the 26th International Geological Congress, Paris, France, July 7–17, 1980.

Cooke, G., J. B. Davis, J. Kovacs, B. Rock, and H. Stewart (1980). *Lost River, West Virginia: An interim report of the NASA/Geosat Test Case Study.* Paper presented at the 6th Annual Pecora Symposium, Sioux Falls, South Dakota, April 13–17, 1980.

Goetz, A. F. H. (1980). *The NASA/Geosat Test Case Program.* Paper presented at the American Society of Photogrammetry Meeting, St. Louis, Missouri, March 10, 1980.

Goetz, A. F. H., and M. J. Abrams (1983). *New techniques for clay mineral identification by remote sensing.* Paper presented at the AAPG Annual Meeting, Dallas, Texas, April 6–10, 1983.

Lang, H. R. (1982a). Finding the Lost River gas field: Lineament density analysis in hydrocarbon exploration. *1982 International Geoscience and Remote Sensing Symposium (IGARSS '82) Digest, I,* WA-4, 1.1–1.5. IEEE Geoscience and Remote Sensing Society, Munich, Germany, June 1–4, 1982.

Lang, H. R. (1982b). *Summary of NASA-Geosat Gas Test Site, Lost River, West Virginia.* Paper presented at the 1982 ACSM–ASP Convention, 48th Annual Meeting, Denver, Colorado, March 14–20, 1982.

Lang, H. R. (1982c). *The use of vegetation density mapping for hydrocarbon exploration in arid regions.* Paper presented at the ERIM International Symposium on Remote Sensing of Environment: Second Thematic Conference, Remote Sensing for Exploration Geology, Ft. Worth, Texas, December 6–10, 1982.

Lang, H. R. (1983). *Remote sensing for oil exploration.* Paper presented to the Coast Geological Society, Ventura, California, April 13, 1983.

Lang, H. R., and K. W. Baird (1981). Spectral stratigraphy of the Fort Union/Wasatch Transition: Patrick Draw Geosat Petroleum Test Site, Wyoming. *1981 International Geoscience and Remote Sensing Symposium (IGARSS '81) Digest, I,* 589–594. IEEE Geoscience and Remote Sensing Society, Washington, D.C., June 8–10, 1981.

Lepley, L. K., M. J. Abrams, and L. Readdy (1982). *Mineralogical remote sensing of surface expressions of deep-seated porphyry copper deposits at Safford Mining District, Arizona.* Paper presented at the ERIM International Symposium on Remote Sensing of Environment: Second Thematic Conference, Remote Sensing for Exploration Geology, Ft. Worth, Texas, December 6–10, 1982.

Rock, B. N. (1982). Mapping of deciduous forest cover using simulated Landsat-D TM data. *1982 International Geoscience and Remote Sensing Symposium (IGARSS '82) Digest, I,* WP-5, 3.1–3.5. IEEE Geoscience and Remote Sensing Society, Munich, Germany, June 1–4, 1982.

Sadowski, R., and M. J. Abrams (1982). *Mapping hydrothermal alteration using aircraft VNIR scanners at the Rosemont porphyry copper deposit.* Paper presented at the ERIM International Symposium on Remote Sensing of Environment: Second Thematic Conference, Remote Sensing for Exploration Geology, Ft. Worth, Texas, December 6–10, 1982.

Stewart, H. E., M. J. Abrams, and M. D. Matthews (1979). *A status report on a multisensor approach to hydrocarbon exploration: The NASA/Geosat Test Case Study.* Paper presented at the American Society of Photogrammetry Annual Meeting, Washington, D.C., March 20, 1979.

Section 2

Sensor Assessment Report

Mark Settle
National Aeronautics and Space Administration

Michael J. Abrams
James E. Conel
Alexander F.H. Goetz
Harold R. Lang
Jet Propulsion Laboratory

Section 2

Sensor Assessment Report

Contents

I. Introduction 2-1
- A. Approach 2-1
- B. Previous Studies 2-1
- C. Description of Site Characteristics 2-2
  - 1. Porphyry copper test sites 2-2
  - 2. Uranium test sites 2-3
  - 3. Petroleum test sites 2-4

II. Remote Sensing Techniques 2-4
- A. Physical Basis of Geologic Remote Sensing 2-4
- B. Description of Instruments and Data 2-5
- C. Interpretation Techniques 2-6

III. Sensor Evaluation 2-7
- A. Summary 2-7
- B. Structural Mapping 2-9
  - 1. Helvetia porphyry copper test site 2-9
  - 2. Patrick Draw petroleum test site 2-9
  - 3. Lost River petroleum test site 2-10
- C. Rock Type/Lithologic Mapping 2-10
  - 1. Silver Bell porphyry copper test site 2-10
  - 2. Lisbon Valley uranium test site 2-11
  - 3. Copper Mountain uranium test site 2-11
  - 4. Patrick Draw petroleum test site 2-14
- D. Mineralogy/Alteration Mapping 2-14
  - 1. Silver Bell porphyry copper test site 2-14
  - 2. Helvetia porphyry copper test site 2-15
  - 3. Safford porphyry copper test site 2-16
  - 4. Lisbon Valley uranium test site 2-17
  - 5. Copper Mountain uranium test site 2-18
- E. Vegetation Mapping 2-19
  - 1. Patrick Draw petroleum test site 2-19
  - 2. Lost River petroleum test site 2-19

PRECEDING PAGE BLANK NOT FILMED

IV. Conclusions and Recommendations 2-19
A. Band Selection by Discriminant Function Analysis 2-20
B. Spatial Resolution 2-20
C. Summary 2-21

References 2-24

Figures

2-1. Generalized absorption spectrum of the atmosphere at the zenith with the named spectral regions examined in the Test Case Project 2-3
2-2. Examples of field spectra acquired in the Test Case Project, illustrating spectral characteristics of typical surface materials in the visible, near, and short wavelength infrared regions 2-5
2-3. NS-001 color ratio composite of the Silver Bell, Arizona, test site 2-12
2-4. Interpretation map of the Silver Bell NS-001 color ratio composite 2-13
2-5. Reflectance spectra for hematite, jarosite, and goethite 2-15
2-6. M^2S color ratio composites of the Helvetia, Arizona, test site 2-16
2-7. Comparison of spatial resolution 2-22

Tables

2-1. Test site locations and characteristics 2-2
2-2. Primary airborne sensor coverage of test sites 2-6
2-3. The most useful remote sensing systems for specific mapping problems at the eight test sites 2-8
2-4. Ranking of available remote sensing systems according to decreasing overall utility (in order of decreasing number of entries in Table 2-3) for solving mapping problems in test site studies 2-9
2-5. Band selection order for Landsat TM, NS-001, and conceptual 30-channel instrument 2-20
2-6. Summary of Landsat TM and NS-001 band selections for rock-type mapping at the porphyry copper sites 2-21

Section 2

Sensor Assessment Report

I. Introduction

A. Approach

This section describes the combined experience of all participating investigators in evaluating available remote sensing systems for geologic mapping as well as for mineral and oil and gas exploration. Findings are based on analysis of the results obtained at each of the eight test sites reported in subsequent sections (Table 2-1). These results provide a basis for determining the geologic utility of sensor systems available prior to 1981 (Figure 2-1) and for developing future sensor systems for geological research and applications. Sensor assessment involves the evaluation of remote measurement techniques in terms of the quantity and quality of geologic information that can be extracted from data acquired by different sensor systems.

The assessment of the geologic capabilities and limitations of existing sensors is broken down into technique areas synonymous with wavelength regions. The three spectral regions sampled in the Joint NASA/Geosat Test Case Project were the visible, near, and short wavelength infrared (0.4 to 2.5 μm), the thermal or mid-infrared (8 to 14 μm), and the active microwave (beyond 1 cm in wavelength) (Figure 2-1). Emphasis is on the visible to short wavelength infrared region because most of the airborne sensor data employed during the Test Case Project were collected in this region.

Surface morphology or image texture is commonly used to delineate geologic structures and discriminate among lithologic units with similar spectral properties. No attempt has been made here to determine the separate contribution of spectral and contextual information to the identification of geologic structures and lithologic boundaries.

B. Previous Studies

Prior to the initiation of the Test Case Project, few in-depth geological studies of remote sensing techniques had been undertaken. An early geological remote sensing study was the Bonanza Project (Lee, 1972). Results were based mainly on multispectral photography since multispectral scanners and the necessary image-processing capabilities were not yet available. The advent of Landsat Multispectral Scanner (MSS) data in 1972 led to several important investigations. Among them were investigations by Goetz et al. (1975), who mapped the Colorado Plateau, and Rowan et al. (1974), who conducted a study of the Goldfield Mining District, Nevada. Both investigations used Landsat MSS data that had been computer image processed. Rowan et al. (1977) made ground spectral measurements with a portable spectrometer. The first comprehensive study using aircraft-acquired multispectral data in the 1- to 2.5-μm region was reported by Abrams et al. (1977). The test area was the Cuprite Mining District, south of Goldfield, Nevada, and the instrument used was the NASA Bendix 24-channel scanner. Results of the Cuprite study helped to justify the 2.08- to 2.35-μm channel of the Landsat 4 Thematic Mapper (TM) multispectral scanner. At the outset of the Project, the only remote sensing data generally available for the newly chosen test sites were Landsat MSS images. The Bendix 24-channel scanner had been retired, and the NS-001 Thematic Mapper Simulator had only recently become available. In addition, an aircraft L-band synthetic aperture radar instrument was operating. As the study progressed, it became clear that the NS-001 Thematic Mapper Simulator provided the most readily interpretable data; hence, heavy emphasis was placed on this sensor during the study. This report represents a detailed analysis of remote sensing techniques as they existed in 1977 at eight test sites.

Table 2-1. Test site locations and characteristics

Site/Staging Location	Commodity/ Operator	Lat/Long Area, km^2	Geologic Setting	Nature of Occurrence	Vegetation Cover Type
Copper Mountain, WY Thermopolis, WY	Uranium Rocky Mountain Energy	43°23'N/107°53'W 400	At base of thrust-faulted Archean Owl Creek Mountains.	Supergene (?) Tertiary age deposits in fractured Archean granitic host rock.	Western Interior pinon-juniper and sage-grass communities; vegetation cover 0 – 30%.
Coyanosa, TX Pecos, TX	Petroleum Exxon & others	31°18'N/103°12'W 1400	Delaware subbasin of the Permian Basin.	Oil and gas production depth from 1200-6000 m. Structural and stratigraphic traps, Permian to Ordovician. Sandstone and carbonate reservoirs, primary and secondary porosity.	Southwestern Sonoran desert and mesquite communities; mesquite, sage, cactus, grass; 30% cultivated; vegetation cover 10 – 60%.
Helvetia, AZ Tucson, AZ	Copper ANAMAX	31°46'N/110°45'W 200	Basin and Range Province, Southern Arizona.	Disseminated copper in Paleozoic limestones.	Sonoran desert community; sage, cactus, pinon-jupiter; vegetation cover 10 – 40%.
Lisbon Valley, UT Moab, UT	Uranium Atlas Minerals Division of Atlas Corp.	38°12'N/109°15'W 200	SW flank of Lisbon Anticline.	Tabular stratabound uranium deposits in sandstone of the Moss Back Member, Chinle Formation.	Great Basin pinon-juniper and sage-grass communities; vegetation cover 0 – 60%.
Lost River, WV Lost River, WV	Petroleum Columbia Gas	39°00'N/78°50'W 200	Valley and Ridge Province of the east-central Appalachian Basin.	Gas production depth of approximately 2100 m. Anticlinal trap, Devonian sandstone reservoir, fracture porosity.	Appalachian pine-hardwood communities; 20% cultivated; vegetation cover 100%.
Patrick Draw, WY Rock Springs, WY	Petroleum Champlin & others	41°30'N/108°31'W 350	Washakie subbasin of the Green River Basin.	Oil production depth of approximately 1400 m. Stratigraphic trap, Cretaceous sandstone reservoir, primary porosity.	Western Interior shrub-grassland and salt desert sage communities; vegetation cover 10 – 60%.
Safford, AZ Tucson, AZ	Copper Phelps Dodge Kennecott	32°55'N/109°40'W 200	Basin and Range Province, Southwest Arizona.	Disseminated copper in Laramide intrusives.	Sonoran desert community; sage, cactus, and pinon-juniper; vegetation cover 10 40%.
Silver Bell, AZ Tucson, AZ	Copper ASARCO	32°25'N/111°30'W 200	Basin and Range Province, Southern Arizona.	Disseminated copper in Laramide intrusives and skarns.	Sonoran desert community; sage, cactus and pinon-juniper; vegetation cover 10 – 40%.

In 1977 the major questions being asked about sensors were:

(1) Is the Landsat MSS adequate for mineral and petroleum exploration purposes?

(2) What spatial resolution is required to solve geologic problems?

(3) Which spectral region is most important for remote sensing, and how many bands are required?

(4) Will the Landsat TM, as envisioned, provide sufficient spatial resolution and adequate spectral coverage? Is the lack of stereo coverage critical?

The rest of this section addresses these questions on the basis of the results obtained during the Joint NASA/ Geosat Test Case Project.

C. Description of Site Characteristics

Brief descriptions of the eight test sites are presented in Table 2-1 and below to provide background information for the discussions of later sections.

1. Porphyry copper test sites. The three porphyry copper sites studied are in southern Arizona. In a classic porphyry copper deposit, Silver Bell, the deposit has been eroded, exposing all alteration zones associated with it. A wide range of altered and unaltered extrusive and intrusive rocks as well as sedimentary rocks crop out in the area. Vegetation cover is scant, offering excellent exposures of the different lithologies.

The Helvetia copper site is in a structurally complex area of Paleozoic and Mesozoic sedimentary rocks. The

ore body is deeply buried; surface indicators include argillic alteration of the country rock and extensive development of calc-silicate skarns and marbles associated with altered limestones.

The Safford District has four known porphyry copper deposits. The two largest are deeply buried, with only minor exposures of the mineralized intrusives at the surface. Surface alteration is mainly limited to the outer propylitic zone of a typical porphyry copper deposit. Volcanic rocks of both premineralization and postmineralization age are exposed in the district.

2. Uranium test sites. There are two uranium sites—Lisbon Valley, Utah, and Copper Mountain, Wyoming. Lisbon Valley encompasses a faulted anticline of Paleozoic and Mesozoic sedimentary rocks. Uranium mineralization is found at depth within fluvial sedimentary units. Surface bleaching of overlying sandstone is spatially coincident with the ore deposits. Mapping alteration patterns, separating and mapping the different sedimentary rock types in the area, and mapping the vegetation cover were accomplished with remote sensing data.

The Copper Mountain site contains uranium deposits in fractured and crushed Archean granites and in Tertiary sediments of the Wind River Basin. Surface alteration or weathering phenomena are spatially coincident with the uranium deposits at depth. Alteration occurs with the mineralization and consists of propylitization of the host rocks and the replacement of pyrite with hematite. The ore-associated alteration is probably masked by iron oxides in the weathering zone and, thus, is not directly observable by remote sensing techniques. The complex Tertiary–Quaternary erosional history of the area is partially interpretable by carefully mapping and analyzing

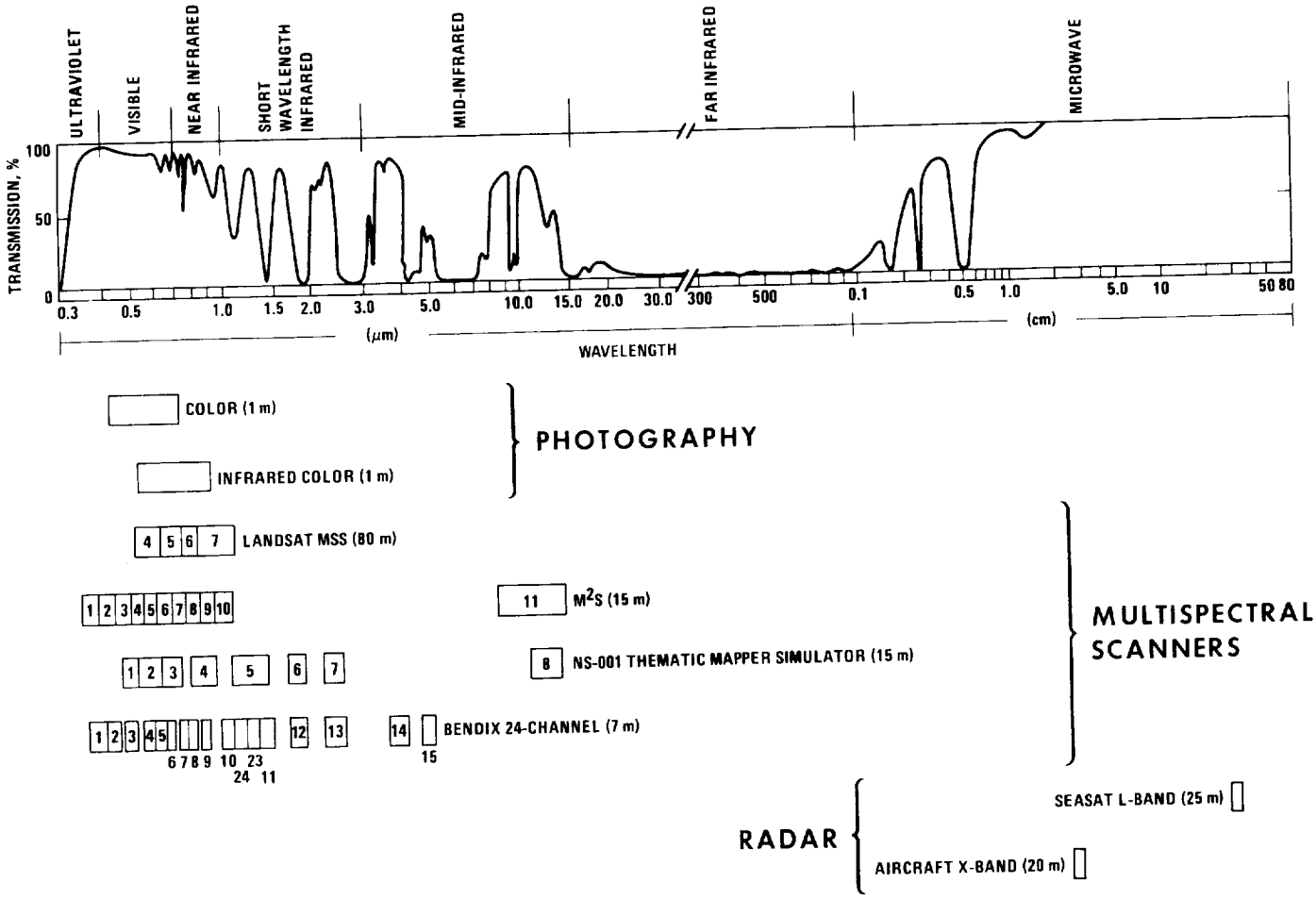

Figure 2-1. Generalized absorption spectrum of the atmosphere at the zenith (after Goetz and Rowan, 1981) with the named spectral regions examined in the Test Case Project. Wavelengths sampled and the spatial resolution of sensors are also illustrated.

Tertiary sedimentary rocks and Quaternary gravel deposits.

3. Petroleum test sites. Three petroleum sites were examined. Patrick Draw, Wyoming, is a typical stratigraphic trap. Surface geology consists of very shallow-dipping Tertiary fluvial and lacustrine sedimentary rocks of variable lithology. Anomalous vegetation distribution may be related to the leaking hydrocarbon reservoir.

Lost River, West Virginia, is the location of a gas field in the Appalachian Mountains. The reservoir is in fractured sandstones at depth situated along an anticlinal fold. Previous regional studies suggested that locations of producing gas fields in the area are confined to zones of enhanced faulting and fracturing. The site is heavily vegetated, with 90 percent forest cover. An important part of the remote sensing study involved mapping the vegetation species. Areal variations were investigated for fracture density and for anomalous vegetation patterns possibly associated with leaking hydrocarbons from subsurface reservoirs.

Coyanosa, in the West Texas Permian Basin, is a prolific oil- and gas-producing area. Production is predominantly from structural traps that are also influenced by local and regional stratigraphic relationships. The surface is moderately vegetated and is characterized by substantial Quaternary sedimentary cover.

II. Remote Sensing Techniques

A. Physical Basis of Geologic Remote Sensing

Two approaches are used for extracting geologic information from remotely sensed data:

(1) In the spectral approach, the known spectral properties of materials can be used to deduce composition from remotely sensed data and to separate units in image data based on spectral reflectance or emittance. This approach is used principally in the analysis of multispectral data and can apply to both vegetated and nonvegetated terrain.

(2) In the photogeologic/photogeomorphic approach, known weathering and erosional characteristics (topographic expression) of earth materials can be used to imply the presence of geological structures at the Earth's surface and to project observed structural relationships into the subsurface. Information contained in an image produced from almost any type of remote sensing data can be useful for photogeologic/photogeomorphic analysis.

Laboratory spectral data have been used to establish the physical basis for remote determination of the composition of earth materials. Laboratory and field data enable spectral features to be related to remotely observed multispectral data of pure and mixed surface materials including minerals, rocks, soils, and plants. This understanding of remotely sensed spectral data has led to sensor designs and image-processing techniques useful in solving a wide variety of geologic mapping and exploration problems.

The wavelengths of interest for geologic remote sensing extend from approximately 0.4 μm to over 50 cm (Goetz and Rowan, 1981). The absorption spectrum of the atmosphere in this region may be divided into segments (as shown in Figure 2-1): ultraviolet, visible and near infrared, short wavelength infrared, mid-infrared, far infrared, and microwave. The existence of major atmospheric absorption bands near 0.3, 0.9, 1.4, 1.9, 2.7, 4.2, 6.0, 9.5, and 15 to 900 μm makes these wavelengths unsuitable for geologic remote sensing.

Spectral reflectance data acquired between 0.5 and 1.1 μm (visible and near infrared) may be used to determine the presence or absence of iron-oxide or hydroxide minerals (e.g., limonite, goethite, and hematite) in soils or rocks and the presence or absence of vegetation (Figure 2-2). The presence of Fe^{+3}-bearing minerals may be inferred from measurements of an absorption band that affects the 0.4- to 0.6-μm interval. The Fe^{+3} electronic transition may be deduced from an absorption band that lies between 0.8 and 1.0 μm. The presence of vegetation is indicated from chlorophyll absorption bands at 0.45 and 0.65 μm.

Spectral reflectance data acquired between 1.0 and 2.5 μm (short wavelength infrared) may be used to denote the presence or absence of hydrous minerals (e.g., clay, mica, and some oxides and sulfates) and carbonate minerals (calcite and dolomite) in soils and rocks; these data may also indicate the state and vigor of vegetation. Important absorption bands occurring in this wavelength region are associated with hydroxyl ions (near 2.2 μm, 2.3 μm, and the short wavelength wing of a 2.77-μm absorption band that extends to 2.0 μm). A strong carbonate absorption band occurs near 2.35 μm. A broad absorption band attributed to leaf water content in vegetation affects the entire 1.5- to 2.5-μm interval. The depth of this absorption band can be related to plant vigor.

Spectral emission data acquired between 8 and 14 μm (mid-infrared, sometimes referred to as thermal infrared) can be used to determine the relative quartz content of soils and rocks. Soil and rock thermal inertia, soil moisture

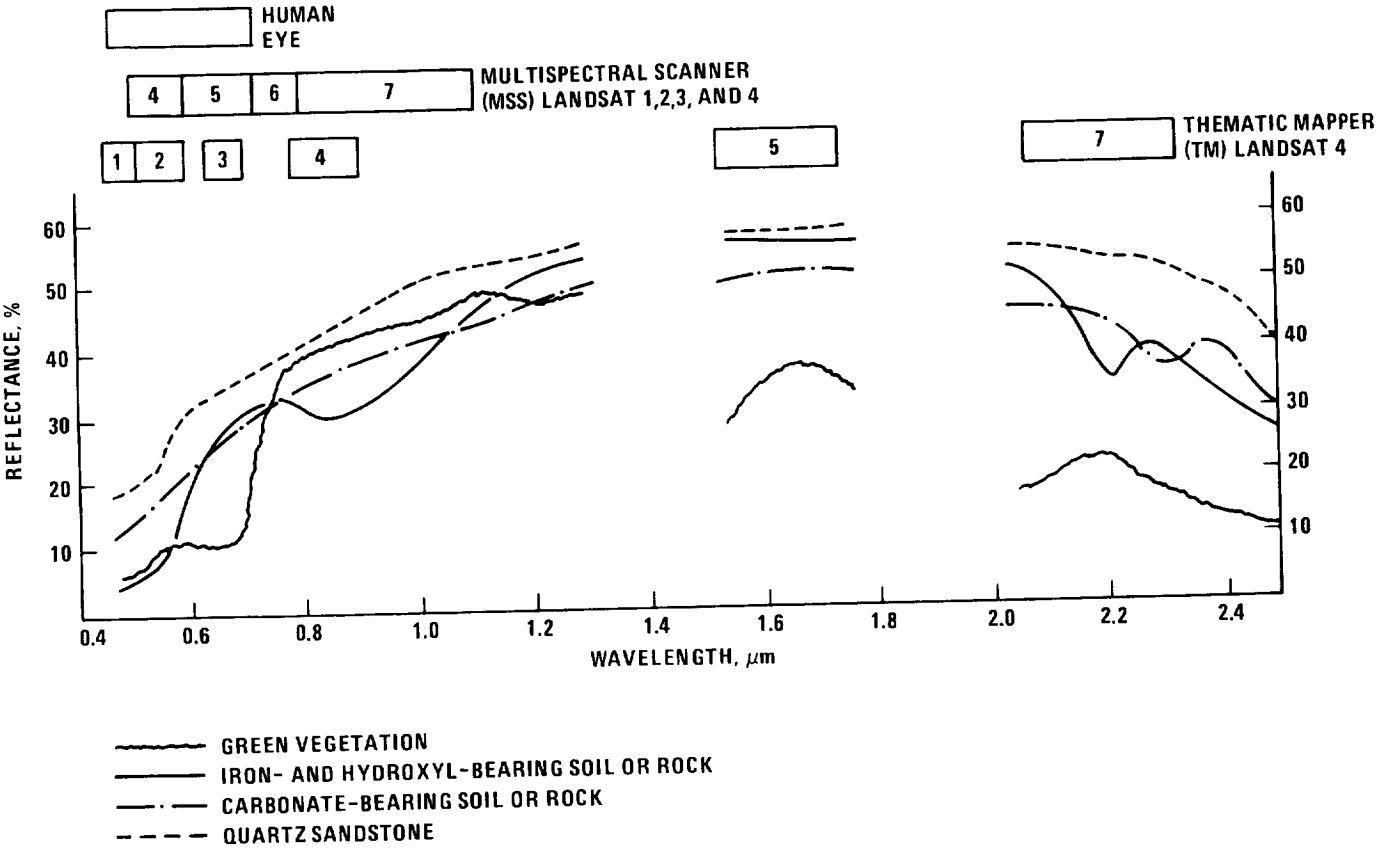

Figure 2-2. Examples of field spectra acquired in the Test Case Project, illustrating spectral characteristics of typical surface materials in the visible, near, and short wavelength infrared regions

content, and vegetation vigor can also be determined from mid-infrared data.

B. Description of Instruments and Data

A detailed description of the instruments and data types used in this Test Case Project may be found in the Technical Appendix, Section 14. A brief description is provided here to facilitate later discussion.

Aerial photographs, radar images from aircraft and satellite instruments, and multispectral scanner data from aircraft (Table 2-2) and satellite platforms were analyzed. The wavelength regions covered by the instruments are shown in Figure 2-1.

Photographs consisted of natural-color and false-color infrared (CIR) positive transparencies acquired with standard large-format camera systems. Color or color infrared film (9 by 9 in.) was routinely collected during aircraft scanner overflights. These photographs, at a scale of approximately 1:40,000, were used at their original scale or were photographically enlarged to match map scales of 1:24,000. Color and color infrared photographs collected during the Skylab missions as part of the S190B experiment were also analyzed. These photographs were 9- by 9-in. transparencies at a scale of 1:500,000 and were analyzed at that scale.

L-band (25-cm) Synthetic Aperture Radar (SAR) data, acquired from the Seasat orbital mission, were digitally correlated, then enlarged to working scales of 1:1,000,000 to 1:250,000. Aircraft radar data were taken at X-band (3 cm) in the multipolarization, synthetic aperture mode. These were optically correlated and analyzed as photographically enlarged prints at a scale of approximately 1:50,000.

Multispectral scanner data were obtained by the Landsat MSS satellite sensor and by aircraft sensors: the 11-channel Modular Multispectral Scanner (M^2S), the NS-001 Thematic Mapper Simulator, and the Bendix 24-channel scanner. Landsat MSS data are obtained in four spectral bands in the 0.5- to 1.1-μm wavelength region.

Table 2-2. Primary airborne sensor coverage of test sites

Commodity	Test Site	Sensor					
		Photography	NS-001	M²S[a]	Bendix 24-Channel	X-Band Radar	L-Band Radar
Porphyry copper	Silver Bell	■	■	■		■	
	Helvetia	■	■	■		■	
	Safford	■	■	■		■	
Uranium	Lisbon Valley	■	■	■	■	■	
	Copper Mountain	■	■	■			
Petroleum	Patrick Draw	■	■	■			
	Lost River	■	■	■		■	
	Coyanosa	■	■	■		■	■

[a]Modular Multispectral Scanner.

Data are acquired digitally; each scene covers a 185- by 185-km area with an instantaneous field of view (IFOV) of 80 m. The M²S scanner has ten channels in the Landsat MSS region, and one channel in the mid-infrared (thermal) region. The IFOV of the data is dependent on the aircraft altitude, but typically was 15 m. Data were acquired with the thermal channel at night for thermal inertia studies. The NS-001 Thematic Mapper Simulator has seven channels in the 0.45- to 2.36-μm region and one channel in the thermal region. The IFOV was typically about 15 m, but varied from site to site as a function of aircraft altitude. The Bendix 24-channel scanner obtained data only over Lisbon Valley. At the time of overflight, only visible and near-infrared channels were operational. The IFOV was about 8 m. All multispectral scanner data were obtained in digital form to permit computer image processing of the data.

C. Interpretation Techniques

Remote sensing data were processed by various means to create photographic products for analysis and interpretation. These either were used in their original transparency form or were photographically enlarged to produce prints at appropriate working scales.

Multispectral image data underwent extensive computer image processing to prepare photographic prints for analysis and interpretation. Detailed descriptions of the computer algorithms used in processing the aircraft images are included in the Technical Appendix, Section 14.

In order to analyze multispectral image data quantitatively, sensor output signals must be corrected to units equivalent to surface reflectance values. The sensor data can then be compared with ground reflectance measurements, and the sensor can be used as a broadband spectrometer for mapping purposes.

Aircraft scanners are generally designed to measure the intensity of surface-reflected solar radiation in digital number (DN) units. Solar radiation passes down through the atmosphere, is reflected by the surface, passes up through the atmosphere between the ground and the scanner, and is recorded by the instrument. The atmospheric component can be either theoretically modeled or empirically removed. For the Test Case Project, the second approach was used: an empirically derived function was applied to remove brightness gradients due to both directional atmospheric scattering and surface geometry.

To convert the gradient-corrected radiance values to relative reflectance, four different techniques were developed:

(1) The reflectance of an identified unit on the ground was estimated. Scanner data were then normalized to the assumed reflectance of this unit, and values relative to this material were obtained (e.g., basalt was used, and a flat reflectance spectrum was assumed). This is a simple method for calibration when no ground spectral data exist.

(2) The ground-based reflectance data for a single unit were used to normalize the scanner data. This is similar to item (1), but is more accurate.

(3) The spectra of several different units were measured in the field, and their reflectance values were compared with scanner DN values to derive a linear relationship between surface reflectance and scanner DN values.

(4) Based on the observation of a Gaussian distribution of scanner brightness values (DN), the minimum, mean, and maximum values for each band were extracted and plotted, versus the similar values determined from a large representative collection of

field reflectance data for the area. These plots provided a linear transformation relating DN values to reflectance in each band.

These four techniques are each applicable under different circumstances, depending on the amount of ground spectral data available. They all produce satisfactory calibrated scanner data, which then allow the scanners to be used as airborne spectrometers.

Interpretation of image data generally proceeded in four steps:

(1) Images and published maps were compared visually, primarily through the use of overlays.

(2) *In situ* measurements of surface reflectance and field samples were collected and the images ground checked to substantiate any interpretive conclusions and to determine the cause of any unusual image features.

(3) Laboratory spectral reflectance, X-ray diffraction analysis, and geochemical analysis of field samples were acquired.

(4) Further visual comparisons were made, and laboratory and field spectral data were integrated.

The boundaries of distinctive spectral features were traced onto mylar overlays of the images, and individual areas were classified and labeled according to spectral characteristics. Maps were then placed on top of the appropriate images and compared with the interpreted overlays. Direct superposition of mapped geology and alteration on the color image products and the different image products on each other were used. Lithologic, alteration, and vegetation separations could be compared and image characteristics qualitatively deduced by examining the image data suites themselves and externally comparing these with theoretical and measured spectra, X-ray diffraction results, field observations, and published maps.

To compensate for geometric distortion in image data, two techniques were used:

(1) A control grid map was constructed by drawing section lines on clear mylar overlayed on images. Support maps were manually rotated or shifted to match the appropriate part of the image as closely as possible; section line grids, major mapped faults, drainages, topographic features, and cultural features were used for alignment.

(2) Image data were digitally registered to base-map data in the computer by first establishing a control grid from a map covering the desired image. Control points or equivalent positions on the map and in the image were located. The computer then calculated the displacements that would map the control points from their location in the image to their desired location in the control grid. Translation, rotation, and second- and higher-order transformations were used to match the image to the control grid.

Ancillary data acquired at the test sites were also analyzed. Portable Field Reflectance Spectrometer (PFRS) (Goetz et al., 1975) spectra were obtained directly in the field in digital form. These data were processed using statistical techniques, such as linear discriminant function analysis, to determine the separability of sampled rock, soil, and vegetation classes and to determine the most important wavelength bands used in the separation. Spectra also were analyzed visually to assess the wavelength intervals where maximum contrast existed between geologically important units.

Lineament analysis from scanner data was accomplished by manually tracing lineaments directly onto mylar image overlays. Overlay interpretations were digitized, and the digital lineament information was statistically analyzed using trend-surface fitting algorithms and other techniques for extracting and displaying directional and density information. The results of these analyses were compared with available geological and geophysical maps of surface and subsurface structures to evaluate the kinds of information interpretable from the image lineament data.

Geochemical survey data were statistically analyzed using multivariate regression programs and trend-surface fitting algorithms to assess the correlation of variables, to assess the areal variability of specific elements, and to search for anomalous values.

III. Sensor Evaluation

A. Summary

For test site studies, remote sensing systems were used to solve specific geologic mapping problems. Interpretive maps, prepared from image data, depict structure, rock types, mineralogy/alteration, and vegetation. The most useful remote sensing systems for mapping features of interest are summarized on a site-by-site basis in Table 2-3. Table 2-4, based on the number of entries of each system in Table 2-3, provides an overall ranking of the seven systems evaluated. Together these two tables illustrate the combined experience of participating investigators in evaluating available remote sensing systems for

geologic mapping as well as for mineral and oil and gas exploration.

Factors other than the characteristics of the sensors themselves also affect rankings. These factors include:

(1) Amount and sophistication of data analysis activities (NS-001 data received the most analytical attention and radar the least).

(2) Availability and quality of data (24-channel data were only available for Lisbon Valley; see Table 2-2).

(3) Whether a mappable component existed or was of interest at a specific test site (vegetation was considered a significant cover component at petroleum and uranium sites and was not considered significant at the porphyry copper sites).

(4) Whether the spectral region sampled by a sensor was appropriate for site-specific problems (M^2S data are suited to iron-oxide mapping, a surface characteristic useful for mapping rock alteration at the porphyry copper sites).

(5) Whether the spatial resolution of a sensor was appropriate for the desired scale of the interpretive map (Landsat MSS and Seasat SAR provide synoptic coverage of large areas with low spatial resolution, useful for regional structural study but of insufficient spatial resolution for detailed stratigraphic study).

(6) Whether multitemporal, repetitive coverage was required to solve a mapping problem (Landsat MSS and to a lesser extent NS-001 and photographic data provided the only repetitive coverage for evaluating seasonal scene variability such as that caused by vegetation phenology).

Specific examples of the geologic information that was obtained through the use of remote sensing techniques at the individual test sites are presented below. All images described in the following discussion appear in subsequent sections of this report.

Table 2-3. The most useful remote sensing systems for specific mapping problems at the eight test sites[a]

Mapping Feature	Porphyry Copper			Uranium		Petroleum		
	Silver Bell	Helvetia	Safford	Lisbon Valley	Copper Mountain	Patrick Draw	Lost River	Coyanosa
Structure								
Regional trends	A	A	A	FA	AF	AB	AB	A
Faults	DF	DF	DF	DF	F	AF	FC	FD
Joints	F			DG	D	FD	FC	FD
Folds				F	F	FD	FC	
Rock Types								
Sedimentary units	F	F	F	DG	F	F	FD	FD
Volcanics	F	F	F					
Igneous acidic	F	F	F		EF			
Igneous intermediate	F							
Metamorphic	F				DF			
Mineralogy/Alteration								
Limonite and goethite	EF	E	E	DF	EF	AF		AF
Hematite	EF	E	E	DF	EF			
Jarosite		E				F		
Clays	F	F	E			F		F
Carbonate	F	F						F
Potassic alteration	F		F					
Phyllic alteration	F		F					
Propylitic alteration	F		AF					
Vegetation								
Trees				DG	DF		FD	
Brush				D			FD	AF
Grasses				D			FD	AF
Mixed soil and vegetation				FG	DF	F	FD	AF

[a]The two most useful systems are shown where applicable.

A Landsat MSS
B Seasat (L-band)
C Aircraft radar (X-band)
D Color aerial photographs
E M^2S
F NS-001
G Bendix 24-channel

Table 2-4. Ranking of available remote sensing systems according to decreasing overall utility (in order of decreasing number of entries in Table 2-3) for solving mapping problems in test site studies

Mapping Feature	Sensor						
	NS-001	Color Aerial Photographs	Landsat MSS	Bendix 24-Channel	M^2S	Aircraft Radar (X-band)	Seasat (L-band)
Structure							■
Regional trends	■		■				
Faults	■	■	■			■	
Joints	■	■		■		■	
Folds	■	■				■	
Rock Types							
Sedimentary units	■	■		■			
Volcanics	■				■		
Igneous acidic	■						
Igneous intermediate	■						
Metamorphic	■	■					
Mineralogy/Alteration							
Limonite and goethite	■	■	■		■		
Hematite	■	■		■	■		
Jarosite	■				■		
Clays	■				■		
Carbonate	■						
Potassic alteration	■						
Phyllic alteration	■		■				
Propylitic alteration	■						
Vegetation							
Trees	■	■	■	■			
Brush	■	■	■	■			
Grasses	■	■	■				
Mixed soil and vegetation	■	■		■			

B. Structural Mapping

1. Helvetia porphyry copper test site. Structural analysis performed for the Helvetia test site illustrates the use of remote sensing data for regional structural studies. Synoptic images provided by the Landsat MSS are ideal for examining the regional structural fabric of an area. A fall scene with low sun elevation was selected to enhance topographic features; a CIR composite was used to enhance tonal or spectral boundaries. A manual lineament analysis was produced on a mylar overlay, and the lineaments were digitized.

Computer processing of lineament data provides an objective method for evaluating what would otherwise be a hopeless maze of lines. Here, simple visual inspection of lineament data failed to reveal significant features or to separate trends from background. A rose diagram summarizing the strike-frequency distribution of the lineament data reveals three trends. These trends correspond to three major deformation events that occurred in the area during the Precambrian, the Paleozoic, and the Laramide orogeny.

Lineaments were also contoured by density to assess the relationship of areal variation in lineament concentration to regional tectonics. The contour map was compared with tectonic boundaries defined on the basis of paleostratigraphic data and with regional residual aeromagnetic data. In both cases, lineament density maps confirmed tectonic trends and features defined by these other geological and geophysical techniques.

2. Patrick Draw petroleum test site. Subtle folds were mapped on the east margin of the Rocky Mountains. Images produced from topographically registered NS-001 data were interpreted at a 1:48,000 scale to detect subtle structures. Individual, thin sandstone beds were traced throughout the area. With the aid of elevation data, these bedding plane traces were used to determine dip and strike throughout the NS-001 image area. This information revealed several previously unmapped folds. The NS-001 spectral information made it possible to identify the extent of discontinuous units that could not be followed with certainty on color aerial photographs. Subsequent examination of stereo aerial photographs and observations in the

field confirmed the existence of these subtle structures, which have limbs that dip only 1° to 3° and are therefore difficult to identify with field mapping techniques alone. Available subsurface data for the Patrick Draw oil field do not confirm the existence of these minor surface flexures in the subsurface. Although oil field productive limits are best defined by stratigraphic variations, these results nevertheless demonstrate the utility of remote sensing methods for mapping subtle folds.

3. Lost River petroleum test site. Areal variations in fracture density were mapped in the Appalachian fold belt. Linear discontinuities in the tone or texture of remotely sensed images, referred to as lineaments, may represent the surface expression of subsurface faults and joints (fractures) (Hodgson, 1974). A lineament study was conducted at Lost River to evaluate operator and image bias in lineament interpretation and to develop efficient methods of lineament analysis for locating potential fractured reservoir targets. Both Landsat MSS and NS-001 data were used to obtain regional and site-specific lineament data. MSS data were interpreted at a scale of 1:500,000, although the resolution capability of the MSS would have allowed mapping at a 1:250,000 scale. Analysis of 1:500,000 Landsat MSS image interpretations prepared by independent interpreters demonstrated that subjectivity in recognizing individual lineaments may be overcome by mapping areal variations in lineament density (number of lineaments/unit area). Such maps show that the Lost River gas field is located beneath an area of high surface lineament density. The NS-001 data were interpreted at an image scale of 1:48,000 for convenient comparison to other existing map data. Lineament density maps at 1:48,000, derived from NS-001 data processed to enhance specific lineament trends, yielded lineament density isopleths that mimic subsurface structural contours on the reservoir of the Lost River gas field.

C. Rock Type/Lithologic Mapping

1. Silver Bell porphyry copper test site. The NS-001 data for Silver Bell provide an example of the utility of NS-001 data for separating rock types. Data were processed using different algorithms, including band ratioing, canonical transformations, principal components (PC) analysis, and supervised classification. Image interpretation results were generally equivalent, indicating that the wavelength regions sampled by the NS-001, rather than the particular processing algorithm, were responsible for lithologic discrimination. The ratio composite image is discussed below.

The ratio composite image was produced by displaying the NS-001 band-ratios 1.65/2.22 μm, 0.66/0.56 μm, and 0.83/1.15 μm as red, green, and blue, respectively (Figure 2-3). (A similarly useful ratio image was produced by using the 1.65-μm band in place of the 1.15-μm band.) This image exhibits a great deal of color contrast among the various rock/alteration types; approximately 25 rock and soil lithologies were separable on the image (Figure 2-4), compared with approximately 6 on color aerial photographs, and 10 on M^{2}S images.

a. Igneous rocks. In general, the most mafic igneous rocks were dark blue to green on the image; intermediate rocks, medium to light blue; and the most felsic rocks, pink to cyan. The Silver Bell andesite was easily discriminated as deep indigo blue, apparently produced by the flat, featureless spectral response of this low albedo material. Exposures of the Mt. Lord Ignimbrite typically exhibited a turquoise blue color, with dark shadows due to the rugged relief formed by the ignimbrites. The Mt. Lord Ignimbrite was confused locally with fresh dacite porphyry, which it resembles petrographically, and in a few instances with Tertiary basalt. The relatively dark bluish image color of fresh dacite porphyry and Mt. Lord Ignimbrite was somewhat anomalous, considering their quartz latitic composition. This was apparently due to the dense, welded character of the two units and their tendency to weather into heavily iron-oxide-stained talus fragments due to the presence of small amounts of pyrite and magnetite.

Exposures of relatively fresh monzonite porphyry and alaskite were also distinct on the color ratio composite image. An alaskite stock was displayed as a pale bluish area, while a monzonite porphyry stock was pale cyan. The pale blue to cyan shades probably result from small amounts of highly dispersed clays, produced by weathering or weak hydrothermal alteration.

Flow-banded quartz latite plugs resembled fresh monzonite, but were separable on the basis of their very pale lavender to white color, indicating a high silica content and the presence of very small amounts of clay. Latite intrusives, compositionally similar to the monzonite porphyry, were not obscured by deep shadows; the latite was pale lavender-brown.

Precambrian granite was generally displayed as yellowish green to yellowish orange. The image characteristics of the Precambrian granite suggest that it is altered and contains clays and limonite. This alteration could result from weathering, hydrothermal alteration, and/or metamorphism.

b. Sedimentary rocks. Consolidated sedimentary rocks rich in iron oxide were dark green on the NS-001 color

composite image because of the effect of the iron charge-transfer absorption in the ultraviolet. Mesozoic red beds and sedimentary rocks of the Precambrian Apache Group both were green on the image, reflecting high iron-oxide and low clay content.

Paleozoic limestone units generally appeared rust-brown. Reliable discrimination of limestone was often hampered by the characteristic formation of resistant landforms, including cliffs and ledges, which produced deep shadows. The effect of contrast enhancement and ratioing is to subdue topography, causing much of the limestone to be displayed as exceptionally dark or light regions. In some areas, the detailed contact relations between Paleozoic limestone and other units were totally obscured.

2. Lisbon Valley uranium test site. This site includes the Lisbon Anticline and to the northeast an adjacent NW-trending anticline, the Lisbon Canyon Anticline, and a parallel syncline, the East Coyote Wash Syncline. The Lisbon Anticline has Pennsylvanian limestones exposed in the axial region. These rocks are overlain by Permian, Triassic, and Jurassic red beds found dipping gently southwest in the southwestern limb. The Lisbon Canyon and East Coyote Wash structures involve only Jurassic and Cretaceous strata; these are thrown into juxtaposition with the Pennsylvanian limestone section along the Lisbon Valley normal fault. The fault structure, with several thousand feet of displacement, dips northeast and parallels all major fold axes. The area is covered by soils of intermediate and immature development and is heavily vegetated locally with stands of piñon–juniper and sage–grassland community plants.

The NS-001 aircraft scanner data were displayed in the form of PC and color ratio composite images to study the distributions of rock types in these structures. These data have a surface resolution of approximately 15 m. For Lisbon Anticline, it is possible to define all of the major conventional lithologic units in the image data, together with finer subdivisions of some formations representing detailed variegated bedding. More detailed bedding relations were used to identify an angular (Permian–Triassic) unconformity present in the section.

Major limestone units are easily separable in all image renditions according to differences in vegetation cover and albedo. In general, the limestones are heavily tree covered. Local variations of tree cover and topographic shadowing produce image patterns that might be confused with possible lithologic variations. Initially, aerial photographic and, to a lesser extent, field observations were used to establish the nature of these areas.

Stratigraphic relations depicted in the image data allowed the structure of the anticline to be delineated and an approximate position of the Lisbon Valley Fault to be established along the axis of the anticline. The Lisbon Canyon Anticline could not be defined in the images (no stratigraphic marker), although detailed analyses revealed the deformation of some units in the structure coincident with minor axial faults mapped by geologists in the field.

In East Coyote Wash Syncline, NS-001 color ratio composite images were used to map the distribution of strata in the structure. A prominent, unmapped stratigraphic subdivision of the Cretaceous upper Burro Canyon Formation was recognized in these data. The new unit graphically delineates the overall structure of the syncline. The outcrop area of this unit contrasts along the synclinal axis to the northwest in accordance with published observations of Burro Canyon sedimentation patterns.

While detailed field checking all of the relations was not possible, it is evident that most of the major image unit subdivisions correspond to major albedo or color differences in the rocks, to differences in vegetation cover, or to shadows. All color relations found in the images could be explained from ground data or alternatively by examination of aerial photographs. For these problems, the NS-001 and M^2S spectral resolutions were thus judged to be adequate.

The geologic interpretation of image data for this site was hampered mostly by areal resolution of the images and by the lack of stereoscopy. Where field checking of interpretations was not possible, aerial photographs were used, and it was usually possible to resolve controversial issues by examination of these, particularly in stereo.

3. Copper Mountain uranium test site. The Copper Mountain site is located on the south flank of the Owl Creek Uplift, a Laramide-age overthrust of Precambrian, Paleozoic, and Mesozoic rocks southward into Wind River Basin. Uplift and erosion subsequently filled the basin with deposits of Eocene, Oligocene, and Miocene tuffaceous sedimentary rocks that buried preexisting landforms. Post-Pliocene uplift and erosion have reexcavated the mountains and basin and led to development of a series of erosion surfaces and Quaternary sedimentary deposits along the mountain front.

NS-001 multispectral aircraft scanner data were used to investigate stratigraphic problems in the Eocene and Quaternary sediments. A comparison of published geologic maps with the PC maps derived from NS-001 data showed

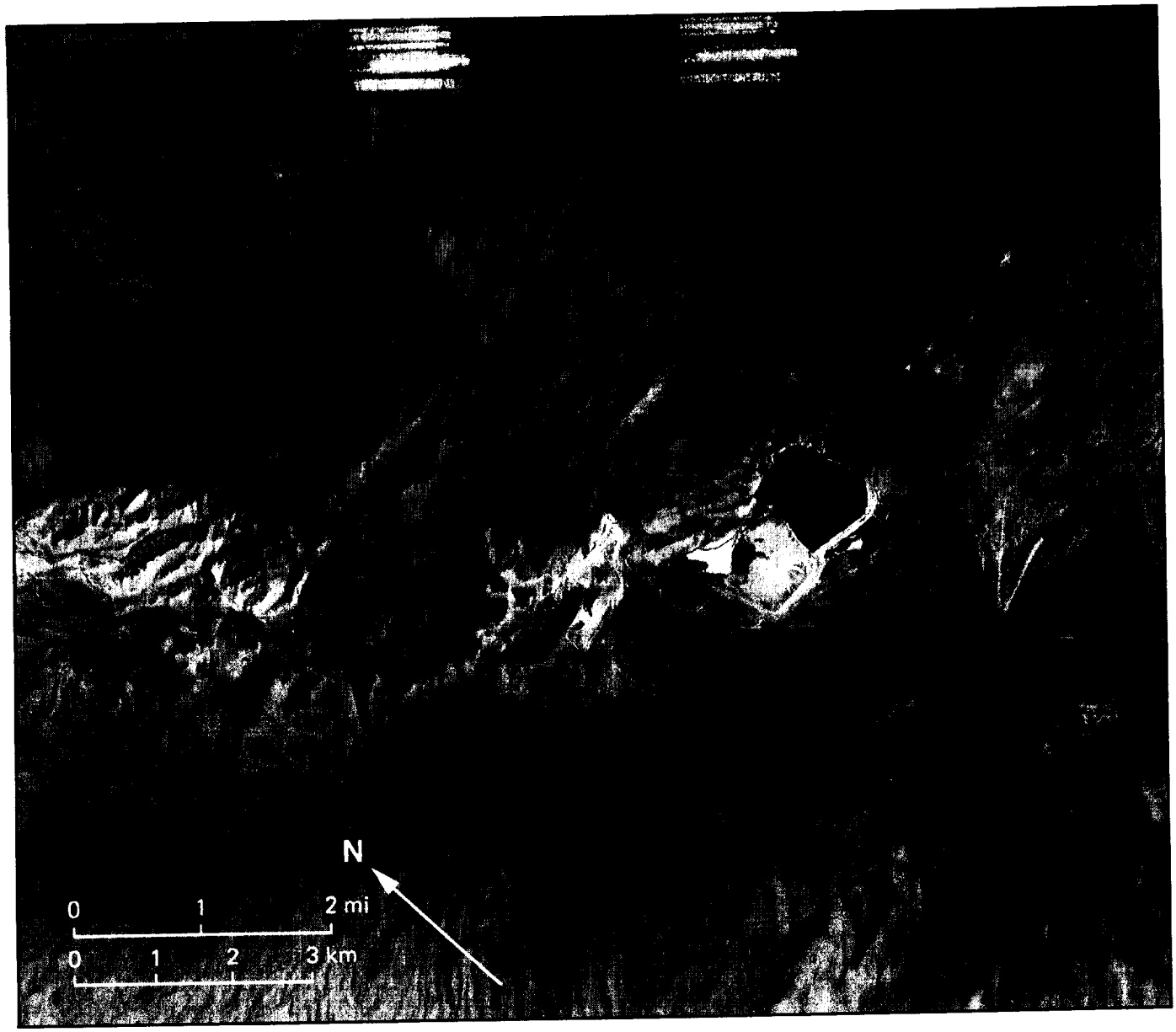

Figure 2-3. NS-001 color ratio composite of the Silver Bell, Arizona, test site. Band-ratios 1.65/2.22 μm, 0.66/0.56 μm, and 0.83/1.15 μm are displayed as red, green, and blue, respectively.

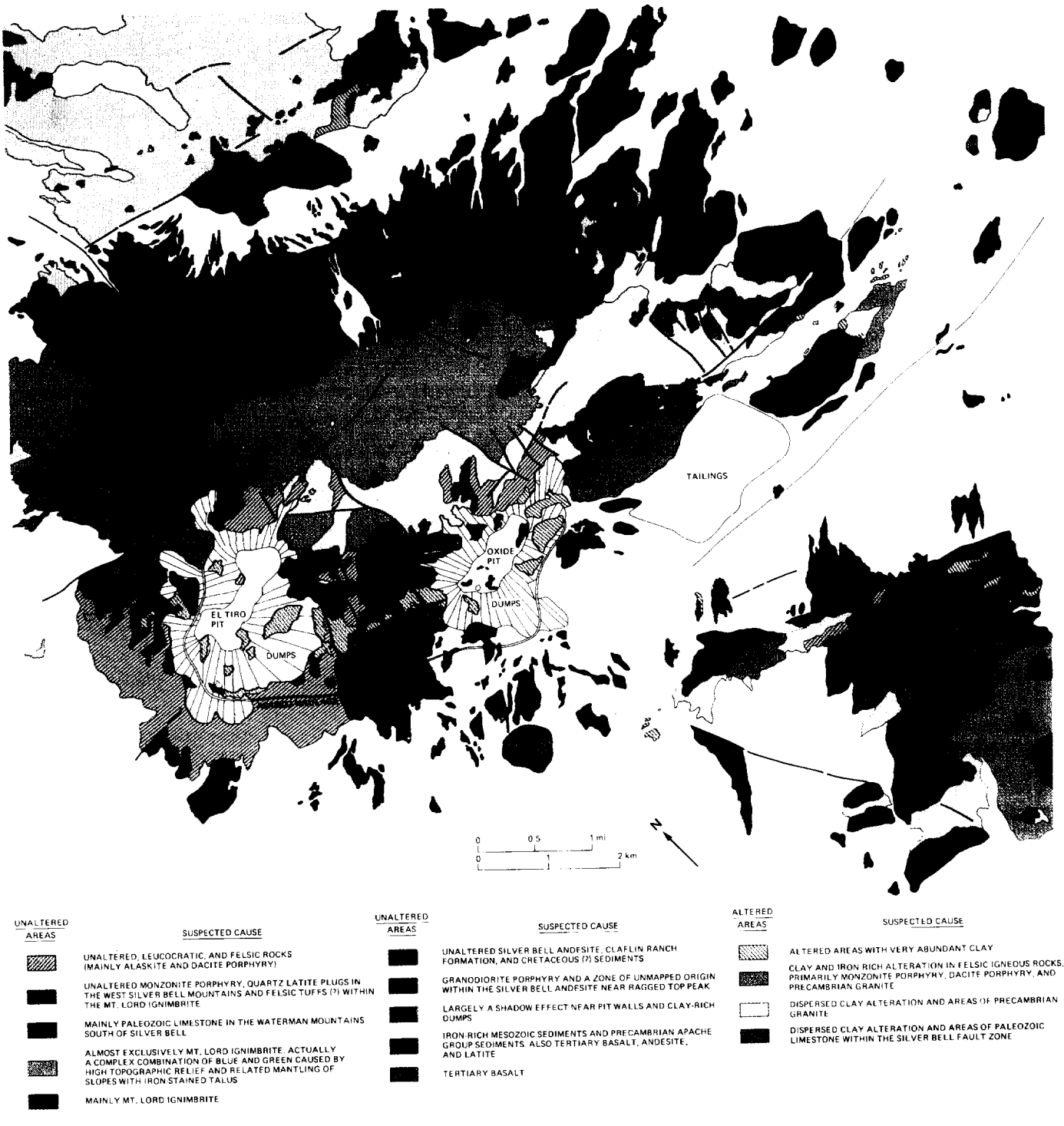

Figure 2-4. Interpretation map of the Silver Bell NS-001 color ratio composite (Figure 2-3)

remarkable coincidences and notable disagreements. Some of the stratigraphic problems identified are as follows:

(1) Subregional and local stratigraphic correlations derived from colors in the images evoked alternate interpretations to the published mapping interpretations. The Eocene sedimentary record represented by the Wind River Formation and Wagon Bed Formation is characterized by variegated but nondescript sediments, complicated physiography, and confusing depositional relations involving complex erosional episodes, diverse lithology, and highly variable topographic relief. Colluvial masking of surface units is widespread, and this masking phenomenon can be easily confused with the local reworking of one formation within another. These relations are often not resolvable by conventional photogeologic interpretation. The NS-001 image data provided objective evidence upon which to propose some new correlations. NS-001 data were used to define major (noncontroversial) stratigraphic boundaries in an unambiguous fashion and to extend these relationships throughout the area. From this basis, local modifications in the correlation schemes were established at smaller spatial scales.

(2) The system of Quaternary stratigraphic units present at the test site was identified in the NS-001 image data. On the basis of observed variations in image tone, it was possible to subdivide units previously undivided in published geologic maps. Reference to topographic maps showed that the image units so defined were separable on a topographic basis and represented distinct ages in alluvial fan development and dissection. Separate fans identified in the scanner images are characterized by variable source materials, vegetation cover, soil development, and possibly surface, macroscopic particle-size distribution. These fan characteristics can, in turn, be related to successive stages of uplift and erosion within the study area.

4. Patrick Draw petroleum test site. Strata in the Patrick Draw test site are poorly exposed. Rare exposures seen in the field are a monotonous sequence of drab-colored shales, mudstones, and sandstones that are laterally discontinuous. For these reasons, field mapping bedrock units in the area is difficult. Early interpretations of NS-001 color composite images revealed an unmapped stratigraphic unit that could be traced throughout the entire test site. Evaluations of published soil maps, analyses of laboratory and field spectral and mineralogical data, and observations in a trench traversing the unit confirmed the lithostratigraphic validity of the unit and demonstrated that its image expression was the result of the following characteristics:

(1) The unit is less resistant and generally finer grained than adjacent units. It is gypsiferous, includes the thickest and highest stratigraphic occurrence of coal, and is characterized by calcite-cemented sandstones.

(2) Residual soils above the unit are grass-bearing, gypsiferous clay loams, while soils over adjacent units are sage-bearing, sandy loams.

(3) Reflectance in all NS-001 bands is higher for the unit than for adjacent strata. NS-001 band-ratio values for the unit indicate absorption features attributable to kaolinite, montmorillonite, jarosite, and gypsum.

This result demonstrates the value of NS-001 multispectral data for detailed stratigraphic analysis. NS-001 band locations and spatial resolution are sensitive to subtle vegetation and mineralogical changes not readily discernible in Landsat MSS data, aerial photographs, or field observations. With the aid of ancillary field and laboratory spectral data and mineralogical analyses of residual soils, NS-001 image spectral units can be related to bedrock stratigraphy.

D. Mineralogy/Alteration Mapping

1. Silver Bell porphyry copper test site. The best discrimination of hydrothermally altered rocks at the Silver Bell site was provided by the NS-001 Thematic Mapper Simulator data. Several different processing algorithms were applied to these data, including band ratioing, canonical transforms, principal components, and supervised classifications. The first two processes were the most satisfactory since they were designed to enhance the spectral characteristics of altered rocks.

A color ratio composite image was prepared by using green, blue, and red filters for band-ratios 0.66/0.56 μm, 0.83/1.15 μm, and 1.65/2.22 μm, respectively (see Figure 2-3). The effect of this processing is to enhance iron-oxide-rich areas in green, due to the presence of the Fe charge-transfer absorption band in the ultraviolet, and clay-rich areas in red, due to the hydrous minerals absorption band near 2.2 μm. Areas of hydrothermal alteration, with mixtures of clay, sericite, and limonite, would appear as orange to yellow, due to the combination of red and green color components. The ratioing process resulted in a stark contrast between the dark-toned unaltered rocks, in shades of blue and green, and the hydrothermally altered rocks, in bright yellow to orange. The main Silver Bell alteration

zone was vividly outlined as a yellowish-orange band, almost perfectly coincident with the boundary of the phyllic/potassic alteration zones on the available alteration map. No discrimination could be made between phyllic and potassic alteration because both appear as yellowish-orange areas due to physical overprinting of the phyllic zone on the potassic core.

Peripheral alteration, corresponding mainly to propylitic and/or argillic alteration, was visible in numerous outcrops of Mt. Lord Ignimbrite, monzonite, and dacite porphyry on either side of the main alteration zone. The peripheral alteration areas were yellowish-green to yellowish-brown patches with mottled or dispersed patterns and often vague, poorly defined boundaries. These features probably reflect the dispersed, nonpervasive distribution of clay minerals and the gradational transition into fresh rocks.

Evidence of hydrothermal alteration was visible in two areas: (1) reddish-orange outcrops of limonite-stained Precambrian granite north of the Ragged Top Fault, and (2) a small, semicircular area of yellow to orange hue in granodiorite porphyry south of the fault. The latter area is caused by a zone of clay, limonite, and copper oxides within a small prospect tested by several drill holes. Small, dispersed zones of apparent alteration were also seen in the Mt. Lord and the Claflin Ranch Formation in the West Silver Bell Mountains and in Precambrian granite in the Waterman Mountains. Some of the yellowish areas in the West Silver Bell Mountains correlate with weak argillic-type alteration on the surface.

2. Helvetia porphyry copper test site. Hydrothermal alteration products exposed at this test site include various iron-oxide/hydroxide minerals. The different species of iron-oxide minerals, specifically hematite (Fe^2O^3), goethite ($FeO{\cdot}OH$), and jarosite ($KFe_3(OH)_6(SO_4)_2$), have different spectral reflectance characteristics and are not necessarily derived from the same sources. Jarosite is almost always associated with hydrothermal alteration processes. Hematite often results from oxidation of pyrite and chalcopyrite in porphyry copper deposits associated with carbonate rocks and is a prominent constituent of gossans. Goethite is more widely distributed, but can also be an alteration product. M²S data have narrow spectral bands, which might allow separation of these minerals. Figure 2-5 shows representative reflectance spectra for hematite, jarosite, and goethite, along with the M²S band intervals. The spectra are displaced vertically for clarity.

The spectral absorption bands in all three curves are due to electronic transitions involving ferric iron. Typically,

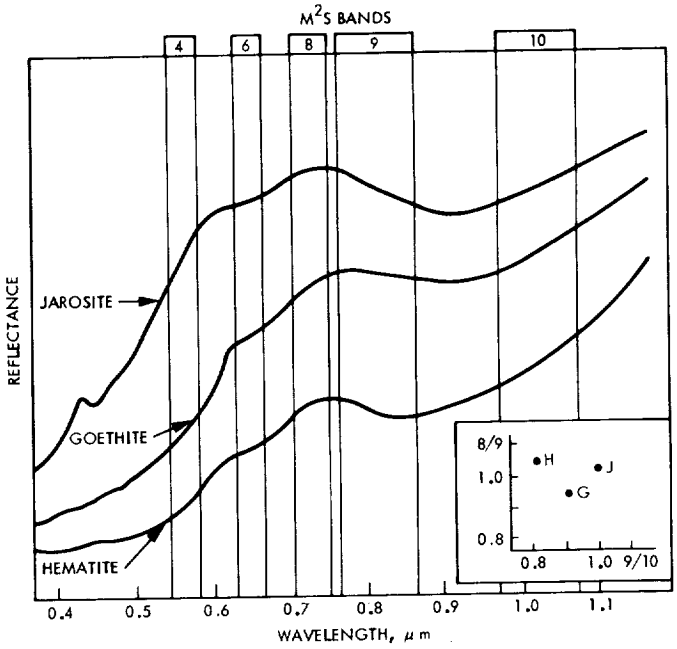

Figure 2-5. Reflectance spectra for hematite, jarosite, and goethite (from Hunt and Ashley, 1979). Spectra are offset vertically for clarity; also shown are the M²S band intervals for channels 4, 6, 8, 9, and 10. The inset figure shows M²S values for band-ratios 8/9 and 9/10 for hematite (H), goethite (G), and jarosite (J) derived from these spectra.

there are three broad features located near 0.45, 0.65, and 0.9 μm and a strong band in the ultraviolet, which produces the rapid falloff in reflectance to shorter wavelengths. Only jarosite shows the 0.45-μm band, while all three spectra depict the 0.65-μm band. But most significant is the position of the 0.9-μm band. In jarosite and goethite, this band is centered at about 0.93 μm; in hematite, the band is displaced toward the shorter wavelength at about 0.85 μm. Although the M²S bands are not ideally placed over these regions, the positions of bands 8, 9, and 10 should produce different reflectance values for the three minerals. By reading off the reflectance values in these three bands, the equivalent 8/9 and 9/10 band-ratio values were calculated and plotted (inset graph, Figure 2-5). In their pure form, the three minerals are clearly separable. This analysis was applied to the M²S image data by construction of two ratio composite images; one with band-ratios 4/6, 6/8, and 8/9; the other with band-ratios 4/6, 6/8, and 9/10. Then two images were displayed using blue for 4/6, green for 6/8, and red for either 8/9 or 9/10 (Figure 2-6).

Examination of the two ratio composite images indicated that the preliminary analysis of iron-oxide separations was borne out. On the 8/9-ratio image, hematitic arkoses were orange, and iron-oxide-bearing rocks that are

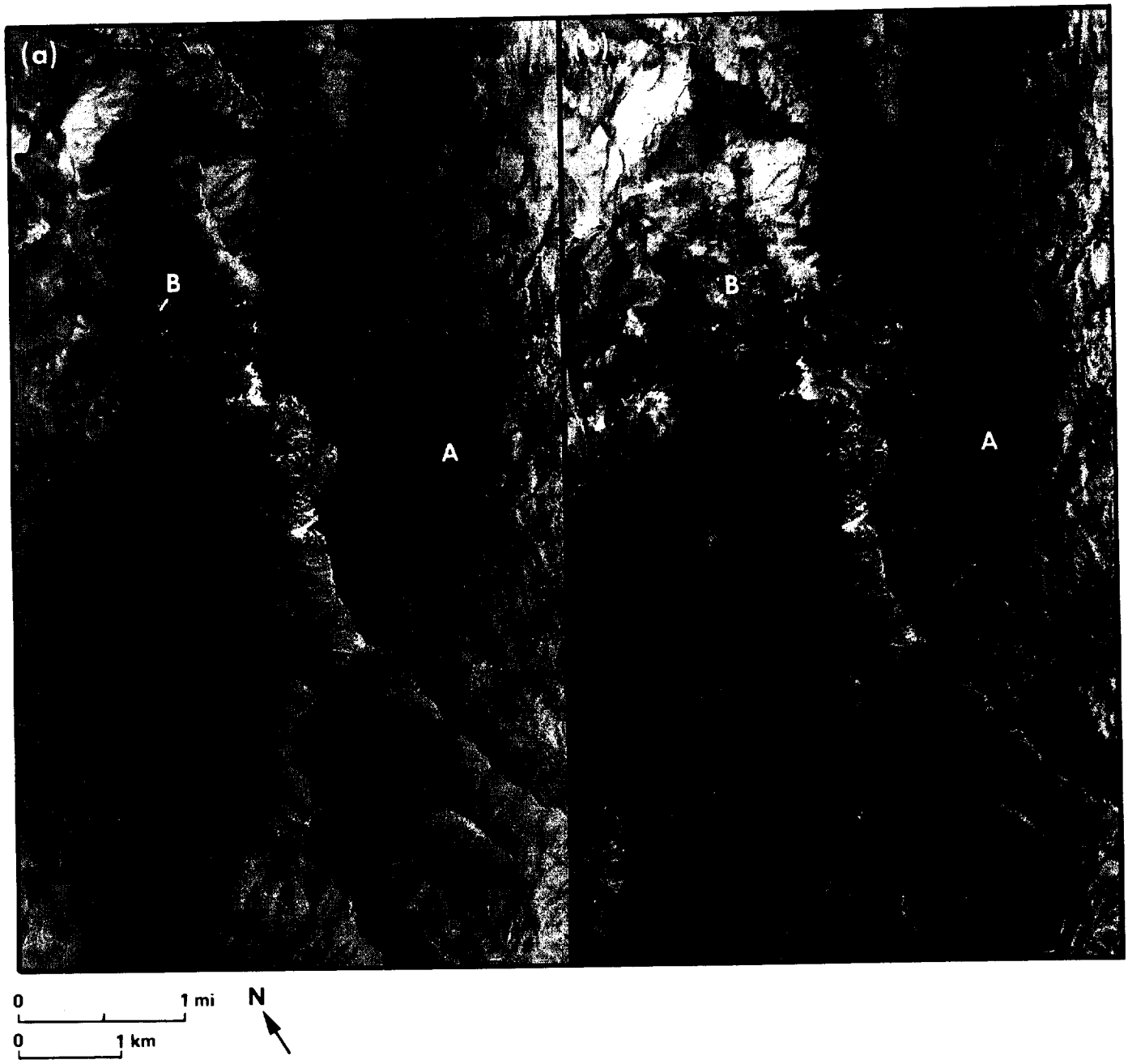

Figure 2-6. M^2S color ratio composites of the Helvetia, Arizona, test site: (a) band-ratios 4/6, 6/8, and 9/10 are displayed as blue, green, and red, respectively; (b) band-ratios 4/6, 6/8, and 8/9 are displayed as blue, green, and red, respectively.

dominantly goethitic were yellow. In the 9/10 ratio, the arkoses were dark brown; this color change verifies the graphical data of Figure 2-5. A jarositic mine dump was yellow on both the 8/9 and 9/10 images, as would be predicted from the data of Figure 2-5. The narrowness of the M^2S spectral bands, despite their nonideal positions, allows separation of iron-oxide minerals based on the shift of the ferric-iron absorption band near 0.9 μm.

3. Safford porphyry copper test site. One of the prime objectives of the Safford test site study was to evaluate remote sensing instruments for their ability to discriminate alteration zones. The Landsat MSS spectral bands and spatial resolution were adequate for mapping the large limonitic (weathered pyritic) zone over the Kennecott ore body. The best Landsat MSS image for mapping this zone was the PC image, in which the third PC sharply deline-

ated limonite. The three-ratio (4/5, 5/6, 6/7) color composite also delineated the same area, but as a more diffuse, less obvious zone. The Landsat MSS three-ratio image was advantageous because the spectral signatures can be identified by their image color coding. For example, not only was the limonitic zone coded in the expected orange–red tone, but a propylitic Mesozoic andesite outcrop was mapped in this image as a cyan tone as would be predicted from the laboratory spectra of these rocks.

A Landsat MSS band 4, 5, 7 CIR composite image depicted the same limonitic zone in the expected yellow tones at about the same distinctiveness as the color ratio image. However, the CIR image did not portray the Mesozoic andesite as distinctly as did the ratio image. Lithologic differences in the postore Datil Volcanics overlying the host rock were more sharply delineated on the CIR image.

One of the main limitations of the Landsat MSS data was spatial resolution. None of the digital Landsat MSS images showed the limonitic porphyry stocks exposed in the area, although these were delineated by the color photographs and multispectral aircraft scanner images. These limonitic zones are about the size of one MSS picture element or pixel (80 m).

The spectral ranges of the visible and near-infrared channels used from the M²S scanner are similar to Landsat MSS channels. An M²S color ratio composite image showed the same color coding of geologic features as the Landsat MSS ratio image. However, the image improvement resulting from the 8-fold increase in spatial resolution was dramatic. Small limonitic porphyry outcrops were clearly shown on M²S images. This comparison demonstrates the value of increased spatial resolution.

The increased spectral resolution of the M²S produced additional mineralogic information not available from the Landsat MSS, including detection of copper oxides and mixed alteration zones. The bandwidths of the M²S scanner are less than one half that of the Landsat MSS; twice as many M²S spectral bands occupy the same spectral range as the Landsat MSS. The geologic information content of the NS-001 Thematic Mapper Simulator images was also increased by the 8-fold increase in spatial resolution. As in the case of M²S images, NS-001 images clearly portrayed limonitic porphyries.

Compared with the M²S, the NS-001 has less spectral resolution in the shorter wavelength region; thus, some mineralogic discrimination was lost. However, the extension of the NS-001 spectral range to bands centered at 1.6 and 2.2 μm enabled the use of the NS-001 to map the clay-type alteration directly. This capability cannot be achieved with the spectral range of the M²S and Landsat MSS sensors. Because the ability of the NS-001 to detect phyllic alteration zones did not depend on the presence of limonitic gossans, NS-001 data reveal more than 90 percent of the phyllically altered areas by virtue of the clay absorption band at 2.2 μm and the increased reflectivity of phyllically altered rock at 1.6 μm.

An NS-001 color ratio composite image (3/2, 4/5, 6/7) was particularly useful for relating image spectra to mineralogy. A canonical transform image was not useful, but did segregate phyllically altered areas into two subcategories. Used together, the canonical transform and the color ratio composite images enabled phyllic alteration to be separated into three categories: (1) latites and quartz monzonite, (2) leached, pyritic vent breccia and tuff, and (3) heavily argillized areas. Together these two images also allowed the resolution of tonal confusion between alteration zones and dense clumps of vegetation. The NS-001 images did not distinctly segregate the limonite gossans (pyritic zones) within the phyllic zones. The M²S images were the best for sharply defining the ferric and copper oxides.

A "thermal inertia" image was generated by combining three images as a false-color composite: an albedo (panchromatic solar reflectance) image was combined with a daytime thermal infrared image and a nighttime thermal infrared image. The thermal inertia image revealed hydrothermally silicified rocks of the most intensely altered quartz-sericite (phyllic) halo. These silicified areas were delineated by their combination of high albedo and high thermal inertia, i.e., relatively cool daytime temperature and warm nighttime temperature.

4. Lisbon Valley uranium test site. The Wingate Sandstone is a rose-colored, fine-grained eolian unit of Jurassic (?) age. In Lisbon Anticline, the sandstone forms a dip slope on the southwest limits and is a prominent cliff-former. In the Big Indian Uranium Mining District, comprising approximately the northwest one-quarter of this structure, the Wingate Sandstone is bleached to buff and white colors. In the past, exploration geologists had noted a general correlation between bleached Wingate Sandstone exposed at the surface and the presence of uranium mineralization at depth within the underlying Chinle Formation (Moss Back Member). However, previous exploration models were of a very local, empirical type, generally not making use of this information. The historical development of this district relied mainly on extension drilling to recover mineralized channel structures in the Moss Back Member of the Chinle Formation.

The Bendix 24-channel (7.5-m resolution) and NS-001 (15-m resolution) multispectral image data were used to map and define the position of bleached Wingate outcrop in Lisbon Anticline. In addition to outcrops throughout the Big Indian District, the images permitted (1) mapping bleached strata in the southern part of the anticline, and (2) establishing an immediate correlation between altered rocks in northern and southern areas. For comparison, a detailed photogeologic analysis of Wingate bleaching was made using color aerial photographs. On the basis of this analysis, it was possible to recognize three general facies within the section: bleached sandstone, unbleached sandstone, and an intricately banded transition facies between the two. Furthermore, using stereoscopic aerial photographs, the relative stratigraphic relation of these units could be established and mapped throughout the structure. These relations, when transferred to a topographic map, showed bleached outcrops at high elevations along the anticlinal crest and transition facies at lower elevations along the limb.

Detailed interpretations of the Bendix 24-channel data were also made by the use of transparent overlays. The image bands were combined in a canonical transform image designed to separate bleached and unbleached rock. The data with a surface resolution of 7 m allow interpretations very roughly comparable to those of the aerial photographs with a surface resolution of approximately 1 m. It was possible to separate bleached and unbleached facies of this sandstone and certain of the thicker bedded units of the banded transition facies as well. In addition, image units corresponding to drill roads and pads, shadows, vegetation, and soils were mapped. One new image unit with an apparent bedded aspect, observed in these interpretations, did not correspond to the usual stratigraphic layering of the Wingate and remains geologically unexplained.

The NS-001 multispectral scanner data were used to extend these interpretations to the southern outcrops. The detail recoverable in these extensions was less than that in the Bendix 24-channel data because of poorer surface resolution (15 m), but an offsetting advantage was the existence of stereoscopic image coverage for a few important outcrops. The existence of stereoscopic images permitted determination of strike and dip for some important horizons. It was evident from this cursory analysis that stereoscopic coverage enhances the value of any image data as a geologic mapping tool.

The separation of bleached and unbleached facies of these units was possible in Landsat MSS, Bendix 24-channel and NS-001 aircraft data, in color composites and color ratio composites, and in PC and canonical transform images. Spectrally, the bleached and unbleached rocks differ in strength of Fe^{+3} absorption present and in albedo. No additional bands would seem to be required to establish these separations.

5. Copper Mountain uranium test site. Uranium mineralization at Copper Mountain is found in Precambrian granitic rocks beneath partially exhumed Eocene-age pediment surfaces and other Eocene landforms. The mineralization, confined to highly fractured rocks along fault zones, represents the remains of more extensive deposits that existed prior to the exhumation of the present erosional surface. The pediment surfaces, where exposed, are veneered by a complex assemblage of iron oxide and hydrate iron oxide, and have a bright rusty-orange appearance in the field.

Exploration geologists defining and developing the Copper Mountain uranium resource developed a supergene genetic model for the mineralization in which the granitic rocks overlying mineralized zones (together with once present but now eroded tuffaceous sediments) acted as sources of uranium. Surface waters leached the uranium, transporting it to depth and discoloring the surface rocks. M²S and NS-001 multispectral scanner data were used to map the distribution of this alteration/weathering effect throughout the Copper Mountain test site. From the M²S data, Landsat MSS band-equivalent color ratio composites (4/5, 4/6, 6/7), found useful in previous studies for mapping iron oxidation and vegetation, were prepared. The distribution of oxidation effects mapped throughout the study site in 11-channel M²S data showed the most intense oxidation over areas corresponding to the topographically well-defined pediment surface along the range front. In addition, the oxidation extended over numerous valleys, ridges, and talus slopes higher in the range. Oxidized outcrops corresponded lithologically to granite, Precambrian metasediments, and Cambrian brown sandstones alike. In addition, the NS-001 data were analyzed with the PC transformation. The distribution of oxidation in the NS-001 images was more restricted. In this case, the zones of most intense effects were depicted separately and were physiographically confined to exhumed granitic portions of the pediments.

The image-derived weathering patterns were compared with the distribution of uranium mineralization based on exploration drilling. This comparison shows that the NS-001 data provided a more accurate delineation than the M²S data of limits of the oxidation effects associated with mineralization. Some aspects of the observed oxidation patterns were identifiable because the physiography was

analyzed independently of topographic maps and field studies.

Oxidation patterns other than pediments corresponded to exhumed paleotopographic landforms characterized by smooth slopes and rotten, decomposed granite rock (grus-mantled) at the surface. These results emphasize the importance of topographic information in the analysis of image data.

Attempts to map prominent surface outcrops of ore-associated hematite elsewhere using automatic machine classification (Bayes-Maximum likelihood) methods were unsuccessful because the field-established training areas were small and hard to locate accurately in the image data. Both of these problems would have been reduced or eliminated by increased spatial resolution in the scanner data.

E. Vegetation Mapping

1. Patrick Draw petroleum test site. An interior sage–grassland community constitutes the vegetation cover at the Patrick Draw site. NS-001 data were used as variables in a supervised classification computer analysis to produce an accurate map of percent vegetation cover in a 350-km^2 area. The first seven NS-001 bands were used as variables for the classification. This procedure proved to be both time and cost effective and resulted in a map of vegetation density that could not have been produced using Landsat MSS data, aerial photographs, or conventional field botanical methods. The resulting vegetation density map and field observations revealed normal variability in plant density and led to the identification of an area of abnormally low vegetation cover, characterized by stunted sage and a lack of associated grass cover. Surface geochemical data suggest that this occurrence of stunted sage may be a response to hydrocarbon seepage from the gas cap of the Patrick Draw reservoir.

2. Lost River petroleum test site. The Lost River test site is completely vegetated, largely by natural deciduous tree species. NS-001 data were used as variables in discriminant function/supervised classification computer analyses to produce accurate maps of 10 local vegetation communities in a 600-km^2 area. Data were acquired during peak fall-foliage display. Spectral separations among species were based on differences in leaf pigment in the visible portion of the spectrum, and leaf structure and water content most prominent in the 1- to 1.3-μm spectral region (NS-001 band 5) and around 1.6 μm (band 6). The 15-m pixel size was significant for mapping because it corresponds approximately to the size of individual tree crowns. The five NS-001 bands and band ratios most useful for mapping vegetation communities were 6, 2/5, 4/5, 5, and 2/6. Again, this procedure proved to be a time- and cost-effective means of mapping vegetation, which would have been impossible using Landsat MSS data, aerial photographs, or conventional field botanical mapping methods. The resulting vegetation map of the test site revealed normal variability of plant distribution and led to the identification of two areas of abnormal maple tree concentration. The abnormal maple concentrations may be related to hydrocarbon seepage from the subsurface reservoir of the Lost River gas field.

IV. Conclusions and Recommendations

This Test Case Project was primarily concerned with the evaluation of remote sensing data obtained by optical scanner systems, both spacecraft and aircraft. The major sensor-related variables considered in this evaluation were spectral resolution and band position, and spatial resolution.

The spectral resolution of existing sensors employed in this Project was dictated primarily by engineering considerations. The M^{2}S scanner covered the wavelengths short of 1.0 μm in 10 spectral bands, and the wavelength range was limited by the spectral sensitivity of silicon detectors. The NS-001 scanner was built to simulate the TM flown on Landsat 4 and 5, with the addition of a band in the 1.0- to 1.3-μm region. The positions of the bands were dictated by atmospheric windows, and the width of individual bands was relatively broad to increase the signal-to-noise ratio. The width and positioning of these spectral bands are not necessarily optimum for identifying surficial materials. Laboratory spectra and theoretical studies suggest that sensor systems possessing a larger number of narrower spectral bands than presently available can potentially provide more specific mineralogical and vegetation information for mapping purposes.

The 0.4- to 2.5-μm wavelength region can be divided into three major parts (Goetz and Rowan, 1981; Hunt 1977): the 0.4- to 1.1-μm region, which includes most of the electronic transitions in the transition elements, notably iron; the 1.1- to 2.0-μm region, which includes absorption features in minerals, and variations in leaf structure and water content in vegetation; and the 2.0- to 2.5-μm region, which includes the overtone bending–stretching vibrations for minerals containing OH, CO_3, and SO_4 ions. To describe the spectral reflectance characteristics of minerals, particularly in the 2.0- to 2.5-μm region, a spectral sampling of 0.01 μm or better is required. Imaging systems with such capabilities are now being built. At the time of

this Test Case Project, the construction of sensor systems with spectral sampling intervals narrower than approximately 0.05 μm was not anticipated. A study was conducted, as described below, to determine the relative advantages of increasing the spectral resolution significantly over the resolution of existing scanner systems used in this study.

A. Band Selection by Discriminant Function Analysis

Discriminant function analyses were performed on the PFRS field data to assess the ability of various sets of wavelength bands to separate rock types on the basis of spectral reflectance. Rock types encountered at the porphyry copper test sites were considered in this analysis. Three instruments were simulated: the Landsat TM (six bands), the NS-001 Thematic Mapper Simulator (seven bands; 1.0- to 1.3-μm band in addition to the six TM bands), and a hypothetical 30-channel instrument with 0.05-μm-wide, equally spaced bands over the 0.475- to 2.475-μm range. The analysis provided the order of band selection, based on the ability of the instruments to separate the classes of materials input as training data. A summary of the band selection order is presented in Table 2-5. The Landsat TM and NS-001 analyses are combined since the only difference between these sensors is the presence of the 1.15-μm band on the NS-001. In all cases, the order of band selection was the same for the TM and NS-001, except the 1.15-μm band was additional to the NS-001 analyses.

The Silver Bell analysis of the NS-001 scanner exhibits a nearly one-to-one correspondence in both the wavelength position and order of spectral bands that were identified as optimally suited for rock-type discrimination in the analysis of the hypothetical 30-channel scanner. The most important band was the 1.65-μm band, followed by the 2.22-μm band. From a statistical standpoint, the TM bands are the optimum bands for discriminating the suite of altered and unaltered rocks sampled at Silver Bell. The 1.15-μm band was the last one selected, suggesting that exclusion of this band from the TM would have little effect on the efficiency of detecting Silver Bell type alteration.

The Helvetia analysis shows a similar behavior for the first three bands selected. The 30-channel analysis then selected three bands in the 2.2-μm region, presumably to separate altered clay-bearing rocks from carbonates. The 0.83- and 1.15-μm bands were not selected in the first seven bands in the 30-channel analysis.

A somewhat poorer correlation exists for the Safford analysis. The 1.15-μm band was selected third, indicating that it is fairly important for separating the suite of rocks sampled at Safford. The 2.2-, 0.5-, 0.9-, and 1.55-μm regions were selected in the 30-channel analysis as the most important. These channels fairly closely match several of the TM channels.

A summary of the Landsat TM and NS-001 band selection order for the three copper sites is found in Table 2-6. The seven bands were examined for the order chosen, then ranked by summing up the three orders for each test site. For example, the 0.48-μm band was selected third at Silver Bell, first at Helvetia, and seventh at Safford, for a total score of 11. By this criterion, the overall most useful was the 1.65-μm band, followed by the 2.2-μm band. The NS-001 1.15-μm band was ranked fifth-sixth; the least useful was the 0.83-μm channel.

B. Spatial Resolution

The requirements for spatial resolution in satellite remote sensing systems have been debated since the 1960s. The IFOV of the Landsat MSS detectors was dictated by swath width, signal-to-noise ratio requirements, and data rate. In the Test Case Project, it has been shown in all of the test sites that images with 80-m pixels are primarily

Table 2-5. Band selection order for Landsat TM, NS-001, and conceptual 30-channel instrument

Silver Bell		Helvetia		Safford	
TM[a]	30 Δλ	TM[a]	30 Δλ	TM[a]	30 Δλ
1.65	1.60	0.48	0.50	2.22	2.15
2.22	2.15	0.66	0.70	1.65	2.20
0.48	0.50	1.65	1.70	1.15[b]	0.50
0.56	0.55	1.15[b]	2.30	0.83	2.05
0.66	0.70	0.56	2.20	0.56	0.90
0.83	0.60	0.83	2.05	0.66	1.55
1.15[b]	2.20	2.22	0.55	0.48	1.65

[a]Center wavelength of Landsat TM bands, μm.
[b]1.00- to 1.30-μm band on NS-001, not on Landsat TM.

Table 2-6. Summary of Landsat TM and NS-001 band selections for rock-type mapping at the porphyry copper sites

Band[a]	Priority Order (Silver Bell, Helvetia, Safford)	Total	Average Ranking
0.48	3, 1, 7	11	3
0.56	4, 5, 5	14	5, 6
0.66	5, 2, 6	13	4
0.83	6, 6, 4	16	7
1.15[b]	7, 4, 3	14	5, 6
1.65	1, 3, 2	6	1
2.22	2, 7, 1	10	2

[a]Center wavelength, μm.
[b]1.00- to 1.30-μm band on NS-001, not on Landsat TM.

useful for regional mapping. It is safe to assume that, in all but the most poorly mapped areas of the Earth, useful mapping for exploration purposes needs to be carried out at a scale of 1:48,000 or better. By simple extrapolation from the Landsat MSS experience, this translates to a requirement for a pixel size of 15 m or smaller. Coincidentally, this is the average pixel size in the aircraft scanner data used in this study.

All of the aircraft scanner data used in this Project were analyzed and processed at their original resolution between 12 and 18 m. However, because the data are in digital form, the spatial resolution was degraded in order to examine the effect of more limited spatial resolution on detectability of geologic features. An NS-001 color ratio composite image for the Silver Bell test site was spatially degraded, and a small area was selected for detailed analysis. A cubic convolution resampling algorithm was used to produce pixels of 30- and 80-m size. For comparison, the same area was extracted from the Landsat MSS CIR composite (bands 4, 5, and 7), and the Landsat MSS color ratio composite (ratios 4/5, 5/6, and 6/7); all five images (Figure 2-7) were at a scale of 1:48,000, a common scale used by exploration geologists for analysis and mapping.

Several different-sized features were examined. An area of altered syenodiorite could be located on all of the NS-001 images because of its tonal contrast with the surroundings. The syenodiorite was also discernible on the Landsat MSS ratio picture as a red area (iron oxides). The dimensions of this area are about 300 by 300 m: on the 12-m data, they are 25 by 25 pixels; on the 30-m data, they are 10 by 10 pixels; on the 80-m data, they are 4 by 4 pixels.

Small outcrops of altered monzonite appeared yellow on the NS-001 data. At 80 m they were only single pixels, but could still be recognized. These outcrops were not discernible on the Landsat MSS images due to their lack of spectral contrast with surrounding units. An extension of the Barite Fault was expressed as a drainage alignment. It was easily mapped at 12- and 30-m resolution, but was not detectable in 80-m resolution images. The same behavior was displayed by several dikes. These were easily seen on the 12-m data, were more difficult to pick out on the 30-m data, and disappeared altogether on the 80-m data.

The spatial resolution afforded by the NS-001 scanner provides data, at a scale of 1:48,000, that can be used for structural analysis, lithologic mapping, and geobotanical surveys. While this resolution may be sufficient for many applications, the studies at Lisbon Valley, and Copper Mountain in particular, showed that stereoscopic aerial photography acquired at a high spatial resolution (1 m) is needed to solve local structural problems and map variegated surface units. In many cases, detailed problems can only be handled with the use of aircraft data. In some cases, low-resolution multispectral data can be substituted for high-resolution aerial photographs as seen in the Lisbon Valley and Patrick Draw test sites.

C. Summary

The results of the study can best be summarized by addressing the four questions stated earlier in this section.

(1) Is the Landsat MSS adequate for mineral and petroleum exploration purposes?

The results of the Test Case Project clearly show that the MSS provides regional information of relevance to mineral and petroleum exploration, but in order to more fully approach the problems, higher spatial resolution, not available from the MSS, and increased spectral coverage are required. At all of the test sites, the addition of wavelength bands

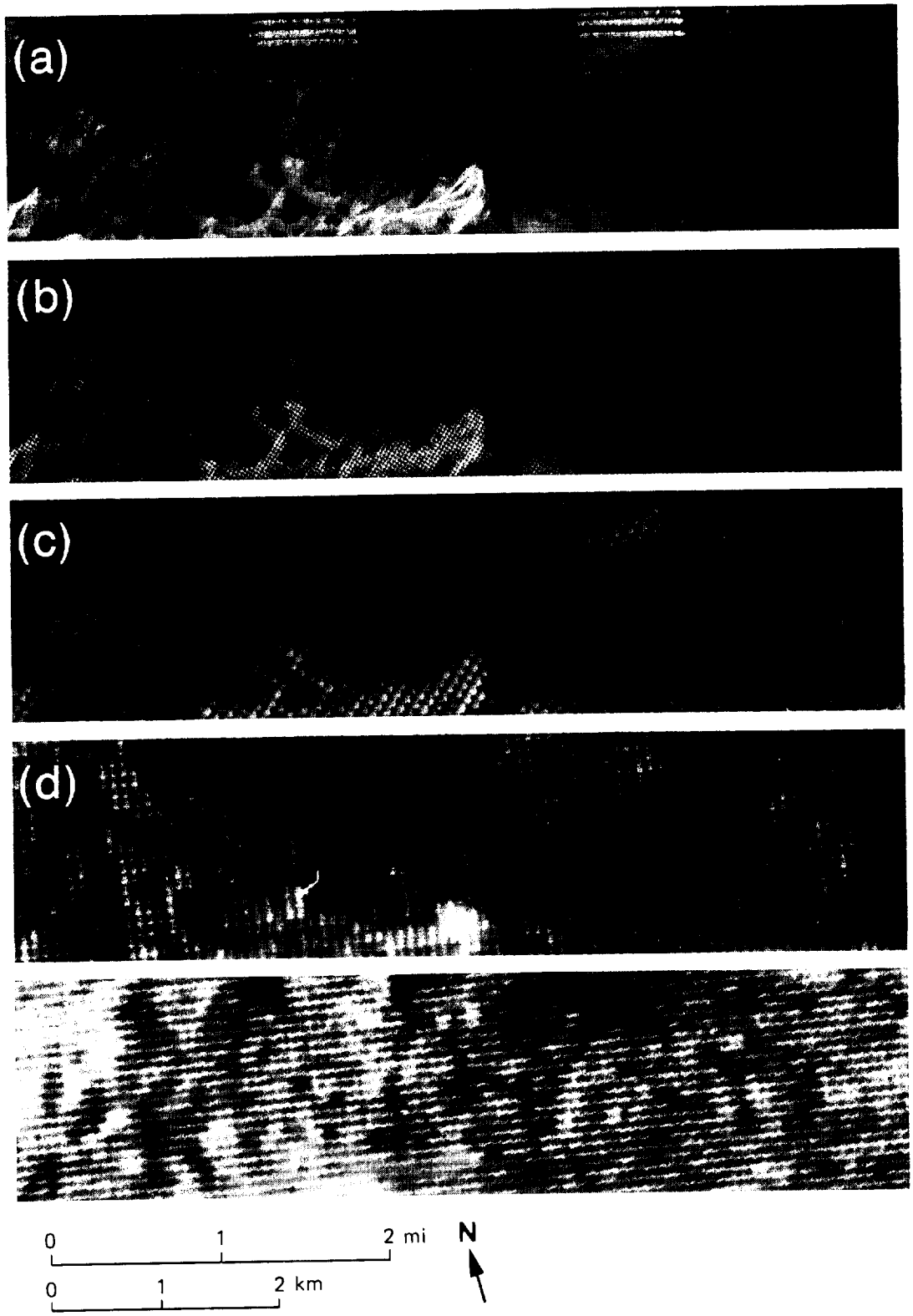

Figure 2-7. Comparison of spatial resolution. Portion of NS-001 ratio composite of Silver Bell, Arizona (Figure 2-3), at resolutions of: (a) 12 m; (b) 30 m; and (c) 80 m. Landsat data of 80-m resolution: (d) false-color infrared composite, MSS bands 4, 5, 7; (e) ratio composite, 4/5, 5/6, 6/7.

beyond 1.0 μm was considered critical in separating units on the basis of mineralogy and vegetation cover. Since exploration often requires mapping at a scale of at least 1:48,000, a scanner pixel size of 15 m or less is necessary.

(2) What spatial resolution is required to solve geologic problems?

The spatial resolution required is directly proportional to the mapping scale. In the Test Case Project, pixel sizes ranged from 80 m for the Landsat MSS to 1 m for aerial photography. NS-001 data from Silver Bell were degraded from a 15-m pixel to 30- and 80-m pixels. Several dikes that were easily seen in the original NS-001 data were difficult to discern in the 30-m Landsat TM equivalent data and were not visible in the 80-m Landsat MSS equivalent image. In six of the eight test site studies, the spatial resolution provided by the NS-001 data was adequate. At the Lisbon Valley and Copper Mountain sites, several problems could only be resolved by use of 1-m resolution aerial photography. Therefore, a definite spatial resolution, applicable to all exploration problems, could not be established. However, space-acquired data with a 15-m IFOV would appear to be sufficient for many problems.

(3) Which spectral region is most important for remote sensing, and how many bands are required?

The Test Case Project concentrated mostly on the 0.4- to 2.5-μm wavelength region. Field and laboratory spectral reflectance data, combined with theoretical considerations, show that the spectrum must be sampled with broad bands in the 0.4- to 1.0-μm region and beyond 1.0 μm, at least at 1.6 μm and in the region of 2.2 μm. These are intentionally the regions covered by the NS-001 and Landsat TM scanners. At the Safford District, it was possible to use spectral bands with a bandwidth of 0.05 μm to separate different iron oxides according to the position of the Fe^{+3} electronic transition and the slope of the spectral curve between 0.4 and 0.7 μm. Identification of individual minerals, in particular those containing OH, requires much higher resolution, on the order of 0.01-μm sampling. Therefore, the scanners operating presently are adequate in spectral coverage and spectral resolution to detect major lithologic boundaries and structural features. To achieve significantly better results (i.e., mineral identification), much higher resolution spectral imaging systems will have to be built.

(4) Will the Landsat TM, as envisioned, provide sufficient spatial resolution and adequate spatial coverage? Is the lack of stereo coverage critical?

The Landsat TM is now in orbit aboard Landsat 4 and 5. The spectral coverage is adequate but not ideal. For instance, the TM bands short of 1 μm are not optimally placed to map differences in iron-oxide mineral composition. Based on the experience at the Lost River, West Virginia, test site, at longer wavelengths the lack of a band centered at 1.15 μm limits the value of the TM in vegetation mapping. The bands centered at 1.6 and 2.2 μm are valuable in lithologic mapping, particularly in alteration zones, as demonstrated particularly well in the porphyry copper test sites.

The lack of stereo coverage greatly inhibits the interpretation of stratigraphic and structural relationships. Presently, necessary topographic information must be obtained from stereo aerial photography, digital terrain data, or topographic maps.

In summary, the TM will provide a major new contribution to remote sensing geology. Many of the results of the Test Case Project can be achieved in comparable regions using space-acquired TM images.

References

Abrams, M. J., R. P. Ashley, L. C. Rowan, A. F. H. Goetz, and A. B. Kahle (1977). Mapping of hydrothermal alteration in the Cuprite Mining District, Nevada, using aircraft scanner imagery for the 0.46–2.36 μm spectral region. *Geology, 5,* 713–718.

Goetz, A. F. H., F. C. Billingsley, A. R. Gillespie, M. J. Abrams, R. L. Squires, E. M. Shoemaker, I. Lucchita, and D. P. Elston (1975). *Application of ERTS images and image processing to regional geologic problems and geologic mapping in northern Arizona* (JPL Technical Report 32-1597). Pasadena, California: Jet Propulsion Laboratory.

Goetz, A. F. H., and L. C. Rowan (1981). Geologic remote sensing. *Science, 211,* 781–791.

Hodgson, R. A. (1974). Review of significant early studies of lineament tectonics. In R. A. Hodgson, S. Parker-Gay, Jr., and J. Y. Benjamins (Eds.), *Proceedings of the First International Conference of the New Basement Tectonics.* Salt Lake City: The Utah Geological Association.

Hunt, G. R. (1977). Spectral signatures of particulate minerals in the visible and near infrared. *Geophysics, 42*(3), 501–513.

Hunt, G. R., and R. P. Ashley (1979). Spectra of altered rocks in the visible and near infrared. *Econ. Geol., 74,* 1613–1629.

Lee, K. (1972). *Bonanza Project–1971* (Remote Sensing Report 72-5). Colorado School of Mines.

Rowan, L. C., A. F. H. Goetz, and R. P. Ashley (1977). Discrimination of hydrothermally altered and unaltered rocks in visible and near infrared multispectral images. *Geophysics, 42*(3), 522–535.

Rowan, L. C., P. H. Wetlaufer, A. F. H. Goetz, F. C. Billingsley, and J. H. Stewart (1974). Discrimination of rock types and detection of hydrothermally altered areas in south-central Nevada by use of computer-enhanced ERTS images. *U.S. Geol. Surv. Prof. Pap. 883.*

Section 3

Porphyry Copper Commodity Report

Michael J. Abrams
Jet Propulsion Laboratory

David Brown
Texasgulf Inc.
Tucson, Arizona

Section 3

Porphyry Copper Commodity Report

Contents

I. Porphyry Copper Overview 3-1
A. Geologic Settings 3-1
B. Characteristics 3-1
1. Classic model (Southwest United States) 3-2
2. Regional variants 3-2
C. Porphyry Deposit Ore Genesis Models 3-2
D. Remote Sensing Characteristics 3-4

II. Background and Site Selection 3-6
A. Background 3-6
B. Site Selection 3-7
1. General criteria 3-7
2. Specific criteria of selected sites 3-7

III. Summary of Previous Work 3-9

IV. Comparative Analysis of Test Site Results 3-11

V. Extrapolation to Similar and Different Environments 3-13

VI. Implication for Mineral Exploration in General 3-14

VII. Future Work 3-15

References 3-16

Bibliography 3-17

Figures

3-1. Worldwide distribution of porphyry copper deposits 3-1
3-2. Idealized cross-sectional views of alteration zoning and mineralization zoning for southwestern U.S. porphyry copper deposits 3-3
3-3. Mineralogy of alteration facies for porphyry copper deposits 3-4

PRECEDING PAGE BLANK NOT FILMED

3-4. Laboratory spectra of selected hydrous minerals illustrating distinct absorption bands in the 2.0- to 2.4-μm wavelength region 3-6
3-5. Locations of porphyry copper test sites in Arizona 3-8
3-6. Diagrammatic field spectrum illustrating positions of diagnostic iron and clay absorption bands 3-11

Tables

3-1. Porphyry copper deposit model and remote sensing characteristics 3-5
3-2. Results of discriminant function analyses: Landsat 4 TM versus 30 $\Delta\lambda$ 3-12

Section 3

Porphyry Copper Commodity Report

I. Porphyry Copper Overview

A. Geologic Settings

Porphyry copper deposits in the Earth's crust generally occur in continental-margin or island-arc regions associated with ancient or recent plate subduction and calc-alkaline magmatism. Current theories favor an origin by ascension and progressive differentiation of a copper-rich magma derived from partial melting in the upper mantle region.

On a global basis, the great majority of porphyry copper deposits occur in the circum-Pacific area, corresponding to a region of Mesozoic to Recent seafloor spreading and plate subduction (Figure 3-1). A number of separate provinces are recognized throughout the circum-Pacific region, corresponding to distinct clusters of deposits. The major porphyry provinces include the Andean orogen of western South America, the southwestern U.S. Province, the Canadian Cordilleran region, and the Southwest Pacific Islands.

Porphyry copper deposits are also found in the so-called Alpide Belt, a Mesozoic–Cenozoic orogen stretching from Yugoslavia and Rumania southeastward to Iran and Pakistan (Sillitoe, 1972). Porphyry-type occurrences of copper and molybdenum are reported in various other parts of the world, including the Appalachian orogen of eastern North America; Precambrian and Paleozoic-age systems also occur in New England, Quebec, and New Brunswick (Schmidt, 1978).

The host rocks for porphyry deposits are largely a function of their regional geologic setting. Continental-margin and island-arc deposits tend to be hosted by co-magmatic/andesite volcanic and volcaniclastic rocks formed in continental slope or back-arc environments. Continental deposits are typically found in shelf-type sedimentary rocks, Precambrian basement rocks, or subaerial volcanic rocks.

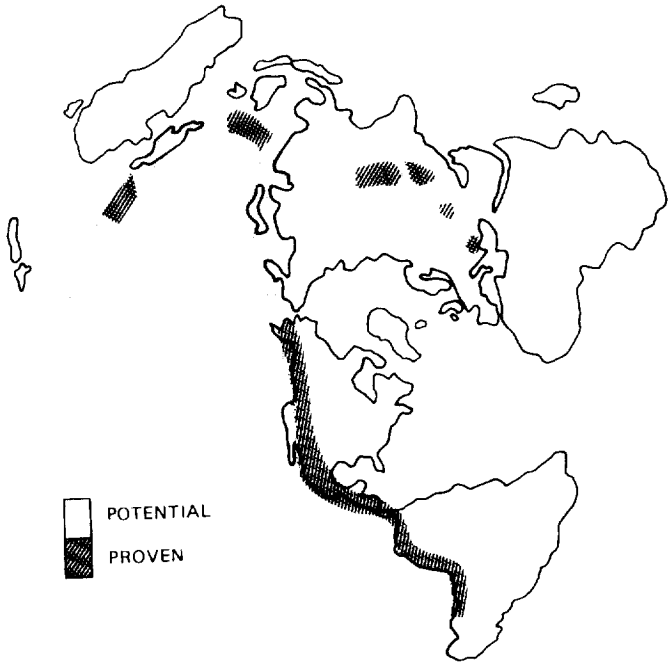

Figure 3-1. Worldwide distribution of porphyry copper deposits

B. Characteristics

Porphyry copper deposits have a number of characteristics that distinguish them as a unique class of deposits. These common features are, to a large extent, qualitative and intuitive in nature, and no one deposit is likely to contain all of the essential elements.

1. Classic model (Southwest United States). A generalized description of a "typical" porphyry copper deposit has been developed by Lowell and Guilbert (1970). The Lowell–Guilbert model is based on a comparison of 27 major North and South American porphyries. The model is definitely biased toward the characteristics of the southwestern U.S. porphyries, and it is the model implicitly adopted to describe the Geosat test sites.

According to Lowell and Guilbert, the typical porphyry copper deposit is associated with an irregular elongate stock, 1230 by 1850 m in size, and progressively differentiated from quartz diorite to quartz monzonite. The stock is typically emplaced into Late Cretaceous sedimentary and volcanic rocks, although Precambrian, Paleozoic, and Mesozoic rocks are also common preore hosts.

The typical ore body is steep walled and cylindrical, with gradational boundaries and dimensions of 1075 by 185 m. The average ore body contains 140 million tons of material, of which 70 percent occurs in the igneous host rocks and 30 percent in preore wall rocks. The typical deposit contains 0.45 percent hypogene copper, 0.35 percent supergene copper, and 0.015 percent molybdenum.

Alteration occurs as a series of concentric shells coaxial with the ore body (Figure 3-2). The innermost and earliest zone is the potassic core (K-feldspar–biotite–quartz), surrounded progressively outward by the phyllic zone (quartz–sericite–pyrite), argillic zone (quartz–kaolinite–montmorillonite) and propylitic zone (epidote–calcite–chlorite) (Figure 3-3). Over the same interval, metallization varies from chalcopyrite–molybdenite–pyrite to pyrite–chalcopyrite to an outer galena–sphalerite assemblage with minor gold and silver. Occurrence of mineralization gradually changes from disseminations in the core to stockworks of fracture fillings and microveinlets and finally to discrete veins and replacements on the periphery.

The original vertical column of hydrothermal alteration is believed to have spanned approximately 3100 m, with the upper reaches formed in a subvolcanic environment only a few kilometers below the surface. Porphyritic igneous textures, breccia pipes, radial and concentric diking, and vertically telescoped zoning all indicate a relatively shallow depth of formation.

2. Regional variants. Modifications to the Lowell–Guilbert model are necessary to adequately describe the characteristics of the Southwest Pacific island-arc deposits and the plutonic and volcanic-type deposits found in British Columbia. The Southwest Pacific deposits are generally hosted by quartz diorite or granodiorite intrusives, which are often emplaced into their co-magmatic mafic volcanic pile. Mineralization is often accompanied by intense structural deformation and subsequent telescoping of alteration and "dumping" of mineralization (Lowell and Guilbert, 1970, p. 107). Gold, rather than molybdenum, is often found with copper in the main ore zone.

Hydrothermal alteration systems in the Southwest Pacific deposits are often "dry" compared to the classic model, and extensive zones of bleaching and phyllic alteration are usually lacking. Alteration in many deposits consists of early pervasive propylitization cut by younger, vein- and fracture-controlled K-feldspar, biotite, and quartz–sericite alteration (Titley, 1975). Magnetite, calcite, and albite are also common alteration products in some deposits.

The porphyry deposits of British Columbia were classified on a morphological basis by Sutherland–Brown (1976), who recognized three distinctive types of deposits: phallic, volcanic, and plutonic. The phallic type basically corresponds to the classic model of Lowell and Guilbert, while the volcanic type shares many similarities with the island-arc deposits of the Southwest Pacific. Characteristics of the British Columbia volcanic-type deposits include shallow depth of formation, volcanic host rocks of marine origin, presence of linear, fault-controlled breccias, and a patchy, asymmetric pattern to alteration and mineralization.

The plutonic type of deposit is typified by the Highland Valley District of southern British Columbia. These porphyries develop within zoned, batholith-sized plutons emplaced into consanguineous volcanic rocks. In section, the host plutons typically are broad, flat, mushroom-shaped bodies concentrically zoned from a mafic border to a felsic interior. Individual ore bodies tend to occur in a central position around the perimeter of the interior felsic phase.

Mineralization in the plutonic-type deposits often occurs in regular-spaced veins developed in several stages. Alteration generally occurs as vein envelopes superimposed on broad, pervasive alteration patterns. Mineral zoning often consists of a bornite-rich core surrounded by a chalcopyrite zone, which grades outward to a pyritic perimeter. Molybdenum is a common ore constituent, but it does not generally exhibit a clear systematic zoning pattern.

C. Porphyry Deposit Ore Genesis Models

The major goal of existing genetic models is to describe the source of the metals and ore-bearing fluids, the origin of observed alteration patterns, and the cause of stockwork fractures and veins. Current models designed to explain these features generally fall into two broad categories,

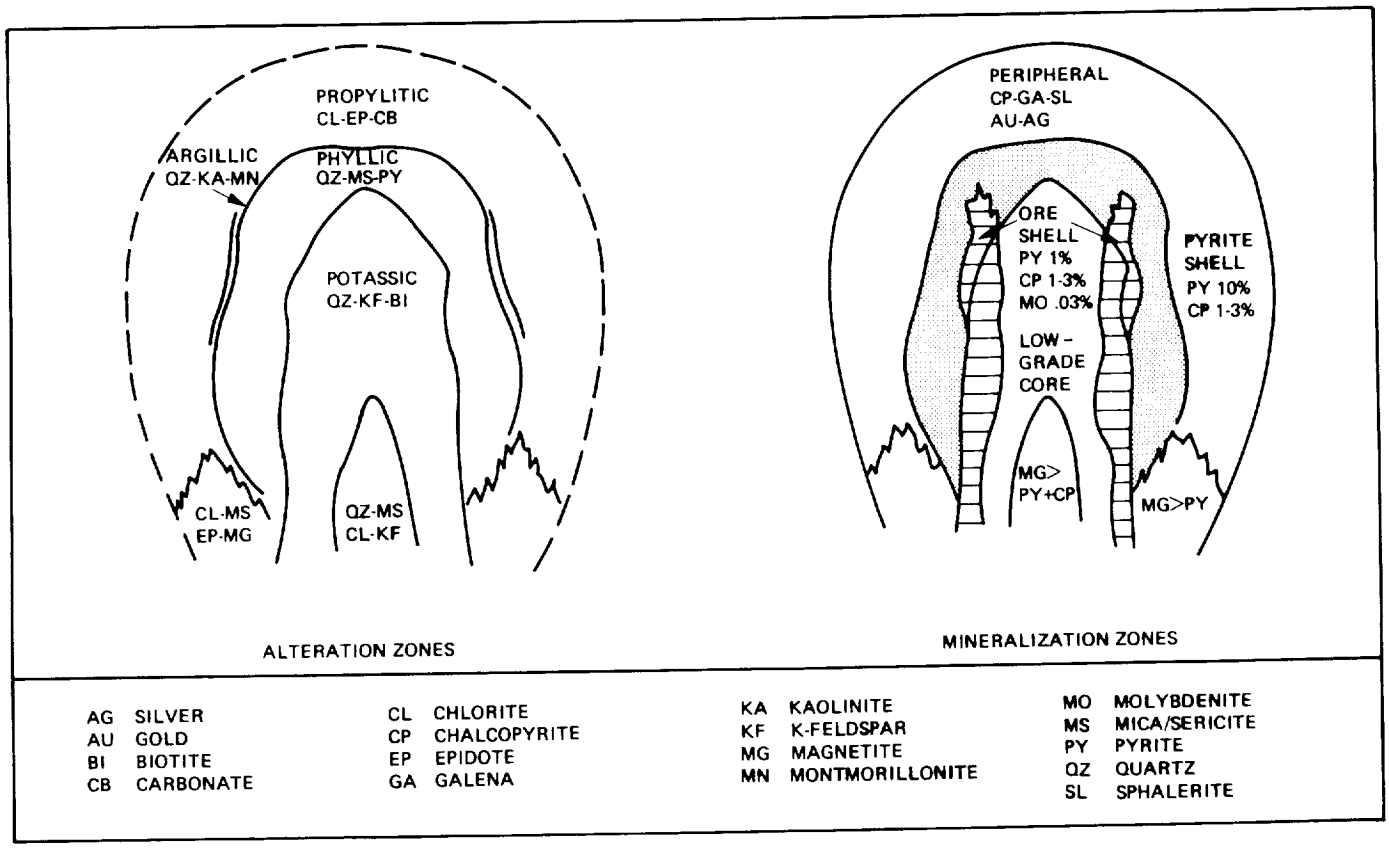

Figure 3-2. Idealized cross-sectional views of alteration zoning and mineralization zoning for the southwestern U.S. porphyry copper deposits (Lowell and Guilbert, 1970)

depending on the role of magmatism in the ore-forming process: the orthomagmatic group and the groundwater convective group (Henley and McNabb, 1978).

The orthomagmatic model stems from pioneering studies of alteration at Butte, Montana (Meyer and Hemley, 1967; Sales and Meyer, 1948). The model was further developed and described by other workers, including Lowell and Guilbert (1970) and Rose (1970). The orthomagmatic model is essentially a closed system in which a separate aqueous phase evolves from a cooling pluton. Emplacement of the pluton into a relatively shallow crustal level results in a sudden pressure drop, with consequent retrograde boiling and intense hydrofracturing by the exsolved fluid phase. Alteration zoning results from a decrease in the K^+/H^+ ratio upward and outward in the convecting hydrothermal system. The result of this physiochemical environment is the deposition of anhydrous K-bearing minerals, such as biotite and K-feldspar, in the interior of the deposit, and hydrous minerals, such as sericite, in the outer envelope of the system.

The convective models of porphyry copper formation have been developed rather recently from mathematical modeling of the fluid dynamics associated with a cooling pluton (Gerlach et al., 1975; Norton, 1978). In contrast with the orthomagmatic models, the intrusive body assumes a more passive role as a heat engine and a source of the metals. The hydrothermal fluids are considered on the basis of isotopic evidence to be groundwater entrained by the advancing magma column to form a large cylindrical convective system in the cupola of the pluton. The convecting meteoric water dissolves metals from the pluton and re-precipitates them at cooler and shallower levels.

A variant of the convection theory proposed by Henley and McNabb (1978) combines features of both types to explain hydrothermal zoning patterns. Their model takes advantage of the isotopic and fluid inclusion evidence for two independently evolved fluids in porphyry deposits—a low-temperature, meteoric fluid responsible for the outer phyllic, argillic, and propylitic zones, and a denser, high-salinity fluid developing the potassic core. A buoyant mag-

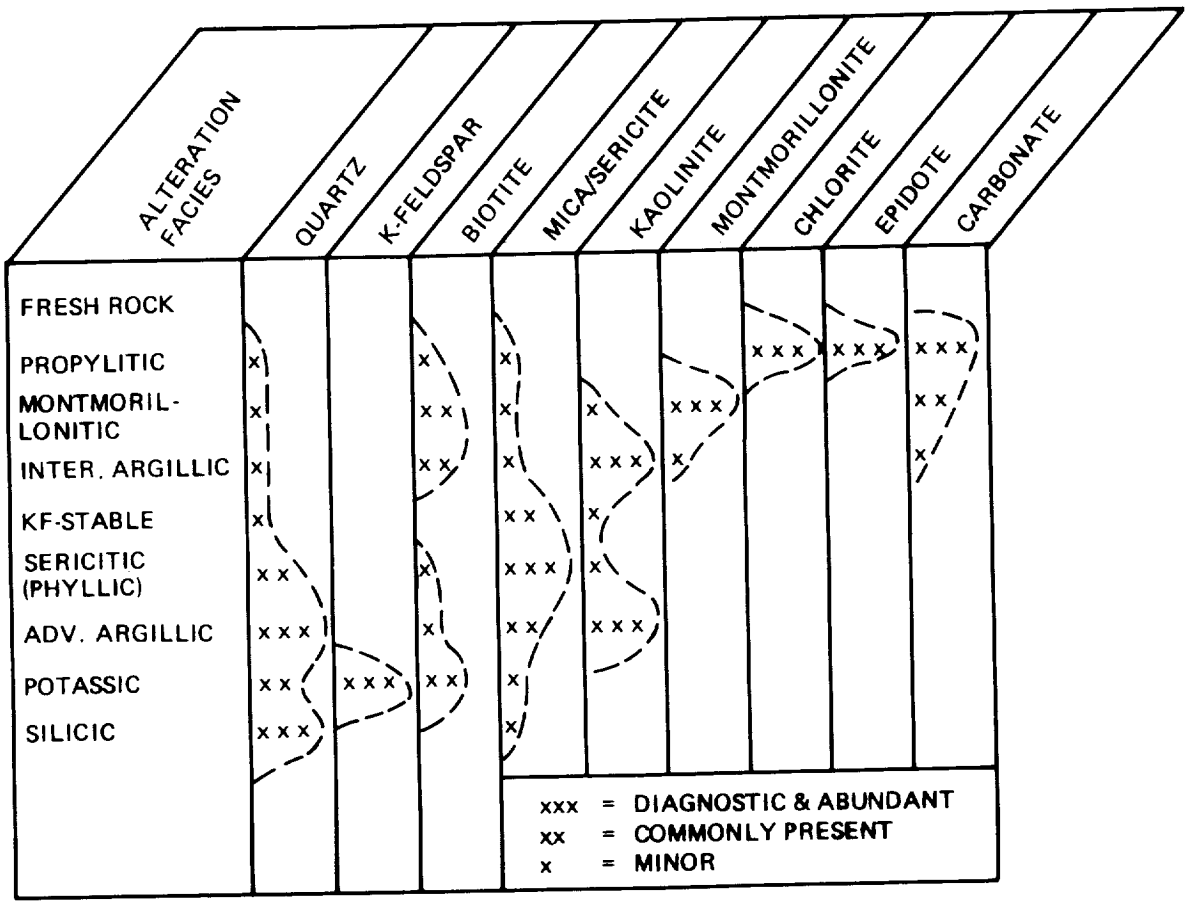

Figure 3-3. Mineralogy of alteration facies for porphyry copper deposits

matic vapor plume carrying the ore metals penetrates and interacts with a separate groundwater system in the cupola region of the pluton. Metal deposition occurs in the zone of mixing and dispersion between these two fluid types, in a region of temperature, salinity, f_{O_2}, and pH variations.

A plate tectonic model proposed by Sillitoe (1972) relates the formation of porphyry deposits to concepts of the new global tectonics. According to Sillitoe's model, porphyry deposits are formed when the oceanic crust partially melts along subduction zones at the elongate compressive junctures between lithospheric plates. The ore metals are derived from the mantle at mid-oceanic spreading centers and transported laterally to the subduction zones as basaltic lava and pelagic sediments. The oceanic plate is thrust downward into the mantle along a dipping Benioff Zone. Partial melting of the oceanic slab creates calc-alkaline magmas, which rise diapirically into the overlying continental crust. Crystallization of these magmas generates a metal-rich fluid phase that is concentrated to form a cylindrical ore body along the lines of the orthomagmatic and convective models.

Sillitoe's plate tectonic model illustrates certain aspects of porphyry copper deposits, such as their episodic distribution and concentration along parallel, linear belts. The theory is especially applicable to the Southwest Pacific island-arc deposits and the South American Cordilleran deposits. However, the model does not provide a completely satisfactory explanation for all porphyry deposits, particularly those in the western United States, where a direct link with plate tectonic activity is more obscure. The presence of flat-dipping and imbricate subduction zones in the western United States, as postulated by Lipman et al. (1972), may provide a partial explanation for the more diffuse and apparently random temporal distribution of porphyries in the western United States.

D. Remote Sensing Characteristics

An examination of porphyry copper genesis models, with consideration of the remote sensing techniques available, allows identification of possible remote sensing characteristics applicable to this study. The Lowell–Guilbert com-

posite model of a typical porphyry copper deposit is presented in Table 3-1. Also listed for each entry are ratings of which characteristics might be detectable by remote sensing.

A few characteristics are definitely detectable (2). Faults controlling emplacement and geometry of the ore body can be recognized using remote sensing image data. Different scales and resolution characteristics of the data allow rec-

Table 3-1. Porphyry copper deposit model and remote sensing characteristics[a]

Rock Type	Characteristics	Remote Sensing Possibility[b]
Preore host rock	1. Precambrian–Late Cretaceous sediments and metasediments	1
Igneous host rock	2. Quartz monzonite stock	1
	3. 65 m.y.a.	0
	4. Northeast and northwest faults controlling structures	2
	5. Elongate, irregular shape	1
	6. 1230 by 1850 m	1
	7. Passive emplacement	1
	8. Stocks more prevalent than dikes	1
	9. Intrusion sequence: diorite–quartz, monzonite–quartz porphyry	1
	10. All rocks mineralized	1
Ore body	11. Oval, pipelike shape	1
	12. Boundaries–original and postore	1
	13. 70 percent in igneous host	0
	14. 1075 by 1850 m	1
	15. Grade: 0.80 percent copper, 0.015 percent molybdenum	0
	16. 770 m extent beyond ore	1
Hypogene alteration	17. Peripheral zone: chlorite, epidote, skarn	1
	18. Outer zone: chlorite, epidote, calcite	1
	19. Intermediate zone: quartz, kaolinite, sericite	2
	20. Inner zone: quartz, sericite, pyrite	2
	21. Innermost zone: quartz, K-feldspar, biotite, sericite	2
	22. Zoning sequence, from center: potassic, phyllic, argillic, propylitic	1
	23. Peripheral zone: galena, sphalerite, silver, gold	0
Hypogene mineralization	24. Outer zone: pyrite, galena, sphalerite	0
	25. Intermediate zone: pyrite, chalcopyrite, bornite	0
	26. Inner zone: pyrite, chalcopyrite, molybdenite	0
	27. Innermost zone: pyrite, chalcopyrite, molybdenite	0
	28. Zoning sequence from center: (chalcopyrite, molybdenite), pyrite (galena, sphalerite, silver, gold)	1
	29. Peripheral zone: veins	0
Occurrence of sulfides	30. Outer zone: veins and veinlets	0
	31. Intermediate zone: veinlets	0
	32. Inner zone: veinlets, disseminated	0
	33. Innermost zone: disseminated	0
Breccia pipes	34. Present and mineralized	1
Crackle zone	35. Present	1
Supergene sulfides	36. Chalcocite more prevalent than covellite	0

[a] Model from Lowell and Guilbert (1970).

[b] 0 -- Unlikely to be detectable
1 – Possibly detectable
2 – Definitely detectable

ognition of structural features of different size and extent. These range from regional systems visible in Landsat and Seasat data, to district faults and fractures visible on moderate-resolution aircraft scanner data and aerial photographs, to small faults, fractures, and dikes visible on high-resolution images. Integration of these data allows synthesis of a structural model showing regional stress patterns and local control of ore geometry. Hypogene alteration patterns should be detectable, based on spectral characteristics of associated mineral assemblages. Hydrous minerals (sericite, kaolinite, montmorillonite, and alunite) have distinct spectral absorption bands in the 2.0- to 2.4-μm wavelength region (Figure 3-4). Silicified materials show fairly distinctive thermal behavior. They have high densities, conductivities, and thermal inertia. It should be possible to discriminate the presence of these phases and, with sufficient spectral resolution, to identify several of them.

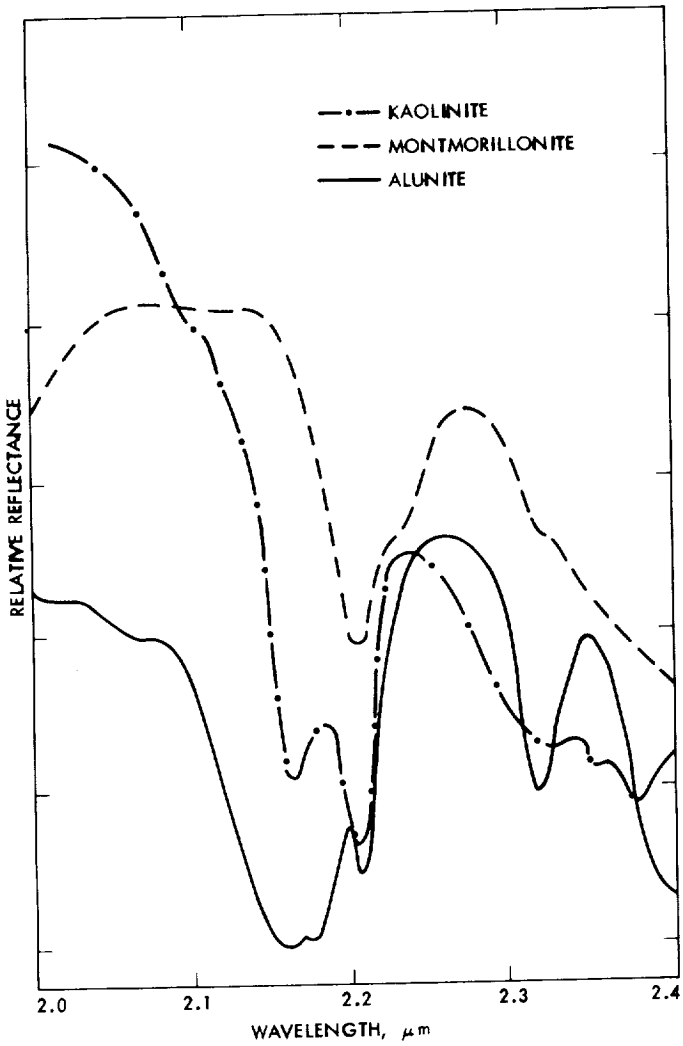

Figure 3-4. Laboratory spectra of selected hydrous minerals illustrating distinct absorption bands in the 2.0- to 2.4-μm wavelength region

A large number of characteristics fall into the category of possibly detectable (1). In some cases, some aspect of the characteristic may be detectable, or at least inferences may be made from remote sensing data as to its presence. In Table 3-1, characteristics 1, 2, 9, and 10 concern general lithologic mapping abilities. Rock-type discrimination and separation depend on many factors: spectral reflectance characteristics, geomorphological appearances, thermal behavior, radar backscatter characteristics, vegetative cover, etc. Insofar as there are local differences between units reflecting any of these parameters, rock types may be separable. Characteristics 5, 6, 7, 8, 11, 12, 14, 34, and 35 depend on many factors; the most important are rock-type contrast and adequate spatial resolution. Recognition of stocks, dikes, breccia pipes, and crackle zones is primarily resolution dependent. Given enough spatial resolution detail, a skilled photointerpreter, using conventional techniques, can probably recognize these features. The dimension of the host rock and ore body obviously are controlled by exposure and erosion level. In the best cases, the two probably could not be separated, although the combined presence may be recognizable based on spectral differences and other photogeological criteria. Zoning sequences of hypogene alteration and mineralization might be inferred by recognition of individual zones. Pyrite zonation may be detectable by analyzing the spectral characteristics of its oxidized by-products (limonite, jarosite, hematite, and goethite), and by estimating the amount of oxides exposed at the surface. Again, level of erosion obviously is a major controlling factor.

Characteristics that are not detectable (0) include age of the deposit, percent of ore in the host rock, grade of ore, and mineralogical composition and habit of ore minerals and sulfides. These minerals are too sparse in the rocks to produce distinctive spectral features; the difference between veins–veinlets and disseminated sulfides requires handlens or microscopic examination to determine.

II. Background and Site Selection

A. Background

Nonrenewable resource exploration is a complex and costly undertaking, requiring the use of as wide a range of tools as is feasible. Remote sensing represents one such tool, which can be used at several stages in the exploration process. In the past, Landsat Multispectral Scanner (MSS) images and aerial photography have been the most frequent types of data used, mainly in the early reconnais-

sance phases of an exploration project. These data are not the best available because they are not specifically designed for geologic purposes. Several experimental sensors were available through NASA to apply to problems and determine whether improvements could be made.

Areas of known copper mineralization offered several attractive features as prospective test sites for evaluating the geologic utility of more advanced types of remote sensing techniques. A model for the genesis of ore bodies was fairly well developed and understood, allowing potential remote sensing characteristics to be identified and used as guides for processing and interpreting data. The southwestern United States is one of the great copper provinces of the world; consequently, appropriate test sites were numerous and representative of this type of deposit. Many Geosat companies were actively involved in porphyry copper exploration and mining, so that industry expertise and involvement were assured.

B. Site Selection

1. General criteria. The Porphyry Copper Test Site Committee met in 1977 to select three test sites for the Project. The overriding criteria for site selection were:

(1) The site must be typical of porphyry copper deposits. This implied the presence of a mineralized and mineralizing intrusive body, alteration zones, and known copper mineralization.

(2) The site must be well exposed. Vegetation cover should be minimal, providing good outcrop exposures. This was necessary to simplify interpretations of image patterns and to provide the optimal and ideal starting point for a remote sensing study. At a future time, more vegetated sites might be examined after the fundamental characteristics of the deposits were determined.

(3) Cultural disturbance must be minimal. This implies the converse – that most of the characteristic features were visible and not terribly disturbed. However, due to the size of a porphyry copper hydrothermal system, even the presence of open-pit operations, mills, concentration tanks, etc., would not necessarily eliminate a potential site from consideration.

(4) Land ownership must not be a problem and, preferably, the site would be owned by a Geosat member company. Ownership would provide easy ground access and cooperation of the company geologists and other experts. Land ownership was crucial to avoid problems that might arise as a result of the remote sensing work. Should new target areas be discovered during the study, problems with public disclosure, land plays, and other undesirable scenarios would be avoided.

(5) Adequate background information must be available. Such things as geological, alteration, structural, geophysical, and soils maps should have already been completed for the site. In addition, reports on the geology, mineral occurrence, etc., should also be available. Selecting an existing, developed mineral deposit would greatly increase the probability of this material existing; having the site owned by a Geosat member company would enhance the possibility of accessing company proprietary information.

(6) The sites must provide a variety of occurrences of copper deposits with different levels of erosional exposure. It was hoped that sites could be found that were moderately to deeply eroded, allowing study of all the alteration zones and the intrusive. Deposits that were only slightly eroded and more poorly exposed were considered as well, since these deposits present a more realistic analog of those found in current frontier exploration areas.

2. Specific criteria of selected sites. Eight to ten candidate sites were nominated for consideration. These were narrowed down, and three final sites were selected: Silver Bell, Helvetia, and Safford (Figure 3-5). All three sites are located in southern or southeastern Arizona.

The Arizona copper province was chosen because deposits there are typical of porphyry copper deposits. This region is one of the major copper-producing regions of the world. Sites in this area were readily accessible, and exposures were excellent due to the semiarid climate. In addition, more research on copper mineralization had been done in this area than in any other.

The characteristics of the three sites selected met the original criteria. Silver Bell is a large, producing porphyry copper deposit located northwest of Tucson and is owned by the American Smelting and Refining Company (ASARCO), a Geosat member. This deposit is considered a classic porphyry copper. There has been considerable study of the deposit over the last 70 years, ranging from masters' theses to ASARCO geological and alteration mapping. The deposit has been eroded fairly deeply, exposing all the alteration zones associated with porphyry copper deposits. These range from intense potassic zones at the center to pervasive, weak propylitic zones at greater distances. A wide range of rock types outcrop in the area, occurring as both altered and unaltered facies. Rock types are dominantly

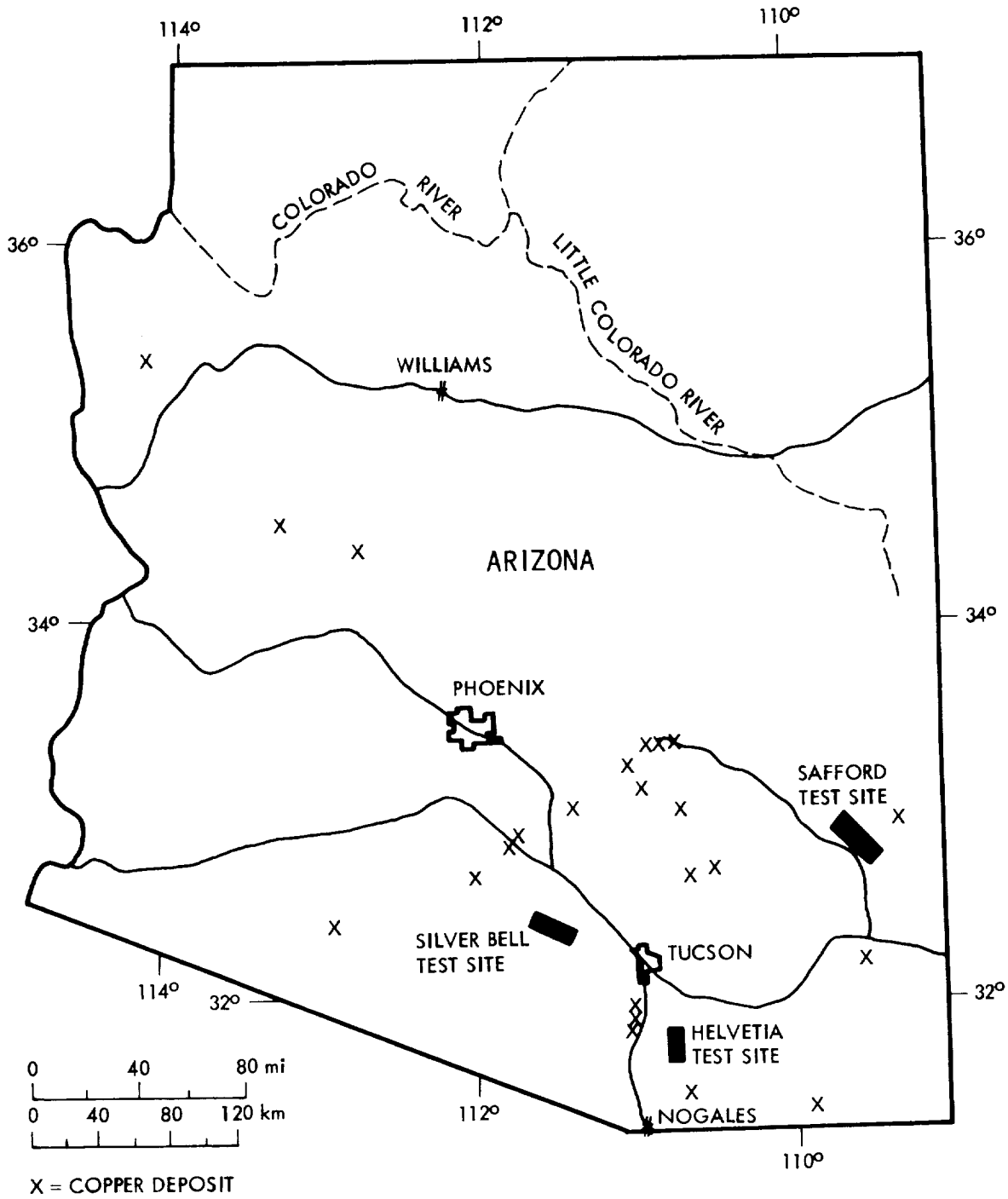

Figure 3-5. Locations of porphyry copper test sites in Arizona; other copper deposits shown with X

intrusive and extrusive igneous rocks, with sedimentary limestone and sandstone also represented. Vegetation cover is scant, except in drainages where it is quite heavy. Two large open-pit mines currently operated by ASARCO attest to the presence of economic quantities of ore.

The Helvetia deposit is located south of Tucson in an old mining district. This site was selected for several reasons: a different suite of rock types is present, dominated by Paleozoic and Mesozoic sedimentary rocks and Cretaceous volcaniclastic assemblages. The ore body is also buried; surface indicators were the alteration (argillic and pyritic) of the country rock and the presence of calc-silicate skarns and marbles associated with alteration of limestones. The area is structurally complex, has moderate to severe topographic relief, and has moderate vegetation cover. Mining activities are limited to several old shafts, and exploratory drilling being conducted by the present owners, AMAX, a Geosat member.

The Safford District is located east of Tucson, near the New Mexico border. The area has four known porphyry copper deposits, one of which has been mined by open-pit methods. The other three have been explored and outlined with drilling in preparation for mining. These three deposits are deeply buried, with only minor outcrops of the mineralizing intrusive showing at the surface. Surface alteration is mainly limited to the outer zones of a typical porphyry copper deposit—propylitic alteration is pervasive, with minor shows of quartz–sericite alteration along veins. Mainly volcanic rocks of both premineral and postmineral affinities are exposed in the district. The ore bodies are hosted by the intrusives and postmineral volcanics. Structural control of the ore bodies has long been considered a major exploration parameter, but extensive postmineral cover makes these deposits difficult exploration targets. Minimal vegetation cover due to the semiarid climate and minimal cultural disturbance made the site attractive for study. Access to one of the deposits was made available by Phelps Dodge Corporation, a Geosat member. Additional information about the other deposits was made available through Kennecott Copper Corporation.

Overall, the selection of these three sites presented excellent opportunities to test remote sensing for porphyry copper exploration. A wide range of rock types was available for improving lithologic mapping capabilities. Various levels and degrees of alteration were exposed for examination. Silver Bell, the best exposed, offered the opportunity to study all the zones of the alteration system. Safford, the poorest exposed, most closely represented the type of area that is currently the focus of exploration interest. The proximity of the sites to each other facilitated logistical arrangements for fieldwork, allowing all three sites to be visited in a single trip if desired.

III. Summary of Previous Work

Previous remote sensing applications for copper exploration have covered a wide range of subjects. Readdy (1978) conducted a comprehensive study of the application of photogeologic analysis for porphyry copper and hydrothermal alteration in arid and semiarid environments. He primarily examined aerial photography, but also used a limited number of radar and single-band Landsat MSS images for several porphyry copper deposits, including Safford. Readdy concluded that several features characteristic of porphyry copper deposits were well defined in his photographs. These features included the zone of crackle breccia related to mineralization, the limonite-stained leached capping, and sometimes the surrounding alteration zones. Less well defined were igneous intrusives and structural settings. Readdy's conclusions from the study of Safford were (1) the best results for mapping regional features were obtained from analysis of Landsat images; (2) radar images and high-altitude aerial photographs were similarly useful for reconnaissance studies of district scale features; and (3) large-scale aerial photographs were useful for detailed mapping of lithology, structure, alteration, and anomalous zones. He recommended that explorationists use the various scales of images available for photogeologic analyses.

One of the first applications of Landsat MSS data was to make structural studies by interpreting lineaments from images, then to attempt to relate these features to known structures, and finally to determine unrecognized structures by inference. Three studies illustrate this application. Ramos (1977) examined the mineral potentials of basement cratonic areas in South America on the basis of mechanical analyses of their tectonic framework. Favorable targets based on tensional release were selected through the application of different deformational models and the identification of the stage and type of deformation. Correlations with geophysical data strengthened the interpretations and led to several successful mining exploration programs.

In a similar study, Kuosmanen (1977) examined Landsat MSS data in Finland in conjunction with geophysical maps. He found that several regional lineaments appeared to correlate with the distribution of ore deposits and mineral showings (specifically nickel, iron, and copper–lead–zinc mineralization). Extraction of the maximum amount of information required the combined study of seasonal

Landsat data with interpretation of geological, geophysical, and geomorphological maps.

Wilson (1975) studied the geologic framework of porphyry copper deposits on Landsat MSS images. He used non-computer-enhanced bulk data at scales from 1:1,000,000 to 1:250,000 to perform lineament and circular feature extraction. The areas examined included the regions of Ray, Arizona; Ely, Nevada; Ok Tedi, New Guinea; Silverton, Colorado; and Tanacross, Alaska. Wilson was able to recognize many new linear and circular features not previously shown on published maps. Circular features seemed to be related to intrusive or volcanic phenomena, such as caldera structures. Linear features not correlated with existing mapped faults were not field checked, so they could not be validated. A general conclusion Wilson reached is that the images *by themselves* are not useful for mineral exploration. Rather, other data must be combined with the images to remove ambiguity. The main advantages of the Landsat data were (1) synoptic viewpoint, (2) extrapolation of favorable known mineral provinces or structures, (3) detection of intrusions in structurally simple environments, and (4) drainage maps in remote, poorly mapped regions.

Landsat MSS data have also been used to characterize the anomalous iron-oxide coloration often associated with porphyry copper deposits. Schmidt (1976) used computer-processed data to identify features that were indicators of sulfide-bearing rocks for an area in Pakistan. Two approaches were used: in the first approach, false-color composites were examined visually to locate areas similar in appearance to a control area of known mineralization; in the second approach, computer classification algorithms were used to identify unknown areas with similar spectral features to the control area. In the first experiment, seven areas were selected for further work. Field checking three of these failed to confirm mineralization; the others were not checked. The computer-classified image outlined 23 target areas; field checking nine of these revealed that five contained hydrothermal alteration, with pyrite and limonite present at the surface. The 14 false alarms were not described, so there is no way to determine the cause of the misclassification. The supervised classification technique seems to have been using the spectral characteristics of iron-oxide materials (Figure 3-6) and bleaching associated with the known ore body to locate similar areas elsewhere.

Krohn et al. (1979) evaluated computer-processed Landsat MSS ratio images to distinguish hydrothermally altered rocks associated with porphyry copper and disseminated gold deposits along the Battle Mountain–Eureka mineral belt in Nevada. Detection of altered rocks was based on the distinctive spectral reflectance of limonite. The pattern of limonitic rocks depicted on the images closely agreed with mapped alteration at the Copper Canyon and Copper Basin deposits. The disseminated gold deposits were poorly represented due to the absence of limonite. Other limonitic but unaltered sedimentary and volcanic rocks presented the largest obstacle to discriminating altered rocks in this area. *In situ* reflectance spectra indicated differences between altered and unaltered rocks in the 1.0- to 2.5-μm spectral region, which would remove this ambiguity.

The combined use of Landsat MSS data for structural information and for alteration mapping was reported by Raines (1978). He analyzed data for the porphyry copper province in northern Sonora, Mexico. The regional tectonic pattern was interpreted to consist of NNE-trending features related to Precambrian structures, NNW-trending lineaments related to Basin and Range faults, and lesser features with N–S and WNW trends. Areas of limonitic rocks were outlined on the images using computer-enhanced ratio composites as the principal base. Seven areas were selected on the basis of favorable structural setting and presence of limonitic materials. Geophysical and geochemical surveys further clarified the nature of the targets. One was selected for exploratory drilling. Preliminary results suggest the discovery of a major hydrothermal system with potential economic copper, lead, silver, and barite reserves.

A final illustration of the use of Landsat MSS data for copper exploration was reported by Bolviken et al. (1977). They examined the effect of naturally heavy-metal poisoned vegetation on Landsat images for an area in Norway. A training area was selected where copper poisoning was known to occur, resulting in barren areas in the birch–pine forest or in a change in the ground-cover vegetation community. Supervised classification algorithms were used to identify other possible copper-poisoned areas. Fieldwork was planned to check these areas to assess the success of this technique.

Several studies have presented results of analysis of multispectral aircraft scanner data for alteration detection and mapping. In an early report, Abrams and Siegal (1976) examined 24-channel aircraft data over Red Mountain, Arizona, a porphyry copper deposit. These data were supplemented with field reflectance measurements. Contour maps produced from spectrometer data using the 1.6/2.2-μm band ratio clearly delineated the alteration associated with the deposit. This was attributed to the presence of clay minerals associated with the altered rocks (Figure 3-6). Band-ratio images produced from the aircraft data allowed discrimination of the limonitic altered rocks from unaltered rocks.

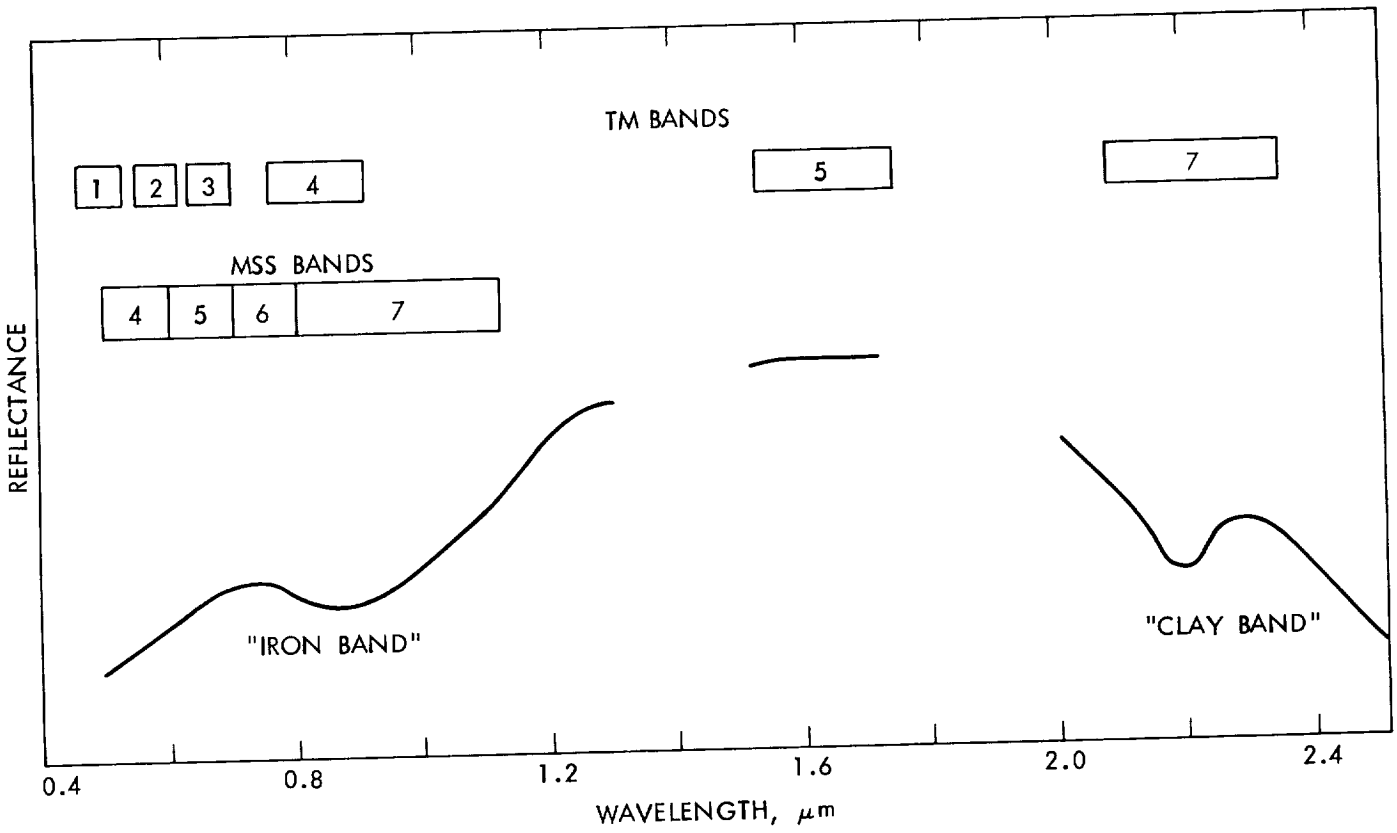

Figure 3-6. Diagrammatic field spectrum illustrating positions of diagnostic iron and clay absorption bands. Also shown are bandpasses of the Landsat MSS and TM sensors.

Two similar studies reported the use of Thematic Mapper Simulator data for alteration mapping. This aircraft scanner has the same bands that are available on Landsat 4, launched in July 1982. In the Cuprite, Nevada District, Abrams et al. (1977) used color ratio composite images to map alteration zones in an area of bleached, solfatarically altered rocks. Abrams et al. were able to separate opalized rocks, silicified rocks, opalized rocks with limonite, and hematitic deuterically altered rocks. Band ratios were selected to enhance mineralogical spectral characteristics related to alteration assemblages. The band-ratio 1.6/2.2 μm enhanced the presence of hydrous/clay minerals; another ratio, 1.6/0.48 μm, brought out the presence of iron-oxide minerals (Figure 3-6). A third ratio, 0.6/0.83 μm, was chosen to separate bleached rocks. This same ratio scheme was used by Prost (1980) for an area near Battle Mountain, Nevada. Clay-rich, nonlimonitic altered rocks were discriminable on the aircraft images, but they were not separable using Landsat MSS data.

Finally, a statistical study of porphyry copper characteristics was reported by DeGeoffroy and Wignall (1972). They tabulated 170 geological characteristics for 58 commercial deposits from the Cordilleran Belt. These data were processed using characteristic analysis to extract the 44 most typical characteristics of the deposits. Regression and classification formulas were then used to correlate these characteristics to the gross dollar value of the deposits. These results were used to rate objectively several porphyry prospects. The 10 most important characteristics were phyllic alteration, passive intrusive implacement, regional fault control, K-biotite alteration, propylitic phase mineralization, presence of hornfels aureole, disseminated sulfides and veinlet sulfides, argillic alteration, and granitoid phase mineralization.

IV. Comparative Analysis of Test Site Results

The three test sites were selected according to both their similarities and differences. Silver Bell and Safford represent classic porphyry copper deposits, differing mainly in their level of erosional exposure. Therefore, the features exposed at the surface—alteration assemblages and structural control—were alike. Helvetia represented a somewhat different environment since it consisted of a mineralized section of carbonate rocks with only limited exposures of phyllic, propylitic, and argillic alteration.

Instead, skarn alteration and hematite development from pyrite were the dominant features. Techniques that were successful at Silver Bell were also successful at Safford. The same applications were less successful at Helvetia due to the rock and alteration differences.

Landsat Multispectral Scanner (MSS) data provided some information on alteration at all three sites. Using a color ratio composite of band-ratios 4/5, 5/6, and 6/7, areas with iron oxides present at the surface are identifiable. These areas include both altered rocks and iron-rich unaltered rocks (such as red beds). This technique was originally developed by Rowan et al. (1974) and has proven repeatable in any arid or semiarid environment. The limited spatial and spectral resolution of the Landsat MSS data made separation of rock types difficult. The Landsat wavelength bands are both too broad and at nonideal positions for separating many geologic materials. In addition, the 80-m resolution is too coarse for resolving small targets, such as dikes and small outcrops.

The aircraft Modular Multispectral Scanner (M^2S) 11-channel data, with better spectral and spatial resolution than Landsat, provided a worthwhile comparison of what improvements in both of these characteristics could be provided. At all sites, smaller outcrops and features could be discriminated due to the 18-m resolution. The presence of several wavelength bands in the 0.7- to 1.0-μm region allowed apparent separation of hematitic versus goethitic/limonitic materials at both Helvetia and Safford. This ability is important for explorationists since the two forms of iron oxides often come from different sources and can provide mineralogical information about alteration assemblages. For instance, at Helvetia the large hematitic area is a result of the weathering of pyrite to hematite. The pyrite is an alteration product, probably associated with the deposition of the ore body.

The high-resolution aerial photographs were useful at Safford and Helvetia for mapping fine drainage patterns and delineating anomalous patterns of geologic interest. At Safford, a drainage anomaly lies over the Dos Pobres intrusive and ore body and is probably due to the fracturing of the buried intrusive being expressed at the surface. At Helvetia, the altered arkoses show a finer drainage pattern than surrounding rocks and can be separated according to their texture and color differences. The inappropriate spectral sensitivity of color photography provides little color contrast between rock types. Only a few different units can be separated, based only on tonal differences. The addition of textural information permits separation of a few more units; however, this type of data only has the advantage of high spatial resolution compared to the multispectral scanner data analyzed. As such, small features like dikes are discriminable.

The radar data examined were moderately useful at some of the sites. The major limiting factor (at Silver Bell and Safford) of the X-band data was the poor quality of the data. This precluded a fair assessment of the utility of this kind of data for geologic applications at the copper sites. Seasat data were processed and examined at Silver Bell and Safford. At both sites, lithologic discrimination was minimal and limited to separation of bedrock from alluvium. Regional structural features, however, were well expressed on the Seasat images and provided a worthwhile complement to the Landsat MSS structural information.

The thermal data were of equal use at all three sites. In general, some separation of rock types was possible, although never as much as could be obtained using the other multispectral data types.

The single most useful data set over all the test sites was the NS-001 Thematic Mapper Simulator data. Discriminant function analyses performed on the field reflectance data simulating the Landsat 4 Thematic Mapper (TM) bands and a conceptual 30-channel instrument (30 equally spaced bands 0.05 μm wide) indicated that the TM bands were well chosen for separating the rock types at the copper sites. A summary of these analyses is presented in Table 3-2.

Table 3-2. Results of discriminant function analyses: Landsat 4 TM versus 30 $\Delta\lambda$

Test Site	Center Band Wavelength, μm	
	Landsat 4	30 $\Delta\lambda$
Silver Bell	1.65	1.60
	2.22	2.15
	0.48	0.50
	0.56	0.55
	0.66	0.70
	0.83	0.60
Helvetia	0.48	0.50
	0.66	0.70
	1.65	1.70
	0.56	2.30
	0.83	2.20
	2.22	2.05
Safford	2.22	2.15
	1.65	2.20
	0.83	0.50
	0.56	2.05
	0.66	0.90
	0.48	1.55

The table lists the order of selection of the six Landsat 4 bands and the first six bands of the 30 equally spaced bands. The Silver Bell analysis exhibits a nearly one-to-one correlation in both the order of band selection and the particular bands selected. From a statistical standpoint, the TM bands are ideally chosen for discriminating the suite of altered and unaltered rocks sampled at Silver Bell. The Helvetia analysis shows similar behavior for the first three bands (the most important selected by the discriminant function program). A somewhat poorer correlation exists for the Safford analysis; however, the 2.2-, 0.5-, 0.9-, and 1.55-μm regions were selected in the 30-$\Delta\lambda$ analysis as the most important. These channels fairly closely match some of the channels of the TM.

The results of analysis and interpretation of the image products substantiate the statistical analysis. Again, the NS-001 Thematic Mapper Simulator data were the most useful for separating and discriminating the geologic units found at the three test sites. A consistent ability of these data was in delineation of areas of alteration. At Silver Bell, potassic, phyllic, and propylitic alteration zones were separable; at Helvetia, argillic and skarn zones were separable; at Safford, propylitic and phyllic zones were separable. The presence of wavelength bands in the region of iron-oxide and clay-mineral absorption features was critical for this success.

General rock-type separation was also successful using the NS-001 Thematic Mapper Simulator data. Although the statistical analyses using the discriminant function algorithm seemed to indicate that more bands would provide improved separation, image analysis showed that the wavelength regions of the bands were more important. At Silver Bell, all the mapped geologic units were separable using a number of processing algorithms (including ratio products or canonical transform images). At Helvetia and Safford, the canonical transform images provided the best visual separation of the units, although the ratio images proved useful. This indicates that the separability of the units is an inherent feature of the spectral information provided by the data and is less dependent on the processing algorithm. A detailed comparison at Silver Bell of images produced from several algorithms supports this conclusion.

V. Extrapolation to Similar and Different Environments

Remote sensing deals primarily with discrimination rather than identification. There are only a few minerals or mineral groups that can be identified from existing remote sensing imaging systems. These include iron oxides, which have characteristic absorption bands between 0.4 and 1.0 μm; certain hydrous minerals, such as clays, alunite, and pyrophyllite, that have absorption bands between 2.0 and 2.5 μm; and some carbonates that also have a strong absorption band between 2.0 and 2.5 μm. Some other materials can be identified according to albedo and geomorphic features. These include basalt flows and playa lakes: basalt flows are extremely dark in all bands between 0.4 and 2.5 μm; playa lakes are very bright. Surface forms and drainages provide additional information which permits identification of these materials. With the exception of these few materials, however, most rock types cannot be identified. Rather, the result of image processing of remote sensing data is to produce images that provide separation of different units by allowing an interpreter to draw boundaries around similar-looking areas and contacts between dissimilar units.

Fortunately, in the case of porphyry copper deposits, iron oxides and hydrous minerals are key indicators of hydrothermal alteration zones. At the three test sites, it was possible, using the NS-001 scanner data, to identify the presence of these minerals and, therefore, infer possible alteration. This requires no *a priori* information—merely adequate exposures of surface materials and outcrops. If these sites had been unknown targets, i.e., no ancillary information was available except that the region was favorable for finding porphyry copper mineralization, the three deposits or districts would have been identified as promising areas for further work. The remote sensing data would have provided an excellent reconnaissance tool for targeting possible favorable exploration sites.

The use of moderate resolution, large coverage data such as Landsat, and a model for how and where porphyry copper deposits occur would provide some information for selecting favorable regions. The southwestern United States is a known porphyry copper province. Structural analysis of Landsat data can provide a regional perspective of the tectonic pattern and point to favorable structural settings for exploration (an excellent case history has been reported by Raines, 1978). Once targets have been selected, processing image data to identify areas with iron-oxide and hydrous minerals present delineates smaller areas for more detailed groundwork.

For the three copper sites, success was achieved in separating many of the rock types present. However, without some type of ancillary information (maps and/or field checking), the interpretations depict remote sensing units that cannot be uniquely identified. Some type of additional data is needed to convert the interpretations to geologic maps. A brief trip to the site, with preplanned traverses,

can provide these data. The images can be used as guides to indicate which areas are important for field sampling. A minimum number of areas need to be visited since the images define the extent of each unit. This can result in a very efficient method for constructing first-level geologic maps of an area.

This study concentrated on arid or semiarid environments, with low to moderate vegetation cover and good outcrops. The degree of success achieved strongly indicates that the techniques described here could be extrapolated to similar environments elsewhere, such as South America, Australia, or Afghanistan/Iran. The problems arising from other types of physiographical and ecological environments are more relief, more vegetation, more soil cover, and less outcrop.

Remote sensing data acquired over areas of moderate to severe relief have problems that make extracting information difficult. The presence of shadowed areas and areas with small horizontal projections introduces atmospheric scattering contributions to the radiance measured by the scanner. To some extent these can be modeled or estimated, then compensated for. However, no method yet devised is entirely satisfactory. The problem of determining the actual spectral response of materials in shadows is still being examined. Severe relief also reduces the horizontal projection of areas the scanner "sees," thus reducing the size of targets being examined and requiring greater spatial resolution than if relief were more moderate.

The spectral response of vegetation is such that, with greater than 40 percent areal coverage, the signature of iron oxides in the 0.4- to 1.0-μm region is masked (Siegal and Goetz, 1977). The effect of increased vegetation cover on the response of hydrous minerals at 2.0 to 2.5 μm was not examined in this study. However, from examination of individual spectral curves, vegetation absorption bands in this region will probably also mask those absorption bands. In general, the increased vegetation cover (more than about 40 percent) will prevent the use of spectral remote sensing data to detect alteration phenomena.

An alternative possibility has been suggested by the work of Collins (1978) and Birnie and Francisa (1981), who have used very high spectral resolution radiometers to detect geobotanical anomalies related to base-metal mineralization. They found that two types of spectral features were associated with vegetation growing on mineralized pyritic ground. One was a shift in the position of the steep increase in reflectance at 0.67 μm; the other was a change in the ratio of reflectances at 0.565 and 0.465 μm. Collins as well as Birnie and Francisa suggest that different types of vegetation can produce spectral anomalies in different parts of the spectral region. More work is necessary before these effects are fully understood. Nevertheless, it does suggest a possible remote sensing method for exploring for copper mineralization in heavily vegetated areas.

VI. Implication for Mineral Exploration in General

The southwestern United States porphyry copper deposits are characterized by several surface features that are common to other types of deposits. These are structural control, hydrothermal alteration zones, and presence of a mineralizing intrusion. The structural control has been documented by other workers and generally consists of preferential areas of crustal weaknesses that provide favorable conduits for upwelling intrusive and mineralizing fluids. These areas contain faults or fractures commonly associated with deep-seated basement structures. Intersections of these features can provide the favorable loci for mineralization. Hydrothermal alteration zones are due to the physiochemical reactivity of magmatic and/or meteoric fluids that are associated with intrusive or extrusive bodies. Circulating fluids change the mineralogy of the country rocks and can produce distinctive and diagnostic assemblages. The zoned alteration sequence developed in association with porphyry copper deposits is a classic example of this interaction. Fluids, often carrying minerals, are generated by and from the intrusive body. Alteration is most intense closest to the intrusion and decreases in intensity away from the intrusion. The presence of an intrusive body can sometimes be directly detected when erosion has exposed the body; it is also possible to detect covered, but near-surface intrusions, by subtle changes in the surface topography, drainage patterns, or fracture patterns.

Many other types of deposits share some or all of these features. The techniques developed in this study should be directly applicable to the deposits that occur in similar climatic zones (arid to semiarid). Using Lindgren's (1933) classification of ore deposits and considering those deposits with similar wall-rock alteration, hypothermal, mesothermal, and epithermal deposits are favorable classes.

Hypothermal deposits form at depths of 3 to 15 km and at temperatures of 300° to 600° C, are associated with deep-seated acid plutonic rocks, and contain ores of gold, tin, molybdenum, tungsten, copper, lead, zinc, and arsenic; alteration includes sericitization in siliceous rocks and chloritization. Examples are gold of Kirkland Lake, Ontario, and Kalgoorlie, West Australia, and tin of Cornwall.

Mesothermal deposits include porphyry coppers. They form at depths of 1 to 5 km and at temperatures of 200° to 300° C, are in or near intrusive igneous rocks, and contain ores of gold, silver, copper, arsenic, lead, zinc, nickel, cobalt, tungsten, molybdenum, and uranium; alteration includes sericitization, argillization, propylitization, and carbonitization. Other porphyry-type deposits are associated with molybdenum, tin, and gold mineralization. The results of this study should be directly applicable to exploration for these types of deposits. Porphyry molybdenum deposits differ from copper deposits only in the dominant ore minerals and in the wetness of the intrusion. As a result, alteration zones are spatially more restricted and often telescoped. Nevertheless, phyllic, quartz–sericitic, argillic, and propylitic alteration zones are common and diagnostic. Structural settings and control are similar, if not identical. The presence of faults and/or fractures acting as conduits and preparing sites for mineralization are characteristic features of porphyry molybdenum deposits. Tin and gold deposits do not develop the intensity of alteration seen at copper and molybdenum deposits. Nevertheless, argillic and propylitic alteration are common and can be looked for.

Epithermal deposits form near the surface and at temperatures of 50° to 200° C, are associated with extrusive or near-surface intrusive rocks, and contain ores of lead, zinc, gold, silver, mercury, antimony, selenium, bismuth, and uranium; alteration includes sericitization, argillization, kaolinization, and dolomitization. Examples are gold of Goldfield and Comstock, Nevada, and silver of Tonopah, Nevada. Previous work at these Nevada locations has demonstrated the power of the TM bands for mapping alteration facies (Abrams et al., 1977). In the Goldfield area, five different types of alteration were separable: intense argillic, silicification, opalization, opalization with iron oxides, and deuteric. These results should be extendable to other vein deposits and epithermal systems where alteration is present.

In addition, some deposits, such as Kuroko massive sulfide deposits, are associated with volcanic-hydrothermal activity on the seafloor. Alteration includes sericitization and chloritization.

Structural control is a general feature of most of the deposits described above. Intrusive and extrusive rocks and hydrothermal fluids are localized in the crust at zones of structural weaknesses, regardless of the type of deposit that may form.

VII. Future Work

Based on the results of the porphyry copper test site project, several areas for further study can be recommended.

The abilities to map alteration zones need to be tested over other porphyry copper deposits in both similar and different environments. The large number of deposits in the southwestern United States offers an opportunity to evaluate the techniques in identical structural, physiographic, and climatic terrains. Deposits in other types of terrains should also be investigated. The semiarid region selected for this study minimized problems due to vegetation cover, extensive soil development, and moderate to severe relief. The success achieved warrants attempts to extrapolate the results in more difficult areas. At the same time, these areas are liable to represent more closely those areas currently being explored in parts of the world outside the United States. In particular, work by other investigators on geobotanical spectral anomalies needs to be aggressively pursued since the majority of the poorly explored parts of the world are heavily vegetated.

A logical extension of this study is to examine deposits of related minerals, such as porphyry molybdenum, tin, and gold deposits. Starting with the study of deposits in arid or semiarid environments, the techniques developed here can be tested for extension to a variety of mineral commodities. Because hydrothermal alteration phenomena are quite similar for a multitude of ore deposits, the success demonstrated in this study should have wide applicability.

The characteristic mineral assemblages produced by hydrothermal events suggest a need for further study and development of instrumentation to perform direct mineralogical identification. The Shuttle Multispectral Infrared Radiometer (SMIRR) experiment is a first step along those lines, demonstrating the capability to identify certain clay minerals directly. Development of an imaging system is the next step in remote sensing technology aimed at mapping alteration phenomena.

References

Abrams, M., R. Ashley, L. Rowan, A. Goetz, and A. Kahle (1977). Mapping of hydrothermal alteration in the Cuprite Mining District, Nevada, using aircraft scanner images for the spectral region 0.46 to 2.36 μm. *Geology, 5*, 713–718.

Abrams, M. J., and B. S. Siegal (1976). *Detection of alteration associated with a porphyry copper deposit in southern Arizona* (JPL Technical Memorandum 33-810). Pasadena, California: Jet Propulsion Laboratory.

Birnie, R., and J. Francisa (1981). Remote detection of geobotanical anomalies related to porphyry copper mineralization. *Econ. Geol., 76*(3), 637–647.

Bolviken, B., F. Honey, S. Levine, R. Lyon, and A. Prelat (1977). Detection of naturally heavy-metal poisoned areas by Landsat-1 digital data. *J. Geochem. E., 8*, 457–471.

Collins, W. (1978). *Airborne spectroradiometer detection of heavy-metal stress in vegetation canopies.* 5th IAGOD Symposium, Snowbird, Utah. (Programs and Abstracts)

DeGeoffroy, J., and T. K. Wignall (1972). A statistical study of geological characteristics of porphyry–copper–molybdenum deposits in the Cordilleran Belt—Application to the rating of porphyry prospects. *Econ. Geol., 67*, 656–668.

Gerlach, T. M., D. L. Norton, and J. E. Knight (1975). Porphyry pluton environments; computed mass transfer for reactions between hydrothermal fluids and sedimentary host rocks. *Econ. Geol., 70*, 1320–1321. (Abstract)

Henley, R. W., and A. McNabb (1978). Magmatic vapor plumes and ground-water interaction in porphyry copper emplacement. *Econ. Geol., 73*, 1–20.

Krohn, D., M. Abrams, and L. Rowan (1979). Discrimination of hydrothermally altered rocks along the Battle Mountain–Eureka, Nevada, mineral belt using Landsat images. *U.S. Geol. Surv. Open File Rep. 78-585.*

Kuosmanen, V. (1977). *Investigation of Landsat imagery on correlations between ore deposits and major shield structures in Finland* (Final Report, Landsat Follow-on Investigation 28-600). Greenbelt, Maryland: Goddard Space Flight Center.

Lindgren, W. (1933). *Mineral deposits.* New York: McGraw–Hill.

Lipman, P. W., H. J. Prostka, and R. L. Christiansen (1972). Cenozoic volcanism and plate-tectonic evolution of the western United States. *Philos. Trans. R. Soc. Lond., 271*, 217–284.

Lowell, J. D., and D. M. Guilbert (1970). Lateral and vertical alteration–mineralization zoning in porphyry ore deposits. *Econ. Geol., 65*(4), 373–408.

Meyer, C., and J. J. Hemley (1967). Wallrock alteration. In H. Barnes (Ed.), *Geochemistry of hydrothermal ore deposits.* New York: Rinehard and Wilson.

Norton, D. (1978). Sourcelines, sourceregions, and pathlines for fluids in hydrothermal systems related to cooling plutons. *Econ. Geol., 73,* 1–28.

Prost, G. (1980). Alteration mapping with airborne multispectral scanners. *Econ. Geol., 75,* 894–906.

Raines, G. (1978). Porphyry copper exploration model for northern Sonora, Mexico. *U.S. Geol Surv. J. Res., 6*(1), 51–58.

Ramos, V. A. (1977). Basement tectonics from Landsat imagery in mining exploration. *Geol. Mijnbouw, 56*(3), 243–252.

Readdy, L. (1978). *Porphyry copper and hydrothermal alteration investigation* (Final Report to U.S. Geological Survey). (Report PB-291205)

Rose, A. W. (1970). Zonal relations of wallrock alteration and sulfide distribution at porphyry copper deposits. *Econ. Geol., 65,* 920–936.

Rowan, L. C., P. H. Wetlaufer, A. F. H. Goetz, F. C. Billingsley, and J. H. Stewart (1974). Discrimination of rock types and detection of hydrothermally altered areas in south–central Nevada by the use of computer-enhanced ERTS images. *U.S. Geol. Surv. Prof. Pap. 883.*

Sales, R. H., and C. Meyer (1948). Wallrock alteration at Butte, Montana. *AIME Trans., 178,* 9–33.

Schmidt, R. G. (1976). Detection of hydrothermal sulfide deposits, Saindak area, West Pakistan. *U.S. Geol. Surv. Prof. Pap. 929,* 89–91.

Schmidt, R. G. (1978). The potential for copper–molybdenum deposits in the eastern United States. *U.S. Geol. Surv. Prof. Pap. 907-E.*

Siegal, B., and A. Goetz (1977). Effect of vegetation on rock and soil type discrimination. *Photogr. E. R., 43*(2), 191–196.

Sillitoe, R. H. (1972). A plate tectonic model for the origin of porphyry copper deposits. *Econ. Geol., 67,* 184–197.

Sutherland–Brown, A. (1976). General aspects of porphyry deposits of the Canadian Cordillera–morphology and classification. In Porphyry deposits of the Canadian Cordillera, A. S. Brown (Ed.), *Can. Inst. Min. Met. Spec. Vol., 15.*

Titley, S. R. (1975). Geological characteristics and occurrences in the southwestern Pacific. *Econ. Geol., 70,* 499–514.

Wilson, J. C. (1975). *Research on recognition of the geologic framework of prophyry copper deposits on ERTS-1 imagery* (Final Report, Landsat Investigation 21769). Greenbelt, Maryland: Goddard Space Flight Center.

Bibliography

Armstrong, R. L., J. E. Harakal, and V. F. Hollister (1976). Age determinations of Late Caenozoic porphyry copper deposits of the North American Cordillera. *Trans. Inst. Mining Met., Sect. B, 85,* 239–244.

Banks, N., and N. Page (1977). Some observations that bear on the origin of porphyry copper deposits. *U.S. Geol. Surv. Open File Rep. 77-127.*

Barr, D. A., P. E. Fox, K. E. Northcote, and V. A. Preto (1976). The alkaline suite porphyry deposits: A summary. *Can. Inst. Min. Met. Spec. Vol., 15*, 359–367.

Bogdanov, B. (1976). *Massive sulfide and porphyry copper deposits in Tethys region.* 25th IGC Meeting. (Abstract)

Botbol, J. M. (1971). An application of characteristic analysis to mineral exploration. *Can. Inst. Min. Met. Spec. Vol., 12*, 92–99.

Branch, C. D. (1976). Development of porphyry copper and stratiform volcanogenic ore bodies during the life cycle of andesitic stratovolcanoes. In *Volcanism in Australasia*, 337–342.

Christopher, P. A., and N. C. Carter (1976). Metallogeny and metallogenic epochs for porphyry mineral deposits in the Canadian Cordillera. *Can. Inst. Min. Met. Spec. Vol., 15*, 64–71.

Corn, R. M. (1975). Alteration–mineralization zoning, Red Mountain, Arizona. *Econ. Geol., 70*, 1437–1447.

DeGeoffroy, J., and T. K. Wignall (1971). A probabilistic appraisal of mineral resources in a portion of the Grenville Province of the Canadian Shield. *Econ. Geol., 66*, 466–479.

DeGeoffroy, J., and T. K. Wignall (1973). Statistical models for porphyry–copper–molybdenum deposits of the Cordilleran Belt of North and South America. *Can. Mining Met. Bull., 66*, 84–90.

Drummond, A. D., and C. I. Godwin (1976). Hypogene mineralization: An empirical evaluation of alteration zoning. *Can. Inst. Min. Met. Spec. Vol., 15*, 52–63.

Emmons, W. (1927). Relations of disseminated copper ore in porphyry to igneous intrusives. *Amer. Inst. of Min. Met. Eng. Trans., 75*, 797–815.

Gilmour, P. (1977). Mineralized intrusive breccias as guides to concealed porphyry copper systems. *Econ. Geol., 72*, 290–303.

Grew, P. C. (1976). Stress corrosion cracking and porphyry copper mineralization. *EOS, 57*, 321.

Horton, D. J. (1978). Porphyry-type copper–molybdenum mineralization belts in East Queensland, Australia. *Econ. Geol., 73*, 904–921.

Hutchinson, R. W., and R. W. Hodder (1972). Possible tectonic and metallogenic relationships between porphyry copper and massive sulfide deposits. *Can. Inst. Min. Met. Trans., LXXV*, 16–22.

James, A. H. (1971). Hypothetical diagrams of several porphyry copper deposits. *Econ. Geol., 66*, 43–47.

Jensen, M. L. (1975). Summary of space imagery studies in Utah and Arizona. *NASA Earth Resources Survey Symposium* (NASA TM X-58168, G-9). Houston: Johnson Space Center, 673–712.

Kesler, S., L. Jones, and R. Walker (1975). Intrusive rocks associated with porphyry copper mineralization in island arc areas. *Econ. Geol., 70*, 515–526.

Kesler, S., J. Sutter, and M. Issigonis (1976). Tectonic evolution of porphyry copper mineralization in Panama. *GSA Abstracts With Programs, 8*(6).

Kesler, S., J. Sutter, M. Issigonis, L. Jones, and R. Walker (1977). Evolution of porphyry copper mineralization in an oceanic island arc: Panama. *Econ. Geol., 72*, 1142–1153.

Kirkham, R. V. (1971). Intermineral intrusions and their bearing on the origin of porphyry copper and molybdenum deposits. *Econ. Geol., 66*, 1244–1249.

Laznicka, P. (1976). Porphyry copper and molybdenum deposits of the USSR and their plate tectonic settings. *Trans. Inst. Mining Met. Sect. B, 85*, 14–32.

Livingston, D. E. (1973). A plate tectonic hypothesis for the genesis of porphyry copper deposits of the southern Basin and Range Province. *Earth Plan., 20*, 171–179.

Livingston, D. E., R. L. Maryer, and P. E. Damon (1968). Geochronology of the emplacement, enrichment, and preservation of Arizona porphyry copper deposits. *Econ. Geol., 63*, 30–36.

Lowell, J. D. (1974). Regional characteristics of porphyry copper deposits of the Southwest. *Econ. Geol., 69*, 601–617.

Lukanuski, J. N., A. E. Nevin, and S. A. Williams (1976). Locomotive-type post-ore fanglomerate as exploration guides for porphyry copper deposits. *AIME Trans., 260*, 326–331.

Mitchell, A. H. G. (1976). *Tectonic settings for emplacement of subduction-related magmas and associated mineral deposits* (Special Paper No. 14). Geological Association of Canada.

Mitchell, A. H. G., and M. S. Garson (1972). Relationship of porphyry copper and circum-Pacific tin deposits to Palaeo-Benioff Zones. *AIME Trans.*, B10–B25.

Moore, W. J., and J. T. Nash (1974). Alteration and fluid inclusion studies of the porphyry copper ore body at Bingham, Utah. *Econ. Geol., 69*, 631–645.

Mustard, D. K. (1976). Porphyry exploration in the Canadian Cordillera. *Can. Inst. Min. Met. Spec. Vol., 15*, 17–20.

Ney, C. S., R. J. Cathro, A. Panteleyer, and D. C. Rotherham (1976). Supergene copper mineralization. *Can. Inst. Min. Met. Spec. Vol., 15*, 72–78.

Ney, C. S., and V. F. Hollister (1976). Geologic setting of porphyry deposits of the Canadian Cordillera. *Can. Inst. Min. Met. Spec. Vol., 15*, 21–29.

Nielsen, R. L. (1968). Hypogene texture and mineral zoning in a copper-bearing granodiorite porphyry stock, Santa Rita, New Mexico. *Econ. Geol., 63*, 37–50.

Nielsen, R. L. (1976). Recent developments in the study of porphyry copper geology: A review. *Can. Inst. Min. Met. Spec. Vol., 15*, 487–500.

Oyarzirn, M., and J. Frutos (1975). Porphyry copper and tin-bearing porphyries: A discussion of genetic models. *J. Phys. Earth Planetary Interiors, 9*(3), 259–263.

Pitcher, S. H., and J. J. McDougall (1976). Characteristics of some Canadian Cordillera porphyry prospects. *Can. Inst. Min. Met. Spec. Vol., 15*, 78–82.

Rico, B. S. (1975). *Some geologic and exploration characteristics of porphyry copper deposits in a volcanic environment, Sonora, Mexico.* Master's thesis, University of Arizona.

Rose, A. W. (1970). Zonal relations of wallrock alteration and sulfide distribution at porphyry copper deposits. *Econ. Geol., 65*, 920–936.

Sales, R. H. (1954). Genetic relations between granites, porphyries, and associated copper deposits. *AIME Trans.*, 499–505.

Saul, J. (1978). Circular structures of large scale and great age on the Earth's surface. *Nature, 271*, 345–349.

Seraphim, R. H., and V. F. Hollister (1976). Structural settings. *Can. Inst. Min. Met. Spec. Vol., 15*, 30–43.

Sillitoe, R. H. (1972). A plate tectonic model for the origin of porphyry copper deposits. *Econ. Geol., 67*, 184–197.

Titley, S. R., and T. L. Heidrick (1978). Intrusion and fracture styles of some mineralized porphyry systems of the southwestern Pacific and their relationship to plate interactions. *Econ. Geol., 73*, 891–903.

Williams, S. A. (1976). *Petrographic criteria unique to porphyry copper deposits.* 25th IGC Meeting. (Abstract)

Section 4

Silver Bell, Arizona, Porphyry Copper Test Site Report

Michael J. Abrams
Jet Propulsion Laboratory

David Brown
Texasgulf Inc.
Tucson, Arizona

Section 4

Silver Bell, Arizona, Porphyry Copper Test Site Report

Contents

I. **Introduction** 4-1

A. Rationale for Site Selection 4-1

B. Site-Specific Objectives and Problems 4-1

C. Remote Sensing Model 4-2
1. Ore zones 4-2
2. High pyrite zones (pyrite halo) 4-2
3. Potassic alteration 4-2
4. Phyllic/argillic alteration 4-2
5. Propylitic alteration 4-2
6. Tactite alteration 4-2
7. Breccia pipes 4-2
8. Structural features 4-2

D. Data Sources and Interpretation Methods 4-2
1. Remote sensing data 4-2
2. Support data 4-3
3. Geophysical support data 4-3
4. Procedures for interpreting and comparing data 4-4

II. **Description of Site** 4-4

A. General Description 4-4

B. Physiography and Geomorphology 4-5

C. Cultural and Land Use Patterns 4-6

D. Geologic History 4-6
1. Stratigraphic evolution 4-6
2. Structural evolution 4-9
3. Emplacement of mineral deposits 4-10
4. Hydrothermal alteration patterns 4-11
5. Discovery and development history 4-12

PRECEDING PAGE BLANK NOT FILMED

III. Discussion of PFRS Data 4-14
A. Introduction 4-14
B. Spectral Measurements 4-14
IV. Sensor Simulations Using PFRS Data 4-20
V. M²S Image Spectra 4-22
VI. Calibration of NS-001 Data 4-29
VII. NS-001 Image Spectra 4-31
VIII. Image Analysis and Interpretation 4-32
A. Color Aerial Photographs 4-32
B. Radar Data 4-34
C. Landsat MSS Images 4-35
D. M²S 11-Channel Scanner Aircraft Images 4-37
E. NS-001 Aircraft Images 4-45
1. Standard color ratio composite image (uncalibrated) 4-45
2. Canonical transformation image (11 groups—igneous rocks only) 4-48
3. Canonical transformation image (18 groups—all rock types) 4-51
4. Supervised classification 4-51
5. Principal components analysis 4-53
6. Summary of NS-001 results 4-58
F. Thermal Data 4-59
G. Comparison of Spatial Resolution 4-63
IX. Conclusions 4-65
Acknowledgments 4-70
References 4-71
Figures
4-1. Location of Silver Bell test site in southern Arizona 4-4
4-2. Map of Silver Bell test site showing features described in this section 4-5
4-3. Silver Bell geologic map 4-7
4-4. Simplified geologic cross sections of Silver Bell 4-8
4-5. Pre-Laramide regional structure 4-9
4-6. Silver Bell structural map showing mapped faults and dikes and showing structures inferred from geophysical data 4-10
4-7. Alteration map of Silver Bell District 4-12
4-8. Alteration zoning at Silver Bell 4-13
4-9. Location of sample sites for PFRS data acquisition and mineralogical analyses 4-15
4-10. PFRS reflectance spectra for rocks measured at Silver Bell: (a) dacite; (b) dacite, propylitic; (c) dacite, phyllic; (d) dacite, potassic 4-16
4-11. PFRS reflectance spectra for rocks measured at Silver Bell: (a) alaskite, propylitic; (b) alaskite, potassic/propylitic; (c) alaskite, potassic; (d) alaskite, phyllic 4-17

4-12. PFRS reflectance spectra for rocks measured at Silver Bell: (a) monzonite, potassic; (b) monzonite, propylitic; (c) granodiorite; (d) Mt. Lord; (e) Mt. Lord, phyllic 4-18
4-13. PFRS reflectance spectra for rocks measured at Silver Bell: (a) Claflin Ranch; (b) Silver Bell mudflow; (c) basalt; (d) limestone; (e) red beds 4-19
4-14. Results of linear discriminant function analysis for alaskites 4-23
4-15. Results of linear discriminant function analysis for dacites 4-24
4-16. Results of linear discriminant function analysis for 11 igneous rock groups 4-25
4-17. Results of linear discriminant function analysis for 18 rock groups 4-26
4-18. Image spectra from M²S 11-channel data for 15 rock types at Silver Bell 4-28
4-19. Image spectra from M²S 11-channel data derived by normalizing raw DN values to imaginary basalt curve with equal reflectance values in all channels 4-30
4-20. Calibration of NS-001 data 4-32
4-21. NS-001 image spectra derived from calibrated data 4-33
4-22. Comparison of PFRS spectra and NS-001 calibrated image spectra for limestone and altered dacite 4-34
4-23. Color aerial photograph of Silver Bell area 4-35
4-24. X-band aircraft radar image of Silver Bell area 4-36
4-25. Seasat L-band radar image of Silver Bell area 4-38
4-26. Structural interpretation of Seasat radar image (Figure 4-25) 4-39
4-27. Landsat color ratio composite 4-40
4-28. Interpretation of Landsat color ratio composite (Figure 4-27) showing lineaments and areas that have iron-oxide minerals 4-41
4-29. Aircraft scanner coverage of Silver Bell test site for M²S and NS-001 data overflights 4-42
4-30. M²S 11-channel color ratio composite 4-43
4-31. Interpretation map of M²S color ratio composite (Figure 4-30) 4-44
4-32. NS-001 color ratio composite 4-46
4-33. Interpretation map of NS-001 color ratio composite (Figure 4-32) 4-47
4-34. NS-001 canonical transform image. Axes derived from discriminant function analysis of 11 rock groups using PFRS data 4-49
4-35. Interpretation map of NS-001 canonical transform image (Figure 4-34) 4-50
4-36. NS-001 canonical transform image. Axes derived from linear discriminant analyses of 18 rock groups using PFRS data 4-52

4-37. (a) Training areas for supervised classification of NS-001 data; (b) classification map for Mt. Lord 4-54
4-38. Classification maps for NS-001 data: (a) altered dacite; (b) unaltered dacite; (c) Claflin Ranch; (d) granodiorite 4-55
4-39. Classification maps for NS-001 data: (a) Ragged Top; (b) Silver Bell 1; (c) basalt; (d) red beds 4-56
4-40. Classification maps for NS-001 data: (a) monzonite; (b) alaskite; (c) limestone; (d) Silver Bell 2 4-57
4-41. Thematic map produced from NS-001 supervised classification 4-58
4-42. Plot of loadings on first four eigenvectors (V1, V2, V3, V4) from NS-001 principal components analysis 4-59
4-43. Principal components values for first four eigenvectors (V1, V2, V3, V4) for 13 rock groups from NS-001 data 4-60
4-44. Principal components images from NS-001 data 4-61
4-45. Principal components color composite from NS-001 data 4-62
4-46. Interpretation map of NS-001 principal components composite (Figure 4-45) 4-63
4-47. M²S thermal data for Silver Bell 4-64
4-48. Color composite of M²S data 4-65
4-49. Interpretation map of M²S thermal-albedo color composite (Figure 4-48) 4-66
4-50. Composite of Silver Bell test site 4-67
4-51. Comparison of spatial resolution 4-68

Tables

4-1. Scales and sources of remote sensing data for Silver Bell test site 4-3
4-2. Stratigraphic section, Silver Bell 4-6
4-3. Mineralogy from X-ray analyses 4-15
4-4. Absorption bands in PFRS spectra 4-20
4-5. Sensor simulation bands 4-21
4-6. Rock-type groups 4-21
4-7. Summary of classification accuracies for 20 analyses 4-22
4-8. Rock types from M²S data 4-27
4-9. Raw DN values and standard deviations from M²S data 4-27
4-10. M²S relative reflectance normalized to basalt 4-29
4-11. Silver Bell basalt: PFRS average curve 4-31
4-12. M²S reflectance values normalized to PFRS basalt spectrum 4-31
4-13. NS-001 DN values versus percentage reflectance (PFRS) 4-31
4-14. 1.6/2.2-μm image spectra and PFRS ratios 4-34
4-15. M²S 11-channel bands 4-43
4-16. Wavelength bands of NS-001 scanner 4-45
4-17. Silver Bell training areas 4-53
4-18. Statistics of training areas 4-53
4-19. Training area accuracy 4-59
4-20. Eigenvalues and eigenvectors for NS-001 data 4-59
4-21. Principal components values 4-59

Section 4

Silver Bell, Arizona, Porphyry Copper Test Site Report

I. Introduction

A. Rationale for Site Selection

The Silver Bell area was chosen as one of the three porphyry copper test sites for several geological and nongeological reasons. First, the rock types and alteration patterns in the district are well exposed at the surface. Soil and vegetation cover are minimal, and topographic relief is generally moderate. Second, the Silver Bell District offers an opportunity to study an unusually elongated zone of alteration and mineralization in which the structural and zoning patterns are tightly compressed into a relatively narrow area. Third, the area contains a diverse mixture of plutonic, volcanic, and sedimentary rocks typical of many porphyry copper districts in the southwestern United States.

Because of the long mining history of the Silver Bell District, the area has been well studied, and a wealth of support data is available to help interpret the remote sensing data. The presence of active mining operations offers the opportunity to study an area modified by pits and dumps.

The Silver Bell area was also chosen because of the cooperation of the American Smelting and Refining Company (ASARCO) management in allowing access for ground support work. ASARCO also agreed to provide certain proprietary data to aid in interpretation of the district, including a geologic map and an alteration map.

B. Site-Specific Objectives and Problems

The overall objective of the Silver Bell test site study was to assess the usefulness of a number of multispectral scanner systems as mapping tools in a known porphyry copper environment. The various imaging systems, alone and in combination with each other, were evaluated for their ability to discriminate the major rock types, alteration patterns, and structural elements associated with Silver Bell porphyry copper mineralization. The major observable features include:

(1) Main zone alteration – Definition of the main Silver Bell alteration zone and detection of zoning patterns within it.

(2) Peripheral alteration – Identification of other alteration zones peripheral to the main structural zone; also, identification of alteration areas separate from or unrelated to the main zone, but associated with hydrothermal activity in other parts of the district.

(3) Rock types – Discrimination of the main lithologies in the area, based on their individual spectral characteristics.

(4) Structural features – Identification of major structural elements, including regional northwest faults, transverse faults, and northeast porphyry dike swarms.

The Silver Bell area offers some special challenges to meeting these various objectives. First, much of the geology in critical areas is obscured by dump material and steep-walled open pits, which would not ordinarily be present in an actual exploration site. Spotty "windows" of data must be extrapolated from peripheral areas into the obscured ore bodies.

A second problem concerns the relation of surficial material to ore mineralization located an average of 30 m

below the surface. Recognition of primary alteration and structural patterns may be difficult because of the effect of extensive supergene oxidation and leaching near the surface.

C. Remote Sensing Model

The remote sensing model adopted for this test case consists of the various color, tonal, textural, and vegetative characteristics expected for the different lithologic and structural features of the Silver Bell area. The general aspects of the model are similar to a photogeological model for porphyry copper deposits in arid environments, developed by Readdy (1978). This photogeological model was derived by comparing Landsat images, radar images, color aerial photographs, and thermal infrared data of the Sar Chesmah, Iran, and Safford, Arizona, deposits. The Readdy model has been adapted and modified to describe the features of the porphyry copper mineralization at Silver Bell.

1. Ore zones. The main ore zones at Silver Bell include subcircular to elliptical zones of chalcocite enrichment in the Oxide, El Tiro, and North Silver Bell areas. These areas should have a fine-textured drainage pattern due to stockwork zones, crackle breccias, or closely spaced parallel fractures. Soil development may be more abundant as a result of more easily weathered material. Vegetation anomalies may coincide with ore zones, either as reduced growth due to metal toxicity or as more abundant growth resulting from the presence of potash and phosphates (Readdy, 1978).

2. High pyrite zones (pyrite halo). The "pyrite halo" at Silver Bell consists of that portion of the main alteration zone outside the main ore deposits. The pyritic zones are characterized by low copper concentrations, high pyrite/copper sulfide ratios, and a relative abundance of jarositic limonite.

The presence of sericite and clay minerals in the pyritic zone tends to produce an overall lighter tone in contrast to the darker tones of surrounding fresh rocks. A diagnostic brick-red or yellowish-brown color is characteristic of the capping produced by oxidation of copper-poor sulfides. The pyritic zone may correspond to a more subdued topography with rounded ridges due to relatively high fracture density and the presence of soft clays and sericite (Readdy, 1978).

3. Potassic alteration. No direct detection of the potassic alteration products, such as K-feldspar, biotite, or anhydrite, is likely to be possible. However, indirect separation of potassic alteration may be possible through the spectral characteristics of spatially associated features. For example, the potassic zones may have slightly different amounts of clays and sericite and higher hematite to goethite plus jarosite ratios than adjacent phyllic or argillic alteration zones.

4. Phyllic/argillic alteration. Phyllic and argillic alteration at Silver Bell generally coincides with the pyritic zone, the general characteristics of which have already been summarized. In addition to the indirect tonal and geomorphic features, the main alteration minerals—sericite, clays, and limonite—should be detectable by their diagnostic spectral absorption bands.

5. Propylitic alteration. Areas of propylitic alteration should have an overall light tone and a pale greenish tint in the visible region of the spectrum due to the presence of minerals such as albite, epidote, and chlorite. Also, the presence of small amounts of limonite from the oxidation of pyrite should be detectable on Landsat and aircraft images.

6. Tactite alteration. Detection of most tactite zones is unlikely because of the small size of outcrops and the lack of spectrally diagnostic primary minerals. Some of the tactite bodies at Silver Bell form craggy, resistant knobs or ridges due to their hardness (Merz, 1967). Also, the abundance of minerals such as garnet, magnetite, and diopside should give tactite units a generally dark tone relative to adjacent igneous rocks or unaltered limestone. Some mineralized tactites may contain enough limonite from primary sulfides to be detected on the basis of iron absorption characteristics.

7. Breccia pipes. Several small breccia pipes are present in the North Silver Bell area. These pipes are silicified and sericitized areas which form resistant knobs and ridges. The Silver Bell breccia pipes average only 30 to 60 m in size and, thus, should only be visible in high-spatial resolution image data because of their slight positive topographic relief.

8. Structural features. Regional basement structure appears to control the locus of intrusion and mineral emplacement at Silver Bell. In addition, local northeast fractures and dike swarms acted to localize more intense mineral development. Structure at various scales should be identifiable from the various image types, depending on their scale and resolution.

D. Data Sources and Interpretation Methods

1. Remote sensing data. Remote sensing data acquired for the Silver Bell test site include aircraft and Seasat radar, Landsat Multispectral Scanner (MSS) images, aircraft

multispectral scanner data, and color aerial photography. The scales at which these data were used and the sources of these data are shown in Table 4-1.

The aircraft radar data examined consist of four glossy prints at a scale of approximately 1:100,000, covering essentially the equivalent area of a Landsat 1:125,000 enlargement. The four prints include two different look directions (northeast and northwest), each with two different polarizations. The Seasat data are an approximately 1:125,000 image covering a roughly 80- by 70-km area, or the approximate southeast quarter of the Phoenix Landsat frame.

Landsat data consist of three full-frame color composites of the Phoenix scene, recorded during three different seasons (winter, spring, and summer, 1976 to 1977). The computer tapes for these three frames were further processed by various band ratioing and principal components techniques, and printed as 1:125,000 enlargements, covering roughly 8 percent of the full-frame area. Each image covers a rectangular area of about 37 by 25 km.

The aircraft photographic and scanner data were acquired by a NASA C-130 overflight at an altitude of approximately 4500 m. The scale of the images produced is approximately 1:24,000. The NS-001 Thematic Mapper Simulator scanner coverage consists of a single northwest-oriented swath approximately 20 by 15 km in size, with an instantaneous field of view (IFOV) of 12 m. The computer-processed NS-001 data were printed onto three separate images, covering the southeast, central, and northwest parts of the district.

Table 4-1. Scales and sources of remote sensing data for Silver Bell test site

Data	Scale	Source	Date
Seasat	1:125,000	Jet Propulsion Laboratory (JPL)	October 1978
Aircraft SLAR	1:100,000	Johnson Space Center (JSC)	April 1979
Landsat MSS	1:125,000; 1:500,000	JPL (processed from EROS Data Center tapes)	March 1976 December 1976 June 1977
11-channel M^2S	1:24,000	JSC	August 1977 May 1978
NS-001 (Thematic Mapper Simulator)	1:24,000	JSC	October 1978
Color aerial photography	1:24,000	JSC	October 1978

The aircraft Modular Multispectral Scanner (M^2S) 11-channel images were acquired at a slightly higher altitude than the NS-001 data, and cover a wider area, with an IFOV of 15 m. The processed portion of the 11-channel images consists of a single color ratio composite image covering the central part of the district.

2. Support data. Ancillary data used in the interpretation of the Silver Bell remote sensing data include geological and geophysical information from both published and unpublished sources. Detailed geologic data on the main part of the district are provided by an unpublished ASARCO map at a scale of approximately 1:12,000. This map, compiled from several sources, shows fine structural and lithologic details, including the location of the numerous northeast-striking monzonite porphyry dikes.

ASARCO's geologic map covers only the central and eastern parts of the Silver Bell Mountains, and not the outlying parts of the test site. Generalized data on the entire Silver Bell and West Silver Bell Mountains are provided by an unpublished Texasgulf, Inc., geologic map. This map, at a scale of 1:24,000, was compiled by D. M. Brown from published sources and reconnaissance mapping.

The distribution of alteration types within the main Silver Bell structural zone was taken from ASARCO's alteration maps, printed as clear mylar overlays at a 1:24,000 scale. Richard and Courtright's published map (1966) shows the outline of intense hydrothermal alteration as well as the distribution of tactite bodies and mineralized fractures. The Richard and Courtright map was enlarged onto a 1:24,000 mylar overlay format to be compatible with the other geologic data.

Volcanic stratigraphy and petrographic descriptions of the igneous rock types within the main part of the mining district are found in a dissertation on the eastern Silver Bell Mountains by Watson (1964). Watson's geologic map was incorporated into the ASARCO and Texasgulf compilation maps.

Geological information for the remainder of the test site is provided by a variety of published references including Banks and Dockter (1976) and McClymonds (1959). Regional geologic data on the 1:500,000 Arizona State Geologic Map (Wilson and Moore, 1969) and 1:375,000 Pima and Santa Cruz Counties Geologic Map (Wilson et al., 1960) were useful, primarily in interpreting Landsat images.

3. Geophysical support data. A detailed aeromagnetic map of the Silver Bell region was used to provide verification of structural features identified on the images. The aero-

magnetic data are on a mylar overlay, at a scale of 1:24,000. The data are from 1973 –1974 surveys flown for Texasgulf by Applied Geophysics, at a flight height of 200 m and 0.5-km line spacing. Most of the test site area is also covered by a less-detailed aeromagnetic survey flown for the U.S. Geological Survey in 1976, with a flight height of 1300 m (barometric) and a line spacing of 1.5 km (USGS, 1980).

Regional geophysical data for interpretation of high-altitude Landsat and Seasat images consist of the Arizona residual aeromagnetic map (Sauck and Sumner, 1970) and the Bouguer gravity map of Arizona (Aiken, 1975). The aeromagnetic data are on a 1:500,000 mylar overlay, while the gravity data are on a 1:1,000,000 paper print.

4. Procedures for interpreting and comparing data. The Silver Bell data were interpreted in three basic steps: (1) visual comparison between images and support data, primarily through the use of overlays; (2) ground checking the site to substantiate any interpretive conclusions and to check the cause of any unusual features or discrepancies; and (3) further visual comparisons and integration with laboratory and ground spectral data.

The boundaries of distinctive spectral features were traced onto mylar from the various images, and the individual areas were classified and labeled according to similar spectral characteristics. Black-and-white transparencies of the geological or geophysical data were then placed on top of the appropriate images and compared with the interpreted overlays. This technique of using transparent overlays with contact boundaries and structure allowed the direct superposition of mapped geology on the color image products as well as the simultaneous comparison of data sets. The interpretive overlays were also placed on top of a colored print of the Texasgulf district geologic map in order to compare lithologic separations.

Alteration data were compared to the images in the same manner as the lithologic and structural data. Mylar overlays of the ASARCO-supplied alteration zones and the Richard and Courtright sketch of the main alteration zone were placed directly over the 1:24,000 aircraft images and compared with visually interpreted features.

The various geologic and alteration overlays did not fit the images exactly because of slight scale differences and geometric distortion of the images. To compensate for this, the overlays were manually rotated or shifted to match the appropriate part of the image as closely as possible. The matching was done by using topographic, drainage, or cultural features as guides.

II. Description of Site

A. General Description

The Silver Bell test site is located in Pima and Pinal Counties, Arizona, approximately 60 km northwest of Tucson (Figure 4-1), centered at lat. 32°25′ N, long. 111°30′ W. The site is reached by driving 30 km north of Tucson on Interstate Highway 10, then 30 km west on a paved county road to the Silver Bell townsite.

The test area covers a rectangular strip approximately 20 by 15 km, centered over the Silver Bell Mountains, an area of generally moderate relief with elevations ranging from 600 to 1400 m. The site is bounded on the northwest by the West Silver Bell Mountains, a low-lying group of hills. Coverage extends southward to the northern end of the Waterman Mountains, a moderately rugged range similar in relief and elevation to the Silver Bell Mountains. The test site is bounded by two intramountain basins: the Avra Valley on the east and the Aguirre Valley on the west (Figure 4-2).

The climate of the area is semiarid, with an average annual rainfall of 25 cm. The site supports a typical growth of Sonoran desert vegetation, including palo verde and ironwood trees, saguaro cactus, and salt cedar trees along certain washes.

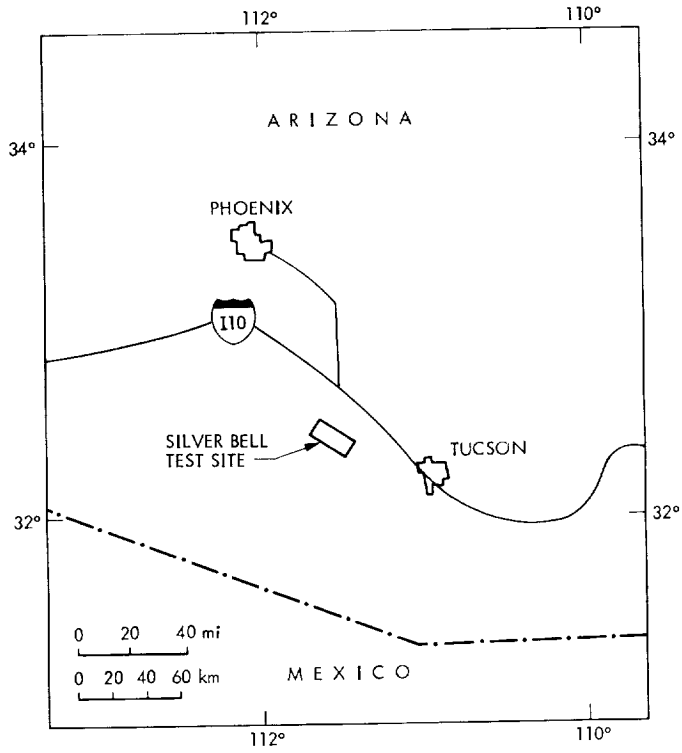

Figure 4-1. Location of Silver Bell test site in southern Arizona

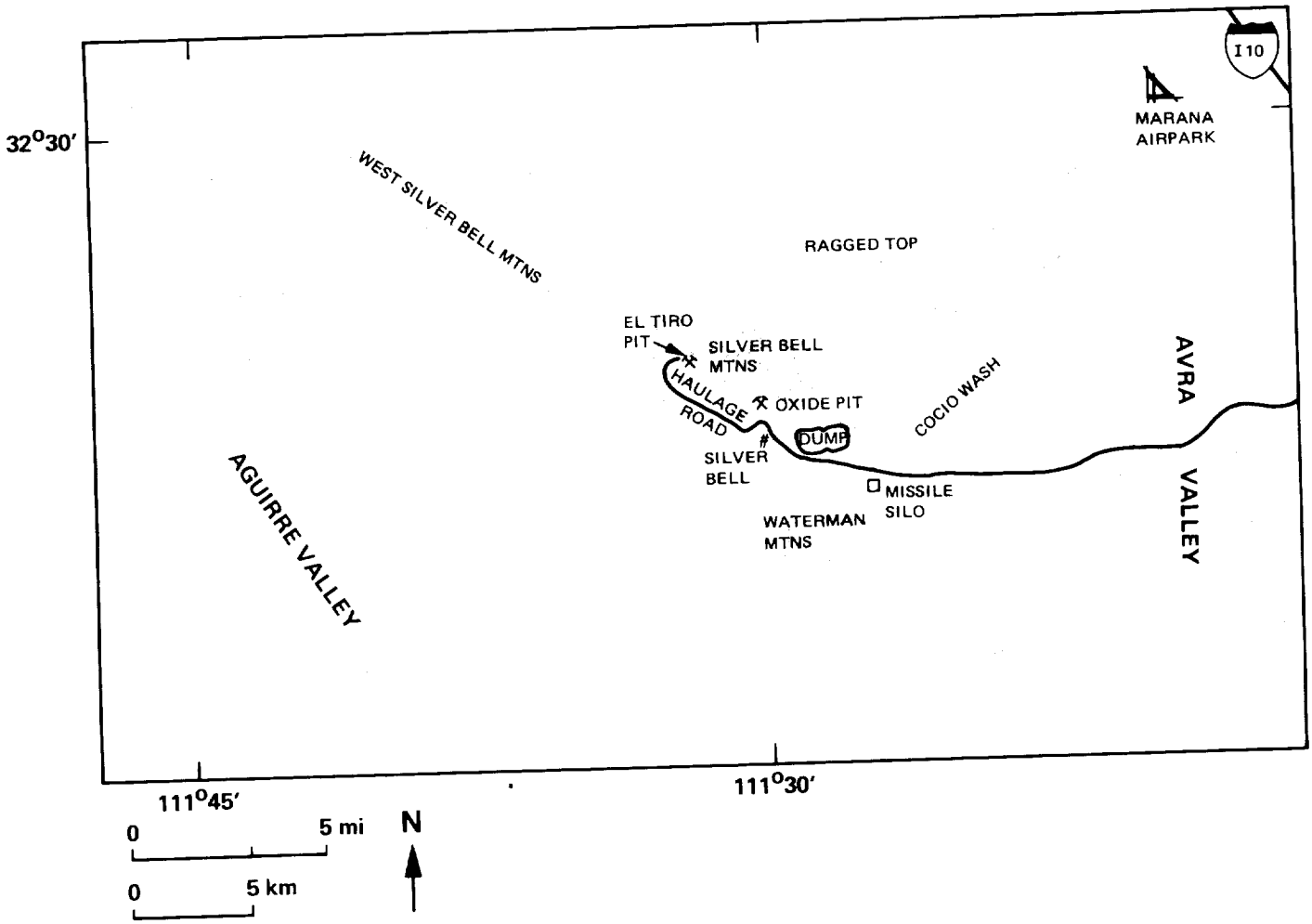

Figure 4-2. Map of Silver Bell test site showing features described in this section

Vegetative cover is generally sparse and varies from 10 to 15 percent in lower elevations to as much as 20 to 25 percent in higher elevations and along major washes.

The amount of outcrop exposure averages about 30 to 40 percent in the central parts of the Silver Bell and West Silver Bell Mountains. Exposure in the pediment areas varies from 0 to 10 percent, with outcrops occurring mainly as small isolated hills and along arroyo bottoms. Surficial cover consists of 0.1 to 2 m of colluvium and talus on ridges and hill slopes. The pediment aprons adjacent to the mountain ranges are covered by 0 to 10 m of semiconsolidated gravels topped by a thin veneer of soil.

The colluvial deposits found on hill slopes are generally a mixture of rock fragments and iron-oxide-stained soil and clay. Rock fragments vary in size from a few millimeters up to boulders 0.5 to 1.5 m across, with the average size being approximately 20 cm. The composition of talus and colluvial rock fragments closely reflects the adjacent and subjacent geology since the fragments are derived by essentially in-place weathering of parental rocks (Richardson and Miller, 1974).

B. Physiography and Geomorphology

The Silver Bell and Waterman Mountains have moderately steep slopes in their central higher elevations and more rounded, subdued hills and ridges on their margins. Slopes near the higher peaks, such as Silver Bell Peak, average about 40° to 50°. The steepest topography occurs on Ragged Top Peak, a craggy volcanic neck at the north end of the Silver Bell Mountains, where steep cliffs with 60° to 70° slopes are common. The limestone units of the Waterman Mountains also form very steep escarpments and rugged ridges with slopes of 50° to 70°. Landslopes on the pediments surrounding the ranges average only a few degrees.

The mountain ranges in the Silver Bell area are drained by networks of dry gullies and ravines with steep gradients.

These drainages coalesce outward from the central parts of the ranges into progressively wider and lower-gradient dry washes. On Landsat images, the washes define a distinctive radial pattern on a circular pediment apron approximately 40 km in diameter. In detail, the washes have a braided, subparallel pattern and are incised into the pediment surface, which is an older, distinctly iron-oxide-stained feature.

The weathering processes at Silver Bell, typical of southwestern deserts, are mainly mechanical rather than chemical in nature. Soil profiles are poorly developed or absent, and caliche zones are commonly present within soil horizons. Weathered rock materials are slowly moved downhill by rock falls, by slumping, and by debris flows during heavy rains. The detrital material in arroyos and washes is provided by rapid runoff and erosion of materials into the higher tributary gullies during heavy winter rains and torrential summer thunderstorms. During the brief periods of flash flooding, the major washes may carry sand, silt, and entrained boulders as much as several kilometers from the source areas.

C. Cultural and Land Use Patterns

The Silver Bell test site is a sparsely populated area used mainly for mining and cattle grazing. Roads are few and far apart, and the only town within the test site area is Silver Bell, a small ASARCO housing settlement of several hundred people. The central part of the Avra Valley to the north and east of the test site is irrigated and cultivated for cotton and other crops.

The largest man-made features within the test site are the pits, dumps, and tailings in the central part of the district. These features cover approximately 5 percent of the total area of the test site. A prominent feature used as a reference point in the image interpretation is ASARCO's paved haulage road along the west side of the two open pits. The haul road shows up clearly as the hook-shaped line connecting the El Tiro Pit with the concentrator adjacent to the Oxide Pit (Figure 4-2).

Other cultural features visible in the area include a gas pipeline and pumping station east of the Silver Bell Mountains. Also, a U.S. Air Force Titan missile silo is visible as a rectangular white scar just south of the ASARCO tailings pond.

D. Geologic History

1. Stratigraphic evolution. The oldest rocks exposed within the Silver Bell test site are Precambrian granite and diabase found north of the Ragged Top Fault and in the Waterman Mountains (Table 4-2; Figures 4-3 and 4-4). The Precambrian granite is overlain unconformably by younger Precambrian Apache Group conglomerate and quartzite,

Table 4-2. Stratigraphic section, Silver Bell

Age	Unit	Lithology
Tertiary–Recent	Sediments	Pediment gravels, alluvium
Oligocene–Miocene	Andesite, basalt	Flows
	Ragged Top stock	Quartz latite
	Andesite, latite dikes	
Cretaceous–Paleocene	Monzonite	Monzonite, syenodiorite stocks, plugs, dikes
	Granodiorite	Granodiorite, andesite stocks, plugs, dikes
	Mt. Lord Formation	Quartz latite tuffs
	Silver Bell Formation	Andesite flows, breccias, tuffs, conglomerates
	Dacite porphyry	Sill (?)
	Claflin Ranch Formation	Flows, tuffs, volcanoclastics
	Alaskite	Quartz monzonite stock
Mesozoic	Village red beds	
	Arkose	Amole equivalent
Paleozoic	Scherrer Formation	Quartzite
	Naco Limestone	
	Escabrosa Limestone	
	Martin Limestone	
	Abrigo Limestone	
	Bolsa Quartzite	
Precambrian	Apache Group	Quartzite, conglomerate
	Oracle Granite	
	Diabase	
	Pinal Schist	

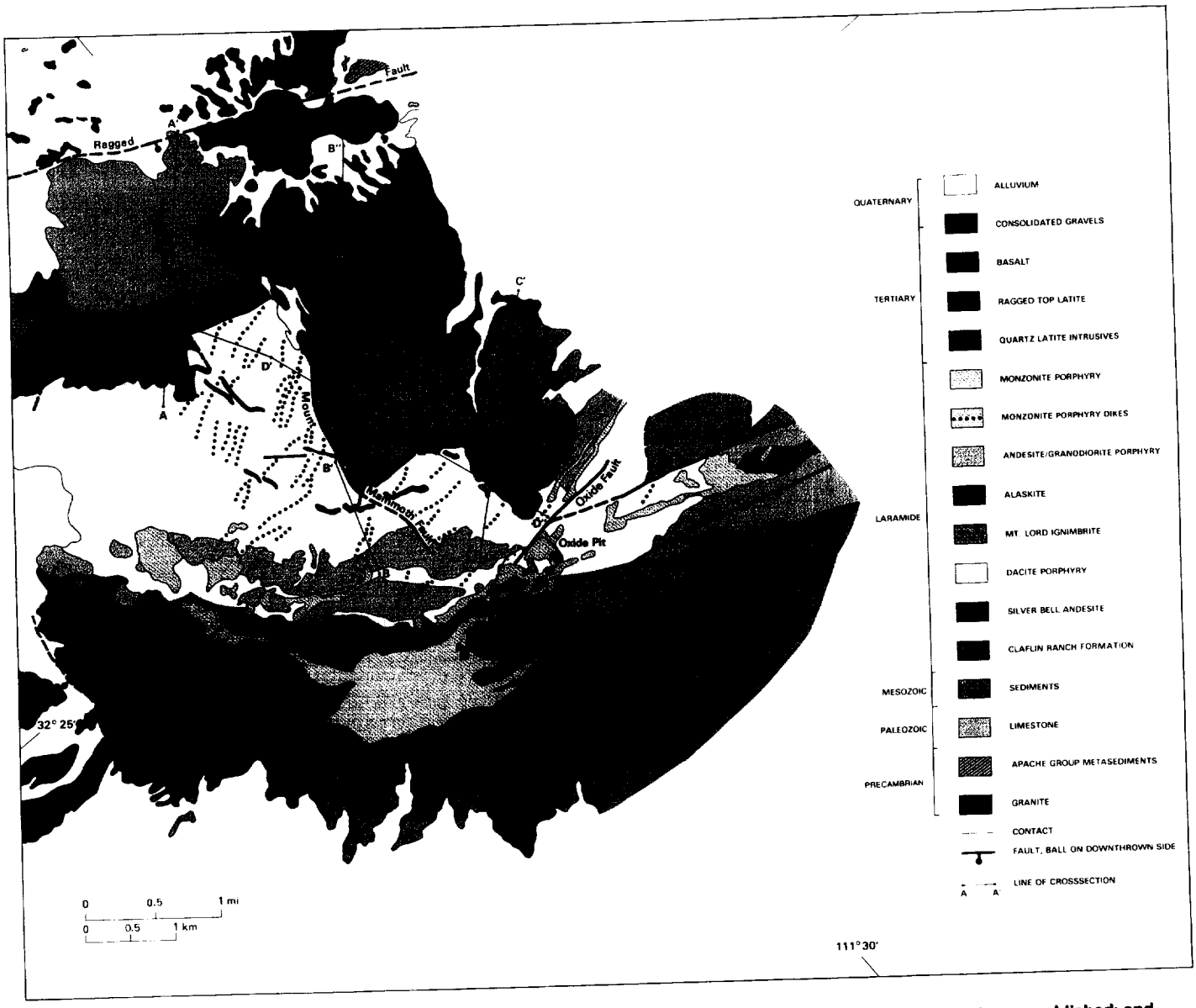

Figure 4-3. Silver Bell geologic map (compiled by D. Brown from Texasgulf mapping, unpublished; ASARCO mapping, unpublished; and various published maps). Indicated cross sections appear in Figure 4-4.

which are exposed only in a narrow strip north of the Ragged Top Fault.

The Precambrian rocks are overlain by a shallow marine sequence of Paleozoic deposits with an original composite thickness in excess of 1300 m. The Paleozoic section, from oldest to youngest, consists of the Bolsa Quartzite and Abrigo Limestone (Cambrian), Martin Limestone (Devonian), Escabrosa Limestone (Mississippian), Naco Limestone (Pennsylvanian), and a series of unnamed Permian limestone, shale, and quartzite. The most complete Paleozoic sections are preserved in the thrust sheets of the Waterman Mountains; exposures elsewhere are incomplete sections limited to isolated fault blocks or pendants within Laramide intrusives.

The Paleozoic formations are overlain by a sequence of Mesozoic clastic deposits formed in a continental environment. Outcrops of the Mesozoic rocks are restricted mainly to the low-lying area between the Silver Bell fault zone and the Waterman Mountains. The exact age of the clastics is unknown, but they may include rocks of Triassic age as well as local equivalents of the Cretaceous Bisbee Group. Their lithology is quite heterogeneous and includes red beds, conglomerates, arkoses, quartzites, limestones, and intercalated volcanics.

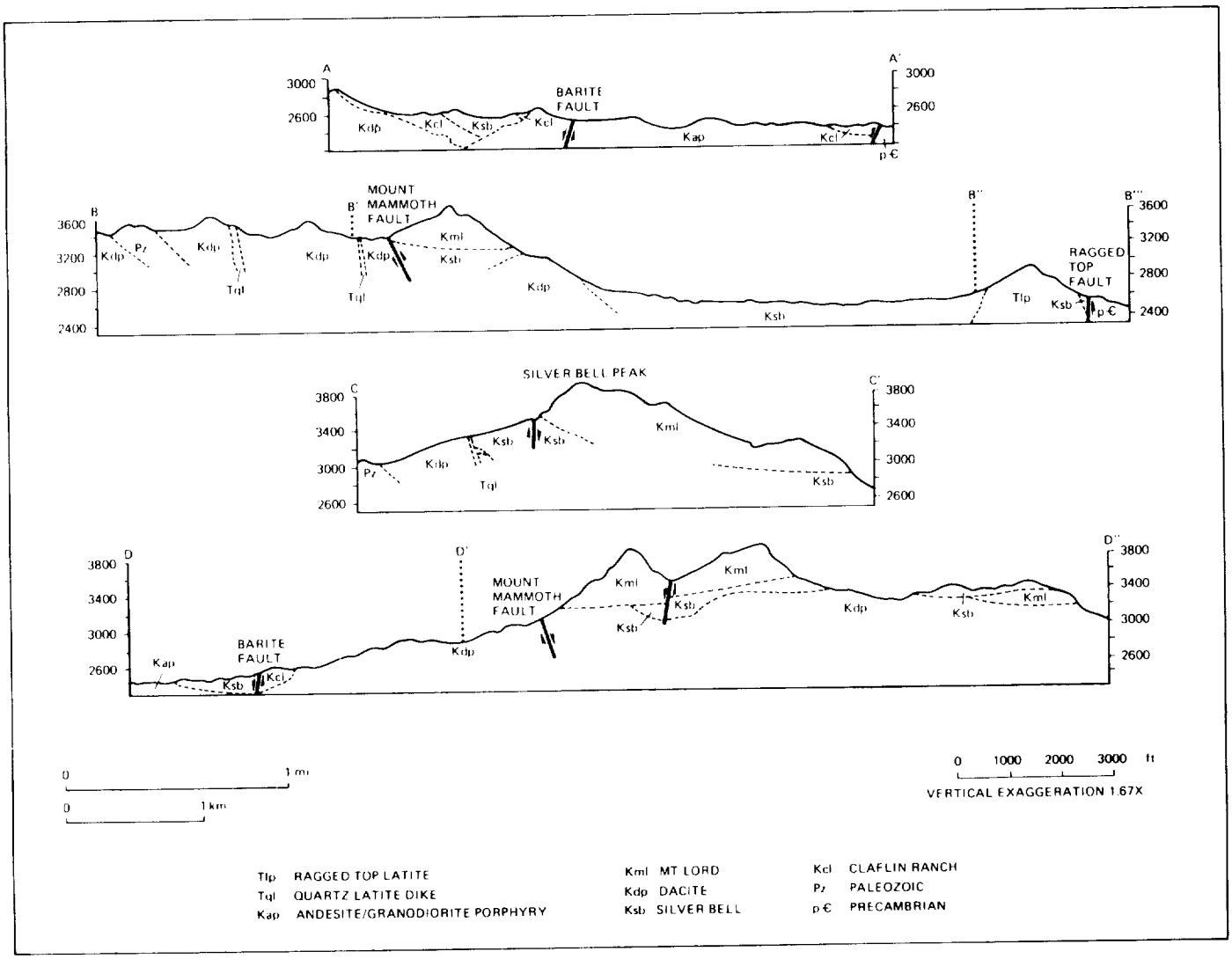

Figure 4-4. Simplified geologic cross sections of Silver Bell. See Figure 4-3 for lines of sections.

Sometime following deposition of the Mesozoic clastics, but prior to the onset of Laramide volcanism, a Cretaceous stock of alaskite was emplaced into the North Silver Bell area. Following the emplacement of the elongate alaskite stock, the Silver Bell area was subjected to intense structural deformation and rapid vertical uplift in early Laramide time. During this period, coarse conglomerates, tuffs, and flows of the Claflin Ranch Formation were deposited on a surface of considerable relief.

The beginning of significant Laramide igneous activity was marked by the intrusion of a large dacite porphyry mass which moved up along the Silver Bell fault zone and spread laterally eastward as a sill. The dacite probably evolved as an explosive, fluidized mass which made room for itself by forcing its way between a Paleozoic/Mesozoic floor and a Claflin Ranch roof (Watson, 1964).

Laramide volcanic activity continued with the deposition of a thick pile of andesitic flows, flow breccias, and lahars known as the Silver Bell complex. This unit makes up a large portion of the Silver Bell and West Silver Bell Mountains. Eruption of the Silver Bell andesites was closely followed by the extrusion of the Mt. Lord Formation, a sequence of predominantly rhyodacitic ash-flow tuffs that presently form much of the higher elevations of the central and northern Silver Bell Mountains. Nearly contemporaneous with the Silver Bell andesites and Mt. Lord tuffs were several stocks of granodiorite porphyry and northeast-trending andesitic dikes.

The culmination of Laramide activity began about 65 million years ago with the intrusion of syenodiorite porphyry dikes along east to northeast-trending tensional fractures emanating eastward from the main Silver Bell

structural zone. Shortly following syenodiorite emplacement, monzonite porphyry invaded the main Silver Bell structural zone, forming irregular stocklike bodies and sending dike swarms northeastward along the same tensional fractures occupied by the earlier syenodiorite (Watson, 1964).

Following the main period of hydrothermal alteration and copper mineralization in latest Laramide time, a long period of relative quiescence ensued during early Tertiary time. Igneous activity was renewed in Oligocene–Miocene time, with the intrusion of andesite and quartz latite dikes and the Ragged Top latite stock. Miocene-age flows of andesite, latite, and basalt were extruded at about the same time, possibly fed by some of the andesite and latite intrusions.

The youngest deposits in the Silver Bell area are unconsolidated to semiconsolidated alluvial deposits of Upper Tertiary to Recent Age. These surficial deposits were formed during erosion of the region following Basin and Range uplift in late Tertiary time.

2. Structural evolution. As depicted by Richard and Courtright (1966) (Figure 4-5), the structure of the Silver Bell area prior to the onset of Laramide igneous activity consisted of four subparallel blocks separated by three major west–northwest faults. These faults are designated, from north to south, the Ragged Top Fault, the Silver Bell fault zone, and the Waterman Fault. The area between the Ragged Top and Silver Bell Faults is designated the Silver Bell structural block, which encompasses the main part of the Silver Bell Mountains.

The Silver Bell Fault exerted a major influence on the emplacement of Laramide monzonite porphyry intrusives and associated porphyry copper deposits. The original trace of the fault zone is marked by the elongation of monzonite stocks and by the trend of the main Silver Bell alteration zone, which strikes west–northwest for two-thirds of its length on the south, then swings nearly north–south near its northern end. The northeast side of the fault zone is marked by a line of elongate, garnetized Paleozoic screens with straight, northwest-trending margins. The intrusion of monzonite porphyry along the Silver Bell structural zone may have caused doming in the area, creating a northeast tilt of 20° to 40° to the Silver Bell structural block (Watson, 1964).

East of the Silver Bell fault zone, the northeast-tilted volcanic and sedimentary units are cut by numerous transverse structures (Figure 4-6) striking north–northeast and east–west, at nearly right angles to the Silver Bell fault zone.

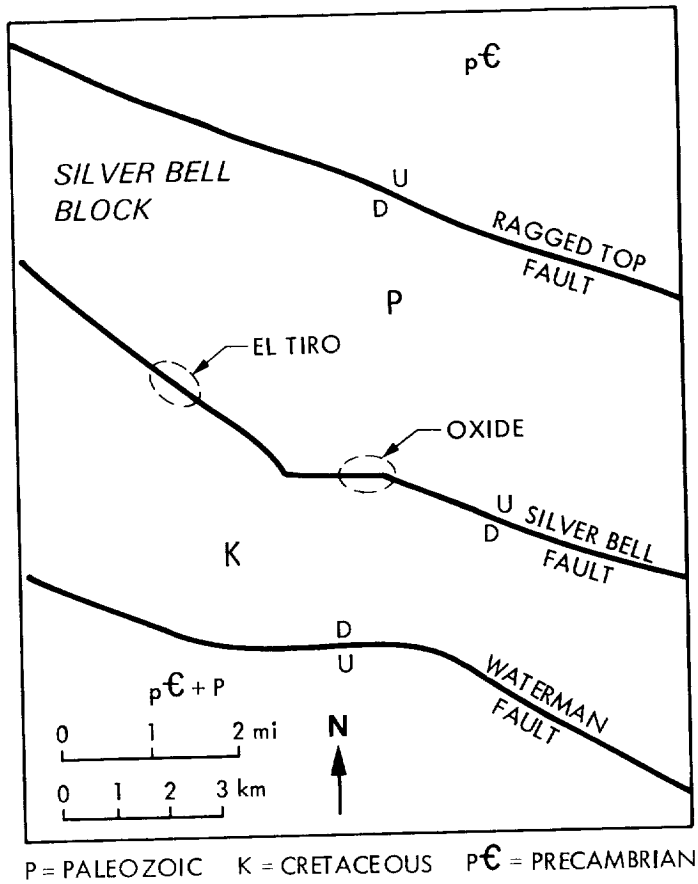

Figure 4-5. Pre-Laramide regional structure (Richard and Courtright, 1966)

These transverse structures are believed to have developed as tensional openings during doming and tilting of the Silver Bell structural block (Watson, 1964). The transverse structures include high-angle faults and swarms of porphyritic dikes. Two of the major transverse faults are the Barite and Mount Mammoth Faults, east of the El Tiro Pit. These two subparallel faults strike north–northeast for a distance of roughly 3 km, transecting the entire Silver Bell Mountains. A third major transverse structure is the Oxide fault zone, a diffuse zone of monzonite and syenodiorite porphyry dikes striking eastward out of the Oxide deposit for a distance of approximately 2 km.

Other transverse faults of northeast to east–west trend are also present in the Waterman Mountains and in the West Silver Bell Mountains. The north end of the West Silver Bell Mountains is transected by an apparent westward extension of the Ragged Top Fault, which juxtaposes Precambrian granite to the north against Laramide volcanic rocks on the south (Banks and Dockter, 1976). The southeast end of the West Silver Bell Mountains is bounded by a straight, northeast-trending feature that appears to be a

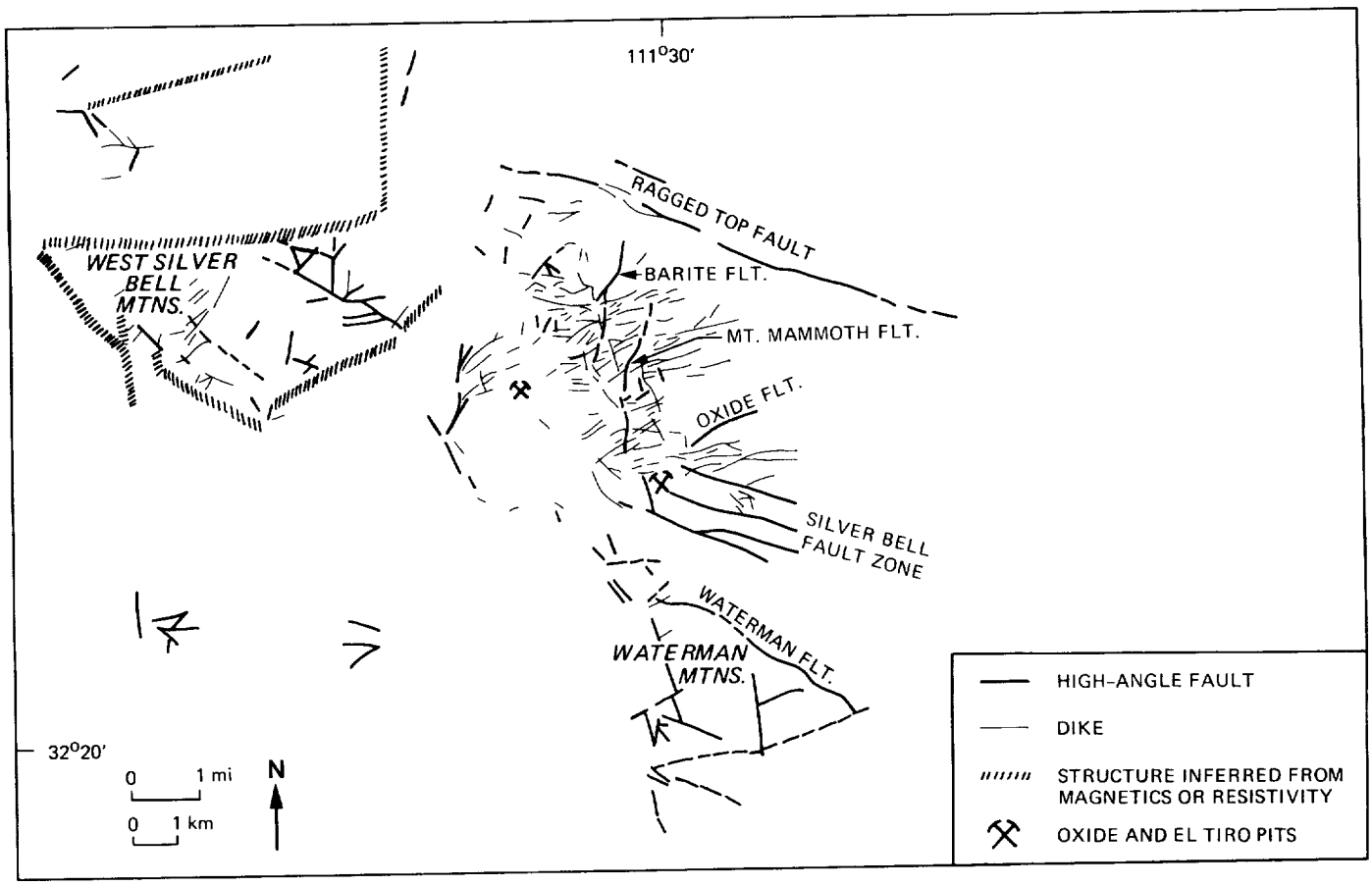

Figure 4-6. Silver Bell structural map showing mapped faults and dikes and showing structures inferred from geophysical data (compiled from ASARCO, unpublished information; Banks and Dockter, 1976; McClymonds, 1959; Texasgulf, unpublished information; Watson, 1964)

possible left-lateral fault, based on apparent offset of the volcanic stratigraphy between the Silver Bell and West Silver Bell Mountains (D. M. Brown–Texasgulf company data). This transverse fault is not exposed, but its existence is supported by aeromagnetic data and by the very straight, northeast alignment of Mammoth Wash along its trend. A third transverse fault of east–west trend has been interpreted in the central part of the West Silver Bell Mountains from magnetic and resistivity data (D. M. Brown–Texasgulf company data).

The structure of the Waterman Mountains block consists of a northwest-trending recumbent fold plunging to the southeast (McClymonds, 1959). This fold structure has been broken by several northwest-trending high-angle thrust or reverse faults. The main northwest structure is the Waterman Fault, a reverse fault which forms a high ridge with a prominent escarpment along the northeast side of the range. The Waterman Fault places upper Paleozoic carbonate rocks on the southwest against Mesozoic clastic rocks within a topographically low area to the northeast.

The central and western parts of the Waterman Mountains are formed by a triangular wedge of lower Paleozoic sediments resting on local inliers of Precambrian granite (McClymonds, 1959). The wedge is faulted against upper Paleozoic rocks on the northeast by a northwest-trending high-angle structure subparallel to the Waterman Fault.

The northwest faults and folds in the Waterman Mountains are displaced by a younger set of northeast to east–northeast strike-slip faults. The largest fault of this system is an inferred east–northeast strike-slip zone south of the central portion of the range (McClymonds, 1959).

3. Emplacement of mineral deposits. According to Watson (1964), three separate periods of mineralization are evident in the Silver Bell area:

(1) An early, minor period of lead-copper mineralization spatially associated with the granodiorite porphyry.

(2) The major period of Laramide porphyry copper mineralization along the Silver Bell structural zone.

(3) A final period of mid-Tertiary (?) lead-copper mineralization in epithermal vein systems of northeast trend.

Lead–zinc–silver replacement deposits at the Indiana Mine in the northern Waterman Mountains may be correlative with the Tertiary mineralization in the Silver Bell Mountains (McClymonds, 1959). Small copper- and zinc-bearing skarns in the West Silver Bell Mountains are probably the same age as the Laramide porphyry copper deposits, based on their association with similar monzonite porphyry intrusives (D. M. Brown–Texasgulf company data).

The porphyry copper deposits in the Silver Bell District were formed about 65 million years ago, in close spatial association with the monzonite intrusives in the Silver Bell structural zone (Watson, 1964). The majority of copper mineralization occurs within the limits of the main alteration zone, a narrow, somewhat arcuate band of pervasive quartz–sericite alteration and discontinuous garnetized limestone bodies. This alteration zone extends the entire length of the side of the Silver Bell Mountains over an exposed distance of approximately 12 km.

Two small porphyry copper deposits were formed along the main alteration zone – the El Tiro deposit on the north and the Oxide deposit on the southeast. Both of these deposits are elliptical in plan view, with horizontal dimensions of approximately 2500 by 2000 m. The deposits appear to be controlled by the intersection of the main alteration zone with northeast-trending dike swarms.

Sulfide mineralization occurs throughout the length of the main alteration zone along systems of tensional fractures and mineralized veins, which generally strike at right angles to the main zone (Richard and Courtright, 1966). The predominant orientation of the mineralized veins is northeast to east–northeast, with a minor north–northwest set, except in the Oxide deposit, where the north–northwest vein set is locally the dominant trend (Galey, 1979). The spacing of fractures appears to be much closer within the limits of the two main porphyry deposits, reflecting the influence of crosscutting structures.

Primary pyrite and chalcopyrite were deposited along the closely spaced parallel fissures to form sheets of near-vertical veinlets. Individual veinlets typically consist of quartz and sulfides, varying in thickness from paper thin to several centimeters and in spacing from several centimeters to a meter (Richard and Courtright, 1966). The primary fracture-controlled mineralization in the igneous rocks of the main alteration zones was accompanied by the formation of tactite mineralization in the Paleozoic limestones. The strongest development of tactites occurred just north of the El Tiro deposit, near the old Atlas Mine, and on the east side of the El Tiro deposit, near the old Union and Mammoth Mines. The average grade of these garnet–diopside–chalcopyrite tactites is about 0.7 to 0.8 percent copper.

Uplift and erosion of the Silver Bell area in early to middle Tertiary time produced extensive leaching and supergene oxidation of the primary mineralization (Loghry, 1972). As a result of this leaching, supergene chalcocite blankets were formed over the El Tiro and Oxide deposits and in the North Silver Bell area. The original protore grades of 0.2 to 0.4 percent copper were enriched to 0.7 to 0.8 percent copper within the chalcocite blankets. The oxidation process converted the upper portion of the main alteration zone to an extensive leached cap, consisting of clays, sericite, iron oxides, and copper carbonates and silicates.

4. Hydrothermal alteration patterns. Published descriptions of hydrothermal alteration at Silver Bell have been written by Kerr (1951) and Richard and Courtright (1966). Kerr's work included a microscopic study of alteration products in the four major intrusive rock types. Some of the important alteration products identified in his study include kaolinite, montmorillonite, illite, sericite, chlorite, alunite, jarosite, and quartz. Kerr divided the intrusive types into four alteration stages, representing a paragenetic sequence from fresh (Stage 1) through sericitic and silicified (Stage 4).

Richard and Courtright illustrate the general outline of the main alteration zone and describe its relation to disseminated copper mineralization (Figure 4-7). They also show the distribution of tactite alteration within the main zone of alteration.

Neither Kerr nor Richard and Courtright describe alteration patterns in terms of classic zoning models, nor do they mention the existence of potassic alteration associated with ore mineralization. The only published references to alteration zoning at Silver Bell are by Lowell and Guilbert (1970) and Graybeal (1982). Lowell and Guilbert tabulated data on 27 major porphyries, where they describe four separate zones: (1) an innermost potassic zone (quartz, K-feldspar, and sericite), (2) an inner phyllic zone (quartz, sericite, and tactite), (3) an intermediate argillic zone (quartz, sericite, kaolinite, and tactite), and (4) an outer propylitic zone (chlorite, calcite, sericite, and montmorillonite). Graybeal's description of the El Tiro area includes a map of alteration zoning that depicts potassic, phyllic, propylit-

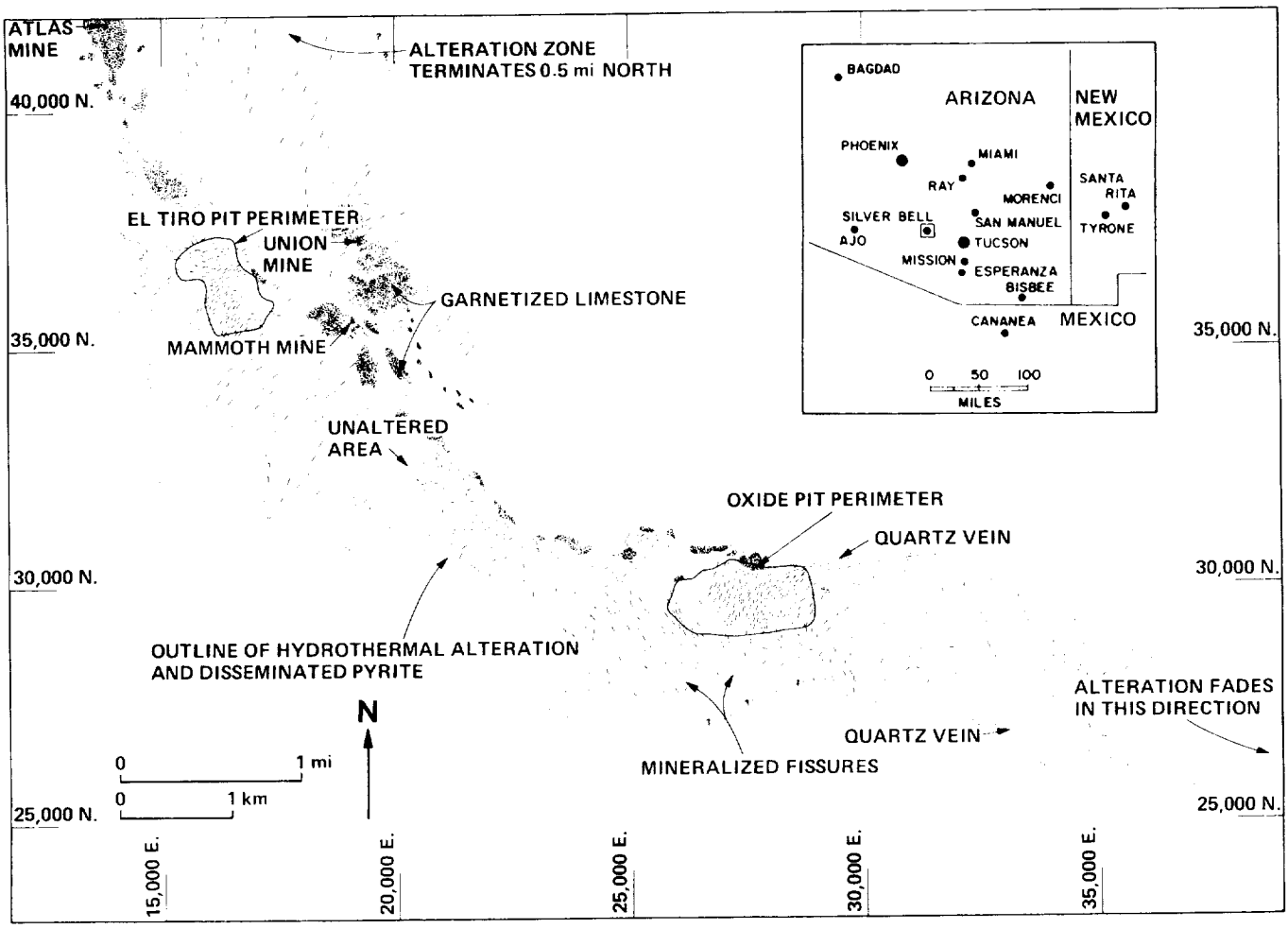

Figure 4-7. Alteration map of Silver Bell District (reprinted from Richard and Courtright, 1966)

ic, and skarn assemblages in a 4- by 6-km area around the El Tiro Pit.

An unpublished alteration map of the Silver Bell District was supplied by ASARCO to aid in our interpretation of aircraft images. ASARCO's map separates the main alteration zone into phyllic and potassic zones. The map also divides the outlying propylitic alteration zone into four subtypes, depending on the relative abundances of epidote, chlorite, and calcite (Figure 4-8).

On the ASARCO map, potassic alteration occurs as two centrally located, narrow bands near the El Tiro and Oxide deposits. Phyllic alteration occurs symmetrically on either side of the two central potassic zones. The two phyllic zones merge east of the Oxide Pit into a single narrow band near the east end of the main alteration zone. (Presumably, the distribution of phyllic and potassic alteration on ASARCO's map is based at least partly on drill hole data since potassic alteration is often difficult to recognize on the surface.)

The four propylitic subzones collectively define two symmetrical and parallel bands on either side of the central phyllic/potassic zone. The propylitic alteration is shown to extend an average of 600 m northeast and 900 m southwest of the phyllic zones. Chlorite is most strongly developed within a central band on the southwest side of the main alteration zone. Epidote is distributed widely throughout the propylitic zone, while vein calcite generally occurs only on the outermost fringes.

5. Discovery and development history. Mining operations at Silver Bell date back to 1863 when high-grade copper deposits were discovered in tactites at or near the surface near the present-day El Tiro Pit. Between 1865 and 1930, approximately 50,000 tons of copper were recovered from underground mines, principally the Union and Mammoth Mines (Kerr, 1951). Around 1909, the disseminated copper possibilities in the igneous rocks were recognized and a churn-drilling program resulted in the partial delineation of the Oxide and El Tiro ore bodies (Richard and Court-

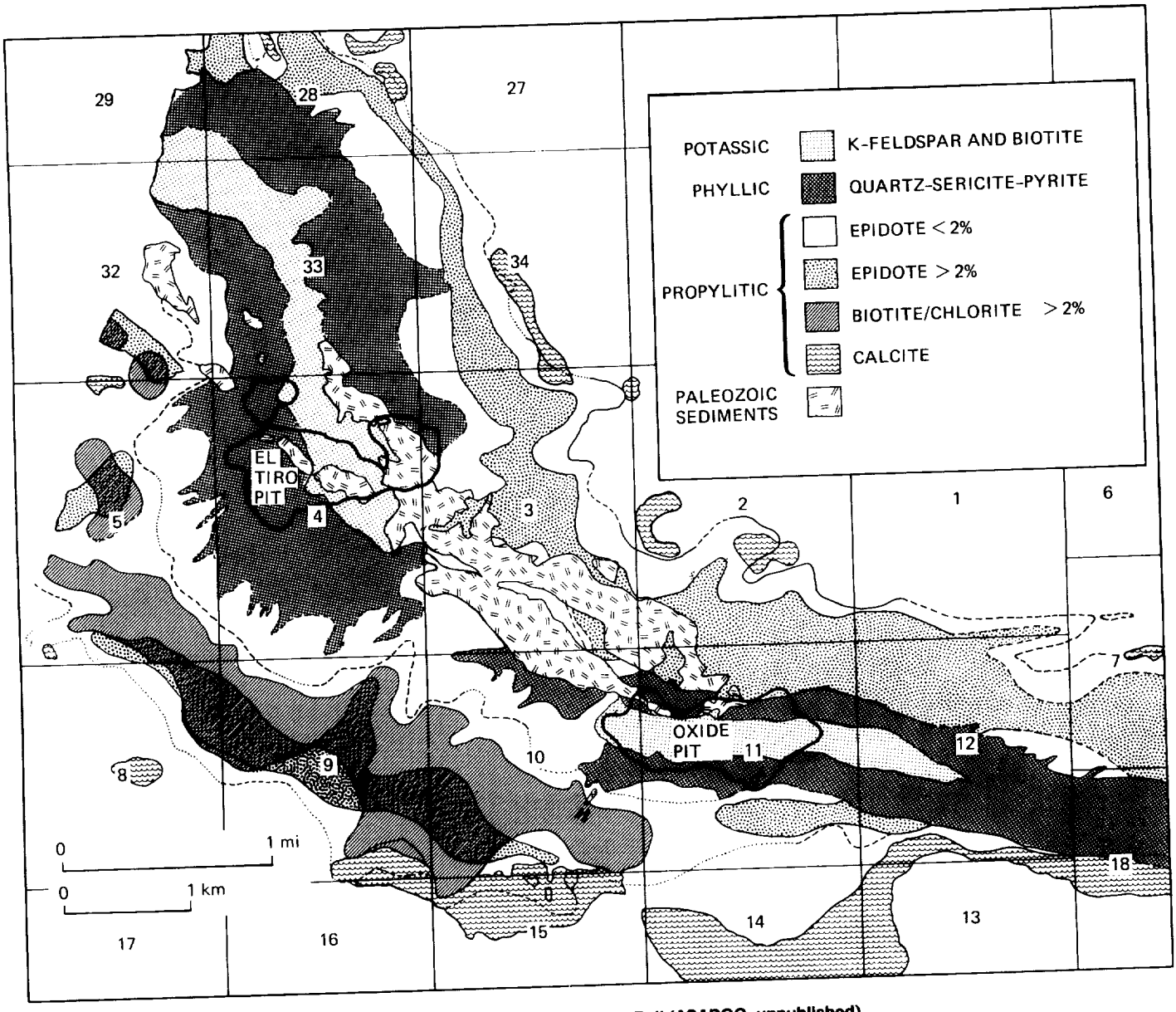

Figure 4-8. Alteration zoning at Silver Bell (ASARCO, unpublished)

right, 1966). However, the grade of the disseminated deposits was too low to mine at that time. Underground mining continued on the tactite deposits until 1930, when mining operations were suspended at the start of the Depression.

ASARCO began an extensive mapping program at Silver Bell in the early 1940s. A churn-drilling program was begun in 1948 on the El Tiro and Oxide deposits. Drilling was largely guided by the interpretation of surface alteration and the study of limonites (hematite, goethite, and jarosite) in leached cappings overlying chalcocite ore. Following the completion of surface drilling, a decision was made to put the two disseminated deposits into production. Production began in 1954, with an initial capacity of 7500 tons of ore per day. Current milling operations process approximately 15,000 tons of ore per day.

The combined reserves of the Oxide and El Tiro deposits are estimated to be 100 million tons (Lowell and Guilbert, 1970). Total production through 1976 was 35 million tons of ore from the Oxide Pit and 38 million tons from the El Tiro Pit (estimated from March 1976 ASARCO mine handout data). Approximately 85 percent of present production is from enriched chalcocite ore and 15 percent is from tactite ore. Approximately 10 tons of copper is recovered daily from oxide-leaching operations.

Recent exploration in the district has centered around the North Silver Bell area, where ASARCO has drilled out an area of discontinuous chalcocite enrichment beneath highly leached and sericitized outcrops of dacite porphyry. A portion of this mineralization extends westward into the area of the old Atlas Mine, currently owned by the BS&K Mining Company. Union Oil Company did exploratory drilling on the BS&K property in the mid-1970s and intersected chalcocite mineralization in some of their holes.

Exploration has been conducted recently by various mining companies in outlying parts of the test site area, including the West Silver Bell Mountains and the eastern Silver Bell Mountains. In spite of the failure of these efforts to locate significant new porphyry deposits, the exploration potential of the region remains relatively high. This conclusion is based mainly on the significant amounts of alluvial and Tertiary volcanic cover in the surrounding area and on the strategic location of the area on a belt of porphyry deposits stretching southeastward into northern Sonora (the so-called Cananea–Silver Bell structure). The Silver Bell fault zone and its neighboring structures, the Waterman and Ragged Top Faults, appear to be subparallel links in this postulated Laramide-age structural zone.

Extension of the major northwestern structures beyond their presently known limits in the Silver Bell and Waterman Mountains is entirely feasible, based on existing geophysical and geological data. With continued exploration, it is very likely that additional porphyry deposits will be found along the buried continuation of the Silver Bell zone or related northwestern structures, such as the Ragged Top Fault.

III. Discussion of PFRS Data

A. Introduction

In situ spectral reflectance measurements can provide valuable information linking mineralogy, spectral response, and multispectral scanner data. Measurement of spectral reflectance was done using JPL's Portable Field Reflectance Spectrometer (PFRS), described in the Technical Appendix, Section 14. The PFRS records a continuous bidirectional reflectance spectrum in the 0.45 to 2.45-μm wavelength region of a 200-cm^2 area on the ground. By sequentially measuring the reflectance of a white standard target, then ratioing the two curves, a relative reflectance curve is obtained. Further processing in the laboratory by computer then converts the relative reflectance to absolute reflectance, based on laboratory measurements of the white standard.

In operation, several measurements are taken of the same unit in the field over a 10- by 10-m area. These measurements can then be averaged to obtain a reflectance curve representative of a particular material. One of the main benefits of such a procedure over laboratory spectral measurements is that soils, dead vegetation, rubble, etc., more representative of the naturally occurring surface and of what is viewed by an aircraft or satellite scanner, are included in the field of view of the PFRS.

In addition, the continuous PFRS curves provide a data base for simulating various scanner instruments by computing appropriate bandpass intervals. Using modeled scanners, various statistical analyses can be performed on this data set to examine separability of various rock units. Examples of these analyses are discussed in Paragraph IV.

B. Spectral Measurements

PFRS measurements were acquired at Silver Bell for eighteen different rock types (Figure 4-9; sample sites are indicated by numbers beginning with "5"). Laboratory X-ray diffraction analyses were done on samples for some of the rocks to determine their mineralogy (Table 4-3). The average reflectance spectra and one standard deviation envelopes are shown in Figures 4-10 through 4-13.

The first four spectra (Figure 4-10) are of dacite, both unaltered and altered. The unaltered dacite spectrum (Figure 4-10a) has moderate albedo; a pronounced absorption band near 2.2 μm; a weak, broad band near 0.9 μm; and a falloff in reflectance from 0.6 μm toward the ultraviolet. The 2.2-μm feature is an Al–O–H vibrational feature (Hunt and Ashley, 1979), due here to the presence of minor kaolinite and mica. The other two features are attributable to electronic transitions in ferric iron (Hunt et al., 1971).

The spectrum of propylitically altered dacite (Figure 4-10b) is similar to the unaltered dacite with a few differences; the ultraviolet falloff in reflectance is stronger; the 2.2-μm absorption band is deeper; and there is an additional absorption band near 2.33 μm. The first two features are probably due to increased concentrations of ferric iron and kaolinite compared to the unaltered rock. The 2.33-μm band is due to the presence of chlorite, a common propylitic mineral resulting from alteration of biotite and other mafic minerals. The band is caused by vibrational processes in the Mg–O–H bonds in the chlorite structure (Hunt and Salisbury, 1970).

The spectrum of phyllically altered dacite (Figure 4-10c) has the typical overall appearance of intensely altered igneous rocks: high reflectance at 1.6 μm, with large

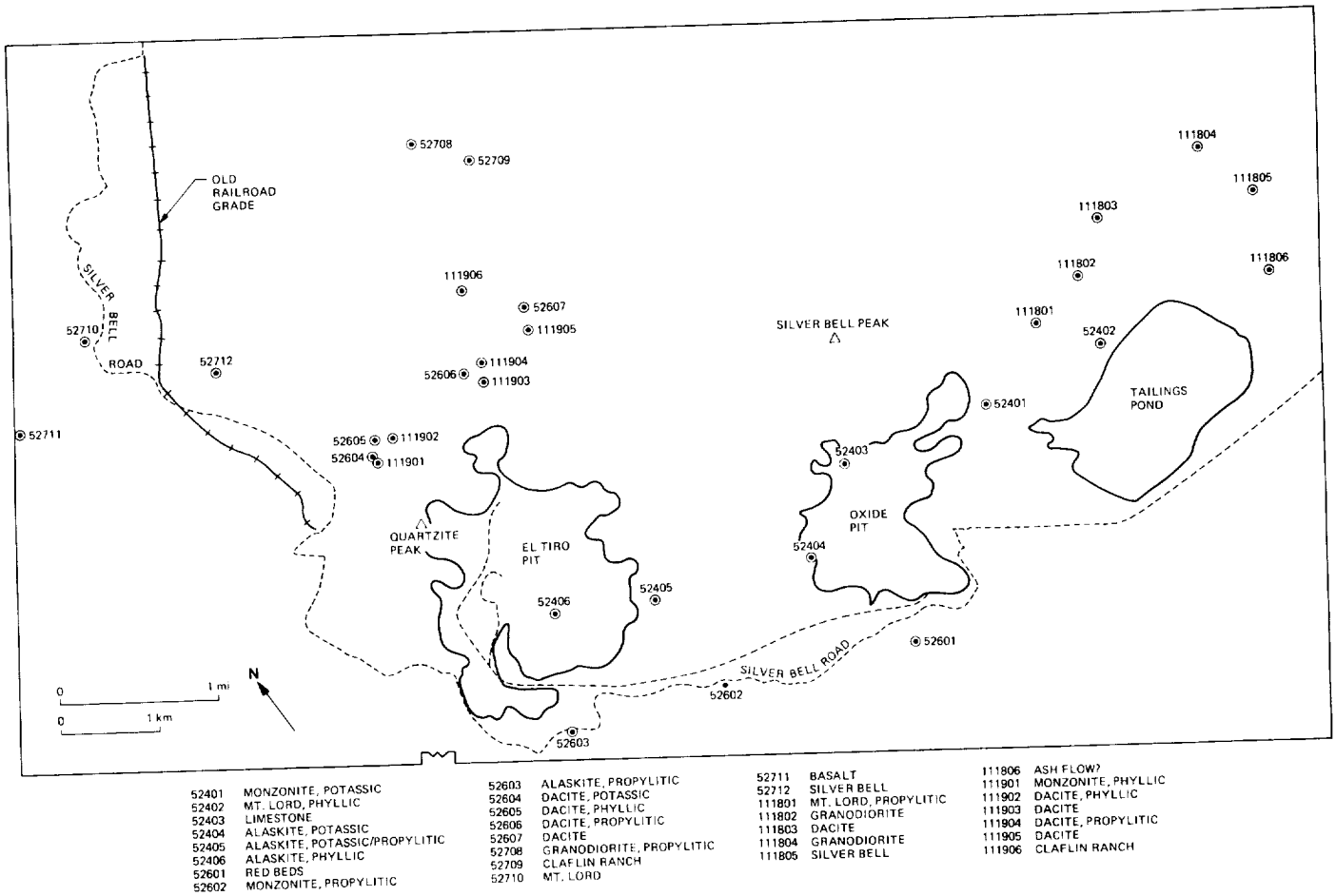

Figure 4-9. Location of sample sites for PFRS data acquisition and mineralogical analyses

decreases toward both shorter and longer wavelengths (Hunt and Ashley, 1979). In detail, ferric-iron absorption features are prominently displayed below 0.6 μm and at 0.65 and 0.9 μm. The intense absorption band at 2.2 μm is due to fine-grained mica (sericite). The characteristic alteration minerals of the phyllic zone are quartz, sericite, and iron oxide/hydroxide. Spectral features of this unit reflect this mineralogical composition. The spectrum of potassically altered dacite (Figure 4-10d) is similar to phyllically altered dacite, but with lower albedo. At Silver Bell, the potassic zone has been overprinted by phyllic alteration; in reality, this unit is more properly called potassic/phyllic. The minerals that characterize potassic alteration (K-feldspar and quartz) have no characteristic absorption features in this spectral region; the spectrum is dominated by features due to the phyllic alteration mineral assemblage.

The spectra of alaskite show similar behavior compared to the dacite spectra. Propylitically altered alaskite (Figure 4-11a) has absorption bands due to ferric iron. The 2.33-μm band is absent because the development of chlorite in this unit is weak. The other three alaskite spectra potassic/propylitic (Figure 4-11b), potassic (Figure 4-11c), and phyllic (Figure 4-11d)—show the effects of overprinting by phyllic alteration. The development of iron oxides from oxidation of pyrite and mafic minerals produces the strong absorption bands at 0.65, 0.9, and short of 0.6 μm. The strong band at 2.2 μm is due to development of sericite and kaolinite from alteration of feldspars.

The spectrum of potassically altered monzonite (Figure 4-12a) again shows absorption bands characteristic of phyllic

Table 4-3. Mineralogy from X-ray analyses

Dacite	Quartz, albite, kaolinite, mica, biotite
Dacite, propylitic	Quartz, andesine, mica, kaolinite, chlorite
Dacite, phyllic	Quartz, albite, mica, goethite
Monzonite, phyllic	Quartz, sanidine, mica, biotite, goethite
Granodiorite	Quartz, sanidine, montmorillonite, goethite
Mt. Lord	Quartz, albite, biotite, kaolinite
Claflin Ranch	Quartz, albite, mica, kaolinite, goethite
Silver Bell	Quartz, andesine, hematite
Limestone	Calcite, goethite, quartz
Red beds	Quartz, albite, hematite, kaolinite

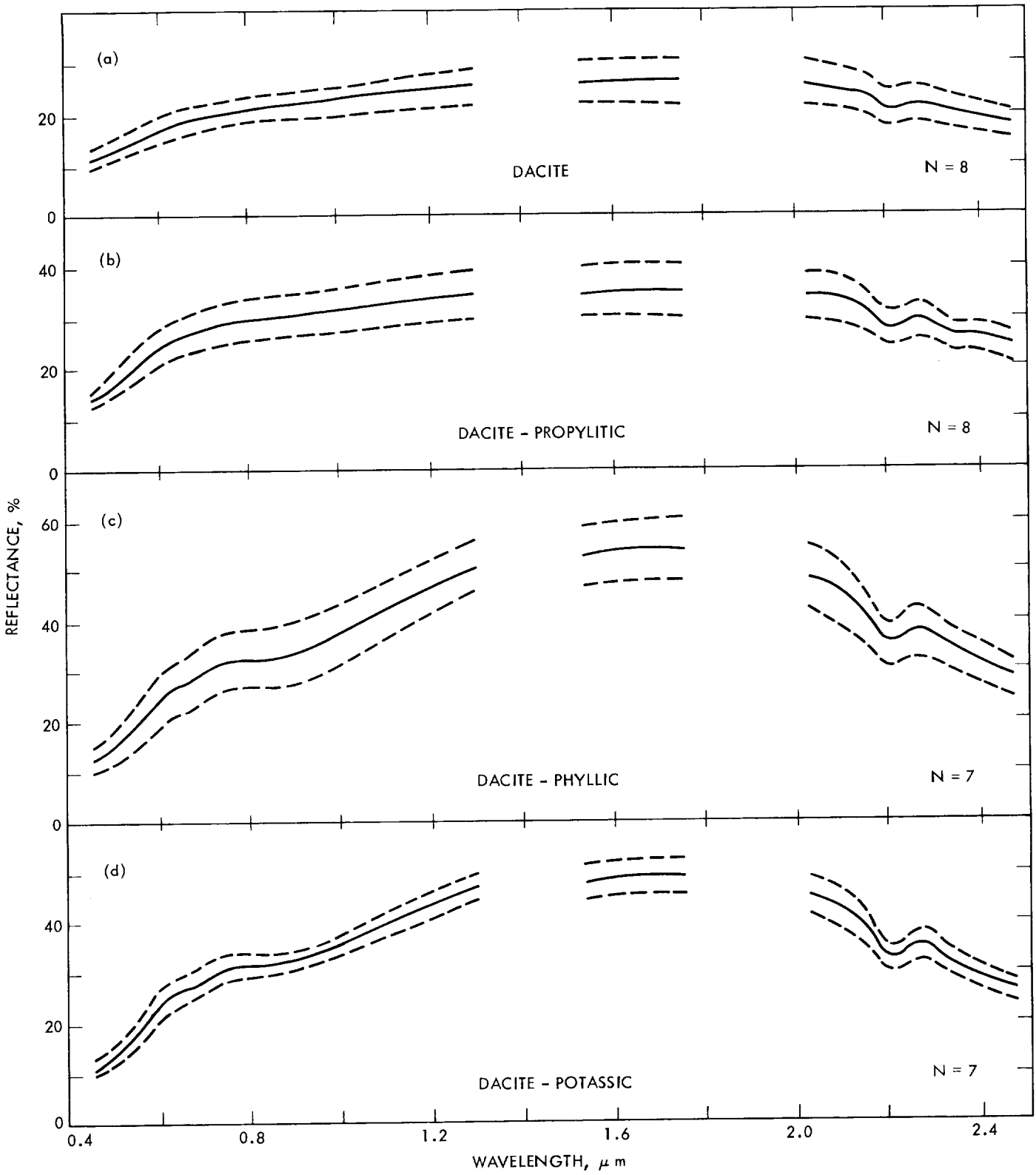

Figure 4-10. PFRS reflectance spectra for rocks measured at Silver Bell: (a) dacite; (b) dacite, propylitic; (c) dacite, phyllic; (d) dacite, potassic. Dashed lines are one standard deviation envelopes. Gaps at 1.4 and 1.9 μm are due to atmospheric water absorption. *N* is number of PFRS measurements represented by the average curve.

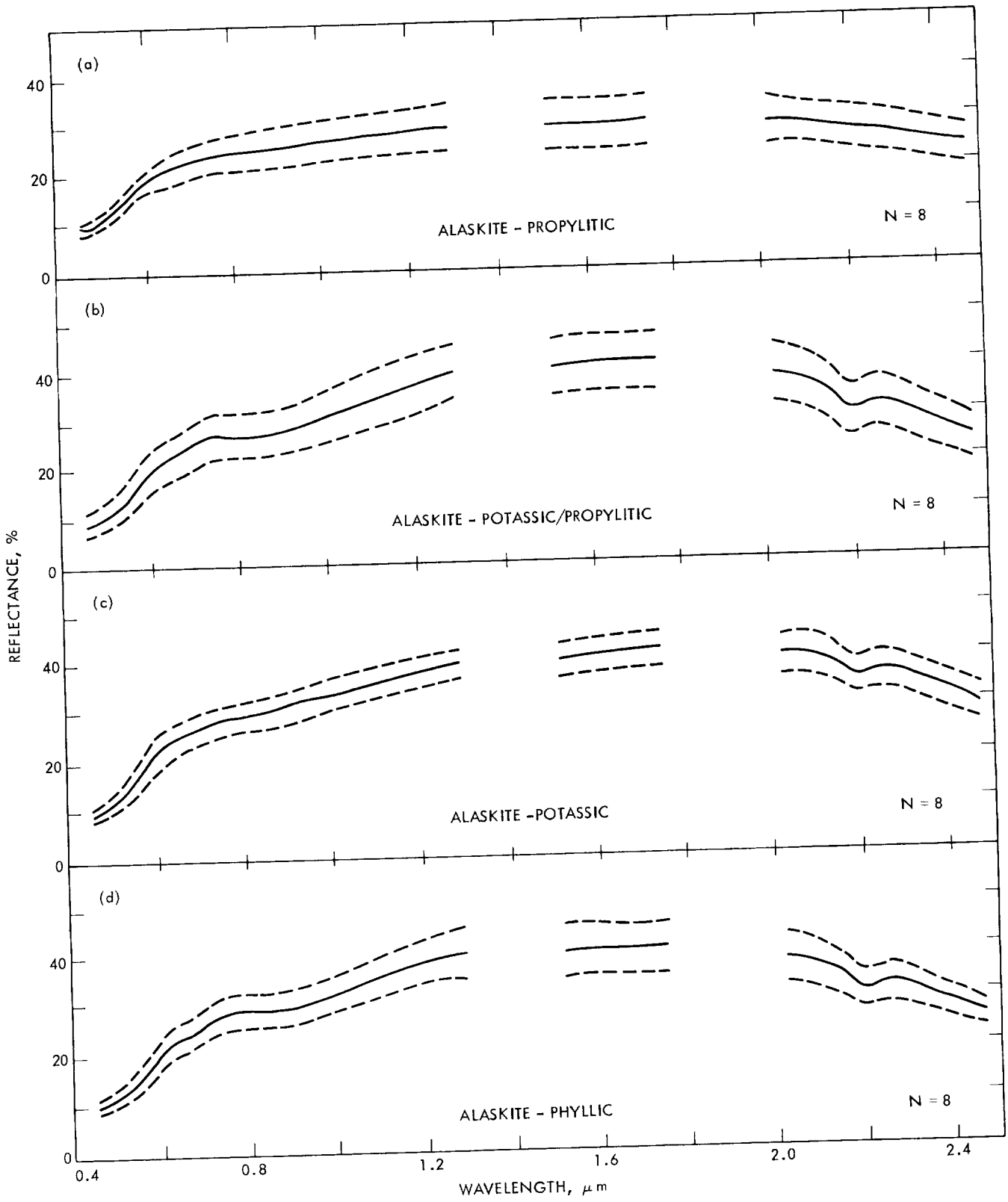

Figure 4-11. PFRS reflectance spectra for rocks measured at Silver Bell: (a) alaskite, propylitic; (b) alaskite, potassic/propylitic; (c) alaskite, potassic; (d) alaskite, phyllic. Dashed lines are one standard deviation envelopes. Gaps at 1.4 and 1.9 μm are due to atmospheric water absorption. *N* is number of PFRS measurements represented by the average curve.

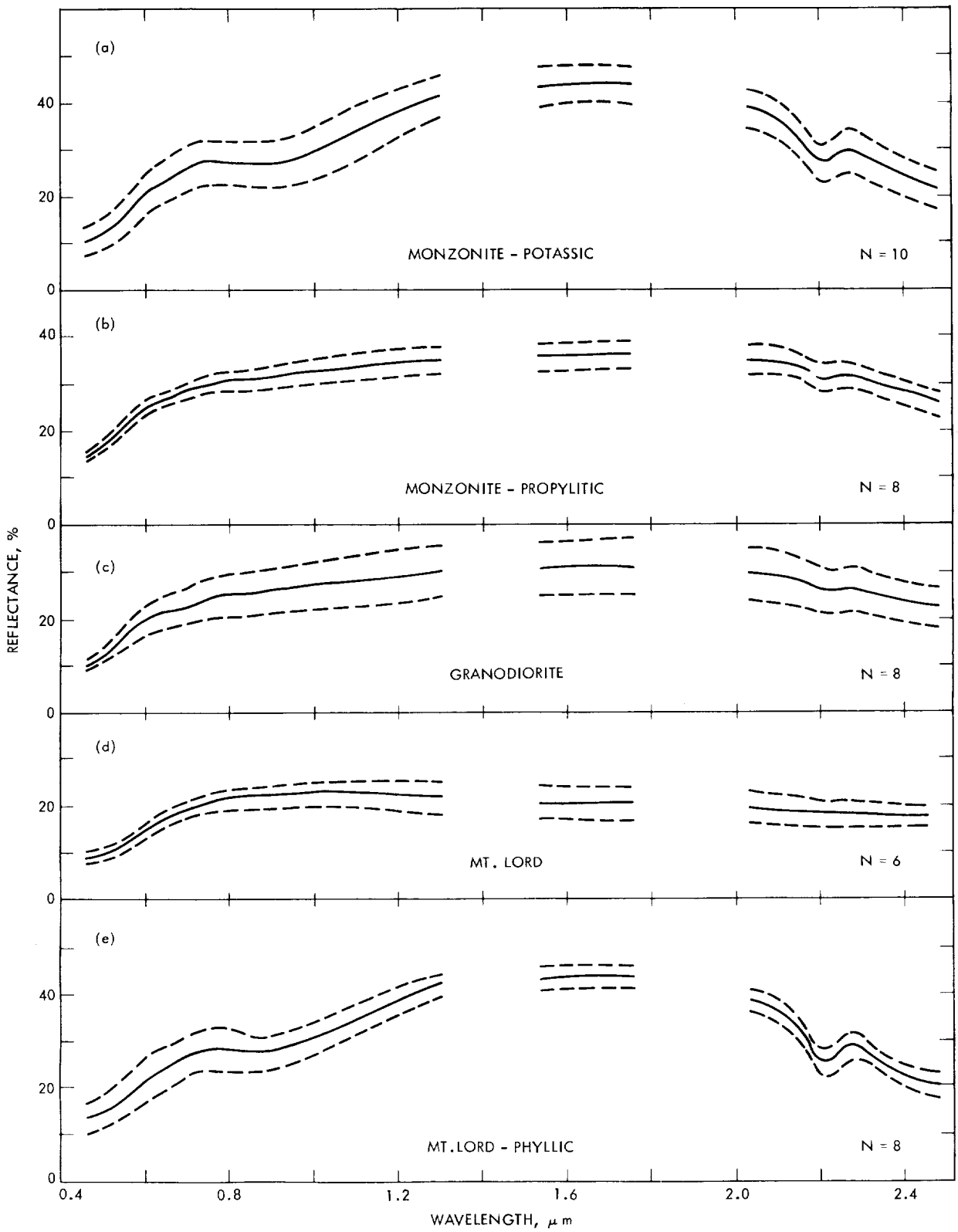

Figure 4-12. PFRS reflectance spectra for rocks measured at Silver Bell: (a) monzonite, potassic; (b) monzonite, propylitic; (c) granodiorite; (d) Mt. Lord; (e) Mt. Lord, phyllic. Dashed lines are one standard deviation envelopes. Gaps at 1.4 and 1.9 μm are due to atmospheric water absorption. *N* is number of PFRS measurements represented by the average curve.

C-2

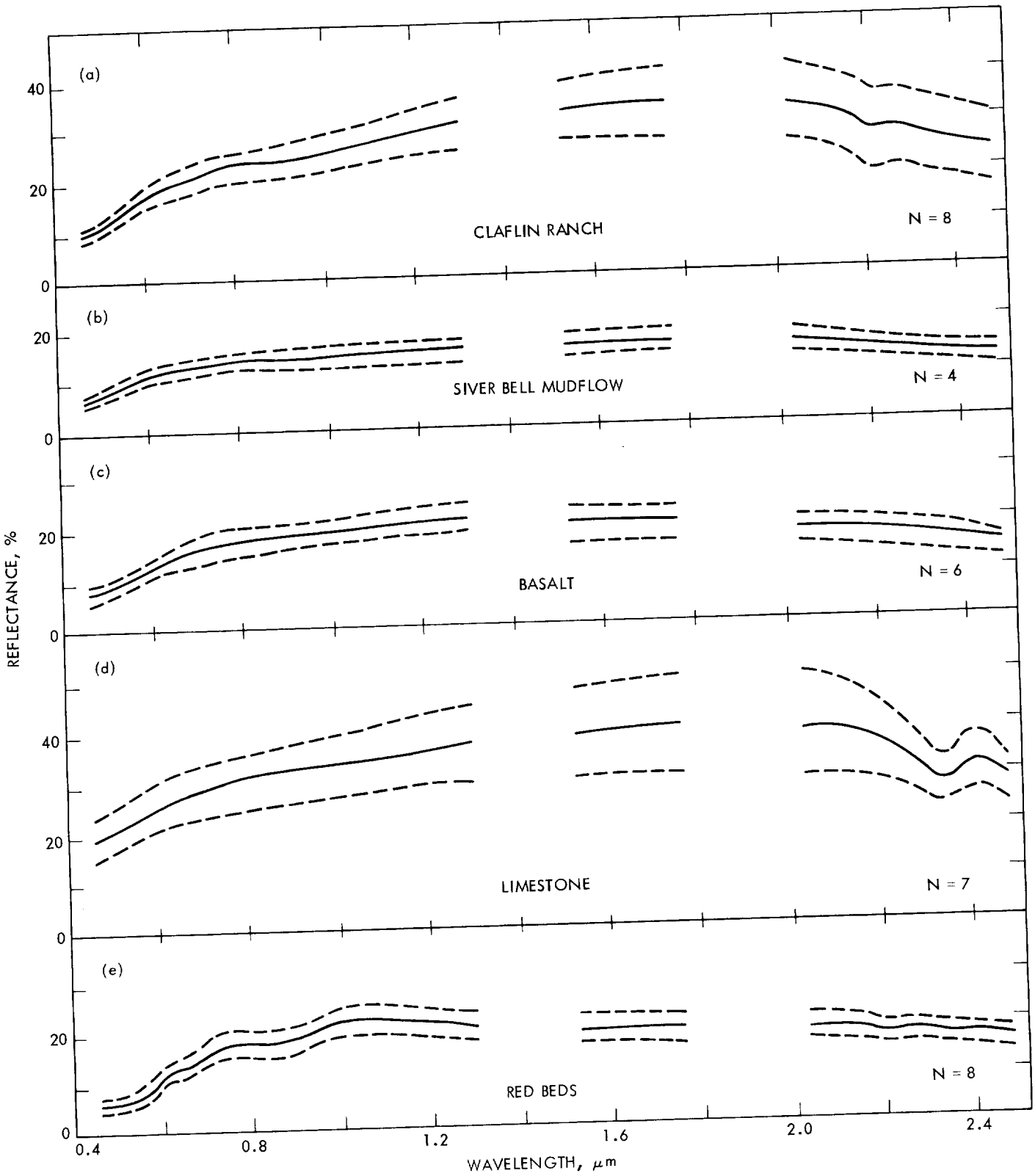

Figure 4-13. PFRS reflectance spectra for rocks measured at Silver Bell: (a) Claflin Ranch; (b) Silver Bell mudflow; (c) basalt; (d) limestone; (e) red beds. Dashed lines are one standard deviation envelopes. Gaps at 1.4 and 1.9 μm are due to atmospheric water absorption. *N* is number of PFRS measurements represented by the average curve.

overprinting. The propylitically altered monzonite (Figure 4-12b) has reduced albedo, weak iron-oxide bands, a weak 2.2-μm band from kaolinite, and a possible subtle 2.33-μm Mg–O–H band from chlorite.

The unaltered Mt. Lord spectrum (Figure 4-12d) has low overall albedo and shows only a falloff toward the ultraviolet from ferric iron. The phyllically altered Mt. Lord (Figure 4-12e) shows strong, well-developed absorption bands from ferric iron and sericite/kaolinite at 0.65, 0.9, and 2.2 μm. The 0.9-μm band is deeper than that shown by either phyllically altered dacite or alaskite, suggesting a larger concentration of ferric minerals.

The spectrum of Claflin Ranch (Figure 4-13a) has weak absorption bands from ferric iron and clays and appears to be weakly altered. The spectra of Silver Bell mudflow (Figure 4-13b) and basalt (Figure 4-13c) are similar: low albedo overall and weak iron-absorption bands.

The limestone spectrum (Figure 4-13d) is dominated by the presence of an intense absorption band, near 2.35 μm, due to vibrational processes of the carbonate radical (Hunt and Salisbury, 1971). Weak iron-absorption bands indicate the presence of ferric minerals in the limestone.

The spectrum of red beds (Figure 4-13e) shows low albedo but very well-developed ferric-iron bands at 0.65 and 0.9 μm due to hematite. Weak bands at 2.2 and 2.35 μm are due to minor amounts of clay and chlorite, respectively. The falloff in reflectance from 1.0 μm toward longer wavelength is typical of dark, highly pigmented sedimentary rocks (Conel et al., 1978).

A summary of the absorption bands seen in the 18 spectra is shown in Table 4-4. The bands are attributable to ferric iron, hydroxyl ion, and carbonate ion processes. Other than features caused by these constituents, albedo is the only characteristic of the spectra which allows them to be differentiated by visual inspection. The four Landsat wavelength bands are in the 0.5- to 1.1-μm region and are quite broad. Iron oxides and albedo are the main features that will influence the appearance of rocks on the Landsat data. The M²S scanner has narrower bands in the same wavelength region; this should allow possible separation of iron oxides. The NS-001 Thematic Mapper Simulator has bands beyond 1.0 μm, including one centered near 2.2 μm. Data from this sensor should allow discrimination of hydroxyl- and carbonate-bearing materials and should provide better discrimination of altered rocks based on their high albedo at 1.6 μm.

Table 4-4. Absorption bands in PFRS spectra

Rock Type	Absorption Band, μm[a]					
	0.4	0.65	0.9	2.2	2.33	2.35
Dacite	M	W		M		
Dacite, propylitic	S			M	W	
Dacite, phyllic	S	M	S	S		
Dacite, potassic	S	M	S	S		
Alaskite, propylitic	S		W			
Alaskite, potassic/propylitic	S	W	M	S		
Alaskite, potassic	S	W	W	M		
Alaskite, phyllic	S	M	M	M		
Monzonite, potassic	S	M	S	S		
Monzonite, propylitic	S		W	M		
Granodiorite	S	M	W	M		
Mt. Lord	S					
Mt. Lord phyllic	S		S	S		
Claflin Ranch	M		M	M		
Silver Bell mudflow	M		W			
Basalt	M		W			
Limestone	M		W			S
Red beds	S	M	M	W	W	

[a] W weak
M moderate
S strong

IV. Sensor Simulations Using PFRS Data

One use of the field spectral reflectance data is to extract wavelength regions corresponding to various scanners and examine how well these simulated instruments can separate various rock types. This analysis does not consider many other factors which affect the signal recorded by an actual scanner instrument. Such factors as atmospheric contributions, effects of field of view on pixel mixing, instrument response parameters, etc., will also influence a particular instrument's ability to separate various materials. Here only position and width of spectral bands as related to the spectral separability of rocks sampled at Silver Bell are questioned. Similar studies have examined separability of plutonic rocks (Blom et al., 1980) and rocks associated with sedimentary uranium deposits (Conel et al., 1980).

In this section, some tests performed using 135 PFRS spectra obtained for 18 rock or alteration types are described. The procedure used was either to obtain the actual instrument filter curves or to approximate the curves with a step function, then to convolve each curve with the PFRS data to obtain a weighted value representing the spectral response.

For this analysis, wavelength regions of five instruments were used. The number and wavelength intervals of the channels are shown in Table 4-5. The sensors are Landsat MSS, M²S 11-channel scanner, Landsat 4 Thematic Map-

Table 4-5. Sensor simulation bands

Landsat MSS 4 channels	M^2S 11-Channel 10 channels	Landsat 4 6 channels	NS-001 7 channels	Idealized 30 channels[a]
0.5–0.6 μm	0.33–0.44 μm	0.45–0.52 μm	0.45–0.52 μm	0.475–0.525 μm
0.6–0.7	0.44–0.48	0.52–0.60	0.52–0.60	0.525–0.575
0.7–0.8	0.49–0.54	0.63–0.69	0.63–0.69	0.575–0.625
0.8–1.1	0.54–0.58	0.76–0.90	0.76–0.90	•
	0.58–0.62		1.00–1.30	•
	0.62–0.66	1.55–1.75	1.55–1.75	•
	0.66–0.70	2.08–2.35	2.08–2.35	2.425–2.475
	0.70–0.74			
	0.76–0.86			
	0.97–1.065			

[a]30 equally spaced channels of 0.05-μm width between 0.475 and 2.475 μm.

per, NS-001 Thematic Mapper Simulator scanner, and an imaginary instrument with 30 equally spaced bands of 0.05-μm width between 0.5 and 2.45 μm. Four analyses were performed for each of the five sensor simulations, examining different groups of rocks. Group A consisted of four types of altered alaskite, Group B consisted of four types of altered and unaltered dacite, Group C consisted of 11 types of altered and unaltered igneous rock, and Group D included all 18 types of rock sampled with the PFRS (Table 4-6).

Analysis was done using a procedure called stepwise linear discriminant function analysis. The aim of discriminant function analysis is to find a set of functions of selected variates (wavelength bands) allowing classification of spectral observations into one of a designated number of populations. In practice, the available (observable) set of discriminant variates may be restricted in number, and the objective may then be to determine how well separation of specified groups is achieved using these restricted variate sets.

The stepwise discriminant analysis program BMD07M of the BMD Biomedical Computer Program Series (Dixon, 1974) was used for analyses reported here. This program has been described in detail by Jennrich (1977). The following discussion is from Conel et al. (1978).

Basically, a stepwise discriminant analysis is a sequence of simple analyses that moves from one analysis to the next by adding or deleting classification variables from the linear discriminant functions. The selection of variables at each

Table 4-6. Rock-type groups

A	B	C	D
Alaskite, potassic	Dacite, potassic	Monzonite, potassic	Monzonite, potassic
Alaskite, potassic/ propylitic	Dacite, phyllic	Alaskite, potassic	Mt. Lord, phyllic
Alaskite, phyllic	Dacite, propylitic	Alaskite, potassic/ propylitic	Limestone
Alaskite, propylitic	Dacite, unaltered	Alaskite, phyllic	Alaskite, potassic
		Monzonite, propylitic	Alaskite, potassic/ propylitic
		Alaskite, propylitic	Alaskite, phyllic
		Dacite, potassic	Red beds
		Dacite, phyllic	Monzonite, propylitic
		Dacite, propylitic	Alaskite, propylitic
		Dacite	Dacite, potassic
		Granodiorite	Dacite, phyllic
			Dacite, propylitic
			Dacite
			Granodiorite
			Claflin Ranch
			Mt. Lord
			Basalt
			Silver Bell

step is controlled to maximize the ratio of the between-group dispersion to the within-group dispersion. The output of the analysis produces the following data:

(1) Group classification function coefficients; these are linear functions used for classifying cases into groups.

(2) Posterior probabilities that case x in Group G came from Group H.

(3) A classification matrix giving the number of cases n_{GH} in Group G whose Group H posterior probability was greatest; these "truth tables" are useful for displaying the success of the classification.

(4) Canonical discriminant functions; these are linear functions that define coordinate transformations providing maximum separation of groups relative to the scatter within groups. These may also be referred to as canonical variates.

For each of the 20 analyses performed, the classification matrix, classification accuracy, and order of input of bands is presented in Figures 4-14 through 4-17. A summary of classification accuracies is shown in Table 4-7.

Overall, Landsat's four wavelength bands were the least adequate in terms of classification accuracy and ability to separate rock types in each group. Accuracy was higher for Groups A and B with few groups, and lower for Groups C and D with more groups. At the opposite extreme, a theoretical scanner having 30 bands in the 0.5- to 2.45-μm region would be able to separate all the rock types almost perfectly, at least from a statistical point of view.

Examination of the analyses of the Landsat 4 Thematic Mapper and NS-001 sensors reveals that, in every case, the 1.65- and 2.2-μm bands are the first two selected (hence the most important). This is a result of the presence at Silver Bell of altered rocks with high hydrous mineral content. The 1.6/2.2-μm ratio is fairly diagnostic of the presence of these types of rocks in the absence of vegetation. Addition of the 1.15-μm band found on the NS-001 scanner compared to Landsat 4 generally provided only marginal improvement in classification accuracy. For Groups C and D, the 1.15-μm band was the last or next to last to be entered, implying that this wavelength region does not contain significant information for separating the rock types examined here.

A significant result emerges upon examination of the Group D test using Landsat 4 and the 30 $\Delta\lambda$ variable sets (Figure 4-17). The first five bands selected from the 30 equally spaced variables are 1.60, 2.15, 0.50, 0.55, and 0.70 μm; the order of selection of the Landsat 4 bands is 1.65, 2.22, 0.48, 0.56, and 0.66 μm. The coincidence of these two selections is remarkable. It implies that given a choice of any 0.05-μm wide bands in the 0.45- to 2.45-μm region, the optimal spectral regions for separating the rock types sampled at Silver Bell are those of the Landsat 4 scanner. This is a completely unpredictable result with significance for the capabilities of Landsat 4 to provide data useful for certain geologic applications.

Table 4-7. Summary of classification accuracies for 20 analyses, percent correct

Sensor	Alaskite (A)	Dacite (B)	Igneous (C)	All (D)
Landsat MSS	81	93	64	65
M^{2}S 11-channel	91	97	89	90
Landsat 4	97	90	89	83
NS-001	97	93	91	89
30 equal	100	100	100	98

The accuracies for the Group D analyses indicate a phenomenon that is perhaps an artifact in this analysis: accuracy increases with the number of bands. Separation can always be achieved statistically given sufficient variables. This was not examined from a theoretical basis, but should be in the future.

V. M^{2}S Image Spectra

A multispectral scanner records data that are proportional to scene radiance. Radiance, in turn, is a function of a material's reflectance, instrument response, field of view, atmospheric effects, etc. If all of the terms could be modeled or measured, it would be possible to use a scanner as a radiometer, extracting the scene reflectance term. Values of reflectance could then be used to infer mineralogical composition based on reflectance and absorption characteristics in the wavelength bands measured by the scanner. The following paragraphs describe various empirical approaches to determine scene reflectance using the M^{2}S 11-channel data and the NS-001 data.

In an attempt to produce image spectral reflectance curves, the August 18, 1977 M^{2}S 11-channel data were examined. Areas representing 15 different rock types at Silver Bell were selected from the image (Table 4-8). Each area contained about 400 pixels. The average digital number (DN) values and standard deviations for the 15 areas were computed from the raw data for each of the 10 visible and near-infrared spectral bands (Table 4-9). These data were plotted and appear as the dashed curves in Figure 4-18. The most obvious feature of the curves is that they bear no resemblance to real spectral reflectance curves (compare to

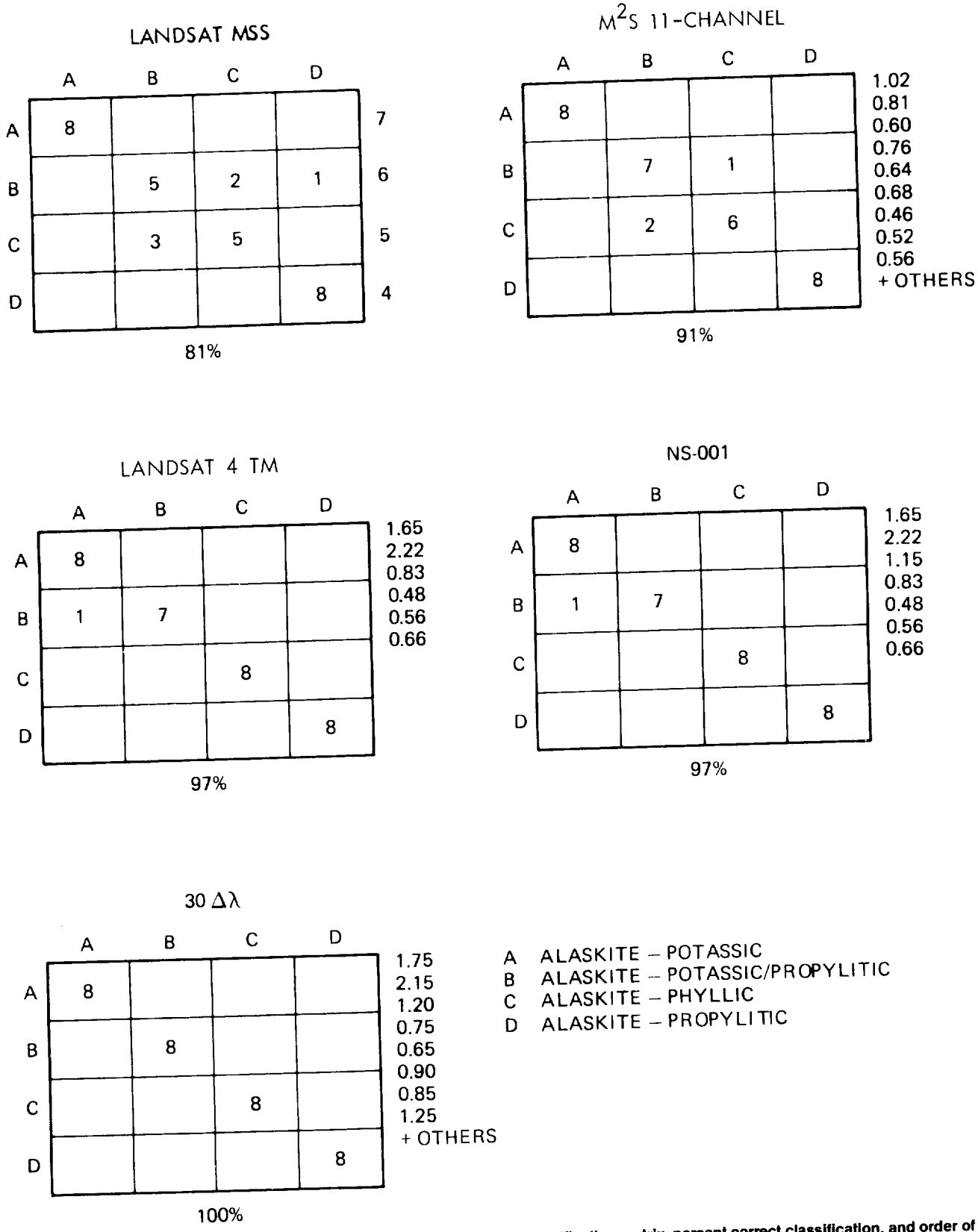

Figure 4-14. Results of linear discriminant function analysis for alaskites: classification matrix, percent correct classification, and order of band selection are shown

LANDSAT MSS

	A	B	C	D	
A	7				6
B	1	6			4
C			7	1	5
D				8	7

93%

M^2S 11-CHANNEL

	A	B	C	D	
A	7				1.03
B		7			0.52
C			7	1	0.60
D				8	0.72
					0.81
					0.56
					0.64
					0.46
					+ OTHERS

97%

LANDSAT 4 TM

	A	B	C	D	
A	6	1			1.65
B		7			2.22
C			7	1	0.83
D			1	7	0.48
					0.66
					0.56

90%

NS-001

	A	B	C	D	
A	7				1.65
B		7			2.22
C			7	1	1.15
D			1	7	0.48
					0.66
					0.83
					0.56

93%

30 $\Delta\lambda$

	A	B	C	D	
A	7				1.60
B		7			2.15
C			8		2.35
D				8	1.65
					2.25
					2.40
					2.20
					1.10
					+ OTHERS

100%

A DACITE – POTASSIC
B DACITE – PHYLLIC
C DACITE – PROPYLITIC
D UNALTERED DACITE

Figure 4-15. Results of linear discriminant function analysis for dacites: classification matrix, percent correct classification, and order of band selection are shown

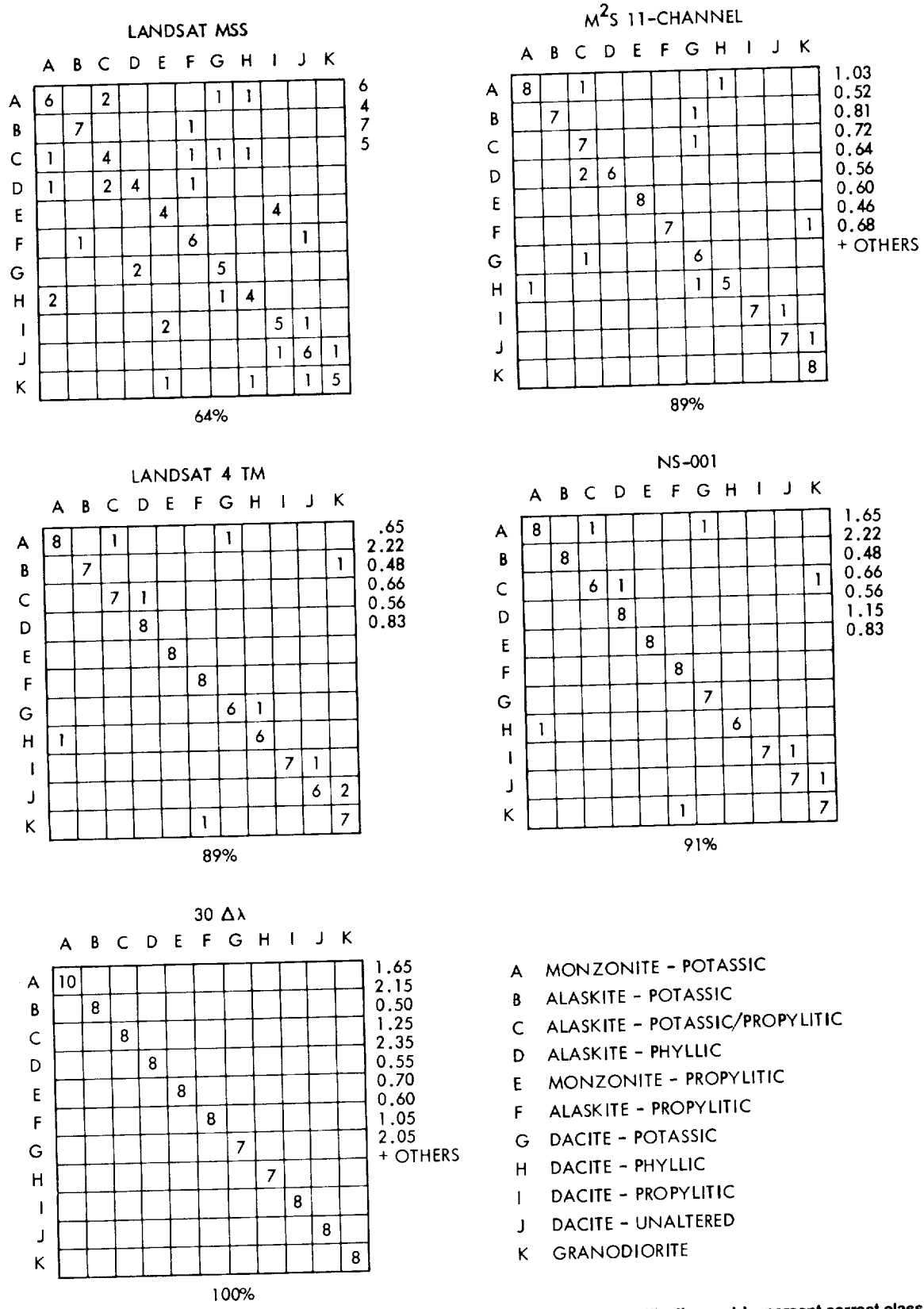

Figure 4-16. Results of linear discriminant function analysis for 11 igneous rock groups: classification matrix, percent correct classification, and order of band selection are shown

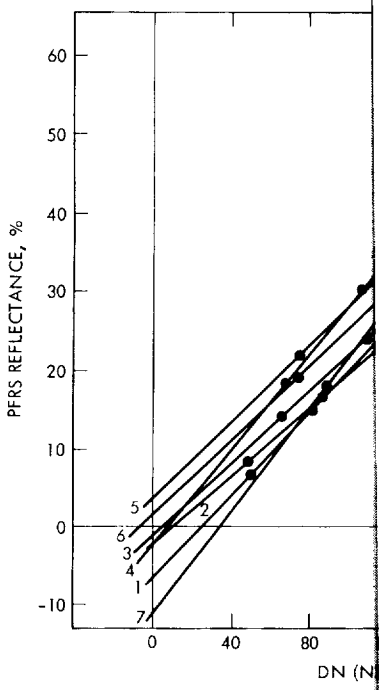

Figure 4-20. Calibration of NS-001 dat are plotted against PFRS reflectance v

extracted, and the average DN each of the 13 areas. The units e and 2 formations, basalt, dacite 1 Mt. Lord, Claflin Ranch, granodi limestone, and red beds.

The DN values versus the se points are shown in Figure 4-21. tion procedure, DN values are p Both DN and reflectance scal y-axis.

The lowest reflectance is shown of 15 percent at 1.15 μm. The absorption band at 0.83 μm. Th the other curves. Laboratory spec Silver Bell often displayed this appears that some miscalibration and values are too high.

The curve for red beds (unit nounced falloff in reflectance lengths. This is consistent with its results in the major absorption in of which is seen in the blue and gr

The curve for dacite 1 (unit 4) s in the 2.2-μm band. The area fr

Table 4-14. 1.6/2.2-μm image sp

Unit	Image Spectr
1 Silver Bell 1	1.33
2 Silver Bell 2	1.46
3 Basalt	1.71
4 Dacite 1	1.55
5 Dacite 2	1.45
6 Ragged Top	0.97
7 Mt. Lord	1.58
8 Claflin Ranch	1.21
9 Granodiorite	1.46
10 Alaskite	1.09
11 Monzonite	1.11
12 Limestone	1.24
13 Red beds	1.0

sponding to gross variations in andesite and most Tertiary volcan gray- to maroon-colored regions. dacite porphyry, monzonite, and tary units all have similar brown

Paleozoic limestones show up relief areas with a light gray c trending quartz latite dikes in t

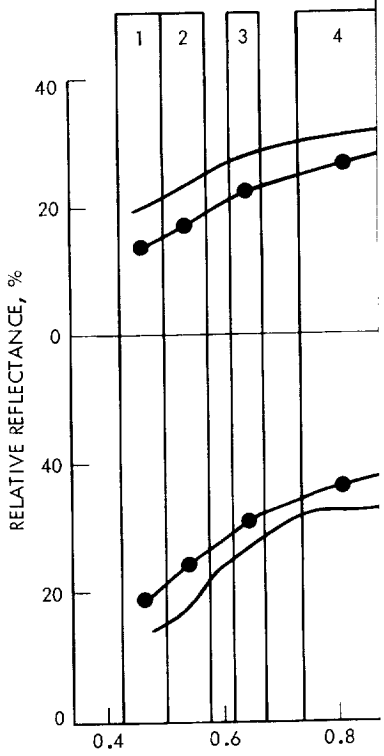

Figure 4-22. Comparis

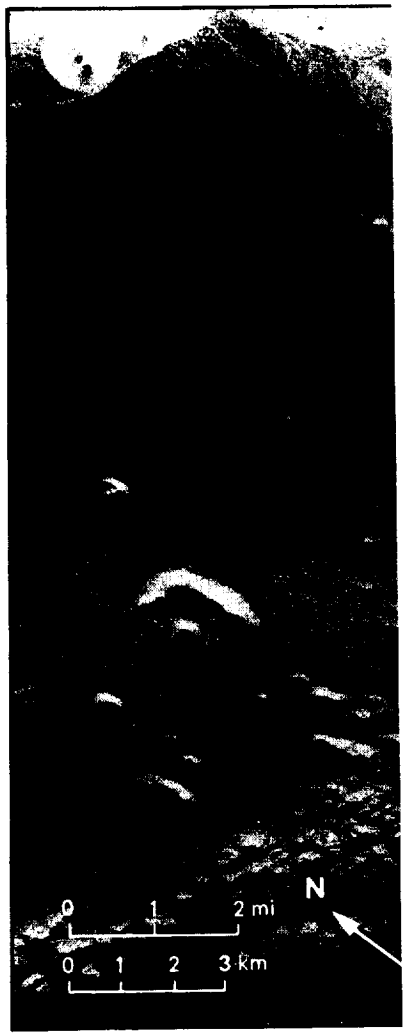

Figure 4-24. X-ba

can be highlighted (Rowan et al. shown in Figure 4-27, a portion of in June 1977. This composite w band-ratios 4/5, 5/6, and 6/7 a respectively. No atmospheric corre to the data prior to ratioing. Are the surface are displayed in sh (Figure 4-28).

Alteration within the main Sil shows up as several reddish-orang to the most highly iron-oxide-sta pyrite to limonites). The North Silv visible north of the El Tiro Pit. S of main zone alteration are also v of the Oxide Pit. A dispersed, pur the Oxide Pit corresponds to iron-

Table 4-8. Rock types from M²S data

1. Ragged Top	6. Limestone	11. Alaskite
2. Granodiorite	7. Precambrian	12. Monzonite
3. Basalt	8. Silver Bell 1	13. Mt. Lord 1
4. Red beds	9. Dacite, propylitic	14. Mt. Lord 2
5. Dacite, phyllic	10. Claflin Ranch	15. Silver Bell 2

PFRS curves, Figures 4-10 through 4-13). This is because the raw DN values represent radiance values recorded by the sensors, with instrument gain factors, atmospheric scattering, and solar irradiance terms convolved in a complicated fashion. In theory, it is possible to determine or model all of these terms and then apply corrections to the raw data to extract reflectance values. A far easier method is either (1) to use ground spectral reflectance measurements for calibration values and then compute the relative reflectance values from the raw DN values, or (2) to assume that the shape of the curve for one rock type is known and use that for calibration. The latter technique was used by assuming that the basalt reflectance curve is flat in the 10 channels of data. This is a fairly good approximation since actual reflectance curves of unvegetated, fresh basalt are mostly flat and featureless, except for a slight decrease in reflectance below 0.6 μm.

A major reason for attempting this calibration is to simulate a real situation when remote sensing data are acquired over an area where no field spectral measurements exist. If it is known that a particular rock type outcrops in the area, and the reflectance properties of this rock type can be approximated, there is a fair possibility of being able to calibrate the data by this method. In theory any recognizable rock would suffice, but recognition is a key factor. Basalt has fairly constant properties, as do water and a few other materials.

It was assumed, therefore, that the DN values for basalt (unit 3) represented the same reflectance values for each channel. The basalt DN value for a given channel was divided into the values for the other 14 rock types, and their relative reflectances determined. A list of values is found in Table 4-10. These values are plotted in Figure 4-19.

The overall impression is that these curves look more or less like actual reflectance measurements. There is a general decrease in relative reflectance toward shorter wavelengths, which is characteristic of almost all naturally occurring rocks. The spike in channel 7 seen in all of the curves appears to be artificial. Some problems are to be expected since one data point is being used to estimate two parameters. Grossly simplified, reflectance is proportional to observed radiance with an offset term:

$$\text{Reflectance} \approx a\text{Rad} + b$$

where a and b are constants, incorporating all multiplicative factors and all additive factors. These include instrument gains and offsets, atmospheric path radiance terms (both multiplicative and additive), etc. (For a complete discussion of the problem of reflectance versus instrument response, refer to the Lisbon Valley, Utah, Uranium Test Site Report, Section 8, Appendix A.)

Probably the two most prominent spectral features are the dips in reflectance at 0.55 and 0.8 μm. These are the

Table 4-9. Raw DN values and standard deviations from M²S data

Rock Group	Channel									
	1	2	3	4	5	6	7	8	9	10
1	194,7	201,11	141,8	111,7	107,7	113,8	117,9	139,9	157,10	180,12
2	170,3	173,4	125,3	100,3	93,3	95,3	94,4	113,3	124,3	131,4
3	133,2	125,2	88,2	69,1	64,2	66,2	63,2	83,2	91,3	91,3
4	145,3	137,4	95,3	74,2	73,2	78,3	79,3	101,3	111,4	123,4
5	166,5	171,8	123,6	100,6	98,6	104,7	108,8	132,9	142,9	159,8
6	162,8	166,11	119,8	95,7	88,7	90,7	90,8	114,8	129,9	142,10
7	161,2	151,2	103,1	82,1	83,1	90,2	92,2	114,2	125,2	136,3
8	170,4	172,5	123,3	98,2	91,2	93,2	92,2	111,2	121,3	127,4
9	168,3	174,5	126,4	102,3	95,3	98,3	98,4	121,4	135,4	145,4
10	170,6	175,9	126,7	102,6	97,6	101,6	101,7	123,6	136,5	147,4
11	152,4	153,6	111,4	91,4	89,4	94,5	95,6	117,5	132,5	143,6
12	152,3	156,5	115,4	95,3	90,3	93,3	96,3	116,3	131,4	139,4
13	151,6	149,9	105,7	85,6	82,7	87,9	89,10	113,11	127,11	137,13
14	163,2	160,3	113,3	90,3	85,3	89,4	90,5	110,5	121,6	124,6
15	171,6	173,8	122,5	96,4	90,4	92,5	92,6	113,6	125,7	130,8

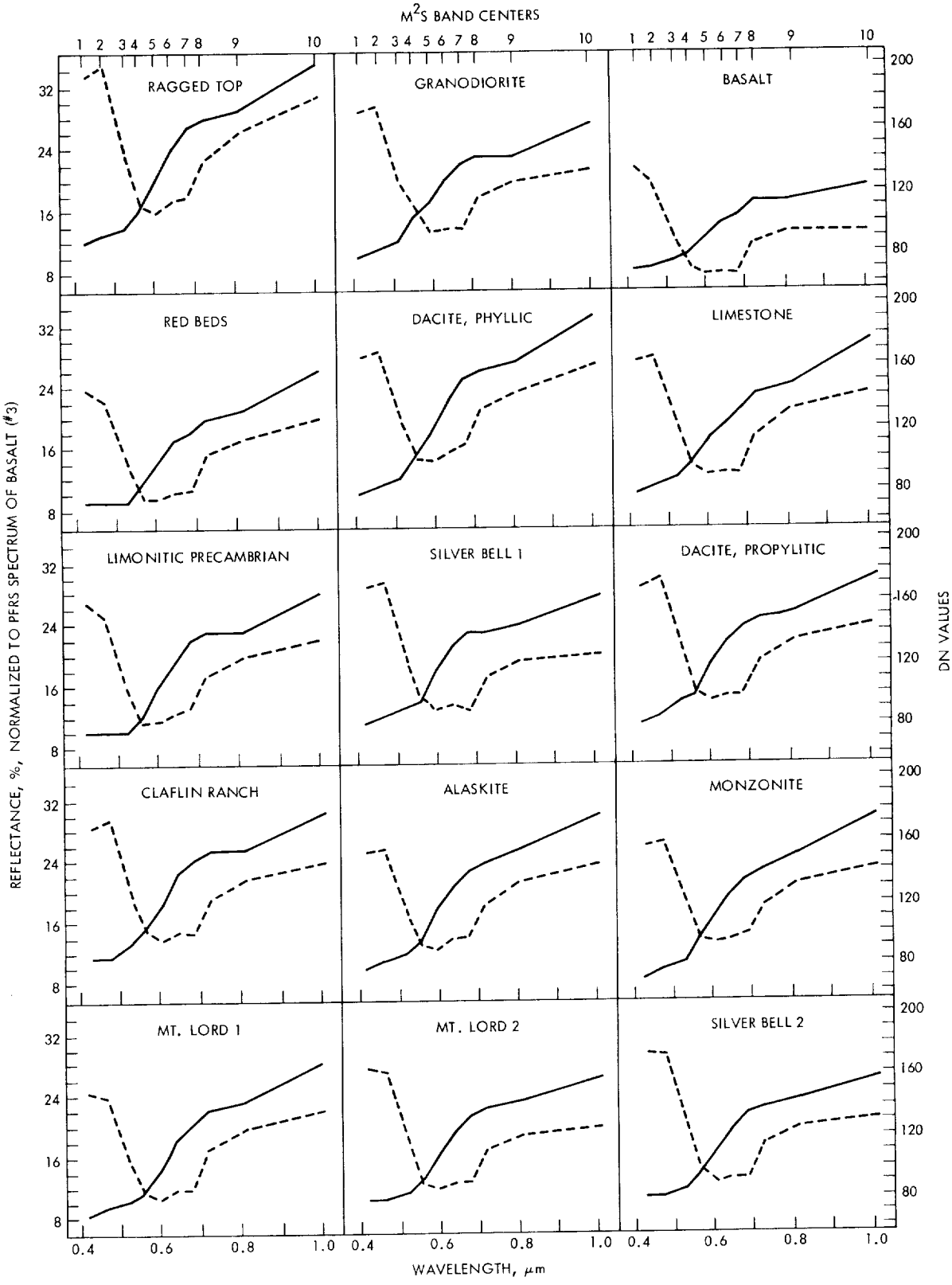

Figure 4-18. Image spectra from M²S 11-channel data for 15 rock types at Silver Bell. Dashed curves are raw DN values. Solid curves are spectra normalized to PFRS basalt spectrum (unit 3).

Table 4-10. M^2S relative reflectance normalized to basalt

Rock Group	Channel									
	1	2	3	4	5	6	7	8	9	10
1	1.46	1.61	1.60	1.61	1.67	1.71	1.81	1.67	1.73	1.98
2	1.28	1.18	1.42	1.45	1.45	1.43	1.47	1.36	1.36	1.42
3	1.0	1.0	1.0	1.0	1.0	1.0	1.0	1.0	1.0	1.0
4	1.09	1.10	1.08	1.07	1.14	1.18	1.23	1.22	1.22	1.37
5	1.25	1.37	1.40	1.46	1.53	1.57	1.69	1.59	1.56	1.73
6	1.22	1.33	1.35	1.38	1.38	1.36	1.41	1.36	1.42	1.56
7	1.21	1.21	1.17	1.19	1.30	1.36	1.44	1.36	1.37	1.49
8	1.28	1.38	1.40	1.41	1.42	1.41	1.44	1.34	1.33	1.38
9	1.26	1.39	1.43	1.48	1.48	1.48	1.53	1.46	1.48	1.59
10	1.28	1.41	1.43	1.48	1.52	1.53	1.58	1.48	1.49	1.62
11	1.14	1.22	1.26	1.32	1.39	1.42	1.48	1.41	1.45	1.57
12	1.15	1.25	1.31	1.38	1.41	1.41	1.48	1.40	1.44	1.54
13	1.13	1.19	1.20	1.23	1.28	1.32	1.37	1.36	1.40	1.51
14	1.23	1.28	1.28	1.30	1.33	1.35	1.41	1.32	1.33	1.36
15	1.29	1.38	1.39	1.39	1.39	1.39	1.44	1.36	1.37	1.43

locations of iron-oxide absorption bands. They are best developed in curves 4 and 7, which are red beds and limonitic Precambrian rocks. The shapes of the rest of the curves are fairly similar, the major difference being albedo. This is not surprising since the 0.4- to 1.0-μm region is not very useful for rock-type discrimination compared to the region beyond 1.0 μm due to the absence of major absorption bands other than those produced by iron.

This technique seems to provide an adequate means for calibrating aircraft scanner data (and presumably satellite data) when no ground spectral measurements are available. All that is required is recognition of a rock type in the image for which a spectral curve can be confidently estimated.

A more rigorous approach to calibration is to use field spectral measurements as the reference curve. PFRS data for basalt at Silver Bell were used to normalize data for the other rock types. The average PFRS reflectance curve for basalt was examined to determine the relative reflectance values for the 10 channels of the M^2S. These values appear in Table 4-11, with the DN values determined from the digital M^2S tape data. The basalt PFRS reflectance value was divided by its DN value for each channel to determine a scaling factor to apply to the remainder of the image data. The DN values (Table 4-9) were multiplied by the appropriate channel scaling factor to arrive at relative reflectance values for the other 14 units (Table 4-12). These values are plotted against channel number and wavelength and appear in Figure 4-18 as solid curves.

The shapes of all of the curves are quite similar: there is a falloff in reflectance toward short wavelengths, and three absorption bands are present—one at 0.8 μm, a major one at 0.45 μm, and a suggestion of a band at 0.65 μm. These features can all be attributed to the presence of iron oxides in the rocks. These curves are quite similar to those obtained by the PFRS. Differences can be attributed to problems in sampling—the PFRS data are made up of 10 spectra per 8- by 8-m site, the M^2S "spectra" are 5- by 5- to 10- by 10-pixel areas which sample 40- by 40- to 80- by 80-m areas. Overall, these curves indicate that this calibration method provides an excellent empirical approach to converting sensor radiance measurements to relative reflectance values, thus compensating for the contribution of atmospheric scattering, instrument response, etc., without actually knowing or modeling these terms.

VI. Calibration of NS-001 Data

Multispectral scanner data, which are a function of the gain factor of the instrument, the transmittance of the atmosphere, the surface reflectance, direct solar illumination, skylight illumination, radiance contributed by atmospheric scattering, radiance contributed by surface outside the IFOV, and instrument offset values (Slater, 1980), are recorded onboard a sensor platform in terms of radiance. In general, image processing algorithms are designed to maximize relative differences between surface units and operate on the DN values recorded by the instrument. Judging by the many successful applications, this approach is both pragmatic and useful. However, there are several areas where recovery of the surface reflectance component is desired for various analyses. A few of these are reported in later paragraphs.

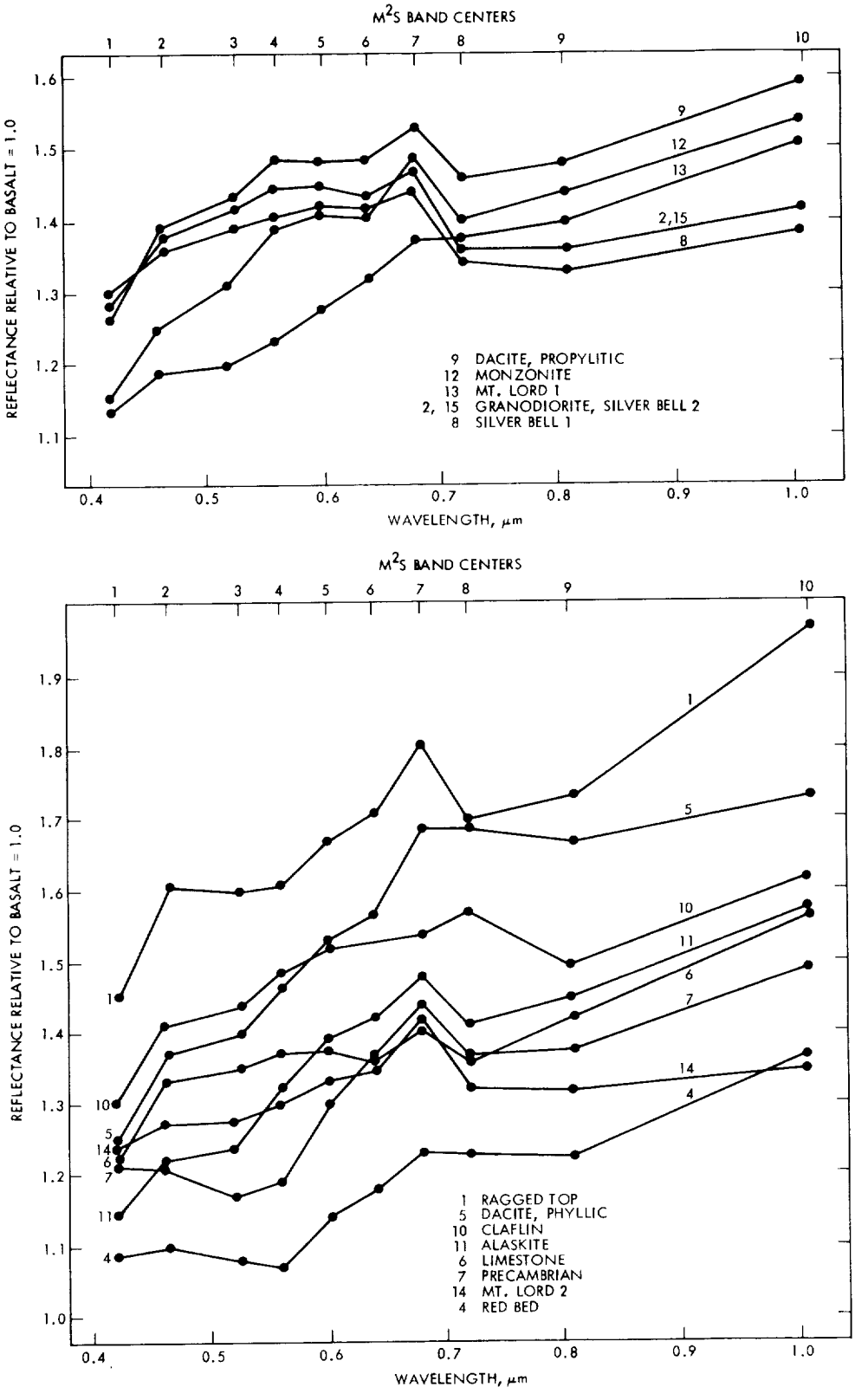

Figure 4-19. Image spectra from M²S 11-channel data derived by normalizing raw DN values to imaginary basalt curve with equal reflectance values in all channels

Table 4-11. Silver Bell basalt: PFRS average curve[a]

Channel	Reflectance (A), %	DN (B)	A/B
1	8	133	0.06
2	8	125	0.064
3	9	88	0.10
4	10	69	0.145
5	12	64	0.188
6	14	65	0.215
7	15	64	0.234
8	17	83	0.20
9	17	91	0.187
10	19	91	0.209

[a]M²S 11-channel reflectance from PFRS data (estimated at channel midpoint).

Table 4-13. NS-001 DN values versus percentage reflectance (PFRS)

Channel	DN (R)[a]	R (R)[b]	DN (M)[c]	R (M)[d]	m[e]	b[e]
1	49.9	6.5	69.6	11.7	0.26	-6.6
2	48.6	8.4	87.2	16.8	0.22	-2.2
3	66.3	14.0	109.0	23.9	0.23	-1.4
4	67.8	18.1	96.0	26.7	0.31	-2.6
5	76.0	21.8	133.8	35.8	0.24	3.4
6	75.8	19.0	179.7	44.0	0.24	0.7
7	88.0	17.9	126.3	30.2	0.32	-10.3

[a]DN values of red beds.
[b]Reflectance of red beds.
[c]DN values of monzonite.
[d]Reflectance of monzonite.
[e]$R = m\mathrm{DN} + b$.

There are many different ways to approach the problem of extracting reflectance from the radiance data. Most methods involve estimation or measurement of the atmospheric terms (see Rogers and Peacock, 1973, Ross, 1973, and Turner et al., 1975, for examples). An empirical approach was used here. Reflectance measurements obtained by the PFRS in the field for red beds and monzonite units at Silver Bell provided calibration points. Areas were identified on the images corresponding to those measured on the ground. The DN values for each channel were extracted from the image data for these areas, and plots of PFRS reflectance versus DN values were constructed. Table 4-13 lists the values used and the slope and intercept of the lines relating reflectance to DN:

$$R_i = m_i \mathrm{DN}_i + b_i$$

where R_i is the reflectance of the ith channel, DN_i is the DN value from the NS-001 data, and m and b are constants. The straight line approximations (Figure 4-20) assume that reflectance is a linear function of measured radiance (DN). This method lumps all the atmospheric and instrument terms into a multiplicative and an additive correction term. Although this is an unsophisticated approach, results using this technique indicate that it is fairly accurate. Its ease of implementation further recommends its use for general applications.

VII. NS-001 Image Spectra

The calibrated NS-001 data were used to create image spectra for 13 rock units. Areas were identified on the image based on the geologic map. A 5- by 5-pixel area was

Table 4-12. M²S reflectance values normalized to PFRS basalt spectrum

Rock Group	Channel 1	2	3	4	5	6	7	8	9	10
1	12	13	14	16	20	24	27	28	29	37
2	10	11	12	15	17	20	22	23	23	27
3	8	8	9	10	12	14	15	17	17	19
4	9	9	9	11	14	17	18	20	21	26
5	10	11	12	15	18	22	25	26	27	33
6	10	11	12	14	17	19	21	23	24	30
7	10	10	10	12	16	19	22	23	23	28
8	10	11	12	14	17	20	22	22	23	27
9	10	11	13	15	18	21	23	24	25	30
10	11	11	17	15	18	22	24	25	25	30
11	9	10	11	13	17	20	22	23	25	30
12	9	10	11	14	17	20	22	23	25	30
13	9	10	11	12	15	19	21	23	24	29
14	10	10	11	13	16	19	21	22	23	26
15	11	11	12	14	17	20	22	23	24	27

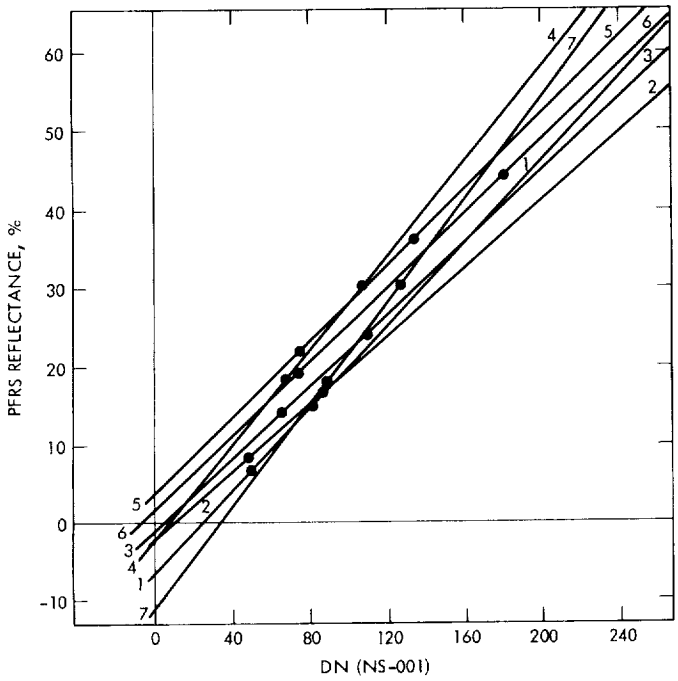

Figure 4-20. Calibration of NS-001 data. DN values for each channel are plotted against PFRS reflectance values for the same rock types.

extracted, and the average DN value was calculated for each of the 13 areas. The units extracted were Silver Bell 1 and 2 formations, basalt, dacite 1 and 2, Ragged Top latite, Mt. Lord, Claflin Ranch, granodiorite, alaskite, monzonite, limestone, and red beds.

The DN values versus the seven wavelength interval points are shown in Figure 4-21. As a result of the calibration procedure, DN values are proportional to reflectance. Both DN and reflectance scales are plotted along the y-axis.

The lowest reflectance is shown by basalt, reaching a value of 15 percent at 1.15 μm. The curve shows an apparent absorption band at 0.83 μm. This feature is absent from the other curves. Laboratory spectra of rock samples from Silver Bell often displayed this iron absorption band. It appears that some miscalibration of band 4 (0.83 μm) exists and values are too high.

The curve for red beds (unit 13) shows the most pronounced falloff in reflectance toward the short wavelengths. This is consistent with its high iron content, which results in the major absorption in the ultraviolet, the wing of which is seen in the blue and green wavelength regions.

The curve for dacite 1 (unit 4) shows a very strong falloff in the 2.2-μm band. The area from which this value was extracted is mapped as intense phyllic alteration, with the highest percentage composition of sericite and kaolinite of all the areas sampled. It also shows a very sharp falloff toward the ultraviolet, a result of the high iron-oxide content produced from oxidation of sulfide minerals.

If we calculate the 1.6/2.2-μm ratio for the 13 samples and compare them to the ratio calculated from the PFRS data, a further calibration problem seems to be indicated (Table 4-14). Based on ratios obtained from laboratory or field spectra, it appears that the values for 1.6 μm are too high, or those for 2.2 μm are too low. There are several possible explanations for this discrepancy. PFRS data were acquired for 8- by 8-m areas on the ground, and the image data represent 60- by 60- to 100- by 100-m areas; the image data include shadows and some vegetation. Thus, directly comparing the two is only as valid as the sampling schemes involved.

Direct comparison of the image spectra with PFRS spectra shows the relative accuracy of this technique. Figure 4-22 presents the spectra of limestone and altered dacite. The shapes of the PFRS and image spectra are quite similar; PFRS absorption bands are seen in the image spectra as lower reflectances in the corresponding wavelength regions. The differences in albedo of the two pairs of curves suggest the effects of sampling problems mentioned previously. However, the close similarities of the two types of spectral data indicate that this method produces image spectra which are faithful approximations of measured, continuous reflectance data.

This analysis leads to two general conclusions: (1) calibration procedures are extremely difficult to implement to achieve accurate reflectance values; and (2) the relative reflectances obtained, however, generally show the major spectral features and are valuable for relative comparisons of materials.

VIII. Image Analysis and Interpretation

A. Color Aerial Photographs

The color aerial photographs of Silver Bell are average in general quality and color contrast. Their main use in this study was to identify roads, pits, dumps, and topographic forms as an aid in registering the location of scanner features (Figure 4-23).

The overall separation of rock types and structures in the photographs is poor, although the resolution of details, such as vegetation, is very good. The photographs display five or six different tones of brown, red, and gray, corre-

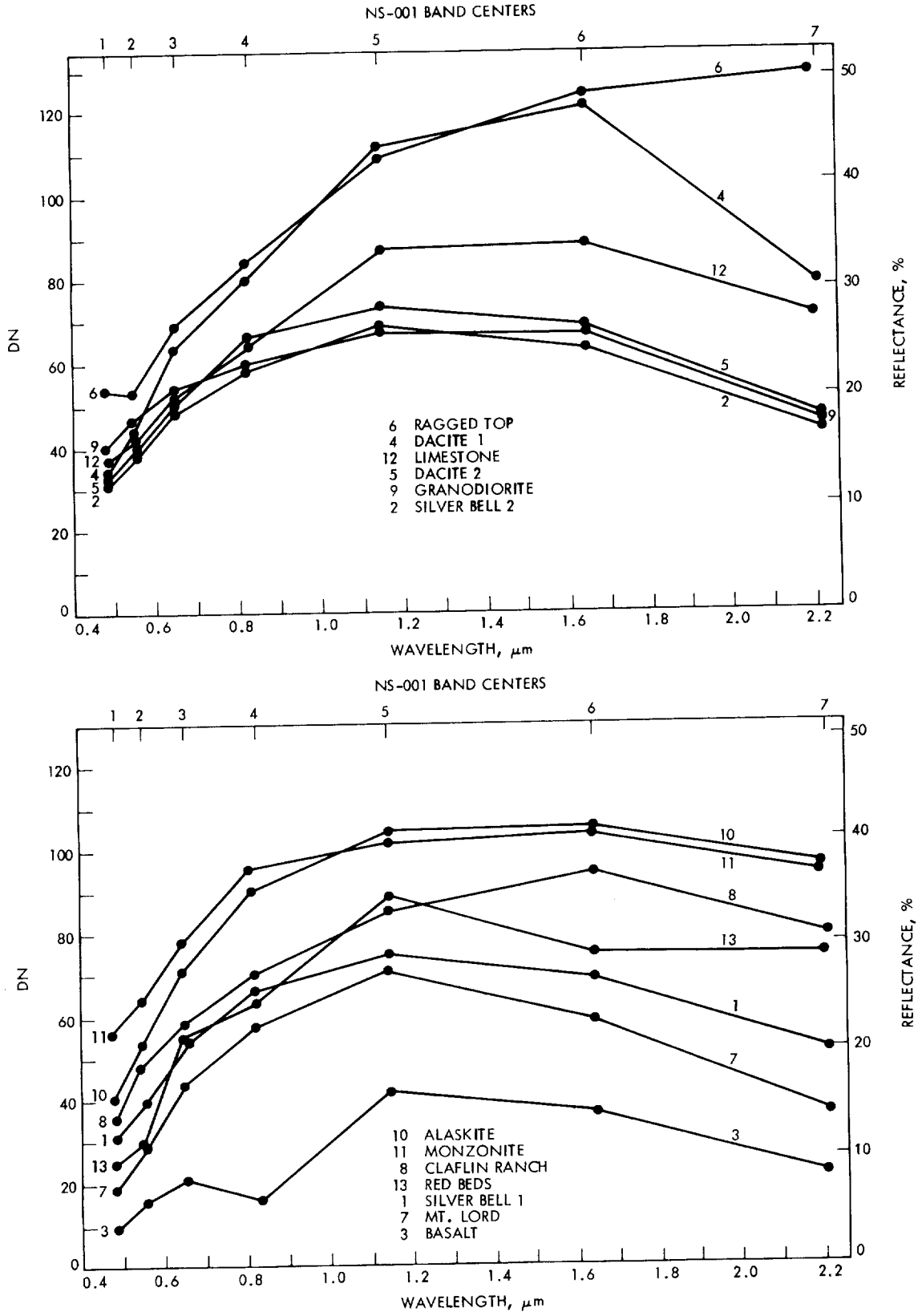

Figure 4-21. NS-001 image spectra derived from calibrated data. Values for 13 rock groups were extracted from image DNs.

Table 4-14. 1.6/2.2-μm image spectra and PFRS ratios

Unit	Image Spectra Ratio	PFRS Ratio
1 Silver Bell 1	1.33	1.17
2 Silver Bell 2	1.46	
3 Basalt	1.71	1.22
4 Dacite 1	1.55	1.49
5 Dacite 2	1.45	1.25
6 Ragged Top	0.97	
7 Mt. Lord	1.58	1.41
8 Claflin Ranch	1.21	1.21
9 Granodiorite	1.46	1.23
10 Alaskite	1.09	1.07
11 Monzonite	1.11	1.12
12 Limestone	1.24	1.0
13 Red beds	1.0	1.0

sponding to gross variations in lithology. The Silver Bell andesite and most Tertiary volcanic outcrops appear as dark gray- to maroon-colored regions. The Mt. Lord Ignimbrite, dacite porphyry, monzonite, and various clastic sedimentary units all have similar brown to reddish-brown tones.

Paleozoic limestones show up as quite distinctive, high-relief areas with a light gray color. Some of the north-trending quartz latite dikes in the Silver Bell Mountains are also easily recognizable because of their grayish color and etched, rib-like erosional forms.

The main Silver Bell alteration zone is barely distinguishable from unaltered rocks as a faint pink-tinged area. Other altered areas, such as the granodiorite porphyry stock northwest of Ragged Top Peak, appear as bleached, light-toned areas distinctive from the main zone alteration.

B. Radar Data

The Seasat (L-band) and Goodyear aircraft (X-band) systems are designed to enhance structural features through the detection of variations in surface roughness, topography, and surface moisture content (Blom and Elachi, 1981). Both the aircraft and Seasat radar data for Silver Bell are disappointing in their information content. Some of the major regional structures are visible on both low- and high-altitude radar images, but many of the lineaments interpreted from the images show little or no correlation with mapped structures.

On the aircraft radar (Figure 4-24), portions of the Ragged Top Fault, the subparallel Mt. Mammoth and Barite Faults, and some of the major faults in the Waterman Mountains are visible. A few indistinct lineaments east of

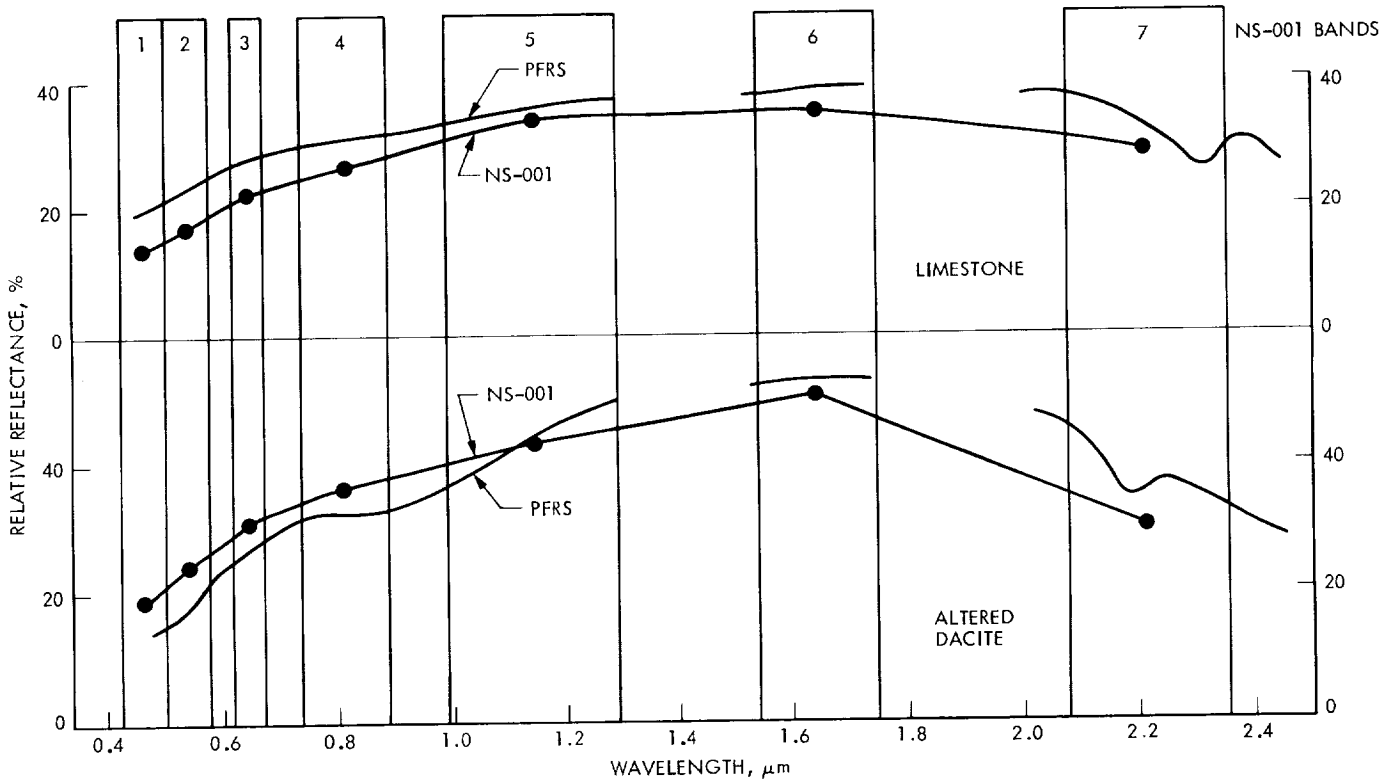

Figure 4-22. Comparison of PFRS spectra and NS-001 calibrated image spectra for limestone and altered dacite

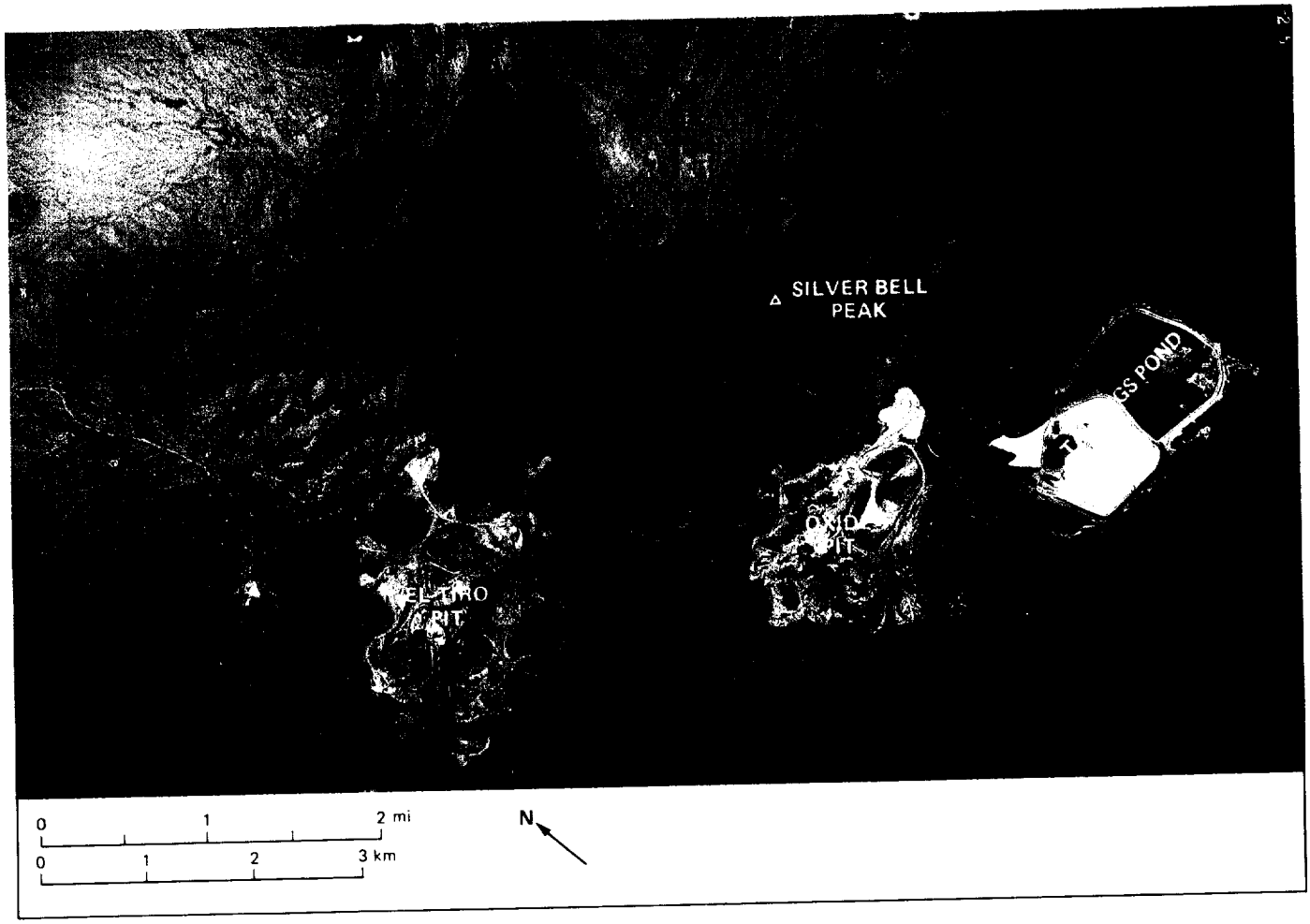

Figure 4-23. Color aerial photograph of Silver Bell area. Photograph obtained simultaneously with NS-001 data overflight.

the Oxide Pit appear to correlate with elements of the main Silver Bell Fault/alteration zone. The remainder of the main zone northwest of the Oxide Pit is obscured in dark shadows, caused by steep pit and dump walls.

The dominant trends of lineaments on the aircraft radar are west–northwest and north northeast, parallel to the Ragged Top–Silver Bell and Barite–Mt. Mammoth fault systems, respectively. Northeast lineaments, corresponding to the porphyry dike swarms and transverse faults, are rare and when present do not usually correlate well with known structures. Look direction and polarization appear to make little difference in the quality of the aircraft radar images; all four of the different images examined appear to be very similar in nature.

Because of the lower resolution, fewer structural features are evident on the Seasat image (Figure 4-25), and those present correlate with major, district-scale structures (Figure 4-26). The main features visible in the Silver Bell District are northeast- and northwest-trending lineaments. A faint portion of the west–northwest Silver Bell structural zone is apparent just east of the Oxide Pit area. The transverse, northeast-trending structures in the West Silver Bell Mountains are quite obvious. The northeast-trending Mt. Mammoth and Barite Faults show up clearly as a single line extending across the entire Silver Bell Mountains.

C. Landsat MSS Images

The low spatial resolution of Landsat multispectral data (80 m) makes the discrimination of many rock types and structures difficult or impossible. The most easily recognizable features are iron-oxide-rich alteration areas and red bed sedimentary rocks. By producing a color ratio composite (CRC) of the Landsat data, the presence of iron oxides

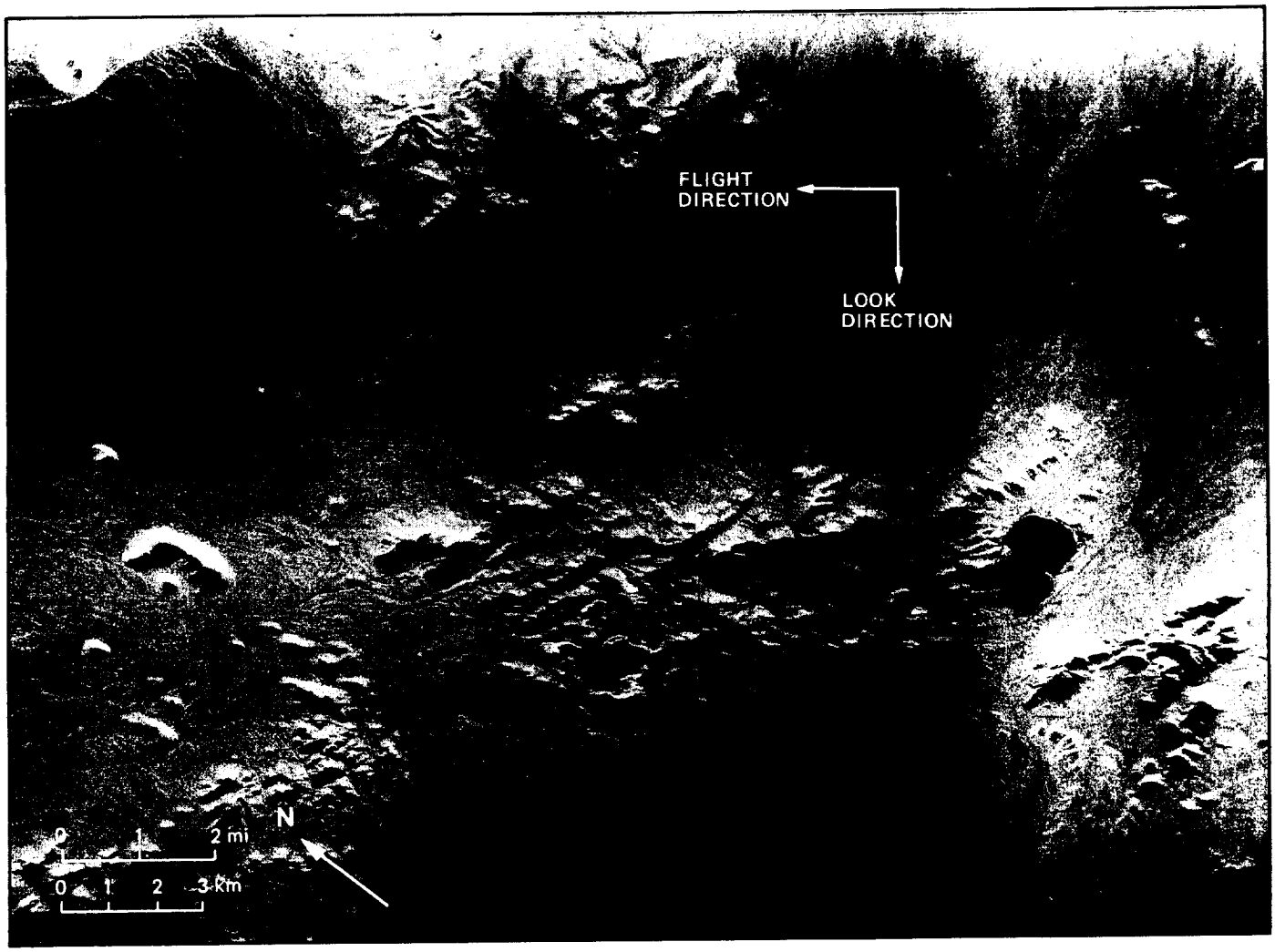

Figure 4-24. X-band aircraft radar image of Silver Bell area (acquired with NASA Goodyear System)

can be highlighted (Rowan et al., 1974). One example is shown in Figure 4-27, a portion of a Landsat scene acquired in June 1977. This composite was created by displaying band-ratios 4/5, 5/6, and 6/7 as blue, green, and red, respectively. No atmospheric correction factors were applied to the data prior to ratioing. Areas having iron oxides on the surface are displayed in shades of red and orange (Figure 4-28).

Alteration within the main Silver Bell structural zone shows up as several reddish-orange patches, corresponding to the most highly iron-oxide-stained areas (oxidation of pyrite to limonites). The North Silver Bell alteration is clearly visible north of the El Tiro Pit. Slightly smaller segments of main zone alteration are also visible northwest and east of the Oxide Pit. A dispersed, purple-colored zone north of the Oxide Pit corresponds to iron-rich Mt. Lord Formation in the topographically high and vegetated area near Silver Bell Peak.

The Ragged Top fault zone is highlighted on the Landsat CRC by a northwest-elongate, teardrop-shaped area of reddish Precambrian granite and Apache Group sediments, located southeast of Ragged Top Peak. A very faint reddish line marks the trace of alteration along the fault northwest of Ragged Top Peak.

Other reddish areas of apparent iron-oxide concentrations are visible: (1) in the range of volcanic hills northeast of Ragged Top Peak; (2) in the eastern part of the West Silver Bell Mountains; and (3) along Waterman Pass, south of the Waterman Mountains. The first area may be caused by Precambrian granite on the low-lying pediment northeast of Ragged Top (Brown, unpublished mapping). The

second area corresponds to Mt. Lord welded tuffs with secondary iron oxides on weathered outcrops from oxidation of ferromagnesian minerals. The third area appears to be caused by a combination of Mesozoic sedimentary red beds and Laramide quartz latite volcanics (Banks and Dockter, 1976; Brown, unpublished mapping). The volcanic and sediment rocks have small amounts of disseminated pyrite and are spatially associated with several small mineral prospects shown on the topographic map.

Lineaments present on the Landsat CRC images are accentuated by the growth of vegetation along relatively straight washes. The east–northeast faults inferred from geophysics in the West Silver Bell Mountains are clearly defined by two subparallel lineaments. A prominent east–northeast lineament at the south end of the Silver Bell Mountains is caused by the straight alignment of Cocio Wash, a major drainage feature near the ASARCO tailings pond. The Cocio Wash lineament does not correspond to any known geologic structure, but its trend does parallel a subtle east–northeast edge in the low-altitude aeromagnetics, suggesting control by some unrecognized major fault.

Some of the known faults in the district appear to be more regional in extent on Landsat than they are indicated on geologic maps. The north-trending Barite and Mt. Mammoth Faults are visible on the Landsat images as two indistinct lineaments, extending southward across the entire range of the Silver Bell Mountains into the Waterman Mountains. Northward, the Mt. Mammoth Fault appears to bend north–northwest and extend for a considerable distance onto the pediment slope beyond the Silver Bell Mountains. On the March Landsat frame, the Ragged Top Fault appears faintly to extend through the West Silver Bell Mountains, and possibly under the Aguirre Valley, to the south end of the Slate Mountains, 15 km to the west.

The smaller-scale structures of the Silver Bell area, including the dike swarms, are not visible on Landsat images due to their low spatial resolution. Very few of the numerous high-angle faults in the district can be discerned, except where their presence is accentuated by development of iron oxides, such as along the Ragged Top Fault and the Oxide fault zone, or by vegetation along washes.

The Landsat data for Silver Bell were also processed by principal components (PC) transformation and the data displayed as several contrast-enhanced color composite images at a scale of 1:125,000. The three principal component images examined contain very little useful geological information and are degraded relative to the untransformed Landsat images. The hydrothermally altered areas that are visible on Landsat CRCs are virtually indistinguishable from surrounding iron-oxide-rich pediments on the PC transformations. The main effect of the processing is to enhance the differences among various soil and alluvium types in the pediment areas and valleys. Because PC transformations operate on all the data input to the algorithm, spatially large areas will dominate the statistics and force selection of axes to maximize the variance of those areas. Small, albeit spectrally different areas will not be accounted for and probably not separated on the PC images. In this example, alluvial and agricultural areas comprise over 80 percent of the scene, so the axes will be selected to maximize the variance of these units.

D. M²S 11-Channel Scanner Aircraft Images

Data from the August 1977 M²S 11-channel scanner flight (see Figure 4-29 for areal coverage) were used to produce a color ratio composite simulating the product described in the previous section about Landsat. Specifically, Landsat ratios 4/5, 5/6, 6/7 were approximated using M²S ratios 0.56/0.63 μm, 0.63/0.72 μm, and 0.72/0.81 μm + 1.03 μm (Table 4-15). The center wavelengths of these bands are similar to the Landsat bands, but the bands are narrower. Landsat band 7 was approximated by averaging two M²S bands. The color composite was produced by displaying the three above ratios in blue, green, and red, respectively (Figure 4-30). The scanner data were processed to remove gross geometric distortions introduced by the aircraft velocity/scanning rate asynchrony. No further attempt was made to improve the geometric accuracy by rubber-sheet stretching. In addition, no atmospheric correction factors were applied to the data prior to ratioing.

On the 11-channel image of Silver Bell, pediments with dispersed iron oxides appear yellowish-orange, vegetation is blue, dumps are white to yellowish-white, and iron-oxide-rich outcrops are red to orange. In general, the spectral data are comparable to Landsat, with some increase in rock type discrimination due to higher spatial resolution and narrower band widths.

Areas rich in iron oxides are displayed vividly and accurately by the ratioing process. However, zones of hydrothermal alteration cannot be discriminated from nonaltered iron-rich areas, due to the lack of spectral reflectance data beyond 1.05 μm (Figure 4-31).

Iron oxides within the main Silver Bell alteration zone are displayed as deep red areas adjacent to the El Tiro and Oxide Pits. The North Silver Bell area is especially obvious as an elongate red zone coincident with overlapping phyllic and potassic alteration. The southeastern portion of the Silver Bell alteration zone also shows up as an elongate, bright red band just southeast of the Oxide Pit.

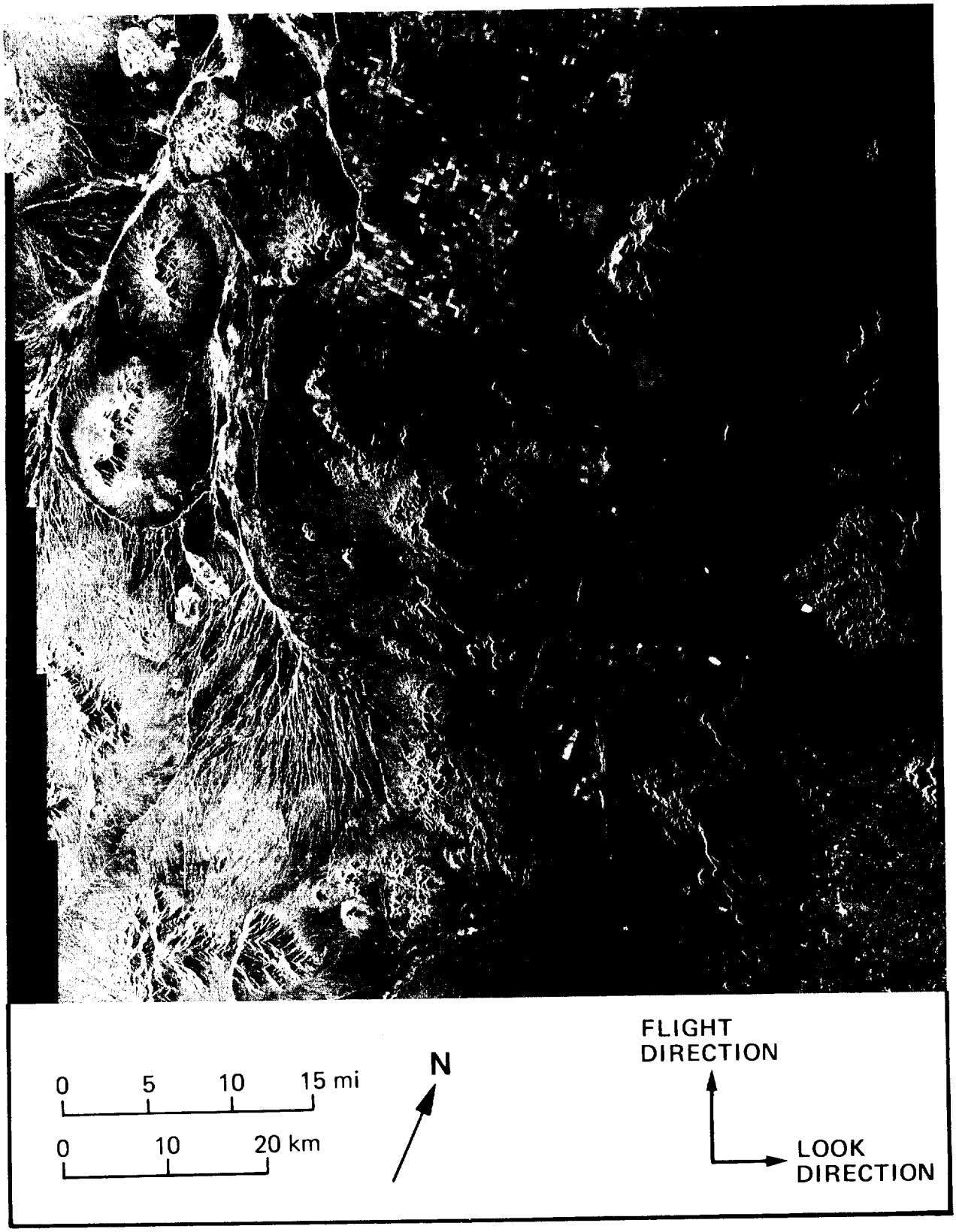

Figure 4-25. Seasat L-band radar image of Silver Bell area

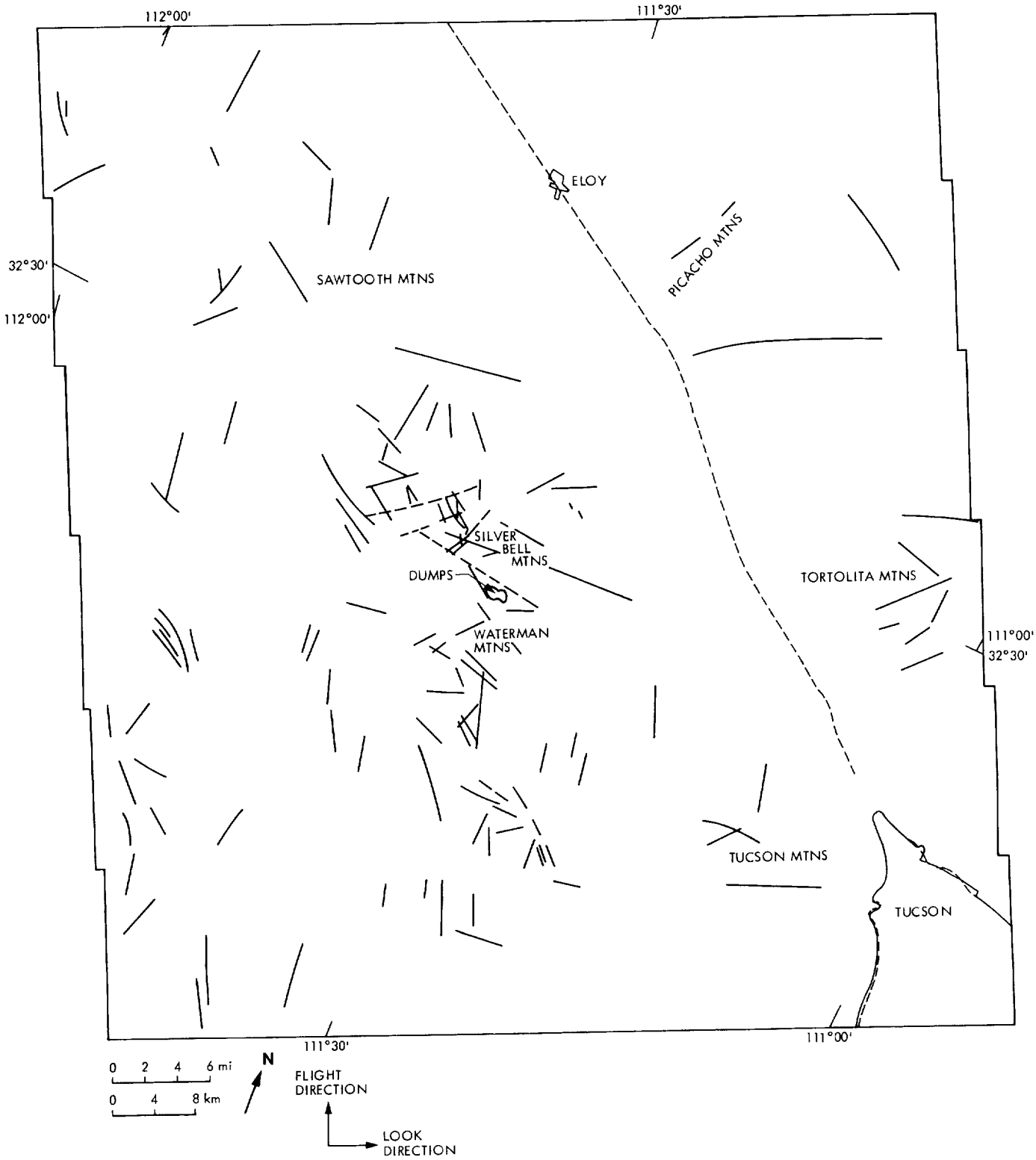

Figure 4-26. Structural interpretation of Seasat radar image (Figure 4-25)

Figure 4-27. Landsat color ratio composite. Band-ratios 4/5, 5/6, and 6/7 are displayed as blue, green, and red, respectively. Area covered is 40 by 40 km (scene no. 2873-17010, June 13, 1977).

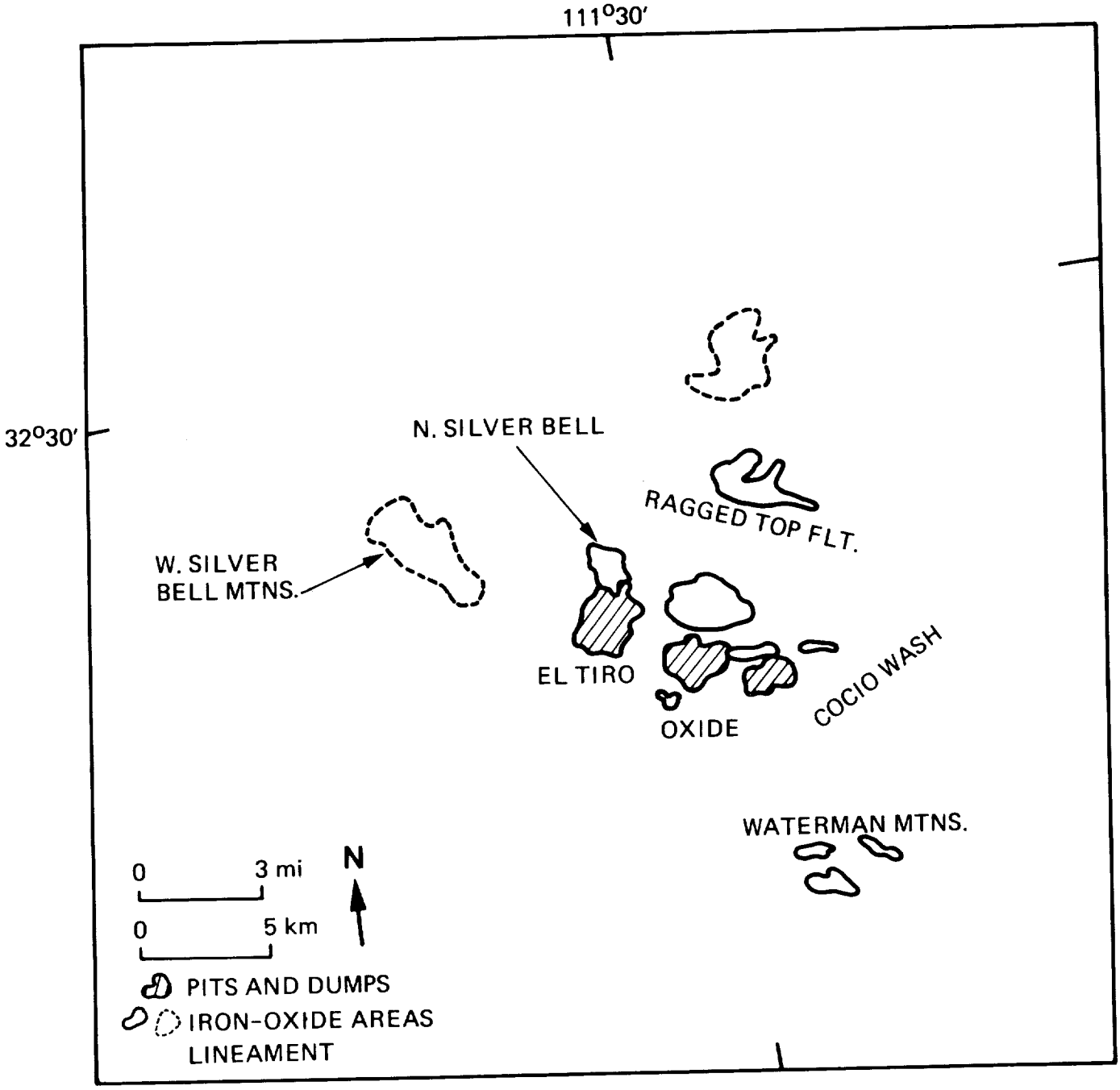

Figure 4-28. Interpretation of Landsat color ratio composite (Figure 4-27) showing lineaments and areas that have iron-oxide minerals

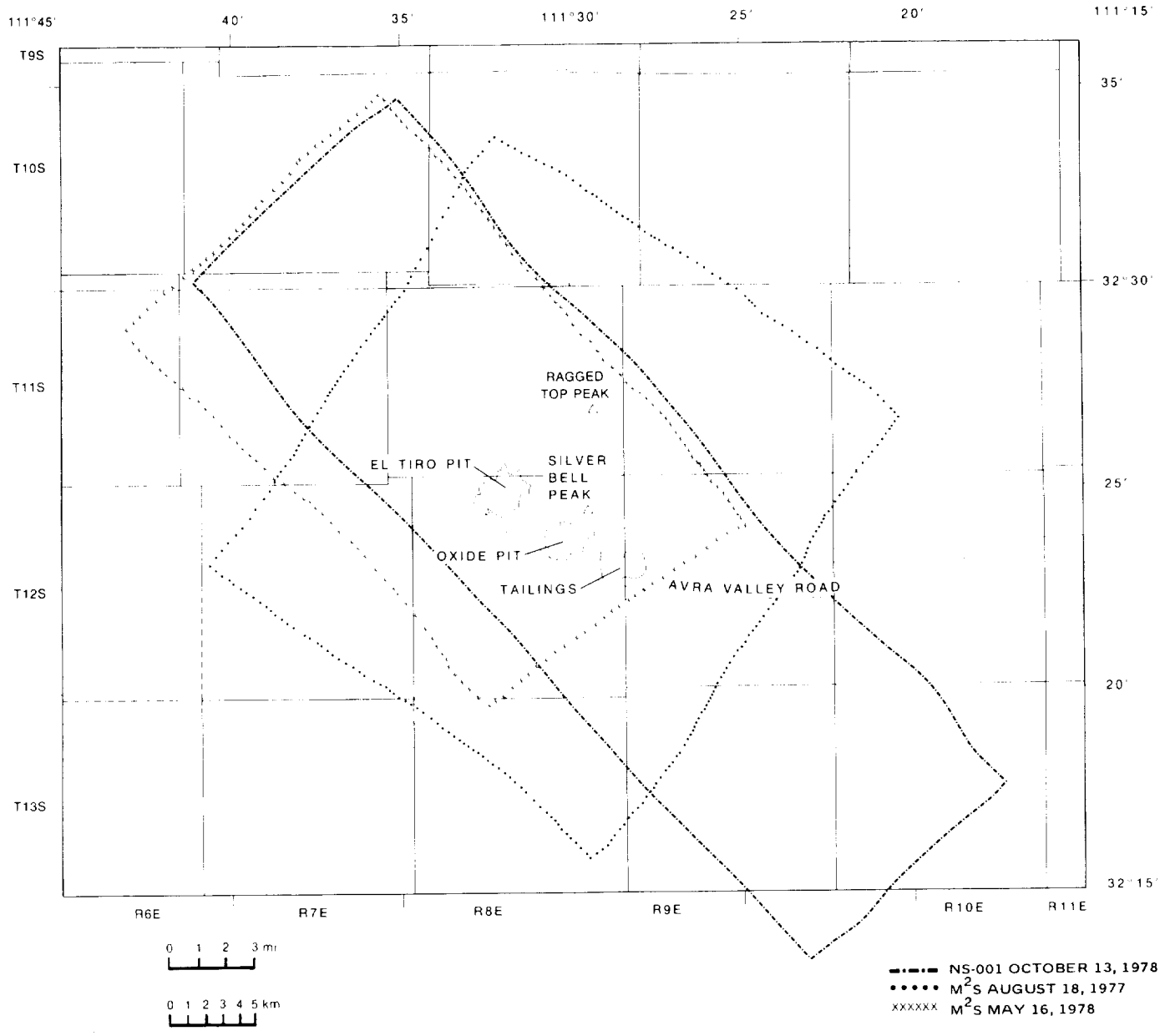

Figure 4-29. Aircraft scanner coverage of Silver Bell test site for M^2S and NS-001 data overflights

Other prominent reddish patterns coincide with outcrops of Mesozoic red beds, southwest of the Oxide Pit, and with Precambrian sediments and granite along the eastern portion of the Ragged Top fault zone. Several red patches in the Waterman Mountains are probably caused by exposures of Mesozoic red beds and Laramide quartz latite, but these areas were not field checked. Irregular areas of red coloration are scattered widely throughout the exposures of Mt. Lord ashflow tuffs in the Silver Bell and West Silver Bell Mountains. These red areas are probably caused by weathering and oxidation of ferromagnesian minerals, and locally by weak hydrothermal alteration.

The presence of moderately heavy vegetation in higher elevations (which appears in blue) such as the Silver Bell Peak area and the Waterman Mountains, hampers the separation of lithologies. In the lower, less-vegetated areas, anywhere from five to seven different lithologic units may be identified.

Outcrops of Tertiary basalt and Laramide Mt. Lord Ignimbrite are similar in appearance, showing up as lavender- to magenta-colored areas, grading locally into deep red. The Laramide granodiorite stock west of Ragged Top Peak is clearly delineated as a C-shaped area with a very

Table 4-15. M^2S 11-channel bands

Channel	Wavelength, μm
1	0.33–0.44
2	0.44–0.48
3	0.49–0.54
4	0.54–0.58
5	0.58–0.62
6	0.62–0.66
7	0.66–0.70
8	0.70–0.74
9	0.76–0.86
10	0.97–1.065
11	8.05–13.7

pale lavender color. Separation of the granodiorite on the 11-channel image is probably facilitated by the presence of weak hydrothermal alteration, causing a slight increase in overall reflectance and a reduced density of vegetation growth (evident in Figure 4-23).

The Ragged Top latite intrusive shows up as a deep blue vegetated area, surrounded by a green-colored talus apron, which conceals the contacts of the latite with adjacent rocks. The large, low-lying area of Silver Bell Formation southwest of Ragged Top can be separated on the basis of a mottled, lavender and blue pattern, resulting from moderate iron oxides combined with the concentration of plant growth along fine networks of arroyos.

Propylitically altered dacite porphyry and Claflin Ranch Formation both have a greenish-brown to olive-drab coloration evident in outcrops to the northeast of the El Tiro Pit. This color pattern could possibly be due to two factors related to the propylitic alteration: (1) a slight increase in reflectance, and (2) slight steepening of the shoulder in the spectral curve between 0.5 and 0.9 μm, resulting in increased green and red components from the appropriate ratio.

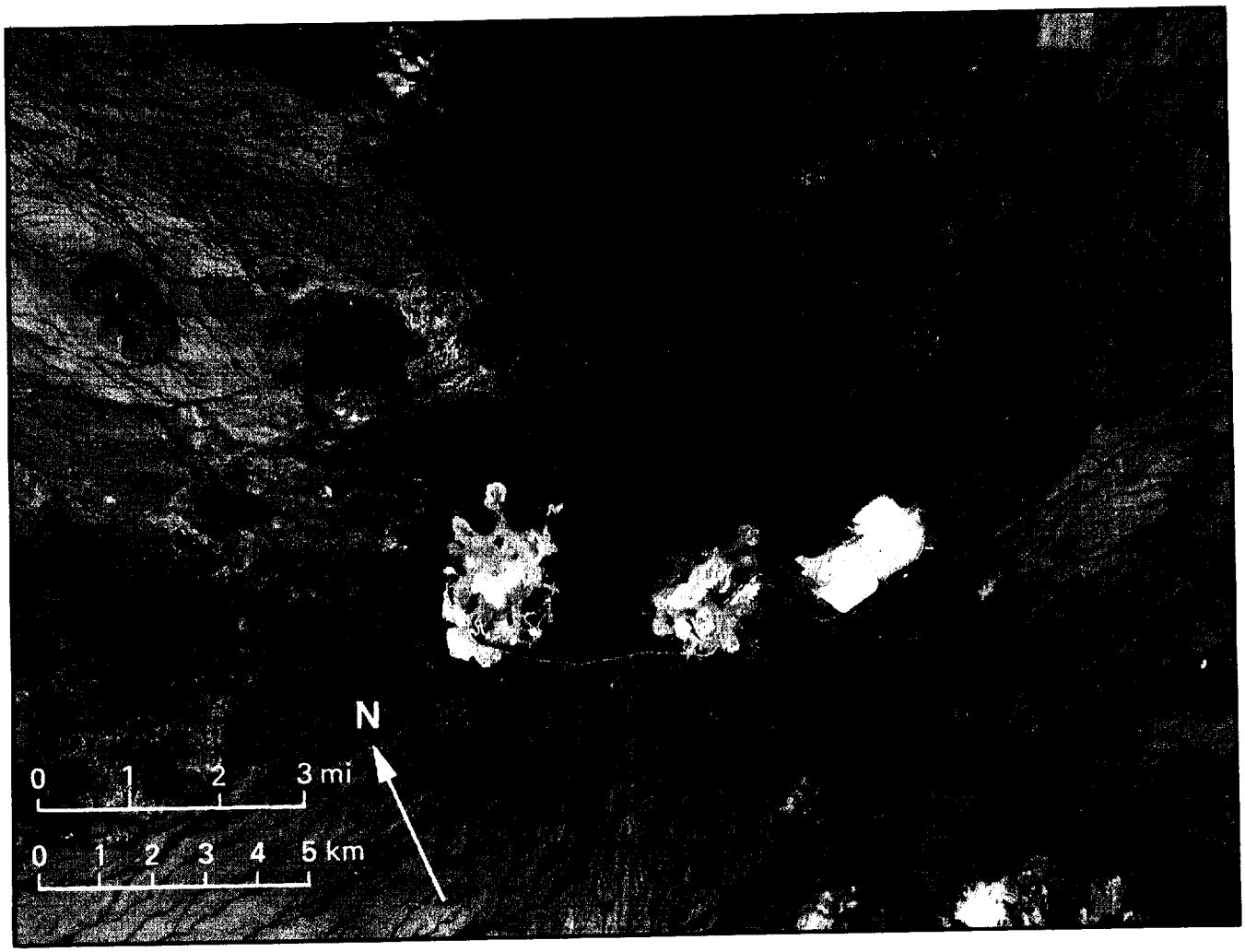

Figure 4-30. M^2S 11-channel color ratio composite. Ratios were chosen to simulate Landsat composite.

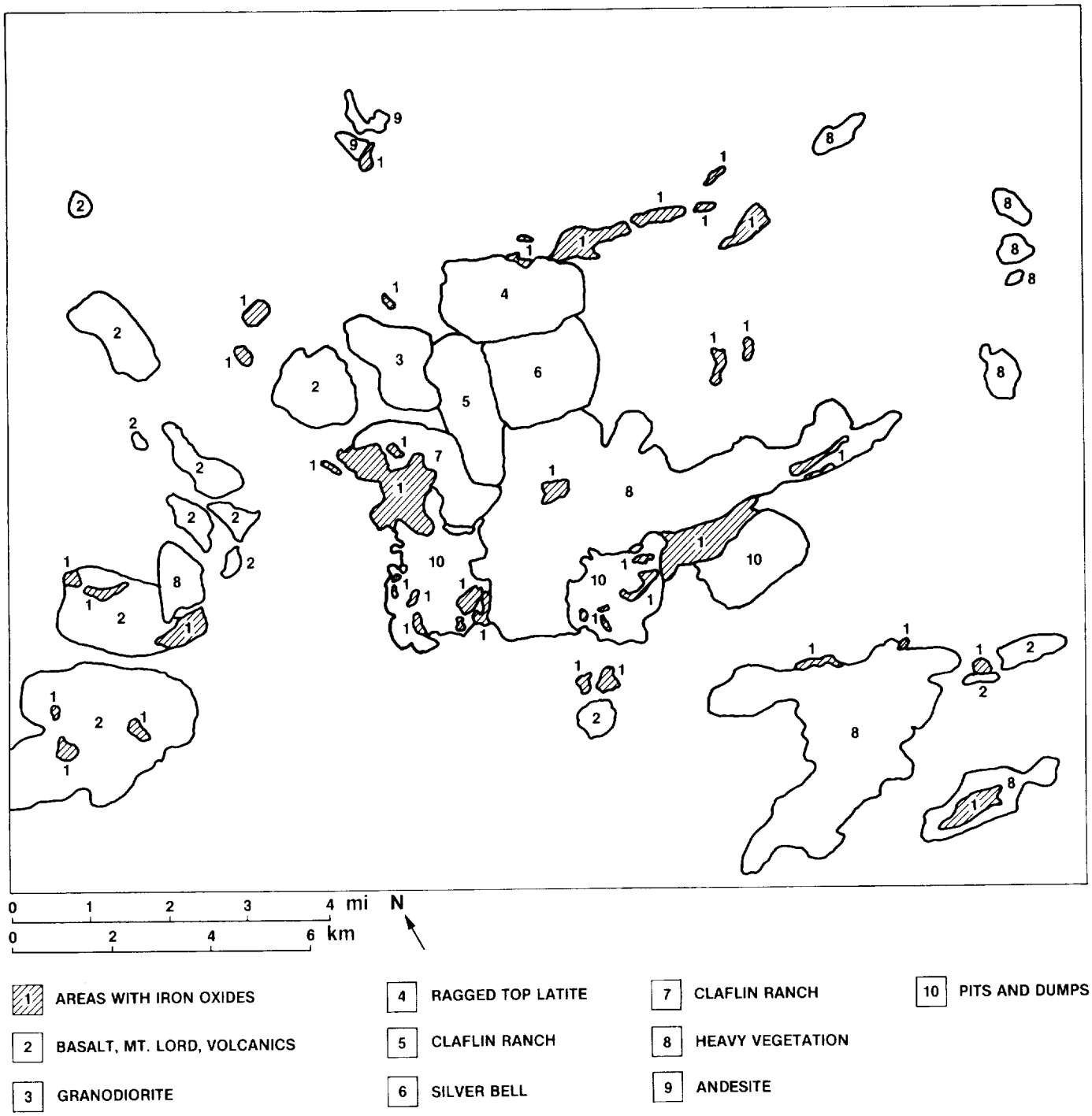

Figure 4-31. Interpretation map of M^2S color ratio composite (Figure 4-30)

Most Tertiary volcanics in the test site area show up on the 11-channel image as nondiagnostic pink- to violet-colored areas. An exception is the andesite/latite flows in the pediment area north of Ragged Top Peak. These flows have a distinctive yellowish-white appearance, indicating a relatively flat reflectance response compared to other volcanic rocks in the area. The nature of these light-toned rocks was not investigated during this study.

E. NS-001 Aircraft Images

The NS-001 Thematic Mapper Simulator scanner data (see Figure 4-29 for areal coverage) are by far the most useful data for rock-type and alteration discrimination of the different imaging systems examined for Silver Bell. The relatively high content of geological information on the NS-001 images can be largely attributed to the inclusion of spectral reflectance data in the clay absorption region near 2.2 μm.

The NS-001 data (Table 4-16) for Silver Bell were processed into a number of displays, including a color ratio composite, six different images produced by canonical transformation of the spectral data based on linear discriminant analysis of the PFRS data, principal components transformation, and supervised classification thematic maps. The six transformed images correspond to six different axial rotations performed on various combinations of the 18 rock-type groups of PFRS data. In addition to the various CRC images, a density-slice image was also produced by color coding the 1.6/2.2-μm ratio.

The uncalibrated CRC image provides discrimination of most of the various rock types in the test site area. Some of the transformed images calibrated with PFRS data enable a further subdivision of certain rock types, caused by differing degrees of hydrothermal alteration. Two of the transformed images appear to have the highest visual information content, based on comparisons with the support geological data.

1. Standard color ratio composite image (uncalibrated). Figure 4-32 was prepared by using green, blue, and red filters for band-ratios 0.66/0.56 μm, 0.83/1.15 μm, and 1.6/2.2 μm, respectively. The scanner data were processed to remove the gross geometric distortions due to the aircraft velocity/scan rate asynchrony. Examination of the individual bands indicated the presence of a brightness gradient in the scene perpendicular to the flight track. This gradient was characterized by computing a one-line average of the entire picture, smoothing the resulting curve, replicating the curve to the same number of lines as in the original data, then adjusting the scene values according to this gradient "picture." No atmospheric corrections were applied to the data prior to creation of band ratios.

Table 4-16. Wavelength bands of NS-001 scanner

Channel	Wavelength, μm
1	0.45–0.52
2	0.52–0.60
3	0.63–0.69
4	0.76–0.90
5	1.00–1.30
6	1.55–1.75
7	2.08–2.35
8	10.4–12.5

The effect of the ratioing process is to enhance iron-oxide-rich areas in green, due to the presence of the Fe^{+3} absorption band short of 0.56 μm, and clay-rich areas in red, due to the hydrous minerals absorption band near 2.2 μm. Areas of hydrothermal alteration, with mixtures of clay, sericite, and limonite, show up as orange to yellow areas, due to the combination of red and green color components.

The processed NS-001 CRC image of Silver Bell is a brightly colored print with a great deal of color contrast among the various rock/alteration types. Approximately 20 to 25 different lithologic units are separable on the image, depending on the boundaries assigned by the individual interpreter (Figure 4-33). This compares with approximately 5 to 6 separate units on the color aerial photographs and 9 to 10 separate units on the 11-channel image.

a. Hydrothermal alteration. The ratio combination used in producing the CRC results in a stark contrast between the dark-toned unaltered rocks, in shades of blue and green, and hydrothermally altered rocks, in bright yellow to orange. The main Silver Bell alteration zone is vividly outlined as a yellowish-orange band, almost perfectly coincident with the limits of hydrothermal alteration outlined by Richard and Courtright (1966) and with the boundary of the phyllic/potassic alteration zones on ASARCO's alteration map. No discrimination can be made between phyllic and potassic alteration because both appear as yellowish-orange areas.

Peripheral alteration, corresponding mainly to propylitic and/or argillic alteration, is visible in numerous outcrops of Mt. Lord ignimbrite, monzonite, and dacite porphyry, on either side of the main alteration zone. The peripheral alteration areas are yellowish-green to yellowish-brown patches with mottled or dispersed patterns and often vague, poorly defined boundaries. These features probably reflect the dispersed, nonpervasive distribution of clay minerals and the gradational transition into fresh rocks.

Evidence of hydrothermal alteration is visible near the Ragged Top Fault in two areas: (1) reddish-orange outcrops of Precambrian granite north of the fault, and (2) a small, semicircular area of yellow to orange hue in granodiorite porphyry south of the fault. The latter area is caused by a zone of clays, limonite, and copper oxides around a small prospect tested by several drill holes (Brown, unpublished mapping).

Figure 4-32. NS-001 color ratio composite. Ratios 0.66/0.56 μm, 0.83/1.15 μm, 1.6/2.2 μm are displayed as green, blue, and red, respectively.

Small, dispersed zones of apparent alteration can also be seen in the Mt. Lord and Claflin Ranch Formations in the West Silver Bell Mountains, and in Precambrian granite in the Waterman Mountains. None of these areas were field checked during this study. Some of the yellowish areas in the West Silver Bell Mountains correlate with weak argillic-type alteration on the surface (Brown, unpublished mapping).

b. Igneous rocks. In general, the most mafic igneous rocks show up on the NS-001 ratio as dark blue to green, intermediate rocks as medium to light blue, and the most felsic rocks as pink to cyan. Fresh Silver Bell andesite is easily discriminated as deep indigo blue areas, apparently produced by the lack of hydrous minerals and relatively flat spectral curve. Exposures of Mt. Lord Ignimbrite typically exhibit a turquoise-blue color, with deep shadows due to the rugged relief formed by the ignimbrites. The Mt. Lord Ignimbrite can be confused locally with fresh dacite porphyry, which it resembles petrographically, and in a few instances with Tertiary basalt. The relatively dark, bluish tint of the fresh dacite porphyry and Mt. Lord Ignimbrite is somewhat anomalous, considering their average quartz latitic composition. This is apparently due to the dense,

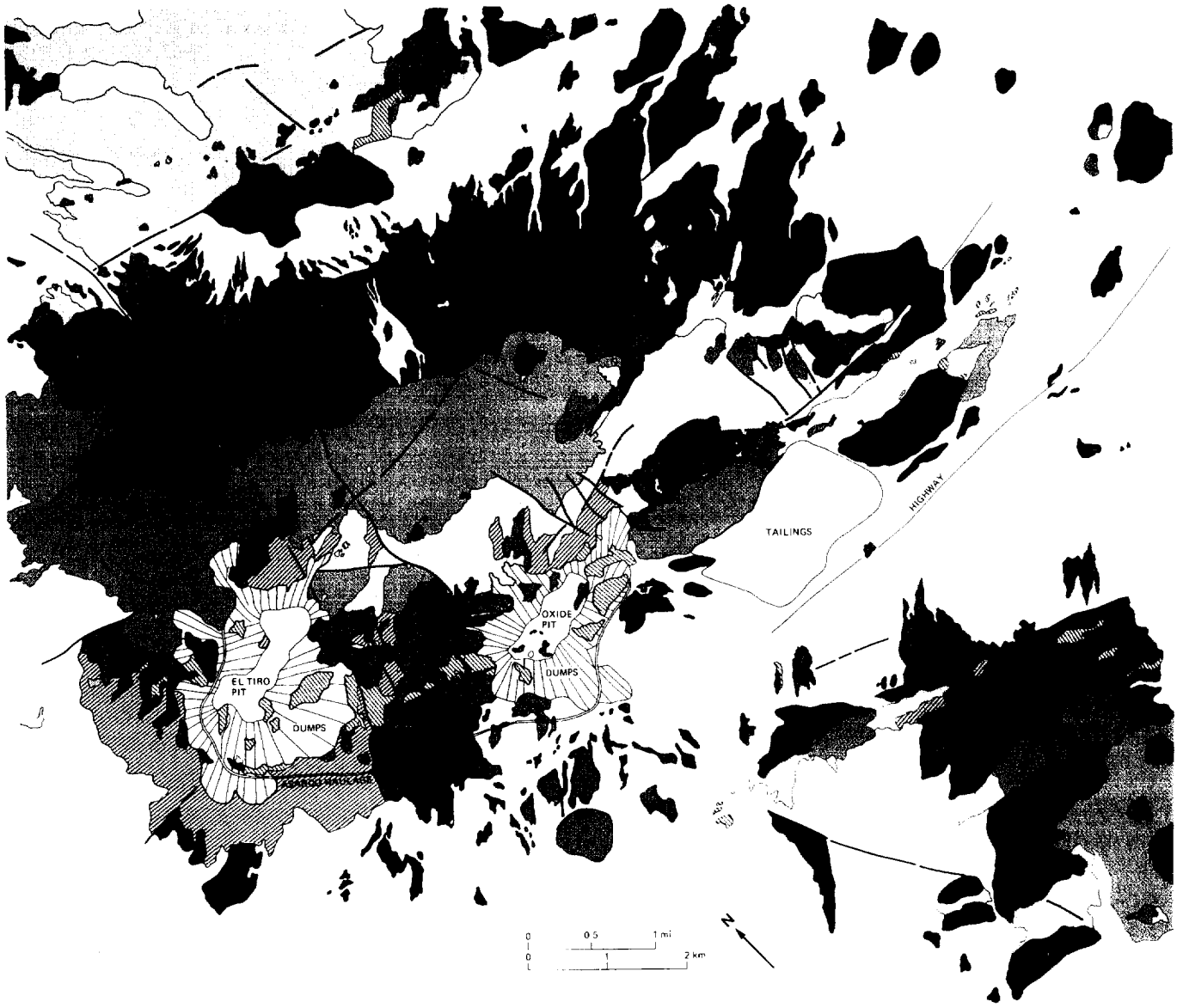

UNALTERED AREAS	SUSPECTED CAUSE
	UNALTERED, LEUCOCRATIC, AND FELSIC ROCKS (MAINLY ALASKITE AND DACITE PORPHYRY)
	UNALTERED MONZONITE PORPHYRY, QUARTZ LATITE PLUGS IN THE WEST SILVER BELL MOUNTAINS AND FELSIC TUFFS (?) WITHIN THE MT. LORD IGNIMBRITE
	MAINLY PALEOZOIC LIMESTONE IN THE WATERMAN MOUNTAINS SOUTH OF SILVER BELL
	ALMOST EXCLUSIVELY MT. LORD IGNIMBRITE, ACTUALLY A COMPLEX COMBINATION OF BLUE AND GREEN CAUSED BY HIGH TOPOGRAPHIC RELIEF AND RELATED MANTLING OF SLOPES WITH IRON-STAINED TALUS
	MAINLY MT. LORD IGNIMBRITE

UNALTERED AREAS	SUSPECTED CAUSE
	UNALTERED SILVER BELL ANDESITE, CLAFLIN RANCH FORMATION, AND CRETACEOUS (?) SEDIMENTS
	GRANODIORITE PORPHYRY AND A ZONE OF UNMAPPED ORIGIN WITHIN THE SILVER BELL ANDESITE NEAR RAGGED TOP PEAK
	LARGELY A SHADOW EFFECT NEAR PIT WALLS AND CLAY-RICH DUMPS
	IRON-RICH MESOZOIC SEDIMENTS AND PRECAMBRIAN APACHE GROUP SEDIMENTS, ALSO TERTIARY BASALT, ANDESITE, AND LATITE
	TERTIARY BASALT

ALTERED AREAS	SUSPECTED CAUSE
	ALTERED AREAS WITH VERY ABUNDANT CLAY
	CLAY AND IRON-RICH ALTERATION IN FELSIC IGNEOUS ROCKS, PRIMARILY MONZONITE PORPHYRY, DACITE PORPHYRY, AND PRECAMBRIAN GRANITE
	DISPERSED CLAY ALTERATION AND AREAS OF PRECAMBRIAN GRANITE
	DISPERSED CLAY ALTERATION AND AREAS OF PALEOZOIC LIMESTONE WITHIN THE SILVER BELL FAULT ZONE

Figure 4-33. Interpretation map of NS-001 color ratio composite (Figure 4-32); all alluvial areas left white

welded character of the two units and their tendency to weather into very dark, heavily iron-oxide-stained talus fragments due to the presence of small amounts of pyrite and magnetite.

Exposures of relatively fresh monzonite porphyry and alaskite are visible west of the ASARCO haulage road. The alaskite stock is displayed as a pale bluish area west of the El Tiro Pit, while the monzonite porphyry stock northwest of the Oxide Pit has a pale cyan color. The pale blue to pink shades probably result from small amounts of highly dispersed clays, produced by weathering or weak hydrothermal alteration.

The flow-banded quartz latite plugs near the south end of the West Silver Bell Mountains resemble the fresh monzonite, but are separable on the basis of their very pale lavender to white color, indicating a high silica content and presence of very small amounts of clays. The Ragged Top latite intrusive falls compositionally in the same category as the monzonite porphyry; where not obscured by deep shadows, the latite has a pale lavender-brown coloration.

Precambrian granite is generally displayed as yellowish-green to yellowish-orange areas north of the Ragged Top Fault and in the Waterman Mountains. The appearance of the Precambrian granite suggests that it is an inherently altered unit containing clays and limonite. This alteration could be a result of three effects: weathering, hydrothermal alteration, and metamorphism.

c. Sedimentary rocks. Consolidated sedimentary rocks rich in iron oxide show up as dark green regions on the NS-001 image, due to the effect of the Fe^{+3} absorption band in the ultraviolet. The Mesozoic red beds west of the Silver Bell Mountains and the Precambrian Apache Group sedimentary rocks southeast of Ragged Top Peak are both green on the image, reflecting their high iron-oxide and low clay content.

Paleozoic limestone units generally appear as rust-brown areas on the NS-001 image. Reliable discrimination of limestones is often hampered by the characteristic formation of resistant landforms, including cliffs and ledges, which produce deep shadows. The effect of computer enhancement and ratioing is to subdue topographic features, causing much of the limestone exposures to be displayed as exceptionally dark or light regions. This effect is particularly apparent in the Waterman Mountains, where much of the detailed contact relations between Paleozoic limestone and other units is totally obscured.

d. Structure. The enhancement of lithologic units on the NS-001 image tends to emphasize certain structural details through the juxtaposition of contrasting colors on opposite sides of fault contacts. On the other hand, the 12-m resolution is insufficient to identify some of the finer structural details visible on aerial photographs, such as dikes and minor faults.

One of the most obvious structural features visible on the NS-001 image is the Ragged Top Fault, which is strikingly enhanced by yellowish-orange and green Precambrian exposures along its trace. The Barite and Mt. Mammoth Faults are also enhanced on the image, through the presence of propylitically altered dacite porphyry between the two faults. The Barite and Mt. Mammoth Faults appear to extend approximately 4 and 2 km, respectively, farther south than they are shown on existing geologic maps. This agrees with the more regional nature of the two faults interpreted from the Landsat images.

Several short, 0.5-km, north-trending linear features are present in yellowish-appearing, altered exposures immediately north of the ASARCO tailings pond. These were field checked and found to be small faults with minor copper-oxide and specularite mineralization. The faults cut propylitically altered granodiorite porphyry. The structures are not shown on existing geologic maps of the district.

Elements of the broad Oxide fault zone, striking east–northeast out of the Oxide Pit, are visible as indistinct linear features corresponding to porphyry dikes and a thick quartz vein shown on the ASARCO geologic map. Much of the Oxide fault zone appears as a dispersed yellowish area, indicating weak argillic or propylitic alteration.

Alteration boundaries on the NS-001 image also highlight portions of the southeast end of the west–northwest-trending Silver Bell fault zone, where it is well exposed southeast of the Oxide Pit. The sharp, straight edges of phyllically altered monzonite outcrops accentuate the fault zone for a length of about 5 km beyond the Oxide Pit, where the zone disappears under alluvium.

2. Canonical transformation image (11 groups–igneous rocks only). Figure 4-34 was prepared using the canonical transformations derived from the linear discriminant analysis for 11 groups of PFRS spectral data (Paragraph IV), corresponding to the 11 different types of altered and unaltered igneous rocks. The canonical variables (V1, V2, and V3) were displayed through blue, green, and red filters, respectively.

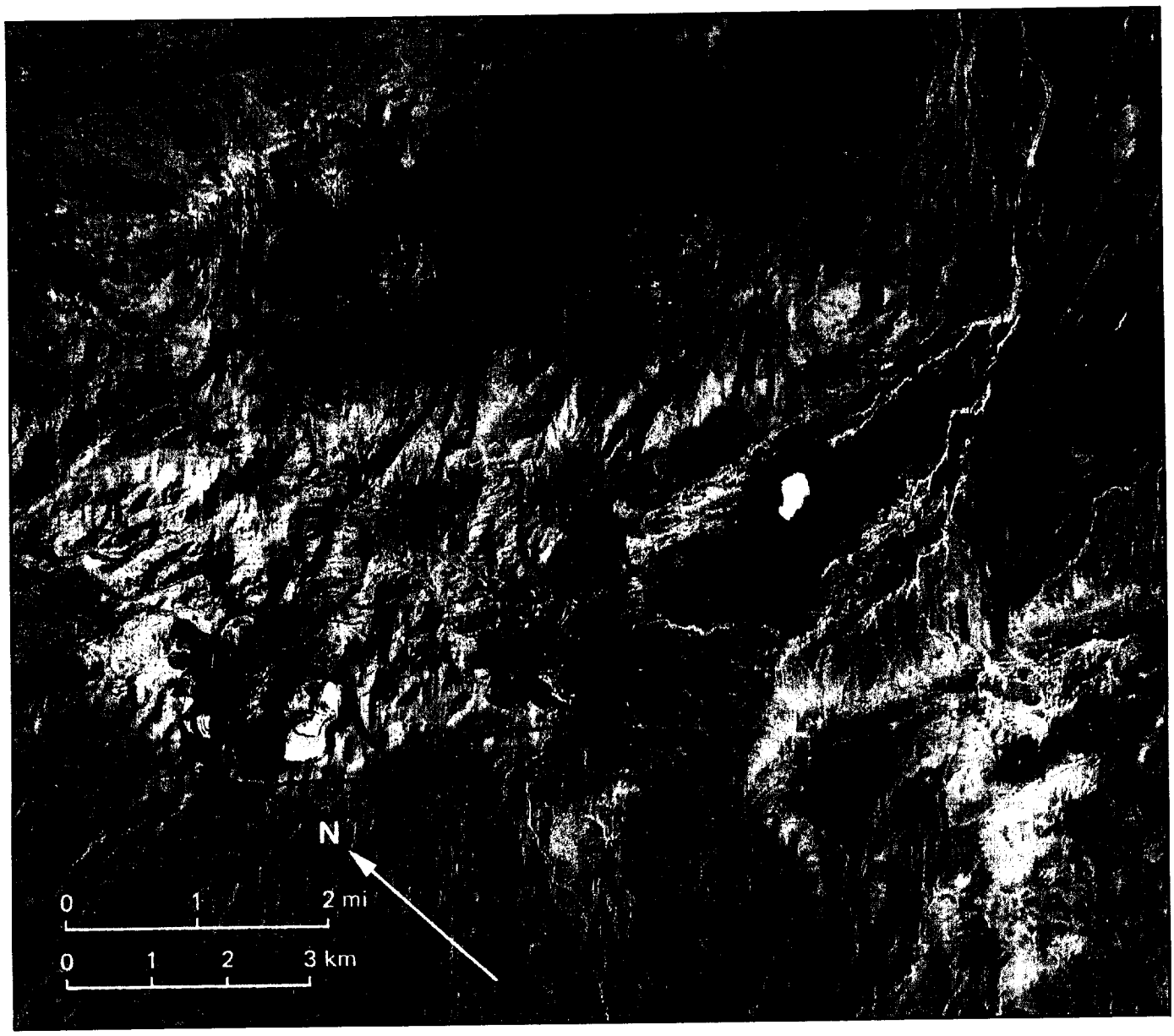

Figure 4-34. NS-001 canonical transform image. Axes derived from discriminant function analysis of 11 rock groups using PFRS data. V1, V2, and V3 are displayed as blue, green, and red, respectively.

Because the linear discriminant function analysis was performed on reflectance data (PFRS measurements) and the NS-001 data are proportional to radiance, it was necessary to convert the scanner data to values proportional to reflectance. The calibration curves (Figure 4-20) computed from comparison of PFRS values and scanner DN values for the same areas were applied to the scanner data prior to transforming the data using the canonical transformations.

Of the six different canonical transformations (CTs) examined, this particular combination provides the greatest visual separation of hydrothermal alteration types. The image displays a vivid array of color patterns corresponding to various alteration subtypes. Many areas lumped together as one alteration type on the ratio image are split into markedly distinctive units on the CT image (see Figure 4-35 for interpretation).

Areas of alteration appear as various shades of orange, blue, lavender, and yellow on the image. Alteration within the main Silver Bell structural zone is separable into two very distinctive patterns: an outer orange region, corresponding to mapped propylitic alteration, and an inner blue/lavender region, corresponding to exposures of phyllic

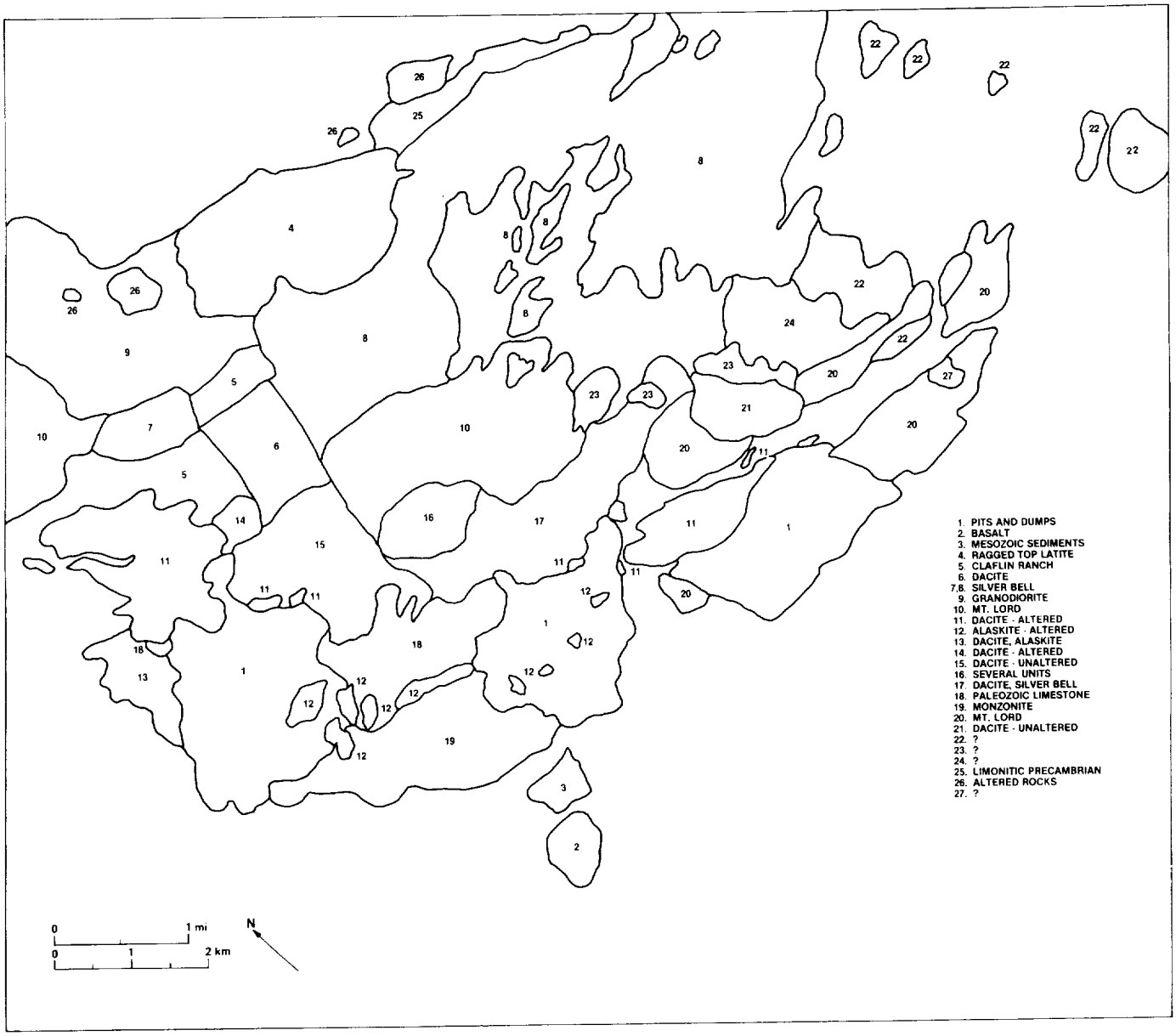

Figure 4-35. Interpretation map of NS-001 canonical transform image (Figure 4-34)

alteration. A third alteration category appears as several small orange patches within the core of the bluish phyllic zone east of the El Toro Pit. These orange areas, which appear identical to propylitic alteration, correlate spatially with zones of potassic alteration shown on the ASARCO alteration map. The similar appearance of the potassic and propylitic zones indicates that the overall makeup of the two alteration types, in terms of clay and iron-oxide content and spectral reflectance, must be quite similar. This is consistent with the PFRS data shown in Paragraph III.

Propylitic alteration appears more extensive on the CT image than shown on ASARCO's alteration map. Orange-colored areas of propylitic alteration are widespread in igneous rocks on both sides of the Silver Bell fault zone, but the most intense development appears to occur in the exposures of granodiorite porphyry, monzonite porphyry, and dacite porphyry east of the Oxide Pit. These exposures were field checked and found to contain extensive outcrops having dispersed epidote and clay and traces of limonite after pyrite.

The Oxide fault zone is very strongly highlighted, due to the apparent presence of strong propylitic alteration in the monzonite dikes along the east–west zone. Other areas of apparent propylitic-type alteration include the rocks between

the Mt. Mammoth and Barite Faults (northwest of Ragged Top Peak) and the monzonite porphyry stock west of the Silver Bell fault zone.

A very distinctive, lavender-colored area shows up within the propylitically altered rocks east of the Oxide Pit. This area, which is not covered by any detailed geologic maps, was field checked and the color was found to be caused by dacite porphyry with a gently east-dipping flow foliation. The dacite is weakly altered to epidote and clays.

The overall lithologic discrimination capability, including both altered and unaltered rocks, is about the same or slightly less than the ratio composite. Approximately 18 rock-type classes may be separated on the transformed image, generally corresponding to the same units separated on the untransformed products. Most of the decreased separability can be attributed to the poor discrimination between the alaskite and monzonite stocks and Paleozoic limestones, all three of which appear uniformly orange in color on the transformed image. Improved separability of the altered rocks indicates the value of this processing technique.

3. Canonical transformation image (18 groups – all rock types). Figure 4-36, produced using spectral data for all 18 rock-type groups, is shown because it appears superior to the other transformations in *overall* discrimination of rock types. The same general units visible on the NS-001 ratio composite are present on the transformed image, but the lithologic boundaries are greatly enhanced and made much more distinct by the presence of highly contrasting color patterns. The separation of alteration types, however, is not as clear as that presented by the transformation product made by using the combination of 11 igneous rock types.

Most of the major rock units mapped in the Silver Bell test area can be discriminated on this CT image. On the image, Mt. Lord Ignimbrite is a blue-green color, and Claflin Ranch Formation and granodiorite porphyry exposures appear yellowish-tan. Fresh dacite porphyry is pale green with a faint lavender tint. Monzonite and alaskite are both violet in color. Mesozoic red beds and Precambrian Apache Group sediments are dark blue, while Paleozoic limestones are variable, ranging in appearance from purplish-brown to pale green. Other rock types are rendered as less diagnostic shades of green, lavender, and pink.

Clay-rich areas of alteration appear bright pink on the image, while areas of propylitic alteration are violet colored, similar to fresh monzonite and alaskite. Propylitic and phyllic alteration can only be discriminated with difficulty within the main Silver Bell alteration zone, due to their similar appearance.

In general, the same structural features visible on the other NS-001 products are accentuated on the 18-group CT image. Both the Ragged Top Fault and the Mt. Mammoth/Barite systems are very clearly defined. However, the Barite and Mt. Mammoth Faults do not clearly extend through the monzonite stocks, as they appear to do on the 11-group CT image. The Oxide fault zone also shows up, but not with the same clarity and resolution which the propylitically altered dikes bring out on the 11-group CT image.

4. Supervised classification. Calibrated NS-001 data were input into a supervised classification scheme to evaluate this processing technique for mapping purposes. Previous work using this algorithm for geologic purposes has met with mixed success (Siegal and Abrams, 1975). This is due to the nature of geologic materials: units are not very homogeneous, producing large variance in training set statistics; boundaries are often gradational rather than sharp; the pixel size can result in mixed pixels having signatures of several units; etc. Nevertheless, because this procedure requires minimal interface by an analyst and is quite automated, it was felt that it was worthwhile to examine it.

Thirteen different rock types were selected and represented by 16 training areas outlined on an image of the Silver Bell area (Table 4-17 and Figure 4-37a). A program called FASTCLAS was used to identify all other pixels in the scene which had similar spectral values in the seven visible and near-infrared NS-001 bands. This program is a hybrid parallelepiped–Bayesian Maximum Likelihood classifier (refer to the Technical Appendix, Section 14, for details). The mean DN values and standard deviations for each group in each of the seven channels are shown in Table 4-18.

Pictures showing the results of the classification for each of the 13 units are shown in Figures 4-37 through 4-40. Mt. Lord (Figure 4-37b) was accurately mapped. Some areas seem to represent alluvium derived from outcrops, particularly southeast of Ragged Top. Altered dacite (Figure 4-38a), or more appropriately phyllic alteration, was properly depicted. The two regions west and east of Ragged Top are weakly altered Precambrian rocks along the Ragged Top Fault. Unaltered dacite (Figure 4-38b) maps outcrops in areas adjacent to the training area. Areas south of Silver Bell Peak were not recognized.

This training area is probably in propylitic material, so less altered dacite and dacite interbedded with Silver Bell are not recognized. Claflin Ranch (Figure 4-38c) identified some areas of granodiorite west of Ragged Top; the large area in the northeast is probably Silver Bell, although no adequate maps exist to verify the accuracy of the classifica-

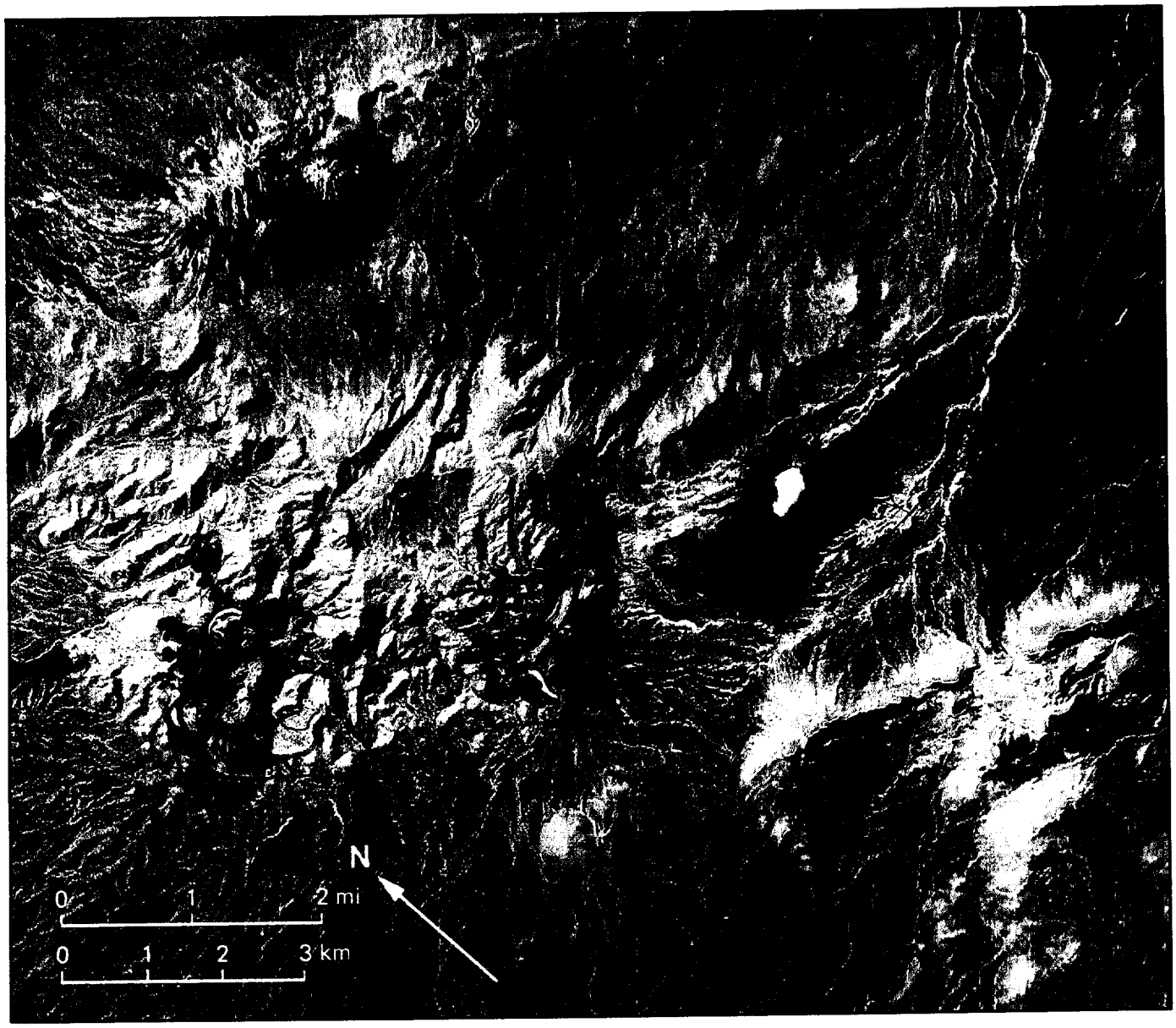

Figure 4-36. NS-001 canonical transform image. Axes derived from linear discriminant analyses of 18 rock groups using PFRS data. V1, V3, and V4 are displayed as red, blue, and green, respectively.

Table 4-17. Silver Bell training areas

Unit	Number	Number of Pixels
Mt. Lord	1	9850
Dacite, altered	2	5450
Dacite, unaltered	3	3025
Claflin Ranch	4	2650
Granodiorite	5	5625
Ragged Top latite	6	5625
Silver Bell 1	7	5625
Basalt	8	2025
Red beds	9	625
Monzonite	10	3025
Alaskite	11	625
Limestone	12	2025
Silver Bell 2	13	1225

tion. Granodiorite (Figure 4-38d) includes some areas of Silver Bell immediately to the south. Ragged Top (Figure 4-39a) includes areas in the Waterman Mountains, probably of high albedo material. Areas in the dumps were also included in this class. Silver Bell 1 (Figure 4-39b) includes the areas south and southeast of Ragged Top. Misclassified were areas south of the Oxide Pit, which are red beds. Basalt (Figure 4-39c) picked up the basalt outcrops, but also included some areas of shadow (low albedo) in the Waterman Mountains. Red beds (Figure 4-39d) classified only the two outcrops and none of the subcrop or alluvial areas. Monzonite (Figure 4-40a) seems to include everything that was not similar to the other classes. Accuracy for this class is clearly the lowest of all the classes and includes a great deal of alluvial area. This may imply that, spectrally, monzonite is most similar to weathered alluvium, regardless of its relative source. Alaskite (Figure 4-40b) classified correctly some of the mapped alaskite. Also included erroneously was a large area north of Ragged Top. Limestone (Figure 4-40c) correctly classified the limestone outcrops between and west of the two pits. Also included were large areas in the Waterman Mountains, which contain limestone outcrops. Silver Bell 2 (Figure 4-40d) classified fairly accurately outcrops not classified in Figure 4-39(b). A color version combining the 13 thematic maps is shown in Figure 4-41.

Table 4-18. Statistics of training areas

Unit	Channel Mean, Standard Deviation						
	1	2	3	4	5	6	7
1	19,4	29,4	44,4	58,3	70,4	58,4	38,5
2	34,5	44,4	63,5	80,5	110,6	121,7	79,6
3	33,4	42,3	51,3	62,3	73,3	67,4	47,4
4	36,3	48,3	59,3	69,3	86,3	94,4	78,4
5	39,4	47,3	54,4	58,3	67,3	68,4	45,4
6	53,5	55,5	69,5	84,6	109,6	119,6	123,7
7	35,3	38,2	48,3	58,3	68,3	63,3	43,4
8	9,2	16,2	23,2	17,3	42,3	36,3	21,3
9	26,2	30,2	54,3	65,3	82,3	73,3	74,4
10	56,4	64,3	77,4	96,3	102,3	104,4	94,4
11	40,3	54,3	70,4	89,3	104,3	105,3	95,4
12	34,5	41,4	52,5	64,5	86,5	87,5	71,6
13	31,3	40,3	53,3	67,3	75,3	67,3	50,3

This exercise mainly indicates that success of supervised classification rests largely on the statistics of the training areas and how well they represent the areas to be identified. A test of the homogeneity of the training areas was performed using linear discriminant analysis. Table 4-19 shows the accuracy with which each training area was grouped into its class. Accuracies ranged from 100 percent for basalt to 53 percent for limestone. Some of the inaccuracies are due to shadows in the training areas, resulting in large standard deviations and overlap of the values between the groups. Overall accuracy of 74 percent is fair, but again reflects the problems with this type of analysis. Improvements could be made by using ratio values in addition to raw bands. This would compensate for some of the problems of shadowing. Also, more careful selection of training areas to insure homogeneity and obtain more representative sampling of the varied units is indicated.

5. Principal components analysis. The seven visible and near-infrared wavelength bands of the NS-001 data were input to a PC analysis. (These data were the calibrated data, where DN is proportional to reflectance.) The first four eigenvectors and their associated eigenvalues are shown in Table 4-20. These vectors are also plotted in Figure 4-42. V1, which has most of the scene variation, is basically an average of each of the seven bands, or the average albedo. V2 contrasts the bands long of 1 μm with those short of 0.7 μm. V3 is heavily weighted on bands 4 and 5 (positive) and band 7 (negative). V4 is heavily weighted on bands 4 and 7 (positive) and bands 5 and 6 (negative).

The DN values from 13 training areas for 13 units were extracted from the NS-001 image data for the seven channels. These values were convolved with the four eigenvectors to produce the PC values:

$$PC_{11} = A_{11}B_{11} + A_{12}B_{12} + \cdots + A_{17}B_{17}$$

where A_{1n} are the n weights of eigenvector 1, B_{11} to B_{17} are the DN values for unit 1 in the seven bands. These values are shown in Table 4-21 and plotted in Figure 4-43.

The values on vector 1 rank the units by albedo: the lowest value is for basalt, then Mt. Lord; the highest value is Ragged Top. An image of V1 is shown in Figure 4-44(a). Ragged Top, the pits, and one dump are white; basalt,

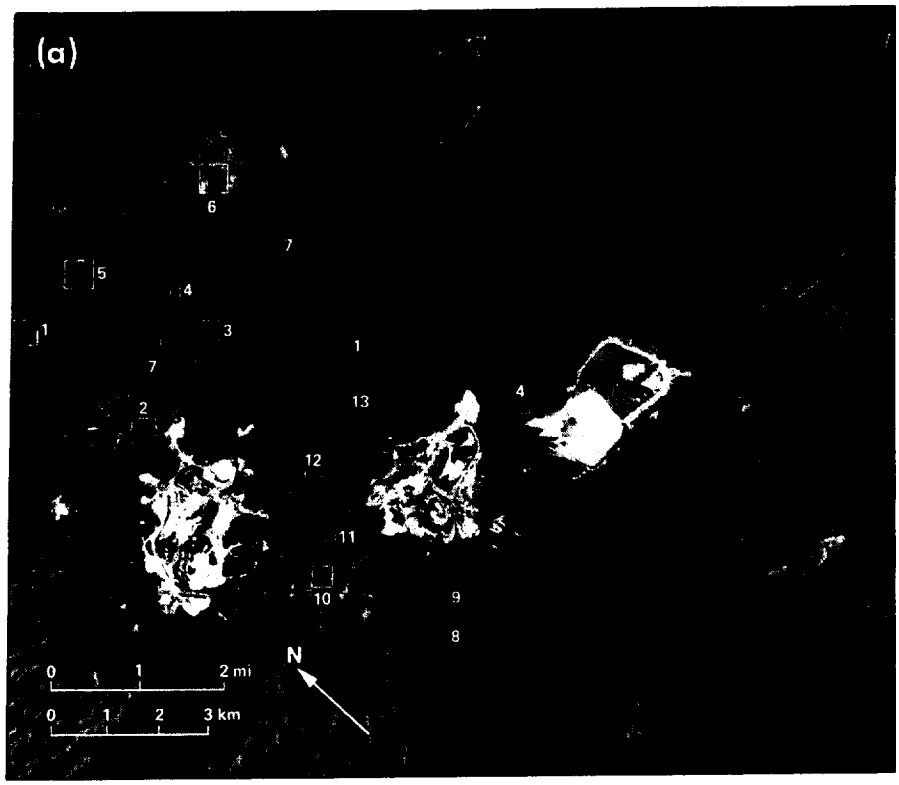

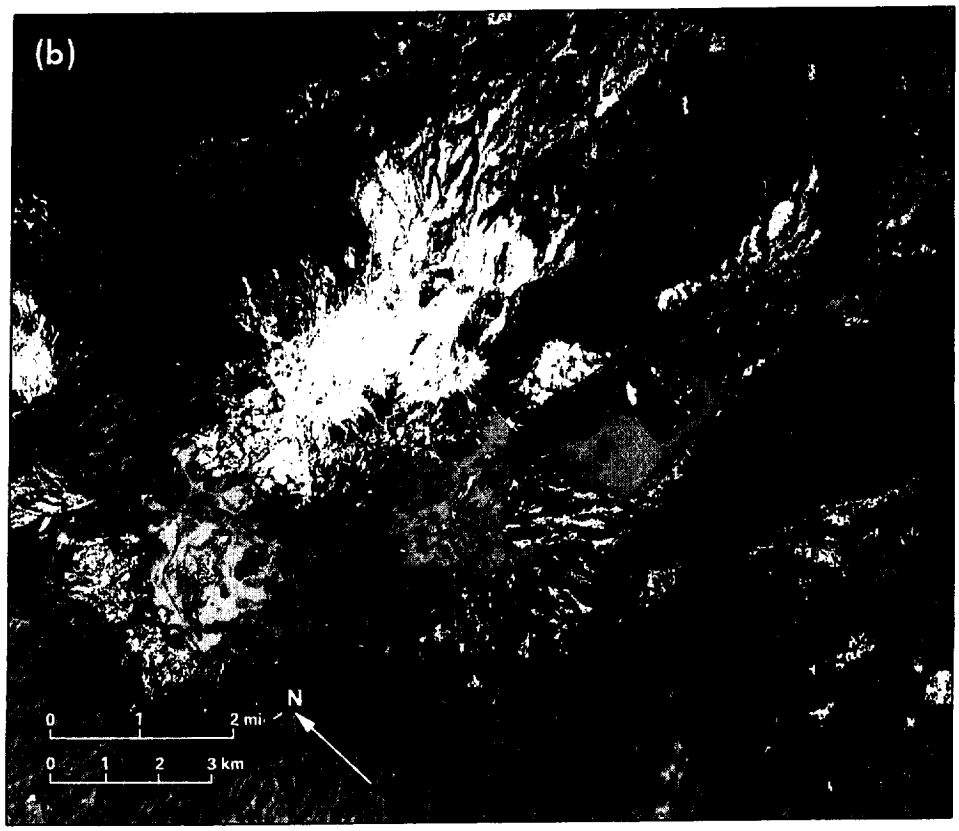

Figure 4-37. (a) Training areas for supervised classification of NS-001 data; (b) classification map for Mt. Lord

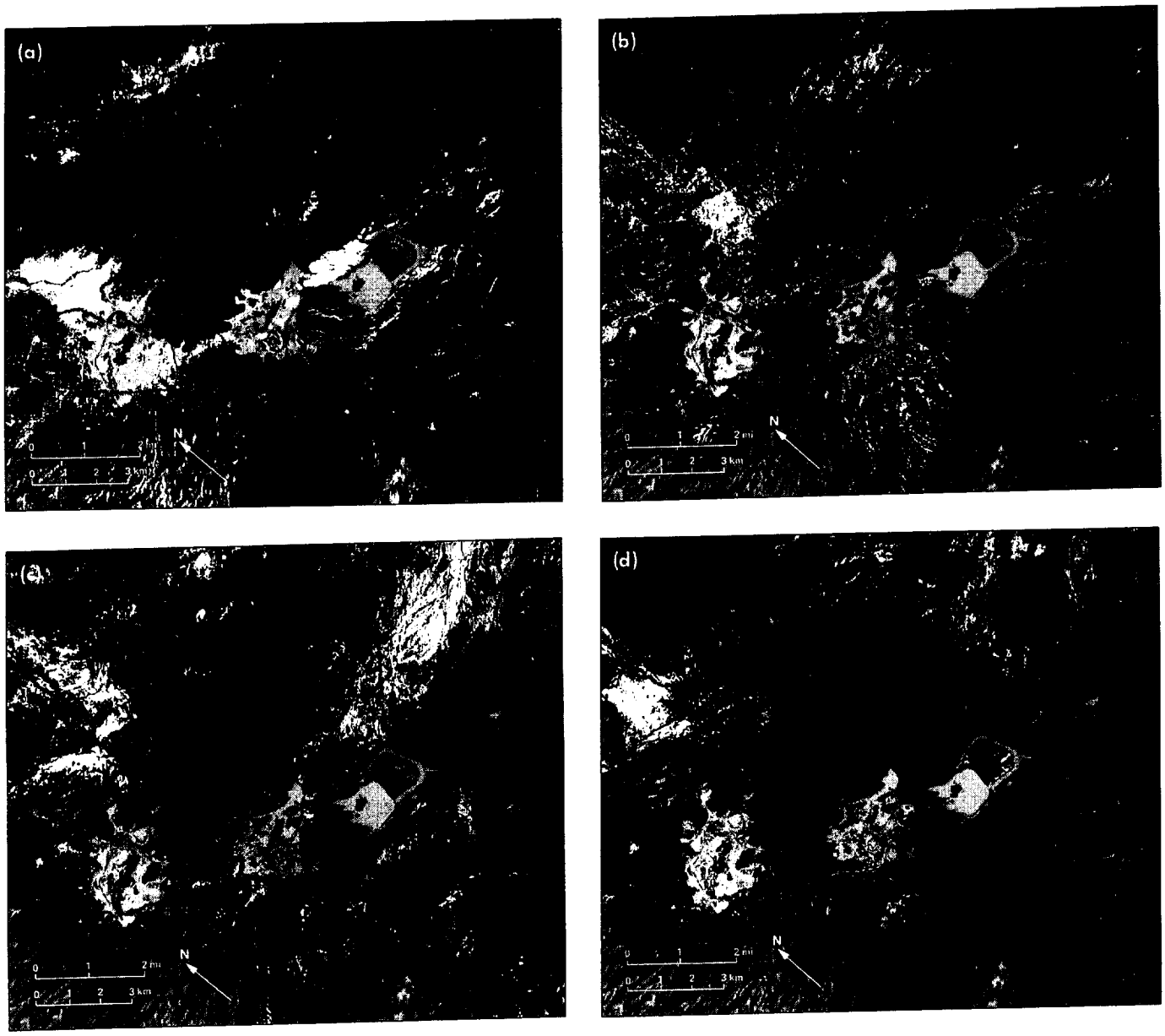

Figure 4-38. Classification maps for NS-001 data: (a) altered dacite; (b) unaltered dacite; (c) Claflin Ranch; (d) granodiorite

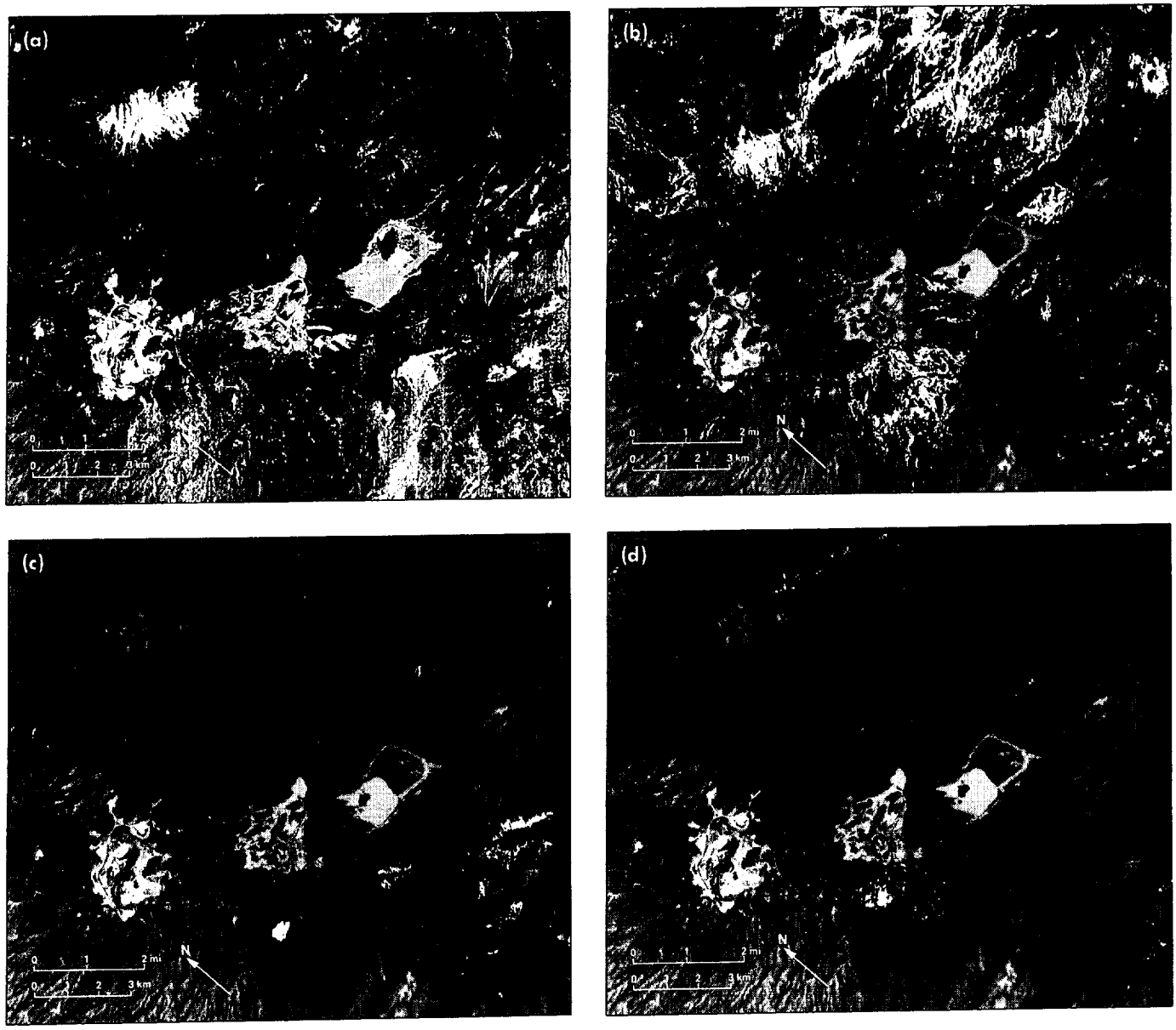

Figure 4-39. Classification maps for NS-001 data: (a) Ragged Top; (b) Silver Bell 1; (c) basalt; (d) red beds

Mt. Lord, and shadows are darkest. Altered dacite, limestone, and monzonite are light gray. Examination of a picture of V2 (Figure 4-44b) and the V2 vector shows dacite, Ragged Top, alaskite, red beds, limestone, and Claflin Ranch as bright (high values). The darkest areas are the dumps and pits.

V3 contrasts band 4 and band 7 (Figure 4-44c); the highest values are produced by dacite, Mt. Lord, Silver Bell, and vegetation; the lowest values are basalt, Ragged Top, the pits, and the dumps.

V4 is basically bands 4 plus 7 minus bands 5 plus 6. The lowest values are found for phyllically altered material (black on Figure 4-44d) and areas of the pits. Red beds and Ragged Top have the highest values.

In general, the individual principal components images provide some lithologic separation. In the case of V1 and V4, the image appearances can be related to spectral features. V1 is average albedo, V4 contrasts the brightest part of the spectrum (at 1.6 μm) with the falloff on either side. This value is largest for altered rocks.

A color composite was produced by displaying V1, V2, and V3 as red, green, and blue, respectively (Figure 4-45). An interpretation map is also shown as Figure 4-46, where similar-colored areas have been assigned the same number and then identified using the geologic maps. Fifteen units (other than alluvium) were recognizable. Unit 1 includes areas of phyllic alteration and limonitic Precambrian rocks. Unit 2 lumps weakly altered dacite, dacite–Silver Bell, and Mt. Lord. Unit 3 includes Silver Bell and Mt. Lord. Unit 4 is only Mt. Lord. Unit 5 represents Ragged Top latite, granodiorite, and limestone. Units 6 and 7 are Silver Bell. Unit 8 is Claflin Ranch. Unit 9 includes Precambrian and Paleozoic rocks of West Silver Bell. Unit 10 includes intrusive rocks—monzonite, alaskite, and granodiorite. Unit 11 is a mixture of dacite and Claflin Ranch. Unit 12 is Claflin Ranch and Silver Bell. Unit 13 is Claflin Ranch. Unit 14 is Silver Bell. Unit 15 is basalt. In general, a few units are uniquely separated; the Silver Bell and Claflin Ranch complexes are distributed over several units, reflecting their variable lithologic compositions (basalts, andesites, flow breccias, agglomerates). Overall, this type of processing has produced an image with fair geologic information.

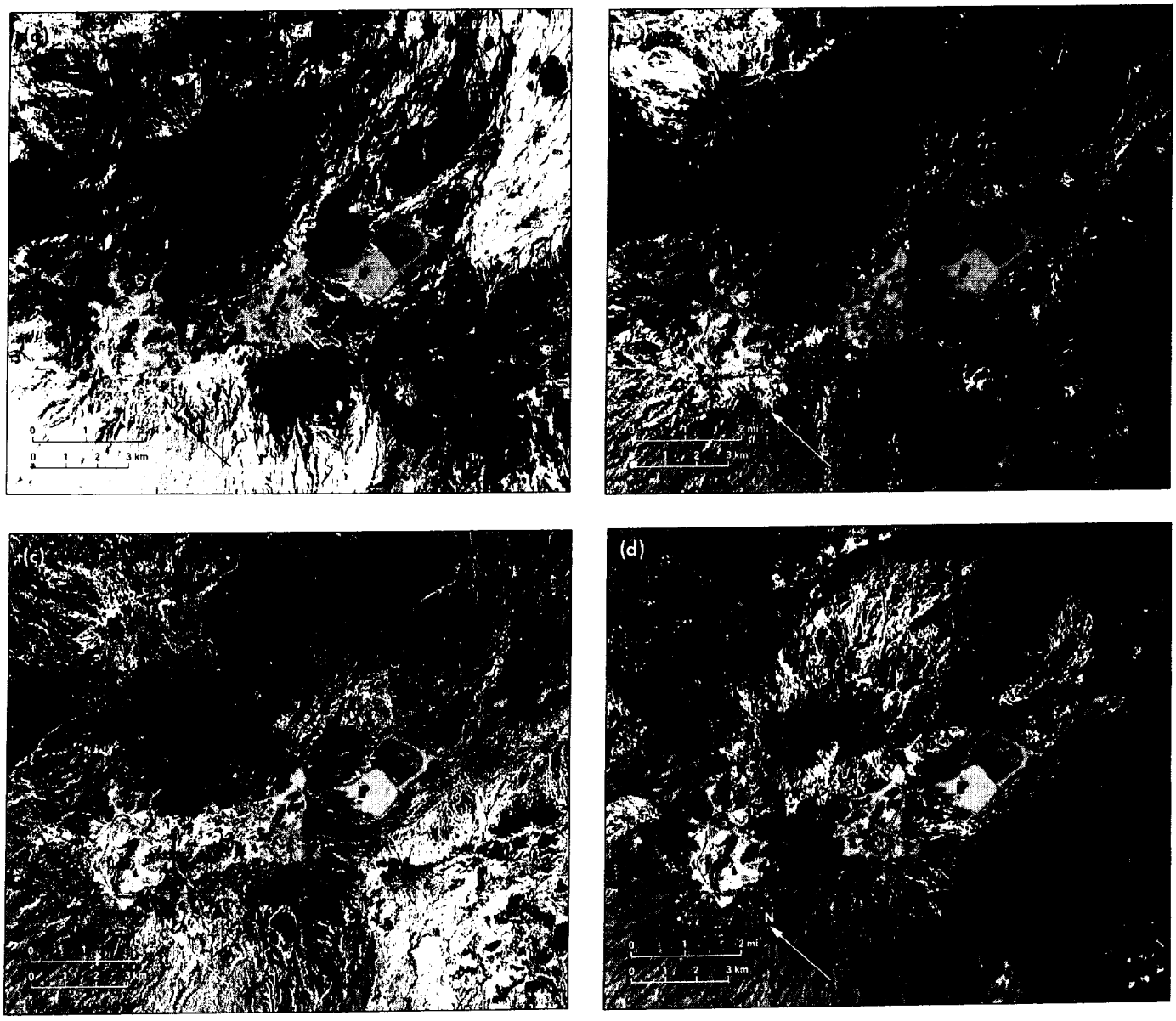

Figure 4-40. Classification maps for NS-001 data: (a) monzonite; (b) alaskite; (c) limestone; (d) Silver Bell 2

Figure 4-41. Thematic map produced from NS-001 supervised classification: Mt. Lord, pink; altered dacite, red; unaltered dacite, lavender; Claflin Ranch, green; granodiorite, light orange; Ragged Top, light blue; Silver Bell 1, dark blue; basalt, white; red beds, brown; monzonite, yellow; alaskite, orange; limestone, gray; Silver Bell 2, cyan; unclassified, black

6. Summary of NS-001 results. This section describes the results of four different kinds of image processing techniques applied to the NS-001 data. Ratioing and principal components transformations require the least amount of knowledge about the scene. PC analysis is an unsupervised technique that produces new, uncorrelated images which display the scene variance along each axis. Because this method operates on statistics from the whole scene, it is biased by the relative areal extent of each unit in the scene. If the area examined contains a large fraction of unimportant surficial cover (vegetation, for example), this method is liable to produce unsatisfactory results relative to separation of the other, more important materials. In the case of Silver Bell, most of the scene contained areas of interest so the separations produced by the technique were satisfactory.

Ratioing requires selection of the particular bands which will be used to create the CRC. A general knowledge of the materials in the scene and their spectral characteristics

Table 4-19. Training area accuracy

Group	Pixels Correct, %
Mt. Lord	61
Dacite, altered	88
Dacite, unaltered	66
Claflin Ranch	83
Granodiorite	83
Ragged Top	79
Silver Bell 1	72
Basalt	100
Red beds	91
Monzonite	70
Alaskite	91
Limestone	53
Silver Bell 2	58

leads to selection of particular band-ratio combinations to enhance the display of those materials. Conversely, ratios can be selected to enhance certain mineralogical constituents (such as iron oxides and clays) and the images used to search for the presence of these materials, even in totally unknown areas. The former approach was used here, with outstanding results.

Supervised classification techniques require *a priori* knowledge of the distribution of materials in a scene in order to select proper training areas. The main advantage (and disadvantage!) of this technique is the production of a thematic map which displays the results of the classification without further interaction by an interpreter. No skill is required to use the thematic map; however, all of the textural and contextual information is correspondingly eliminated, preventing an interpreter from bringing to bear his professional skills and geological expertise on the interpretation. As such, this technique is philosophically the least desirable approach to image processing for geologic mapping.

Canonical transforms require the greatest amount of *a priori* information. Field spectral measurements must be available (at least in this particular application) to serve as the basis for discriminant function analysis. However, the gratifying results point to this technique as the most powerful of those presented here.

Table 4-20. Eigenvalues and eigenvectors for NS-001 data

Eigenvalue	Eigenvector	Channel						
		1	2	3	4	5	6	7
4392	V1	0.34	0.31	0.36	0.36	0.34	0.42	0.49
340	V2	-0.61	-0.41	-0.26	-0.06	0.26	0.39	0.40
170	V3	-0.25	-0.05	-0.04	0.75	0.35	-0.07	-0.50
55	V4	-0.15	-0.05	-0.01	0.43	-0.34	-0.59	0.57

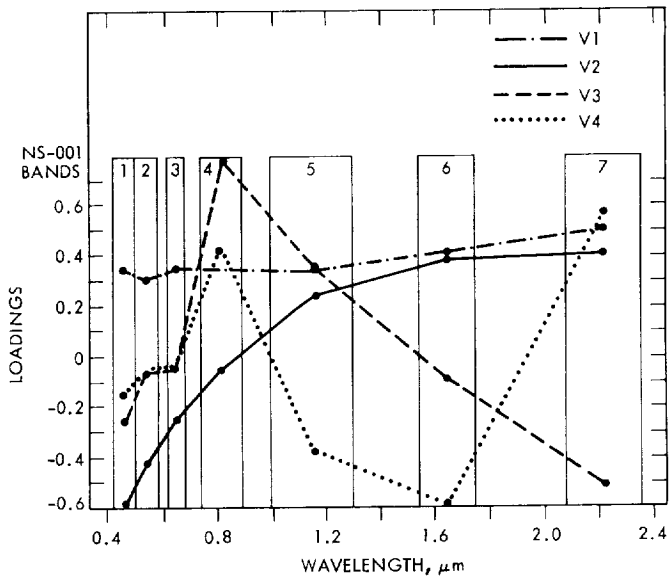

Figure 4-42. Plot of loadings on first four eigenvectors (V1, V2, V3, V4) from NS-001 principal components analysis

While this section is certainly not an exhaustive treatment of image processing techniques, a wide enough variety of algorithms was considered to conclude that it is the spectral regions covered by the NS-001 Thematic Mapper Simulator (and Landsat 4 Thematic Mapper) and the resulting information content which allow satisfactory geologic maps to be interpreted using any of the processing schemes.

F. Thermal Data

Midday and predawn thermal data were obtained on August 17–18, 1977, using the M²S scanner. The day thermal image (Figure 4-47a) depicts warm areas in white and cold areas in black. The coldest areas are the stream beds

Table 4-21. Principal components values

Unit	Vector			
	1	2	3	4
Mt. Lord	118	17	37	-16
Dacite 1	204	47	38	-38
Dacite 2	142	10	32	-19
Claflin Ranch	180	29	23	-19
Granodiorite	142	1	25	-20
Ragged Top	239	45	13	-13
Silver Bell 1	134	7	29	-18
Basalt	63	15	10	-19
Red beds	156	35	25	-8
Monzonite	226	19	33	-14
Alaskite	214	36	32	-14
Limestone	167	30	24	-21
Silver Bell 2	145	13	34	-15

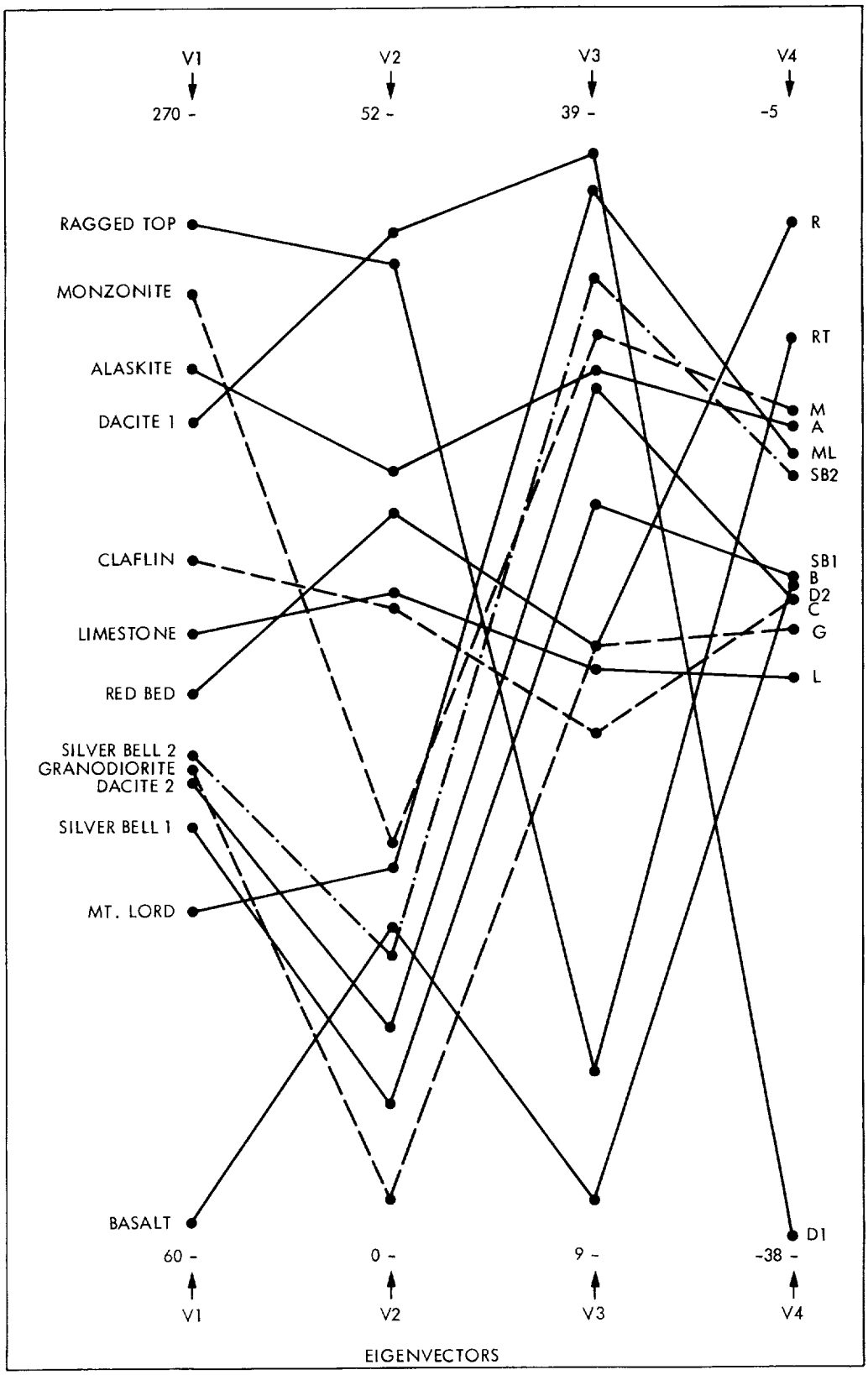

Figure 4-43. Principal components values for first four eigenvectors (V1, V2, V3, V4) for 13 rock groups from NS-001 data

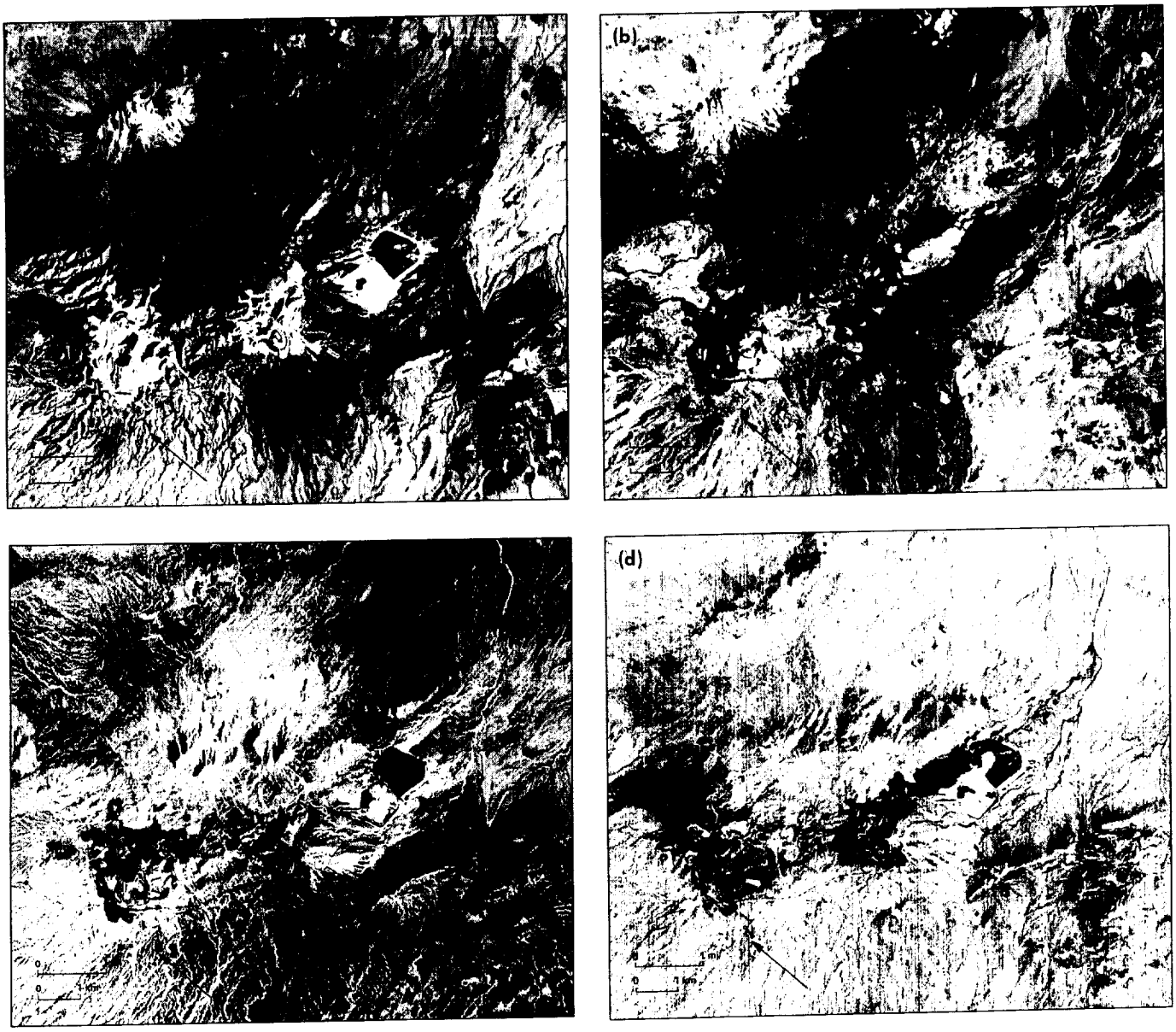

Figure 4-44. Principal components images from NS-001 data: (a) V1; (b) V2; (c) V3; (d) V4

with vegetation, parts of the dumps, and Ragged Top (high albedo, reflects solar energy). Warm areas are basalt outcrops and alluvium. In general, there is less information in these data than the average albedo image (acquired at the same time) (Figure 4-47b). The night or predawn thermal image (Figure 4-47c) is very noisy, and the data show a limited range of temperature values. In general, outcrop areas are warmer than alluvium, although topographic effects are an additional factor as seen at Ragged Top and Silver Bell Peak—which are relatively cooler.

A more useful display of thermal properties is produced by calculating apparent thermal inertia (ATI) (Kahle et al., 1981). ATI is an approximation of the modeled thermal inertia, and is calculated as:

$$\text{ATI} = \frac{1 - A}{\Delta T}$$

where A is albedo, and ΔT is the difference between day and night temperature values. To produce an ATI image, day–night thermal data are coregistered and the difference between them computed. An average albedo value is computed by weighting the 10 channels of visible and near-infrared data (obtained simultaneously with the day thermal) with the solar spectrum. An ATI image is shown as Figure 4-47(d);

Figure 4-45. Principal components color composite from NS-001 data. Components V1, V2, and V3 are displayed as red, green, and blue, respectively.

high ATI values are bright, low values are dark. The brightest areas are moist areas in the dump, vegetation in streams, basalt outcrops, the Waterman Mountains, Ragged Top, silicified knobs and quartzite west of Oxide Pit, and Mt. Lord west of Ragged Top Peak. These are all dense materials, which have high thermal inertia, or wet areas (water has high TI). Lowest ATI values are in the dumps and pits and in the alluvial fans. These are areas of very low density material, hence low TI. Dacite has moderately low ATI, probably due to reduced density due to phyllic alteration.

A more effective method to display thermal data is to produce a color composite of the thermal and albedo data. Figure 4-48 is a picture using night thermal as blue, day thermal as green, and albedo as red. This process allows the interrelationship of thermal and albedo properties to be depicted on a single, more easily interpretable image. An interpretive map for this image is shown in Figure 4-49. The dumps are bright red, indicating high albedo and low temperatures in both the day and night thermal data. Ragged Top is magenta, indicating high albedo and relatively warm temperatures at night and cold temperatures in the

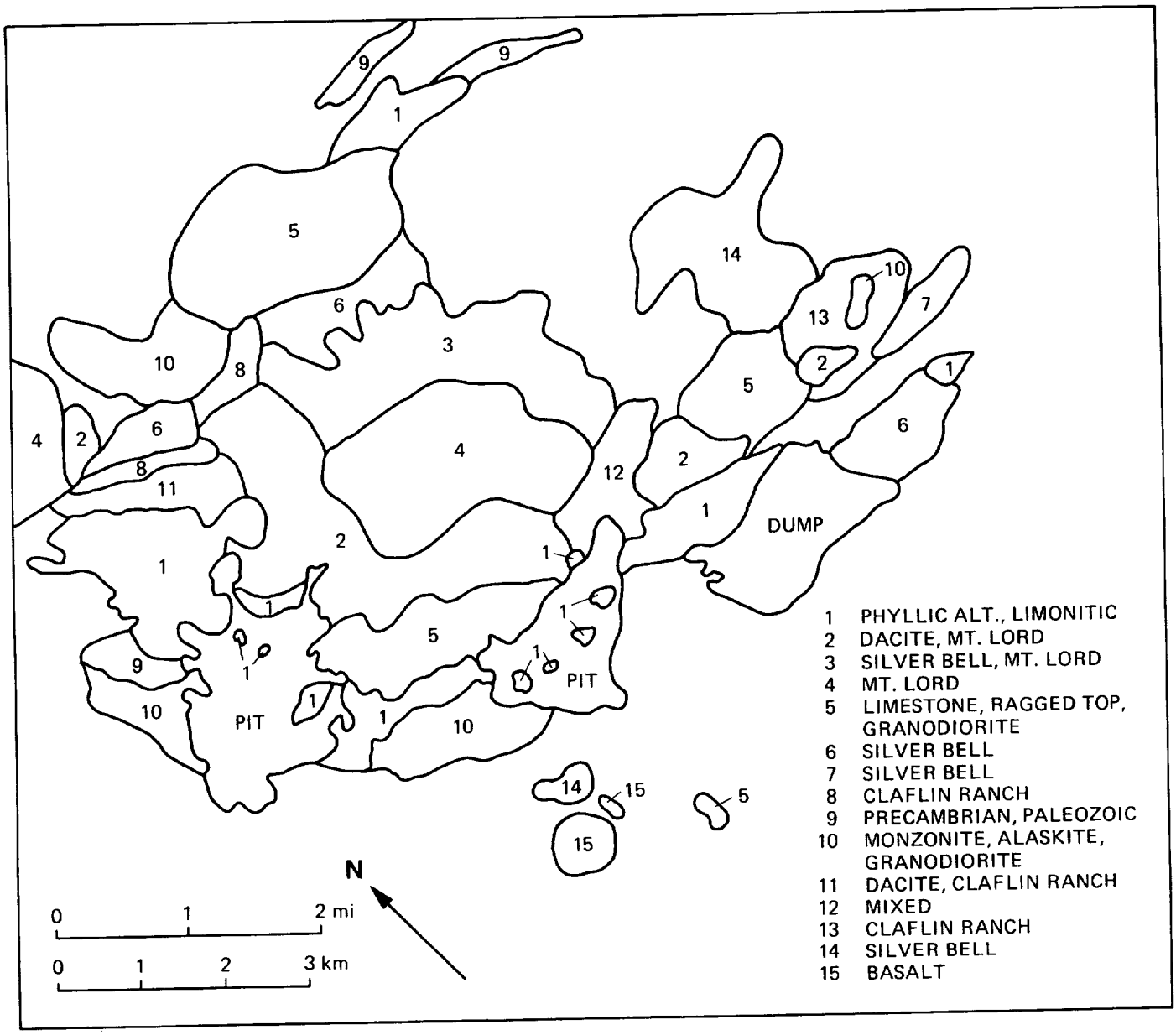

Figure 4-46. Interpretation map of NS-001 principal components composite (Figure 4-45)

day. A fair number of geologic units are distinguishable on this image: Silver Bell complex, Mt. Lord, basalt, and Mesozoic sediment. Alaskite, monzonite, and limestones are not separable; granodiorite and dacite also look similar. While not as informative as NS-001 data, this combination provides an acceptable level of rock-type separations. However, no additional information is found compared to NS-001 data.

G. Comparison of Spatial Resolution

All of the aircraft scanner data examined and presented in this report were analyzed and processed at their original resolution of between 12 and 18 m. However, because the data are in digital form, it is possible to degrade the spatial resolution in order to examine the effect of more limited spatial resolution on detectability of geologic features.

The NS-001 ratio data used to produce Figure 4-32 were digitally degraded for this task. The area selected for analysis is outlined in Figure 4-50(a). A cubic convolution resampling algorithm was used to produce pixels of 30- and 80-m size. These are shown, with the original 12-m data, in Figures 4-51(a), (b), and (c). For comparison, the same area was extracted from the Landsat false-color

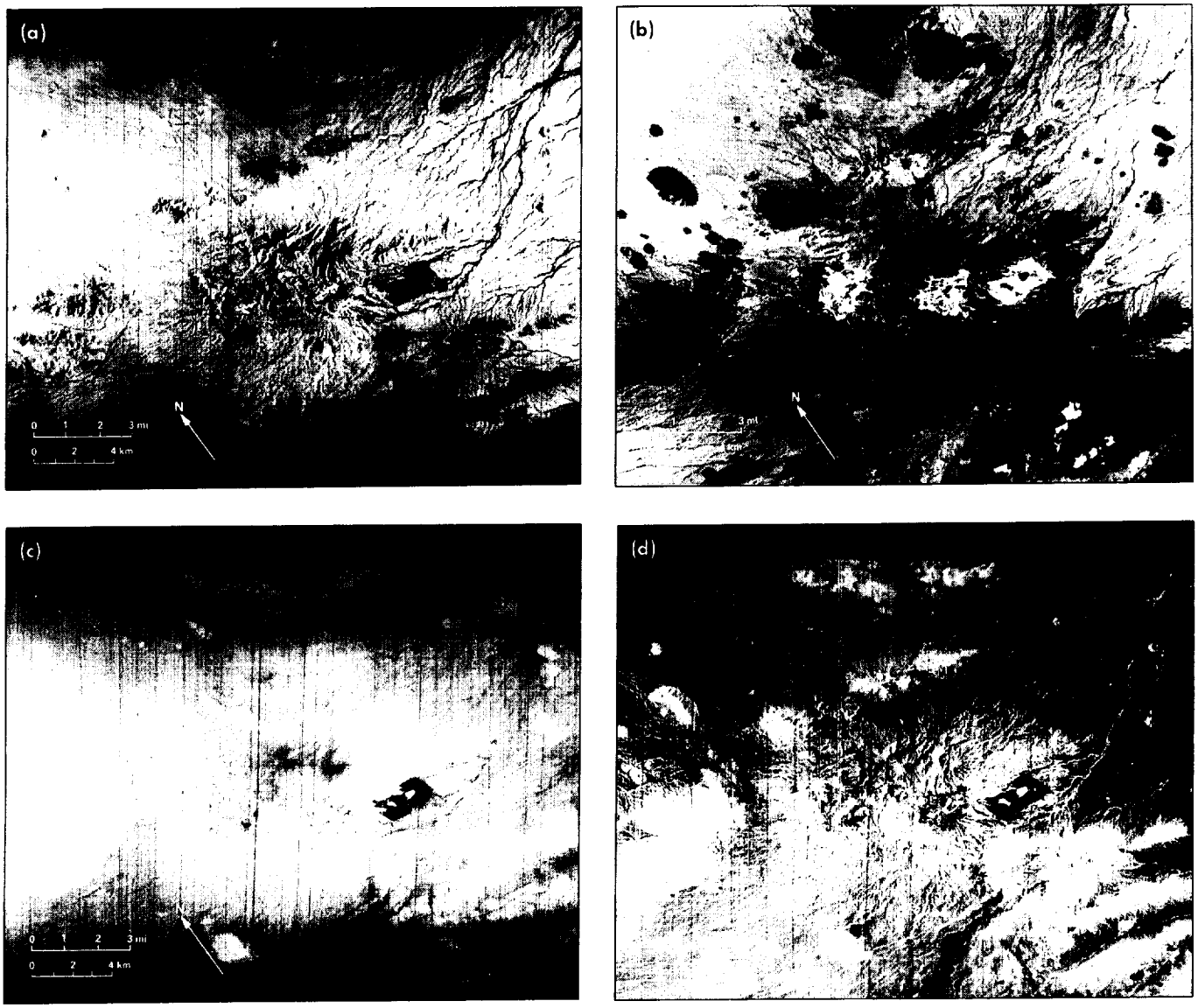

Figure 4-47. M^2S thermal data for Silver Bell: (a) day thermal; (b) albedo; (c) night thermal; (d) apparent thermal inertia. High temperatures or reflectance values are bright.

infrared (CIR) composite (bands 4, 5, and 7), and the Landsat color ratio composite (ratios 4/5, 5/6, and 6/7); these are shown in Figures 4-51(d) and (e). All five images were originally at a scale of 1:48,000, which is a common scale used by explorationists for analysis and mapping.

Several different-sized features were selected for examination and are indicated in the sketch map appearing in Figure 4-50(b). One of the dumps of the Oxide Pit (#1) is shown for location purposes. On the NS-001 data, it appears as a pink area due to the dominance of clay minerals present. On the Landsat CIR, it appears as light blue to white, and on the Landsat ratio image as yellow.

The area of altered syenodiorite (#2) is locatable on all the NS-001 images as a yellow-green area due to its tonal contrast with the surroundings. It is also discernible on the Landsat ratio image as a red area (iron oxides). The dimensions of this area are about 300 by 300 m; on the 12-m data, they are 25 by 25 pixels; on the 30-m data, they are 10 by 10 pixels; on the 80-m data, they are 4 by 4 pixels.

The small outcrops of phyllically altered monzonite (#3) appear as yellow on the NS-001 data. At 80 m they are only single pixels, but can still be recognized because of color contrast with their surroundings. They are not discernible on the Landsat images due to their lack of spectral distinction in the Landsat bands.

The extension of the Barite Fault (#4) is expressed as a drainage alignment. It can easily be mapped at 12- and 30-m resolution, but disappears at 80-m resolution.

The same behavior is evinced by several dikes (#5, #6). These are easily seen on the 12-m data, are more difficult to pick out on the 30-m data, and disappear on the 80-m data.

From the above analysis, it appears that 80-m data are inadequate for recognition of small, key features associated with the Silver Bell deposit. At 30m – the resolution of the Landsat 4 Thematic Mapper – the features are detectable.

IX. Conclusions

Analysis of the Silver Bell remote sensing data reveals that airborne scanner images, particularly the NS-001 Thematic Mapper Simulator data, are superior to more con-

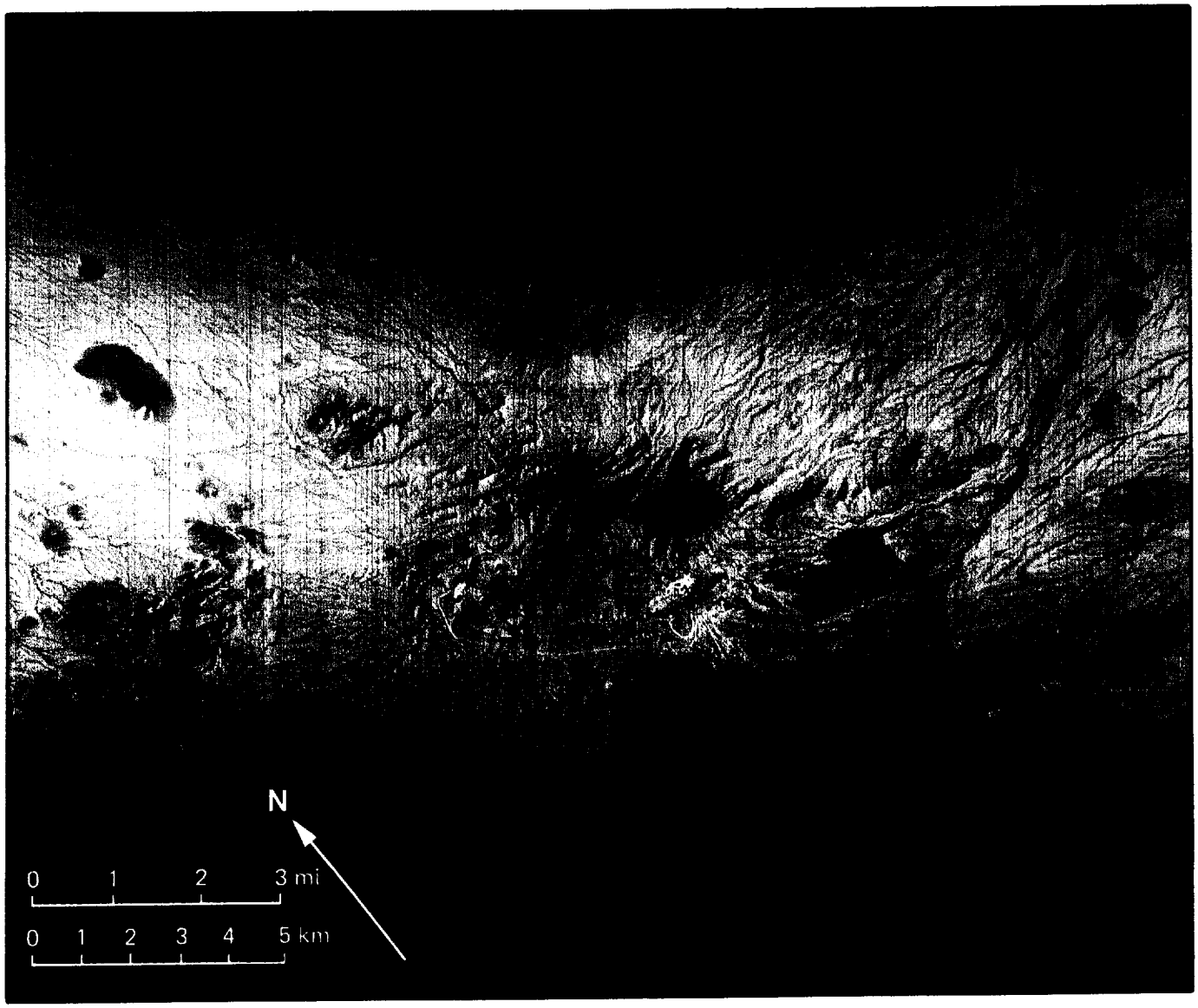

Figure 4-48. Color composite of M²S data. Day thermal, night thermal, and albedo are displayed as green, blue, and red, respectively.

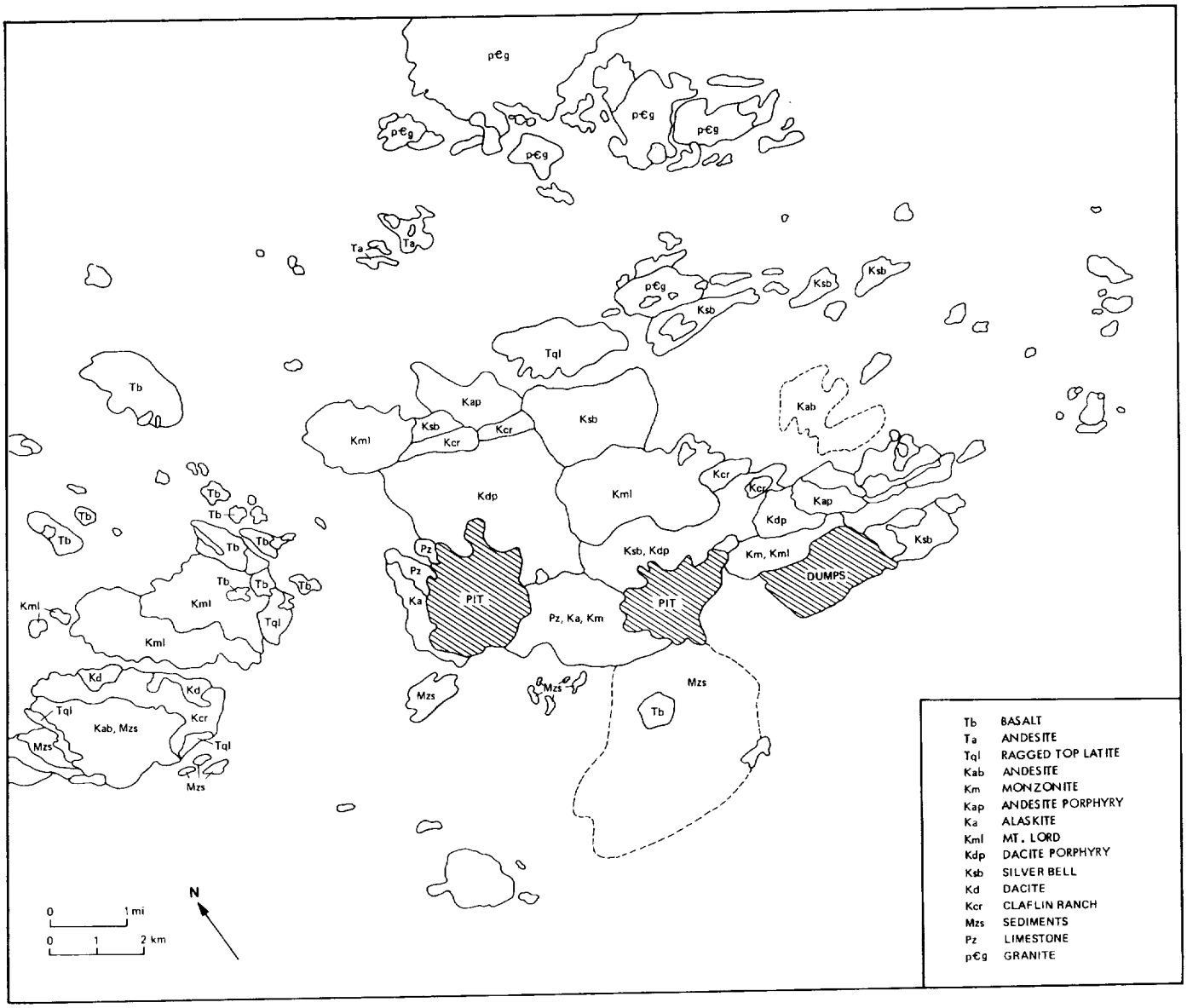

Figure 4-49. Interpretation map of M²S thermal-albedo color composite (Figure 4-48)

ventional systems such as Landsat MSS and color aerial photography in terms of overall structural and lithologic information. The effectiveness of the NS-001 data can be attributed partly to relatively high spatial and spectral resolution, but even more to their ability to detect reflectance features due to clay absorption near 2.2 μm. The Landsat and radar data are useful mainly to delineate regional structures in the district.

The results of the remote sensing interpretation suggest that both high-altitude and low-altitude sensor data would be important in designing an exploration program for an area similar to Silver Bell. Landsat and Seasat data, used in conjunction with regional aeromagnetic data, can identify prospective exploration targets on the basis of coincident alteration and structural features. The close relationship between regional faults, hydrothermal alteration, and copper mineralization is well documented for the Silver Bell District, and this study has demonstrated the feasibility of identifying regional structures through the integrated application of aeromagnetic data and Landsat images.

Several aspects of the Silver Bell remote sensing data appear unique relative to published data for the test site. Among these unique aspects is the ability of the NS-001 images to delineate previously unidentified areas of hydro-

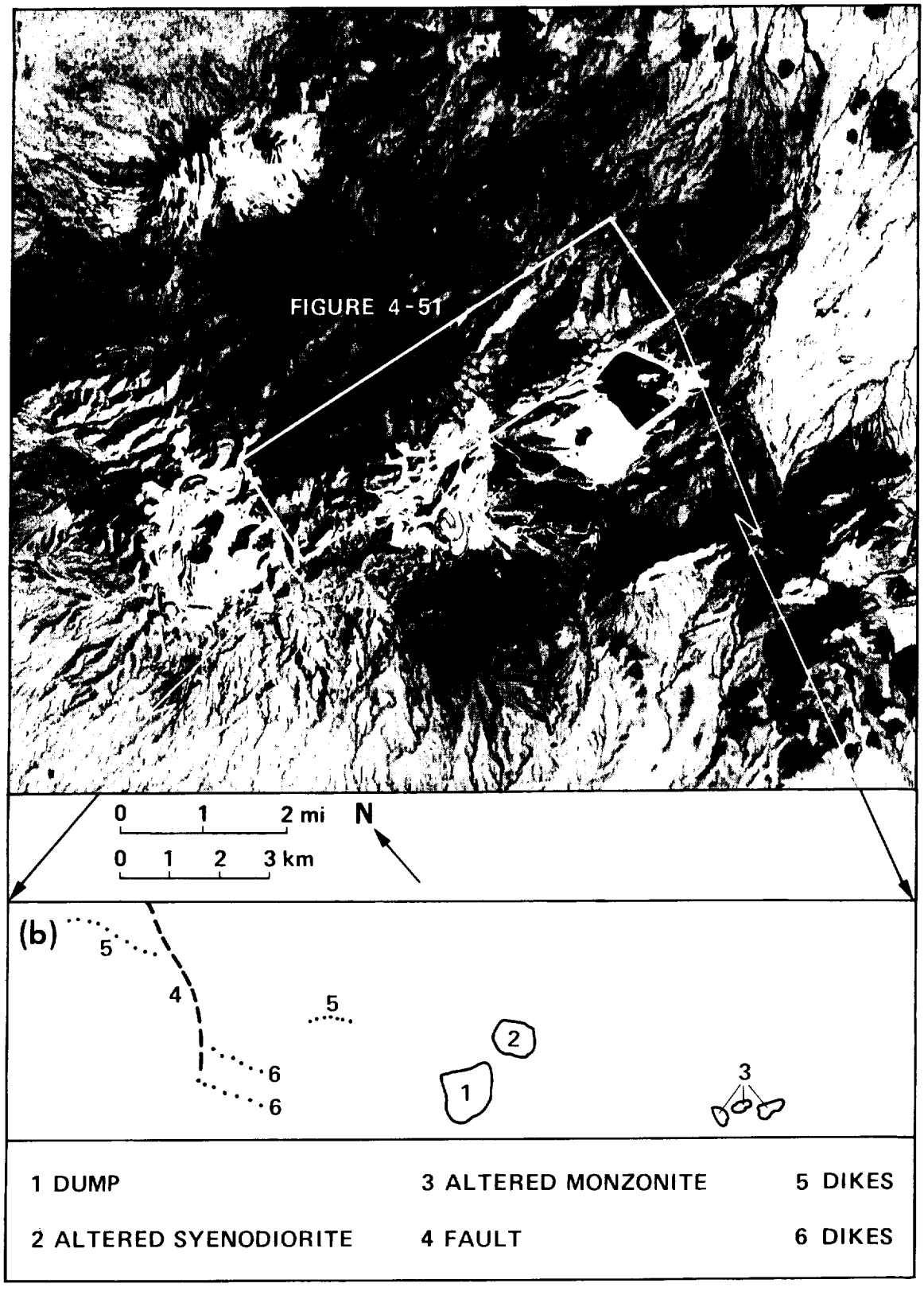

Figure 4-50. Composite of Silver Bell test site: (a) outline of area of Figure 4-51 used for resolution comparisons; (b) features in Figure 4-51 discussed in text

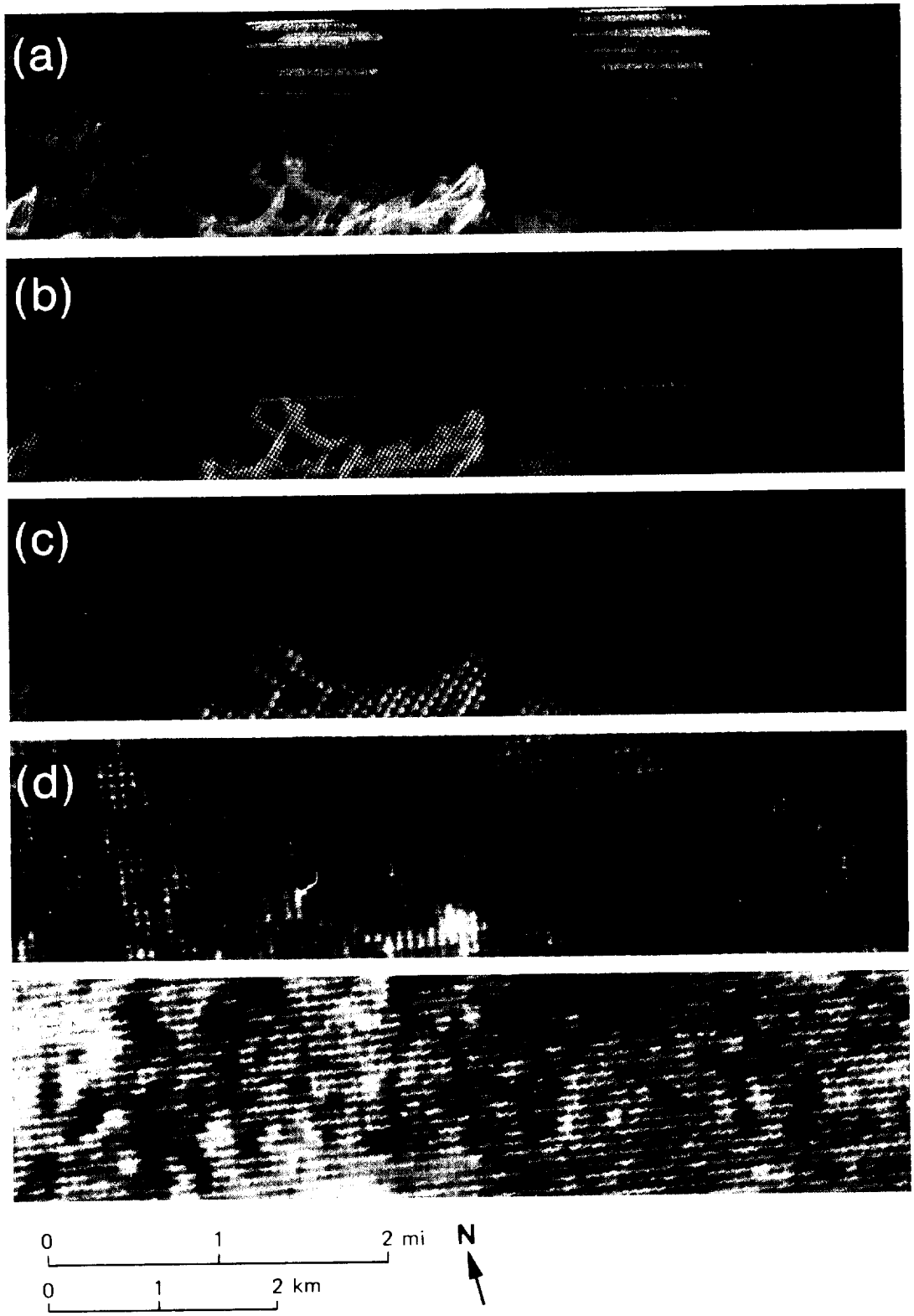

Figure 4-51. Comparison of spatial resolution. Portion of NS-001 ratio composite (Figure 4-32) at resolutions of: (a) 12 m; (b) 30 m; (c) 80 m. Landsat data of 80-m resolution: (d) false-color infrared composite, 4, 5, 7; (e) ratio composite, 4/5, 5/6, 6/7. Area covered is outlined in Figure 4-50(a).

thermal alteration, including the north Ragged Top area, central Waterman Mountains, and West Silver Bell Mountains. In each of these areas, the Thematic Mapper Simulator was able to discriminate very subtle and apparently dispersed concentrations of clay minerals and iron oxides which were not shown on any existing geologic maps.

A second result that is unique to the remote sensing data is the nonuniform, structurally controlled distribution of peripheral propylitic/argillic alteration. This relationship is brought out by some of the NS-001 images, which display propylitically altered areas as discrete patches or blocks, rather than pervasive alteration over broad, continuous intervals. In many cases, these discrete patches are elongated west–northwest to east–west, parallel to the trend of the main Silver Bell fault zone. This distribution pattern is especially noticeable east of the Silver Bell fault zone, where the most intense propylitic alteration appears to have been channeled along certain fault and dike zones.

A third unique aspect of the data is the apparent ability of Landsat and airborne radar data, used in conjunction with regional aeromagnetic and gravity data, to extend some of the known fault zones well beyond their mapped limits. Examples cited in this report include the possible continuation of the Barite/Mt. Mammoth fault system for 3 to 4 km south of the El Tiro Pit, and the possible extension of the Ragged Top Fault across the West Silver Bell Mountains, possibly as much as 6 km west of its known limits.

A rather surprising result emerged from the statistical analyses of the PFRS data. The discriminant function program, given 30 equally spaced 0.05-μm-wide wavelength bands in the 0.45- to 2.45-μm region, selected as its first six bands wavelength regions almost identical to those on the Landsat 4 Thematic Mapper. These bands provide the optimal separation of the 18 rock-type groups used in the analysis.

Attempts were made to use the aircraft scanner data to produce "image spectra." Several approaches were examined to calibrate the data, including *ad hoc* assumptions about the reflectance of a particular material and fitting of image data to field-measured reflectance values for an area in the scene. The resulting image spectra were satisfactory approximations of field-measured spectra. Absorption bands characteristic of ferric iron and hydrous minerals could be seen or inferred. These results suggest that proper calibration of image data can allow them to be used to provide spectral reflectance "curves," which in turn allow some inference of mineralogical composition.

Various computer processing techniques were applied to the NS-001 data, including band ratioing, principal components, supervised classification, and canonical transforms. Virtually every one tried and described in the report produced images providing satisfactory separation of the geologic units. Although some were better than others, it is concluded that, given the proper spectral bands, a variety of techniques will prove satisfactory.

Examination of the thermal data provided no additional information not found in the visible and near-infrared data. Nevertheless, some separation of units was possible using simple three-component color composites of day and night thermal data and albedo data. If this were the only data set available, some degree of discrimination of rock types would be possible. However, given a choice of data types, this one would not be an early selection.

Simulation studies of various spatial resolutions were performed by degrading the 12-m NS-001 data to 30- and 80-m pixel sizes. These data were then analyzed at an original scale of 1:48,000, a common mapping scale used by exploration geologists. All important features detectable on the 12-m data were also visible on the 30-m data. These included small outcrops of altered rocks and individual dikes. At 80-m spatial resolution, small features were not visible. This indicates that multispectral data from the Landsat 4 Thematic Mapper scanner will be of enormous use to exploration geologists, even at a scale of 1:48,000. Resolution, up to a point, is not the limiting factor on interpretation of critical geologic information. Rather it is the position of wavelength bands in appropriate spectral regions which is the critical factor in determining whether multispectral data will be useful or not.

The results of this test site study should have wider applications, both to porphyry copper deposits and to other mineral deposits. Certainly in any area of the world where vegetation cover is minimal and porphyry-associated alteration is exposed, the Thematic Mapper will allow recognition of the presence of alteration zones. In addition, those mineral occurrences whose paragenesis involves hydrothermal alteration of host and country rocks should also be recognizable. An immediate extension can probably be made to porphyry molybdenum deposits, whose alteration assemblages are quite similar to those of prophyry copper systems. Epithermal deposits with argillic alteration should be detectable given adequate spatial resolution.

Acknowledgments

We would like to thank Sal Anzalone, Jim Gailey, and Cliff Delbert of ASARCO for their help, for allowing us access to the Silver Bell property, and for use of ASARCO maps. Without their willing cooperation, this test site report would not have been possible. Texasgulf made available the services of David Brown who was a major contributor to the writing, data analysis and interpretation, and to the field investigations. Daryl Madura and Ron Alley of JPL worked long and hard to convert meaningless numbers to usable images. Finally, we thank the reviewers, whose critical comments helped improve the final manuscript.

References

Aiken, C. L. V. (1975). *Residual Bouguer gravity anomaly map of Arizona.* University of Arizona, Department of Geosciences. (Scale 1:1,000,000)

Banks, N. G., and R. D. Dockter (1976). Reconnaissance geology map of the Vaca Hills Quadrangle, Arizona. *U.S. Geol. Surv. Map MF-793.*

Blom, R., M. Abrams, and H. Adams (1980). Spectral reflectance and discrimination of plutonic rocks in the 0.45 to 2.45 μm region. *J. Geophys. Res., 85,* 2638–2648.

Blom, R., and C. Elachi (1981). Spaceborne and airborne imaging radar observations of sand dunes. *J. Geophys. Res., 86,* 3061–3073.

Conel, J., M. Abrams, and K. Baird (1980). Uranium: Spectral discrimination of alteration phenomena in sediments. *Mod. Geol., 7,* 115–135.

Conel, J., M. Abrams, and A. Goetz (1978). *A study of alteration associated with uranium occurrences in sandstone and its detection by remote sensing methods* (JPL Publication 78-66). Pasadena, California: Jet Propulsion Laboratory.

Dixon, W. (Ed.) (1974). Multiple regression with case combinations. *Biomedical computer programs.* Los Angeles: University of California Press.

Galey, J. L. (1979). *General geology and hydrothermal alteration of the Silver Bell porphyry copper deposit.* Paper presented to the SEG Field Conference, Tucson area porphyry copper deposits.

Graybeal, F. (1982). Geology of the El Tiro area. In S. Titley (Ed.), *Advances in geology of the porphyry copper deposits.* Tuscon: University of Arizona Press, 487–505.

Hunt, G., and R. Ashley (1979). Spectra of altered rocks in the visible and near infrared. *Econ. Geol., 74,* 1613–1629.

Hunt, G., and J. Salisbury (1970). Visible and near-infrared spectra of minerals and rocks: I. Silicate minerals. *Mod. Geol., 1,* 283–300.

Hunt, G., and J. Salisbury (1971). Visible and near-infrared spectra of minerals and rocks: II. Carbonates. *Mod. Geol., 2,* 23–30.

Hunt, G., J. Salisbury, and C. Lenhoff (1971). Visible and near-infrared spectra of minerals and rocks: III. Oxides and hydroxides. *Mod. Geol., 2,* 195–205.

Jennrich, R. (1977). Stepwise discriminant analysis. In K. Enslein, A. Ralston, and H. Wilf (Eds.), *Statistical methods for digital computers, Volume III of mathematical methods for digital computers.* Wiley-Interscience Publication, 76–95.

Kahle, A., J. Schieldge, M. Abrams, R. Alley, and C. LeVine (1981). *Geologic applications of thermal inertia imaging using HCMM data* (JPL Publication 81-55). Pasadena, California: Jet Propulsion Laboratory.

Kerr, P. F. (1951). Alteration features at Silver Bell, Arizona. *Geol. Soc. America Bull., 62,* 451–480.

Loghry, J. D. (1972). *Characteristics of favorable cappings from several southwestern porphyry copper deposits.* Master's thesis, University of Arizona.

Lowell, J., and D. Guilbert (1970). Lateral and vertical alteration-mineralization zoning in porphyry ore deposits. *Econ. Geol., 65,* 373–408.

McClymonds, N. E. (1959). Paleozoic stratigraphy of the Waterman Mountains, Pima County, Arizona. *Arizona Geol. Society, Southern Arizona Guidebook II,* 67–76.

Merz, J. J. (1967). *The geology of the Union Hill area, Silver Bell District, Pima County, Arizona.* Master's thesis, University of Arizona.

Readdy, L. A. (1978). *Porphyry copper and hydrothermal alteration investigation* (Final Report to U.S. Geological Survey). (Report PB-291205)

Richard, K., and J. H. Courtright (1966). Structure and mineralization at Silver Bell, Arizona. In Titley and Hicks (Eds.), *Geology of the porphyry copper deposits, southwestern North America.* Tucson: University of Arizona Press, 157–163.

Richardson, M. L., and M. L. Miller (1974). *Report and interpretations for the general soil map of Pima County, Arizona.* U.S. Department of Agriculture, Soil Conservation Service Report.

Rogers, R., and K. Peacock (1973). A technique for correcting ERTS data for solar and atmospheric effects. *Symposium on Significant Results of ERTS-1* (NASA SP-327). Washington, D.C.: National Aeronautics and Space Administration, 1115.

Ross, D. (1973). Atmospheric effects in multispectral photographs. *Photogr. E. R., 39,* 377–384.

Rowan, L., P. Wetlaufer, A. Goetz, F. Billingsley, and J. Stewart (1974). Discrimination of rock types and detection of hydrothermally altered areas in south-central Nevada by the use of computer-enhanced ERTS images. *U.S. Geol. Surv. Prof. Pap. 883.*

Sauck, W. A., and J. S. Sumner (1970). *Residual aeromagnetic map of Arizona.* Tucson: University of Arizona Press. (Scale 1:1,000,000)

Siegal, B., and M. Abrams (1975). Geologic mapping using Landsat data. *Photogr. E. R., 42*(3), 325–337.

Slater, P. (1980). *Remote sensing: Optics and optical systems.* Reading, Massachusetts: Addison–Wesley Publishing Co.

Turner, R., W. Malila, R. Nalepka, and F. Thomson (1975). Influence of the atmosphere on remotely sensed data. *Proc. SPIE, 51,* 101, "Scanners and Imagery Systems for Earth Observations."

U.S. Geological Survey (1980). Composite aeromagnetic map of the Papago area, Arizona. *U.S. Geol. Surv. Open File Rep. 80-56.* (Scale 1:250,000)

Watson, B. N. (1964). *Structure and petrology of the eastern portion of the Silver Bell mountains, Pima County, Arizona.* Doctoral dissertation, University of Arizona.

Wilson, E. D., and R. T. Moore (1969). *Geologic map of Arizona*. Arizona Bureau of Mines and U.S. Geological Survey.

Wilson, E. D., R. T. Moore, and R. T. O'Haire (1960). *Geologic map of Pima and Santa Cruz Counties, Arizona*. Arizona Bureau of Mines. (Scale 1:375,000)

Section 5

Helvetia, Arizona, Porphyry Copper Test Site Report

Michael J. Abrams
Jet Propulsion Laboratory

Ray Sadowski
AMAX Exploration, Inc.
Tucson, Arizona

Gary L. Prost
AMOCO Production Co.
Denver, Colorado

Section 5

Helvetia, Arizona, Porphyry Copper Test Site Report

Contents

I. Introduction 5-1
A. Overview 5-1
B. Rationale for Site Selection 5-1
C. Site-Specific Objectives and Problems 5-1
D. Remote Sensing Model 5-2
1. Structural features 5-2
2. Lithological features 5-2
3. Alteration detection 5-2
E. Data Sources 5-3
F. Interpretation Methods 5-3

II. Description of Site 5-4
A. Location 5-4
1. Geographic description 5-4
2. Physiographic description 5-4
B. Geologic History 5-4
1. Stratigraphic evolution 5-4
2. Structural evolution 5-10
3. Emplacement of mineral deposits and alteration 5-15
C. History and Production 5-16

III. Evaluation of Nonimage Remote Sensing Data 5-20
A. PFRS Spectra 5-20
1. Introduction 5-20
2. Spectral measurements 5-20
3. Statistical analysis of PFRS data 5-24
B. M²S Image-Derived Spectra 5-27
1. Introduction 5-27
2. Procedure and spectra 5-27

IV. Evaluation of Photography, Radar, and Landsat Data 5-29
A. Color Aerial Photography 5-29
1. Introduction 5-29
2. Interpretation of photographs 5-29

PRECEDING PAGE BLANK NOT FILMED

B. Radar Data ... 5-34
1. Introduction ... 5-34
2. Aircraft X-band radar data ... 5-34
3. Seasat satellite L-band data ... 5-35
C. Landsat MSS Data ... 5-35
1. Introduction ... 5-35
2. Lineament analysis ... 5-35
3. False-color infrared composite ... 5-46
4. Color ratio composite ... 5-47
5. Principal components analysis ... 5-53
6. Comparison with stream sediment geochemistry ... 5-55

V. Evaluation of Aircraft Multispectral Scanner Data ... 5-57
A. Introduction ... 5-57
B. M^2S 11-Channel Data ... 5-57
1. Ratio composites ... 5-57
2. Thermal infrared data ... 5-60
C. NS-001 Thematic Mapper Simulator Data ... 5-68
1. Introduction ... 5-68
2. Ratio composite ... 5-68
3. Canonical transforms ... 5-68

VI. Summary and Conclusions ... 5-70

Acknowledgments ... 5-75

References ... 5-76

Figures

5-1. Porphyry copper model in carbonate rocks ... 5-2
5-2. General location of the Helvetia test site in southeastern Arizona ... 5-5
5-3. Topographic map of the Helvetia test site showing selected place names ... 5-6
5-4. Soils map of the Helvetia test site ... 5-7
5-5. Geologic map of south–central Arizona ... 5-11
5-6. Sahuarita Quadrangle ... 5-12
5-7. Geologic map of Empire Mountains Quadrangle ... 5-14
5-8. Diagrammatic east–west cross section through Rosemont area ... 5-16
5-9. Tectonic map of the Santa Rita Mountains, with inset enlarged map of Helvetia–Rosemont area ... 5-17
5-10. Summary of the tectonic record of the Santa Rita Mountains ... 5-18
5-11. Alteration map of the Santa Rita Mountains showing major structures and silicified, argillized, and skarn metamorphosed areas ... 5-19
5-12. PFRS sample sites in the Helvetia–Rosemont area ... 5-22
5-13. PFRS reflectance curves of rock types measured in the field: (a) Cretaceous volcanics, iron-oxide altered; (b) quartz monzonite porphyry; (c) Cretaceous arkose; (d) Concha Limestone; (e) limestone conglomerate ... 5-23

5-14. PFRS reflectance curves of rock types measured in the field: (a) Escabrosa Limestone; (b) Bolsa Quartzite; (c) Abrigo Limestone; (d) arkose conglomerate; (e) Cretaceous volcanics 5-25
5-15. Results of linear discriminant function analysis of PFRS data for three limestones 5-27
5-16. Results of linear discriminant function analysis of PFRS data for 10 rock types 5-28
5-17. M^2S image spectra 5-30
5-18. Comparison of field-acquired PFRS reflectance spectra and calibrated M^2S image spectra 5-31
5-19. Mosaic of color aerial photographs of a 5- by 5-km area around Rosemont 5-32
5-20. Interpretative map of Figure 5-19 showing recognizable linear features (faults or shear zones), dikes, and lithologic contacts 5-33
5-21. Drainage map produced by tracing streams and drainages from a color aerial photograph 5-36
5-22. Contour map of drainage density from Figure 5-21 5-37
5-23. X-band aircraft image of the Helvetia–Rosemont area: north–south flight line with illumination to the west 5-38
5-24. Interpretative map of Figure 5-23 showing linear features recognized and mapped faults 5-39
5-25. X-band aircraft image of the Helvetia–Rosemont area: northeast–southwest flight line with illumination to the northwest 5-40
5-26. Interpretative map of Figure 5-25 showing linear features recognized and several topographically expressed elliptical features 5-41
5-27. Seasat orbital L-band radar image including Helvetia–Rosemont area 5-42
5-28. Lineament interpretation of Seasat radar data in Figure 5-27 5-43
5-29. Structural trends in southeastern Arizona derived from analysis of mapped faults 5-44
5-30. Lineament interpretation map produced from October 1975 Landsat scene over southeastern Arizona 5-45
5-31. Rose diagram summarizing strike-frequency distribution of lineaments interpreted from Landsat scene 5-46
5-32. Contour map of lineament density using data from Figure 5-30 5-48
5-33. Simplified residual aeromagnetic map of southeastern Arizona with Titley's (1976) northwest trends superposed 5-49
5-34. False-color infrared composite of Landsat scene 1678-17210 acquired June 1, 1974 5-50
5-35. Geologic map of Arizona covering area of Landsat frame in Figure 5-34 5-51
5-36. Landsat color ratio composite of 40- by 40-km subarea centered near Helvetia 5-52

5-37. Typical spectral reflectance curves for vegetation and iron oxide ... 5-53
5-38. Elliptical scatter pattern of data in two multispectral channels, X_1 and X_2 ... 5-54
5-39. Eigenvector loadings for Landsat PCs (V1, V2, V3, V4) ... 5-54
5-40. PC color composite with geographic features referred to in text ... 5-56
5-41. Ternary plot of PC values for representative Landsat reflectances of limestone (L), vegetation (V), hematitic iron oxide (H), and goethitic iron oxide (G) ... 5-57
5-42. Geologic and alteration interpretation map of PC color image shown in Figure 5-40 ... 5-58
5-43. Stream sediment survey in Santa Rita Mountains showing areas of high copper concentrations ... 5-59
5-44. Flight lines and coverage of aircraft multispectral scanner data over Helvetia test site ... 5-61
5-45. M²S 11-channel color ratio composite of Helvetia–Rosemont area ... 5-62
5-46. Interpretation map of Helvetia M²S ratio image in Figure 5-45 ... 5-63
5-47. Spectral reflectance curves for hematite, goethite, and jarosite ... 5-64
5-48. M²S color ratio composites from August 1977 data ... 5-65
5-49. M²S thermal infrared images ... 5-66
5-50. M²S thermal infrared–albedo color composite ... 5-67
5-51. NS-001 color ratio composite ... 5-69
5-52. Geology/alteration interpretation map of the Helvetia area NS-001 image in Figure 5-51 ... 5-71
5-53. NS-001 Thematic Mapper Simulator data ... 5-73

Tables

5-1. Remote sensing data ... 5-3
5-2. Helvetia test site soils and vegetation ... 5-8
5-3. Rocks of the Santa Rita Mountains, Arizona ... 5-9
5-4. Explanation of symbols of Empire Mountains Quadrangle geologic map ... 5-15
5-5. Gold, silver, copper, lead, and zinc produced in the Helvetia District, 1908–1950 ... 5-21
5-6. Spectral bands of five simulated sensors ... 5-26
5-7. Rock types identified in the M²S image ... 5-28
5-8. M²S DN values and standard deviations ... 5-29
5-9. PFRS and M²S DN values for hematitic arkose ... 5-29
5-10. Deformations of southeastern Arizona ... 5-46
5-11. Reflectance and calculated ratio values for vegetation and iron oxide ... 5-53
5-12. Eigenvalues, variability, and loadings for Helvetia MSS PCA ... 5-54

5-13. Percent reflectances for surface materials 5-57
5-14. PC values for four surface materials 5-57
5-15. Wavelength bands of M²S and NS-001 scanners 5-60

Section 5

Helvetia, Arizona, Porphyry Copper Test Site Report

I. Introduction

A. Overview

The Helvetia test site report is one of three test site studies on the application of remote sensing technology to geologic mapping related to porphyry copper deposits. (A summary of porphyry copper deposit genesis, a remote sensing model, a comparison of results of the three test sites, and applications to other types of deposits can be found in the Porphyry Copper Commodity Report, Section 3.) This report presents the detailed results of a regional and local examination of a porphyry copper deposit located in a structurally complex sedimentary environment. A wide range of imaging systems was used to obtain remote sensing data. These data were computer processed and interpreted for geologic information. Ancillary nonimage data, geophysical data, and geochemical data were used in conjunction with the remote sensing data to aid in understanding the analyses of the image data. The results of this test site report contributed to the Sensor Assessment Report, Section 2, which summarizes the findings from all the test sites relating to the evaluation of the remote sensing technology examined.

B. Rationale for Site Selection

The Helvetia area was selected as one of the three porphyry copper test sites because it contains a wide range of lithologic units and alteration types that have moderate soil and vegetation cover. Local lithologies consist of sedimentary, volcanic, and intrusive members; alteration ranges from weak phyllic alteration of igneous rocks to skarn alteration of carbonate rocks. Skarn alteration is not present or well exposed at the Silver Bell and Safford porphyry copper test sites. The Helvetia site area contains two known copper deposits, Peach-Elgin and Rosemont, which are undisturbed except for drill roads, several historic mine shafts, and small dumps.

Access to the area is good; it is located near major highways from Tucson, and many secondary dirt roads crisscross the test site. The area is controlled by ANAMAX Mining Company, a 50 percent partnership between AMAX and Anaconda. ANAMAX willingly agreed to contribute their data and the cooperation of company geologists for this study.

C. Site-Specific Objectives and Problems

The overall objective of the Helvetia test site study was to evaluate the utility of remote sensing techniques and instruments as mapping tools in a semiarid environment over an area having known copper deposits. The various data sets were evaluated for their usefulness in discriminating different rock types, alteration types, and structural elements associated with the Helvetia area. The major features examined were:

(1) Rock types—Discrimination of various outcropping rock types, including sedimentary rocks (limestone, quartzite, arkose, volcanic sediments, and gravels); intrusive rocks (quartz latite porphyry, granite, and dikes); and volcanic rocks (andesite, pyroclastics, and tuff).

(2) Alteration—Delineation of alteration zones and separation of alteration types into phyllic/argillic, propylitic, skarn, and hematitic.

(3) Structural features—Delineation of complex structural patterns that characterize the area. Features of regional extent may control the loci of mineraliza-

tion, while more local structural elements have produced a complex pattern of disrupted stratigraphic outcrops.

The Helvetia area offers particular problems for this study due to the great diversity of lithologies, alteration types, and structural elements. The geological complexity challenges both the capabilities of the remote sensing technology and the interpreters' skills to derive useful, accurate geologic information.

D. Remote Sensing Model

The remote sensing model is based on some of the features described in the Porphyry Copper Commodity Report, Section 3, and on other features peculiar to a carbonate host-rock environment. Possible observable characteristics consist of various color, tonal, and textural properties associated with structural and lithological features at Helvetia.

1. Structural features. Regional basement structures appear to have a profound influence on the geology and ore emplacement in southeastern Arizona (Heidrick and Titley, 1982). These structures may have surface expressions such as faults, fractures, or lineaments observable on synoptic satellite data like Landsat. Regional geophysical data can provide a basis for correlating features observed on remotely sensed data with geologic and tectonic controls. On a larger scale, Helvetia should show evidence of its complex tectonic and deformational history (see Paragraph II.B for details). Features associated with this activity would include faults, fractures, dikes, and lineaments possibly detectable on moderate- to high-resolution images, such as aerial photographs or aircraft scanner data.

2. Lithological features. The large variety of rock types exposed in the Helvetia area should have spectral and geomorphic differences that would provide a means of separating the main units by analysis of remotely sensed data. Most carbonates, for example, have a strong absorption band near 2.35 μm, which should be detectable with NS-001 Thematic Mapper Simulator data; variations in albedo, iron-oxide content, and other spectral characteristics should permit some separation of the other rock types.

3. Alteration detection. A wide range of alteration types are present at the test site. The presence of quartz monzonitic intrusives provides the necessary thermal and fluid source for hydrothermal fluids associated with porphyry copper deposits. Phyllic/argillic alteration may be detectable as geomorphic anomalies. More likely, however, the presence of clay minerals and iron-oxide minerals can be detected directly by their diagnostic spectral reflectance characteristics. Propylitic alteration may be detectable from its dark tone and pale greenish color, indicating the presence of ferrous-oxide minerals such as chlorite and epidote. Hematitic areas resulting from oxidation of hydrothermal pyrite will be detectable due to the intense 0.85-μm absorption band of hematite and the characteristic brick-red color caused by the strong falloff in reflectance toward the ultraviolet absorption band. A large enough area of hematitic alteration will be discernible on virtually any type of remote sensing data covering the visible and near-infrared region.

Skarn alteration is a result of hydrothermal fluid reactions with carbonate rocks. Generally, an outer marble zone encloses an exoskarn composed of garnet, diopside, and hedenbergite (Figure 5-1). Between this zone and the intrusive lies the endoskarn, composed of biotite, chlorite, anhydrite, and K-feldspar. The ore zones found within both exoskarns and endoskarns contain copper sulfides, pyrite, and magnetite (Enaudi, 1982). These latter minerals weather to produce detectable iron-oxide concentrations when

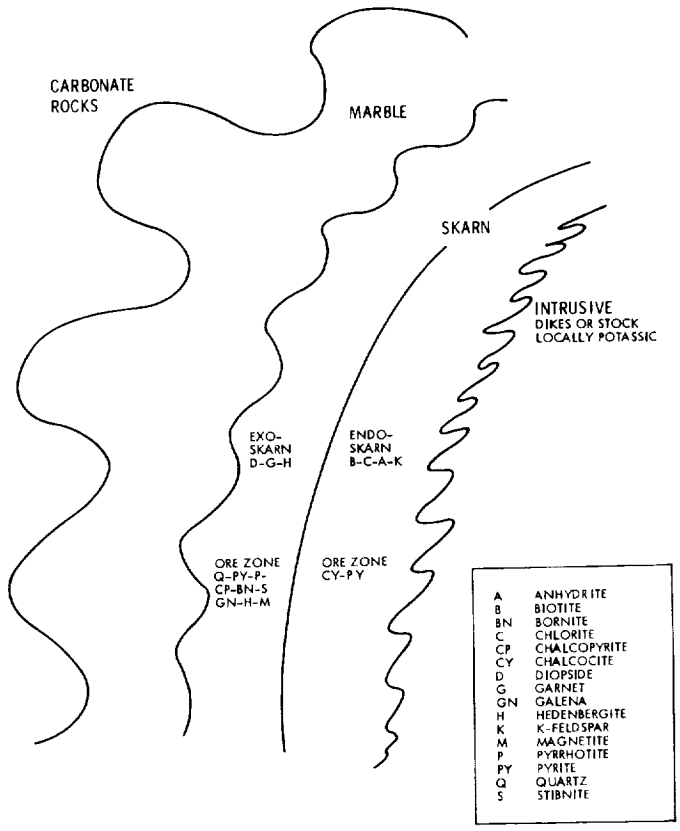

Figure 5-1. Porphyry copper model in carbonate rocks. An intrusive in contact with carbonate rocks develops a skarn zone containing ore minerals and various calc-silicate minerals. The carbonate is metamorphosed to marble (adopted from Lowell and Guilbert, 1970).

exposed at the surface. The development of marble can be detected by its lighter tone or by possible absorption features due to introduced iron or other ionic constituents.

E. Data Sources

The data collected and analyzed for this study included remote sensing data, field spectral reflectance measurements, and ancillary support maps. Remote sensing data analyzed included seasonal Landsat coverage, color aerial photography, Seasat L-band radar data, dual polarization X-band radar data, Modular Multispectral Scanner (M^2S) data, and NS-001 Thematic Mapper Simulator scanner data. The dates of data acquisition, spectral band coverage, and scales at which the data were analyzed are shown in Table 5-1. Data were obtained in digital form on computer-compatible tapes, with the exception of the aerial photographs and radar data, which were obtained as photographic products. Field spectral reflectance measurements were obtained using JPL's Portable Field Reflectance Spectrometer (PFRS) during June 1978. Data were acquired in digital form for further computer processing.

Ancillary support data used in the interpretation of Helvetia remote sensing data included geologic and geophysical information from both published and unpublished sources. Geologic maps included U.S. Geological Survey publications (Creasey and Quick, 1955; Drewes, 1970, 1971a, 1971b, 1971c, 1972a, 1972b, 1973, 1976, 1980; Finnell, 1970) and an unpublished geologic map provided by AMAX Exploration at a scale of 1:24,000. Soils maps of the area were obtained from the U.S. Soil Conservation Service (Richardson et al., 1979). Geologic information on stratigraphy and structure was extracted from Drewes' publications, cited above.

Geophysical support data consisted of two regional maps at a scale of 1:500,000: the Residual Aeromagnetic Map of Arizona (Sauck and Sumner, 1970) and the Residual Bouguer Gravity Anomaly Map of Arizona (Aiken, 1975). Data from a low-level, detailed aeromagnetic survey were provided by AMAX Exploration.

F. Interpretation Methods

Interpretation of the Helvetia data involved an iterative process of laboratory analysis of computer-processed remote sensing data, field checking of the site to substantiate any interpretative conclusions and to determine the cause of any unusual features, and further processing and integration of data in the laboratory.

The processed remote sensing images were interpreted in the laboratory by several analysts who traced boundaries onto transparent mylar overlays. This was done without use of geologic maps to minimize bias during the interpretation. The image data were scaled similarly to support maps, so the overlays could later be placed over the maps for comparison and labeling of interpreted units. When the various geologic overlays did not fit the maps exactly due to residual geometric distortion in the aircraft data, photographic or optical techniques were used to compensate by rotating and shifting the overlays to fit locally. This matching was done using topographic, cultural, and drainage features as control points. The technique of creating transparent interpretative overlays allowed intercomparisons of results between various data sets.

Fieldwork was undertaken at several stages during the project. After preliminary image processing of the aircraft scanner data, *in situ* spectral measurements of distinct geo-

Table 5-1. Remote sensing data

Data Type[a]	Date	Spectral Bands	Resolution, m	Scale	Source
Color aerial photographs	August 19, 1977 May 16, 1978 October 9, 1978	Visible, polychromatic	3	1:24,000	Johnson Space Center (JSC)
Landsat MSS	June 1, 1974 March 25, 1975 October 8, 1975	4 bands between 0.5 and 1.1 μm	80	1:500,000 1:125,000	EROS Data Center
Radar	April 27, 1979	X-band: VV, VH, HH, HV	25	1:62,500	JSC
M^2S scanner	August 19, 1977 May 16, 1978	11 bands: 10 between 0.4 and 1.1 μm, 1 at 8.0 -13.5 μm	18	1:62,500	JSC
NS-001 scanner	October 8, 1978	8 bands: 7 between 0.5 and 2.3 μm, 1 at 10.4–12.5 μm	12	1:62,500	JSC

[a]Refer to the Technical Appendix, Section 14, for a detailed description of the instruments.

logic units were obtained. Analysis of these data aided further processing of the image data. Additional field trips were undertaken to verify the results of the image interpretation and to examine the lithological character of image units. Each trip provided new information and ideas that applied to later image processing and aided in interpretation of the images.

II. Description of Site

A. Location

1. Geographic description. The Helvetia test site is located in southeastern Arizona in Pima County, approximately 50 km southeast of Tucson (Figure 5-2). Access to the eastern part of the area from Tucson is available from Interstate Highway 10 east, Arizona Highway 83 south, and graded dirt roads. The western part of the area is reached via Interstate Highway 89 south from Tucson, then paved and dirt roads to the site.

The area studied in detail covers approximately 800 km^2 and is bounded by a rectangle with vertices at lat. 32°05′ N, long. 110°45′ W; lat. 31°55′ N, long. 110°35′ W; lat. 31°45′ N, long. 110°55′ W; and lat. 31°40′ N, long. 110°45′ W (Figure 5-2).

Several mining districts are in the area. These are the Helvetia District, the Rosemont District, the Greaterville District, and the Sycamore Canyon District. At the present time, mining activities are not being conducted in the area, although exploration efforts by several mining companies continue.

2. Physiographic description

a. Topographic relief. The test site is located in the Basin and Range Province. Two mountain ranges are included in the area: the Empire Mountains and the northern part of the Santa Rita Mountains. Alluvial slopes and valleys surround the mountains. Relief is rugged in the ranges and gentle in the foothills and intermountain valleys. A maximum elevation of 2045 m (6650 ft) occurs in the southern part of the area; alluvial slopes on the west side descend to an elevation of 1200 m (4000 ft) (Figure 5-3).

b. Climate. The climate of the area is semiarid, typical of that of a steppe; average annual precipitation is about 50 cm. About one-half of the annual precipitation falls during thundershowers in July and August. Winter precipitation usually lasts for several days; snowfall is rare, although at higher elevations, accumulations of several centimeters are not uncommon. Temperatures range from occasional summer highs in excess of 40° C to winter lows of −5° C. The average daily high and low are 25° C and 10° C.

c. Soil and vegetation cover. Soil distribution and composition and associated vegetation cover types are presented in the soils map (Figure 5-4) and Table 5-2 (Richardson et al., 1979).

d. Land use. The test site is located in the Coronado National Forest. The land is used primarily for grazing purposes, supporting a moderate cattle population. Camping and four-wheel-drive vehicle usage is permitted in the area. Agriculture or farming is not practiced in the area. In past years, mining activities provided a major input to the area's economic base; however, active mining is not being conducted presently.

B. Geologic History

1. Stratigraphic evolution. The oldest known rocks in the area are regionally metamorphosed Precambrian rocks conventionally assigned to the Pinal Schist (Table 5-3; also see Figures 5-5, 5-6, 5-7, Table 5-4, and Figure 5-8). In most nearby areas, this formation is a muscovite–chlorite or muscovite–biotite schist, but locally it consists largely of biotite gneiss and granite gneiss and only a small amount of schist. These rocks were deformed, metamorphosed, and intruded, either during one geologic event or separately in the given sequence, by a large pluton of Continental Granodiorite. The rocks were uplifted and deeply eroded before the deposition of a sequence of Paleozoic rocks.

The Paleozoic rocks of the Santa Rita Mountains are believed to have lain unconformably on the Precambrian crystalline rocks, although they are now invariably faulted upon them. The Paleozoic rocks form a concordant marine sequence that begins with the Bolsa Quartzite of Middle Cambrian age, contains several disconformities, and ends with the Rainvalley Formation of late Early Permian or slightly younger age. Nearby areas have no Permian rocks younger than the Rainvalley Formation. This marine sequence was deposited in a shallow continental sea. Its internal disconformities mark a succession of epeirogenic fluctuations of an otherwise tectonically stable region.

Moderate tectonic activity marked the interval between the deposition of Permian rocks and the onset of the Laramide orogeny in mid-Cretaceous time. Toward the end of the Permian time, the region was uplifted and the sea retreated; in Early Triassic time, the area now occupied by the Santa Rita Mountains was faulted, the uplifted block was deeply eroded, and a thick pile of volcanic and sedi-

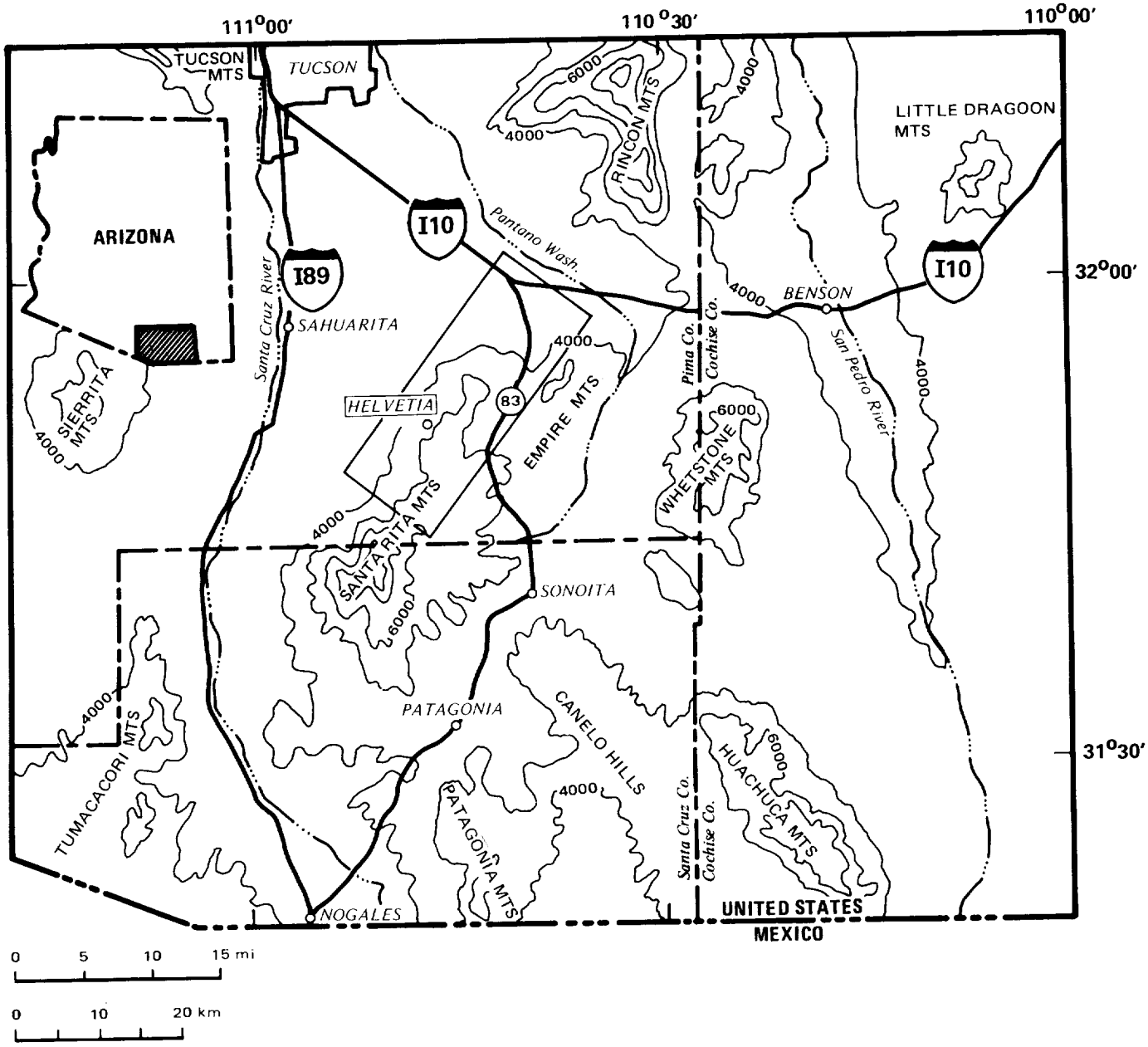

Figure 5-2. General location of the Helvetia test site in southeastern Arizona. The small test site is outlined. Contours are in feet; contour interval is 1000 ft.

mentary rocks of the Mount Wrightson and Gardner Canyon Formations was deposited in a fault-block basin. Near the end of Triassic time, a stock of the Piper Gulch Monzonite was intruded, perhaps along an old fault zone, forming the Santa Rita fault scar. During the Jurassic Period, a large stock or small batholith of granite intruded the southern part of the area. Faulting and erosion followed and, during Early Cretaceous time, the Temporal Formation, Bathtub Formation, and Bisbee Group were deposited in a continental environment. Both the local relief and tectonic activity decreased during this interval and, before its close, a shallow sea briefly encroached upon the area for the last time.

The initial impulse of the Laramide orogeny occurred during mid-Cretaceous time, when the Upper Cretaceous Fort Crittenden Formation was deposited unconformably upon the Lower Cretaceous Bisbee. The deposition of coarse clastic rocks and resumption of volcanism mark the upper part of Fort Crittenden, and widespread volcanism is

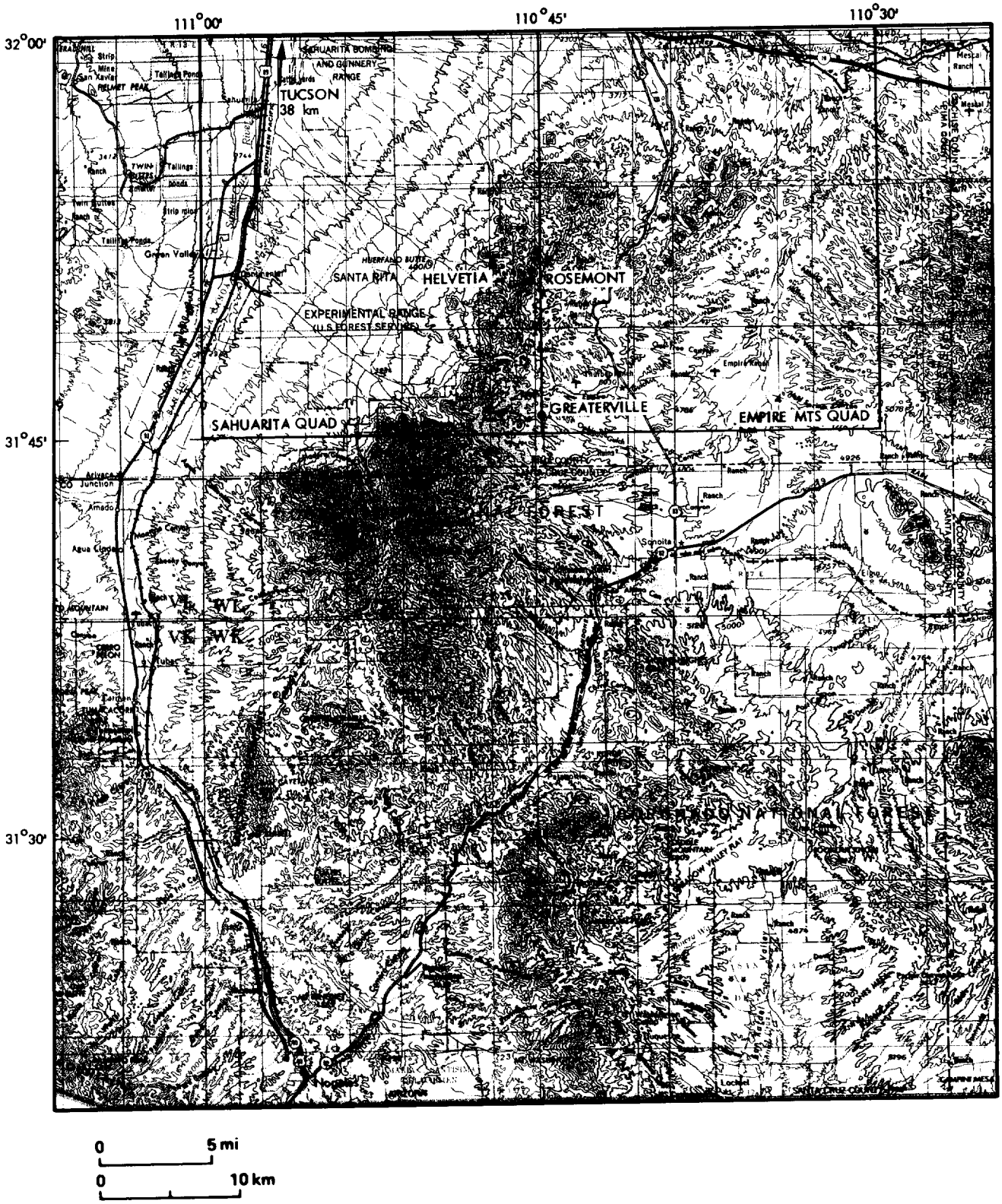

Figure 5-3. Topographic map of the Helvetia test site showing selected place names referred to in this section. Contours and elevations are in feet.

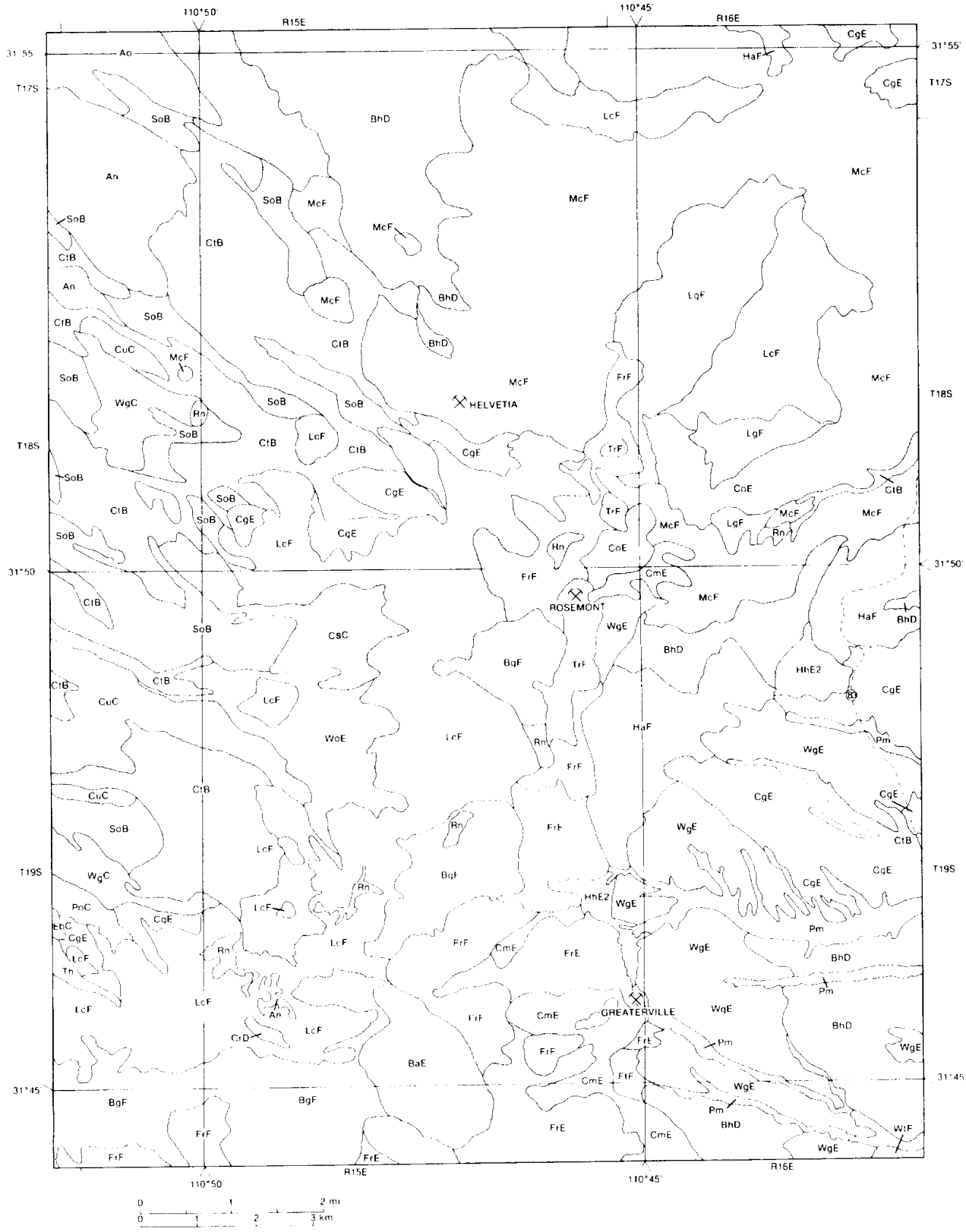

Figure 5-4. Soils map of the Helvetia test site. Key to the units is found in Table 5-2 (Richardson et al., 1979).

Table 5-2. Helvetia test site soils and vegetation

Symbol	Name	Composition	Slope, %	Elevation, m	Vegetation
An	Anthony	Gravelly, sandy loam	0–5	890–1170	Mesquite, paloverde, burroweed, three-awns, bush muhly, cacti
Ao	Anthony	Gravelly loam	1–5	890–1170	Mesquite, paloverde, burroweed, three-awns, bush muhly, cacti
BaE	Barkerville–Gaddes	Cobbly loam	10–30	1540–2300	Oak, piñon, juniper, manzanita, grama grasses
BgF	Barkerville–Gaddes	Gravelly, granitic	10–30	1540–2300	Oak, piñon, juniper, manzanita, grama grasses
BhD	Bernardino–Hathaway	Gravelly, clay loam	2–30	1230–1600	Mesquite, grama, cane beard grass
CgE	Caralampi	Gravelly, sandy loam	10–40	920–1540	Grama, mesquite, mimosa
CmE	Casto	Gravelly, sandy loam	10–40	1540–2000	Oak, juniper, manzanita, grama
CoE	Chiricahua	Cobbly, sandy loam	10–45	920–1660	Grama, mesquite, catclaw, mimosa, ocotillo, agave, cacti
CrD	Chiricahua–Lampshire	Cobbly, sandy loam	5–35	920–1660	Grama, mesquite, catclaw, mimosa, ocotillo, agave, cacti
CsC	Comoro	Sandy loam	5–10	920–1540	Oak-savannah
CtB	Comoro	Sandy loam	0–5	920–1540	Desert shrubs
FrE	Faraway–Rock	Cobbly, sandy loam	10–30	1540–2310	Oak, juniper, piñon, manzanita, grama, bluestem
FrF	Faraway–Rock	Cobbly, sandy loam	30–60	1540–2310	Oak, juniper, piñon, manzanita, grama, bluestem
Ge	Grabe	Loam	0–3	920–1660	Desert shrubs, grasses
HaF	Hathaway	Gravelly, sandy loam	20–50	1100–1660	Black side oats, grama, three-awns, mesquite, yucca
HhE2	Hathaway	Gravelly, sandy loam	1–40	1100–1660	Black side oats, grama, three-awns, mesquite, yucca
LcF	Lampshire–Chiricahua	Cobbly loam	15–50	1050–1660	Grama, bluestem, ocotillo, mesquite, mimosa, oak, juniper
LgF	Lampshire–Graham	Cobbly loam	20–60		Grama, bluestem, ocotillo, mesquite, mimosa, oak, juniper
McF	Mabray–Chiricahua	Gravelly loam	8–45	920–1690	Ocotillo, whitethorn, sotol, catclaw, grama, tridens
Pm	Pima	Clay loam	0–3	920–1540	Grass, shrubs
PoC	Pinaleno	Gravelly, sandy loam	0–10	920–1230	Mesquite, grama, three-awns, burroweed, cacti
Rn	Rock	Outcrop	15–60	1230–2580	Oak, juniper, manzanita, mimosa, grasses
SoB	Sonoita	Gravelly, sandy loam	1–8	1170–1540	Mesquite, burroweed, three-awns, grama
Th	Torriflurents	Sandy, clay loam	1–5	920–1840	Desert shrub, grasses
TrF	Tortugas–Rock	Cobbly loam	25–60	1480–2150	Cliff rose, sumac, ocotillo, grama, mesquite, oak, juniper
WgC	White House	Gravelly loam	0–10	1015–1660	Grama, mesquite, three-awns, oak
WgE	White House	Gravelly loam	10–35	1015–1660	Grama, mesquite, three-awns, oak
WtF	White House–Hathaway	Gravelly loam	5–45	1015–1660	Grama, mesquite, three-awns, oak

recorded in the succeeding Salero Formation. During this time, the Corona stock was emplaced in the northern part of what is now the Santa Rita Mountains. Major northeastward-directed thrust faulting marked the tectonic climax of the Piman phase of the Laramide orogeny during the time of deposition of the Salero Formation (probably Campanian time). The Piman phase culminated a few million years later with a series of multiple intrusions of rocks known as the Josephine Canyon Diorite, Madera Canyon Granodiorite, and Elephant Head Quartz Monzonite.

During Early Paleocene time, about 63 to 58 million years (m.y.) ago, the area was tectonically quiet. The Josephine Canyon stock, a large epizonal body, was partly exposed by erosion, and the volcanic and sedimentary rocks of the Gringo Gulch Volcanics were deposited. The Gringo Gulch pluton and other small bodies were probably emplaced during that time.

In Late Paleocene time, tectonic and volcanic activities were renewed in the northern part of the area to record the Helvetian phase of the Laramide orogeny. Minor northwestward-directed thrust faulting was penecontemporaneous with the emplacement of a group of small stocks named the "Helvetia stocks." Quartz latite porphyry intrusives that are locally referred to as "ore porphyry" because of their association with mineralization were intruded at the close of the Helvetian phase of the Laramide orogeny.

Between the Paleocene and Oligocene times, the local geologic record is fragmentary. Mineralized quartz veins were emplaced in the southern part of the area, and some rhyolitic volcanic rocks and andesitic intrusive rocks were emplaced in the northern part. The area was strongly eroded and possibly block faulted to form the ancestral Santa Rita Mountains.

During the Late Tertiary and Quaternary times, the area was block faulted several times, and gravel of several formations filled the basins next to the raised and gently southeastward-tilted Santa Rita Mountains. The latest magmatic activity is recorded by basalt flows, of Miocene or Pliocene age, that are intercalated in the oldest unit of

Table 5-3. Rocks of the Santa Rita Mountains, Arizona

Age	Groups, Formations, and Members		Description	Estimated Thickness, ft
Holocene	Youngest gravel and low-level terrace deposits		Gravel and intercalated sand; infantile gray soil on low-level terrace gravel	0 – 300 ±
Pleistocene: Late Pleistocene	Intermediate-level pediment and terrace deposit		Gravel and sand; capped by weakly developed red soil	0 – 400 ±
Pleistocene: Middle Pleistocene	High-level pediment deposits		Gravel and sand; capped by well-developed red soil	0 – 50 ±
Pleistocene and Pliocene	Basin-fill gravel		Gravel, sand, and silt, commonly pinkish-gray and slightly indurated; locally includes tuffaceous beds	0 – 2,000 ±
Pliocene and Miocene (?)	Gravel of Nogales		Gravel, sand, and silt; rich in volcanic clasts; commonly pale red, poorly sorted, and slightly indurated	0 – 1,000 ±
Late (?) Oligocene	Rhyolite intrusives of the northern Santa Rita Mountains		Rhyolite porphyry of a plug and of the Gardner Canyon and Box Canyon dike swarms	
	Dikes and stock of the San Cayetano Mountains		Rhyodacite porphyry dike swarm and medium-coarse-grained light-gray granodiorite	
	Igneous complex of the southern Santa Rita Mountains	Dikes and laccoliths in the Grosvenor Hills area	Rhyodacite vitrophyre, medium-gray to light-gray	
		Grosvenor Hills Volcanics: Rhyodacite member	Rhyodacite lava flows, agglomerate, tuff, and welded tuff	150 – 2,200
		Grosvenor Hills Volcanics: Rhyolite member	Rhyolite tuff; a little welded tuff and lava	500 +
		Grosvenor Hills Volcanics: Gravel and silt member	Gravel and silt; a little limestone and shale	0 – 200
Oligocene to Paleocene	Quartz vein swarm		Mineralized quartz veins of the southern Santa Rita Mountains	
	Rhyolitic volcanics		Rhyolitic tuff and lava of Wasp Canyon	
	Olivine andesite plugs		Vesicular and amygdaloidal plugs at Deering Spring	
	Andesite dikes and sills		Small andesite intrusives; include some dacite and diorite intrusives	
Paleocene	Greaterville intrusives		Quartz latite porphyry dikes and plugs, light-gray to grayish-orange-pink; contains stubby bipyramidal quartz phenocrysts; associated with mineralization	
	Helvetia stocks		Granodiorite to quartz monzonite stocks and a quartz diorite stock, medium coarse grained	
	Cottonwood Canyon dike swarm		Quartz latite porphyry, finely porphyritic to coarsely porphyritic	
	Gringo Gulch plugs		Hornblende dacite porphyry; partly very coarsely porphyritic; microgranodiorite in core of one plug	
	Volcanics of Red Mountain		Rhyolitic and andesitic pyroclastic rocks, intensely altered	
Paleocene (?)	Gringo Gulch Volcanics	Upper member	Rhyolitic to dacitic tuff, sandstone, and a capping andesite lava	900 +
		Lower member	Rhyolitic and dacitic pyroclastic rocks and some flows; contains intercalated epiclastic rocks	700 +
	Elephant Head Quartz Monzonite		Stocks of coarse-grained quartz monzonite and an aplitic phase	
	Madera Canyon Granodiorite		Stock of coarse-grained hornblende granodiorite, and porphyritic and leucocratic phases	
	Josephine Canyon Diorite		Large stock of fine-grained diorite and quartz diorite and a late quartz monzonite phase	
Late Cretaceous	Salero Formation	Upper member	Sedimentary and volcanic rocks	3,500 ±
		Arkose member	Arkose and conglomerate; largely facies of welded tuff member	500 ±
		Welded tuff member	Rhyodacite welded tuff	1,200 ±
		Exotic block member	Dacitic volcanics containing large exotic blocks	1,000 ±
		Lower member	Dacitic volcanics	400 ±
	Fort Crittenden Formation	Upper red conglomerate member	Volcanic conglomerate; some sandstone and siltstone	1,400 +
		Rhyolitic tuff member	Tuff, in part intercalated in upper red conglomerate member	0 – 650
		Brown conglomerate member	Arkosic conglomerate; some sandstone and siltstone	2,000 +
		Lower red conglomerate member	Volcanic conglomerate; some sandstone and siltstone	800 – 1,200
		Shale member	Fossiliferous gray shale; some sandstone and conglomerate	4,550 +
	Bisbee Group	Turney Ranch Formation	Sandstone and red siltstone	1,500 +
		Shellenberger Canyon Formation	Siltstone and arkose	1,600 +
		Apache Canyon Formation	Arkose and siltstone; some limestone lenses	1,500 – 2,000
		Willow Canyon Formation	Arkose and conglomerate	2,200 +
		Glance Conglomerate	Limestone- and granite-cobble conglomerate	0 – 1,500 +
Early Cretaceous	Bathtub Formation	Upper member	Dacitic volcanics and tuffaceous sandstone	0 – 1,500 +
		Middle member	Rhyolitic to andesitic volcanics	800 – 1,500
		Lower member	Conglomerate and volcanic sandstone	700 ±

Table 5-3 (Continued)

Age	Groups, Formations, and Members		Description	Estimated Thickness, ft
	Temporal Formation	Upper member	Conglomerate and rhyolitic volcanics	600 – 1,000
		Middle member	Rhyolitic to latitic volcanics and conglomerate	100 – 400
		Lower member	Rhyolitic to dacitic volcanics and fanglomerate	200 – 1,300
Jurassic	Squaw Gulch Granite		Large stock of coarse-grained pink rock ranging in composition from granite to quartz monzonite	
Early Jurassic and Late Triassic	Canelo Hills Volcanics		Arkosic sandstone and conglomerate, tuff and tuffaceous sandstone, and quartzite	600 +
	Piper Gulch Monzonite		Stock of very coarse-grained dark-gray rock ranging in composition from monzonite to quartz monzonite	
Triassic	Gardner Canyon Formation	Upper member	Red mudstone, dacitic volcanics, and conglomerate	1,800 +
		Lower member	Red siltstone and chert-pebble conglomerate	200
	Mount Wrightson Formation	Upper member	Eolian sandstone and andesitic to rhyodacitic volcanics	2,000 +
		Middle member	Rhyolitic to latitic volcanics; some sandstone and conglomerate	5,000 ±
		Lower member	Dacitic to andesitic volcanics and sandstone	1,500 +
		Rainvalley Formation	Limestone and dolomite; a little sandstone	0 – 300
		Concha Limestone	Limestone, thick-bedded, cherty, dark-gray	400 – 575
	Scherrer Formation	Upper quartzite member	Quartzite, pale reddish-gray, fine-grained	140 ±
		Middle dolomite member	Dolomite, light- to medium-gray	120 ±
		Lower quartzite and basal siltstone members	Quartzite, pale yellowish-gray, fine-grained; basal reddish-gray siltstone	460 ±
Early Permian	Naco Group	Upper member	Limestone, moderately thick bedded, medium-gray, slightly cherty	380 +
	Epitaph Dolomite	Lower member	Mainly light brownish-gray marlstone and dolomitic siltstone; locally contains some argillite and gypsum; basal 180 ft contains intercalated dark- to medium-gray medium-thick-bedded dolomite	620 ±
		Colina Limestone	Limestone, dark-gray, medium-thick-bedded	350 ±
Early Permian and Late Pennsylvanian		Earp Formation	Siltstone and shale, reddish-gray; contains some sandstone and chert-pebble conglomerate	800 ±
Late and Middle Pennsylvanian		Horquilla Limestone	Limestone, fine-grained, thin-bedded to moderately thick bedded, medium- to light-gray; contains siltstone beds in upper half and two thin conglomerate beds near base	1,000 ±
Mississippian		Escabrosa Limestone	Limestone, coarse-grained, thick-bedded, cherty, medium-gray, crinoidal	560 ±
Devonian		Martin Formation	Brown dolomite, gray limestone, siltstone; some sandstone	400 ±
Late and Middle Cambrian		Abrigo Formation	Shale, quartzitic sandstone, and thin-bedded limstone	740 – 900
Middle Cambrian		Bolsa Quartzite	Quartzite, coarse-grained, thick-bedded, light- to brownish-gray and purplish-gray; thin basal conglomerate	460 ±
Precambrian		Continental Granodiorite	Granodiorite porphyry and quartz monzonite porphyry; contains aplite and fine-grained quartz monzonite intrusives	
		Pinal Schist	Hornblende gneiss, granite gneiss, and schist	

Broken lines indicate that the adjacent formations are contemporaneous or that their relations are uncertain.

gravel along the Santa Cruz River a few kilometers southwest of the Mount Wrightson Quadrangle.

2. Structural evolution. The rocks of the Santa Rita Mountains are abundantly faulted and less commonly folded. Most faults are complex high-angle structures consisting of many normal faults and some reverse and tear faults. Other faults are low-angle structures, which are mainly thrust faults but which include some faults whose genetic environment is unknown. A few thrust faults are steeply inclined because of tilting or local irregularities along the fault plane. Most folds are small open flexures or drag folds, but a few are nearly isoclinal and have large amplitudes.

The Santa Rita Mountains consist of three major structural units whose internal characteristics vary from unit to unit and whose boundaries are marked by major fault zones. The units are referred to here as the southwestern, central, and northeastern units (Figure 5-9). The rocks in the southwestern unit are typically inclined gently to the south and are cut by many normal faults. The rocks in the central unit are inclined moderately to the east and are cut by only a few faults, but they are folded in places. The rocks of the northeastern unit are also commonly inclined moderately to the east, but they are cut by many thrust and tear faults and are folded in many places. Because of differences in their structural position and magmatic history, the three units, at times, developed rock sequences independently of each other.

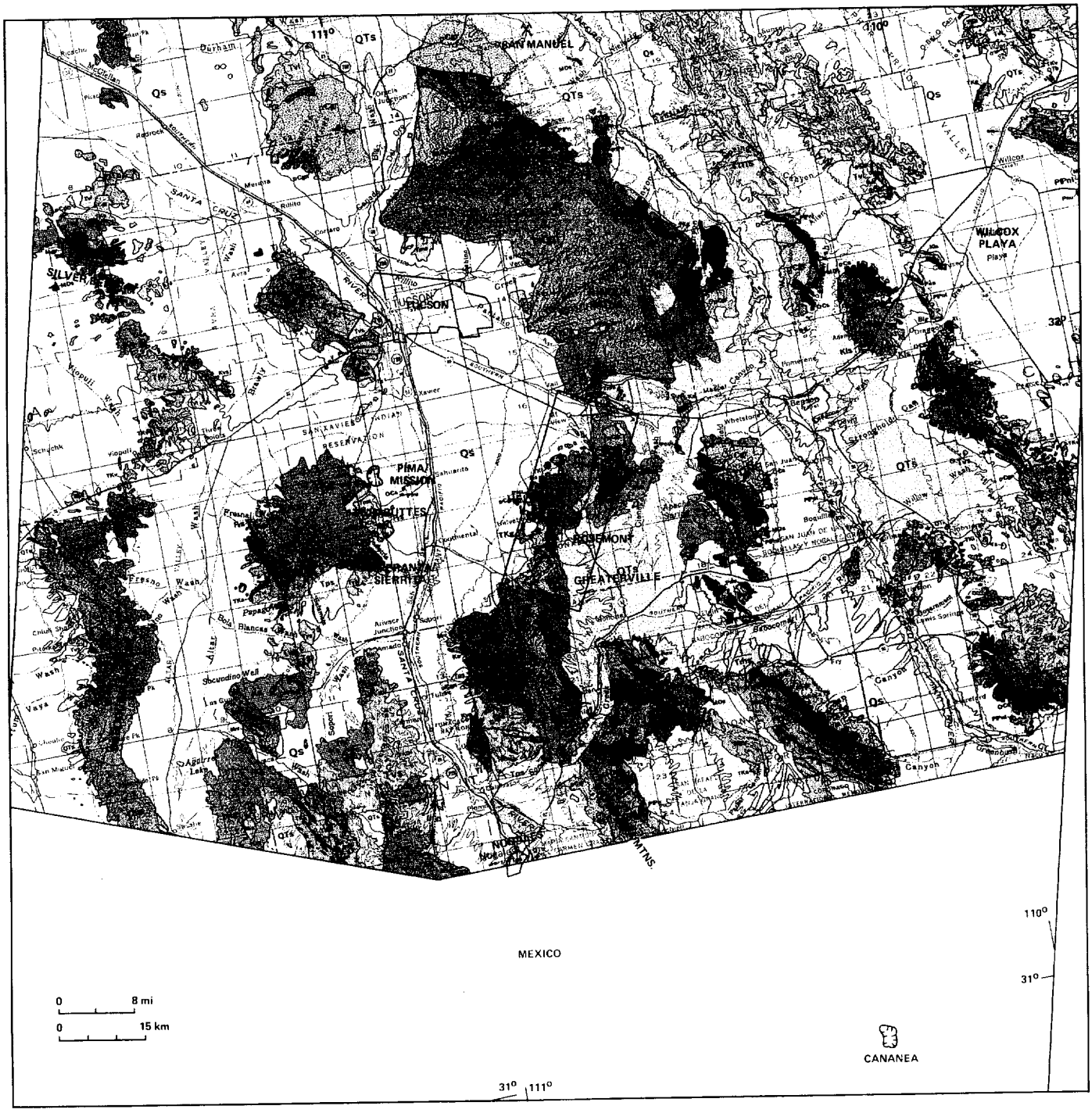

Figure 5-5. Geologic map of south–central Arizona (Wilson et al., 1969). Outline of small test site is shown.

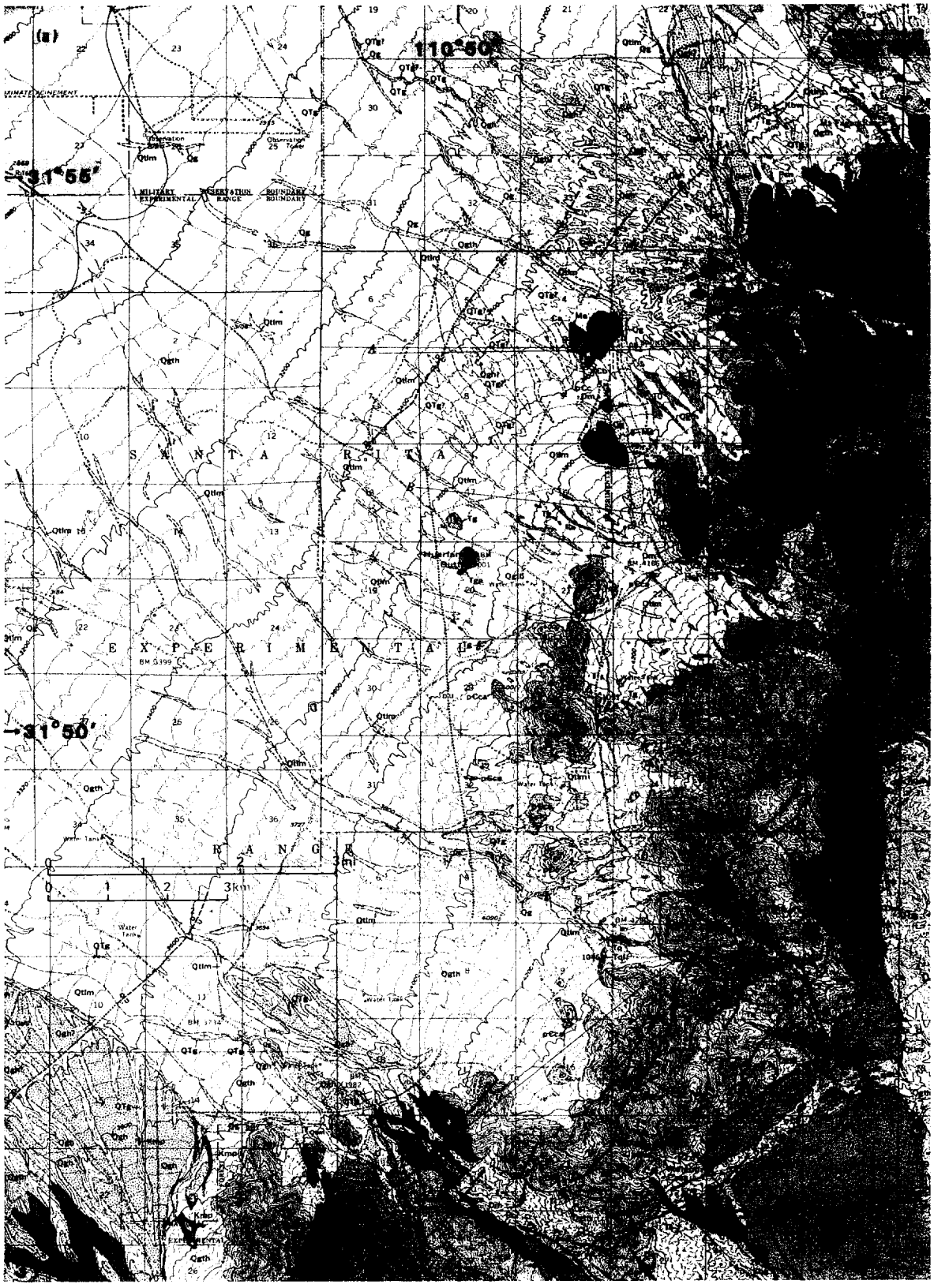
(a)
110°50'
31°55'
31°50'
SANTA RITA
EXPERIMENTAL
RANGE
0 1 2 3km
0 1 2 3mi

(b)

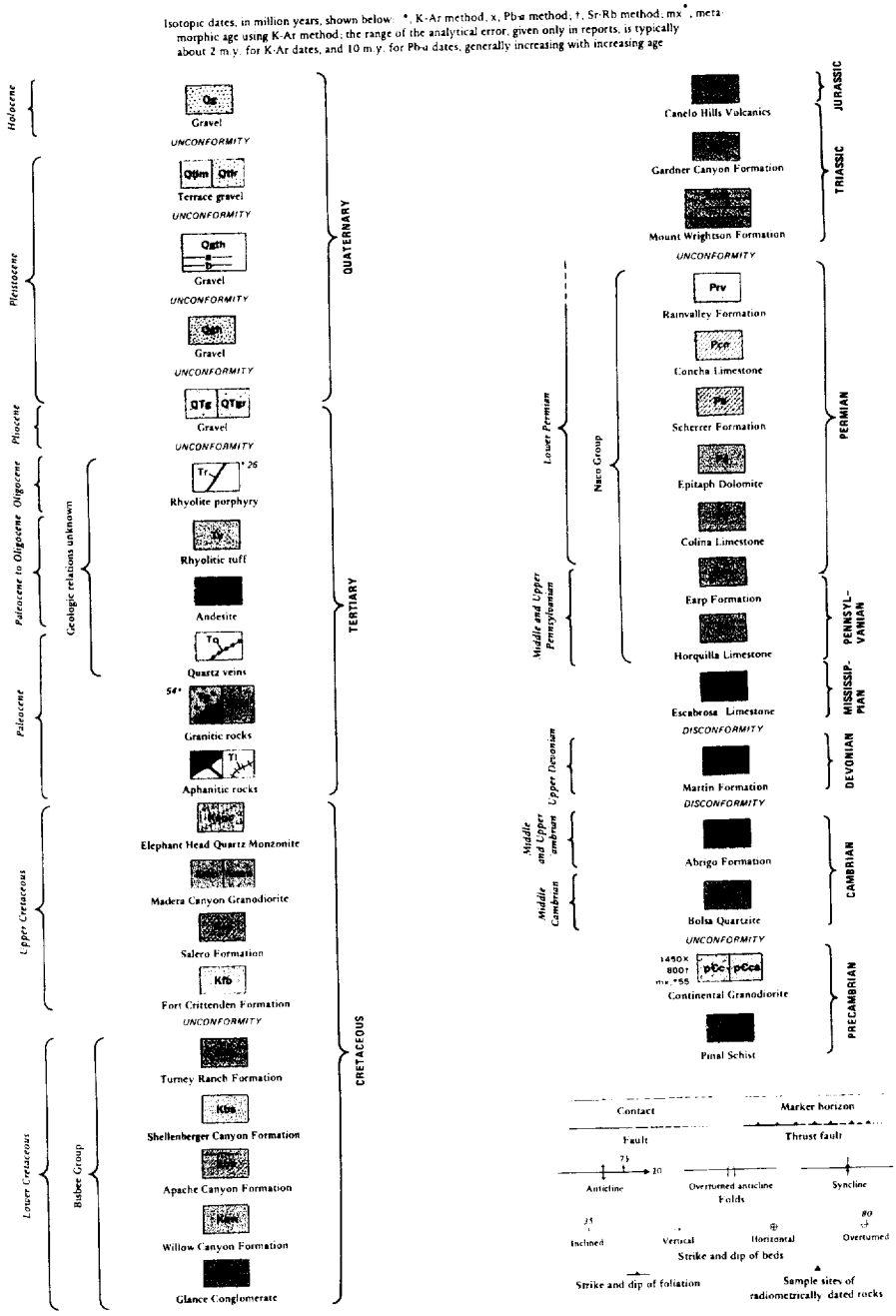

Figure 5-6. Sahuarita Quadrangle: (a) geologic map (Drewes, 1971b); (b) explanation for geologic map

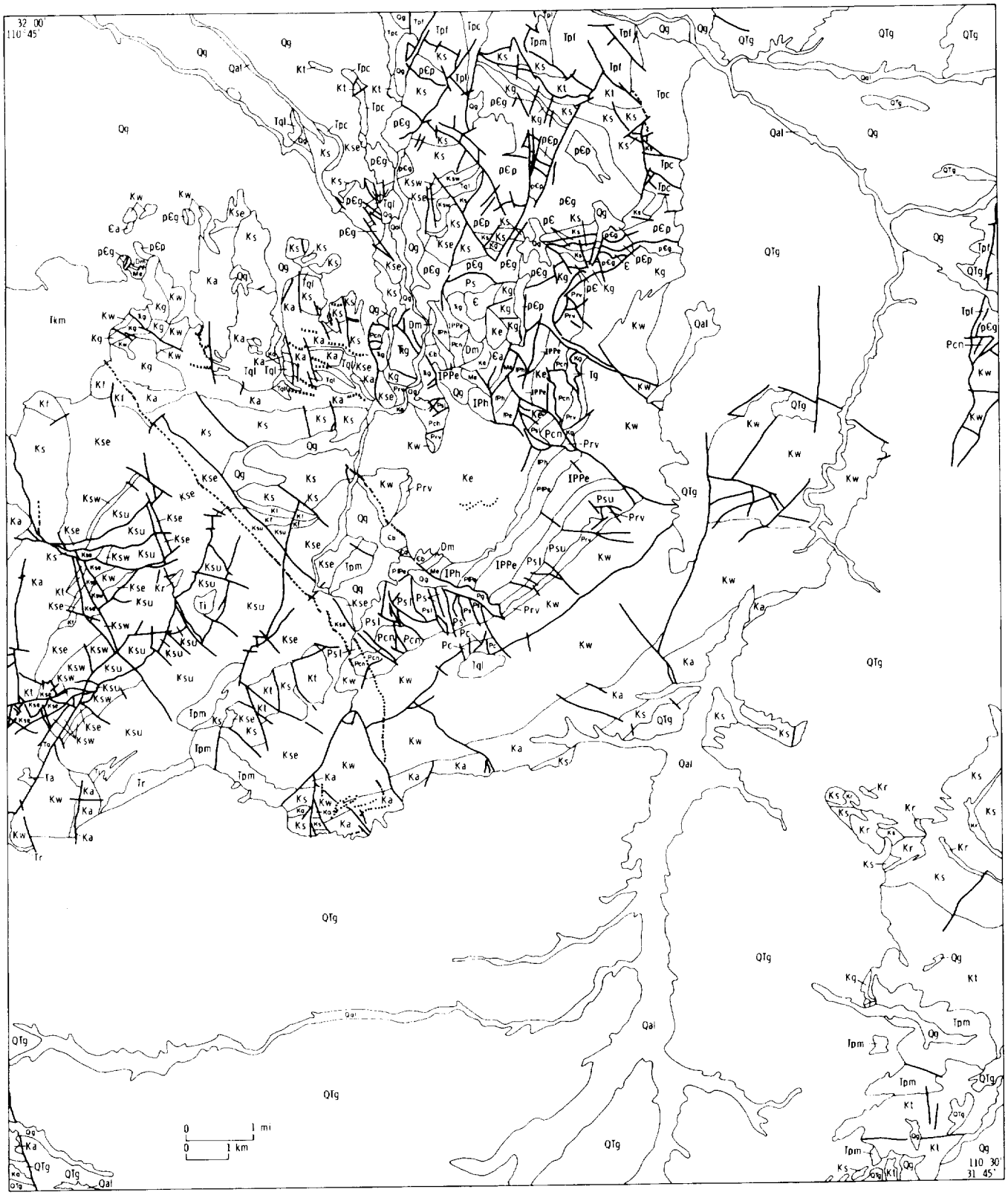

Figure 5-7. Geologic map of Empire Mountains Quadrangle (Finnell, 1970). Explanation of symbols is in Table 5-4.

Table 5-4. Explanation of symbols of Empire Mountains Quadrangle geologic map

Symbol	Age	Unit
Qal	Pleistocene–Holocene	Alluvium
Qg	Pleistocene–Holocene	Pediment, fan gravels
QTg	Pleistocene	Gravel and basin fill
Tp	Oligocene–Miocene	Pantano Formation
Tpc		Claystone unit
Tpa		Andesite flow
Tpf		Conglomerate
Tpl		Limestone–sandstone
Tpm		Mudflow
Tr	Tertiary	Rhyolitic tuff
Ti	Tertiary	Rhyolitic plugs
Ta	Tertiary	Andesite
Tql	Paleocene	Quartz latite porphyry
Tkm	Paleocene–Cretaceous	Quartz monzonite
Kg	U. Cretaceous	Quartz diorite
Ke		Quartz monzonite of Empire Mountains
Ks		Salero Formation
Ksu		Conglomerate, breccia
Ksw		Rhyodacitic tuff
Kse		Andesitic flow
Kr		Rhyodacitic sills, dikes
Kf	U. Cretaceous	Fort Crittenden Formation (conglomerate)
Kt	L. Cretaceous	Turney Ranch Formation (mudstone)
Ks		Shellenberger Canyon Formation (mudstone)
Ka		Apache Canyon Formation (limestone–shale)
Kw		Willow Canyon Formation (sandstone)
Kg	L. Cretaceous	Glance Conglomerate
Tg	Triassic	Gardner Canyon (mudstone)
Prv	Permian	Rainvalley Formation (limestone)
Pcn		Concha Limestone
Ps		Scherrer Formation
Psu		Calcareous sandstone
Psl	Permian	Calcareous sandstone
IPPe	Pennsylvanian-Permian	Earp Formation (siltstone)
IPh	Pennsylvanian	Horquilla Limestone
Me	Mississippi	Escabrosa Limestone
Dm	Devonian	Martin Formation (dolomite)
€	Cambrian	Undifferentiated
€a	Cambrian	Abrigo Limestone
€b	Cambrian	Bolsa Quartzite
p€	Precambrian	Undifferentiated
p€g	Precambrian	Granitoid igneous rocks
p€p	Precambrian	Pinal Schist

The major fault zones separating the three structural units are belts along which rocks are more abundantly and complexly deformed than the rocks within the units themselves. The Santa Rita fault zone and fault scar separate the southwestern and central structural units, and the Sawmill Canyon fault zone separates the central and northeastern units. These fault zones are identifiable in the mountains southeast of the Santa Rita Mountains, and they may be recognizable to the northwest as well.

The tectonic development of the area (Figure 5-10) is similar to that of the surrounding region, and only the local record of the development during the Mesozoic time is more complete than the regional record. The most ancient rocks—the Pinal Schist and Continental Granodiorite—show Mazatzal revolution effects which are typical of central Arizona. Alternating upward and downward, epeirogenic movements throughout the Paleozoic Era are recorded by a marine sequence whose continuity is interrupted by several disconformities. Strong vertical movements, largely on faults, occurred at intervals from the Triassic to the Early Cretaceous times; two stocks were injected into the rocks of the area at about the end of the Triassic and during Middle Jurassic times.

During the Laramide orogeny, which lasted from about 90 to 53 m.y. ago, the area was severely deformed. The orogeny apparently took place in two phases, an early (Piman) phase and a late (Helvetian) phase, which were separated by a period of tectonic quiescence 10 to 20 m.y. in duration. The Piman phase began with folding in the early Late Cretaceous time and culminated with northeast-directed thrust faulting of what was probably a single, relatively thin plate mainly composed of bedded rocks. Abundant subsidiary tear faults and folds deformed the plate during the Piman phase, and some favorably oriented segments of older faults were reactivated. The Piman phase ended with the emplacement of several large stocks in the late Late Cretaceous time. The Helvetian phase of Late Paleocene age comprised northwest-directed thrust and tear faulting and emplacement of small stocks. At the close of the Helvetian phase, plugs and dikes of quartz latite porphyry intruded the faults, and mineralizing fluids associated with these intrusive rocks spread along the faults.

In post-Laramide time, the area was deformed largely by normal faults. Many of these faults were associated with Late (?) Oligocene volcanism; others were related to intrusion of several dike and vein swarms into east- to northeast-trending tension fractures. During the Late Tertiary time, the area was tilted gently southeast on a range-front fault, along which the youngest movement was Late Pleistocene (Drewes, 1972b).

3. Emplacement of mineral deposits and alteration. Many areas of the Santa Rita Mountains that lie adjacent to

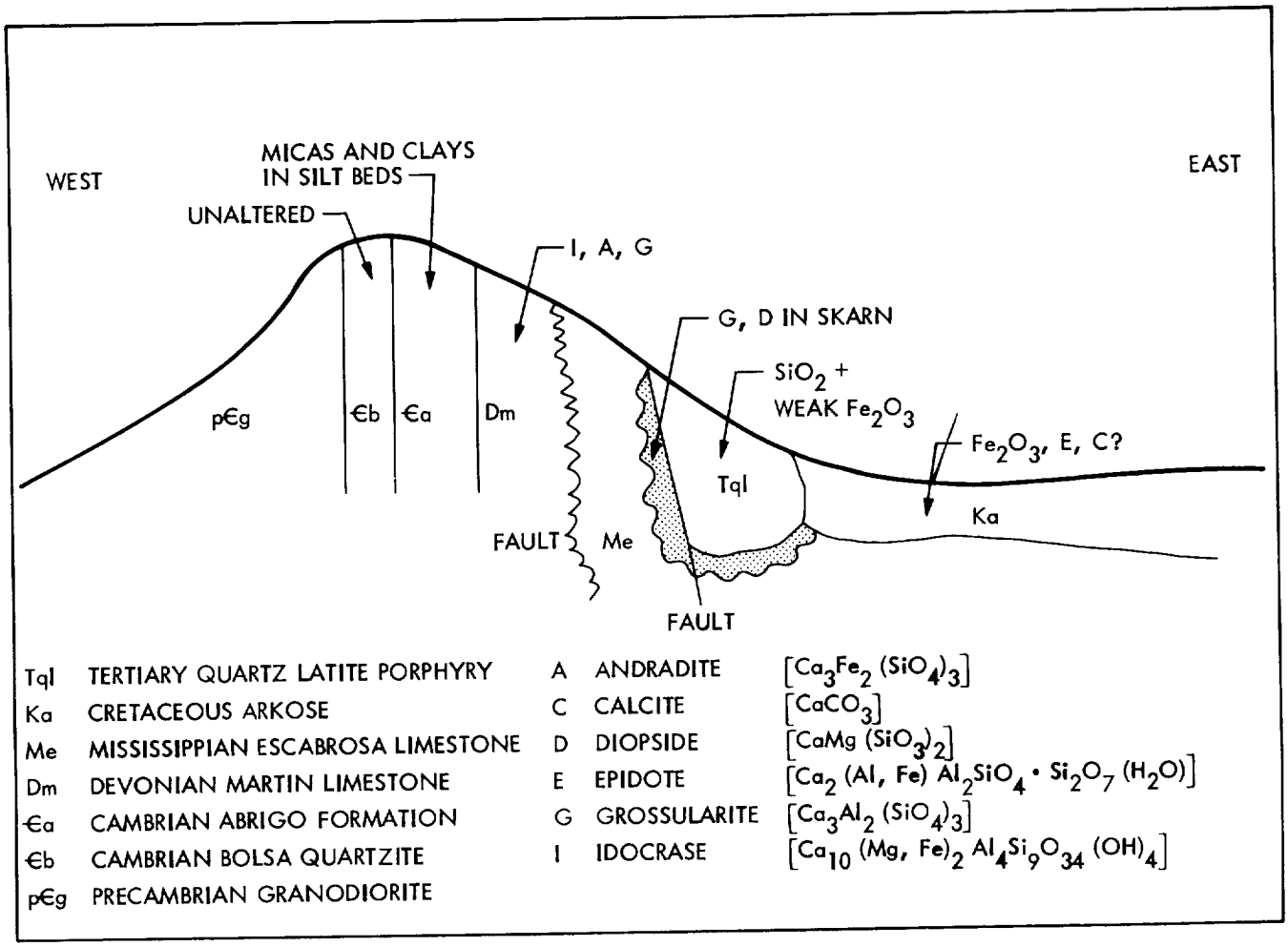

Figure 5-8. Diagrammatic east–west cross section through Rosemont area. Structure, alteration minerals, and skarn are shown.

northwestern fault zones and Laramide intrusives show either strong argillic or skarn alteration (Figure 5-11). Carbonate lithologies show the alteration sequence of marble in pure limestones, calc-silicate minerals in silty limestones, and hornfels in siltstones. Felsic volcanic rocks, intrusives, and clastic sedimentary rocks display weak phyllic or weak argillic alteration. At the Rosemont Camp, quartz latite shows weak phyllic alteration, while the Cretaceous arkose shows weak argillic alteration. The arkose was selectively pyritized and then oxidized to an orange–red color at scattered outcrops throughout the area. The majority of the arkose, however, were pervasively stained by hematite to a deep-red or reddish-brown color that shows little direct association with pyrite. Still other areas within the arkose were propylitized and show the presence of epidote nodules. Cretaceous andesite also present at the Rosemont deposit was selectively altered to pervasive epidote or hematite/jarosite. Fresh pyrite was observed within rocks of the hematite/jarosite zone.

Virtually all the mineral deposits are in rocks that have been hydrothermally or dynamically altered (Drewes, 1973). Some deposits are disseminated in, or are replacements of, favorable lithologies; other deposits occur as epigenetic veins. Many of the calc-silicate skarn zones contain high concentrations of metals. Deposits are also concentrated in vein swarms and along faults around the ore porphyries.

The ore porphyries in the Greaterville and Helvetia Districts are quartz latite porphyries and occur as six plugs and associated dikes. Radiometric dating of biotite concentrates from samples indicates an age of 56 m.y. (Drewes, 1973), or Late Paleocene time. The porphyries were probably emplaced at shallow depths from fairly fluid magmas.

C. History and Production

Mineral exploration began in the Santa Rita Mountains about 1705, shortly after the first visits of Father Kino to

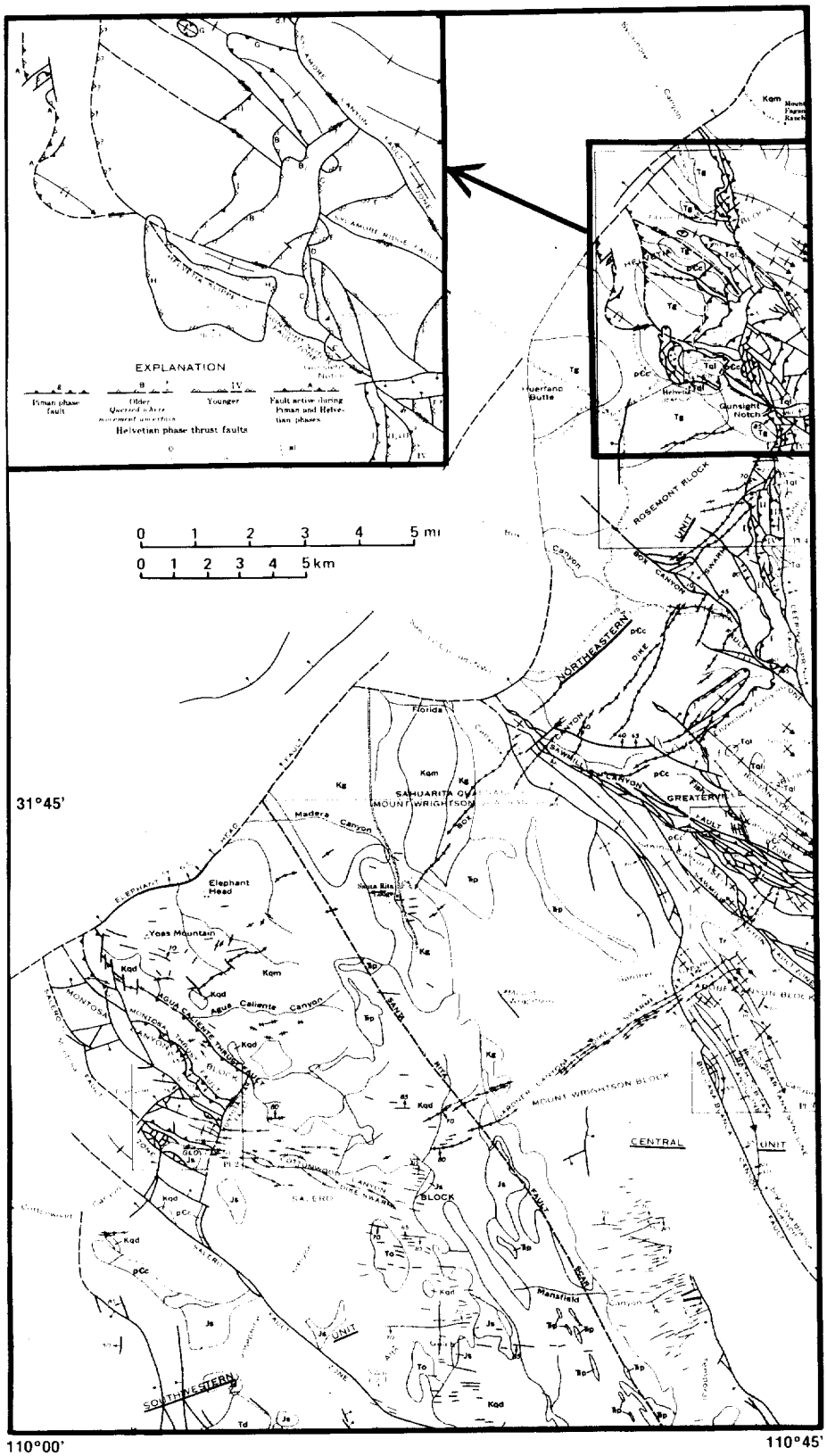

Figure 5-9. Tectonic map of the Santa Rita Mountains, with inset enlarged map of Helvetia–Rosemont area (Drewes, 1972b)

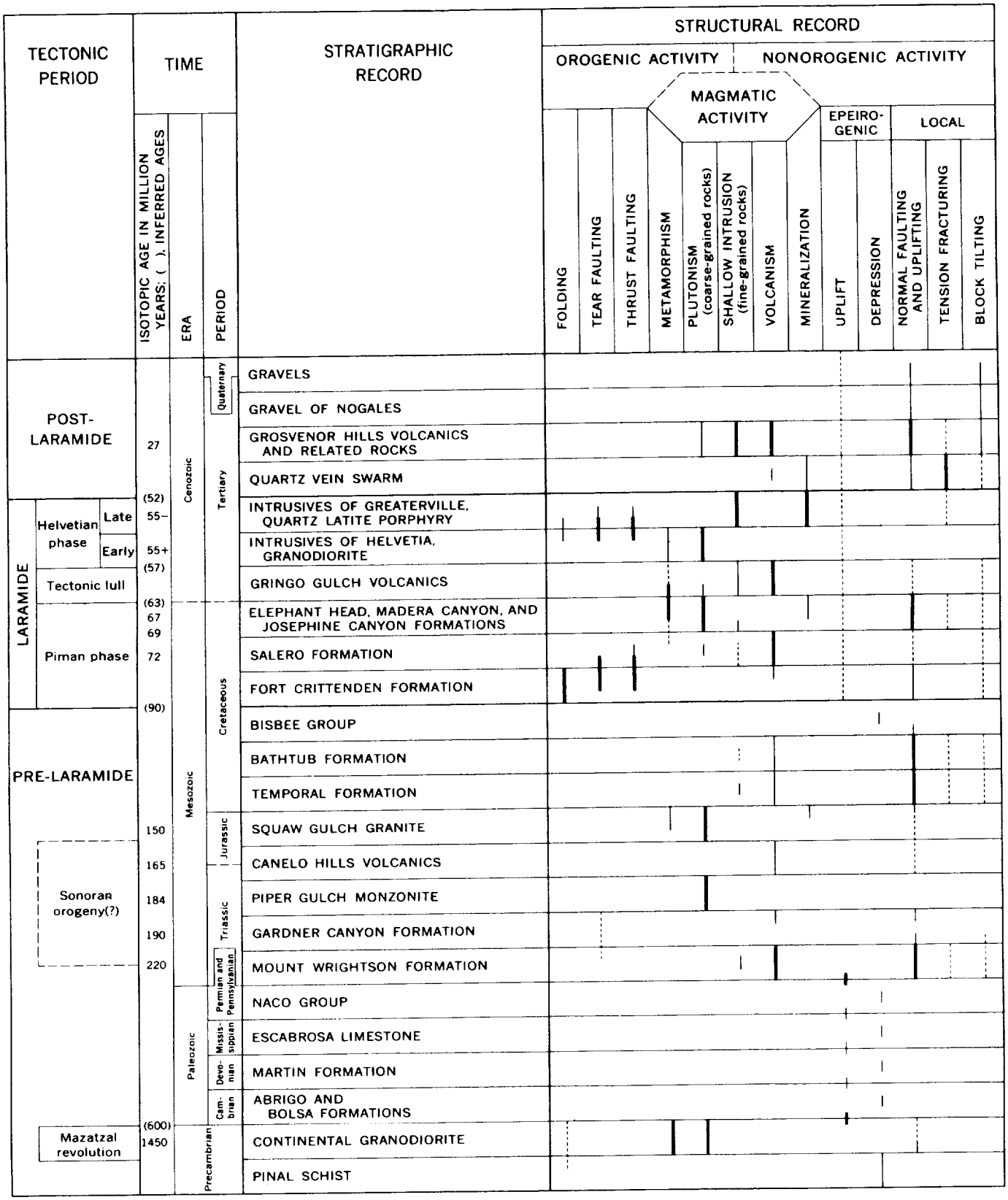

Figure 5-10. Summary of the tectonic record of the Santa Rita Mountains (Drewes, 1972b)

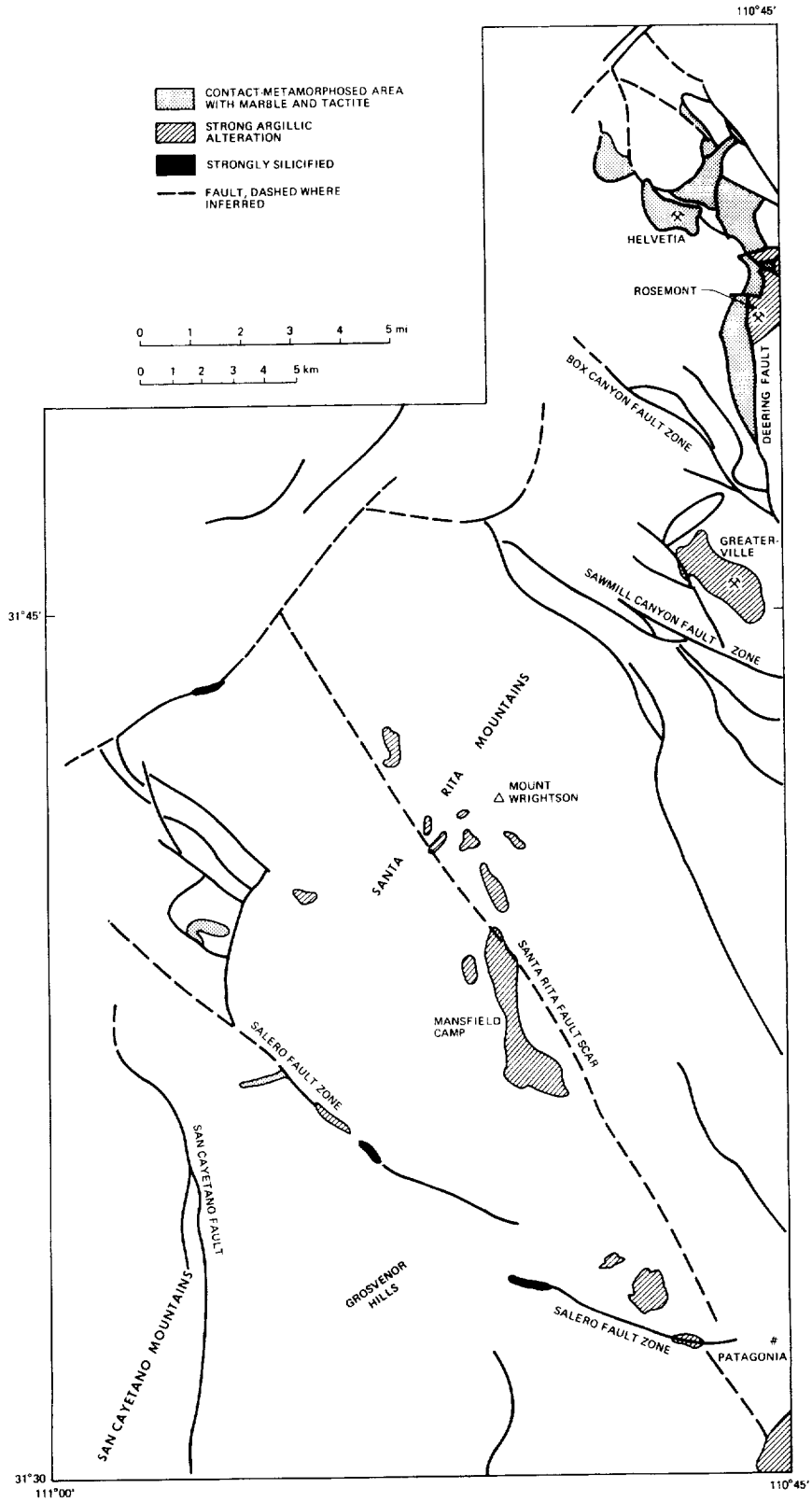

Figure 5-11. Alteration map of the Santa Rita Mountains showing major structures and silicified, argillized, and skarn metamorphosed areas (Drewes, 1973)

the Indian villages along the Santa Cruz River. Silver may have been mined before the close of the 18th century from the Montosa, Alto, Salero, and Montezuma Mines along the west flank of the southern part of the range. Exploration activity was increased after the Gadsden Purchase in 1853, when the region was transferred from Mexico to the United States. The Old Frijole Mine, reported to be the oldest in the Helvetia District, was opened in 1880 and operated for several years. Ore from the district was treated at the Columbia smelter, located on the west side of the Santa Rita Mountains near Old Tiptop Campsite. This smelter was succeeded in 1884 or 1885 by the Mohawk smelter, owned and operated by the Rosemont Mining and Smelting Company, which mined from workings near the Rosemont Camp on the east slope of the Santa Rita Mountains.

In the early 1890s, the Helvetia Copper Company of New Jersey acquired holdings near the town of Helvetia and operated until 1901. The company is reported (Schrader, 1915, p. 96) to have spent $800,000 on development work that included 8 to 10 km of aerial tramway and a new smelter, and also to have produced about $400,000 worth of copper from ore that averaged 8 to 10 percent copper and contained a small amount of silver and gold.

In 1903, the Helvetia Copper Company of Arizona began operations that continued until 1911. Its principal holdings were the Black Horse, Copper World, Heavy Weight, Isle Royal, Leader, and Old Dick Mines. This company built and operated a smelter in 1905 that was closed in 1907, and thereafter the ore was shipped to the Old Dominion smelter in Globe, Arizona. The total production is not known, but the following partial production figures are given by Schrader (1915, p. 97). In 1907, about $40,000 in ore was shipped and, in 1908, 11,000 tons, valued at $157,000. In 1909, 1434 tons of copper ore averaging about 5.5 percent copper was shipped to the Old Dominion smelter and, in 1910, the output was valued at $109,000. The company discontinued operations in 1911.

The yearly production of the Helvetia District from 1908 to 1950 is given in Table 5-5. Unfortunately, the individual production of all the mines of the district was never recorded. Since 1940, however, the bulk of the ore produced from the Helvetia District has come from the Rosemont lease, Copper World, Mohawk, and Narragansett Mines.

The Helvetia–Rosemont area is currently under option by the ANAMAX Mining Company. Recent exploration activities have included diamond drilling, induced polarization surveys, and geochemical sampling. The initial reserves of the Rosemont porphyry copper deposit, estimated in 1973, are 340 million short tons of ore averaging 0.63 percent copper (Gilmour, 1982).

III. Evaluation of Nonimage Remote Sensing Data

A. PFRS Spectra

1. Introduction. *In situ* spectral reflectance measurements can provide valuable information linking mineralogy, spectral response, and multispectral scanner data. Measurement of spectral reflectance was done using JPL's Portable Field Reflectance Spectrometer (PFRS), described in detail in the Technical Appendix, Section 14. The PFRS records a continuous, bidirectional reflectance spectrum in the 0.45- to 2.45-μm wavelength region of a 200-cm^2 area on the ground. By sequentially measuring the reflectance of a white standard target, then ratioing the two curves, a relative reflectance curve is obtained. Further processing by computer then converts the relative reflectance to absolute reflectance based on laboratory measurements of the white field standard.

In operation, 8 to 10 measurements were taken of the same unit in the field over a 10- by 10-m area. These measurements can then be averaged to obtain a reflectance curve representative of a particular material. One of the main benefits of such a procedure over laboratory spectral measurements is the inclusion in the PFRS field of view of soils, dead vegetation, rubble, etc., which are more representative of the naturally occurring surface that is actually viewed by an aircraft or satellite scanner.

In addition, the continuous PFRS curves provide a data base for simulating various scanner instruments by sampling reflectance values within selected wavelength intervals. Various statistical analyses can be performed on this data set to examine separability of various rock units using modeled scanner bandpasses.

2. Spectral measurements. PFRS measurements were acquired within the Rosemont District at 15 sites representing 10 different rock types (Figure 5-12): Cretaceous arkoses in an iron-oxide alteration zone; quartz monzonite porphyry (quartz latite); Cretaceous arkose; Concha Limestone; limestone conglomerate; Escabrosa Limestone; Bolsa Quartzite; Abrigo Limestone; arkose conglomerate; Cretaceous volcanics. Average reflectance curves and one standard deviation envelopes for each unit are shown in Figures 5-13 and 5-14; each curve is an average of 6 to 16 measurements. Mineralogy of the samples was determined by X-ray diffractometry.

The variability of the measurements for a given rock type is 2 to 6 percent reflectance. This is due to the natural variability of surfaces measured with an instrument having a

Table 5-5. Gold, silver, copper, lead, and zinc produced in the Helvetia District, 1908–1950[a]

Year	Number of Producing Lode and Placer Mines	Ore, tons	Gold, value	Silver, oz	Copper, lb	Lead, lb	Zinc, lb	Total Value
1908	3	892	$61	949	91,164	374		$12,611
1909	2	11,187	597	11,698	1,156,604			157,038
1910	3	124						
1911	2							
1912	4	467						6,353
1913	6	739	64	1,170	62,805	10,392	236,117	24,185
1914	2							
1915	6	2,506	248	3,300	349,945			63,161
1916	11	14,609	289	19,300	1,958,825	71,903		499,820
1917	10	18,499	269	24,525	2,615,613	19,171		736,496
1918	8	16,302	56	17,828	2,156,486	12,406	489,163	595,931
1919	7	3,357	300	5,479	414,370	58,432		86,607
1920	6	2,516	8	6,295	401,244	3,618		80,988
1922	1							
1923	8	683	163	5,024	69,633	40,590		17,360
1924	4	202	31	1,459	33,585	9,018		6,130
1925	8	319	80	2,500	41,972	6,000		8,300
1926	5	73	100	150	9,272	3,000		1,765
1927	4	116	136	73	15,332	2,761		2,359
1928	4	150	140	70	18,750	2,700		3,042
1929	6	756	34	852	84,823	2,774		15,592
1930	3	2,258	185	1,282	145,882	80		19,648
1931	1	40						
1934	3	32	*3,495	102	3,475			379
1935	1							
1937–1938	11	1,403	*3,535	14,874	43,099			20,255
1939	5	69	*105	439	8,875	213		1,336
1940	2	1,115	*280	1,409	163,080			19,710
1941	8	440	*445	1,966	58,300	8,300		9,205
1942	3	4,465	*385	3,631	449,000	3,000		57,497
1943	11	3,639	*945	5,549	309,600	26,200	41,000	51,532
1944	10	20,240	*1,785	11,025	1,070,800	67,100	134,000	174,827
1945	7	29,188	*560	10,239	1,516,600	29,500	78,000	224,089
1946	6	44,577	*13,370	12,714	1,904,000		20,000	334,531
1947	9	29,891	*4,340	9,936	1,264,400	3,000	41,800	284,346
1948	9	11,695	*490	5,466	606,400	27,300	27,600	145,584
1949	4	3,170		2,464	266,700	18,200	30,300	61,403
1950	4	1,514	*105					105
Total		227,333	$32,601	181,768	17,290,634	426,032	1,097,980	$3,722,185

[a]Creasey and Quick, 1955.
Asterisk indicates conversion from ounces to dollar value.

field of view of 200 cm^2. More or less soil, rock fragments, outcrop, and grass randomly occur in the field of view; in addition, some heterogeneity of the rock-type mineralogy may be expected on scales of a few meters. The average curves are more representative of a larger field of view such as might be imaged by a scanner. While no systematic attempt was made to obtain data on a detailed grid basis, obtaining a number of measurements in a 10- by 10-m area provides a more useful approximation of a natural surface's reflectance characteristics.

Cretaceous volcanics with iron-oxide alteration (Figure 5-13a) show three major absorption features in the reflectance curve. The dip at 0.85 μm and smaller features at 0.65 and 0.45 μm are due to ferric iron oxide in the form of hematite. The sample site is located in the large hematitic alteration area east of the Rosemont deposit and appears brick red in the field. Hematite is developed from oxidation of pyrite; casts of pyrite and occasional cubes of pyrite were observed on some outcrops. The dip at 2.2 μm is due to the presence of kaolinite, whose major absorption band

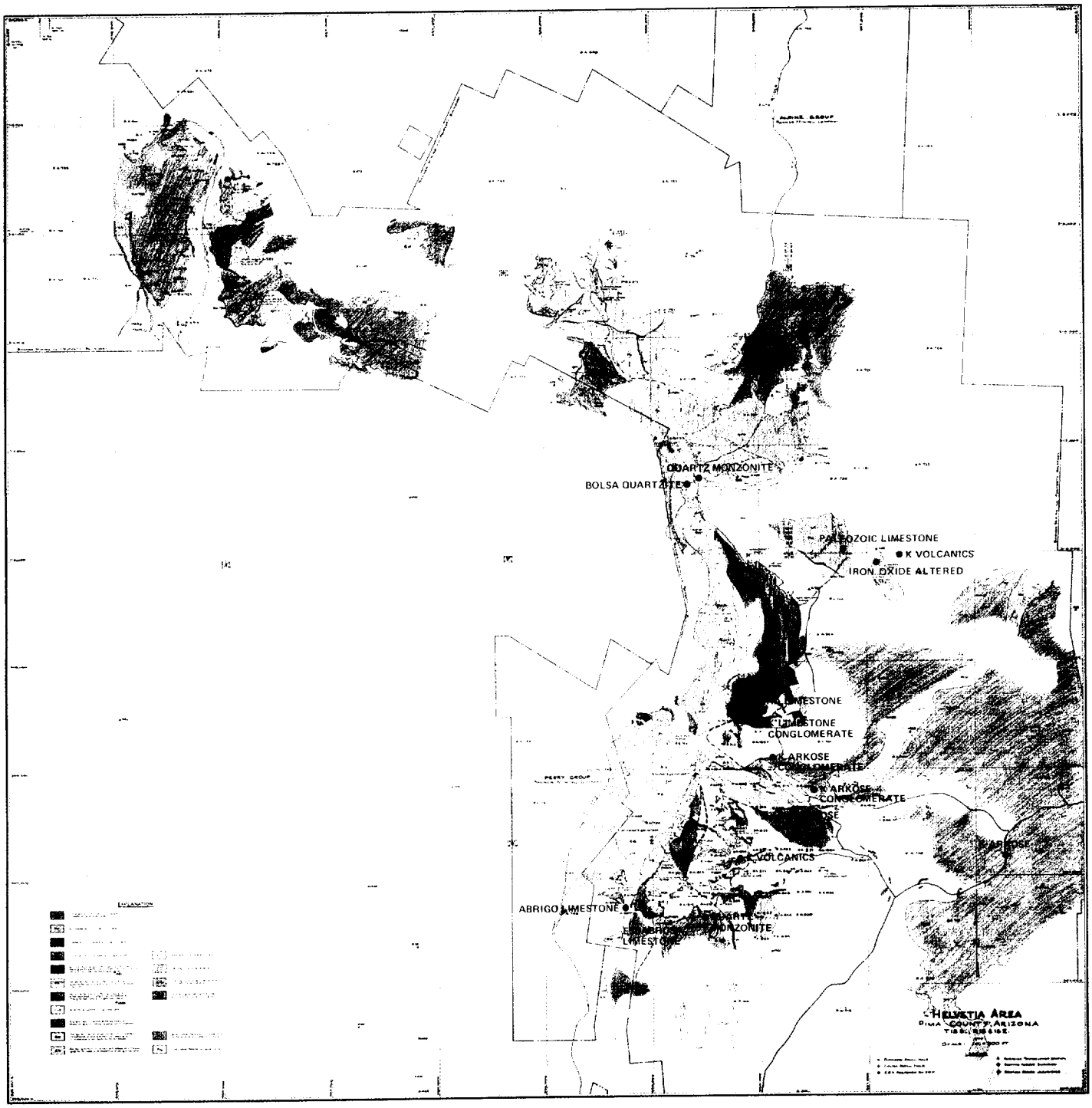

Figure 5-12. PFRS sample sites in the Helvetia—Rosemont area. Base is geologic map from AMAX (unpublished).

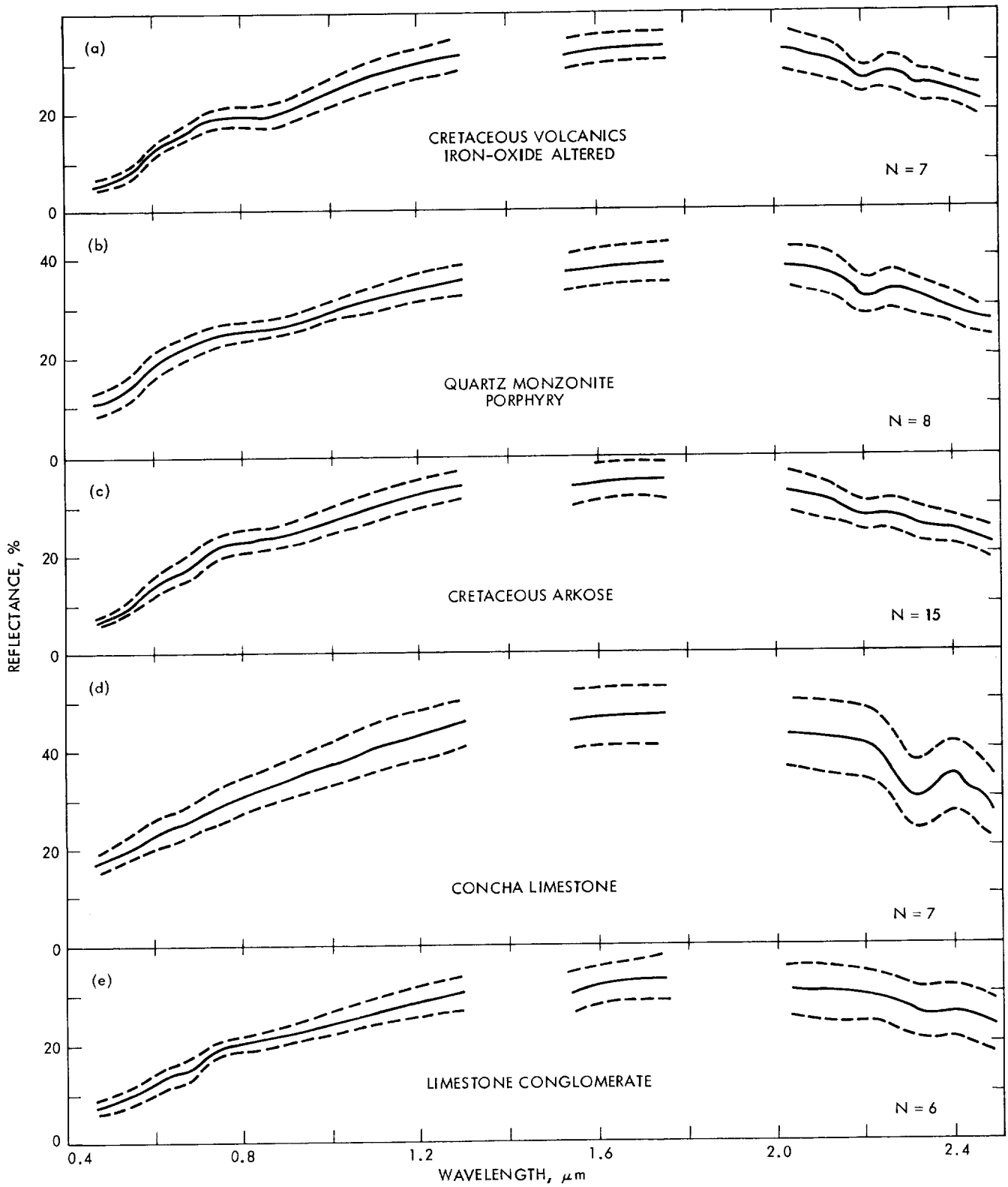

Figure 5-13. PFRS reflectance curves of rock types measured in the field: (a) Cretaceous volcanics, iron-oxide altered; (b) quartz monzonite porphyry; (c) Cretaceous arkose; (d) Concha Limestone; (e) limestone conglomerate. Dashed lines are one standard deviation envelopes. Locations are shown in Figure 5-12. The two gaps in the spectral curves are in regions of energy absorption by atmospheric water. *N* is number of PFRS measurements represented by the average curve.

in this wavelength region is at this position (Hunt et al., 1973). The high reflectance at 1.6 μm is typical of hydrothermally altered rocks whose spectral response is dominated by the iron charge transfer band in the ultraviolet, causing the sharp falloff in reflectance at shorter wavelengths, and the major water band at about 2.7 μm, causing the falloff at longer wavelengths. These features can be exploited in the scanner data to highlight the presence of iron oxides and hydrous minerals.

The quartz monzonite porphyry curve (Figure 5-13b) is from an area of alteration, characterized by oxidation of mafic minerals to iron oxides and alteration of feldspars to clay (phyllic/argillic alteration). Iron-oxide bands are moderately well expressed—the broader absorption feature near 0.9 μm indicates the presence of limonitic/goethitic iron oxides, rather than hematite; the 2.2-μm absorption band is due to the presence of kaolinite.

Cretaceous arkose (Figure 5-13c) again shows iron-oxide and clay-related absorption bands. The iron bands indicate a combination of hematite and goethite; the 2.2-μm band is not as deep as the previous two curves, suggesting weaker clay development. The spectral features are due to oxidation of the original mafic minerals and probably are not related to hydrothermal alteration phenomena.

The three limestone curves (Figures 5-13d, 5-14a, and 5-14c) for Concha, Escabrosa, and Abrigo are quite similar. They show a smooth, featureless rise in reflectance from 0.4 to 1.6 μm and a major absorption band at 2.35 μm. This band is due to overtone and combination tones of the internal vibration of the CO_3 radical (Hunt and Salisbury, 1971a). The falloff toward short wavelength and lack of discrete absorption bands may indicate the presence of small amounts of ferric iron. The carbonate absorption band can be used in scanner data to highlight the presence of these limestones.

The limestone conglomerate (Figure 5-13e) shows a slight dip at 2.35 μm due to carbonate, a band at 0.65 μm from iron, and a general flattening of reflectance between 0.8 and 1.2 μm, also due to iron.

Bolsa Quartzite (Figure 5-14b) shows similar iron features between 0.4 and 1.2 μm and a slight band at 2.2 μm. The sample site is in an outcrop area near the quartz monzonite intrusive; copper-oxide mineralization occurs nearby along fractures in the quartzite, indicating hydrothermal fluid activity. The clay band is due to alteration of feldspars in interbedded shales and the soil derived from them. The generally low reflectance values are due to opaque minerals which depress the curve. Clean quartzites are lighter and spectrally featureless.

Arkose conglomerate (Figure 5-14d) and Cretaceous volcanics (Figure 5-14e) are quite similar. Iron-oxide absorption bands are evident at 0.45, 0.65, and more broadly near 0.9 μm. The feature at 2.35 μm is due to the presence of an Mg–O–H absorption band found in some mafic minerals; these rocks do not contain any carbonate.

3. Statistical analysis of PFRS data

a. Introduction. The continuous 0.45- to 2.45-μm wavelength region spectra acquired by the PFRS provide an opportunity to simulate the spectral bandpasses of existing and theoretical scanners. By computing the equivalent band responses of these instruments, it is possible to examine on a statistical basis separability of rock types as a function of wavelength bands. This type of analysis has been used in the past to examine plutonic rocks (Blom et al., 1980) and sedimentary rocks associated with uranium mineralization (Conel et al., 1980). A more general study (Wiersma and Landgrebe, 1980) presented a scheme for analytical design of multispectral sensors using an overall performance measure, probability of correct classification.

This type of analysis covers only one aspect of sensor performance, the spectral bandpasses. Other factors, such as atmospheric effects, spatial averaging due to variable field of view, radiometric sensitivity, and instrument response, are not considered. Nevertheless, the spectral regions are probably the most important factor affecting the ability to separate various rock types.

b. Discriminant function analysis. The technique used here is stepwise linear discriminant function analysis, part of the BMDO7M computer package from the University of California at Los Angeles (Dixon, 1970). The mathematics of discriminant analysis are fully discussed by Jennrich (1977).

Briefly, the program develops group classification functions (linear combinations of the surveyed spectral channels) based upon training data (sets of PFRS measurements) provided by the user for each group. The classification functions result from linear operations performed on each variable (each spectral channel) and are developed in a stepwise fashion by surveying the available variables and adding the most useful variables to the analysis. The utility of each variable for discrimination among the groups is thus assessed. After development of the group classification functions, the members of the training sets are classified, allowing one to determine to what degree sufficient information exists in the data to discriminate among the chosen groups. The output of the program includes mat-

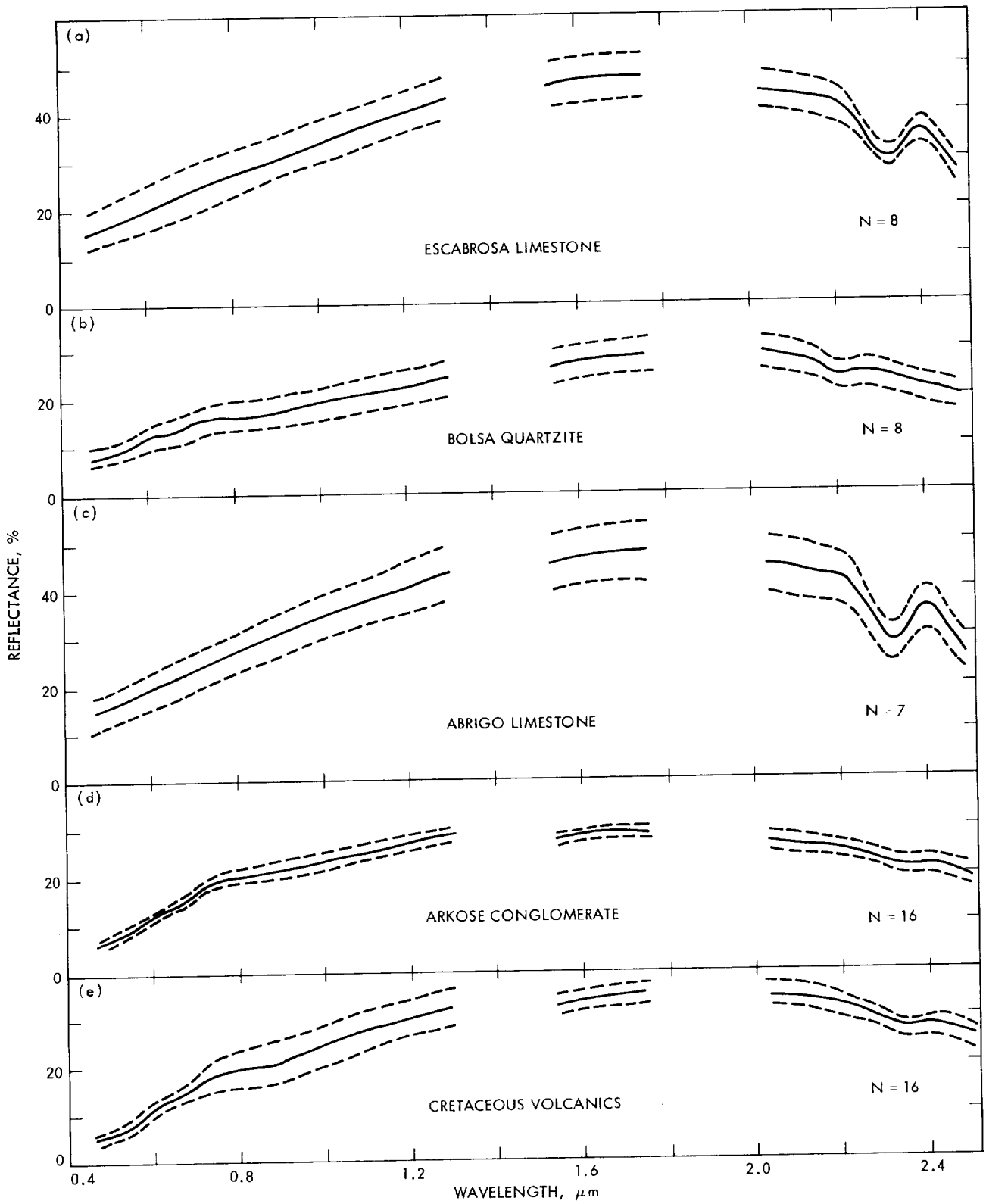

Figure 5-14. PFRS reflectance curves of rock types measured in the field: (a) Escabrosa Limestone; (b) Bolsa Quartzite; (c) Abrigo Limestone; (d) arkose conglomerate; (e) Cretaceous volcanics. Dashed lines are one standard deviation envelopes. Locations are shown in Figure 5-12. The two gaps in the spectral curves are in regions of energy absorption by atmospheric water. *N* is number of PFRS measurements represented by the average curve.

rices that depict the classification accuracies, order of band selection in terms of relative importance for classification, and group classification functions for classifying unknown members.

c. Results of the analysis. For the Helvetia PFRS data, two different groups of rocks were examined: three limestones and ten different rock types. The spectral bands of five different sensors were simulated: Landsat Multispectral Scanner (MSS), M²S 11-channel, Landsat 4 Thematic Mapper (TM), NS-001, and a theoretical scanner with 30 equally spaced wavelength bands 0.05 μm wide (Table 5-6). For the first four sensors, filter functions for the respective bands were convolved with the PFRS spectra to calculate the equivalent band reflectance values. These values were then the variables used for the analysis.

The first series of the analysis examined separability among the three limestones—the Escabrosa, Abrigo, and Concha—using 29 PFRS spectra as the data base. In the field, the Escabrosa and Concha appeared quite similar—medium to dark gray, coarsely crystalline, massively bedded. The PFRS spectra, however, appear similar for all three units. Figure 5-15 presents matrices, percent correct classification, and order of band selection for the five sensors analyzed.

The classification matrices depict the assignment of spectra to the three groups. For example, in the Landsat MSS matrix, three spectra of A are correctly classified as A; one is incorrectly classified as B; three are incorrectly classified as C. Correct assignments occur along the principal diagonal. Landsat MSS wavelength bands are the poorest in accuracy, providing 62 percent correct classification (18 of the 29 spectra). Using 10 wavelength bands from the M²S scanner (no thermal channel), 83 percent accuracy is achieved. The first band, 0.52 μm, is where the three have different relative reflectances: 15, 17, and 19 percent for Abrigo, Escabrosa, and Concha, respectively. Similar relative differences occur at the other wavelengths; after inclusion of more of the variables, only five samples are misclassified. Landsat 4 bands are less accurate: 76 percent. The 1.65-μm band is the first one selected, followed by bands at 0.83 and 0.56 μm. At 1.65 μm, Concha Limestone has the largest reflectance difference compared to the other two (41 versus 47 percent). In the 0.83- and 0.56-μm bands, the Escabrosa and Abrigo have different reflectances from each other. The addition of the 1.15-μm band with the NS-001 improves the accuracy to 90 percent. This band is selected second; all three limestones differ in reflectance values here. Using the 30-channel scanner, complete separation of the groups is achieved. Four of the first seven bands selected are between 2.0 and 2.4 μm, the region where the pronounced carbonate absorption feature occurs. The other three bands are at wavelength positions similar to the 0.56-, 0.66-, and 0.83-μm bands of Landsat 4. This implies that these bands are well suited for separating these particular rock groups. They were selected for inclusion on the satellite scanner on the basis of vegetation spectral characteristics, not on rock characteristics. It is fortuitous that the coincidence will benefit geologists also.

The second analysis involved 10 rock-type groups of PFRS data (Figure 5-16). Classification accuracy for the four real scanners is relatively poor, ranging from 50 percent for Landsat to 68 percent for Landsat 4 and NS-001. Some of the misclassifications are minor (one limestone is classified as another); others are major. This seems to indicate that wavelength bands on existing instruments are not well suited for separating this particular suite of rock types. One possible explanation may be in the variability of spectra included for any particular group. The inhomogeneity of a single unit sampled in the field can be due to the presence of more or less lichen cover, different degrees of weathering, variable proportions of soil versus outcrop, variable grass cover, and natural inhomogeneity in the unit. A far more extensive sampling scheme could solve these problems. The 30-channel conceptual scanner provides 95 percent classification accuracy. Again, the first four bands selected are similar to the 0.56-, 0.66-, 1.65-, and 2.2-μm

Table 5-6. Spectral bands of five simulated sensors

Landsat MSS	M²S 11-channel	Landsat 4 TM	NS-001	30Δλ
0.5–0.6 μm	0.33–0.44 μm	0.45–0.52 μm	0.45–0.52 μm	0.425–0.475 μm
0.6–0.7	0.44–0.48	0.52–0.60	0.52–0.60	0.475–0.525
0.7–0.8	0.49–0.54	0.63–0.69	0.63–0.69	0.525–0.575
0.8–1.1	0.54–0.58	0.76–0.90	0.76–0.90	•
	0.58–0.62		1.00–1.30	•
	0.62–0.66	1.55–1.75	1.55–1.75	•
	0.66–0.70	2.08–2.35	2.08–2.35	2.425–2.475
	0.70–0.74			
	0.76–0.86			
	0.97–1.065			

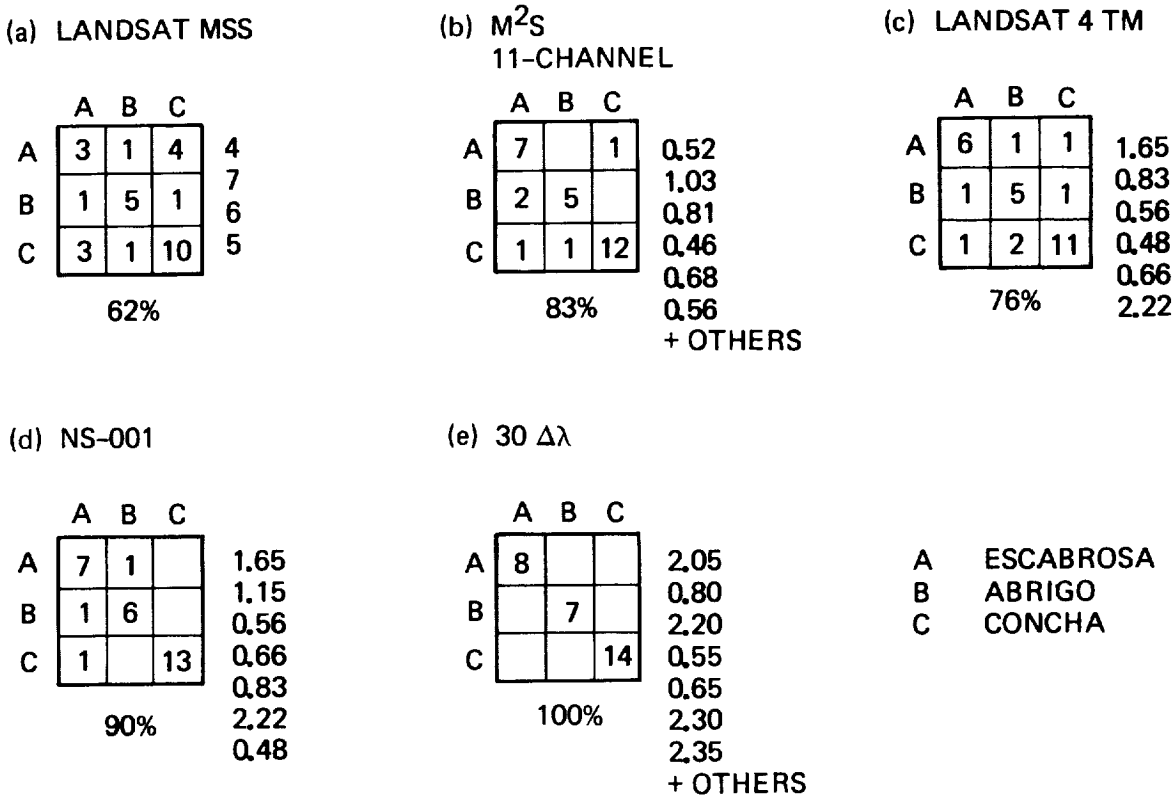

Figure 5-15. Results of linear discriminant function analysis of PFRS data for three limestones. Five scanners were simulated from the continuous spectral data: (a) Landsat MSS; (b) M²S 11-channel; (c) Landsat 4 TM; (d) NS-001; (e) 30 Δλ. Classification matrix, percent correct classification accuracy, and order of band selection are shown.

bands of Landsat 4. The major difference is the width of the 30 wavelength bands, 0.05 μm compared to an average width of 0.13 μm for the Landsat 4 Thematic Mapper bands. This indicates that narrower spectral bands may be necessary to separate the particular group of rocks analyzed here.

B. M²S Image-Derived Spectra

1. Introduction. Multispectral scanners record radiance values which are a function of many factors: instrument detector response characteristics, reflectance of the ground surface, atmospheric transmittance between ground and sensor, upwelling atmospheric radiance between ground and sensor, atmospheric scattering contributions, and transmittance of the optical system (Slater, 1981). To use a scanner as an imaging spectrometer, it is necessary to extract the ground reflectance term from the other radiance contributions by calibrating the data in some fashion. There are two different approaches to accomplish this: (1) to measure and/or model all the contributions other than the reflectance term, and (2) to use ground reflectance measurements as calibration points and fit the radiance data to the measured reflectance values. Various attempts have been made to determine analytical solutions based on modeling and measurements of atmospheric terms and instrument factors (Hulstrom, 1975; Turner et al., 1975). These approaches are difficult and approximate due to inaccuracies in atmospheric models, sensor characterizations, and atmospheric measurements. The second method is empirical, requiring only ground spectral reflectance measurements in the area imaged by the scanner. This latter approach is used here to calibrate the M²S data and produce relative reflectance curves for various rock-type units.

2. Procedure and spectra. Eleven rock types were selected (Table 5-7), and outcrop areas were identified in the M²S image based on the geologic map. Digital number (DN) values were extracted from the digital data for the 10 visible and near-infrared channels for areas of about 5-by-5 to 10-by-10 pixels for each rock type (75- by 75-m to 150- by 150-m areas). These values and their standard deviations are shown in Table 5-8.

Hematitic arkose was chosen as the unit to use for calibration because PFRS spectra for this outcrop were available and the area was large enough on the image to be confidently located and delineated. The PFRS reflectance curves for this unit were used to calculate the equivalent

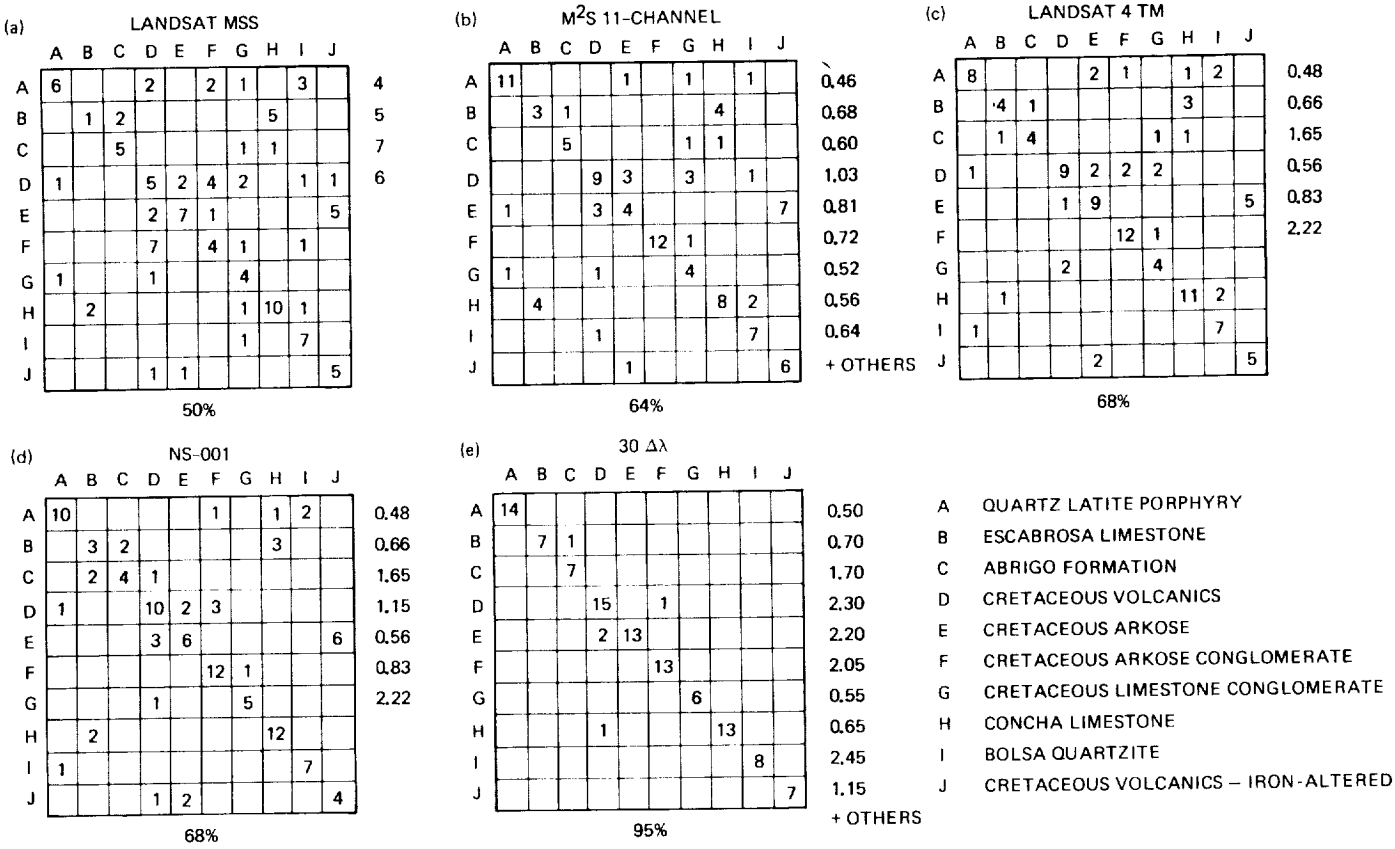

Figure 5-16. Results of linear discriminant function analysis of PFRS data for 10 rock types. Five scanners were simulated from the continuous spectral data: (a) Landsat MSS; (b) M²S 11-channel; (c) Landsat 4 TM; (d) NS-001; (e) 30 Δλ. Classification matrix, percent correct classification, and order of band selection are shown.

wavelength response for each of the 10 M²S bands. The PFRS values and DN values are shown in Table 5-9. By dividing PFRS values by DN value (A/B in Table 5-9), a scaling factor was determined that related PFRS reflectance to DN values within each spectral channel of the M²S.

The calibration procedure then consisted of multiplying the scaling factor times the DN values for each of the rock types for each channel to produce relative reflectance values. Plots of the raw DN values and the corresponding relative reflectance values are shown in Figure 5-17.

Table 5-7. Rock types identified in the M²S image

Group	Rock Type
1	Hematitic arkose
2	Concha Limestone
3	Willow Canyon sandstone
4	Altered Concha Limestone
5	Altered latite porphyry intrusive
6	Precambrian granodiorite
7	Hermosa Limestone
8	Shellenberger siltstone
9	Earp sandstone
10	Tertiary granodiorite
11	Bolsa Quartzite

The shapes of the raw DN spectra are all quite similar and bear no resemblance to actual reflectance curves. This is due to the DN values being proportional to measured radiance values, convolved with the atmospheric and instrumental factors previously discussed. The latter effects are dominant, judging from the U-shape of the curves. After calibration, the image spectra appear similar to measured reflectance curves. The dominant feature is the general falloff in reflectance toward shorter wavelengths. This is due to the presence of an intense iron absorption band in the ultraviolet; the falloff is one wing of this band. Other absorption bands due to iron oxides dominate this part of the electromagnetic spectrum (Hunt and Salisbury, 1971b). In particular, hematite shows absorption features centered near 0.57, 0.67, and 0.85 μm; goethite has features near 0.55, 0.6, and 0.95 μm. Possible evidence for the presence of iron-oxide minerals can be seen, particularly in the curves for Tertiary granite, Bolsa Quartzite, and Shellenberger

Table 5-8. M²S DN values and standard deviations

Group	No. Pixels	Channel/Central Wavelength, μm								
		1/0.42	2/0.46	3/0.52	4/0.56	5/0.60	6/0.64	7/0.68	8/0.72	9/0.81	10/1.0
1	400	63,4	66,5	57,4	50,4	49,5	52,6	51,7	80,7	94,7	102,9
2	400	106,7	118,9	92,6	75,5	69,5	70,5	68,5	97,4	111,5	111,5
3	400	106,5	120,7	95,5	78,4	75,4	78,4	80,5	112,4	132,5	146,5
4	400	86,6	96,8	79,5	66,4	61,4	62,4	61,5	91,4	108,4	115,5
5	400	75,3	81,4	69,3	59,3	56,3	58,4	58,5	88,4	103,5	112,6
6	400	97,4	109,5	89,4	77,4	73,5	76,6	76,6	114,5	140,4	151,5
7	225	109,3	126,3	102,2	85,2	79,2	82,3	82,3	118,3	140,3	152,4
8	400	101,3	113,4	91,3	78,3	73,4	76,4	75,5	102,4	116,5	121,7
9	100	111,2	121,1	95,1	80,1	74,1	76,1	76,1	114,1	140,2	148,3
10	225	116,3	134,3	109,3	94,2	90,3	94,3	86,3	132,3	156,3	169,3
11	400	127,3	132,3	100,2	84,2	81,3	85,3	86,4	116,4	133,4	142,3

siltstone. A dip in reflectance occurs at 0.85 μm, a pronounced low at 0.55 μm, and a dip at 0.65 μm (granite curve).

A direct comparison of two of the image spectra with actual PFRS spectra is presented in Figure 5-18 for Shellenberger siltstone and altered intrusive. The altered intrusive has a weak absorption band at about 0.9 μm, and a strong falloff toward the short wavelength, particularly between 0.6 and 0.5 μm. These features can be clearly seen in both curves for the intrusive. Shellenberger curves have stronger absorption features than the intrusive in both curves. The deeper 0.9-μm band is clearly evident, as is the more pronounced drop in reflectance between 0.6 and 0.5 μm.

The image spectra produced by this simple calibration technique allow the aircraft scanner to be used as a spectrometer, providing spectral "curves" which depict mineralogical information. There are, however, limitations inherent in this procedure. First, there is the spectral resolution restriction due to the positions and number of spectral bands on the instrument. In the case of the M²S scanner, there are only two bands beyond 0.75 μm; therefore, only crude resolution of the shape of the 0.9-μm ferric iron absorption band is possible. Second, this procedure compares two different sampling schemes: the PFRS curves are averages of eight measurements covering an area of about 10 by 10 m; the M²S curves are computed from pixel averages covering an area about 150 by 150 m. If the sampled unit is homogeneous at this scale, the two curves will appear similar; if greater heterogeneity occurs, the PFRS sampling bias and lack of ability to measure a very large area can make the curves appear quite different. The similarity of the two examples shown suggests that the two units examined are relatively homogeneous at the varied measurement scales. A more systematic ground sampling scheme could verify the value of this approach.

Table 5-9. PFRS and M²S DN values for hematitic arkose

Channel	PFRS, %		
	Reflectance (A)	DN (B)	Factor (A/B)
1	5	64	0.08
2	6	66	0.09
3	7	57	0.12
4	8	50	0.16
5	13	49	0.27
6	15	52	0.29
7	17	51	0.33
8	19	80	0.24
9	19	94	0.20
10	25	101	0.25

IV. Evaluation of Photography, Radar, and Landsat Data

A. Color Aerial Photography

1. Introduction. True-color aerial photography was acquired simultaneously with each of the aircraft multispectral scanner data overflights. The photographs were obtained using a 6-in. focal length camera and recorded on 9- by 9-in. film transparencies with 60 percent overlap between succeeding frames. The photographs were used in the field for location purposes and were also interpreted for geologic information. They were used at their original scale of about 1:70,000, and interpretive overlays were produced either from the original transparencies or from contact prints.

2. Interpretation of photographs. A photograph centered near Rosemont is shown in Figure 5-19. This photo-

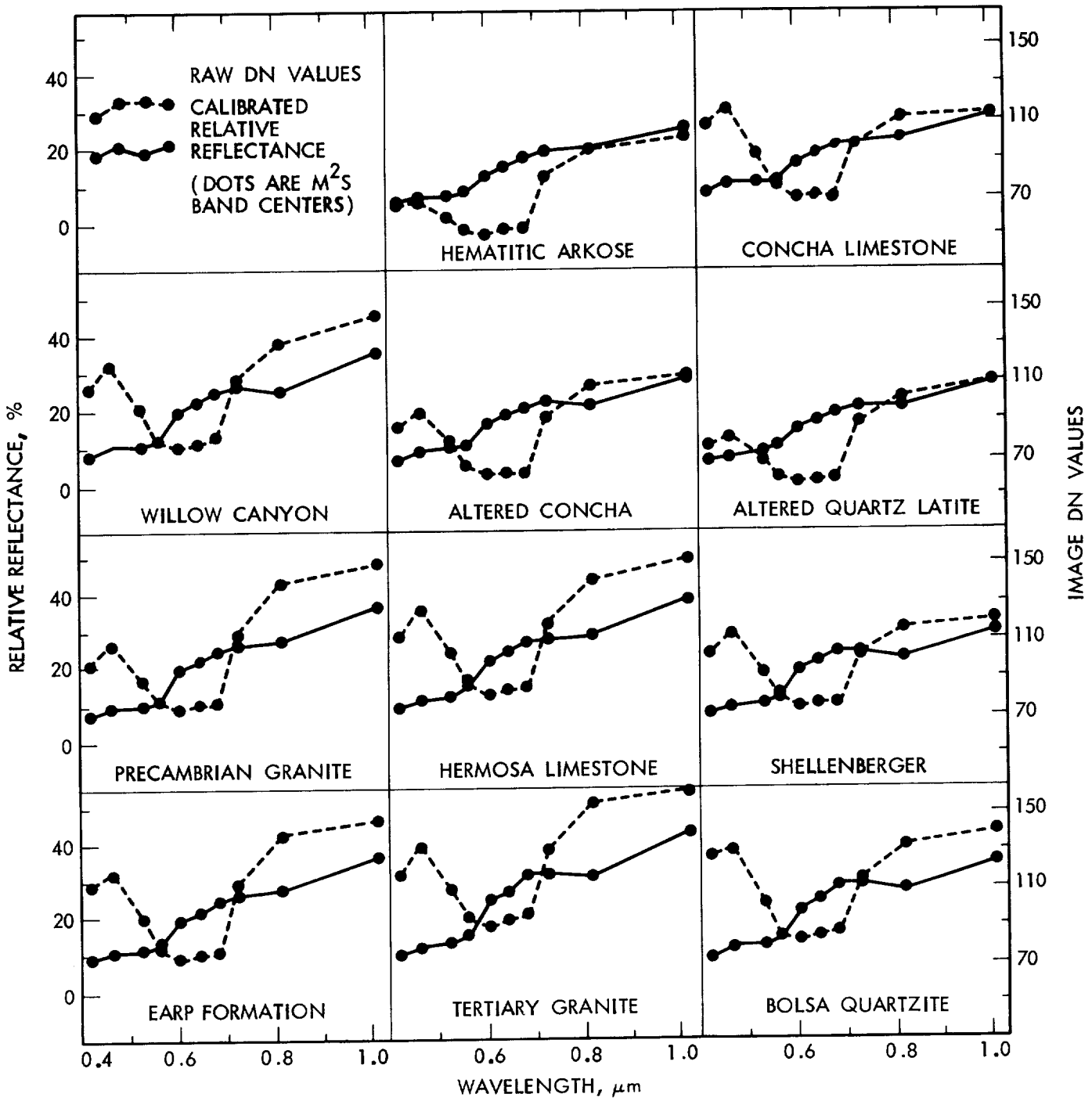

Figure 5-17. M²S image spectra. Raw DN values (broken lines) and calibrated relative reflectance values (solid lines) are shown for 11 rock types. Dots are M²S band centers. Calibration procedure transforms U-shaped raw DN curves to curves resembling measured reflectances.

graph was interpreted, and the results are shown in Figure 5-20. One of the most obvious features in the photograph is the large reddish area corresponding to the argillic and hematitic alteration of the Cretaceous volcanic sediments and arkoses. The distinctive tonal anomaly produced by development of hematite allows this area to be easily identified. Paleozoic limestones appear light gray in color in the northern part of the photograph, and darker in the south. Their distinctive color allows them to be recognized and identified as limestones. Precambrian granites can be dis-

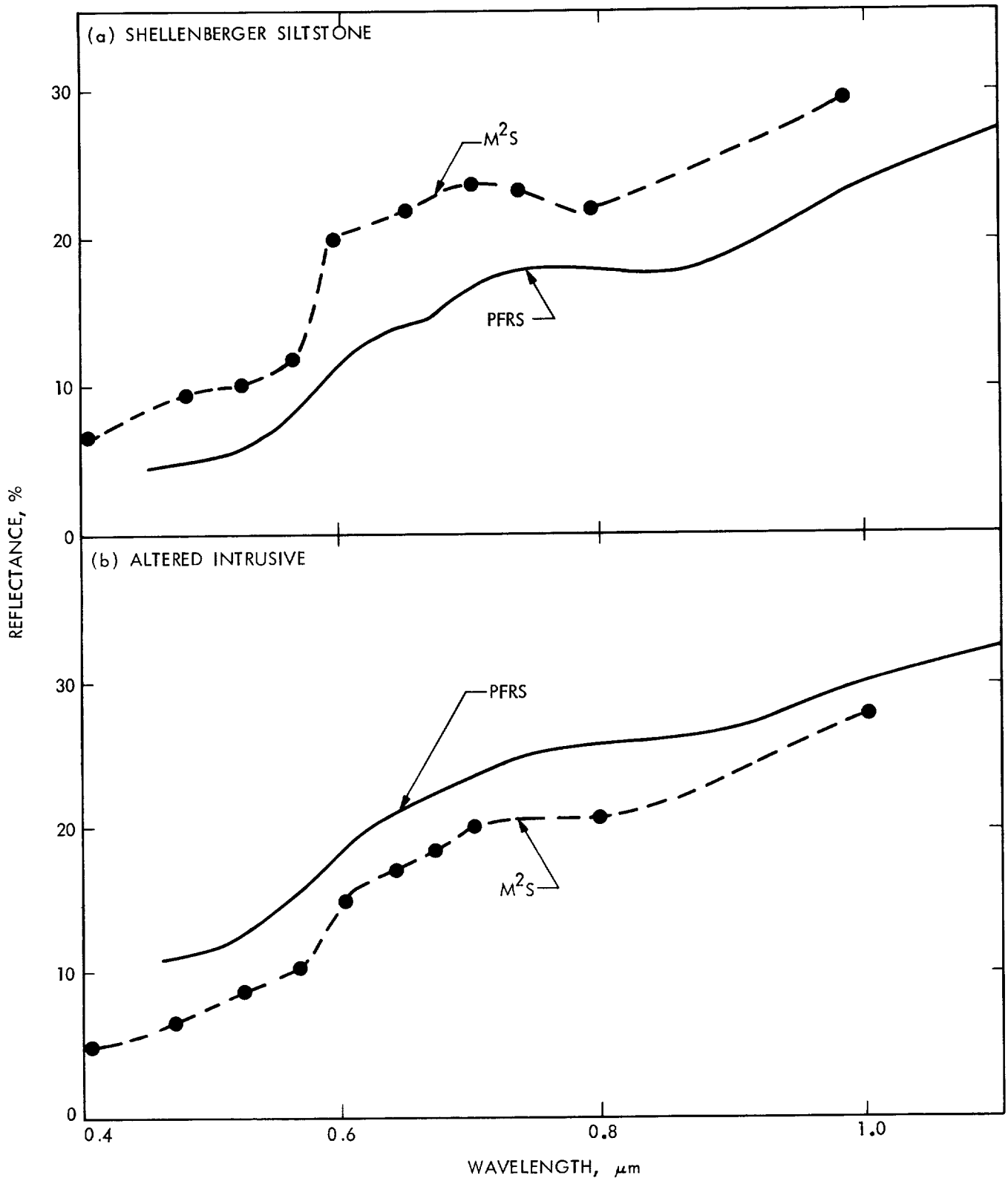

Figure 5-18. Comparison of field-acquired PFRS reflectance spectra and calibrated M^2S image spectra: (a) Shellenberger siltstone; (b) altered intrusive. The calibration procedure produces image spectra curves with similar shapes, but offsets in overall relative albedo.

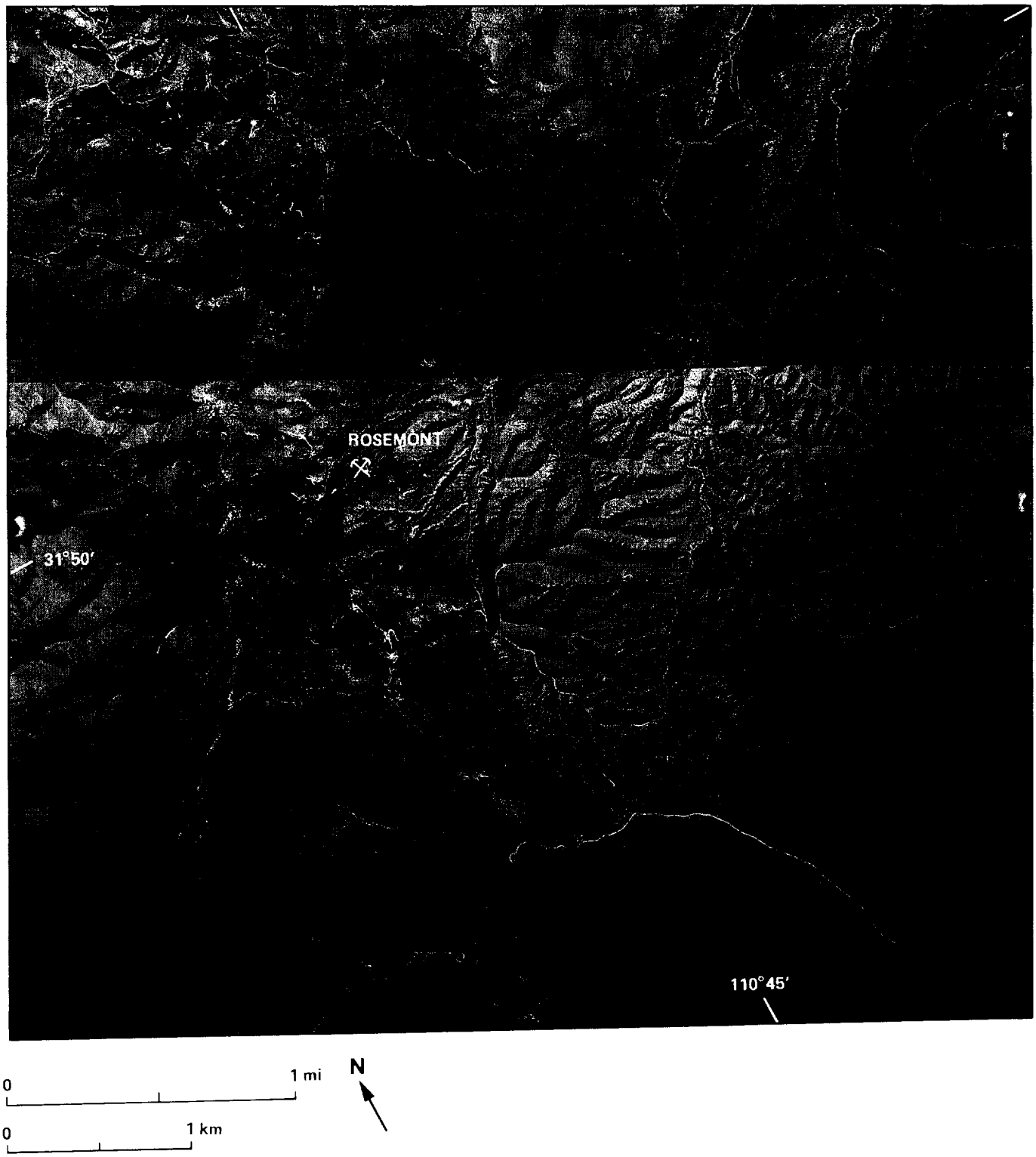

Figure 5-19. Mosaic of color aerial photographs of a 5- by 5-km area around Rosemont. Photographs were acquired October 13, 1978 coincident with NS-001 near-noon overflight.

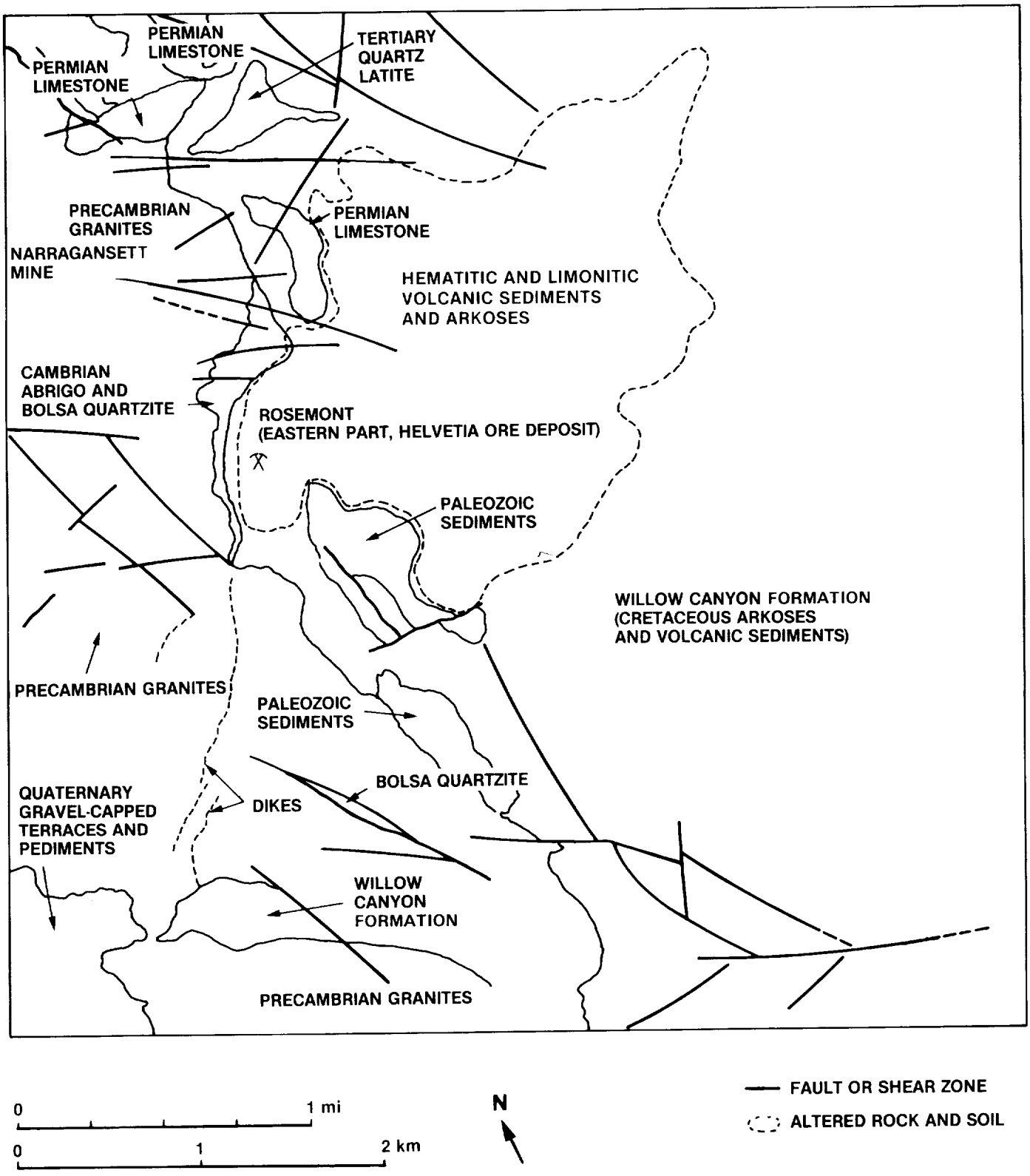

Figure 5-20. Interpretative map of Figure 5-19 showing recognizable linear features (faults or shear zones), dikes, and lithologic contacts. Hematitic arkose is a prominent mappable feature. Formation names were obtained by subsequent comparison with geologic maps.

criminated based on uniform texture, vegetation cover, and tone. The Abrigo and Bolsa Quartzite form resistant knobs and ridges at the range crest and can be delineated based on their geomorphic appearance. The arkoses and sediments that underlie the eastern half of the photograph present a uniform appearance of fine-grained dendritic drainage patterns, low to moderate topography, and a tan color. Tertiary dikes in the southwestern part of the photograph are recognizable by their sharp linear appearance crosscutting the topography and by their white color. Faults, shear zones, and lineaments are mainly expressed by straight topographic alignments, dominantly streams or drainages. Small faults are inferred where apparent offsets can be mapped in the Permian limestones.

A drainage analysis was done using the aerial photograph overlapping to the north. The drainages were traced onto transparent mylar (Figure 5-21), and a 10-by-10 grid was superposed on the map. The numbers of drainages were counted for each cell, then contoured (Figure 5-22). This procedure was done to determine if some of the rock types could be characterized and separated based on their geomorphology. Drainage density is controlled by substrate porosity, permeability, jointing, fracturing, bedding, etc. The high density of drainages in the lower right corner corresponds to the area of Quaternary–Tertiary gravels, which are relatively unconsolidated and develop a fine dendritic drainage pattern. The east–west-trending high (value of 25) corresponds to the altered arkoses. The higher drainage density compared to similar unaltered rocks to the north may reflect physical breakdown of the rock due to alteration. The altered rock is softer than unaltered materials and more susceptible to drainage development. Bedrock areas have the lowest drainage density and develop a coarser overall texture.

B. Radar Data

1. Introduction. Microwave remote sensing is a relatively new field, initially developed during World War II. Active radar systems have been used to generate radar images for a variety of geoscience studies. Radar has several advantages and differences compared to conventional camera systems. The major advantage is radar's ability to penetrate clouds, smoke, and fog; in addition, because the system is an active one providing its own illumination, data can be obtained at virtually any time. The major difference lies in those physical parameters and characteristics that affect the radar backscatter and, hence, control the appearance of the imaged terrain. The signal strength returned to the radar antenna is a function of the transmitted power, wavelength, polarization, and viewing geometry. Geometric and physical properties of the surface also strongly influence the radar return. Surface roughness is one factor that determines whether an area will look bright or dark on a radar image. For root-mean-square (rms) surface roughness much less than one-tenth of the radar's wavelength, the surface will appear smooth and generally bright; for surface roughness approximately one wavelength, the surface will appear rough and dark since most of the transmitted energy will be scattered and little will be returned to the radar receiver. The electrical properties of the surface (complex dielectric constant) will also affect the radar return. Significant increases in the dielectric constant usually result from changes in moisture content; an increase in moisture content increases the reflectivity and therefore the level of the signal return (MacDonald, 1980).

Two different synthetic aperture radar data sets were examined for Helvetia: aircraft X-band data, in like- and cross-polarized returns, and satellite L-band radar data acquired by Seasat. The X-band data were at 3-cm wavelength, and the L-band were at 25 cm.

2. Aircraft X-band radar data. Two flight directions were used to obtain aircraft X-band data with Johnson Space Center's radar system: north–south and northeast–southwest with a depression angle of 40° to 60°. The look-directions were to the west and northwest, respectively. For each of the data passes, both like-polarized (HH) and cross-polarized (HV) data were acquired simultaneously. Examination of the two polarizations failed to reveal any significant differences between them. According to MacDonald (1980), where the terrain is rough in comparison to the radar wavelength, there should be little difference between polarizations. It is only for very smooth surfaces, such as grassland or marshland regions, that a marked difference will occur.

The north–south line is shown in Figure 5-23. The east sides of topographic features are bright (illuminated) and the west sides are shadowed. Two main characteristics of this image bring out geologic features: texture and linear features. The young alluvial fans on the west side of the range appear smooth; they are only weakly dissected and are fairly homogeneous. In marked contrast are the Quaternary–Tertiary gravel deposits in the southeastern quarter of the picture, which show an extremely well-developed drainage pattern and appear much "busier." The Tertiary–Cretaceous sediments and volcanics in the northeastern part of the scene show more rounded topography and a coarser drainage pattern. Granite, sediments, and other rocks forming the Santa Rita Mountains stand out in stark topographic relief.

Mapping of linear and curvilinear features is shown in Figure 5-24. These features are recognized mainly by

drainage alignments, straight drainage segments, and straight ridge crests. Some of these features correspond to mapped faults (i.e., Sycamore Canyon Fault). Thrust faults are not recognizable since they do not have topographic expression. Some features may correspond to previously unmapped faults. However, these were not field checked, so no conclusion can be made regarding their origin.

Similar features are observable on the northeast–southwest line (Figures 5-25 and 5-26). The interpretative map shows several elliptical features of unexplained origin and a large north–south-trending lineament going through the Rosemont District. The southern part of this feature corresponds to the mapped Deering Fault. However, the northern extension is not mapped and may indicate that this fault is more regionally extensive than previously recognized.

3. Seasat satellite L-band data. The Seasat orbital radar satellite operated for 3 months during 1978 and acquired 100-km swath-width images over 100 million square kilometers of the land and sea surface of the Earth. The system was an active L-band radar, with a depression angle of 70°. Because of this viewing geometry, extreme foreshortening resulted where foreslopes as seen by the radar exceeded about 20° (Ford et al., 1980). The scene covering the Helvetia area was digitally processed at JPL and covers about 100 by 100 km, centered over the Sierrita Mountains (Figure 5-27). The look-direction is from the west as can be inferred from the shadowing. The layover distortion is quite obvious in the mountains – all the peaks and ridges "lean" toward the west and topography is compressed on the west side of the mountains. The darkest areas in the scene (except for shadowed areas) are the tailings associated with the copper mines on the east side of the Sierritas. These are smooth relative to L-band wavelength and are inclined nonperpendicular to the look-direction; therefore, most of the radar signal is reflected away from the receiver.

Almost no tonal information can be seen relative to differences in rock type. The major variation is due to drainage density and topographic differences between bedrock areas (brighter) and alluvial regions (darker). Most of the information discernible in the data is related to topography. A lineament interpretative map of the image is shown in Figure 5-28. Some of the lineaments coincide with mapped faults depicted by Drewes (1980) such as the Sawmill Canyon and Duval Faults. Most of the lineaments do not correspond to recognized faults and are probably fortuitous straight topographic elements (drainages and ridges) that are not structurally controlled. Without detailed field examination, the cause of these features cannot be determined.

C. Landsat MSS Data

1. Introduction. The Helvetia Landsat data consisted of three scenes acquired in June 1974, March 1975, and October 1975. The data were computer processed for interpretation; the full scenes were interpreted at a scale of 1:500,000; subscenes were analyzed at 1:125,000. Processing algorithms used were decorrelation enhancement, band ratioing, and principal components analysis (see the Technical Appendix, Section 14, for details of computer algorithms). Color photographic products were made from the enhanced data for maximum display of information, and prints were used as working copy.

Landsat data were acquired in four spectral bands in the 0.5- to 1.1-μm wavelength region. Each scene covered an area of 185 by 185 km, with an instantaneous field of view of 80 m. The time of satellite overpass was approximately 10 A.M. local time, with repeat coverage of the same area every 18 days. Data were recorded in digital format for computer processing and enhancement.

2. Lineament analysis. The synoptic, equal-illumination images provided by Landsat present an ideal opportunity for examining the regional structural fabric of an area. Many workers have mapped lineaments from Landsat data. Shoemaker et al. (1978) used Landsat images to extend the known traces of the Bright Angel and Mesa Butte fault systems in northern Arizona. Sawatzky and Raines (1982) examined lineaments in Sonora, Mexico, using Landsat data. They interpreted lineaments from images, digitized the lineament data, then computed strike-frequency histograms and determined numerically significant trends. Maps depicting concentrations of linear features having significant trends were compared with geologic and geophysical data to produce a synthesis of a regional tectonic model. Details of their results will be discussed later in comparison with work done on Helvetia.

Computer processing of lineament data provides an objective method for evaluating what would otherwise be a hopeless mass of lines on a map. Often, visual inspection fails to reveal significant features or trends to be extracted from a lineament interpretation map.

An early study using mapped faults as input data was done by Carson (1969) for an area in southeastern Arizona and southwestern New Mexico. He digitized 2500 faults from published and unpublished geologic maps, then used a computer algorithm to count the length-weighted fault elements for 1° increments. Trends of higher than background values were plotted and indicated as "structural trends," which may correlate with tectonic boundaries or subsurface basement features (Figure 5-29). Carson found

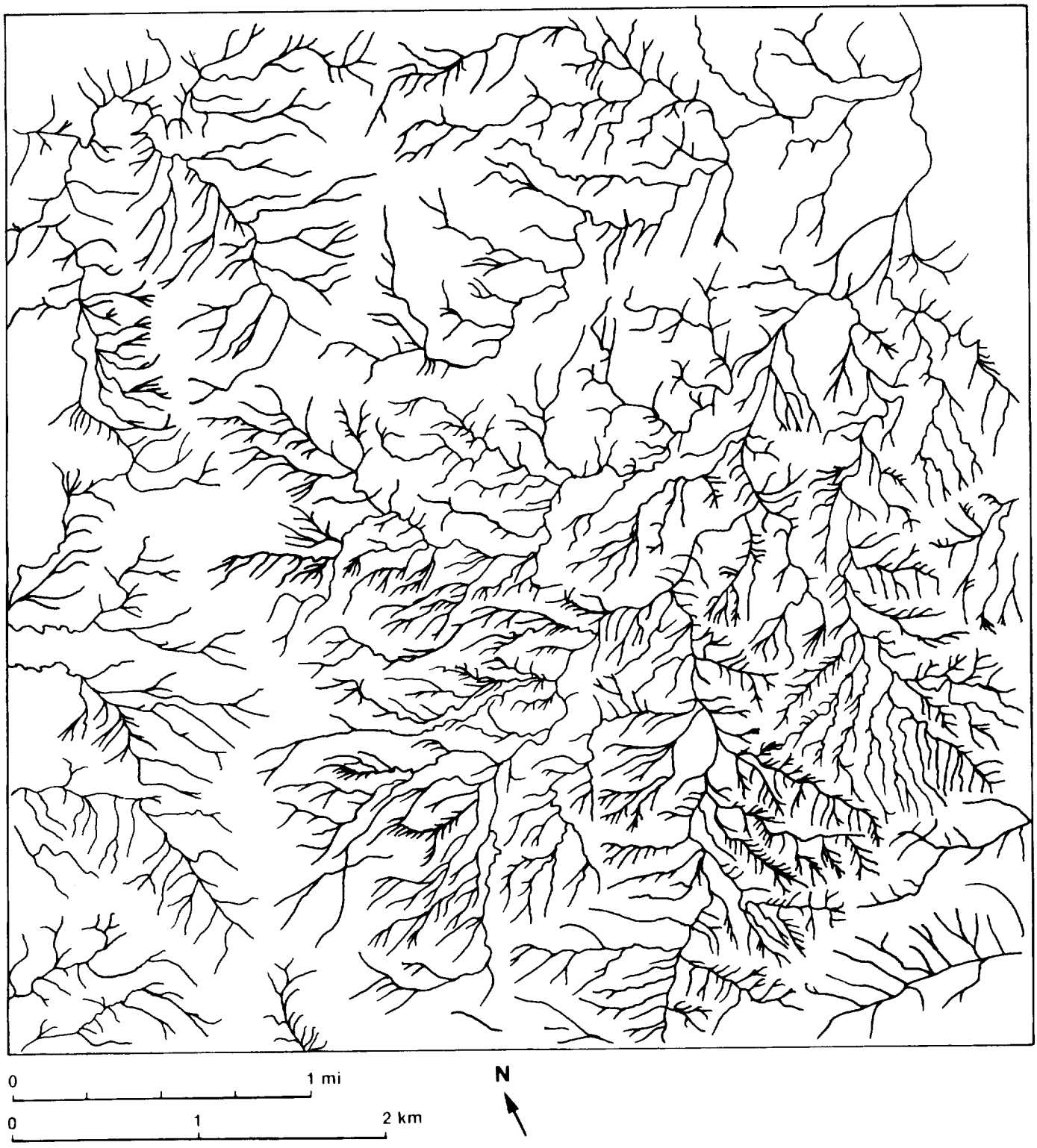

Figure 5-21. Drainage map produced by tracing streams and drainages from a color aerial photograph

C-3

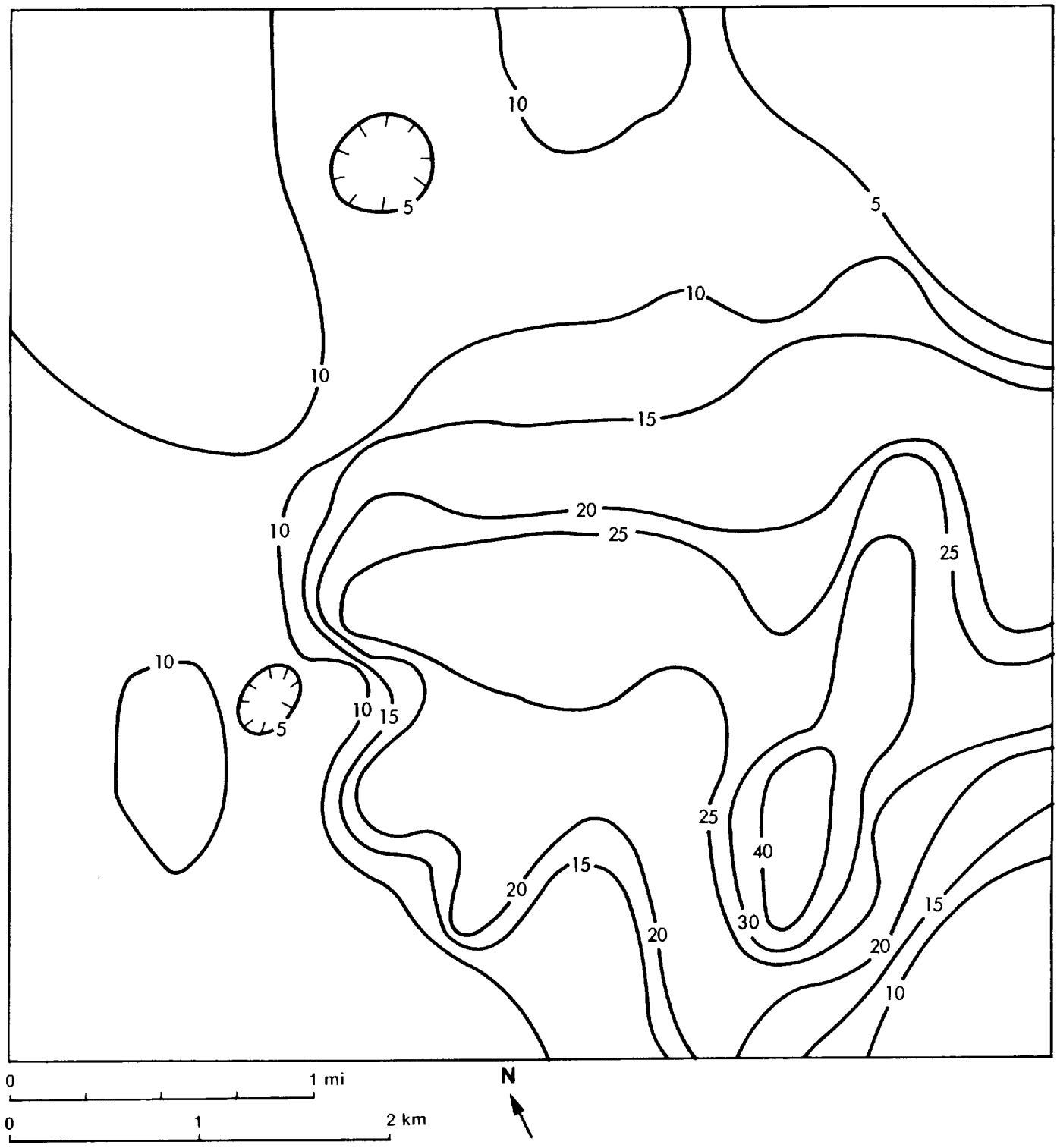

Figure 5-22. Contour map of drainage density from Figure 5-21. Highest density overlies Quaternary–Tertiary gravels in lower right corner of map.

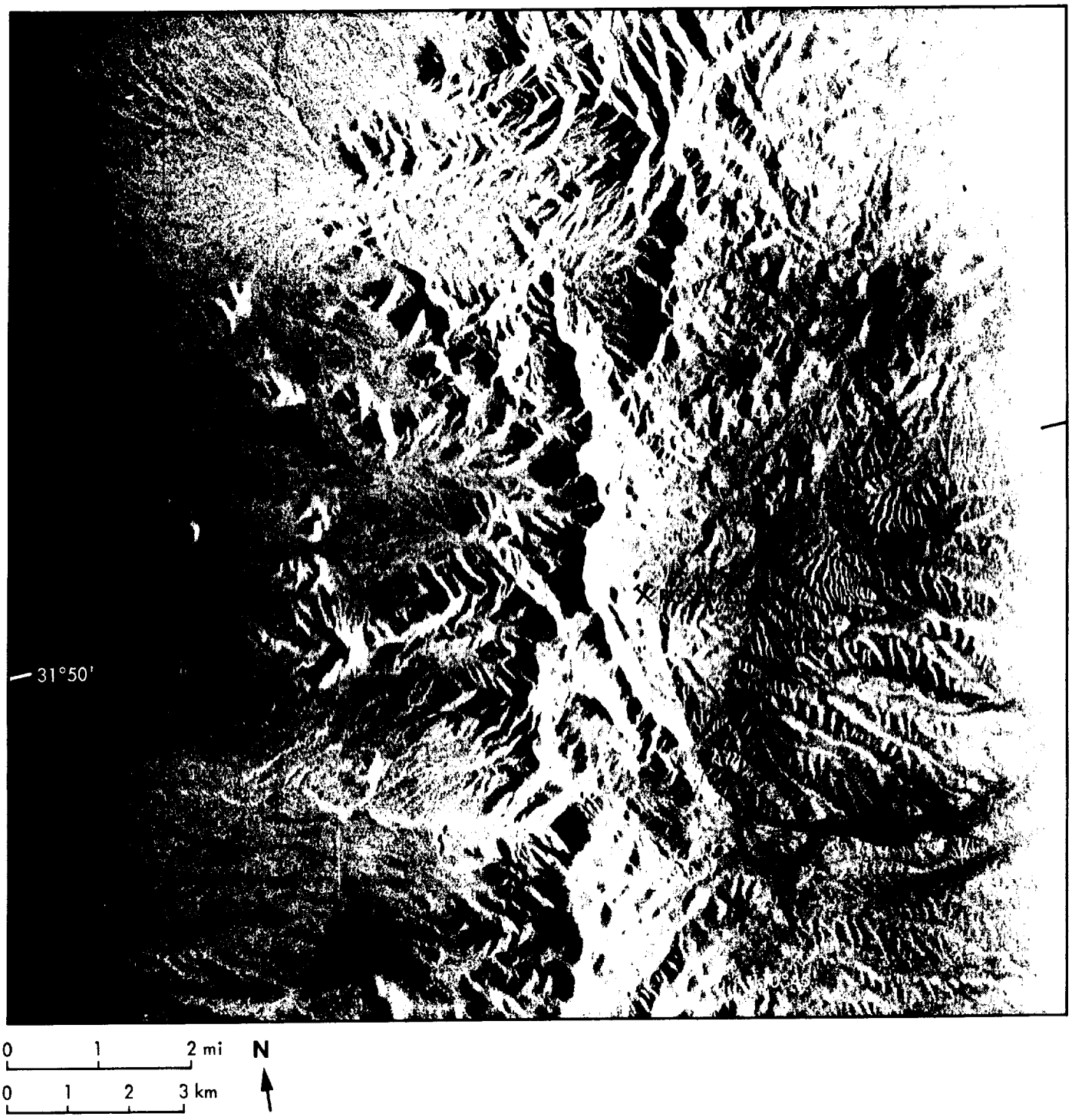

Figure 5-23. X-band aircraft image of the Helvetia–Rosemont area: north–south flight line with illumination to the west

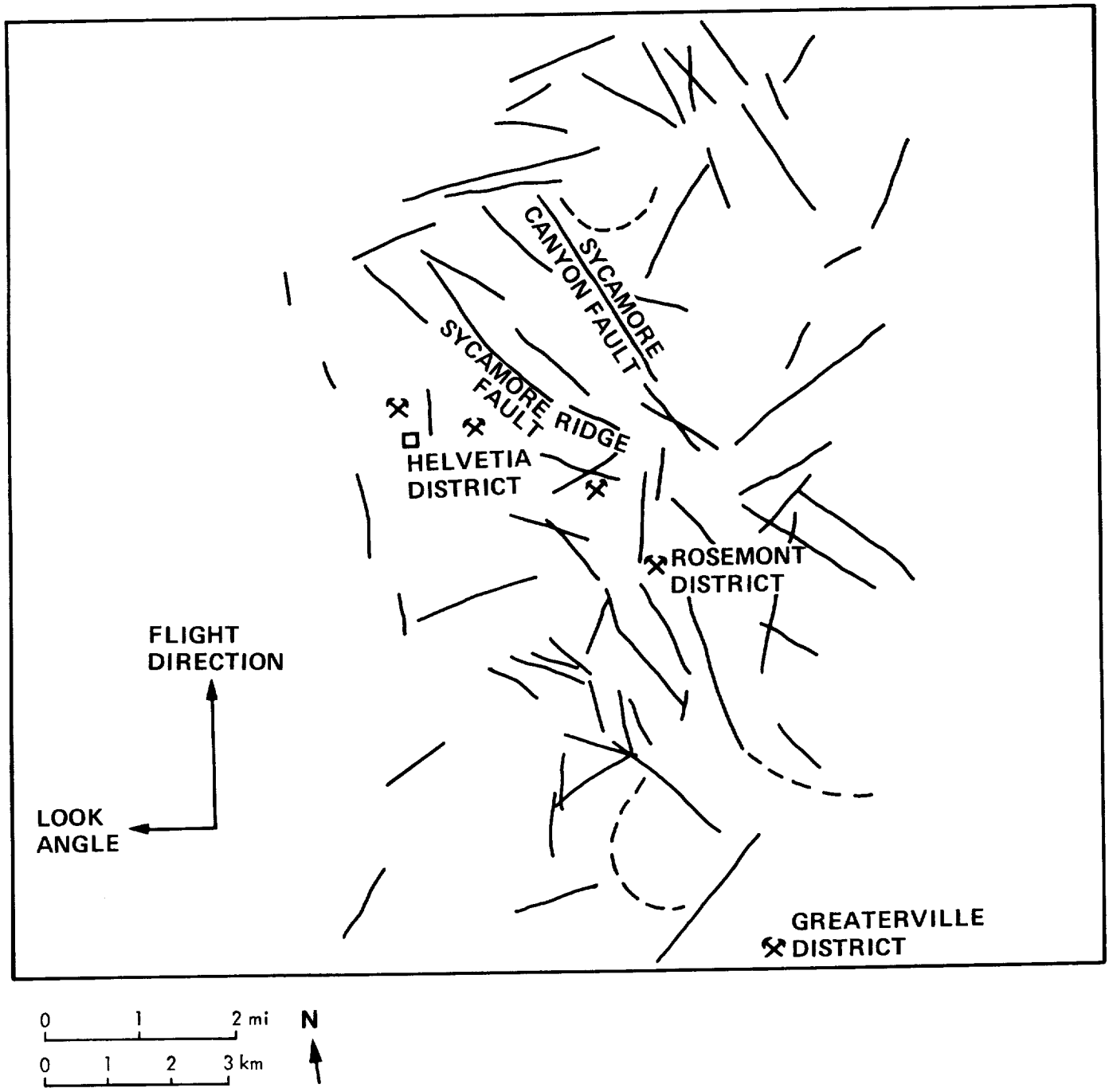

Figure 5-24. Interpretative map of Figure 5-23 showing linear features recognized and mapped faults

Figure 5-25. X-band aircraft image of the Helvetia–Rosemont area: northeast–southwest flight line with illumination to the northwest

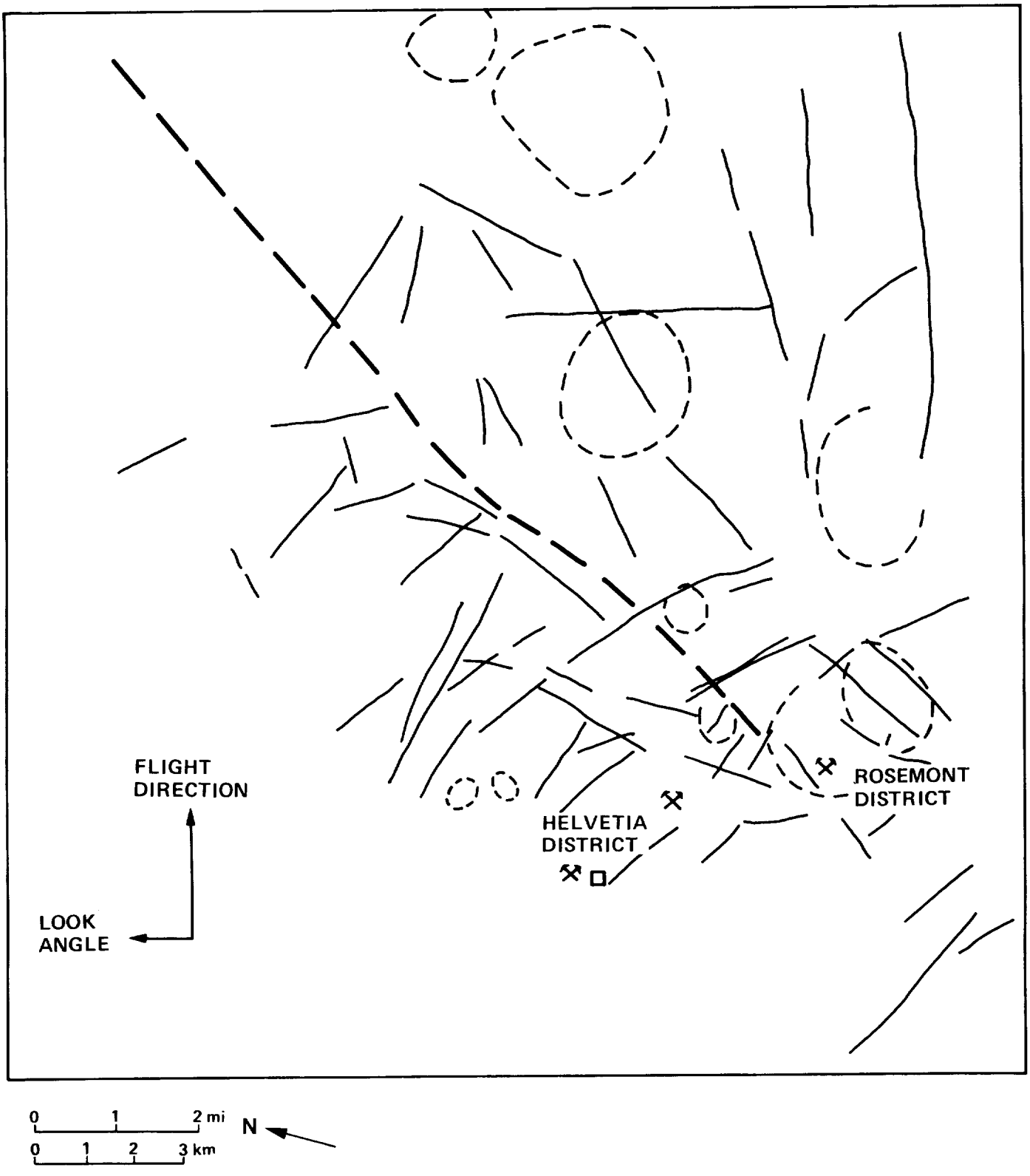

Figure 5-26. Interpretative map of Figure 5-25 showing linear features recognized and several topographically expressed elliptical features

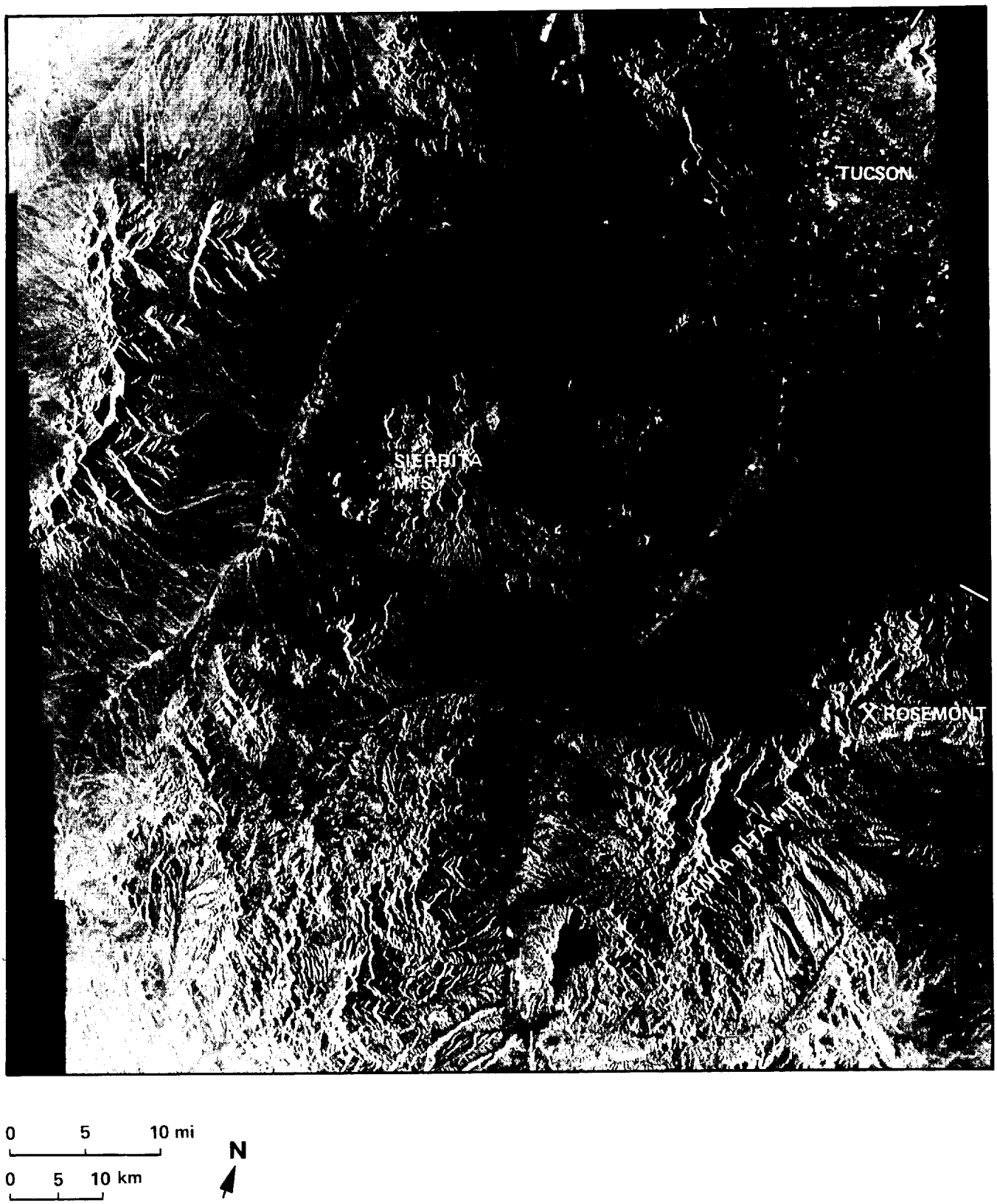

Figure 5-27. Seasat orbital L-band radar image including Helvetia–Rosemont area. Lithologic discrimination is minimal; the principal information that can be extracted is structural or topographic.

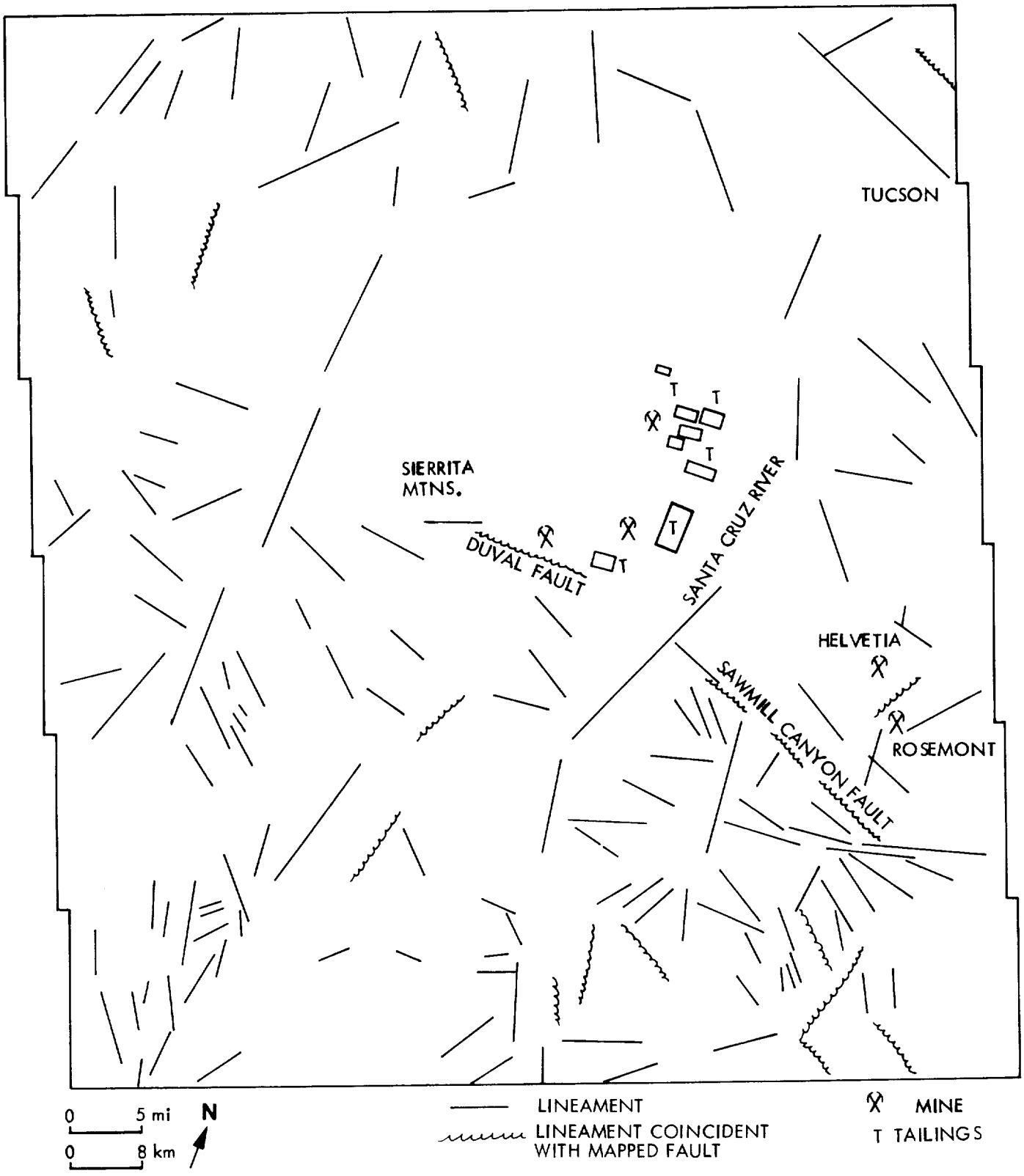

Figure 5-28. Lineament interpretation of Seasat radar data in Figure 5-27. Several lineaments correlate with mapped faults; most do not.

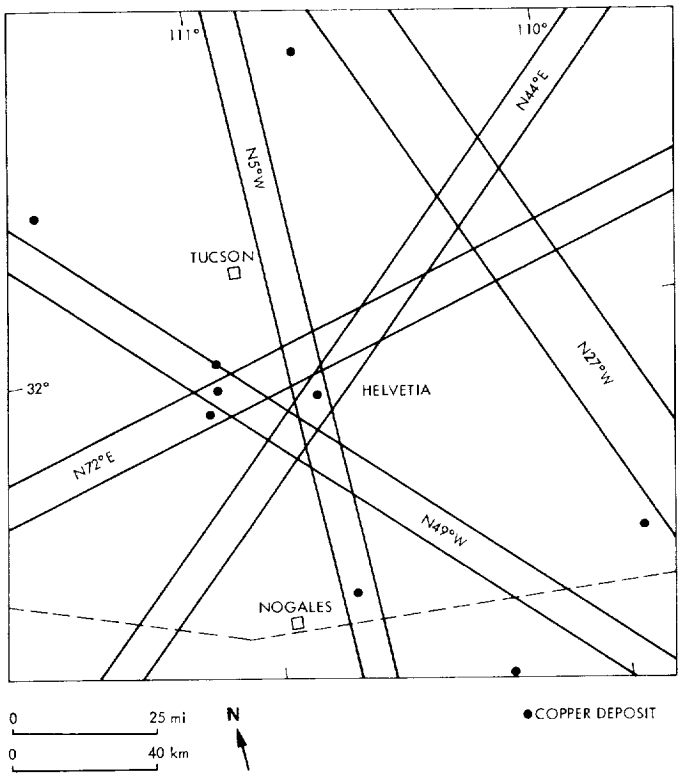

Figure 5-29. Structural trends in southeastern Arizona derived from analysis of mapped faults (Carson, 1969)

five trends in the area covered by the Helvetia Landsat coverage: N 49° W, N 27° W, N 5° W, N 44° E, and N 72° E, four of which intersect near the Helvetia, Pima/Mission, Twin Buttes, Sierrita, and San Xavier copper deposits. These will be compared with a similar analysis using Landsat data later in this section.

The October Landsat frame for Helvetia was interpreted for lineament features. In this analysis, a lineament is defined as a linear or curvilinear feature identifiable by an interpreter from an image. These features may be faults, fractures, joints, lithologic contacts, cultural features, or artifacts. They are expressed on the image by tonal or textural discontinuities or alignments. A map of the lineaments is shown in Figure 5-30. The product used for interpretation was a color composite of bands 4, 5, and 7 (false-color infrared composite). The October frame was selected as the one with the lowest sun elevation of the three scenes available to enhance topographic features; a color composite was used to enhance tonal or spectral boundaries. The lineament map was digitized, and computer algorithms were used to compute information. The frequency versus azimuth of lineaments for the entire scene was computed and plotted as a rose diagram (Figure 5-31). Three trends stand out above the background: N 50° W, N 45° E, and N 85° E. These correlate with three of Carson's trends based on map information. Davis (1981), in his paper on tectonics of southeastern Arizona, lists eight directions of deformation since Precambrian time (Table 5-10). The N 45° E trend appears to correlate with his older Precambrian trend, which is better expressed in northern Arizona (Shoemaker et al., 1978) and northern Sonora, Mexico (Sawatzky and Raines, 1982). The N 50° W trend corresponds to his Paleozoic and Mesozoic faulting and folding events. The N 85° E trend correlates with the Laramide faulting that was accompanied by intrusions and porphyry copper mineralization.

The lineaments were counted on a 10- by 10-km grid, and the total density was contoured (Figure 5-32) to examine the pattern of concentration and to assess how it might relate to regional tectonics. Also shown in Figure 5-32 are five tectonic boundaries, defined by Titley (1976), based on paleostratigraphic and fault evidence for Mesozoic boundaries. The lines define tectonic blocks, which have had different histories of deformation and sedimentation. The lineament density map is negatively correlated with Titley's boundaries; i.e., his lines correspond to density lows. This may be due to the development of valleys and thick sequences of valley fill along these structural zones, so that higher density of lineaments would be seen in the mountain blocks between the zones.

The major trend seen on the lineament contour map is a strong northwest grain. This correlates overall with Titley's northwest-trending structural blocks.

Comparison with Carson's trends based on map data (Figure 5-29) shows some correlation. His N 27° W trend corresponds to the lineament density high going north–northwest through the Dragoon Mountains. The N 49° W trend parallels the Sawmill Canyon trend and a series of lineament density highs. The N 44° E trend is weakly expressed by an alignment of density highs southwest of Nogales, in the Santa Rita Mountains, in the Rincon Mountains, and northeast of the Rincons. The N 5° W and N 72° E trends are not corroborated by the density map.

The Residual Aeromagnetic Map of Arizona (Sauck and Sumner, 1970) lends strong support to Titley's theory of northwest-trending structural blocks (Figure 5-33). The dominant magnetic grain is northwesterly. A large continuous zone of magnetic lows follows the Sawmill Canyon structure; a zone of highs lies along the Silver Bell–Bisbee structure. There is also excellent evidence for the Dragoon structure shown as a series of northwest-trending highs; Carson's trends match rather poorly with the magnetic data. This may indicate that his analysis, which relied on an uneven grid of ground mapping, may have used the wrong

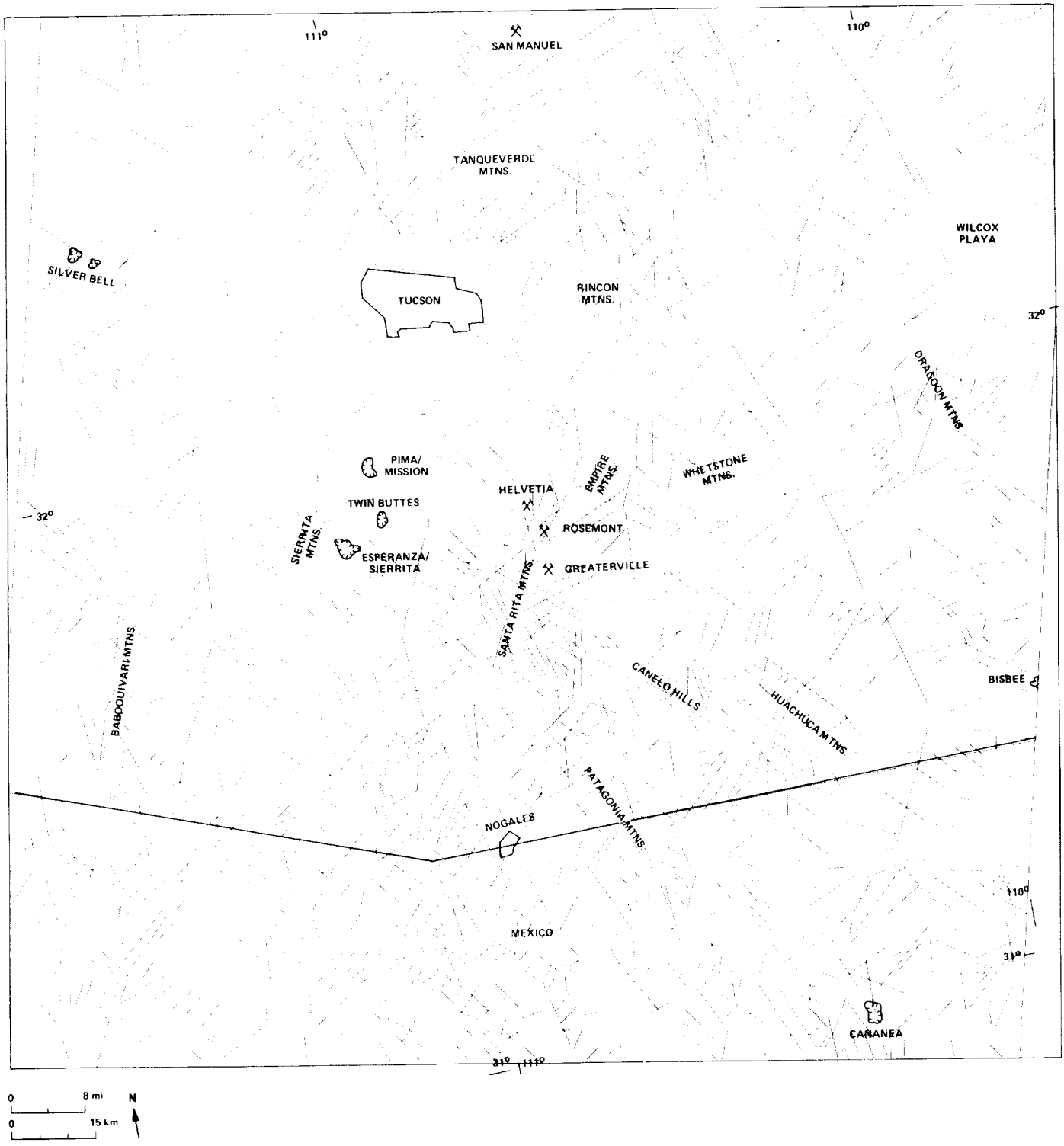

Figure 5-30. Lineament interpretation map produced from October 1975 Landsat scene over southeastern Arizona. The Rosemont–Helvetia test site is at the center of the map.

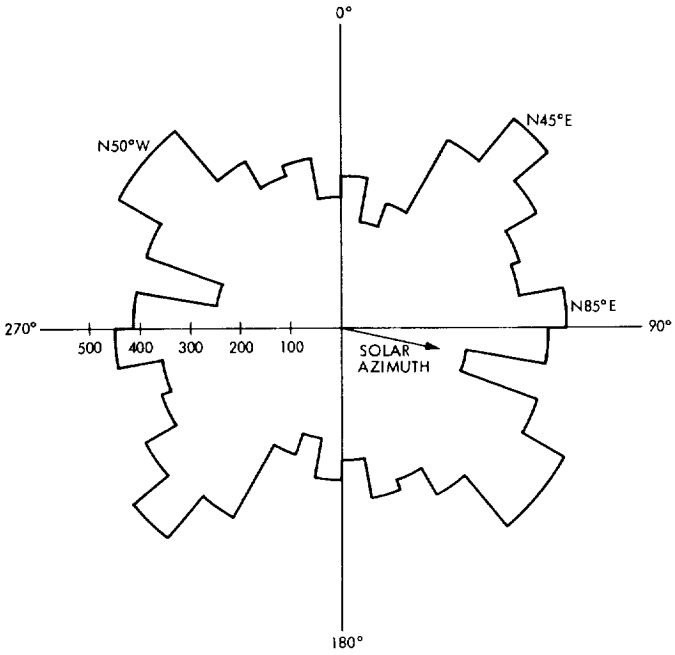

Figure 5-31. Rose diagram summarizing strike-frequency distribution of lineaments interpreted from Landsat scene. Trends above background occur at N 50° W, N 45° E, and N 85° E.

data base for structural analysis. This work was done prior to Landsat data availability, and this serves to emphasize one of the major uses of Landsat data.

Sawatzky and Raines (1982), in their Landsat interpretation of Sonora, Mexico, recognized zones of northeast-trending lineaments which they interpreted as zones of shearing. These zones were intersected by northwest-trending zones. The intersections seemed to have a high correlation with occurrence of alteration and mineral deposits.

The U.S. extension of their northwest-trending zone lines up with the lineament density high between Nogales and the Baboquivari Mountains, also defined by Titley as the Comobabi–Nogales zone. One of their northeast zones, if projected into the United States, would extend through Nogales into the Helvetia scene. Some indication of this feature can be seen as an alignment of lineament density highs at Nogales and the Santa Rita Mountains.

3. False-color infrared composite. The June 1974 Landsat scene was processed using decorrelation stretching. This algorithm, developed by Soha and Schwartz (1978), is a color enhancement procedure. Data from bands 4, 5, and 7 were input into the program and a principal components rotation was performed. The data then fell on three new orthogonal axes. A stretch was performed on the new axes, and the stretched data were then retro-rotated back to the

Table 5-10. Deformations of southeastern Arizona[a]

Age	Direction	Nature
Older Precambrian	N 50° E	Folding
Precambrian	N 15° W	Rifting
Paleozoic	N 40° W	Faulting
Jurassic–Cretaceous	N 46° W	Folding, thrusting
Laramide	N 80° E	Faulting, intrusion
Paleocene–Eocene	N 31° W	Core complex deformation
Oligocene–Miocene	N 31° W	Faulting
U. Miocene	N 20° W	Basin–Range faulting

[a]After Davis (1981).

original 4–5–7 coordinate space. A color composite was made by displaying MSS bands 4, 5, and 7 as blue, green, and red, respectively (Figure 5-34). The effect of this process is to maintain the hue information and to exaggerate the intensity and saturation of the colors.

As a result, the processed picture is dominated by several colors. Heavily vegetated mountain areas are bright red; this changes to pink as the vegetation density decreases at lower elevations. The red color is due to high reflectance in band 7 by vegetation. Blue areas represent spectrally flat materials of varying albedo. Because Rayleigh atmospheric scattering is strongest at shorter wavelengths, spectrally flat materials have a blue contribution from the atmosphere in band 4, stronger than the scattering component in the red or infrared. Blue areas also include tailings piles at mine locations, basalts, and Wilcox Playa. These areas contain materials whose spectral reflectance values are about the same in each of the Landsat bands, although of different overall albedos.

Green and yellow areas coincide with valley fill material and sediment trains derived from outcropping intrusive rocks. Spectrally, the green color arises from materials whose reflectance in band 5 is much higher than in band 4, and the same or higher than in band 7. Materials having iron oxides on the surface are the main class that fits this scheme. Similarly, yellow areas are those having high reflectance in bands 5 and 7. Iron-oxide-stained soil or rocks with some vegetation growing on them meet these requirements. Indeed, most of the yellow areas are older, more dissected alluvial fans, which support a higher density of vegetation than younger fans.

Comparing this image with the geologic map of Arizona (Figure 5-35) indicates that in some areas geologic units are separable on the image; in others they are not. In the northwestern part of the scene, Tertiary volcanic rocks are all dark blue (around Silver Bell, west of Tucson, and at

the northeast end of the Baboquivari Mountains). In the Tortolita Mountains northwest of Tucson, a clear distinction is seen between the pink northwestern half and the blue–pink southeastern half of this mountain range. The map indicates Precambrian granite as the major rock type, with only small outcrops of gneiss in the southwest. The image suggests that the map may be incorrect. The geology in the Tanqueverde and Rincon Mountains north and east of Tucson is obscured on the image by heavy vegetation cover. On the east and south flanks of the Rincons, Tertiary granite appears pink; Paleozoic sediments are bright blue. North of the Dragoon Mountains and west of Wilcox Playa, Tertiary granite is again pink; Paleozoic limestone is medium blue. Vegetation again obscures the geology in the Dragoon Mountains.

In the Whetstone Mountains and Empire Mountains, Cretaceous sediments are green; vegetation covers most of the central part of the Whetstones. Outcrops of Paleozoic rocks southeast of the Whetstone Mountains are dark blue. The Tertiary granite outcrop in the center of the Empire Mountains appears as an orange spot, distinct from the surrounding sedimentary rocks.

The area around Helvetia shows little detail at this scale, except for a yellow–orange spot east of Rosemont, corresponding to the hematitic arkose outcrop. While the main body of the Santa Ritas to the south is heavily vegetated, the block of Tertiary volcanic sediments to the southwest appears dark blue and pink, indicating differences in lithology not shown on the map.

The Huachuca Mountains are heavily vegetated. Similarly, little detail is discernible in the Canelo Hills. The area between the Canelo Hills and the Patagonia Mountains has blue areas (Tertiary arkose) and green areas (Tertiary rhyolite) clearly separated.

In the Sierrita Mountains, Tertiary granite appears pink. Tertiary volcanics are black to dark blue, and Paleozoic sediments are blue and light blue.

In this semiarid region, where vegetation is not abundant, good geologic discrimination is possible from this type of processed Landsat MSS image. A comparison with the published 1:500,000 state geologic map suggests that additional lithological information not shown on the map can be recognized. In more poorly mapped arid regions of the world, Landsat data can provide substantial geologic information suitable for reconnaissance mapping at a scale of about 1:500,000. At higher elevations, vegetation cover dominates the spectral response of the areas and obscures the underlying geology.

4. Color ratio composite

a. Introduction. Band ratioing of Landsat data for geological applications was first reported by Rowan et al., (1974). Ratioing is an effective method for distinguishing among rock types because the main spectral differences in the visible and near-infrared spectral regions are found in the slopes of the reflectivity curves. Absorption bands are broad and weak, and are difficult to use for discrimination of rock types on standard MSS images. In addition, the ratioing process removes first-order brightness effects due to topographic slope and enhances subtle color variations between materials.

By examination of spectral reflectance data, Rowan et al. (1974) determined that a composite of ratios 4/5, 5/6, and 6/7 would provide an effective means for discrimination of hydrothermally altered areas and of regional rock and soil units.

This combination was used to produce the color ratio composite (CRC) image presented in Figure 5-36. Band-ratios 4/5, 5/6, and 6/7 were assigned colors of blue, green, and red, respectively, to produce this CRC image. The June 1974 Landsat scene was used since it had the highest sun elevation and, therefore, the fewest shadows of the three scenes available. The image shown is a subscene covering an area of 40 by 40 km centered near Helvetia. The data were destriped, but no atmospheric corrections were applied.

b. Analysis and interpretation of image. The particular combination of band ratios and color assignments used displays vegetation in blue and iron oxides in red and orange. Typical spectra of vegetation (representative of chlorophyll reflectance in a general sense) and iron oxides are shown in Figure 5-37. The Landsat bandpasses are also indicated. Calculated ratio values for 4/5, 5/6, and 6/7 are shown in Table 5-11.

Vegetation has a relatively high 4/5 value due to high reflectance in the green part of the spectrum (band 4) and low reflectance in the red (band 5) due to absorption of energy by chlorophyll. The infrared response in bands 6 and 7 produces a ratio less than 1. The 5/6 value is low, also due to the chlorophyll band. Iron oxide has a low 4/5 value due to the sharp falloff in reflectance toward the ultraviolet, and a ratio greater than 1 in the 6/7 value due to the ferric iron absorption band near 0.9 μm. Therefore, iron-oxide areas will have a strong red component (high 6/7 value), no blue component (low 4/5 value), and a green component (high 5/6 value). These areas will appear orange to red depending on the relative amount of green.

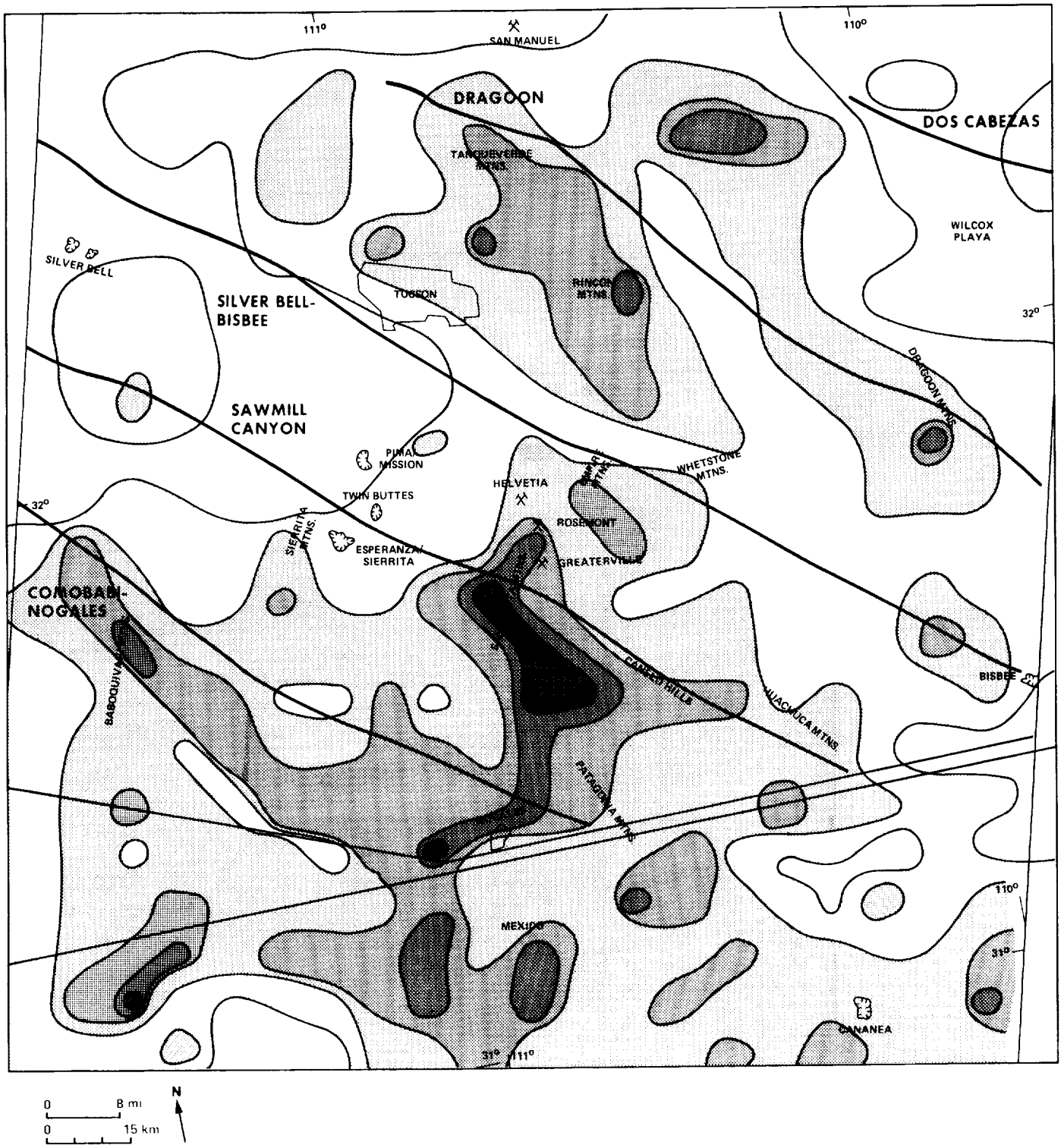

Figure 5-32. Contour map of lineament density using data from Figure 5-30. Also shown are northwest structural trends from Titley (1976). Contour interval is three lineaments per grid cell; the darkest pattern encloses areas with lineament density greater than 16.

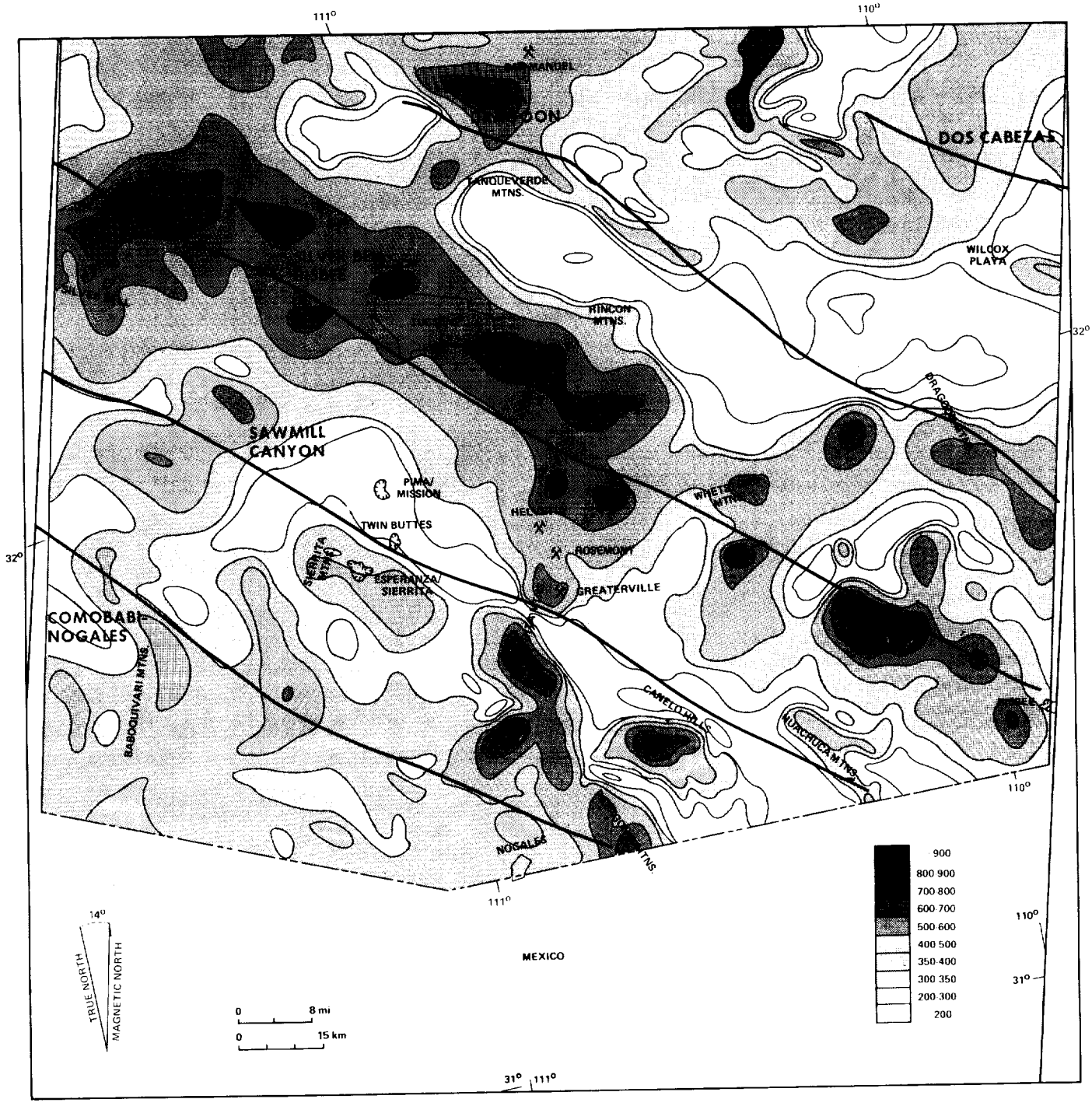

Figure 5-33. Simplified residual aeromagnetic map of southeastern Arizona with Titley's (1976) northwest trends superposed (map from Sauck and Sumner, 1970)

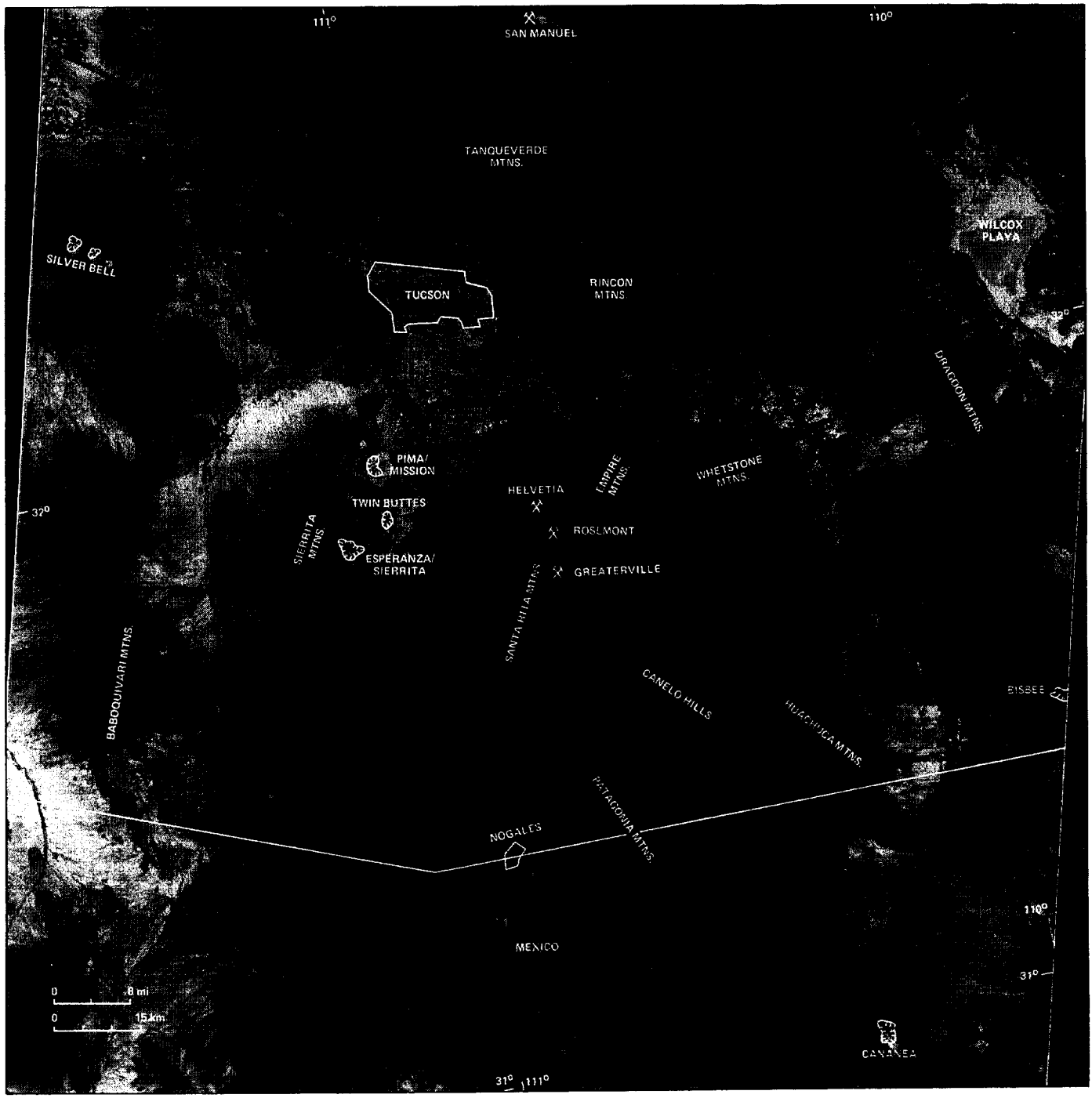

Figure 5-34. False-color infrared composite of Landsat scene 1678-17210 acquired June 1, 1974; MSS bands 4, 5, and 7 are displayed as blue, green, and red, respectively

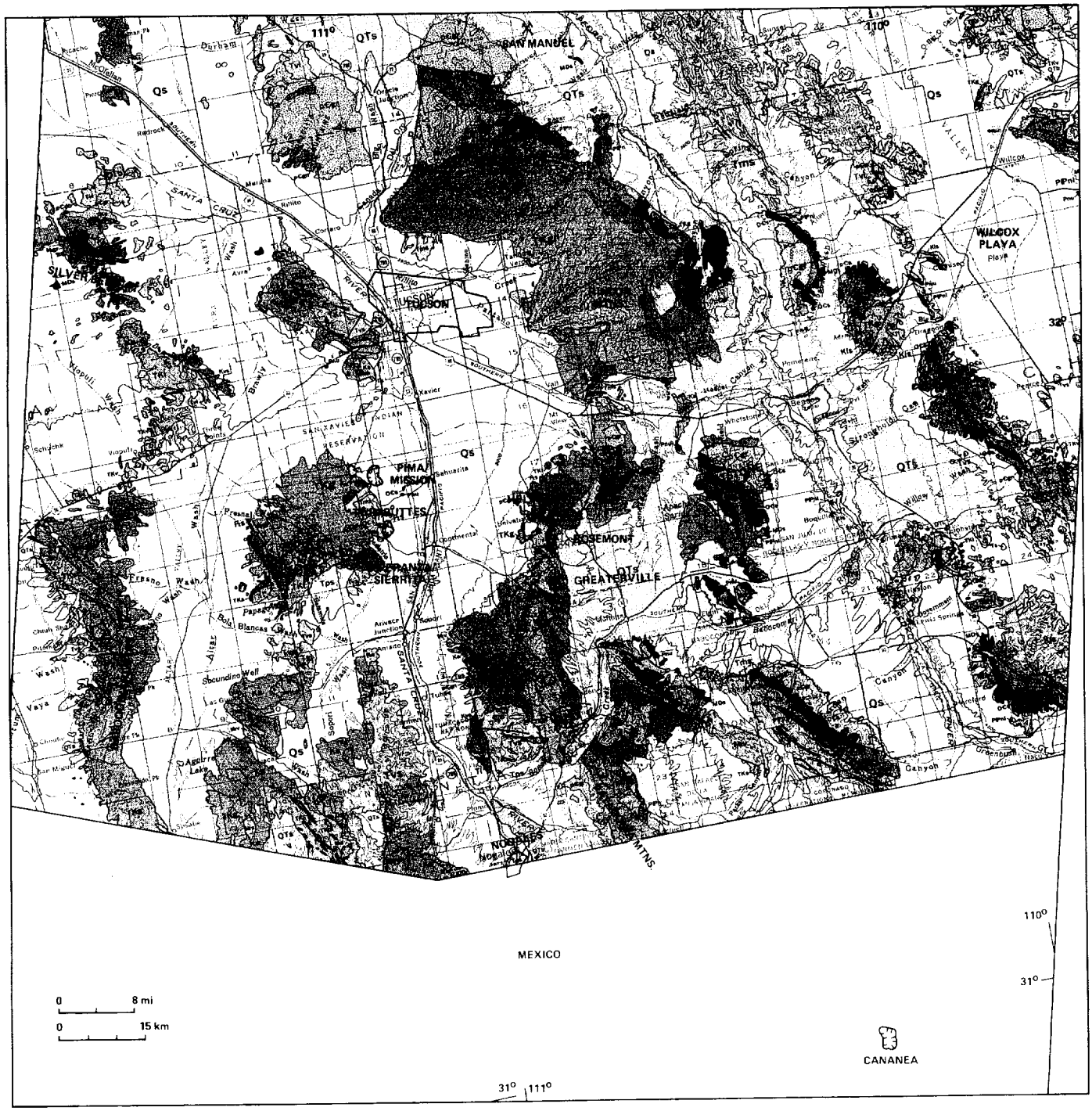

Figure 5-35. Geologic map of Arizona covering area of Landsat frame in Figure 5-34 (Wilson et al., 1969)

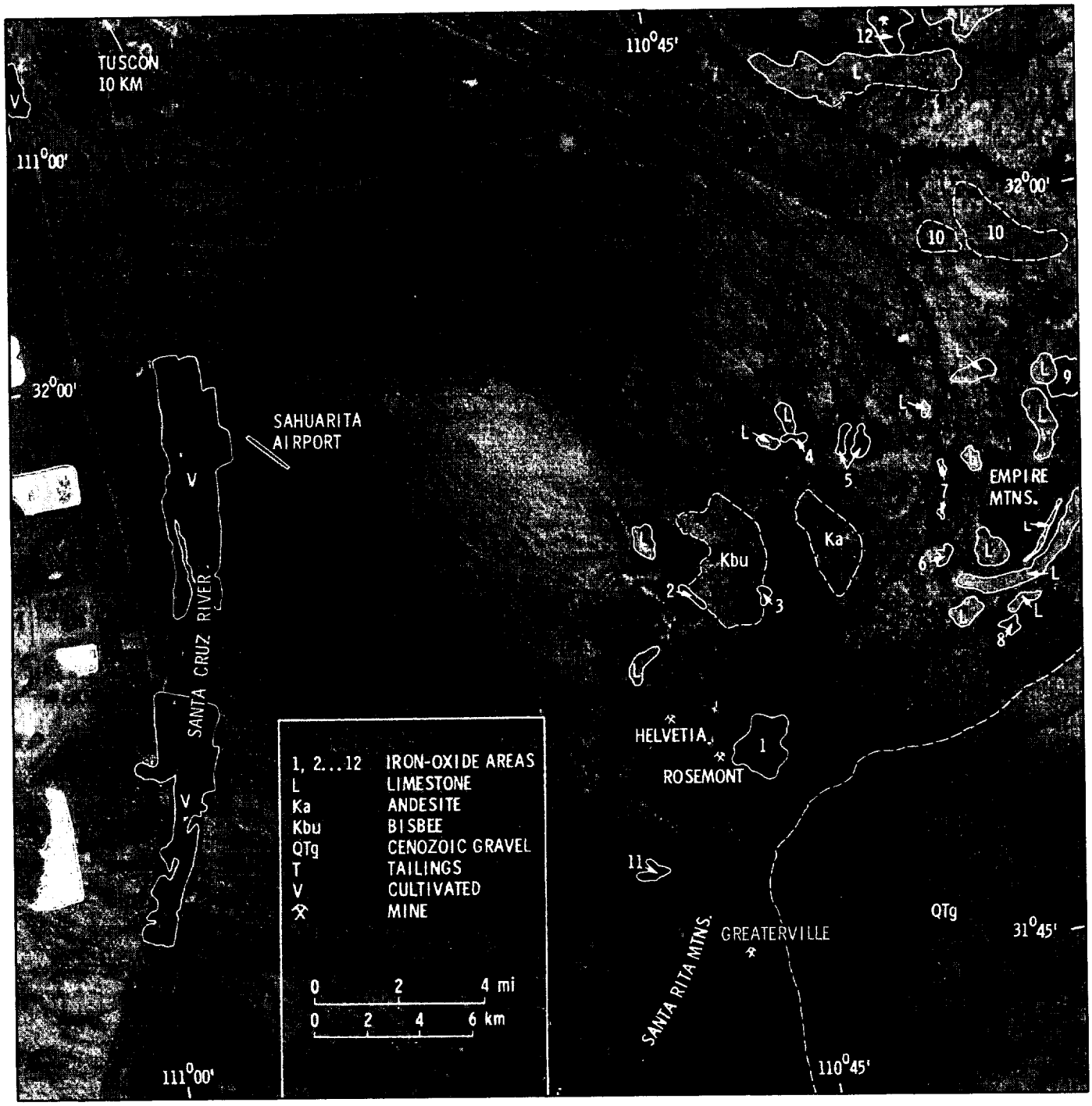

Figure 5-36. Landsat color ratio composite of 40- by 40-km subarea centered near Helvetia. MSS band-ratios 4/5, 5/6, 6/7 are displayed as blue, green, and red, respectively. Interpretative overlay shows lithologic units and areas of iron oxide. Solid and dashed lines indicate sharp and gradational contacts, respectively (Landsat scene 1678-17210, June 1, 1974).

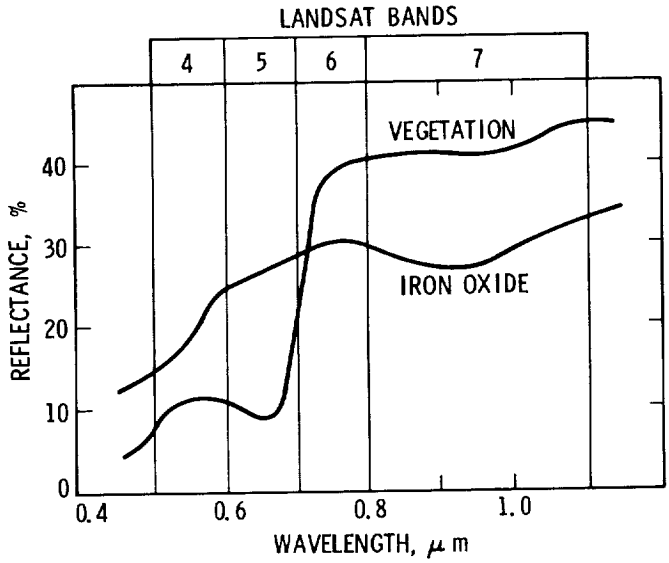

Figure 5-37. Typical spectral reflectance curves for vegetation and iron oxide. The Landsat MSS band intervals are also indicated.

Twelve iron-oxide areas are outlined in the CRC image (Figure 5-36), excluding red–orange areas obviously corresponding to alluvium or gravels. Area 1 is the hematitic arkoses east of Rosemont. Area 2 is a linear zone in Sycamore Canyon, where altered latite porphyry occurs. Area 3 was not field checked and remains unexplained. Outcrops of altered latite porphyry also occur in areas 4, 5, 6, and 7, near and west of the Empire Mountains.

The Cuprite Copper Mine is located within area 4; pits and prospects are found within the other three areas of alteration. Areas 8 and 12 correspond to outcrops of Tertiary conglomerate. Drewes (1980) describes the rock as a red, poorly indurated conglomerate. The presence of a mine in area 12 (the Heavy Boy Copper Mine) is puzzling since no intrusive is mapped nearby. Areas 9 and 10 are parts of the Bisbee Formation; locally the Bisbee is quite ferruginous, explaining its appearance on the CRC image. Area 11 is located in Precambrian granite and was not field checked.

Paleozoic limestones (L in Figure 5-36) are separable by their light-blue color. They are recognizable wherever they are not covered with heavy vegetation. There is some separation of parts of the outcrops of the Bisbee (Kbu) and andesite (Ka), although these units do not appear the same elsewhere on the image, presumably due to lithologic changes.

Table 5-11. Reflectance and calculated ratio values for vegetation and iron oxide

Material	MSS Band				Ratio		
	4	5	6	7	4/5	5/6	6/7
Vegetation	12	10	33	41	1.2	0.3	0.8
Iron oxide	18	27	30	28	0.7	0.9	1.1

Areas labeled V are cultivated fields along the Santa Cruz River. The dark-blue color was explained earlier. Heavy vegetation also occurs along stream drainages and at higher elevations of the Santa Rita Mountains. Areas labeled T are tailings associated with mining activities.

The large white area in the center of the image corresponds to alluvial material derived from limestone outcrops to the southeast. Indeed, it is possible to identify the drainage feeding this area and to trace it back toward the mountains and limestone source area; the drainage appears as a thin, white stream.

The variable appearance of other alluvial areas reflects differences in composition of the parent source material, different weathering conditions, and variable vegetation cover. Most of the drainages discernible on the image appear in blue colors due to the presence of moderate to heavy vegetation. The dominant orange–red color of the fans is due to the presence of iron oxides on the surface. The source for the iron oxides is either due to a weathering phenomenon (oxidation of mafic materials) or reflects the presence of iron-oxide minerals in the parent source materials. The area marked QTg in the southeast corner of the image is green to blue in color, generally indicating a lack of iron-oxide minerals and the presence of a moderate vegetative cover.

Overall, the lithologic information interpretable from the color ratio composite is limited by the presence of vegetation, the modest spatial resolution of the Landsat MSS, and the small number of spectral bands available. Areas with iron oxides present on the surface are readily identifiable; this provides valuable information relating to the search for possible hydrothermally altered rocks.

5. Principal components analysis

a. Introduction. Principal components analysis (PCA) has been used in statistical processing of data for a considerable time (Hotelling, 1933) and is well illustrated in many texts (Davis, 1973, for example). The method produces new uncorrelated variables (components), which are linear combinations of the original variables and are orthogonal to each other. The new axes for the variables are computed to maximize the scene variance along the first axis or component containing the greatest proportion of the variance,

followed by the next components which contain successively less of the scene variance. In this fashion it is often possible to ignore the latter components because they contain little or no useful information. This is especially true with Landsat data; thus, the original four MSS bands can often be reduced to the first three principal components (PCs). Geometrically, PCA can be viewed as a rotation and translation of the original coordinate axes to new axes passing through the data. A hypothetical example in two-dimensional space is shown in Figure 5-38.

PCA is a method for reducing the dimensionality of data by removing intervariable correlation and compressing it onto one or a few new axes, usually less than the total original data. In Landsat data, about 80 to 90 percent of the scene variability can be accounted for by the first PC. This variable is usually an average of the values of the four bands, i.e., albedo (Podwysocki et al., 1977). The components can be combined into a color display by assigning blue, green, and red colors to any triplet of the available variables.

b. Analysis of Helvetia PCA. The October Landsat data for the 40- by 40-km Helvetia subscene were processed using PCA. The eigenvalues, percent variation, and loadings for each of the components are shown in Table 5-12. In addition, the loadings are plotted in Figure 5-39.

The first component accounts for 92 percent of the scene variability. The coefficients for the four MSS bands are all positive and about equal. This component can be interpreted as albedo; most of the information in the scene is therefore related to the overall brightness of the materials and not to any absorption bands in their spectral reflectance response. This also implies that the four bands are very highly correlated; when the reflectance increases in one band, it also increases in other bands. The second component accounts for 6 percent of the variability in the scene. It is positively weighted on the infrared bands (6 and 7) and negatively weighted on the green and red bands (4 and 5). This component would tend to emphasize vegetation since vegetation has high reflectance in the infrared bands and relatively low reflectance in the green and red bands. Component 3 accounts for 1 percent of the scene variability; it is heavily weighted on band 4, with lesser weighting on bands 5 and 7. The fourth component accounts for less than 1 percent of the variability and is positively weighted on band 6 and negatively weighted on bands 5 and 7.

Table 5-12. Eigenvalues, variability, and loadings for Helvetia MSS PCA

Component	Eigenvalue	Total Variance, %	Band Loadings			
			4	5	6	7
1	1177	92	0.36	0.65	0.55	0.38
2	81	6	-0.38	-0.49	0.33	0.72
3	11	1	0.85	0.46	-0.15	0.21
4	8	<1	0.07	-0.36	0.75	-0.55

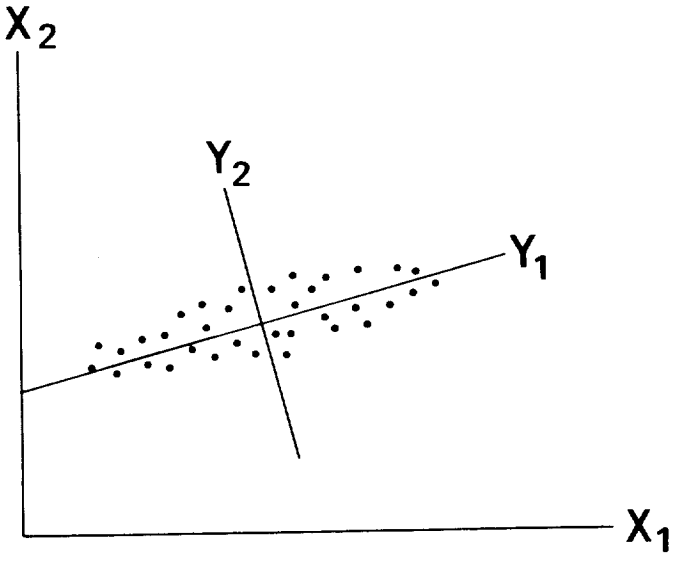

Figure 5-38. Elliptical scatter pattern of data in two multispectral channels, X_1 and X_2. The PCA creates a new set of coordinate axes (components) such that the first component (Y_1) accounts for most of the variability. The second axis (Y_2) is chosen orthogonal to the first.

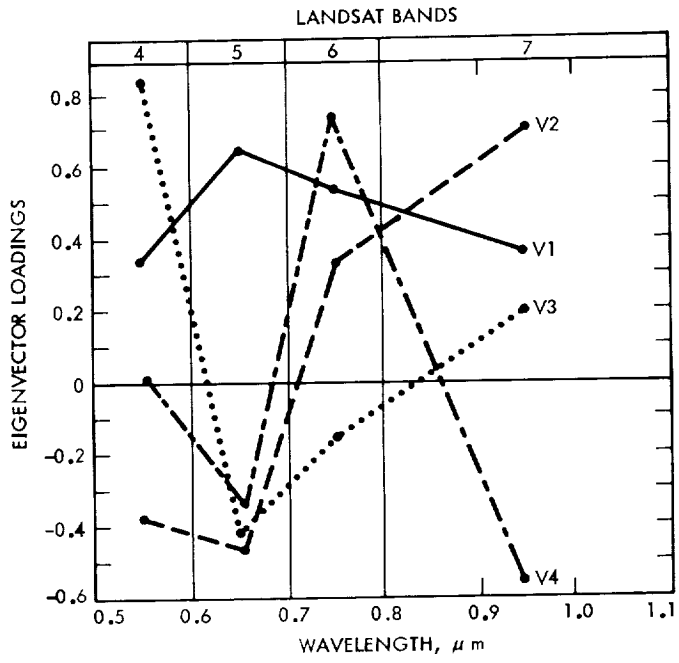

Figure 5-39. Eigenvector loadings for Landsat PCs (V1, V2, V3, V4). Landsat MSS band intervals are shown at the top of the figure.

The individual components were examined as black-and-white images; the first three components showed tonal variations in the scene. The fourth component was made up mainly of noise and thus contained the least amount of usable information. Therefore, the first three components were used to make a false-color composite. Examination of several different combinations led to the selection of one particular display which presented color differences in a pleasing manner to the analyst. Other combinations are equally permissible; however, an individual's bias or preference for certain color schemes dictates the choice of a particular combination. The image shown in Figure 5-40 used the first three components, with color assignments for components 1, 2, and 3 (called V1, V2, and V3) of magenta, yellow, and cyan, respectively. These colors were produced by complementing the primary colors green, blue, and red.

The colors that appear on the image can be related to the spectral reflectance of the surface materials in the following manner. First, typical Landsat reflectance values are determined or measured for several materials. In this example, vegetation, goethitic iron oxide, hematitic iron oxide, and limestone were used (Table 5-13). Reflectance values were calculated from PFRS spectra for these materials in the equivalent MSS bandpasses.

These values were convolved with the factor loadings for the first three components to compute PC values. For example, vegetation in V1 would be:

$$\text{Veg (V1)} = 0.36\,(12) + 0.65\,(10) + 0.55\,(33) + 0.38\,(41) = 44$$

Values for the four materials in the three components are shown in Table 5-14.

Using these relative values, it is possible to predict the color that would result on the images. The PC values were normalized to determine the relative contribution of the three colors (Table 5-14). The range of values for each raw PC was first rescaled to 0 to 100; for example, the raw V1 values (44, 51, 34, and 43) became 59, 100, 0, and 53. Next, the rescaled PC vectors for each of the four materials were expressed as fractional values; for example, rescaled vegetation values of 59 (V1), 100 (V2), and 100 (V3) became normalized values of 0.22 (59/259), 0.39 (100/259), and 0.39 (100/259). Plotting these values on a ternary diagram (Figure 5-41) shows that goethitic iron oxide lies near the magenta (V1) point, vegetation lies equally between cyan and yellow on the green line, limestone lies equally between magenta and cyan on the blue line, and hematitic iron oxide lies near the yellow point. Examining the color image (Figure 5-40) indicates that vegetation in the Santa Rita Mountains and in cultivated fields along the Santa Cruz River is green; the hematitic arkose east of Rosemont is orange–yellow; the goethitic alluvial fans along the Santa Cruz River are magenta; and the limestone outcrops, such as those in the Empire Mountains, are blue.

A more detailed interpretation map of the color PC image is shown in Figure 5-42. Alluvial areas and terrace gravels are magenta (goethitic), orange (hematitic), or blue/cyan (material derived from limestone source areas upstream). They can be identified as alluvium, based on their geomorphic appearance; drainages are well developed with little or no topographic relief. The Santa Cruz River Valley and Cienega Creek are green where there are cultivated fields or heavy vegetation. The Santa Rita Mountains are dominantly green due to heavy vegetation cover. Occasionally, nongreen areas appear where vegetation is less and bedrock or soils show through. Paleozoic limestones are various shades of blue. Arcuate outcrops are traceable on the southeast flank of the Empire Mountains; small outcrops are mappable around Helvetia and at the bottom edge of the image on the east and west sides of the Santa Rita Mountains. Orange to red areas exclusive of the pediments correspond to several different units. Those associated with limonitic alteration are indicated with the stipple pattern on the map. These areas are outcrops of quartz latite porphyry or quartz monzonite in the Empire Mountains, and hematitic arkose east of Rosemont. They all correspond to areas of hydrothermally altered rocks and have past or present mining activities. Other limonitic areas correspond to outcrops of Cretaceous conglomerate and red eolian sandstone east of Mt. Wrightson.

6. Comparison with stream sediment geochemistry. A detailed geochemical reconnaissance was performed between 1962 and 1969 and reported by Drewes (1973). Several hundred samples of alluvium were collected in the Santa Rita and San Cayetano Mountains and were analyzed by chemical and semiquantitative spectrographic methods for 29 to 39 elements. The distribution of high copper values is shown in Figure 5-43. A similar, although not identical, pattern was also mapped for lead, tin, zinc, silver, and molybdenum (not shown here). The highest concentrations of copper (225 to 3000 ppm) occur near Helvetia, Rosemont, northwest of Greaterville, and west of Mt. Wrightson. The Helvetia, Rosemont, and Greaterville anomalies are associated with ore deposits at these locations; the high concentration west of Mt. Wrightson was not explained.

Comparing the stream sediment geochemistry with the results of the Landsat analysis would provide a strong impetus for further interest in this region for mineral exploration. In the early stages of exploration, a reconnais-

Figure 5-40. PC color composite with geographic features referred to in text. The area covered is 40- by 40-km centered near Helvetia. PCs 1, 2, and 3 are displayed in magenta, yellow, and cyan, respectively (Landsat scene 20260-17145, October 9, 1975).

Table 5-13. Percent reflectances for surface materials

Material	Reflectance in MSS Bands, %			
	4	5	6	7
Vegetation	12	10	33	41
Goethitic iron oxide	18	27	30	28
Hematitic iron oxide	18	24	28	32
Limestone	15	20	25	30

sance program that started with regional Landsat analysis and followed up with geochemical surveying would have targeted the most promising areas for more detailed geological and geophysical work. The iron-oxide anomalies inferred from Landsat data at Rosemont and Greaterville, when considered in conjunction with the geochemical anomalies, would have provided sufficient justification for land acquisition and further development.

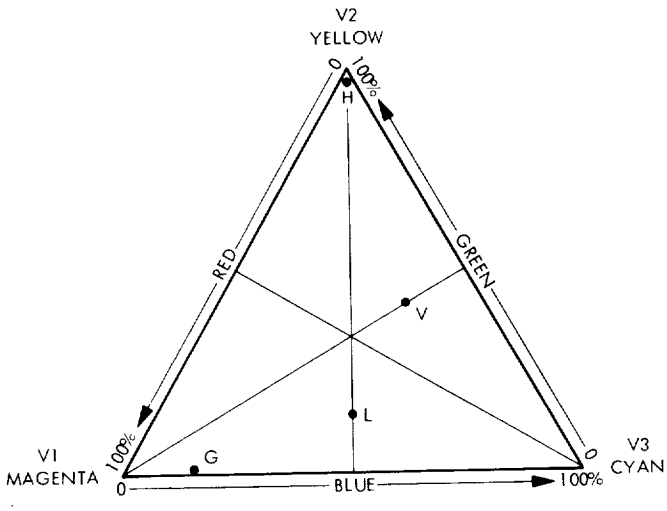

Figure 5-41. Ternary plot of PC values for representative Landsat reflectances of limestone (L), vegetation (V), hematitic iron oxide (H), and goethitic iron oxide (G). Values were normalized and plotted along magenta, cyan, and yellow axes.

V. Evaluation of Aircraft Multispectral Scanner Data

A. Introduction

Aircraft multispectral scanner data were acquired during three overflights with two instruments. The M²S 11-channel scanner was flown twice at approximately 12:00 noon local time: in August 1977 with an instantaneous field of view (IFOV) of 10 m and in May 1978 with an IFOV of 15 m; these overflights also provided a nighttime pass with only the thermal channel to examine the thermal characteristics of the surface. In October 1978, also near noon, data were obtained with the NS-001 Thematic Mapper Simulator with an IFOV of 12 m. Wavelength regions of the instruments are listed in Table 5-15. The areal coverage of each of the flights is shown in Figure 5-44.

B. M²S 11-Channel Data

1. Ratio composites

a. Landsat CRC equivalent. The August 1977 data were used to create a color ratio composite image. The bands used were 4/6, 6/8, and 8/(9 + 10); this combination was selected to simulate a Landsat 4/5, 5/6, 6/7 ratio composite (discussed in Paragraph IV.C.4) and to examine both the spectral information available and the improved spatial resolution capability. The three ratios were displayed in blue, green, and red, respectively (Figure 5-45). An interpretation map produced from this image is shown in Figure 5-46.

With this particular color scheme, vegetation will be blue; iron-oxide-bearing rocks will be in shades of red. A prominent feature seen on the image is a deep-red area east of Rosemont, corresponding to the hematitic arkoses of the Willow Canyon Formation (Kbwa). Orange areas in the scene correspond to outcrops of Precambrian granite, altered quartz latite intrusive, Cretaceous volcanic and sedimentary rocks, and Paleozoic sedimentary rocks. Limestones appear as light yellow to white (Rainvalley and Concha Formations in the northern part of the scene) where they are unaltered. Concha Limestone outcrops containing considerable organic matter appear gray northeast of Rosemont. Outcrops of tactite-altered limestone at Rosemont appear in pale-gold colors.

Table 5-14. PC values for four surface materials

Materials	Raw			Rescaled			Normalized		
	V1	V2	V3	V1	V2	V3	V1	V2	V3
Vegetation	44	31	9	59	100	100	0.22	0.39	0.39
Goethitic iron oxide	51	10	4	100	0	16	0.85	0	0.15
Hematitic iron oxide	34	12	3	0	9	0	0	1.0	0
Limestone	43	15	6	53	24	50	0.41	0.20	0.39

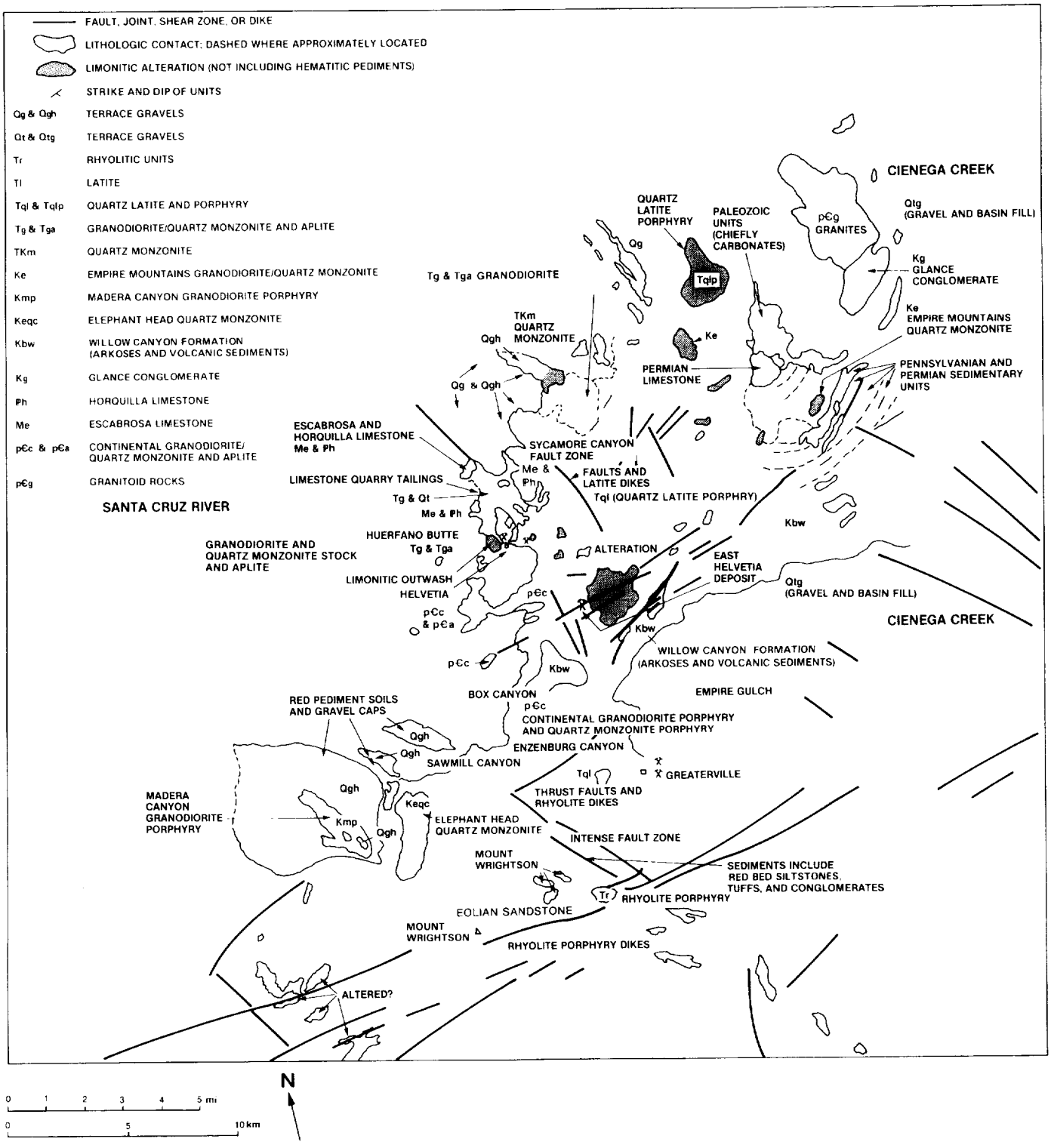

Figure 5-42. Geologic and alteration interpretation map of PC color image shown in Figure 5-40

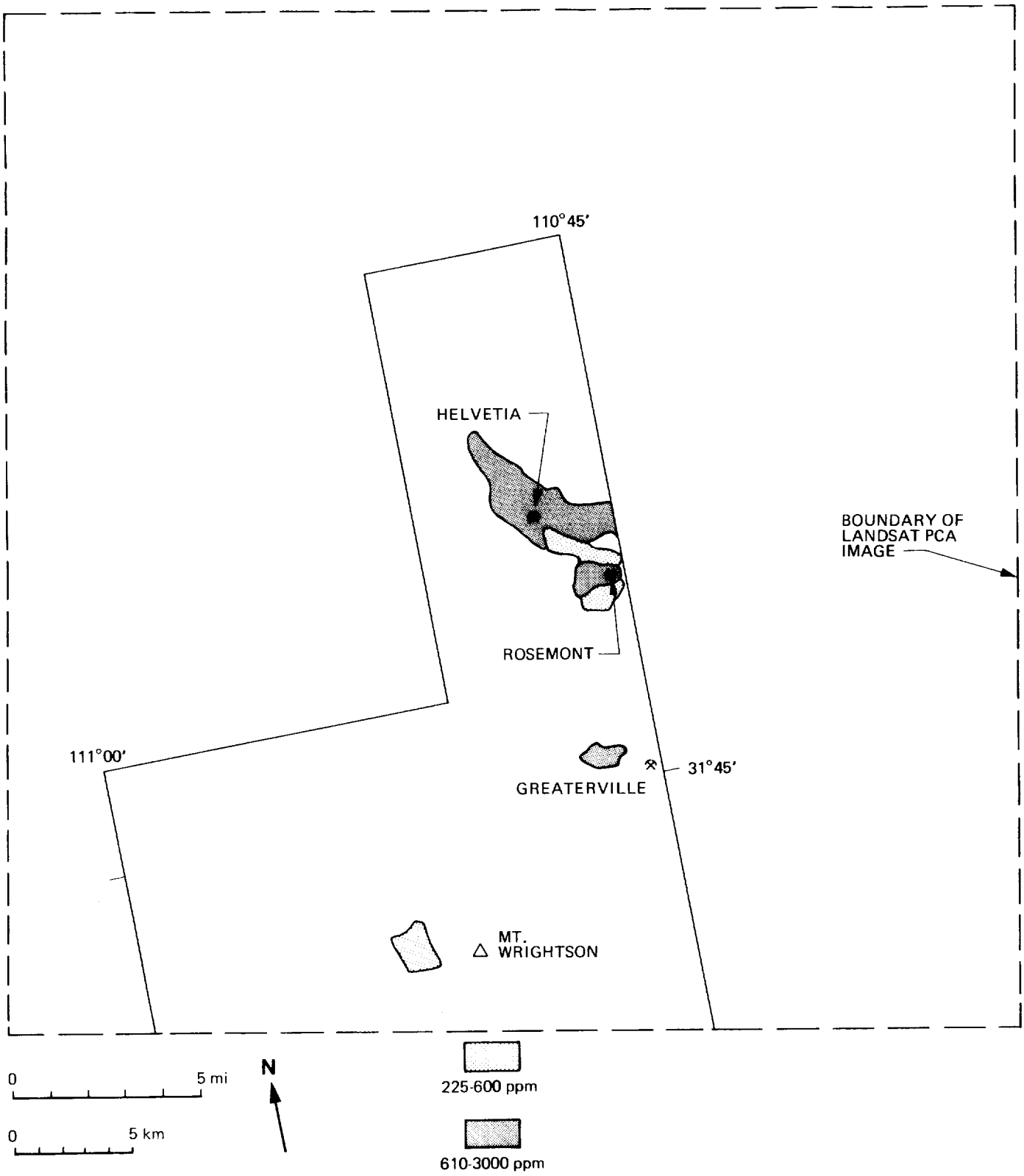

Figure 5-43. Stream sediment survey in Santa Rita Mountains showing areas of high copper concentrations (Drewes, 1973). Solid line indicates boundary of surveyed area.

The spectral information and the overall appearance of this image is similar to the Landsat color ratio composite (Figure 5-36). The major difference is the improved spatial resolution (15 m versus 80 m) provided by the aircraft data. Small outcrops are discernible, such as the dikes in the south and the quartz latite in the north; these cannot be seen on the Landsat MSS data.

b. Iron-oxide discrimination. The different species of iron-oxide minerals (collectively referred to as limonite)—specifically hematite (Fe_2O_3), goethite ($FeO \cdot OH$), and jarosite ($KFe_3(OH)_6(SO_4)_2$)—do not have the same spectral reflectance characteristics, nor are they necessarily derived from the same sources. Hematite often results from oxidation of pyrite and chalcopyrite at porphyry copper deposits and is a prominent constituent of gossans. Goethite is more widely distributed, but can be an alteration product. Jarosite is a ferric-sulfate mineral that is almost always associated with hydrothermal alteration processes. The M²S data have narrow spectral bands that might allow separation of these minerals. Representative reflectance curves for hematite, goethite, and jarosite (Hunt and Ashley, 1979) are shown in Figure 5-47, along with the M²S band intervals. The curves are displaced vertically for clarity.

The spectral absorption bands seen in all three curves are due to electronic transitions involving ferric iron. There are typically three broad features located near 0.45, 0.65, and 0.9 μm and a strong band in the ultraviolet, which produces the rapid falloff in reflectance to shorter wavelengths. Only jarosite shows the 0.45-μm band, while the 0.65-μm band is apparent in all three minerals. But the position of the 0.9-μm band is most significant. In jarosite and goethite, this band is centered at about 0.93 μm; in hematite, the band is displaced toward shorter wavelengths at about 0.85 μm. Although the M²S bands are not ideally placed over these regions, the positions of bands 8, 9, and 10 should produce different reflectance values for the three minerals. By sampling the reflectance values in these three bands, the equivalent 8/9 and 9/10 band-ratio values were calculated. These are plotted in the inset graph in Figure 5-47. The three minerals are clearly separable along the two axes. This analysis was applied to the M²S image data by construction of two ratio composites—one with band-ratios 4/6, 6/8, and 8/9; the other with ratios 4/6, 6/8, and 9/10. These two images, using blue for 4/6, green for 6/8, and red for 8/9 or 9/10, are shown in Figure 5-48.

Examination of the two ratio composites indicates that the preliminary analysis of iron-oxide separations is borne out. On the 8/9 ratio (Figure 5-48b) the hematitic arkoses (A) are orange, and other iron-oxide areas, which are dominantly goethitic, are yellow; they have less red component. In the 9/10 ratio composite (Figure 5-48a), the arkoses (A) are now dark brown; they have less red. This color change verifies the graphical data of Figure 5-47. A mine dump (B) is yellow on the 8/9 image (Figure 5-48b), indicating the relatively high 8/9 ratio value and therefore a large red component. On the 9/10 ratio composite (Figure 5-48a) the dump (B) is still yellow, suggesting the presence of jarositic material. This dump was visited in the field and verified to be jarositic. By using the two images together, and by taking advantage of the narrowness of the M²S spectral bands (despite their nonideal positions), it is possible to separate iron-oxide minerals based on the shift of the ferric iron absorption band near 0.9 μm.

2. Thermal infrared data. Daytime and nighttime predawn thermal infrared (TIR) data were acquired with the M²S scanner during the May 16–17, 1978 overflights. TIR data can provide additional lithologic discrimination information, compared to reflectance data, because they respond to differences in the physical properties of materials, such as density, conductivity, and diffusivity, rather than to surface properties. Vegetation cover and moisture content, however, can greatly affect the thermal characteristics of an area and overwhelm the actual material's thermal response. Meteorological conditions at the time of the overflights were acceptable for obtaining these data; there had been no precipitation for at least 96 hours prior to the flights and winds were low.

TIR data can be used directly and the day or night data examined independently; or a calculated parameter called apparent thermal inertia (ATI) can be derived from the temperature and albedo data. ATI is an approximation of thermal inertia and is calculated as $(1-A)/\Delta T$, where A is average albedo and ΔT is the difference between the day

Table 5-15. Wavelength bands of M²S and NS-001 scanners

M²S		NS-001	
Band	Wavelength, μm	Band	Wavelength, μm
1	0.33–0.44	1	0.45–0.52
2	0.44–0.48	2	0.52–0.60
3	0.49–0.54	3	0.63–0.69
4	0.54–0.58	4	0.76–0.90
5	0.58–0.62	5	1.00–1.30
6	0.62–0.66	6	1.55–1.75
7	0.66–0.70	7	2.08–2.36
8	0.70–0.74	8	10.4–12.5
9	0.76–0.86		
10	0.97–0.065		
11	8.05–13.50		

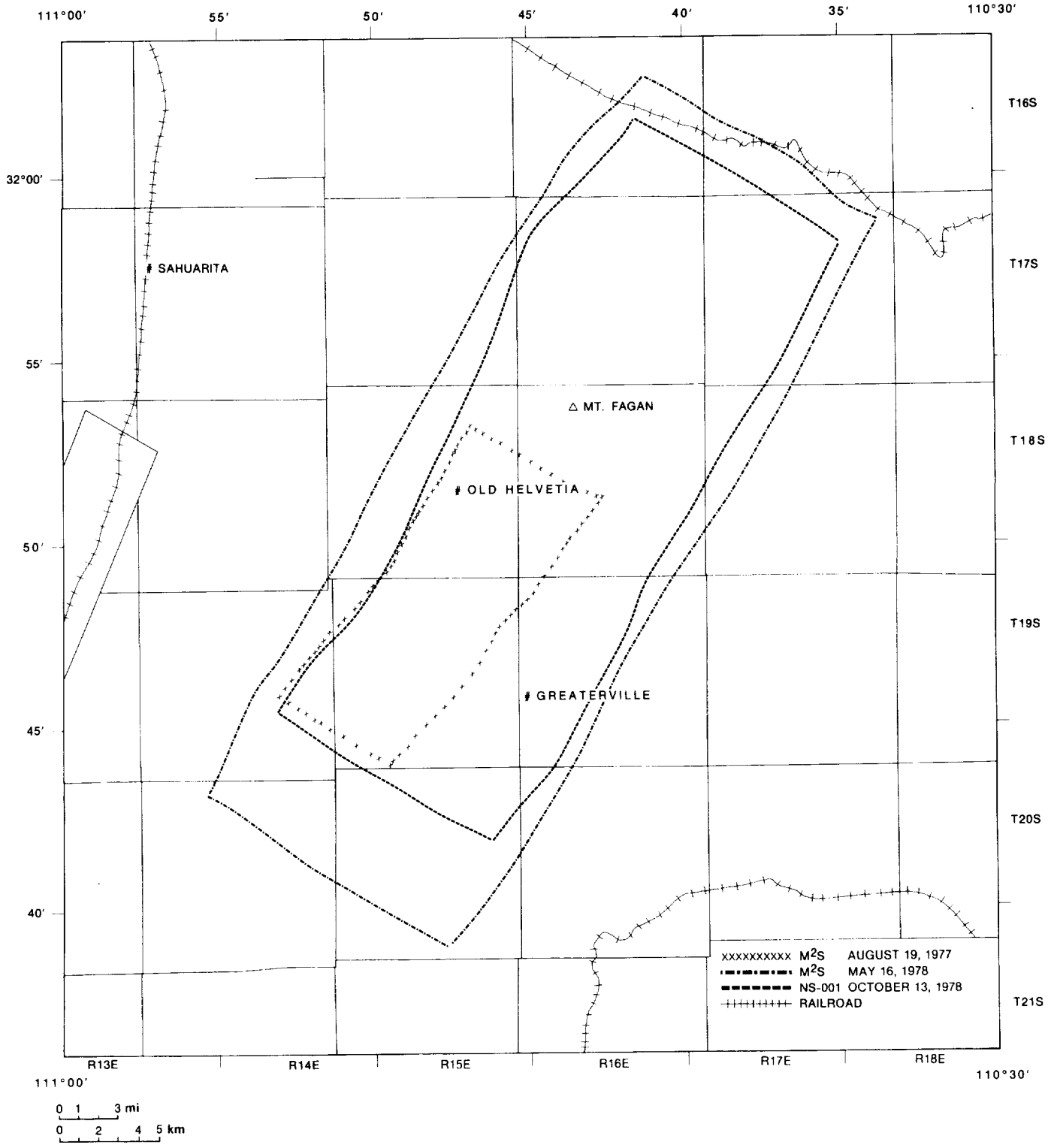

Figure 5-44. Flight lines and coverage of aircraft multispectral scanner data over Helvetia test site. Coverage from M²S 11-channel scanner and NS-001 Thematic Mapper Simulator is shown.

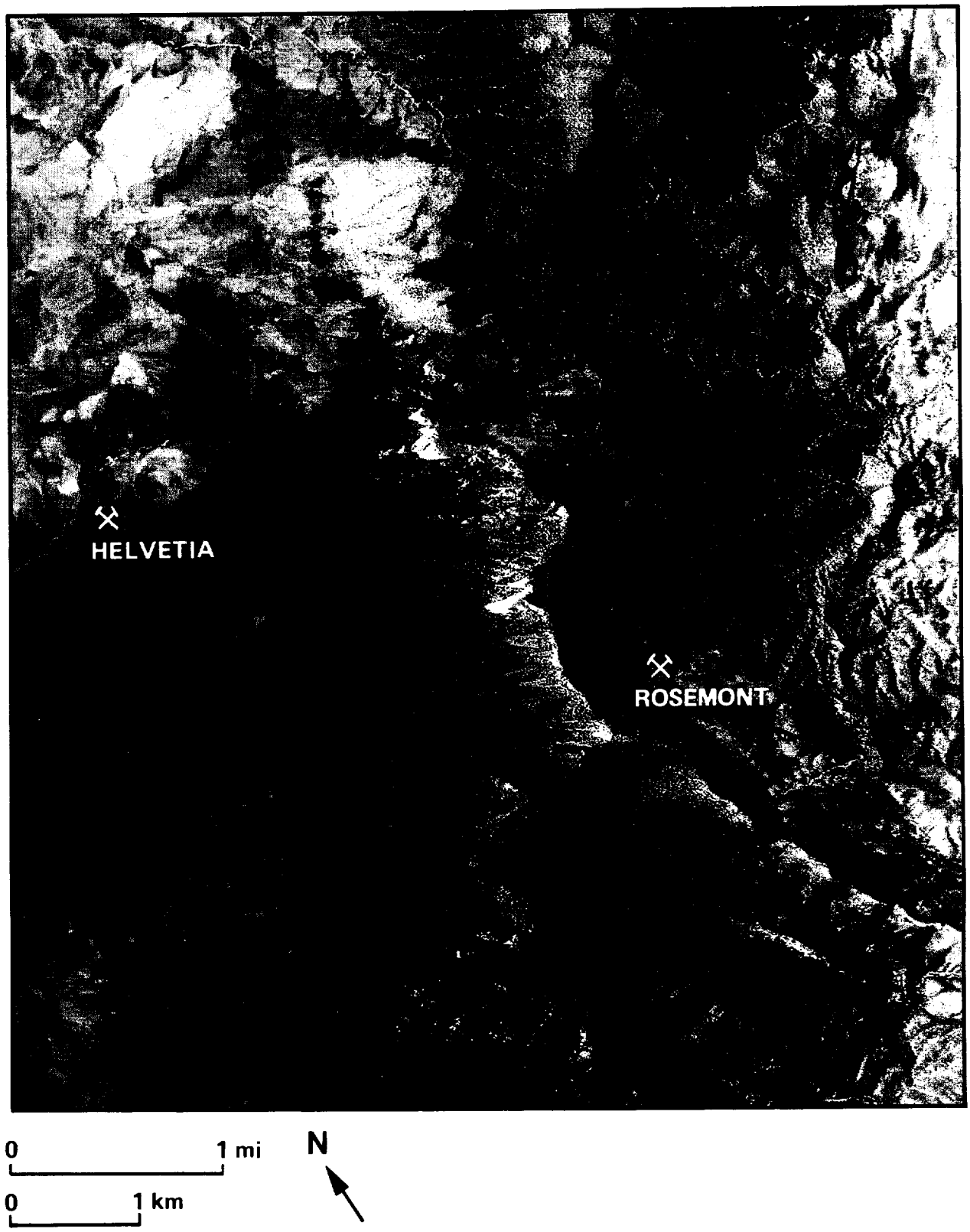

Figure 5-45. M^2S 11-channel color ratio composite of Helvetia–Rosemont area. Band-ratios 4/6, 6/8, and 8/(9 + 10) are displayed as blue, green, and red, respectively (August 1977 overflight data).

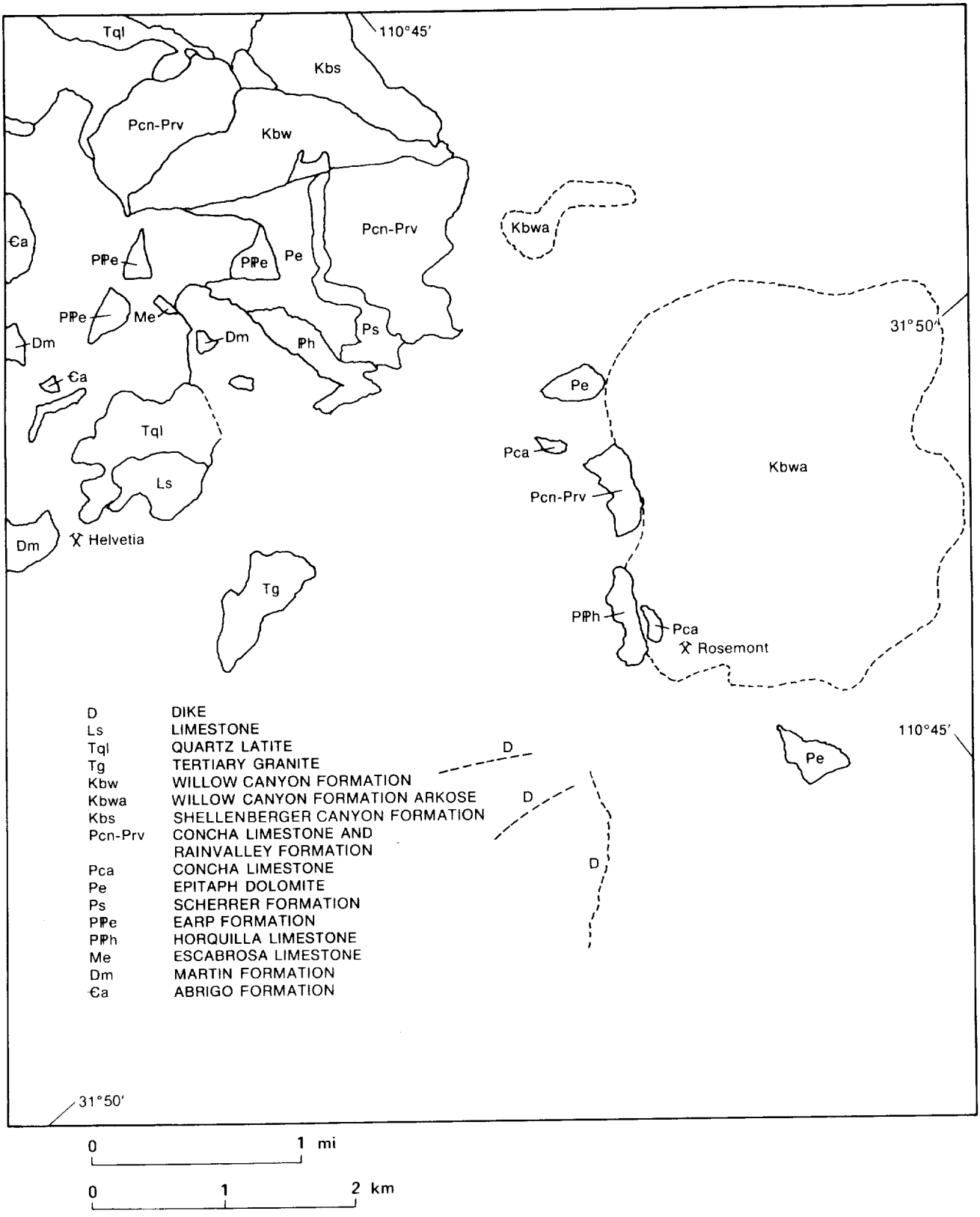

Figure 5-46. Interpretation map of Helvetia M^2S ratio image in Figure 5-45

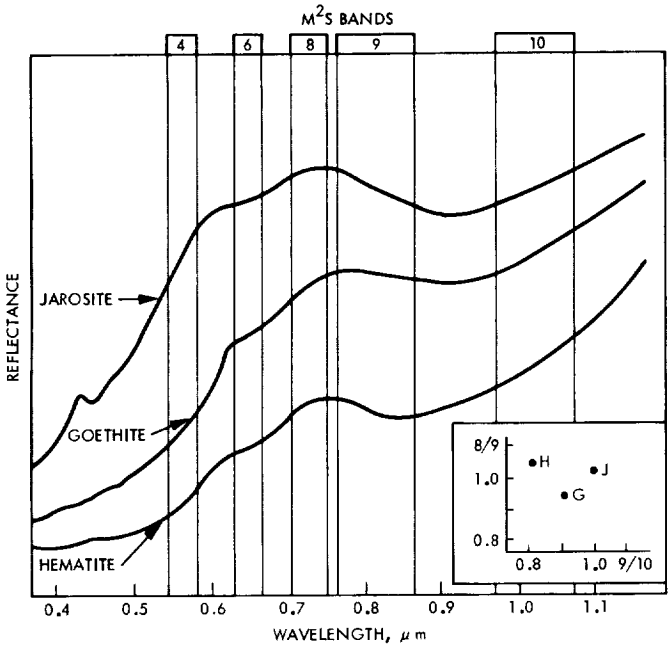

Figure 5-47. Spectral reflectance curves for hematite, goethite, and jarosite (Hunt and Ashley, 1979). The curves are offset vertically for clarity; also shown are the M²S band intervals for channels 4, 6, 8, 9, and 10. The inset figure shows calculated M²S values for band-ratios 8/9 and 9/10 for hematite (H), goethite (G), and jarosite (J).

and night temperature data. Thermal inertia (TI) is a parameter that provides a measure of a material's resistance to temperature change due to heat fluxes. It is represented by the quantity $(K\rho c)^{1/2}$ where K is conductivity, ρ is density, and c is specific heat capacity. TI is a body property of a material that can provide information about composition where the surface may be masked by weathering, staining, or other processes that cause reflectance measurements to be unrepresentative of the entire material. TI cannot be measured directly and must be inferred using models developed to interpret remotely sensed visible and thermal data convolved with terms accounting for heat fluxes (Gillespie and Kahle, 1977). Since the computational procedure to determine TI is difficult, an approximation using ATI is both simpler to implement and yields fairly equivalent results (Kahle et al., 1981). In practice, an ATI image is produced by registering the day and night temperature images, computing a difference image, calculating albedo by weighting the visible and near-infrared channels with the solar constant, then dividing $(1 - A)$ by the ΔT data.

For Helvetia, the albedo, day temperature, night temperature, and ATI images are shown in Figure 5-49. The day temperature data (Figure 5-49b) are dominated by vegetation and topographic effects. South sun-facing slopes are consistently brighter (warmer) than north-facing slopes. Higher elevations are darker (cooler) than lower elevations due to the presence of increased vegetation cover and the effect of elevation on temperature. The night temperature image (Figure 5-49c) again shows major topographic effects. The major drainages are dark (cool) due to vegetation. A small pond (A) is bright (relatively warm) because water retains its heat at night relative to other materials; higher elevations tend to be cooler than lower elevations. However, some differences in temperature related to rock-type differences are apparent. An oval bright area (B) corresponds to outcrops of altered quartz latite porphyry; field checking revealed that the rocks are silicified, resulting in high thermal inertia and relatively warmer nighttime temperature. Other bright areas are outcrops of granite (C) and unaltered limestone (D). Limestone that has been altered to skarn and marble appears dark (E). In the field, the marbles are very broken up, in contrast to the massive habit of the fresh limestones. Bedding is visible in the Cretaceous rocks (F) due to changes in lithologies which have varying thermal properties. The noisier appearance of this image is due to the severe contrast stretch used to display the narrow range of DN values (temperatures).

Basically, the same features are discernible on the ATI image (Figure 5-49d), with the addition of more topographic detail. Bright areas are generally rock outcrop exposures of granite and Paleozoic sediments. Most of the Cretaceous sediments are dark (lower apparent TI) due to their lower densities, conductivities, and/or specific heat.

A more effective technique for displaying thermal data is to produce a color composite of three components (Kahle et al., 1981). In such a display, the interrelationship between day and night thermal patterns is visible as color differences on the image. The albedo, day thermal, and night thermal images were used to produce Figure 5-50 by displaying the three components as cyan, magenta, and yellow, respectively. The interpretation map overlayed on the color image indicates which units were separable on the image. Boundaries were drawn around similar appearing areas; the interpretation was then compared with a geologic map to assign formation names to the outlined areas.

The variations recognizable on this image are due to tonal (color) and textural differences. Tonal differences are a combination of thermal and albedo variations. Textural differences are geomorphic and are mainly controlled by drainage textures. These, in turn, are due to several properties of the surface materials: porosity, permeability, hardness, jointing, fracturing and faulting, and bedding.

Precambrian granites are variable in color, but tend to appear as light orange or purple. Texturally, the areas dis-

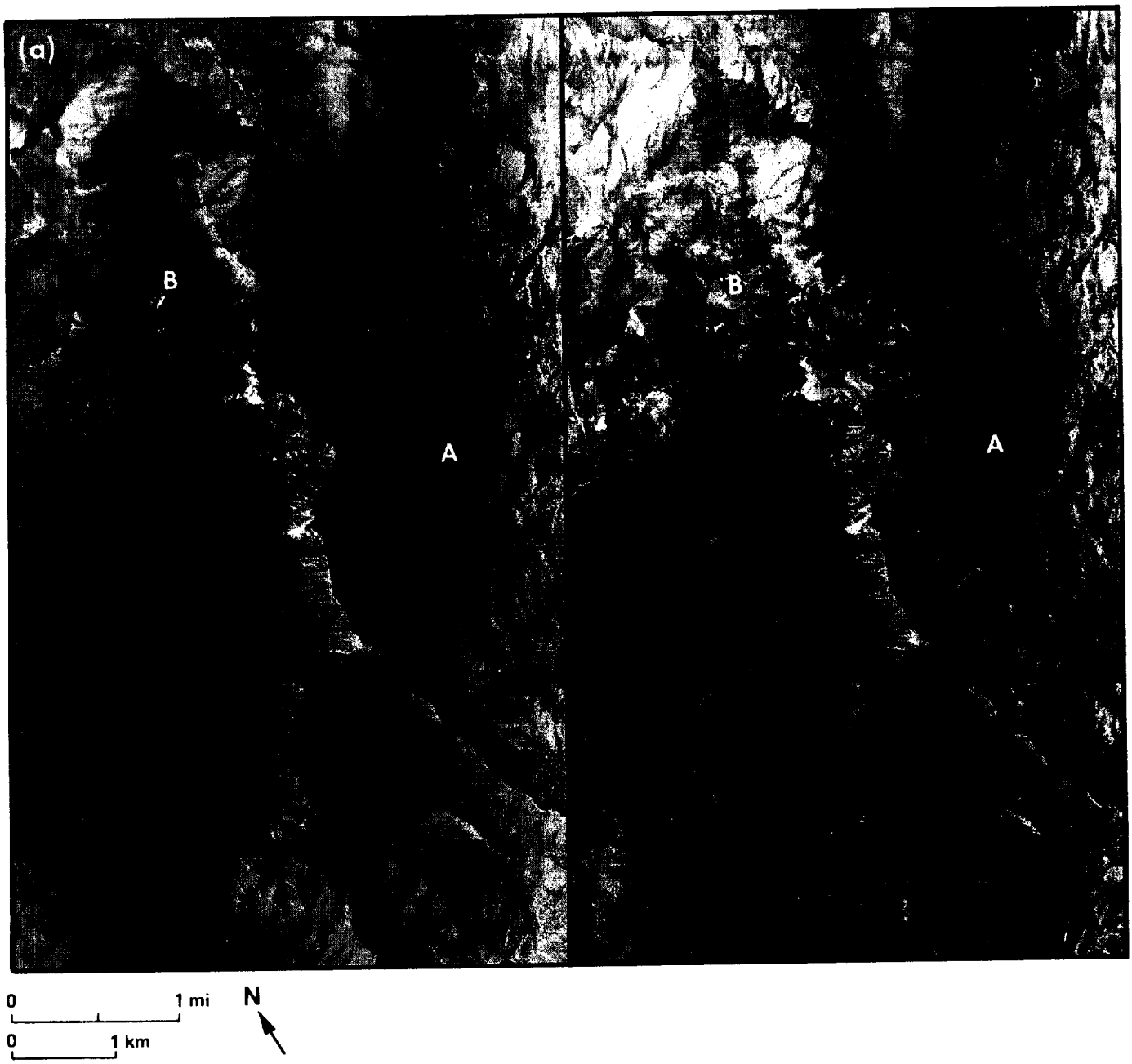

Figure 5-48. M²S color ratio composites from August 1977 data: (a) band-ratios 4/6, 6/8, and 9/10 are displayed as blue, green, and red, respectively; (b) band-ratios 4/6, 6/8, and 8/9 are displayed as blue, green, and red, respectively

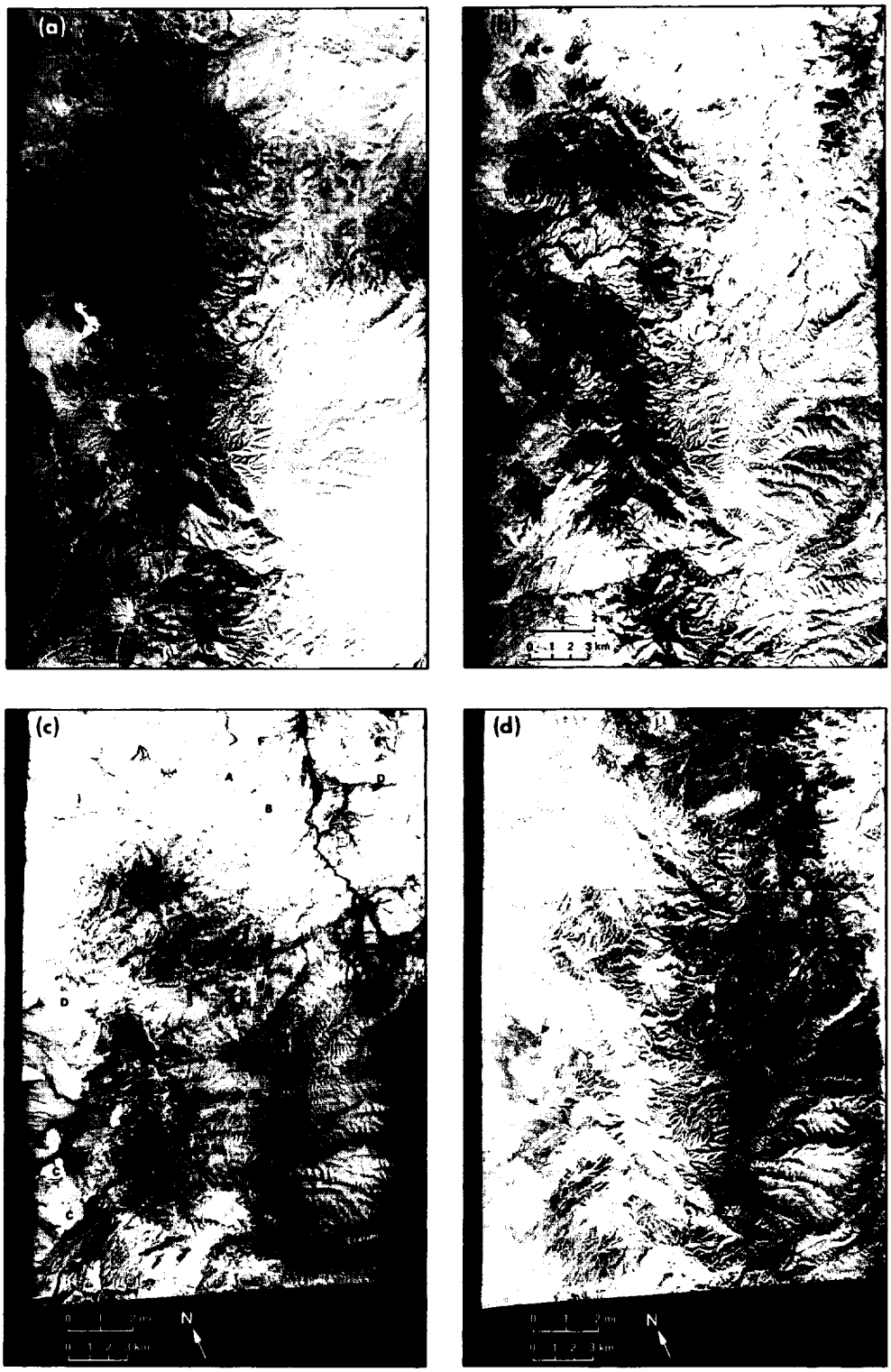

Figure 5-49. M²S thermal infrared images: (a) average albedo; (b) day temperature; (c) night temperature; (d) apparent thermal inertia. Data from May 16–17, 1978 flights.

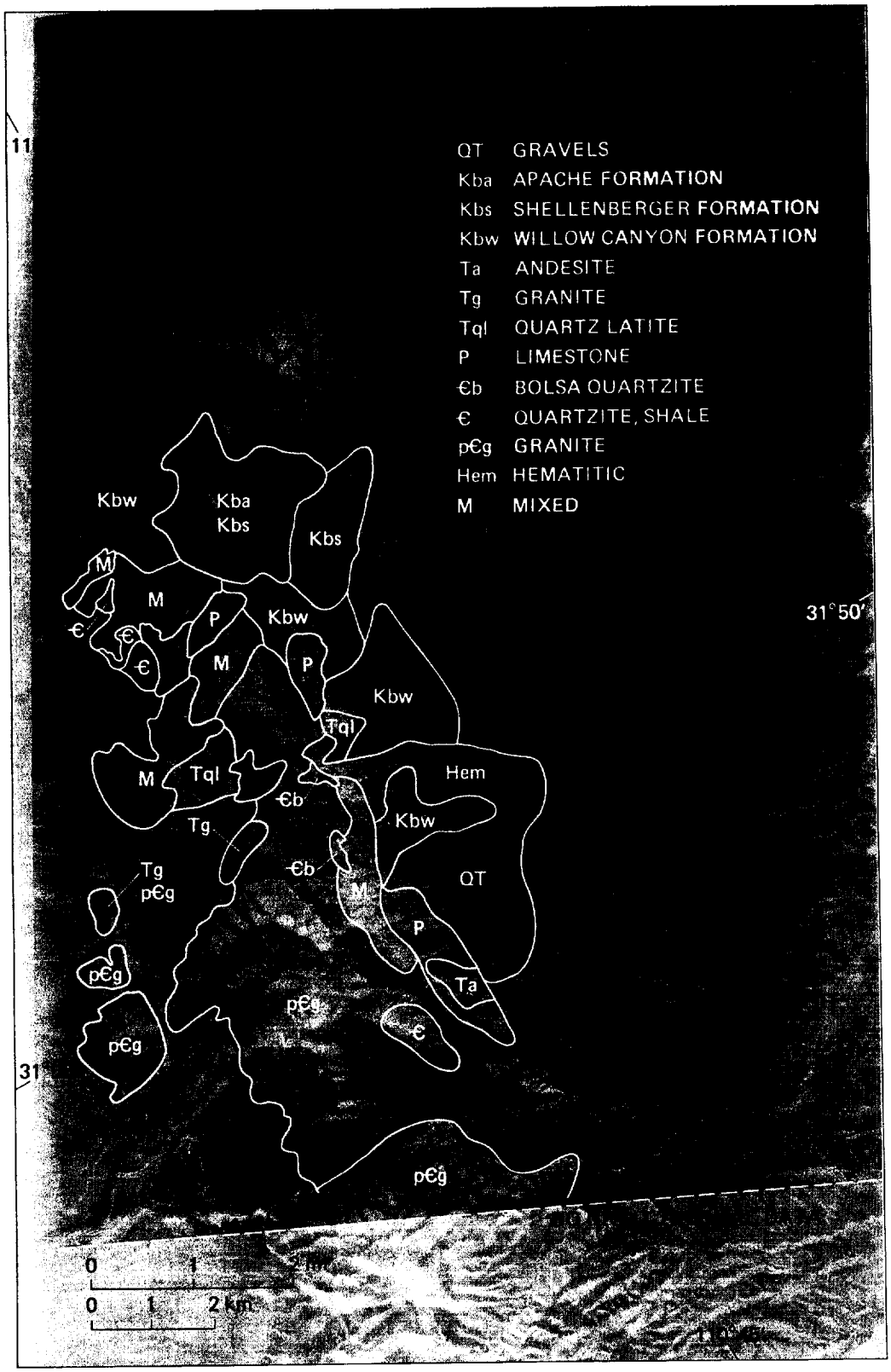

Figure 5-50. M²S thermal infrared–albedo color composite. Albedo, day thermal, and night thermal data are displayed as cyan, magenta, and yellow, respectively. Overlayed is an interpretation map indicating separable units.

play a dendritic drainage pattern, with smooth ridges and regularly spaced stream channels. The Tertiary granite (Tg) is orange, indicating either low albedo, high daytime temperature, or a combination of these effects. The Shellenberger Formation siltstones (Kbs) are purple, indicating low albedo, low daytime temperature, and high nighttime temperature; this behavior is consistent with a lithology of dark, well-indurated material. The Bolsa Quartzite (Ꞓb) is yellow–orange, indicating low albedo, high daytime temperature, and low nighttime temperature.

Although this display allows better separation of lithologies than the individual thermal images, it is not as good as information that is available from visible and near-infrared data. Indeed, no new separations could be interpreted compared with the latter data.

C. NS-001 Thematic Mapper Simulator Data

1. Introduction. Data from the NS-001 Thematic Mapper Simulator were acquired on October 13, 1978 over Helvetia, with a spatial resolution of about 12 m. This scanner has the same spectral bands as the Landsat 4 Thematic Mapper scanner, with an additional band at 1.0 to 1.3 μm. The data were computer processed to reformat the bands and remove panorama distortion due to the scan mirror profile. The noise level of the data was found to be low enough for further processing without the necessity for cosmetic rectification. Two different image products will be examined in this section—a color ratio composite and a color composite produced by canonical transforms from stepwise linear discriminant function analyses of PFRS data.

These two types of enhancements were selected according to previous experience gained from image processing of data at other sites. Band ratioing is a well-established technique for enhancing subtle spectral differences between materials and, at the same time, subduing uneven illumination effects due to topography. The method of using canonical transforms based on stepwise linear discriminant function analysis is a statistically optimum method for determining separability of studied rock types. It is an objective approach, limited mainly by the bias introduced in the sampling scheme used to select the groups to be separated. The better these groups are characterized by the selected measurements (in this case the PFRS spectra), the more valid the resulting transformations will be.

2. Ratio composite. Based on a study of the reflectance properties of minerals associated with altered rocks (Abrams et al., 1977), three ratios were selected to produce a color composite for Helvetia. The color image shown in Figure 5-51 was created by displaying band-ratios 6/7, 3/2, and 4/5 in red, green, and blue, respectively. No atmospheric corrections were applied to the ratioed data. The 6/7 ratio is sensitive to the presence of hydrous minerals due to their 2.2-μm absorption band; the 3/2 ratio was selected to highlight the presence of iron-oxide materials, taking advantage of the marked falloff to shorter wavelengths due to the ferric iron charge transfer band in the ultraviolet; the 4/5 ratio was selected to separate unaltered rock types. A detailed interpretation map produced from this image is shown in Figure 5-52.

The dark blue–green areas (A) in the left-central part of Figure 5-51 are outcrops of Permian limestone that are unaltered. In the field, these are massive blue–gray rocks with no iron staining. Farther to the south, these same mapped lithologies appear olive green (B); these are areas where the limestone has been altered to skarn and marble; the green color indicates the presence of some iron oxide, which is what was observed in the field. A large green area (C) corresponds to the hematitic alteration of the Cretaceous arkoses. Several small yellow areas (D) indicate the presence of both iron oxides and hydrous minerals. These correspond to outcrops of argillically altered quartz latite porphyry and Tertiary volcanics. Other yellow areas, particularly the large area in the lower left corner of the image, correspond to surface materials that have iron oxide and moderate vegetation cover. The spectral reflectance of vegetation is such that water bands affect the 6/7 ratio and produce a red contribution in the image similar to hydrous minerals; other ratio combinations (not shown) remove this ambiguity. The orange patch (E) at the bottom center of the image corresponds to an outcrop of Epitaph Dolomite. The color indicates the presence of some iron oxide and either hydrous minerals or a strong carbonate band. The pink area (F) is an outcrop of Concha Limestone in the Helvetia klippe. The color is due to the presence of a strong hydroxyl or carbonate absorption band. Other rock units which are separable on the image are shown in the interpretation map. In general, a large number of the mapped rock types are separable using the NS-001 data. The added spectral bands and improved spatial resolution provide for more information than is available from Landsat MSS data.

3. Canonical transforms. The linear discriminant function analyses of the PFRS data described in Paragraph III.A were used to produce new image transforms of the Helvetia NS-001 data. Briefly, the analyses produced linear combinations of the input variables (in this case, the NS-001 spectral bands) which separated the rock-type groups used as training data. Because the statistical analysis was based on PFRS data, which are in terms of reflectance values, a method had to be implemented to convert the NS-001 radiance values to reflectance. The easiest way to do

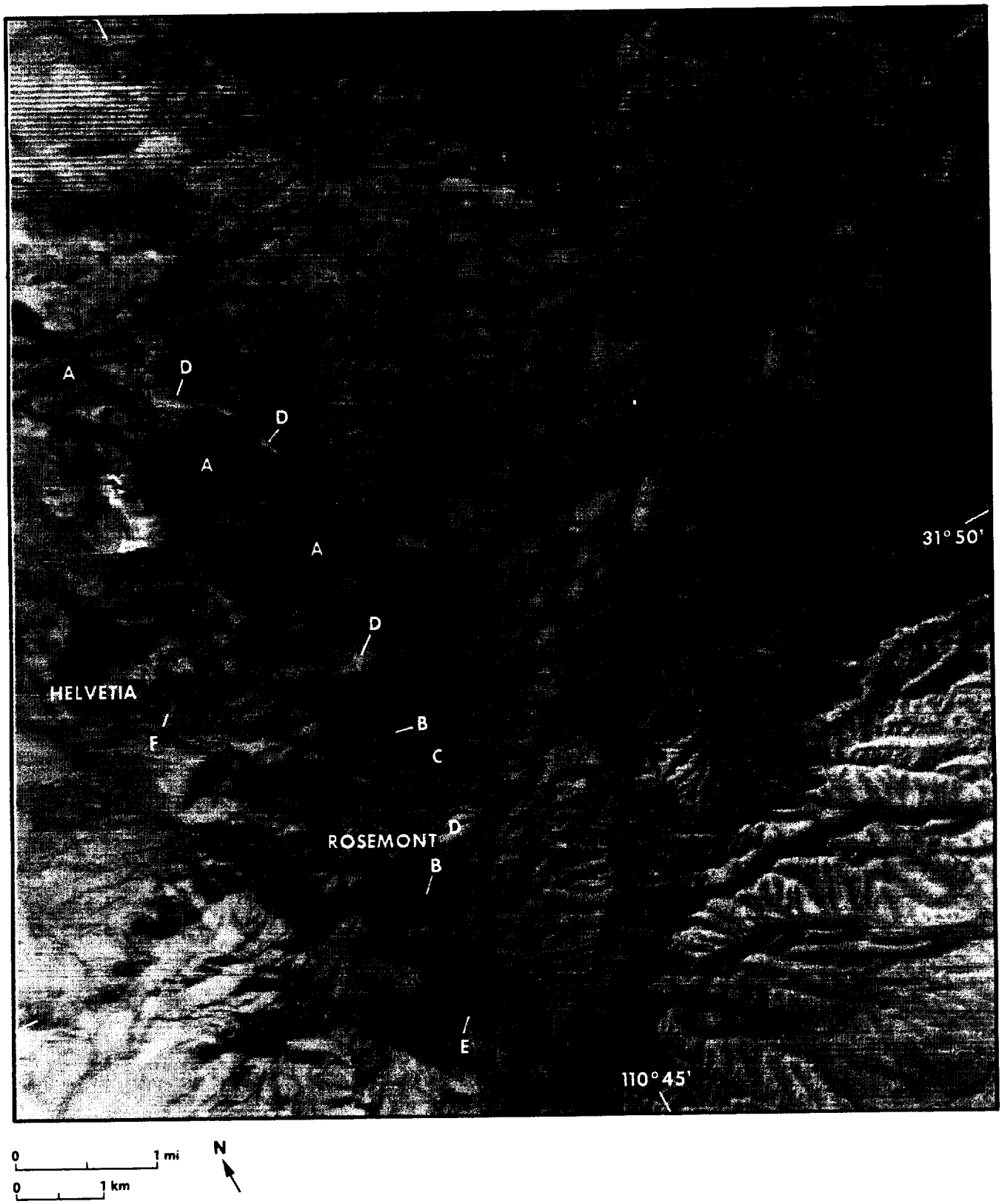

Figure 5-51. NS-001 color ratio composite. Band-ratios 6/7, 3/2, and 4/5 are displayed as red, green, and blue, respectively. Area covered is 12 by 14 km (data acquired October 13, 1978). Scanner noise in the 6/7 ratio is responsible for the horizontal striping seen.

this was to apply the calibration algorithms computed from the Silver Bell NS-001 data to the Helvetia data (refer to the Silver Bell, Arizona, Porphyry Copper Test Site Report, Section 4, Paragraph VI). It was felt that this approach was valid because the two sites were flown less than an hour apart and they are only about 60 km from each other. It was assumed, therefore, that the instrument response did not change during the intervening time and that the atmospheric conditions were the same or very similar.

Seven variables were used as inputs, and seven new linear combinations (canonical variates) were produced as outputs. Of these, the first, second, and fourth were selected for creation of a color composite by displaying them as green, red, and blue, respectively. This particular combination was chosen after examination of a larger number of possibilities. The third variate was not used because it appeared to have less new information than the fourth, although in theory, the first canonical variate has most of the separation, the second the next lower amount, and so forth. The resulting color image, with an interpretative overlay, is shown in Figure 5-53.

A general observation is that, compared to the ratio composite (Figure 5-51), this image shows major effects due to topography and uneven solar illumination. To the first order, ratioing subdues this phenomenon; because the canonical transforms are combinations of the original variables, shadowing effects remain in the new data displays.

The Paleozoic limestones (11,12,13) are bright to dark red, the altered limestones being darker in color. Their distribution is strikingly highlighted in this particular color scheme, and it is also due to the weighting of the PFRS samples with respect to the number of limestone classes used in the analyses. The altered quartz latite porphyry outcrops (9) are lavender in color. The hematitic Cretaceous arkose (HEM) is yellow–green; in this rendition, it appears similar to some of the Precambrian granites. The Cambrian sediments along the range crest (17) are dark pink, while west of the crest they are green, probably reflecting differences in mineralogy. The Cretaceous rocks in the northeastern quarter of the scene are generally separable. However, when compared to the geologic map, only a few units can be separated in detail. The large amount of shadowing produces a confusing array of colors on the image.

Overall, compared to the ratio composite, this product has somewhat less information. In part, this is due to the PFRS sampling bias. Had more systematic measurements of the Cretaceous sediments been made, their separation would probably have improved. This technique proved to be the most effective at Silver Bell, where most of the geologic units in the entire scene were spectrally measured with the PFRS.

VI. Summary and Conclusions

The Helvetia porphyry copper test site in southeastern Arizona was selected because of the geologic features encompassed by this mining district. A wide variety of rock types is exposed in the area. These include lithologies ranging in age from Precambrian to Quaternary, and consist of sedimentary rocks (limestone, sandstone, shale, arkose, conglomerate, quartzite) and igneous rocks (granite, quartz latite porphyry, andesite, tuff, volcaniclastics). This wide range provided an ideal opportunity to examine the spectral characteristics of a wide lithologic assemblage and to assess the separability of these rock types using remote sensing techniques. Alteration associated with base-metal mineralization has affected many of these assemblages. Alteration types include weak argillic, propylitic, hematitic, and skarn-related metamorphic minerals. These differ from the types of alteration found at the Silver Bell and Safford test sites and provide an opportunity to study the spectral characteristics of a wider range of alteration types associated with mineralization. The structural complexity of the area presented tectonic features of different scales for study. Regional tectonic patterns were examined from synoptic scale images; local, smaller structural features were studied using larger scale images.

Remote sensing data were obtained either from existing archival facilities (EROS Data Center, Sioux Falls, South Dakota) or from Johnson Space Center, which provided multispectral scanner data acquired by the M^{2}S and NS-001 scanner instruments. Data which were analyzed consisted of (1) color aerial photography, (2) L-band Seasat satellite radar data, (3) X-band aircraft radar data, (4) Landsat Multispectral Scanner data, (5) M^{2}S 11-channel multispectral scanner data (visible, near-infrared, and day–night thermal data), and (6) NS-001 Thematic Mapper Simulator data. Ancillary information was obtained *in situ* using JPL's Portable Field Reflectance Spectrometer.

Data analysis/interpretation was an iterative process of laboratory analysis of computer-processed remote sensing data, field checking of the site to substantiate any interpretive conclusions, and further processing and integration of data in the laboratory.

In situ spectral reflectance measurements were obtained using JPL's PFRS. Examination of these 0.45- to 2.45-μm spectra indicated that the major spectral absorption fea-

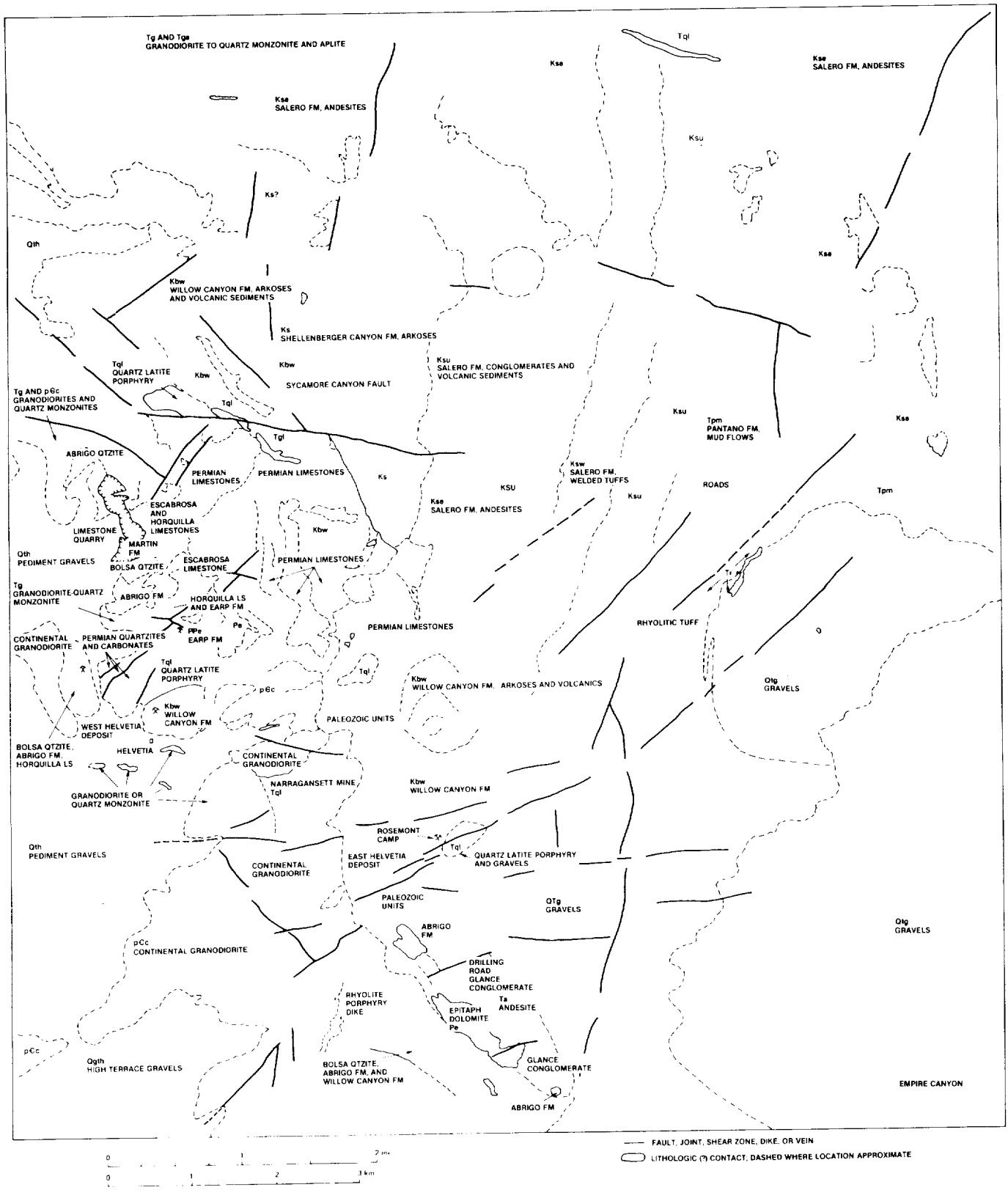

Figure 5-52. Geology/alteration interpretation map of the Helvetia area NS-001 image in Figure 5-51. Rock type boundaries and structural features recognizable on the image are shown (see Drewes, 1971b, for description of units).

tures associated with sampled rock types were attributable to the presence of iron oxides, carbonate, and hydrous minerals (such as clays). Statistical analyses of these data were undertaken using linear discriminant function analysis. Wavelength regions corresponding to Landsat MSS, M²S 11-channel scanner, Landsat 4 TM, NS-001 Thematic Mapper Simulator, and a conceptual 30-channel, equal-wavelength bands scanner were computed from the data for the analyses. Examining the separability of 10 different sampled rock types indicated that Landsat MSS was the least effective instrument examined. Separation accuracy was about equal for the M²S, Landsat 4 TM, and NS-001 simulations. Increasing the number of bands to 30 and narrowing them to 0.05 μm allowed almost complete separation of the rock types. The linear transformations which were computed by the analysis technique were later used to process the image data since these transformations are statistically optimal for separating the sampled rock groups.

Imaging scanners can also be used as spectrometers, albeit limited by the number and position of the bands recorded. The M²S data were used to produce image spectra in the 0.4- to 1.1-μm range. Calibration of the image data was done by forcing the radiance values of one geologic unit to match the ground-measured PFRS reflectance values. The resulting image spectra had acceptable shapes, and absorption features corresponding to ferric iron bands were evident. Comparison of several image spectra with PFRS measurements revealed an excellent correspondence in the shape of the curves, with an offset in the overall reflectance values. The one-point calibration method used was responsible for this behavior. Nevertheless, this exercise indicated that image data can be used to produce image spectra which provide spectral information relatable to mineralogical composition.

The color aerial photography allowed some discrimination of lithologic units. Limestones appeared gray on the photographs; the hematitic arkoses were dark red and quite distinct. Small features, such as dikes, were identifiable based on their geomorphic appearance: long, semicontinuous linear features. The limited spectral range of color film did not allow separation of most of the units. A drainage density analysis indicated that areas of Precambrian to mid-Mesozoic rocks were different than areas underlain by Cretaceous rocks and Tertiary gravels. The hematitic arkoses showed up as an area of moderately high drainage density.

Radar data provided mainly structural information. Tonal differences seen on both the satellite and aircraft radar data were limited to separation of bedrock and alluvium. The little lithologic information present was attributable to differences in geomorphic appearance, dominantly drainage density and pattern. Numerous lineaments and circular/elliptical features seen on the images were primarily due to drainage patterns. A few could be correlated with mapped faults, but most had no correspondence to previously recognized features. Further field checking of these features would be required to determine whether they had any geologic significance.

Landsat MSS data were computer processed and analyzed for both structural and lithologic information. A statistical lineament analysis was performed on a full scene of Landsat data; results were compared with other published structural analyses based on mapped fault data, Landsat data analysis for an adjoining area to the south in Mexico, and regional residual aeromagnetic data. Three distinct lineament trends were seen on the lineament analysis: N 50° W, N 45° E, and N 85° E. These correlated with three of the structural trends recognized by Carson (1969) from analysis of mapped faults. The N 50° W trend corresponds to Titley's (1976) Mesozoic northwest structural trends which define distinct litho-tectonic blocks in southeast Arizona. The boundaries correspond to zones of lower lineament density; the blocks are areas of higher density. In general, this is due to the development of alluviated valleys along the boundaries and to the mountain blocks between them. Lineament density highs mapped by Sawatzky and Raines (1982) from Landsat data in Sonora, Mexico, project into southeastern Arizona and line up with several trends found from this lineament study. This type of analysis of Landsat data provides a powerful tool for study of regional tectonic features. The synoptic view provided is ideal for examining large areas under uniform illumination conditions.

Lithologic information derivable from Landsat MSS data was examined using three types of computer-enhanced image products: false-color infrared composite, color ratio composite, and principal components analysis. The false-color infrared composite for a full Landsat scene was compared to the state geologic map. In areas of high relief, vegetation cover dominated the spectral reflectance characteristics and masked the underlying geology. At lower elevations, various mapped geologic units were recognizable. These included outcrops of granite, volcanic rocks, and limestones. Valley fill material was separable based on both tonal and geomorphic appearances. Iron-oxide-bearing areas were spectrally distinct due to ferric iron absorption bands which occur in the Landsat wavelength region. CRC and PC images were produced for a 40- by 40-km subarea of a Landsat frame. These two processing algorithms enhance spectral separability of materials: CRC at the expense of brightness (topographic) information, and PCA at the expense of easy interpretation of the physical

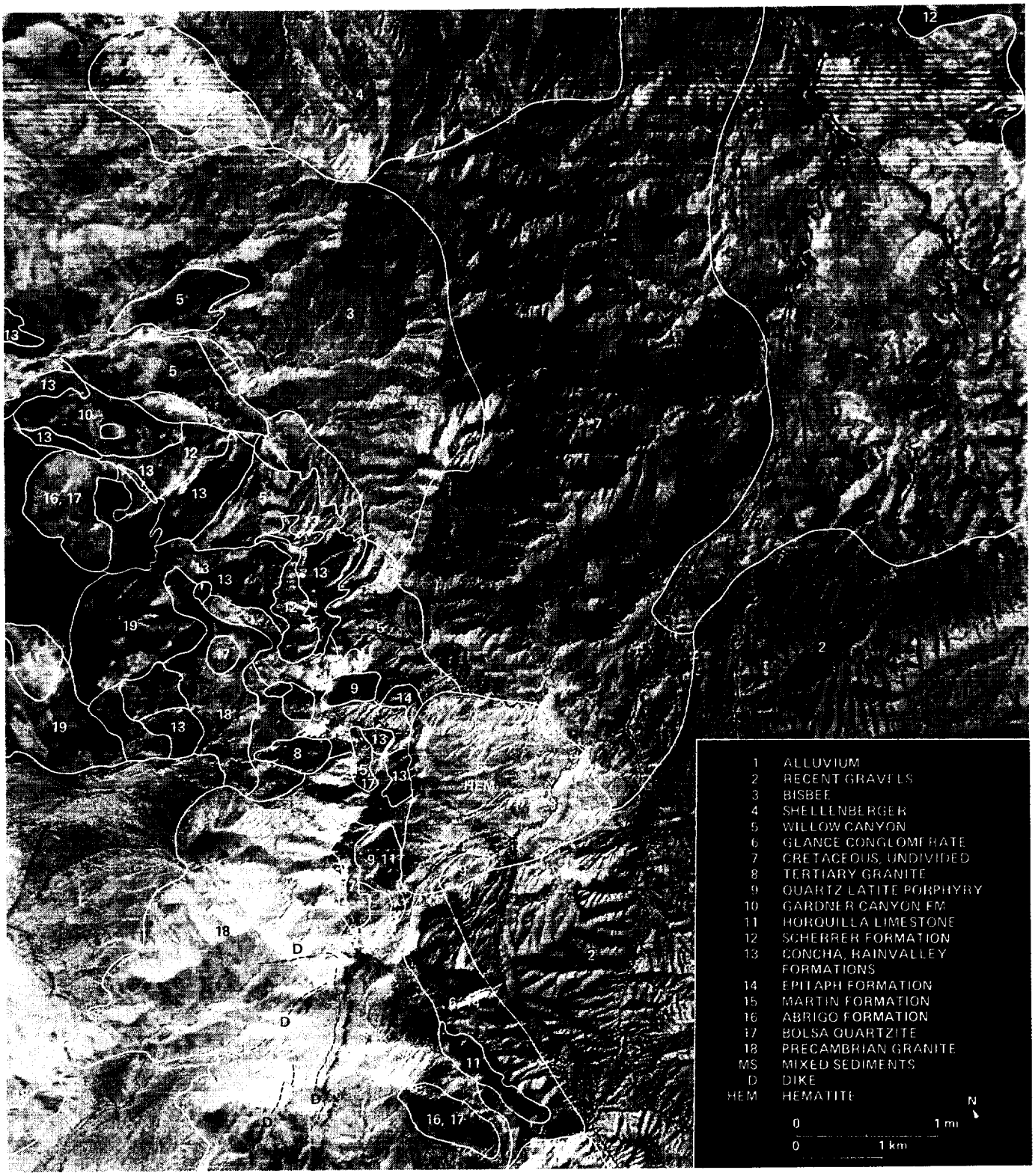

Figure 5-53. NS-001 Thematic Mapper Simulator data. Color image produced using canonical transformations determined from linear discriminant function analyses of PFRS data. Interpretive overlay also shown. Same area as Figure 5-51.

meaning of the output product. Interpretation of the CRC and PC images allowed many mapped geologic units to be separated based on differences in spectral response. Areas of iron-oxide development, some of which are associated with alteration, were particularly evident. The PC image additionally produced some separation of hematitic from goethitic materials. This was seen by the different tonal appearance of alluvial fans east of the Santa Cruz River and in the area of hematitic arkoses east of Rosemont. A stream sediment geochemical survey was compared to the results of the Landsat data analyses. Anomalously high concentrations of copper (also zinc, silver, and lead) were found in several areas that corresponded to iron-oxide occurrences mapped from the Landsat data. In an exploration program, these two converging pieces of data could provide sufficient justification to consider more detailed groundwork, geophysical surveys, and other exploration activities.

The main limitation of the Landsat MSS data was the moderate spatial resolution (80 m). The detailed geology of the test site was not discernible on the images. In addition, the limited number and positions of the Landsat MSS spectral bands reduced the information relevant for lithologic separation.

Aircraft M²S multispectral scanner data were processed and interpreted to examine the effects of improved spatial and spectral resolution on geologic information compared with Landsat MSS data. Color ratio composites produced using different bands in the 0.75- to 1.0-μm region allowed separation of different iron oxides based on the shift of the ferric iron absorption band near 0.9 μm. Areas with jarosite, goethite, or hematite were distinct on the images. The improved spatial resolution (18 m) compared to that of Landsat (80 m) allowed fairly detailed interpretation maps to be constructed; small geologic features, such as dikes, were evident on the images. However, the spectral region covered (0.4 to 1.0 μm) was still inadequate for separating many of the rock types exposed at the test site.

Thermal infrared data were analyzed from day–night overflights with the thermal channel of the M²S scanner. The day and night images were examined separately; apparent thermal inertia was calculated from the day and night thermal data and from the computed albedo image. Although there was some geologic information in each of these products, topographic effects dominated the images. Separation was best between rock types with widely varying thermal properties such as alluvial fill and silicified volcanic rocks. A more effective display of these data was achieved by combining the day and night thermal and albedo data to create a color additive composite. Many more rock types were separable on the combined image than on any individual image. Nevertheless, no new information was seen compared to NS-001 data.

The most geologic information was provided by the NS-001 Thematic Mapper Simulator data. This instrument provided the same spectral bands as those on the Landsat 4 Thematic Mapper; however, the aircraft platform allowed higher spatial resolution (15 m versus 30 m). Color ratio composites and canonical transforms were used to produce displays for interpretation. Delineation of most of the geologic units occurring at the test site was possible because of the wider spectral range covered by the instrument. Altered rocks were distinct, based on spectral characteristics due to the presence of iron oxides and hydrous minerals; altered and unaltered limestones were clearly separated; many of the Cretaceous sediments were separable also. Of all the multispectral data sets examined, this one was unequivocably the best. The main improvement provided by the NS-001 data was in the spectral region covered by the scanner. The addition of wavelength bands in the 1.0- to 2.5-μm region provided mineralogical information not contained in the 0.4- to 1.0-μm region. The 2- to 2.5-μm region is particularly important for detection of hydrous minerals and carbonates, both of which are present in rocks at the Helvetia test site.

From an exploration viewpoint, this test site study covered many elements of a reconnaissance exploration project. Regional analysis was done using Landsat data for structural mapping and lithologic separation. Particular attention was given to mapping the distribution of iron-oxide occurrences; this is one of the main mineralogies identifiable using Landsat data and is also important due to its association with alteration systems. Integrating these data with regional geophysical data and stream sediment geochemistry strengthened the geologic interpretation of possible anomalous areas of potential significance. Aircraft scanner data and radar data were then used to examine in greater detail a smaller area targeted from the regional analysis. These data allowed better geologic interpretations to be made and highlighted small areas of alteration. The next step would be further detailed geophysical measurements, and then sample collection and analysis to determine whether an ore body was present. Had this been a virgin, unexplored area, there is no doubt that the remote sensing analysis detailed in this report would have successfully led to the discovery of the porphyry copper deposit.

Acknowledgments

We would like to thank ANAMAX Corporation for allowing us access to their site, and to thank AMAX for providing the services of Ray Sadowski during the study and for the valuable advice of company geologists. Image processing at JPL of enormous amounts of data would have been impossible without the dedication of Ron Alley. Field assistance was provided by Mustafa Ukayli. Finally, we thank the personnel of Johnson Space Center's flight support facility, particularly Gordan Hrabal, for the excellent job they did acquiring the aircraft scanner data.

References

Abrams, M., R. Ashley, L. Rowan, A. Goetz, and A. Kahle (1977). Mapping of hydrothermal alteration in the Cuprite Mining District, Nevada, using aircraft scanner imagery for the 0.46–2.36 μm spectral region. *Geology, 5*, 713–718.

Aiken, C. (1975). *Residual Bouguer gravity anomaly map of Arizona.* Tucson: University of Arizona Press.

AMAX Exploration. *Geology of Helvetia area.* Unpublished map. (Scale 1:24,000)

Blom, R., M. Abrams, and H. Adams (1980). Spectral reflectance and discrimination of plutonic rocks in the 0.45 to 2.45 μm region. *J. Geophys. Res., 85*, 2638–2648.

Carson, W. (1969). *Computerized lineament tectonics and porphyry copper deposits in S.E. Arizona and S.W. New Mexico.* Doctoral dissertation, Stanford University, Palo Alto, California.

Conel, J., M. Abrams, and K. Baird (1980). Uranium: Spectral discrimination of alteration phenomena in sediments. *Mod. Geol., 7*, 115–135.

Creasey, S., and G. Quick (1955). Copper deposits of part of Helvetia Mining District, Pima County, Arizona. *U.S. Geol. Surv. Bull. 1027-F.*

Davis, G. (1981). Regional strain analysis of the superposed deformations in S.E. Arizona and the Eastern Great Basin. *Ariz. Geol. Soc. Digest, XIV*, 155–172.

Davis, J. C. (1973). *Statistics and data analysis in geology.* New York: John Wiley & Sons.

Dixon, W. (Ed.) (1970). BMDO7M stepwise linear discriminant analysis. *BMD biomedical computer programs.* Berkeley: University of California Press, 233–253.

Drewes, H. (1970). Structural control of geochemical anomalies in the Greaterville Mining District, southeast of Tucson, Arizona. *U.S. Geol. Surv. Bull. 1312-A.*

Drewes, H. (1971a). Geologic map of the Mount Wrightson Quadrangle, southeast of Tucson, Santa Cruz and Pima Counties, Arizona. *U.S. Geol. Surv. Misc. Geol. Invest. Map I-614.*

Drewes, H. (1971b). Geologic map of the Sahuarita Quadrangle, southeast of Tucson, Pima County, Arizona. *U.S. Geol. Surv. Misc. Geol. Invest. Map I-613.*

Drewes, H. (1971c). Mesozoic stratigraphy of the Santa Rita Mountains, southeast of Tucson, Arizona. *U.S. Geol. Surv. Prof. Pap. 658-C.*

Drewes, H. (1972a). Cenozoic rocks of the Santa Rita Mountains, southeast of Tucson, Arizona. *U.S. Geol. Surv. Prof. Pap. 746.*

Drewes, H. (1972b). Structural geology of the Santa Rita Mountains, southeast of Tucson, Arizona. *U.S. Geol. Surv. Prof. Pap. 748.*

Drewes, H. (1973). Geochemical reconnaissance of the Santa Rita Mountains, southeast of Tucson, Arizona. *U.S. Geol. Surv. Bull. 1365.*

Drewes, H. (1976). Plutonic rocks of the Santa Rita Mountains, southeast of Tucson, Arizona. *U.S. Geol. Surv. Prof. Pap. 915.*

Drewes, H. (1980). Tectonic map of Southeast Arizona. *U.S. Geol. Surv. Misc. Geol. Invest. Map I-1109.*

Enaudi, M. (1982). Description of skarns associated with porphyry copper deposits. In S. Titley (Ed.), *Advances in geology of the porphyry copper deposits.* Tucson: University of Arizona Press.

Finnell, A. (1970). *Preliminary geologic map of the Empire Mountains Quadrangle, Pima County, Arizona.* U.S. Geol. Surv. Open File Map.

Ford, J., R. Blom, M. Bryan, M. Daily, T. Dixon, C. Elachi, and E. Xenos (1980). *Seasat views North America, the Caribbean, and Western Europe with imaging radar* (JPL Publication 80-67). Pasadena, California: Jet Propulsion Laboratory.

Gillespie, A., and A. Kahle (1977). Construction and interpretation of a digital thermal inertia image. *Photogr. E. R., 43,* 983–1000.

Gilmour, P. (1982). Grades and tonnages of porphyry copper deposits. In S. Titley (Ed.), *Advances in geology of the porphyry copper deposits.* Tucson: University of Arizona Press.

Heidrick, T., and S. Titley (1982). Fracture and dike patterns in Laramide Plutons and their structural and tectonic implications: American Southwest. In S. Titley (Ed.), *Advances in geology of the porphyry copper deposits.* Tucson: University of Arizona Press.

Hotelling, H. (1933). Analysis of a complex of statistical variables into principal components. *J. Educ. Psyc., 24,* 417–441; 498–520.

Hulstrom, R. (1975). Spectral measurements and analyses of atmospheric effects on remote sensor data. *Proc. SPIE, 50,* 90.

Hunt, G., and R. Ashley (1979). Spectra of altered rocks in the visible and near infrared. *Econ. Geol., 74,* 1613–1629.

Hunt, G., and J. Salisbury (1971a). Visible and near-infrared spectra of minerals and rocks: II. Carbonates. *Mod. Geol., 2,* 23–30.

Hunt, G., and J. Salisbury (1971b). Visible and near-infrared spectra of minerals and rocks: III. Oxides and hydroxides. *Mod. Geol., 2,* 195–205.

Hunt, G., J. Salisbury, and C. Lenhoff (1973). Visible and near-infrared spectra of minerals and rocks: VI. Additional silicates. *Mod. Geol., 4,* 85–106.

Jennrich, R. (1977). Stepwise discriminant analysis. In K. Enslein, A. Ralston, and H. Wilf (Eds.), *Statistical methods for digital computers, Volume III of mathematical methods for digital computers.* Wiley-Interscience Publication, 76–95.

Kahle, A., J. Schieldge, M. Abrams, R. Alley, and C. LeVine (1981). *Geologic application of thermal inertia imaging using HCMM data* (JPL Publication 81-55). Pasadena, California: Jet Propulsion Laboratory.

Lowell, J., and D. Guilbert (1970). Lateral and vertical alteration-mineralization zoning in porphyry ore deposits. *Econ. Geol., 65*, 373–408.

MacDonald, H. (1980). Techniques and applications of imaging radars. In B. Siegal and A. Gillespie (Eds.), *Remote sensing in geology*. New York: John Wiley & Sons, 297–336.

Podwysocki, M., F. Gunther, and H. Blodget (1977). *Discrimination of rock and soil types by digital analysis of Landsat data* (Report X-923-77-17). Greenbelt, Maryland: Goddard Space Flight Center.

Richardson, M., S. Clemmons, and J. Walker (1979). *Soil survey of Santa Cruz and parts of Cochise and Pima Counties, Arizona.* Phoenix: University of Arizona. (National Cooperative Soil Survey)

Rowan, L., P. Wetlaufer, A. Goetz, F. Billingsley, and J. Stewart (1974). Discrimination of rock types and detection of hydrothermally altered areas in south–central Nevada by the use of computer-enhanced ERTS images. *U.S. Geol. Surv. Prof. Pap. 883.*

Sauck, W., and J. Sumner (1970). *Residual aeromagnetic map of Arizona.* Tucson: University of Arizona Press.

Sawatzky, D., and G. Raines (1982). Geologic use of linear-feature maps derived from small scale images. *Proceedings of the 3rd Basement Tectonics Symposium*, in press.

Schrader, F. (1915). Mineral deposits of the Santa Rita and Patagonia Mountains, Arizona. *U.S. Geol. Surv. Bull. 582.*

Shoemaker, E., R. Squires, and M. Abrams (1978). Bright Angel and Mesa Butte fault systems of northern Arizona. In R. Smith and G. Eaton (Eds.), Cenozoic tectonics and regional geophysics of the Western Cordillera, *Geol. Soc. of Am. Mem. 152*, 341–367.

Slater, P. (1981). *Remote sensing: Optics and optical systems.* Reading, Massachusetts: Addison–Wesley Publishing Co.

Soha, J., and A. Schwartz (1978). Multispectral histogram normalization contrast enhancement. *5th Canadian Symposium on Remote Sensing.* Victoria, British Columbia, August 1978, 86–94.

Titley, S. (1976). Evidence for Mesozoic linear tectonic pattern in S.E. Arizona. *Ariz. Geol. Soc. Digest, X*, 71–101.

Turner, R., W. Malila, R. Nalepka, and F. Thomas (1975). Influence of the atmosphere on remotely sensed data. *Proc. SPIE, 51*, 101.

Wiersma, D., and D. Landgrebe (1980). Analytical design of multispectral sensors. *IEEE Trans. Geosci. Rem. Sens., GE-18*(2), 180–189.

Wilson, E., R. Moore, and J. Cooper (1969). *Geologic map of Arizona.* Phoenix: Arizona Bureau of Mines. (Scale 1:500,000)

Section 6

Safford, Arizona, Porphyry Copper Test Site Report

Larry Lepley
Tucson, Arizona

Michael J. Abrams
Jet Propulsion Laboratory

Leigh Readdy
Tucson, Arizona

Section 6

Safford, Arizona, Porphyry Copper Test Site Report

Contents

I. Introduction 6-1
- A. Overview 6-1
- B. Rationale for Site Selection 6-1
- C. Site-Specific Objectives 6-1
- D. Remote Sensing Model 6-2
  - 1. General porphyry model 6-2
  - 2. Ore zones 6-2
  - 3. High pyrite zones 6-2
  - 4. Phyllic/argillic alteration 6-3
  - 5. Propylitic alteration 6-3
  - 6. Plugs, dikes, and tuffs 6-3
  - 7. Mineralized porphyries 6-3
  - 8. Structural features 6-3
- E. Data Sources and Interpretation Methods 6-4
  - 1. Remote sensing data 6-4
  - 2. Support data 6-5
  - 3. Geophysical support data 6-6
  - 4. Procedures for interpretation and comparison of data 6-6

II. Description of Site 6-6
- A. General Description 6-6
- B. Soils and Physiography 6-7
- C. Vegetation 6-7
- D. Cultural and Land Use Patterns 6-7
- E. History and Production 6-7
- F. Geologic History 6-9
  - 1. Stratigraphic evolution 6-9
  - 2. Structural evolution 6-9
  - 3. The Laramide porphyry copper deposits 6-11
- G. Summary of Observable Features 6-23

PRECEDING PAGE BLANK NOT FILMED

III. Field and Laboratory Spectral Measurements 6-23
A. Field Spectra 6-23
1. Description and procedure 6-23
2. Spectral measurements 6-24
3. Statistical analysis of PFRS data 6-26
B. Laboratory Spectra 6-31
1. Introduction 6-31
2. Methods 6-31
3. Results 6-35

IV. Image Analysis and Interpretation 6-39
A. Introduction 6-39
B. Mapping of Alteration 6-39
1. Potassic zone 6-40
2. K-feldspar–quartz–biotite assemblage 6-40
3. Biotitization 6-41
4. Phyllic zone 6-41
5. Albitization 6-42
6. Chloritic zone 6-42
7. Argillic zone 6-42
8. Propylitic zone 6-42
9. Pyritic halo 6-42
C. Remote Sensing Data 6-42
1. Color photography 6-42
2. Radar data 6-43
3. Landsat MSS data 6-51
4. M²S 11-channel data 6-58
5. NS-001 data 6-65
6. M²S thermal data 6-80

V. Conclusions and Recommendations 6-81
A. Evaluation of Data 6-81
1. Photographic data 6-81
2. Radar data 6-88
3. Landsat MSS 6-88
4. M²S 11-channel scanner 6-89
5. NS-001 Thematic Mapper Simulator 6-89
6. M²S thermal data image 6-89
B. Signatures for Alteration of Andesitic Rocks 6-90
C. Recommendations 6-90
1. Sensors and sensor combinations 6-90
2. Digital processing techniques 6-91
3. Field verification techniques 6-91
4. Sequencing of data acquisition, processing, and verification 6-91

Acknowledgments 6-92

References 6-93

Figures

6-1. Idealized cross-sectional views of alteration zoning and mineralization zoning for southwestern U.S. porphyry copper deposits 6-3

6-2. Location of Safford test site in southeastern Arizona 6-4
6-3. General soil map of the Safford area 6-8
6-4. Geologic map of Safford District 6-10
6-5. Geologic sections of Safford District 6-11
6-6. Geologic terraces in the Safford area. 6-13
6-7. Surface alteration map of Safford District 6-14
6-8. The Lone Star District: (a) alteration patterns; (b) pyrite halo 6-21
6-9. Location map showing PFRS sample sites and sites where samples were obtained for laboratory analyses 6-24
6-10. PFRS reflectance curves of alluvium, basalt, and tuff units measured in the field. 6-27
6-11. PFRS reflectance curves of andesite and quartz monzonite units measured in the field. 6-28
6-12. Results of linear discriminant function analysis of PFRS data 6-30
6-13. Image pseudo-spectra of solid, freshly broken rock surfaces (D_B, F_B), solid weathered surfaces (D_W, F_W), and powdered rocks (D_P, F_P) of (a) phyllically altered mylonite and (b) argillized porphyry as might be seen by five bands of the M²S scanner 6-34
6-14. Image pseudo-spectra of solid, freshly broken rock surfaces (A_B, B_B), solid weathered surfaces (A_W, B_W), and powdered rocks (A_P, B_P) of propylitically altered andesite as might be seen by five bands of the M²S scanner 6-35
6-15. Image pseudo-spectra of solid, freshly broken rock surfaces (F_B, D_B), solid weathered surfaces (F_W, D_W), and powdered rocks (F_P, D_P) of (a) argillized porphyry and (b) phyllically altered mylonite as might be seen by six bands of the NS-001 scanner 6-36
6-16. Image pseudo-spectra of solid, freshly broken rock surfaces (A_B, B_B), solid weathered surfaces (A_W, B_W), and powdered rocks (A_P, B_P) of propylitically altered andesite as might be seen by six bands of the NS-001 scanner 6-37
6-17. Image pseudo-spectra of five M²S and six NS-001 channels of sample 2c taken from one of the noncorrelating sites where some scanner images indicate phyllic alteration and others do not 6-38
6-18. Color aerial photograph of area around the Dos Pobres deposit 6-44
6-19. Interpretation map of color aerial photograph (Figure 6-18) showing iron-oxide anomaly and curvilinear features associated with the buried Dos Pobres deposit 6-45
6-20. Drainage map of area around the Dos Pobres deposit showing fine-textured pattern over the deposit 6-47
6-21. Color photograph from Skylab 4 S190B experiment, acquired February 1974 6-48
6-22. Interpretation map of lineaments and curvilinear features mapped from Skylab S190B color photograph (Figure 6-21) 6-49

6-23. Seasat L-band image of Safford area, acquired October 5, 1978 ... 6-50
6-24. Enlarged Seasat L-band radar image of Safford District ... 6-51
6-25. Interpretation of linear and curvilinear features detectable on enlarged Seasat image (Figure 6-24) ... 6-52
6-26. Aircraft X-band radar image of Safford area ... 6-53
6-27. Interpretation map produced from aircraft X-band radar image of Safford area (Figure 6-26) ... 6-54
6-28. Full-frame Landsat MSS scene of Safford area ... 6-55
6-29. Enlargement of Landsat CIR composite (Figure 6-28) covering a 32- by 34-km area ... 6-56
6-30. CRC of Landsat data covering a 50- by 50-km area around Safford ... 6-57
6-31. Typical spectral reflectance curves for vegetation and iron oxide ... 6-58
6-32. PC composite of Landsat data covering a 50- by 50-km area around Safford ... 6-59
6-33. Structural and limonite interpretation based on three processed Landsat MSS scenes ... 6-60
6-34. Spectral reflectance curves for hematite, goethite, and jarosite ... 6-61
6-35. M²S CRC. Band-ratios 4/6, 6/8, and 8/9 are displayed as blue, green, and red, respectively ... 6-62
6-36. M²S CRC. Band-ratios 4/6, 6/8, and 9/10 are displayed as blue, green, and red, respectively ... 6-63
6-37. Interpretation map of M²S CRCs (Figures 6-35 and 6-36) showing areas of iron-oxide anomalies found on the two images ... 6-64
6-38. Location of area interpreted for soil units using M²S data ... 6-66
6-39. Soil map of area analyzed from M²S data ... 6-67
6-40. M²S CRC of a portion of the Safford area used for soil mapping ... 6-68
6-41. Interpretation of M²S ratio image (Figure 6-40) ... 6-69
6-42. NS-001 CRC. Band-ratios 3/2, 4/5, and 6/7 are displayed as green, blue, and red, respectively ... 6-71
6-43. NS-001 CRC. Band-ratios 3/2, 4/6, and 6/7 are displayed as green, blue, and red, respectively ... 6-72
6-44. Interpretation map of NS-001 3/2, 4/5, and 6/7 ratio image (Figure 6-42) ... 6-73
6-45. Enlargement of NS-001 band-ratio composite (3/2, 4/5, 6/7) over Dos Pobres deposit ... 6-74
6-46. Geologic map of Dos Pobres area ... 6-75
6-47. Interpretation of spectral anomalies on NS-001 ratio image of Dos Pobres area (Figure 6-45) ... 6-76
6-48. Density slice of NS-001 6/7 band ratio ... 6-77
6-49. Lineament interpretation produced from NS-001 band-ratio image ... 6-78

6-50. Lineament interpretation produced from Landsat MSS data for the same area as NS-001 data, Figure 6-49 6-79
6-51. Canonically transformed NS-001 data 6-82
6-52. Interpretation map of canonically transformed NS-001 image (Figure 6-51) showing areas interpreted to be hydrothermally altered 6-83
6-53. General geologic map of Safford District with Kennecott area (Figure 6-54) outlined 6-84
6-54. Kennecott deposit: (a) color aerial photograph; (b) enlargement of NS-001 canonical transform image; (c) Kennecott alteration map; (d) interpretation of NS-001 image 6-85
6-55. M²S thermal and albedo data 6-86
6-56. Color composite of M²S thermal and albedo data 6-87

Tables

6-1. Scales and sources of remote sensing data for Safford test site 6-5
6-2. Description of units on soil map (Figure 6-3) 6-9
6-3. Geologic column and geochronology 6-12
6-4. Sample numbers and rock types 6-25
6-5. PFRS spectral absorption features 6-29
6-6. Wavelength bands (μm) of instruments used for statistical analysis of PFRS data 6-29
6-7. Comparison of mapped lithology and alteration, color on digital images, X-ray mineralogy, and laboratory spectral features 6-32
6-8. Predicted and observed image colors for phyllic and propylitic alteration 6-34
6-9. Color assignments for remote sensing scanner images 6-39
6-10. Percent reflectance and ratio values for vegetation and iron oxide in Landsat MSS bands 6-58
6-11. MSS and M²S bands 6-61
6-12. Ratio values and M²S ratio colors for phyllic and propylitic alteration 6-66
6-13. Description of soil units 6-70
6-14. NS-001 bands 6-70
6-15. Ratio values and NS-001 colors for phyllic and propylitic alteration 6-70
6-16. Thermal behavior and predicted image colors for various materials 6-81
6-17. Sensor configurations and results of classification analysis 6-90

Section 6

Safford, Arizona, Porphyry Copper Test Site Report

I. Introduction

A. Overview

The Safford test site report presents the results of the remote sensing data evaluation project for the Safford, Arizona, porphyry copper district. This report is divided into three parts:

(1) *Background information.* This part includes a description of the physiography, geology, and mineral emplacement history of the deposits; detailed descriptions of the types of data analyzed and the data interpretation methods used; and a remote sensing model describing characteristics of the deposits which might be detectable by remote sensing methods.

(2) *Spectral analysis.* This part includes a description of laboratory and field spectral measurements of rocks and soils found at the test site and provides the foundation for the later image analysis description by relating spectral properties to mineralogy. This information is useful both for interpreting the image data and for guiding the development of image processing techniques.

(3) *Image analysis.* This part includes a description of the results of the various image data sets evaluated individually, then integrated and interpreted jointly. Appearances of rock types on the images are related to the spectral properties determined in the spectral analysis portion.

B. Rationale for Site Selection

The Safford (Lone Star) District was chosen because it contains three known, deeply buried porphyry copper deposits (Kennecott, Dos Pobres, and San Juan). Only minor outcrops of these mineralized intrusives show at the surface, and surface alteration is mainly limited to the outer zones of a typical porphyry copper deposit. The center of the Kennecott deposit is covered by postmineral volcanic rocks. The Dos Pobres deposit is not only deeply buried, but is split by a normal fault. The down-faulted block is now covered by several hundred meters of alluvium. In contrast to the well-exposed Silver Bell site, only the outer fringes of the alteration associated with the buried deposits are exposed. This represents the present real-world situation in exploration for concealed deposits. In addition to the three deeply buried porphyry systems, the district contains a small deposit (Sanchez) that has a reasonable amount of exposure, although its surface has been disturbed by past mining efforts.

Vegetation cover and cultural disturbances for the deeper porphyry systems are minimal. Access to one of the deposits and to unpublished maps and reports was made available by Phelps Dodge Corporation, a Geosat member. Published information on the district and on the Kennecott deposit showed that the area had been well studied and contains typical porphyry copper deposits (Dunn, 1978; Robinson and Cook, 1966). More recently, detailed information has been published on the Dos Pobres deposit (Langton and Williams, 1982).

C. Site-Specific Objectives

The overall objective of the Safford test site study was to assess the usefulness of a number of remote sensing systems as mapping tools in an environment of known, deeply buried porphyry copper deposits.

The secondary objective of this study was to use a variety of remote sensing instruments to define the characteristic signatures for alteration in andesitic volcanic rocks. Particular emphasis was placed on the NS-001 Thematic Mapper Simulator. The NS-001 was configured to provide an analog to the Thematic Mapper (TM) which is on board the Landsat 4 satellite.

The Safford District provided a unique test case since there are four porphyry systems within a small area. Evaluation of the imaging systems, as single data sources and in various combinations, could therefore be made to document their application to the discrimination of several major rock types, alteration patterns, and the structural elements associated with each of these deposits. Specific objectives included the identification and definition of:

(1) Phyllic alteration representative of the outer zone of sulfide mineralization in the buried deposits

(2) Propylitic alteration associated with both district-wide autometamorphism of the andesites and a second phase associated with the mineralization events

(3) Different host-rock lithologies

(4) Major structural elements including regional faults, transverse faults, and porphyry dike swarms

D. Remote Sensing Model

The primary part of the remote sensing model is the general model of porphyry copper deposits within the Basin and Range Province. This was used to define spectral modeling features expected to be observable through images that could be obtained from three scanner devices. These instruments include the Landsat 4-channel Multispectral Scanner (MSS), the Modular Multispectral Scanner (M^2S) 11-channel scanner, and the Landsat 4 TM as simulated by the NS-001 scanner. The model could also be used to evaluate an idealized, synthetic 30-channel array from a theoretical point of view. For comparison, a photogeologic model based on conventional color aerial photography was also considered. This model is limited by the availability of only three broad spectral bands available to color film and to the human eye. However, more textural, morphological, and other spatial information is available from the photography because of the high spatial resolution of photographic film.

1. General porphyry model. A very general Basin and Range porphyry copper model has been defined by various authors in Titley and Hicks (1966) and by Lowell and Guilbert (1970). This model consists of a set of nested shells of sulfide mineralization and alteration mineral assemblages which are superimposed on an intrusive center (Figure 6-1). The intrusive center is commonly at least partially porphyritic, if not a true porphyry. In plan view, the generalized form of the systems and zones within the system are circular to elliptical. Three dimensionally, they resemble a cylinder, which may taper inward slightly with depth, capped by domal zones roughly paralleling the intrusive host. Mineralized and altered dikes may extend upward and away from the intrusive.

The hypogene alteration assemblage usually changes progressively from the core outward through potassic, phyllic, argillic, and propylitic alteration zones. The mineral assemblages that constitute these various alteration zones depend upon the host-rock chemistry. In the deeply buried porphyry deposits of the Safford District, phyllic (quartz–sericite) and argillic alteration are restricted to the more acidic intrusive masses and dikes and to a tuff-filled vent. Some minor phyllic alteration, seen as weak disseminations of sericite associated with quartz, occurs in fractures in the andesite adjacent to the dikes and in widely spaced fractures in the andesite. Argillic alteration has a similar mode of occurrence. Propylitic alteration is widespread in the andesites. This propylitic alteration is composed of biotite, chlorite, epidote, calcite, and albite in the fabric of the andesite as well as in veinlets. Portions of this widespread propylitic alteration are probably autometamorphic, but at least some of this alteration is related to the porphyry copper mineralization event.

2. Ore zones. The ore zones are not exposed in the Dos Pobres and Kennecott deposits (see Figure 6-2 for locations). However, the mineralizing intrusions, the structures controlling the locus of intrusions and mineral emplacement, the intermediate and outer alteration zones, and the leached cappings derived from the sulfide system are partially exposed.

3. High pyrite zones. The "pyrite halo" at the Kennecott site coincides with that portion of the main alteration zone outside the main ore zone. Pyritic zones are characterized by low copper concentrations, high-pyrite/copper sulfide ratios, and relative abundance of jarositic limonite.

The presence of sericite and clay minerals in the pyritic zone tends to produce an overall lighter tone in contrast with the darker tones of surrounding fresh rocks. A diagnostic brick-red or yellowish-brown color is characteristic of the capping produced by oxidation of copper-poor sulfides. The pyritic zone may be characterized by a subdued topography with rounded ridges caused by relatively high fracture density and the presence of soft clays and sericite (Readdy, 1978).

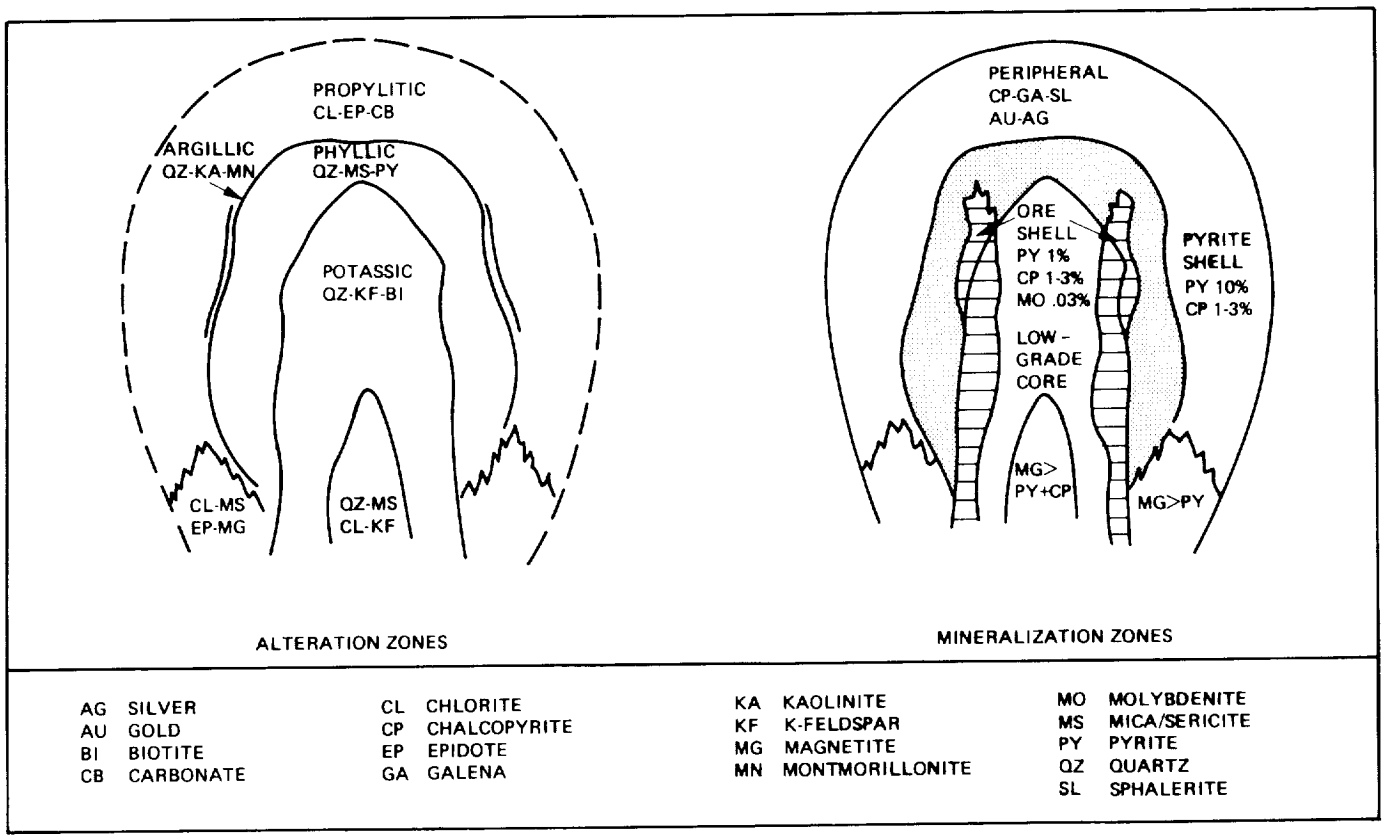

Figure 6-1. Idealized cross-sectional views of alteration zoning and mineralization zoning for southwestern U.S. porphyry copper deposits (Lowell and Guilbert, 1970)

4. Phyllic/argillic alteration. Phyllic and argillic alteration generally coincide with the pyritic zone, the general characteristics of which have already been summarized. In addition to the indirect tonal and geomorphic features, the main alteration minerals—sericite, clays, and limonite—can be detected directly by their diagnostic spectral absorption bands. The iron and hydroxyl absorption bands make phyllic and argillic alteration highly visible on both Landsat and aircraft images.

5. Propylitic alteration. Areas of propylitic alteration should have an overall light tone and a pale greenish tint in the visible region of the spectrum due to the presence of minerals such as albite, epidote, and chlorite. The presence of small amounts of limonite from the oxidation of pyrite should also be detectable on Landsat and aircraft images. The Mesozoic andesite host rocks are pervasively propylitically altered by autometamorphism. Therefore, the objective of the model was to discriminate between propylitic and phyllic alteration. The propylitic zones would show less intense iron and hydroxyl absorption bands.

6. Plugs, dikes, and tuffs. Eocene rhyolite, quartz latite, latite, and dacite plugs, dikes, and associated tuffs are exposed at the Kennecott property and north of the Phelps Dodge ore body (Dos Pobres). Some of these outcrops are hundreds of meters in length and width and should be visible against the andesitic Cretaceous–Paleocene metavolcanics.

7. Mineralized porphyries. Mineralized Paleocene–Eocene quartz monzonite, tonalite, and granodiorite porphyries are exposed at or near the Dos Pobres, San Juan, and Kennecott deposits. These generally contain abundant sericite and limonite (iron-oxide minerals) and thus should be discernible with TM spectral bands.

8. Structural features. Mineralization was controlled by NE–ENE faulting that also controlled the emplacement of the porphyry stocks and dikes. The relative stratigraphic position of dike swarms, mineralized fractures, and alteration zones are difficult to map by conventional methods because of the lack of marker units in the premineral andesite. The phyllic alteration generally follows the northeasterly structures. The predictive model was that these should be mappable by their spectral contrast with the surrounding andesite wherever the alteration zones are wider than the 10-m resolution of the NS-001 scanner.

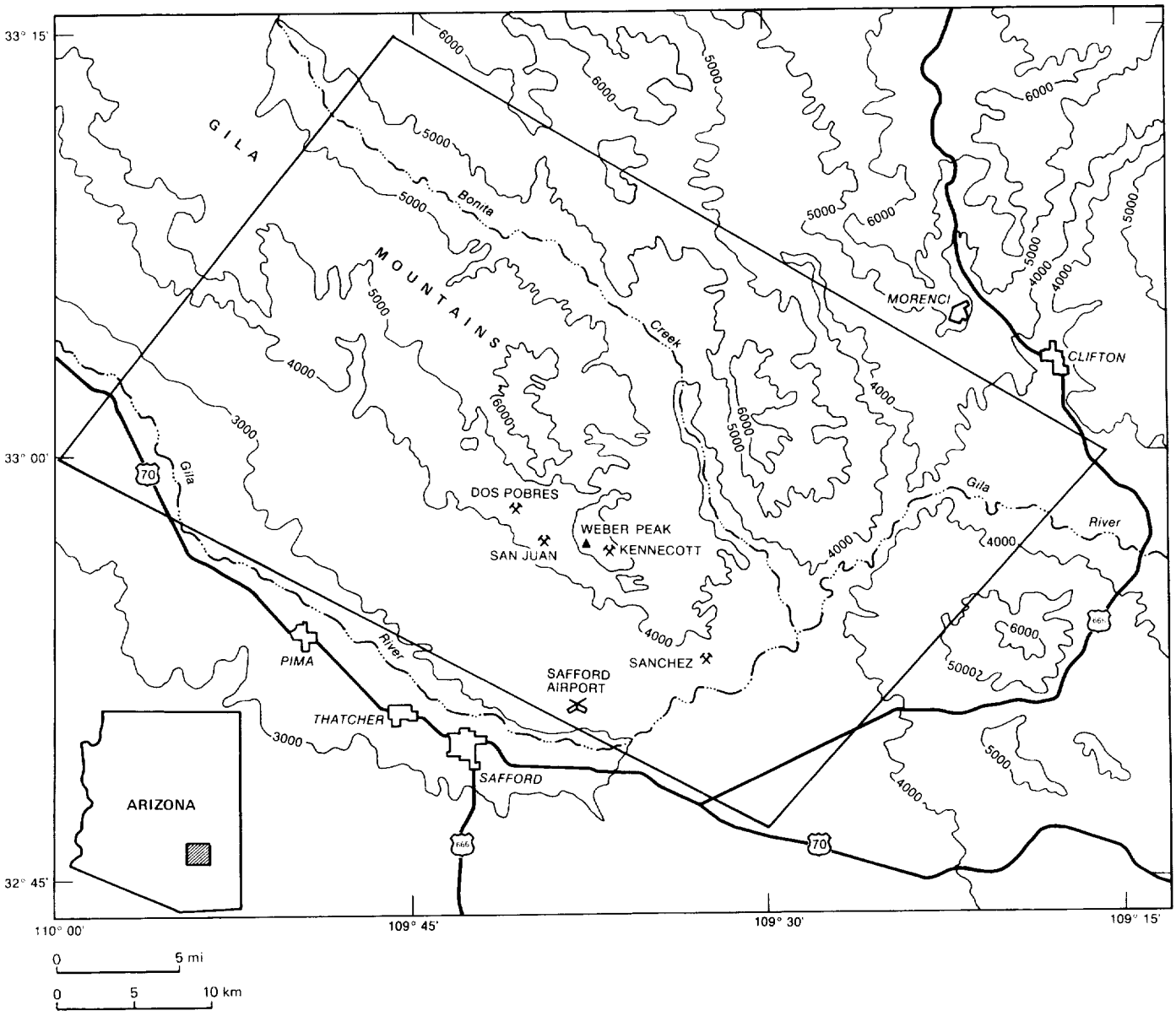

Figure 6-2. Location of Safford test site in southeastern Arizona; topographic contours in feet

The postmineral northwesterly Butte (Foothill) Fault should be mappable from all sensors because it is marked by the contact between Tertiary alluvium against Mesozoic metavolcanics. Many of the other larger faults were also anticipated to be mappable on most of the sensor products (images) because of their reasonably strong topographic expression.

E. Data Sources and Interpretation Methods

1. Remote sensing data. Remote sensing data acquired for the Safford test site include color aerial photography, Landsat MSS images, aircraft multispectral scanner data, and radar images from both aircraft and Seasat. The scales and sources of these data are included in Table 6-1.

The aircraft color aerial photography was acquired by NASA during October 1978. The stereo color aerial photographs are at a scale of 1:48,000. Nonstereo enlargements of this photography at a scale of 1:24,000 were also used.

Glossy prints, produced at JPL, of the following three stereo sets of Skylab color photographs were interpreted:

Table 6-1. Scales and sources of remote sensing data for Safford test site

Data	Scale	Source	Date
Color aerial photography	1:24,000; 1:48,000	Johnson Space Center (JSC)	August 1977 October 1978
Skylab photography	1:500,000; 1:750,000	JPL (reproduced from EROS Data Center transparencies)	September 1973 February 1974
Landsat MSS	1:125,000; 1:500,000	JPL (processed from EROS Data Center tapes)	December 1973 October 1976 March 1977
11-channel M^2S	1:24,000	JSC	August 1977 October 1978
NS-001	1:24,000	JSC	October 1978
Aircraft SLAR	1:250,000	JSC	May 1978
Seasat (SAR)	1:1,000,000	JPL (digitally processed)	October 1978

(1) S190B Earth Terrain Camera, SO-242 film, prints at 1:500,000 scale, acquired on SL-3, September 1973

(2) S190B Earth Terrain Camera, SO-242 film, prints at 1:500,000 scale, acquired on SL-4, February 1974

(3) S190A Hasselblad Camera, SO-356 film, prints at 1:750,000 scale, acquired on SL-4, February 1974

Landsat MSS data consist of three scenes of the Safford area, recorded at three different seasons (spring, winter, and summer). The computer tapes for these three frames were further processed by band ratioing and principal components techniques and printed as 1:125,000 enlargements, covering roughly 8 percent of the full-frame area. Each enlargement covers a rectangular area of about 37 by 25 km.

Scanner data using the 11-channel M^2S system were acquired by NASA simultaneously with the color aerial photography during October 1978. The C-130 overflight was at an altitude of approximately 5000 m. The images produced are at approximately 1:24,000 scale. These 11-channel data cover a NW-oriented swath of 20 by 45 km with an instantaneous field of view (IFOV) of 15 m.

The NS-001 scanner data consist of a WNW-oriented swath 30 by 11 km in size with an IFOV of 12 m. Due to a brief malfunction of the NS-001 scanner, a 1.6-km-wide strip of data is missing from that swath. The missing 1.6- by 11-km strip is unfortunately centered over the San Juan Mine, so the remote sensing model was not tested over that deposit.

The aircraft radar data examined consist of two glossy prints at a scale of approximately 1:250,000 covering essentially the equivalent area of the Landsat 1:125,000 enlargement, with a north-looking direction and two different polarizations.

2. Support data. Ancillary data used in the interpretation of the Safford images include geological and geophysical information from both published and unpublished sources. Detailed geologic data on the Dos Pobres deposit and the surrounding area are provided by an unpublished Phelps Dodge geologic map at a scale of approximately 1:4,800. This map shows structural and lithologic details, including the location of the ENE-mineralized shear zones, the Trans-Butte Fault, the Dos Pobres Anticline, and the Red Dyke fault zone. The contact between the Cretaceous–Paleocene metavolcanic host rock and the nonmineralized Eocene Baboon metavolcanics is shown; and, most importantly, the small (25- to 75-m) heavily altered Paleocene porphyry outcrops are shown. This map was accompanied by an unpublished Phelps Dodge geologic report by J. M. Langton and S. A. Williams that has only recently become available in published form (Titley, 1982).

The principal detailed geologic data for the entire Safford District is provided by three unpublished 1:24,000 maps provided by Bear Creek Mining Company (Kennecott Copper Corporation). These maps, compiled by Annan Cook in the early 1960s, include separate sheets for alteration, geology, and structure. The mineralized and altered ENE shear zones, the mineralized porphyry dikes, the metavolcanic host rocks, the Lone Star parent pluton, and the outline of the phyllic alteration zones are shown.

It is important to note that these Kennecott maps were compiled many years before the Geosat Test Case studies but were not released until January 1980, several months after JPL had processed the multispectral scanner data to produce the images evaluated as part of this study. The digital data processing was completed without recourse to the Kennecott support data which included the only district-wide alteration maps of appropriate scale and detail. The timing of the release fortuitously provided the researchers with a double-blind experiment wherein information derived from remote sensing data could be compared with information produced by conventional techniques.

A number of other sources of geological information exist for the district. A master's thesis by Blake (1971) describes the San Juan Mine area. A 1:45,000 geologic map of the Safford District, modified after R. Greer, was released by Phelps Dodge Corporation. Published information includes 1:45,000 to 1:150,000 scale geologic maps of the Safford (Lone Star) District by Dunn (1978). Geologic cross sec-

tions in the literature are the Safford (Kennecott) deposit by Robinson and Cook (1966), the Dos Pobres deposit by Langton and Williams (1982), and other parts of the district by Dunn (1978). Geochemical, mineralization, and geophysical maps of the Safford deposit are shown by Robinson and Cook (1966). A district geochemical map is shown by Horsnail (1978). An evaluation of the photogeologic features such as natural color, tone, photographic texture, landform, and drainage characteristics related to the porphyry systems in the district has been reported by Readdy (1978).

3. Geophysical support data. Regional aeromagnetic and gravity maps are available (Lyzonski et al., 1980; Sauck and Sumner, 1970) and regional analyses of these have been made (Lepley, 1978). Although these maps may help explain the location of the district within a larger area, these small-scale (1:500,000 to 1:1,000,000) maps are too coarse for meaningful analyses of the district (i.e., the test site itself). However, such geophysical data can be used with Landsat MSS images and Skylab photographs to relate metallogenesis to regional tectonics. These geophysical maps are not sufficiently detailed for analysis at district scale and, therefore, will not be discussed further in this report.

4. Procedures for interpretation and comparison of data. Interpretation of the Safford data proceeded in four steps:

(1) Visual comparison between images and support data, primarily through the use of overlays

(2) Ground checking—collection of samples at the site to substantiate any interpretive conclusions and to check the cause of any unusual features or discrepancies

(3) Laboratory spectral reflectance and X-ray diffraction analysis of the samples

(4) Further visual comparisons and integration with laboratory and ground spectral data

The boundaries of distinctive spectral features were traced onto mylar from the various images, and the individual areas were classified and labeled according to similar spectral characteristics. Maps with supporting geological data were then placed on top of the appropriate images and compared with the interpreted overlays by the quick-flip technique. Direct superposition of mapped geology and alteration on the color image products and the different image products on each other was used. Lithologic and alteration separations were compared, and image spectral signatures were qualitatively deduced by internally comparing the image data suites themselves and externally comparing these with theoretical and measured spectra, X-ray diffraction results, field identification, and support maps.

The geologic and alteration maps did not fit the images exactly because of slight scale differences and geometric distortion of the scanner images. To compensate for this, a control grid map was constructed by drawing section lines on clear mylar overlayed on one of the 1:24,000 NS-001 images. This grid map was constructed with the aid of 1:24,000 translucent mylar orthophotomaps supplied by the U.S. Department of Agriculture Soil Conservation Service.

The support maps were manually rotated or shifted to match the appropriate part of the image as closely as possible. The matching was done by using the section line grids, major mapped faults, and the cliff edge of postore volcanic rocks as guides.

II. Description of Site

A. General Description

The Safford test site is located in Graham County, southeastern Arizona. The area studied in detail is defined by a NW–SE polygon with coordinates of lat. 32°48′ N, long. 109°30′ W; lat. 33°00′ N, long. 110°00′ W; lat. 33°00′ N, long. 109°17′ W; and lat. 33°15′ N, long. 109°47′ W (Figure 6-2).

The deposits studied are in the Safford (or Lone Star) District on the southwestern flank of the Gila Mountains, one of several NW-trending ranges characteristic of the Basin and Range physiographic province of southeastern Arizona. This range is on the eastern side of the mountain region or Mexican Highlands that separates the Colorado Plateau Province from the Sonoran Desert (Robinson and Cook, 1966). The area has one major drainage area, the Gila River, which runs from southeast to northwest; Bonita Creek drains the northern part of the area and flows into the Gila River northeast of Safford. Several streams flow intermittently in a southwestern direction from the Gila Mountains and join the Gila River.

Four separate porphyry copper deposits occur within a narrow NW-trending belt along the southwestern flank of the Gila Mountains. From northwest to southeast these are the Dos Pobres ore body operated by the Phelps Dodge Corporation, the San Juan open-pit operation leased by the Phalen Oil Company, the Safford deposit of Kennecott, and the Sanchez deposit held by Inspiration Copper.

Major access to the region is provided by U.S. Highway 70 from the northwest and Interstate Highway 10 and U.S.

Highway 666 from the south and west. U.S. Highways 70 and 666 intersect at the town of Safford, about 15 km southwest of the mining district.

Graham County has an arid climate, with light precipitation, large temperature changes, plentiful sunshine, and low humidity. Mean annual precipitation ranges from about 20 cm near Safford to more than 90 cm on Mt. Graham, 22 km southwest of Safford. About one-half of the precipitation occurs during the summer and comes as brief but often heavy showers. Light to moderate precipitation occurs during the winter months.

The mean annual temperature ranges from about 20°C in the lower valley to about 8°C in the higher mountains. Summer daytime temperatures of 32°C or higher can be expected at lower elevations, and quite often exceed 37°C.

B. Soils and Physiography

The test site area, as depicted on the general soil map of Graham County (Figure 6-3), contains eight mapped soils in floodplains and alluvial fans (Table 6-2). These are:

(A1) Soil ranging from clay loam to sand loam

(B2) Broad grass-covered areas of brown loam or clay loam

(B3) Soil on low terraces or rounded ridges with gravelly loam surfaces

(B4) Soil on high terraces and valley slopes consisting of brown gravelly, sandy loam

(B7) Soil formed on basalt bedrock and on alluvium derived from basalt bedrock

(C5) Deeply dissected terrace fronts—gravelly loam

(D1) Slopes on footslopes of Gila Mountains—reddish-brown clay horizons or cobbly clay loam

(D3) Basalt hills and low mountains—dark-brown cobbly clay loam; rock outcrops common

The maximum elevation of 1850 m is reached at Weber Peak; extensive alluvial fans extend southwesterly from the mountain range down to the Gila River trough at an elevation of 840 m.

C. Vegetation

Vegetation association types are related to the different soil classes:

(A1) Mesquite, catclaw, creosote, cacti, saltbush, cottontop, bush muhly, and three-awns; cottonwood, willow, and tamarisk along stream channels

(B2) Grass covered; blue grama with some tobosa and hairy grama

(B3) Creosote, cholla, mesquite, and annual grasses

(B4) Creosote, whitethorn, catclaw, mesquite, and annual grasses at lower elevations; curly mesquite, tobosa, snakeweed, and wolfberry at higher elevations

(B7) Creosote, snakeweed, saltbush, mesquite, cactus, ocotillo, tobosa, and grama

(C5) Mesquite, creosote, tarbush, catclaw, cacti, and whitethorn

(D1) Short grass cover, dominantly tobosa, but with blue grama, three-awns, scattered juniper, and mesquite

(D3) Tobosa, with minor cone beard grass, side oats grama, and black grama; in addition, north-facing slopes have Mormon tea, guajillo, juniper, and piñon; south-facing slopes have ocotillo, cacti, and snakeweed

In general, vegetation density is minimal. Thick growths, dominated by willows, are found along well-watered streams. Fans and terraces support only a modest cover of grasses, cacti, and shrubs among scattered trees. Most of the year, vegetation cover is less than 20 percent. During the brief rainy season, grasses flourish and coverage increases to 70 to 80 percent. At higher elevations along rocky outcrops, trees become more prevalent, and grasses and shrubs decrease in abundance; coverage, nevertheless, does not exceed 30 percent.

D. Cultural and Land Use Patterns

The Gila River Valley is extensively cultivated for irrigated crops of cotton, sorghum, alfalfa, barley, and corn. The unirrigated areas, such as those surrounding the porphyry systems, are used as desert range for producing beef cattle. Farming is the dominant enterprise of the Gila River Valley, but cattle ranching, mineral exploration, and mining are the primary land uses of the area around the porphyry deposits.

E. History and Production

Information pertaining to the Safford District prior to 1950 is scanty. Of the four known porphyry copper deposits (San Juan, Dos Pobres, Kennecott, and Sanchez), no information was found for the Sanchez deposit, and only early information was found for the San Juan deposit.

Most of the development and production at the San Juan deposit was accomplished from 1900 to 1920 (Blake, 1971). Production for 1905 was 110,000 lb of copper, 223 oz of sil-

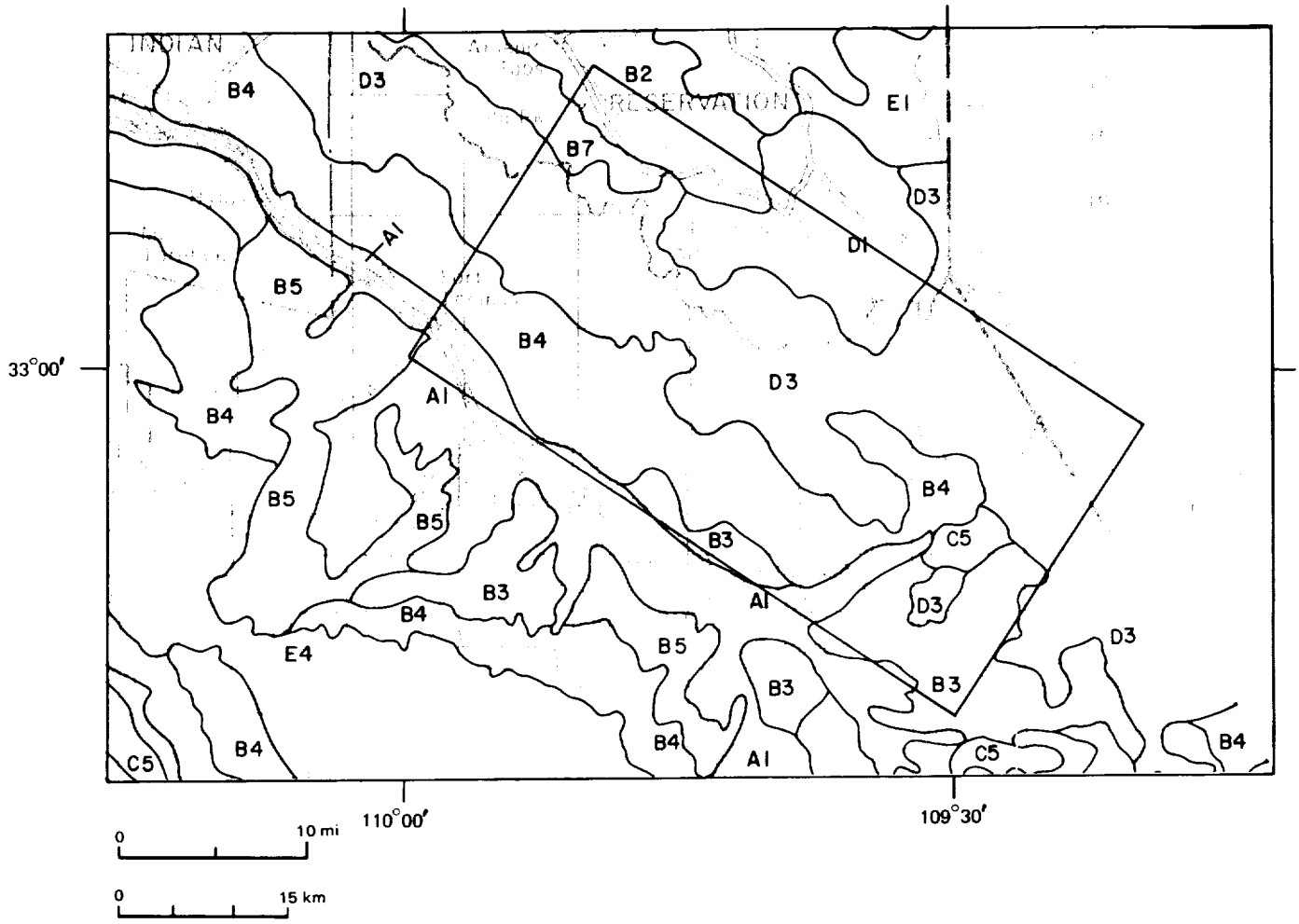

Figure 6-3. General soil map of the Safford area (U.S. Department of Agriculture, 1973). Test site area in box. For explanation of units, see Table 6-2.

ver, and 6 oz of gold. Lack of information covering the period from 1920 to 1948 suggests that the mine was idle. In 1951, Tuab Mineral Corporation secured a lease on the San Juan Mine and adjoining claims. In 1955, the Bear Creek Mining Company (the exploration branch of Kennecott Corporation) initiated a geological mapping and geochemical sampling program in the region and later dropped its option on the San Juan area. The latest work to take place was initiated in 1967 by the Phalen Oil Company, which optioned the property in hopes of doing further exploration work and leaching the deposit.

The Dos Pobres area was optioned in 1957 by Phelps Dodge Corporation, based on geochemical surveying and on geological and leached capping interpretations of unusual outcrops. Drilling begun in 1957 encountered sufficient mineralization to warrant purchase of the optioned claims. Further exploration and drilling of a development shaft, crosscuts, and drifts have confirmed reserves of approximately 400 million tons of 0.72 percent copper sulfide ore (Langton and Williams, 1982).

Discovery of the Kennecott ore deposit occurred in 1949 when the Consolidated Copper Mines Corporation and the American Metal Company, Ltd. optioned claims in the area, drilled nine holes both through the basalt-covered area and in the outcropping mineralized rhyolites, and encountered low-grade copper mineralization. In 1955 Bear Creek Mining Company optioned the area, based on reconnaissance geological mapping without knowledge of the previous drilling results. After further geological mapping, geophysical surveying, and geochemical sampling, a diamond drilling program was started. The property was purchased by Kennecott Corporation in 1959, when drilling indicated the presence of a sizable low-grade copper deposit. Since then, development work has been carried out. Estimates of reserves range from 500 to 2000 million tons of 0.5 percent copper ore (Lowell, 1978).

Table 6-2. Description of units on soil map (Figure 6-3)

Soil Type	Class and Association	Characteristics
Hot, arid soils of the lowlands	A1 Grabe–Gila–Anthony	Deep medium and moderately coarse textured, nearly level to gently sloping soils.
Hot, arid soils of the uplands	B2 Forrest–White House	Deep, fine textured, nearly level to gently rolling soils on alluvial fans with lime accumulation to moderate depths.
	B3 Pinaleno–Bitter Springs–Tres Hermanos	Deep, gravelly, moderately coarse to moderately fine textured, nearly level to gently rolling soils on alluvial fans.
	B4 Continental–Pinaleno–Cave	Deep and shallow, gravelly, fine to medium textured, nearly level to steep soils on alluvial fans.
	B7 Continental–Gila–Fluventic Camborthids	Deep, fine to medium textured, nearly level to very steep soils on terraces.
	C5 Calciorthids–Torrifluvents	Deep and shallow, gravelly, medium to coarse textured, nearly level to steep soils on deeply dissected terrace fronts.
Hot, semiarid soils of the hills and mountains	D1 Rimrock–Graham	Moderately deep and shallow, cobbly, gravelly, fine textured, undulating to steep soils overlying basalt bedrock on plains and hills.
	D3 Graham–House Mountain–Lithic Torriorthents	Shallow, gravelly and cobbly, fine to moderately fine textured, rolling to very steep soils, and basalt rockland on hills and mountains.

F. Geologic History

1. Stratigraphic evolution. Except for small xenoliths of Precambrian quartzite and Pleistocene–Recent sedimentary deposits, the geologic column of the district consists of extrusive and intrusive igneous rocks (Figures 6-4 and 6-5). Table 6-3, modified after Langton and Williams (1982), summarizes the geologic history of the region. The older Safford metavolcanic series, in which the four separate porphyry copper deposits occur, consists of dark-gray, massive porphyritic andesite and fine-textured flow breccia with intercalated tuff beds.

The older Safford volcanics are overlain uncomformably by the intermediate composition Baboon metavolcanic series. This series consists of dacite, andesite, latite, flow breccia, and tuff.

The younger Gila Mountain volcanic series, consisting of basalt flows, tuff, and agglomerate, disconformably overlies the intermediate Baboon volcanics. The premineral Safford metavolcanic rocks have been intruded by the Lone Star quartz diorite pluton, a representative of the underlying parental magma from which the metavolcanics were derived. The disseminated copper mineralization is associated with stocks of quartz monzonite porphyry, exposed at the San Juan, Sanchez, and Dos Pobres deposits and encountered at depth at the Kennecott deposit.

The andesite and comagmatic quartz diorite plutons have been cut by latite and quartz latite dikes in NE-trending swarms. Dunn (1978) interprets the latite dikes as being related to the quartz diorite, and the quartz latite dikes as being related to the mineralizing quartz monzonite porphyry stocks.

A large, near-vertical pipe of mineralized tuff is partially exposed near the center of the Kennecott deposit. Gently dipping beds suggest a collapse origin by removal of magma at depth (Dunn, 1978).

The postmineral volcanic rocks of the district can be divided into three units: (1) Upper Eocene hornblende andesite dikes, sills, and plugs; (2) Miocene–Pliocene siliceous tuffs, rhyolite, and agglomerates; and (3) Late Pliocene basalt flows and interbedded tuffs.

2. Structural evolution. Analogous to the Morenci–Metcalf District 32 km to the northeast, the major fault zones strike N–S, ENE–WSW, and NW–SE. The NW faults are parallel to the elongated regional structural belt, conceivably part of an older right-lateral system. Elongation of the premineral outcrop belt and irregular alignment of quartz monzonite porphyry stocks within the district are both thought to be a reflection of the same regional structures that controlled the NW-trending faults.

The most prominent structural features at the porphyry deposits are NE–ENE-trending mineralized fractures and dikes. At least six major NE-striking faults cut the premineral andesite – the Lone Star, Trojan, Weber Peak, Dry

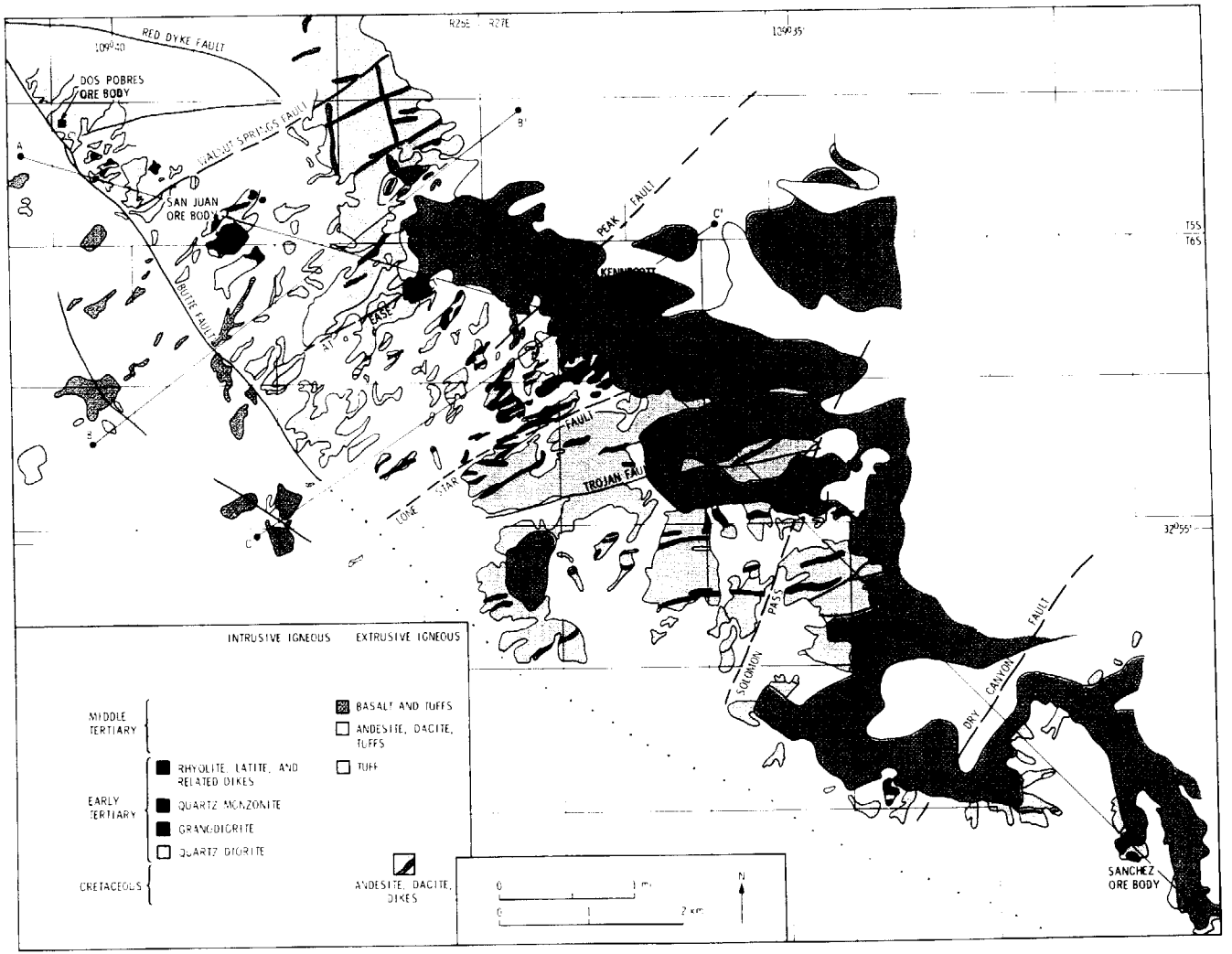

Figure 6-4. Geologic map of Safford District (modified from unpublished Kennecott company map)

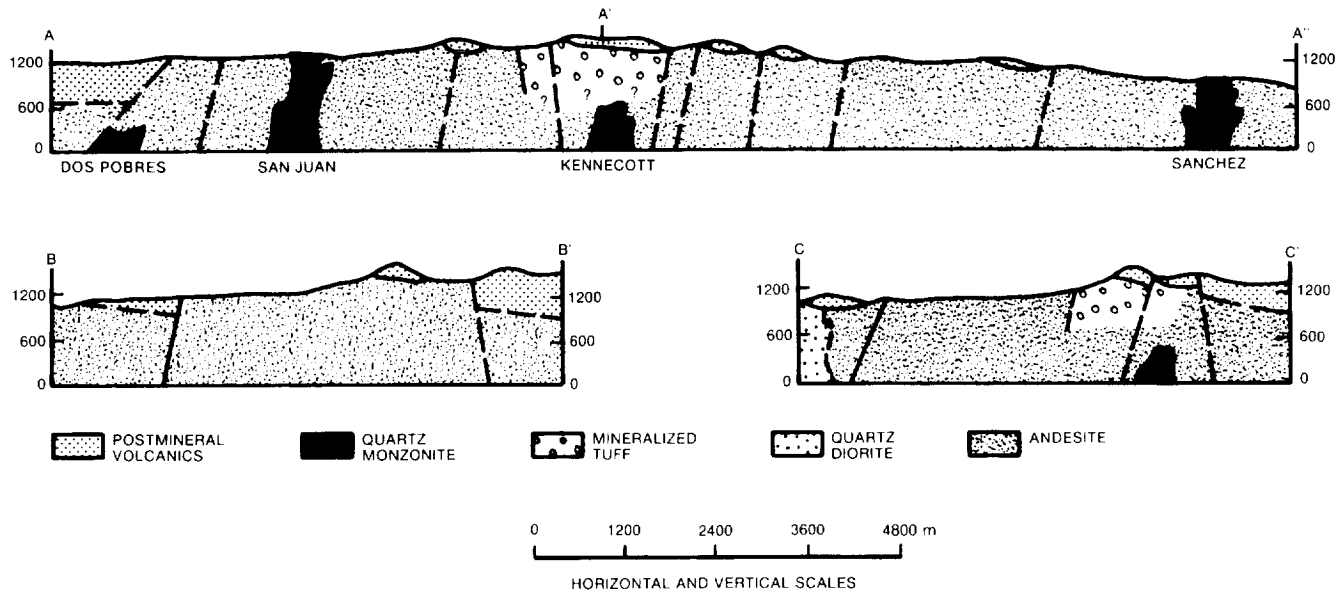

Figure 6-5. Geologic sections of Safford District (Dunn, 1978). Approximate lines of sections are shown in Figure 6-4.

Canyon, Solomon Pass, and Walnut Springs Faults (Dunn, 1978). The NE-striking faults apparently controlled the emplacement of the intrusive centers and the location of the porphyry copper deposits. Copper mineralization along the Lone Star and At Ease Faults indicates their early existence. The apparently comagmatic productive quartz monzonite stocks at the four porphyry copper deposits seem to have been displaced vertically 500 to 750 m by early Tertiary movements along these NE-striking faults (Figure 6-5). NE-trending fractures and faults are regional features common in many of the Laramide stocks in Arizona (Rehrig and Heidrick, 1976).

NW–SE *en echelon* faults are the most pronounced features in the district. Reactivation by gravity movement since Miocene time has resulted in approximately 1000 m of vertical offset along the Butte Fault. Postmineral vertical displacement on the other NW-striking faults is no more than 100 m. The displacement of marker units within the volcanic rocks indicates that these faults were reactivated during the period of postmineral volcanism.

The Safford Basin, occupied by the Gila River, is filled by as much as 900 m of sediments derived from the surrounding mountains (U.S. Department of Agriculture, 1970). The sediment was carried into the closed basin by sluggish streams. Three sediment units are recognized: the lowest unit is 100 to 150 m thick and consists of gravel, conglomerate, and dark clay; the middle unit is as much as 600 m thick and is made up of fine-grained locally derived material; and the uppermost unit consists of thin gravel deposits. Deposition of sediments in the basin ended when structural uplift of the area began. During this period, tilting and minor faulting accompanied the formation of the Gila River. Downcutting by the river alternated with periods of stabilization, forming terraces. Five major terraces were created in this way (Figure 6-6).

3. The Laramide porphyry copper deposits. The general geology of each of the four porphyry copper systems is discussed. This provides a reference against which the results of the remote sensing interpretations can be compared. These discussions also refine the predictive model relating to the remote sensing signature of the various lithologies of each porphyry system. Of the Safford test site deposits, the Dos Pobres and Kennecott (Lone Star) deposits are the best documented in the literature. These two deposits are also less disturbed than the San Juan and Sanchez deposits. They are therefore better test sites for remote sensing exploration for deeply buried porphyry copper deposits. For the following discussions, refer to the geologic map (Figure 6-4) and the alteration map (Figure 6-7).

a. The Dos Pobres deposit. The description of this deposit is primarily taken from Langton and Williams (1982), augmented by field observations by the authors.

The Dos Pobres deposit is the northwestern-most test target within the area of this study. This deposit is approximately 14 km north of Safford. The elevation of the surface over the ore body varies from 900 to 1300 m above sea level. The location of this deposit is shown on Figures 6-2 and 6-4.

Table 6-3. Geologic column and geochronology[a]

Name	Rock Type	Thickness, ft	Age	Events	Dates, m.y.
Alluvium, terrace gravels, basin fill	Sands, clay beds, gravels, siltstones, conglomerates	0–2000+	Pleistocene–Recent	Younger pediment, basin fill, and gravel development	
	UNCONFORMITY				
Gila Mountain volcanics	Basalt and rhyolite dikes, sills, plugs. Basalt flows, tuffs, rhyolites, agglomerates, vent debris, basal conglomerate	0–3000+	Miocene–Pliocene	Basaltic volcanism	
				Major Basin and Range gravity faulting, minor tilting, erosion, and oxidation	
				Intrusion–Extrusion of Gila Mountain volcanics contemporaneous with development of older pediment	
	UNCONFORMITY			Hiatus, faulting, minor folding and tilting	
Baboon metavolcanics–metavolcaniclastics	Hornblende andesite dikes, sills, plugs		Eocene	Extrusion of Upper Baboon agglomerates	46 ± –36 ±
				Late, prolific retrograde veining	46 ±
				Extrusion of Lower Baboon volcanics and pyroclastics	47 ± –46 ±
	Propylitized andesite agglomerates, flow breccias, mud flows, lithic tuffs, conglomerates	0–1500+	Eocene	Intrusion of hornblende andesite magma(s)	47 ± –36 ±
				Degassing and subsequent crystallization of productive rest magma(s) with accompanying hydrothermal phase	47.8 ± 1.8
	UNCONFORMITY			Uplift, faulting, minor folding, continued volcanism	
				Crystallization of productive porphyry dikes	52.2 ± 2.0
				Early pervasive mesozonal contact metamorphism and hydrothermal alteration	56.9 ± 2.2
Productive porphyries	Tonalite–quartz monzonite–monzonite–granodiorite porphyry stock(s), dikes, sills		Paleocene–Eocene	Intrusion of productive magma(s)	59 ± –47 ±
				Uplift, faulting, NE-folding, erosion, deposition of volcaniclastic sediments	
Lone Star pluton(s)	Quartz diorite–granodiorite batholith		Upper Cretaceous–Paleocene	Crystallization of Lone Star pluton(s)	67 ± –60 ±
				Intrusion of Lone Star magma(s) into Safford volcanics and subsequent contact metamorphism	69 ± –60 ±
Safford metavolcanics–metavolcaniclastics	Metamorphosed hornblende and pyroxene andesite flows, breccias, agglomerates, wackes, mud flows	3500+	Upper Cretaceous–Paleocene	Extrusion of Safford volcanics	70 ± –60 ±
				Intrusion of Lone Star magma(s) into Precambrian metasediments and subsequent contact metamorphism	69.8 ± 2.7
	UNCONFORMITY			Uplift, faulting erosion	
	Amphibolite, gneiss, granite, quartzite, schist		Precambrian		

[a] Langton and Williams, 1982.

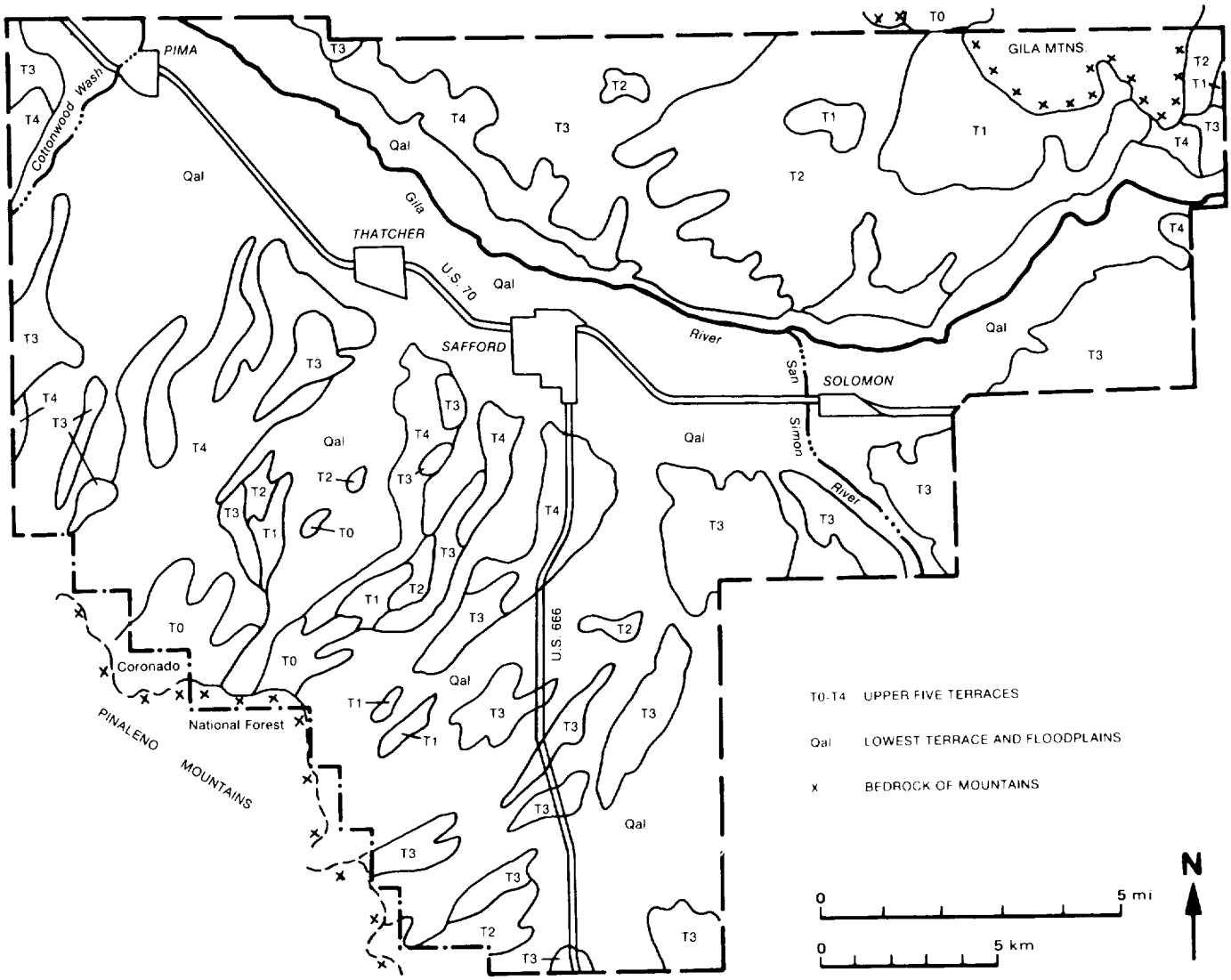

Figure 6-6. Geologic terraces in the Safford area. T0 designates the oldest and highest terraces; T1 through T4 designate progressively more recent and lower terraces; Qal designates the present floodplain of the Gila River (U.S. Department of Agriculture, 1970).

Lithology. There are four primary lithologic units in the immediate area of the Dos Pobres deposit. These are, as defined by Langton and Williams (1982), the Safford metavolcanics, the "productive" porphyries, the hornblende andesite dikes and sills, and the Baboon metavolcanics. Each of these lithologic units is briefly described below.

(1) *Safford metavolcanics.* More than 75 percent of the potentially economic copper mineralization at Dos Pobres occurs within the Safford metavolcanics. This unit is a metamorphosed sequence of Cretaceous–Tertiary volcanic rocks. The majority of these volcanic rocks are andesitic in composition, but dacites, dacite tuffs, and latites have also been recognized. Most of the flows and volcanic breccias are hornblende or pyroxene andesites. These units have been pervasively altered in the vicinity of the ore body; the character of this alteration is discussed later. The fragmental nature of the flow breccias is often obscured by the effects of metamorphism or hydrothermal alteration. It is probable that the fragmental nature of the volcanic rocks has been accentuated by crackling. Contact metamorphism of these andesites by the main granodiorite has been dated at 69.8 ± 2.7 m.y. (Langton and Williams, 1982).

(2) *"Productive" porphyries.* Some of the higher copper grade values occur in the dikes or phacoliths in the upper levels of the deposit. With increasing depth

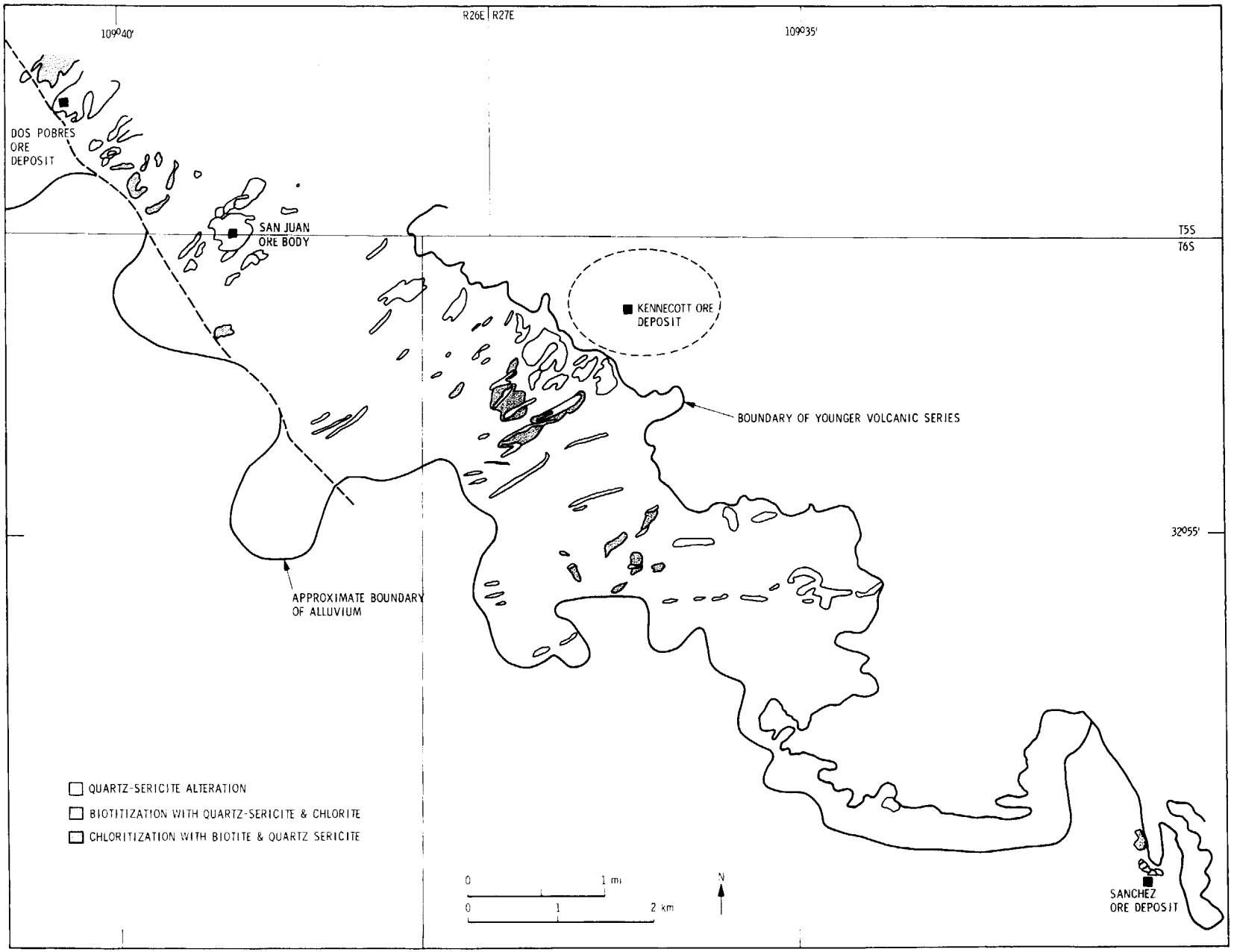

Figure 6-7. Surface alteration map of Safford District (modified from unpublished Kennecott company maps)

the porphyries become progressively lower grade and eventually relatively barren. The principal "productive" or mineralized porphyry is generally a quartz monzonite. However, the mineralized porphyry ranges in composition to a tonalite or granodiorite.

The freshest samples tend to be granodioritic. Phenocrysts within these fresh samples consist of embayed quartz, plagioclase, hornblende, and dark-brown biotite set in a matrix of the same minerals as well as quartz and orthoclase. Langton and Williams (1982) conclude that "it seems likely that the porphyry was indeed a granodiorite originally, and that it was modified locally and erratically by late magmatic effects."

The productive porphyry is generally observed as dikes or fragments of dikes in the central portion and is dated at 52.2 ± 2.0 m.y. A stock of the porphyry, dated at 47.8 ± 1.8 m.y., occurs at depth in the northwestern part of the deposit.

(3) *Hornblende andesite dikes and sills.* Hornblende andesite dikes and sills are most obvious in the ENE-trending shear zones away from the center of mineralization. Most of them are clearly consanguineous with the Baboon volcanic rocks. Large titaniferous hornblende phenocrysts, often more than 1 cm long, occur in these nonmineralized intrusives. These dikes are evidently late and postmineral and have acted as dilutents to the ore zone. The grade of copper mineralization near these dikes is almost always lower than in the core of the ore body. No hornblende andesite dikes or sills have been recognized in the center of the porphyry deposit. The thickness of these dikes varies considerably between the two andesitic volcanic units. In the Safford metavolcanics, these dikes are generally only 1 m thick. However, these dikes may exceed 60 m in thickness within the lower portion of the Baboon sequence.

(4) *Baboon metavolcanics.* The Baboon metavolcanics are composed of propylitized andesitic agglomerates, flow breccias, mud flows, and lithic tuffs of Tertiary age. These outcrop north of the ore body and thicken to more than 500 m in a northwesterly direction. The Baboon sequence has been locally hydrothermally altered. However, these units have not been metamorphosed either by the productive porphyries or by the parental pluton(s). Propylitization appears to be autometamorphic away from the ENE-trending shear zones; propylitization is clearly hydrothermal near the ore body. The lower members of the Baboon metavolcanics are intruded by hornblende andesite dikes which are of late or postmineral age. Upper units of this series contain large xenoliths of the same dike rocks.

Structure. An important structure strongly influencing the geometry of the ore body is the Butte (Foothill) Fault (Figure 6-4), which offsets the southern part of the ore body 700 m downward. Several ENE-trending faults which cut the ore body have had considerable postmineral displacement. These same structures were the principal channels along which the productive porphyries were emplaced and along which the ore-bearing fluids migrated. These faults had recurrent movement and down-faulted the ore zone in a step-like pattern from southeast to northwest. The offsetting movement along the ENE faults was essentially contemporaneous with the major vertical displacement of the Butte Fault.

Crackle brecciation, which constitutes the dominant fracturing in the mine area, is extensively developed in the metavolcanics but is not as well developed in the productive porphyries. The crackling or fracturing not related to postmineral faulting appears to be of hydrothermal origin. Langton and Williams (1982, p. 341) describe this: "Simple parting across fragments and large phenocrysts, with virtually no displacement of the respective boundaries, is typical of the character of this fracturing and is seen throughout the orebody."

Contact breccias often host the highest ore grade material. These zones are intimately associated with the porphyries. Contact breccias are more important in the upper portions of the deposit and appear to have formed early in the intrusion history. The upper extremities of porphyry dikes grade into the breccias, which contain numerous fragments of the metavolcanics embedded in the porphyry.

A megabreccia incorporating large fragments of metaandesite, porphyry, and the contact breccia formed as a later event. Langton and Williams (1982) relate this megabreccia to "de-gassing of the productive rest-magma."

Erosion appears to have been more extensive to the southeast of the ore body, and the Baboon volcanics are no longer present 6 km away in this direction. As mentioned previously, the Baboon volcanics thicken to at least 500 m to the northwest of the ore body.

Although low-angle faulting has been recognized at the Dos Pobres ore body, it is difficult to trace for any distance along the strike and should not be detectable on the NS-001 images.

Subsequent to the mineralization, the Miocene–Pliocene Gila Mountain volcanic rocks were extruded onto an erosion surface. Exposed at this erosional surface were the Laramide intrusives and consanguineous metavolcanics. These volcanic rocks form a blanket that obscures the target zone from the imaging sensors. The source of these volcanic rocks was to the northeast along Bonita Creek. Pediment formation along the southwestern front of the Gila Mountains occurred contemporaneously with this period of volcanism. The amount of gravel derived from these volcanics thickens rapidly toward the center of the Safford Valley. These pediment gravels obscure a significant portion of the test site area. However, numerous small- to medium-sized outcrops of altered units are exposed through the thinner part of the pediment gravels.

The last major tectonic event in the district is represented by Basin and Range block faulting. The NW-trending faults were particularly active. Normal gravity displacements in excess of 600 m have been recognized on several of these high-angle structures. Adjustments along N–S- and NE-trending faults also occurred, but of lesser magnitude than on the Butte, Red Dyke, and Valley Faults. Erosion and oxidation of the ore body prior to the deposition of the Gila Mountain volcanics, and similar erosion, oxidation, and development of extensive thicknesses of clay beds, basin fill, terrace gravels, and alluvium during Pliocene and Recent periods, established the present surface environment. This is the complicated surface that was imaged by the various remote sensing instruments as part of this test case study.

Alteration. The earliest alteration change to occur in the productive porphyry was the replacement of hornblende by biotite flakes. The biotite flakes appear to be identical in character to the biotite phenocrysts. In some cases biotite may also have crystallized as frilly rings or overgrowths on the larger biotite books. Langton and Williams (1982) attribute this alteration to a late magmatic age. Coarse-grained primary biotite was deformed by flowage; new or late magmatic biotite was not. This biotite alteration may have taken place while the wall rocks, adjacent to the productive porphyry, were undergoing mesozonal metamorphism.

As cooling of the porphyries continued, late magmatic biotite ceased to form and a new mineral assemblage began to crystallize. This assemblage was quartz + orthoclase + magnetite + bornite. The quartz and orthoclase grew in the matrix at the expense of plagioclase and late magmatic biotite. Metamorphosis of the porphyry from a granodiorite to a quartz monzonite probably began as late magmatic but continued into the deuteric stage. This late magmatic to deuteric alteration is often fracture controlled and pervasive. Veinlets of quartz and orthoclase accompanied by bornite are seen filling fractures. These veinlets have a distinctly hydrothermal aspect and probably coincided with the main pulse of mineralization and associated K-metasomatism in the wall rocks.

This episode ended with simple deuteric alteration, and the surviving biotite was partially replaced by coarse clinochlore and blebs of epidote with accessory rutile. The chlorite developed from the biotite may have been accompanied by minute platelets of hematite. During this deuteric alteration, plagioclase was altered, weakening to a mixture of shreddy sericite and some earthy epidote. Usually only the cores of plagioclase phenocrysts are so afflicted, with the sodic rims remaining unchanged. Sulfides were deposited in veins and veinlets at this time, with chalcopyrite and bornite developing in a gangue of quartz, carbonate, and chlorite.

In some areas the porphyry shows incipient alteration to a quartz–sericite assemblage. This alteration is also of deuteric age and occurs in areas where more sulfur was available; such alteration is seldom complete. There is a tendency in this assemblage for quartz in the groundmass to grow to the point of coalescing, and for all remaining feldspars and altered mafites to be partially replaced by sericite. Any chlorite that survived this alteration is highly magnesian. Pyrite may appear in the sulfide assemblage and bornite gives way to chalcopyrite. These sulfide minerals occur in quartz veinlets or may be disseminated in sites of former mafites. Alteration of this nature is uncommon and seldom complete. This is typical of low-sulfur porphyry copper systems; the best example of such alteration is observable locally on the southeast side of the ore body.

During the progression of alteration from fresh to deuteric to new biotite, the rock chemistry changed with a decrease in SiO_2 and an increase in Ti, Na, Al, and Fe. These chemical changes are mainly due to the development of abundant new biotite. The K_2O content remains relatively stable, which reflects the loss of orthoclase during new biotite growth and implies no real K-metasomatism within the intrusive.

Langton and Williams (1982, p. 343) conclude:

> The elements that show considerable change are those whose mobility is closely tied to the presence of sulfur. Calcium is the best example, for it is quickly removed when sulfur is available; elements such as Si and Al increase only because they are residual, and there is a corresponding decrease in the volume of the original

rock. The assemblage quartz–sericite–rutile derives readily from plagioclase-sphene in the presence of sulfur, and the loss of Ca from plagioclase is inevitably the major change.

The alteration in the andesites that host the productive porphyries and the majority of the copper values has a somewhat more complex history. The andesitic volcanic rocks exhibit an epizonal metamorphic (alteration) event of almost regional extent. This is believed to represent the composite effect of two processes. One of these processes was the slow cooling of the thick, rapidly extruded andesitic pile, resulting in autometamorphism. Langton and Williams (1982) suggest the presence of a slowly cooling heat source at depth as the second cause for the abnormally strong epizonal effects in the andesitic volcanic rocks of the district. These effects are in contrast to weaker effects in many other thick mafic volcanic piles. The logical source of heat at depth is the granodiorite or a parent pluton of batholithic dimensions.

The andesites demonstrate an alteration assemblage characterized by stability of epidote and pennine. These alteration minerals may completely replace mafic minerals by a mixture of coarse-grained epidote prisms embedded in pennine. Epidote partially replaces plagioclase; the remainder of the plagioclase not replaced by epidote is albitic. Excess iron in the system is developed from alteration of mafic minerals and from accessory magnetite. This excess iron forms tiny hematite tablets *in situ*. Calcite is commonly present but not abundant in the volcanic rocks. Calcite may form patchy crystalloblasts in the matrix of the andesitic volcanics. In contrast to the andesites, dacites responded differently and are altered to an assemblage of quartz–sericite–pennine with epidote rare or absent.

A second thermal alteration event was imposed on the volcanics in the aureole around the Dos Pobres deposit. This resulted from rising temperatures that related to intrusion of the productive magma. During the thermal event, epidote and pennine formed, often as continued development of the same earlier formed minerals, but with exaggerated growth. During this stage of alteration, plagioclase was sometimes completely destroyed. Clots or pods of coarse-grained epidote, with interstitial calcite and pennine, spread crystalloblastically and invaded the surrounding matrix. The process of formation of these clots initiated from a variety of centers; these include phenocrysts, especially reactive xenoliths, or merely at intersections of fractures. Some of these clots show epidote veinlets extending away in one or two directions. This zone dies out away from the productive porphyry and eventually blends into the regional propylitization, which has an identical mineralogy in the alteration assemblage. The alteration effects of this aureole cannot be seen with any certainty beyond about 600 m from the periphery of the ore body.

Mesozonal metamorphism began as temperature rose, accompanying the final emplacement of the productive magma. Alteration accompanying this phase of the emplacement cycle is one where the earlier alteration assemblages were destroyed and the andesites exhibit abundant secondary actinolitic hornblende and brown biotite. This event has been dated at 56.9 ± 2.2 m.y. from these ferromagnesium alteration minerals (Langton and Williams, 1982). Both minerals occur as small crystals that replace both relict plagioclase and the pre-existing hornblende. The new actinolitic hornblende is not iron rich; disseminated, dust-like magnetite is a common accessory mineral in the alteration assemblage. In many samples the disseminated magnetite is concentrated in hazily defined areas, indicating that these zones may represent former cognate xenoliths.

This early mesozonal metamorphism was a transient stage. More K_2O was added to the system during mesozonal conditions, and the alteration mineral assemblage yielded to a metasomatic one. This metasomatic alteration represents the main pulse of K-metasomatism which accompanied the mineralization. In the zones where this has been most intense, it affects even the productive porphyry dikes. The result of the most intense K-metasomatism is that these dikes may be so heavily replaced by secondary biotite that they are visually indistinguishable from the andesites, except for the ghost of biotite phenocrysts.

Crackling was an important alteration and ore emplacement mechanism during the period of mesozonal K-metasomatism. Crackling appears to have been relatively unimportant during the preceding mesozonal metamorphism. However, the crackling associated with the K-metasomatism provided fractures that served as pathways for the mineralizing fluids and that are now veinlets carrying quartz, orthoclase, apatite, bornite, and chalcopyrite.

The zone of secondary biotite may be observed by visual inspection of samples up to 500 m away from the center of the ore body. The biotite zone gradually fades and merges into the surrounding propylitic assemblage. Toward the outer margin of the zone, biotite becomes paler and assumes a green color. This shift in color of secondary biotite is first shown by biotite that has formed at the expense of plagioclase, while the biotite apparently developed in the rock matrix because the same area is still brown. Eventually, even the secondary biotite in the matrix takes on a green color.

Oxidation and erosion were the dominant forces at work on the area of the ore body during Oligocene and early Miocene times. At this time, minor supergene alteration and enrichment were superimposed on the hypogene ore in the Dos Pobres deposit. "The central portion of the Dos Pobres chalcopyrite-bornite ore pipe was partially leached, thoroughly oxidized, and locally enriched to depths of approximately 1,200 m (2,900 ft. level)" (Langton and Williams, 1982, p. 351). Chrysocolla and cuprite are the dominant copper oxides over the center of the sulfide ore. Hematitic, jarositic, and goethitic limonite cappings on the southeast side of the ore body reflect former minor chalcocite enrichment in the vicinity of the productive porphyries at a level now exposed by erosion.

b. The San Juan deposit. The San Juan deposit is a small porphyry copper system that is located between the Dos Pobres and Kennecott deposits. The mineralized porphyry has had fairly extensive surface disturbance which reduces its usefulness as a test case. In addition, during the NS-001 data overflight there was a short malfunction of the scanner and no data for the immediate San Juan deposit were collected. The majority of the information on this deposit comes from Blake's (1971) master's thesis.

Lithology. In the San Juan Mine area, a composite stock composed primarily of quartz monzonite porphyry with a lesser amount of granodiorite porphyry intrudes the andesitic volcanic rocks. Small bodies of granite porphyry and quartz diorite porphyry also occur in this area. Blake (1971) reports that, texturally, portions of the quartz monzonite porphyry approach the appearance of a quartz latite porphyry.

Mineralization. The mineralization at the San Juan deposit consists primarily of pyrite and chalcopyrite. The ratio of pyrite to chalcopyrite varies from 20:1 (with 3 to 5 volume-percent sulfide in the pyrite halo) to 1:1 (with an average of 2 to 3 volume-percent sulfide in the central zone). Disseminated sulfides in the quartz-feldspar groundmass of the porphyry preceded the period of stockwork sulfide deposition. Blake (1971) recognized the development of magnetite which accompanied the sulfide deposition at this property. Chrysocolla is the most abundant copper oxide mineral present in the exposed portion of the San Juan mineralization.

The supergene environment at the San Juan deposit has not been conducive to the development of a stable chalcocite zone. It is possible that a chalcocite blanket may have formerly existed above the San Juan stock. If so, this has been completely removed. At the San Juan deposit, a weak goethitic and mixed limonite capping has developed.

Structure. The main structural ore control at the San Juan deposit is the NE-trending San Juan shear zone. This 1000-m wide zone of shearing is separated from the Lone Star shear zone by 1000 to 1300 m of less sheared andesitic volcanics. The shearing in the San Juan zone is more intense near the San Juan stock. Other fracture directions include NW, E–W, and NNE trends which intersect at the San Juan stock. Mineralization is localized in fractures within and adjacent to the stock and in nearby breccia pipes and breccia dikes.

In addition to the San Juan shear zone, there are weaker NW-, E–W-, and NNE-mineralized structures. Blake (1971) recognizes a radiating structural pattern in the San Juan stock area which he relates to forceful emplacement of the stock. Dikes have been emplaced along these fracture directions.

The shattered contact zone of the Laramide stock and the adjacent Cretaceous porphyritic andesites formed the major loci for emplacement of copper mineralization (Blake, 1971). Some of the mineralization occurs as true disseminations within the quartz–potash feldspar groundmass of the intrusive rocks.

Small breccia pipes and breccia or pebble dikes occur near the San Juan deposit. Blake (1971) mapped at least four small breccia pipes in the San Juan Mine area. Numerous highly fractured areas and breccia dikes are also shown on Blake's maps. The largest of these pipes is aligned northeast with a long axis of 150 m and a width of approximately 80 m. This pipe is located northwest of the San Juan stock. Two smaller pipes, each approximately 80 by 40 m, occur within the San Juan stock. Another pipe southeast of the stock is associated with a small quartz diorite porphyry intrusive. This pipe has a diameter of approximately 60 m.

Formation of the breccia pipes in the San Juan Mine area clearly postdates the emplacement of the San Juan stock and associated dikes. Fragments of the plutonic rocks are incorporated into the breccias. Blake (1971) related these pipes to the last phase of the mineralization process. The pipes are slightly mineralized and the brecciated fragments are sericitically altered. Breccia fragments vary in size from rock flour to fragments measuring over 30 cm in diameter. However, most of the breccia fragments are less than 30 cm in size. Angular fragments predominate, but some rounded fragments occur. The breccia dikes in the San Juan area tend to follow the northeast shear trend. These dikes are narrow and do not exceed 2 m in width (Blake, 1971).

Slight silicification associated with the quartz–sericite alteration of the breccia pipes sometimes results in development of moderate topographic highs. The breccia pipe outcrops are frequently iron stained as a result of oxidation of associated pyrite.

Alteration. In the San Juan area, there is a K-feldspar–quartz–biotite–sericite zone centered on the intrusive. This is surrounded by a zone where quartz and sericite have been introduced primarily along widely spaced small fractures. The overall extent of this quartz–sericite zone as defined by Blake (1971) is smaller than and encompassed by the pyritic halo which measures 2300 by 3000 m. The quartz–sericite zone is surrounded by a progressively changing propylitic zone. This zone includes in places the development of secondary biotite, albite, and chlorite along with the normal propylitic assemblage of epidote–chlorite–calcite.

c. The Kennecott deposit. This section, which is based primarily on the published paper of Robinson and Cook (1966), describes the Kennecott (Lone Star) deposit. The deposit is located south and east of the Dos Pobres and San Juan deposits.

Lithology. The host rocks (older volcanics), which contain the Kennecott ore body, consist of Cretaceous to early Tertiary andesitic and dacitic volcanic rocks. These have been intruded by quartz diorite, granodiorite, and quartz monzonite porphyry stocks, rhyolite, latite, quartz latite, and related dikes. Postmineral basalt and more acidic mid- to late Tertiary volcanic rocks of the Gila Mountain volcanic sequence cover a significant portion of the ore body.

In the vicinity of the Kennecott deposit, the Lone Star stock has been emplaced in the NE-trending Lone Star shear zone. This stock is primarily composed of quartz diorite, with minor amounts of granodiorite. A body of quartz monzonite is exposed at the northeast edge of the stock. This elongate, composite intrusive has intruded the porphyritic andesite of the older volcanic rocks. The pluton has dimensions of at least 2500 by 1300 m. The Lone Star stock has resisted later shearing and is not the main ore host rock.

Following emplacement of the Lone Star stock, a dike swarm of acidic to intermediate composition was emplaced in the porphyritic older andesite. Robinson and Cook (1966) relate some of these quartz latite, rhyolite, quartz diorite, and granodiorite dikes to a volcanic vent. This vent-like area has some of the characteristics of a breccia pipe. The vent is composed of acid volcanics similar in composition to the dike swarm. Robinson and Cook (1966, p. 253) state:

> Some of the dikes probably emanate from a rhyolitic plug, and together with pyroclastics, crystalline tuff, and tuff breccia they fill a steep-sided deep-seated vent 2,000 by 1,500 feet in area and at least 2,000 feet in vertical extent.

Robinson and Cook (1966) conclude that the volcanic vent itself predates the mineralization. The associated dike swarm and related fracturing comprise the loci for mineralization. Individual dikes vary from a few centimeters up to 600 m in width. Strike length is variable. The longest dikes may have strike lengths of 600 to 1300 m (Robinson and Cook, 1966).

Small breccia pipes and breccia or pebble dikes occur near the Kennecott deposit (Robinson and Cook, 1966). These are primarily aligned along N 50°–65° E-trending fractures. In the area of the Lone Star stock, three small breccia pipes, up to 15 m in diameter, occur near the At Ease Fault. Small pebble or breccia dikes up to 30 cm in width extend from these pipes (Robinson and Cook, 1966).

Mineralization. The ore body consists of the primary sulfide minerals pyrite and chalcopyrite, with lesser amounts of bornite and other hypogene sulfides. Pyrite is the most abundant sulfide present, with a pyrite-to-chalcopyrite ratio of 10:1 to 21:1 and with total sulfide of 4 to 8 volume-percent in the pyrite zone. A portion of the pyrite zone for this deposit is exposed at the surface south of the deposit.

In addition to chalcopyrite in the Kennecott ore body, small amounts of bornite and molybdenite and trace amounts of galena, sphalerite, and tetrahedrite are noted by Robinson and Cook (1966). At the Kennecott deposit there appears to be a deeper, molybdenite-bearing central zone with molybdenite in quartz veinlets (Robinson and Cook, 1966).

Robinson and Cook (1966) conclude that the disseminated sulfides in thin quartz veinlets at the Kennecott deposit preceded the stockwork sulfide deposition. Replacement of magnetite and ferromagnesian minerals by sulfides occurred at the Kennecott deposit. Magnetite was also developed during alteration of mafic rock-forming minerals away from the main part of the ore zone. Magnetite and wolframite occur in small quartz-carbonate veins.

The history of supergene mineralization in the district is complicated by a complex structural and erosional history. In addition to the vertical block movements controlled by the NE-trending faults, there are normal faults following a northwest trend such as the Butte Fault. The result is the removal of variable amounts of the sulfide system at each

of the porphyry deposits in the district. At the Kennecott ore body, removal of the pyrite halo that existed above the enrichment blanket resulted in partial destruction of the chalcocite zone by oxidation and partial leaching.

The supergene copper minerals include chrysocolla, chalcocite, and covellite. The supergene history of the Kennecott ore body as described by Robinson and Cook (1966) can be used to understand the supergene processes at the other deposits of the Safford District. Following hypogene mineralization, the Kennecott ore body was subjected to oxidation and leaching. Pyrite present in the halo above the copper protore provided sufficient acid for effective leaching of the copper to take place. Uplift occurred along NE and NW structures and erosion exposed the top of the leaching system. Once the pyritic material was consumed by supergene processes or removed by erosion, the lower pyrite central zone became deficient in leaching potential. Subsequent periods of uplift resulted in partial destruction of the chalcocite blanket. The net result is the development of a buried leached capping up to 300 m thick, with an average thickness of 140 m (Robinson and Cook, 1966). Under this capping is an ore body consisting of three classes of ore: oxide, mixed, and sulfide. In the supergene sulfide zone, chalcocite and covellite replace chalcopyrite and bornite, and coat pyrite.

At least a portion of the oxidation and enrichment history of the Kennecott ore body predates the Tertiary intermediate volcanic rocks. Fragments of leached capping are found in the basal conglomerate beneath these volcanics.

Less than 1 m^2 of leached capping is exposed over the Kennecott ore body. This exposure occurs in a small window in the overlying younger volcanic rocks (Robinson and Cook, 1966). In the suboutcrop, the capping consists of brown–red–maroon-stained andesite and intrusive rock (Robinson and Cook, 1966); goethite and hematite are the predominant limonite minerals, but some jarosite is present. Jarosite, associated with alunite, clay, and turquoise, is also present along fractures. The predominance of goethite with hematite in the suboutcrop capping gives way to jarosite and veinlets of alunite over the pyrite halo (Robinson and Cook, 1966). If the postmineral volcanic rocks had been removed by erosion, a conspicuous leached capping would have been visible over the ore zone.

Structure. The main structural controls of mineralization in the Safford District, in general, and for the Kennecott deposit are the NE-trending shear zones. Movements along this trend may date from the Precambrian. Certainly, pre-Early Tertiary movement occurred to prepare the zones of structural weakness that served as loci for pluton emplacement, dike swarms, and breccia pipe development.

Mineralization at the Kennecott deposit is related to the area of closely spaced NE-trending dikes emplaced along the major shear zone. Both the dikes and well-fractured andesites are mineralized. On the 1200-m level of the Kennecott (Safford) ore body, dikes comprise approximately 25 percent of the mineralized area (Robinson and Cook, 1966), similar to the productive porphyries at Dos Pobres. Primary mineralization occurs preferentially where numerous, closely spaced, small dikes intrude the porphyritic andesite.

The Lone Star shear zone is bounded by the NE-trending Lone Star and At Ease Faults (Figure 6-4). This shear zone extends at least 5000 m from the Lone Star stock and 1600 m under the Tertiary volcanic rocks. Robinson and Cook (1966) conclude that this zone represents a horst block with a possible upward displacement of 250 m.

The mineralization at the Kennecott ore bodies occurs peripherally to the subvolcanic vent previously mentioned. In this area, the strongly sheared porphyritic andesites are cut by the closely spaced dike swarm (Robinson and Cook, 1966).

Alteration. Figure 6-8 shows alteration patterns and pyrite distribution as mapped in the field approximately 20 years ago (Robinson and Cook, 1966). An area measuring approximately 3600 by 1800 m was subjected to fairly extensive hydrothermal alteration. However, only about one-half of this area is exposed, with the remainder being covered by the postmineral Tertiary volcanics.

A strongly developed quartz–sericite zone exists in the southwestern portion of the central area of intense alteration. This quartz–sericite zone adjoins and is partially superimposed on a large area where secondary biotite is pervasive. This strong secondary biotite zone lies to the southwest of the center of intense alteration. The quartz–sericite and secondary biotite zones correspond to the spatial distribution of the Kennecott ore body. Surrounding these two zones are chloritic and propylitic alteration assemblages as roughly concentric zones. Portions of the quartz–sericite and the chloritized zones correspond to the pyritic halo. According to Robinson and Cook (1966) the propylitic alteration zone is unmineralized except where traversed by shear zones, veins, or dikes that are accompanied by sulfide minerals.

Boundaries of alteration zones are fairly arbitrary because the mineralogical changes are transitional and overlap-

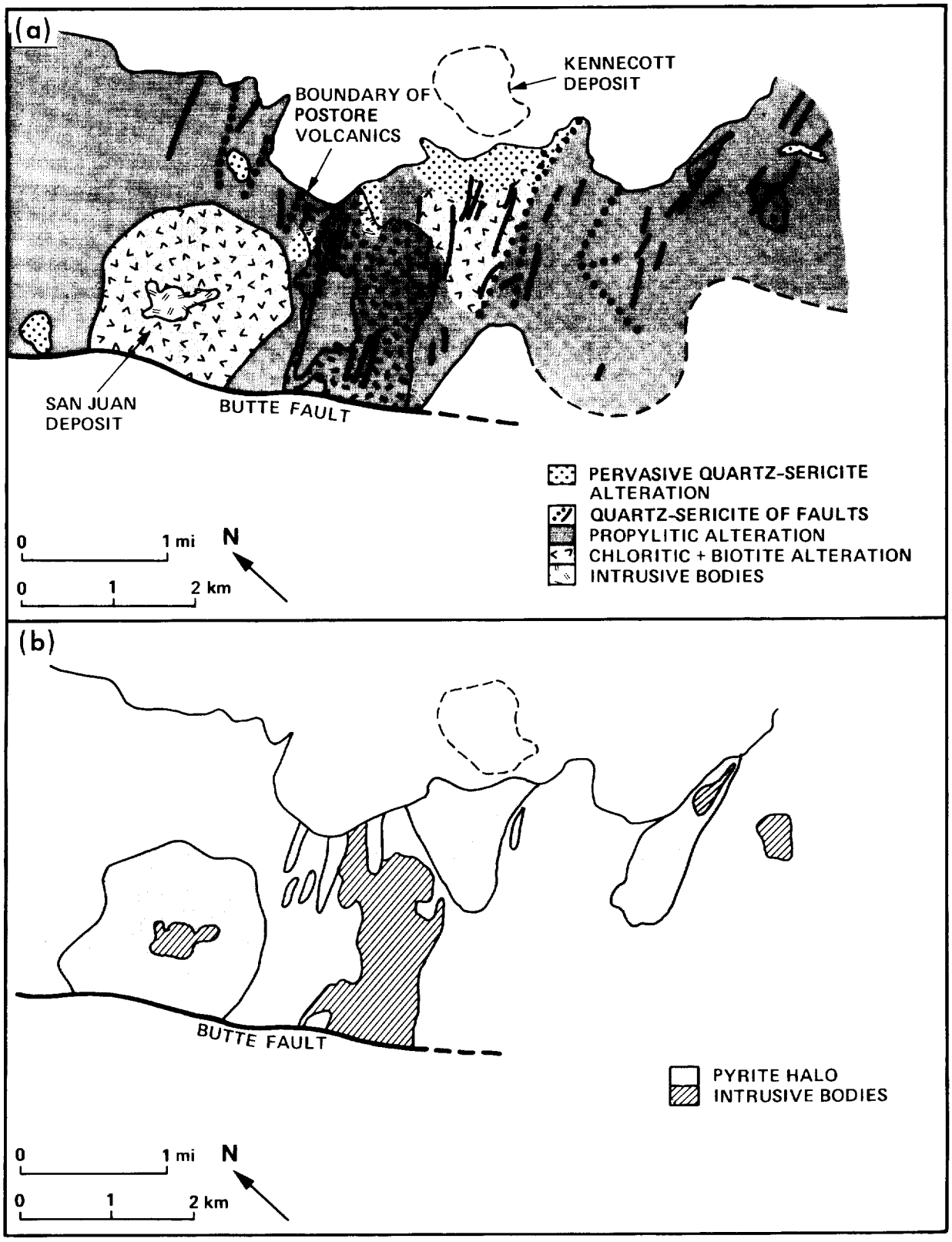

Figure 6-8. The Lone Star District (modified from Robinson and Cook, 1966): (a) alteration patterns; (b) pyrite halo

ping. This is particularly the case in the porphyritic andesite host rock. The distribution of the host-rock lithologies plays an important part in the alteration mineral assemblage formed at the Kennecott and other porphyry deposits in this district. For example, while there may be very weak and thin seams of quartz–sericite alteration cutting the andesites, this alteration assemblage is more restricted to the more acid rock types. The quartz–sericite alteration assemblage is primarily restricted to the post-older andesite intrusive complex and to the pyroclastic lithic tuff and volcanic vent debris. Sericite occurs in almost all the dikes and along their contact zones with the porphyritic andesite for a distance of more than 3000 m southwest of the ore body. This dike-associated sericite transects the chloritic and propylitic alteration zones. Sericite is clearly formed later than the biotitization because sericitization occurs along veins, shears, and contacts that cut the zone of biotitization.

Plagioclase, as both phenocrysts and groundmass material within the intrusives, has been thoroughly converted to sericite and quartz. This has taken place mainly along veinlets.

Potash feldspar makes up 15 to 20 percent of the groundmass of the intrusives; this K-feldspar is probably primary. However, the concentration of K-feldspar along veins indicates addition or migration of potassium during alteration. Secondary K-feldspar and associated quartz and sericite are abundant along veins that cut the porphyritic andesite near the ore zone.

Robinson and Cook (1966, p. 260) describe the biotite zone as follows:

> The rocks mainly affected by this type of alteration are the porphyritic andesites. Hornblende and augite were replaced by brown biotite in flakes, clots, and, more rarely, in veinlets carrying sulfides. The strongest biotitization—10 to 50 percent and averaging about 20 percent—is developed around the intrusive plugs and dikes in and adjoining the orebody. The acidic to intermediate intrusive rocks have secondary biotite developed in only minor amounts, a few percent, along quartz veinlets. Other occurrences in these intrusives, if ever present, were probably destroyed by the later sericitic alteration phase....

Chlorite is the most widely distributed alteration mineral within the alteration halo. In fact, the distribution of chlorite in the area of the Kennecott deposit extends over all the other alteration assemblages. A 300- to 900-m-wide zone ascribed to predominantly chloritic alteration surrounds and overlaps the biotitized and sericitized zones on the southwest side of the ore body. The Bear Creek Mining Company and Kennecott geologists who mapped this zone defined the chloritic zone as being where chlorite predominated over biotite in the replacement of mafic minerals. Since this was done by field mapping methods, greenish biotite may have been misidentified, and the actual chloritic zone may be of a smaller extent than mapped.

Propylitic alteration in the zone around the Kennecott ore body is the most widespread of the alteration zones. Epidote and chlorite sometimes associated with calcite are the alteration minerals present in this zone. Much of what has been called widespread propylitic alteration may have been caused by autometamorphism of the andesitic volcanic rocks. It appears that at least some part of the propylitic mineral assemblage is related to hydrothermal processes.

d. The Sanchez deposit. The Sanchez deposit is a small porphyry copper deposit at the extreme southeastern end of the test site area. This deposit has had a considerable amount of disturbance from mining activity, which diminishes its usefulness as a test case target for development of mineral exploration criteria. Very little published information exists regarding this deposit. The primary sources used for the basis of this discussion are Robinson and Cook (1966) and Readdy (1978).

Lithology. In the area of the Sanchez deposit there are altered quartz monzonite intrusives which host the copper mineralization, porphyritic andesite, younger Tertiary volcanics, and intrusive dike rocks of diorite to quartz monzonite composition.

Mineralization. From the presently available data it appears that the upper portion of the primary copper zone and the overlying pyrite halo have been removed from the Sanchez deposit by erosion. The level of the presently exposed porphyry system appears to correspond to the central part of the chalcopyrite zone. The goethitic capping and the abundant copper oxides in this deposit are indicative of a low pyrite-to-chalcopyrite ratio.

Structure. The Sanchez deposit is cut by four directions of fracturing. These are the same NE, NW, E–W, and N–S trends that exist elsewhere in this district. The deposit has a structural setting similar to the other three porphyry systems but apparently lacks the well-developed system of dikes that is common to the others. This may be the result of the level of erosion of the porphyry system.

Alteration. The predominant alteration assemblage present in the quartz monzonite porphyry is argillic. Propylitic alteration is present in the porphyritic andesites.

G. Summary of Observable Features

From the descriptions of the sulfide and alteration systems present in this test site, it can be seen that many of these target areas are of adequate size for detection by the various remote sensing surveys. The more limited alteration zones, such as those associated with small dikes, may be below the spatial limits of direct detection. However, they will provide a contribution to the spectral signature of the area imaged.

There are a number of reasons why differences should be anticipated between field-mapped alteration and leached capping patterns and those mapped from various remote sensing images. These include the integrating aspects of the sensors and field mapping of fresh exposures versus sensor imaging of weathered surfaces.

Field geologists, when mapping alteration and leached cappings, break the rock to get a fresh, unweathered surface for rock type, alteration, and mineralogical identification. Field mapping therefore records the fresh rock characteristics. What the remote sensors image are complex mixtures of surficial materials. These mixtures include the weathered surface skin of outcrops, desert varnish and other coatings, soil, weathered and relatively fresh rock fragments that have migrated from their original position, dust coatings, plants, etc.

Another important difference between mapping in the field and mapping from remote sensing images is that a considerable amount of subjectivity is involved in field mapping alteration zones. The field geologist is constantly making rapid decisions as to which alteration zone an outcrop represents, often based on only cursory inspection of hand samples. He also does not have the time to examine a fresh sample of every outcrop within a large target area in order to prepare an alteration map to guide further exploration. He must, of necessity, work relatively rapidly to form an integrated interpretation of the pattern of alteration in the overall area.

The field geologist will therefore examine the main outcrops and make, at times, widely spaced traverses. He will also avoid mapping alteration and capping information from transported material. Since the sensor reports the net reflectance signature for all of the material within each single resolution element, it therefore mixes surficial materials with outcrops. In any case, the airborne scanners only record the surface characteristics of the material.

Altered rock units are frequently more susceptible to the development of new mineral species as weathered coatings than are the corresponding unaltered rocks. This is definitely the case at the Safford site. The field and reflectance evidence suggests that chlorite is more prevalent in the weathered surface than in fresh exposures of the altered rock.

As a result of the above factors, the NS-001 Thematic Mapper Simulator should provide a useful map of the alteration pattern. However, there will be differences in what this scanner will identify as the alteration class versus what exists in the fresh rock. This is not really a major problem. Once the target pattern has been recognized, the geologist can go into the field and provide the required refinements.

III. Field and Laboratory Spectral Measurements

A. Field Spectra

1. Description and procedure. *In situ* reflectance measurements were obtained at Safford in the area of the Dos Pobres deposit. Twelve units were sampled at a total of fifteen different sites. The measurement procedures consisted of making 8–10 measurements over a 10- by 10-m area for a given geologic unit (Figure 6-9, Table 6-4).

Data were obtained with JPL's Portable Field Reflectance Spectrometer (PFRS). This instrument consists of a separate optical head and amplifier–recorder assembly. In the field, a 5- by 40-cm (200-cm^2) area is viewed, and the bidirectional reflectance spectrum in the 0.45- to 2.45-μm region is recorded with moderate spectral resolution ($\Delta\lambda/\lambda$ = 0.02 to 0.04). Immediately following, a reflectance spectrum is measured of a white standard (Fiberfrax®, a ceramic wool) placed at the same orientation as the sampled area. In the laboratory, the sample spectrum is divided point by point with the Fiberfrax® spectrum to produce a normalized spectrum of reflectance relative to the Fiberfrax®. A further correction is made to convert the relative spectrum to absolute reflectance based on laboratory measurements of the Fiberfrax's® response.

The major advantage of the field measurement technique over laboratory spectral measurements is that the data obtained are more representative of naturally occurring conditions. Under natural *in situ* conditions, the instrument's field of view includes soils, various rock fragments, dead and live vegetation, etc., rather than 1-cm^2 powders or chips of rock material which are measured using laboratory instruments. In addition, a larger area is measured and, by acquiring many samples in a 10- by 10-m area, then averaging the spectra, the spectral characteristics of a larger area can be approximated.

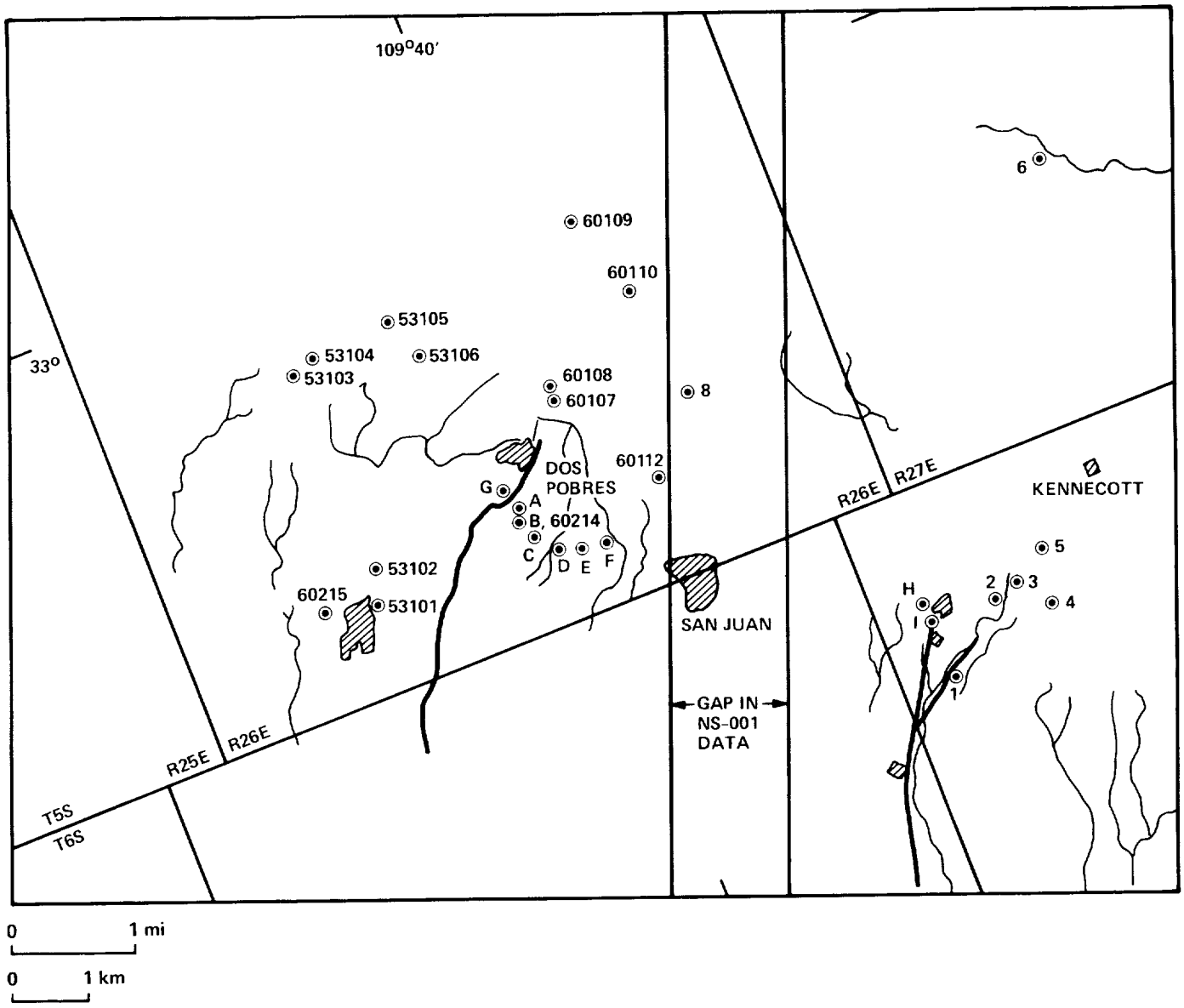

Figure 6-9. Location map showing PFRS sample sites and sites where samples were obtained for laboratory analyses. Heavy lines are roads; light lines are streams.

Spectral measurements were obtained in the field to aid in characterizing the spectral reflectance properties of the rocks and soils exposed at the Safford site. Samples were collected at each measurement site and were returned to the laboratory for mineralogical analyses. By comparison of the spectra and the mineralogy, a direct link could be established between chemical composition and spectral characteristics. This knowledge is invaluable for interpreting the remote sensing image data.

In addition, the PFRS spectra provide a data base for statistically examining the separability of different rock types as a function of wavelength regions examined. Examples of this type of analysis will be presented later. And, finally, analysis of the spectra can help in selection of image processing algorithms to apply to the aircraft scanner data. This facet will also be presented later.

2. Spectral measurements. The spectral reflectance characteristics of rocks and minerals in the 0.4- to 2.5-μm region are due to electronic processes and vibrational processes (Hunt and Ashley, 1979). Electronic processes are responsible for features that appear at wavelengths shorter than about 1.2 μm and are dominated by the presence of iron.

Table 6-4. Sample numbers and rock types

Measurement Type	Sample No.	Rock Type
PFRS	053101, 060110	Tertiary basalt
	053102	Alluvium, basaltic
	053103	Andesite
	053106, 060108	Andesite, weak propylitic
	053104, 060216	Andesite, propylitic
	060214	Andesite, hematitic
	053105	Alluvium, rhyolitic
	060112	Soil, limonitic boulders
	060215	Quaternary basalt
	060109	Latite tuffs
	060107	Quartz monzonite
	060111	Andesite conglomerate
Laboratory	A	Andesite, propylitic
	B	Andesite, propylitic
	C	Quartz monzonite, sericitic
	D	Quartz monzonite, sericitic
	E	Quartz monzonite, sericitic
	F	Quartz monzonite, sericitic
	G	Andesite, propylitic
	H	Latite, sericitic
	I	Latite, sericitic
	1	Latite, sericitic
	2	Latite, sericitic
	3	Latite, sericitic
	4	Andesite, propylitic
	5	Tertiary basalt
	6	Dacite
	7	Dacite
	8	Andesite

Electronic transitions involve either the transfer of an electron between two ions (intervalence charge transfer) or transitions between the crystal field perturbed energy levels of an ion. The former process is responsible for the ferric iron band centered in the near-ultraviolet range; it is this mechanism which produces the sharp falloff in reflectance to shorter wavelengths. The latter mechanism produces three fairly broad features in the spectra of ferric oxides that occur between 0.75 and 0.95 μm, between 0.55 and 0.65 μm, and near 0.45 μm. The presence of ferrous iron is most typically evidenced by the prominent appearance of a broad band near 1 to 1.1 μm.

From 1.2 μm to longer wavelengths, all features exclusively involve vibrational transitions of the hydroxyl (OH) groups. Single or multiple features at 1.4 μm are due to the first overtone of the fundamental OH stretching vibration, or to a combination of the fundamental stretching modes of two different OH groups. Unfortunately, this region is overlapped by a water absorption band in the atmosphere, so no energy from the sun reaches the surface. Therefore, this region is only of use for laboratory measurements.

Features or bands appearing near 2.2 μm are due to combinations of the OH fundamental stretch with the Al–O–H fundamental bending mode. These features appear slightly different in different materials because the OH groups occur in somewhat different environments. It is common for this feature to appear in phyllosilicates that possess a dioctahedral structure, such as kaolinite, muscovite, and montmorillonite.

When a feature appears near 2.3 μm in the absence of one at 2.2 μm, it is typically due to a combination of the OH stretching mode with the fundamental bending mode of Mg–O–H, such as in biotite. Single or multiple absorp-

tion bands near 2.35 μm are typical of the presence of overtones of the C–O stretching mode in carbonates.

The average PFRS spectra for the twelve measured units are shown in Figures 6-10 and 6-11. Also shown in dashed lines is the one standard deviation envelope for the average curves. The first three spectra are of Quaternary alluvium of varying composition. The spectrum of soil/limonitic boulders (Figure 6-10a) is of moderately low albedo. Weak absorption bands can be seen at 0.65 and 0.95 μm; also apparent below 0.7 μm is a strong falloff in reflectance toward the ultraviolet. These three features are attributable to the presence of ferric iron and are due to conduction bands and electronic processes (Hunt et al., 1971).

The spectrum of Quaternary alluvium/basalt (Figure 6-10b) is dominated by the presence of basaltic chips and boulders. Low albedo and weak absorption bands are indicative of the presence of iron oxide. There is a suggestion of an absorption band near 2.3 μm, which may be due to ferrous iron. The spectrum of Quaternary alluvium/basalt and rhyolite (Figure 6-10c) is similar to the previous spectrum but lacks the weak 2.3-μm band. Higher overall albedo is attributed to the presence of lighter-colored rhyolite fragments in the field of view. These three alluvium curves are of unaltered materials, based on the absence of absorption bands associated with clay minerals.

The spectrum of Quaternary–Tertiary basalt (Figure 6-10d) is basically flat with low albedo. Weak ferric iron absorption bands and the falloff in reflectance toward the ultraviolet are the only distinctive spectral features seen. The spectrum of Tertiary basalt (Figure 6-10e) is virtually identical to that of Quaternary basalt, but with slightly lower albedo.

The spectrum of latite tuffs (Figure 6-10f) shows subtle absorption bands at 0.65, 0.9, and 2.2 μm. The first two are due to ferric iron; the third band, just beyond 2.2 μm, is due to minor montmorillonite present on the rock surface. The 2.2-μm region contains diagnostic absorption bands due to Al–O–H and Mg–O–H vibrational processes, which can permit direct identification of the dominant clay mineral present (Hunt et al., 1973).

The next five spectra (Figure 6-11, a through e) are of andesites. Unaltered fresh andesite (Figure 6-11a) is fairly featureless spectrally. Weak iron absorption bands indicate the presence of ferric iron. Weak propylitic alteration (Figure 6-11b) produces no apparent spectral changes. The hand specimens of this material showed weak chloritization of biotite flakes, but no overall change in the matrix. Strong propylitic alteration (Figure 6-11c) was characterized by intense development of chlorite and epidote. Spectrally, a strong absorption band at 2.35 μm is attributed to a combination of ferrous iron and Mg–O–H hydroxyl bands (Hunt and Salisbury, 1970). The hematitic andesite spectrum (Figure 6-11d) is from a shear zone along the Butte Fault. In the field, the rock is a bright orange–red color due to the presence of pervasive hematite. The reflectance spectrum shows major absorption bands near 0.85 μm (ferric iron) and at 2.2 μm (kaolinite). A minor absorption band at 0.65 μm and the strong falloff in reflectance toward the ultraviolet are also due to ferric iron. The overall shape of this curve, with maximum reflectance at 1.6 μm of 35 percent, is characteristic of hydrothermally altered rocks (Abrams et al., 1977). The propylitically altered andesite conglomerate spectrum (Figure 6-11e) shows a minor absorption band at 2.35 μm and falloff in reflectance toward the ultraviolet. The low albedo suppresses the other iron absorption bands; otherwise this curve would look similar to the propylitized andesite curve (Figure 6-11c).

The spectrum of quartz monzonite porphyry (Figure 6-11f) shows weak iron absorption bands at 0.65 and 0.9 μm and a weak absorption band at 2.2 μm due to kaolinite. In hand specimens, this rock appeared weakly altered, with visible alteration of feldspars to clays. The weakness of the 2.2-μm band suggests only minor presence of clay minerals.

A summary of the absorption features described above is shown in Table 6-5. The spectral characteristics can be attributed to the presence of iron and clay minerals. These are basically the only constituents that commonly produce absorption bands in the 0.45- to 2.45-μm region. Higher spectral resolution would allow more precise definition of the hydroxyl bands near 2.2 μm. Moderate resolution is sufficient to detect the shift toward the longer wavelength of the 0.9-μm ferric band between goethite and hematite. Overall albedo is the other characteristic feature of rocks measured in this wavelength region.

3. Statistical analysis of PFRS data. The continuous 0.45- to 2.45-μm wavelength region spectra acquired by the PFRS provide an opportunity to simulate the wavelength responses of existing and theoretical scanners. By computing the equivalent band responses of these instruments, it is possible to examine the separability of rock types as a function of wavelength bands on a statistical basis. It should be noted that many other factors are ignored in this analysis. Such things as instrument response, spatial resolution, atmospheric effects, variable field of view, etc., are not considered and probably play a significant part in determining separability of materials when real instruments are used. Wavelength bands, however, are probably the major variables, with other effects being of lesser importance. This

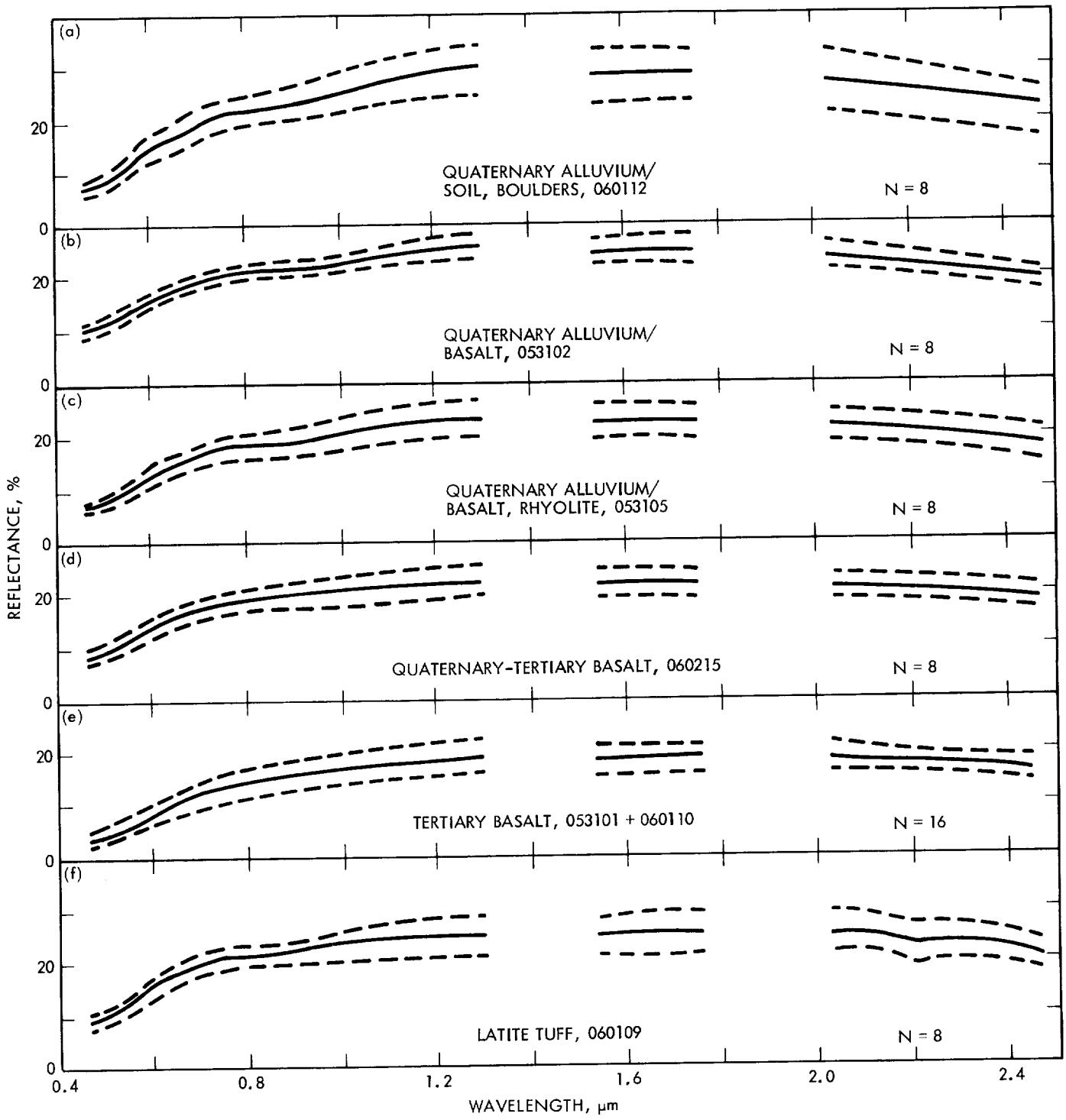

Figure 6-10. PFRS reflectance curves of alluvium, basalt, and tuff units measured in the field. Average reflectance (solid lines) and one standard deviation envelopes (dashed lines) are shown. *N* is number of PFRS measurements represented by the average curve. Gaps at 1.4 and 1.9 μm are due to atmospheric water absorption.

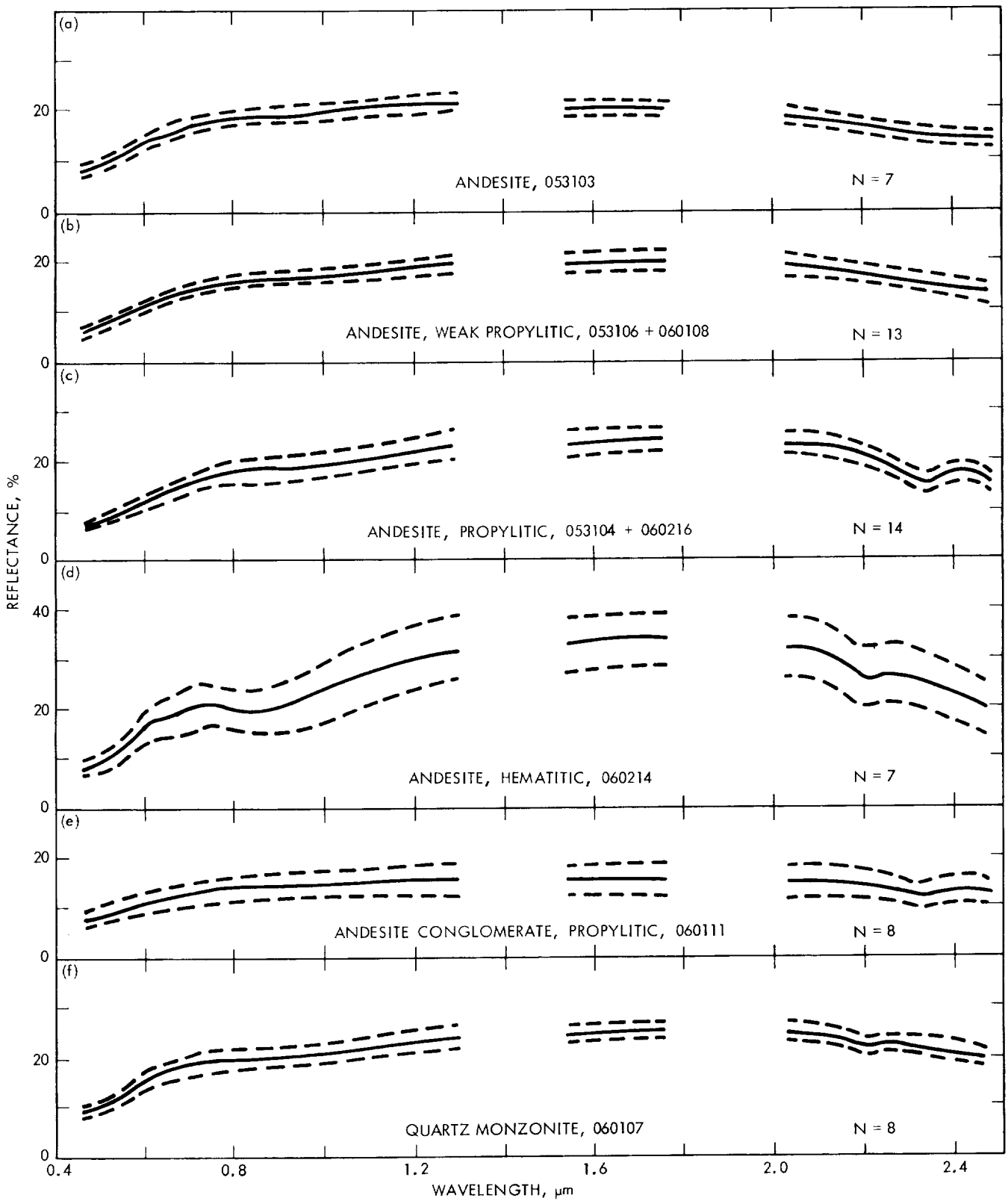

Figure 6-11. PFRS reflectance curves of andesite and quartz monzonite units measured in the field. Average reflectance (solid lines) and one standard deviation envelopes (dashed lines) are shown. *N* is number of PFRS measurements represented by the average curve. Gaps at 1.4 and 1.9 μm are due to atmospheric water absorption.

Table 6-5. PFRS spectral absorption features

Rock Type	Wavelength, μm[a]				
	0.5	0.65	0.9	2.2	2.35
Quaternary alluvium/limonitic soil	M	W	W		
Quaternary alluvium/basalt	W	W	W		W?
Quaternary alluvium/basalt, rhyolite	M	W	W		
Quaternary–Tertiary basalt	M	W	W		
Tertiary basalt	M	W	W		
Latite tuffs	M	W	W	W	
Andesite	M		W		
Andesite, weak propylitic	M		W		
Andesite, propylitic	M		W		S
Andesite, hematitic	S	W	M	S	
Andesite conglomerate, propylitic	W				M
Quartz monzonite	M	W	W	W	

[a]W – weak, M – moderate, S – strong.

Table 6-6. Wavelength bands (μm) of instruments used for statistical analysis of PFRS data

Landsat MSS	M²S	Landsat 4 TM	NS-001	30 Δλ
0.5–0.6	0.33–0.44	0.45–0.52	0.45–0.52	0.425–0.475
0.6–0.7	0.44–0.48	0.52–0.60	0.52–0.60	0.475–0.525
0.7–0.8	0.49–0.54	0.63–0.69	0.63–0.69	0.525–0.575
0.8–1.1	0.54–0.58	0.76–0.90	0.76–0.90	•
	0.58–0.62		1.00–1.30	•
	0.62–0.66	1.55–1.75	1.55–1.75	•
	0.66–0.70	2.08–2.35	2.08–2.35	2.425–2.475
	0.70–0.74			
	0.76–0.86			
	0.97–1.065			

type of analysis has been used in the past to examine plutonic rocks (Blom et al., 1980) and sedimentary rocks associated with uranium mineralization (Conel et al., 1980). A more general study (Wiersma and Landgrebe, 1980) presented a scheme for analytical design of multispectral sensors using an overall performance measure, probability of correct classification.

The technique used here is stepwise linear discriminant function analysis, part of the BMD07M computer package from UCLA (Dixon, 1970). The mathematics of discriminant analysis are fully discussed by Jennrich (1977).

Briefly, the program develops group classification functions based upon training data (sets of PFRS measurements) provided by the user for each group. The classification functions result from linear operations performed on each variable (each spectral channel) and are developed in a stepwise fashion by surveying the available variables and adding the most useful to the analysis. The utility of each variable for discrimination among the groups is thus assessed. After development of the group classification functions, the members of the training sets are classified, allowing one to determine to what degree sufficient information exists in the data to discriminate among the chosen groups. The output of the program includes matrices that depict the classification accuracies, the order of band selection, and the group classification functions for classifying unknown members.

Equivalent reflectances for bandpasses of five instruments were calculated from the PFRS data for the twelve different rock types measured. The five instruments were Landsat 1, 2, and 3 MSS; the M²S 11-channel scanner; the Landsat 4 TM; the NS-001 scanner; and a conceptual instrument with 30 equally spaced wavelength bands 0.05 μm wide in the 0.45- to 2.45-μm region (Table 6-6). The results of the analysis are shown in Figure 6-12. The classification matrix has correct classifications along the principal diagonal; misclassifications are off-diagonal elements. The overall correct classification percentage is shown under each matrix; the order of band selection is shown to the right of each matrix.

The lowest accuracy (46 percent) was achieved using the Landsat MSS wavelength bands. The broad spectral coverage of each band (0.1 μm or more) and the limited spectral region covered are responsible for their performance. Subdividing the same wavelength region into additional, narrower channels similar to those that exist on the M²S scanner improved the accuracy to 63 percent.

Landsat 4 TM bands provided 55 percent accuracy. The addition of the 1.15-μm band using the NS-001 scanner improved the accuracy to 65 percent. The first two bands selected in both tests were the 2.22- and 1.65-μm bands. These bands were selected for the Landsat 4 TM to provide improved discrimination of geologic materials, particularly altered rocks.

Finally, the 30-channel equal wavelength test achieved almost perfect accuracy. This suggests that very narrow spectral bands may be required to separate geologic materials.

An inherent bias in this analysis is the sampling scheme used. This analysis is applicable to the particular group of rocks measured at the Safford test site. Similar analyses done at the Silver Bell test site (Section 4) achieved much higher accuracies with the Landsat 4 TM and NS-001 wavelength bands. The rock types measured were dominated by hydrothermally altered materials, which have large spectral reflectance contrasts in the 1.65- and 2.22-μm region.

(a) LANDSAT MSS

	A	B	C	D	E	F	G	H	I	J	K	L	
A	2		2		3			1	2	3		3	5
B		6										2	4
C	1	1	5	1									7
D	1		1		1	1			8	1			6
E	2		1		1			1		2		1	
F		6			1	3			2			1	
G							6					2	
H	1		1			1	1	4					
I				1					7				
J										8			
K			1								6		
L	1	1						1		1		2	

46%

(b) M^2S 11-CHANNEL

	A	B	C	D	E	F	G	H	I	J	K	L	
A	7	1		1				2				4	1.03
B		6										2	0.52
C			6				1						0.81
D	4			6		1	1		2				0.72
E			1		6		1						0.60
F		4		2		5			2				0.64
G			1				7						0.68
H			1		1	1	1	3				1	+OTHERS
I						1			7				
J										8			
K							1				6		
L	1	1	1									3	

63%

(c) LANDSAT 4 TM

	A	B	C	D	E	F	G	H	I	J	K	L	
A	6				2			2				4	2.22
B		7										1	1.65
C			7										0.83
D			3	7			1		3				0.56
E					3			1		2		2	0.66
F		6				4			3				0.48
G							8						
H	1	1						6					
I						1			7				
J								1		7			
K							1				6		
L	1	1	1									2	

55%

(d) NS-001

	A	B	C	D	E	F	G	H	I	J	K	L	
A	7				2							5	2.22
B		7										1	1.65
C			7										1.15
D				8		1	2		3				0.48
E					5			1		2			0.83
F	1	1		3		3	2		3				0.66
G							8						0.56
H	1	1			1			5					
I				1					7				
J										8			
K											6		
L	1	1	1									2	

65%

(e) $30\Delta\lambda$

	A	B	C	D	E	F	G	H	I	J	K	L	
A	15											1	2.15
B		8											2.20
C			7										0.50
D				13					1				2.05
E	1				7								0.90
F						13							1.55
G							8						1.20
H								8					1.65
I				1		1			6				+ OTHERS
J										8			
K											7		
L												6	

95%

A	TERTIARY BASALT
B	ALLUVIUM, BASALT
C	ANDESITE
D	ANDESITE, PROPYLITIC
E	ALLUVIUM, BASALT/RHYOLITE
F	ANDESITE, WEAK PROPYLITIC
G	QUARTZ MONZONITE
H	LATITE TUFF
I	ANDESITE CONGLOMERATE
J	ALLUVIUM, LIMONITIC
K	ANDESITE, HEMATITIC
L	QUATERNARY BASALT

Figure 6-12. Results of linear discriminant function analysis of PFRS data. Percent correct classification, order of band selection, and classification matrix are shown for five simulated scanners.

Nevertheless, the linear discriminant analysis technique produces statistically optimal discriminant functions for the groups analyzed. In a later paragraph, these functions will be applied to the image data, and the visual separability of rock types will be assessed.

B. Laboratory Spectra

1. Introduction. Field checking the digital images raised a number of questions about the spectra of rocks and minerals and remote sensing spectrometry by the scanners. First, it was obvious that the weathered rind of the phyllic rocks was different than the freshly broken core. The fresh surface is used by field geologists for identification and mapping, whereas remote sensing instruments record the spectral reflectance of the weathered rind. Second, most published reflectance spectra of rocks and minerals are from powdered samples, wherein the rind would have been diluted by the fresh rock. Also, it is known that decreasing the particle size by grinding affects the reflectance spectra. Third, in some areas the different image configurations did not correlate in their classification of phyllic versus propylitic alteration. Samples collected at sites of typical altered areas as defined by the digital images were subjected to mineralogical and laboratory spectral analyses to answer some of these problems.

2. Methods

a. Sample collection. During field checking of the images, 17 rock samples were collected from the surface (Figure 6-9). The sample sites represent spectral classes as shown by patterns on the NS-001 and M^2S images taken into the field. The alteration and geologic maps released by Kennecott were also consulted in selection of sample sites. Where surface materials at the sites were mixed, each of the rock types was included in the sample and these were analyzed separately.

b. Analyses of the samples. Splits of the samples were analyzed by three laboratory techniques:

(1) Reflectance spectra of both weathered surfaces and of interior (broken, fresh) surfaces of solid samples were obtained. Two spectra of each sample or subsample were produced to compare weathered and unweathered rock. The integrating sphere reflectometer at the University of Arizona's Optical Science Center was used to produce reflectance spectra that scanned the 0.4- to 2.7-μm wavelength region.

(2) Reflectance spectra of whole rock powdered samples spanning the 0.4- to 2.5-μm wavelength region were obtained with JPL's UV5240 Beckman Spectrophotometer (also using an integrating sphere).

(3) X-ray diffraction analyses were performed of powdered samples by JPL.

The three spectra of each sample were examined and unusual features or recognizable chemical signatures were noted.

c. Tabulation of data. Notations from examination of the three spectra and results from the X-ray diffraction analysis were tabulated for each sample and subsample. Eight other parameters were added to the table:

(1) The image color codes from five scanner images: (a) NS-001 band-ratio composite, (b) NS-001 principal components (PC) composite, (c) M^2S 4/6, 6/8, 8/9 band ratios, (d) M^2S 4/6, 6/8, 9/10 band ratios, and (e) M^2S thermal infrared color composite image

(2) Classification of sample sites by the Kennecott alteration map

(3) Classification of sample sites by the Kennecott geology map

(4) Comments based on field examination or on the macroscopic appearance of the sample

The resulting 12 by 20 matrix is presented as Table 6-7.

As an example, samples 2b, 2c, and 2d in Table 6-7 were taken from a site classified by the Kennecott maps as Mesozoic latite dikes with quartz–sericite alteration. The site is adjacent to the Lone Star shear zone and near propylitically altered Mesozoic andesite. In the field, greenish material the field geologists called chrysocolla was seen on sample 2c. The X-ray diffraction results from sample 2c, showing the presence of quartz and feldspar with muscovite and kaolinite, would agree with the mapped classification of quartz–sericite (phyllic) and latite. The Beckman spectra from the powdered sample 2c shows the expected high reflectance and 2.2-μm notch at the infrared end of the spectrum. However, the high reflectance at the visible end of the spectrum is more typical of propylitic rocks but could also be attributed to chrysocolla. The spectrum of the solid weathered surface shows the same hybrid characteristics. The X-ray diffraction (XRD) analysis of sample 2b shows the typical array of phyllic minerals but, in addition, shows the presence of chlorite, a propylitic mineral. This hybrid alteration is confirmed by the subdued reflectance spectrum of the fresh surface typical of propylitic rocks and the clay signature in the spectrum of the weathered surface. Sample 2d contains both epidote and major quartz.

The expected color codes on digital images for phyllic zones and for propylitic zones and the observed color code

Table 6-7. Comparison of mapped lithology and alteration, color on digital images, X-ray mineralogy, and laboratory spectral features

Sample No.	Description of Company Maps		Color on Digital Images					X-Ray Mineralogy	Chemical or Mineralogical Features From Laboratory Spectra			Field Observations
	Lithology	Alteration	NS-001 Canonical Transform	NS-001 3/2, 4/5, 6/7	M^2S 4/6, 6/8, 8/9	M^2S 4/6, 6/8, 9/10	Thermal: High TI + Albedo		Powdered	Broken Surface	Weathered Surface	
6	Tertiary dacite		Yellow	Yellow	Red	Black		Major quartz Major andesine Major cristobalite Minor muscovite Minor kaolinite	High albedo, flat spectrum	High albedo, trace hematite	Lower albedo than fresh surface, high at 1.6 μm	Post caldera or "rhyolite" dome; phyllic
7	Tertiary dacite				Gray?	Gray?		Major quartz Major andesine Minor kaolinite Trace hematite	High albedo, strong ferric oxide, weak at 2.2 μm	High albedo, high ferric	High albedo, deep ferric at 0.9 μm, high IR	
3	Mesozoic quartz latite or latite	Quartz–sericite	Yellow	Yellow	Brown	Black	Yes	Major andesine quartz Minor kaolinite Minor sericite Trace hematite	High albedo, kaolinite, chlorite (?)	High albedo, high blue (Cu?)	High ferric oxide band, deep at 2.2 μm	Pyritic zone, phyllic
1	Mesozoic latite	Quartz–sericite	Red	Yellow	Red–orange	Brown	?	V. major quartz Minor sericite V. minor albite, hematite, sanidine, epidote	Hematite (0.9 μm), 2.2 μm "clay"	V. high albedo, high 1.6- to 2.2-μm ratio	Dark in visible, v. bright at 1.6 μm	Phyllic, with epidote and sericite
2b	Mesozoic latite + andesite	Quartz–sericite + chloritization	Yellow–red–brown	Yellow	Brown	Brown–black	Yes	Major quartz Andesine Minor chlorite Minor montmorillonite	Chlorite (?)	Chlorite (?), low albedo	Looks phyllic–high at 1.6 μm, low at 2.2 μm	Mineralized; phyllic–propylitic boundary at Lone Star shear zone
2d	Mesozoic latite + andesite	Quartz–sericite + chloritization	Yellow–red–brown	Yellow	Brown	Brown–black	Yes	Major andesine Major quartz Minor epidote Minor muscovite	Minor 0.85- and 2.2-μm bands			Mineralized; phyllic–propylitic boundary at Lone Star shear zone
2c	Mesozoic latite + andesite	Quartz–sericite + chloritization	Yellow–red–brown	Yellow	Brown	Brown–black	Yes	Quartz, feldspar Minor muscovite Minor kaolinite	V. high in IR; 2.2 μm band, peak at 0.6 μm	Similar to weathered but attenuated	Peak at 0.6 μm, deep at 0.68 μm	Mineralized; phyllic–propylitic boundary at Lone Star shear zone
1	Mesozoic latite + andesite	Quartz–sericite + chloritization	Red	Yellow	Gray	Gray	?	V. major quartz Minor muscovite Minor illite V. minor hematite	High albedo, weak ferric iron band	Similar to weathered but attenuated	Deep at 0.9 μm, high in IR, deep at 2.2 μm	Narrow dike, phyllic, sericitized, near propylitic
D_p	Quartz monzonite	Quartz–sericite, goethitic	Red	Yellow	Red	Black	Yes	Major quartz Major kaolinite Major muscovite Major illite (sericite) V. minor hematite, albite	Hematite, kaolinite	Dark visible–high IR, deep at 2.2 and 0.5-μm bands	High at 1.6 μm, exaggeration of broken surface	Phyllic porphyry, silicified, albitized, argillized

Table 6-7 (Continued)

Sample No.	Description of Company Maps		Color on Digital Images					X-Ray Mineralogy	Chemical or Mineralogical Features From Laboratory Spectra			Field Observations
	Lithology	Alteration	NS-001 Canonical Transform	NS-001 3/2, 4/5, 6/7	M^2S 4/6, 6/8, 8/9	M^2S 4/6, 6/8, 9/10	Thermal: High TI + Albedo		Powdered	Broken Surface	Weathered Surface	
D_m	Quartz monzonite	Quartz–sericite	Red	Yellow	Red	Black	Yes	V. major quartz Major alunite Minor hematite	Hematite, alunite	Deep at 2.2 μm, low visible–high IR	High at 1.6 μm, exaggeration of broken surface	Phyllic, microfabric mylonite
E	Quartz monzonite	Quartz–sericite	Red	Yellow	Red–white	Black	?	Major kaolinite Major sericite Minor quartz, hematite	Hematite, kaolinite	Deep at 2.2 μm, low visible–high IR	High at 1.6 μm, exaggeration of broken surface	Phyllic–argillic
F	Quartz monzonite	Quartz–sericite	Red	Red	Red	Tan	No	V. major quartz Major sericite Minor alunite, hematite	Hematite (deep), kaolinite	High albedo, unusual because same as weathered	Deeper 0.5-, 0.9-μm bands	Argillic
C	Quartz monzonite	Quartz–sericite, hematitic	Red	Yellow	Red	Black	No	Major albite, quartz Major chlorite Minor sericite V. minor kaolinite, hematite	Chlorite	Low albedo, flat, strong chlorite (2.3 μm)	Strong at 0.9 μm, high at 1.6 μm, low at 2.2 μm	Phyllic rind, propylitic core, latite (?)
G	Mesozoic andesite	Propylitic	Blue	Violet	Gray	Cyan	No			V. low albedo, chlorite	0.95-μm band	Propylitic
A	Mesozoic andesite	Propylitic	Blue	Brown	Cyan	Gray	No	Major quartz, muscovite Minor andesine, chlorite V. minor calcite	Chlorite–calcite, 2.2 μm	Low albedo, green chlorite	Low albedo, high at 1.6 μm	Propylitic
B	Mesozoic andesite	Propylitic	Blue	Brown	Cyan	Gray	No	Major quartz, muscovite Minor calcite Minor montmorillonite	2.2 μm clay band, 2.3 μm calcite, deep 0.55-μm band	High visible, peak at 0.6 μm (chlorite), falling in IR	V. low albedo, weak at 2.2-, 2.3-μm bands	Propylitic
4	Mesozoic andesite	Propylitic	Brown	Green	Cyan	Cyan	No	Major andesine Major quartz Minor chlorite	V. flat	No 0.9-μm band, high blue	Weak at 2.2 μm	Propylitic, host rock
H	Mesozoic latite	Quartz–sericite	Tan	Yellow–green	Brown–orange	Gray	?	Major quartz Minor muscovite, illite V. minor epidote, albite Trace hematite	Hematite, muscovite, epidote (?)		Very bright at 1.6 μm, dark visible	Mixed float, including basalt
5	Tertiary basalt		Brown	Green	Pink	Pink		Fresh rock Major andesine, diopside Minor cristobalite Weathered rock Major andesine Minor hematite Minor Mn calcite Minor Cu oxides	Fresh Flat spectrum Weathered Weak at 0.5 μm, higher IR	V. low albedo	Low visible, high IR	Younger, post-Laramide; appears to be mineralized

for the 2b-2c-2d sample site on the images are listed in Table 6-8. In this example the tabulated results show that the samples from site 2 are of hybrid alteration, as indicated by the mixed results from image codes and laboratory analyses.

d. Image pseudo-spectra. The spectra of Figures 6-13 through 6-17 were constructed from the laboratory reflectance spectra by plotting, at the band centers of the M²S and NS-001 scanners, the spectral values of powdered samples picked from the pen-line graphs drawn by JPL's Beckman spectrophotometer. The spectra of fresh (broken) rock surfaces and weathered rock surfaces were taken from numerical printout sheets generated by the University of Arizona's integrating sphere reflectometer.

Figures 6-13 and 6-14 were drawn to simulate the spectra as might be seen by the five reflective M²S bands based upon the laboratory spectral measurements. Figures 6-15 and 6-16 simulate the spectra as might be seen by the six NS-001 bands used. Figures 6-13 and 6-15 represent phyllic alteration, and Figures 6-14 and 6-16 represent propylitic alteration. Figure 6-17 shows both M²S and NS-001 spectra of one sample from an area of anomalous noncoincidence between the digital images. Two image configurations (both M²S) classified the source area of this sample as propylitic and two other configurations (both NS-001) as phyllically altered.

The three types of laboratory reflectance spectra represent freshly broken solid surface, weathered surface rind, and powdered samples (minus 80 mesh). The laboratory spectra that best represent the surfaces seen by remote sensing instruments are the spectra of the weathered surfaces of solid rock samples. The mineralogies of these weathered rinds are sometimes different from those of the fresh interiors that would be used by field geologists to classify rocks. Spectra of the fresh surfaces are useful to correlate with the mineralogy as mapped by field geologists. Spectra of powdered samples present two difficulties in their use: (1) the reduction in particle size by grinding modifies the spectra, and (2) the weathered rind is diluted

Table 6-8. Predicted and observed image colors for phyllic and propylitic alteration

Images	Predicted Color		Observed Color
	Phyllic Alteration	Propylitic Alteration	Samples 2c, 2b, 2d
NS-001 canonical (Figure 6-51)	Red	Blue	Yellow + brown to red
NS-001 3 ratios (Figure 6-42)	Yellow	Blue	Yellow
M²S 8/9 ratio (Figure 6-35)	Red	Cyan	Brown
M²S 9/10 ratio (Figure 6-36)	Black	Light gray	Black
Thermal composite (Figure 6-56)	Magenta pink	Blue–gray green	Magenta pink

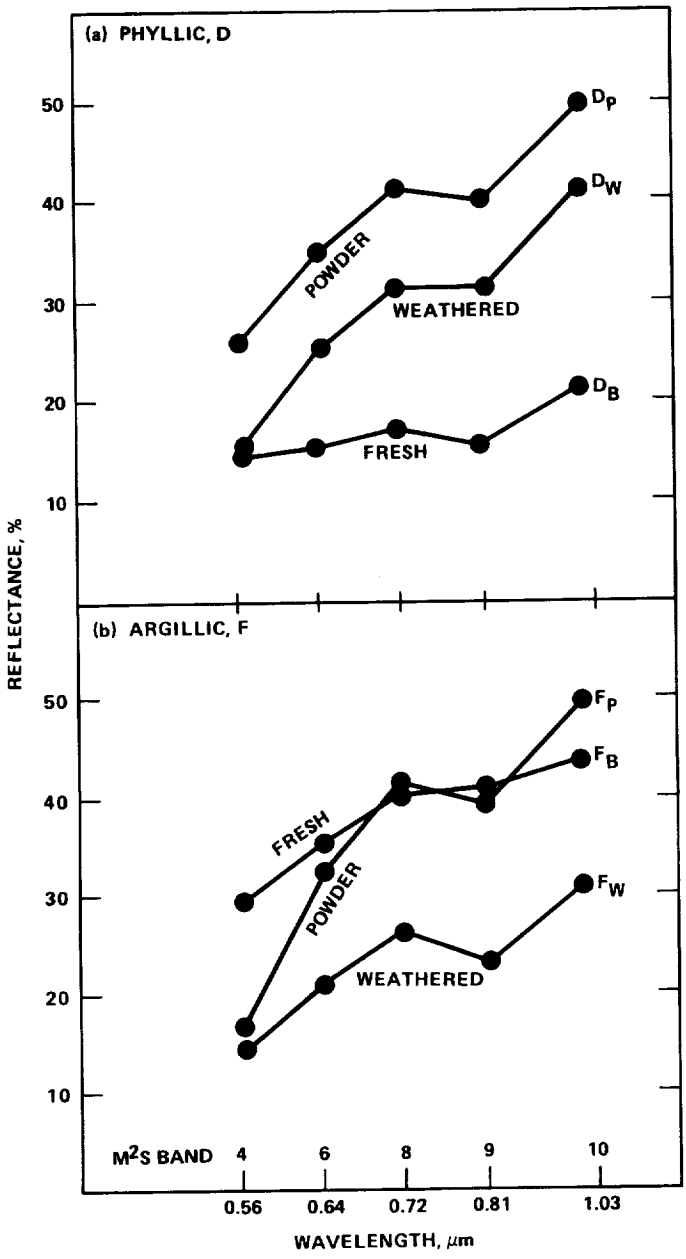

Figure 6-13. Image pseudo-spectra of solid, freshly broken rock surfaces (D_B, F_B), solid weathered surfaces (D_W, F_W), and powdered rocks (D_p, F_p) of (a) phyllically altered mylonite and (b) argillized porphyry as might be seen by five bands of the M²S scanner

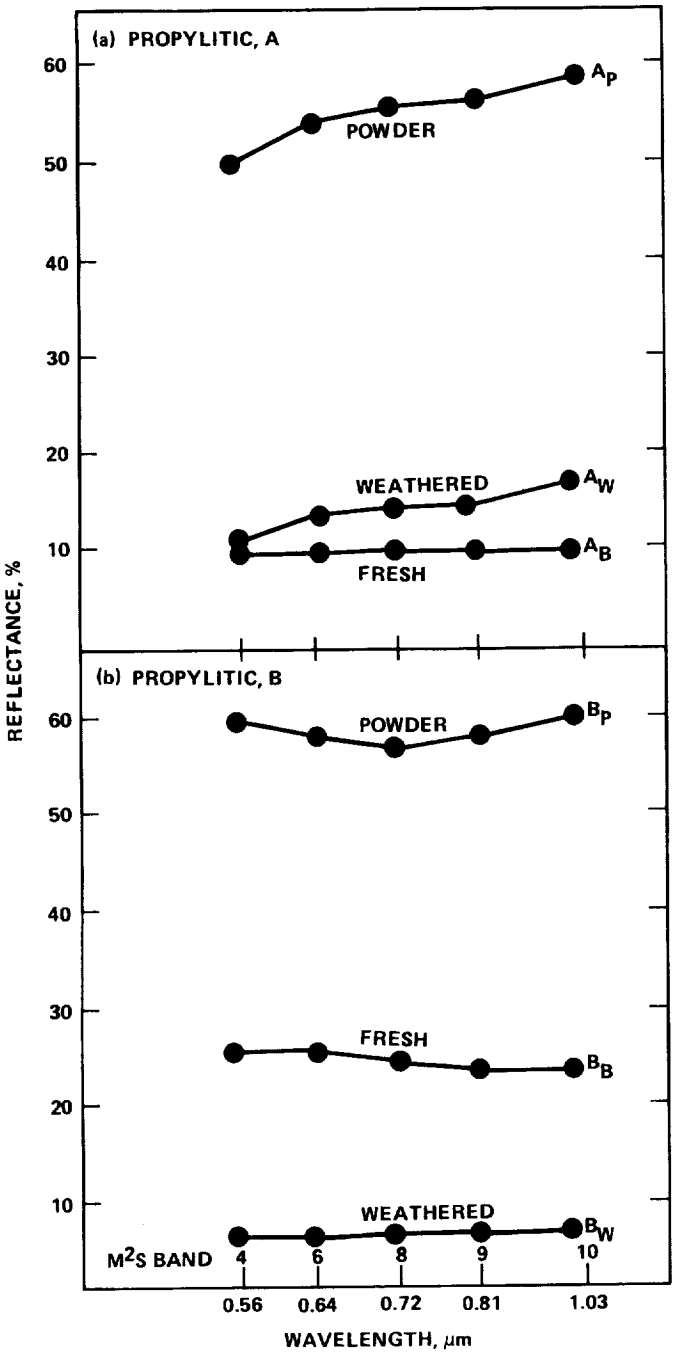

Figure 6-14. Image pseudo-spectra of solid, freshly broken rock surfaces (A_B, B_B), solid weathered surfaces (A_W, B_W), and powdered rocks (A_p, B_p) of propylitically altered andesite as might be seen by five bands of the M²S scanner

by mixing with the fresh rock core. Spectra of powdered samples are useful for two reasons: (1) they provide a comparison to the mineralogic and chemical analyses by X-ray and other methods that use powdered samples, and (2) they can be compared with spectra in the literature.

Silicates and carbonates, such as those found in the propylitic zones, are relatively transparent to visible light, and the effect of decreasing particle size is to increase the albedo, i.e., silicates produce a light streak. However, in the case of ferric oxides, the reflectivity to visible light decreases with decreasing particle size, i.e., ferric oxides produce dark streaks. Iron oxides are transopaque, that is, opaque in the visible and transparent in the infrared region. This optical property produces a crossover between the spectral curves for different particle size ranges. The crossover effect is notable in rocks from the phyllic zones. Powdered phyllic rocks show decreased reflectance in the visible spectrum and increased reflectance in the infrared, i.e., to infrared sensors, iron oxide would appear as a white streak.

3. Results. The combined data set analyzed was composed of (1) the three reflectance spectra (outer rock surface, fresh broken inner rock surface, and powdered rock), (2) the tabulated mineralogical, lithological, spectral, and image data, and (3) the image-pseudo spectra. Some new explanations were provided for (1) the lack of consistent correspondence between alteration patterns as displayed on some of the different types of scanner images, and (2) the high reflectivity at 1.6 μm displayed by the weathered rind of phyllic rocks. Figures 6-13 and 6-15 show the sets of three types of spectra for two samples of phyllically altered rock, D (Figure 6-13a) and F (Figure 6-13b). Sample D is representative of phyllic alteration containing major quartz, alunite, and hematite. Sample F is from a highly argillized outcrop. Important features include:

(1) A strong transopaque crossover effect is shown by the powdered sample F_p and the fresh sample F_B, probably caused by the iron oxide present.

(2) An unusual situation, possibly unique to heavily argillized areas, exists: the weathered surface F_w is darker than the fresh core F_B.

(3) The three spectra from sample D show a progression typical of most phyllic samples: a monotonic increase in albedo from the fresh surface D_B to the weathered surface D_W and finally to the brightest powdered D_p. This progression implies that at least part of the difference between fresh and weathered surfaces of phyllic rocks is due to the particle-size decrease associated with argillization or to the mechanical disintegration associated with supergene processes.

Figures 6-14 and 6-16 show simulated M²S and NS-001 spectra of two typical samples of propylitically altered Mesozoic andesite. The spectra of the solid rock surfaces show no consistent change in albedo between weathered and unweathered surfaces. These propylitic rocks seem to be more resistant to weathering than the phyllic rocks.

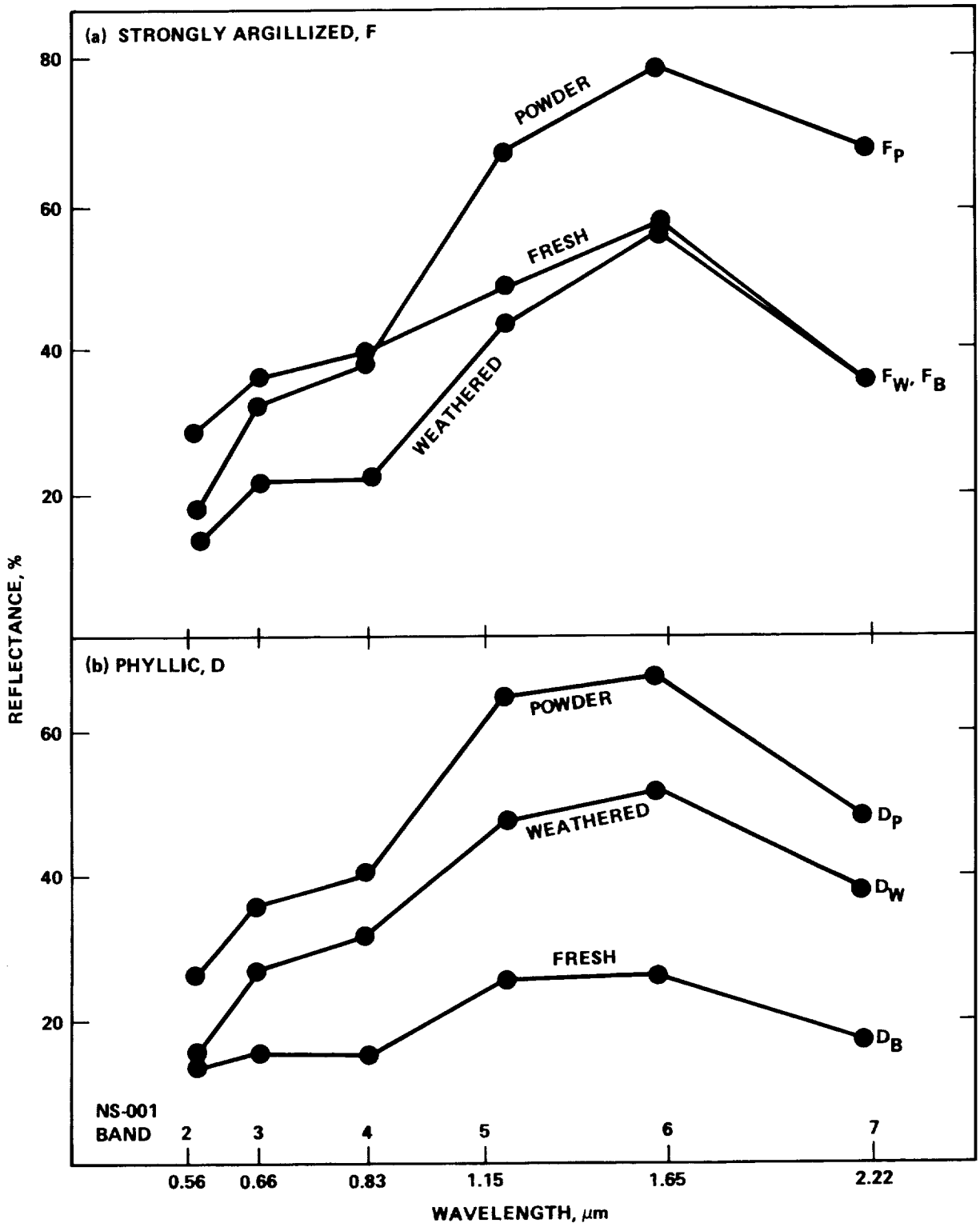

Figure 6-15. Image pseudo-spectra of solid, freshly broken rock surfaces (F_B, D_B), solid weathered surfaces (F_W, D_W), and powdered rocks (F_p, D_p) of (a) argillized porphyry and (b) phyllically altered mylonite as might be seen by six bands of the NS-001 scanner

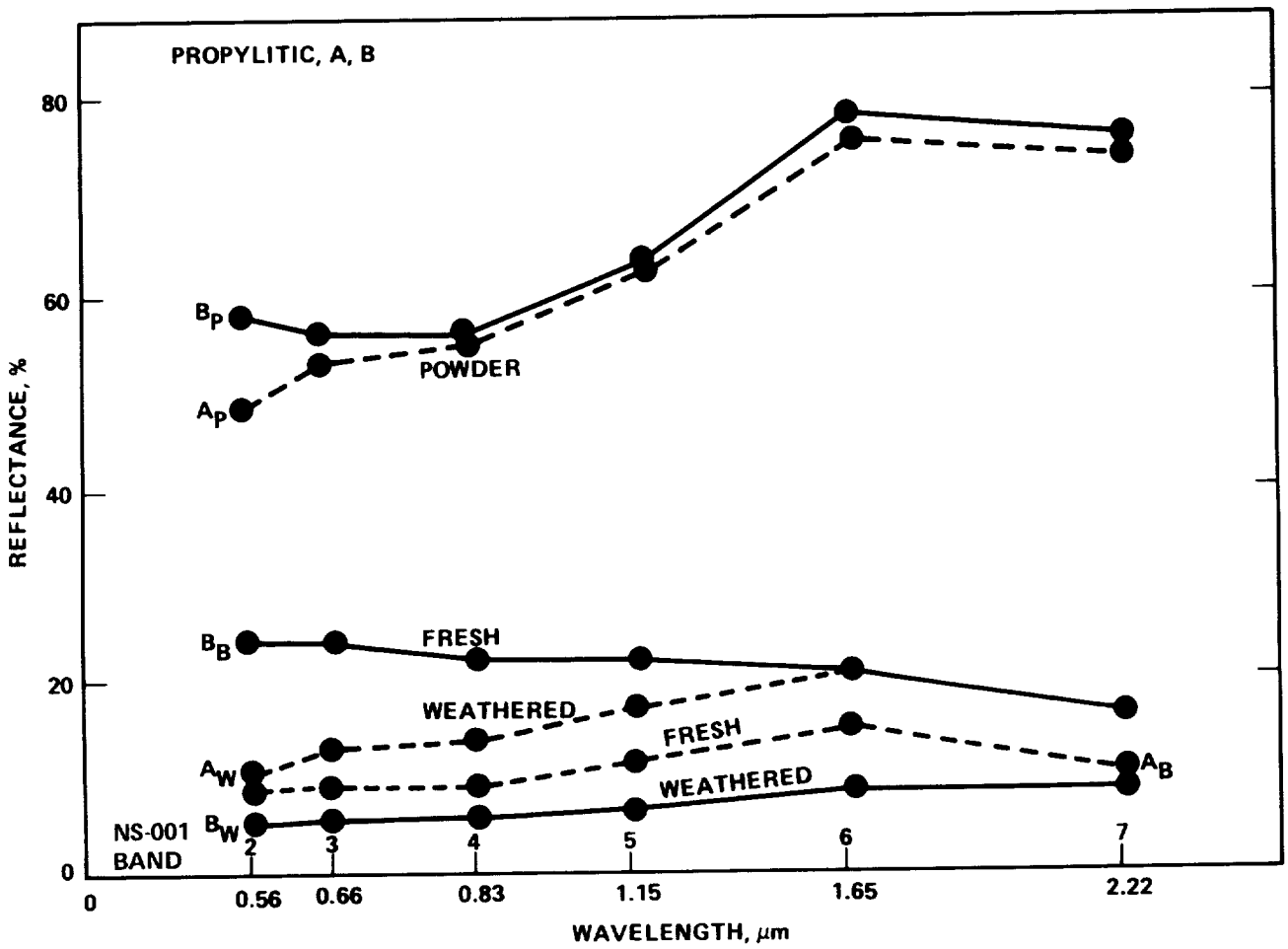

Figure 6-16. Image pseudo-spectra of solid, freshly broken rock surfaces (A_B, B_B), solid weathered surfaces (A_W, B_W), and powdered rocks (A_p, B_p) of propylitically altered andesite as might be seen by six bands of the NS-001 scanner

Note the extreme increase in albedo and the altered curve shapes shown by the powdered samples. The analogous albedo increases in the visible range caused by grinding the samples can be observed in the white streak that is obtained from silicate and carbonate minerals typical of the propylitic zones. The lack of transopaque crossover indicates the lack of ferric oxide and clay minerals.

Figure 6-17 shows the NS-001 and M^{2}S simulated spectra of sample 2c from one of the anomalous sites where classifications of alteration types by different image types did not agree. Sample 2c is from an area previously mapped by Kennecott as a dike of latite altered to quartz–sericite, but closely surrounded by chloritized andesite. The sample contained the typical phyllic assemblage of quartz, muscovite, kaolinite, ferric oxide (or pitch limonite) after sulfides, and a thin coating of chrysocolla. The infrared region of all of the 2c spectra are typical of the phyllic rocks. The strong transopaque crossover (high reflectance in the infrared compared to visible wavelengths) is indicative of the ferric oxides, and the steep slope between 1.6 and 2.2 μm confirms the presence of the kaolinite. However, the visible end of the spectra more closely resembles that of propylitic rocks. The increase in the 0.56-μm reflectance is indicative of the presence of the chrysocolla.

The results of the three types of spectral analysis, X-ray diffraction mineralogy, coding by five digital images, and previous field mapping are listed in Table 6-7. The data summarized here confirm that the phyllic–propylitic separation by the digital scanner images is for the most part correct. In a few areas the classifications of the images fail to correlate between these images. The example of sample 2c was discussed above (lack of correlation due to presence of chrysocolla). In another case, sample H contained minerals indicative of both phyllic and propylitic alteration.

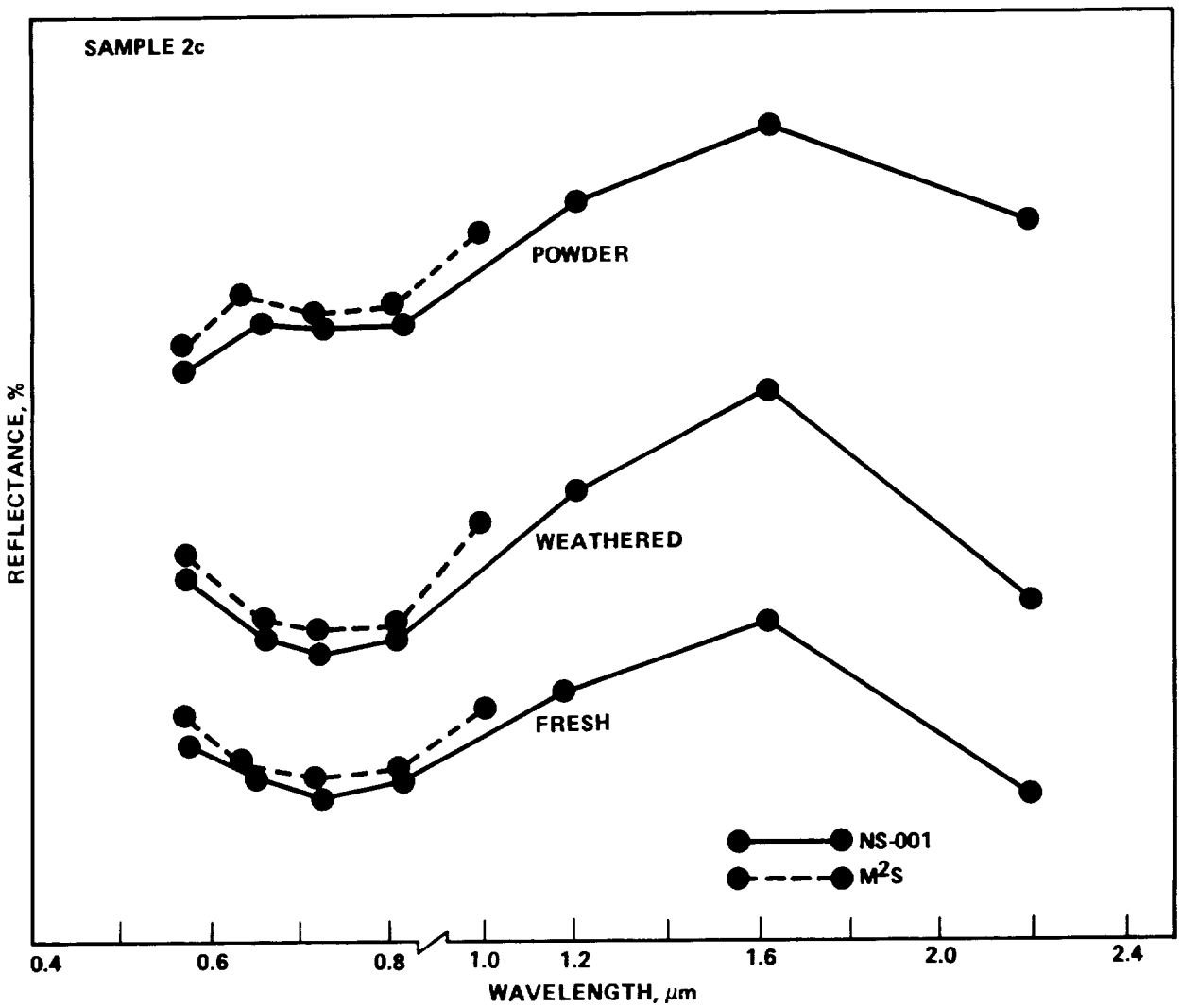

Figure 6-17. Image pseudo-spectra of five M²S and six NS-001 channels of sample 2c taken from one of the noncorrelating sites where some scanner images indicate phyllic alteration and others do not. Note that the spectra beyond 0.8 μm indicate phyllic alteration, whereas the spectra below 0.8 μm indicate propylitic alteration. Also note scale change after 0.9 μm.

In the areas of noncorrelation between the M²S 4/6, 6/8, 8/9 and the M²S 4/6, 6/8, 9/10 images, these noncorrelations were previously assumed to be due to differences in species of ferric oxide in the leached capping. Laboratory studies could not confirm that assumption. Instead, the major difference was found to be on the shortwave (4/6) end of the spectrum, where the green minerals chlorite, epidote, and chrysocolla tended to increase the 4/6 ratio. These green propylitic minerals were found in samples that also had phyllic characteristics including low 9/10 ratios indicative of ferric oxide also found in the samples (3, I, 2d, 2c, H). In other areas, such as at the site of sample I, the ground was covered with float containing both alteration types.

The area of sample C was classified as phyllic by all four scanner configurations. However, sample C was found to have a phyllic weathered rind over a propylitic core.

Table 6-8 was used to derive a significant modification to the remote sensing model. The table reveals that the combination of the five image types makes possible not only the 100 percent correct discrimination between the major alteration types (propylitic and phyllic), but also between mineralogical subdivisions within these two types. Degrees of argillization or silicification and some lithologic differences are discriminated within the color-coded images.

IV. Image Analysis and Interpretation

A. Introduction

Efforts in the analysis and interpretation of the remote sensing data were not equally distributed, but were concentrated on those data sets that offered the highest potential value to exploration in environments similar to the Safford District. The types of information sought from the data were general lithologic separations and mapping capabilities, separation of different types of alteration, and mapping of regional and local structural features. In all interpretations, analysis was guided by the remote sensing model developed earlier, which focused the interpreters' attention to seek certain expected features associated with Safford District type porphyry copper deposits.

More than 20 remote sensing image types were analyzed to produce more than a dozen interpretive maps from a selection of these images. These included aerial and space photography, airborne and Seasat radar, and aerial and space multispectral images. The multispectral images were produced from three different scanners by several different digital processing algorithms. The multispectral data included day–night thermal infrared image sets for thermal inertia studies. A summary of the color images and band assignments appears in Table 6-9.

Analysis of the multispectral color composites was done in three steps:

(1) The images were taken into the field. Those areas in which the images indicated phyllic alteration were examined. Representative rock samples were collected for laboratory analysis.

(2) The laboratory studies, described in Paragraph III.B, included X-ray diffraction and reflection spectroscopy. The X-ray and reflection data were used to relate mineralogy to spectral patterns seen in the images.

(3) In the study of the correspondence or lack of correspondence between the different images of the same area, the laboratory and field observations were synthesized to develop a modified remote sensing model.

B. Mapping of Alteration

One of the primary objectives of the test site study was to see if it was possible to map the alteration patterns present. In addition to mapping the gross alteration pattern, the use of the multispectral scanner images to discriminate and map the various types of alteration was to be tested. The alteration associated with each of the deposits has already been briefly discussed. However, it is appropriate here to provide a general discussion of the types of alteration and their overall distribution with respect to the known porphyry systems within the district. In addition, general notes are provided on the types of problems that should be anticipated. Any program to map alteration from spectral signatures must make allowances for a number of factors. This discussion will provide a background against which the results and problems encountered during this test case can be measured.

Hypogene alteration, associated with the porphyry copper systems of the Safford District, is similar to that found at other porphyry copper deposits. There is a pattern

Table 6-9. Color assignments for remote sensing scanner images

Image	Color Assignment		
	Blue	Green	Red
Landsat color additive composite (Figure 6-28)	MSS 4	MSS 5	MSS 7
Landsat color additive composite (Figure 6-29)	MSS 4	MSS 5	MSS 7
Landsat color ratio composite (Figure 6-30)	4/5	5/6	6/7
Landsat principal components composite (Figure 6-32)	V1	V2	V3
M^2S color ratio composite (Figure 6-35)	4/6	6/8	8/9
M^2S color ratio composite (Figure 6-36)	4/6	6/8	9/10
M^2S color ratio composite (Figure 6-40)	5/2	6/8	8/10
NS-001 color ratio composite (Figure 6-42)	3/2	4/5	6/7
NS-001 color ratio composite (Figure 6-43)	3/2	4/6	6/7
NS-001 color ratio composite (Figure 6-45)	3/2	4/5	6/7
NS-001 density slice of 6/7 ratio (Figure 6-48)			
NS-001 canonical transform (Figure 6-51)	V1	V3	V2
NS-001 canonical transform (Figure 6-54)	V1	V3	V2
M^2S thermal composite (Figure 6-56)	Night thermal	Day thermal	Albedo

of superimposed zones with a potassic core surrounded by phyllic, argillic (?), and propylitic zones. There are, however, some significant variations in the alteration assemblages which appear to be related to the chemical composition of the andesite host rock.

The overall extent of hydrothermal alteration in the Safford District is difficult to determine in the field. This results from two main factors: minerals characteristic of the propylitic zone also occur as deuteric products in the older andesites, and widespread postmineral cover is present. Both of these factors will also influence the ability to discriminate the extent of alteration on the remote sensing images. The distribution and character of hydrothermal alteration in the San Juan and Kennecott areas have been well documented by Blake (1971) and Robinson and Cook (1966).

Details regarding the type and distribution of alteration for the Dos Pobres deposit have been documented by Langton and Williams (1982). The general types and distribution of alteration at this deposit are similar to those in the San Juan and Kennecott deposits. However, biotitization at the Dos Pobres deposit exceeds the intensity of that reported for the Kennecott deposit.

The altered and pyritized zone at the Kennecott deposit is known to cover an area 4000 by 2000 m. Half of this altered zone is covered by postmineral volcanic rocks (Robinson and Cook, 1966).

In the San Juan area, the pyritic halo measures 2200 by 2800 m and exceeds the quartz–sericite zone (Blake, 1971). The outer edge of the propylitic zone is not well defined but, as shown on the mapping by Blake (1971), extends at least 300 m beyond the pyritic zone.

The alteration assemblages that exist at the Dos Pobres, Kennecott, and San Juan deposits include: K-feldspar–quartz–biotite–(anhydrite?)–sericite, quartz–sericite, biotitization, albitization, argillization (kaolinite–montmorillonite–alunite), chloritization, and propylitization (epidote–chlorite–calcite). All of these zones are gradational and have overlapping boundaries. In addition, overprinting of alteration zones occurs where there has been retrograde alteration.

1. Potassic zone. The potassic zone is identified by the introduction or redistribution of potassium feldspar and biotite. This alteration zone is roughly conformable to the central portion of the sulfide system. The distribution of hydrothermal K-feldspar in the Safford District is conformable with the center of the sulfide system. Hydrothermal biotite extends beyond the K-feldspar zone within the porphyry systems in the Safford District.

There is a problem in relation to the significance of much of the biotite in the Cretaceous–Early Tertiary hornblende andesite. Although this biotite indicates a net increase in potassium, in the andesite this biotitization appears to represent the zone usually occupied by phyllic, argillic, or in some instances propylitic alteration in less mafic host rocks. The presence of minor amounts of chlorite in this zone of biotitization may mask its true signature on multispectral scanner images.

2. K-feldspar–quartz–biotite assemblage. Typical potassic alteration occurs at all of the ore bodies within the district. This is characterized at San Juan by stockwork or veinlets containing K-feldspar and quartz, and in the groundmass of the quartz monzonite porphyry stock by abundant secondary K-feldspar. The potassic feldspar is recrystallized near veinlets and replaces plagioclase (Blake, 1971).

Shreddy or wispy grains of biotite replace rims of primary biotite in the intrusive. Small shreds of secondary biotite also occur in the groundmass of the intrusive associated with sulfides, quartz, and K-feldspar. Some of the hydrothermal biotite, replacing hornblende in the andesites immediately adjacent to the San Juan stock, may not correlate with the classic "potassic" zone.

A portion of the potassic alteration zone defined by Blake (1971) appears to include biotite formed in the andesite that would correlate with phyllic alteration in less mafic terrains. This portion of the 1.5-km-long potassic zone (Blake, 1971) corresponds to the pyritic halo which is usually associated with phyllic alteration. There is a general absence of secondary potassium feldspar in this portion of Blake's (1971) potassic alteration zone.

In the Lone Star stock area of the Kennecott deposit and within the Dos Pobres deposit, potassium feldspar occurs in and along veins in the various intrusive rocks. Abundant K-feldspar also occurs in veins which contain quartz and sericite that cut portions of the andesite near the volcanic vent and associated dikes (Robinson and Cook, 1966). Small amounts of secondary biotite are associated with quartz veins that cut the intrusives (Robinson and Cook, 1966).

Small amounts of rutile and apatite are noted by Blake (1971) as accessory minerals in the K-feldspar–biotite alteration zone at the San Juan Mine. Rutile occurs as needles within the wispy, secondary biotite formed at the expense of the primary biotite. Apatite is associated with

quartz–K-feldspar–biotite veins and veinlets. The presence of apatite in this zone is interesting and possibly important with regard to geobotanical indicators of similar zones, particularly since Lowell and Guilbert (1970) noted small amounts of apatite in veinlets and as disseminated grains in the potassic zone in other deposits. The occurrence of higher quantities of potassium and phosphate, if liberated into the soil, should tend to promote more vigorous plant growth which could be detectable in aerial photographs. However, no botanical indicators were noted during the present study of the Safford test site.

3. Biotitization. The biotitization referred to in this discussion is limited to the development of abundant biotite replacing hornblende and augite in the andesites of the Safford District. As previously stated, much of this biotitization appears to correlate with the phyllic or argillic alteration zones of other porphyry copper deposits. The amount of potassium added to that contained in the host andesite as hornblende is comparable to that added during sericitization of less mafic rocks.

Biotitization at the Dos Pobres and Kennecott deposits is strongest adjacent to the dikes and plugs. Robinson and Cook (1966) report a content of up to 20 percent secondary biotite in the andesites near the ore zone at the Kennecott deposit. Langton and Williams (1982) report even higher biotite contents for similar settings in the Dos Pobres ore body. This hydrothermal biotite occurs as clots, flakes, and shreddy aggregates replacing hornblende and augite, and as veinlets.

The secondary biotite zone as shown by Robinson and Cook (1966) at the Kennecott ore bodies extends at least 1600 m in an E–W direction. This zone is open to the north and measures at least 900 m in a N–S direction. Within the center of the Kennecott ore body, the main alteration suite is quartz–sericite overlapping a lesser amount of quartz–K-feldspar. This phyllic alteration suite in the intrusive rocks at the center of the ore body is another indication of the probable correlation of the biotitization in the andesites with the phyllic zone.

At the San Juan Mine, a similar zone of biotitization in the andesites is reported by Blake (1971). Near the San Juan stock, hornblende in the andesites is completely replaced by biotite. The overall zone containing secondary biotite measures roughly 1.5 km in diameter and is centered on the San Juan stock.

Blake's (1971) mapping of alteration shows a zone of moderate biotitization measuring 300 by 600 m bordering the San Juan stock to the south. Two much smaller zones of moderate biotitization occur just to the northeast and northwest of the stock. These zones contain biotite replacing from 25 to 50 percent of the hornblende and augite (?) present in the andesite. In the remainder of the biotitized zone, as shown by Blake (1971), less than 25 percent of the hornblende and augite (?) have been replaced by biotite. Biotitization decreases away from the stock. A similar pattern of potassic alteration and biotitization is reported at the Dos Pobres ore body.

4. Phyllic zone. In the Safford District, quartz–sericite (phyllic) alteration is mainly confined to intrusives, stocks and dikes, and mineralized fractures within the ore bodies and surrounding pyritic halos. Chloritic alteration is closely associated with the phyllic zone in this district. However, chlorite, and to some degree epidote, is nearly ubiquitous in the district.

A phyllic alteration zone is centered on the Kennecott ore body (Robinson and Cook, 1966). The phyllic zone at this deposit conforms to the distribution of the post-older andesite intrusive dike complex and to the more acid volcanic tuffs and associated volcanic vent. Sericite extends beyond the main phyllic zone, with traces present in all of the dike rocks. Sericite is also present along structures in the chloritic and propylitic alteration zones. Sericite occurs up to 3000 m southwest of the Kennecott ore body in dikes and along fractures (Robinson and Cook, 1966). This widespread, albeit sparse, sericitic alteration may partially represent leakage from a deeper portion of the Kennecott ore body.

The main zone of phyllic alteration associated with the Kennecott ore bodies is 2200 by 1600 m wide (Robinson and Cook, 1966). The quartz–sericite alteration is primarily confined to the intrusive rocks. Sericitization is developed in the andesite as *narrow* zones along fractures and grades into biotitization. Sericite replaces secondary biotite along veins and fractures that cut the biotitized zone. Rocks of this zone are characterized by bleaching that ranges from light gray to white in color (Robinson and Cook, 1966). These zones are poorly exposed and are not readily apparent on the color or panchromatic aerial photographs of the area. Linear light-toned patches in the Dos Pobres ore zone are visible on the color aerial photographs and represent sericitic alteration along fractures.

The phyllic zone at the San Juan Mine is mainly confined to the stock and to mineralized structures. This zone, which measures 2600 by 1600 m, consists of silica flooding in the intrusive and sericite development along both sulfide-bearing fractures and as partial replacement of plagioclase. The phyllic zone at San Juan is erratic and overlaps

the potassic, argillic, and propylitic zones. Its distribution is primarily related to mineralized fractures.

5. Albitization. Robinson and Cook (1966) determined that prior to the development of sericite, the andesine plagioclase in the andesite was altered to oligoclase or albite. Similar sodic metasomatism also occurs in the intrusives. This is another example of sodium replacement of calcium in plagioclase (albitization) associated with potassic to phyllic alteration zones in the porphyry environment such as reported by Anderson et al. (1955) at Bagdad, Arizona.

6. Chloritic zone. A zone of more intense chlorite development is closely associated with the sericitic and biotitic zones in the Safford District. It appears that these higher chlorite areas correspond to portions of the phyllic and argillic zones. According to Robinson and Cook (1966, p. 260), "Chlorite is the most widely distributed alteration mineral and occurs in all stages of alteration."

In the chloritic zone, chlorite is the most abundant *alteration* mineral present. Chlorite is present in much smaller amounts in the propylitic zone.

A 300- to 600-m-wide chlorite alteration zone occurs near the Kennecott ore body (Robinson and Cook, 1966). This chlorite zone overlaps the biotite and sericite zones to the southwest of the Kennecott ore body.

Blake (1971) does not specifically define a chloritic zone at the San Juan Mine. However, Robinson and Cook (1966) do recognize a stronger zone of chlorite development peripheral to the biotite zone in this area.

7. Argillic zone. Argillic alteration is not pervasively developed at the San Juan or Kennecott ore bodies. Argillic alteration of probable supergene origin occurs in the monzonite stock at the Sanchez porphyry deposit.

Kaolinite and illite are associated with fractures in the San Juan stock (Blake, 1971). Kaolinite accompanies sericite along fractures in the andesites near the ore bodies (Blake, 1971; Robinson and Cook, 1966). Montmorillonite develops in the andesites at the outer edges of the argillically altered zones. Alunite is associated with the argillic alteration in the Kennecott deposit, which suggests a possible supergene origin for the argillic alteration (Robinson and Cook, 1966).

The argillic zone is erratic and overlaps the phyllic and part of the propylitic zones. A portion of the chloritic zone may equate with the environment that usually develops hypogene argillic alteration.

Supergene argillic alteration occurs with the leached capping in the intrusive rocks at the Kennecott deposit (Robinson and Cook, 1966). Supergene alteration may reasonably be expected to occur in similar environments at the Lone Star and Dos Pobres deposits.

8. Propylitic zone. Propylitic alteration is widespread in the Safford District. A portion of the pervasive zone of epidote, chlorite, and calcite development within the older andesites may be of deuteric origin.

The propylitic alteration of the Cretaceous (?) older andesites is characterized by the development of epidote, chlorite, and calcite (Robinson and Cook, 1966). Epidote, replacing hornblende and plagioclase, is the main diagnostic mineral. Much of this epidote may be deuteric or autometamorphic in origin. Chlorite is generally confined to the groundmass of the andesite. Small grains of secondary quartz are associated with sites of former plagioclase phenocrysts. Incipient, minor sericite may be developed along cleavage in hornblende and plagioclase phenocrysts (Blake, 1971).

9. Pyritic halo. The pyritic halo which usually corresponds to the phyllic alteration zone in porphyry copper deposits is associated with biotitic and chloritic alteration zones in the Safford District. Pyrite is closely associated with the replacement of hornblende and primary biotite by chlorite or secondary biotite. Pyritization in the propylitic zone is generally confined to fractures and dikes (Blake, 1971). The pyritic halo about the San Juan stock measures 3000 by 2300 m (Blake, 1971). This zone contains 3 to 5 percent pyrite by volume. At the Kennecott ore body, the pyrite halo contains from 4 to 8 percent pyrite by volume. This pyritic halo is over 3100 m long and up to 3000 m wide.

C. Remote Sensing Data

1. Color photography. Natural color photography of the Safford test site area was interpreted with respect to the geologic features indicative of the porphyry copper systems. These images include very high quality color photographs from the Skylab S190B experiment and high quality aerial photographs taken by NASA as part of the test site overflights. In addition, previous workers in the area have reported the use of low-altitude color aerial photographs to document features of the porphyry copper systems (Readdy, 1978).

The exposures of leached cappings in the test site area are large enough for detection and mapping using 1:24,000 aerial photographs. However, on the Skylab photographs, the color anomalies associated with the oxidation and

leaching of the exposed sulfide mineral assemblage are very indistinct. The shift in color toward red related to hematitic limonite in small areas at the Dos Pobres deposit is discernible under high magnification on the 1:500,000 image. The brownish cast related to goethite coatings developed from breakdown of sulfides is not readily observable. This is probably overwhelmed by the goethite on normal weathering surfaces in the andesite. The largest of the breccia pipes in the San Juan Mine area can be detected as a small anomalous dark-brown equidimensional feature on the Skylab photographs. This feature would not be sufficient to target this as an area of exploration interest.

The changes in coloration that are discernible on the conventional (1:24,000) color aerial photographs (Figure 6-18) do provide useful exploration guides to the porphyry systems in this test site (Figure 6-19). The reddish colors related to hematitic limonite at the Dos Pobres deposit were clearly evident (dotted outline on Figure 6-19). A drainage map interpretation (Figure 6-20) was also produced from the aerial photograph of the Dos Pobres area. A finer textured pattern was observed over the buried ore deposit. This may be caused by a crackle zone in the intrusive or by fracturing and shattering of the intrusive affecting the surface drainage characteristics. These two observations (iron oxides at the surface and drainage anomaly) would focus exploration interest in the Dos Pobres area. Similarly the mixed goethite–jarosite–hematite cappings associated with the Kennecott and San Juan deposits were discernible on other photographs. The capping at the Sanchez deposit is only weakly observable on conventional color aerial photographs.

The Skylab S190B photographs are of excellent quality, and a considerable amount of information can be interpreted from these images (Figure 6-21). Examples of features that can be interpreted include approximate bedrock–alluvial contacts, major lithologic boundaries, linear features related to fracture systems, and circular features, some of which are attributable to the intrusive centers, others of which may represent calderas, etc. An interpretation showing the major structural features of the Skylab photography is presented as Figure 6-22.

The dikes associated with the Dos Pobres and Kennecott ore bodies are not discernible as dikes on the Skylab photographs. Although structural directions are clearly defined on these color photographs, the dikes themselves are not identifiable. Many of the dikes are also not identifiable on the 1:24,000 conventional photographs. Initially, this is surprising because many of the porphyritic dikes are clearly large enough to be identified, and the color contrast between the dike rock and the porphyritic andesite should be substantial. However, the surface rind of many of the dikes is similar in color to that of the weathered surface of the andesite. Some of the larger dikes with the greatest development of sericite and argillic minerals, however, are readily identifiable on the standard color aerial photographs.

The color photography, both aerial and Skylab, was extremely useful in support of the interpretation of the scanner images. The color photographs provide a comfortable reference base for identification of individual features. The color photographs also do not suffer from the geometrical distortions characteristic of the scanner data and can therefore be used to identify the proper location of features discriminated on the scanner data.

One of the advantages of the Skylab color photographs is that stereo coverage is available. Stereo is a very useful adjunct for image interpretation. The ability to provide stereo coverage from remote sensing instruments on satellites would be valuable for future resource studies.

2. Radar data

a. Introduction. Microwave remote sensing is a relatively new field, initially developed during World War II. There are two different areas of sensor utilization, active and passive. The active systems have been employed to generate radar images for a variety of geoscience studies. Radar has several advantages and differences compared to conventional camera systems. The major advantage is radar's ability to penetrate clouds, smoke, and fog; in addition, because the system is an active one providing its own illumination, data can be obtained at virtually any time from any direction. The major difference lies in those physical parameters and characteristics which affect the radar backscatter and, hence, control the appearance of the image terrain. The signal strength returned to the radar antenna is a function of the transmitted power, wavelength, polarization, and viewing geometry. Geometric and physical properties of the surface also strongly influence the radar return. Surface roughness is one factor that determines whether an area will appear bright or dark on a radar image. For root-mean-square surface roughness much less than one-tenth of the radar's wavelength, the surface will appear smooth and generally bright; for surface roughness approximately one wavelength, the surface will appear rough and dark because most of the transmitted energy will have been scattered and little will be returned to the radar receiver (MacDonald, 1980). The electrical properties of the surface (complex dielectric constant) will also affect the radar return. Significant increases in the dielectric constant usually result from changes in moisture content; an increase in moisture content increases the reflectivity and therefore the level of the signal return.

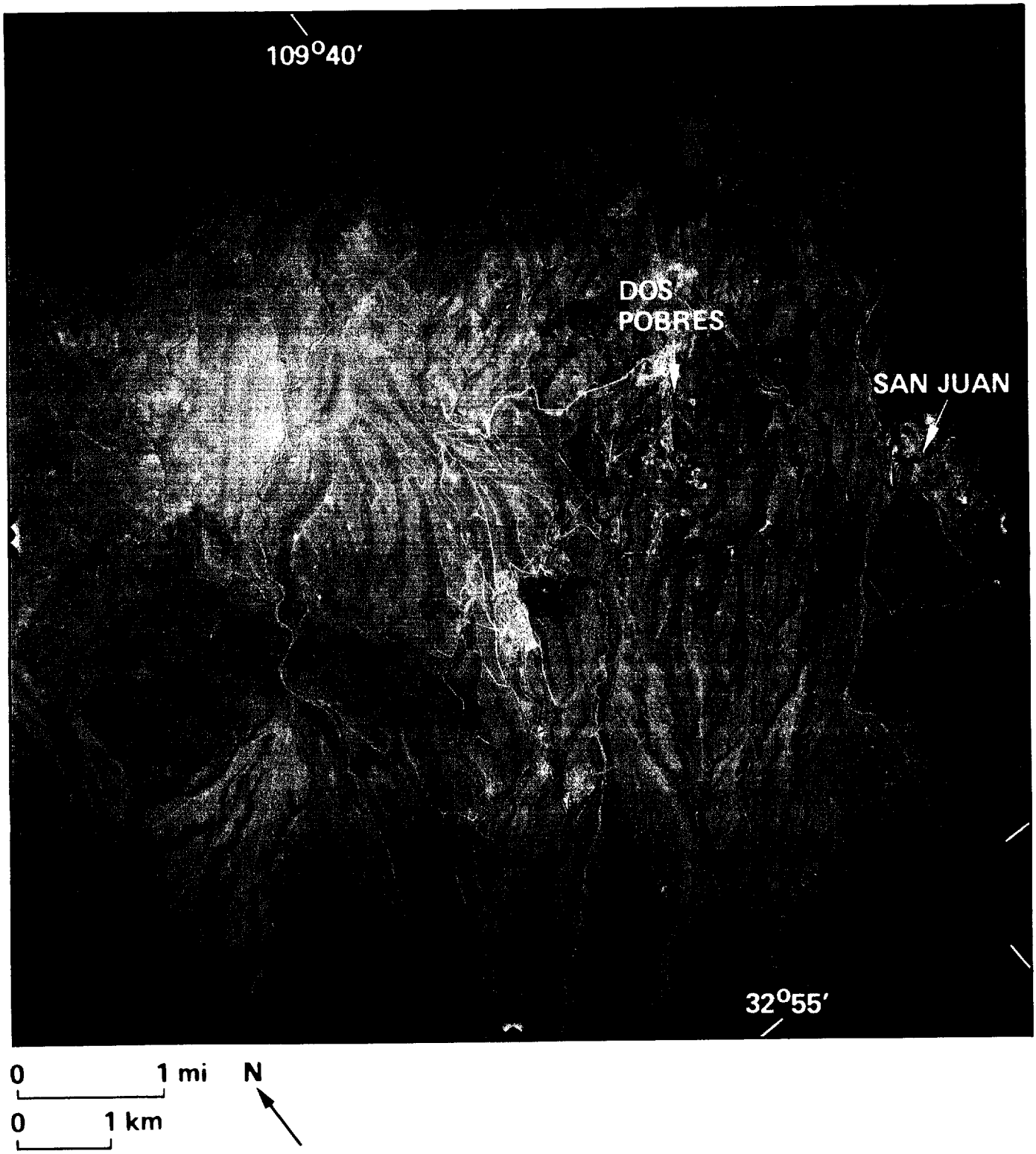

Figure 6-18. Color aerial photograph of area around the Dos Pobres deposit. Photograph was acquired August 1977 simultaneously with M^2S data overflight.

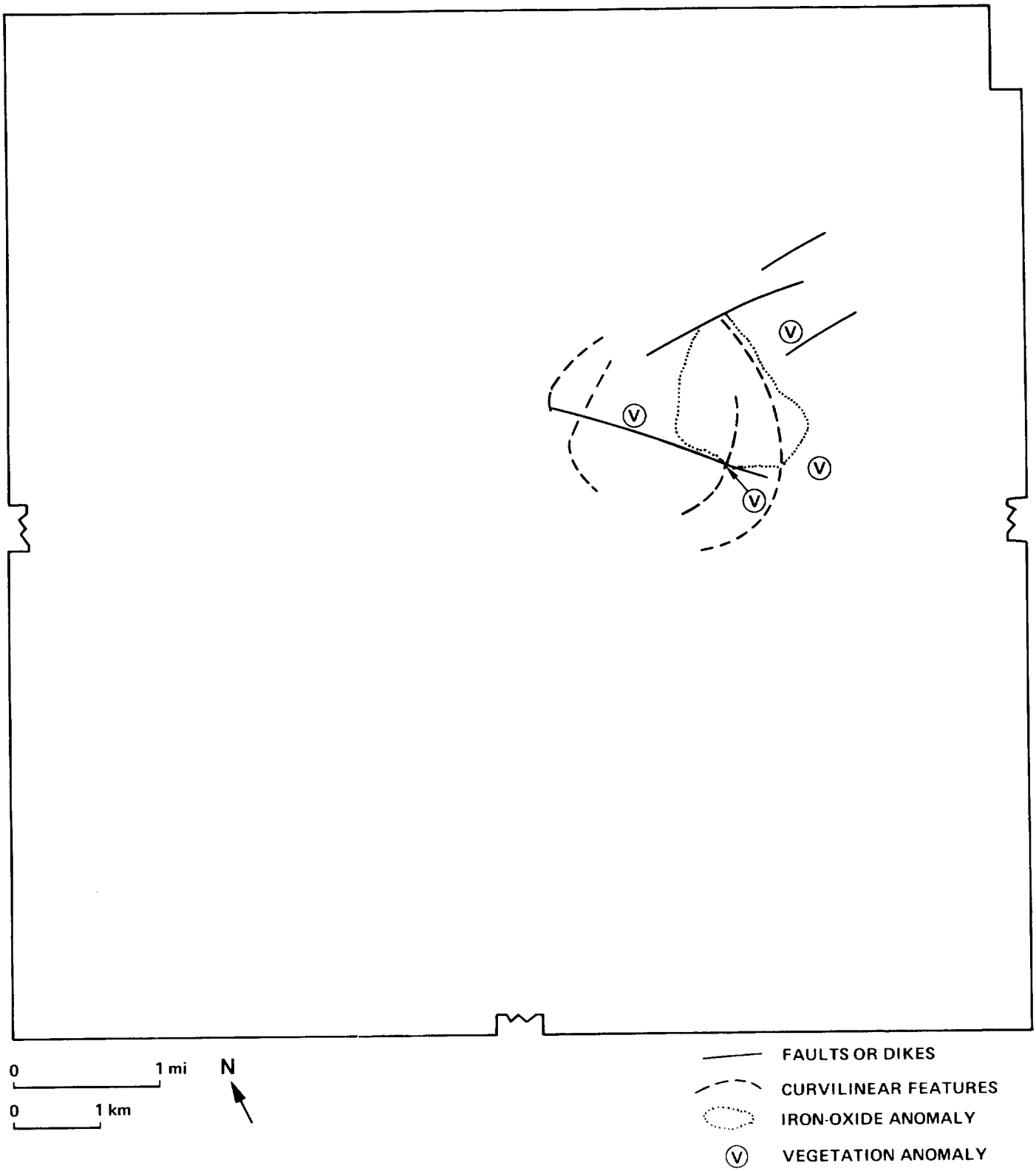

Figure 6-19. Interpretation map of color aerial photograph (Figure 6-18) showing iron-oxide anomaly and curvilinear features associated with the buried Dos Pobres deposit

Two different synthetic aperture radar data sets were examined for Safford: aircraft X-band data, in like- and cross-polarized returns, and satellite L-band radar data acquired by Seasat. The X-band data were at 3-cm wavelength, and the L-band data were at 25 cm.

b. Seasat satellite L-band data. The Seasat orbital radar satellite operated for 3 months in 1978, acquiring 100-km swath-width images over 100 million km^2 of the land and sea surface of the Earth. The system was an active L-band radar, with a depression angle of 70°. Because of this viewing geometry, extreme foreshortening resulted whenever a foreslope as seen by the radar exceeded about 20° (Ford et al., 1980). The scene covering the Safford area was digitally processed at JPL and covers about 100 by 100 km.

The Safford test site is in the upper right part of Figure 6-23. The image suffers from the effects of layover distortion of the mountain peaks. Because of this layover effect, many of the faults and fracture systems do not show up as linear elements but as alignments of topographic saddles which, on the image, appear to be notches. In other cases, fault zones show up as linear disruptions of smaller topographic ridges and as linear textural boundaries. The overall visual result from the radar shadow enhancement of the topography and the bright radar return from the westerly facing slopes is upsetting to the average viewer. However, for those familiar with interpretation of radar imagery, particularly from the early systems, many structural features become immediately apparent. In general, however, the structural detail available and the ease with which this information can be interpreted favors the use of Skylab photography, Landsat images, and airborne radar systems.

On the Seasat image studied as part of this test site evaluation, features that apply to porphyry copper exploration in the district can be identified. These features are all structural and/or physiographic in nature. Rough interpretation of the small portion of the Seasat image that covers the Safford test site (Figure 6-24) is shown in Figure 6-25. Shown are the NE, NW, nearly N–S, and E–W fracture patterns.

Also shown are circular features characterized by a change in topography that contain the Dos Pobres and Kennecott deposits. In addition, there are several circular features in the younger volcanics which have previously been identified from interpretation of Landsat MSS and other images by Readdy (1978). Circular features are frequently found at and near porphyry copper systems. Certainly not all such features are related to porphyry systems. However, features such as intrusives, crackle zones, alteration patterns, calderas, and breccia pipes frequently have at least some degree of circular pattern development (Readdy, 1978).

c. Aircraft X-band data. A side-looking airborne radar (SLAR) image using the NASA-operated X-band radar system was also collected over the test site. This radar image is shown in Figure 6-26. An interpretation of this image is presented as Figure 6-27. The same general pattern of fracturing detectable on the Skylab photography and Seasat image is noted. More detailed structural information can be interpreted from this image than from the Seasat scene. This results from several factors, the first and most obvious of which is the difference in scale of the images interpreted. Second, the airborne radar scene had more optimal illumination with respect to incidence angle; the airborne image (Figure 6-26) does not suffer from extreme topographic distortion (layover) of the ridges and peaks. A previously published interpretation of the area using the Goodyear/Aero Service X-Band Synthetic Aperture Radar (SAR) system (Readdy, 1978) developed a very similar interpretation to that developed from this aircraft SLAR system.

The steep incidence angle built into the Seasat system is optimal for the study of relatively flat features such as sea state and sea ice. However, this steep angle reduces the usefulness of Seasat data for mountainous areas. In mountainous areas the excessive layover, or geometric distortion of the higher topographic features toward the imaging system, detracts from the general use of the image for interpretation in support of mineral exploration. In fact, without the use of some geometrically accurate image such as Skylab photography or a Landsat scene, even a very experienced image interpreter may not be able to interpret the Seasat image. One method of reducing the amount of this disorientation is to view the Seasat scene from a direction facing into the direction of radar illumination from the satellite.

Changing to a lower incidence angle for future satellite radar systems would reduce the layover problem, but this would introduce larger areas of deep radar shadowing. If future systems could be designed to have both variable look-direction and variable incidence angle, this would introduce the flexibility needed to partially offset both problems. The proposed multiple look-direction would allow the collection of coverage which accentuates different tectonic directions and would also fill in data obscured by radar shadow on images collected on different passes.

The present Seasat data are useful but are not as interpretable for this test site as the other imaging systems. This is primarily a result of the more mountainous character of the test site terrain.

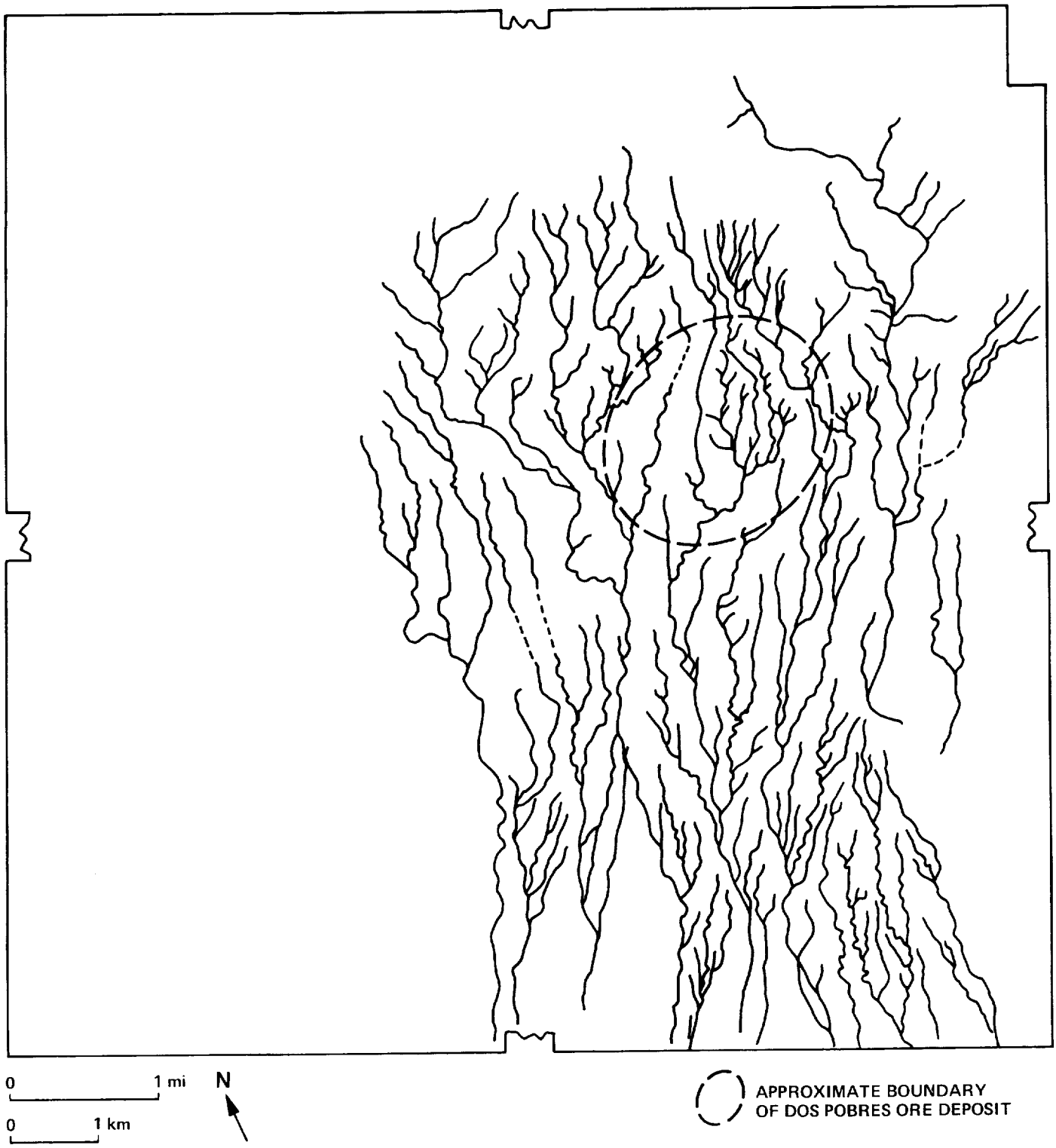

Figure 6-20. Drainage map of area around the Dos Pobres deposit showing fine-textured pattern over the deposit. Interpretation was made from color aerial photograph (Figure 6-18).

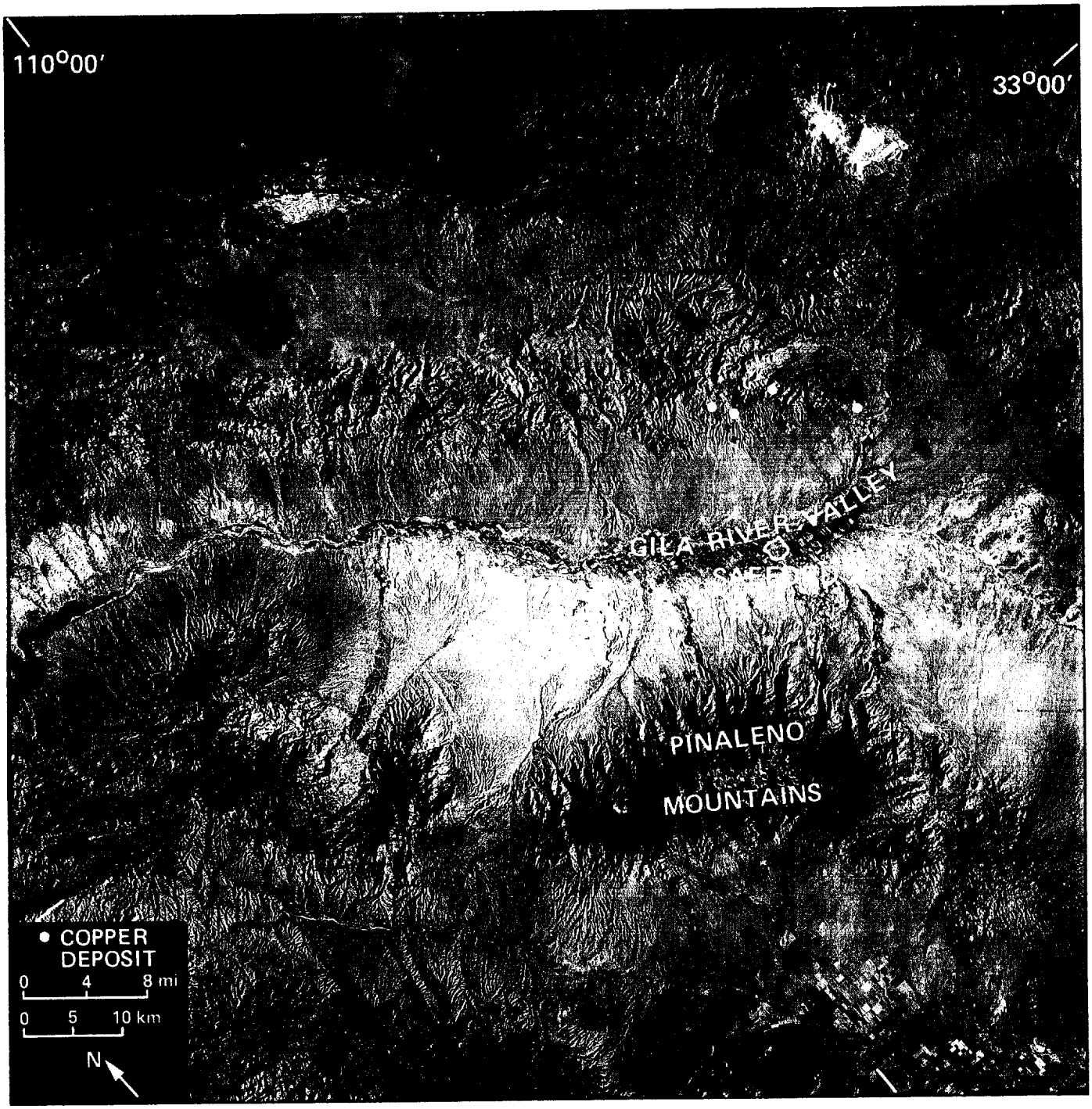

Figure 6-21. Color photograph from Skylab 4 S190B experiment, acquired February 1974. White dots represent the four copper deposits in the Safford District.

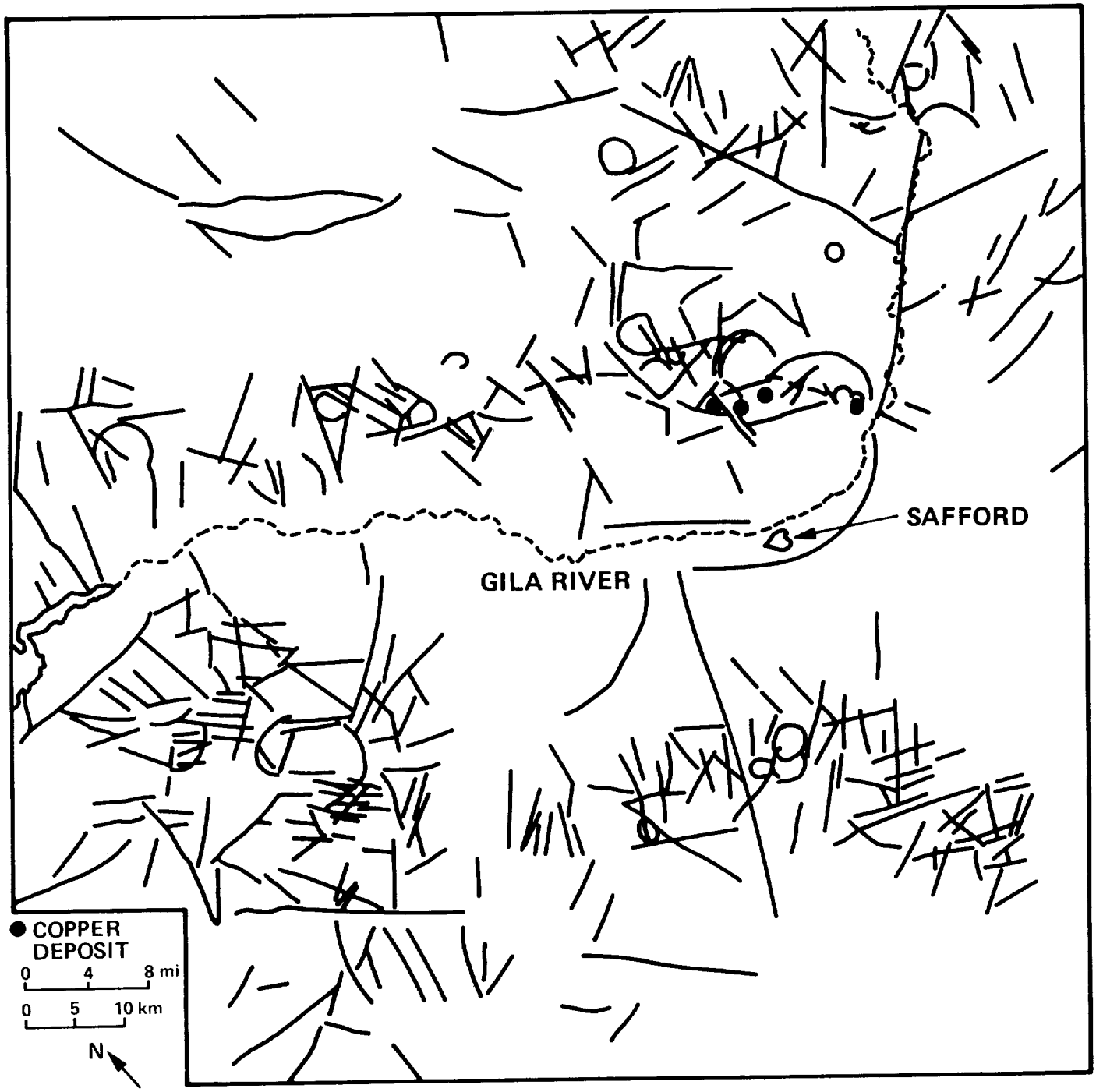

Figure 6-22. Interpretation map of lineaments and curvilinear features mapped from Skylab S190B color photograph (Figure 6-21)

C-4

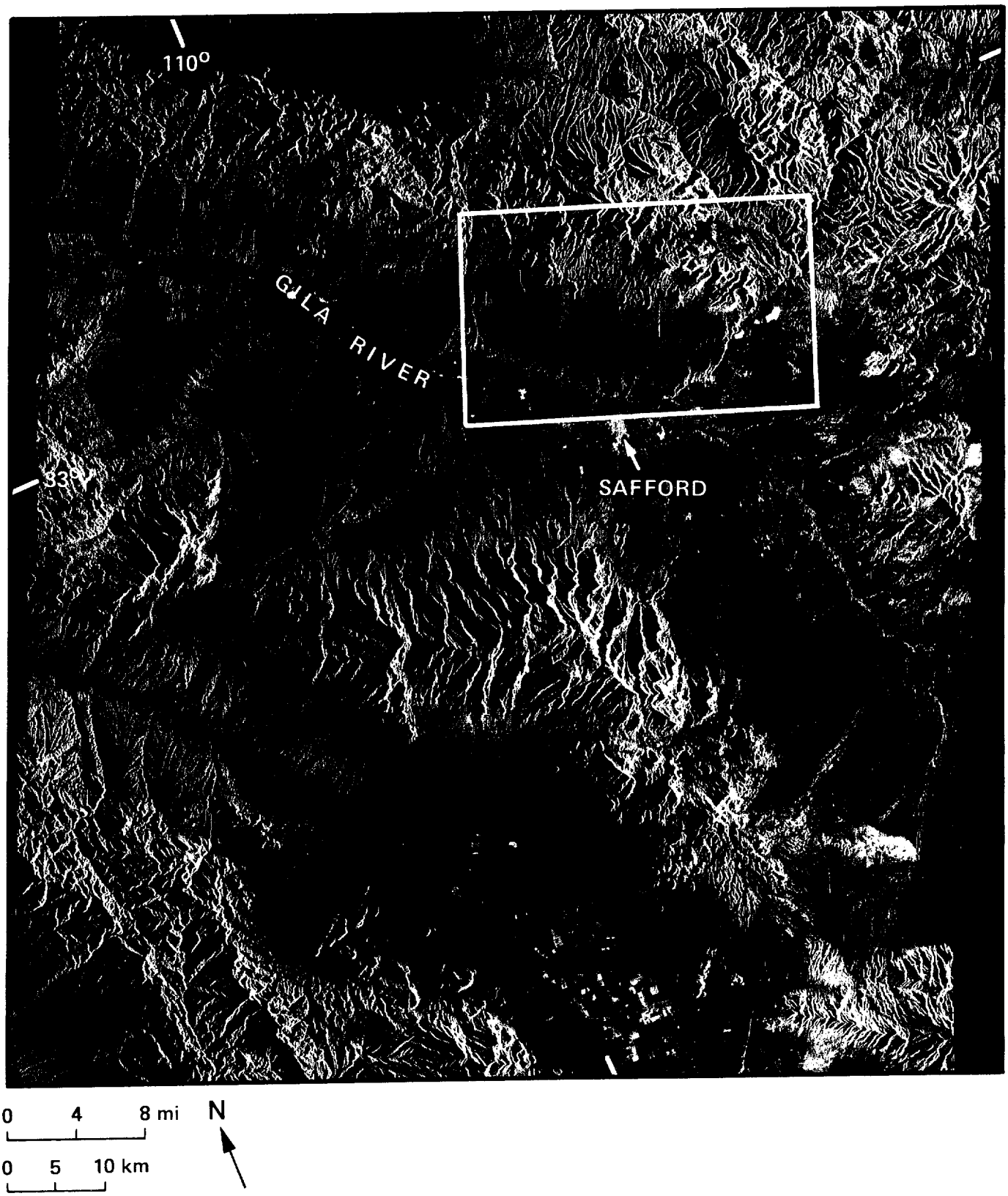

Figure 6-23. Seasat L-band radar image of Safford area, acquired October 5, 1978. Outline of enlarged area (Figure 6-24) and X-band aircraft radar image (Figure 6-26) is shown. Radar illumination is from the east.

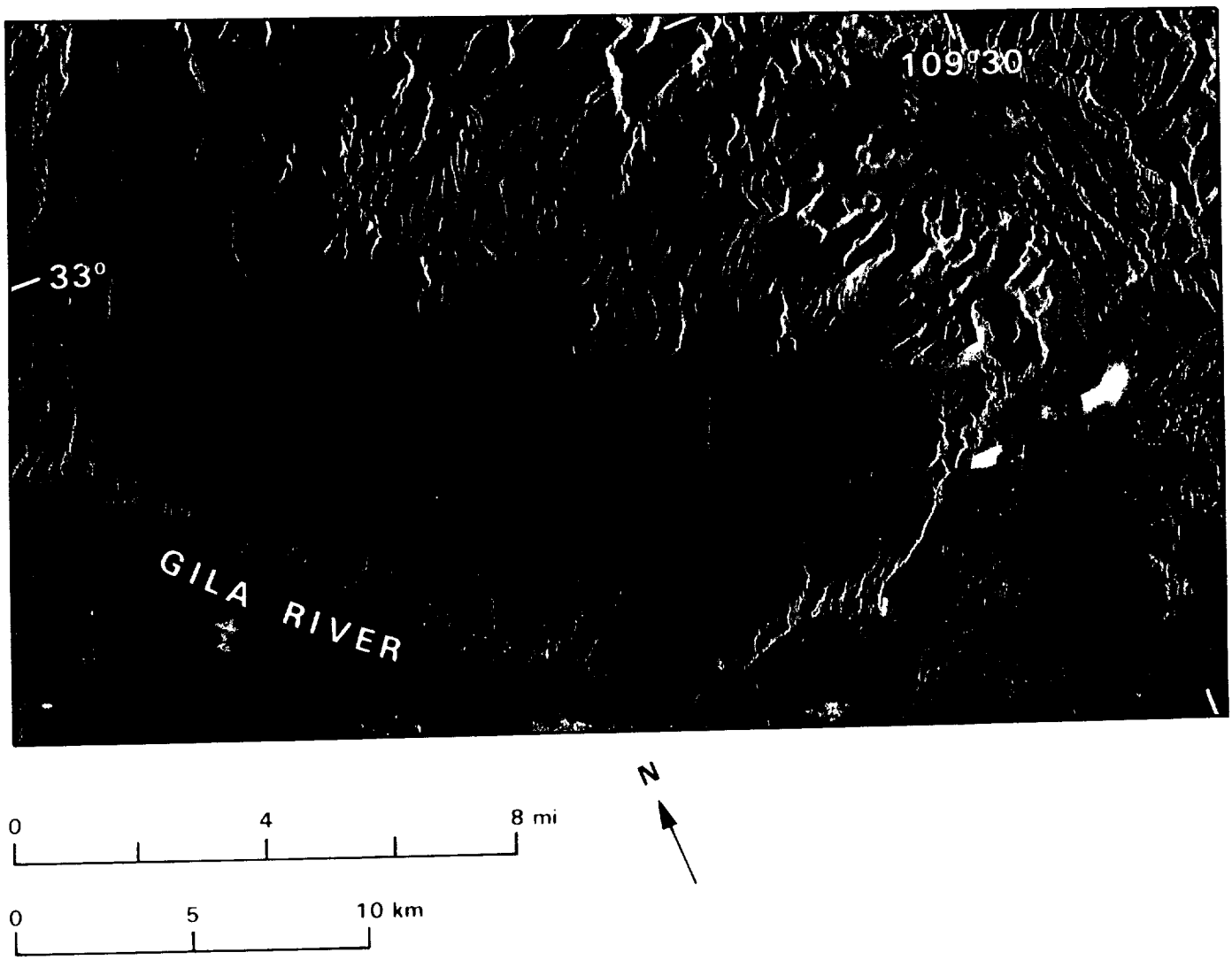

Figure 6-24. Enlarged Seasat L-band radar image of Safford District

3. Landsat MSS data. Digital tapes of three Landsat MSS scenes (acquired December 10, 1973; October 11, 1976; March 31, 1977) were processed by three different image enhancement algorithms: contrast enhanced, false-color infrared (CIR) composites; band ratioing; and principal components analysis (PCA). For each date, the full Landsat scene was processed using the three algorithms; in addition, 50- by 50-km subareas were extracted from the data over the area of the Safford test site. The nine resulting images were individually analyzed; the three most satisfactory are discussed here.

a. False-color infrared composite. The October Landsat scene produced the best image of this type (Figure 6-28). The data were processed using a color enhancement technique that rotates the data values in three spectral bands (4, 5, and 7) onto three new uncorrelated axes. Digital values in each axis are stretched and then retro-rotated to the original coordinate system (Soha and Schwartz, 1978). The effect of this process is to greatly exaggerate scene contrast, but at the same time preserve the original hues present in the scene.

Enhanced digital values for bands 4, 5, and 7 can subsequently be displayed as blue, green, and red, respectively, to form a CIR composite. Lithologic differences within the younger volcanic rocks that cap the district can be mapped from enlargements of this image. Yellow tones mark the high ferric-iron content of the weathered pyritic outcrop of Mesozoic latites and tuff associated with the Kennecott deposit (Figure 6-29). The high red and near-infrared reflectances (bands 5 and 7) and low green reflectance (band

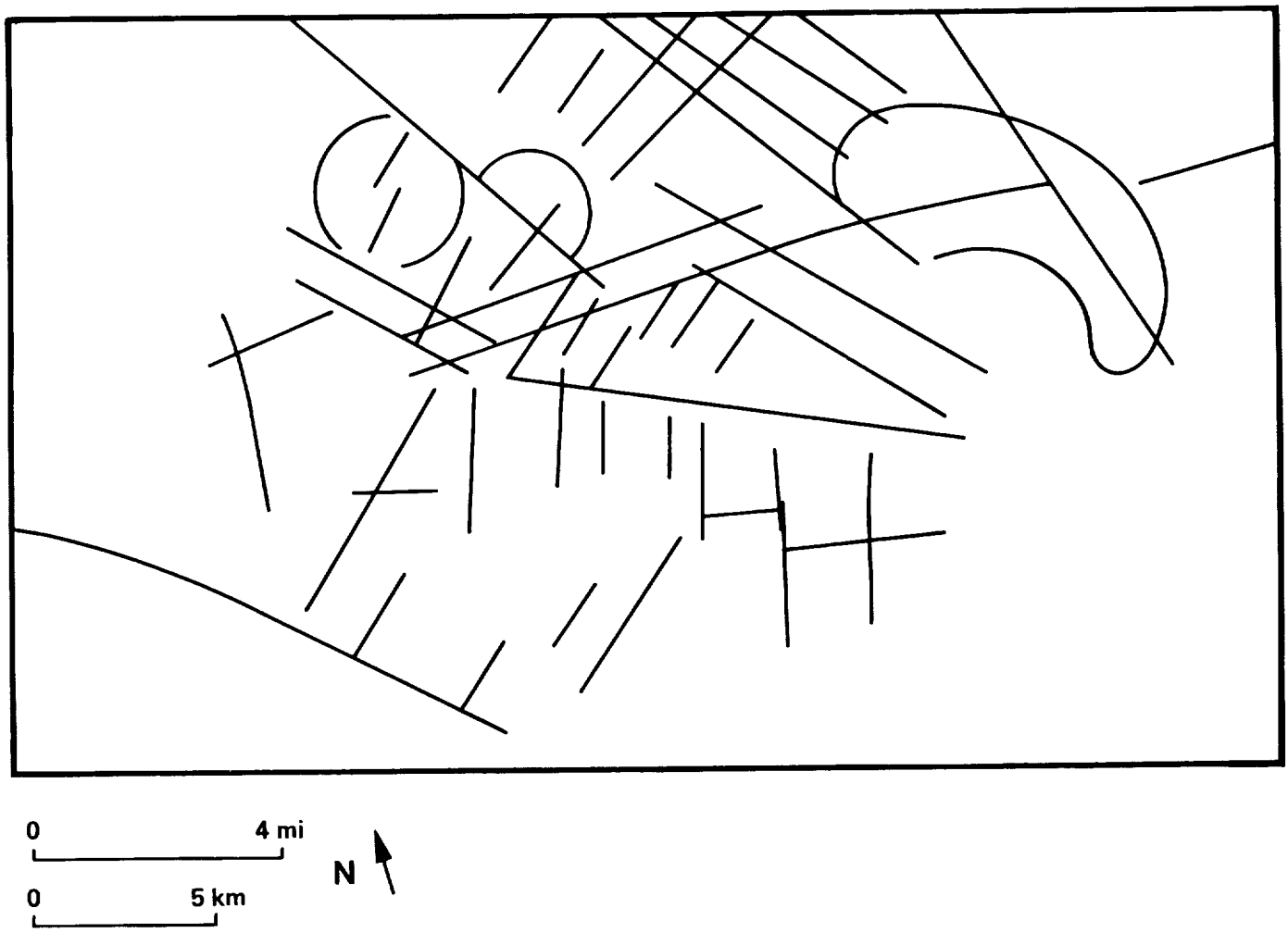

Figure 6-25. Interpretation of linear and curvilinear features detectable on enlarged Seasat image (Figure 6-24)

4) of iron oxide would explain the yellow color on the image. As is usual with this type of product, green vegetation is displayed in red color; dumps, pits, and some rocks and soils are blue; water is black.

b. Color ratio composite. Band ratioing of Landsat MSS data for geological applications was first reported by Rowan et al. (1974). Ratioing is an effective method for distinguishing among rock types because the main spectral differences in the visible and near-infrared spectral regions are found in the slopes of the reflectivity curves. Absorption bands are broad and weak and are difficult to use for discrimination of rock types on standard MSS images. In addition, the ratioing process removes first-order brightness effects due to topographic slope and enhances subtle reflectance variations between materials. By examining spectral reflectance data, Rowan and others determined that a composite of MSS band-ratios 4/5, 5/6, and 6/7 would provide an effective means for discrimination of hydrothermally altered areas and of regional rock and soil units.

This combination was used to produce the color ratio composite (CRC) image presented in Figure 6-30. Band-ratios 4/5, 5/6, and 6/7 were assigned colors of blue, green, and red, respectively, to produce a CRC image. The October 1976 Landsat scene was used because it had the highest sun elevation and, therefore, the fewest shadows of the three scenes available. The image shown is a subscene covering an area 50 by 50 km centered near Safford.

The particular combination of band ratios and color assignments used displays vegetation in blue and iron oxides in red and orange. A typical spectrum of vegetation and iron oxides is shown in Figure 6-31. The Landsat MSS bandpasses are also indicated. Ratio values for 4/5, 5/6, and 6/7 are shown in Table 6-10.

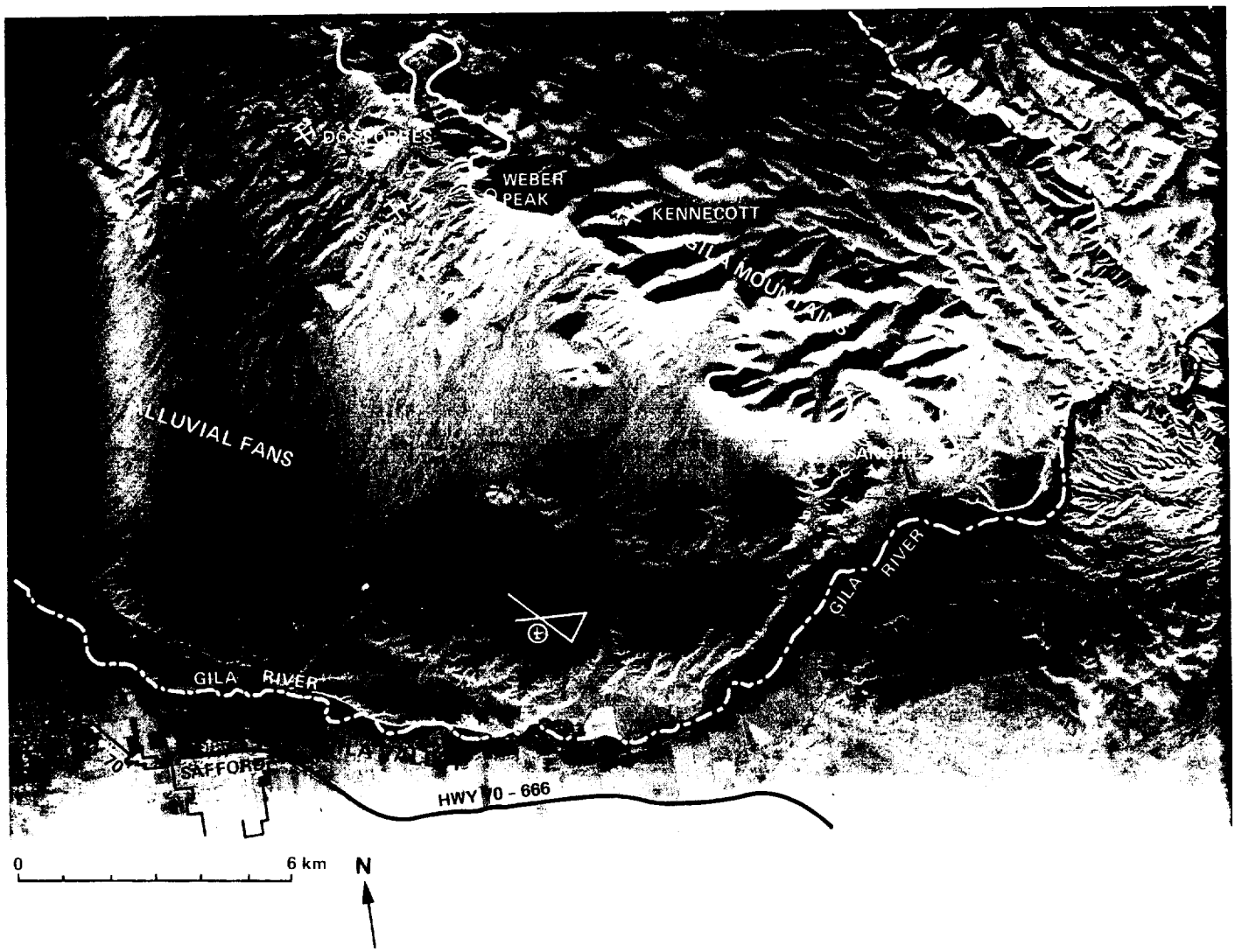

Figure 6-26. Aircraft X-band radar image (cross-polarized horizontal-vertical) of Safford area. Illumination direction from the south.

Vegetation has a relatively high 4/5 value due to high reflectance in the green part of the spectrum (band 4) and low reflectance in the red (band 5) due to absorption of energy by chlorophyll. The infrared response in bands 6 and 7 produces a ratio less than 1. The 5/6 value is low due to the chlorophyll band also. Iron oxide has a low 4/5 value due to the sharp falloff in reflectance toward the ultraviolet, and a ratio greater than 1 in the 6/7 value due to the Fe^{3+} absorption band near 0.9 μm. It will have a strong red component (high 6/7 value), no blue component (low 4/5), and a green component (high 5/6). These areas will appear orange to red depending on the relative amount of green.

The red-orange color on the image (dashed outline on Figure 6-30) at the location of pervasive quartz-sericite alteration within the pyrite halo over the Kennecott ore body is due to the presence of iron oxides developed from oxidation of pyrite and mafic minerals. Other red areas can be seen on the image, primarily in the alluvial fans south of the mountains. Iron oxides there result from the weathering of surface materials and presence of debris from altered outcrops upstream. In general, the CRC is inferior to the CIR composite for several reasons: (1) remote detection of the large alteration halo at the Kennecott ore body is about the same, (2) topographic information present in the color infrared composite is lost on the ratio image, and (3) the small amount of lithologic discrimination on the color infrared image is not well shown on the ratio image.

c. Principal components analysis. Principal components analysis has been used in statistical processing of data for a considerable time and is well illustrated in many texts (Davis, 1973, for example). The method produces new variables

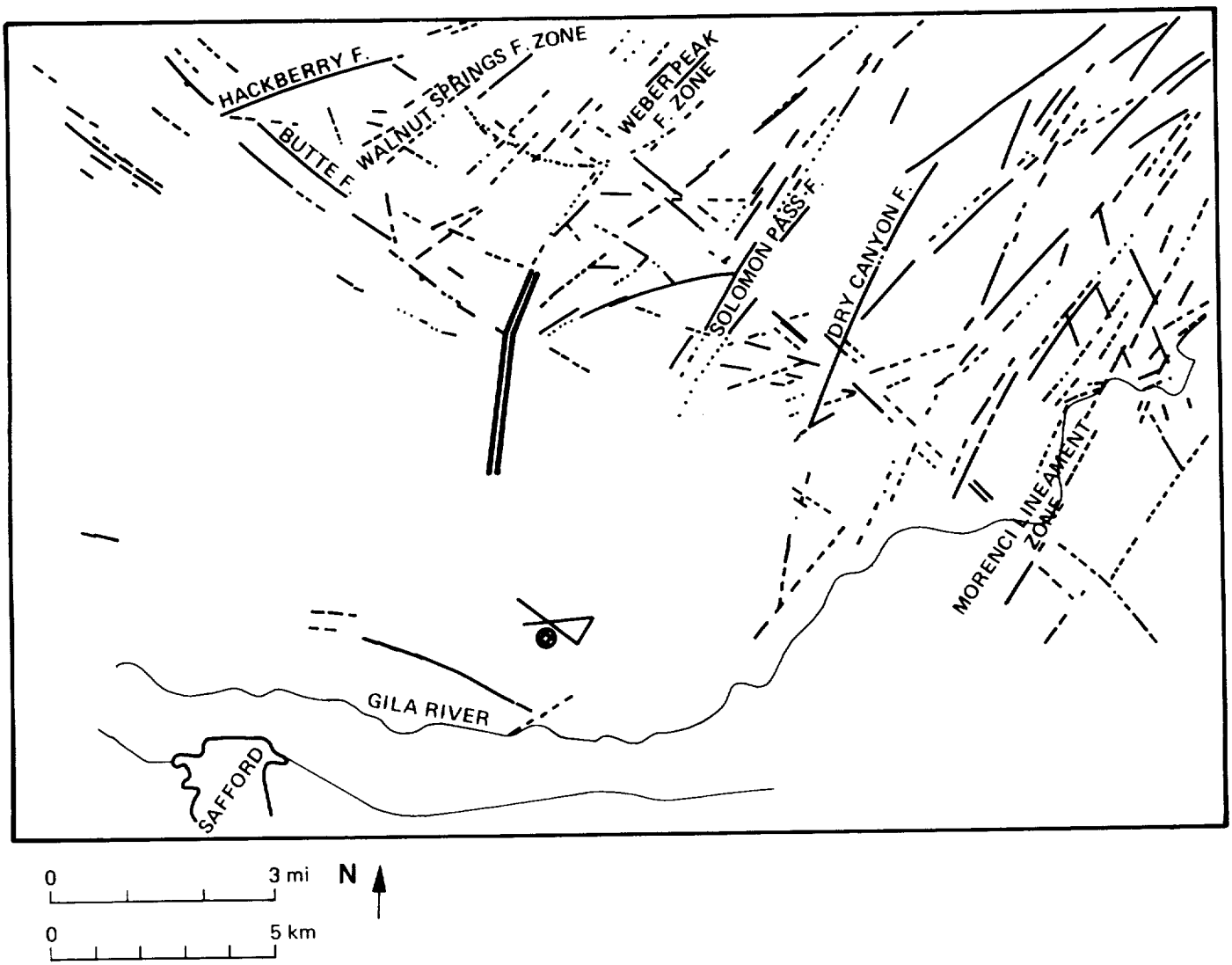

Figure 6-27. Interpretation map produced from aircraft X-band radar image of Safford area (Figure 6-26). Heavy double line is a road; solid lines represent more prominent lineaments than dashed lines.

(components) which are linear combinations of the original variables and are orthogonal to each other. The axes for the new variables are computed to maximize the variance in the transformed data set along the first axis. The second variable axis has the next highest level of variance and is orthogonal to the first. Succeeding axes are determined in similar fashion. Geometrically, a PCA can be viewed as a rotation and translation of the original coordinate axes to new axes passing through the data.

PCA is a method for reducing the dimensionality of data by removing intervariable correlation and compressing it onto one or a few new axes, usually less than the total original data. In Landsat MSS data, about 95 percent of the scene variability can be accounted for by the first principal component (PC). This variable is usually an average of the four bands, i.e., albedo (Podwysocki et al., 1977). The components can be combined into a color display by assigning blue, green, and red colors to any triplet of the available variables.

The March data were used to produce the composite of a 50- by 50-km subarea centered near Safford. The first three components were displayed as blue, green, and red, respectively (Figure 6-32). Tonal contrasts on the image help to delineate structural zones not visible on the ratio image. Lithologic discrimination within the younger volcanics is shown as well as on the infrared composite. However, the boundary between the younger volcanics and the Mesozoic volcanics is not well shown on this image. The phyllic alteration halo over the Kennecott ore body is better shown than on the other Landsat MSS images.

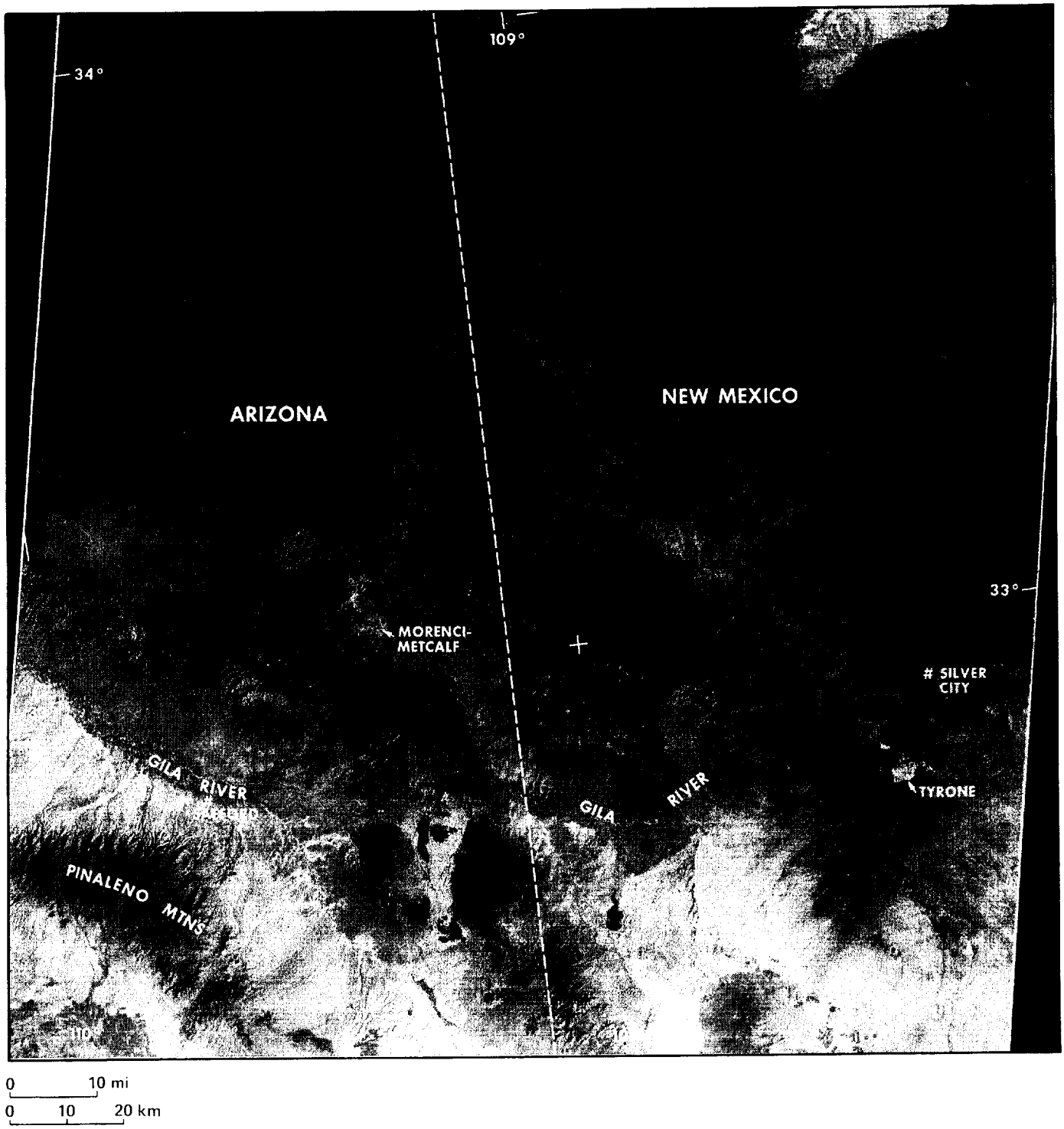

Figure 6-28. Full-frame Landsat scene of Safford area. Bands 4, 5, and 7 are displayed as blue, green, and red, respectively (Landsat scene no. 11541–16265, acquired October 11, 1976). Morenci–Metcalf and Tyrone are two large open-pit copper mines.

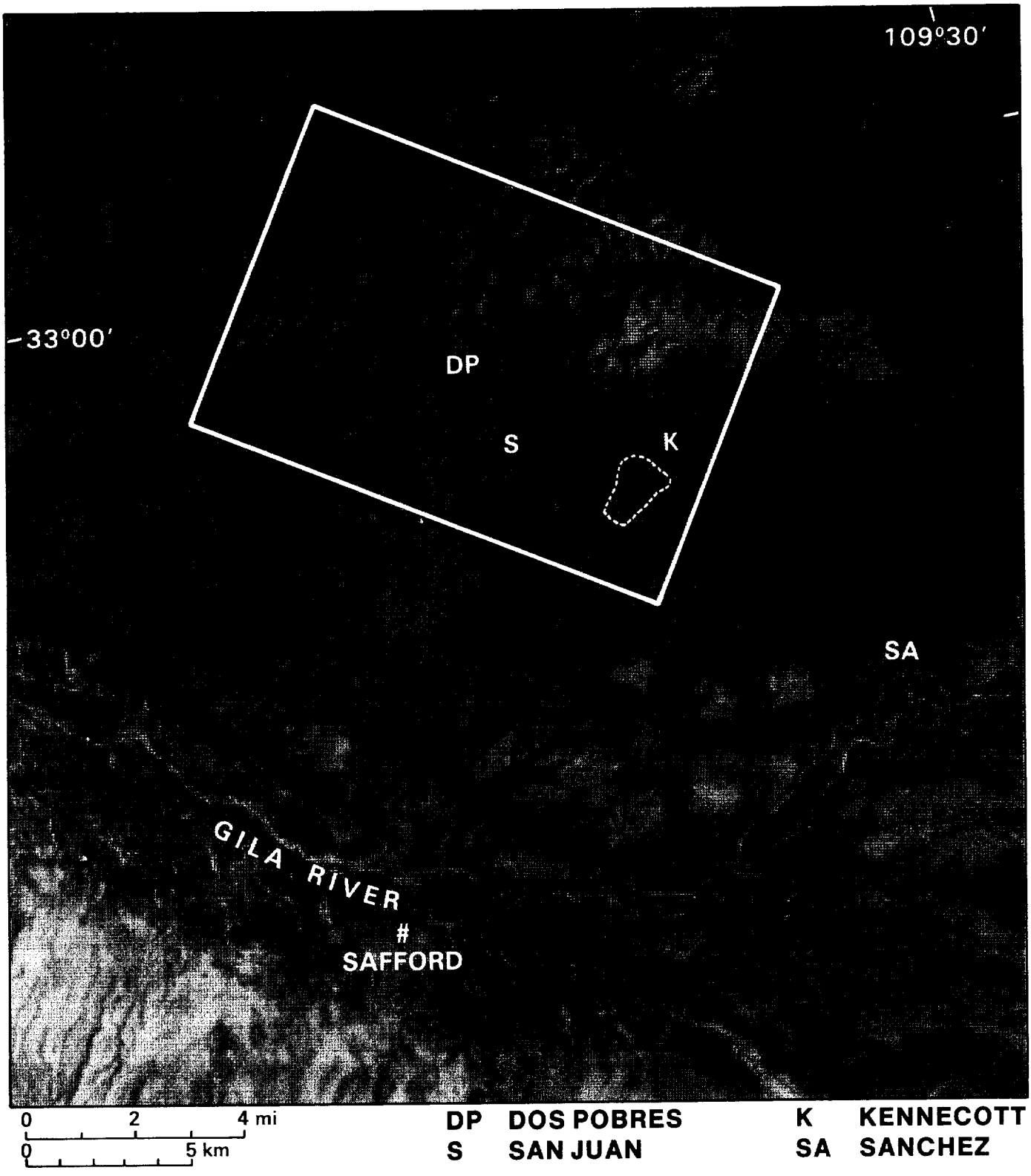

Figure 6-29. Enlargement of Landsat CIR composite (Figure 6-28) covering a 32- by 34-km area. Outline shows area of M^2S images (Figures 6-35 and 6-36). Dashed outline encloses iron-oxide-stained altered rocks associated with Kennecott deposit.

Figure 6-30. CRC of Landsat data covering a 50- by 50-km area around Safford. Band-ratios 4/5, 5/6, and 6/7 are displayed as blue, green, and red, respectively (Landsat scene no. 11541–16265, acquired October 11, 1976).

d. Summary of evaluation of Landsat MSS images. The combined use of the three images—principal components, color ratio composite, and color infrared composite—produced the most geologic information (Figure 6-33). The CIR image provided good geomorphic information, some lithologic information, and some alteration patterns. The PC image showed the sharpest delineation of the alteration halo fringing the Kennecott ore body, some lithologic patterns, and some structural information.

It is important to note that *none* of the images showed the altered outcrops of the Dos Pobres deposit. This probably is due to the 80-m resolution of the MSS. The Dos Pobres alteration zones are approximately one pixel in size, whereas the zone of pervasive phyllic alteration at Kennecott is closer to 100 pixels in size.

4. M²S 11-channel data

a. Introduction. The analysis of the M²S images is discussed next because the spectral range of the five bands chosen for image generation falls within the spectral range of the Landsat MSS bands described in the previous paragraph. The M²S bands and their center wavelengths are listed in Table 6-11.

One of the main advantages of the M²S data over Landsat MSS data is the narrowness of the spectral bands. This characteristic was used to separate altered rocks at Safford.

b. Iron-oxide discrimination. The different species of iron-oxide minerals, specifically hematite (Fe_2O_3), goethite ($FeO \cdot OH$), and jarosite ($KFe_3(OH)_6(SO_4)_2$), do not have the same spectral reflectance characteristics, nor are they necessarily derived from the same sources. Hematite often results from oxidation of pyrite and chalcopyrite at porphyry copper deposits and is a prominent constituent of gossans. Goethite is more widely distributed, but can be an alteration product. Jarosite is a ferric sulfate mineral which is almost always associated with hydrothermal alteration processes. The M²S possesses relatively narrow spectral bands which might allow separation of these minerals. Representative reflectance curves for hematite, goethite, and jarosite (Hunt and Ashley, 1979) are shown in Figure 6-34, along with the M²S band intervals. The curves are displaced vertically for clarity.

Table 6-10. Percent reflectance and ratio values for vegetation and iron oxide in Landsat MSS bands

Material	MSS Band, %				Ratio		
	4	5	6	7	4/5	5/6	6/7
Vegetation	12	10	33	41	1.2	0.3	0.8
Iron oxide	18	27	30	28	0.7	0.9	1.1

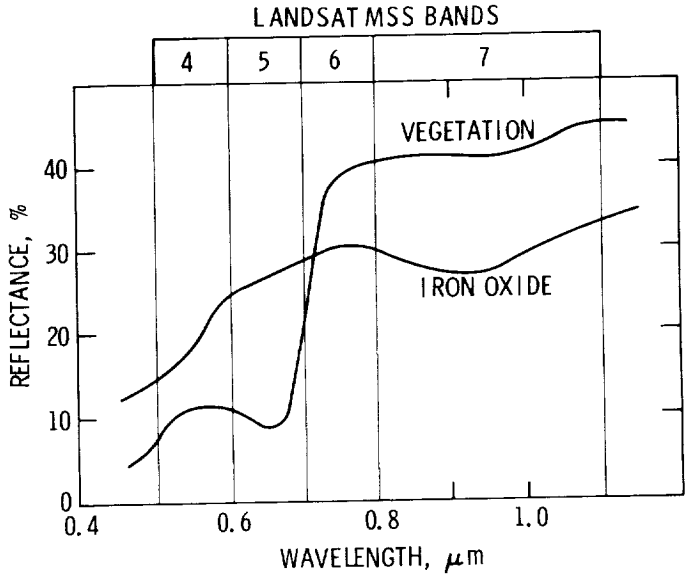

Figure 6-31. Typical spectral reflectance curves for vegetation and iron oxide. The Landsat MSS band intervals are also indicated.

The spectral absorption bands seen in all three curves are due to electronic transitions involving ferric iron. There are typically three broad features located near 0.45, 0.65, and 0.9 μm and a strong band in the ultraviolet, which produces the rapid falloff in reflectance to shorter wavelengths. Only jarosite shows the 0.45-μm band; the 0.65-μm band is apparent in all three minerals. But most significant is the position of the 0.9-μm band. In goethite and jarosite, this band is centered at about 0.93 μm; in hematite, the band is displaced toward the shorter wavelength at about 0.85 μm. Although the M²S bands are not ideally placed over these regions, the positions of bands 8, 9, and 10 should produce different reflectance values for the three minerals. By determining the reflectance values in these three bands, the equivalent 8/9 and 9/10 band-ratio values were calculated. These are plotted in the inset graph in Figure 6-34. The three minerals are clearly separable along the two axes. This analysis was applied to the M²S image data by construction of two ratio composites: one with band-ratios 4/6, 6/8, 8/9; the other using 4/6, 6/8, and 9/10. These two images were displayed using blue for 4/6, green for 6/8, and red for 8/9 or 9/10 (Figures 6-35 and 6-36).

c. Image analysis. The appearance of the phyllic and propylitic zones on the M²S ratio images can be predicted by referring to the spectral graphs of Figures 6-13 and 6-14. In Figure 6-13, note the spectral plots of the weathered surfaces of the argillic sample F_w and the phyllic sample D_w. These can be compared to the spectra of the weathered surfaces of the propylitic samples A_w and B_w in Figure 6-14 to note the qualitative differences in the band ratios. The

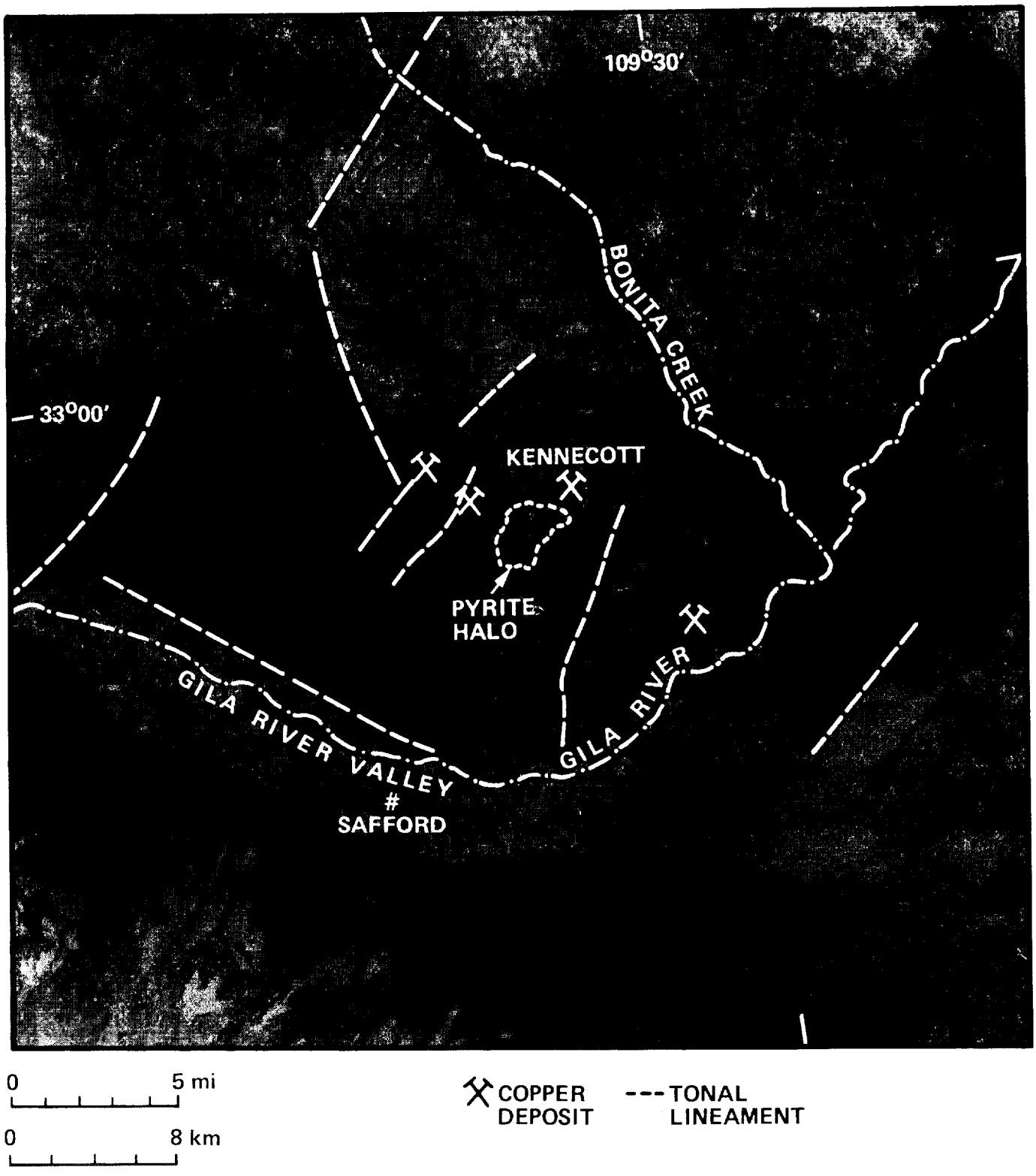

Figure 6-32. PC composite of Landsat data covering a 50- by 50-km area around Safford. Components 1, 2, and 3 are displayed as blue, green, and red respectively (Landsat scene no. 20799–16532, acquired March 31, 1977).

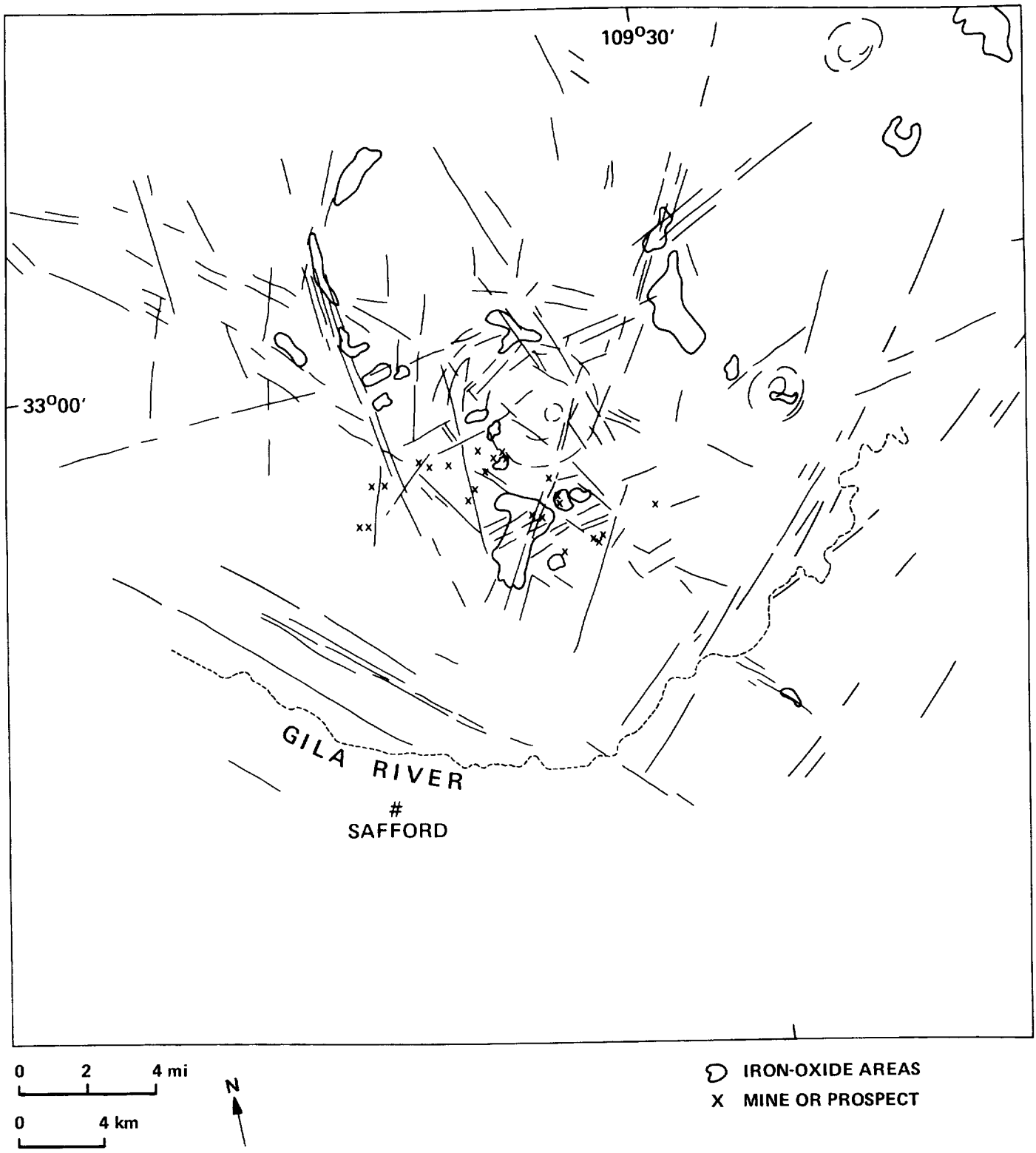

Figure 6-33. Structural and limonite interpretation based on three processed Landsat MSS scenes: principal components composite, color ratio composite, and color infrared composite

relative ratio values and the predicted colors on the ratio images are shown in Table 6-12.

Phyllically altered rocks have low 4/6 and 6/8 ratio values due to the general falloff in reflectance toward shorter wavelengths caused by the ultraviolet ferric-iron absorption band. The 8/9 ratio is high because of the contrast between the shoulder (band 8) and the trough (band 9) of the 0.9-μm ferric-iron absorption band. Similarly, the 9/10 ratio is low because of the contrast between the trough and the other shoulder (band 10) of this band. The resulting color on the ratio composite for phyllically altered materials should be red for the "8/9" image (low blue, low green, high red) and black to brown for the "9/10" image (low blue, green, red). A similar analysis of propylitically altered materials indicates that they should be displayed as cyan on the "8/9" image and white to gray on the "9/10" image.

When the two ratio images (Figures 6-35 and 6-36) are compared to the Kennecott alteration map (Figure 6-7), the red ("8/9" image) or black ("9/10" image) areas correspond with the most intensely altered zones as predicted in Table 6-12. The cyan and silver–gray areas correspond to the propylitic zones on the Kennecott map (Figure 6-37).

These spectral contrasts are mostly due to the increased ferric oxide in the phyllic zone. Iron causes a decreased reflectance in bands 4 and 9, and an increased reflectance in bands 8 and 10. Note the area of phyllic alteration south of the word "Kennecott." On the "8/9" image, this area is red, and the postmineral volcanic cover to the north is blue. On the "9/10" image, the altered area is black, and the postore volcanic cover is magenta–blue.

There are some areas of known phyllic alteration, however, where these image codes break down. Figure 6-37 shows the outline of the red-colored areas of the "8/9" images. Note, for example, that at the location of samples 2 and 3, only the "9/10" image identifies this zone.

The first hypothesis attempted to explain these differences by the shift in wavelength of the absorption of different ferric-oxide species. Hunt and Ashley (1979) show an absorption feature for hematite at 0.85 μm, for goethite at 0.94 μm, and for jarosite at 0.93 μm (Figure 6-34). Laboratory analyses of the samples did not confirm this hypothesis.

Table 6-11. MSS and M^2S bands

MSS Band	Wavelength, μm	M^2S Band	Wavelength, μm
4	0.5–0.6	4	0.54–0.58
		5	0.58–0.62
5	0.6–0.7	6	0.62–0.66
6	0.7–0.8	8	0.70–0.74
		9	0.76–0.86
7	0.8–1.1	10	0.97–1.065

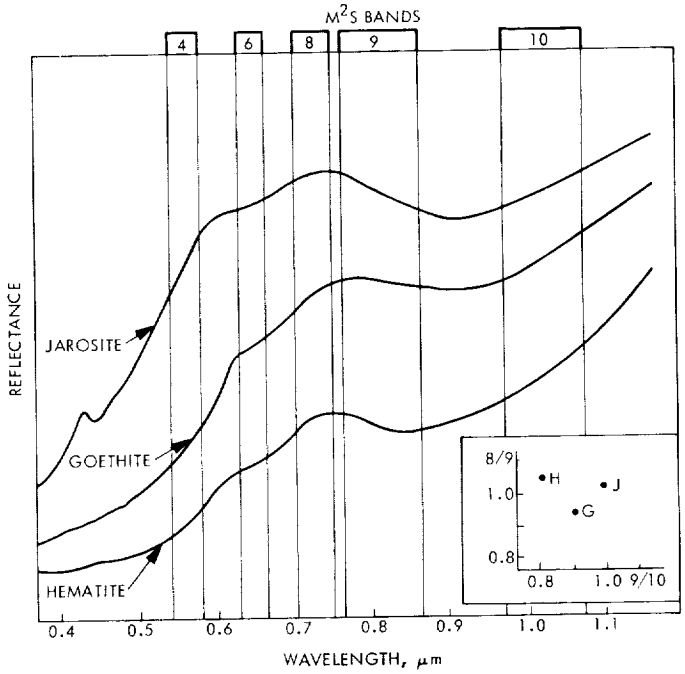

Figure 6-34. Spectral reflectance curves for hematite, goethite, and jarosite (from Hunt and Ashley, 1979). The curves are offset vertically for clarity; also shown are the M^2S band intervals for bands 4, 6, 8, 9, and 10. The inset figure shows calculated M^2S values for band-ratios 8/9 and 9/10 for hematite (H), goethite (G), and jarosite (J).

Examination of the spectra as compared to ocular and XRD analysis of the samples revealed some features that support a second hypothesis. Note the spectral trace of sample 2c in Figure 6-17. The 9/10 portion of the curve (between 0.8 and 1.0 μm in that figure) is similar to that part of the spectra of the phyllic sample D in Figure 6-13. However, the shorter wavelength portion of the 2c trace more closely resembles the propylitic samples A_w and B_w in Figure 6-14. Note also that, in addition to this spectral appearance, the band 4 (0.56 μm) reflectance increased. This "tail" may be due to the presence of chrysocolla and/or chlorite, both of which were found in the sample. The areas of samples 2 and 3 that were shown in a noncorrelative manner by the two M^2S images are composed of rocks that have the characteristics of *both* propylitic and phyllic alteration. The XRD analysis of samples 2b, 2d, and 2c shown in Table 6-7 lists kaolinite, muscovite (sericite), chlorite, and epidote.

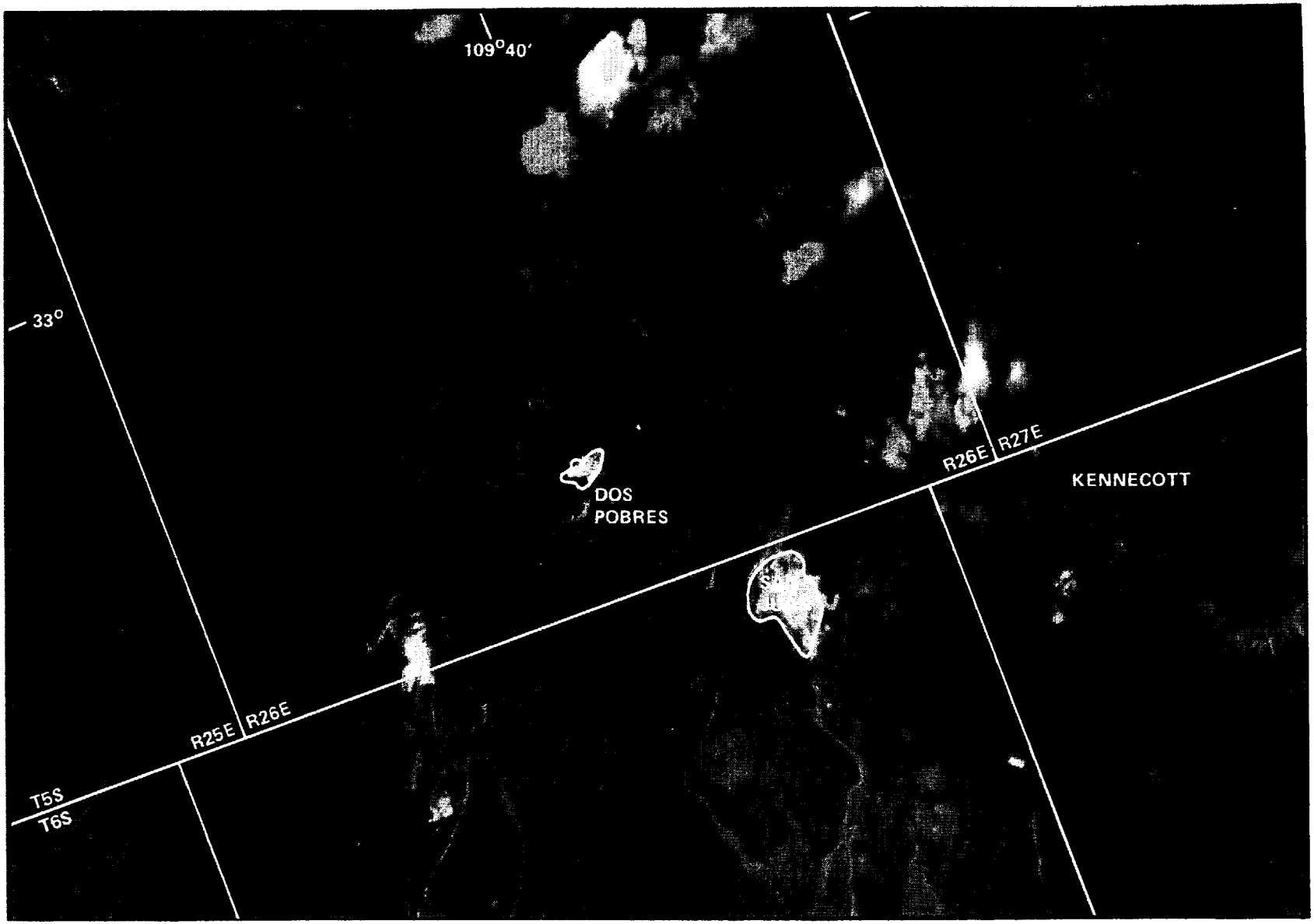

Figure 6-35. M²S CRC. Band-ratios 4/6, 6/8, and 8/9 are displayed as blue, green, and red, respectively. Light-blue and pink features in the north–central part of the image are clouds and cloud shadows, respectively.

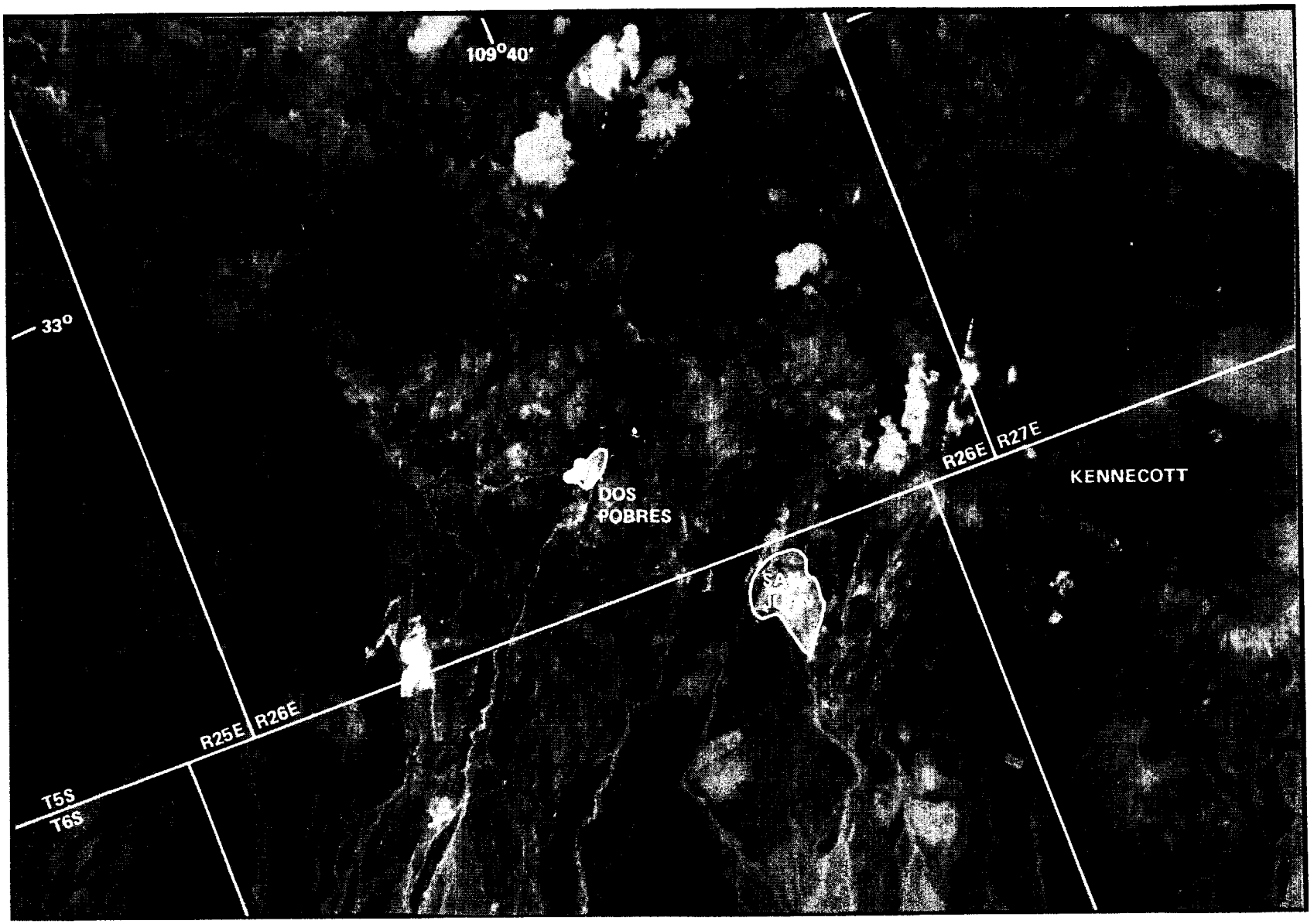

Figure 6-36. M^2S CRC. Band-ratios 4/6, 6/8, and 9/10 are displayed as blue, green, and red, respectively.

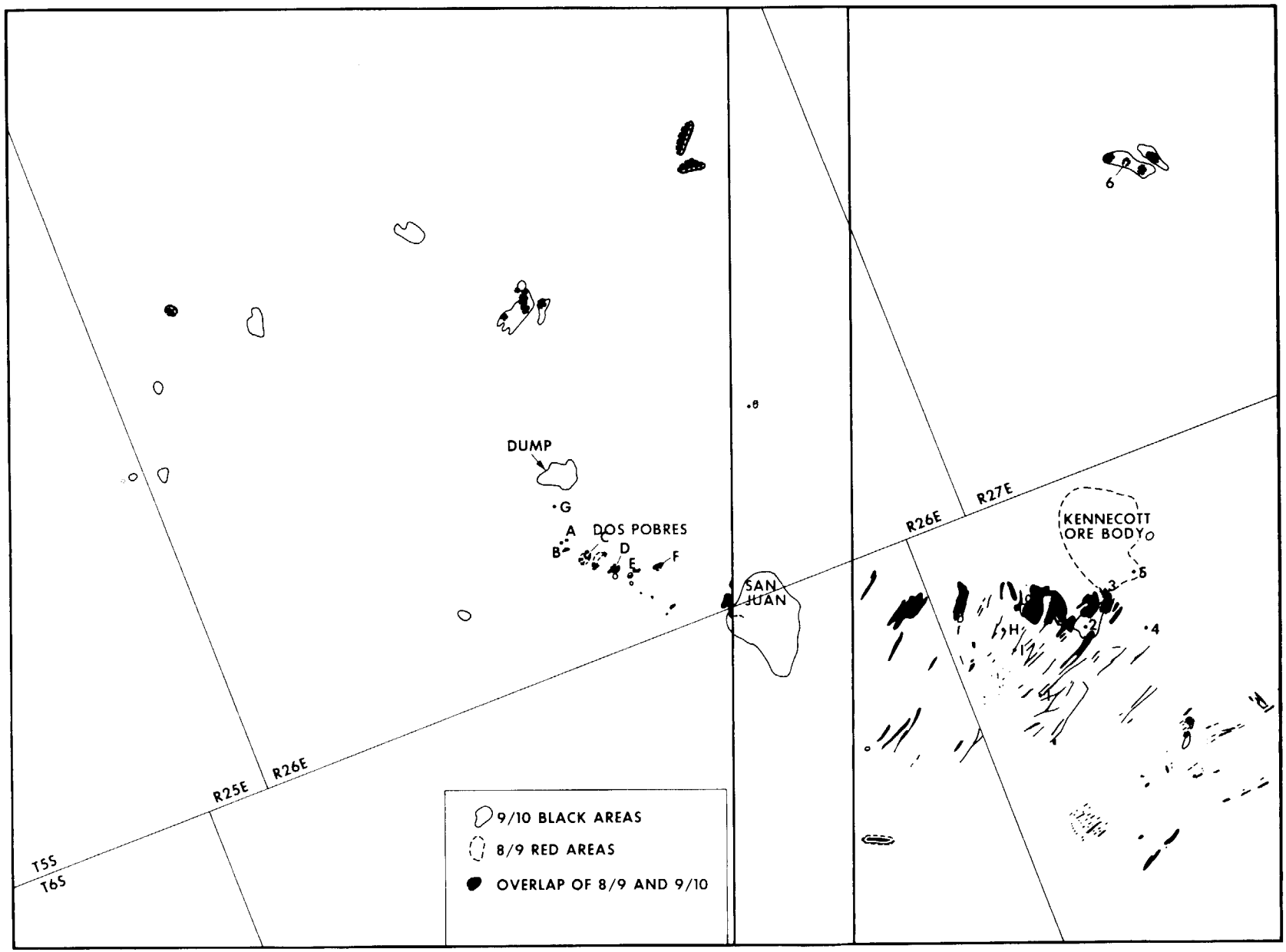

Figure 6-37. Interpretation map of M^2S CRCs (Figures 6-35 and 6-36) showing areas of iron-oxide anomalies found on the two images. Letters and numbers are sample locations shown in Figure 6-9.

d. Mapping of soils

Introduction. Examination of several ratio composites of the M²S data suggested that significant separation of the alluvial fan materials could be made. An area was selected for examination northeast of the town of Safford (Figure 6-38). This area is also covered by the USDA soil survey of the Safford area (U.S. Department of Agriculture, 1970); a compilation of the soil map is shown in Figure 6-39. Thirteen units are depicted on the soil map; a summary of their characteristics is presented in Table 6-13 (U.S. Department of Agriculture, 1970). Most of the units are gravelly sandy loams, developed on terraces and alluvial fans built up on the south flank of the Gila Mountains by streams draining into the Gila River. Their visual colors range from brown to reddish-brown.

Analysis of ratio composite. A CRC was selected because it seemed to show the clearest separation of soil units. This composite (Figure 6-40) was produced by displaying band-ratios 5/2, 6/8, and 8/10 as blue, green, and red, respectively. The grid on the image is distorted (compare to location map, Figure 6-38) because the data were not geometrically rectified to correct for aircraft motions. With this particular band combination, vegetated areas will be black since they have very low ratio values; materials with iron oxides will have a high blue component due to the high reflectance at 0.60 μm relative to 0.46 μm (5/2 ratio).

An interpretation map (Figure 6-41) was produced by outlining areas on the CRC that were separable by image color and geomorphic appearance. These areas were then assigned the soil designation appearing on the USDA map. Therefore, adjacent units on the interpretation map can have the same designation because they represent a single soil unit by USDA criteria, but appear different on the CRC image.

In general, all the USDA soil units can be separated on the CRC. The blue areas on the CRC correspond to CtB and PvC, which are the red–brown soils (the spectrally distinctive iron oxides present are responsible for the red color). The CtB unit can be separated on the CRC into two distinct units– the blue unit on the tops of the terraces, and an orange–green unit at the terrace breaks. The PuB unit is a distinctive orange color; the soil map and description of this unit do not show it as having a different visual color from other units. Presumably, there is some marked spectral difference in the infrared for this unit, although it was not examined in the field.

While the ratio image allows separation of most of the units depicted on the USDA soil map, additional separations based on spectral differences can be made. These new units were not field checked, but presumably are subunits of soil classes which the USDA does not distinguish. Some of these differences are due to the different techniques used to define a unit. The soil mappers consider physiography, slope, surface composition, and *depth profile* when defining a soil unit. The addition of information from the third dimension implies that units appearing similar on the surface could be classified into different units, and vice versa. The image units are limited to the surface of materials and, hence, lack any depth information. On the other hand, spectral characteristics in the infrared *are* included, unlike the visual color characteristics used by the USDA. Nevertheless, the analysis of the image certainly indicates that remote sensing data can greatly contribute to soil mapping.

5. NS-001 data

a. Band-ratio images. The NS-001 scanner differs from the M²S and Landsat MSS scanners most significantly in bands 6 and 7. The NS-001 bands used and their wavelengths are listed in Table 6-14.

Two band-ratio images (Figures 6-42 and 6-43) were analyzed in detail. The first image was produced using all six bands listed in Table 6-14. Later, a band-ratio image was produced using only those five bands that correspond to the five bands on the Landsat 4 TM. The two band-ratio configurations display 3/2 in green, 6/7 in red, and 4/5 or 4/6 in blue (band 5 on the NS-001 scanner does not exist on the TM). The lack of overall image clarity and sharpness (compared to Figure 6-51, for example) is due to suppression of topographic highlighting, which is a result of the ratioing process (Rowan et al., 1974).

By referring to the spectral graphs of Figures 6-15 and 6-16, the color coding of the phyllic and propylitic zones can be predicted on the band-ratio images (Table 6-15). Qualitatively, both configurations give the same results, which can be confirmed by comparing the two images.

In both of the band-ratio images, high ferric-oxide areas would be depicted as green due to iron absorption in band 2, resulting in large values for the 3/2 ratio. Clay areas would be shown as red due to clay (OH) absorption in band 7. Phyllic areas would show both colors and appear yellow on the images. Propylitic areas would have the opposite behavior and appear blue on the images.

Figure 6-44 was traced from the first configuration (using 4/5 instead of 4/6) because (1) it was available early in the project, and (2) it was nominally scale-matched to the 1:24,000 Kennecott maps. The figure also shows areas of

Table 6-12. Ratio values and M^2S ratio colors for phyllic and propylitic alteration

Alteration	M^2S Ratio Composite, Figure 6-35				M^2S Ratio Composite, Figure 6-36			
	Ratio	Color Assignment	Value	Image Color	Ratio	Color Assignment	Value	Image Color
Phyllic	4/6	Blue	Low	Red	4/6	Blue	Low	Black to brown
	6/8	Green	Low		6/8	Green	Low	
	8/9	Red	High		9/10	Red	Low	
Propylitic	4/6	Blue	High	Cyan	4/6	Blue	High	White to gray
	6/8	Green	High		6/8	Green	High	
	8/9	Red	Low		9/10	Red	High	

quartz–sericite alteration traced from the Kennecott alteration map. The yellow "phyllic" color encompasses most of these mapped quartz–sericite areas. Most of the excessive yellow color extends downslope from the most intensively altered areas of the Kennecott deposit. Field checking showed that quartz–sericite-altered latite float was thinly spread over the propylitically altered andesite in these areas. The NS-001 band-ratio image is more inclusive of known phyllic alteration than are the M^2S band-ratio images, but the M^2S images more sharply defined the smaller number of more intensely altered zones than did the NS-001 images. Another important difference is that, due to effects of deuteric alteration, the NS-001 images showed rather large areas of the postore Tertiary dacite volcanic rocks north of the deposits, coded with the same shade of yellow as the phyllic Mesozoic latites.

A more detailed interpretation of the Dos Pobres area was made possible by an enlarged print (Figure 6-45) of the NS-001 ratio image of that area. Striping in the image, trending NNE–SSW, is due to noise in the 6/7 ratio component. Comparison with the geologic map (Figure 6-46) and with the aerial photograph indicated that the geometry of the map was inaccurate. This was a result of the surveying method used to produce the map. Despite the inexact fit, it was possible to use a zoom transfer scope to compare the map and the image.

Intensely colored yellow and orange areas on the image correspond with the mapped quartz monzonite and latite porphyries. Field checking showed that these "productive" porphyries are indeed phyllically altered in contrast to the propylitically altered andesites that they intrude. One of these porphyry intrusions is coded red instead of yellow on the image (Figure 6-45). This area is outlined around the sample point F on the cartoon map of Figure 6-47. The field check showed this intrusion to be heavily argillized, thus explaining the preponderance of the high 6/7 band ratio sensitive to clays. An erroneous interpretation of this red spot could have been made. A yellow-coded area (clay + iron oxide) containing vegetation (magenta code) could also have produced a red-coded anomaly (yellow + magenta = red). This interpretation was ruled out by referring to the aerial photographs, which showed denser vegetation.

An image was constructed from the single ratio of the 1.6-μm (band 6) and 2.2-μm (band 7) channels by assign-

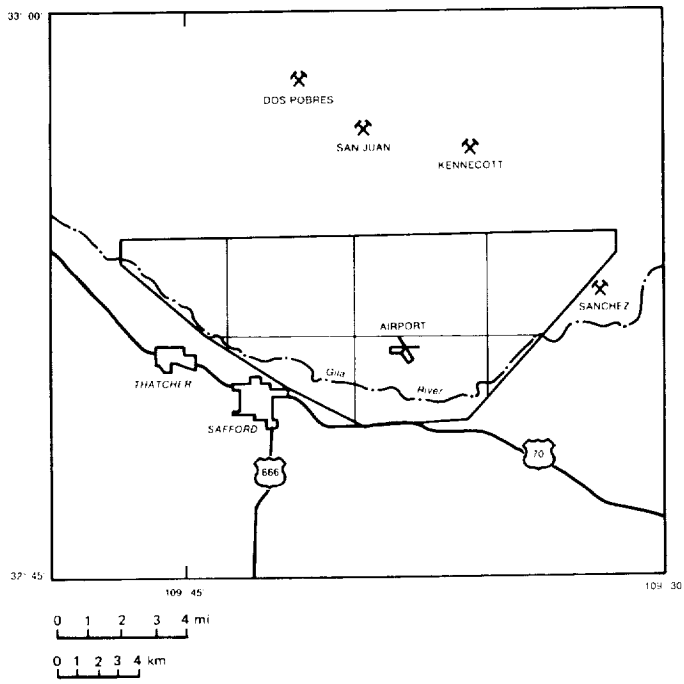

Figure 6-38. Location of area interpreted for soil units using M^2S data

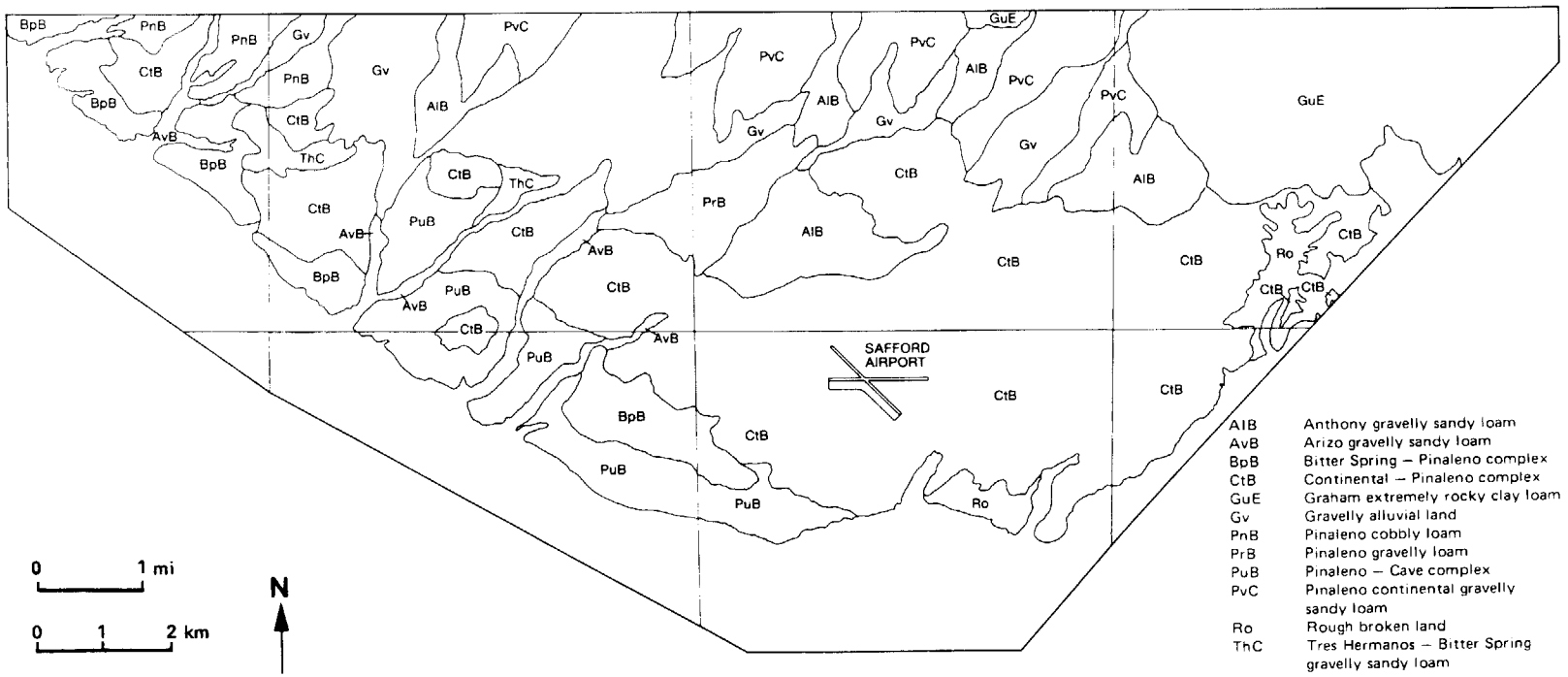

Figure 6-39. Soil map of area analyzed from M²S data (U.S. Department of Agriculture, 1970)

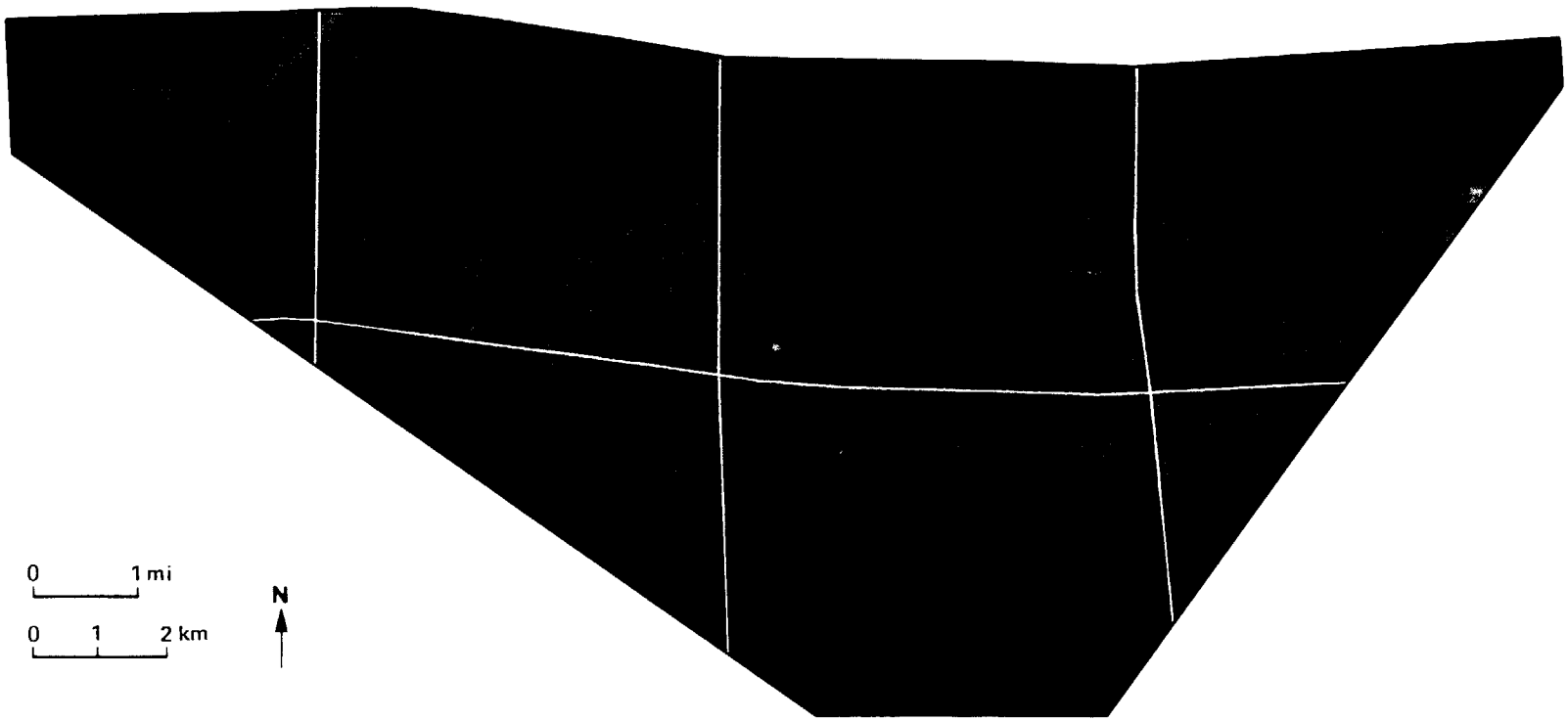

Figure 6-40. M^2S CRC of a portion of the Safford area used for soil mapping. Ratios 5/2, 6/8, and 8/10 are displayed as blue, green, and red, respectively.

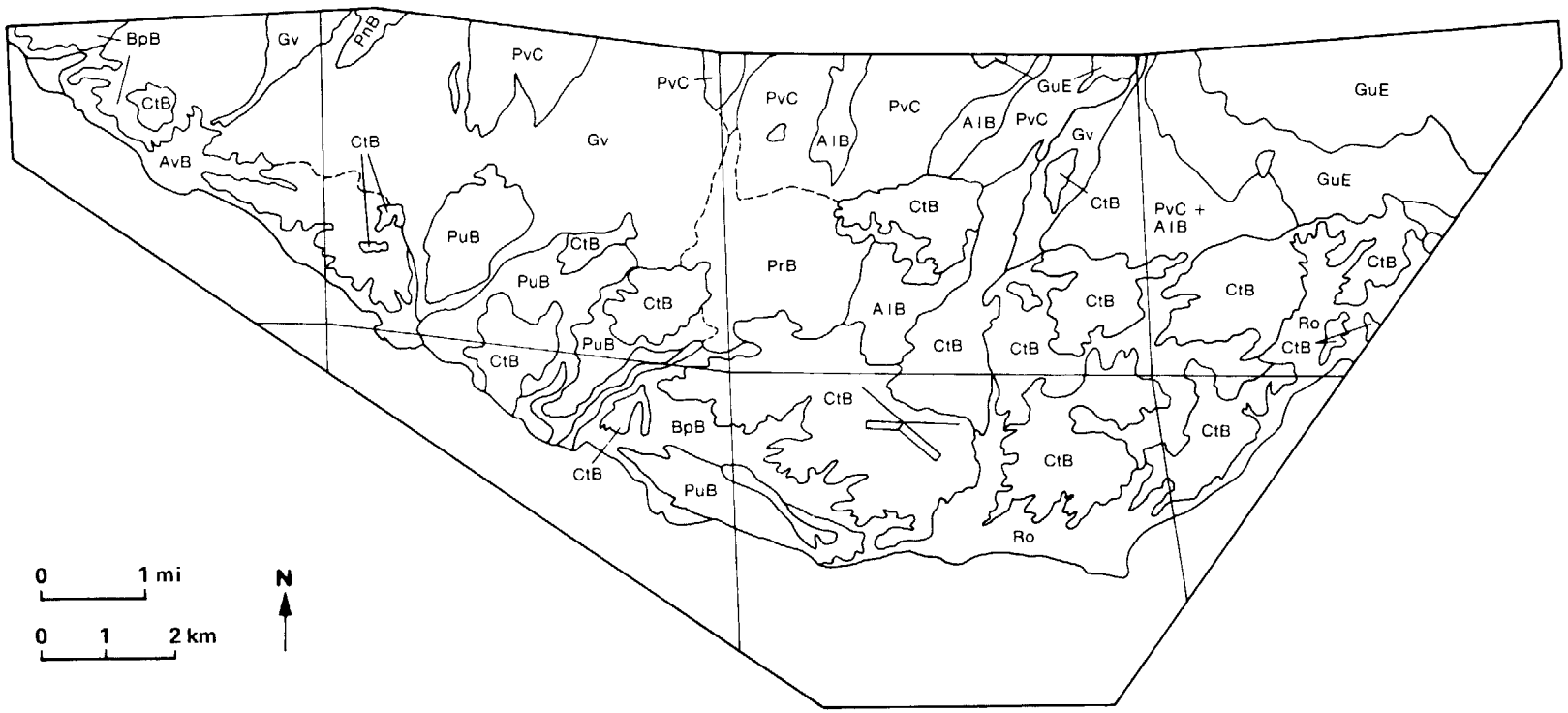

Figure 6-41. Interpretation of M^2S ratio image (Figure 6-40). Unit designations were added by comparison with the soil map (Figure 6-39).

Table 6-13. Description of soil units

Unit	Occurrence	Composition	Visual Color (Munsell Color)
AlB	Alluvial fans	Gravelly sandy loam	Brown (10 YR 5/3)
AvB	Washes below terraces	Gravelly sandy loam	Brown (10 YR 5/3)
BpB	Lower terraces	Gravelly sandy loam	Light brown (7.5 YR 6/4)
CtB	Terraces	Gravelly sandy loam	Red–brown (5 YR 4/4)
GuE	Outcrop and talus	Rocky clay loam	Red–brown (5 YR 4/3)
Gv	Fans and washes	Gravelly alluvium	
PnB	Lower terraces	Cobbly loam	Brown (7.5 YR 5/4)
PrB	Terraces	Gravelly sandy loam	Brown (7.5 YR 5/4)
PuB	Terraces	Gravelly sandy loam	Brown (7.5 YR 5/4)
PvC	Terraces	Gravelly sandy loam	Red–Brown (5 YR 4/3)
Ro	Terrace breaks		
ThC	Flats of lower terraces	Gravelly sandy loam	Pink (7.5 YR 7/4)

ing colors to ranges of values of the 6/7 ratio (Figure 6-48). The highest ratio values were coded black; decreasing values were coded brown, blue, green, orange, red, and finally white. The high noise level in this image results from use of only a single ratio to produce the picture, and the 2.2-μm channel on the NS-001 had a higher noise level than other channels. This noise is accentuated by the ratioing process. The resulting image shows that the black areas, which have the highest 6/7 ratio value (maximum clay content), conform closely to those areas coded yellow or red on the three-ratio NS-001 image. On the three-ratio image, vegetation is coded magenta (red and blue). The single-ratio image confused clay (coded red on the three-ratio image) with vegetation in only one case (the well-watered willow thicket that extends downstream from the reservoir at Dos Pobres, magenta area in Figure 6-45). The oak trees on the plateau and the desert scrub below were not mapped as clay on the 6/7 ratio map.

The single-ratio image was useful for two purposes:

(1) To distinguish between semiarid vegetation and clay alteration

(2) To demonstrate the power of the two TM bands at 1.6 and 2.2 μm

Table 6-14. NS-001 bands

NS-001 Band	Center Wavelength, μm
2	0.56
3	0.66
4	0.83
5	1.15
6	1.65
7	2.22

A lineament map (Figure 6-49) was prepared from the NS-001 band-ratio image to demonstrate that the brightly colored digital scanner images show structural features better than do the high-resolution aerial photographs. For example, even though the mineralized or highly altered latite dikes too small to be directly seen on the NS-001 image were visible on the color aerial photographs, many faults, the shear zones controlling these dikes, and the copper mineralization and associated phyllic minerals were more easily mapped from the scanner image. The fault and fracture zones are delineated by tonal discontinuities on the NS-001 and other scanner images, whereas some of these same structures are tonally featureless on the color aerial photographs. In other words, the digital images are more sensitive to mineralogical discontinuities that mark structural zones.

A lineament map of the same area was constructed from the digital Landsat MSS images and enlarged to the same scale to produce a matching map (Figure 6-50). Note that these two lineament maps, made from images of disparate scale and spatial resolution, are highly complementary. Used together as overlays, the traces of most of the known faults

Table 6-15. Ratio values and NS-001 colors for phyllic and propylitic alteration

Ratio	Color Assignment	Phyllic	Propylitic
4/5 or 4/6	Blue	Low blue	High blue
3/2	Green	High green	Low green
6/7	Red	High red	Low red
Image color		Yellow	Blue

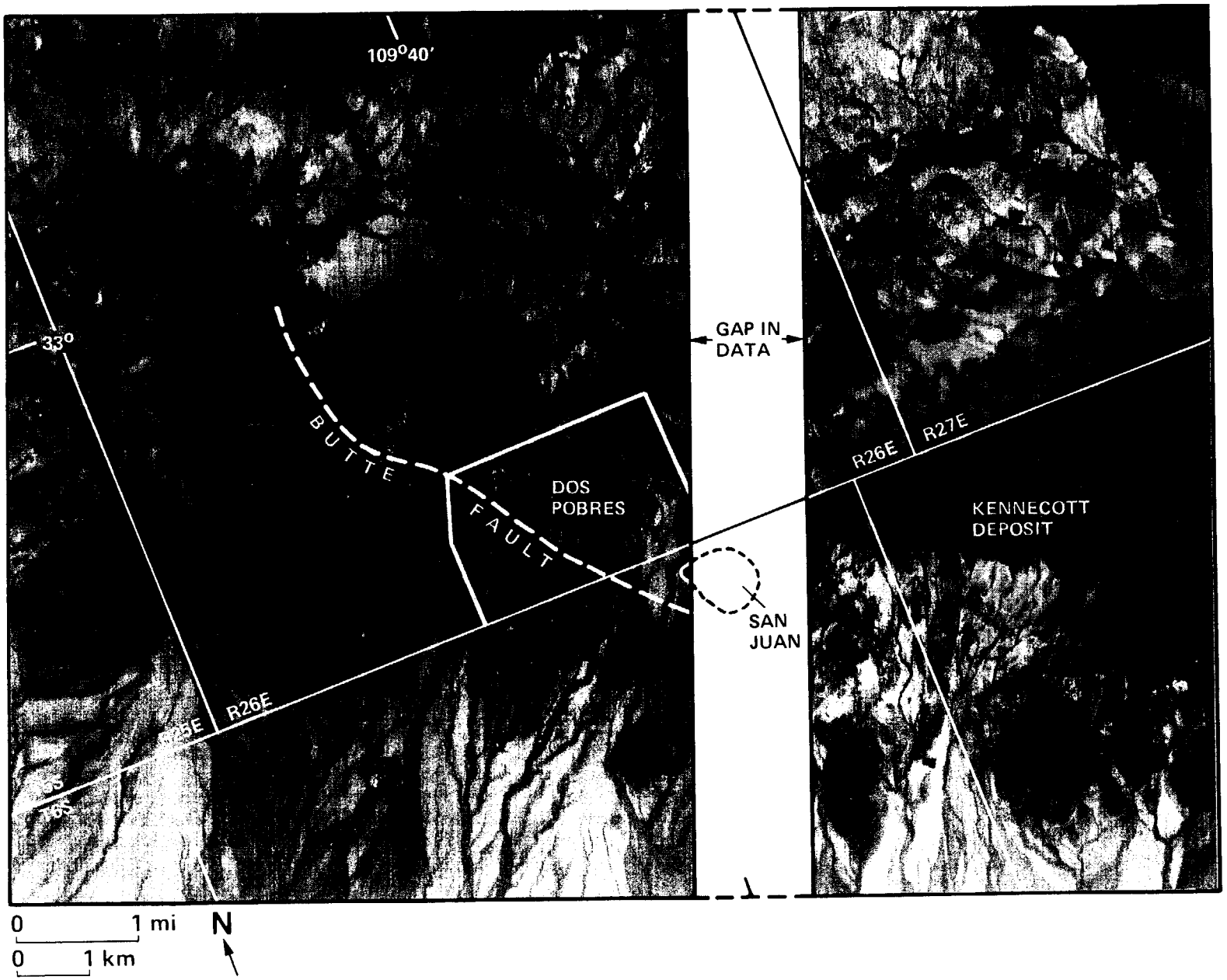

Figure 6-42. NS-001 CRC. Band-ratios 3/2, 4/5, and 6/7 are displayed as green, blue, and red, respectively. Heavily outlined area around the Dos Pobres deposit represents enlarged area of Figure 6-45.

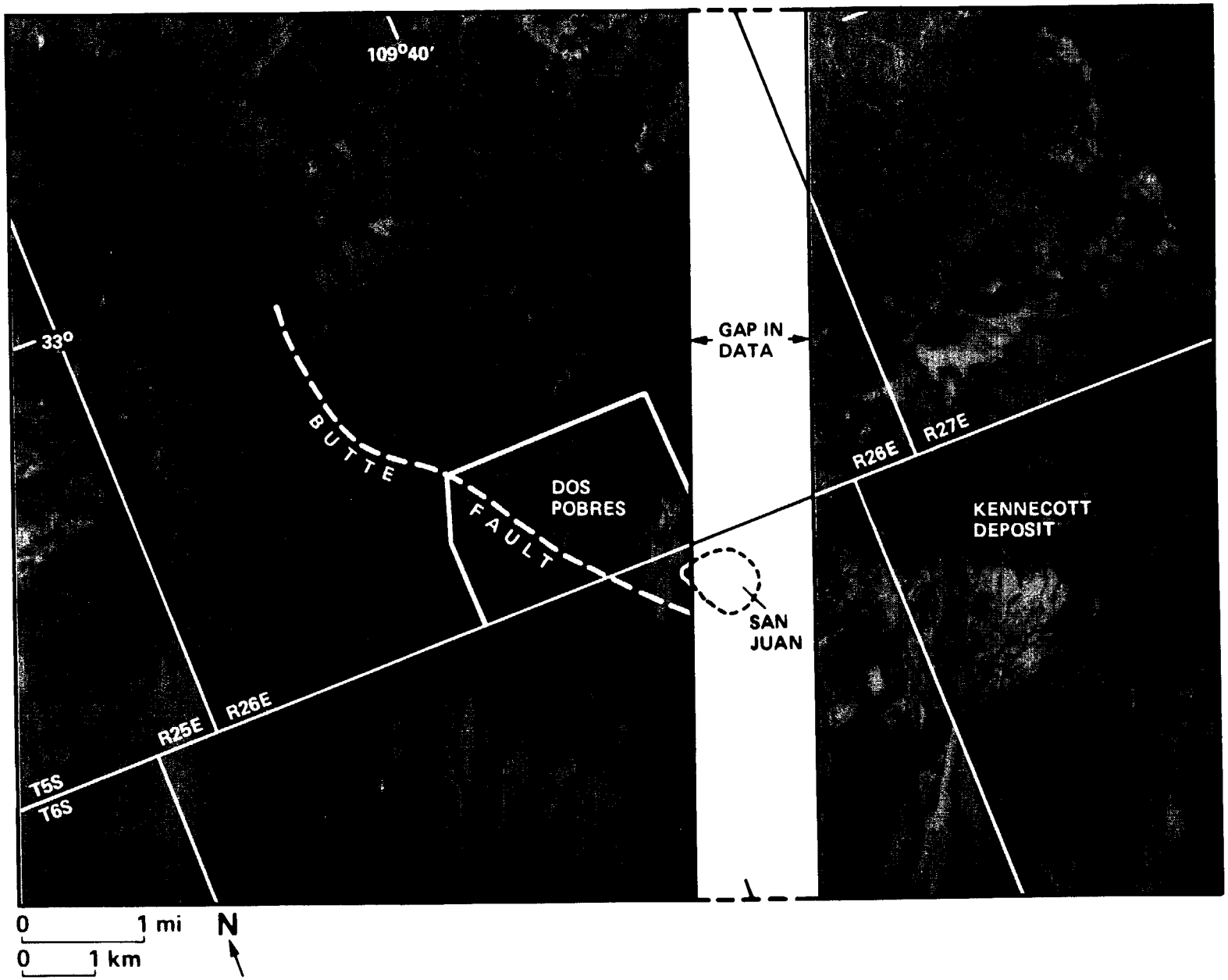

Figure 6-43. NS-001 CRC. Band-ratios 3/2, 4/6, and 6/7 are displayed as green, blue, and red, respectively.

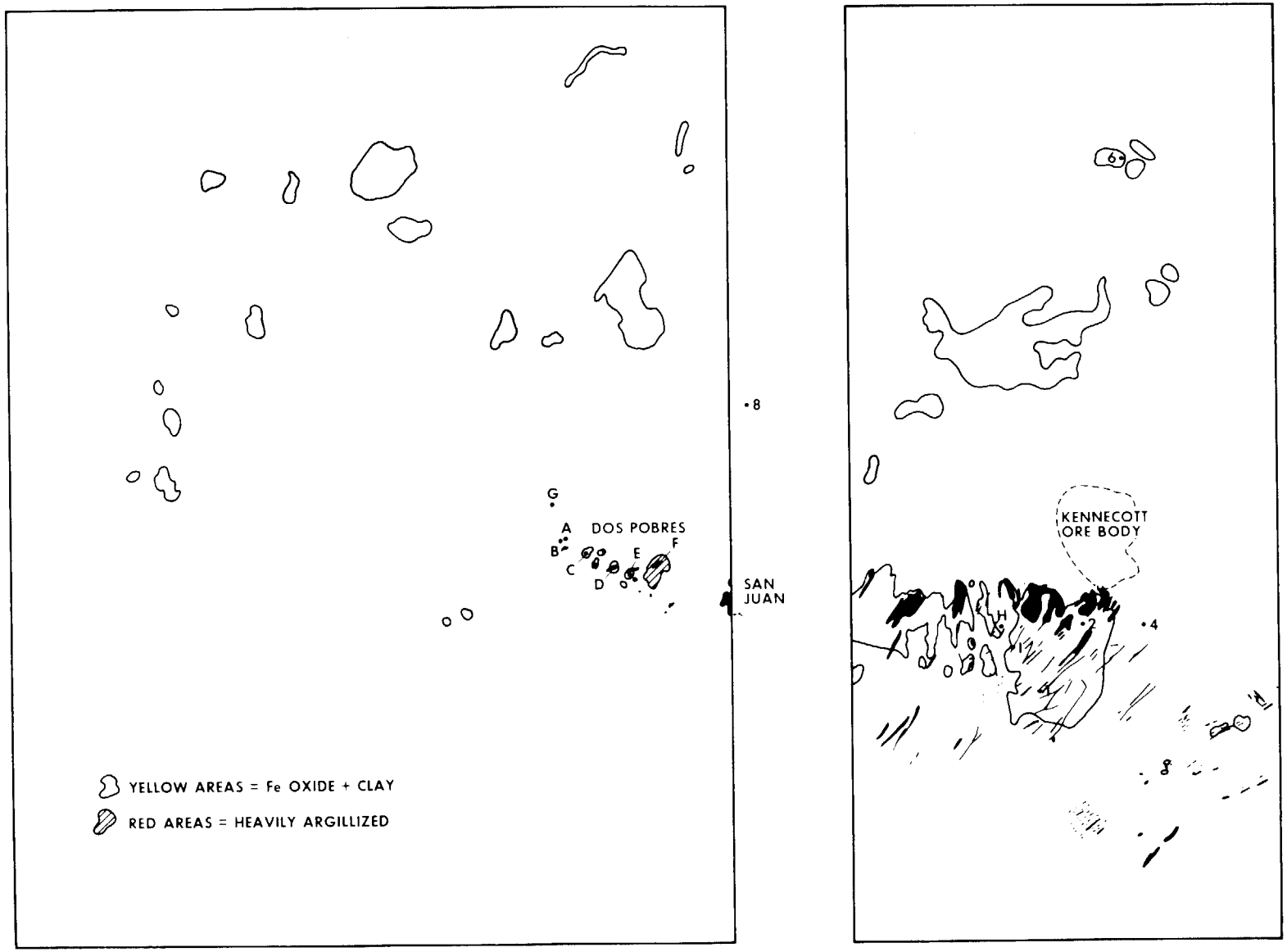

Figure 6-44. Interpretation map of NS-001 3/2, 4/5, and 6/7 ratio image (Figure 6-42). Black areas are quartz–sericite alteration from Kennecott company map.

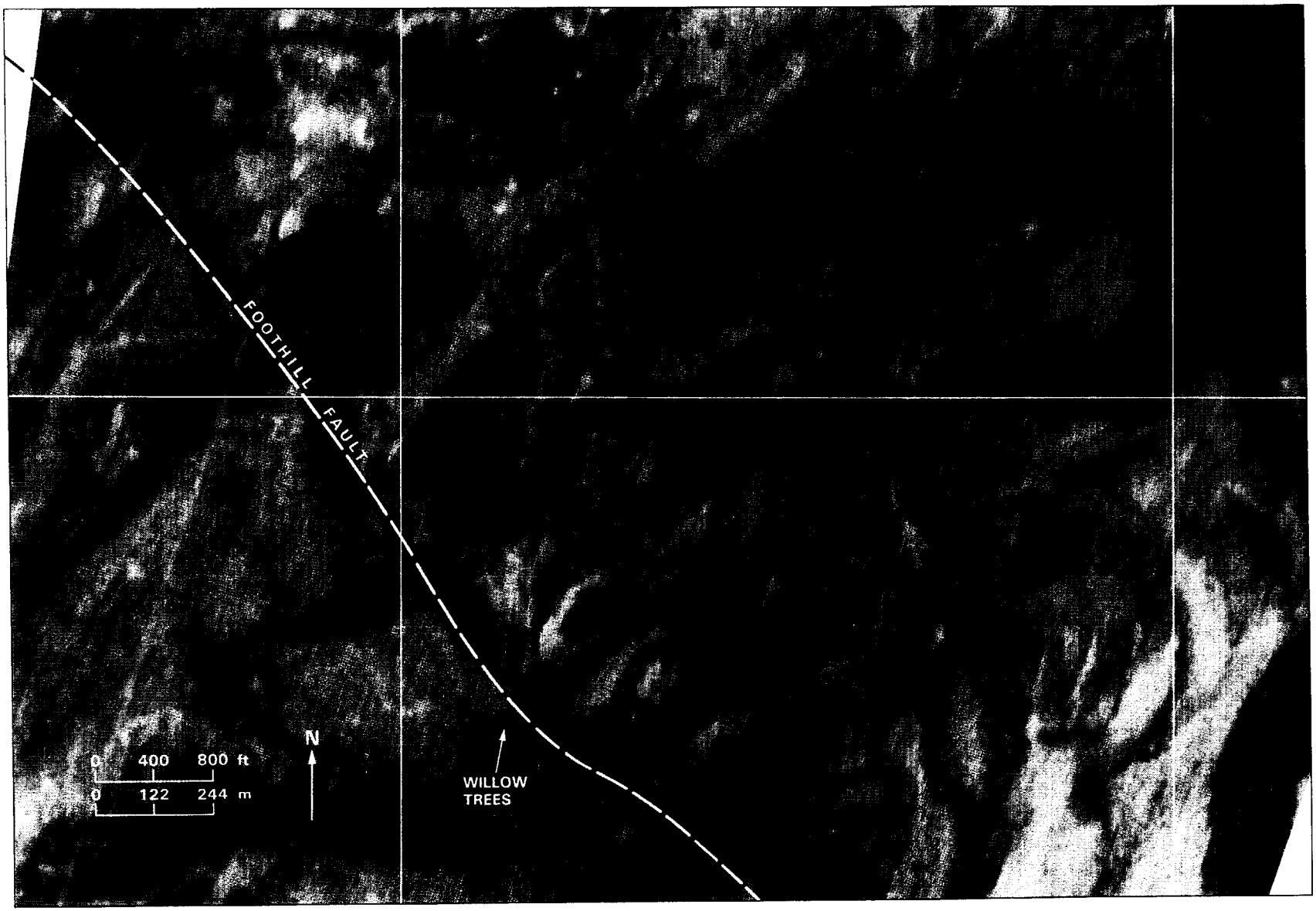

Figure 6-45. Enlargement of NS-001 band-ratio composite (3/2, 4/5, 6/7) over Dos Pobres deposit

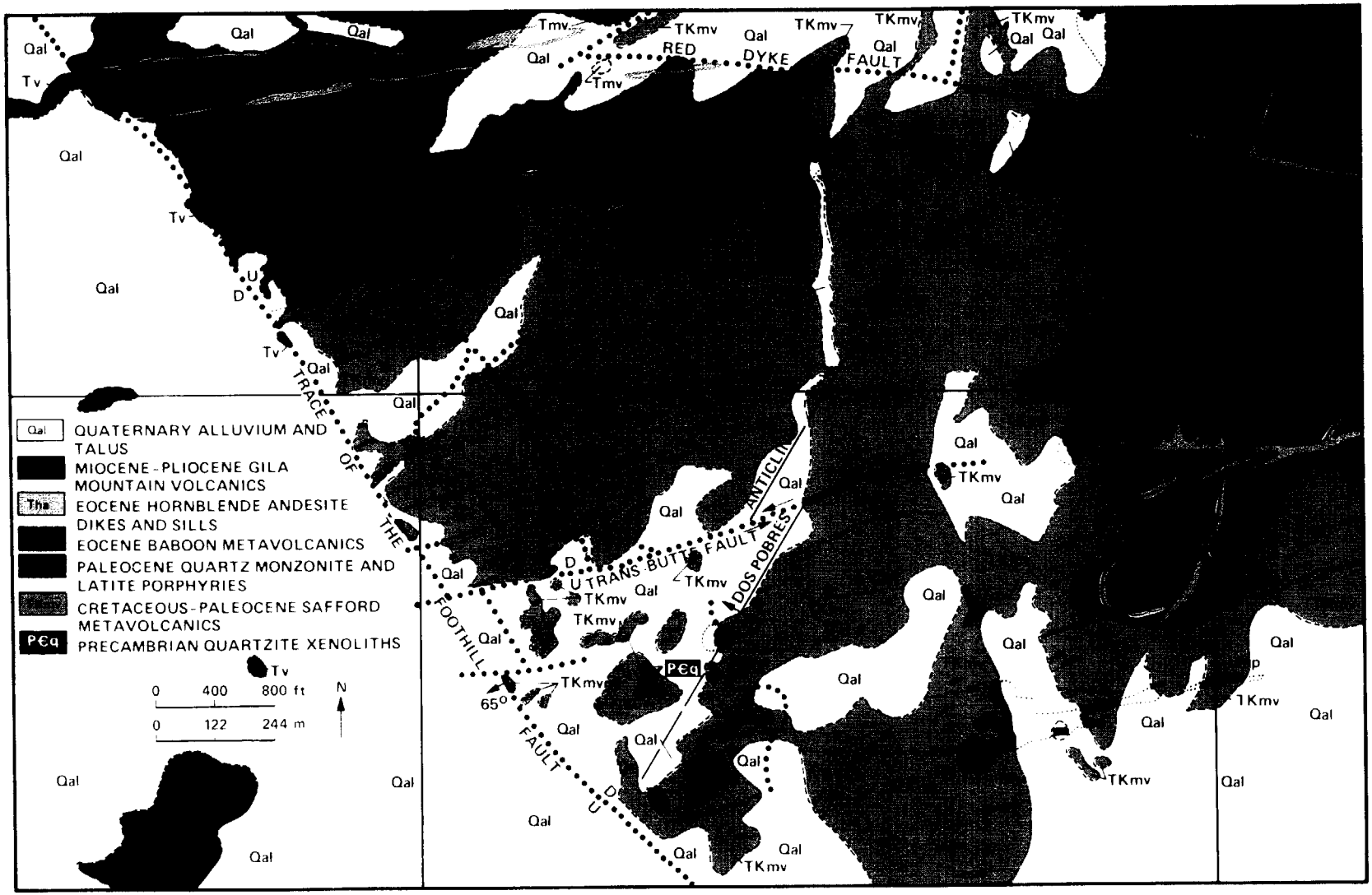

Figure 6-46. Geologic map of Dos Pobres area, supplied by Phelps Dodge Corporation

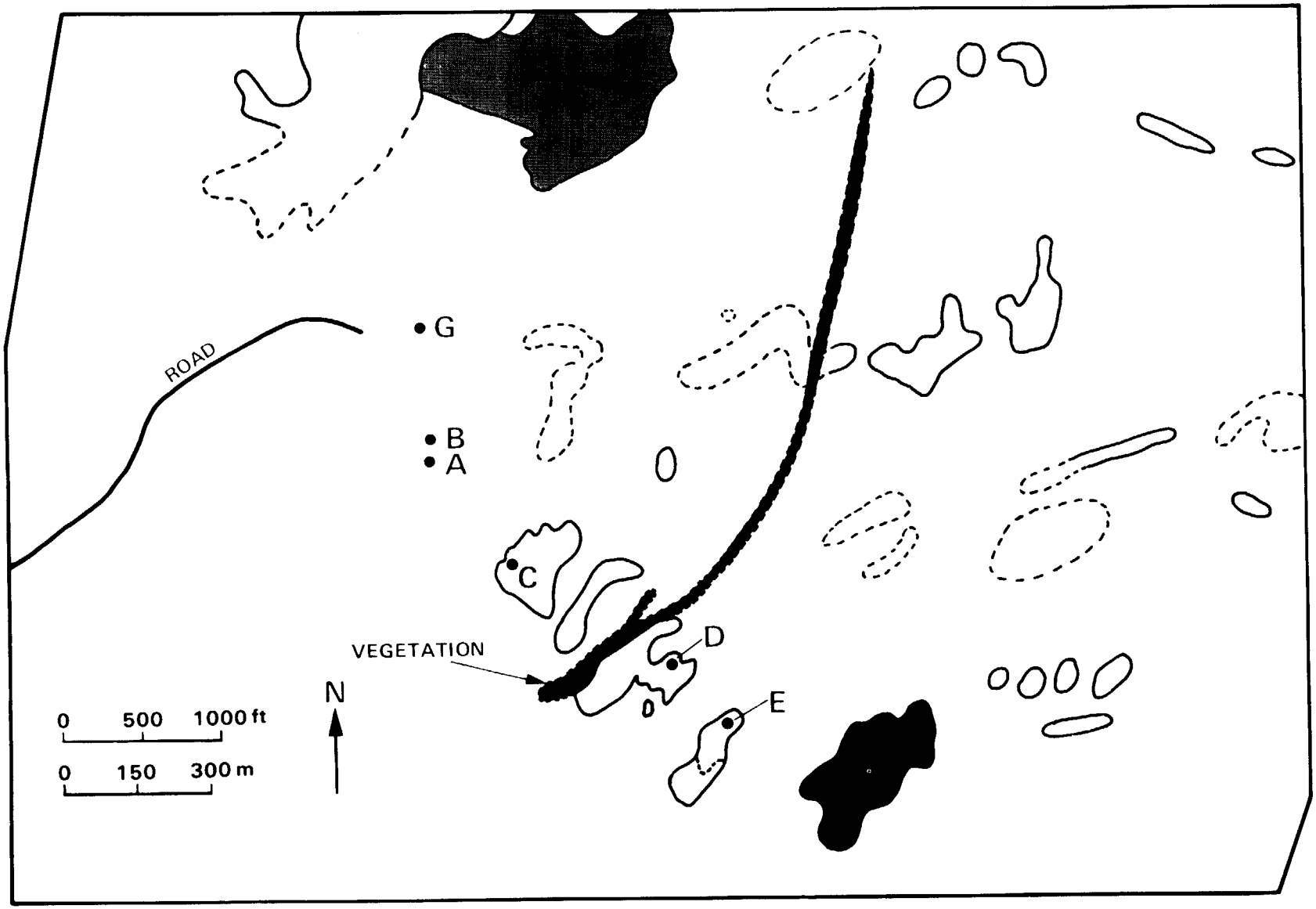

Figure 6-47. Interpretation of spectral anomalies on NS-001 ratio image of Dos Pobres area (Figure 6-45). Dashed areas are more diffuse yellow areas. Apparent inconsistencies with ratio image are due to reproduction degradations of original image from which interpretation was made.

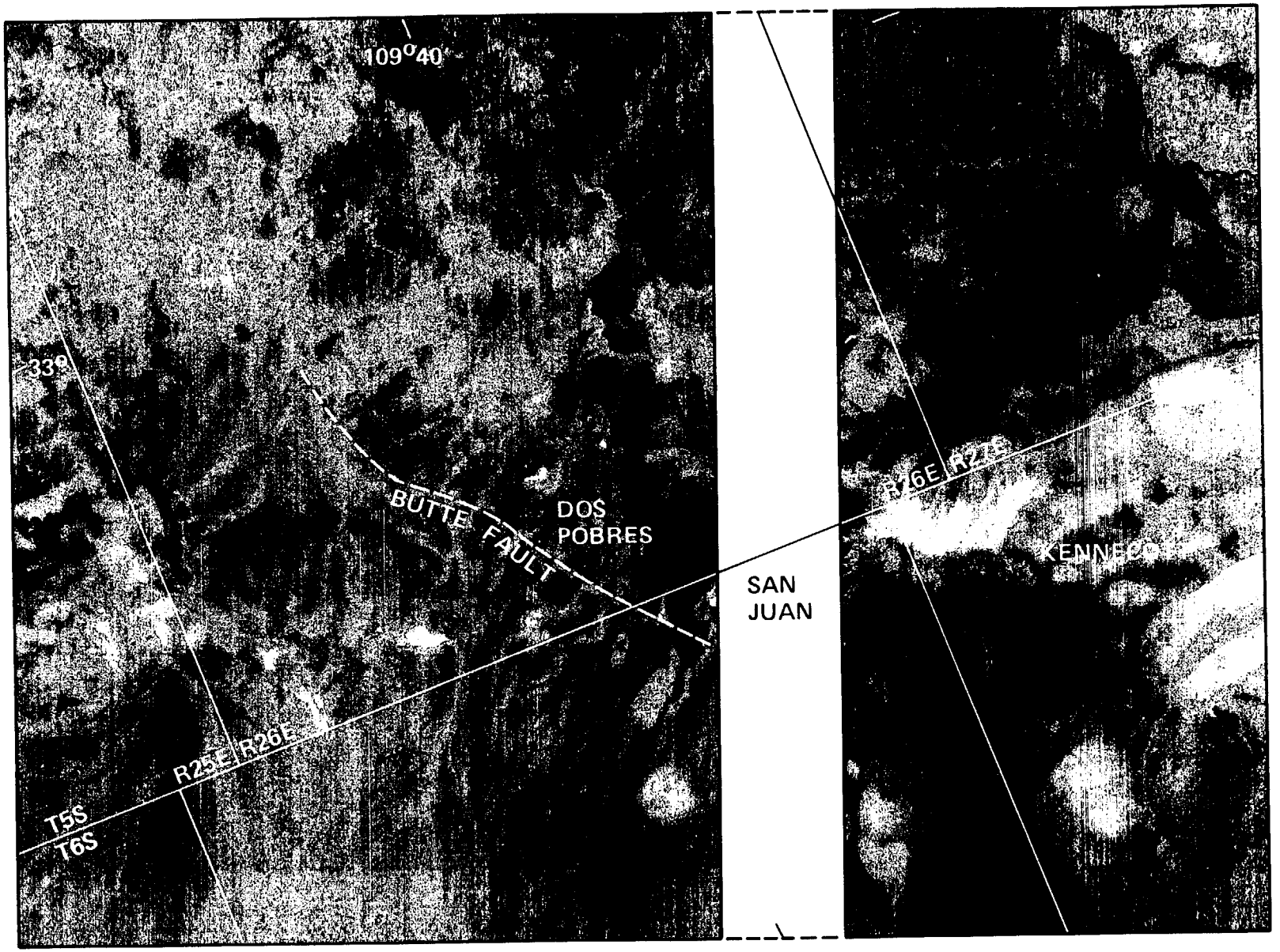

Figure 6-48. Density slice of NS-001 6/7 band ratio. Colors progress from black (highest ratio values) through brown, dark blue, blue, green, orange, red, and white (lowest ratio values).

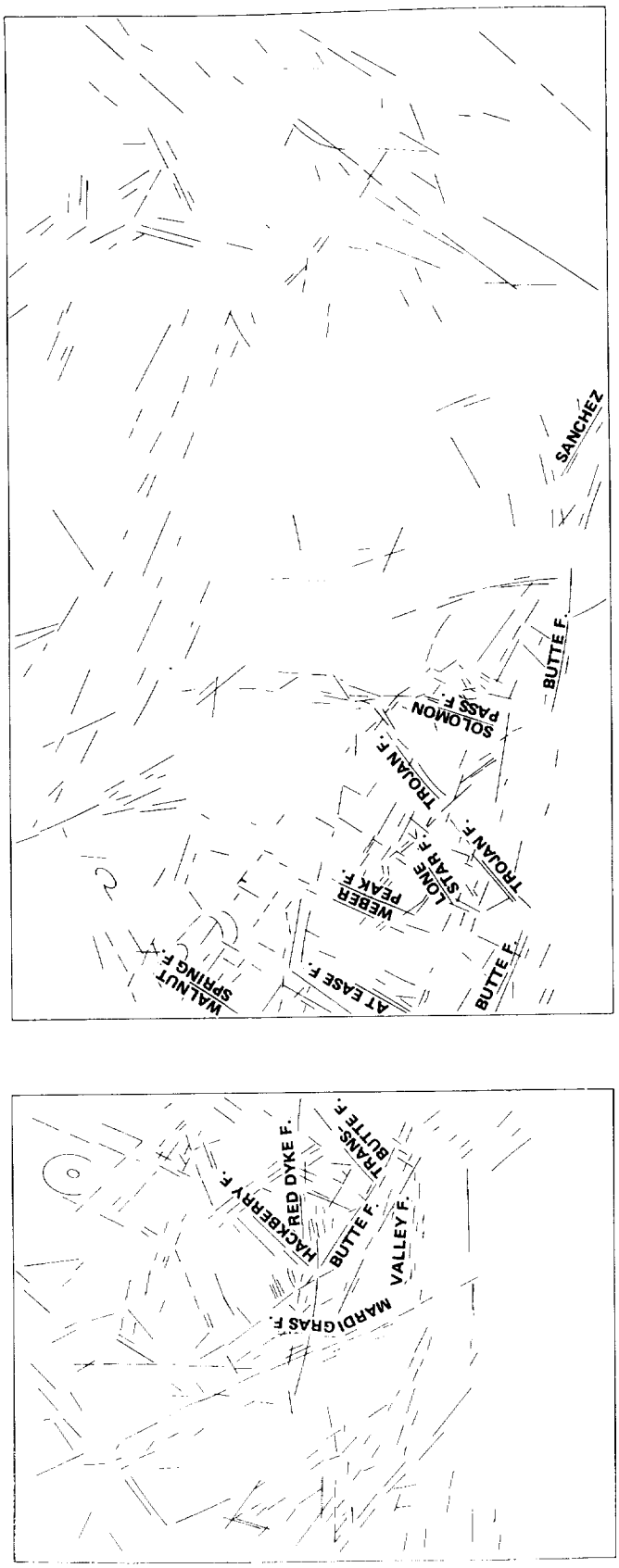

Figure 6-49. Lineament interpretation produced from NS-001 band-ratio image

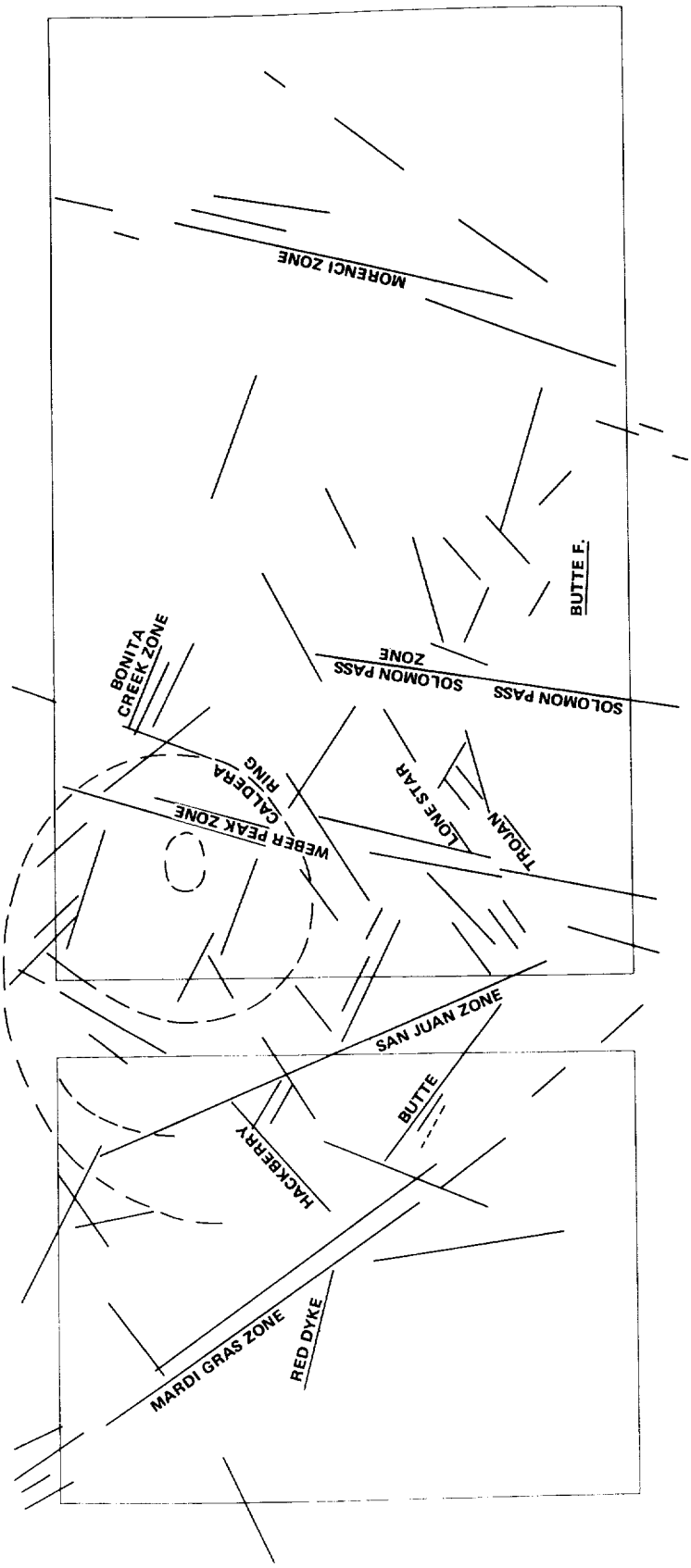

Figure 6-50. Lineament interpretation produced from Landsat MSS data for the same area as NS-001 data, Figure 6-49 (Landsat scene no. 11541–16265, acquired October 11, 1976; sun elevation 35°, azimuth 133° used for analysis)

mapped by Dunn (1978) and Robinson and Cook (1966) are displayed. In addition, possible extensions of these faults are traced through the overlying valley alluvium and plateau basalts. The 3-km-diameter circular feature on the plateau composed of dacite (and possibly rhyolite) is more evident on the color infrared Landsat MSS composite than on the aircraft scanner image.

b. Canonical image. The NS-001 image (Figure 6-51) was produced by canonical transformation. Canonical transforms use rotated spectral axes to increase spectral separation of the units. This is a supervised procedure; parameters for the transformation were based on the linear discriminant analysis of the PFRS data (Paragraph III). This program produces linear combinations of the original variables (wavelength bands) which were applied to the image data to create new images.

The discriminant function analysis was done using reflectance data from the PFRS training sets. The NS-001 raw data represent radiance values. To convert the scanner data to reflectance, a calibration procedure was used based on work done at the Silver Bell, Arizona, test site. At Silver Bell, ground reflectance measurements were compared to scanner digital number (DN) values for the same areas to create a linear function which related DN value to reflectance. These transfer functions were applied to the Safford data prior to transforming them to the canonical variates. It was felt that the Silver Bell calibrations could be used because the two data sets were obtained with the same instrument only 1 hour apart, with similar weather conditions.

Comparison of the canonical image with the field examinations shows the following correlations:

1st vector (blue)	Propylitic Mesozoic andesites (and some vegetation)
2nd vector (red)	Most of the phyllic Mesozoic latite dikes and quartz monzonite porphyries
3rd and 2nd vector (red + green = yellow)	Altered younger dacites and the most intensely altered, pyritic, quartz–sericite, Mesozoic lithic tuff, granodiorite, and latite (and some well-watered vegetation)
1st, 2nd, and 3rd vector (white)	Unaltered younger dacite on the plateau

It is interesting to compare the interpretation (Figure 6-52) made from the NS-001 canonical image with that made from the NS-001 ratio image (Figure 6-44). One important difference between these two NS-001 images is evident. The area that is colored yellow (phyllic) in the ratio image is subdivided into two categories in the canonical image. Most of the phyllic areas are coded red, but the most intensely altered areas are coded yellow. Field observations have shown that these yellow-coded areas are most intensely pyritized and silicified, and they contain more copper-oxide mineralization (chrysocolla).

The canonical image has the disadvantage that chemical or mineralogical cues cannot be inferred from the color codes as they are from band-ratio images. The canonical image has the advantage that *a priori* ground information such as field spectra and previous mapping can be used to achieve data compression and to enhance subtle spectral differences between specific target rock types. The canonical image is best used in conjunction with the band-ratio image.

The canonical image showed the desert vegetation as blue, and well-watered vegetation as yellow. However, the rock types that could be confused with vegetation on the canonical image were different than on the three-ratio image. Used together these two images eliminate the vegetation problem. For example, the heavily argillized area F at Dos Pobres was coded red on the canonical image and thus could not have been confused with vegetation as it could have been on the three-ratio image.

The area around the Kennecott deposit (Figure 6-53) was examined in detail by enlarging a section of the NS-001 canonical transform image (Figure 6-54b) and comparing it with the aerial photograph (Figure 6-54a) and the Kennecott alteration map (Figure 6-54c). Very little separation of alteration types can be seen on the aerial photograph. The NS-001 enlargement, however, displays the altered rocks as three different colors: blue, red, and yellow. An interpretation map of this image was produced (Figure 6-54d) and color coded with the same colors as seen on the image. Comparison with the alteration map shows a striking similarity between the two. Propylitically altered rocks (blue on the image) are accurately portrayed. The red areas on the image correspond almost perfectly with areas mapped as quartz–sericite alteration and chloritization with quartz–sericite. Yellow areas are also quartz–sericite alteration. Field checking of the area revealed that the yellow areas were more intensely altered and mineralized than the red areas.

This example illustrates the accurate, detailed alteration mapping that can be done using the NS-001 data; taking into account a moderate decrease in spatial resolution, Landsat 4 TM data will provide a powerful tool for geological resource exploration.

6. M²S thermal data. A predawn - near-noon pair of thermal images were acquired with the M²S scanner on August 17 – 18, 1977. The nighttime thermal image was

geometrically registered to the daytime image for further processing of the day–night pair. An average albedo image was produced from the 10 channels of visible and near-infrared data, which were obtained during the daytime pass.

Thermal infrared data can provide additional lithologic discrimination information compared to reflectance data because thermal infrared data represent differences in the physical properties of materials, such as density, conductivity, and diffusivity, rather than surface properties. Vegetation cover and moisture content, however, can greatly affect the thermal characteristics of an area and overwhelm the thermal behavior of the rocks and soils present. Meteorological conditions at the time of the overflights were acceptable for obtaining these data; there had been no precipitation for at least 96 hours prior to the flights, and winds were low.

The following black-and-white images and color composite of the M^2S data were evaluated: (1) albedo image (Figure 6-55a), (2) daytime thermal infrared (Figure 6-55b), (3) nighttime thermal infrared (Figure 6-55c), (4) temperature difference created by subtracting the nighttime thermal data from the daytime thermal data (Figure 6-55d), and (5) a color composite produced by displaying the daytime thermal as green, the nighttime thermal as blue, and the albedo as red (Figure 6-56).

The separate black-and-white images were examined and found not to be geologically useful in themselves, but were valuable as accessory data to construct and verify a thermal remote sensing model for the Safford area. A more effective method for displaying the data is to combine them into a single image by color compositing (Kahle et al., 1981). In this way, the interrelationship between daytime and nighttime thermal patterns is visible as color differences on a single image.

A remote sensing model was developed for Safford. Highly silicified phyllic host rocks are expected to have higher visible and near-infrared reflectance as well as higher thermal conductivity and density than the surrounding rocks. The higher conductivity and density would produce an effective high thermal inertia. In other words, these siliceous rocks would be relatively cool in the daytime (because the heat from the sun's radiation would reflect and be conducted downward) and warm at night (because the heat would conduct upward). Using similar arguments, the appearance of the various materials on the color composite would have predictable colors on the image. A summary of the behavior and color appearances predicted is shown in Table 6-16.

Table 6-16. Thermal behavior and predicted image colors for various materials

Material	Albedo (red)	Daytime Infrared (green)	Nighttime Infrared (blue)	Image Color
Siliceous rocks	High	Low	High	Magenta–pink
Basalt	Low	High	Low	Green
Propylitic rocks	Low to moderate	Moderate	Moderate	Cyan–gray
Argillic rocks or clay-rich soil	High	High	Low	Yellow
Vegetation	Moderate to high	Low	Low	Red

Evaluation of the color composite (Figure 6-56) verifies this model. Also shown in Figure 6-56 are outlines of the magenta–pink zones (siliceous rocks) seen in the color composite. The areas include the most intensely altered, silicified, pyritized Mesozoic latites and lithic tuffs associated with the Kennecott deposit. Comparison with Robinson and Cook's (1966) maps indicates that these high-albedo, high-thermal inertia areas not only coincide with the pyrite halo, but also delineate an area mapped as "galena and gold occurrences."

The thermal composite delineated this area more effectively than the other data sets examined. Even on the NS-001 images, the galena and gold (pyrite) area is only marginally separable. The thermal analysis demonstrates the usefulness of these data and points to the potential benefits of data from the TM thermal band.

V. Conclusions and Recommendations

A. Evaluation of Data

More than two dozen remote sensing images of the Safford District, acquired from seven different sensors, were evaluated. Objectives were to determine their usefulness as tools for mapping in an environment of deeply buried copper deposits. This was a double-blind evaluation because the most important ground truth alteration and geologic maps were released by Kennecott Corporation only after the digital images were produced at JPL. The Kennecott maps were compiled nearly 20 years ago.

1. Photographic data. Color photographs at vastly different scales were interpreted. The Skylab photographs were at 1:500,000 and 1:750,000 scale, whereas the aerial photographs were at 1:48,000 and 1:24,000, a disparity of 10X to more than 30X.

The reddish tones associated with the leached pyritic zones over the ore bodies were discernible on the Skylab

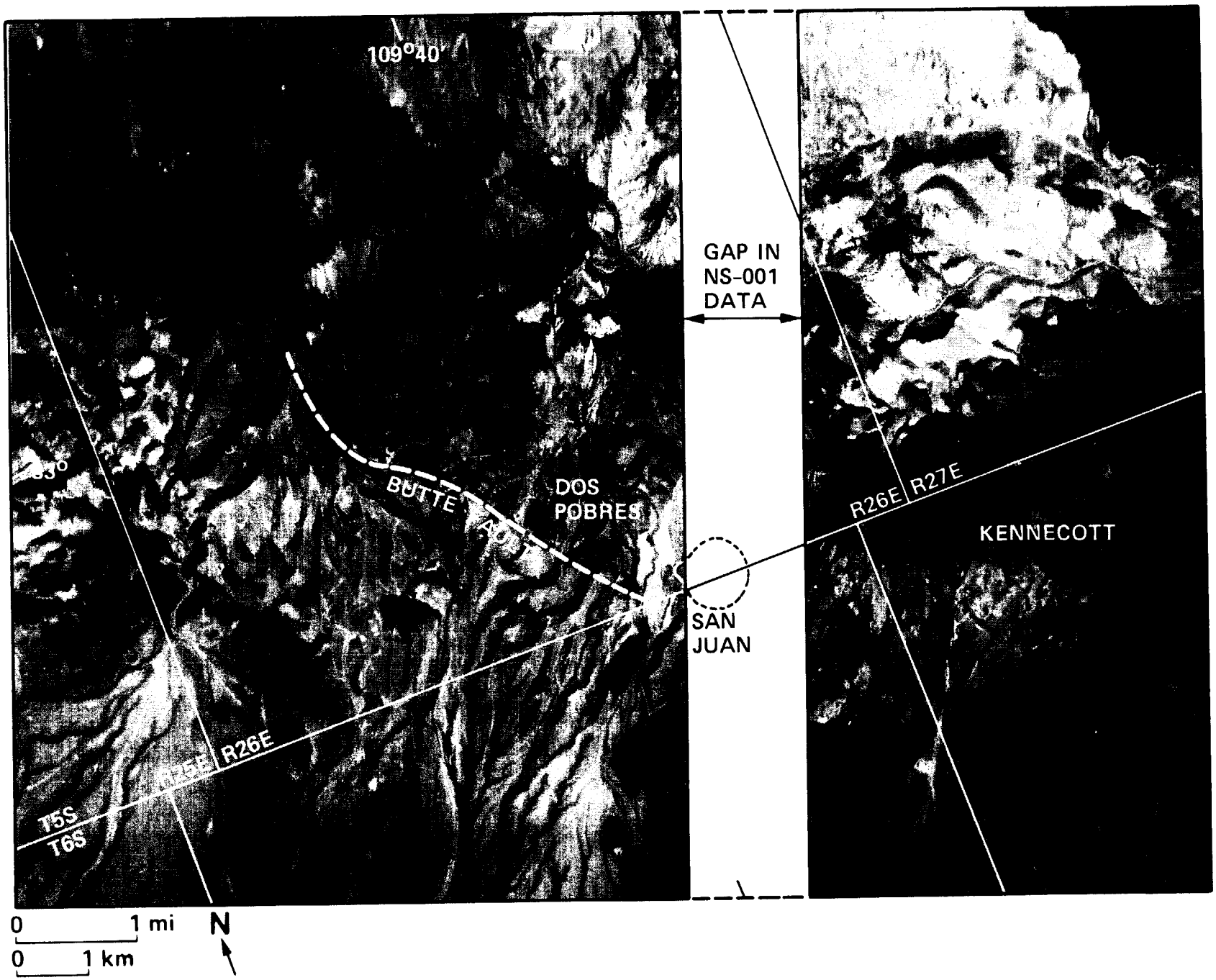

Figure 6-51. Canonically transformed NS-001 data. Components 1, 2, and 3 are displayed as blue, red, and green, respectively.

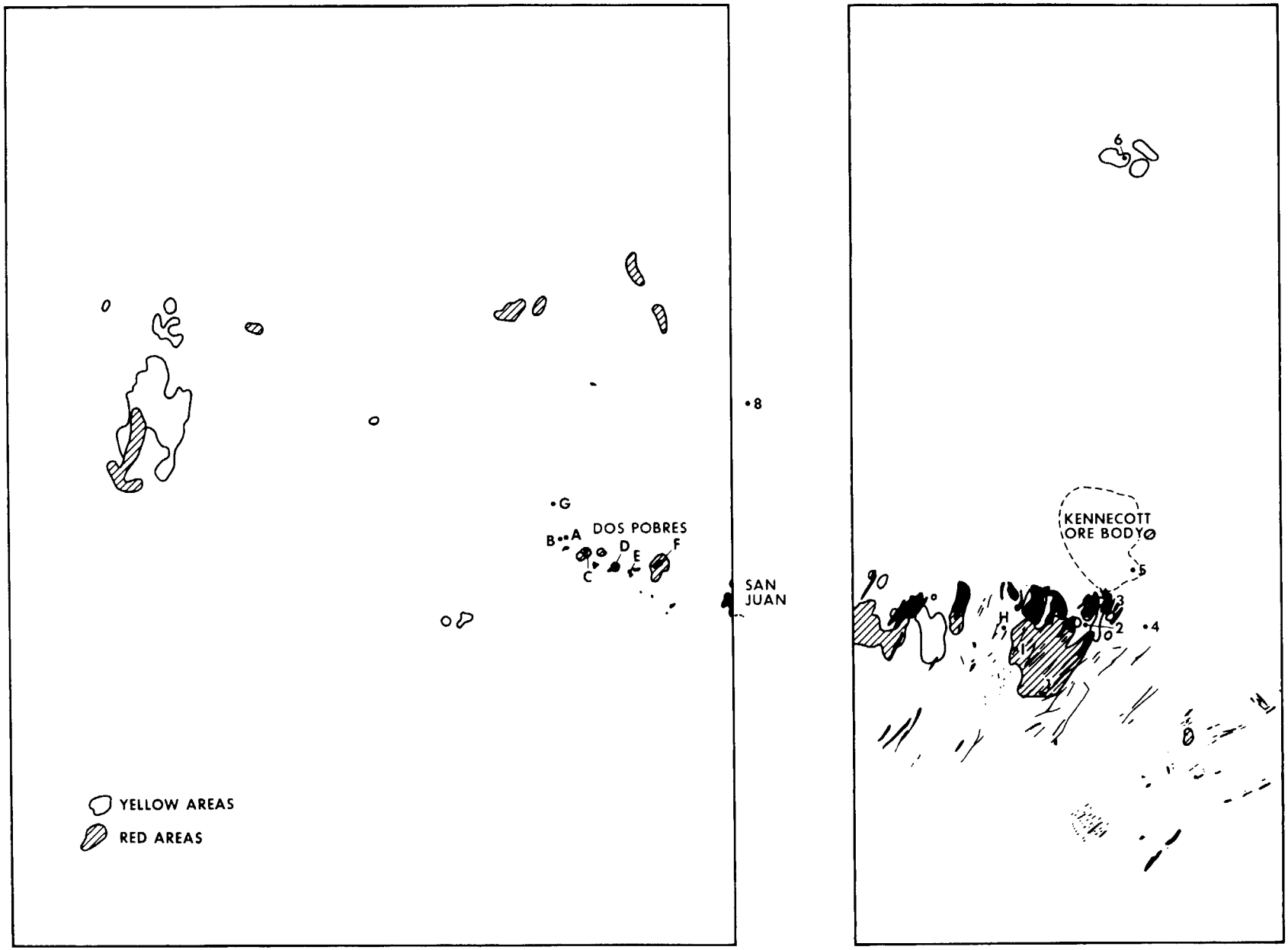

Figure 6-52. Interpretation map of canonically transformed NS-001 image (Figure 6-51) showing areas interpreted to be hydrothermally altered. Heavy black areas are quartz–sericite alteration from Kennecott company map.

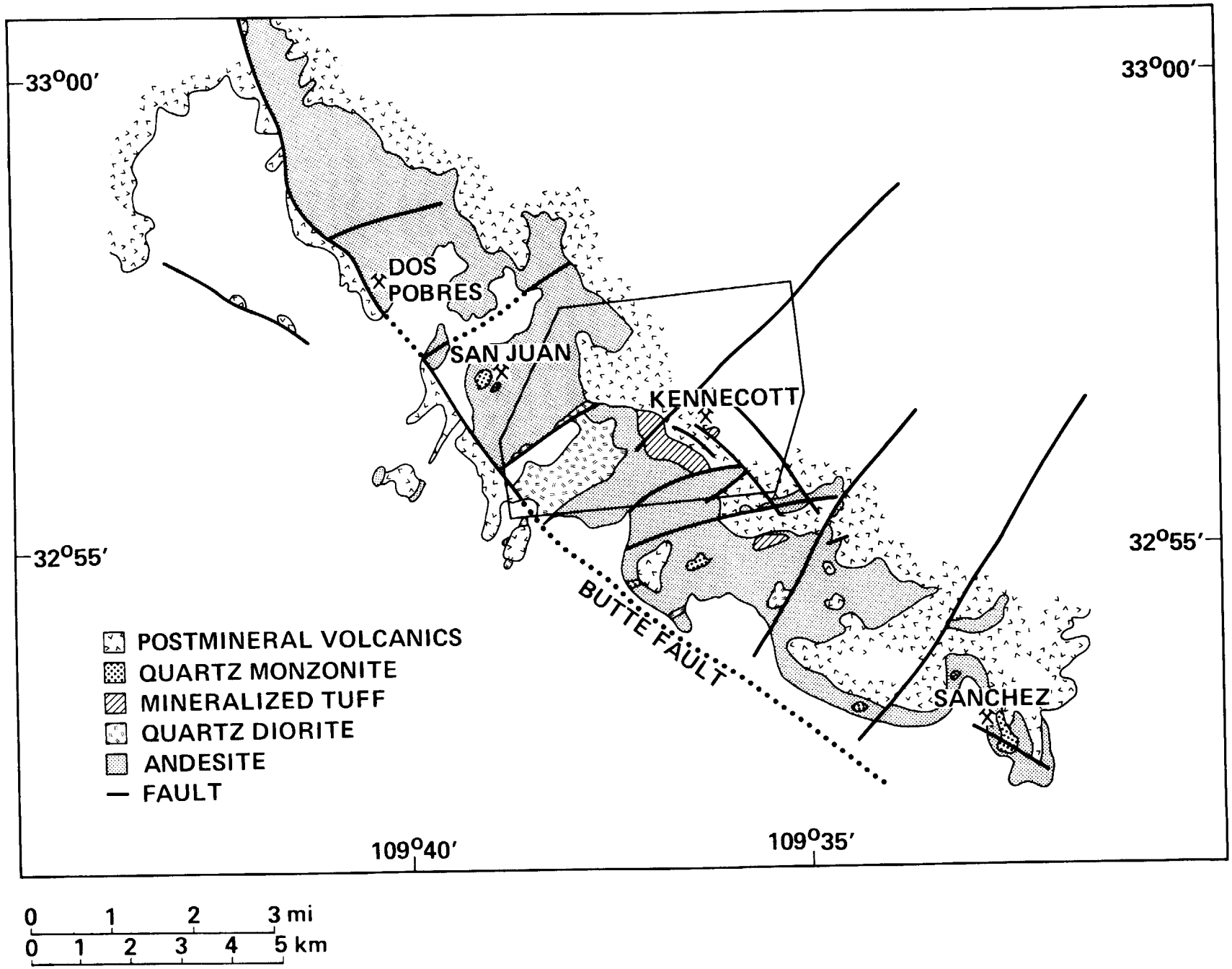

Figure 6-53. General geologic map of Safford District with Kennecott area (Figure 6-54) outlined (Dunn, 1978)

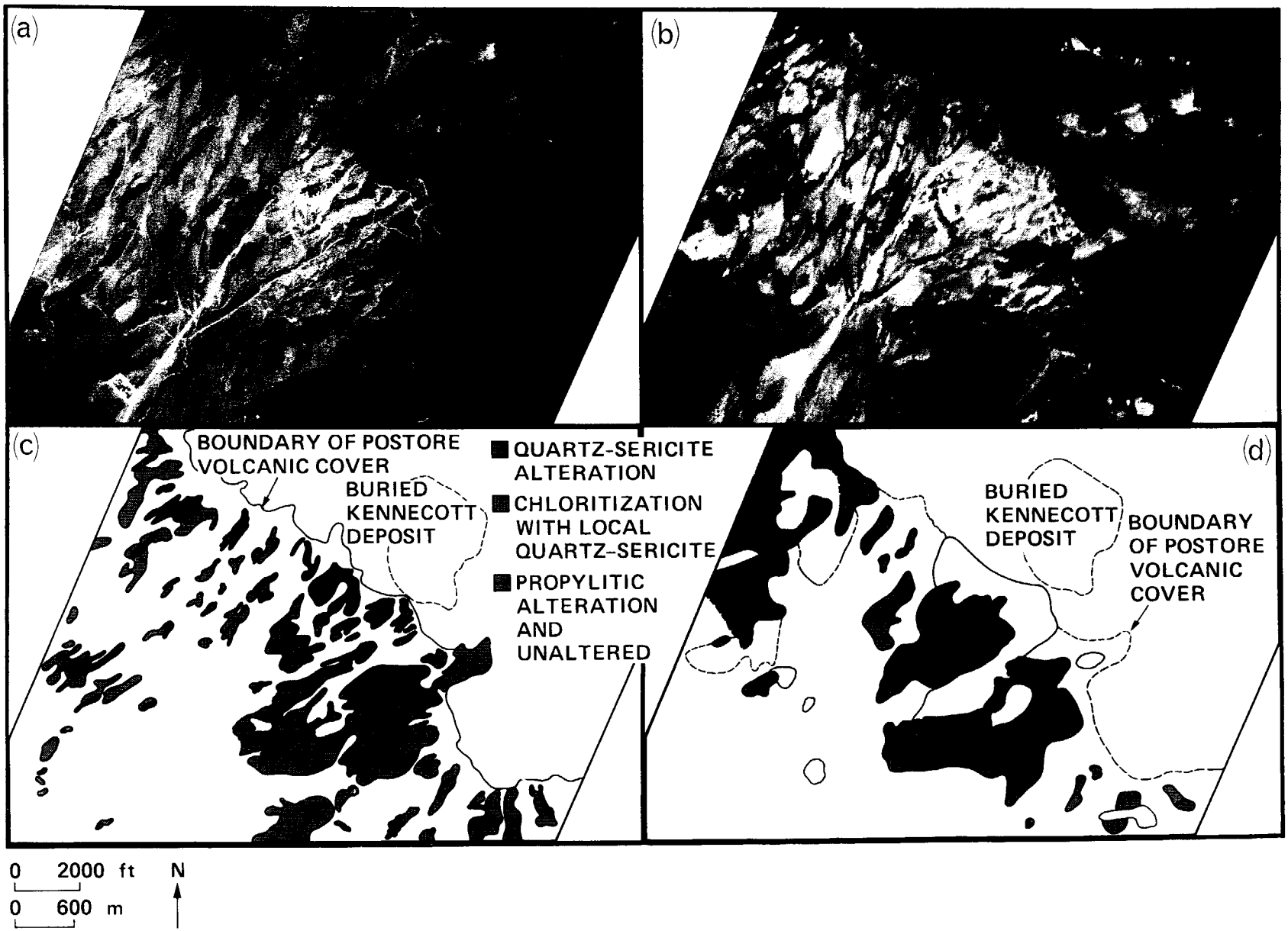

Figure 6-54. Kennecott deposit: (a) color aerial photograph; (b) enlargement of NS-001 canonical transform image; (c) Kennecott alteration map; (d) interpretation of NS-001 image

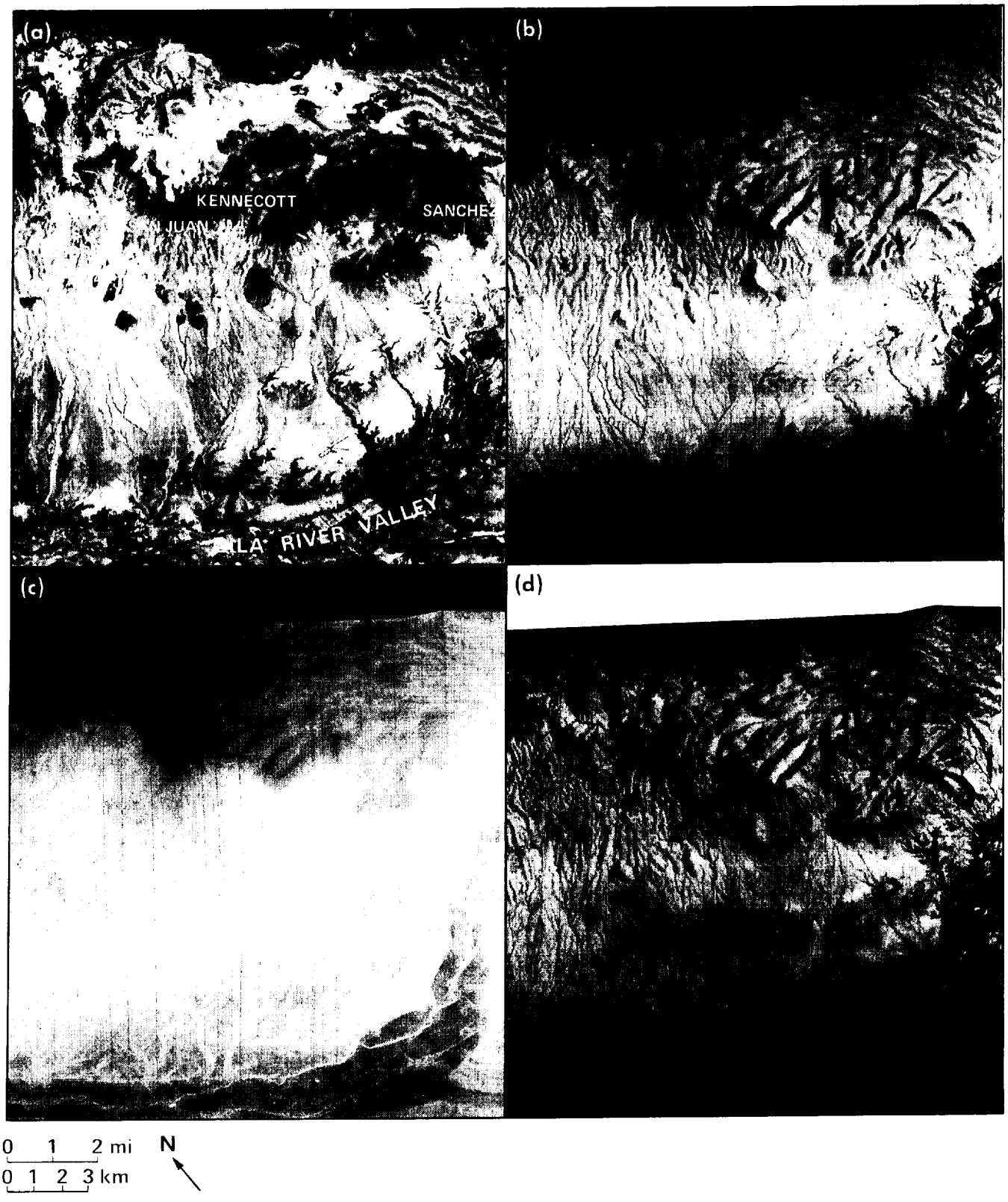

Figure 6-55. M^2S thermal and albedo data: (a) albedo image computed from 10 channels of visible and near-infrared reflectance data; (b) daytime thermal data; (c) nighttime thermal data; (d) thermal difference (daytime thermal minus nighttime thermal). Data acquired August 17–18, 1977.

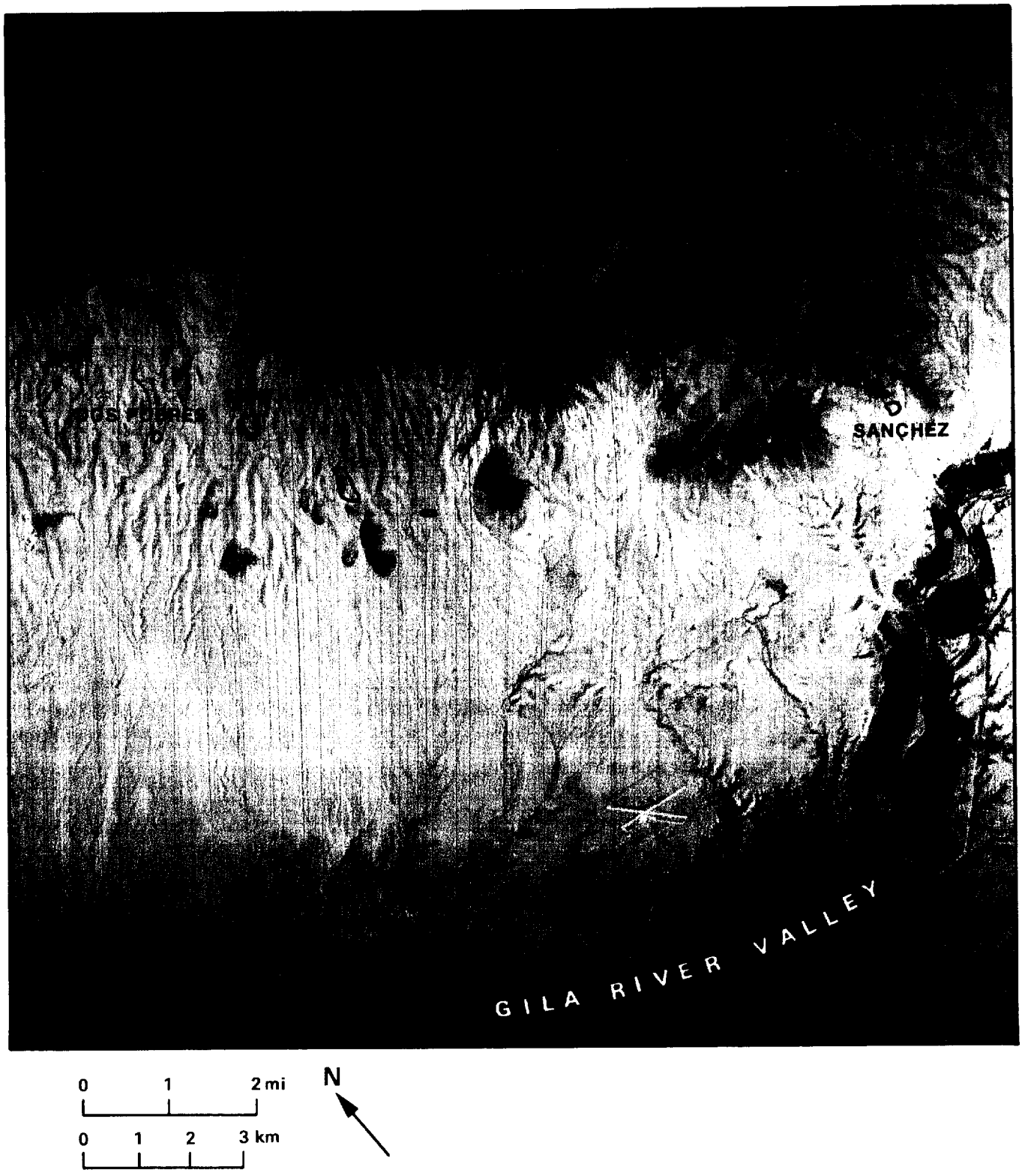

Figure 6-56. Color composite of M^2S thermal and albedo data. Day thermal, night thermal, and albedo data are displayed as green, blue, and red, respectively. Outlined red areas are suspected siliceous rocks corresponding to silicified, pyritized rocks.

photographs only with magnifying lenses. At the aerial photographic scales, these limonitic areas were easily discernible although not as distinct as on the multispectral digital images.

The photographic sets are superior to the other images in two respects: higher spatial resolution and stereopsis. These two attributes make the photographic sensors most useful for geographic orientation and for fine geomorphic details. Color aerial photographs that matched the scale of the electronic digital images were indispensable for navigation and positioning during field checks of the digital images.

The spectral range of color film is not well suited for lithologic discrimination in the Safford District. The latite dikes were expected to be visible due to their high contrast against the Mesozoic andesite that they intruded. However, the weathered rind of the latite had taken on the color of the weathered rind of the andesites, and thus many of the dikes were not visible in the color photographs. The spectral studies show that, in the infrared wavelength regions beyond the capabilities of film, the weathered rinds of these two rocks are easily distinguished by their contrasting reflectivities.

2. Radar data. The airborne SLAR and the Seasat SAR images differ in several ways. The airborne SLAR images are at relatively large scale. The microwave look-angle is toward the north, two images of different polarization (like-polarized horizontal-horizontal [HH] and cross-polarized horizontal-vertical [HV]) were used, and the radar depression angle was shallow (closer to horizontal). The Seasat SAR is at relatively small scale, the look-angle is toward the west, one polarization was used, and the depression angle was closer to vertical.

The most important difference is in the depression angle. The steep depression angle of Seasat SAR causes severe geometric distortion known as layover. The layover effect is detrimental to geologic interpretation of the mountainous area. In the flatter intermountain areas, the steep depression angle fails to enhance small scarps and other subtle features enhanced by shallow-angle SARs. The shallow depression angle of the airborne SLAR produces images wherein the geomorphic features, and thus structural features (and sometimes lithology and alteration), are enhanced. The shallow depression angle causes the backside of mountains to be lost due to the shadowing effect. That shadowing effect can be corrected by the use of multiple look-directions.

When radar images are used for mapping geologic structures, multiple look-directions are advisable for all SAR systems, regardless of depression angle. Topographic lineaments of certain directions relative to the look-angle are enhanced and other directional sets are subdued. Optimum tectonic interpretation requires a directionally balanced data set.

Scale is the least important factor in SAR systems because spatial resolution of the systems is not directly dependent upon the altitude of the sensor as it is with angular systems such as scanners and cameras. Both the Seasat and the airborne radar imaging systems produce images with excellent geomorphic information and good structural information, but were only marginally useful for mapping lithology and alteration. In a poorly mapped or cloud-covered environment, multiple look-angle, multiple or shallow depression angle, satellite or airborne SLAR images would be extremely valuable for the easily interpretable geomorphic and geographic information. For the semiarid, well-mapped Safford District, little additional information was contained in the radar images.

3. Landsat MSS. The Landsat spectral bands and spatial resolution are adequate for mapping the large limonitic (weathered pyritic) zone over the Kennecott ore body. The best image for mapping this anomaly is the PC image, in which the third PC sharply delineates the limonite against the background of the first PC.

A few major lineaments through the district are seen as tonal anomalies. These particular lineaments are more distinctly shown by the PC image than by the ratio image or by the CIR image.

The three-ratio (4/5, 5/6, 6/7) color composite also delineated the same limonitic zone, but as a more diffuse, less obvious anomaly. The Landsat three-ratio image is advantageous in that spectral signatures can be perceived by the color coding. For example, not only is the limonitic zone coded in the expected orange–red tone, but the propylitic Mesozoic andesite outcrop is mapped in this image as a cyan tone as would be predicted from the laboratory spectra of these rocks.

The 4, 5, 7 CIR composite shows the same limonitic zone in the expected yellow tones at about the same distinctiveness as does the CRC image. However, the CIR image does not map the Mesozoic andesite rock as a distinct tone as does the ratio image. Lithological differences in the post-ore volcanic rocks overlying the host rock are the most sharply delineated on the CIR composites. For mapping regional structure, the October CIR Landsat image is quite

effective because the topography is enhanced by the low solar illumination. One of the main limitations of the Landsat MSS is spatial resolution. None of the digital Landsat images showed the limonitic porphyry stocks exposed at the Dos Pobres area, although these were delineated by the color photographs and the multispectral aerial scanner images. These Dos Pobres limonitic zones are about the size of one Landsat MSS pixel (80 m).

In summary, all three digital versions of the Landsat MSS images have their contributions and they should be used together—the fall CIR image for structure and lithology of younger volcanic rocks, the three-ratio composite for spectral modeling and mineralogy, and the PC image for defining the limonitic zones.

4. M²S 11-channel scanner. The spectral range of the visible and near-infrared channels used from the M²S scanner spans a spectral range similar to the Landsat MSS channels. The M²S three-ratio "8/9" image shows the same color coding of geologic features as does the Landsat MSS three-ratio image. However, the image improvement resulting from the eight-fold increase in spatial resolution is dramatic. The small limonitic porphyry outcrops at Dos Pobres are clearly shown on the M²S images, but are not resolved by the Landsat images. This comparison is a clear demonstration of the economic value of increased spatial resolution.

The increased spectral resolution of the M²S produced additional mineralogic information not available from the MSS, including possible detection of copper oxides and mixed alteration zones. The bandwidth of the M²S scanner is less than one-half that of the Landsat MSS, and twice as many M²S spectral bands occupy the same spectral range.

The same advantages were seen in mapping the distribution of soils in the southeastern part of the test site. Information interpretable from the M²S ratio images almost perfectly matched the soil boundaries mapped by the U.S. Department of Agriculture. This analysis suggests that narrow spectral bands, even in the Landsat MSS wavelength region, and high spatial resolution can be of great value for mapping Quaternary geology and pedology.

5. NS-001 Thematic Mapper Simulator. The geologic information content of the NS-001 images was also increased by the eight-fold increase in spatial resolution. As in the M²S images, the limonitic porphyries at Dos Pobres were clearly mapped on all of the NS-001 images.

Compared to the M²S, the NS-001 scanner has less spectral resolution in the shorter wavelength end of its spectral range and, thus, some subtle mineralogic discrimination is lost. However, the extension of the spectral range to include bands centered at 1.6 and 2.2 μm enabled the use of the NS-001 data to directly map clay-type alteration—impossible with the M²S and Landsat MSS sensors. Because the ability of the NS-001 scanner to map phyllic alteration zones did not depend on the presence of limonitic gossans, the NS-001 data enabled us to map more than 90 percent of the phyllically altered areas by virtue of the clay absorption band at 2.2 μm and the increased reflectivity of phyllically altered rock at 1.6 μm.

The three-ratio NS-001 image was particularly useful for spectral modeling, i.e., relating image spectra to mineralogy. The canonical transform image was not useful in spectral modeling, but did separate phyllically altered areas into two subcategories. Used together, the canonical transform and the three-ratio image enabled the phyllically altered zones to be separated into three categories: (1) latites and quartz monzonite, (2) leached, pyritic vent breccia and tuff, and (3) heavily argillized areas. The combination of these two images also resolved possible tonal confusion between certain alteration zones and dense clumps of vegetation. The NS-001 image did not distinctly map the limonite gossans (pyritic zones) within the phyllic zones. The M²S images were the best for sharply defining the ferric and copper oxides.

Structural features were clearly defined on the NS-001 images. In spite of the inferior spatial resolution of the scanner, structural discontinuities were better defined by tonal edges on these images than on aerial photographs.

6. M²S thermal data image. The "thermal inertia" image was generated by combining three images as a false-color composite: an albedo (panchromatic solar reflectance) image with a daytime thermal infrared image and a nighttime thermal infrared image. The hydrothermally silicified rocks of the most intensely altered quartz–sericite (phyllic) halo of the Kennecott deposit were mapped in the thermal inertia image. These silicified areas were delineated by their combination of high albedo and high thermal inertia, i.e., relatively cool daytime temperature and warm nighttime temperature, and were difficult or impossible to detect using other data.

The use of the thermal band of the M²S scanner has demonstrated the increased mineralogical information that can be made available by the addition of thermal wavelengths to remote sensing systems.

B. Signatures for Alteration of Andesitic Rocks

Discriminant analysis was applied to test the accuracy of correctly identifying twelve groups of PFRS field spectra (a total of 111 spectra) using the spectral bands of five different multispectral configurations. The sensor configurations and the results are repeated in Table 6-17.

The percentage correct is closely related to the number of channels. The slight deviation from this progression by the 10-channel M^2S sensor is most probably due to its lack of channels in the 1.6- and 2.2-μm regions.

Although field spectra are undoubtedly best for calibration of sensors or for channel selection, laboratory spectra of discrete rock samples were also used to relate mineralogy and state of weathering to the spectra. Three kinds of spectra were compared for each of twenty surface rock samples collected in the Safford District. The sample mineralogy as derived from X-ray diffraction and examination with a handlens was compared to these spectra. To this data set the image codes were added from two remote sensors, the NS-001 sensor in two-image configurations and the M^2S sensor in three-image configurations. These data were tabulated in a 12-column by 20-row matrix (see Table 6-7).

The weathered rind of most rock samples from the phyllic zone produced different spectra than did the interior, freshly broken surfaces. The largest spectral differences are in the infrared region. This spectral contrast is important to note because remote sensing instruments map spectral signatures of weathered rinds, whereas field geologists usually classify outcrops by freshly broken rock surfaces.

The grinding of samples to produce powdered-rock spectra severely distorts the spectra. It follows that spectra of powdered minerals commonly published in the literature should be used with caution.

The spectra of powdered rocks were compared with spectra of solid weathered rinds of argillized and nonargillized rocks. The spectra of argillic rinds approach the form of the spectra of powdered rocks. Both of these spectral classes have relatively high infrared reflectances. One possible explanation is that the increased reflectance of argillized rock is due to the decreased particle size in the conversion of feldspar to clay. In a system containing two relatively broad bands at 1.6 and 2.2 μm, such as the TM, the increased reflectance at 1.6 μm may be even more useful than the absorption at 2.2 μm for mapping clay. In some of the spectra, the 2.2-μm absorption band does not really deepen with increasing clay content—it remains approximately the same while the 1.6-μm reflectance increases.

Table 6-17. Sensor configurations and results of classification analysis

Sensor	Accuracy, %
30-channel	95
10-channel M^2S[a]	63
7-channel NS-001[a]	65
6-channel Landsat 4 TM[a]	55
4-channel Landsat MSS	46

[a]No thermal channel.

Table 6-7 shows that with the use of five sensor configurations (NS-001 canonical transform and three-ratio transform; M^2S "8/9" ratio, "9/10" ratio, and thermal inertia images) 100 percent accuracy was obtained in identifying the alteration types among the 18 samples having the five image codes. This result concurs with the results of the discriminant analysis indicating that increasing the number of wavelength bands increases geologic information.

C. Recommendations

1. Sensors and sensor combinations. For mapping the alteration zones associated with deeply buried porphyry ore bodies of the type contained in the Safford District, multichannel electronic sensors of the type used in this study are far superior to photography. Although the reflective and thermal infrared channels between 0.7 and 13.0 μm are the most important for geological remote sensing, the visible range (0.4 to 0.7 μm) is effective if the spectral bands are sufficiently narrow and closely spaced.

The field and laboratory studies have shown that, for the most effective geologic mapping, many channels may be needed—on the order of 15 or more. Spectral bands located at reflectance maxima are as important as those located at absorption minima. The spectrometric data show that narrow (0.05 μm or less) bands centered at 0.6 and 0.75 μm and a broader band at 1.6 μm (as in Landsat 4 TM) would be very effective mates for the ferric absorption bands adjacent to these highs at 0.45, 0.65, and 0.90 μm. An ideal geologic multispectral remote sensor might have a band centered at every 0.05-μm interval from 0.45 to 1.25 μm, a single band centered near 1.6 μm, narrow bands at every 0.02 μm from 2.0 to 2.6 μm, and a band at every 1.0 μm from 8.5 to 13.5 μm.

Experience in the field shows that stereo color photographs, nominally scale-matched to the digital images, are an invaluable complement to the digitally processed hard copy. The higher resolution, stereoscopic, natural-color

format of the photographs helps interpretation of ambiguities in the digital images, helps locate target areas for digital classifications, and aids in navigation and positioning during field checks. An aerial camera of suitable focal length to cover the usable swath width of airborne electronic sensors should be included in airborne remote sensing packages. To aid in interpretation of satellite images such as the Landsat 4 TM, the use of higher resolution color or color-infrared image data such as the SPOT sensor (a high spatial resolution French satellite system to be launched in 1984) or high-altitude aerial photography is recommended. In areas where SAR would be beneficial, the use of shallow depression angle, multidirectional SAR is recommended.

2. Digital processing techniques. The simpler and the more complex digital techniques together produce complementary sets of images. Color additive composites are the least expensive and preserve the geomorphic information best. CRCs can be used to enhance and display the spectral character of ground areas. PC and canonical transform images can sometimes be used to map subtle but geologically important spectral classes, but they are the most expensive images to produce.

All three types of images should be produced, but not all at once. The simplest algorithms should be produced first and used for preliminary fieldwork before the more esoteric algorithms are applied.

3. Field verification techniques. Extra copies of the multispectral images should be cut into manageable-size sheets, no larger than 8 x 10 in. (200 x 280 mm) that will easily fit into a notebook or clipboard. The photographs and other images should be laminated between clear plastic. All photographs, maps, and images should be nominally scale-matched (within 10 percent). The digital images will guide the field traverses to examine spectral anomalies.

4. Sequencing of data acquisition, processing, and verification

a. Landsat MSS. A multiseasonal set of standard CIR Landsat MSS images can be used to select the optimal seasonal conditions of vegetation, fog, snow cover, dust, and other environmental factors important to the acquisition of geological remote sensing data. The more expensive but more geologically suited data can be selected by using this relatively inexpensive data set.

b. Aerial survey. An aerial remote sensing survey would then be designed with the instrument array and channel selection whose configuration would depend upon the geological targets and their geological and environmental backgrounds. Experiences with the Safford test case demonstrate that maximizing the number of spectral channels and spectral resolution will maximize the geological information produced. Aerial cameras with color or color-infrared film should be included in the sensor system.

c. Preliminary image processing and interpretation. In a digital image laboratory, color additive and/or color ratio images should be produced with the aid of all appropriate geological information available at that time.

A set of scale-matched multispectral hard copy, aerial photographs, and existing maps should be produced for use in the next stage—field checking and field spectrometry. Preliminary interpretation will delineate target areas, road access, and other information useful for reconnaissance.

d. Preliminary fieldwork. With the scale-matched set of digital images, aerial photographs, and maps in hand, the remote sensing geologist should conduct reconnaissance traverses guided by targeted anomalies shown on the images. These traverses include the use of a field spectrometer and the collection of surface samples for later laboratory analysis.

e. Laboratory work. The extent of laboratory work depends upon the degree of development of the geological model in the target area. If the environment is not well understood, the analysis of the samples might include reflectance spectrometry of the solid weathered surface, X-ray diffraction, X-ray fluorescence, wet chemical analysis, trace metal chemistry, and petrography.

f. Final image processing and secondary interpretation. The spectral data collected with the field spectrometer can be used to calibrate the multispectral data for canonical analysis and other higher level digital processing. The geological knowledge gained on the field traverses and the results of the laboratory analyses should be used to synthesize a geological remote sensing model that will be applied to the development of algorithms for the production of the final digital images.

An interpretive map would be constructed from the final digital image (or images). Potentially mineralized areas or important areas that are difficult to interpret are targeted to help direct the final field checks.

g. Final field checks. With field-configured copies of the final digital images added to the remote sensing package, the field geologist is now ready to take the package to the field. He will check problem areas and mineral targets and reinterpret the images as required; additional samples may be collected; geologic information is added to the maps. Detailed groundwork can then begin in selected areas.

Acknowledgments

Anthony Hauck, who represented Phelps Dodge Corporation on the Geosat porphyry copper panel, released proprietary geologic maps of the Dos Pobres property and of the district (later published by Langton and Williams, 1982). Phelps Dodge also provided access to Dos Pobres for our field measurements, and A. M. Schern and David Bogges provided field guidance and assistance on the property. Phelps Dodge and ANAMAX Corporations paid for laboratory spectral measurements of samples taken from the test site. Phelps Dodge provided funds for Lepley's travel to the Test Case Workshop in Denver. G. D. Van Voorhis released proprietary geologic and alteration maps of the district and a structure map of the Kennecott (Safford) deposit, compiled by Annan Cook. Through Neal Gamble and Don Fountain, Kennecott provided access to their deposit, and Annan Cook, who compiled the Kennecott maps, gave us field guidance during our sampling and field observations on the Kennecott property.

Douglas Pease, State Soil Scientist of the USDA's Soil Conservation Service in Phoenix, made available unpublished mylar orthophotographs and soil maps of the area.

References

Abrams, M., R. Ashley, L. Rowan, A. Goetz, and A. Kahle (1977). Mapping of hydrothermal alteration in the Cuprite Mining District, Nevada, using aircraft scanner images for the spectral region 0.46 to 2.36 μm. *Geology, 5,* 713–718.

Anderson, C., E. Scholz, and J. Strobell (1955). Geology and ore deposits of the Bagdad area, Yavapai County, Arizona. *U.S. Geol. Surv. Prof. Pap. 278.*

Blake, D. W. (1971). *Geology, alteration, and mineralization of the San Juan Mine area, Graham County, Arizona.* Master's thesis, University of Arizona, Tucson.

Blom, R., M. Abrams, and H. Adams (1980). Spectral reflectance and discrimination of plutonic rocks in the 0.45 to 2.45 μm region. *J. Geophys. Res., 85,* 2638–2648.

Conel, J., M. Abrams, and K. Baird (1980). Uranium: Spectral discrimination of alteration phenomena in sediments. *Mod. Geol., 7,* 115–135.

Davis, J. (1973). *Statistics and data analysis in geology.* New York: John Wiley & Sons.

Dixon, W. (Ed.) (1970). BMD07M stepwise linear discriminant analysis. *BMD biomedical computer programs.* Berkeley: University of California Press, 233–253.

Dunn, P. (1978). Geologic structure of the Safford District, Arizona. *Ariz. Geol. Soc. Digest, XI.* Tucson: University of Arizona Press, 9–15.

Ford, J., R. Blom, M. Bryan, M. Dailey, T. Dixon, C. Elachi, and E. Xenos (1980). *Seasat views North America, the Caribbean, and Western Europe with imaging radar* (JPL Publication 80-67). Pasadena, California: Jet Propulsion Laboratory.

Horsnail, R. (1978). Safford District, Graham County, Arizona. *J. Geochem. E., 9,* 241–243.

Hunt G., and R. Ashley (1979). Spectra of altered rocks in the visible and near infrared. *Econ. Geol., 74,* 1613–1629.

Hunt, G., and J. Salisbury (1970). Visible and near-infrared spectra of minerals and rocks: I. Silicate minerals. *Mod. Geol., 1,* 283–300.

Hunt, G., J. Salisbury, and C. Lenhoff (1971). Visible and near-infrared spectra of minerals and rocks: III. Oxides and hydroxides. *Mod. Geol., 2,* 195–205.

Hunt, G., J. Salisbury, and C. Lenhoff (1973). Visible and near-infrared spectra of minerals and rocks: VI. Additional silicates. *Mod. Geol., 4,* 85–106.

Jennrich, R. (1977). Stepwise discriminant analysis. In K. Enslein, A. Ralston, and H. Wilf (Eds.), *Statistical methods for digital computers, Volume III of mathematical methods for digital computers.* Wiley-Interscience Publication, 76–95.

Kahle, A. B., J. P. Schieldge, M. J. Abrams, R. E. Alley, and C. J. LeVine (1981). *Geologic application of thermal inertia imaging using HCMM data* (JPL Publication 81-55). Pasadena, California: Jet Propulsion Laboratory.

Langton, J., and S. Williams (1982). Structural, petrological and mineralogical controls for the Dos Pobres orebody. In S. Titley (Ed.), *Advances in geology of the porphyry copper deposits.* Tucson: University of Arizona Press.

Lepley, L. K. (1978). *Geophysical lineaments of Arizona* (Technical Report). University of California, Los Alamos National Laboratory.

Lowell, J. (1978). Case histories of discoveries. *Ariz. Geol. Soc. Digest, XI.* Tucson: University of Arizona Press, 175–178.

Lowell, J, and D. Guilbert (1970). Lateral and vertical alteration-mineralization zoning in porphyry ore deposits. *Econ. Geol., 65*(4), 373–408.

Lyzonski, J. C., J. S. Sumner, C. L. V. Aiken, and J. S. Schmidt (1980). *The complete residual Bouquer gravity anomaly map of Arizona (IGSN71).* Tucson: Arizona Bureau of Geology and Mineral Technology. (Scale 1:1,000,000)

MacDonald, H. (1980). Techniques and applications of imaging radars. In B. Siegal and A. Gillespie (Eds.), *Remote sensing in geology.* New York: John Wiley & Sons, 297–336.

Podwysocki, M., F. Gunther, and H. Blodget (1977). *Discrimination of rock and soil types by digital analysis of Landsat data* (Report X-923-77-17). Greenbelt, Maryland: Goddard Space Flight Center.

Readdy, L. A. (1978). *Porphyry copper and hydrothermal alteration investigation* (Final Report to U.S. Geological Survey). (Report PB-291205)

Rehrig, W., and T. Heidrick (1976). Regional tectonic stress during the Laramide and late Tertiary intrusive periods, Basin and Range Province, Arizona. *Ariz. Geol. Soc. Digest, X.* Tucson: University of Arizona Press, 205–228.

Robinson, R. F., and A. Cook (1966). The Safford Copper Deposit, Lone Star Mining District, Graham County, Arizona. In S. Titley and C. Hicks (Eds.), *Geology of the porphyry copper deposits.* Tucson: University of Arizona Press.

Rowan, L., P. Wetlaufer, A. Goetz, F. Billingsley, and J. Stewart (1974). Discrimination of rock types and detection of hydrothermally altered areas in south-central Nevada by the use of computer-enhanced ERTS images. *U.S. Geol. Surv. Prof. Pap. 883.*

Sauck, W., and J. Sumner (1970). *Residual aeromagnetic map of Arizona.* Tucson: University of Arizona Press. (Scale 1:1,000,000)

Soha, J., and A. Schwartz (1978). Multispectral histogram normalization contrast enhancement. *Proceedings of the 5th Canadian Symposium on Remote Sensing,* Victoria, B.C., August 1978, 86–94.

Titley, S. (1982). *Advances in geology of the porphyry copper deposits.* Tucson: University of Arizona Press.

Titley, S., and C. Hicks (Eds.) (1966). *Geology of the porphyry copper deposits.* Tucson: University of Arizona Press.

U.S. Department of Agriculture (1970). *Soil survey, Safford area, Arizona.* Washington, D.C.: U.S. Government Printing Office.

U.S. Department of Agriculture (1973). *General soil map, Graham County, Arizona* (M7-L-22961-1). Portland, Oregon: USDA–SCS.

Wiersma, D., and D. Landgrebe (1980). Analytical design of multispectral sensors. *IEEE Trans. Geosci. Rem. Sens., GE-18*(2), 180–189.

Section 7

Uranium Commodity Report

John W. Gabelman
Utah International, Inc.
San Francisco, California

James E. Conel
Jet Propulsion Laboratory

7-14. Distri
11-ch
7-15. Canni
uranit
plotte
(and C
patter

Tables

7-1. Chara
7-2. Backg
7-3. Data s

Section 7
Uranium Commodity Report

Contents

I. Introduction 7-1
A. Background and Objectives 7-1
B. Program and Site Selection 7-1

II. General Geology of Uranium Deposits 7-3
A. Uranium Occurrence Compared to Other Resources 7-3
B. Geochemical Behavior of Uranium and Its Accumulation Into Mineral Deposits 7-5
C. Significance of Rock Alteration 7-5
D. Forms of Uranium Occurrence 7-6
E. Major Types of Uranium Deposits 7-8
1. Veins 7-8
2. Sandstone impregnations—Uravan mineral belt type 7-9
3. Large continuous sandstone impregnations 7-12
4. Quartz–pebble conglomerates 7-14
5. High-temperature replacement disseminations 7-15
6. Unconformity-related deposits 7-16

III. Remote Sensing in Uranium Exploration 7-18
A. Case Histories 7-20
1. Mapping of alterations using satellite images 7-20
2. Other spectral, textural, and structural studies 7-22
B. Summary 7-23

IV. Geologic Overview of Test Sites 7-24
A. Lisbon Valley District 7-24
B. Copper Mountain District 7-26

V. Summary of Test Site Results 7-27
A. Nature and Utilization of Remote Sensing Information 7-27
B. Lisbon Valley 7-28
C. Copper Mountain 7-29

PRECEDING PAGE BLANK

VI. Remote Sen

A. Lisbon V

1. Explo
2. Inform
3. Timin

B. Copper M

1. Explo
2. Inform
3. Discus

VII. Extrapolatio

A. Bleachin

B. Iron Oxi

VIII. Implication

IX. Direction of

X. Summary

References

Figures

7-1. Area
7-2. Area
7-3. Gene
7-4. Plan mine and t
7-5. Sche vana
7-6. Sche boun end c
7-7. Gene sand Wyo
7-8. Sche leadi fault
7-9. Diag of fr
7-10. Geol nifer of va
7-11. Gene ore b
7-12. Sche the e
7-13. Distr depo Lisb

Section 7
Uranium Commodity Report

I. Introduction

A. Background and Objectives

The Joint NASA/Geosat Test Case Project has focused on applying remote sensing methods to geologic mapping and exploration. The purposes were to define how remote sensing could be used for geologic mapping and to determine how these methods could potentially contribute to resource exploration. This commodity report summarizes the application of multispectral imaging techniques to uranium exploration. Detailed results of all phases of these investigations, including geologic mapping and image analysis, are presented in accompanying reports for the two uranium test sites, Lisbon Valley, Utah (Section 8), and Copper Mountain, Wyoming (Section 9).

In past remote sensing applications, Landsat Multispectral Scanner (MSS) data have been applied to uranium exploration in two ways: (1) through the mapping of surface-exposed iron-oxide alteration effects and (2) through the mapping of the variations in lineament or vegetation density as a guide to unravelling stratigraphy or structure related to uranium distribution. These applications were hampered by the poor spatial resolution (~80 m) and limited (wide-band) spectral sampling of Landsat MSS data.

Present applications represent a significant extension of the remote sensing method beyond that usually undertaken with satellite data. With NASA's aircraft-mounted multispectral scanners, surface spatial resolution over the sites has improved by a factor of five to ten, thus making the image data more nearly comparable to aerial photography in spatial resolution. The spectral observation interval of 0.4 to 2.4 μm, with spectral channels as narrow as 0.04 μm, significantly improves classification, discrimination, and identification beyond that possible with Landsat MSS and perhaps conventional aerial photographs.

From a geologic point of view, the new uranium test site applications provide a challenge in relating the remote sensing data to the genesis of ore deposits. New geologic insights have emerged at both sites, somewhat reconciling existing empirical exploration models with surface geology and thereby developing a better appreciation of both the strengths and weaknesses of remote sensing data.

B. Program and Site Selection

The uranium test site selection committee met in 1977 to select sites for the Project. The criteria for site selection were as follows:

(1) Districts rather than single deposits were to be selected to ensure some generality of the results. These would include deposits of large size and grade to maximize geologic contrasts with surrounding rocks and to provide large targets. Different types of uranium occurrences would be represented among the districts. Ore bodies would be present at a sufficiently shallow depth to permit study of both the deposits and halo, or "umbrella," effects in the outcrops over them. The districts would present maximum exposures of a diversity of rock type, structure, and, if possible, alteration.

(2) Cultural disturbances were to be minimal, though some effect was recognized to be inevitable. Typically, active uranium-producing areas contain drill pads, access roads, mine dumps, and production facilities. These ordinarily form a small portion of the total surface, but the effects are detectable at the resolution of satellite or aircraft scanner observations and thus need to be accounted for. For example, exploration drill sites can be spaced at intervals from a few meters to a few hundred meters, although confined mainly to regions of ore accumulation in the subsurface. In these places, together with the

connecting access roads, the vegetation cover and topsoil are often removed or completely disturbed, exposing partially weathered or fresh rocks beneath. Areas of older mining activity, since abandoned and partly or completely revegetated, may be difficult to recognize at the present time. Most of these disturbances may be identified and accounted for in the interpretations by employing aerial photographs or by making field observations.

(3) The districts were to be of largely single controllership, preferably by a Geosat member company, to assure access for fieldwork in the test site areas, to minimize requests for proprietary data, and to avoid problems of disclosure or land ownership should new areas of exploration interest emerge during the investigation.

(4) Sufficient background data were to be available to permit evaluation of the remote sensing results. Such information would include surface and subsurface geologic maps, distributions of mineralization and rock alteration, soil type, and vegetation communities.

The array of districts initially considered was based on the following considerations. Nearly 95 percent of domestic uranium production has come from large lenses and pods that are strata-bound in nearly flat sandstone beds and 5 percent in steep, tabular, vein deposits (Gabelman et al., 1981). Other exotic deposits include small replacement lenses in limestone and large, low-grade, replacement disseminations in volcanic tuff or granite. Accumulations termed *resources*—referring to much less quantified and even undiscovered deposits—include an increasing proportion of large, low-grade, replacement disseminations, but these are largely unexplored and their characteristics poorly known.

Most veins and limestone replacement lenses are too small to be resolved spatially in satellite images (30 to 80 m), but they might be detected at resolutions attainable with aircraft scanners ($\sim$15 m). Some veins are sufficiently long and recognizable to be the object of geometric fault/lineament studies.

Those test sites selected also had to be suitable for spectral studies of the rock types and rock alteration products present. The uranium mineralization process is thought to alter large volumes of rock to new minerals and to form ore bodies as "plums in a pudding" (Gabelman and Boyer, 1958). This process usually generates a marked contrast between the altered uranium-bearing "matrix" and its unaltered surroundings. Thus, districts containing small ore lenses in sandstone or veins may be discriminated by analyzing the altered matrix using the spectral reflectance properties of altered rocks.

The chief task of the uranium subpanel was to identify and select a few districts of widely differing characteristics and deposit types. The types selected included the following:

(1) A district of "giant" ore bodies in sandstone (Lisbon Valley, Utah)

(2) A district of many small, scattered ore bodies in sandstone (Uravan mineral belt, Colorado)

(3) A district of large replacement disseminations in crystalline intrusive rocks (granite) (Copper Mountain, Wyoming)

(4) Districts of large replacement or impregnation disseminations in volcanic tuff or tuffaceous sediments (Date Creek Basin, Arizona; McDermitt Caldera, Nevada; Lakeview, Oregon)

(5) A district containing large buried deposits (known by drilling) but whose surface had not yet been disturbed by mining activities (east side of San Juan Basin, New Mexico)

Using the criteria given earlier, the subpanel selected two sites, Copper Mountain, Wyoming, and Lisbon Valley, Utah.

The characteristics of these deposits are given in Table 7-1. The two test areas have deposits that represent very different types of apparent alteration, host rocks, structural or stratigraphic environment, and apparent age of deposits. In both areas, uranium ranges from near-surface to moderate depth. Both areas also are covered by similar vegetation communities of approximately the same areal density.

Cultural disturbances at the sites are locally intense, especially in areas of active mining or exploration. The disturbances related to mining consist of drill roads, exploration drill sites, mine workings, haulage roads, dumps, and production facilities. Oil wells and refining facilities are present at Lisbon Valley but lie mostly outside the mining areas.

Of far greater areal significance at the Lisbon Valley site, though not in areas of active mining, is the disruption of the indigenous piñon–juniper vegetation community by a Bureau of Land Management (BLM) rangeland reclamation program. The measures taken in this program consisted of removing the tree (and shrub) cover, stacking slash material at local sites, and subsequently reseeding the areas with range grasses. The affected areas are several square kilometers in area and needed to be accounted for mainly

Table 7-1. Characteristics of the uranium test sites

Characteristic	Lisbon Valley, Utah	Copper Mountain, Wyoming
Latitude/longitude	38°12′ N/109°15′ W	43°23′ N/107°53′ W
Test site area, km^2	200	400
Nature of deposits		
Type	Strata-bound	Stockwork or vein (supergene?)
Host rock	Sandstone of Triassic age	Archean granite
Age	Triassic (?)	Tertiary
Depth, m	Few to 200	15 to 100
Alteration	Bleaching, leaching of Fe^{+3} oxide	Propylitic + limonitic/ hematitic
Production (or reserves) of U_3O_8	> 70,000,000 lbs	Proprietary (probably < 6,000,000 lbs)
Mineralization	Uraninite $(U^{+4}_{1-x} U^{+6}_{x}) O_{2-x}$ Coffinite $(U(SiO_4)_{1-x}(OH)_{4x})$	Sooty pitchblende
Geologic setting	Flanks of salt anticline	Crushed and fractured zones along normal faults above overthrust
Climate	Semiarid	Semiarid
Vegetation (estimated % cover)	Piñon-juniper and sage grassland (0 to 70)	Juniper and sage grassland (30)

in geological mapping from image data. Apart from grazing by cattle and wildlife, vegetation is essentially undisturbed at the Copper Mountain site.

All cultural effects related either to mining activity, petroleum production, or rangeland reclamation can be identified and accounted for from aerial photographs at both test sites.

A variety of topographic, geologic, soil and vegetation maps, plant species lists, and geophysical and geochemical surveys was available or was acquired during the course of the investigation. These are listed in Table 7-2. Refer to individual test site reports for details of many of these surveys.

II. General Geology of Uranium Deposits

A. Uranium Occurrence Compared to Other Resources

The technology for discovering valuable deposits of any mineral resource depends on the mode of occurrence and whether that mode is suited to economic exploitation. There are three broad geometric types. The simplest type is the planar distribution, such as extensive sedimentary layers of coal, phosphate, or limestone. Veins along faults are steeply inclined forms of such planar bodies but are much less continuous. The second type, of intermediate complexity, is relatively restricted pools of liquid, gas, hydrocarbons, or their solid counterparts. Mineral bodies of planar shape but of limited lens-like extent, such as replacements of limestone, are of this type. The third type, of greatest complexity, is concentrations of trace elements (including uranium). Such deposits are geologically rare. They are of very restricted geographical distribution, of limited size, and usually of irregular shape.

A variety of geological processes are capable of concentrating any trace element into economic deposits, and different groups of processes are responsible for different elements. Useful recognition parameters for valuable trace-element deposits appear complex. A few processes are eventually recognized as possible candidates for the genesis of economic deposits. These interpreted processes and their results become models that routinely are preferred in exploration.

Like most trace elements, uranium is present in extremely low abundances, averaging 2 to 3 ppm in most rocks. To constitute an economic deposit, uranium must be concentrated by at least three orders of magnitude above these levels. Uranium deposits are mostly created by chemical/geological processes in already-formed rocks and thus are epigenetic deposits, as opposed to syngenetic deposits that form contemporaneously with the rocks. The genetic ingredients required to form a valuable deposit are (1) a

Table 7-2. Background data for uranium test site investigations

Data	Lisbon Valley, Utah[a]	Copper Mountain, Wyoming[a]
Topographic maps		
Regional (1:250,000)	P	P
Test site (1:24,000)	P	P
Detail (1:12,000)	N/A	Pr/A
Geologic maps		
Regional (1:250,000 and 1:500,000)	P	P
Test site (1:24,000)	P	P
Uranium occurrence data		
Discovery	P	P
Production	P	N/A
Reserves	Pr	Pr
Subsurface structural data from oil well, drill hole and seismic	P	P
Soil maps (1:4,470 and 1:250,000)	P	P
Vegetation community maps (1:4,470 and 1:33,000)	P	Pr/A
Field vegetation surveys, species, and/or abundance	P	Pr/A, S
Field/laboratory spectral reflectance surveys	S	S
Geophysical surveys		
Gravity	P	P
Magnetic	P	Pr/A
Soil and bedrock geochemistry		
X-ray diffraction mineralogy	S	S
Elemental geochemistry	N/A	Pr/A
Ore deposits and petroleum		
X-ray diffraction mineralogy	S	N/A
Carbon isotopes	S	N/A
Sulfur isotopes	S	N/A
Previous remote sensing studies	N/A	P

[a] P Public information, including maps, reports, papers and unpublished theses
S Study conducted during this investigation
Pr/A Proprietary but available for this investigation
Pr Proprietary; not available for this investigation
N/A Not available or not acquired

uranium source, (2) a mobilization mechanism, (3) a transportation mechanism, (4) a concentration mechanism, and (5) a fixation (precipitation) mechanism. Together, these constitute the mineralization process. The same process and ingredients are valid for a number of economically valuable elements besides uranium. For uranium the process is complicated by the variety of geological environments in which it occurs and by the character of host rocks, their composition, geometry, and location. The combination of mineralization and environmental conditions that produces a valuable deposit is unusual enough for both the process and its products to be relatively rare—hence the high deposit value.

Uranium differs from other trace elements by being of newest utility to society. Other than radioactivity, its most significant property is solubility in the oxidized (U^{+6}) state. High solubility makes uranium very mobile, especially in near-surface environments. Like better-known soluble elements (e.g., iron, manganese, copper), uranium thus forms many compounds in a large variety of environments. Probably not all modes of deposition have been recognized, and some are not fully understood (e.g., the evaporitic uraniferous "calcretes"). Historically, the recognized forms of uranium concentration progressed from veins to pegmatities, sandstone impregnations, quartz–pebble conglomerates, limestone replacements, replacement disseminations,

and rich breccia masses (described in Paragraph II.E). Each form was found to be more prolific than its predecessors, and the model describing each became the preferred model for further exploration.

Uranium exploration has been conducted by surface sampling and drilling in areas offering a suitable combination of environmental factors. A number of new deposits of both old and new types were discovered during the exploration surge of the 1970s based on criteria learned from deposits discovered during the boom of the 1950s. However, the number discovered was small compared to the earlier boom, and the aggregate value of the new discoveries fell far short of the amount spent collectively by industry in discovering them. Also, these deposits are probably not representative of the number of each type nor of the number of types that exist. Thus, knowledge of uranium occurrence is still incomplete, and discovery opportunities are still favorable when suitable exploration incentives prevail.

The following descriptions of the general features of uranium deposits and districts are drawn from field experience since 1953, and some descriptions are unpublished. During that interval, uranium became the most studied and documented of all economic mineral commodities, and a huge literature has resulted. Some examples are the proceedings of the International Atomic Energy Agency Vienna conferences and the many reports prepared by Bendix Field Engineering Company, national laboratories (Livermore, Berkeley, Los Alamos, Oak Ridge), and other contractors for the U.S. Department of Energy during the National Uranium Resource Evaluation Program. A recently published summary of the genesis of the important types of uranium deposits has been given by Nash et al. (1981).

B. Geochemical Behavior of Uranium and Its Accumulation Into Mineral Deposits

The lithophile element uranium and its close geochemical companion thorium are delivered to the crust in peralkaline and calc-alkaline magmas. These elements crystallize together in a variety of late magmatic minerals. Transfer from initial distributions in the mantle is accomplished with uranium in the form of volatile halide species (F, Cl) and is aided by the chemical incompatibility of uranium in common rock-forming materials of the crust and mantle. Possibly 50 to 75 percent of the Earth's uranium has been transferred (Gabelman, 1977) along with thorium and other incompatible elements.

Uranium and thorium thus become concentrated in the final aqueous and volatile residual fluids accompanying magmatic crystallization. Fixation of uranium occurs in the chemically reduced (U^{+4}) state in which it is insoluble. Uranium and thorium in their original crustal state are most associated with the granite-rhyolite clan of igneous rocks, the final products of magmatic differentiation.

Uranium and thorium locally are concentrated together into primary high-temperature epigenetic deposits as disseminated replacements and veins. The bulk of juvenile uranium delivered to continental rocks becomes disseminated in magmatic rocks such as alkaline granites and rhyolitic tuffs at a level of 3 to 5 ppm. That portion delivered through ocean-ridge fault zones at spreading tectonic-plate boundaries in alkaline basalts mostly ends up in seawater as suggested by the low abundances observed (0.14 ppm) in oceanic basalts.

Once resident in the continental crust, soluble uranium, but not thorium, can be mobilized through leaching and erosional processes. Such mobilization usually results in still greater dispersion. However, given suitable environmental conditions and a precipitation mechanism, uranium can be concentrated secondarily into economic deposits. The concentration rather than further dispersion of mobilized uranium is more difficult and depends greatly on local geologic conditions. For crustal uranium, the critical ingredients for concentration during lateral (laterogene) or downward (supergene) migration are (1) a suitable liberation agent or mechanism, (2) suitable transport agents and pathways, and (3) suitable precipitants, which in simple cases need be only a reductant to change soluble U^{+6} to the insoluble U^{+4} state. Argument surrounds the distinction between deposits of hypogenic (primary) uranium (separated from thorium prior to concentration) and deposits of supergenic or laterogenic (recycled) uranium. The preponderance of opinion lies with recycling of crustal uranium because the processes are simpler.

C. Significance of Rock Alteration

Alteration accompanying metallic ore deposition is a consistent associate of magmatic-related or mantle-emanation-related epigenetic mineralization processes (Meyer and Hemley, 1967). Altered-rock halos around ore bodies or altered matrices of districts resulting from these processes have been useful guides in metal exploration. An important type of alteration accompanying uranium mineralization produces chlorite, epidote, albite, clay, silica, quartz sericite, and secondary alkali feldspars, depending on temperature. The aggregate is termed collectively "propylite." These products are almost always present regardless of the types of metals concentrated during the metallization phase of the mineralization process. Whether such rock alteration is a precedent of uranium mineralization has always been controversial. Those preferring the interpretation of

transport and deposition of uranium from groundwater have been reluctant to accept pervasive propylitic alteration because such alteration is thought to require fluids more corrosive than ordinary dilute groundwater and because a hypogene mineralization mechanism would thereby be implied. Experience from years of widespread uranium exploration has proved the presence of mineralogically anomalous ore-body halos and district matrices. These constitute altered rock (see, for example, Gabelman and Boyer, 1958). The pervasive rock alteration in uranium districts is now more widely accepted. However, complications have arisen over the definitions and causitive agents of the alteration. The changes recognized typically are of low-temperature origin and could result from a variety of processes. Confusion clouds the distinction of alterations produced in reducing environments and later elevated into the vadose zone to become oxidized and weathered. Many regard oxidation/weathering as the most significant alteration associated with sandstone uranium occurrences.

Reduction (ferric to ferrous iron in clay), iron chloritization, argillization, bleaching, pyritization, hematization, and silicification are types of alteration also found with uranium mineralization. These occur at depth independently of surficial oxidation and weathering. Oxidation and weathering of alteration minerals produce limonite and kaolin. Confusion surrounds the genetic distinction of supergene limonite from hematite. Hematite forms spontaneously from hydrated iron oxide at the surface at mildly elevated temperatures (Berner, 1969). Limonite and hematite are not thermodynamically interconvertible under shallow conditions once hematite is formed as the stable phase. Even under chemically reducing conditions, such as in paludal environments or in interaction with epigenetic fluids, the production of limonite from hematite is controversial. One possibility is that an intermediate suite of minerals may be formed: iron-rich green clays (montmorillonite, nontronite), chlorite, and the sulfides pyrite and marcasite. These may undergo subsequent oxidation and hydration reactions to produce limonite and goethite.

D. Forms of Uranium Occurrence

Uranium is so widespread geologically and geographically in concentrations from less than 1 ppm to greater than 20 percent that methods for classifying occurrences as deposits need to be discussed. The following are in general use. Uranium can be more or less uniformly disseminated throughout rocks such as black shale or phosphate or can be strongly concentrated. The former are called uranium dispersions and the latter concentrations. Although some dispersions have been investigated for exploitation at very high uranium prices, they have not been able, historically, to compete with concentrations and are mostly of scientific interest. Dispersions formed in a rock coincidentally with the formation of a rock are "natural abundances." These would represent the extremely large, low-grade deposits at the minimum of the size-richness range. Potentially economic examples include Florida phosphate rock (100 ppm U_3O_8), Swedish alum shale (200 to 300 ppm U_3O_8), American Chattanooga shale (65 ppm U_3O_8), and Vermont Conway granite (11 ppm U_3O_8).

Economic uranium geology centers around uranium concentrations (Figure 7-1). "Concentration" is synonymous with "grade" or richness. Those concentrations far below the current limit of economic exploitation (and probably always so) are informally called "occurrences" (Figure 7-2), although accurately any concentration is also an occurrence. Concentrations slightly below the economic limit, which might fluctuate from ore to waste with changing price, are marginal deposits. Concentrations above this economic limit are called "deposits," an abbreviation for "ore deposit," although all concentrations likewise technically might be called deposits. "Ore" is formally defined as any natural product that can be mined at a profit. The qualifier "ore" is often dropped to avoid the implication of economic viability before an ore deposit is evaluated. Deposits are evaluated in terms of the total quantity of valuable commodity they contain, portrayed as the product of volume and grade.

Deposits of potential economic interest are further classified by the method of entry and fixation of the valuable element (U, Cu, Pb, Zn, Au, Ag, etc.) in the rock. The two basic types of entry are incorporation with the rock as it is formed (syngenesis) and emplacement in an already-formed rock (epigenesis). Early in the history of uranium geology, these alternatives were the dominant issue for uranium deposits in sandstone of the Colorado Plateau. Now, recognizing that an epigenetic concentration mechanism is required because the initial syngenetic abundances are so low, geologists debate the issue less, although many still consider uranium to be of syngenetic origin in either igneous or sedimentary rocks.

Two additional fundamental processes further qualify epigenetic concentration: the filling of open cavities in rock by precipitation from fluids and the metasomatic replacement by fluid diffusion through solid rock.

Metasomatic replacement involves ion exchange to form new minerals that grow by replacement in the matrix. All combinations of these extremes are found in nature. Some examples are fault fillings (veins); small fracture or joint fillings (stockworks); pore fillings, as in sandstones near

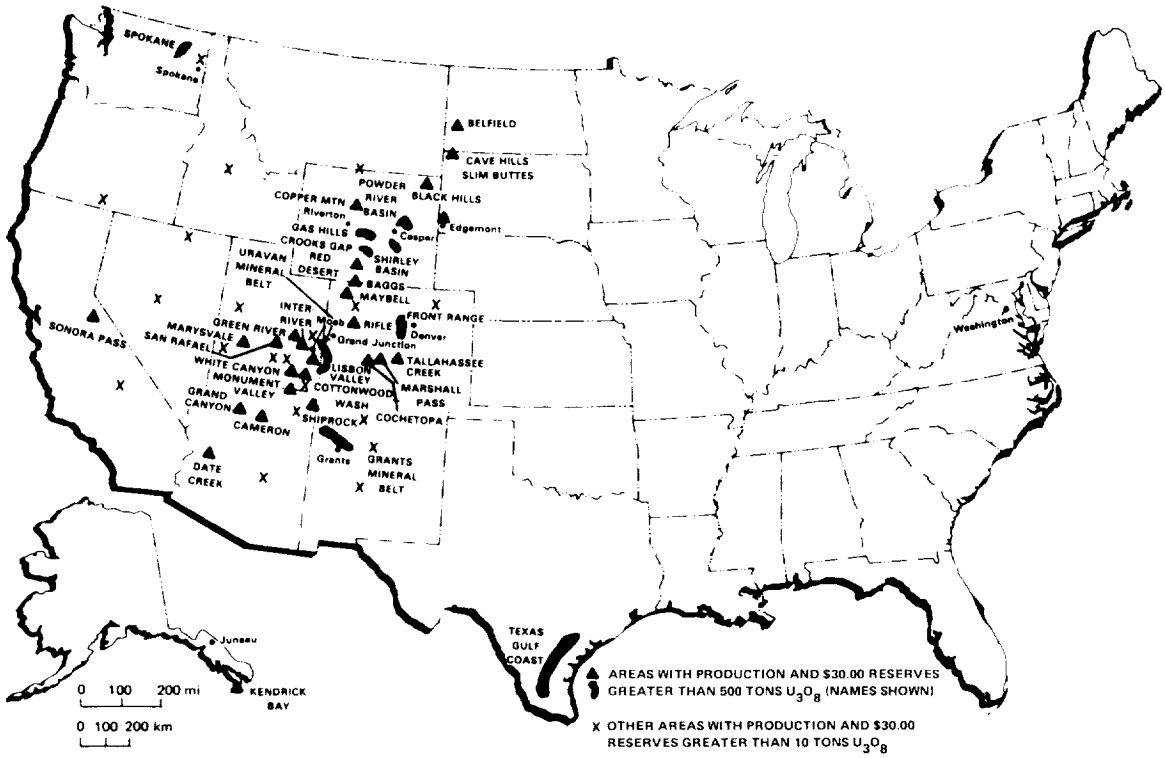

Figure 7-1. Areas of significant uranium deposits in the United States (unpublished map, courtesy of U.S. Department of Energy, Grand Junction, Colorado)

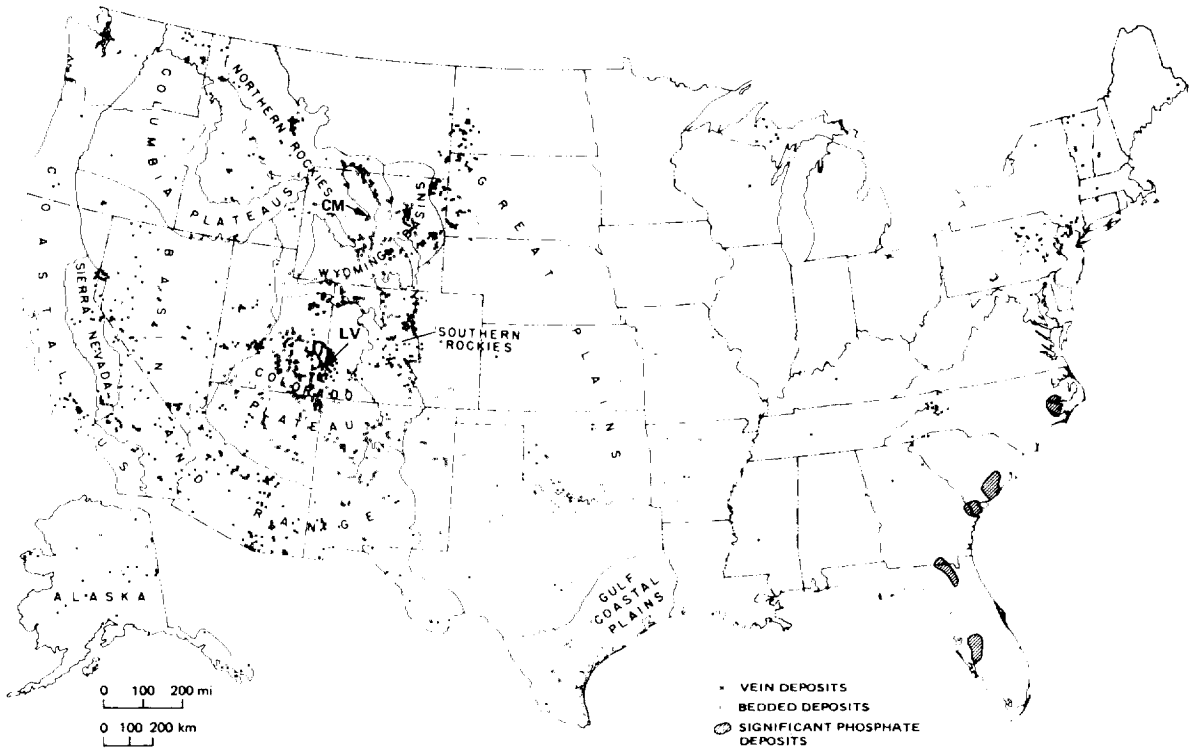

Figure 7-2. Areas of uranium occurrence in the United States. CM is Copper Mountain. LV is Lisbon Valley (unpublished map, courtesy of U.S. Department of Energy, Grand Junction, Colorado).

fractures (impregnations); widespread pore fillings (impregnation disseminations); replacement of fault or fracture walls (replacement veins); large, rich replacement areas, independent of fractures (massive replacements); and replacements as small, isolated grains widely and pervasively distributed throughout a rock (replacement disseminations).

E. Major Types of Uranium Deposits

Uranium in some small quantity occurs in most types and distributions of rocks so that it can be said to be geochemically persistent. However, concentrations above 0.1 percent U_3O_8 in rocks generally have been required for a deposit to be of potential economic interest. The following equivalents are rough guides for uranium deposits to qualify as ore bodies at prices of $25 to $30 per pound of U_3O_8, assuming metallurgical viability:

(1) 0.05% U_3O_8 for 10^9 rock tons

(2) 0.1% U_3O_8 for 10^6 rock tons

(3) 0.15% U_3O_8 for 10^5 rock tons

(4) 0.2% U_3O_8 for 10^4 rock tons

(5) 0.3% U_3O_8 for 10^3 rock tons

These grades are not high compared to those required for most other economic elements; the minimum represents a concentration ratio of only about two orders of magnitude over the average crustal abundance levels for different rocks.

During the first half of this century, the major types of deposits discussed below were discovered more by systematic prospecting of large areas than by prospecting based on the use of genetic models. In all cases the criteria of discovery were anomalous levels of gamma radiation at the surface or, much less frequently, the presence of uranium minerals at the surface. Although many discoveries were "blind" (drilling beneath barren outcrop to a discovery at depth), all blind occurrences were downdip or along trends from known mineralized outcrops. Therefore, very few deposits in new areas or environments can be said to have been found only by geological prediction. However, discoveries of new geologic information were very commonplace, and many such discoveries were significant enough to change the entire complexion of uranium geology and search technology. One example is the discovery at Grants, New Mexico, in 1951, that uranium in the Colorado Plateau occurred outside the Uravan mineral belt. Another discovery in 1951–1952 was that uranium occurred in formations other than Jurassic Morrison sandstones, that is, in Wyoming Tertiary sandstones. A third discovery at Lisbon Valley, Utah, in 1953 was that yellow oxidized ores changed to black unoxidized ore at depth. This last phenomenon had been predicted by Coffin (1921).

The three major types of uranium deposits discovered through 1965 were veins, sandstone impregnations, and quartz–pebble conglomerates. A fourth type, the large "Rossing" low-grade replacement dissemination, was brought into prominence after 1965. A fifth type, the large, rich, "unconformity-related" deposit, was recognized in the early 1970s; and a sixth type, the large, rich, "Roxby Downs" breccia deposit, was discovered in the late 1970s.

Recently, Adams (1981) and Adams and Smith (1981) described the geology and recognition criteria for six types of uranium deposits including the conglomerates. Conventional veins are not described, but a new class of unconformity-related vein-like deposits is defined (the fifth type listed above). Four subtypes of sandstone impregnations are recognized: the Salt Wash type, roll-type in continental sandstones, fluvial-shallow marine host-rock type, and humate (plant-derived petroleum) type.

1. Veins. Vein deposits became the first classic and preferred type of deposit. In form and character veins are similar to veins of other elements, but uranium veins seldom occur in districts of other metal veins. The exceptions—Joachimsthal, Czechoslovakia (the original vein deposit producing district); Eldorado, Canada; and Shinkolobwe, Belgian Congo (Zaire)—contained abundant silver, which was mined first; discovery of uranium was made subsequently. These districts supplied the early limited market. When demand was created during World War II, the initial search for geologically similar districts was unsuccessful. These districts continue to be unique. However, when the simple pitchblende vein type was discovered (Beaverlodge, Canada; Limousin, France; Urgeiria, Portugal; Schwartzwalder, Colorado; Menzenschswand, West Germany), it became a more common prototype. The difference appears to be a regional zoning of metals in which uranium becomes more abundant away from conventional metal mining districts. Such veins have accounted for about 5 percent of production.

A typical vein occupies a fault or fissure to produce a planar body usually steeply inclined with respect to the surface. Local directional changes in strike or dip frequently cause linear, wider, and richer "shoots" that are often preferred mining sites. The fluids that bring metals to fractures to create veins remain unidentified but presumably can be of any origin (magmatic, metamorphic, connate, meteoric, etc.). Most likely the bulk of fluid, at least at shallow depths, is meteoric. The sources of metallic

ions are equally unknown and probably are multiple. The fixation of ions into minerals is dominated by wallrock replacement at depth, changing to mostly simple precipitation at the surface. Chemical reduction by an unidentified extrinsic or intrinsic agent is usually required. In terms of remote sensing, veins intersect the surface as lines, as traces of faults, or as extremely large-scale joints. Because of their scale, they may be more easily recognizable in satellite images than in aerial photographs.

Uraniferous-shatter stockworks (of which Copper Mountain, Wyoming, is an approximate representative) are a form of vein deposit. Rather than along one or a few major persistent veins, mineralization has occurred along all available fractures throughout a larger area than that traversed by any single fracture. However, average grade and total volume of mineralized ground are correspondingly lower.

2. Sandstone impregnations – Uravan mineral belt type. The classical sandstone impregnations were discovered early in this century during the radium boom in sandstones of the Jurassic Morrison Formation of western Colorado. Oxidized uranium minerals impregnated the pores and replaced cement preferentially in the highest ("Third Rim") of three sandstone units. These units with intervening mudstones comprise the Salt Wash Member. These sediments are fluvial, abounding in riverbed and floodplain depositional features including channels, crossbedding, and interfingering sandstone–mudstone transitions. They are rich in carbonized plant debris that "fixed" the migratory uranium locally.

A peculiar, unresolved feature is that uranium deposits occur only in restricted districts within the widespread, uniform lithology of the Salt Wash Member. Most districts are grouped within 30 mi of several laccolithic mountains. The Uravan belt forms a 1- to 9-mi-wide band wrapped around the south, east, north, and northwest sides of the La Sal laccoliths at a distance of 27 to 30 mi (Figure 7-3). Several districts are within this ring, closer to the mountains, but the belt is not continuous. Rather, "trends" cross the belt (like spokes) at intervals of 8 to 10 mi and contain uranium deposits while intervening areas are barren.

Within districts, deposits tend to occupy the thickest portions of sandstone beds. These are broad, filled riverbeds and display sinuous trends typical of stream channels (e.g., Deremo Mine, Figure 7-4). However, in detail, the channel fills are never uniform sandstone bodies but show small-scale interfingering, anastomosing lenses of sandstone and mudstone, both rich in well-preserved carbonized or silicified plant fragments.

Vanadium is the principal exotic element in these ore impregnations, exceeding uranium by a factor of two to four. There are several primary vanadium minerals, but only two primary black uranium minerals – pitchblende and coffinite. These oxidize to yellow carnotite, the hydrous potassium uranyl vanadate.

Valuable vanadium–uranium impregnations occupy only small portions of the sandstone lenses. In plan view, the ore bodies are locally linear but, overall, form complex networks resembling joint patterns (Figure 7-4). It is only the groups of such networks, or the limits of the entire volume enclosing them, that illustrate the larger channel-fill ore pattern. Actual ore bodies are separated, small, and irregularly shaped. Large-scale underground or open-pit mining never has been economically feasible, so the viable extraction method has been the "dog hole," in which two or three men follow the ore. These practices created underground mine workings of highly irregular shape. The distribution, size, shape, and exact position of these small ore bodies never have been predictable, and it has proved impossible to calculate reserves in advance of development. Yet persistently following some sand lens, mudstone stringer, or fracture usually discloses another small ore body that could sustain small, independent mining. Thus, the Uravan belt has operated longer and more continuously than any other district in the Colorado Plateau. Large-company mining has never been feasible, but several (e.g., Union Carbide) have found it profitable to maintain custom mills to support independent mines.

The most notable features of Uravan ore bodies are ore "rolls," a long-established miner's term described by Shawe (1956) (Figure 7-5). A roll is a "C"-shaped ore-waste boundary oriented across the bedding with a downdip convex shape. This "C" may bound a large irregular ore body, or where the body is particularly small, both contacts may be parallel to illustrate a "C"-shaped ore body with wings lensing-out at the top and bottom of the sandstone bed. Rolls are not a consistent feature, however. They are believed to illustrate fronts of diffusion, advective transport, and ore impregnation that migrate along the bed. The Deremo cross-trend (Figure 7-4), including the Deremo Mine in the southern part of the mineral belt, is the only trend to contain large ore bodies, spaced closely enough to sustain large-scale mining operations.

Ore bodies are contained within alteration halos consisting dominantly of bleached sandstone (originally dull hematitic red). Bleached rock commonly constitutes the matrix of an entire district and may extend to other formations. A more local feature of the bleaching alteration is the concentration of hematite introduced just outside the

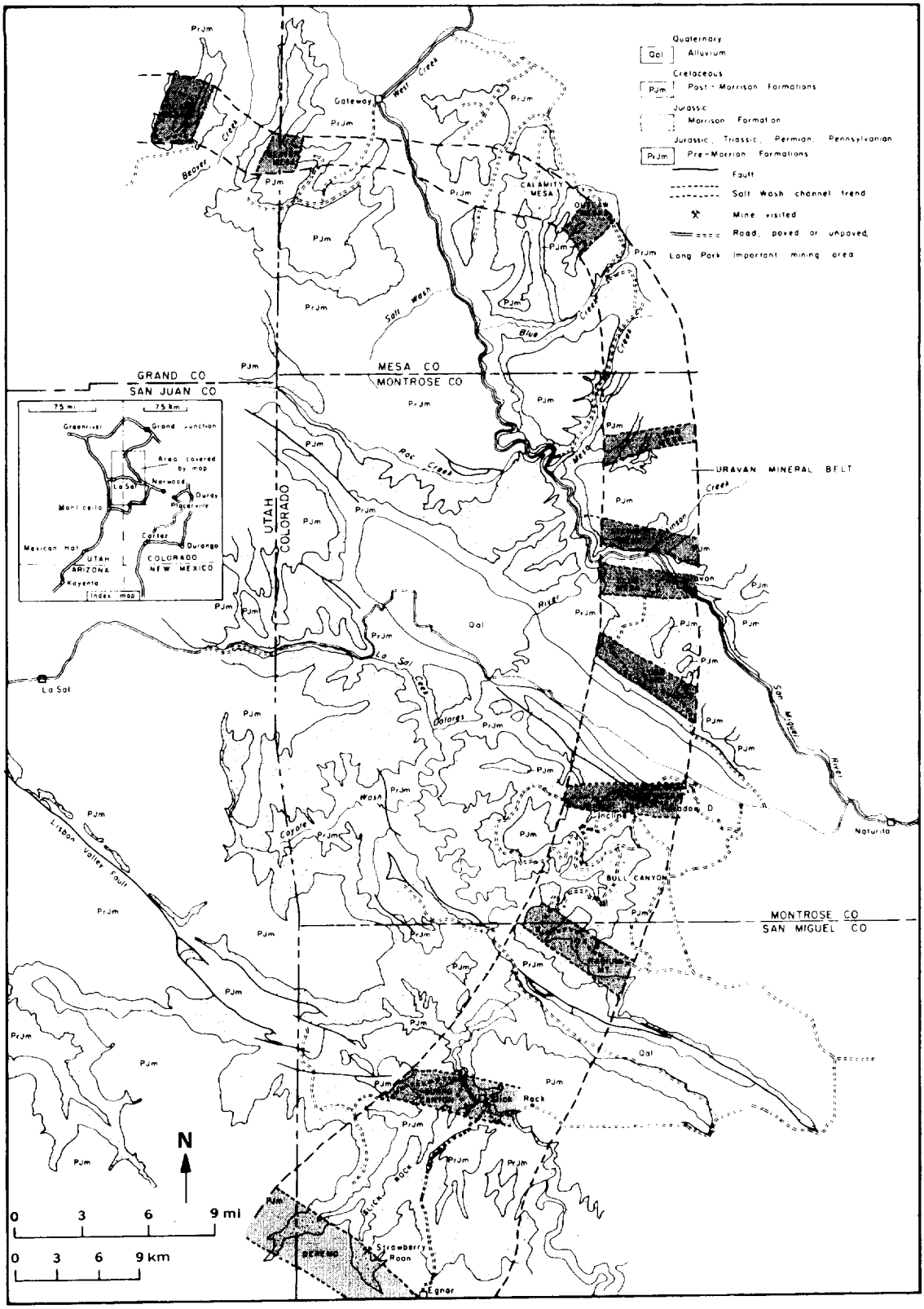

Figure 7-3. Generalized geologic map of the Uravan mineral belt. Major producing areas are shown as cross trends ("channel trend") (U.S. Atomic Energy Commission, 1959).

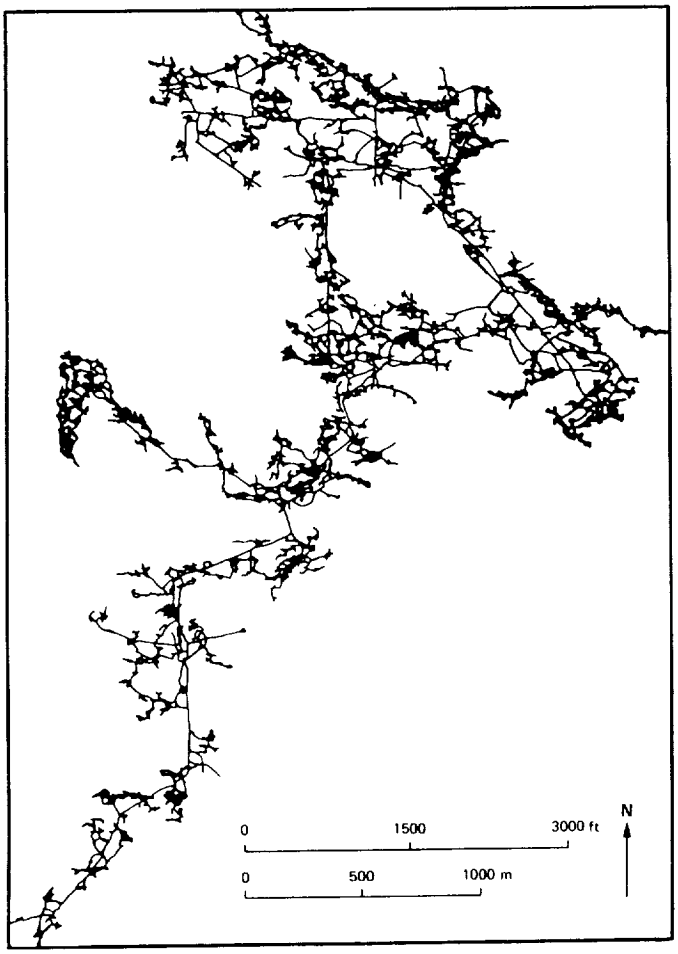

Figure 7-4. Plan view of the Deremo Mine, south end of the Uravan mineral belt, showing the small size of individual stopes and the complexity of the workings (Thamm et al., 1981)

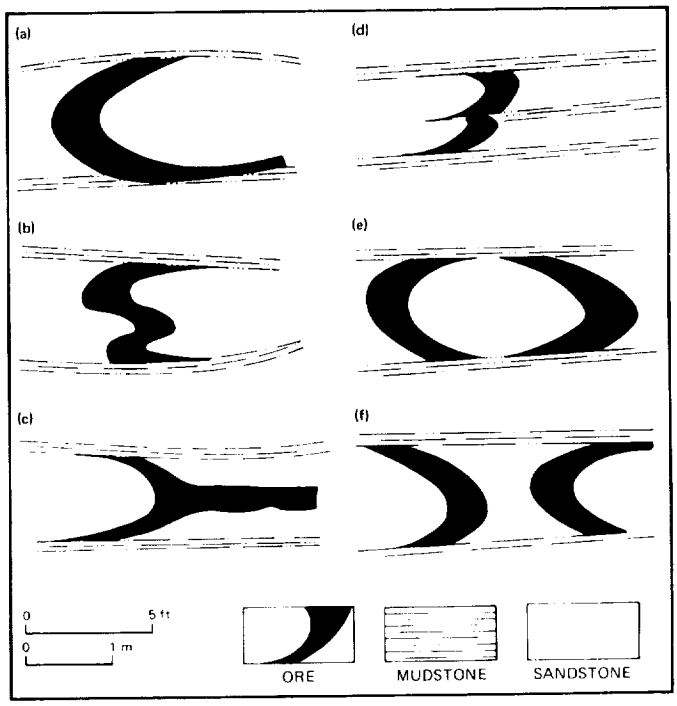

Figure 7-5. Schematic cross sections for various shapes of uranium–vanadium roll deposits (Shawe, 1956): (a) "C" roll; (b) "S" roll; (c) socket roll; (d) two rolls separated by a thin layer of mudstone; (e) mirror-image "C" rolls—convex loop of roll front; and (f) mirror-image "C" rolls—concave loop of roll front

zone of strongest bleaching (Figure 7-6). A more regional feature of the alteration important to ore, for which both syngenetic and epigenetic origins are still debated, is the occurrence of reduced green (ferrous) mudstone (less so sandstone) that forms a larger, outer-district matrix for the bleached and hematitic rock. Those favoring a syngenetic origin argue that still-preserved carbon prevented this depositional environment from ever becoming oxidized and that the coloring pigments present were therefore never hematitic. Epigeneticists emphasize the transgressive boundaries between green and red rocks and the local distribution of green mudstone in most of these areas. They claim that most of the original hematite in Colorado Plateau red beds is detrital and derived by erosion from laterites.

In early years, genetic interpretation of Uravan ores was about evenly divided between syngenetic deposition with the fluvial sandstones and epigenetic deposition from telethermal fluids migrating along aquifers from feeder centers (such as the laccoliths) or veins (such as the Cashin copper–vanadium mineralized zone). Years of investigation have shown that the ores are epigenetic in their present concentrated form, but the preponderance of opinion favors syngenetic emplacement of uranium into the Salt Wash Member or at least the Morrison Formation in the tuff component of mudstone in the overlying Brushy Basin Member. Uranium was thought to be liberated from Brushy Basin rocks by groundwater and fixed below by accumulations of carbon trash. Several problems exist for this model. There is, for example, a low correlation in detail between uranium and carbon. The uranium content of any district far exceeds the amount present initially in the district at reasonable abundance levels, and the means of funneling fluids to deposition points rather than dispersing them further throughout the aquifer are not evident.

The same features characterizing the Uravan belt deposits also characterize the uranium deposits found anywhere in the Salt Wash Member: the small size, irregular shape, and discontinuity within large clusters of deposits. These

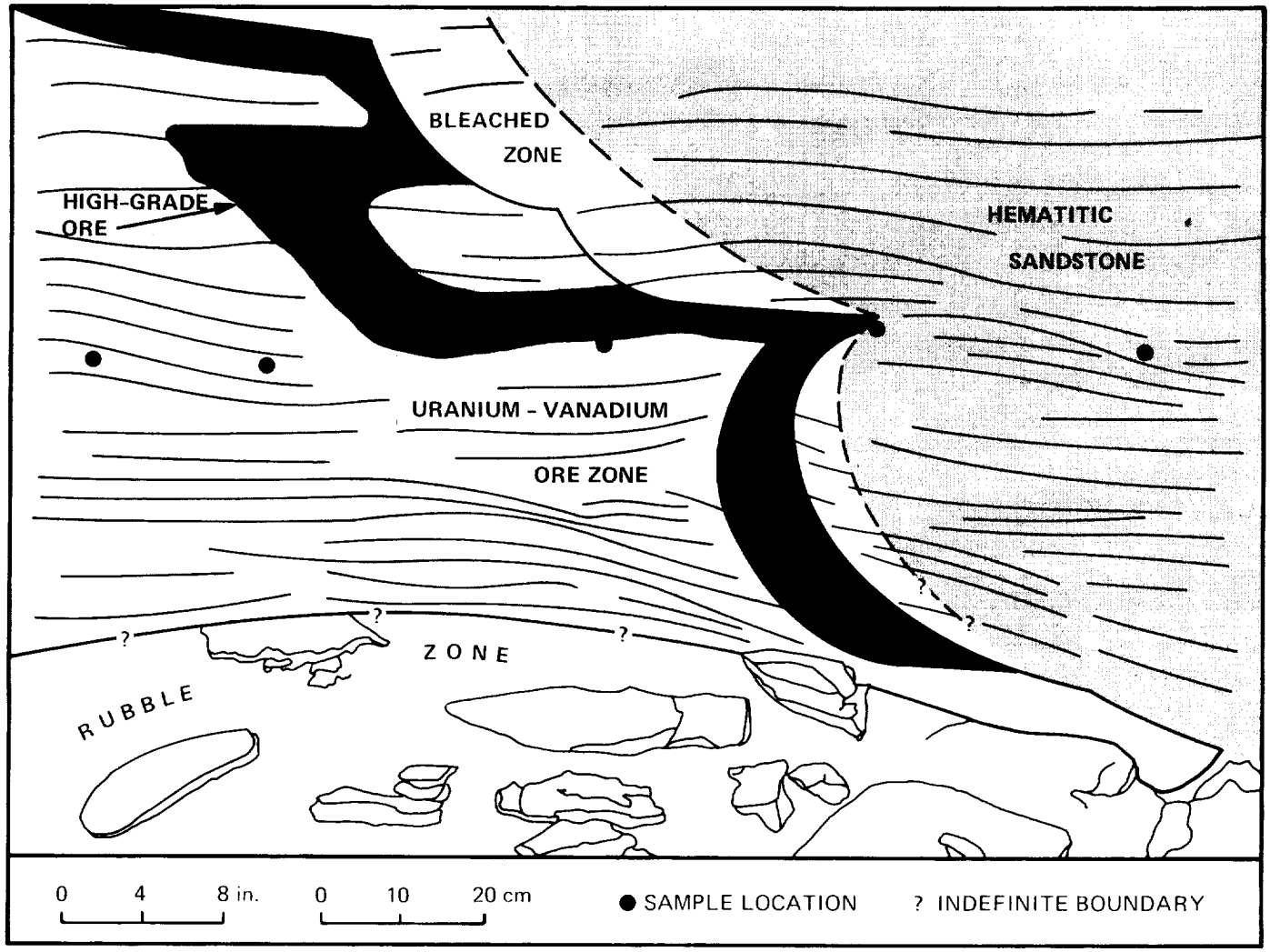

Figure 7-6. Schematic cross section of an oxidation-reduction boundary entirely within sandstone, Deremo Mine, south end of the Uravan mineral belt (Thamm et al., 1981)

features probably reflect the irregular sedimentary structures of the original host rock. Such structures change radically over short distances yet constitute a formation-wide characteristic.

3. Large continuous sandstone impregnations. In contrast to the Uravan or Salt Wash type of deposit, there is really only one other type: the large, more continuously mineralized deposit that is more regular and definable in trend and more uniform in grade. This type is worthy of large-scale underground or open-pit extraction and, once recognized, quickly becomes the province of large mining companies.

The first minor "giant" impregnation recognized was the Monument 2 impregnation in Shinarump conglomerate at the base of the Triassic Chinle Formation in Monument Valley, Arizona. Here also epigenetic, secondary, uranium minerals (carnotite with minor pitchblende) impregnated a river channel fill composed of conglomerate. Carbon trash was still a common occurrence in these deposits; in addition, copper and silver were found in locally economic quantities. Large deposits were rare, although exploration to find others quickly identified a multitude of smaller deposits. Large, reasonably straight, conglomerate channels in the otherwise medium-grained sandstone were barren, but small tortuous channels were more prolific. A few similar deposits (Happy Jack, Pick Mine) proved to be giants.

In about 1952, Steen discovered a major primary pitchblende ore deposit in the Moss Back sandstone, also at the

base of the Chinle Formation at Lisbon Valley, Utah. This discovery changed the nature of the uranium industry. A string of similar deposits, like beads, was quickly identified around the faulted Lisbon Valley Anticline. None of these could be said to occur in well-defined channels, although such an interpretation was advanced by Steen (1953). The ore accumulations appeared as massive impregnations without "roll" boundaries or local control by mudstone–sandstone geometry. The ore averaged 0.2 to 0.5 percent U_3O_8 with V_2O_5 to U_3O_8 ratios ranging from 0.07:1 to 3.34:1 (Johnson and Thordarson, 1966). In textural detail the ore was a uniform impregnation. The distribution of uranium was not controlled by carbon fragments, although much plant material was present. This ore became a subtype known as Moss Back ore. The deposits are strata-bound in the basal sandstone member of the thick Chinle Mudstone Formation. They are of different character than the Salt Wash deposits even where the two ore types are nearly superimposed stratigraphically one above the other, such as at Dry Valley and East Mesa near Lisbon Valley. The Lisbon Valley deposits were also considered to be derived from mudstones in the Upper Chinle, which, as does the Brushy Basin Member, contain a uranium-enriched tuffaceous component. Other models of ore derivation are as follows: (1) Uranium was derived from the arkosic component of the Moss Back conglomerates, and (2) uranium was liberated from granitic source rocks in the Uncompagre Uplift to the east and was transported surficially through the channel system in Moss Back time. Regionally, the same problem of ore localization exists in that only a small portion of the uniformly favorable sandstone lithology is productive. Factors that may indicate genesis are the altered rock matrices, unusual accessory and trace element suites (V, Cu, Ag, Co, Ni, REE), and relations to nearby intrusive or subvolcanic centers, but these factors have yet to be included in models of ore occurrence. The addition of juvenile emanations into the groundwater system, though unpopular, has not been eliminated as a mineralization mechanism.

Uranium was discovered in the Poison Canyon Sandstone Tongue of the Brushy Basin Member of the Morrison Formation at Grants, New Mexico, in 1951, following the discovery of replacement pitchblende deposits in the stratigraphically lower Todilto Limestone. Eventually uranium was found in the sandstones of Westwater Canyon Member and Cretaceous Dakota Sandstone. Although the surficial deposits were too scattered and small for anything other than small operation, the primary black ores in the Westwater Canyon Member soon became the world's largest and principal source. The ore was a uniform impregnation of massive sandstone without control by local depositional features or carbon trash (except in the Poison Canyon and Dakota).

Ore apparently was fixed by humates that had flowed in the aquifer much as liquid petroleum. Ore bodies were of two types: (1) long, narrow trends extending for miles, possibly parallel to the Jurassic stream channel direction, that are rich in molybdenum sulfide and were considered controlled by very subtle broad stream channels; and (2) so-called "stacks" of deposits, obviously related to transgressive faults, that lack molybdenum sulfide and were considered redistributions of the former. The deposits of this "humate" type eventually were found to occupy a belt more than 75 mi long along the northeast flank of the Zuni Uplift. This belt is still the world's greatest uranium producer.

The ores are considered Jurassic in age and thus penesyngenetic by most workers. The uranium source is attributed to the tuff component of the Brushy Basin Member, and concentration is thought to have been caused by diagenesis. However, the same problems of limited areal distribution in a lithologically uniform matrix remain, which suggest that uranium may have arrived at these sites already concentrated to a significant degree. Also, Tertiary uranium mineralization occurred along the eastern extension of the belt in the Rio Grande graben; this suggests post-Jurassic mineralization at Grants. Other interpretations include fluvial derivation from the Jurassic landmass to the south, magmatic hydrothermal fluids derived from the nearby Mt. Taylor volcano (long defended by Kerr, 1958), telethermal migration of magmatic fluids from more distant sources, and feeding into aquifers from deep sources through diatremes without magmatic transport (Gabelman, 1956, 1977).

Further exploration of fluvial sandstones in other regions resulted in the discovery of major districts in the Wyoming basins and Texas Gulf Coast Province of Texas. The deposits in the Wind River and Shirley Basins of Wyoming proved to be giants second only to those of the Grants uranium belt. These impregnations were the first significant deposits discovered in Tertiary sandstones, thus removing restrictions on the possible ages of uranium concentration in sandstones. The dominant form of the primary or unoxidized ore zone beneath the water table in the Wyoming deposits was recognized, when exposed by mining, as that of the "C" roll in cross section (Harshman, 1974); but these rolls were gigantic compared to those of the Uravan belt and extended for miles as highly contorted "ribbons." These have been interpreted to represent fronts between oxidizing and reducing conditions in fluids migrating through aquifers (Figure 7-7).

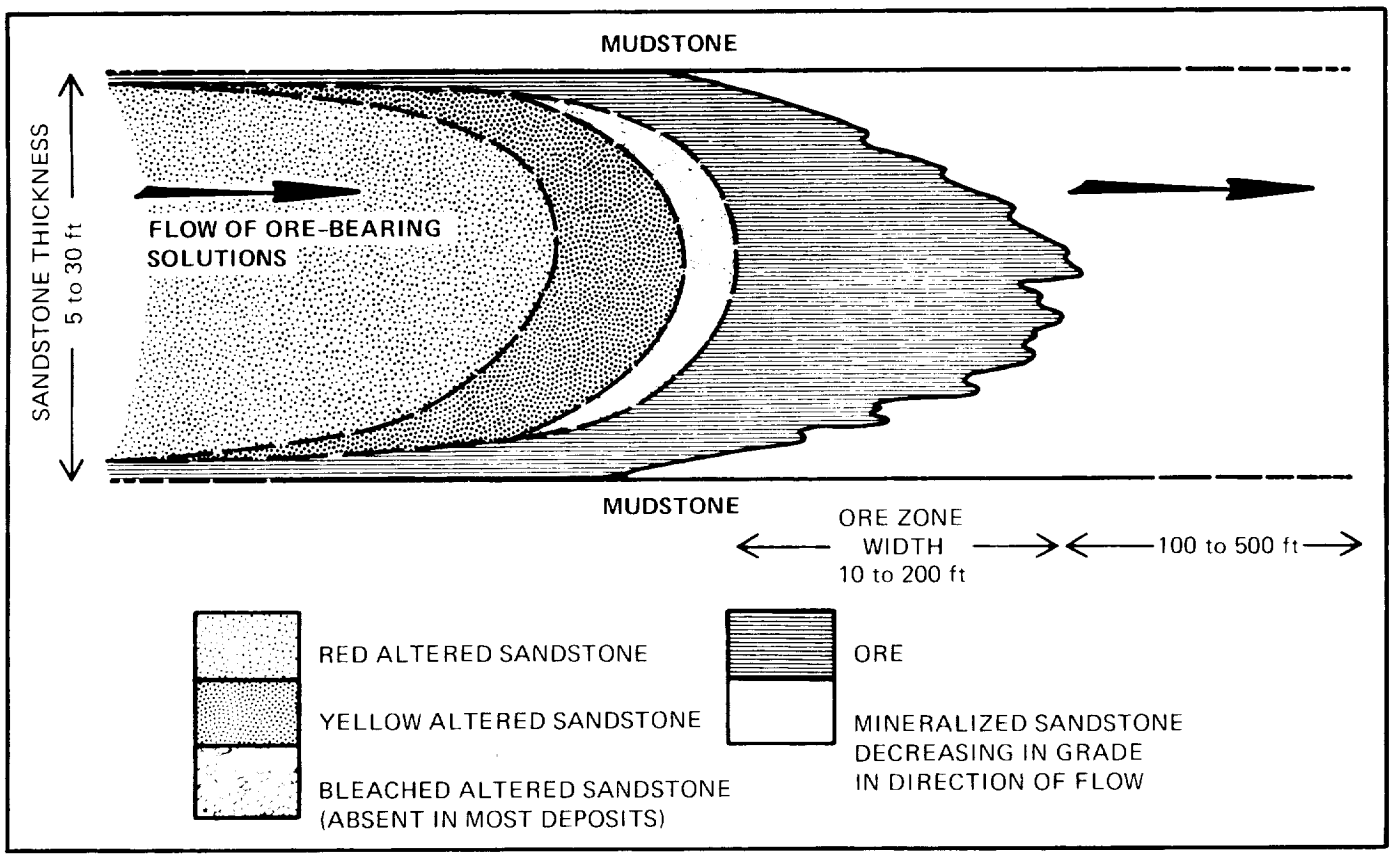

Figure 7-7. Generalized composite cross section of edge of altered sandstone tongue and ore body, Powder River Basin, Wyoming, showing character of altered sand near roll front (Harshman and Adams, 1981)

The Texas deposits proved smaller than those in Wyoming. They are found in marginal marine as well as continental sandstones and exhibit roll features very similar to those in Wyoming. These deposits were found to be related to the distribution of growth faults that characterize the Gulf Coast. Some geologists interpret them to have developed from pressurized fluids rising along the faults to the outcrop (Gabelman, 1977) and then descending through aquifers to form uranium concentrations (Adams and Smith, 1981; Gabelman, 1977) (Figures 7-8 and 7-9).

4. Quartz–pebble conglomerates. The unexpected occurrence of uranium in Proterozoic auriferous quartz–pebble conglomerates of the South African Witwatersrand was discovered by W. Bourret and G. Bain during the Manhattan Project, before the recognition of large U.S. sandstone deposits at Grants. These conglomerates supplied the bulk of uranium for that project. The grade, though remarkably uniform, is very low (<0.1 percent U_3O_8), and uranium would not be economical if it were not for the independent, economic viability of gold. This permits uranium recovery as a by-product. The uranium and gold are unusually persistent in conglomerate beds of equally remarkable continuity. Based on continuity of the conglomerates, the uranium occurrences have been interpreted as fossil placers (Figure 7-10).

The significant production of these deposits stimulated attempts to find others like them elsewhere. Direct comparison with South African deposits led F. Joubin to drill successfully the Blind River, Ontario, Proterozoic quartz–pebble conglomerates. These conglomerates lacked gold; anomalous radioactivity of uranium-free outcrops was previously interpreted to result from thorium. Joubin demonstrated that insoluble thorium was also absent and that the radiation observed was due to uranium leached from the surface (Griffith, 1967, p. 96). The Blind River (now Elliott Lake) conglomerates are slightly richer than the Witwatersrand (averaging about 0.11 percent U_3O_8) and are economically viable at higher uranium prices. The conglomerates themselves are not as continuous as those of the Witwatersrand, and the distribution of uranium probably originated as part of a paleodrainage system.

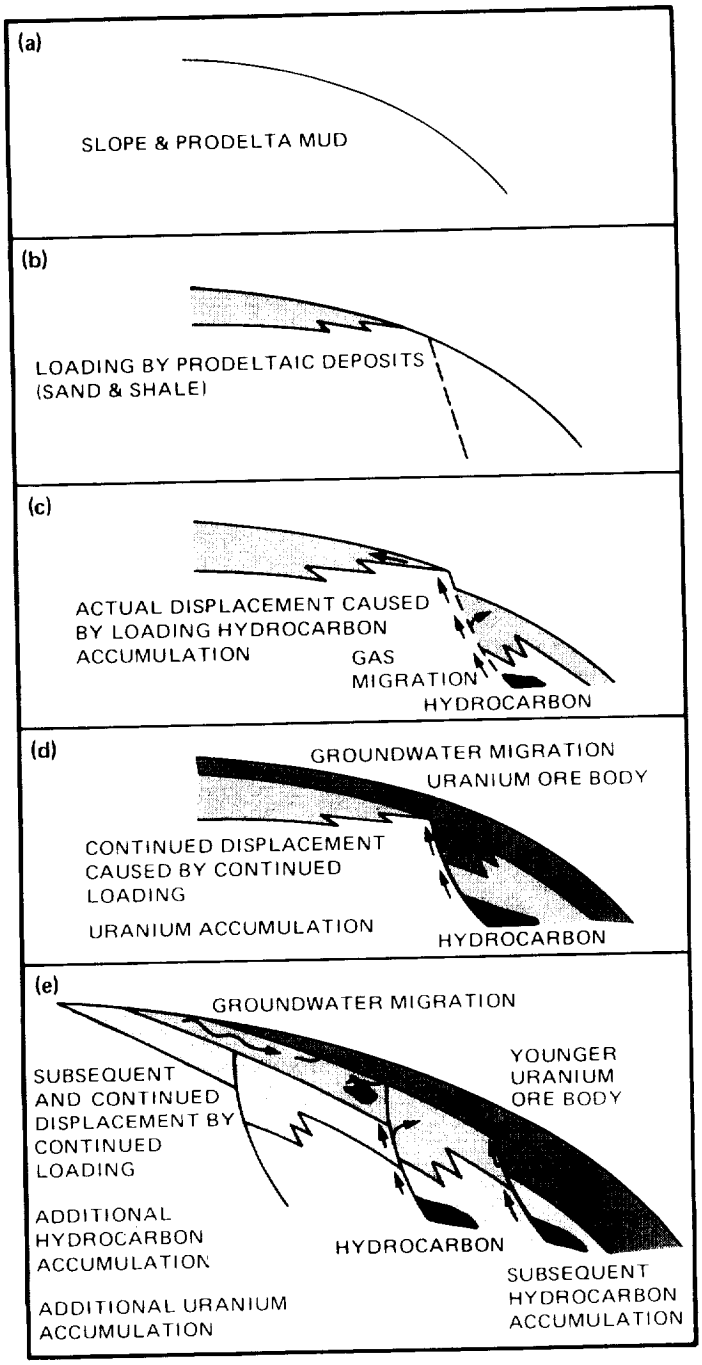

Figure 7-8. Schematic cross sections showing the sequence of events leading to the formation of uranium deposits related to fault-derived H_2S, south Texas. H_2S introduction likely preceded and followed roll-front formation but was not synchronous (Adams and Smith, 1981).

Although Proterozoic quartz–pebble conglomerates are relatively common, only three other localities in the world boast uraniferous conglomerates, and none has proved economically significant. One is in Russia and the other two are in Brazil (Jacobina is mined for gold; the Quadrilatero Ferrifero has virtually no gold but does contain uranium).

The genesis of quartz–pebble conglomerate deposits was long debated. Placer syngenesis was suggested by strata-binding, by the presence of refractory minerals such as zircon and brannerite, and by the rounded detrital appearance of pyrite and pitchblende. Epigenesis was supported by the secondary textures of pyrite, pitchblende, and gold. These textures were attributed to remobilization by syngeneticists. The preponderance of opinion has swung to a placer origin. Among the serious problems attending this interpretation is how pitchblende and pyrite, both readily oxidizable and soluble, escaped leaching during transport since the Proterozoic Era. It is now hypothesized that a global reducing atmosphere existed during the Proterozoic Era, prior to the development of oxygen in the atmosphere that occurred with the advent of plants.

5. High-temperature replacement disseminations. High-temperature replacement deposits were long suspected to comprise the logical intermediary between felsic intrusives (granite or syenite) with high thorium–uranium abundances and the moderate- to low-temperature uranium veins. No very large, economically significant deposit of this type was identified until Rossing, South West Africa (Namibia), was announced in the late 1960s. Concentration of uranium and thorium in such a deposit is an example of the classical concentration of metals and volatiles in residual fluids during magmatic differentiation. This fluid further segregates and mineralizes rock through the well-known deuteric, pegmatitic, and hydrothermal phases. The process and products of mineralization are well exhibited in "porphyry" deposits of other metals such as copper, molybdenum, tin, and tungsten. Rock alteration (clay, chlorite, quartz, silica, secondary feldspars, biotite, etc.) forms by replacement of crystallized rocks and walls of fractures. Metal deposition occurs when local conditions of temperature and pressure cause the fluids to become saturated. Fluid motion is inhibited when deposition destroys permeability. The result is a texture of uniformly distributed (but randomly scattered) grains, first of metal oxides, followed by metal sulfides.

Several uranium deposits with high thorium content, including Bancroft, Ontario, and Bokan Mt., Alaska, exhibit transitional features from enriched magmatic rocks, pegmatites, and veins and were candidates for "porphyry" type uranium deposits. However, this class of deposit did not gain recognition until the Rossing type, long known for its uraniferous pegmatites, was understood. The type is now better known as the "alaskite" type than as a replacement dissemination.

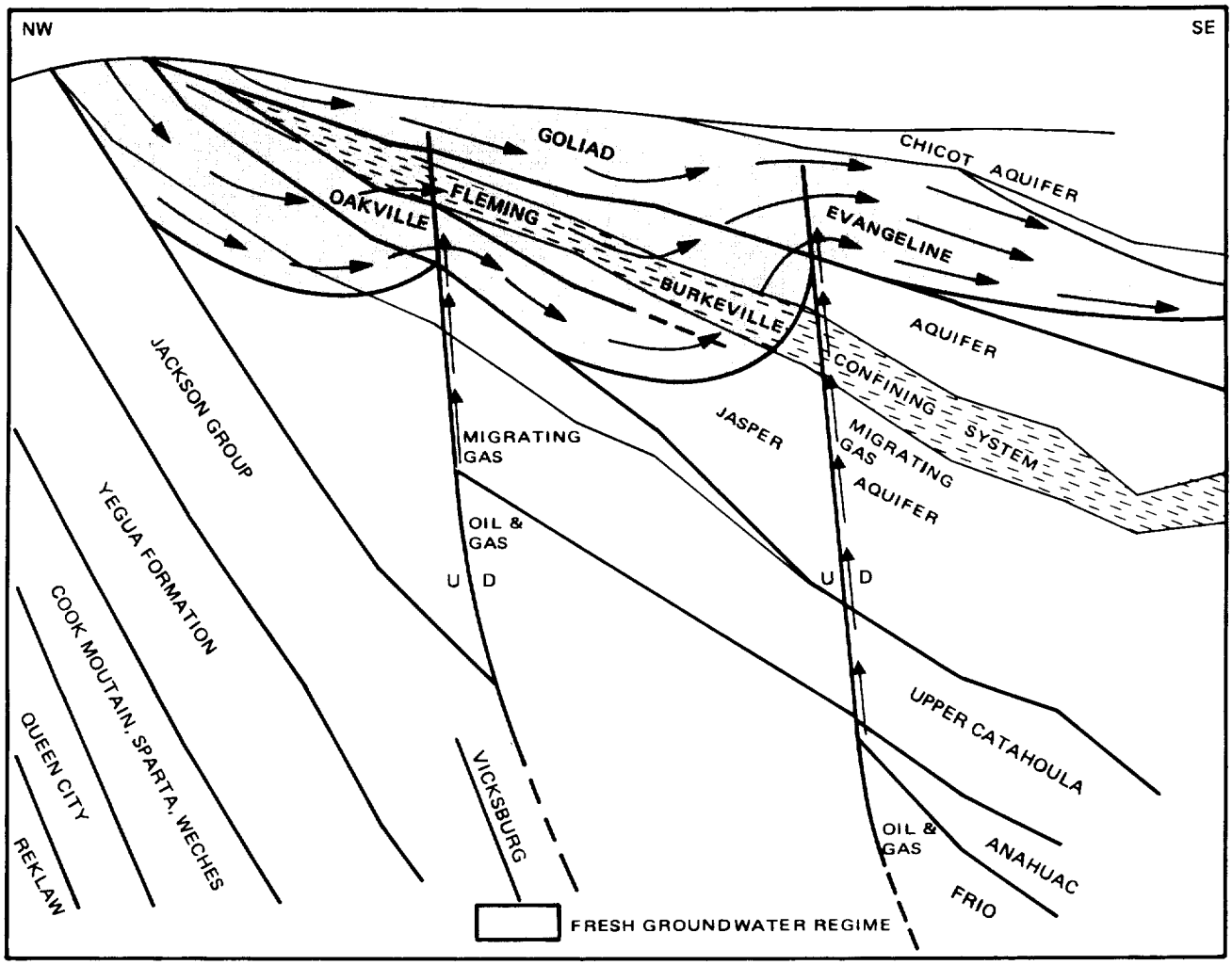

Figure 7-9. Diagrammatic cross section showing the migration paths of fresh groundwater and fault-related H_2S, south Texas (modified from Baker, 1979)

6. Unconformity-related deposits. Deposits closely associated with unconformities became established during the 1970s with the discovery of several very large, rich uranium deposits in Proterozoic Athabasca Sandstone in Canada and in the crystalline Archean rocks immediately beneath basal Proterozoic unconformities in Canada and Australia. In some, uranium impregnates regolith or breccia. The most distinctive feature with genetic implications is that grade seems to decrease with depth so that the bulk of concentrated uranium is geometrically near the unconformity. Field experience suggests this feature also is common to many deposits exposed at the present surface and is the result of secondary supergene enrichment. Nevertheless, some of these deposits, particularly those in Australia, extend to depths that seem improbable for supergene enrichment. It is also possible that primary mineralization occurred at the Earth's surface during a time interval represented by the unconformity.

Most of the deposits occur under some structural (fault) control or at least occur in structurally prepared open ground, so that the qualifier "veinlike" is added by Button and Adams (1981) (Figures 7-11 and 7-12). However, few are simple tabular veins. This class of deposit is generally thought to have resulted at a time of intense uranium mineralization near the beginning of the Proterozoic Era, about 1.7 billion years ago.

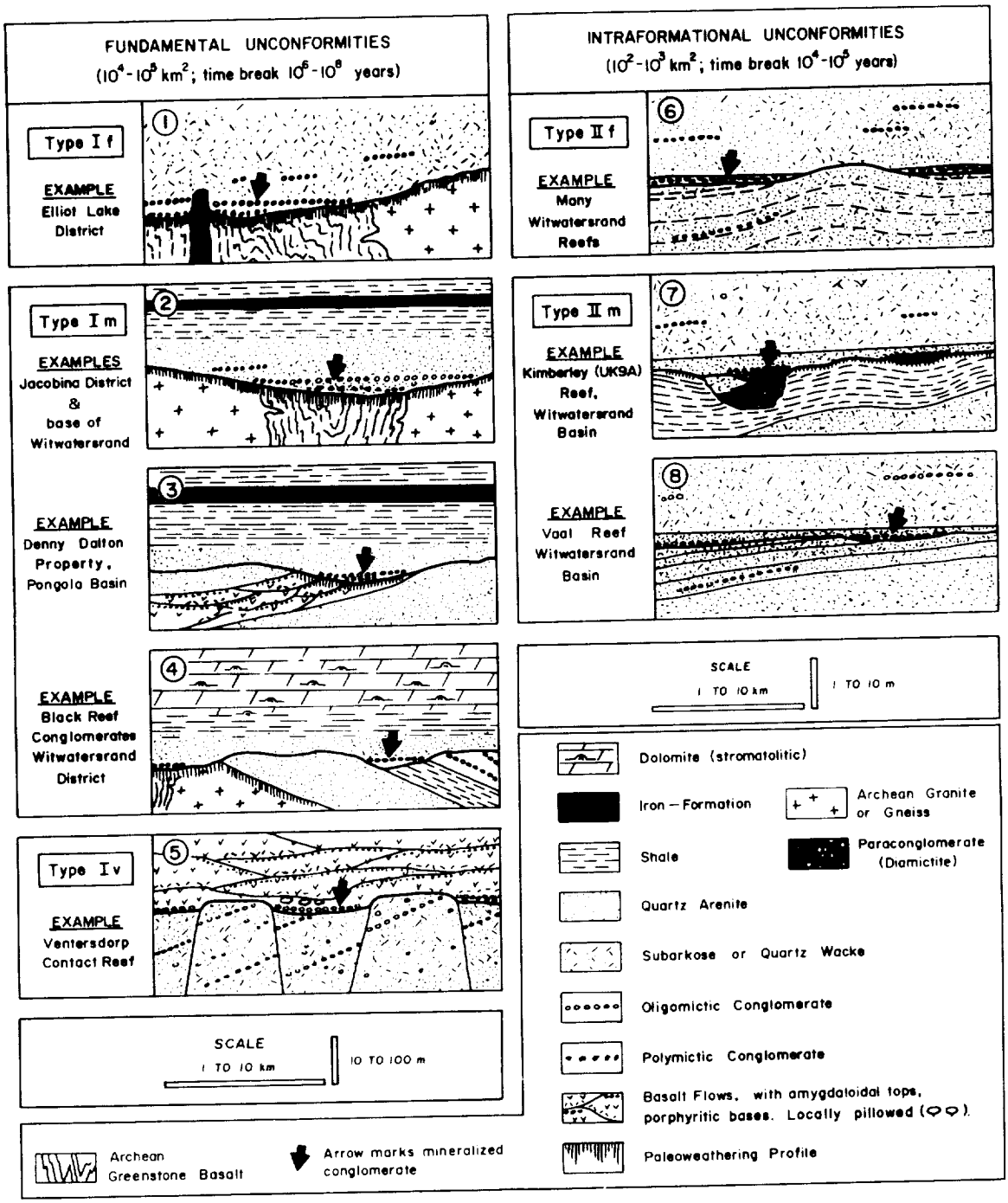

Figure 7-10. Geologic sketches showing the development of uraniferous conglomerates along or close to unconformities of varying types (Button and Adams, 1981)

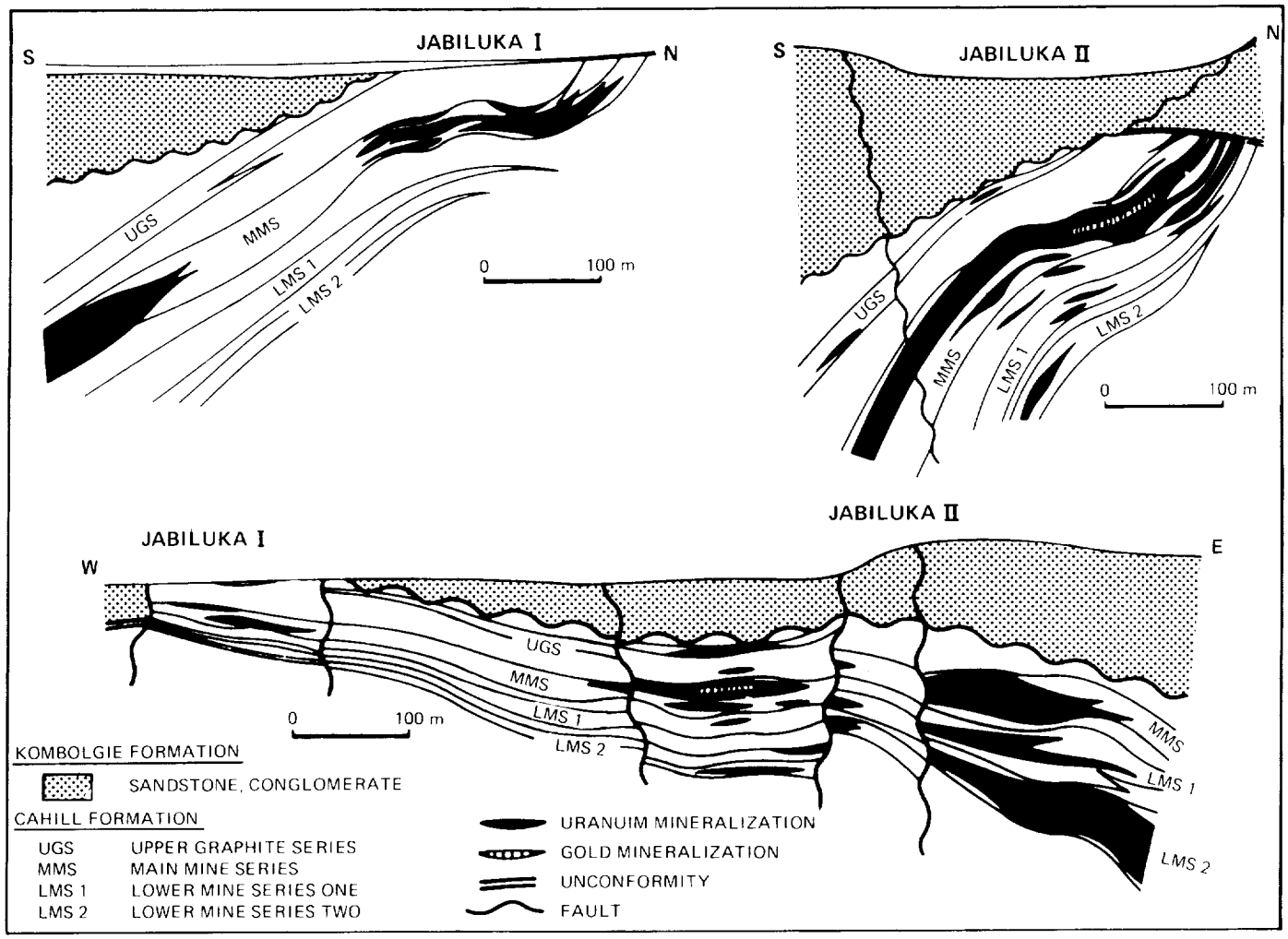

Figure 7-11. Generalized cross sections of the Jabiluka I and Jabiluka II ore bodies (from Needham, 1982)

III. Remote Sensing in Uranium Exploration

Remote sensing broadly refers to the detection of any physical parameter from a distance; its application to mineral exploration involves the subsequent geological interpretation of any parameter measured. A variety of parameters has been measured from a distance in uranium exploration, including gamma radiation, radon gas, magnetism, gravity, electromagnetic response, and photographic (visual) appearance of the surface.

Of these parameters, gamma radiation has been the most used because uranium is one of only three abundant, naturally radioactive elements (K, Th, and U). Gamma-ray energy measurements (spectroscopy) differentiate these three elements.

Black-and-white aerial photography has been the second most significant remote sensing method. The use of photographs has not led to the direct identification of uranium deposits, but so many deposits were found in unmapped areas during early exploration efforts that a rapid method of geological mapping was needed to portray the setting of deposits. Later, color aerial photography became widely used, especially after the geometric relations and significance of rock alteration halos and matrices became apparent.

Generally, however, remote geophysical and geochemical methods have not been highly useful. Their main use has been over outcrops of uraniferous host formations. Since uranium in sandstones is dominantly strata-bound, most

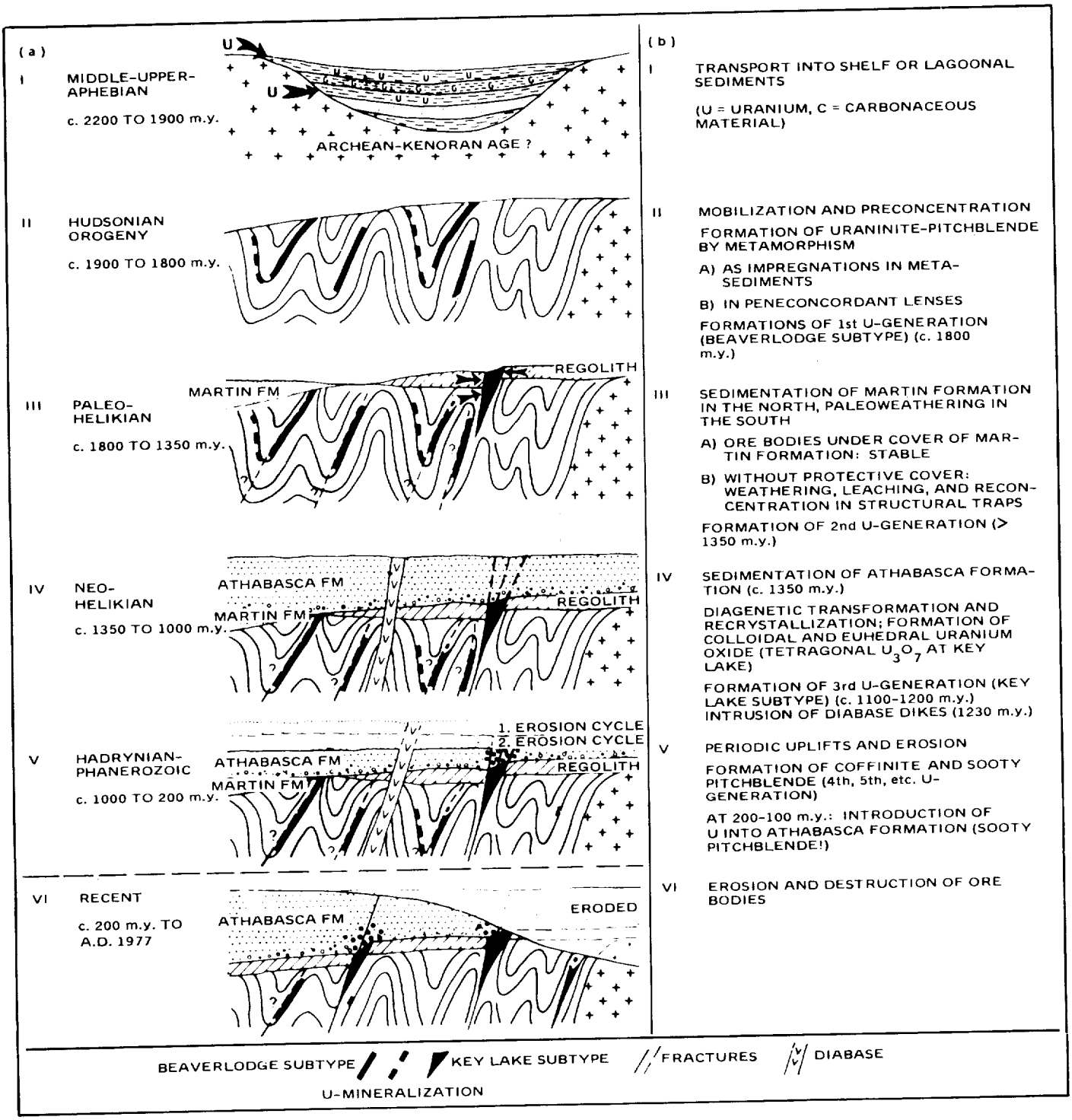

Figure 7-12. Schematic cross sections depicting the geologic stages in the evolution of vein-like uranium deposits (from Dahlkamp, 1978): (a) cross sections; (b) uranium-related processes

geologists believed remote sensing methods were useless for deposits buried in sedimentary rocks because of the lack of noticeable migration across sedimentary formations. Burial was also believed to effectively shield any other type of deposit from detection. However, radon gas liberated from uranium deposits easily seeps to the surface where it can be readily measured, even from aircraft. So, from this perspective, remote detection was taken seriously.

Barringer Research is investigating the feasibility of using sensitive airborne and surface chemical methods to detect other uranium-related ions, elements, or uranium itself that might have migrated vertically to the surface through perhaps thousands of feet of cover. This commercial group is also investigating the use of so-called laser-sounding techniques from aircraft to stimulate directly visible fluorescence in uranium-bearing minerals exposed at the Earth's surface. The U.S. Geological Survey (Watson and Theisen, 1977) has investigated solar-stimulated fluorescence of uranium minerals.

Effectively then, gamma-ray and radon emanations are the only physical parameters derivable from remote observations that are well-established for direct recognition of uranium deposits. Both of these have been highly developed specifically for uranium detection, and each is attended by an enormous literature. Review of these applications is considered beyond the scope of this section. Here we address the previous applications of spectral reflectance-like measurements from satellites to uranium exploration.

A. Case Histories

Twelve studies utilizing satellite remote sensing and focusing on uranium problems are summarized here. The majority used distinctive spectral properties of limonite and hematite for mapping altered ground associated with uranium occurrences in sandstone. Others employed statistical classification schemes combining geologic, structural, geochemical, geophysical, and Landsat MSS data in a search for correlations between such data and the distribution of uranium.

1. Mapping of alterations using satellite images. Salmon and Pillars (1975) studied iron-oxide alteration accompanying roll-type uranium deposits in Wind River Basin, Wyoming. These deposits have bleached alteration tongues, stained locally by limonite, that extend into unaltered, drab gray–green sandstone. The ore bodies occur at the interface between altered and unaltered rocks and typically are crescent shaped (hence, "C" roll). Laboratory reflectances of 20 representative field samples from throughout the basin were used to construct spectral signatures for Landsat MSS bands. A relationship was established between response-weighted reflectances for bands 4 and 5 and Munsell hues of the field specimens. Empirically, the best correlation existed between the reflectance in band 4 (0.5 to 0.6) and Munsell hue (i.e., distinctions between red, yellow, and white).

The ratio of Landsat MSS band 5 to band 4 (5/4) produced good separations between red and yellow (or tan) and green to white rocks but could not discriminate between samples of yellow and tan, geologically important color distinctions that the eye perceives with ease. Improved discrimination between important colors was considered possible using the Landsat MSS ratio 7/6. Analog-level slicing of the Landsat MSS image for Wind River Basin successfully delineated areas of Triassic red beds but could not separate areas of limonitic stain. It was suggested that 5/4 ratios might be applicable in the Powder River Basin, where hematitic alteration is the pervasive updip coloration associated with roll-type uranium deposits.

Spirakis and Condit (1975) studied alteration halos in the Triassic Chinle Formation near Cameron, Arizona. Limonite, jarosite, gypsum, and alunite found in alteration halos produce an overall buff–yellow pigmentation that contrasts with the typical light purple to gray of this formation. These colors are used as a guide to ore but are not always indicative of uranium-related alteration. Landsat MSS data were processed to produce simulated natural-color images in which most rock units appeared as they do in the field. Spatial filters were applied to aid identification of structural features. The methods used did not distinguish altered ground in the images. The second method used Landsat MSS band-ratios 5/4, 6/4, and 7/4. Spectral-band cluster analysis was used to identify optimum enhancements of contrast to make altered rock more recognizable. The process accentuated altered areas within the Chinle Formation together with other nonaltered blue–gray mudstone units. In fact, reflectance differences between units were significant and seemingly sufficient to separate altered from unaltered Chinle rocks with additional processing.

Offield (1976) used Landsat MSS data to map iron discoloration related to uranium occurrences in the Eocene Battle Spring Formation at Crooks Gap in south-central Wyoming. Ore occurs in rolls that are associated with tongues of reddish sandstone rich in iron-oxide pigment. No uranium has been found in unaltered (drab white to tan) sandstones in this area. Areas of red altered sandstone were distinguishable in the images from unaltered sandstones using the Landsat MSS band-ratio 4/5.

Vincent (1977) searched for Landsat MSS-equivalent signatures of oxidized topsoil found on weathered uranium deposits in arkosic sandstone. An artificial spectral signature (a so-called discriminating reflectance function) thought to be representative of such deposits was derived. This involved using the weighted reflectances of iron oxides, grass, and unaltered arkose in typical deposits. The ratio of this artificial function to the signatures from normal Triassic red beds enhanced the differences between these and unmineralized red rocks. This technique proved superior to other methods, such as simple color ratio composites, for recognizing altered red sandstones.

Kober and Proctor–Gregg (1977) examined Landsat MSS data from 50 known uranium occurrences in the western United States. Images were analyzed with an analog-hybrid video-processing system. The brightness distributions in the four Landsat MSS bands were determined for alteration halos around the known occurrences. These brightnesses define a spectral signature in the Landsat bands. To isolate the signature, the logarithms of the actual brightness levels were plotted versus the cumulative probability of brightness (Beta transform) for normal rocks. The signatures then were used as discriminants in displaying the Landsat MSS images. Kober and Proctor–Gregg (1977, p. 83) found that

> . . . the discriminants are highly individualistic and only locally valid. At least at the dimensionality of [the] study (bandwidth, resolution, scale), it is not possible to generate a signature specification and then expect it to be generally valid for recognition of alteration. The value of the results . . . may extend known ore bodies.

Marrs et al. (1973) used color composite Landsat MSS images covering 10,000 km^2 of the Powder River Basin, Wyoming, in a search for uraniferous-altered areas. Orange and red ground could be distinguished only with considerable difficulty. Such colored areas were identified in a N–S-trending belt about 15 km wide and 65 km long that included the Pumpkin Buttes uranium district. Comparisons with field maps showed that these outcrops at the north end of the area are more widely distributed than apparent from the color composite images; the mapped belt of coloration trends southeast and diverges markedly from the pattern delineated on the color composite. In the northern part, mixed results were obtained by matching areas appearing altered on the color composite images with uranium occurrences. The difficulties have been attributed to the way soil and vegetation mask intrinsically weak alteration effects and to the fact that other red rocks that are unrelated to altered ground are mapped on the image.

Raines et al. (1978) used computer-enhanced Landsat MSS images of the southern Powder River Basin, Wyoming, to define facies and linear structural features within the Wasatch Formation that could be related to the occurrences of uranium. The facies distribution is separable at the surface because vegetation density and types (sage and grass) are controlled by the local substrate. These indications of surface facies were confirmed in the subsurface by determining sandstone/mudstone ratios in exploration drill holes. The newly defined geologic features are spatially related to known uranium mineral occurrences and are believed connected to uranium mineralization in three ways. First, major uranium occurrences are almost completely restricted to facies of the Wasatch of intermediate grain size. This facies probably marks the axial zone of the depositional basin. Second, the axial zone marks the boundary between domains containing structural lineaments of differing orientation. The structural details influenced the fluvial pattern and sedimentation and, hence, the flow of uranium-bearing groundwater. Third, the current basin axis is marked by a recently active fault that appears to have a relation to both groundwater chemistry and the distribution of relatively modern sandstone. The mapping of altered ground was attempted using color ratio composite images (4/5, 5/6, 6/7). Limonitic clinker beds resulting from coal fires were the only limonitic materials separable; vegetation obscured limonitic altered rock associated with most uranium occurrences.

Levinson et al. (1979) employed a video image analysis system to map hematite-pigmented (altered) sandstone in the Pumpkin Buttes uranium area. There, altered sandstone is masked by soil and by vegetation cover. The Landsat MSS ratio 7/4 proved to be most efficient for discriminating obscured altered outcrops. The ratio 5/4 was useful where vegetation cover was minimal. Alteration maps prepared from images were compared with alteration maps constructed by field mapping. Fifty-two percent of the areas depicted as anomalous on the Landsat MSS images corresponded to areas mapped as "sandstone" in the field, units that contain uranium concentrations. Many of these mismatches resulted from geometric distortions of the image data and from failure to resolve small outcrops in the video-processed Landsat composite, since video processing generally degraded the spatial resolution to 150 m. A similar analysis was made with video-processed, color aerial photography which was of high spatial but poorer spectral resolution. Sixty percent of the areas mapped as altered sandstone in the field corresponded to altered areas mapped from photographs. The original field mapping accounted only for sandstone units within areas of red (altered) sandstone as mapped by Sharp and Gibbons (1964). The aerial

photographic survey extended the number of outcrops of known "uranium-altered" red sandstone by 18 percent.

2. Other spectral, textural, and structural studies. In an interesting use of integrated geophysical and Landsat MSS data in desert terrain, Missallati et al. (1977) applied a stepwise linear discriminant function method to Landsat MSS, geologic, radiometric, and magnetic data over an area of uranium-bearing crystalline rocks in southeastern Libya. The region of interest was sampled areally by means of a Landsat-based grid at the dimensions of 6 by 8 pixels. Within each such cell, the values of variables (up to 43) in the analysis were determined, including the following:

(1) Areal percentage of different lithologies including Precambrian metasediments, two Paleozoic granites and one rhyolite, Paleozoic sandstone, Tertiary sandstone and basalt, minor pegmatites and quartz veins (8 variables).

(2) Lengths of geologic contacts between the eight possible lithologic units (22 variables).

(3) A distance from cell center to any major structural feature (1 variable).

(4) Aeroradiometric and aeromagnetic values measured at cell centers (2 variables).

(5) Landsat MSS digital raw values (4 variables) and band ratios (6 variables) averaged over cell dimensions.

Before discriminant analysis, geologic and other variables obtained by grid sampling were analyzed statistically and transformed to normal distributions using arc sine, square root, or logarithmic transformations. A study of the correlation matrix (two-variable) showed low (negative) or moderate (positive) correlation between the Landsat MSS and geologic variables; the aeroradiometric data were positively correlated with Landsat MSS bands (0.79 to 0.90); the aeromagnetic data positively correlated with band 7 (0.67); the radiometric and magnetic data positively correlated with each other (0.66).

Discriminant functions were constructed based on all geographic cells in the study area. Two groups were established from the aeroradiometric data as either anomalous (>1200 counts per second [cps]) or nonanomalous (<1200 cps). These functions, constructed to include geologic, geophysical, and MSS data, were then used to reclassify the study area regardless of the initial classification provided by radiometric data. New areas reclassified as anomalous were discovered by this procedure. The principal advantage gained by adding MSS data to the discriminant functions was the improved classification accuracy for nonanomalous terrain. The most important variables in the analysis were contact relationships between geologic units. The main contribution of MSS data emerged as the brightness of band 6 and the ratio of bands 7/4. The main contribution of geophysical data was aeromagnetic intensity.

A simple interpretation of these results is obtained by comparing the geologic map with a map of areas favorable for exploration. This shows that the discriminant technique outlined regions of Ordovician-age rhyolite within which the originally defined subareas of anomalous radioactivity were contained.

It would be interesting as a further exercise to first base development of the discriminant functions on training areas of limited size, picked on the basis of local aeroradiometric data but including only geologic variables, and second to reclassify the remaining regions excluding the geophysical data. The Landsat MSS and geologic variables thus could guide classification of the latter regions without support of the geophysical data. The results could be expected to be similar because (1) the anomalous areas reside in rhyolitic terrains, important variables in the discriminant functions, and (2) the radiometric data are not important variables in this function.

Conel et al. (1978, 1980) studied reflectance properties of altered sandstone within tabular uranium occurrences in the Morrison Formation, Utah, and associated with roll-type deposits in the Wasatch Formation, Powder River Basin, Wyoming. They used a high spectral resolution portable field reflectance spectrometer operating in the spectral region 0.45 to 2.5 μm to obtain spectra of outcrops. Alteration minerals at the Utah site consisted of poorly crystallized hydrated oxides of iron ("limonite"). Alteration minerals within the Wyoming deposits were characterized spectrally and mineralogically as goethite and hematite. Collections of spectral reflectance curves were analyzed using discriminant analysis. This yielded the definition of spectral bands useful for distinguishing such alteration minerals from other hydrothermal alteration products commonly associated with base-metal deposits and iron-oxidized volcanic, batholithic, and sedimentary rocks. For the suites of rocks studied (pooled collection of 586 spectra), the NS-001 Landsat 4 Thematic Mapper Simulator (6 channel) always provided superior discrimination to the Landsat MSS. The overall best classification by discriminant functions (95 percent) was provided by a hypothetical scanner system employing 30 equal spectral bands (0.05 μm) between 0.4 and 2.5 μm, excluding regions of atmospheric water-vapor absorption. Bands of this width

permit classification according to the clay type present, principally montmorillonite versus kaolinite. The first five bands chosen (1.25, 0.95, 2.20, 2.15, and 2.05 μm) allowed separation of unaltered, uranium-altered, and hydrothermally altered groups with 93 percent correct classification. These bands are outside the visible range, and only one measures reflectance related to the alteration (iron oxides) present. The classification, instead, centered mainly on the spectral distinction of the clay type present. The inclusion of other bands (up to 11) increased the success of classification to 95 percent. Some general notions about spectral classification emerged: First, the choice of the fewest variables for any given rock (or vegetation) discrimination problem usually is unknown beforehand; thus, the design of a scanner optimized for all geological (or geobotanical) applications based on a minimum number of widely spaced bands would be difficult. Second, the system that classifies rocks the best generally is that scanner system employing the most channels with the narrowest bands. Physically, this means the best separations can be achieved by employing the most information, short of statistically overfitting the data. The Landsat 1, 2, 3 MSS and Landsat 4 Thematic Mapper (TM) systems in this sense are inferior to spectrometer-like systems with large numbers of channels, although the utility of Landsat 4 TM is greatly improved over that of the earlier Landsat MSS system by including near-infrared channels, specifically 1.6 and 2.2 μm.

The field data were used to construct canonical variates for Landsat MSS bands. A Landsat 1 image of the San Rafael Swell was transformed to recover the uraniferous-altered training areas. The procedure was unsuccessful because the differences in reflectance in the Landsat MSS bands poorly discriminate such rock alteration and because the outcrops sought were below the size of system resolution (80 m).

Earth Satellite Corporation (1979) made an extensive study of the textural properties of Landsat MSS data and sought to correlate texture with the distribution of uranium deposits in the United States, including the Copper Mountain District, Wyoming. Texture in images refers to the spatial distribution of gray levels: Coarse texture is characterized by slow change over many pixels and fine texture by rapid change. In general, the analysis of texture was found to be improved if principal component images were analyzed. For Copper Mountain, texture measures were prepared from band 5 and band 7 data bases. Edge enhancement (high-pass filtering) on band 5 provided the "least negative" result. A tenuous relationship was reported between east–west lineaments and uranium areas. Since the uranium deposits at Copper Mountain occur in intensely fractured granite, the poor correlation obtained was attributed to the poor spatial resolution of Landsat MSS images. For uranium deposits in general, no type of texture specific to such deposits resolvable at the scale of the satellite data was found. Discrimination is poor because of scene variability and system resolution.

Data classification schemes designed to highlight areas of potential uranium mineralization in the Montrose, Colorado, 1° by 2° quadrangle, were reported by Bolivar et al. (1981). The data sets employed included hydrogeochemical and stream sediment analyses for 23 elements, U/Th ratios, airborne geophysical survey data, location of 90 uranium occurrences, geologic maps, and Landsat MSS data displayed as raw bands and adjusted for atmospheric effects. A good correlation between uranium abundance in water and outcrops of the black Mancos Shale was reported. A factor analysis was made of all data sets. The MSS raw band data are all highly correlated with themselves (0.82 to 0.98) but are uncorrelated with all other data sets used. This result might have been anticipated since the MSS data are predominantly measures of the reflectance of vegetation, soil, and rock outcrops. The chemical data refer to point measures of stream sediments and water, and the radiometric and magnetic data to mineral and elemental species. None of these are directly responsible for the reflectance properties of rocks and vegetation.

B. Summary

The investigations described here employed the Landsat MSS system (4 bands, 0.4 to 1.1 μm) to search for an iron-oxide or limonite spectral signature characterizing uranium alteration to separate this signature from those of uninteresting rock types. The Landsat MSS ratios 4/5, 4/6, 5/6, and 6/7 were generally found useful for this purpose. Successful applications were possible where physical dimensions of altered outcrops exceeded by many times the spatial resolution of the Landsat MSS data (i.e., 80 m).

Integrating geophysical and geochemical data with MSS image data and using MSS data for structural studies related to uranium distribution have yielded mixed results. The most successful approach used discriminant functions to classify likely occurrences of uranium. Geologically, these results increased the number of known anomalous areas contained within rhyolitic terrain to include additional outcrops of rhyolite.

Studies seeking a relationship between image texture and uranium distribution generally were not successful. For Copper Mountain, this approach suffered mainly from the

poor spatial resolution of MSS images compared to the structural controls that govern distribution of uranium at that site.

The discrimination of uranium-related alteration via satellite data could be improved with (1) sensors utilizing spectral bands extending out to 2.5 μm, (2) increased spatial resolution to scales on the order of 10 as opposed to 100 m, and (3) systematic analyses of the influence of vegetation, soil cover, or other alien components on alteration reflectance.

IV. Geologic Overview of Test Sites

This section summarizes the geology of the uranium test sites and reviews attributes of the genetic models that may be observable at each site using aircraft multispectral scanner data.

A. Lisbon Valley District

The Lisbon Valley District (Figure 7-2) in San Juan County, Utah, in the east–central part of the Colorado Plateau, is the site of Steen's 1952 discovery of giant-sized "black" primary uranium ore in sandstone. This discovery revolutionized the uranium industry and for the first time brought major mining companies into the national crash exploration effort to supply the United States with an atomic weapons stockpile. In addition to its historic significance, the district is unique among the major producers for its variety of geologic features and the extent of their surface expression.

The Lisbon Valley District encompasses a NW-trending, elongated anticline on the southwest flank of the larger Gypsum Valley diapiric salt anticline. The Lisbon Valley fold has been faulted longitudinally along its axis, placing Cretaceous-age Dakota Sandstone in juxtaposition with the Permian-age Cutler Formation. The raised southwestern portion of the fold constitutes a structural and stratigraphic block that comprises the uranium district. Within the block, formations from Pennsylvanian through Jurassic age are exposed in a curved, SW-dipping hogback series terminated along the Lisbon Valley Fault.

Deeper in the anticline are accumulations of oil and gas occupying distinct Mississippian, Devonian, and Pennsylvanian reservoirs, together with a wide distribution of nonproducing but still petroliferous rocks. The reservoirs probably have been faulted, and the nonproducing and petroliferous source zones fractured and deformed by salt flowage in the anticline. Petroleum from many of these more extended sources may have leaked to higher stratigraphic intervals, possibly even to the surface, along fractures. The distribution of probable source rocks is shown in Figure 7-13.

Uranium was first discovered during the pre-World War I radium boom in the Big Buck sandstone bed of the Cutler Formation near the valley bottom, but these oxidized deposits proved erratic in grade, scattered in distribution, and uneconomic. By drilling downdip from the outcrop to determine if larger concentrations occurred at depth in the Big Buck horizon, Steen accidentally discovered the largest ore body then known in the stratigraphically higher Moss Back conglomerate at the base of the Triassic, a horizon not then known to be uraniferous. The deposit also contained black unoxidized pitchblende (UO_2), rather than oxidized carnotite [$K_2(UO_2)_2(VO_4)_2 \cdot 3H_2O$], which previously typified all the known uranium ores in sandstone. Thus, the distinction between primary and secondary ores was generated and has become a cornerstone of uranium geology. The legendary staking and drilling boom that followed disclosed a necklace-like string of ore body "beads" in the Moss Back within a limited elevation zone. Lithologic controls, such as porous sandstone units, are vague for the alignment or shape of ore bodies. Within a short time a variety of generic interpretations arose, including the following three:

(1) Localization of uranium in poorly defined paleostream channels adjacent to indigenous organic trash accumulations (Steen, 1953); the proposed source rocks were tuff components in the Moss Back or overlying Upper Chinle sediments.

(2) A fossil oxidized hydrocarbon (dead oil) accumulation (Wood, 1968) that selectively fixed subsequently migrating uranium; this interpretation is favored by a locally high asphaltite content in the ore.

(3) Ore fluids rising from depth, mineralizing the Moss Back horizon and bleaching iron from the Wingate Sandstone at least 800 ft stratigraphically above the ore horizon (Gabelman and Boyer, 1958); the genetic problems were not resolved as the district developed and as potash beds and oil accumulations were discovered in deep horizons beneath the uranium.

The district has never ceased to be a significant producer, and Atlas Minerals Corporation has effected a consolidation to nearly single controllership. The continued significance of the district as a producer, the variety of resources and geological features, and the excellent exposures of color-contrasting rocks make this district very favorable for a test of remote sensing and interpretation techniques. The Lisbon Valley District was selected as a Geosat test site because the above characteristics offer clear examples for both geologic mapping and the study of uranium geology.

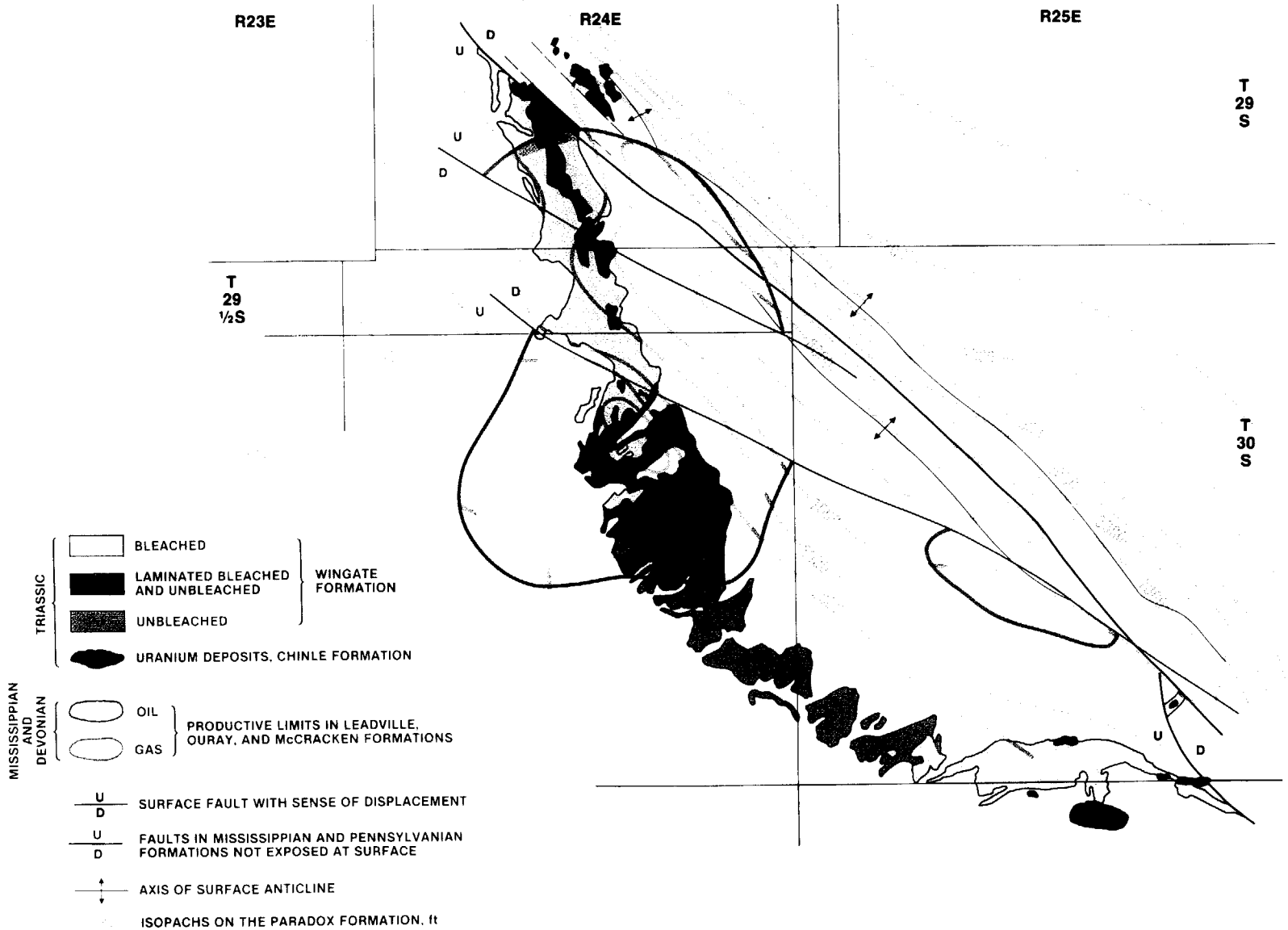

Figure 7-13. Distribution of bleached Wingate outcrops, Chinle ore deposits, and Mississippian oil and gas accumulations on Lisbon Valley Anticline. Solid lines around ore bodies represent approximate economic limits of mineralization. Isopachs represent distribution of Paradox Formation, potential source rocks for petroleum accumulations in the anticline (Parker, 1966).

The distribution of Wingate Sandstone alteration (bleaching) offers an important problem for remote sensing studies. Loring (1958) pointed out the areal correlation between sandstone bleaching and Moss Back uranium distribution in the Big Indian District. Gabelman and Boyer (1958) conjectured that bleaching represented a stratigraphically transgressive alteration event linked genetically to ore deposition. The spatial distribution of bleaching has not been mapped anywhere in the anticline. This distribution is of obvious importance in any discussion of origin for the alteration or its connections with ore deposition.

Bleached and unbleached rocks can be separated based on a number of spectral and geomorphic criteria. For example, bleached sandstones are characterized by the absence of red hematite pigment, presence of minor amounts of kaolinite, and absence of calcite cement. Unaltered sandstones are stained red and contain calcite cement but little or no clay. Bleached strata are friable and form rounded outcrops that support an extensive cover of piñon and juniper. Unbleached sandstones are resistant, display good jointing, and are relatively poorly vegetated. Contrasts in iron pigmentation and vegetation cover are surface characteristics especially amenable to analyses using multispectral scanner data. Carbonates and clay minerals have distinctive absorption bands as well, but these tend to be washed out by the presence of iron-oxide pigments or vegetation.

B. Copper Mountain District

The Copper Mountain District is on the north margin of the early Tertiary Wind River sedimentary basin, Fremont County, Wyoming (Figure 7-2). The basin margin is marked by an east-trending complex zone of faults along which the curving Owl Creek Mountains arch was thrust toward the basin during its uplift and along which basin subsidence later was intensified. At Copper Mountain the Precambrian granites have been cut by normal faults. These rocks are covered by an onlapping sequence of conglomerates, sandstones, and mudstones comprising the Eocene Wagon Bed (Teepee Trail) and Wind River Formations. The district is named for copper occurrences in the Precambrian rocks.

Long after uranium was discovered in the Eocene Wind River Formation in the Gas Hills (in 1952) some 50 km (30 mi) south in the basin, uranium (autunite) was encountered in about 1956 in a granite boulder and cobble regolith comprising the base of the Wagon Bed Formation at Copper Mountain (Arrowhead Mine). This deposit was one of the first discovered in basal sediments directly overlying granite, and it represented a new depositional and exploration environment. The granitic rocks were suspected as a source for uranium incorporated syngenetically in the conglomerates and concentrated by both syngenetic and diagenetic processes. Additional accumulations could also be attributed to downward percolation of uranium from volcanic tuffaceous rocks (now missing) higher in the Tertiary section. The predominance of autunite (uranium phosphate), compared to uranium vanadates and carbonates in the Gas Hills, favored the granitic source and also suggested that autunite concentrations were oxidized accumulations from pitchblende veins in the granite. The genetic controversy was whether uranium concentrations would extend significantly down into the granite as veins or stockworks or would be confined to the superjacent sediments. This controversy had major economic consequences.

Surface radiometric prospecting soon disclosed autunite concentrations higher in the Wagon Bed (Teepee Trail) Formation in carbonaceous siltstone (Rex deposit) as well as some associated with asphaltite in stockworks deeper in the granite (Gem deposit).

The distinction among products resulting from reducing environments, sedimentation, epigenetic primary rock alteration, and supergene oxidation/weathering strongly influenced exploration of the Copper Mountain District. The trend in early interpretation was to consider mineralization in all occurrences as supergenetic. A colorfully anomalous zone of oxidized granitic rocks generally confined to a partly exposed pediment surface was recognized and interpreted in terms of the supergene model. This zone was considered a residual weathering product (Yellich et al., 1978) that accompanied the leaching uranium from the granite and thus was considered of speculative though conceptually well-defined genetic significance for the uranium accumulations. Exploration following the model of lateral and downward secretion from the weathering zone was successful and led to discoveries in fracture works along altered fault zones at depth. The Canning Ranch and Fuller resources were thereby discovered. Deep drilling in the fault zones disclosed unoxidized sooty pitchblende along fractures at depth, polymerized hydrocarbon precipitant, and an associated red earthy hematite, which was interpreted as resulting from reactions involving pyrite during the precipitation of uranium.

In addition to near-surface oxidation (weathering) of dark minerals and the association of earthy hematite with ore at depth, the host and the source granitic rock displayed propylitic alteration, which might be linked to previous mineralization episodes. Propylitic alteration is recognized specifically at depth in the uranium accumulations. The distribution of such alteration at the surface is unknown

and constitutes a problem for future study. Any propylitized rock near the surface has possibly undergone weathering, so the geologic/remote sensing problem would be to recognize and separate such altered zones in the presence of a masking weathering alteration.

The Copper Mountain District was selected as a test area providing good problems for both geologic mapping and uranium exploration using remote sensing methods for the following reasons:

(1) A suspected zone of supergene and propylitic rock alteration at the surface was correlated with the presence of uranium mineralization at depth.

(2) There were excellent exposures of Tertiary and Quaternary sediments and Precambrian granites.

(3) An intensive Department of Energy/Rocky Mountain Energy (DOE/RME) program existed and was focused on the study of uranium district "halos" using geochemical and geophysical surveys (Bramlett et al., 1979, 1980).

(4) The area was under the single controllership of RME, thus permitting access to property and to proprietary information about the deposits and geology of the test site.

V. Summary of Test Site Results

A. Nature and Utilization of Remote Sensing Information

The aircraft and satellite multispectral scanners, in addition to conventional aerial photographs, provided the principal data sets utilized in this study (Table 7-3). These instruments record essentially broadband solar radiance that either is reflected by the Earth's surface, mainly in the spectral region 0.4 to 4.0 μm, or is absorbed by the surface and re-emitted as thermal radiation, principally in the spectral region 8 to 14 μm. The measurements contain, in addition to the wanted surface signal, important atmospheric absorption and scattering effects that must be removed before quantitative interpretation of the data.

Two methods of interpretation are possible: (1) as surface spectral reflectance or emittance, or (2) photogeologically, as images. The first method requires calibration of the radiance using ground observations of reflectance or emittance to remove scattering effects introduced by the atmosphere. The second method can be advantageously used with or without these calibrations.

Ultimately, the images and/or spectral observations are used to infer the stratigraphic, structural, and geomorphic relations in the test sites together with the distributions of possible uranium-related alteration, alluvium, colluvium, eolian deposits, soils and vegetation, or mixtures of these.

All such discrimination (or identification) exercises use digital image processing methodology to separate and correlate surface cover types. The images are commonly presented as band composite, band-ratio composite, and principal component, or canonical transform (linear band combination) renditions. All such methods exploit the reflectance properties of surfaces to achieve desired separations, using either specific absorptions (band ratios) or more generalized descriptions of the entire spectrum (principal component).

Table 7-3. Data sets acquired for the uranium test case program

Sensor	Wavelengths	No. Channels Utilized	Areal Resolution, m	Site[b]	
				Lisbon Valley	Copper Mountain
Photography	Color, color IR		1	A	A
24-channel, μm	0.34–4.0[a]	14	7	A	NA
M^{2}S 11-channel, μm	0.38–1.06, 8.05–13.7[a]	10	15	N	A
NS-001, μm	0.45–2.35, 10.4–12.5[a]	7	15	A	A
Landsat MSS, μm	0.4–1.1[a]	4	80	A	A
X-band, cm	2.8		20	N	NA
L-band (Seasat), cm	23.5		25	N	N

[a]See Technical Appendix, Section 14, for specific band assignments.

[b]A Data sets analyzed in detail for this study.

NA Data not acquired at the site.

N Data sets acquired at the site but not analyzed in this study.

Inferences regarding the relation between supposed surface-exposed rock alteration and uranium mineralization at depth are possible through so-called exploration models. Considerable effort in field observations and photogeologic interpretation of the images and aerial photographs has been devoted to establishing for the uranium test sites plausible remote sensing exploration models where none existed before. The problems involved proved to be very difficult: The remote sensing approach forces a reinterpretation of all of the conventional arguments concerning genesis of the uranium deposits in terms of effects observable at the surface. This useful reevaluation has led to new geologic insights for both test sites and is one of the most useful functions of the remote sensing approach. This section summarizes the geologic and remote sensing results for the uranium test site investigations.

For further discussion of the physical basis of the remote sensing method and detailed comparisons of sensors, refer to the Petroleum Commodity Report (Section 10) and to the test site reports (Section 8, especially the Appendixes, and Section 9).

B. Lisbon Valley

The Geosat uranium test site at Lisbon Valley represented a unique opportunity to apply remote sensing techniques to a major sandstone uranium district. The structural setting, lithologic diversity, presence of mappable alteration, and generally good rock exposures enhanced these investigations and provided excellent cases for application of the methods. Aircraft multispectral scanner images have been used to map, for the first time, the distribution of altered rocks in the area. These distributions have been related spatially to the distribution of uranium ore bodies and to oil and gas accumulations or petroleum source rocks in the subsurface.

At Lisbon Valley the principal geologic feature of interest was the differential bleaching of Wingate Sandstone. The distribution of bleached and unbleached rock over most outcrops on the southwest limb was first mapped using stereoscopic color aerial photographs. Six informal facies of the formation were identified. These consist of bleached, unbleached, and partially bleached strata, together with possible photogeologically inseparable (but intertonguing) layers of Wingate and the overlying Kayenta Formation. Such photogeologic interpretations, in which the rock surface can be assigned definite lithologic characteristics, formed the basis for subsequent interpretation of the image data.

Bendix 24-channel aircraft scanner images were used to obtain the distribution of bleaching throughout the Big Indian District. Specific canonical transforms were prepared from 10 channels of data (0.46 to 2.36 μm) optimized to separate bleached and unbleached units. Six units were identified in these images over the Wingate outcrops. These units correspond only in part to those derived from the aerial photographic interpretation. The geological significance of some of the image units (those not identifiable in the photointerpretation) is unclear. These may represent (1) new unrecognized patterns of alteration that crosscut stratigraphic horizons, (2) mixtures of cover types spatially unresolvable in the scanner data, or (3) artifacts in the image color patterns from the particular contrast stretches employed. Stereoscopic coverage in the image data would have significantly aided further stratigraphic and structural interpretation.

The NS-001 Thematic Mapper Simulator data were used to prepare principal component transforms and color ratio composites of the entire Lisbon Valley test site. Separation of bleached and unbleached Wingate Sandstone could be obtained using both of these image processing techniques. In addition, all of the major formations and many subunits were mapped, on the basis of both topographic relations and differences in spectral reflectance properties. A major unconformity separating Paleozoic and Mesozoic strata was represented. The Lisbon Valley Fault can be distinguished by topographic alignments and by truncation of important rock units where such units intersect the fault. Major areas of cultural disturbance (stripping of tree cover for land reclamation) can be identified and mapped.

The NS-001 data were more useful than Landsat MSS data. The NS-001 data have higher surface resolution, and stereoscopic coverage is available.

The distribution of bleached Wingate Sandstone and the general stratigraphic relations present in the Lisbon Valley Anticline may also be recovered from Landsat MSS images of the test site. While these images highlight bleached outcrops, surface resolution of $\sim$80 m precludes detailed geologic analysis of the bleaching patterns present.

The distributions of bleached rock obtained from photogeologic and image analyses were compared with the distribution of uranium mineralization in the Moss Back and Cutler Formations. Bleached rocks are inferred to have formed a cap near the crest of Lisbon Valley Anticline. The cap has been faulted and erosionally dissected with breaching of the anticline so that the initial distribution of remnant bleached sandstone is unknown. Uranium deposits of the Moss Back/Cutler Group lie geometrically beneath pervasively bleached or partly bleached outcrops (Figure 7-13), and all are located at elevations near the apparent

subhorizontal boundary between bleached and unbleached rock in the structure. Uranium deposits are essentially absent beneath unbleached outcrops. Bleached rocks and uranium deposits lie above oil and gas accumulations or other petroleum source rocks in the anticline. There is thus a triple spatial coincidence of bleaching, uranium deposits, and oil and gas reservoirs or source rock in the anticline. This suggests a causal relation between some members of the group. Other examples of this type of association are known, for example, the bleaching of red beds in anticlines over petroleum accumulations at Cement, Velma, Chickasha, and Eola fields in Oklahoma (Donovan, 1974; Ferguson, 1979, 1981). Exploration for uranium has been contemplated at some of these sites (J. D. Ferguson, personal communication, 1981).

The preference in this study was to work with principal component images for studies at the Lisbon Valley site. These renditions possess three generally desirable properties: (1) spectral reduction, that is, representation of the scatter in multiple spectral planes by a smaller number (i.e., three or four) of statistically independent variables, (2) partial independence from atmospheric effects if computed from the scene covariance matrix, and (3) total independence from atmospheric effects if computed from the scene correlation matrix. The principal components may be computed without prior geologic knowledge of a site, and they provide a statistically significant separation of spectrally differing units in the scene. Specialized linear transformations such as the canonical transform provide superior discrimination of specified spectral image units, as was demonstrated in mapping of bleached rocks at this site.

C. Copper Mountain

At Copper Mountain, strata-bound mineralization and alteration occur only in the Eocene formations overlying the crystalline basement. This sedimentary cover does not offer nearly as much economic promise for uranium occurrence as does the basement. Mineralized rock in the crystalline basement is reasonably uniform to the surface, and the mineralization is predominantly fracture controlled in distribution. At depth, the primary parameter is the existence and recognition of a possible altered-rock matrix occurring with fracture-controlled ore concentrations. The alternate interpretations are whether the fractures guided (1) a hypogene fluid charged with primary ions that propylitized the rocks through which circulation occurred, or (2) supergene groundwater that redistributed shallow ions secondarily, leaving an oxidized surficial horizon leached of uranium. In either case, the water involved could be dominantly or entirely meteoric. Further, the actual alteration products are represented at the surface as oxidized residue of the original alteration, introducing the yet more important factor of weathering. Separating the conjectured hypogene alteration in such a weathered layer is an unresolved problem. The problems pertinent to economic exploration are (1) recognizing the weathered equivalents of ore-selective matrices (i.e., propylitic) and (2) deciding if the weathered surface layer by itself constitutes the source for at least a portion of the uranium found at depth. At the resolution of Landsat MSS images, the ore bodies themselves, even if exposed, are too small to be recognizable. This is not a problem for airborne multispectral scanners with high spatial resolution. The mineralized rocks projected to the surface are in any event covered in detail by Tertiary sedimentary rocks and are thus inaccessible to direct observation.

The focus of this study was determining the distribution of surface oxidation representing, on the supergene model, the distribution of at least a portion of the uranium source rock. The oxidation effects were depicted in detail over a wide area in color ratio composite images of the Modular Multispectral Scanner (M^2S) 11-channel data utilizing the Landsat MSS equivalent band-ratios 4/5, 4/6, and 6/7 (Figure 7-14). A simple density slice of a single band ratio (4/6) highlighted the oxidation patterns and mapped these according to "intensity" of oxidation. This ratio measures strength (depth) of the charge-transfer band due to Fe^{+3} in the iron oxides and the iron hydroxide reflectance spectrum.

Analysis of the images revealed details of the surface oxidation pattern that were previously unsuspected. Mapping by geologists of the controlling company (RME) showed an E-W-trending belt of surface-weathered crystalline rocks coincident with partly exhumed pediment surfaces along the base of the mountains, with oxidation extending from the West Fork of Dry Creek on the west to the Paleozoic–Precambrian boundary on the east. The boundary of oxidation to the north coincides roughly with the limits of pediment erosion at the mountain base; to the south, exposures of oxidized granite are limited by Tertiary sediment cover. All known uranium occurrences throughout the test site both in Tertiary rocks and in the granites beneath the surface are associated with weathered granites in the western half of the belt.

The new patterns of oxidation recovered from analysis of the scanner data are far more intricate (Figure 7-14). The western half of the previously mapped oxidized belt was depicted as oxidized in the scanner results, thereby establishing a definite image representation for this intensely weathered terrain. This correspondence was then used to interpret the remainder of the image. The eastern portion

Figure 7-14. Distribution of oxidized granitic outcrops from the M²S 11-channel color ratio composite and ratio density slices. Geologic boundaries for the Archean, Paleozoic, and Tertiary/Quaternary sedimentary rocks from Thaden (1980b, 1980c, 1980d, 1980e)

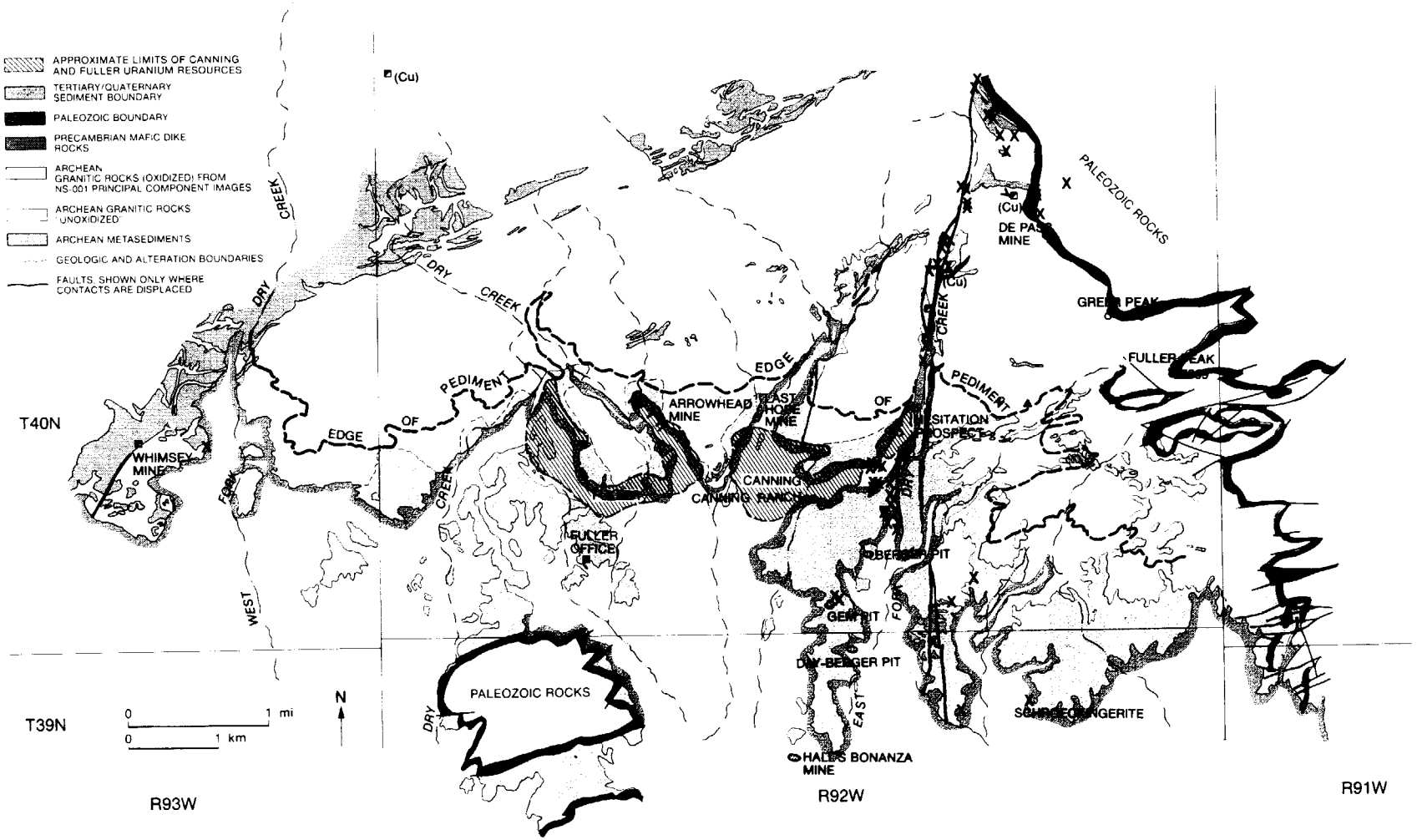

Figure 7-15. Canning and Fuller resources (in granitic rock) and minor uranium prospects in granite and Tertiary sediments plotted with respect to the distribution of Wagon Bed (and Quaternary) sediments and surface oxidation patterns in granitic rock obtained from NS-001 image. Geologic boundaries for the Tertiary, Paleozoic, and Precambrian units from Thaden (1980b, 1980c, 1980d, 1980e). Other sources include Thaden (1980a, 1980e); Yellich et al. (1978) (shafts, cuts, adits, pits, tar springs; see Figure 9-48); RME, Denver, Colorado (drill hole data to August 1978); NASA–JSC aerial photography, August 1979 (drill hole data to August 1979, based on approximate location).

of oxidized granite originally mapped extended from the East Fork of Dry Creek to the Paleozoic–Precambrian boundary; this portion is depicted as unoxidized in image data. The discrepancies arise from directional surface reflectance effects in the image data. Additional oxidized areas were recognized in the images to form an intricate pattern extending over much of the remaining crystalline terrain along stream valleys and along NE-trending fracture zones marking faults that cut the granites. The oxidation effects depicted are extremely difficult to recognize on the ground or from aerial photographs. Mapping by conventional field procedures is thus difficult or even impossible. This may explain why these effects were overlooked or not included in the original field mapping.

The deeply weathered zones of granites are coincident with old pediment surfaces that have been exhumed from beneath the Tertiary sediment cover. Such weathering may be attributed to pre-Tertiary subareal weathering but may also be of more modern origin. The newly delineated oxidized areas in images, on the other hand, fall over complex topography, including paleotopography along old stream valleys topographically above the pediments. They are thought to represent areas more recently exhumed from beneath the Tertiary cover.

Based on experience with the correlation between oxidized granitic terrain and uranium mineralization elsewhere in the study area, it was speculated informally that the newly depicted areas of surface alteration might constitute additional targets of exploration interest. Subsequent examination by RME geologists of granitic (oxidized) rocks along a shear zone extending up into the mountains behind the frontal pediment surface disclosed the presence of anomalous radioactivity. These additional areas were evidently unanticipated based upon the previous field mapping and upon the exploration model employed.

The distribution of oxidation was also examined using principal component transforms of the NS-001 imagery. The distributions obtained differ from those given by the M^{2}S results. Intensely oxidized terrain in this second interpretation is essentially confined to the pediments and to narrow zones in the granites following mafic dike swarms or trains of metamorphic inclusions.

The oxidation patterns from M^{2}S and from NS-001 images were compared with the distribution of uranium mineralization throughout the test site. These mineralized patterns were inferred from the distributions of exploration drill holes, old mines, adits, prospect pits, etc. The distribution of mineralization falls within the pattern of heavily weathered granitic rocks and in general corresponds most favorably with the distribution provided by the NS-001 results (Figure 7-15).

The ore-altered matrix association consisting of pitchblende-coated fractures in propylitically altered granite was discovered solely by examining cores. This association is a valuable tool to exploration geologists. The weathered surface masks or modifies this alteration in the mineralized areas. It has not been mapped at the surface by company geologists, and it has not been possible to study it with the scanner data.

VI. Remote Sensing Exploration Models

A remote sensing exploration model relates the distribution of surface alteration, lithology, structure, etc., either on an empirical or a deterministic basis, to the subsurface distribution of mineralization. Studies at the Lisbon Valley and Copper Mountain test sites have resulted in two empirical models. This section reports our findings and describes problems raised by the geologic relations implied.

A. Lisbon Valley

1. Exploration strategies. No specific exploration models were known for the uranium deposits at Lisbon Valley beyond direct mining or surface drilling to locate extensions of existing ore bodies along trends in the host fluvial sandstone channel systems. Bleaching of sandstone outcrops was recognized to occur above ore-bearing strata in 1958 (Loring, 1958) but apparently was not used as an exploration guide.

Some general rules governing the distribution of ore had been recognized earlier: (1) Uranium in the Chinle and Cutler Formations occurs immediately adjacent to the (Paleozoic–Mesozoic) angular unconformity separating the two (Malan, 1968), and (2) where present, ore is confined to an elevation interval of 6200 to 6700 ft drawn on the top of the Cutler Formation (Lekas and Dahl, 1956). An exception to this rule is the Atlas Minerals Velvet (1979) deposit in the southern ore district. The estimated elevation of this body is 5200 to 5700 ft; its stratigraphic position is uncertain.

2. Information supplied by remote sensing method. The correlation shown in Figure 7-13 between Wingate bleaching and major ore accumulations is satisfying but not perfect. For example, while bleaching over the North Alice Mine is geometrically conclusive, the Wingate over the larger Mi Vida Mine is in the transition zone of bleaching, and the major Louise Mine also lies beneath only partly bleached rock.

Remote sensing methods depict the present and not the initial distribution of bleach effects. Similarly, mining depicts the present, not necessarily the initial nor the complete distribution of ore. Large canyons (Mi Vida, Expectation) cut the Wingate Sandstone in the transition region, exposing the Upper Chinle Formation and Moss Back Member beneath. Analysis of cross sections reveals that erosion has removed a substantial amount of bleached rock south of Mi Vida Canyon so that the initial distribution of bleached facies and the distribution of ore deposits might have been more nearly coincident. In the southern part of Lisbon Valley Anticline, *all* known occurrences of ore, including a deposit discovered in 1979 by drilling, are located beneath bleached outcrops. In the central portion of the anticline, Moss Back rocks beneath the unbleached facies contain only a few ore bodies. These ore bodies are extremely localized, and none exceeds a few hundred thousand pounds in size.

A complete analysis of this problem would require knowledge of the complete present distribution of bleaching, including that in the subsurface. This can be obtained only by drilling and is beyond the scope of this project.

3. Timing of mineralization and alteration events

a. Age of mineralization. In addition to the detailed problems of areal correlation, there remains the problem of the timing of the mineralization and bleaching events. Dating of the uranium deposits is uncertain due to possible geochemical alteration of the ore bodies by groundwater action. The most convincing discussion of the uncertainties and significance of the isotopic age is that of Miller and Kulp (1963). They interpreted the isotopic data to indicate primary uranium mineralization during or soon after deposition of the enclosing Chinle rocks, that is, about 210 m.y. ago.

b. Age of bleaching. The time of bleaching cannot be older than the time of Wingate deposition itself, although intraformational sedimentary structures suggest bleached rocks may have been present during the Wingate deposition interval. The upper boundary of bleached Wingate interfingers with red Kayenta sandstone, suggesting bleached rocks were present at that time; but these relationships might also result from permeability variations between these formations. Bleached Wingate strata are truncated by the Lisbon Valley Fault, which is Laramide in age. Thus, the bleaching is in part pre-Laramide in age. The sandstone is a good aquifier, and some iron solution and transport may still occur with the flushing of meteoric water through the system. These observations only loosely constrain the time of mineralizing and sandstone alteration events.

An alternative interpretation is of a serial connection between mineralization and bleaching. That is, a common external agent (petroleum) may have acted sequentially, first as a reductant source for deposition of uranium during Chinle time, and later as a reductant aiding solution and removal of Fe^{+3} pigment during or after deposition of the Wingate. Bleaching, in this interpretation, thus indicates the reducing environmental conditions required for deposition of ore.

A barrier to accepting these relationships as genetically significant is that bleached rocks and ore horizons are separated stratigraphically by hundreds of feet of unaltered red mudstone and sandstone, with no apparent connection between the two.

However, the observed distributions of altered and mineralized rocks are incomplete in that hundreds of feet of Mesozoic and Paleozoic rock have been removed over the axial region, leaving residual outcrops exposed only along the flanks. Thus, many conduits may have existed between these formations that are no longer preserved along the flanks of this structure.

B. Copper Mountain

1. Exploration model. Attention is confined here to mineralization comprising the North Canning Ranch and Fuller resources at Copper Mountain (Figure 7-15); deposits found in the Tertiary rocks are excluded.

Based on analysis of drill cores the North Canning resource was characterized as composed of sooty pitchblende occupying extensive fractured granite along fault zones. The country rock contained low-temperature propylitic alteration and hematite on fractures associated with the mineralization. Concentrations in the subsurface were localized beneath a remnant covering of Tertiary sediments that apparently acted to shield the uranium accumulations beneath from remobilization and redistribution by downward-percolating surface waters. Yellich et al. (1978) suggested a supergene mechanism of concentration in which rocks at the surface were oxidized while being leached of their uranium.

The exploration strategy consisted of a search by drilling for mineralized fracture zones. The primary areas were generally confined to zones of oxidized granite of the pediment as opposed to "fresh" granite exposed outside the pediments. Hematite staining of fractures was also used as a guide. Furthermore, the primary areas were specifically centered on Tertiary outcrops within the belt of oxidized granite. Distribution of propylitization at the surface was evidently not important as a guide inasmuch as it was dif-

ficult to identify in the presence of masking by surface weathering. The limonite staining, however, may be derived from iron-rich chlorites or clays; these could represent the propylitized zone and hence, in a secondary fashion, the original reduction alteration that has significance for the uranium emplacement.

2. Information supplied by remote sensing method. The remote sensing exercises at Copper Mountain specifically were aimed at mapping the distribution of surface oxidation using the image data. The image method proved to be sensitive to the amount and variability of this alteration; as a result, the patterns determined are more extensive and considerably more complicated in distribution than those provided by conventional field mapping.

The image data were used to predict the location of additional favorable ground based on the oxidation criterion. The controlling company (RME) subsequently located surface mineralization in these new areas. The usefulness of the remote sensing image method as a supplement to conventional methods of mapping was thereby demonstrated.

3. Discussion of significance and timing of alteration. Problems concerning the genesis of the ore bodies and of the surface alteration remain. At least six models can be described for the origin of the Copper Mountain deposits:

(1) Precambrian uranium widely dispersed in granite was leached and transported in Tertiary time by either meteoric water heated by deformational friction during thrusting or cold meteoric groundwater. The uranium subsequently was chemically fixed by hydrocarbons migrating from reservoirs in Mesozoic sediments beneath.

(2) Tertiary uranium was dispersed syngenetically in the Wagon Bed and possibly the White River Formations (the "Gas Hills" model). These tuffaceous sediments were leached of uranium by meteoric groundwater, and the uranium precipitated in granite along crushed zones by the reducing action of hydrocarbons or reducing conditions at the water table.

(3) Precambrian uranium in granite was liberated by surficial leaching and erosion of granite and redeposited syngenetically in the Tertiary Wagon Bed (Teepee Trail) gravel and into crushed granite at depth, either in syngenetic concentrations fixed by clay or organic matter in sediments or in epigenetic secondary concentrations fixed by organic matter, hydrocarbons, or other reducing agents (Kendall et al., 1980), possibly with multiple episodes of precipitation and remobilization in veins in granite.

(4) Tertiary uranium was introduced hypogenetically into stockworks controlled by the fracture pattern along the faulted mountain front.

(5) Precambrian uranium was mobilized by hydrothermal waters convectively driven by radioactive heating. Precipitation and alteration took place by closed-system reaction within crushed zones (Shrier and Parry, 1982).

(6) Multiple Tertiary episodes of uranium mineralization involved both tuffaceous and granitic source rocks (Kendall et al., 1980).

Interpretation of the relative ages of mineralization and surface weathering is a difficult problem. Probably a series of mineralizing episodes is represented, some as recent as the Pliocene (S. Reyher, personal communication). The age of weathering is also unspecific. Based on interpretation of drill cores and cuttings, the weathered layer is not present along paleovalleys beneath the Tertiary cover. If this represents erosion of the zone, the age of weathering is pre-Wagon Bed (pre-Middle Eocene), and the weathering can at most be significant, on the supergene model, for the pre-Eocene episodes of uranium deposition.

Field relations also suggest, however, that the surface coloration may develop progressively after removal of Tertiary sediments from the granitic pediment surfaces. Thus, actual timing of the surface coloring is ambiguous. If, however, the weathered zones prove localized over weathered or propylitically altered zones in the granites and these zones prove important as altered matrices or as source rocks for mineralization, then the limonite stain serves as a guide of secondary origin to these "primary" effects. In this sense, the staining may be significant regardless of its actual age.

VII. Extrapolation of Techniques to Other Uranium Districts

The most useful guides to uranium occurrences, bleaching at Lisbon Valley and favorable limonite at Copper Mountain, can be easily extrapolated to other districts.

A. Bleaching of Sediments

Lisbon Valley represents a typical occurrence of strata-bound uranium deposits in one of only four prolific horizons in the entire Colorado Plateau, but the deposits are nearly unique among districts of strata-bound uranium deposits. Lisbon Valley is the only district so far found in a breached, faulted anticline, although the actual control by

either faulting or folding has been questioned. There are, however, many other districts in which strata overlying or adjacent to ore bodies have been bleached or otherwise altered in a manner similar to that at Lisbon Valley. Examples include the Grants uranium belt, New Mexico, and Sinbad Valley of the San Rafael Swell, Utah.

In circumstances where bleaching occurs in the same stratum that binds the uranium deposits, bleaching has been considered, almost since the inception of uranium geology, a process directly related to the concentration of uranium into deposits, that is, the altered matrix in which ore bodies are found. Bleached rock always has been a time-honored exploration guide and can be used for remote sensing interpretations in almost any district of uranium deposits in sedimentary rocks. Indeed, the technique was used extensively during the 1950s by studying color aerial photographs.

Bleaching associated with reduction and uranium (as well as other metal) mineralization represents a change from the original brown or red colors of sediments to pale-green or near-white colors, that is, the change from ferric oxides to ferrous oxides or silicates. This chemical change is generally followed by the conversion of part of the oxides to sulfides. The process is independent of surface weathering and, in fact, would not occur in an oxidizing environment. Bleached weathered rock at the outcrop also can result from the reduction of iron by plant debris or by the removal of iron by suspension or solution in meteoric water.

Distinguishing residual reducing sedimentary environments from reduction imposed epigenetically upon an oxidized sediment can be difficult if evidence of the original reductant (organic material) is not present or if clear cross-cutting stratigraphic relations are absent. These two mechanisms have been debated intensely along with the syngenetic–epigenetic alternatives of uranium genesis.

Stratigraphic separations between ore and bleached rock with no apparent connection between the two retard simple extrapolation. Geologists hesitate to believe that the dilute groundwater thought to be responsible for uranium concentration could penetrate across formations of low permeability to accomplish coordinated changes in selective aquifers. On the other hand, at Lisbon Valley, the Lisbon Valley Fault and possibly other faults of earlier age resulting from diapiric flow of salt might have acted as conduits across the impermeable horizons. Clearer examples may be provided in other areas. For example, at Temple Mountain, Utah, pipe-like collapse structures penetrating Triassic and Jurassic strata form accessible pathways between mineralized horizons and superjacent strata. In that area the Wingate Sandstone is bleached for miles along the outcrop away from the collapse structure, but the intervening Chinle red beds are unaltered, except locally around the pipe itself. These distributions are probably controlled by formation permeabilities; the Wingate is a porous, permeable sandstone whereas the Chinle consists of tight, clay-rich mudstones with high resistance to fluid motion.

Many uranium districts have large areas of surficial, strong-green color, resulting from a reduced state of the iron present. This coloration at Lisbon Valley is largely restricted to the narrow band of Moss Back outcrop. Gray and gray–green rocks of the Moss Back are easily separable on scanner images. This coloration is not so readily accepted as an alteration product; it is usually taken to represent a syngenetic reducing depositional environment. In any case, at other localities its distinction in scanner data would be straightforward.

B. Iron Oxidation and Weathering

For remote sensing, the distinctive features closely associated empirically with uranium concentration at Copper Mountain are weathering of granite and the production of a peculiar variety of limonite. The chance for extrapolation is rather low because the combined types of features and associations at Copper Mountain are fairly uncommon if not unique and because the role of weathering in the concentration of uranium is uncertain. Copper Mountain has few counterparts anywhere, unless the common denominator would be veins or shatterworks in granitic rocks. In that case, there are many counterparts, and the critical controls and guides are essentially the fracture orientation and density which are inaccessible to surface observation at this site.

There is considerable promise for extrapolation of the peculiar limonitic color, even though its association with the mineralization process may be questionable. It has been observed in most granitic terrains that were subjected to relatively low-temperature mineralization, and it is considered a valid common indicator that can be extrapolated regardless of the physiographic nature of the exposures. This particular limonite may result from selective oxidation of the ferrous silicates (clays and chlorites) produced by the invasion of the reducing environment as part of the alteration phase of the mineralization cycle. Visually, this limonite can be distinguished from hematite or limonites of other parentage. In effect then, this limonite serves the same role in recognition as the "greening" or bleaching of sandstones on the Colorado Plateau and indeed can be considered to be of equivalent importance. As with bleaching, it does not directly indicate uranium ore bodies but

rather indicates the type of matrix or the chemical environment in which they can and habitually do occur. However, there are many ferrous clay matrices without uranium ore bodies.

VIII. Implications for Mineral Exploration in General

Epigenetic concentrations of uranium in the Earth's crust differ little in occurrence from most other trace elements. Historically, uranium exploration consisted of examining other metal deposits and districts for anomalous radioactivity. Failure to find significant amounts of uranium associated with concentrations of other trace elements led to the conclusion by many that uranium did not participate in any important way in primary (magmatic, hydrothermal, metamorphic) mineralization processes.

The discovery of large economic deposits in sandstone (and later, other sedimentary hosts) geographically removed from other mineral districts stimulated the conclusion that most economic uranium deposits have an independent origin related to meteoric water supergenesis or laterogenesis. The strata-bound nature of these deposits suggested that uranium was syngenetic with the host sediment and was epigenetic in detail only by virtue of secondary concentration.

Vanadium, copper, barium, molybdenum, lead, and selenium concentrations have been found in sandstones with characteristics similar to those of uranium deposits, and indeed some (vanadium–uranium) are commonly produced together. More commonly the elements do not occur together, but many concentrations nevertheless are enclosed by similar altered-rock envelopes, or in large altered matrices. Further, the superficial associated limonite assemblages are similar. Therefore, the remote sensing techniques developed for uranium exploration in sedimentary terrains should be applicable to the other elements in sandstone.

Such an empirical common denominator as alteration halos should indicate similarity or even association of the genetic processes, although the common genetic factor may be one as innocuous as the corrosive power of ordinary dilute groundwater. The total mineral ion content of groundwater is the key factor in deciding whether such fluids can be a mineralizing (corrosional, transportational, or depositional) agent. Nearly pure (sweet) or dilute (in mineral ions) groundwater should have little effect on the rocks through which it passes, thus requiring long geologic time intervals to accomplish mineralization. Corrosive brines, on the other hand, are known to exist and are capable of producing mineralization in short time intervals (Gabelman, 1970). The hydrothermal fluids that create other metal deposits are brines. Therefore, similar alteration envelopes and even similar metal deposits (depending on the mineral ion transplanted) could be created by similar brines of different genesis. Connate, magmatic, and laterogenic (in geopressured marginal marine basins) brines are all known.

The empirical and conceptual similarities described can be extrapolated from the sedimentary environment to most other host environments for mineralization. First, large alteration matrices and ore-body alteration envelopes are common to most other metal deposit types. The alteration types are similar throughout all district types ranging from high-temperature "porphyry" replacement disseminations to low-temperature sandstone impregnations and are similar for metal types ranging from gold to uranium. In order of rising alteration temperature and intensity, the most common alteration types are propylitization (leaching), argillization (bleaching), silicification, sericitization, biotitization, and feldspathization. The literature is replete with descriptions of zones of these types of alteration being concentric around a bull's-eye of highest temperature alteration and forming a single "district" (as defined by Gabelman, 1976, 1977), usually with many distortions.

Second, similar zonal relationships occur in other types of metal deposits (Barnes, 1979). For example, high-temperature replacement disseminations (both porphyry and nonporphyry), breccia pipes, and stockworks are found within a central zone of pervasively altered rock. Veins and limestone replacements with thin altered-rock envelopes are found marginal to the pervasive "core," usually under structural control. Strata-bound sandstone or shale impregnations occur farther away. "Metallogenically" different metals are arranged along a temperature gradient directed radially outward from the core, ranging from central magnetite through gold, copper, zinc, lead–zinc–copper, lead–silver, sulfosalts, gold, fluorite, barite, uranium, copper–vanadium–uranium, and uranium (Gabelman, 1961, 1976, 1977). However, not all of these are represented in any single district.

Whether the strata-bound sandstone impregnations belong to larger zonal patterns is very controversial. Most sandstone uranium geologists prefer to exclude them. Nevertheless, on the basis of long and extensive studies of the empirical distribution of metal types, Gabelman (1961, 1968, 1970, 1977) and Gabelman and Boyer (1958) have demonstrated the consistent occurrence of sandstone uranium impregnations on the outskirts of most complex metal districts. Further, when groups of mineralogically and geometrically similar districts are coalesced into belts, the belts

frequently define metal zones of regional extent characterized by a single dominant element or small group of elements. Groups of parallel, contiguous regional zones illustrate a paragenetic gradient ranging across some controlling tectonic feature, such as an orogenic mobile belt or cratonal major fault zone, and conforming to that feature in geometry. Gabelman now considers such groups of related metal zones to constitute a regional mineralization belt in which uranium and vanadium are geometrically and paragenetically involved, even though a variety of processes might be responsible for the formation of different types of deposits. Thus, meteoric groundwater activated and converted to brines by tectonic, including magmatic, events becomes mineralizing fluids responding to the same controls as magmatic fluids but acting to form deposits distributed zonally in response to a metallotectonic gradient (Gabelman, 1968, 1976).

In these terms, the remote sensing technology developed for the recognition and evaluation of uranium deposits and districts can be applied to the recognition and evaluation of many other types of deposits. The restraints imposed by the mineralogical, morphological, and structural variations plus problems of exposure must be recognized, but the application should be beneficial. In fact, the scale of synoptic viewing and the amount of area covered by satellite images create a good opportunity to further define and test the regional zonation of varieties of ore deposits. The important differences are the alteration mineral suites involved whose reflectance properties must be established by independent studies.

IX. Direction of Future Research

Remote sensing can impact exploration for uranium in two direct ways: (1) It can provide improved understanding of the geologic setting of mineral deposits through improved geologic mapping of lithology and alteration effects and (2) can provide identification or discrimination of alteration phenomena peculiar to uranium deposits.

Empirical methods correlating occurrences of ore and geologic effects (among which may be alteration) are commonly used in exploration strategy regardless of whether cause and effect can be established. Clearly a thorough understanding of ore genesis and related effects will provide the greatest benefits. The mineral companies, with access to subsurface information plus active exploration programs, are uniquely positioned to aid in the development of the required exploration models.

The detection and discrimination of rock alteration is a remote sensing problem equivalent to lithologic discrimination. Usually lithologic discrimination is carried out using statistical classification methods and image training areas. On the other hand, direct detection requires using high-spectral resolution information and accurately eliminating atmospheric effects.

The high-resolution spectral properties of uranium-related, as well as most other metal-related, alterations have been investigated in detail for a few deposits. Extending field and laboratory observations to more diverse metal environments is essential if quantitative applications of the remote sensing method are to be made.

Investigating other uranium districts will deepen our understanding of the place of remote sensing methods in the uranium exploration process. Sandstone uranium environments have so far achieved most of the attention, but including other types of deposits of "world-class" status comparable to Laguna or Ambrosia Lake (in the Grants uranium belt of New Mexico) is warranted.

X. Summary

The Joint NASA/Geosat Test Case Project for uranium focused on remote sensing studies in two uranium districts: (1) Lisbon Valley, Utah, representing strata-bound uranium deposits in sandstone, and (2) Copper Mountain, Wyoming, which is a stockwork (supergene?) accumulation in Precambrian granite.

The test site investigations used aerial photography, aircraft multispectral scanner data, Landsat MSS images, and field observations to map the distribution of suspected mineral-related alteration and to map the geology of selected areas at each site. The aircraft scanner data covered the spectral region 0.4 to 2.5 μm and were used as principal components, canonical transforms, color ratio composites, and single ratios to map the distribution of sandstone bleaching (Lisbon Valley) and/or surface weathering (Copper Mountain). Major limitations of both aircraft scanner data and Landsat MSS images are spatial resolution and lack of stereoscopic coverage. The best aircraft scanner resolution available is approximately 7 m (Bendix 24-channel, Lisbon Valley), which is a factor of 5 or so poorer than conventional aerial photographs. Use of image data can be expected to increase significantly as the surface resolution capability improves. Stereoscopic coverage will provide important benefits, especially for stratigraphic problems, and will tend to eliminate the need for independent topographic information. Including additional spectral bands plus thermal infrared data will also improve rock discrimination capability. Existing scanner channels were

adequate for the discrimination problems studied here wherever spatial resolution permitted it.

At Lisbon Valley the uranium deposits are found predominately in the Moss Back Member of the Chinle Formation on the southwest flank of Lisbon Valley Anticline 100 to 200 m (300 to 700 ft) beneath an umbrella of bleached or partially bleached Wingate strata and 2500 m (8000 ft) above oil and gas accumulations and source rocks in Mississippian and Pennsylvanian reservoirs located on the flanks of the anticline. The distributions of bleached and pigmented strata have been mapped using aircraft multispectral scanner data. The origin of the bleaching and its relation to mineralization are not fully explained. One theory holds that transgressive mineralizing fluids deposited uranium in the Moss Back and passed through the impermeable section of Chinle rocks above to permeate and bleach the Wingate section. Another possibility is that these fluids, which may have contained a component of hydrocarbons (H_2S and CO_2) from the leaking reservoirs beneath, aided the fixation of Chinle/Cutler ore in Triassic (Moss Back?) time, and later, perhaps by means of fault conduits, provided reductants for the leaching of hematite from Wingate red beds. Empirically, bleaching of the Wingate is correlated with the distribution of uranium mineralization. Other anticlines are known where bleached red beds occur above ore and gas accumulations. These become potential targets for uranium exploration according to the ideas presented here. Bleaching is a widespread phenomenon occurring with uranium and constitutes an available target for remote sensing study.

At Copper Mountain, the uranium resources are located along fracture systems (at 100-m [300-ft] depth) occupying an area at the foot of the Owl Creek Mountains that is coincident with a pediment surface of pre-Eocene age. These accumulations in the granites are covered at the surface by tuffaceous sediments of the Eocene Wagon Bed Formation. The adjacent granite rocks are weathered and heavily limonite- and hematite-stained where they are exposed at the surface. These exposed weathered granites are barren at depth. The distribution of so-called oxidized granite has been mapped in detail using aircraft scanner data. Empirically, the occurrences of uranium, both in the granites and in the Tertiary section, correlate well with the distribution of oxidized rocks.

The origin of surface oxidation and its relation to mineralization are not fully settled. One theory holds that the surface oxidation represents the result of leaching of the granite of its uranium. Uranium present in the accumulation at depth is thus supergene. Other sediment sources of uranium may be required to complete the deposit, but these have never been removed by erosion. The present (residual) resource is protected from additional leaching by the remnant Tertiary sediment cover.

A second theory involves a hydrothermal origin for the uranium and the development of a regional alteration matrix in the granite involving extensive propylitization. This alteration has been masked at the surface by extensive weathering, and mapping of its distribution has not been attempted.

Extrapolating these results to other uranium districts is risky because explorationists feel the Copper Mountain deposit may be unique. Limonitic alteration of the Copper Mountain type is empirically correlated with low-temperature mineralization in granitic terrains and should be a useful exploration tool elsewhere.

References

Adams, S. S. (1981). *Geology and recognition criteria for uraniferous humate deposits, Grants uranium region, New Mexico* (U.S. Department of Energy GJBX-2[81]). Grand Junction, Colorado: Bendix Field Engineering Corporation.

Adams, S. S., and R. B. Smith (1981). *Geology and recognition criteria for sandstone uranium deposits in mixed fluvial-shallow marine sedimentary sequences, south Texas* (U.S. Department of Energy GJBX-4[81]). Grand Junction, Colorado: Bendix Field Engineering Corporation.

Baker, E. T., Jr. (1979). *Stratigraphic and hydrogeologic framework of part of the coastal plain of Texas* (Report 236). Austin: Texas Department of Water Resources.

Barnes, H. L. (Ed.) (1979). *Geochemistry of hydrothermal ore deposits* (2nd ed.). New York: John Wiley & Sons.

Berner, R. A. (1969). Goethite stability and the origin of red beds. *Geochim. Cosmochim. Acta, 33,* 267–273.

Bolivar, S. L., S. H. Balog, K. Campbell, L. E. Fugelso, T. A. Weaver, and G. W. Wecksung (1981). *Multisource data set integration and characterization of uranium mineralization for the Montrose Quadrangle, Colorado* (Informal Report LA-8807-MS). Los Alamos, New Mexico: Los Alamos Scientific Laboratory.

Bramlett, L. B., R. F. Czarnecki, D. A. Emilia, J. C. Pacer, R. M. Sadowski, and J. S. Schmidt (1979). *Uranium geophysics, Copper Mountain, Wyoming* (Preprint 79-336). Paper presented at Society of Mining Engineers of AIME, Fall Meeting, Tucson, Arizona, 1979.

Bramlett, L. B., S. L. Reyher, and G. G. Southard (1980). *Uranium geology and geochemistry, Copper Mountain, Wyoming* (Preprint 80-102). Paper presented at Society of Mining Engineers of AIME, Annual Meeting, Las Vegas, 1980.

Button, A., and S. S. Adams (1981). *Geology and recognition criteria for uranium deposits of the quartz-pebble conglomerate type* (U.S. Department of Energy GJBX-3[81]). Grand Junction, Colorado: Bendix Field Engineering Corporation.

Coffin, R. C. (1921). Radium, uranium, and vanadium deposits of southwestern Colorado. *Colo. Geol. Surv. Bull., 16,* 150–227.

Conel, J. E., M. J. Abrams, and K. W. Baird (1980). Uranium: Spectral discrimination of alteration phenomena in sediments. *Mod. Geol., 7,* 115–135.

Conel, J. E., M. J. Abrams, and A. F. H. Goetz (1978). *A study of alteration associated with uranium occurrences in sandstone and its detection by remote sensing methods* (JPL Publication 78-66, Vol. I). Pasadena, California: Jet Propulsion Laboratory.

Dahlkamp, F. J. (1978). Geological appraisal of the Key Lake U–Ni deposits, northern Saskatchewan. *Econ. Geol., 73,* 1430–1449.

Donovan, T. J. (1974). Petroleum microseepage at Cement, Oklahoma: Evidence and mechanism. *AAPG Bull., 58,* 429–446.

Earth Satellite Corporation (1979). *Geometric pattern recognition techniques applied to Landsat digital data for uranium exploration.* Washington, D.C.

Ferguson, J. D. (1979). The subsurface alteration and mineralization of Permian red beds overlying several oil fields in southern Oklahoma, Parts 1 and 2. *Shale Shaker Digest, 29,* 172–178, 200–208.

Ferguson, J. D. (1981). Formation of diagenetic alteration zones by leaking hydrocarbons over three oil fields in Oklahoma. *AAPG Bull., 65,* 924. (Abstract)

Gabelman, J. W. (1956). Structural control of uranium deposits in the Zuni–Mt. Taylor region, northwest New Mexico. *Econ. Geol., 51*(1), 114. (Abstract)

Gabelman, J. W. (1961). Tectonics, hydrothermal zoning and uranium in the central Andes. *Soc. Geol. Peru Bol., 36,* 67–101.

Gabelman, J. W. (1968). Regional metallotectonic zoning in Mexico. *AIME Trans., 241,* 113–128.

Gabelman, J. W. (1970). Speculations on the uranium ore fluid. *Uranium exploration geology.* Vienna: International Atomic Energy Agency, 315–330. (Panel proceedings)

Gabelman, J. W. (1976). Strata-bound ore deposits and metallotectonic provinces. In K. H. Wolf (Ed.), *Handbook of strata-bound and strataform ore deposits* (Vol. 4). New York: Elsevier Scientific Publishing Company, Amsterdam–Oxford, 75–164.

Gabelman, J. W. (1977). Migration of uranium and thorium: Exploration significance. *Studies in geology* (No. 3). Tulsa, Oklahoma: The American Association of Petroleum Geologists.

Gabelman, J. W., and W. H. Boyer (1958). Relation of uranium deposits to feeder structures, associated alteration, and mineral zones. *United Nations Survey of Raw Material Resources: Second International Conference on Peaceful Uses of Atomic Energy* (Vol. 2), 338–350. (Proceedings)

Gabelman, J. W., W. L. Chenoweth, and E. Ingerson (1981). Uranium. *AAPG Bull., 65*(10), 2274–2282.

Griffith, J. W. (1967). *The uranium industry: Its history, technology and prospects* (Mineral Report 12). Ottawa: Canadian Department of Energy, Mines, and Resources, Mineral Resources Division.

Harshman, E. N. (1974). Distribution of elements in some roll-type uranium deposits. *Formation of uranium ore deposits.* Vienna: International Atomic Energy Agency, 169–183. (Symposium Proceedings)

Harshman, E. N., and S. S. Adams (1981). *Geology and recognition criteria for roll-type uranium deposits in continental sandstones* (U.S. Department of Energy GJBX-1[81]). Grand Junction, Colorado: Bendix Field Engineering Corporation.

Johnson, H. S., Jr., and W. Thordarson (1966). Uranium deposits of the Moab, Monticello, White Canyon, and Monument Valley Districts, Utah and Arizona. *U.S. Geol. Surv. Bull. 1222-H.*

Kendall, R. G., S. L. Reyher, D. Atherley, K. A. Taylor, and D. K. Morton (1980). *Geologic evaluation of the Copper Mountain development project, Fremont County, Wyoming* (unpublished report). Denver, Colorado: Rocky Mountain Energy Company.

Kerr, P. F. (1958). Uranium emplacement in the Colorado Plateau. *Geol. Soc. Am. Bull., 69*(9), 1075–1111.

Kober, C. L., and H. David Proctor-Gregg (1977). *Discrimination of uranium alteration zones in selected areas by use of Landsat MSS imagery* (U.S. Department of Energy Final Report GJBX-4[77]). Grand Junction, Colorado: Bendix Field Engineering Corporation.

Lekas, M. A., and H. M. Dahl (1956). The geology and uranium deposits of the Lisbon Valley Anticline, San Juan County, Utah. In J. A. Peterson (Ed.), *Intermountain Association of Petroleum Geologists, Geology and Economic Deposits of East–Central Utah, 7th Annual Field Conference.* Salt Lake City, 161–168.

Levinson, R. A., R. W. Marrs, and F. Crockell (1979). *Video processing of remote sensor data applied to uranium exploration in Wyoming* (Final Report). Laramie: University of Wyoming, Department of Geology.

Loring, W. B. (1958). *Geology and ore deposits of the northern part of the Big Indian District, San Juan County, Utah.* Unpublished doctoral dissertation, University of Arizona, Tucson.

Malan, R. C. (1968). The uranium mining industry and geology of the Monument Valley and White Canyon Districts, Arizona and Utah. In J. D. Ridge (Ed.), *Ore deposits in the United States, 1933–1967* (Vol. 1). New York: American Institute of Mining, Metallurgical and Petroleum Engineers.

Marrs, R. W., R. M. Breckenridge, R. S. Houston, and F. K. Root (1973). Color anomalies, minerals, and ERTS-1 imagery. *Univ. Wyo. Contr. to Geol., 12*(2). Laramie: University of Wyoming.

Meyer, C., and J. J. Hemley (1967). Wallrock alteration. In H. L. Barnes (Ed.), *Geochemistry of hydrothermal ore deposits.* New York: Holt, Rinehart, and Winston, 166–235.

Miller, D. S., and J. L. Kulp (1963). Isotopic evidence on the origin of the Colorado Plateau uranium ores. *Geol. Soc. Am. Bull., 74,* 609–630.

Missallati, A. A., E. A. Prelat, and R. J. P. Lyon (1977). *Simultaneous use of Landsat digital data with that of geophysical and geological surveys in geomathematical modelling for mineral exploration prediction* (Technical Report 77-10). Palo Alto, California: Stanford University, Remote Sensing Laboratory, School of Earth Sciences.

Nash, J. T., H. C. Granger, and S. S. Adams (1981). Geology and concept of genesis of important types of uranium deposits. *Econ. Geol. (75th Anniv. Vol.),* 63–116.

Needham, R. S. (1982). *Cahill–Northern territory.* Canberra City, Australia: Bureau of Mineral Resources, Geology and Geophysics. (1:100 000 map commentary)

Offield, T. W. (1976). Remote sensing in uranium exploration. *Uranium exploration geology.* Vienna: International Atomic Energy Agency, 731–744. (Panel proceedings)

Parker, J. M. (1966). Lisbon field area, San Juan County, Utah. *AAPG Mem. 9, 2*, 1371–1388.

Raines, G. L., T. W. Offield, and E. S. Santos (1978). Remote sensing and subsurface definition of facies and structure related to uranium deposits, Powder River Basin, Wyoming. *Econ. Geol., 73*(8), 1706–1723.

Salmon, B. C., and W. W. Pillars (1975). *Multispectral processing of ERTS-A data for uranium exploration in the Wind River Basin, Wyoming* (ERIM Report 110400-2-F). Ann Arbor: University of Michigan.

Sharp, W. N., and A. B. Gibbons (1964). Geology and uranium deposits of the southern part of the Powder River Basin, Wyoming. *U.S. Geol. Surv. Bull. 1147-D*, D1–D60.

Shawe, D. (1956). Significance of roll ore bodies in genesis of uranium-vanadium deposits on the Colorado Plateau. In L. R. Page, N. E. Stocking, and H. S. Smith (Eds.), Contributions to the geology of uranium and thorium by the U.S. Geol. Surv. and Atomic Energy Comm. for the U.N. Int. Conf. on Peaceful Uses of Atomic Energy, Geneva, Switzerland, 1955, *U.S. Geol. Surv. Prof. Pap. 300*, 239–241.

Shrier, T., and W. T. Parry (1982). A hydrothermal model for the North Canning uranium deposit, Owl Creek Mountains, Wyoming. *Econ. Geol., 77*, 632–645.

Spirakis, C. S., and C. D. Condit (1975). Preliminary report on the use of Landsat-1 (ERTS-1) reflectance data in locating alteration zones associated with uranium mineralization near Cameron, Arizona. *U.S. Geol. Surv. Open File Rpt. 75-416.*

Steen, C. A., et al. (1953). Uranium operations of the Utex Exploration Company in the Big Indian District, San Juan County, Utah. *U.S. Bur. Mines, Info. Cir. 7669.* Also published in *Mines Mag., 44*(4), 16–23, 40, 1944.

Thaden, R. E. (1980a). Geologic map of the Birdseye Pass Quadrangle, Fremont County, Wyoming. *U.S. Geol. Surv. Geol. Quadrangle Map GQ-1537.*

Thaden, R. E. (1980b). Geologic map of the De Pass Quadrangle, Fremont and Hot Springs Counties, Wyoming. *U.S. Geol. Surv. Geol. Quadrangle Map GQ-1526.*

Thaden, R. E. (1980c). Geologic map of the Gates Butte Quadrangle, Fremont County, Wyoming. *U.S. Geol. Surv. Geol. Quadrangle Map GQ-1538.*

Thaden, R. E. (1980d). Geologic map of the Guffy Peak Quadrangle, Fremont and Hot Springs Counties, Wyoming. *U.S. Geol. Surv. Geol. Quadrangle Map GQ-1527.*

Thaden, R. E. (1980e). Geologic map of the Picard Ranch Quadrangle, Fremont County, Wyoming. *U.S. Geol. Surv. Geol. Quadrangle Map GQ-1539.*

Thamm, J. K., A. A. Kovaschak, Jr., and S. S. Adams (1981). *Geology and recognition criteria for sandstone uranium deposits of the Salt Wash type, Colorado Plateau Province* (U.S. Department of Energy GJBX-6[81]). Grand Junction, Colorado: Bendix Field Engineering Corporation.

U.S. Atomic Energy Commission (1959). *Guidebook to uranium deposits of western United States.* U.S. Atomic Energy Commission RME-141 (open-filed 1966).

Vincent, R. K. (1977). Uranium exploration with computer-processed Landsat data. *Geophysics, 42*(3), 536–541.

Watson, R. D., and A. F. Theisen (1977). Luminescence properties of selected radioactive rocks and minerals. *U.S. Geol. Surv. Open File Rpt. 77-293.*

Wood, H. B. (1968). Geology and exploitation of uranium deposits in the Lisbon Valley area, Utah. In J. D. Ridge (Ed.), *Ore deposits of the United States, 1933–1967* (Vol. 1). New York: American Institute of Mining, Metallurgical and Petroleum Engineers, 770–789.

Yellich, J. A., R. T. Cramer, and R. G. Kendall (1978). Copper Mountain, Wyoming, Uranium Deposit—Rediscovered. *Wyoming Geological Association Guidebook, Thirteenth Annual Field Conference.* Casper: Wyoming Geological Association, 311–327.

Section 8

Lisbon Valley, Utah, Uranium Test Site Report

James E. Conel
Ronald E. Alley
Jet Propulsion Laboratory

Section 8

Lisbon Valley, Utah, Uranium Test Site Report

Contents

I. Introduction 8-1
A. Purpose and Background 8-1
B. Site Selection and Specific Geologic Problems 8-1
C. Remote Sensing Data 8-2
D. Plan of the Section 8-2

II. General Description of the Test Site 8-4
A. Location and Access 8-4
B. Description of the Test Site 8-4
C. Physiography 8-4
D. Climate 8-4
E. Multispectral Scanner Coverage 8-4

III. Vegetation Cover 8-4

IV. Soil Type and Distribution 8-7

V. Geologic Background 8-9
A. Stratigraphy of the Lisbon Valley Area 8-9
1. Pre-Permian stratigraphy and petroleum relations 8-9
2. Permian and later stratigraphy 8-12
B. Geologic Relations at Lisbon Valley 8-20
C. Geologic History of the Salt Anticline 8-20
D. Emplacement of Mineral Deposits 8-24
E. Exploration and Mining History 8-25
1. Exploration history 8-25
2. Mining history 8-26

VI. Reflectance Properties of Cover Types 8-26
A. Background 8-26
B. Laboratory and Field Spectra of Sediments 8-28
1. Cutler Formation 8-28

PRECEDING PAGE BLANK NOT FILMED

2. Moss Back sandstone and upper Chinle red beds 8-31
3. Wingate Sandstone 8-31
4. Kayenta Formation and Navajo Sandstone 8-32
C. Spectral Reflectance of Vegetation 8-32
D. Spectra of Rock Units and Vegetation Derived From Multispectral Scanner Data 8-33

VII. Remote Sensing Objectives, Models, and Approach 8-35
A. Introduction 8-35
B. Connections Among Genetic, Exploration, and Remote Sensing Models 8-36
C. Approach 8-37

VIII. Interpretation of Multispectral Scanner Data at Lisbon Valley 8-37
A. Introduction 8-37
B. Geologic Relations From NS-001 Data 8-38
1. PC images 8-38
2. Color relations in the PC data 8-41
3. Stratigraphic relations 8-41
4. Geomorphic and color representation of structure 8-44
C. Distribution of Alteration in the Wingate Sandstone 8-49
1. Photogeologic mapping 8-49
2. Analysis of bleaching distribution in a canonical transform image of Bendix 24-channel data 8-52
3. Distribution of bleached, unbleached, and laminated sandstone in the Wingate outcrop and in Lisbon Valley Anticline 8-58
D. Removal of Vegetation Signatures in the Image Analysis 8-58
1. General 8-58
2. Estimating tree cover by the band depth method 8-59
3. Removal of vegetation spectral contribution and construction of "vegetation-free" PC images 8-60
E. Comparison of Soil Maps to Geologic and Image Data 8-62
F. Landsat MSS Image Interpretation 8-64
G. Fraunhofer Line Discriminator Observations at Lisbon Valley 8-64
1. General 8-64
2. Description of experiment 8-66
3. Discussion of the image data base 8-66
4. Registration of data to the image base and analysis of anomaly distributions 8-68
5. Conclusion 8-68

IX. Structural and Geochemical Relationship Between Bleaching and the Uranium and Oil and Gas Deposits 8-70
A. Distribution of Uranium and Oil and Gas Deposits With Respect to Distribution of Bleached Wingate Sandstone 8-70
1. Uranium deposit distribution and bleached outcrops 8-70
2. Distribution of petroleum with respect to uranium and bleached outcrops 8-73
B. A Reinterpretation of the Structure Above Lisbon Reservoir 8-76
1. Fault interpretation of Upper Paradox structural surface 8-76
2. Modification to cross sections 8-77

3. Relationship of reservoir and surface structural configurations ... 8-77
4. Discussion ... 8-79
C. Stability Relations for Ferrous and Ferric Iron Species and the Transport of Uranium ... 8-80
D. Relationship to Bleaching of Red Beds in Other Anticlines ... 8-81
1. Cement field, Oklahoma ... 8-81
2. Velma, Eola, and Chickasha fields ... 8-82
3. San Rafael Swell ... 8-82
4. Comparison to Lisbon Anticline ... 8-82
E. Carbon and Sulfur Isotope Measurements on Oil, Gas, and Uranium Ore Samples ... 8-82
1. Background ... 8-82
2. Chemical procedures ... 8-83
3. Uranium ore samples ... 8-84
4. Oil and gas samples ... 8-84
5. Results ... 8-84
6. Summary ... 8-88

X. Summary ... 8-90
A. Geologic Setting ... 8-90
B. Correction and Analysis of Aircraft Scanner Data ... 8-90
C. Geological, Geochemical, and Remote Sensing Results ... 8-91
1. Lisbon Anticline ... 8-91
2. East Coyote Wash ... 8-91
3. Distribution of Wingate alteration ... 8-92
4. Distribution of uranium and of oil and gas with respect to bleached outcrops ... 8-92
5. Isotope studies ... 8-93
D. Other Remote Sensing Measurements and Analyses ... 8-93
1. Spectral reflectance ... 8-93
2. Vegetation signatures and unmixing models ... 8-93
3. FLD observations ... 8-94
4. Landsat MSS images ... 8-94

XI. Conclusions for Remote Sensing Analysis ... 8-94
A. Analysis of the Lisbon Valley Images and Photographs ... 8-94
B. Remote Sensing Radiance Measurements ... 8-94
C. Problems for Future Research ... 8-95

Acknowledgments ... 8-96

References ... 8-97

Appendixes
A. Relation of Scanner DN Values to Ground Reflectance ... 8-103
B. Calibration of the Scanner Data for Ground Reflectance and Estimation of Data Noise Level ... 8-115
C. Principal Components for Lisbon Valley Images ... 8-121
D. Systematics of Correlation Matrices From Lisbon Valley NS-001 Scanner Data ... 8-137
E. Principal Component and Canonical Scatter Diagrams: The Analysis of Mixed Spectral Collections ... 8-143

C-5

F. Additional Renditions of Principal Component Images From the Bendix 24-Channel and NS-001 Scanners, Lisbon Valley, Utah 8-155

Figures

8-1. Location of the Lisbon Valley area, Utah:
(a) general map showing Paradox Basin and Colorado Plateau 8-2
(b) detailed map 8-3

8-2. Ground coverage of the aircraft multispectral scanners and radar systems over the Lisbon Valley test site:
(a) the Bendix 24-channel scanner and the 8-channel NS-001 Thematic Mapper Simulator 8-5
(b) the 11-channel M²S and the X-band aircraft radar 8-6

8-3. Soil map for the Lisbon Valley area 8-8

8-4. Low-oblique aerial view of the unbleached Wingate Sandstone facies 8-15

8-5. Unbleached Wingate Sandstone at Big Indian Wash, Lisbon Valley 8-16

8-6. Low-oblique aerial view of the bleached Wingate Sandstone facies 8-17

8-7. Ground view of the bleached Wingate Sandstone facies 8-18

8-8. Intertonguing relationship between white facies of the Wingate Sandstone and red facies of the Kayenta Formation 8-19

8-9. Intraformational channeling and apparent truncation of bleached laminae in the Wingate 8-20

8-10. Geologic map of the Lisbon Valley area 8-21

8-11. Index of geologic mapping for the Lisbon Valley area 8-23

8-12. Laboratory hemispherical reflectance curves for sediments exposed in Lisbon Anticline 8-28

8-13. Bidirectional field reflectance of sediments exposed in Lisbon Anticline 8-29

8-14. Index map of PFRS and hand specimen sample locations 8-30

8-15. Absorption band centered near 1.65 μm, attributed to the presence of Ti^{+4} in the hematite lattice 8-31

8-16. The differential hemispherical reflectance spectrum of iron-oxide pigment from the unbleached facies of Wingate Sandstone 8-31

8-17. Laboratory spectral reflectance measurements of juniper, piñon pine, and Great Basin sage from the Lisbon Valley test site 8-32

8-18. Broadband spectral reflectance for the NS-001 bands:
(a) juniper; (b) piñon pine; (c) sage 8-33

8-19. Comparison of scanner-derived NS-001 spectral reflectance curves with field spectral measurements obtained with the PFRS 8-34

8-20. Image-derived reflectance curves for areas of vegetation and mixed vegetation and outcrops 8-36

8-21. PC image mosaic of Lisbon Valley area prepared using transform I from seven channels of NS-001 data 8-39

8-22. Index map of image interpretation and photogeologic mapping for the Lisbon Valley area 8-40
8-23. CRC image of NS-001 data for the portion of line 7 interpreted in Figure 8-24 8-46
8-24. Interpretation of CRC image of a portion of line 7 for the NS-001 flight at Lisbon Valley 8-47
8-25. Stratigraphic section for the Dakota Sandstone and Burro Canyon Formation 8-48
8-26. Photogeologic interpretation of a portion of the Wingate Sandstone outcrop with the distribution of bleached, partially bleached, and unbleached facies 8-50
8-27. Photogeologic map of a portion of the Wingate Sandstone outcrop between Ike–Nixon Mine and Dry Wash 8-51
8-28. Classification matrix from discriminant function analysis of the Bendix 24-channel data 8-54
8-29. Canonical scatter diagram for separation of bleached and unbleached Wingate Sandstone in the Bendix 24-channel data of Lisbon Valley 8-54
8-30. Canonical transform image of the Bendix 24-channel scanner data 8-55
8-31. Geologic interpretation of the canonical transform image covering a portion of the Wingate Sandstone outcrop between Big Indian Mine and Big Indian Wash 8-57
8-32. Distribution of vegetation types according to BLM mapping for a portion of the western limb of Lisbon Valley Anticline 8-59
8-33. Color-coded representation of the fractional area of tree cover according to the simple two-component mixing model 8-61
8-34. CIR photomosaic of the area corresponding to Figure 8-33 8-61
8-35. PC image of the northern part of Big Indian District 8-62
8-36. Soil units of Figure 8-3 compared to (a) geologic map and (b) NS-001 image data for the Lisbon Valley area 8-63
8-37. PC image of Landsat MSS scene 20872-16540, San Juan County, Utah 8-65
8-38. Definition of the quantities *a, b, c, d* measured in the FLD experiment 8-66
8-39. Ground track of the FLD for perfectly collimated aircraft track 8-67
8-40. Eight-channel PC image from NS-001 scanner for a portion of the Big Indian District 8-69
8-41. Distribution of Moss Back and Cutler massive ore deposits in the Big Indian District and in the southern part of Lisbon Anticline 8-71
8-42. Distribution of uranium deposits with respect to bleached, unbleached, and laminated Wingate Sandstone in Lisbon Valley Anticline 8-72
8-43. Transverse sections across bleached and mineralized intervals 8-73

8-44. Structural contour map of Mississippian-age reservoir rocks in Lisbon Anticline and the distribution of Wingate bleaching and Moss Back uranium mineralization 8-74
8-45. Cross section along line EE′ showing generalized distribution of Wingate bleaching and relations of bleaching to uranium mineralization and oil and gas accumulations 8-75
8-46. Pennsylvanian Paradox Formation:
(a) structure contours on the upper surface of the formation 8-76
(b) original contour data 8-77
8-47. Reinterpretation of structure sections in Figure 8-46 according to a fault model of the Upper Paradox Formation structural surface:
(a) EE′; (b) FF′ 8-78
(c) GG′ 8-79
8-48. Cross section along the portion AA′ of profile AA‴ showing the relation between doming in Lisbon reservoir and flexure of Wingate Sandstone at the surface 8-80
8-49. Stability fields from ferrous and ferric iron species in equilibrium with FeS_2 and iron hydroxide species superimposed on the stability field for uranyl carbonate and other species in the system $U–O_2–H_2O$ 8-81
8-50. Eh-pH relations of natural environments with the field of simultaneous stability of uranyl dicarbonate and the Fe^{+2}(aq)–Fe-hydroxide system 8-81
8-51. Distribution of δ-values for sulfur isotopes from hydrothermal uranium deposits (Miner's Basin, La Sal Mountains, Utah) and sedimentary uranium deposits (Big Indian Wash and Lisbon Valley) 8-83
8-52. Isotope sample sites for oil and gas reservoirs and for uranium deposits in the anticlines 8-85
8-53. Distribution of sulfur isotopic values found for ore stage pyrite, H_2S, and petroleum (condensate) in Lisbon Anticline 8-88
8-54. Distribution of $\delta^{13}C$ in petroleum (condensate), natural gas, and total organic carbon and carbonate from Moss Back uranium host sandstone 8-89
8-55. Variations in the isotopic carbon composition in some natural materials 8-89

A-1. Bendix 24-channel color composite images 8-107
A-2. Various transformations of the scatter ellipsoid resulting from application of gain factors ϵ_1 and ϵ_2 to radiance variables 8-110
B-1. Calibration curves for channels 1–7 of the NS-001, Lisbon Valley data 8-116
B-2. An example of the areal distribution of DN values in channel 2, line 5, of NS-001 data, Lisbon Valley, for a slice of the range divided into six intervals corresponding to $\pm 1\ \sigma$, ± 1 to $\pm 2\ \sigma$, and $> \pm 2\ \sigma$ about the mean 8-118
B-3. Histogram of gray levels for the 2,426,400 elements in channel 2, line 5, of the NS-001 data, Lisbon Valley 8-119

C-1. Subareas of Lisbon Valley sampled to form PC transform II 8-122
C-2. Spectral reflectance of sandstone and juniper with important absorption bands due to Fe^{+3}, chlorophyll, Al–O–H, and water 8-124
C-3. First four PCs for transform I of NS-001 data, line 6, Lisbon Valley, Utah 8-125
C-4. First four PCs for NS-001 data from Lost River, West Virginia 8-126
C-5. First four PCs for NS-001 data from Silver Bell, Arizona 8-127
C-6. First four PCs for transform II of NS-001 data, Lisbon Valley, restricted area 8-129
C-7. First four PCs for transform III of NS-001 data, line 5, Lisbon Valley 8-131
C-8. First four PCs for transform I of NS-001 data, line 6, Lisbon Valley 8-133
C-9. First four PCs for transform II of NS-001 data, Lisbon Valley, restricted area; principal values and directions from calibrated covariance matrix 8-134
C-10. Eigenvector diagram of the four PCs from the covariance matrix given in Table C-14 8-135
D-1. First four PCs for transform II of NS-001 data, Lisbon Valley, restricted area; principal values and directions from correlation matrix 8-140
E-1. Coordinate system of the PC diagram 8-144
E-2. Detailed relationships between the principal coordinates P, P′, P″ and principal coordinates reduced to the unit plane Q, Q′, and Q″ 8-145
E-3. Resolution of a spectral group P into three end members: P′, P″, and P‴ 8-146
E-4. Examples of scatter ellipses in PC diagrams 8-147
E-5. Four-component systems in two-dimensional displays 8-147
E-6. PC diagram for some rock and vegetation types 8-147
E-7. PC diagram for rock-outcrop and rock-outcrop-and-tree mixtures 8-148
E-8. Canonical variate scatter plots for piñon–juniper, Wingate outcrop, and piñon–juniper and Wingate mixtures 8-148
E-9. Canonical variate scatter diagram for piñon–juniper, Kayenta outcrop, and piñon–juniper and Kayenta mixtures 8-148
E-10. Motion of a point in the PC diagram representing target of uniform reflectance $\overline{R}$ across the 7-channel NS-001 spectrum for the u_1u_2-unit plane between $\overline{R} = 100\%$ and $\overline{R} = 0$ 8-152
E-11. Motion of a point in the PC diagram representing target of uniform reflectance $\overline{R}$ across the 7-channel NS-001 spectrum for the u_2u_3-unit plane between $\overline{R} = 100\%$ and $\overline{R} = 0$ 8-152
F-1. PC image of the NS-001 data for the Lisbon Valley area prepared according to transform II 8-156
F-2. Seven-band PC image of the NS-001 data for Lisbon Valley area prepared according to transform II 8-157

F-3. Seven-band PC image of the Big Indian area prepared from 10 channels of the Bendix 24-channel scanner data 8-158

Tables

8-1. Dominant vegetation types for the Lisbon Valley area 8-7
8-2. Stratigraphy of Lisbon Valley area 8-10
8-3. Petrographic X-ray and chemical analyses of bleached and unbleached Wingate Sandstone 8-14
8-4. Bandpasses for the Bendix 24-channel scanner and the NS-001 used for image analysis at Lisbon Valley 8-28
8-5. Locations of image spectral sites in NS-001 flight lines 5 and 6 at Lisbon Valley 8-35
8-6. Aircraft flight parameters and solar position data for images acquired at Lisbon Valley 8-38
8-7. Color key for the PC image 8-42
8-8. Description of image stratigraphic units for East Coyote Wash Syncline and Lisbon Canyon Anticline 8-45
8-9. Description of photogeologic units identified in Figures 8-26 and 8-27 8-53
8-10. Color key for the canonical transform image 8-56
8-11. BLM vegetation classification for the southwest flank of Lisbon Valley Anticline, Big Indian District 8-59
8-12. Eigenvalues and eigenvectors for PC transform of the NS-001 image, line 5, Lisbon Valley 8-68
8-13. Location and description of uranium ore samples used in isotope studies, Moss Back Member, Chinle Formation, Lisbon Valley 8-86
8-14. XRD analysis of uranium ore samples 8-86
8-15. Paragenetic mineral sequence at Mi Vida Mine 8-87
8-16. Well locations and data on samples for isotope analysis from producing zones and oil and gas reservoirs, Lisbon Valley 8-87
8-17. Chemical analysis of samples from Lisbon Anticline oil and gas reservoirs 8-87
8-18. Sulfur isotope data 8-88
8-19. Carbon isotope data 8-89

A-1. Correlation matrix between two sets of PC images, NS-001 data, line 5, Lisbon Valley 8-112

B-1. Value for the constants k_i' and k_i'' in the calibration equation $DN_i = k_i'\overline{\rho}_i + k_i''$ obtained from three-point least square fits 8-117
B-2. NS-001 raw DN responses with standard deviations at vegetated sites, Lisbon Valley 8-117

C-1. Covariance $\|u_{ij}\|$ and correlation $\|c_{ij}\|$ matrices from NS-001 data, line 6, Lisbon Valley 8-123
C-2. Correlation matrix for the 7-band NS-001 data from Lost River, West Virginia, September 1979 8-123
C-3. Correlation matrix for the 7-band NS-001 data from Silver Bell, Arizona, October 1978 8-123

C-4. Transform I: Eigenvalues and eigenvectors from NS-001 data, line 6, Lisbon Valley, total area 8-124
C-5. Transform II: Covariance $\|u_{ij}\|$ and correlation $\|c_{ij}\|$ matrices from NS-001 data, Lisbon Valley, restricted area 8-128
C-6. Transform II: Eigenvalues and eigenvectors from NS-001 data, Lisbon Valley 8-128
C-7. Transform III: Covariance $\|u_{ij}\|$ and correlation $\|c_{ij}\|$ matrices from the 8-channel NS-001 data, Lisbon Valley 8-130
C-8. Transform III: Eigenvalues and eigenvectors from NS-001 data, Lisbon Valley 8-130
C-9. Constants used to calculate gain- and offset-corrected covariance matrices 8-131
C-10. Transform I: Covariance matrix of the reflectances obtained from element-by-element gain correction of the matrix $\|u'_{ij}\|$ 8-131
C-11. Transform I: Eigenvalues and eigenvectors from the calibrated covariance matrix based on reflectances, NS-001 data, Lisbon Valley 8-132
C-12. Transform II: Covariance matrix of the reflectances obtained from element-by-element gain correction of the matrix $\|u_{ij}\|$ 8-132
C-13. Transform II: Eigenvalues and eigenvectors from the calibrated covariance matrix based on reflectances, NS-001 data, Lisbon Valley 8-132
C-14. Covariance matrix for the area shown in the Landsat MSS image (Figure 8-37) 8-135
C-15. Eigenvalues and eigenvectors from the covariance matrix in Table C-14 8-135
D-1. Hierarchical arrangement of the correlation matrices for NS-001 data of Lisbon Valley and other test sites 8-137
D-2. Loading of seven variables in three factors for Lisbon Valley 8-138
D-3. Transform II: Eigenvalues and eigenvectors computed from the correlation matrix 8-139
E-1. Calculated Euclidean distance amplification factors for various Lisbon Valley PC transformations 8-149
E-2. Comparison of Euclidean separation distances D under various PC transformations for bleached and unbleached Wingate facies, NS-001 data, Lisbon Valley 8-150
E-3. Mean values of principal coordinates and separation distances for bleached and unbleached Wingate Sandstone 8-151

Plates[1]

8-1. Lisbon Valley, Utah: Distribution of bleached, unbleached, and laminated members in the Wingate Sandstone outcrop, southwest flank of Lisbon Valley Anticline

8-2. Lisbon Valley, Utah: Relationships of bleached Wingate Sandstone outcrops to topography

8-3. Lisbon Valley, Utah: Cross section showing relationships of bleached and unbleached strata on the southwest limb of Lisbon Valley Anticline

8-4. Lisbon Valley, Utah: Cross-section AA''' showing the relationship between distribution of the bleached Wingate Sandstone (unit W_1) and the Lekas-Dahl (1956) "magic interval" of uranium mineralization drawn on the upper surface of the Cutler Formation

[1]Plates are contained in Part 3 (envelope) of *The Joint NASA/Geosat Test Case Project.*

Section 8

Lisbon Valley, Utah, Uranium Test Site Report

I. Introduction

A. Purpose and Background

The Joint NASA/Geosat Test Case Project was initiated to evaluate the utility of remote sensing methods for mineral, oil, and gas exploration and for geologic mapping. A complete description of this Project and its history are given in the Project Description, Section 2. A key element of the Project was the anticipated cooperation between NASA and the participating Geosat companies wherein NASA provided aircraft overflight data plus ancillary ground-based observations, and Geosat provided the geologic and subsurface data and access to property.

This section describes remote sensing and geologic investigations carried out at Lisbon Valley, Utah (Figure 8-1), a NASA/Geosat uranium test site that represents a tabular stratabound Colorado Plateau-type deposit in sandstone. The participating Geosat company was Atlas Minerals, Moab, Utah. A second site, located at Copper Mountain, Wyoming, is a probable supergene uranium occurrence with vein or stockwork mineralization dispersed in Precambrian rock. This site is discussed in Section 9.

B. Site Selection and Specific Geologic Problems

Lisbon Valley was chosen as a prototype district representing sandstone-type uranium deposits. This choice from among the possible sandstone occurrences (Uravan, Grants Mineral District, eastern San Juan Basin, and Wyoming Basin) was governed by four considerations:

(1) Geological exposure and mineral resources present. The Lisbon Valley area is located astride a salt anticline with a well-exposed section of Paleozoic and Mesozoic rocks. The stratigraphy and structure are both amenable to remote sensing studies. Major uranium deposits are present that reside in the basal Triassic section composed of the Moss Back Member of the Chinle Formation. A number of other resources are present that may contribute to the remote sensing parameters: (1) oil and gas accumulations buried beneath the southwestern limb in porous dolomitic rocks of Mississippian and Devonian age ,(2) Tertiary-age (post-Laramide) copper deposits in Mesozoic and Paleozoic rocks along Laramide-age faults cutting the anticline, and (3) Cretaceous-age coal deposits in the extreme southeastern portion of the anticline along a major fault.

(2) Outcrops of mineralized and altered rocks. The mineralized lower Triassic section crops out along the entire southwestern flank of the anticline, thus forming a potential target for remote sensing observations. Localized occurrences of ore-bearing rocks lie very near to, but are not exposed at, the surface. Altered (bleached) strata, principally the Triassic Wingate Sandstone, are well exposed above the ore-bearing section. The bleached rocks may be guides to mineralization. The distribution of bleaching was known to follow the distribution of ore beneath; however, the distribution of bleached rocks throughout the anticline had not been mapped, and the spatial relations between bleaching and mineralization had not been worked out.

(3) Property distribution. In a cooperative scientific study with industry like the Geosat Project, it was essential that the pattern of property ownership over the test site be simple and that access to property be available. A major portion of the ground at the Lisbon Valley test site is controlled by the Geosat member company.

(4) Previous geologic investigations. The geology of Lisbon Valley is well mapped at a scale of 1:24,000. Considerable geologic information exists on the distribution and stratigraphic relations of the ore bodies, their mineralogy, and lead-isotopic ages. The lead-isotopic relations provide additional constraints on origin. At depth, the structure of the salt diapir is known from oil and gas geophysical exploration studies and from drilling.

These circumstances offered an opportunity to piece together surface and subsurface elements of the structure and stratigraphy of Lisbon Anticline into an expanded picture relating bleaching now exposed at the surface to the uranium mineralization and to the deeper occurrences of petroleum and petroleum source rocks. These relations had not been worked out previously.

Two principal geologic and image interpretation problems were evaluated: (1) use of scanner data for geologic mapping in the anticline and surrounding areas, and (2) detailed photogeologic and image interpretation of the distribution of bleached and unbleached Wingate strata. In addition, carbon and sulfur isotopic data were obtained for samples of (Moss Back) ore and for samples of oil and gas from the major reservoirs or oil-producing horizons. Also, as a result of the image analysis and supporting geologic studies, possible causal geochemical connections between the presence of oil, gas, and uranium and the occurrence of bleached rock were suggested.

C. Remote Sensing Data

The available remote sensing data consisted of high-resolution aerial photography, aircraft multispectral scanner information, ground-based spectral reflectance measurements, Landsat 1, 2, and 3 satellite data, aircraft X-band radar observations, multifrequency microwave radiometer data, and Fraunhofer Line Discriminator (FLD) image data, the latter provided by the U.S. Geological Survey (USGS). All of these data except the microwave and radar observations were used in this study. The surface resolution of the microwave data was very low (≈1.3 km), and the aircraft flew wide of the area to the northeast. The X-band observations revealed general physiographic features of the site. Since all of these structural and stratigraphic elements were known from existing topographic or geological maps, no additional analyses were performed.

The aircraft multispectral scanner data are discussed in this section. These data cover the approximate spectral range of 0.45–2.5 μm in discrete spectral bands from 0.04 to 0.3 μm in width. The scanners provide measures of solar radiance that has been reflected from the surface. The data include atmospheric scattering effects, which were removed using empirical methods before interpretation. The surface parameter of importance is spectral reflectance, which is averaged in the measurements over surface resolution elements and over spectral interval. The scanners yield a surface spatial resolution of approximately 10 m.

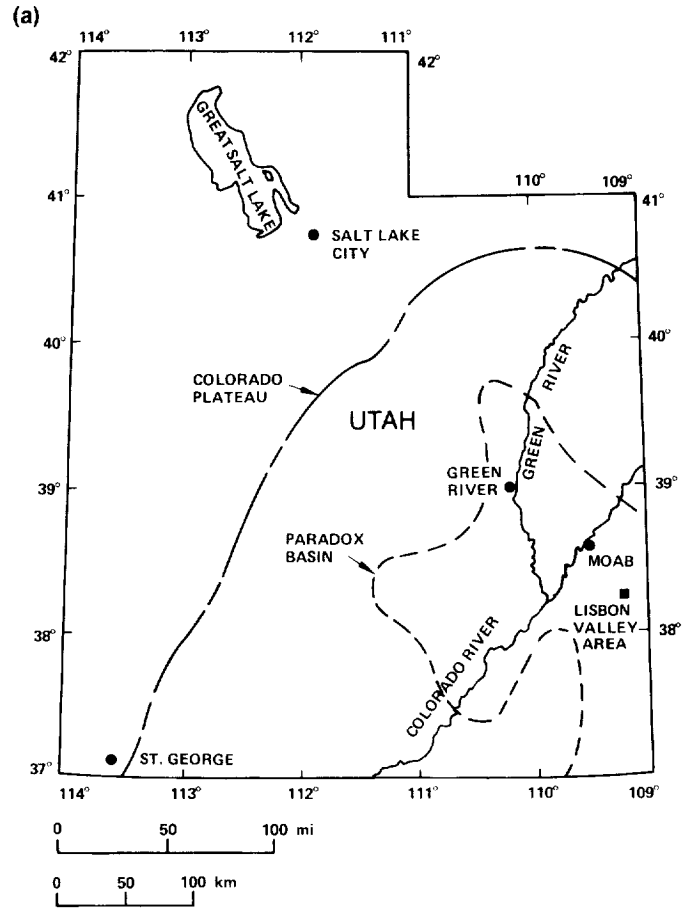

Figure 8-1. Location of the Lisbon Valley area, Utah: (a) general map showing Paradox Basin and Colorado Plateau

D. Plan of the Section

This section is divided into two parts. The first part consists of the geologic descriptions, reflectance measurements, image interpretations, carbon and sulfur isotope studies, and FLD data analysis. The second part includes appendixes that provide analyses of problems relating to the interpretation of remote sensing data as radiance data. Examples of such problems are the relationship between scanner radiance and surface reflectance, and the use of radiance spectral data to study the problem of mixed cover types of the principal components (PCs). These appendixes have mostly been developed as examples from the Lisbon Valley site, but the results also apply to the Copper Mountain test site discussed in Section 9 and in general terms to the other sites.

(b)

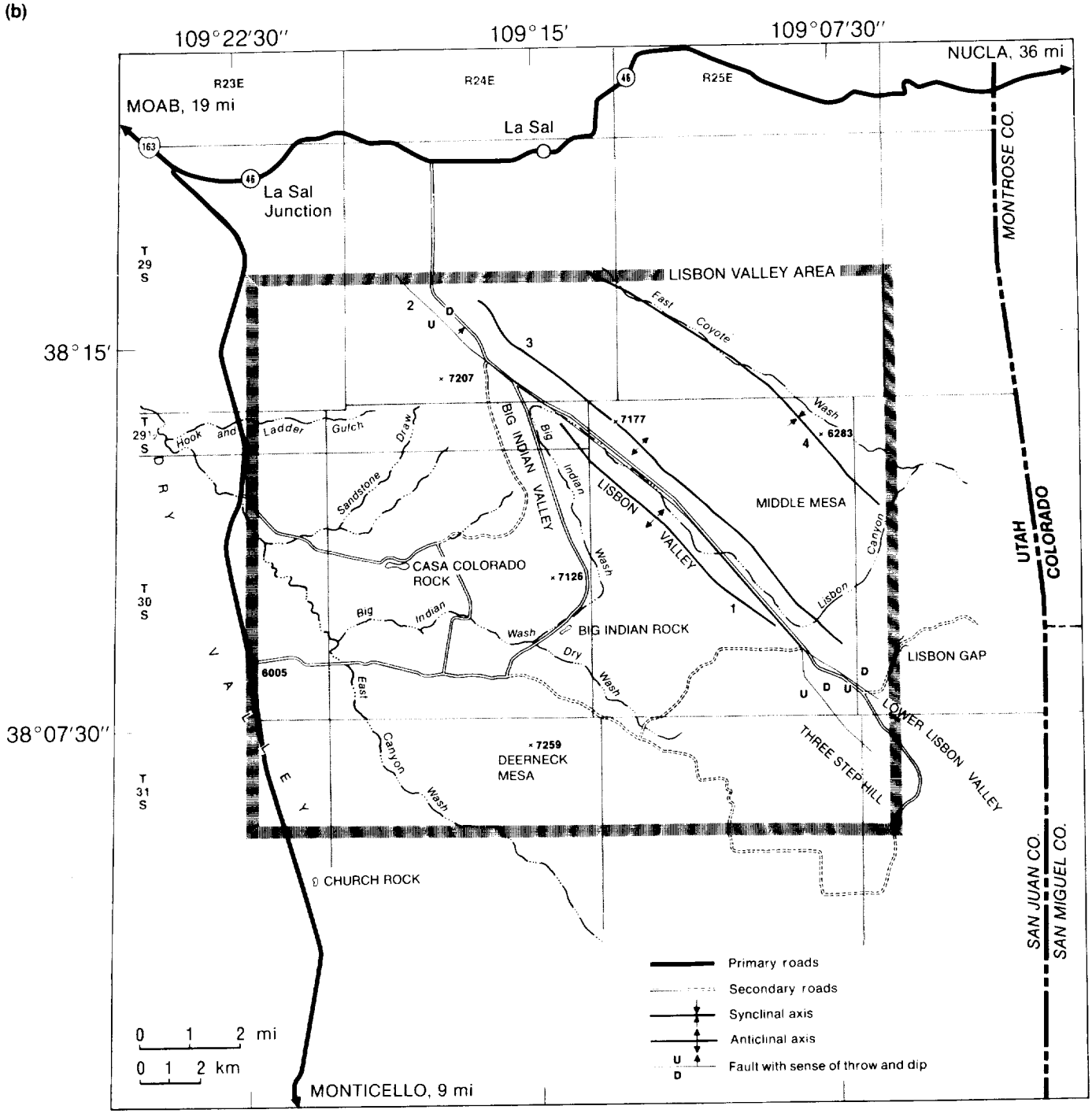

Figure 8-1. Location of the Lisbon Valley area, Utah: (b) detailed map

II. General Description of the Test Site

A. Location and Access

The Lisbon Valley Uranium District is located 34 mi southeast of Moab, Utah, in northern San Juan County, southeastern Utah. Lisbon Valley lies near the center of the Colorado Plateau within the Paradox Basin of Pennsylvanian evaporite sedimentation on the southwestern side of the Paradox fold and fault belt (Figure 8-1; Schneider et al., 1969). The area of study includes the southwestern portion of the Lisbon salt anticline. The Lisbon Valley area is reached by paved highways from Moab or Monticello (U.S. Highway 163) and La Sal Junction (Utah Highway 46). Paved roads from both north and east provide access to the Lisbon Valley area from these major highways. Numerous unpaved dirt roads and unimproved dirt roads provide access to all parts of the study area. Some of these are passable by automobile in dry weather only.

B. Description of the Test Site

The Lisbon Valley test site (Figure 8-1) is bounded by latitudes 38° 5′ 20″ and 38° 16′ 30″ and longitudes 109° 22′ 30″ and 109° 6′ 00″, comprising a total area of 168 mi^2. Within the study area are two major folds: (1) a composite structure consisting of two side-by-side anticlines separated by a normal fault (these are the Lisbon Valley and Lisbon Canyon Anticlines and are referred to collectively as the Lisbon Anticline), and (2) the East Coyote Wash Syncline lying to the northeast of Lisbon Anticline. These large structures were used in the application of multispectral scanner data to geologic mapping problems. For uranium problems, the area of interest is the southwestern limb of Lisbon Anticline, principally in a NW-trending strip lying roughly between Big Indian Valley and lower Lisbon Valley on the northeast side and Hook and Ladder Gulch and Three Step Hill on the southwest.

C. Physiography

Lisbon Valley is one of many NW-trending subsequent stream valleys cut along bleached salt anticlines in the Paradox Basin of the Colorado Plateau (Wood, 1968). Lisbon Anticline lies on the western edge of the deeper part of the basin, together with the Cane Creek, Moab, and Dolores Anticlines. All of these anticlines have Triassic and younger rocks exposed, and all have uranium mineralization in the basal Chinle sandstone beds. The Lisbon Anticline, with its two separate anticlines, was formed by folding during both the Tertiary and Permian periods. The younger Tertiary anticline accounts for the present physiography. Lisbon Anticline covers an area 34 by 14.5 km (21 by 9 mi). Altitudes throughout the test site range from about 6000 to 7200 ft. The area can be characterized as having moderate to rugged topography; the western escarpment of Big Indian Valley comprises the southwestern limb of the structure and consists of a high sandstone-capped cuesta cut by southwest-draining canyons 200 to 500 ft deep. Big Indian Wash, located just southwest of the axis of the anticline, flows generally NW–SE along a course determined by bedding in the nonresistant Permian section to the vicinity of Big Indian Rock. At Big Indian Rock the wash turns abruptly west, crosscutting the west-dipping resistant strata of the west limb to flow westward into Dry Valley. Lisbon Valley to the northeast, on the other hand, generally follows the trace of Lisbon Valley Fault and drains southwest, turning abruptly northeast at Lisbon Canyon to flow outward across the axis of Lisbon Canyon Anticline, eventually emptying into East Coyote Wash.

D. Climate

The climate of the Lisbon Valley area is semiarid, with cool winters and relatively hot summers. From December through March, snow may cover all slopes except those with southern exposure. Thunderstorm activity may occur in summer months.

Weather records for Northdale (Loring, 1958) near the Colorado border at an elevation of 7000 ft show an annual temperature of 44.8° F and a mean annual precipitation of 13.39 in. The highest temperature reading was 103° F in August and the lowest was −10° F in December.

E. Multispectral Scanner Coverage

Flight paths and ground coverages for the multispectral scanners and X-band radar systems flown over the Lisbon Valley test site for the 1976–1979 period are given in Figure 8-2. Geometric rubber sheet corrections are applied to the scanner data to compensate for aircraft motions depicted by distortion of the ground tracks shown in Figure 8-2. Details of this geometric processing are given in the Technical Appendix, Section 14.

III. Vegetation Cover

The Lisbon Valley test site lies within the upper Sonoran climatic zone and is part of the southwest uplands (Colorado Plateau) physiographic province. Most of the area falls within the piñon–juniper belt. The Bureau of Land Management (BLM), Moab, Utah, has prepared maps of the dominant and subordinate plant species for the area, without detailed reference to percent cover, as part of a program of range assessment. A list of dominant plant species present is given in Table 8-1, as compiled from these mapping data. In general, two plant communities can be recognized and are distributed physiographically as follows:

(1) A sage–grassland community (*Artemisia tridentata, Atriplex canescens, Salsola kali, Sarcobatus vermiculatus, Oryzopsis hymenoides, Bouteloua gracilis, Hilaria*

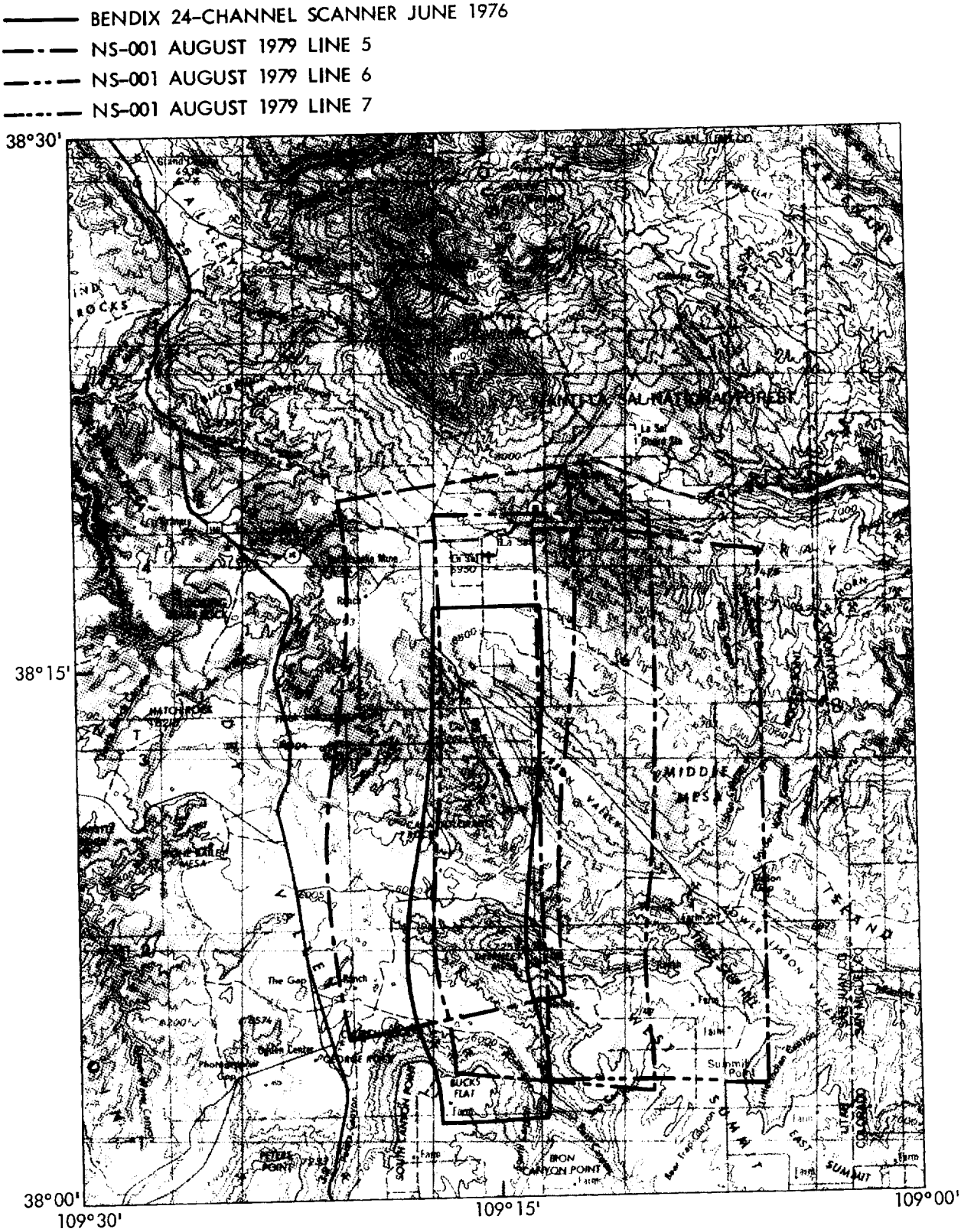

Figure 8-2. Ground coverage of the aircraft multispectral scanners and radar systems over the Lisbon Valley test site: (a) the Bendix 24-channel scanner and the 8-channel NS-001 Thematic Mapper Simulator

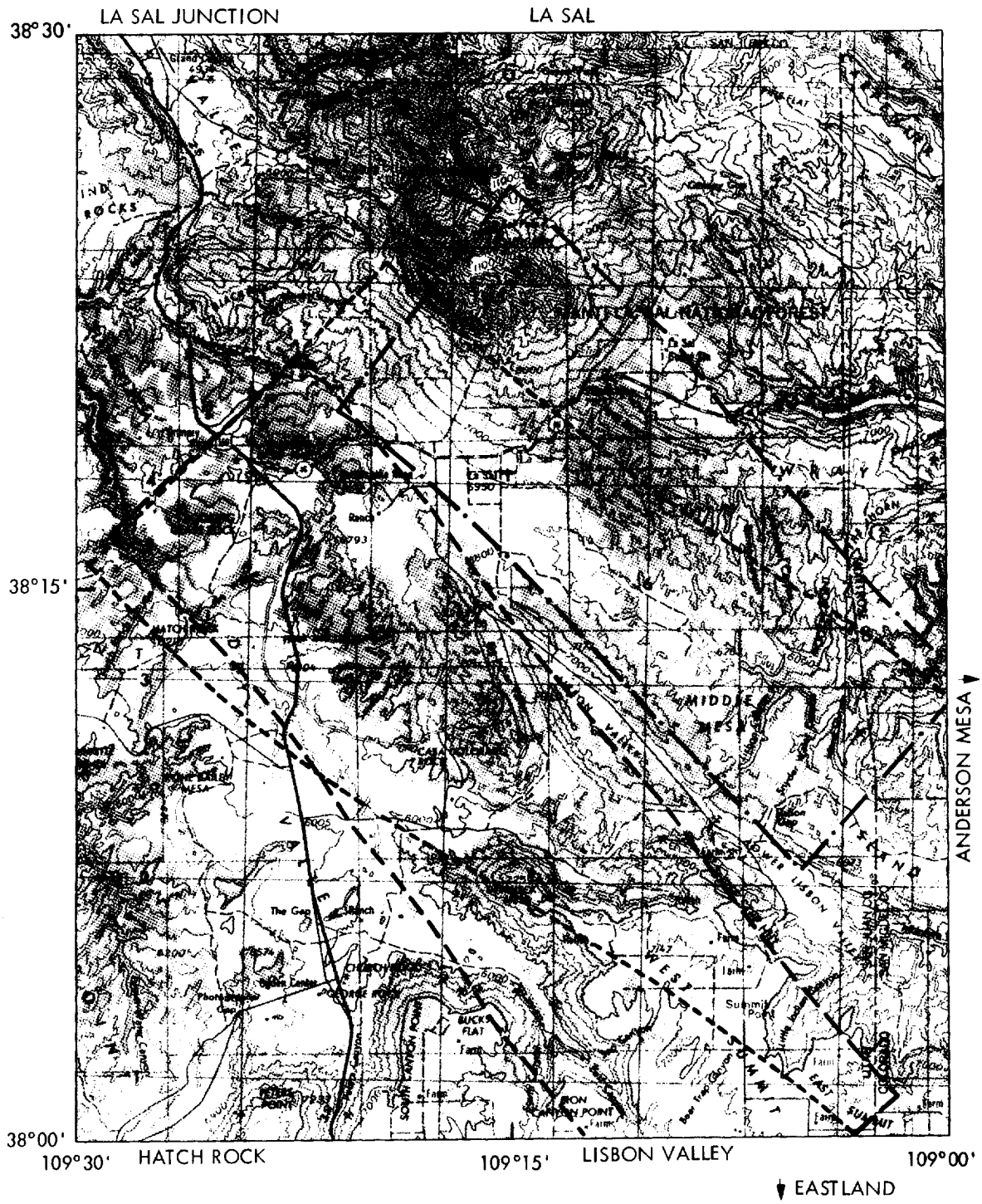

Figure 8-2. Ground coverage of the aircraft multispectral scanners and radar systems over the Lisbon Valley test site: (b) the 11-channel M²S and the X-band aircraft radar

Table 8-1. Dominant vegetation types for the Lisbon Valley area[a]

Vegetation Type	Scientific Name	Common Name
Grasses	*Agropyron cristatum*	Crested wheatgrass
	A. subsecundum	Bearded wheatgrass
	Bouteloua gracilis	Blue grama
	Hilaria jamesii	Galleta grass
	Oryzopsis hymenoides	Ricegrass
	Sporobolus cryptandrus	Spike dropseed grass
	Stipa comata	Needle-and-thread grass
Shrubs	*Amelanchier utahensis*	Utah serviceberry
	Artemisia tridentata	Great Basin sagebrush
	Atriplex canescens	Four-wing saltbush
	A. confertifolia	Shad scale
	Cercocarpus sp.	Mountain mahogany
	C. ledifolius (?)	Mountain mahogany
	C. montanus	Mountain mahogany
	Chrysothamnus sp.	Rabbit brush
	C. nauseosus	Rabbit brush
	Ephedra sp.	Mormon tea
	Eurotia lanata	Wooly winter fat
	Gutierrezia sarothrae	Broomweed
	Purshia tridentata	Antelope bitterbrush
	Salsola kali	Russian thistle
	Sarcobatus vermiculatus	Black greasewood
	Solidago pumila	Rock goldenrod
Trees	*Juniperus osteosperma*	Utah juniper
	Pinus edulis	Two-needle piñon pine

[a] Prepared from unpublished BLM mapping data.

jamesii, Agropyron cristatum, and *Stipa comata)* occupies tops of sandstone mesas, broad alluvial areas within eolian deposits and bottoms of modern streams, places where relatively thick soils have developed.

(2) A piñon–juniper community *(Pinus edulis* and *Juniperus osteosperma* with *Artemisia tridentata, Cercocarpus montanus, Purshia tridentata, Atriplex canescens,* and *Bouteloua gracilis)* occupies moderate to steep slopes and rocky outcrops of limestone and sandstone where soils are absent or poorly developed. Measurements from transects show that the plant cover may vary from bare outcrops to 70 percent coverage in areas of piñon–juniper. Large areas were cleared by chaining with a bulldozer to remove the tree cover as part of a BLM land reclamation program. These chained areas were reseeded with grasses, and shrubs and grasses now cover these sites.

IV. Soil Type and Distribution

The soil distribution map (Figure 8-3) covering Lisbon Valley and adjacent areas is taken from the U.S. Soil Conservation Service general soils map of the Canyonlands area, Grand and San Juan Counties, Utah. The following descriptions are taken from the unpublished Description of the Canyonland Area, Utah, General Soil Map for Broad Land Use Planning (1980). All of the soil types present are dominantly well drained, occur on nearly level to steep slopes, and are characteristic of types present in a dry, subhumid climate zone.

Lisbon Valley, Lower Lisbon Valley, Big Indian Valley, East Coyote Wash, and Middle Mesa are covered by Palma, Cahone, and Hagerman mixed soil types (unit 8, Figure 8-3). This general map unit represents moderately deep to very deep soils developed on nearly level or gently sloping terrain of up to 8 percent grade in eolian deposits and in alluvium derived from sandstone.

Palma soils are generally deep and well drained and occur on upland benches and cuestas. Source materials are eolian deposits derived predominantly from sandstone. The surface layer is yellowish-red, very fine-grained sandy loam. The subsoil may consist of yellowish-red, very fine sandy loam and fine sandy loam. Below this to depths of as much as 48 in. the soils are reddish-yellow, fine sandy loam and loamy fine sand. The vegetation on these soils is mainly big sagebrush, blue grama, galleta, and winter fat.

Cahone soils are generally deep and well drained and occur on upland benches and cuestas. Source materials are mainly eolian deposits derived from sandstone. The surface layer is yellowish-red, fine sandy loam. The subsoil is yellowish-red, sandy clay loam. Below this to a depth of 60 in. or more the soils are pink, fine sandy loam and loam. The vegetation on these soils is mainly big sagebrush, crested wheatgrass, and scattered Utah juniper.

Hagerman soils are also found on upland benches, and cuestas are moderately deep and well drained. These soils form on eolian deposits. The surface layer is brown, very fine sandy loam. The subsoil is brown, sandy clay loam. Below this to a depth of 30 in. or more the soils are strong brown, sandy loam. The vegetation is mainly big sagebrush, snakeweed, globe mallow, and blue grama.

Soils covering the terrain of largely bedrock exposures adjacent to Big Indian Wash, Lisbon Valley, and Lower Lisbon Valley are classified as mixed Rizozo–Rock outcrop–Ildefonso soil types. Unit 9 (Figure 8-3) is mapped mainly on upland benches, cuestas, and fans on slopes ranging from 3 to 30 percent. The vegetation on the soils in this unit is mainly piñon, Utah juniper, big sagebrush, Mormon tea, and galleta. Rizozo soils are shallow and well drained and have formed from residual and eolian deposits. The surface layer is yellowish-red, gravelly, fine sandy loam. Subsoils to a depth of 14 in. are reddish-brown, sandy loam, clay loam, and fine sandy loam. Rock outcrops are soil free. Ildefonso soils form on alluvial

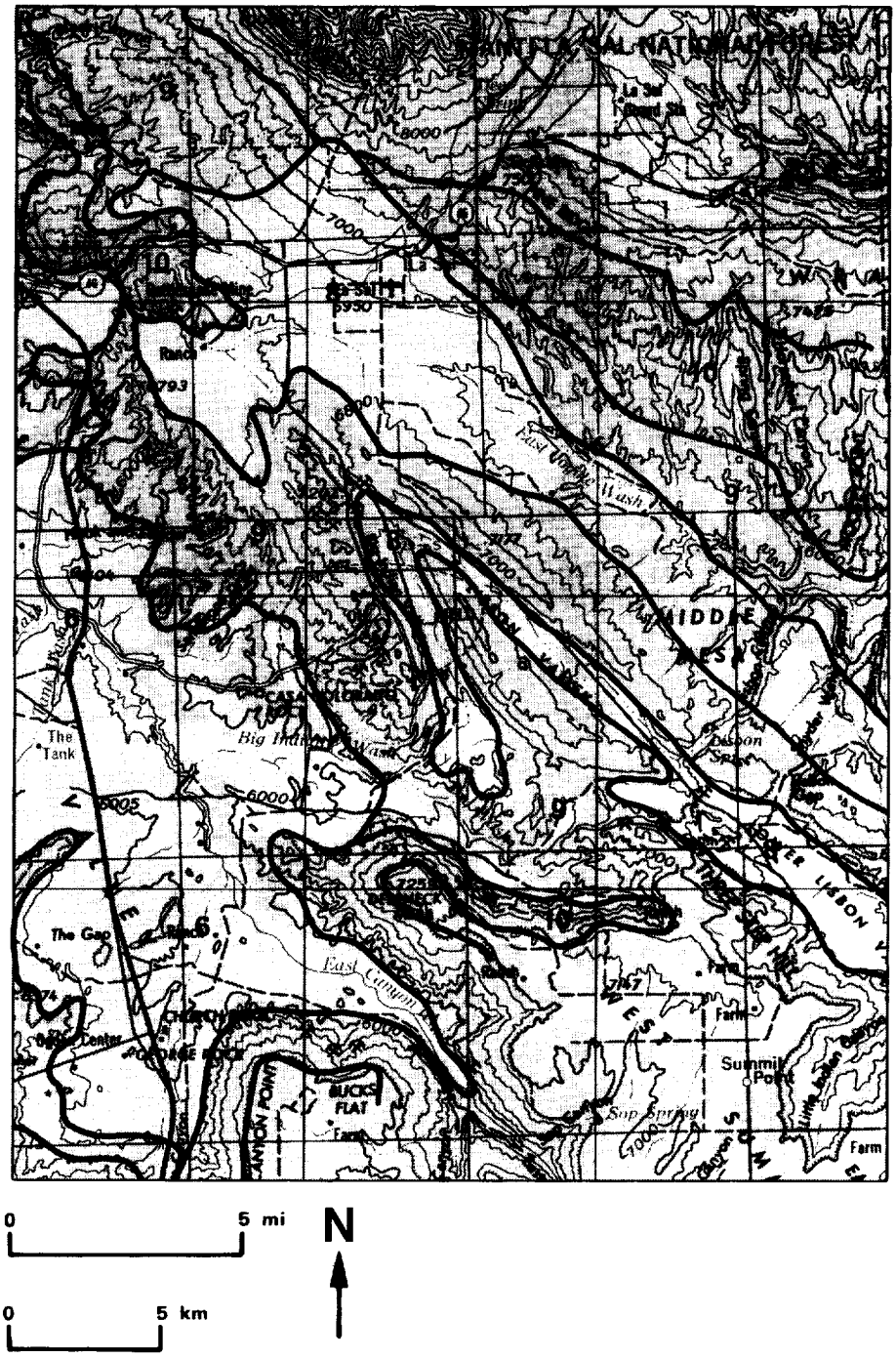

Figure 8-3. Soil map for the Lisbon Valley area (adapted from the general soils map of the Canyonlands area, Grand and San Juan Counties, Utah, as prepared by the U.S. Soil Conservation Service, Moab, Utah, 1980)

fans and are deep and well drained. The surface layer is brown, very stony, fine sandy loam. The subsoil is commonly brown, cobbly, fine sandy loam. Below this to a depth of 60 in. or more the soils are light brown and pink, very gravelly fine sandy loam and extremely cobbly loamy sand.

The sloping area below Deer Neck Mesa is covered by mixed Ustic Torriorthent–Ustollic Calciorthid–Ustollic Haplargid soil types (unit 10, Figure 8-3). These soils occur mainly on hillsides, landslides, and escarpments on slopes 10 to 60 percent. Vegetation consists mainly of Utah juniper, piñon, Indian ricegrass, Utah serviceberry, and Mormon tea.

Ustic Torriorthent soils occur on escarpments and landslides. They may be shallow or deep, but are generally well drained. They form in colluvium derived from sedimentary rocks. The surface layer is yellowish-brown, cobbly sandy loam. Below this to a depth of 15 to 60 in. or more the soils are brown to light gray, very cobbly or very gravelly sandy clay.

Ustollic Calciorthid soils form on south-facing escarpments and hillsides. They may be shallow or deep, but are generally well drained. They form in colluvium and residuum derived dominantly from shale and sandstone. The surface layer is strong brown, gravelly fine sandy loam. The subsoil is strong brown, fine sandy loam and loam. Below this to a depth of 15 to 60 in. the soils are pink and light brown, gravelly loam and sandy clay loam.

The Ustollic Haplargid soils occur on north-facing hillsides and landslides. These soils are very deep and well drained. They form in colluvium derived dominantly from shale and sandstone. The surface layer is strong brown and reddish-brown, stony sandy loam. The subsoil is light reddish-brown and strong brown, stony sandy clay loam. Below this to a depth of 60 in. or more the soils are pink and yellowish-red, stony silty clay loam and sandy clay loam.

Dry Valley represents an area covered by Begay–Windwhistle–Ildefonso mixed soil types (unit 6, Figure 8-3). These soils are moderately deep to very thick and are characterized in part as excessively drained. They represent soils developed on gently sloping surfaces in alluvial deposits, in eolian accumulations, on benches, on terraces, and in valleys.

Begay soils form on benches, on terraces, and in valleys. These soils are very deep and somewhat excessively drained. They form in alluvium and on eolian deposits derived dominantly from sandstone. The surface layer is reddish-brown, fine sandy loam. The subsoil is yellowish-red, fine sandy loam. Below this to a depth of 60 in. or more the soils are yellowish-red and reddish-yellow, loamy fine sand. The vegetation is mainly big sagebrush, spiny hopsage, snakeweed, and blue grama.

Windwhistle soils occur on benches and in valleys. These soils are moderately deep and well drained. They form in eolian deposits over sandstone derived dominantly from sandstone. The surface layer is yellowish-red, very fine sandy loam. The subsoil is yellowish-red, very fine sandy loam. Below this to a depth of 46 in. the soils are light reddish-brown, fine sandy loam and loamy fine sand. Typically such soils are 20 to 40 in. thick. The vegetation is mainly galleta, four-wing saltbush, big sagebrush, Indian ricegrass, and Mormon tea.

Ildefonso soils of this unit are on benches and fans. These soils are very deep and well drained. They form in alluvium derived dominantly from sandstone and shale. The surface layer is brown, gravelly fine sandy loam. The subsoil is brown, gravelly fine sandy loam. Below this to a depth of 60 in. or more the soils are pinkish-white and pink, very gravelly fine sandy loam and extremely gravelly fine sandy loam. The vegetation is mainly blackbrush, snakeweed, and blue grama.

The soil unit subdivisions of Figure 8-3 represent the data presently available concerning the soil types of this area. The classification used is too generalized and the scale of the map is generally too small to permit a comprehensive assessment of the image data for soil mapping purposes. Aircraft and satellite scanner images may be of great assistance in such mapping problems, particularly where units are separable on the basis of characteristic colors or characteristic plant communities. Later the soil map of Figure 8-3 is compared with a geologic map and with aircraft scanner data for the area.

V. Geologic Background

A. Stratigraphy of the Lisbon Valley Area

Table 8-2 provides a summary of the stratigraphic column for the Lisbon Valley area. This information plus subsequent lithologic descriptions have been compiled chiefly from Bohn (1977), Hite and Cater (1972), Huber (1979), Jacobs and Kerr (1965), Lekas and Dahl (1956), Loring (1958), Parker (1966), Schneider et al. (1969), Stokes (1956), Weir and Dodson (1958a, 1958b, 1958c), Weir et al. (1961), and Wood (1968). Lithologic descriptions are supplemented by field observations made as part of the present study. Rocks older than the Pennsylvanian Hermosa Formation are not exposed in the anticline, but are known from well data. Pre-Pennsylvanian strata are included in this compilation to facilitate later discussion of the possible relation of mineral deposits to oil and gas accumulations in the anticline.

1. Pre-Permian stratigraphy and petroleum relations. The pre-Permian stratigraphy is summarized in Table 8-2. None of these sediments crop out in the study area. The middle and lower Cambrian section is represented by shale, siltstone, and

Table 8-2. Stratigraphy of Lisbon Valley area

Age	Group	Formation / Member	Lithologic Description	Thickness, ft
Upper Pleistocene and Recent		Eolian and alluvial	Light-brown, red, and grayish-yellow wind-deposited sand and silt in thin sheets covering tops of mesas and plateaus; grades into stream-deposited sand and silt in valley bottoms.	50 +
		unconformity		
Upper Cretaceous		Mancos Shale	Dark-gray fissile marine shale. Not exposed in area.	500 +
		Dakota Sandstone	Open marine to shoreline and stream channel sandstone conglomerate, shale, mudstone, and coal. Basal conglomerate includes cobbles and boulders from Burro Canyon Formation.	200
Lower Cretaceous		Burro Canyon Formation	Lagoonal, shoreline, stream channel, and mudflat sandstone and conglomerate, variegated mudstone, and dense gray limestone in thin beds.	200, variable
Upper Jurassic		Morrison Formation, Brushy Basin Member	Grayish and reddish bentonitic mudstone, prominent dark-brown lenticular conglomeratic sandstone at base.	225 +
		Morrison Formation, Salt Wash Member	Light-brown lenticular sandstone interbedded with reddish mudstone. Contains thin beds of gray dense limestone at base. Uranium - vanadium deposits occur chiefly in sandstone in upper part.	
Upper and Middle Jurassic		Summerville Formation	Reddish, thin-bedded mudstone with grayish-yellow bed in middle part of formation.	130
	San Rafael Group	Entrada Sandstone	Grayish-yellow, red, and brown, fine-grained crossbedded sandstone.	180
		Carmel Formation	Red siltstone and fine-grained sandstone, gradational contact with overlying Entrada Sandstone; may correlate with lower part of Entrada (Dewey Bridge Member).	75
		unconformity		
Upper and Middle Jurassic	Glen Canyon Group	Navajo Sandstone	White and grayish-yellow, crossbedded, fine-grained sandstone with a few dense light-gray to buff limestone lenses in lower part.	100 - 300
Upper Triassic		Kayenta Formation	Red and purplish-red, fine- to coarse-grained crossbedded sandstone irregularly bedded with red siltstone. Upper and lower contacts gradational and locally intertonguing.	25 - 250
		Wingate Sandstone	Grayish-orange to reddish-brown, fine-grained crossbedded sandstone. Cream to buff ("bleached") facies in northwestern and southeastern exposures in Lisbon Anticline contain trace quantities of asphalic residue coating grain surfaces and interstitially, locally abundant in bleached facies, especially near Lisbon Valley Fault.	300
		Upper Chinle Formation	Red, light-brown, and gray sandstone and conglomerate; red, purplish-red, and greenish-gray mudstone. Indefinite basal zone. Altered green zone a few inches thick parallel to contact but transecting small-scale crossbedding structures where in contact with "bleached" facies of the overlying Wingate Sandstone.	300 - 600
		Moss Back Member, Chinle Formation	Light-brown and gray sandstone and conglomerate and grayish-green mudstone; contains major uranium mineralization.	100
		unconformity		
Middle (?) and Lower Triassic		Moenkopi Formation	Medium- to dark-brown, thin-bedded mudstone, siltstones, and fine-grained sandstone. Does not crop out in field area. Probably present in subsurface northeast of Lisbon Valley Fault.	0 - 550

Table 8-2 (Continued)

Age	Group	Formation/ Member	Lithologic Description	Thickness, ft
Permian		Upper Cutler Formation	Maroon, red, purple, and mottled grayish-yellow and grayish-purple conglomerate, conglomeratic, and coarse- to fine-grained arkosic sandstone interbedded with dark brown, red, and purple siltstone; some thin gray chert beds and isolated gray limestone lenses near base. Basal contact locally gradational.	550–4500
		unconformity		
		Lower Cutler Formation	Sandstone lenses in upper part of Cutler Formation near Moss Back outcrops contain small uranium–vanadium deposits. "Sugar sand" is a prominent light-brown, locally bleached-mottled sandstone unit containing traces of biotite. This unit subcrops beneath the unconformity at the base of Chinle Formation and underlies large uranium deposits in the Moss Back Member. Formation is divided by an unconformity into upper and lower parts by Parker (1966). Represents marine clastic tidal flat and fluvial transition facies.	500–800
Pennsylvanian		Honaker Trail Formation	Gray fossiliferous marine limestone interbedded with brown to reddish-brown, fine- to coarse-grained sandstone and reddish, yellowish, and greenish-gray mudstone; top of formation gradational with overlying Cutler Formation. Fewer red arkosic sandstone beds in basal part.	1600–1900
	Hermosa Group	Upper Paradox Formation	Ismay carbonate cycle of Four Corners area: dolomite, siltstone, gray to black shale, anhydrite.	325–400
		Middle Paradox Formation	Salt with thin beds of black shale, anhydrite, siltstone, and a few earthy dolomite beds.	500–8000
		Pinkerton Trail Formation	Dolomite and limestone, gray, brown, dense, some gray dolomitic siltstone, thin anhydrite beds, some chert in the limestone. Thin gray-green and dark-gray shales.	15–170
		Molas Formation	Red-brown, gray, green, and purple silty to sandy shale.	20–60
		unconformity		
Mississippian		Leadville	Dolomite and limestone.	330–500
Devonian		Ouray Limestone	Limestone.	70–130
		Elbert Formation	Gray-brown dolomite interbedded with green shale.	100–160
		McCracken Sandstone Member	Sandstone and sandy dolomite.	70–140
		Aneth Formation	Glauconitic dolomite with siltstone partings.	200+
		unconformity		
Upper Cambrian		Lynch Dolomite	Dolomite.	200+
Middle and Lower Cambrian		Ophir Formation	Gray and green shale and tan siltstone.	125±
		Tintic Quartzite	Gray-green shale and siltstone at top grading downward to red, pink, and buff coarse-grained sandstone.	400+
		unconformity		
Precambrian			Pink granite; 30 percent quartz, 60 percent feldspar, 10 percent biotite.	

sandstone and the upper Cambrian section by dolomite. Ordovician and Silurian rocks are missing from the sequence or are not identified. Dolomite of the Devonian Aneth Formation rests unconformably upon the Upper Cambrian Lynch Dolomite. Above the Aneth lie the Devonian McCracken Sandstone and Elbert and Ouray carbonate rocks. The McCracken and Ouray act as petroleum reservoirs, but they are not porous and, consequently, are poor producers (Parker, 1966).

The Pennsylvanian section is very different stratigraphically from the Mississippian and Devonian sections, containing in the Paradox Basin an evaporite sequence totaling 5000 to 6000 ft in thickness, and a thinner complementary facies of shelf carbonates.

The basal Pennsylvanian unit is the Molas Formation, which consists of a radioactive red shale together with siltstone and limestone. This formation is separated by an unconformity from Mississippian rocks beneath, along which approximately 145 ft of Leadville Dolomite was removed prior to deposition of the Pennsylvanian unit (Parker, 1966, p. 1384). The Molas grades upward to carbonate rocks of the lower Hermosan Group (Pinkerton Trail Formation). This formation in turn grades upward into an evaporite sequence, including salt, anhydrite, black shale, and dolomite, which constitutes the Paradox Formation that was deposited in the deeper part of the Paradox Basin. Units of the Paradox are arranged in a cyclic fashion; 29 such evaporite cycles can be recognized in the deeper part of the basin and in the section at Lisbon Valley (Hite and Cater, 1972). A typical evaporite cycle consists predominantly of chemical rocks layered in accordance with solubility: (a) silty, calcareous, dolomitic, argillaceous organic-rich black shale, (b) silty dolomites, (c) nodular and laminated anhydrite, and (d) halite with or without potash salts. Boundaries of the Paradox cycles can be defined on the basis of black shale units, but more conveniently on the basis of disconformities present atop each halite unit.

The evaporite cycles can be correlated across the salt basin into equivalent cyclic carbonate facies on the southwestern shelf of the basin that include (basal) algal limestone, silty dolomite and limestone, black argillaceous shale, siltstone, sandstone and silty dolomite, and pelletal–foraminiferal limestone (Hite and Cater, 1972).

The Upper Paradox Formation represents such a carbonate shelf lithofacies. Above the Upper Paradox are carbonate and clastic rocks of the Upper Hermosa Honaker Trail Formation, which represent a return to depositional conditions similar to the preevaporite beds.

The Pennsylvanian (sapropelic) black shale beds have been suggested as potential source rocks for oil and gas accumulation in the Paradox Basin (Peterson and Hite, 1969). Parker (1966) suggests the possible presence of indigenous oil and gas in each of the Devonian, Mississippian, and Pennsylvanian reservoirs. But it also seems likely that some oil and gas have migrated to the Mississippian and Devonian rocks since the Pennsylvanian source beds have been juxtaposed by faulting and flowage against the older Paleozoic reservoir strata. However, in the Lisbon field area the crude oil and gas compositions of hydrocarbons found in Devonian, Mississippian, and (Hermosa) Pennsylvanian rocks are each different, though they possess similar correlation indexes (Parker, 1966).

A few petroleum occurrences have been found in the Paradox salt and in Honaker Trail sandstone (Parker, 1966). The Paradox reservoir is a thin, nonporous earthy dolomite with anhydrite, and is nonproductive. The Hermosa sandstones in the Lisbon field area are not productive because these beds crop out and are buried at a depth of only a few hundred feet. The Hermosa sandstones are productive on the northeast (downthrown) side of Lisbon Valley Fault, where they are found in a faulted anticline and are buried at an average depth of 4000 ft beneath the surface.

2. Permian and later stratigraphy. Detailed discussions of the stratigraphy of rocks exposed in the anticline are available in numerous publications describing the mineral deposits. The stratigraphic units of interest as ore-bearing formations or for the remote sensing observations are described below.

a. Cutler Formation. The Cutler Formation of Permian age is composed predominantly of a fluvial sequence of red beds including dark maroon, red, and purple conglomerates, conglomeratic and coarse- to fine-grained arkosic sandstone interbedded with dark brown, red, and purple siltstone. In the mineralized area, the formation ranges from 900 to 1800 ft thick. A prominent erosional unconformity is located at the top of the formation throughout the salt anticline area. The formation thins from erosion over the salt anticline. Massive sandstones as much as 50 ft thick are found within the formation. These units are well sorted and fine to medium grained with saccharoidal texture, the so-called "sugar sands." The units are quartz-rich with feldspar and minor dark biotite and may represent coastal dune fields reworked into longshore bars (Campbell, 1981). They have a mottled appearance where bleached of iron-oxide pigment. Such sands tend to be heavily bleached in their upper parts, giving way to unbleached rock heavily pigmented with iron oxide at the base.

Uranium in the Cutler Formation is found in the central and northern part of the Lisbon Valley area in the upper part of the formation in distributary fluvial sandstones (Campbell, 1981). Uranium ore pods crop out about 100 ft stratigraphically below the Cutler–Chinle contact and a thousand feet or so northeast

(updip) of the west escarpment of Big Indian Valley. Additional occurrences of ore are found in the massive sandstone units where these subcrop beneath Moss Back ore bodies. (Moss Back stratigraphy is described below.) Red Cutler sandstones are discolored green (reduced) adjacent to ore bodies in the Moss Back; according to Wood (1968), the thickness of a bleached zone below the unconformity is apparently not directly related to the size or distribution of ore, but rather to the thickness of the more porous of the Cutler sandstone beds. Where the authors have observed such effects (Spiller Canyon), the greenish and bleached zones extend a few inches to one foot from ore pods. Green and bleached rocks not associated with mineralization also occur. Bleached sandstones crop out at the surface and may be identified in the images. Greenish Cutler rocks have no obvious outcrop expression because of the small physical scale of the discoloration and thorough mixing at the surface in the debris and soil layer.

b. Chinle Formation. The Chinle Formation of Upper Triassic age consists of fluvial and lacustrine sediments and averages about 400 ft thick along the mineralized zone. The lower Moss Back Member is green to gray green and brown in color and ranges from 10 to 80 ft thick. This unit was deposited on an erosion surface cut into the Cutler Formation. Huber (1979) recognizes two and possibly three fluvial channel systems in the lower strata, representing deposits from stream systems flowing generally west and northwest. The Moss Back Member represents the major uranium host. The unit is predominantly fluviatile, cross-bedded, calcareous fine- to coarse-grained arkose with interbedded sandstone, mudstone, and calcarenite conglomerate. Organic woody trash and coaly material occur in sandy lenses and mudstones in and above the ore sandstones. The upper portion of the member contains greater abundances of calcarenite conglomerate and micaceous mudstone beds. The lower part of the member grades upward into red–brown, purple, lavender, thin-bedded siltstones and mudstones of the Upper Chinle Formation. The Upper Chinle is 275 to 400 ft thick along the mineralized belt. The claystones are lacustrine, with some bentonite, and are believed to have been derived from volcanic ash. Such materials have been suggested as a source of uranium for the ore bodies beneath (Wood, 1968).

The angle of discordance between the Cutler and Chinle Formations varies from 2° to 6° throughout the Big Indian ore belt. Paleotopography on the surface of the unconformity varies from 5 to 30 ft. Wood (1968) remarks that relief is greatest in the area beneath ore bodies in the central part of the ore trend where the largest Permian–Triassic uplift and erosion occurred. However, the ore bodies are erratically distributed with respect to undulations on the unconformity. Topographic relief on the surface evidently generated conditions conducive to development of turbulent Moss Back streams with irregular courses. Numerous intraformational conglomerates and sand lenses resulted. These acted as the favorable sites for eventual uranium deposition.

Conspicuous bleaching of Cutler and Moss Back sediments occurs along the unconformity in the proximity of ore. Wood (1968) suggests that alteration in these places represents strong reducing conditions, either from migratory humates derived from local organic sources, from sulfur-bearing waters leaking from oil and gas reservoirs beneath, or from uranium mineralizing solutions existing in the near ore mineralization.

c. Wingate Sandstone. The Wingate Sandstone is the lowest formation of the Glen Canyon Group and is of Upper Triassic age. The sandstone crops out as a massive cliff former. It caps the escarpment along the west side of Big Indian Wash and forms a dip slope on the southwestern limb of Lisbon Valley Anticline. The sandstone is approximately 300 ft thick. Throughout most of the area the lower portion of the formation is very massive, with large-scale cross-bedding. The upper 100 ft of section is also cross-bedded but divided into numerous layers of sandstone, and the rock has a less massive appearance.

Two facies of Wingate Sandstone are of special interest here as possible significant guides to uranium distribution: (1) an unaltered or unbleached portion, and (2) an altered or so-called bleached section. Mineralogical, petrographical, and chemical data on these two rock types are summarized in Table 8-3. The principal outcrops of the unaltered unit occur from approximately Mi Vida Canyon southward to roughly 1 mi south of Big Indian Wash in the area of Little Valley (Figure 8-4). The unaltered or pristine Wingate facies consists of salmon-color to red-pigmented fine-grained sandstone (Figure 8-5) composed predominantly of quartz with 15 percent microcline and plagioclase feldspar and scarce biotite. The rock has a matrix predominantly of calcite plus hematite pigment.

Altered facies of sandstone crop out from Mi Vida Canyon northward to North Alice Mine where the sandstone is truncated by the Lisbon Valley Fault. To the south, bleached facies occur along the southern boundary of T30S, R25E as far east as Costanza Mine, where the unit is truncated by the Lisbon Valley fault system and its tributaries. In contrast to the unaltered facies, bleached rock is white to buff in outcrop appearance (Figures 8-6 and 8-7), although in some places on cliffs it may be red due to wash from overlying red rocks.

The bleached Wingate facies is typically a fine-grained cross-bedded sandstone composed predominantly of quartz with very little microcline. Calcite and hematite are absent, and kaolinite is abundant in the matrix. Buff-colored portions of the bleached facies typically contain submillimeter-sized, evenly dispersed, limonitic patches, possibly derived from alteration of pyrite. Loring (1958) has discussed limonitic nodules in the Wingate

Table 8-3. Petrographic X-ray and chemical analyses of bleached and unbleached Wingate Sandstone

(a) Thin section analysis

Rock	Mineral									
	Heavy	Quartz	K-Feldspar	Plagioclase	Mica	Calcite	Iron Oxides	Porosity	Sorting	Clay
Unaltered	Magnetite garnet	Mainly	Fresh microcline	Scarce	Biotite (scarce)	As clasts and in matrix	Hematite in matrix	30% (medium)	Poor	<1–5%
Altered		Mainly	Scarce altered to clay	Scarce altered to clay	White mica	None	None	Low	High	Kaolinite montmorillonite in matrix

(b) X-ray diffraction analysis

Unaltered Rock	Mineral									
	Quartz	K-Feldspar	Plagioclase	Mica	Calcite	Iron Oxides	Clay	Heavy Minerals	Chlorite	Other
<2 μm clay unoriented	Major	Major	<1–5%	Minor biotite white mica	Very minor to trace	Very minor hematite	<1–5%		Major	
<2 μm clay oriented	Minor	Minor	<1–5%	<1%	Trace	Trace hematite	Major kaolinite montmorillonite + chlorite		Minor	
Whole sample	Major	Major	Minor	White + trace biotite	Very minor	Trace hematite	Trace kaolinite	Minor grossularite major pyrite	Very minor	Trace pyroxene chalcopyrite

(c) Density and chemistry

Rock	Description	Density, g/cc		Chemistry (Wet & AA), wt %		
		Rock	Silt	Fe^0	Fe^{+2}	Fe^{+3}
Unaltered	Poorly sorted arkosic siltstone	2.676	2.647	0.36	0.04	0.32
Altered	Well-sorted quartzitic siltstone	2.655	2.666	0.18	0.18	0.00

(d) Grain sizes

Sieve Size, mm	Rock, wt %	
	Unaltered	Altered
>0.495	0.88	7.67
>0.351	1.38	3.47
>0.246	5.38	5.31
>0.147	15.76	42.33
>0.090	60.98	27.13
>0.074	9.33	8.29
>0.053	3.12	3.51
>0.045	1.25	0.45
>0.037	0.58	0.62
>0.030	0.56	0.53
<0.030	1.63	0.74

(e) Infrared reflectance bands

Rock	Mineral, λ μm			
	Fe^{+3}	Clay	OH	CO_3
Unaltered	0.88	2.20	1.42	2.35
Altered	0.65	2.18	1.40	

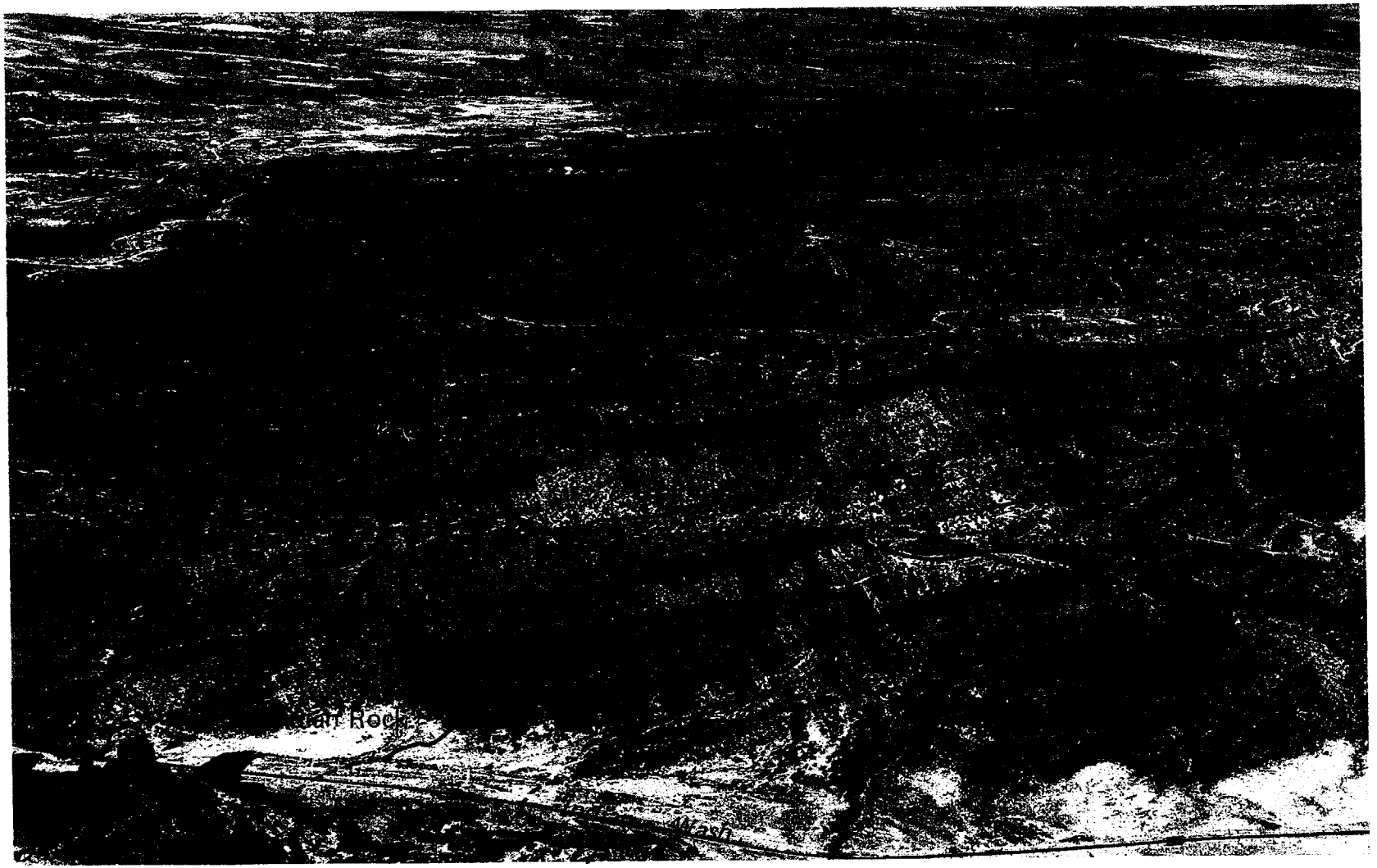

Figure 8-4. Low-oblique aerial view of the unbleached Wingate Sandstone facies, taken January 1980. View is looking northwest along the southwestern flank of Lisbon Valley Anticline north of Big Indian Wash, Secs. 23, 24, T30S, R24E.

Jn	Navajo Sandstone	Trcl	Moss Back Member of the Chinle Formation
Jk	Kayenta Formation	Pc	Cutler Formation
Trw	Wingate Sandstone (unbleached facies)	Pcs	Sugar sandstone unit in the Cutler Formation (note prominent jointing in this unit)
Trcu	Upper Member of the Chinle Formation		

Angular unconformity between Cutler and Chinle strata is also visible in lower right-hand corner of picture.

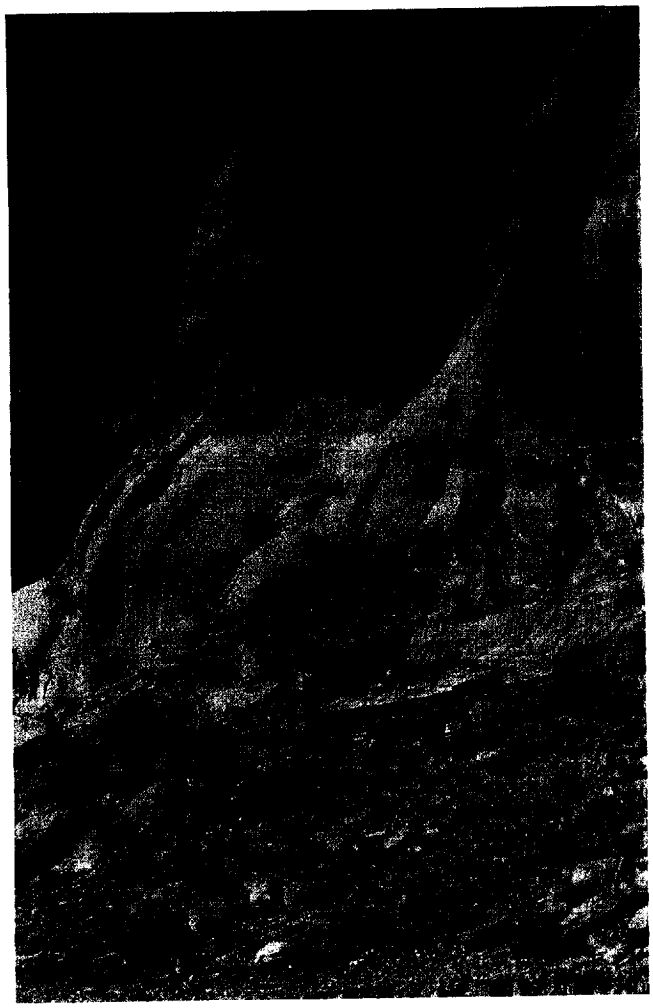

Figure 8-5. Unbleached Wingate Sandstone at Big Indian Wash, Lisbon Valley

Sandstone reported to be pseudomorphous after pyrite. However, in specimens studied thus far, obviously pseudomorphous pyrite or limonitic forms were not identified. Residual asphaltic material has been identified as grain coatings and matrix fillings in the bleached facies from outcrops near Columbia Mine and Costanza Mine, and from cores at the Rio Algom production shaft on the northeast downthrown side of the Lisbon Valley Fault. The asphaltic residues are characterized (distinguished from biotite) by gold fluorescence in carbon tetrachloride when excited under ultraviolet light.

Bleached rocks may be more friable and less resistant to weathering. Prominent joint systems present in unbleached portions of the section (visible in Figure 8-4) may not extend upward through bleached strata. From field observations and study of aerial photographs, the bleached and unbleached facies are connected by a stratigraphically complicated intertonguing relationship. This relationship is explored in detail below where the distribution of bleached rocks is mapped. North of Expectation Canyon the entire section of Wingate strata consists of bleached rock. Interlayered bleached and unbleached strata extend southward from this point to Big Indian Wash where the section is predominantly unbleached. At Big Indian Wash, the laminated bleached and unbleached section is thin and occupies the upper portion of the formation. In southern exposures of the Wingate south of Little Valley, bleached and pigmented sandstone interfinger throughout the stratigraphic section. These relations may be seen in the center of the aerial view of Figure 8-6.

If Wingate bleaching has genetic significance as a guide to the distribution of Moss Back uranium, an important relationship is the age of such alteration relative to the age of mineralization. The age of bleaching is not definitely established. Some constraints are as follows: Bleached Wingate strata are displaced by the Lisbon Valley Fault or related fault structures at both the northwestern and southeastern ends of Lisbon Valley Anticline, which indicates that the alteration is older than the pre-Laramide age of faulting. The Wingate rests conformably upon Chinle red beds beneath. Chinle strata are altered green where they contact bleached Wingate; this indicates that the time of bleaching is after the development of red pigmentation of the Chinle and at some time after deposition of at least a portion of the Wingate. The upper Wingate contact with Kayenta red beds is gradational and locally intertonguing (Figure 8-8). In this relationship detailed boundaries between unpigmented Wingate and red Kayenta rocks are preserved, suggesting that unpigmented sands were available to participate in such depositional processes in Wingate time. Bleached strata may also be truncated in intraformational scour structures (Figure 8-9), suggesting that unpigmented strata were present in the section at that time.

The interpretation of such relationships depends upon history of the formation of the pigment in these rocks and detailed permeability relations between rock units, neither of which is well understood at Lisbon Valley. To interpret age relations in the channel structure depicted in Figure 8-9, it must be assumed (1) that pigmented rocks were present, and (2) that bleaching occurred in the section as an intraformational event prior to channeling. Walker et al. (1981) have discussed the history of pigment development in the Moenkopi Formation. They show that multiple post-diagenetic episodes of hematite crystallization and redistribution have occurred in these strata. Gabelman (1981, personal communication) has described euhedral magnetite in red sandstone of the Cutler Formation that he interprets to represent post-depositional introduction of iron. Development of pigment in the Wingate may have had a complex history similar to that described by these investigators.

Figure 8-6. Low-oblique aerial view of the bleached Wingate Sandstone facies. View is looking northwest along the southwestern flank of Lisbon Valley Anticline near Three Step Hill, Secs. 33, 34, 35, T30S, R25E and Secs. 2, 3, 4, T31S, R25E.

Jk Kayenta Formation

Trw Wingate Sandstone (bleached facies)

Trc, Trcu Upper Member of the Chinle Formation

Lower Chinle (Moss Back) is not exposed in this view. Unsymboled arrow indicates interfingering bleached and unbleached Wingate strata. NW-trending, nearly vertical joints are mostly confined to massive bedded Wingate strata.

Figure 8-7. Ground view of the bleached Wingate Sandstone facies, NW 1/4, Sec. 1, T31S, R25E. Note thinner bedding near the top of formation and massive character of the unit near the base.

An alternate interpretation of time relations for the channel structure depicted in Figure 8-9 is that bleaching postdates scowering. In this case, the distribution may be governed by detailed variation in permeability between the strata. The bleaching would then be post-depositional and offer no constraint on its time of origin.

Based on the photogeologic mapping described below, the anticline (hence, the bleached strata contained therein) may have undergone a small additional deformation since cessation of at least one episode of bleaching. The inferred additional rotations probably coincide with Laramide or post-Laramide anticlinal growth and faulting, but the timing is uncertain.

Superimposed upon the inferred older events are additional post-diagenetic changes, including modern hydrologic effects. For example, the Wingate Sandstone as opposed to the Upper Chinle or Kayenta strata is a good aquifer at the present time and readily carries surface rainwater to depth in mine workings.

d. Kayenta Formation. The Kayenta Formation (Carter and Gualtieri, 1965; Craig and Dickey, 1956) is the middle formation of the Glen Canyon Group and is of Jurassic (?) age. The formation rests on the Wingate Sandstone with which it has locally an intertonguing relationship (Figure 8-8). In the study area, the formation consists of reddish-brown and purplish-gray, fine- to coarse-grained sandstone with cross-beds irregularly interbedded with red siltstone. The composition is made up of subrounded quartz with minor mica, feldspar, and dark minerals. The Kayenta Formation crops out in a series of ledges and benches. The upper beds of the Kayenta are less resistant and form a broad bench that extends to the foot of the Navajo Sandstone cliff. From examination of aerial photographs it is possible to subdivide this unit in the study area into two and possibly more informal members based upon differences in color; however, this subdivision has not been worked out.

The Kayenta Formation is easily distinguished from the Wingate Sandstone, beneath where the latter formation is bleached (unpigmented), since bleaching is confined in detail to the Wingate. Examination of the contact relations, which are generally not well exposed, shows a transition of depositional environment from one favoring development of massive strata with cross-bedding characteristic of the Wingate to thin bedding representative of fluvial conditions of deposition for the Kayenta.

The Kayenta Formation is approximately 200 ft thick throughout most of the study area, but it appears to thin in the southern part of the area near the axis of the Lisbon Valley Anticline.

e. Navajo Sandstone. The uppermost formation of the Glen Canyon Group is the Navajo Sandstone of Triassic (?) and Jurassic age (Carter and Gualtieri, 1965; Craig and Dickey, 1956; Peterson and Pipiringos, 1979). This formation conformably overlies the Kayenta Formation, with which it has an indefinite intertonguing boundary. The Navajo forms steep cliffs, rounded slopes, and hogbacks. The Navajo is fine- to medium-grained massive sandstone which is light gray to pale brown in color. Based on the locally reddish color of this unit in southern Utah and elsewhere (Peterson and Pipiringos, 1979), the Navajo may have been bleached of its original iron-oxide pigmentation in the Lisbon Valley area. The sandstone has large-scale tangential cross-beds which, together with its color, easily distinguish it from the Kayenta beneath. The Navajo is

Figure 8-8. Intertonguing relationship between white facies of the Wingate Sandstone (Rw) and red facies of the Kayenta Formation (Jk). View looking northwest, NW 1/4, Sec. 10, T30S, R24E. Jn = Navajo Sandstone, Je = Entrada Sandstone.

Figure 8-9. Intraformational channeling and apparent truncation of bleached laminae in the Wingate, SE 1/4, Sec. 3, T30S, R24E

weakly cemented and consists of rounded to subrounded quartz with minor quantities of feldspar and dark minerals. The large-scale nature of the cross-bedding indicates the formation is predominantly eolian in origin, although thin beds of limestone occur near the base. The sandstone is approximately 250 ft thick throughout the study area. Carter and Gualtieri (1965) note irregular and abrupt thinning adjacent to the axes of anticlinal salt structures in Paradox and Castle Valleys to the east and north, which indicates that the anticline had been active prior to or during deposition of the formation. A similar thinning is observed over the axis of Lisbon Anticline in the southern part of the study area.

B. Geologic Relations at Lisbon Valley

A geologic map of the Lisbon Valley area, compiled from the published maps of Carter and Gualtieri (1957a, 1957b); Weir and Dodson (1958a, 1958b, 1958c); Weir and Puffett (1960); and Weir et al. (1960a, 1960b, 1961), is given in Figure 8-10. An index map of locations for these quadrangles is shown in Figure 8-11. The total area covered by the mapping shown is approximately coincident with that covered by the NS-001 Thematic Mapper Simulator images of the region. The geologic descriptions provided in this section will facilitate comparison between the existing geologic maps and the image interpretations described later.

The main diapiric salt structure comprising Lisbon Anticline (Figure 8-10) is a composite structure consisting of two side-by-side NW-trending anticlines separated by the steeply NE-dipping Lisbon Valley Fault. The Lisbon Valley Anticline, whose southwest limb and crest are exposed on the southwestern side of the fault, has marine limestone and sandstone of the Pennsylvanian-age Hermosa Formation exposed in the axial region. Southwest across the limb, the Hermosa Formation is overlain by the Cutler Formation. This formation is separated with angular unconformity from the Moss Back Member of the Chinle Formation (the Moss Back is subdivided in the geologic mapping of the figure only in the northern portion of Lisbon Valley Anticline). Above the Moss Back is the upper Chinle Formation. The Chinle Formation is capped by the Wingate Sandstone which, in turn, is overlain by the Kayenta Formation and the Navajo Sandstone. To the south of Lisbon Valley Anticline at Deerneck Mesa and on Three Step Hill (Figure 8-10) are exposed nearly flat-lying rocks of Jurassic age, including the Carmel, Entrada, Summerville, and Morrison Formations. Thin-bedded mudstones and limestones of the Carmel Formation and red sandstones of the Entrada occur to the west and northwest of the Lisbon Valley structure near Colorado Rock.

Northeast of Lisbon Valley Fault lies the axis of the Lisbon Canyon Anticline expressed at the surface in rocks of the Burro Canyon Formation and Dakota Sandstone. The Lisbon Canyon Anticline is cut in the axial region by minor normal faulting that exposes sediments of the Jurassic Morrison Formation.

To the northeast of Lisbon Canyon Anticline lies the NW-trending East Coyote Wash Syncline developed in rocks of the Burro Canyon Formation and Dakota Sandstone. The synclinal axis closely follows the course of East Coyote Wash. Relations in this structure are accentuated by the irregular distribution of Quaternary sediments that occurs atop outcrops of the Dakota and follows drainage courses determined by the synclinal alignment of dips.

The Lisbon Valley normal fault trends approximately N 50° W parallel to the axes of both of the anticlines. The fault dips northeast at approximately 58° at the surface, but the dip may shallow at depth to the northeast (Parker, 1966). The approximate displacement is 2000 ft. Near the southeastern extremity of the anticline (Sec. 35, T30S, R25E) this fault bifurcates. Rocks exposed in the intervening triangular wedge include a complete section from the Moss Back Member of the Chinle through the Mancos Shale. Some of these units (such as the Wingate, Kayenta, and Navajo) are considerably thinner here than in other exposures elsewhere in the area, indicating erosional thinning or nondeposition on the anticlinal axis. Except for short segments near the southern and northern extremities of the anticline, the Lisbon Valley Fault is buried beneath Quaternary gravel and eolian deposits.

C. Geologic History of the Salt Anticline

Geologic development of salt anticlines in the Paradox Basin has been discussed by Hite and Cater (1972) and by Stokes (1956); at Lisbon Valley the geologic history has been summarized by Lekas and Dahl (1956), Parker (1966), and Wood

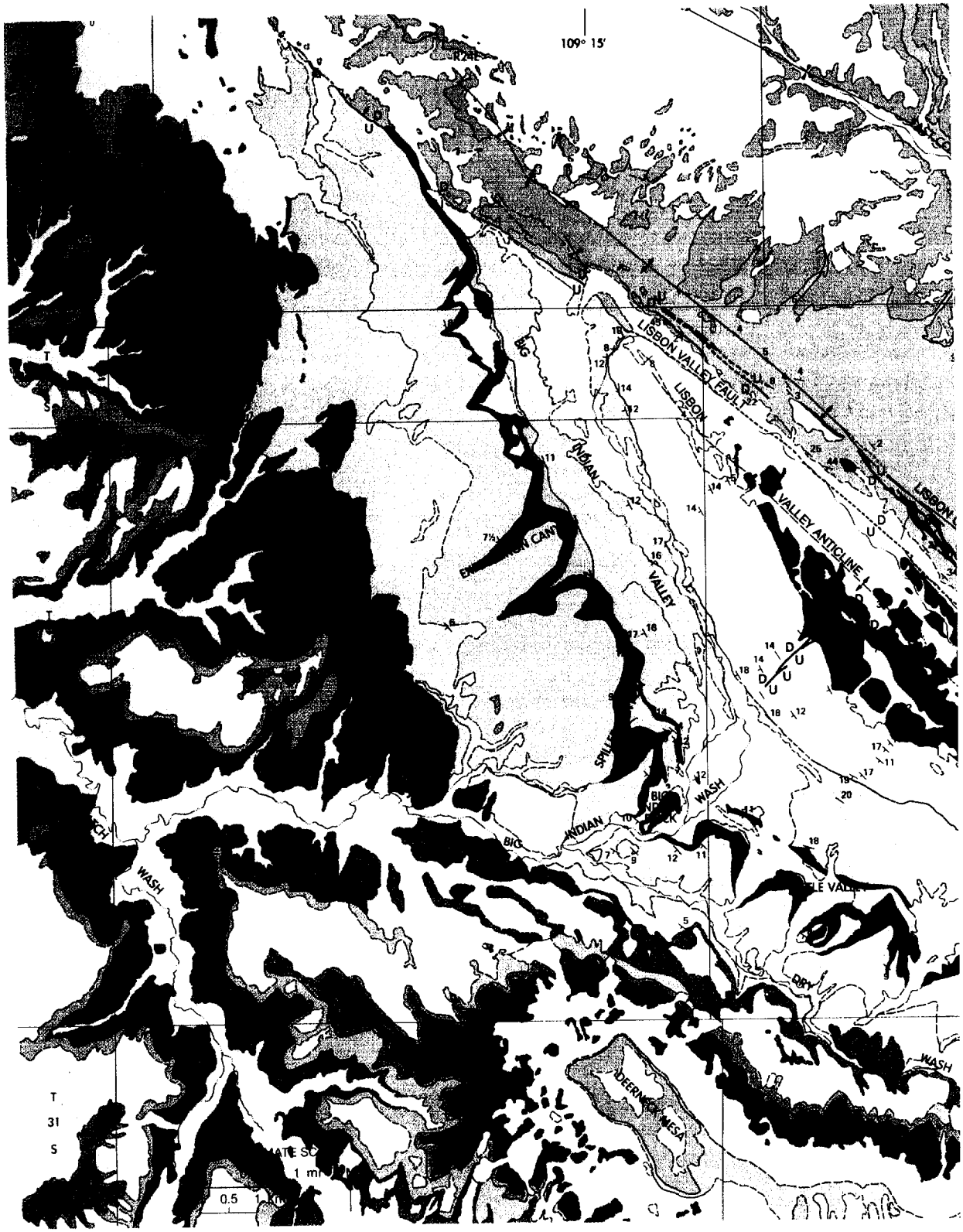

FOLDOUT FRAME

QUATERNARY
- EOLIAN AND ALLUVIAL SAND AND SILT
- LANDSLIDE DEPOSITS

CRETACEOUS
- MANCOS SHALE
- DAKOTA SANDSTONE
- BURRO CANYON FORMATION

JURASSIC
- MORRISON FORMATION
  UPPER UNIT, BRUSHY BASIN MEMBER
  LOWER UNIT, SALT WASH MEMBER
- SUMMERVILLE FORMATION
- ENTRADA SANDSTONE
- CARMEL FORMATION
- NAVAJO SANDSTONE

JURASSIC (?)
- KAYENTA FORMATION

TRIASSIC
- WINGATE SANDSTONE
- CHINLE FORMATION
  UPPER UNIT, RED SILTSTONE MEMBER
  LOWER UNIT, MOSS BACK MEMBER

UNCONFORMITY

PERMIAN
- CUTLER FORMATION WITH SUGAR SANDSTONE UNIT

PENNSYLVANIAN
- HERMOSA FORMATION
  UPPER UNIT
  LOWER UNIT

CONTACT

U / D 50
FAULT, SHOWING DIP
DASHED WHERE APPROXIMATELY LOCATED, DOTTED WHERE CONCEALED
U, UPTHROWN SIDE, D, DOWNTHROWN SIDE

ANTICLINE
TRACE OF AXIAL PLANE, DIRECTION OF PLUNGE, DASHED WHERE APPROXIMATELY LOCATED

SYNCLINE
TRACE OF AXIAL PLANE, DIRECTION OF PLUNGE DASHED WHERE APPROXIMATELY LOCATED

32
STRIKE AND DIP OF BEDS

ADIT

Figure 8-10. Geologic map of the Lisbon Valley area (compiled from sources given on the index map of Figure 8-11)

FOLDOUT FRAME 2

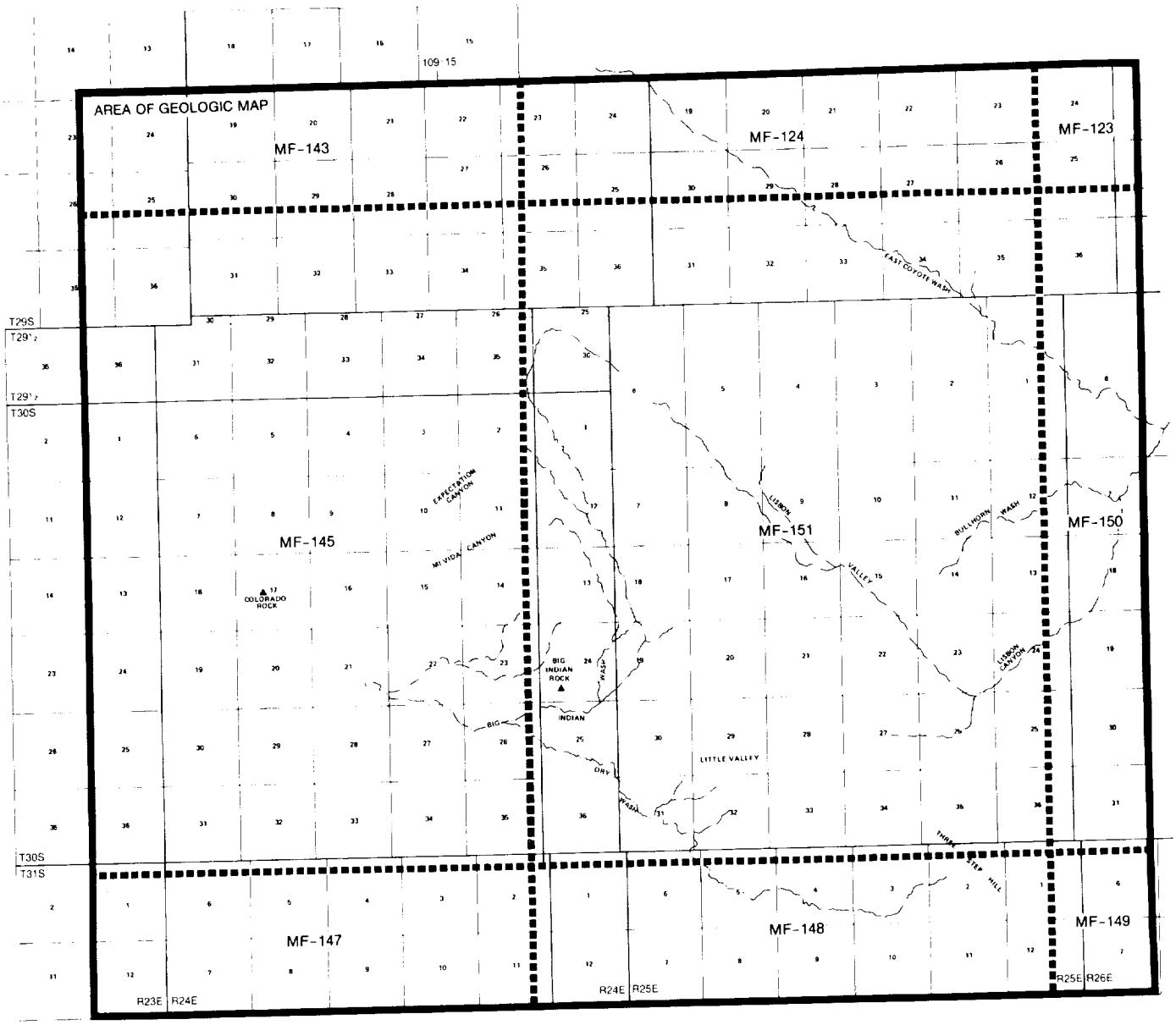

Figure 8-11. Index of geologic mapping for the Lisbon Valley area. Geologic map of Figure 8-10 compiled from Mineral Investigation Field Studies Maps (MF) of the U.S. Geological Survey: MF-123 (Mt. Peale 1SE), Carter and Gualtieri (1957a); MF-124 (Mt. Peale 1SW), Carter and Gualtieri (1957b); MF-143 (Mt. Peale 2SE), Weir et al., (1960b); MF-145 (Mt. Peale 3NE), Weir and Dodson (1958a); MF-147 (Mt. Peale 3SE), Weir and Dodson (1958b); MF-148 (Mt. Peale 4SW), Weir and Dodson (1958c); MF-149 (Mt. Peale 4SE), Weir and Puffett (1960); MF-150 (Mt. Peale 4NE), Weir et al. (1960a); MF-151 (Mt. Peale 4NW), Weir et al. (1961).

PRECEDING PAGE BLANK NOT FILMED

(1968). Geologic events leading to development of Lisbon Anticline are summarized below, based on discussions by Hite and Cater (1972), Parker (1966), and Wood (1968).

(1) Uplift and faulting occurred in Precambrian time, with development of a Precambrian erosion surface.

(2) Cambrian through Mississippian strata were deposited. Ordovician and Silurian strata were missing because of nondeposition or erosion.

(3) Faulting and folding occurred in late Mississippian time, with development of a Lisbon structural feature before deposition of the Early to Middle Pennsylvanian Molas Formation (Parker, 1966). The thinned Mississippian strata coincide in position with the present structural configuration of reservoir rock in Lisbon field.

(4) Oil and gas accumulated in Mississippian and Devonian reservoirs (?).

(5) Erosion took place during Late Mississippian and Early Pennsylvanian time, thinning the Mississippian strata over structural highs.

(6) In Pennsylvanian time a deep basin developed southwest of the NW-trending Uncompagre Uplift into which rocks of the Molas, Pinkerton Trail, and Paradox Salt and Honaker Trail Formations were deposited. Pennsylvanian black shale source beds provided additional oil and gas to Mississippian–Devonian reservoirs.

(7) Salt movement began prior to deposition of Lower Permian Cutler rocks, and possibly as early as Late Paradox time, probably through tectonic movements on the fault system developed in Mississippian time (Elston and Landis, 1960). Most salt flowage took place after development of an unconformity identified by Parker (1966) to divide the Cutler Formation. After Lower Cutler deposition and initiation of rapid salt movement, local depressions formed. Erosion from topography surrounding such lows initiated Upper Cutler deposition, with subsequent large augmentation by sediments from more distant sources.

(8) Jurassic through upper Cretaceous strata were deposited with recurrent salt movement throughout the interval in response to differential loading. The recurrent nature of motion is evidenced by nondeposition of the Moenkopi Formation and by reduced thicknesses of the Chinle Formation, Glen Canyon Group, and other rocks through Morrison in age over the crest and flanks of the salt anticline.

(9) By the end of San Rafael time (Jurassic), salt flowage from areas adjacent to the anticline ceased with exhaustion of the supply of salt there. The salt anticlines were beveled prior to deposition of Morrison and later rocks.

(10) After deposition of the upper Cretaceous Mesaverde Formation, anticlines formed along the old salt anticline structures in response to deep-seated deformation apparently controlled by Precambrian basement structures. These structures were of widespread influence throughout the basin.

(11) Collapse of the crests of the salt anticline occurred in two stages widely separated in time. During the early (post-Cretaceous) stage, grabens formed along crests in a structurally simple pattern of collapse. A second period of collapse began after uplift of the Colorado Plateau. This post-Miocene uplift rejuvenated movements that eventually breached the crests of these fold structures, in some cases exposing the salt core to solution and removal.

D. Emplacement of Mineral Deposits

Miller and Kulp (1963) provided uranium–lead isotopic ages and sulfur isotopic evidence on the origin of Colorado Plateau uranium ores, including those of Triassic and Jurassic age at Lisbon Valley.

Theories of origin for these ore deposits must satisfy the isotopic data as well as geological and other geochemical boundary conditions.

(1) An upper (maximum) age limit of approximately 210 m.y. constrains the age for the bulk of uranium mineralization because the deposits occur in Upper Triassic and Upper Jurassic strata and are not reworked from earlier deposits.

(2) Basement rocks of the Colorado Plateau are about 150 m.y. old.

(3) The deposits are found in porous sandstones generally with organic debris.

(4) The Colorado Plateau deposits taken together are scattered over a 150,000-mi^2 area.

(5) Solution and deposition of uranium have occurred in recent geologic history.

(6) Based on experimental evidence (Miller, 1958), H_2S can precipitate uranium as pitchblende from solutions containing ppb dissolved U; these uranium concentrations are common in Colorado Plateau groundwater. In addition, all of the unoxidized ore deposits contain abundant sulfide.

The measured U–Pb isotopic ages of ores in the Colorado Plateau range from 22 to 255 m.y. Those in Lisbon Valley

span the interval 85 to 207 m.y. The ages, calculated on the basis of ^{238}U–^{206}Pb and ^{235}U–^{207}Pb, agree within 5 percent, but a few disagree by more than experimental error and show lower ^{238}U–^{206}Pb ages (Miller and Kulp, 1963). These U – Pb ages and ^{207}Pb–^{206}Pb ages are typically discordant, the latter being older. Peaks in the distribution of ^{235}U–^{207}Pb ages over the Plateau occur near 200 to 220 m.y. and 60 to 110 m.y., which is interpreted to signify at least two major depositional episodes or alteration events. Two hypotheses have been proposed to deal with these problems: (1) loss of radiogenic lead subsequent to mineral formation, and (2) incorporation of old radiogenic lead at the time of mineral formation. The original radiogenic lead hypothesis (2) was proposed by Stieff et al. (1953) to explain discordant U–Pb ages observed for Colorado Plateau ores. Their measured isotopic ages clustering near 60 m.y. were suggested to represent the (end of Laramide) age of uranium deposition and older ^{235}U–^{207}Pb ages by variable contributions of radiogenic lead from older (up to 1500 m.y.) basement sources of pitchblende. Numerous difficulties with this hypothesis were pointed out by Miller and Kulp (1963), who proposed instead the alteration lead-loss hypothesis.

The lead-loss hypothesis assumes that pitchblende was deposited early in the history of the enclosing sediments and that subsequent perferential loss of radiogenic ^{206}Pb relative to ^{207}Pb accompanied more recent geochemical alteration events. The observed isotopic ages are lower than the true ages on this basis. Preferential loss of an intermediate isotope in the ^{238}U decay series such as radon or radium is a possibility. Such losses are probably enhanced by groundwater activity.

Some sulfides present in all the Colorado Plateau ores show extensive fractionation of the sulfur isotopes; this requires the action of anaerobic bacteria (Miller and Kulp, 1963). These organisms do not metabolize above a temperature of 80° to 90° C. Chinle ore deposits are found to be localized in and near accumulations of organic trash. These observations suggested that uranium-bearing solutions encountered bacterially produced H_2S environments and led to low-temperature formation of pitchblende and iron sulfides.

The following origin and history of Colorado Plateau ores are based on the geochemical and isotopic data of Miller and Kulp (1963). During or shortly after deposition of the sedimentary rocks, groundwater containing a dilute solution of uranium passed through H_2S-saturated environments. Precipitation of uranium occurred in these low-temperature environments. The initial sources of uranium could have included the basement, surface rocks, or permeable rocks containing the present ore bodies. The uranium from these was supplied to the host sandstones by hydrothermal solutions. Groundwater action subsequent to ore deposition produced losses of radiogenic lead in amounts yielding the observed isotopic ratios.

The model of ore genesis proposed by Wood (1968) and summarizing most of the evidence available at that time is similar to the model of Miller and Kulp (1963). Wood discounts the role of hydrothermal activity. The uranium is believed indigenous to the Chinle Formation, released from siliceous glass by diagenesis. Gaseous CO_2 from Mississippian oil and gas reservoirs is thought to play a role in the dissolution and transport of uranium. Coalified plant material together with natural gas or sulfide solutions from the oil and gas reservoirs beneath cause ore precipitation in favorable sites. Emplacement occurred in a static period following deposition of the fluvial Chinle. Deposits were positioned within the ore belt either along a water–gas connate–vadose water interface near the crest of the ancestral Permian anticline or near subcrops of porous Cutler or Moenkopi sediments on the Triassic–Permian unconformity.

The mechanisms described require the presence of carbonaceous debris or external sources of reductants to precipitate uranium. Uranium deposits in the Permian Cutler Formation at Lisbon Valley have been described by Campbell (1981). In these deposits no significant organic carbon was found in the ore zones, and formation of the ore bodies occurred without any obvious reductant.

The precise timing of events leading to mineralization of the Cutler and Chinle rocks is not known. The maximum age is provided by ages of the enclosing rocks. Thus the Chinle ore bodies are no older than Triassic and the Cutler ore bodies no older than Permian. A major hiatus represented by an angular unconformity separates these two formations. The ore bodies are continuous across the unconformity. No geologic evidence known to the writers has suggested both Permian and Triassic mineralizing episodes; therefore, the time of mineralization is Chinle or later. The Pb–U ages are of course uncertain, but Miller and Kulp (1963) argue that the distribution of ages points to a Triassic age of emplacement. Mineralization of Jurassic or later age is found in the Morrison Formation both to the south and to the north of the study area. These later mineralizing episodes may have contributed to the Lisbon Valley deposits or to their reorganization in part.

E. Exploration and Mining History

The exploration and mining history of Lisbon Valley Anticline has been summarized by Wood (1968). The following is excerpted from that paper.

1. Exploration history

The first discovery of uranium–vanadium ore on the Lisbon Valley anticline was made in 1913, at the south end of the anticline, on outcrops of basal Chinle sandstone. In 1948, low-grade uranium deposits were discovered and

developed in Upper Cutler sandstone outcrops along the center of the southwest flank of the anticline. These were the deposits that attracted Charles Steen to the area. In July 1952 Steen drilled the famous 70-foot deep discovery hole on the Mi Vida claim just off the Big Buck claims and down dip from the mines in the Cutler Formation. He encountered about 13 feet of uraninite ore in the Moss Back sandstones, about 100 feet higher stratigraphically than anticipated. Following this discovery, claim staking and exploration drilling progressed rapidly to the northwest and southeast and continued with intensity through 1956. During this ensuing period, the following deposits in the Chinle were discovered by drilling in the north half of the Big Indian ore belt: Standard (Big Buck), Little Beaver, Louise, Texwood-Stinko, Ike-Nixon, La Sal, Columbia, San Juan, Cord (Jen), Radon (Hecla), Far West, and North Alice. A peak in exploration was reached in 1955, when 647,000 feet of drilling was reported. By mid-1956, exploration drilling began to taper off. By the end of 1964, over 4500 holes totalling about 2,200,000 feet had been drilled in the search for uranium on the anticline, and over 3000 holes, spaced 200 to 500 feet apart, had been drilled within the delineated ore belt. This intensity of drilling argues against the existence of any undiscovered large ore deposits in the drilled areas, although a number of small ore deposits may remain undiscovered.

The discovery in 1962 and the mining of uranium ore in 1964 at the Costanza Mine in Secs. 26 and 35, T30S, R25E established the existence of uranium ore on the northeast side of a hinge fault that has more than 2000 feet of displacement. This high angle fault is one of the main bifurcating faults at the south end of the Lisbon Valley Fault. Between May 1964 and July 1965, Humeca Exploration Company drilled five deep holes (2500 feet ±), in the center of Sec. 21, and in the southwest corner of Sec. 22, T29S, R24E. Interpretation of Century Geophysical Company gamma ray logs of these holes indicated that two holes penetrated up to 33 feet of Moss Back sandstone and 2 to 8 feet of uranium ore. This discovery established the occurrence of uranium ore in the downthrown block northeast of the main Lisbon Valley Fault at the north end of the anticline. [These deposits are currently under production by Rio Algom Corporation.]

In 1978, Atlas Minerals announced the discovery by drilling of a major mineral body in the center of Sec. 3, T31S, R25E, adjacent to the Velvet deposit in the NW 1/4, NW 1/4, Sec. 3. The stratigraphic position of this new mineralized zone is uncertain and has been tentatively assigned to the Cutler as opposed to the Chinle section. The new deposits may actually lie in the Moenkopi Formation. From drill core data the Moenkopi is present on the flanks, but is not exposed in the axial region of Lisbon Anticline.

2. Mining history

Vanadium ore production from the Chinle Formation at the Divide and Serviceberry Mines in south Lisbon Valley was reported in 1917, 1940, and 1941. These same mines were reopened in 1948 for their uranium content. Also in 1948, the Big Buck Mines in the Cutler Formation in Big Indian Valley were mined for uranium. Intermittent production from these small deposits continued until 1952. In December 1952, Steen shipped the first ore from the Mi Vida Mine.

Production from the Moss Back sandstone beds has ranged from two to six million pounds of U_3O_8 per year and reached a peak production of over 6,377,000 pounds in Fiscal Year 1958. Due to the exhaustion of a few of the major ore deposits, the ore production rate started dropping in 1960 and has leveled off to about 4,000,000 pounds per year.

In the central and southern deposits, the vanadium content is high enough for that metal to be extracted economically. During the 1948–56 period, vanadium was extracted from ore that was shipped from these mines to some of the processing mills on the Colorado Plateau. However, most of the ore has been processed at the Atlas Corporation alkaline leach mill at Moab, Utah, and to date this mill has recovered only a small amount of vanadium on an experimental basis. Molybdenum assays ranging up to 0.25 per cent are common but very spotty in the Big Indian ores. Those deposits with anomalous molybdenum, such as the North Alice, South Almar, Mi Vida, Standard, and Velvet, normally assay only 0.03 to 0.07 per cent molybdenum.

Up to July 1, 1965, about 6,147,000 tons of ore at a grade of 0.39 percent U_3O_8 containing about 48,530,000 pounds of U_3O_8, had been mined from deposits in the Big Indian ore belt, including production from the Cutler Formation. Continuation of operations to 1971 was anticipated to result in a total production of about 57 million pounds of uranium oxide....

VI. Reflectance Properties of Cover Types

A. Background

The visible and near-infrared (VNIR) reflectance (0.45 to 2.5 μm) properties of rock and vegetation types for the Lisbon Valley test site are presented here. Ground reflectance was determined by *in situ* field measurements, by laboratory studies of outcrop samples from field sites, and by analysis of aircraft multispectral scanner data. The reflectance of sedimentary rocks and of various vegetation types is presented here.

The sedimentary rocks of interest here consist predominantly of continental clastics. Major pigments are iron oxides; clays and carbonate cements contribute additional important features to the reflectance spectra.

The vegetation present consists of lichen, grass, shrubs, and evergreen (piñon–juniper) tree cover. This cover is diverse in species and highly variable in extent. The vegetation component can thus make an important contribution to the macroscopic (pixel size) reflectance determined from the scanner data. The reflectance properties of plants are dominated by the presence or absence of the pigment chlorophyll and by the abundance of imbibed and free water. These are properties that characterize the health or vigor of plant materials. Plants with an open branching structure contribute a variable-density shadow component. The shadow component may dominate the reflectance from heavily tree-covered areas. Some field spectral reflectance measurements of shadow effects are presented in the Patrick Draw, Wyoming, Petroleum Test Site Report, Section 11. The reflectance properties of plants (grasses and shrubs) are also seasonally dependent. This aspect of the reflectance can only be evaluated qualitatively because plant surveys coincident with the times of the aircraft scanner overflights (June 1976 and August 1978) are not available.

In addition to sedimentary rock outcrops and vegetation, soil, alluvial, eolian, and landslide deposits cover large areas of the surface throughout the study area. The distribution of soil cover types was mapped in a preliminary survey by the USDA Soil Conservation Service and has been summarized above. These subdivisions of soil cover are done in a generalized manner at a small map scale and have limited value in interpretation of the image data. Alluvial, eolian, and landslide deposits have been mapped in the area by the U.S. Geological Survey. All of these deposits have extensive soil and vegetative cover. Quaternary alluvial deposits occupy the bottoms of modern streams and the tops of mesa-forming units, such as the Navajo Sandstone and Dakota Sandstone, where extensive grass and shrub cover develops. Eolian cover is widespread in Big Indian Valley. Landslide deposits are found extensively on slopes underlain by nonresistant shales of the Morrison and Burro Canyon Formations. Extensive landslide deposits occur on the flanks of Deerneck Mesa, where they are covered by thick stands of piñon–juniper. These soil and alluvial cover types are diverse. No field spectral measurements have been made of such units.

Characterization of diverse cover types is a problem to which the multispectral scanner data naturally apply. Three approaches are possible: (1) absolute identification using the spectral reflectance by matching aircraft scanner data with laboratory and field spectra, (2) resolution of mixed targets (multiple pixel or subpixel in size) in to specified but perhaps uncharacterized end-member components, and (3) relative classification into groups based on training data sets. Approaches (1) and (2) are discussed here. Refer to the Lost River, West Virginia, Petroleum Test Site Report, Section 12, for an application of classification methods to vegetation problems. Use of images to provide "absolute" broadband spectral reflectance requires a calibration step to remove instrumental and atmospheric effects. An analysis of this problem and details of the required calculations are given in Appendixes A and B.

The problem of mixed scenes (pixels with mixed cover types) has been encountered in crop inventory studies using Landsat data (for an up-to-date survey of methods, see Feiveson, 1979). The usual approach to this problem is a statistical one (Horwitz et al., 1971, and papers cited in Feiveson, 1979), but all approaches share use of the simple areal-additive photometric law of mixing.

A geometrical but nevertheless closely similar method based on use of either principal axes or canonical coordinates is developed here. This method and its applications are presented in Appendix E. The method permits separation of mixed spectral collections into end members present. Advantages of the method are:

(1) It employs the linear reduction properties of these transforms.

(2) The calculations can be done by hand once the principal components are available, or it can be carried out using the BMD software (Dixon, 1974) to provide canonical variables.

(3) It provides an easy geometrical representation of the results.

(4) The raw uncalibrated spectral radiance data not corrected for atmospheric effects may be used.

Field spectral measurements have been carried out using the JPL Portable Field Reflectance Spectrometer (PFRS). This instrument operates in the spectral region 0.45 to 2.5 μm and measures bidirectional reflectance of the undisturbed surface with respect to the field standard Fiberfrax® with a spectral resolution $\lambda/\Delta\lambda$ of approximately 100. The area covered in a typical observation is approximately 200 cm^2. The spectral regions 1.3 to 1.5 μm and 1.75 to 2.0 μm are excluded because of strong atmospheric water extinction. Optical and electronic design of the instrument and procedures of data reduction are described in the Technical Appendix, Section 14. Hand specimens were collected routinely at all field sites for laboratory analysis.

Laboratory spectral reflectance measurements were made using Beckman DK2A and Beckman 5240 Spectrophotometers, both of which operate in the spectral region 0.4 to

2.5 μm. The laboratory instruments measure hemispherical reflectance with respect to smoked MgO with a spectral resolution $\lambda/\Delta\lambda$ of 100 to 500. Laboratory samples are usually pulverized and the P32 (<0.49 mm) mesh size fraction analyzed on loosely packed samples as a simple means of standardizing the measurements.

Aircraft multispectral scanners measure bidirectional radiance in discrete spectral intervals. The bandpasses for instruments used in these studies are included in Table 8-4. The fields of view are between 50 and 225 m^2.

The reduction of radiance values to equivalent average surface reflectance uses model assumptions needed to eliminate atmospheric and instrumental parameters. These are discussed in Appendix A. In general, a linear relation of the form

$$DN_i = k_i' \bar{\rho}_i + k_i''$$

holds with good approximation between average surface reflectance $\bar{\rho}_i$ and encoded scanner radiance DN_i for each scanner channel i. The k_i' and k_i'' are constants determined empirically by comparison to field spectral reflectance data discussed in Appendix B. Ultimately, the determined nondirectional reflectance measures $\bar{\rho}_i$ are referenced to the Fiberfrax® field reflectance standard.

The laboratory data are used routinely to interpret spectral features present in the field measurements. The field data in turn form a basis for interpretation of the scanner results, but detailed photometric reconciliation of the three measurement sets is generally not made.

Table 8-4. Bandpasses for the Bendix 24-channel scanner and the NS-001 used for image analysis at Lisbon Valley

Channel	Bendix 24-channel,[a] μm	NS-001, μm
1	0.34–0.40[b]	0.45–0.52
2		0.52–0.60
3	0.46–0.50[d]	0.63–0.69
4		0.76–0.90
5	0.57–0.63[d]	1.00–1.30
6	0.64–0.68[d,e]	1.55–1.75
7	0.71–0.75[d]	2.08–2.35
8	0.76–0.80[d]	10.4–12.5
9	0.82–0.87[d]	
10	0.97–1.05[d]	
11	1.18–1.30[d]	
12	1.52–1.73[d]	
13	2.10–2.36[b,d]	
14	3.54–4.00[b,c]	

[a] Channels listed were operable and noise free during the June 1976 overflight at Lisbon Valley.
[b] Channel was used in the three-color composite, Figure A-1.
[c] Additional channel was used only in PC analysis of vegetation removal (described in Paragraph VIII. D).
[d] Channel was used for canonical transform image, Figure 8-30.
[e] Channel was excluded from PC analysis of vegetation removal.

B. Laboratory and Field Spectra of Sediments

Sedimentary rocks are the only lithologies present in the Lisbon Valley area. The laboratory and corresponding field reflectance spectra of representative outcrops exposed on the flank of Lisbon Anticline are shown in Figures 8-12 and 8-13. A location map of the field sites studied is given in Figure 8-14. These reflectance spectra generally are dominated by absorption bands contributed from Fe^{+3}, OH, and free water. The spectra of some sedimentary rocks are discussed by Hunt and Salisbury (1976). The following descriptions include some lithologic details to facilitate the interpretations.

1. Cutler Formation. This formation includes red, purple, and deep-maroon iron-oxide-pigmented sediments with granitic clasts and quartzose sugar-textured sandstones. To varying degrees, the sugar sands have been bleached of iron-oxide pigmentation to form mottled mixed red, purple, green, and

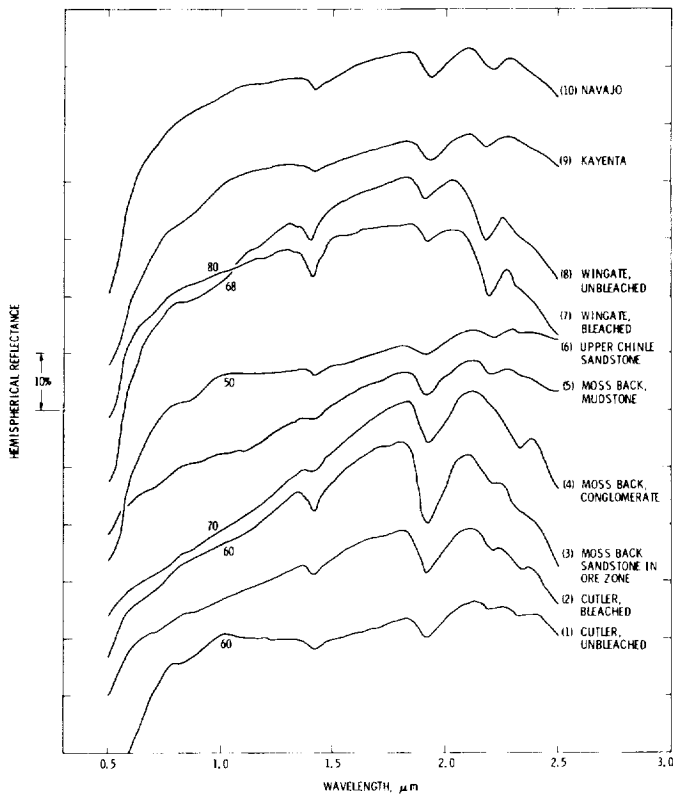

Figure 8-12. Laboratory hemispherical reflectance curves for sediments exposed in Lisbon Anticline. Numbers next to curves give the reflectance values at 1.0 μm.

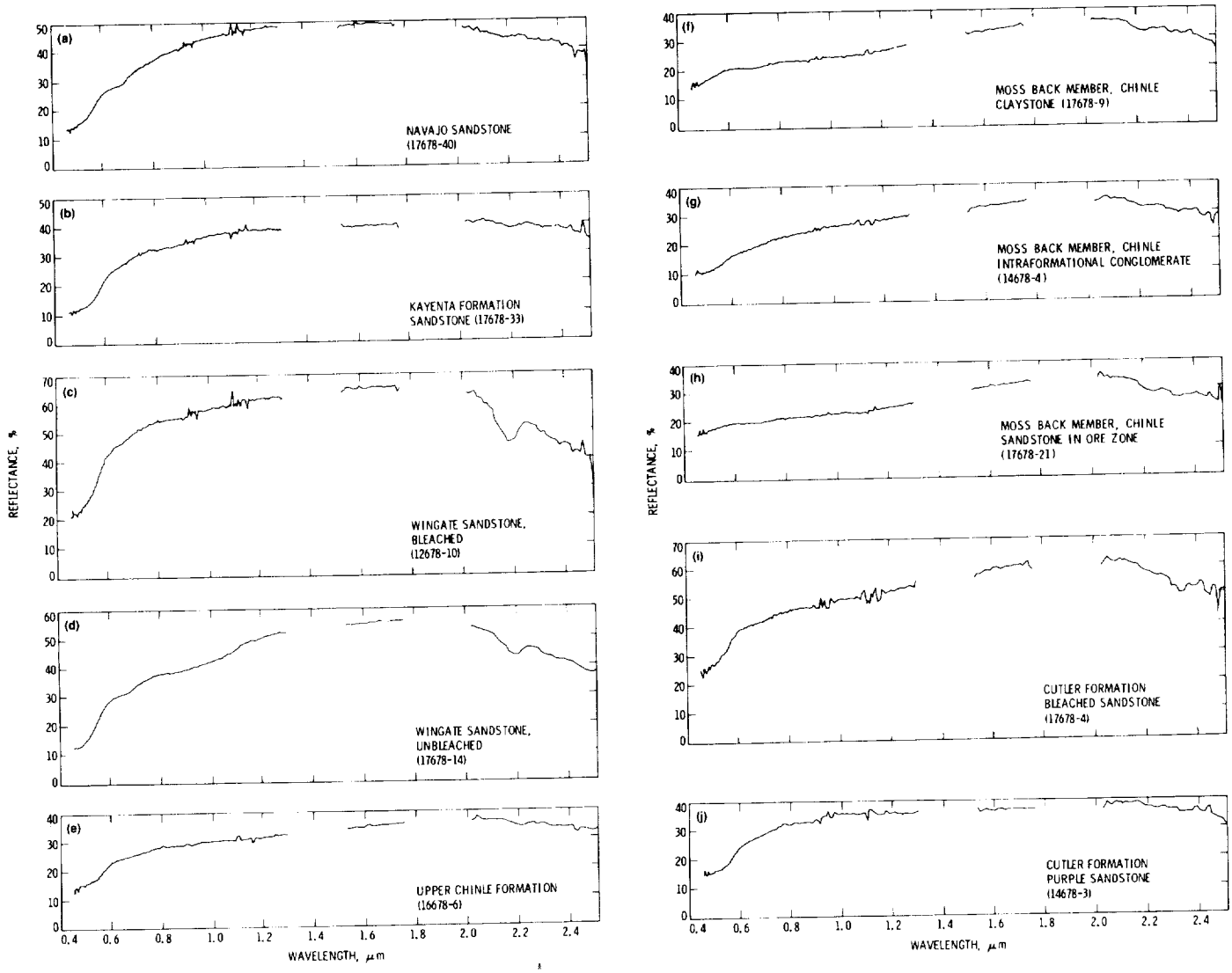

Figure 8-13. Bidirectional field reflectance of sediments exposed in Lisbon Anticline. Measurements were obtained with the PFRS. Numbers are field site identification symbols.

buff outcrops. The deeply pigmented Cutler facies (curve 1, Figure 8-12) shows strong absorption features from Fe^{+3}. Ferric oxide produces a characteristic falloff in reflectance toward the blue, with the wing of a strong ultraviolet absorption near 0.5 μm and a well-defined band at 0.85 μm. A very broad, shallow absorption feature residing between 1.0 and 2.0 μm is characteristic of many ferric oxides (Conel et al., 1978) and may arise from the presence of quadrivalent titanium impurities and oxygen vacancies in the hematite lattice. Morin (1954) discussed the origin of this feature and has shown that it emerges when synthetic pure hematite is artificially doped with titanium (Figure 8-15). Such pigments may develop from weathering of ilmenite.

The reflectance of the Cutler red beds also has weak bands at 2.20 μm due to OH in clay and at 2.35 μm due to carbonate. The presence of kaolinite and calcite is confirmed by X-ray diffraction (XRD) analysis of these samples. Prominent bands due to OH (1.4 μm) and water (1.4 and 1.9 μm) are also present. The reflectance curve for bleached sandstone (curve 2, Figure 8-12) shows a decrease in the presence of absorptions due to Fe^{+3} and an increase in the strength of OH, water, and CO_3^{-2} absorptions in carbonate. These increases possibly resulted when the bands were unmasked during the removal of strongly absorbing iron-oxide pigments, or the bands may have developed with production of clay and introduction of carbonate accompanying alteration of the rock.

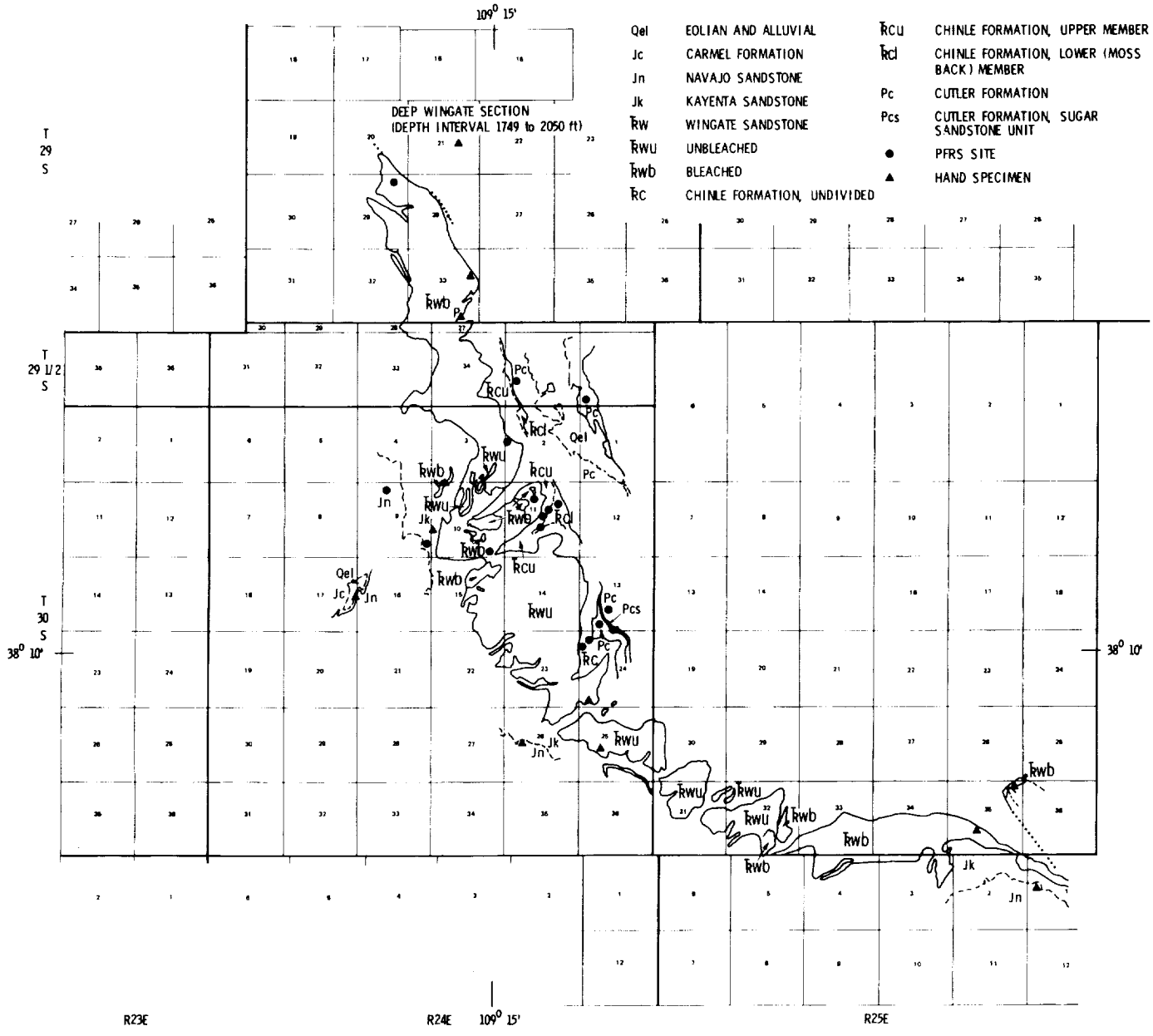

Figure 8-14. Index map of PFRS and hand specimen sample locations

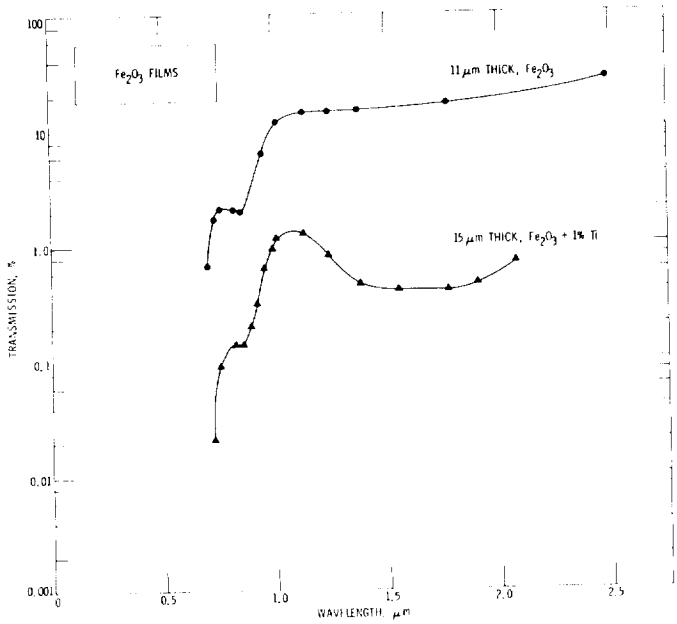

Figure 8-15. Absorption band centered near 1.65 μm, attributed to the presence of Ti^{+4} in the hematite lattice (after Morin, 1954)

2. Moss Back sandstone and upper Chinle red beds. The lower Chinle (Moss Back) sediments include brown and green conglomeratic (cherty) sandstone, siltstone, and minor limestone lenses. The reflectance spectra of greenish-gray Moss Back sediments (curves 3, 4, 5, Figure 8-12) rise from the blue toward the infrared and show a broad, poorly defined absorption near 1.0 μm due to Fe^{+2}, possibly present as constitutional iron in a clay mineral. These curves are characterized by weak bands due to OH absorption at 1.4 μm, by strong bands due to water absorption at 1.9 μm, by minor bands due to kaolinite absorption at 2.20 μm, and by carbonate absorption at 2.35 μm.

The upper member of the Chinle Formation consists mainly of thinly cross-bedded fine sandstones and siltstones, mostly red in color. The reflectance spectrum of sandstone from this member (curve 6, Figure 8-12) again shows the strong ultraviolet 0.85- and 1.6(?)-μm absorption features characteristic of ferric oxide with titanium impurities. A minor absorption band at 2.20 μm from OH is probably due to kaolinite. Poorly developed OH and water bands at 1.4 and 1.9 μm are also present.

3. Wingate Sandstone. Wingate Sandstone in its unaltered (unbleached) state is a massively bedded pink to salmon-colored, fine-grained sandstone. It is bleached (altered) of its original color to a white or beige color throughout the northern and southern parts of the anticline. Partial bleaching (interlayered bleached and unbleached strata) characterizes some portions of the section over the remaining exposures.

The reflectance spectra of bleached and unbleached facies (curves 7, 8, Figure 8-12) portray these changes in mineralogy and pigmentation. Altered sandstone is 10 to 15 percent brighter than its unaltered equivalent. Unaltered rock is characterized by intense ultraviolet absorption and a broad structure near 0.9 μm, both arising from ferric oxide. These features are removed or greatly diminished in strength in the spectra of bleached rock. A very prominent feature at 2.20 μm due to OH in kaolinite is present in both and is seen to be slightly stronger (unmasked?) in bleached sandstone. Unaltered sandstone sometimes displays a very subtle absorption at 2.35 μm from carbonate. From study of laboratory samples, the spectral reflectance of bleached rock is similar in both northern and southern outcrops in the study area.

Iron-oxide pigments in sandstone typically contribute a vanishingly small percentage of the mineral assemblage present and usually cannot be analyzed directly by XRD methods. Spectral reflectance is a sensitive method of characterizing the mineralogy of these compounds and is especially useful when they are present in small amounts. A differential reflectance technique (Conel et al., 1978) was used to examine the reflectance properties of pigmentation alone. Pigment was removed from a sample by dithionite–citrate extraction, and the resulting clean sample was used as a reference in the spectrophotometer, replacing MgO. The ratio reflectance spectrum of pigmented to unpigmented sample is shown in Figure 8-16. A comparison of Figure 8-16 to Figure 8-12 shows that the resolution of the

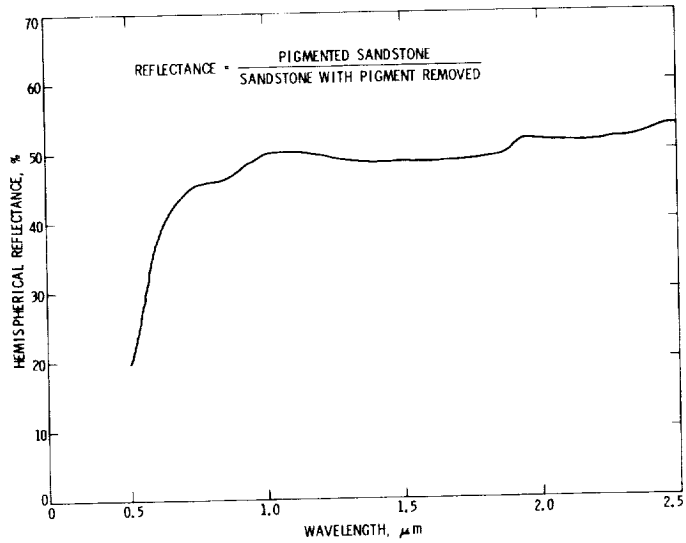

Figure 8-16. The differential hemispherical reflectance spectrum of iron-oxide pigment from the unbleached facies of Wingate Sandstone. Iron oxide was removed from pigmented samples by dithionite–citrate extraction and the resulting clear sample used as a reference in the spectrophotometer. The differential spectrum shows Fe^{+3} absorption bands in the ultraviolet and at 0.85 μm, typical of hematite, and an absence of OH and water absorption features, typical of goethite.

(0.8 to 0.9 μm) Fe^{+3} iron transition has been improved, allowing it to be placed with greater certainty near 0.85 μm. In addition, OH, water, and carbonate absorptions have all been reduced or removed. The resulting spectrum compares favorably with that usually associated with hematite (see Conel et al., 1978, for comparison spectra), but not goethite.

4. Kayenta Formation and Navajo Sandstone. The Kayenta Formation is a series of red, purple, and maroon fluvial, coarse- to fine-grained sandstones stratigraphically located above the Wingate Sandstone. The Navajo Sandstone atop the Kayenta is a white to buff, massive cross-bedded eolian quartz sandstone with minor thin freshwater limestone lenses.

The reflectance spectrum of Kayenta red sandstone (curve 9, Figure 8-12) shows moderately intense ultraviolet absorption and a weak, poorly resolved structure near 0.85 to 0.90 μm, both probably arising from ferric oxide. In addition, the spectrum shows weak structures attributable to OH and water and a prominent band at 2.19 to 2.20 μm from clay.

The reflectance spectrum of Navajo Sandstone (curve 10, Figure 8-12) displays the usual prominent ultraviolet (i.e., rapid falloff in reflectance below 0.7 μm) absorption and, in addition, weak structures near 0.9 and 1.2 μm. The first of these may arise from hydrated iron oxide (goethitic/limonitic) in which the iron absorption shifts to a longer wavelength than that of ferric oxide (hematite). A possible choice for the second is a combination band ($2\nu_1 + \nu_2$) due to OH stretching (ν_1) and H–O–H bending (ν_2) modes (see Hunt et al., 1971).

C. Spectral Reflectance of Vegetation

Laboratory reflectance measurements of Utah juniper (*Juniperus osteosperma*), piñon pine (*Pinus edulis*), and Great Basin sage (*Artemisia tridentata*) are shown in Figure 8-17 as examples of the spectral properties of vegetation types present in the Lisbon Valley area. The detailed reflectance properties of plants involve complex interactions of light with leaf morphology, cell structure, intracellular spaces, protoplasm, chloroplasts, and pigments (chlorophyll) contained within the chloroplasts. Qualitatively, the major features of vegetation reflectance arise from the pigments important in photosynthesis, from the cellulose of cell walls, and from water containing solutes within the cells themselves. The relevant spectral features are discussed in detail by Gates et al. (1965).

As illustrated in Figure 8-17, the reflectance of plants below 0.75 μm is dominated by the presence of chlorophyll and carotenoid pigments. While about ten forms of chlorophyll have been identified, two forms are most frequent in higher plants. Chlorophyll-a has two absorption peaks, at 0.43 and 0.68 μm, while chlorophyll-b absorbs at 0.46 and 0.66 μm. The carotenoids (xanthophylls and carotenes) absorb in the

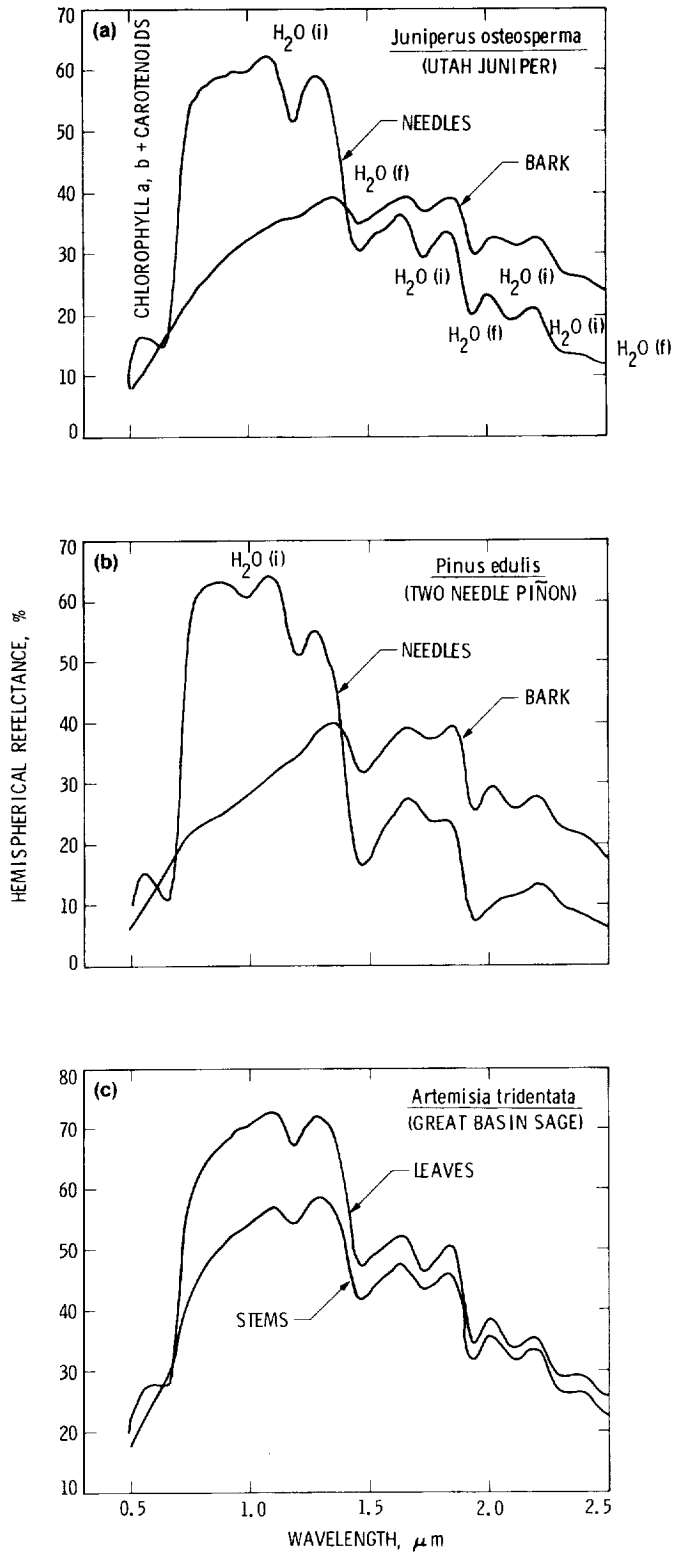

Figure 8-17. Laboratory spectral reflectance measurements of juniper, piñon pine, and Great Basin sage from the Lisbon Valley test site. Prominent absorptions indicated are due to chlorophyll and carotenoids, imbibed water on cell walls (H_2O (i)), and free water (H_2O (f)).

region 0.41 to 0.58 μm. Between these double-peaked absorptions is a region of relatively low absorption (0.55 μm) corresponding to a spectral band of higher reflectance. Pigments involved in photosynthesis fluoresce, possibly contributing to the measured reflectance in the spectral region near 0.7 μm. Chlorophyll shows a brilliant red fluorescence with the maximum fluorescent intensity at a slightly longer wavelength than the red absorption maximum in chlorophyll extending out to and beyond 0.73 μm.

The reflectance of green material beyond approximately 0.8 μm is characterized by strong absorption bands due to both imbibed cell water and free water. Absorptions due to the absorbed component occur at 0.98, 1.19, 1.73, 2.1, and 2.3 μm, while those from the free-water component are found at 1.47 and 1.97 μm in the plant specimens studied. Beyond 2.5 μm, the principal absorption arises from the water fundamental molecular absorption at approximately 3.0 μm.

The reflectance properties of stems and gray scaly parts of twigs and bark are dominated by tannin dyes and cellulose. Characteristically, the absorption bands due to chlorophyll disappear and are replaced by an increased reflectance attributed to the tannins (Figure 8-17). This results in a marked decrease in slope near 0.7 μm, the so-called red rolloff. The loss of free and imbibed water causes the reflectance, beyond 1.4 μm, of gray scaly material to exceed that found in the green parts. All of the associated water absorption bands are of reduced intensity in scaly dead cell material. These general changes accompany senescence of all types of green plants.

To facilitate later comparisons with the derived scanner spectral data, these reflectances are shown in Figure 8-18, averaged over the NS-001 scanner bands. That is, the equivalent scanner reflectances $\bar{\rho}_i$ are computed graphically from

$$\Delta\lambda_i\bar{\rho}_i = \int_{\Delta\lambda_i} \rho(\lambda)d\lambda$$

where $\Delta\lambda_i$ is the spectral bandwidth of channel i, and $\rho(\lambda)$ is the laboratory reflectance at wavelength λ. Considerable spectral detail is lost by this band-averaging procedure. For green plants, the characteristic chlorophyll absorption appears as a sharp kink in the reflectance curve at 0.7 μm. The reflectance is dominated by a broad maximum centered near 1.0 μm and extending between 0.7 and 1.6 μm. The position of this reflectance maximum occurs in band 4 when the chlorophyll pigments are fresh and in band 5 (1.0 to 1.3 μm) when the pigments are degraded.

In bark and twiggy material, the reflectance takes on a characteristic rounded shape from the reduced role (or disappearance) of chlorophyll absorption. The maximum in the reflectance curve shifts to band 6 (centered at 1.65 μm) with disappearance of chlorophyll and reduction of water content.

D. Spectra of Rock Units and Vegetation Derived From Multispectral Scanner Data

The NS-001 multispectral scanner radiance data in channel i (DN_i) may be reduced to an equivalent Lambertian surface reflectance, $\bar{\rho}_i$, using the linear relationship derived in Appendix A,

$$DN_i = k_i'\bar{\rho}_i + k_i'' \qquad (i = 1,2,\ldots,p)$$

with constants k_i' and k_i'' evaluated from the NS-001 scanner data (Appendix B) and from field measurements.

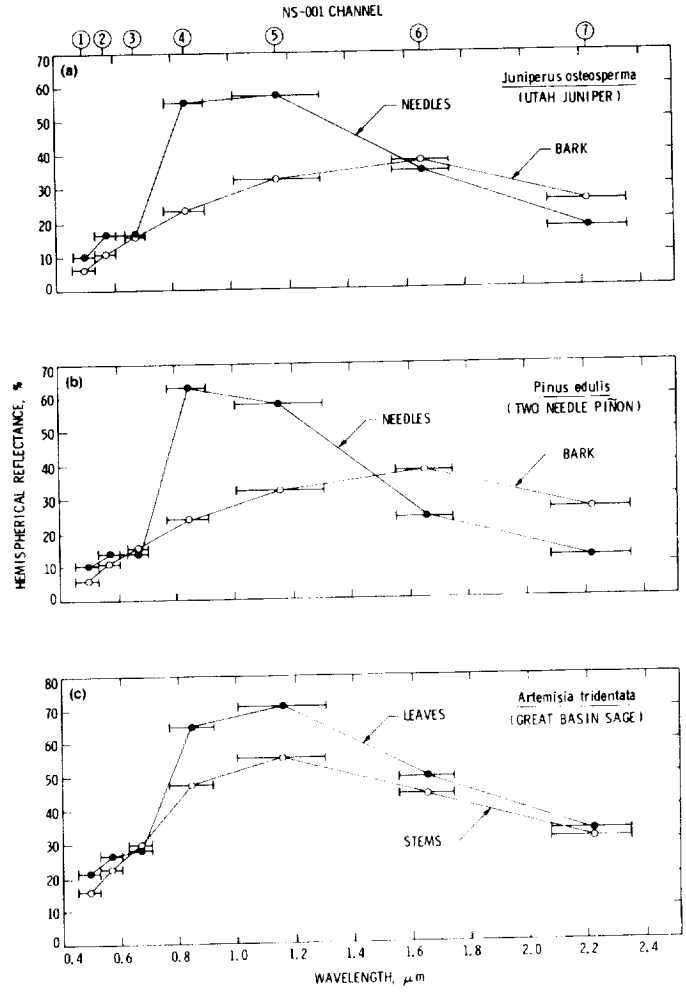

Figure 8-18. Broadband spectral reflectance for the NS-001 bands: (a) juniper; (b) piñon pine; (c) sage. Curves were determined from the laboratory data in Figure 8-17; horizontal bars refer to filter bandpasses of the aircraft instrument.

Some examples of the scanner spectral data are given in Figure 8-19. Locations of the image spectral sites are given in Table 8-5. Vertical bars on spectral points in all cases refer to $\pm 1\ \sigma$ scatter values in the observations derived from the image sampling statistics. The horizontal bars are actual bandwidths of the NS-001 scanner channels and have no statistical significance. To make connections with the field observations, ranges of reflectance values derived from the PFRS observations over the sample sites are plotted with each scanner spectrum. The scanner sample areas are always large when compared to the sites represented in the cumulative PFRS observations. For example, the area covered by 10 pixels is roughly 2250 m^2, whereas for 10 field spectra the area is 2000 cm^2. Thus, the scanner spectral points represent averages of possibly diverse cover types not resolved on the images, including soils, vegetation, and partially shadowed terrain. The macroscopic lighting conditions for the NS-001 data also generally differ from conditions during which PFRS data were taken. Despite the large differences in sampling, there is reasonably good agreement between the two data sets.

The presence of absorption bands may sometimes be delineated in the scanner spectra. Thus, the usually strong charge transfer band below 0.5 μm (channel 1) due to Fe^{+3} is well defined in image spectra 5-22, 5-7, 5-12, 5-15, 5-4, and 6-9 (Figure 8-19). Chlorophyll and carotenoids in plants also absorb strongly below about 0.75 μm (Figure 8-17). The distinction between ferric iron absorption and chlorophyll–carotenoid absorption may not always be clear. Absorptions due to vegetation (piñon–juniper) are probably present in image spectrum 5-12, where the reflectance rises abruptly between bands 3 and 4 and the slope of the image reflectance curve is concave upward. This agrees with the slope of the image spectra derived for juniper, sage, and piñon from laboratory data in Figure 8-18. A well-defined band near 0.85 μm (band 4), probably due to Fe^{+3}, is seen in the spectrum of Cutler red beds (6-9). Green strata of the Moss Back (5-1, 5-2) show a broad but well-defined absorption near 1.0 μm (bands 4 and 5).

A few examples of the image spectra of vegetation types and mixtures of rock outcrops and vegetation are given in Figure 8-20. In all cases, the vegetation types listed are taken from preliminary BLM Range Forage Assessment Surveys of the Lisbon Valley area (U.S. Bureau of Land Management, Moab, Utah, unpublished plant survey data). The dominant species present in each area are listed in relative order of abundance.

Characteristic features of most of these spectra are the (1) lack of any strong absorption assignable to chlorophyll in the plants present, and (2) similarity to the spectra of predominantly (senescent) unpigmented cellulose material (Figure 8-17). The interpretation is that the outcrops sampled were

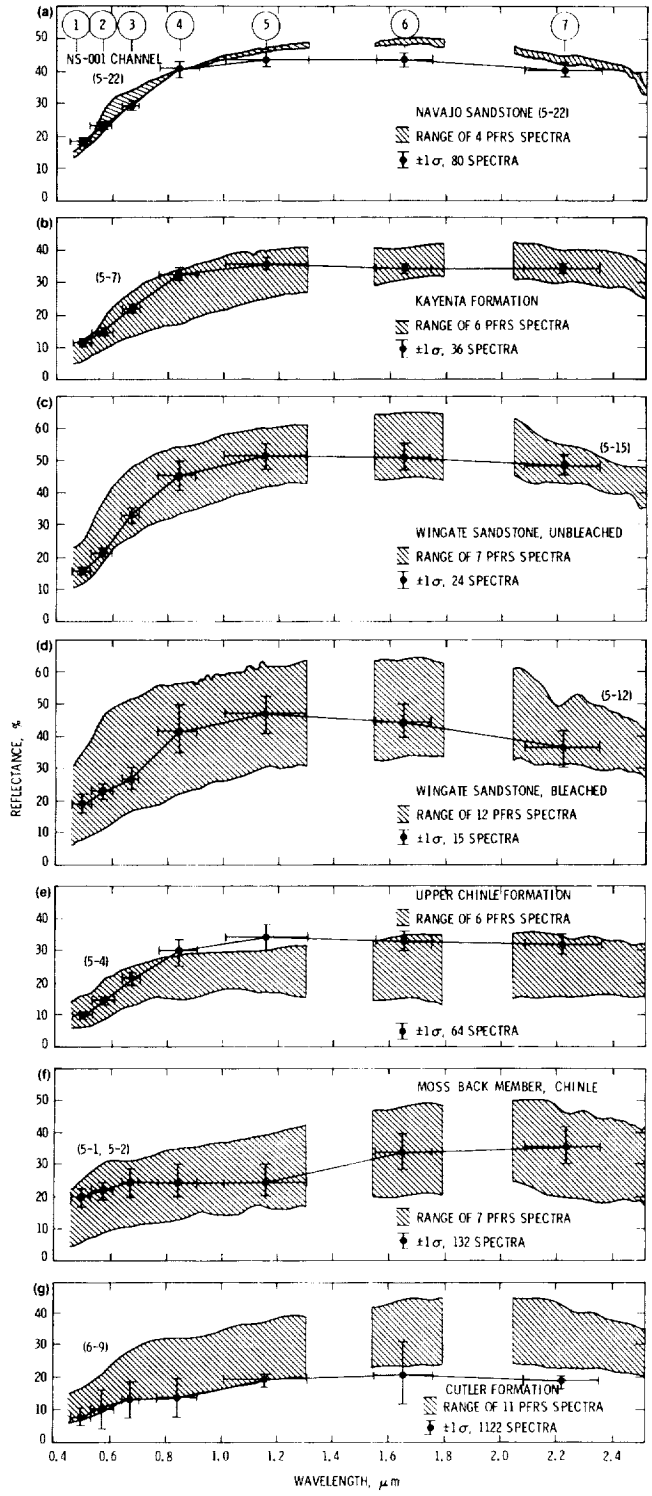

Figure 8-19. Comparison of scanner-derived NS-001 spectral reflectance curves with field spectral measurements obtained with the PFRS. Horizontal bars on the curves refer to filter bandpasses; vertical bars are $\pm 1\ \sigma$ standard deviation for the spectral sample size indicated; numbers in parentheses (5-22, etc.) refer to sample site locations given in Table 8-5.

Table 8-5. Locations of image spectral sites in NS-001 flight lines 5 and 6 at Lisbon Valley[a]

Flight Line and Site No.	Formation or Vegetation Type	Sample Coordinate		Number		
		Starting Line	Starting Sample	Lines	Samples	Pixels
5-1	Moss Back Member, Chinle Formation	1636	800	6	14	84
5-2	Moss Back Member, Chinle Formation	1387	690	6	8	48
5-4	Upper Chinle Formation, 25° slope	1423	630	8	8	64
5-6	Alluvium with sage/grass	1380	331	22	21	462
5-7	Kayenta Formation outcrop	1413	442	6	6	36
5-8	Kayenta Formation + piñon juniper	1413	453	11	17	187
5-10	Wingate Sandstone, bleached, + piñon juniper	1042	465	13	20	260
5-11	Wingate Sandstone, bleached, + piñon–juniper	937	435	8	19	152
5-12	Wingate Sandstone, bleached outcrop	793	361	3	5	15
5-13	Piñon–juniper on Dakota Sandstone	745	540	11	6	66
5-15	Wingate Sandstone, unbleached outcrop	1704	674	4	6	24
5-20	Wingate Sandstone, unbleached outcrop	1817	899	8	9	72
5-21	Wingate Sandstone, unbleached, + piñon juniper	1789	916	13	12	156
5-22	Navajo Sandstone outcrop	1803	537	10	8	80
5-23	Navajo Sandstone and grass	1785	509	5	9	45
6-9	Cutler Formation outcrop	1717	788	33	34	1122

[a]Sample positions may be located by referring to images in Figure C-1.

probably covered by dead grass or by shrubs or trees with sparse leaves and needles at the time of observation (August 28, 1979).

An interesting spectrum is that of piñon–juniper mixed tree cover on a substrate of Dakota Sandstone (5-13). Close examination of aerial photographs shows the tree cover to be continuous. Shadows are probably also present. No evidence of chlorophyll absorption can be seen in the spectrum, leading to the conclusion that the effect of the green parts (compare PFRS spectrum of juniper needles) is largely subordinate to the purely photometric effects produced by shadowing and/or reflectance from woody parts. Some contribution of ground reflectance may also be present.

Examination of the image-derived spectra for major rock units exposed at the Lisbon Valley site shows that these are characterized by reflectance differences $\Delta\bar{\rho}_i$ at all wavelengths roughly 10 percent or greater. In addition to a general difference in brightness (as measured by reflectance) of this magnitude or greater, individual absorption bands due to Fe^{+2} and Fe^{+3} may sometimes be recognized. These differences are generally 10 percent or less. Vegetation modifies the reflectance by introducing shadows, by contributions from dormant or dead surface litter, as well as by contributions from chlorophyll and water absorptions. However, the presence of chlorophyll absorption is subordinate and is seldom recognized in these data for this test site. The estimated noise level in the image data of $\Delta DN \leq 1$ (see Appendix B) suggests that reflectance differences $\Delta\bar{\rho}_i$ on the order of $1/k_i'$ should be observable. From Table B-1, $\Delta\bar{\rho}_i < 0.25$ percent.

VII. Remote Sensing Objectives, Models, and Approach

A. Introduction

Remote sensing methods, primarily aircraft scanner data, were used to map the distribution of cover types, to separate altered from unaltered rocks, and to relate the distribution of

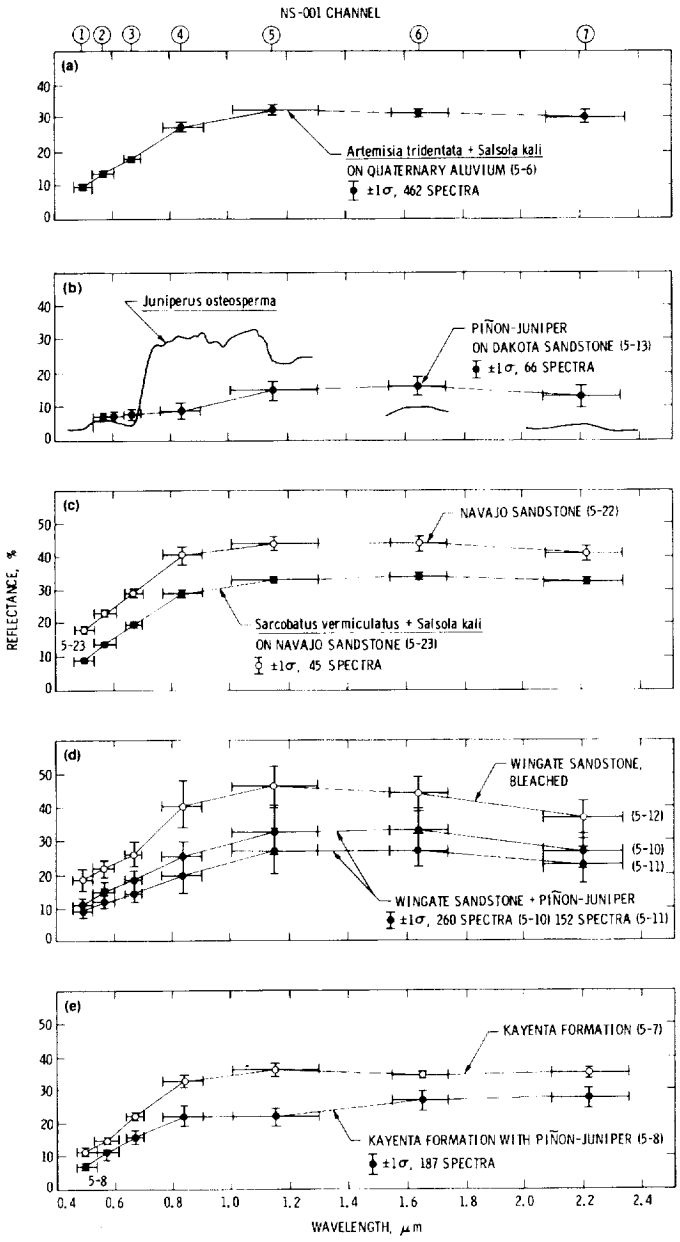

Figure 8-20. Image-derived reflectance curves for areas of vegetation and mixed vegetation and outcrops. Horizontal bars refer to filter bandpasses of the NS-001 scanner; vertical bars are ±1 σ standard deviation for the spectral sample size indicated; numbers in parentheses (5-12, etc.) refer to sample site locations given in Table 8-5. Curve for *Juniperus osteosperma* is a PFRS spectrum.

alteration on the surface to uranium mineralization in the subsurface. The radiance data can easily be used to map variations in surface cover and can be reduced to reflectance for interpretation in terms of ionic or molecular absorption bands present. Generally, however, aircraft scanners do not have sufficient spectral resolution for mineral or plant species identification based on characteristic absorption bands.

Photointerpretative methods based on scanner observations are excellent for mapping variations in iron oxidation and are generally superior to what can be accomplished by field investigation alone. The scanner data include the spectral region to 2.3 μm, which may provide additional absorption features useful for rock-type or vegetation discrimination.

B. Connections Among Genetic, Exploration, and Remote Sensing Models

The stratigraphic, structural, and mineralogical conditions related to distribution of ore in the Big Indian District were summarized by Wood (1968) as described previously. To describe the genesis of these deposits, Wood invoked the so-called multiple accretion hypothesis of Gruner (1956), which has become the basis of explanation for Wyoming-type roll-front sandstone deposits. In this hypothesis, uranium is assumed to be leached from source rocks and carried as a uranyl (+6) carbonate species in groundwater to sites where favorable reducing conditions of deposition are encountered. Deposition may be accomplished by interaction with organic material entrained in the section, or by reductants introduced from the outside, such as petroleum or petroleum-related H_2S supplied by the through-flowing medium. Ore emplacement is usually accompanied by oxidation of pyrite upstream from the accumulations and by concentration of pyrite in the ore zone itself.

These ideas are applied more loosely to the Lisbon Valley (Big Indian District) deposits. Thus, the uranium source rocks are assumed to be red beds of the upper Chinle section, which provided uranium to groundwaters from a tuffaceous component. Accumulations of organic material occupying overbank deposits in the lower Chinle (Moss Back) section acted as reductant sources for deposition. The accumulations were governed in distribution by the geometry of Moss Back streams, which in turn appear related to the orientation of the sugar sandstone bodies of the Cutler section. These sandstones abut the angular unconformity at the base of the Moss Back. No bodies of altered rock corresponding to the alteration tongues of roll deposits have been identified for the Lisbon Valley deposits, either in the section or cropping out at the surface.

The exploration strategy for Big Indian deposits has been to seek out extensions of the Moss Back–Cutler channel system on a piecemeal basis, using surface drilling and subsurface mining methods. Exploration guides are thus largely empirical. Individual operators have employed their own proprietary strategies.

With respect to surface guides to mineralization, Loring (1958) and Gabelman (1970) noted that the Wingate Sandstone was bleached of its usual iron-oxide pigmentation in outcrops throughout the Big Indian Mining District. Loring and Gabelman describe in a general way the proximity of bleached rock

above ore mineralization in the Moss Back Member and Cutler Formation beneath. The bleached facies everywhere are separated stratigraphically from the ore-bearing horizons by 300 ft or so of unaltered Chinle red beds, with no exposed or remnant connection between them. Gabelman and Boyer (1958) have argued that examples such as this one represent transgressive alteration, reportedly common to many mineral districts in which the mineralizing agents emplace ore in one stratigraphic horizon, pass through other strata without apparent effect, only to alter selectively stratigraphically higher rocks.

Bleached rock by such processes has had its supposed original iron-oxide pigment removed or possibly redistributed as hydrated iron-oxide phases.

C. Approach

The aircraft image data, together with high resolution (<1 m) ancillary color aerial photography, form the basis for lithologic, stratigraphic, and structural studies of the Lisbon Valley test site. The existing genetic models for the uranium deposits have no direct consequences detectable from the images. The separation of bleached from pigmented facies, together with the mapping of each, is however possible from the scanner image data. Thus, the distribution of bleached strata was mapped and the empirical correlation already noted between altered sandstone and mineralization distribution exploited.

For detailed geologic analysis, images were analyzed and interpreted by use of overlays. Color boundaries were traced from the images without reference to other data sources such as maps or photographs except where noted. The image interpretations were then compared with geologic, photogeologic, soil, and vegetation maps to help identify the color units separated. These comparisons have led to recognition of units on the image data not previously observed in the present photogeologic or earlier USGS geologic maps of the study area.

VIII. Interpretation of Multispectral Scanner Data at Lisbon Valley

A. Introduction

The airborne Bendix 24-channel multispectral scanner and the 8-channel NS-001 Thematic Mapper Simulator data were used to study the geology of Lisbon Anticline and to map the distribution of bleached and unbleached Wingate Sandstone throughout the length of exposure of this unit on the southwestern limb. The Bendix 24-channel data were acquired in June 1976, before formal inception of the Geosat Project. As shown in Figure 8-2, the area studied lies along a north–south track and covers the northern exposure of Wingate outcrop and stratigraphically adjacent rocks in the Big Indian District. Ten channels of data lying between 0.45 and 2.35 μm are sufficiently noise free to be useful in these analyses (Table 8-4). The image has a spatial resolution of approximately 7 m and constitutes the best scanner data set available for study of detailed stratigraphic relations. Flight parameters and solar position data for this data set are given in Table 8-6. The NS-001 data have seven channels between 0.45 and 2.35 μm plus a thermal channel in the interval 10.4–12.5 μm (Table 8-4). The images consist of three parallel overlapping flight lines covering the entire Lisbon Anticline plus surrounding areas to the northeast and southwest. Flight data and position of the sun for the NS-001 observations are also given in Table 8-6. These data are all essentially noise free and have a nominal ground resolution of approximately 15 m. A good stereoscopic effect occurs in the overlapping image strips. The image results are reproducible; that is, color relations can be preserved from flight line to flight line by detailed adjustments of the contrast (cosmetic) stretches applied. Apart from a residual geometric distortion, this has permitted a manual mosaicking of the three flight lines together to form a single picture for the entire area. Directional effects present in the data for regions of overlap have been ignored in preparation of the mosaic. For the most part these effects, which arise from differences in illumination and viewing geometry between flight lines as well as possible directional properties of the surface reflectance, are small because the sun is in the south and the flight lines are north–south.

The images used for interpretation consist of principal component (PC), canonical transformation, and color ratio composite (CRC) renditions. None of the radiance data have been reduced to "equivalent ground reflectance"; i.e., they are referred to as uncalibrated. As shown in Appendix A, calibration amounts to application of a specialized linear transformation of the radiances.[1] This linear transformation is always superseded by other linear rescaling and cosmetic stretching transformations required for computer processing and data display. It is always possible to achieve the same result without calibration by adjusting the cosmetic part. The cosmetic transformation represents an adjustment to improve visual appearance of the image data; the calibration step for purposes of image display is thus usually superseded by other image transformations.

One basis for first-order evaluation of the image data is the comparison with published geologic maps. The following questions are examined: (1) To what extent do image boundaries delineated on the images recover the existing geologic units and structure? (2) Where are additional geologic relations such

[1] Digital number (DN) is representative of a voltage so the Lambertian (nondirectional) reflectance in the calibration equation is interpreted as a proportionality (nondimensional) constant between radiance and voltage, with the appropriate units for conversion contained in an additional multiplicative factor.

as alteration or rock types provided? (3) Are any relations provided that are not observed in the aerial photographs?

The distribution of bleached Wingate facies had not heretofore been mapped anywhere in Lisbon Anticline. To fill this gap in the existing geologic mapping, stereoscopic color aerial photographs were used to map in detail the surface distribution of bleached rocks. The spatial resolution of these photographs is extremely good (<1 m), and the color and stereoscopic coverage allowed important stratigraphic relations between bleached and unbleached rock to be determined. These photogeologic maps provided a basis for understanding all the color relations in the highest resolution images and, in addition, provided other mappable units not recoverable in the images. The color aerial photographs of Lisbon Anticline were indispensable in deciphering geologic relations depicted in the images; these photographs were used extensively, together with the published geologic maps, to support the interpretations presented.

All images and photographs depict surface effects, which relate to rock outcrops; vegetation cover such as trees, shrubs, grasses, and lichens; shadowing due to slopes and vegetation; soils; eolian materials; and cultural disturbances such as drill roads and pads, mine dumps, and areas cleared of tree cover. In conventional aerial photographs at high resolution, the distinction of many of these is readily made, largely because of familiar "textural" appearance. For example, shadows always appear darker than sunlit areas. In areas of sparse tree cover, individual trees may be separable as dark spots against a lighter-colored background. Roads are obvious because they represent characteristic disturbances of the vegetation, topsoil, or weathered covering. In images, however, the familiar textural information is almost always absent because of poorer spatial resolution, and the familiar color and brightness relationships are translated to a new color system that is dependent on detailed transformations in the image processing. Thus, shadows may appear in any color depending on the image DN scaling relations. Partially shadowed areas and terrain with vegetation appear in still other ways. The color representing a rock unit in an image may also vary with solar illumination. An additional difficulty in using image data alone may be the lack of stereoscopic coverage; stereoscopic capability is crucial in sorting out stratigraphic and structural relationships. The principal value of the image data is the discrimination of correlative rock units together with the separation of various cover types. Image data in these studies have not generally contributed geologic data that are otherwise not available from color aerial photographs. To interpret most image units present, it has been necessary to refer to the photographs.

B. Geologic Relations From NS-001 Data

1. PC images. Figure 8-21 is a mosaic of three PC images of the Lisbon Valley area prepared using seven bands (0.45–2.35 μm) of the NS-001 data. In this rendition the second (V2 = blue), third (V3 = red), and fourth (V4 = green) components have been employed. (Figure 8-22 is an index map of the image interpretation and photogeologic mapping for the area.) The covariance matrix upon which the transform for all three lines is based was prepared by sampling the middle (line 6) of the three flight lines comprising the mosaic (transform I of Appendix C). Initially three separate images were prepared. The transforms for each were obtained from analysis of the convariance matrices peculiar to each flight line. A judgment was then made of which transform provided the best color separations of bleached and unbleached Wingate facies together with the best overall rock group separations.

Analysis of the "physical" content of these components revealed a large contribution from vegetation in the covariance

Table 8-6. Aircraft flight parameters and solar position data for images acquired at Lisbon Valley

Date	Start GMT Stop GMT	Start Latitude Stop Latitude	Start Longitude Stop Longitude	Altitude Above Terrain, ft	Apparent Solar Right Ascension	Solar Declination	Solar Zenith Angle (Mean Position)	Solar Azimuth (Mean Position)
June 15, 1976[a]	21h 18m 20s 21h 21m 25s	38° 18.3′ N 38° 04.1′ N	109° 15.8′ W 109° 16.6′ W	9,800	5h 38m	23° 20′	32° 24′	34° W
August 28, 1979[b]								
Line 5	17h 12m 45s 17h 16m 05s	38° 0.42′ N 38° 19.0′ N	109° 16.5′ W 109° 16.5′ W	16,300	20h 27m	10° 15′	40° 58′	33.4° E
Line 6	17h 21m 05s 17h 24m 50s	38° 19.0′ N 38° 02.9′ N	109° 13.0′ W 109° 12.9′ W	14,700	20h 27m	10° 15′	40° 58′	33.4° E
Line 7	17h 05m 30s 17h 09m 00s	38° 17.7′ N 38° 02.8′ N	109° 09.5′ W 109° 09.4′ W	14,700	20h 27m	10° 15′	40° 58′	33.4° E

[a]Bendix 24-channel scanner
[b]NS-001 Thematic Mapper Simulator

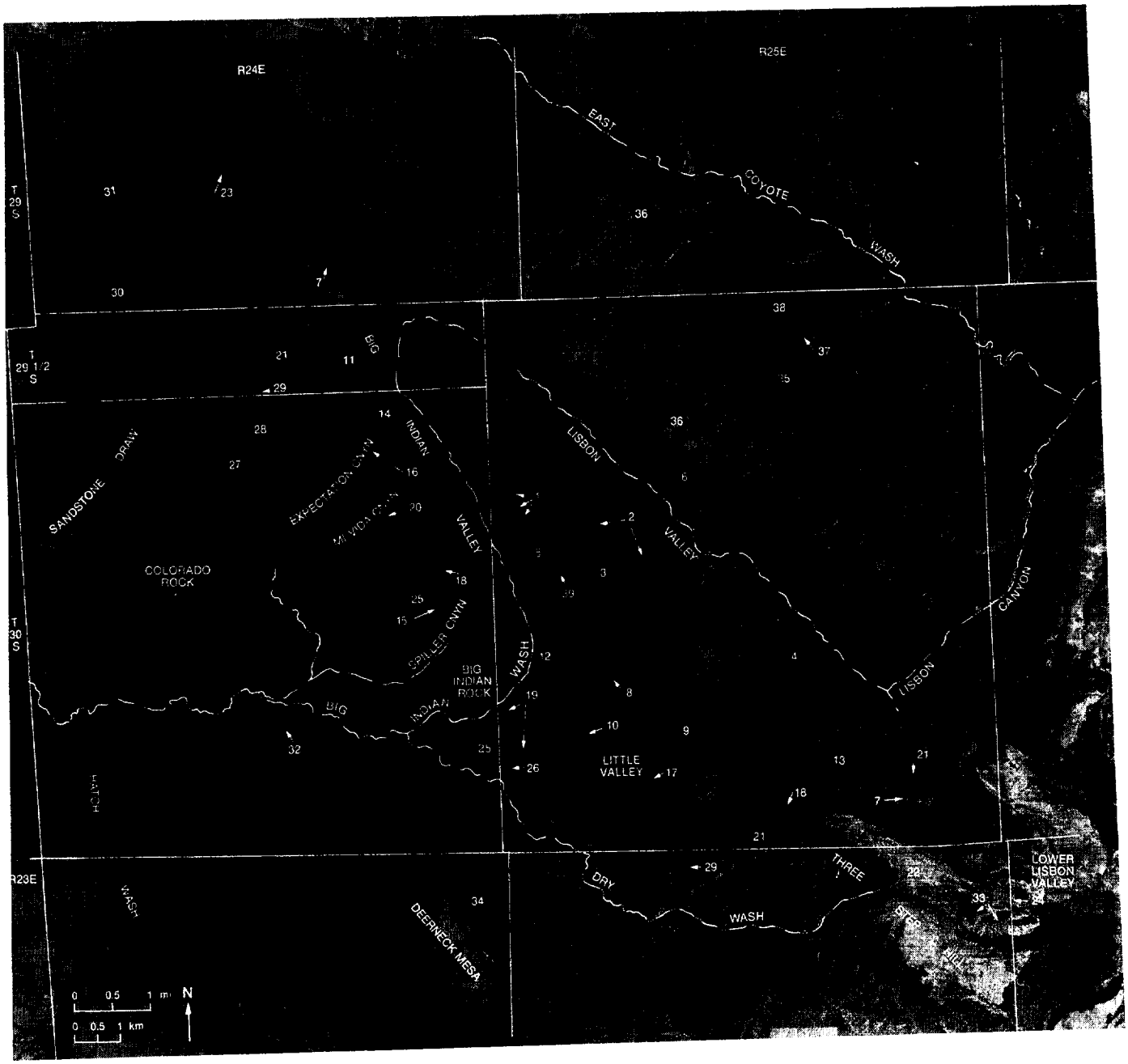

Figure 8-21. PC image mosaic of Lisbon Valley area prepared using transform I from seven channels of NS-001 data (Mission 407, August 28, 1979). V2 = blue, V3 = red, V4 = green. Numbers refer to site locations described in the text.

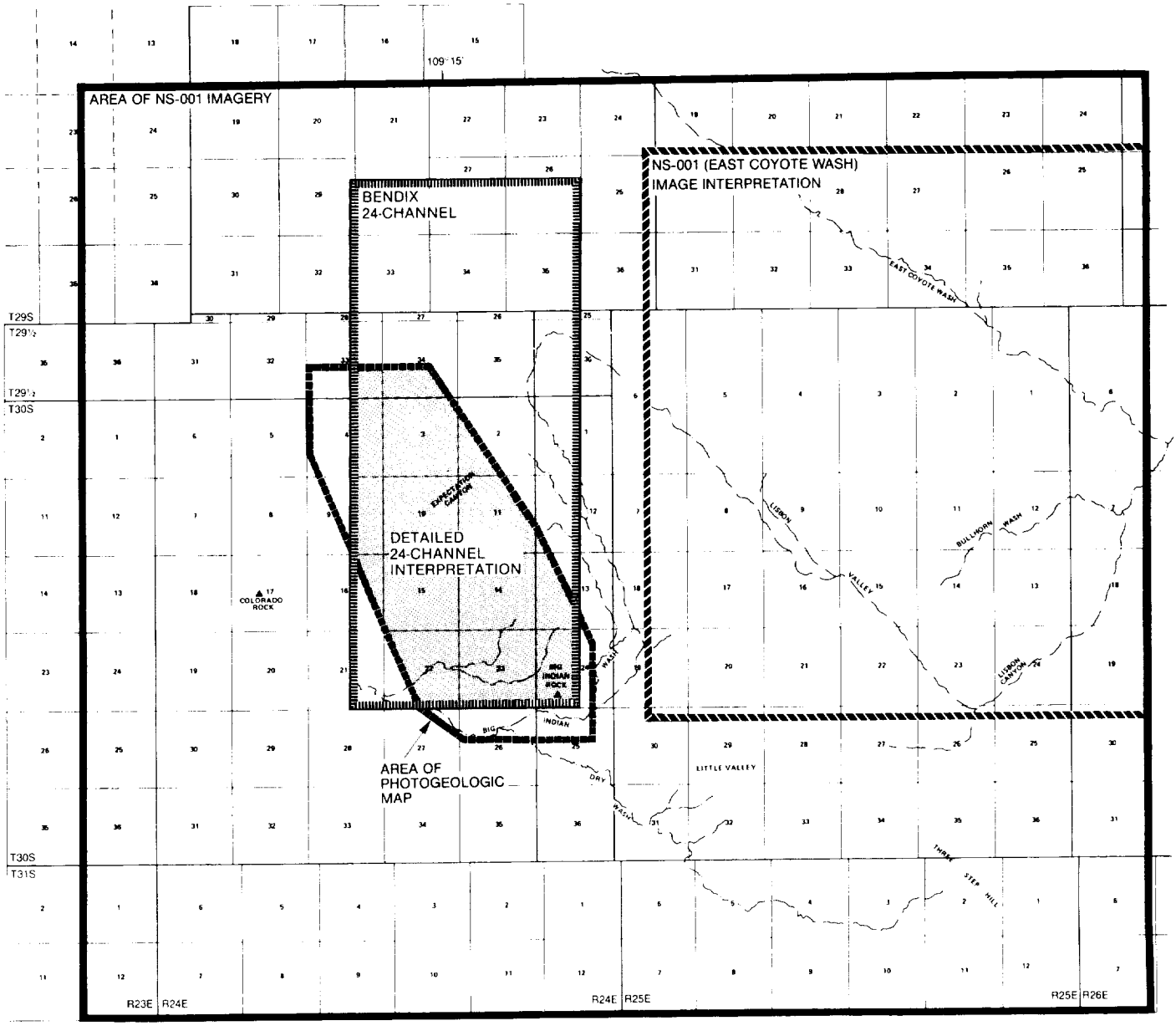

Figure 8-22. Index map of image interpretation and photogeologic mapping for the Lisbon Valley area

matrix for all lines. This is thought to result from extensive sampling of heavily vegetated Quaternary sediments both north and south of the anticline, but also from 10 to 70 percent vegetation cover throughout the anticline itself. In an attempt to improve separations resulting (mainly for Wingate rocks) at this step, all three lines were resampled over areas restricted largely to Wingate outcrops plus stratigraphically adjacent rocks. Images were prepared from transforms based upon the average restricted area covariance matrix (transform II, Appendix C) using various color combinations and combinations of components (V1, V2, V3) or (V2, V3, V4). None of these additional procedures produced results superior to the original versions. The final choice was a matter of subjective preference. Therefore, the PC images were analyzed according to the line 6 transform (transform I); however, most of the relations to be described could have been obtained using other versions as well. Two additional versions of the PC data using transform II are included in Appendix F for comparison.

Failure to secure improvement in the separations by restricted sampling is at first a surprising result. This circumstance is discussed in Appendix E. A summary of the argument follows.

The Mahalanobis-like (Euclidean) distance-squared criterion, representing separation in radiance space of spectral groups, depends multiplicatively upon reflectance differences, transform factors, and scaling factors. Real increases in the distance of separation can be achieved by purely dilitational manipulations of the space through the scaling factors, but the scatter as well as the separation of group means increase by this process. Restricting the sampling area for the transform in question reduces the scatter about the mean values, but does not increase the separation of group means. The inherent separation depends upon differences in reflectance between the groups. However, subsampling may be thought of as beneficial to the extent that resolution of clusters is improved. Geometrically, adjustment of the scaling factors is the basis of decorrelation enhancement when applied to PC data. This method is usually discussed as one for simply expanding the scatter by a nonlinear Gaussian transformation to fill dynamic range (Soha and Schwartz, 1978) plus an inverse transformation to the original color space to preserve color relationships. Since rescaling (stretching) of the PC data (but not the inverse transformation) is usually required for display, the data space is routinely expanded to some extent in the fashion described. The major benefits of the decorrelation treatment are thus present in the PC transformation method.

2. Color relations in the PC data. The physical meaning of the PCs has always been uncertain because general rules do not exist for their interpretation. Mathematically, the successive components can be thought of as empirical basis functions of an orthogonal series representation of the scene-averaged spectral radiance. The separate terms of this expansion may have physical meaning in the same sense as would, say, the separate terms of a Fourier representation of complex motion of a vibrating string. This is an application of the Karhunen-Loeve expansion and is described by Davenport and Root (1958) and by Wiersma and Landgrebe (1980). On a statistical basis each principal axis is oriented in successive directions of decreasing scatter in the data swarm. The first component is often thought to represent albedo, thus describing in an average way differences in brightness between surface cover types (see Appendix E for a graphical proof of this). Other components may possibly be given an approximate physical meaning by comparison with other pure end-member data sets. Thus, PCs 1, 2, and 3 of the Lisbon Valley example have some contributions from vegetation, nearly uniformly band for band. This is apparent when the eigenvector diagram for the Lisbon Valley NS-001 image is compared with the eigenvector diagram for a September (green foliage time) NS-001 image of Lost River, West Virginia (see Appendix C). The fourth PCs differ between the two data sets, and no simple analysis can be offered for them.

Table 8-7 delineates the correspondence between geologic unit (by color) or cover type (principally vegetation) and image color (Figure 8-21) for some important members present. These are qualitative descriptions, but approximate numerical values can be assigned to the image colors by referring to three-component (red, blue, green) color-additive diagrams (see Section 12, Figure 12-32).

3. Stratigraphic relations

a. Pennsylvanian section. Outcrops of the Pennsylvanian Hermosa Formation near the crest of Lisbon Anticline (1)[2] in Lisbon Valley are olive to dark brown and black in appearance. The arcuate belt of Upper Hermosa limestones forms a dip slope covered by piñon and juniper. The bedding of limestone and sandstone units in the upper part is faintly expressed as alternating black, green, and yellow banding on the images.

Sharp notch-like canyons following cross fractures are accentuated by colors representing shadowing in the canyon bottoms. Except in the northern part of Hermosa exposures, the contact between upper and lower units of the formation cannot be delineated. In the northern part, outcrops of the lower unit are covered by alluvium; in the southern part, the alluvial cover is less extensive. Where exposed (2), the lower unit displays thick SW-dipping beds of limestone. The NE-facing shadowed and tree-covered riser slopes of these strata appear as a red-and-green mottled strip in the images. Extensive areas of chained piñon–juniper forest are represented by yellow to yellow–green colors (3), with sharp boundaries between chained and unchained areas. Because of the rough topography, chaining was not continued to the southeast. Here the color pattern represents spotty, tree-covered limestone outcrops surrounded by alluvial cover (4). Outcrops of tree-covered Upper Hermosa rocks (5) are difficult to distinguish from tree-covered outcrops of Burro Canyon and Dakota sediments (6) exposed in a narrow belt across Lisbon Valley Fault.

b. Permian section. The Permian Cutler Formation is exposed as an arcuate belt terminated at both northwest and southwest ends by the Lisbon Valley Fault (7). The red to magenta image colors of this unit contrast sharply with Pennsylvanian rock represented as olive shades. This color difference delineates a well-defined contact between the two units (8).

Alternating red, maroon, magenta, green, and black units of the Cutler section give the unit a distinctive laminated appearance (9). The stratification depicted is in part reinforced by shadowing from the topography. The sugar sands appear as dark olive-green to black triangular or chevron-shaped facets on ridges extending across the outcrop (10). Cutler rocks are covered by eolian deposits (yellow and red areas) in the northwestern portion of the outcrop (11), by Quaternary sediments

[2]Numbers in parentheses indicate site locations in Figure 8-21.

Table 8-7. Color key for the PC image (Figure 8-21)

Geologic Unit or Cover Type	Image Color	Relative PC Values[a]
Vegetation—green grasses or shrubs with high leaf density and strong green pigmentation. Appear deep ruby-red on false-color IR photographs	Deep, moderate, or light blue. Colors correlate with deep red to sparse red on color IR photographs	Deep blue = high V2; low to zero V3, V4
		Light blue = high V2; low V3; high V4
Vegetation—heavy cover of shrubs and (dormant?) grasses	Moderate red—brown	Low V2; moderate V3; moderate V4
Vegetation—dense piñon—juniper cover	Red orange—brown	Low V2; moderate to high V3; low to moderate V4
Deep shadows	Red	Dominant V3; low to zero V2, V4
Highly reflecting buff to white outcrops (saturated, DN ~255)	Black	Saturated (V2, V3, V4) = (0,0,0)
Light gray—green outcrops with sparse vegetation	Olive green or green to brownish black	Green = low to zero V2; low V3; high V4
		Olive green = low V2; low to moderate V3; moderate to high V4
		Brownish black = low V2; low V3; low V4
White to buff outcrops with sparse to moderate tree cover	Light olive	Low V2; low V3; moderate V4
Red- and salmon-colored units including maroon and light strata, mostly with sparse tree and/or shrub cover	Magenta to red	Low to moderate V2; high V3; low V4
Chained (disturbed) piñon—juniper cover over red, purple, and buff units; contains abundant dead tree material plus secondary growth of shrub (sage) and dead grass	Yellow to yellow—orange	Low V2; moderate to high V3; moderate to high V4
Red to brown soils with sparse green vegetation (alluvial flat near Cub-Costanza Mine, NE¼, Sec. 35, T30S, R25E)	Magenta	Moderate to high V2; high V3; low V4

[a] V2—blue
V3—red
V4—green

with vegetation near the mouth of Big Indian Wash (12), along other canyons to the southeast, and over a rectangular area of cultivated alluvium near the termination of this unit by Lisbon Valley Fault further to the east (13). Piñon–juniper cover has been removed in many areas. These areas are generally depicted as yellow or yellow–orange in the images (14).

The Permian rocks are separated by an angular unconformity from the Moss Back sediments above. This relationship can be seen along most of the contact but most prominently at (15) near Big Indian Rock and at Spiller Canyon. Here and elsewhere differences in dip between the two formations are approximately 5°. The trace of the unconformity at the surface is defined, where visible, by the truncation of laminated Cutler strata at the Moss Back–Cutler contact.

c. Triassic strata. The lowest unit in the Triassic section is represented by the Moss Back Member of the Chinle Formation. This is the most important mineralized horizon in Lisbon Valley Anticline. The Moss Back Member is approximately 50 ft thick and forms a resistant cliff above the Cutler sediments. The projected area on the image is consequently small (several pixels). Best exposures, most extensively disturbed by mining activity, occur in canyon bottoms at Expectation, Mi Vida, and Spiller (16) and on the crests of ridges at Little Valley (17). The triangular-shaped outcrops are uniformly dark

olive green to black in all cases. Between the exposures this member is visible as a narrow, continuous dark olive green to black band (18).

Stratigraphically above the Moss Back bench and below the cliff-forming Wingate Sandstone lies the Upper Chinle Formation. The unit forms steep rubbly slopes with little or no visible intraformational stratification, although the unit is thinly bedded. Prominent exposures are found on the slopes of Big Indian Wash (19) and in canyons to the south where the unit is magenta in hue. North-facing exposures below the Wingate Sandstone are often in shadow and consequently display saturated red hues in these images (20). None of the exposures studied show evidences of internal bedding.

The massively bedded cliff-forming Wingate Sandstone dips southwest and south 7° to 8° with good outcrops everywhere on the southwest flank of Lisbon Valley Anticline except below Three Step Hill in the southern part. Here the formation is covered by the Kayenta Formation and is obscured by a heavy tree cover which has been partly removed by chaining.

The Wingate displays a bleached (buff to white in outcrop) and an unbleached (salmon to red in outcrop) facies. Bleached facies in Figure 8-21 appear as light green to dark olive green and black (21), but yellow where piñon–juniper tree cover has been removed (22). Bleached rocks are confined to the northern and southern portions of the anticline. Bleached strata are truncated at both ends (23) and displaced by the Lisbon Valley Fault or branches of this fault (24). Unbleached Wingate sediments occupy the middle portion of the exposed belt (25). These strata are generally portrayed in the images as deep red to brown-red and black on bare outcrops. This description of the "rock equivalent" units present is actually oversimplified. The unit in its upper part can be divided into several mappable units. Only two of these units, however, can be recovered and then only in part using scanner data. These relations are described below.

Tree cover is generally more extensive over bleached portions of the Wingate, locally reaching 50 percent or greater. Vegetation cover makes a significant contribution to the spectral reflectance. The image analysis problems of using spectral reflectance methods to estimate tree cover and of reducing or eliminating vegetation contributions to the reflectance are discussed in Paragraph VIII.D.

d. Jurassic strata. The Kayenta Formation is composed of a series of red, purple, and maroon sandstones conformably overlying the Wingate section. Locally the Kayenta red beds and bleached Wingate facies are interbedded, but outcrops of this composite unit are not separable in the images. The formation supports a uniform (20 to 30 percent) cover of piñon and juniper over all outcrops in the region studied. Two previously unmapped facies of the formation are discernible in the image data. These are confirmed by study of aerial photographs: the stratigraphically lowest unit is deep red in color and is exposed mainly near margins of Kayenta outcrop (27); the stratigraphically highest unit is represented by yellow, orange, and green mottled areas mainly occupying the center of Kayenta outcrops (28). The Kayenta Formation is easily distinguished on the basis of color from pervasively bleached rocks of the Wingate Sandstone in this PC rendition, and isolated erosional remnants of the Kayenta, some previously unmapped, can be found scattered over the Wingate outcrops (29). The Kayenta Formation and *unbleached* facies of the Wingate Sandstone are virtually inseparable in these images, but the actual contact is also mostly covered by alluvium in the interval.

In the southern part of the anticline, north of Three Step Hill, the stratigraphic relations among Wingate, Kayenta, and Navajo rocks are complex. Three sets of images plus color-infrared (CIR) aerial photographs, however, did not satisfactorily resolve all of the stratigraphic problems recognized.

The Navajo Sandstone in the field is a white to buff cross-bedded unit forming low cliffs and mesas. Locally thin buff limestones are present. The extensive outcrops of this unit west of the northern tip of the anticline (30) are displayed as green, olive green, and black and contrast sharply with the intense red, red-orange, and yellow-orange hues of the adjacent Kayenta Formation and Quaternary alluvium (31).

In the area of Big Indian Wash, the Navajo Sandstone is poorly exposed. Outcrops are few and the formation is covered extensively by soils or Quaternary sediments with moderate to heavy grass and shrub cover. Tree cover is sparse and restricted to the edges of soil cover. Contacts with the underlying Kayenta Formation in this area are covered or indistinct.

Low cliffs and outcrops of Navajo Sandstone appear green to black in the images (32). Black outcrops represent areas where the image representation, but not the raw radiance, is saturated (scaled to DN values $\geq$255). Since these outcrops occur mostly on south-facing slopes or slopes opposite the sun, they probably arise from a backscatter (a specular-like) component in the surface reflectance.

In the southern part of the anticline (Three Step Hill), the Navajo Sandstone and bleached facies of the Wingate Sandstone are nearly juxtaposed by the dramatic thinning (~50 ft thick) of intervening Kayenta strata near the crest of the anticline. The separation of these light-colored units in the image data is often difficult. For example, bare outcrops of Navajo Sandstone are black (33) and are surrounded by yellow- and green-mottled areas representing chained and partly tree-covered portions of the unit, respectively. Thus, in these few

cases the Wingate (usually olive green) and the Navajo (usually black) Sandstones are separable primarily on the basis of saturated image color. On the other hand, the distinction of Navajo and Wingate Sandstones (33 and 21) in this area can easily be made from aerial photographs on the basis of the joint patterns present in each. The average spacing of Wingate joints is 100 to 150 ft, with a strike of N 70° W (21). The average spacing of joints in the Navajo is approximately 50 ft, and the strike varies from N 70° W to N 90° W (33). The distinction of joints in the Wingate and Navajo in this area on the images is unfavorable because they closely parallel the direction of image scan lines.

Additional Jurassic strata (Carmel, Entrada, Summerville, and Morrison) crop out in the southern, southwestern, and western portions of the image area near Deerneck Mesa (34). These formations were not important in the investigation of stratigraphic or structural problems in Lisbon Anticline. The images of these outcrops reveal relationships similar to those already described.

e. Cretaceous strata. Predominantly Cretaceous rocks crop out northeast of Lisbon Valley Fault throughout the image area along the axis of Lisbon Canyon Anticline and in the East Coyote Wash Syncline (35). Outcrops are poor, and many of the shallow-dipping or flat-lying strata are largely capped by alluvium (Figure 8-10). The alluvial cover supports an extensive growth of grass and shrubs and, on the sandy or rocky outcrops, dense stands of piñon and juniper. The piñon–juniper cover has been removed over extensive areas (36). Despite these conditions, the image data provide useful information on distribution of rock types, cover types, and structure.

Figure 8-23 is a CRC image covering the northern portion of line 7 of the NS-001 Lisbon Valley data. The color assignments are band-ratios 2/3 = blue, 2/4 = green, 4/5 = red. These band ratios generally distinguish vegetation and rock types in the area of interest. Vegetation-free outcrops of strongly red-colored beds such as the Cutler Formation appear in red or red–brown (high ratio 6/7); gray and green (light colored) outcrops as yellow (low 2/3, high 2/4, high 4/5). Shrub and grass-covered areas are blue–green and green (high 2/3, moderate to high 2/4). Shadowed or heavily tree-covered terrain is magenta (high 2/3; high 4/5). Areas of chained piñon–juniper cover are dark green, sometimes banded due to bulldozer tracks. Examples of these disturbed areas are outlined in Figure 8-24.

The mappable units in the Cretaceous section distinguished in Figure 8-24 are described in Table 8-8. A stratigraphic column including the Dakota and Burro Canyon units is given in Figure 8-25. This section was compiled from descriptions provided by Carter (1956) based on field relations in the Mt. Peale No. 1 Quadrangle in the northern and northeastern portions of the image (Figure 8-23) and map (Figure 8-11) areas. Correlations between these two columns are tentatively made as follows: units 4, 3, and 2 of Figure 8-24 correspond to the middle unit of the Burro Canyon Formation of Figure 8-25 and are not readily distinguishable in Carter's description. Unit 1 corresponds to the lower unit described by Carter (1956) in the Burro Canyon section.

The Dakota–Burro Canyon contact is difficult to identify on the images. On the basis of the image stratigraphic column, the contact is placed at the top of unit 4. In Figure 8-21, unit 4 of Burro Canyon is distinctly shown along East Coyote Wash and in tributary canyons as an olive-green unit (37) that contrasts sharply with red–brown rocks of the Dakota Sandstone above (38). Areas of Burro Canyon outcrops in the synclinal axis are greatly enlarged. On the other hand, if the basal cliff-forming sandstone unit of the Dakota is missing (described by Carter, 1956, to be present), then the middle unit of the Dakota, consisting of dark shales, may rest on the upper and middle units of the Burro Canyon, which contain the quartzite and green shale. Unit 2 of the Burro Canyon section is extensively exposed in the middle portion of the image area and pinches out to the northwest.

The structure of East Coyote Wash Syncline is nicely portrayed by the symmetrical distribution of rock units about its axis. The adjacent Lisbon Canyon anticlinal structure cannot be distinguished. The axes shown for both of these folds were taken from the geologic mapping.

Several of the minor normal fault structures depicted on the geologic map of Weir et al. (1961) can be recognized. These are primarily displayed by truncated rock units depicted by abrupt changes in color.

4. Geomorphic and color representation of structure

a. Folding. The broad anticlinal doming in Lisbon Valley Anticline is displayed in the image data (Figure 8-21) by the arcuate erosional pattern and by the successive rock unit coloration. While a sense of the dips can be obtained from outcrop patterns in valleys from a single image, the relative values can be established by stereoscopic examination of the image where these images overlap. Location of fold axes has not been possible here except, as noted, approximately in the East Coyote Wash structure. Such determination was attempted using stereoscopic image pairs along the axis of Lisbon Valley Anticline, but the lack of well-defined bedding in the Lower Hermosa units and poor image resolution made this impossible.

b. Faulting. Much of the trace of Lisbon Valley Fault, the major normal fault structure breaching this anticline, is covered by alluvium. The general position of the fault can be determined from the image data (Figures 8-21 and 8-24) by the truncation

Table 8-8. Description of image stratigraphic units for East Coyote Wash Syncline and Lisbon Canyon Anticline

Stratigraphic Unit	Map Symbol	Description
Quaternary Alluvium	Q	Magenta and blue, mainly in stream courses.
Mancos Shale		Small outcrops. Not distinguished in images.
Dakota Sandstone/ Quaternary Alluvium	Kd + Q	Generally green. On mesas underlain by Quaternary sediments or soils. These are green with orange–brown. These areas are dominantly grass and shrub covered. On slopes, unit is light blue, some magenta. Rocky, low tree cover.
Burro Canyon Formation	Kbc	
	Kbc+Q	Undifferentiated units with alluvial and soil cover.
	Kbc_4 (unit 4)	Mostly green, but with some yellow and some blue mottling. Principally exposed along stream bottoms and along axis of syncline (East Coyote Wash). Generally lower tree density than unit 1.
	Kbc_3 (unit 3)	Red–brown color. Patchy distribution almost always associated with unit 2. Represents reddish, heavily tree-covered rock type mostly on crests of ridges. Interpreted to belong to Burro Canyon Formation, but actual stratigraphic assignment uncertain.
	Kbc_2 (unit 2)	Yellow- to yellow–cream-colored terrain. Banded meandering pattern on southwestern limb of syncline represents outcrops of gently dipping strata. Extensive patchy and irregular distribution on northeastern limb. Represents light green on gray–green unit with low tree cover. Underlies unit 4 where in contact with this unit.
	Kbc_1 (unit 1)	Mottled blue–green with isolated magenta patches and elongate areas along streams. Represents heavily tree-covered terrain. Shadows on south-facing slopes probably contribute the magenta color in these places.
Morrison Formation	Jmb	Predominantly light red with yellow. Difficult to distinguish from units 2 and 3 of Burro Canyon Formation. Occurs as isolated patches along faults on axes of Lisbon Canyon Anticline and in Lisbon Canyon, and in extensive exposures in canyon bottoms in the northern part of the image.
Cutler Formation	Pc	Predominantly reddish orange and yellow. Distinctive thin layering, alternating in shades of yellow, dark green, and dark red. Occurs in southwest portion of image. Upper unit not mapped, but easily distinguished from overlying Moss Back (Chinle) sandstones, which appear rich yellow–gold, and from underlying Hermosa limestones.
Hermosa Formation	Ph	Mixed pink, yellow–gold, and green. Unit characterized by heavy tree cover (pink area), deep green where tree cover removed. Dip slopes have distinctive patterns of parallel rill-like canyons oriented northeast–southwest. Unit exposed in the southwest and west-central portion of the image.

of important rock units, such as the Cutler, Wingate, Kayenta, and Navajo, at either end of the anticline and by the alignment of streams and alluvial cover throughout the center part of the fold. Areas where dissimilar rock types are mapped by the U.S. Geological Survey (Figure 8-10) as juxtaposed by the faulting, such as at Big Indian Mine, are heavily disturbed by mining activity, and relations there are obscured. Minor fault structures, probably akin mechanically to the Lisbon Valley Fault, are mappable using the image data along Lisbon Canyon Anticline (Figure 8-24). These correspond to structures mapped by the U.S. Geological Survey, but the sense of displacement or motion for these has not been possible to determine from the image data.

Minor normal fault structures are mapped by Weir et al. (1961) in the Hermosa rocks (Sec. 18, T30S, R25E). These small cross structures lie along a sharp V-shaped canyon cutting the dip slope of this upper unit. On the image data, this canyon is displayed by its shadow pattern (39). Seventeen or so additional cross-striking straight canyons of this type can be seen in the images, but it has not been possible to determine displacements.

c. Jointing. The Dakota, Navajo, Kayenta, and Wingate are all transected by joint sets, but the most striking examples occur in the Wingate Sandstone, which is cut by a steeply dipping joint set normal to bedding. The joints strike N 50° W in northwestern Wingate exposures in the anticline and nearly east–west in the southern part.

Jointing is less well developed or absent in bleached strata; prominent jointing is always present in the unbleached, massively bedded section. Locally, two joint sets are developed that intersect each other at an angle of 30°. Individual joints or groups of joints sometimes extend downward through the

Figure 8-23. CRC image of NS-001 data for the portion of line 7 interpreted in Figure 8-24 (band-ratios 2/3 = blue, 2/4 = green, 4/5 = red)

Figure 8-24. Interpretation of CRC image of a portion of line 7 for the NS-001 flight at Lisbon Valley (Mission 407, August 28, 1979) (band-ratios 2/3 = blue, 2/4 = green, 4/5 = red)

Chained	Tree cover removed (disturbed)	Kbc + Q	Burro Canyon Formation and Quaternary deposits undifferentiated
Q	Quaternary deposits	Jmb	Brushy Basin Member, Morrison Formation
Kd + Q	Dakota Sandstone and Quaternary deposits undifferentiated	Pc	Cutler Formation
Kbc	Burro Canyon Formation undivided	Ph	Hermosa Formation
Kbc_1, Kbc_2, Kbc_3, Kbc_4	Informal subunits of the Burro Canyon Formation		

Fold axes placed from USGS mapping by Weir et al. (1961). The symbol x x x marks a section line and indicates change in vegetation resulting from clear-cutting and grazing.

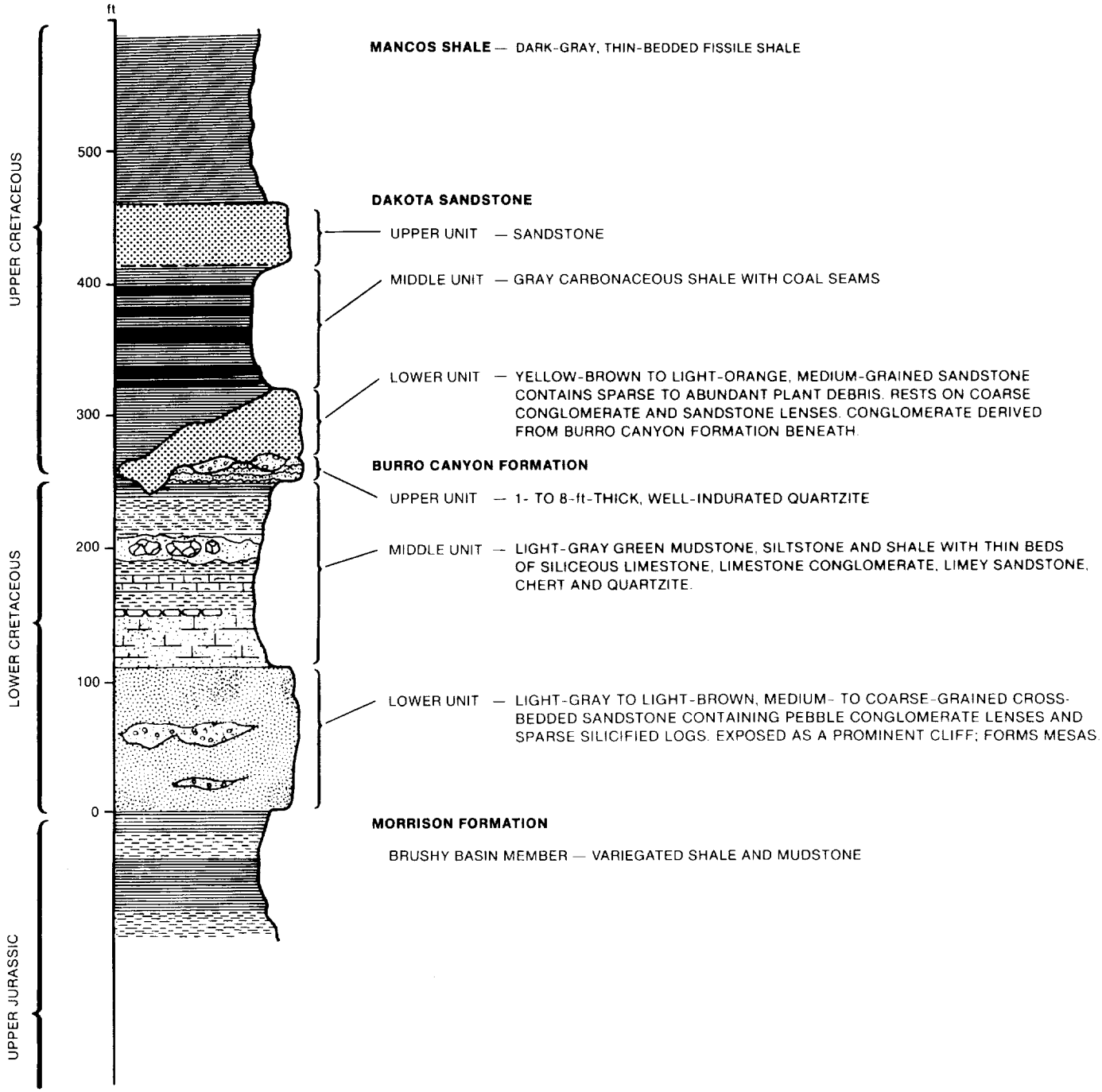

Figure 8-25. Stratigraphic section for the Dakota Sandstone and Burro Canyon Formation (compiled from description by Carter, 1956)

underlying thinly bedded Chinle strata. Elsewhere, the overlying Kayenta rocks display a poorly defined joint system parallel to structures in the subjacent section. Outcrops showing all three units cut by the same structure have not been found.

The joints described above can sometimes be resolved in the images, predominantly in the unbleached facies. Individual joints are manifested by parallel banding with a color pattern that consists of alternating red and black stripes which represent shadows (indistinguishable from outcrops) and outcrops (25).

C. Distribution of Alteration in the Wingate Sandstone

1. Photogeologic mapping. As an aid to sorting out relations of bleached and unbleached sandstone in the anticline, the distribution of bleached facies at the surface was mapped using stereoscopic aerial photographs together with image data. High-resolution (<1 m) color positive aerial photographs of portions of the Lisbon Valley area were obtained simultaneously with acquisition of scanner images in May 1978, but the coverage is incomplete, particularly over Wingate outcrops in the southern part of the anticline. Photography using color infrared filters from a later mission (Mission 407, August 28, 1979) provided additional coverage; however, infrared film is difficult to interpret for geologic problems and was generally unsatisfactory for mapping the outcrops needed.

Figure 8-26 is a photogeologic interpretation of a portion of frame 8 (Mission 381, May 26, 1978) covering the transition region between bleached and unbleached facies. A detailed interpretation based entirely on the use of stereoscopic pairs is given for portions of Secs. 33, 34, T29 1/2 S, R24E and Secs. 2, 3, 4, 9, 10, 11, 14, 15, 16, T30S, R24E. In addition, photogeologic interpretations were extended southward to include parts of Secs. 22, 23, 24, T30S, R24E. A composite photogeologic interpretation map of the area is shown in Figure 8-27.

A stratigraphic column compiled from the photogeologic analysis is presented in Table 8-9. The descriptions include characteristics used for identifying and mapping rock units.

The highest stratigraphic units, located in the center and on the western side of the area, are the Navajo Sandstone and the Kayenta Formation. Each of these formations contains several mappable subunits, but they have not been subdivided here. The Kayenta Formation and the Wingate Sandstone are easily separable on the basis of their color in the mapped area of Figures 8-26 and 8-27. In the SW 1/4 of Sec. 3, the contact between bleached cross-bedded facies of the Wingate and red, thinly bedded Kayenta Formation is an interfingering one. This relationship is shown in Figure 8-8. In the field, the contact is sharp (<1-m stratigraphic interval). In Figure 8-26, the outcrops of the interfingering section are mapped as the unit KW. This unit is thin and difficult to identify except on some slopes where the banding is resolved and apparently is not present everywhere. It may be confused with erosional remnants (previously unmapped by the U.S. Geological Survey) of basal Kayenta sandstone, especially where the Kayenta has been disturbed by drill road clearing. Unit KW has provisionally been placed with the Wingate section, although it probably consists of both Kayenta and Wingate sediments.

The uppermost unit definitely assignable to the Wingate section in the northern part of the area is unit W_1, which is a white ledge-forming sandstone stratigraphically beneath unit KW. All outcrops of white Wingate have been mapped as W_1 in Sec. 3 and to the north. The Wingate section beneath these outcrops of W_1 may be totally bleached; it is not possible to decide this from photogeologic interpretation alone. P. Niesen (personal communication, 1982) observed that the Wingate section is bleached throughout the area north of Expectation Canyon. However, the nature of the contact between bleached and unbleached units is obscure. Outcrops of unit W_1 are not found south of the middle of Secs. 14 and 15. The dip of unit W_1 is 7½° southwest and the strike is N 45° W. This dip is identical to that of other Wingate rocks in the section (Figure 8-10). W_1 thus has a dip equivalent to bedding and does not perceptibly represent a boundary crosscutting the Wingate section.

In the southern part of the mapped area of Figure 8-27, the first Wingate (?) unit below identifiable Kayenta red beds[3] is designated W_0. The distinction of this unit from KW is difficult. Unit W_0 is also closely adjacent stratigraphically to W_1 mapped to the north.

Interpretation of outcrop patterns of W_0 and W_1 in the NW 1/4 of Sec. 14 suggests that W_0 may be stratigraphically higher. Alternatively, these two units may interfinger and thus be an equivalent horizon. If they are equivalent, a geographic limit is placed on the extent of Wingate bleaching in a single stratigraphic horizon, high in the formation, that is continuous and not removed by erosion.

A major stratigraphic unit below W_1, labeled W_5 in Figures 8-26 and 8-27, is composed of intercalated layers of white, red, and pink (bleached and partially bleached) strata. To the north, individual laminae are thick enough to map and units W_2, W_3, and W_4 are examples of these. To the south, the laminations become finer and individual strata are not mapped. Unit W_5 thins to the south and the banding becomes indistinct,

[3]Outcrops of Kayenta are established by comparison with USGS mapping (Figure 8-10).

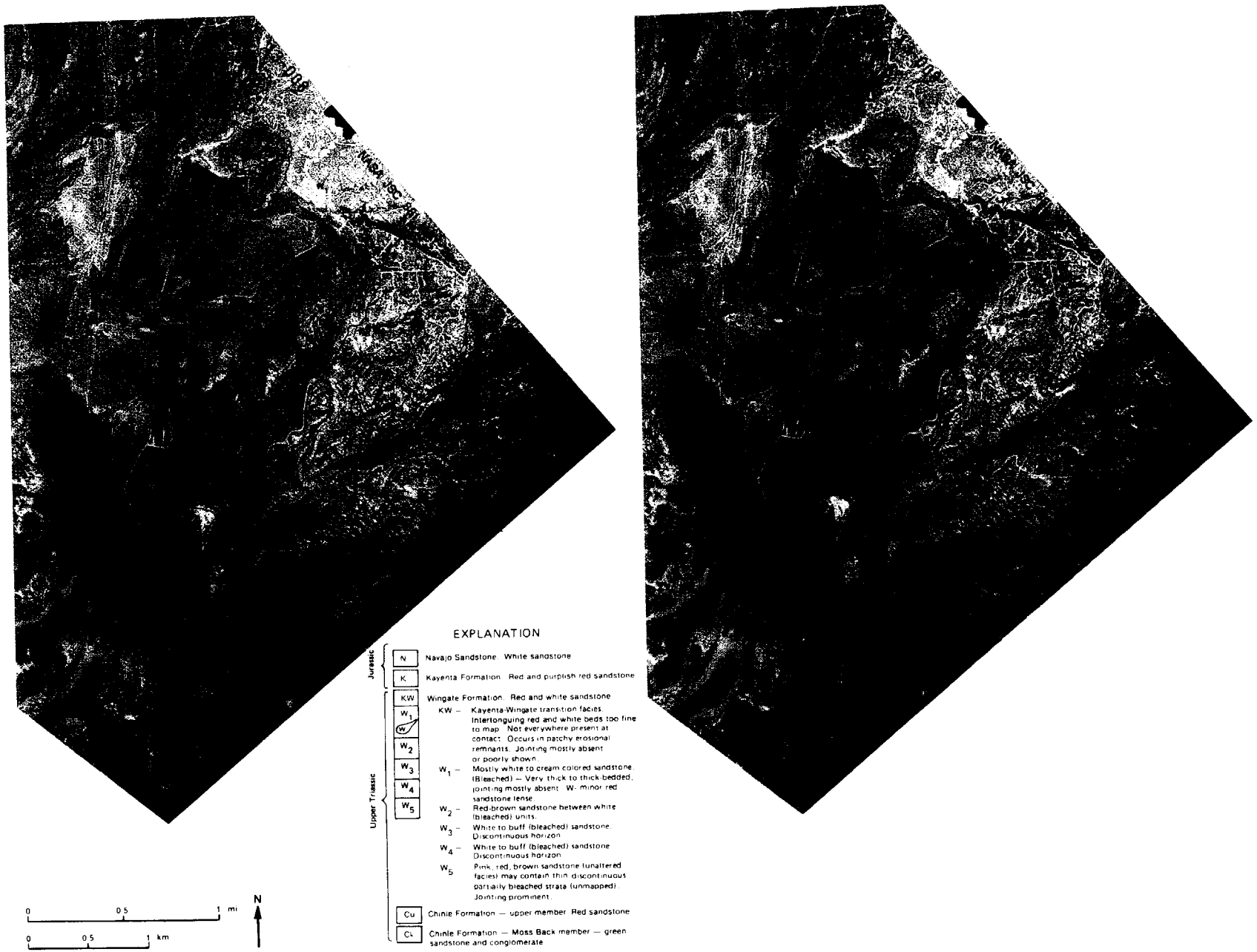

Figure 8-26. Photogeologic interpretation of a portion of the Wingate Sandstone outcrop with the distribution of bleached, partially bleached, and unbleached facies (frame 8, Mission 381, May 26, 1978). Informal members of the Wingate Sandstone were established on the basis of photogeologic mapping.

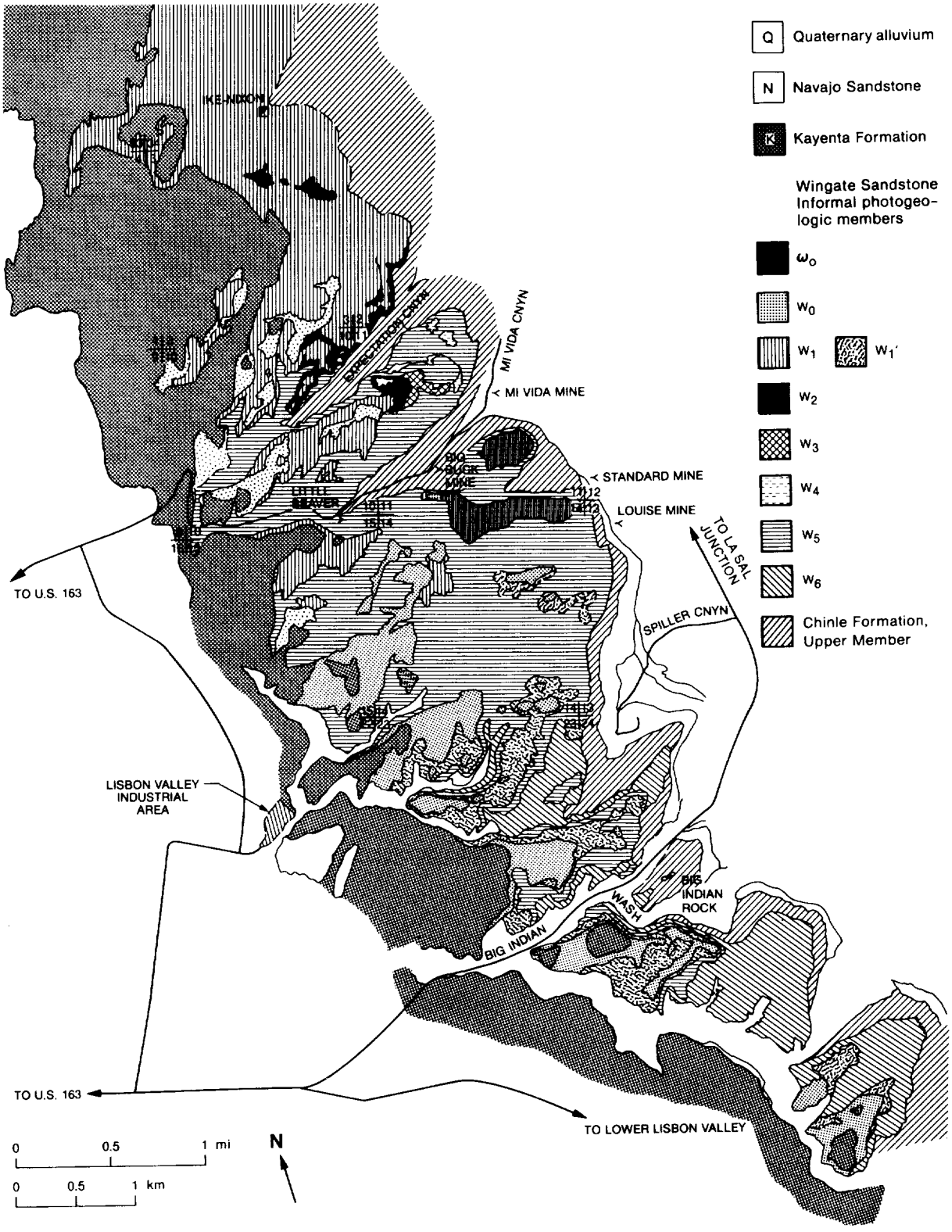

Figure 8-27. Photogeologic map of a portion of the Wingate Sandstone outcrop between Ike–Nixon Mine and Dry Wash. Descriptions of photogeologic units are given in Table 8-9.

but some interfingering of bleached and unbleached strata of this type probably persists across the predominantly unbleached Wingate interval. This laminated unit is heavily jointed in contrast to strata above, which do not display jointing; individual joint blocks isolated by weathering form resistant banded knobs and small domes that give a distinctive geomorphic appearance to this unit.

Unit W_6 represents massive unaltered salmon–pink sandstone that is heavily jointed. Unit W_6 is unbanded or possesses banding at a scale below that resolved in the aerial photographs. On this basis, it is distinguished from unit W_5 above it.

The relationships between bleached and unbleached Wingate rocks in the southern part of the anticline (Sec. 32, T30S, R25E) north of Dry Wash have not been established photogeologically, but from cursory examination of the available photographs the relations appear stratigraphically simpler. The complicated laminated section of the northern part is not prominent. Thick bleached and jointed sandstones appear to lie above a section of massive, unbleached red sandstone. The bleached units pinch out abruptly to the north. Bleached strata are overlain by a pink sandstone horizon resembling W_0 of the northern area. The field nature of these units has not been established. They may represent erosional remnants of basal Kayenta or an upper Wingate horizon of partially bleached and unbleached rocks.

A series of important outcrops containing boundaries between bleached and unbleached rocks crosscutting the Wingate Sandstone occurs (1) along canyon bottoms cut in the dip slope in the southern part of Secs. 33, 34, T30S, R25E, and in the northern part of Secs. 3, 4, T31S, R25E, and (2) along the bottom of a northern tributary to Dry Wash. These outcrops can be seen in a high oblique aerial photograph (Figure 8-6) and are designated by arrows.

2. Analysis of bleaching distribution in a canonical transform image of Bendix 24-channel data. The Bendix 24-channel scanner system was flown along a N–S-orientated flight path (Figure 8-2) over the northwestern portion of Lisbon Valley Anticline on June 15, 1976. Ten channels in the VNIR (Table 8-4) were mostly free of noise and striping and thus suitable for image analysis. Subsequently, however, removal of irregular dark striping from some bands was required to analyze vegetation problems. None of the thermal infrared channels were operative during the flight. The approximate ground resolution of these data is 7 m, more than twice that of the 8-channel NS-001 images.

Analysis of the images has focused on determining the distribution of alteration effects in the Wingate Sandstone, separate from the general problem of geologic mapping. The high spatial resolution of these images allowed detailed comparisons to be made between the photogeologic interpretations of Wingate stratigraphy described above and the image data. Some apparent differences between the photogeologic interpretation and interpretations based on the image data were revealed. The relatively large number of channels available covering a wide spectral range suggested that linear reduction (PC transformation) or classification (discriminant function) techniques could be used advantageously to display the separation of the specified lithologic classes. The analysis in all cases was limited to a combination of 10 bands because of computer storage limitations. Both PC and canonical transform images were prepared from these data. PC images provided less visual separation of bleached and unbleached units as compared with the canonical variate renditions; thus, the latter were used in this analysis. The PC transformation was applied as part of a "tree removal" algorithm discussed below. An example of the PC rendition based on a combination of 10 bands is given in Figure F-3.

Methods of multidimensional classification (i.e., discriminant functions) have been described in detail by Gnanadesikan (1977). Canonical axes in the multiple group classification problem give directions in multidimensional space that maximize the separation between specified groups of observations relative to the scatter within these groups. Canonical variables (here designated CV to distinguish them from the PC variables V) thus optimize the separations for purposes of display. These canonical coordinates are obtained routinely as part of the BMD07 stepwise discriminant function computational package (Dixon, 1974).

The reference observation sets were derived from training areas within the images themselves, and the canonical coordinates were devised to separate four groups: bleached Wingate (BW), unbleached Wingate (UW), alluvium (AL), and all other rock types (OT). The goodness of classification obtained for the 10 variables used is given in the associated classification matrix (Figure 8-28). Overall, the classification into groups is 88 percent correct, with the largest errors (0.5 percent or less) from misclassification of BW as UW, and UW as BW. A detailed analysis of these false classifications has not been made because the separation is excellent. The probable causes of misclassification include (1) contamination of the training sets with members of other classes, or (2) influences of vegetation, principally piñon–juniper and minor shrub and grass cover. Improvement in the separations might be possible using the PFRS collections. Here the trade-offs will always be between separations in relatively meager samples of pure end members (PFRS data) versus separations for a statistically superior sampling of the actual macroscopic cover types present in the image data. There is no advantage in using the PFRS data. Furthermore, the image-derived training sets, even for model sample

Table 8-9. Description of photogeologic units identified in Figures 8-26 and 8-27

Photogeologic Unit	Map Symbol	Description
Navajo Sandstone	N	White, gray, and buff sandstone forming low mesas and gentle dip slopes. Soil developed on flat surfaces with dense shrub and grass cover, sparse to moderate tree cover near edges of soil-covered areas and on adjacent rocky exposures.
Kayenta Formation	K	Red and purplish-gray sandstone; probably represents separate (but unmapped) stratigraphic units. Moderately uniform piñon–juniper cover.
Wingate Sandstone		Informal photogeologic members.
	KW	Transition facies between Kayenta and Wingate. Consists of intertonguing red and white beds too fine to map or in mottled patchy erosional remnants on dip slopes. Not everywhere present at contact. Jointing mostly absent or poorly displayed. Some outcrops heavily disturbed by drill roads. Included in Wingate section to conform with mapping of this undifferentiated formation by Weir and Dodson (1958a, 1958b, 1958c).
	W_0	Mostly grayish-red sandstone. Bedding indistinct. Outcrops generally uniform in color. Stratigraphically lies beneath Kayenta Formation. Relations to KW unit uncertain, possibly the stratigraphic equivalent or a basal unit of Kayenta sandstone. Jointing absent. Moderate to heavy uniform piñon–juniper and shrub cover, except where disturbed by drill pads and roads.
	W_1	Mostly white to cream-colored sandstone. Very thick to very thick bedded. Forms ledges, but generally in rounded outcrops. Jointing usually absent. Where present, joints are very closely spaced and poorly developed; w is a minor red sandstone lense. Moderate to heavy tree cover everywhere except where distributed by drilling and road clearing.
	W_1'	Very light brown to light pink sandstone. Forms resistant ledges. Interpreted to be unbleached or partly bleached stratigraphic equivalent of W_1.
	W_2	Red–brown sandstone between white (bleached) sandstone units. Generally narrow exposures on steep slopes. Sparse to moderate tree cover.
	W_3	White to buff (bleached) sandstone horizon. Local resistant ledges only. Discontinuous horizon.
	W_4	White to buff (bleached) sandstone. Local resistant ledges only. Discontinuous horizon.
	ω_0	Red unit with a few white to mottled outcrops. Subdued topographic expression. Jointing absent. Stratigraphic position uncertain. Appears to lie above W_5, the laminated terrain, in which case it may be the equivalent of W_0. However, appears topographically higher in some juxtaposed outcrops. May represent weathered layer or soil development of modern origin. Moderate tree cover and extensive disturbances with drill roads and pads.
	W_5	Pink, red, brown, and white laminated sandstone facies. Forms resistant outcrops and knobs that display prominent, widely spaced joints. May contain thin, discontinuous, partially bleached strata, most of which are too fine to map. Tree cover generally low to absent except along joints, where dense growths occur, and in patchy areas. Covered by unit resembling ω_0.
	W_6	Red to salmon sandstone, massive bedding, distinguished from W_5 by the general lack of lamination, or by the presence of lamination at a scale below resolution of aerial photographs (<1 m). Unit forms cliffs. Lower part not visible in aerial photographs. Extensive, well-developed jointing, except along outcrops near Kayenta contact. Tree cover sparse, mainly in patches (on W_0?) and along joints.
Chinle Formation	Cu	Upper Member. Red sandstone and siltstone. Forms steep slopes beneath W_6 Wingate cliffs.
	Cl	Chinle Formation–Moss Back Member. Green sandstone and conglomerate. Mainly as V-shaped outcrops in canyon bottoms.

size, tend to be almost normally distributed within the classes, thus keeping within mathematical constraints of the BMD program.

The scatter diagram representation of the first two canonical variables is given in Figure 8-29. Ninety-seven percent of the total dispersion is explained by the first two variables in this plot and 100 percent by the first three variables. A line joining the group means of UW and BW lies outside the (CV1, CV2) plane and has direction cosines with respect to the canonical axes (CV1, CV2, CV3) = (0.8020, 0.5399, 0.2555). This explains the large overlap present in the projection of the first two variables (CV1, CV2) without the associated large error in classification. The direction cosines also show that most of the variation between these groups is described by the first two variables.

	BW	UW	AL	OT
BW	4229	546	105	70
UW	622	12405	98	0
AL	33	34	2433	0
OT	54	6	153	1787

BW BLEACHED WINGATE, 4950*
UW UNBLEACHED WINGATE, 13125
AL ALLUVIUM, 2500
OT ALL OTHER ROCK TYPES, 2000

* NUMBER OF PIXELS SAMPLED

Figure 8-28. Classification matrix from discriminant function analysis of the Bendix 24-channel data (four classes, 10 bands, and 22,575 image spectra)

For representation of the image data in (CV1, CV2, CV3) space, raw DN values from the gradient-corrected image data and the linear transformation formulas were used to compute canonical coordinates for each pixel. These numbers may be both positive and negative and are subsequently rescaled so that all lie between 0 and 255. Further stretches have been applied to adjust visual appearance of the final images.

A canonical transform rendition of the Bendix 24-channel data for Lisbon Valley is shown in Figure 8-30, with the following color assignments: CV1 = red, CV2 = green, CV3 = blue. The principal units, cover types, color assignments, and approximate canonical variate weights are included in Table 8-10.

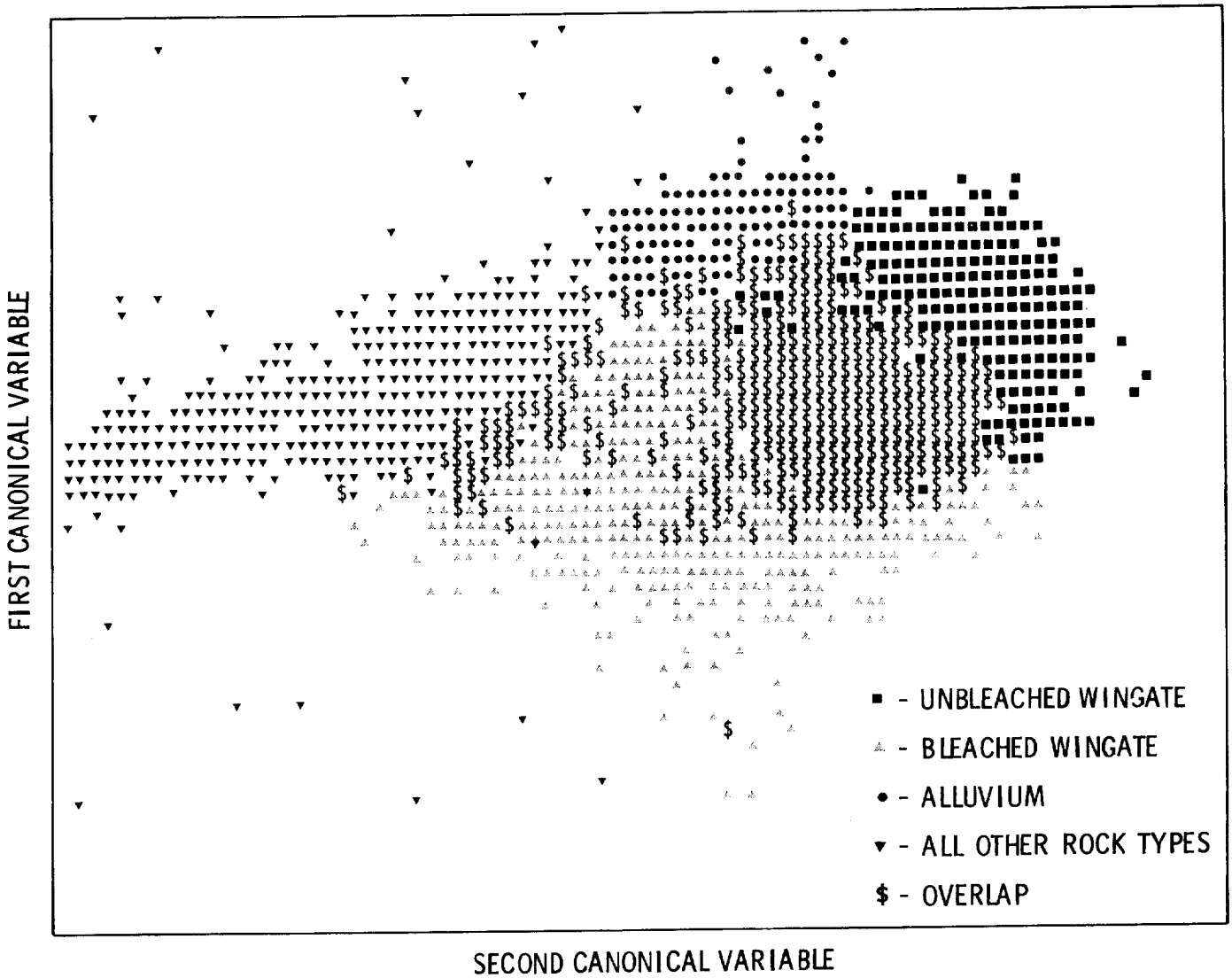

Figure 8-29. Canonical scatter diagram for separation of bleached and unbleached Wingate Sandstone in the Bendix 24-channel data of Lisbon Valley

An interpretation of the canonical transform image is given in Figure 8-31. Boundaries have been drawn to separate image units with similar colors or color relations. A detailed interpretation is provided only for the Wingate Sandstone outcrops. Boundaries of this formation and those of other formations present have been separated by dashed lines where location was aided by reference to the published geologic map (Figure 8-10). In the middle part of Sec. 10 and the southern part of Sec. 3 (T30S, R24E in Figure 8-31), the image-interpreted boundaries largely correspond to those depicted in the photogeologic interpretations in Figures 8-26 and 8-27. In the field relations, light-colored Wingate rocks contrast sharply with multicolored units located stratigraphically to either side, and the image display is consequently good. Throughout Sec. 15, however, the units depicted in the image interpretation may differ substantially from those obtained in the photogeologic interpretation of Figures 8-26 and 8-27. In Figure 8-30, a residual noise striping trends nearly parallel to the scan lines. This banding oscillates in color from gold to cream or white and constitutes a limit on the color distinctions that can be made here. Where the regions depicted mostly correspond to those in the photogeologic interpretation, the same patterns have been used. Elsewhere, the units outlined appear to consist of four types: (1) units that correspond to ω_0 of the photogeologic interpretation and possibly represent soil cover or disturbed ground, (2) units labeled W′ that represent a diverse mixture of ω_0, W_0, W_1, W_5, and W_6, undivided, (3) units that correspond to W_1 and W_2 alone, and (4) units that are spotty, elongate, and in partial shadow. Physically, except for shadowed places, the field units in these areas are characterized by subtle color contrasts in shades of pink, buff, light red, maroon, and light maroon. These field color differences are not resolved in the image data. This may result because more variability is introduced in to the images by inclusion of infrared bands (channels 7–13) in the analysis.

The difference between the image and photogeologic units is important to understand. The photogeologic units are characterized by differences in color, structure, vegetation cover, and stratigraphic position. Image units represent cover types or shadowed areas differentiated purely on the basis of color representation. Image units may not by themselves have stratigraphic significance.

In summary, the image data were useful in mapping the general distribution of altered and unaltered Wingate strata, but an interpretation of these data unsupported by the photogeologic interpretation would be misleading and could not reveal the actual time-stratigraphic significance of the units depicted or their distributions. This may be largely a question of scale. Thus, the comparisons might be improved if images at a 1-m resolution or aerial photographs at a 7-m resolution were used,

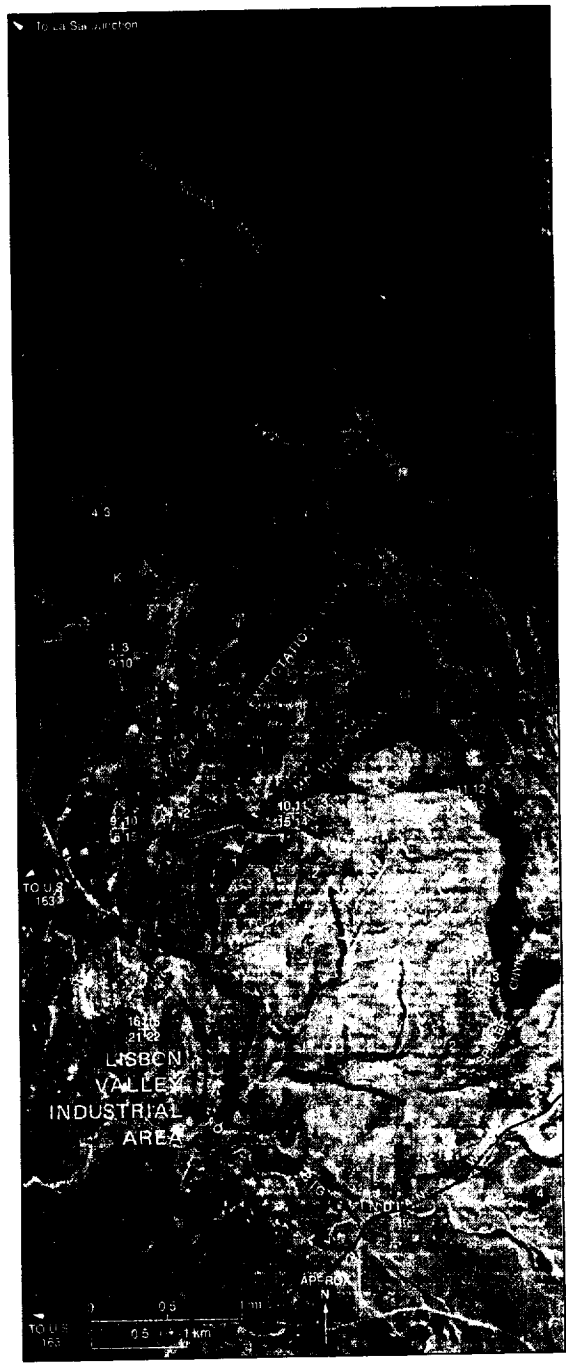

Figure 8-30. Canonical transform image of the Bendix 24-channel scanner data, June 1976. The 10 bands used in the analysis are included in Table 8-4 (CV1 = red, CV2 = green, CV3 = blue). Numbers show type areas for image mapping units described in the text.

Q	**Quaternary alluvium**	**Cu**	**Chinle Formation, Upper Member**
N	**Navajo Sandstone**	**Cl**	**Chinle Formation, Moss Back Member**
K	**Kayenta Formation**		

Table 8-10. Color key for the canonical transform image (Figure 8-30)

Geologic Unit or Cover Type		Image Color	Canonical Coordinate Representation[a]		
			CV1	CV2	CV3
Vegetation	Heavy (5 to 100 percent) piñon juniper cover (outcrops of Dakota Sandstone near Rio Algom Mine). High shadow component.	Medium to deep blue	Low	Low	Moderate to high
	Heavy cover of shrubs and grasses (Cutler outcrops south of Big Indian Mine; alluvial cover east of Rio Algom). Includes areas of chained piñon–juniper with possible secondary growth of shrubs and clump grasses. Not known if grasses are green or yellow (dormant).	Green to olive green	Low	Moderate to high	Low
	Green grasses or shrubs with high leaf density, strong green pigmentation, low shadow component (Big Indian Wash).	Whitish pink to pink	High	Moderate to high	High
	Predominant clump grass cover (alluvium or soil-covered mesas on Navajo Sandstone in Big Indian Wash). Not known if green or yellow (dormant).	Yellow red and yellow brown (golden)	High	Moderate to high	Low to moderate
Shadows	Along some canyons and east- and north-facing edges of mesas.	Deep blue	Low	Low	High
Outcrops	Highly reflecting buff to white outcrops (south-facing slopes below mesas of Navajo Sandstone; north-facing slopes of Entrada; unvegetated outcrops of bleached Wingate).	Red to slightly blackish red	Moderate to high	Low	Low
	Light gray green outcrops with sparse vegetation. (Moss Back outcrops in canyon bottoms and where well-exposed on slopes.)	Dark olive to black	Low	Low to moderate	Low
	White to buff outcrops with moderate tree cover (bleached Wingate outcrops).	Moderate olive green	Low	Moderate	Low
	Maroon and purple sandstone with moderate and heavy tree cover (Kayenta Formation).	Blue (red outcrops with tree cover) to golden (grayish purple outcrops with trees)	Low High	Low Moderate	High Low to moderate
	Salmon or light-red outcrops (unvegetated Wingate exposures north of Big Indian Wash).	Reddish yellow to red brown or golden	Moderate	Moderate	Low
	Reddish to light-reddish units with moderate tree and/or shrub and possibly some grass and soil cover (unbleached Wingate exposure northwest of Spiller Canyon).	Cream to white	High	High	Moderate to high

[a] CV1 red
CV2 green
CV3 blue

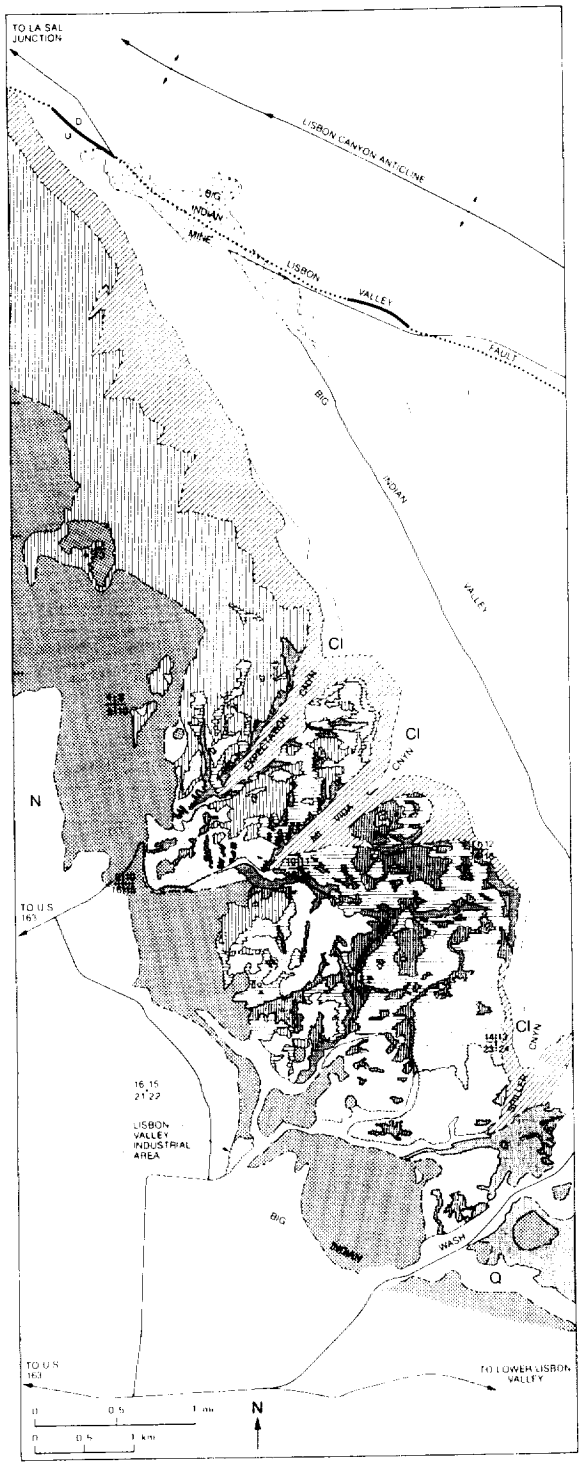

IMAGE	UNITS	APPROXIMATE PHOTOGEOLOGIC EQUIVALENT
Q	**QUATERNARY** UNDIVIDED—PINK AND LIGHT BLUE	
N	**NAVAJO SANDSTONE** UNDIVIDED—YELLOW TO YELLOW-GREEN AND GOLD	
	KAYENTA FORMATION UNDIVIDED BLUE-GREEN AND GOLD	
	WINGATE SANDSTONE INFORMAL UNITS FROM IMAGE INTERPRETATION. RELATIVE STRATIGRAPHIC POSITION INDETERMINATE	
	BRICK RED (OUTCROP) AND OLIVE GREEN (PIÑON-JUNIPER) INTERMIXED (AREA 1)	W_1
	YELLOW-ORANGE TO RED BROWN (AREA 2)	W_{0-} IN PART
	LIGHT YELLOW-ORANGE (AREA 3)	W_{0-} IN PART
	DEEP YELLOW-ORANGE (AREA 4)	W_{0-} IN PART
	BUFF TO CREAM (AREA 5)	W_0
	BLUE TO STEEL GRAY (AREA 6)	NO EQUIVALENT (SHADOWS)
	CHINLE FORMATION—UPPER MEMBER	
Cl	**CHINLE FORMATION**—MOSS BACK MEMBER	

Figure 8-31. Geologic interpretation of the canonical transform image (Figure 8-30) covering a portion of the Wingate Sandstone outcrop between Big Indian Mine and Big Indian Wash

together with stereoscopic coverage. Units interpreted as partially bleached (laminated) in the aerial photographic interpretations are not detected in the image data because (1) the banding is too small to be resolved, and (2) the macroscopic spectral contrasts of laminated units at the resolution of the image data are probably not large enough.

The distribution of the various image units reveals that some altered strata probably extend across the entire Wingate exposure. New image units depicted represent a composite of cover types whose geologic significance is not always clear. Broadly, the image units found parallel the strike of Wingate outcrops, but the distribution over the outcrop is not in accord with that required for correspondence to strategraphic boundaries. For example, if the new image unit possessed a layered distribution, these units would dip more steeply southwest than do the actual Wingate strata.

3. Distribution of bleached, unbleached, and laminated sandstone in the Wingate outcrop and in Lisbon Valley Anticline. Plate 8-1 summarizes the distribution of rock types in the Wingate outcrops as derived from analysis of aerial photographs, the Bendix 24-channel scanner image of Figure 8-30, and the NS-001 (7-channel) scanner images of Figure 8-21. Here the bleached sandstone distribution obtained from the scanner data alone is shown in a vertical bar pattern. The additional boundaries, all approximately located, are taken from analysis of aerial photographs and may or may not be resolved in the scanner images. The generalized outcrop patterns do not have the same stratigraphic significance as the photogeologic map versions (Figures 8-26 and 8-27).

The stratigraphic interpretation was carried outside the bleached areas wherever aerial photographic coverage was sufficient. In addition to the photogeologic boundaries transposed from Figure 8-27, this resulted in the inclusion of small outcrops of unbleached sandstone both on the dip slope and in sections of the E–W-striking outcrops to the south and north of Dry Wash. These irregular roughly E–W-trending exposures appear to crosscut the section. An approximate dip measurement from the outcrop pattern in conjunction with the topographic map gives a value of 7°. This is shallower than the average 10° dip for the formation as a whole. The stratigraphic distribution of bleaching is likely to be governed by detailed variation in permeabilities from layer to layer. The reported difference in dip should thus be viewed with caution. The significance of establishing such a relationship, however, should be clear. If the bleaching was associated with a standing level fluid at some point in the history of anticlinal development, the difference in dip for uniform permeability would represent the increase in tilt of these beds occurring since the cessation of alteration. A crosscutting relationship would establish that (1) the beds were tilted prior to alteration; hence, at least some bleaching originated after deposition and deformation, and (2) further tilting subsequent to alteration had taken place.

The distribution of bleached outcrops with respect to elevation on the southwestern side of Lisbon Valley Anticline is shown in Plate 8-2. To avoid excessive clutter in the drawing, only the outcrop pattern of the stratigraphically highest bleached unit in this section is shown. Some bleached strata within unit W_5 (laminated terrain) persist beyond the limits shown and probably extend across the entire Wingate exposure; these outcrops of banded rocks are not depicted in any of the image data examined and are not shown here.

In both northern and southern areas, bleached strata represent the highest outcropping rocks (7000 ft) and lie closest to the anticlinal crest. The geometry and position of the lower boundary are more uncertain and cannot be determined from surface observations alone. Bleached rocks of the uppermost unit identified as W_1 by photogeologic analysis feather out at 6200 ft near Mi Vida Canyon. In the southern part of the anticline, bleached rocks lie above approximately 6400 ft.

The relations between bleached and unbleached rocks, where mapped, are depicted in the cross section (Plate 8-3) drawn along the line AA'A"A"' in Plate 8-2. The line of section AA"' trends parallel to the Wingate outcrop following an arcuate path with respect to the axis of the Lisbon Valley Anticline. The maximum separation occurs at Point A' (Big Indian Rock), where the distance is 3.3 mi between the anticlinal axis and the line of this cross section. At Big Indian Rock, the sediments transected lie farthest from the crestal region in both distance and elevation. The curved line of this section produces an apparent synclinal geometry in these beds, which from the geologic map (Figure 8-10) is actually a broad but undesignated anticlinal warp.

D. Removal of Vegetation Signatures in the Image Analysis

1. General. Thus far, no attempt has been made to account for the contribution made by vegetation cover in measurement of the distribution of Wingate bleach effects. Examination of the plant distribution image prepared by the BLM for the Lisbon Valley area (Figure 8-32 and Table 8-11) indicates Wingate outcrops to be classified as piñon–juniper terrain. The dominant plant species consist of piñon pine (*Pinus edulis*) and juniper (*Juniperus osteosperma*), plus subordinate species not identified in BLM mapping such as mountain mahogany (*Cercocarpus* sp.), big sagebrush (*Artemisia tridentata*), and various grasses. Ground cover by the dominant and other types of vegetation may vary from 0 to 100 percent. CIR and color photographs of the area reveal the irregular nature of this distribution of tree and shrub cover. Generally, a higher tree density prevails over bleached outcrops of Wingate Sandstone

in the Big Indian District and in the southern portion of the anticline than over outcrops of unbleached strata north of Big Indian Rock.

2. Estimating tree cover by the band depth method. To account approximately for the effects of vegetation, data from the Bendix 24-channel scanner were used (1) to investigate the distribution of tree cover, and (2) to remove the spectral contribution of vegetation so that the differences in spectral response of bleached versus unbleached areas could be estimated separately from the vegetation component. The 24-channel data were used because the spatial resolution (~7 m) is superior and the spectral data are available at a large number of wavelengths. Ten channels of data were used to form reduced spectra for the extraction problems. These are listed in Table 8-4. Channel 6 falls within a major chlorophyll-a and chlorophyll-b absorption feature in piñon, in juniper, and in green plants generally found at 0.65 μm. No major spectral features occur in the reflectance of the Wingate at this wavelength, but the

Table 8-11. BLM vegetation classification for the southwest flank of Lisbon Valley Anticline, Big Indian District

(a) Number abbreviations

Number	Abbreviation	Number	Abbreviation
13	PJ Putr Artr	25	Artr Hija Ager
14	Atco Artr Bogr (Bogr)	26	Artr PJ Chna
15	Artr Ager (Chained) Saka (PJ)		Ager Hija Orhy
16	Ager PJ Artr	28	Artr Atca Bogr
18	Artr Bogr Stco Hija PJ	29	Save Saka
19	Artr (less dense) Bogr (PJ)	30	PJ
20	Atca Bogr (Artr)	33	Ager Artr PJ
21	Artr Bogr Atca Hija	36	Artr Ager
24	Rocky PJ	37	Artr Ager Orhy

(b) Name key

Abbreviation	Scientific Name	Common Name
Ager	*Agropyron cristatum*	Crested wheatgrass
Artr	*Artemisia tridentata*	Great Basin sagebrush
Atca	*Atriplex canescens*	Four-wing saltbush
Atco	*A. confertifolia*	Shad scale
Bogr	*Bouteloua gracilis*	Blue grama
Chna	*Chrysothamnus nauseosus*	Rabbit brush
Hija	*Hilaria jamesii*	Galleta grass
Orhy	*Oryzopsis hymenoides*	Ricegrass
PJ		Piñon juniper
Putr	*Purshia tridentata*	Antelope bitterbrush
Saka	*Salsola kali*	Russian thistle
Save	*Sarcobatus vermiculatus*	Black greasewood
Stco	*Stipa comata*	Needle-and-thread grass

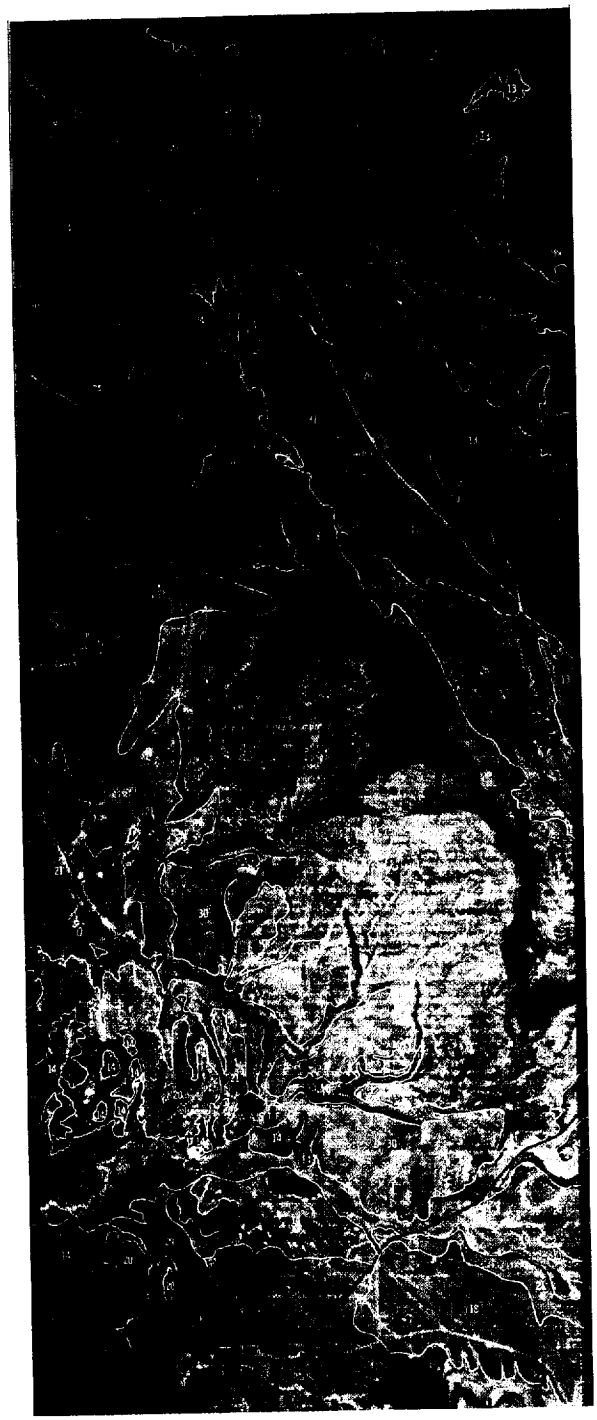

Figure 8-32. Distribution of vegetation types according to BLM mapping for a portion of the western limb of Lisbon Valley Anticline (numbers refer to BLM classification given in Table 8-11). Base is Bendix 24-channel canonical transform image.

field-determined reflectance varies between 40 and 60 percent for both altered and unaltered rocks. This wide variation is not a serious problem in the model because the areally averaged image values used represent the pure rock end member. The radiance level in channel 6 throughout the image may be used to approximate the extent of vegetation cover on a two-component mixing model as follows:

If

N_6 = typical rock DN for channel 6

V_6^j = actual DN at pixel j due to mix of rock and vegetation cover

Then

$$\left.\begin{aligned} V_6^{100} &= \text{DN in channel 6 for 100 percent tree cover} \\ \frac{V_6^j - V_6^{100}}{N_6 - V_6^{100}} &= \text{fraction of rock cover in pixel} \\ 1 - \frac{V_6^j - V_6^{100}}{N_6 - V_6^{100}} &= \text{fraction of vegetative cover in pixel } j \end{aligned}\right\} \quad (8\text{-}1)$$

The result of applying Eq. (8-1) to determine the fraction piñon–juniper (i.e., chlorophyll absorbing) cover over the image area is shown in Figure 8-33. This is a simple density slice representing the fraction of cover, color coded as given in the scale. The constant V_6^{100} was measured from the image data on outcrops of Dakota Sandstone north of Big Indian Mine, where tree density could be seen from high-resolution aerial photographs (Figure 8-34) to approach or equal 100 percent. The values of N_6 were obtained from large exposed areas of (pigmented) Wingate Sandstone cropping out south of Big Indian Rock.

Comparison of the image data with CIR photographs of the same area shows a general correspondence between the distribution of cover represented in these two ways. An inherent ambiguity exists with this simple method in dealing with: (1) shadowed areas where the radiance in the reference channel may be small, but the terrain barren of cover, or (2) in areas where rock reflectance is lower than that of the Wingate over the bandpass of channel 6. The number of components should probably be increased to include three, four, or perhaps more components in a more realistic treatment to permit representation of actual variations in rock reflectance and the presence of multiple plant species. For this purpose, the algorithms of Horwitz et al. (1975) may be useful. A method based on use of PC diagrams can also be employed (see Appendix E).

3. Removal of vegetation spectral contribution and construction of "vegetation-free" PC images. The radiance values in other channels may also be modified to remove the vegetation component. In this instance the image at each wavelength is reconstructed with radiance values representing 100 percent rock.

If

P_i = piñon–juniper response for channel i

D^k = actual DN for channel i in pixel k

r_i = ideal response for rock alone in channel i (unbleached Wingate Sandstone)

Then

$$D^k = \left(1 - \frac{V_6^k - V_6^{100}}{N_6 - V_6^{100}}\right) P_i + \left(\frac{V_6^k - V_6^{100}}{N_6 - V_6^{100}}\right) r_i$$

and

$$r_i = \frac{N_6 - V_6^{100}}{V_6^k - V_6^{100}} \left[D^k - \left(1 - \frac{V_6^k - V_6^{100}}{N_6 - V_6^{100}}\right) P_i \right] \quad (8\text{-}2)$$

To represent the contributions from all channels, these "ideal" rock responses represented by r_i (unbleached Wingate values assumed) for each of the channels used (excluding channel 6) were combined in a PC image. Some of these channels contained a small amount of noise, which was removed before further analysis.

The primary noise in the Bendix 24-channel scanner data consisted of irregularly spaced dark bands rotated slightly from the horizontal. To facilitate interpretation of the PC color composites, the following destriping technique was performed on each channel before the application of the vegetation removal procedure. For strictly horizontal noise, the dark bands were distinguished from the rest of the image by examining the average value of the samples in each line. A high-pass filter applied to a one-sample-wide image created from the line averages produced an estimate of the noise. The noise pattern was then spread out to the full width and subtracted from the original image. The scanner images required a small rotation to place the stripes in a horizontal position before the noise removal procedure could be applied. For approximately one-quarter of the flight line, the angle of rotation was 1.4°; for the remainder it was 0.8°. The image for each channel was first separated and each section rotated appropriately. The destriped sections were then rotated back to their original orientations and mosaicked together. After this destriping, the vegetation removal was performed and the PC color composite produced.

Figure 8-33. Color-coded representation (Bendix 24-channel image) of the fractional area of tree cover according to the simple two-component mixing model given by Eq. (8-1) in the text. Outcrop pattern of the Wingate Sandstone is outlined. Percent vegetation cover is indicated by the scale.

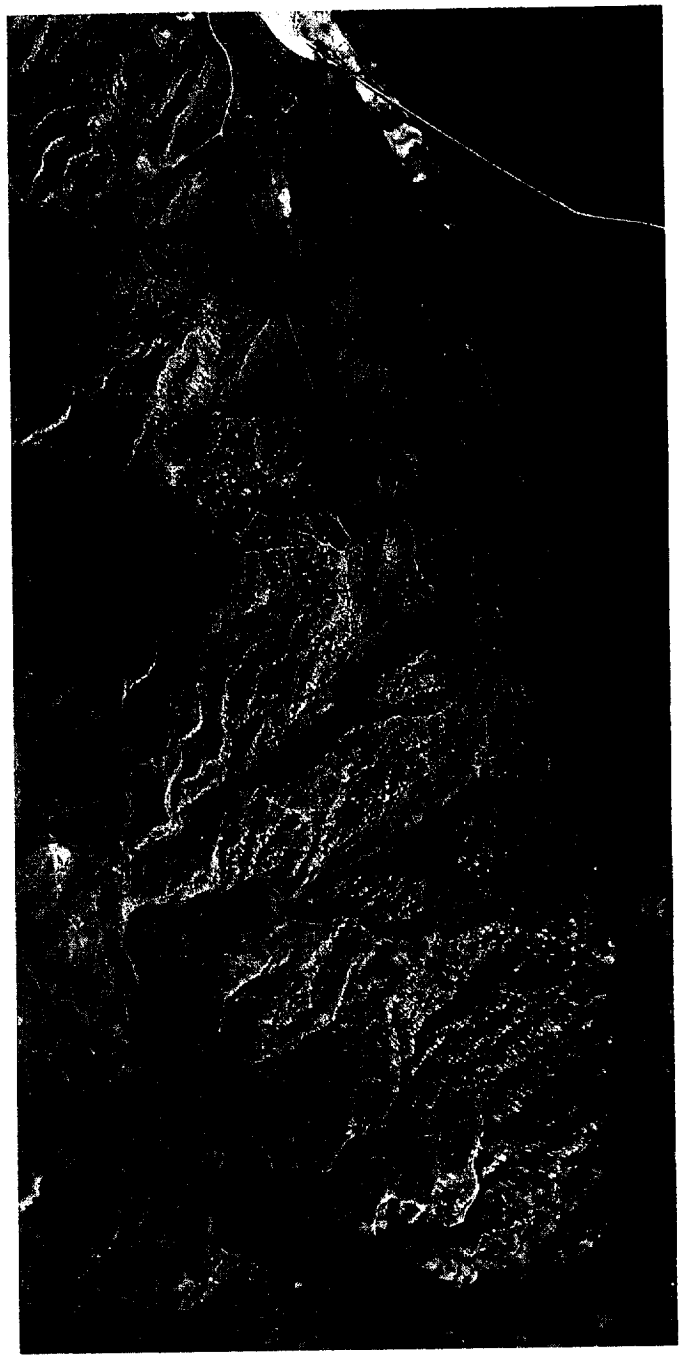

Figure 8-34. CIR photomosaic of the area corresponding to Figure 8-33

The destriped image represents some improvement over the original data, although the noise pattern was not removed completely. The noise removal procedure, however, involves a trade-off between noise reduction and spatial resolution. Each of the two rotations necessitates a resampling of pixels to preserve the line–sample coordinate system. This is accomplished using a four-point interpolation which results in some loss of detail. The enhancement of the data produced by the noise removal procedure was considered worth the loss in resolution.

The resulting PC image is shown in Figure 8-35. The differences between bleached (northern portion) and unbleached (southern portion) outcrops in this image now represent variations in rock reflectance alone, without the influence of vegetation. The two-component reflectance model required exclusion of the inherent difference in reflectance between bleached and unbleached strata. Expanding the treatment to a three-component case (vegetation, bleached, and unbleached) could be expected to enhance the differences in rock-type discrimination sought.

E. Comparison of Soil Maps to Geologic and Image Data

The soil mapping units of Figure 8-3 are compared in Figure 8-36 to the geologic mapping of the Lisbon Valley area and to the NS-001 PC image data. Soil unit 6 (Begay–Windwhistle–Ildefonso) in Figure 8-36(a) occupies Big Indian and Hatch Washes west of the anticline. The area encompassed by this unit is underlain predominantly by Navajo Sandstone with mesas formed of Carmel, Entrada, and Summerville Formations. The mesas are capped and the major drainages are mantled with Quaternary alluvial deposits. These deposits represent a variety of substrates, but none are separated in the soil mapping.

Soil unit 8 (Palma–Cahone–Hagerman) is found throughout Big Indian Valley, Lisbon Valley, and Lower Lisbon Valley, and on the southeastern side of East Coyote Wash. Big Indian Valley follows the strike of SW-dipping Cutler red beds, while Lisbon Valley and Lower Lisbon Valley follow the Lisbon Valley fault zone. The fault brings carbonates of the Hermosa Formation into contact with clastics of the Burro Canyon Formation. The valleys defined by the fault zone are in part filled with alluvium. The soil unit follows the physiographic form of the anticlinal and fault structures without distinction, lumping together the alluvial and rock formations. In the East Coyote Wash area and to the northwest, the soil unit mostly follows outcrops of Dakota Sandstone capped by alluvium along the southwestern flank of East Coyote Wash Syncline.

Soil unit 9 (Rizozo–Rock outcrop–Ildefonso) is developed on a diverse group of rocks including the Hermosa Formation (center of Lisbon Valley Anticline), Cutler, Chinle, Wingate, Kayenta and Navajo sediments (southwest flank of Lisbon Valley Anticline), and outcrops of Burro Canyon Formation (flanks of East Coyote Wash Syncline). Outside Lisbon Anticline, the unit is developed on Burro Canyon and Dakota rocks (Deerneck Mesa).

Figure 8-35. PC image of the northern part of Big Indian District, with all image reflectance values adjusted for removal of vegetation component according to Eq. (8-2) before combining into the PCs. Variation in color along Wingate Sandstone outcrop represents variation in reflectance of "rock alone" between bleached areas in the north and unbleached outcrops in the south (V1 = blue, V3 = green, V4 = red).

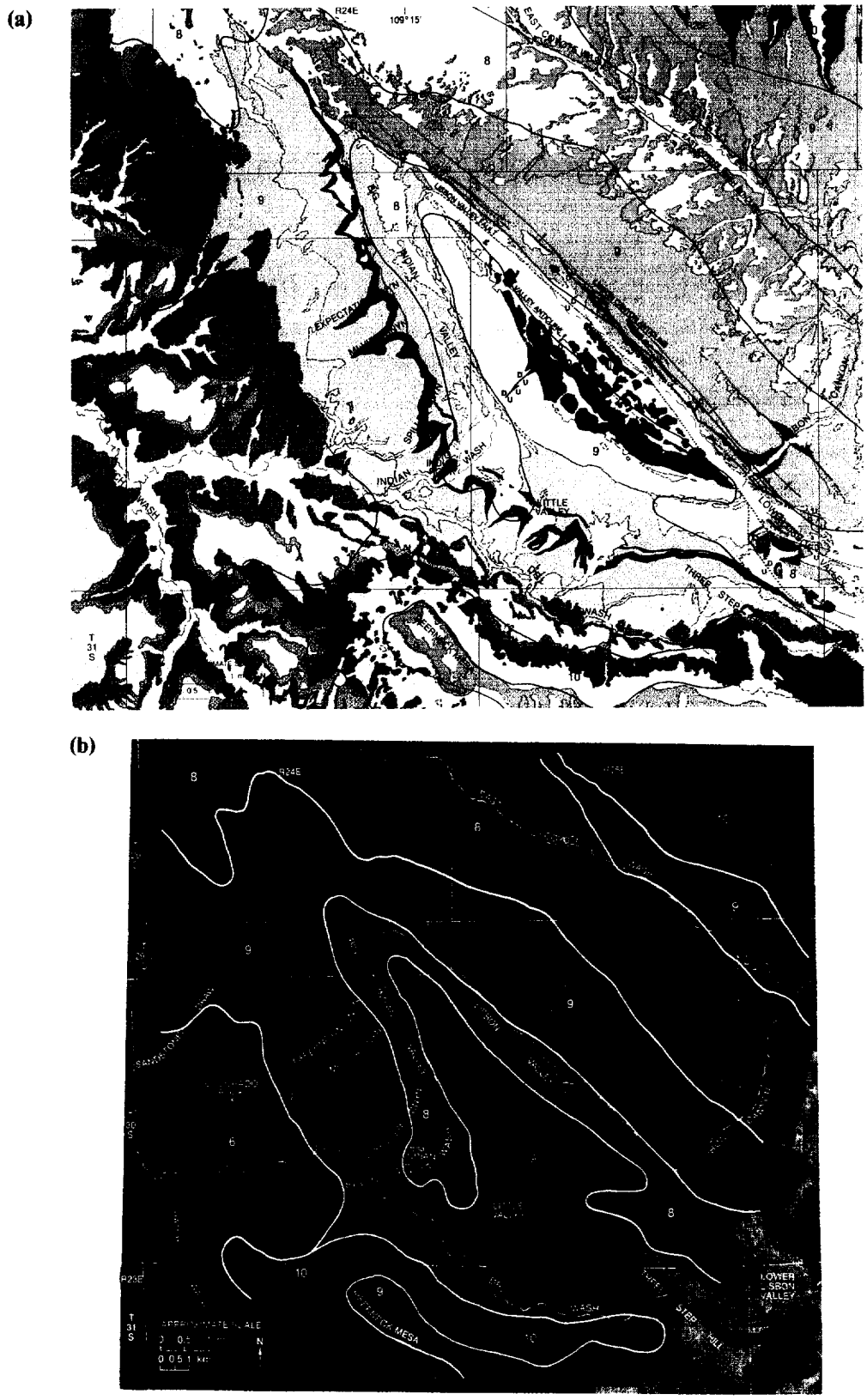

Figure 8-36. Soil units of Figure 8-3 compared to (a) geologic map (see Figure 8-10 for legend) and (b) NS-001 image data for the Lisbon Valley area: unit 6, Begay–Windwhistle–Ildefonso; unit 8, Palma–Cahone–Hagerman; unit 9, Rizozo–Rock outcrop–Ildefonso; unit 10, Ustic Torriorthent–Ustollic Calciorthid–Ustollic Haplargid

Soil unit 10 (Ustic Torriorthents–Ustollic Calciorthids–Ustollic Haplargids) is found on steep slopes flanking Deerneck Mesa, which are underlain by the Morrison Formation. Much of this unit is covered by Quaternary-age land deposits. Additional exposures of soil unit 10 are found over Burro Canyon and Morrison outcrops in the northwest corner of the map.

In Figure 8-36(b), the soil unit distribution is superposed on the NS-001 image data. Little or no systematic relationship can be identified between the two, largely reflecting the lumped and generalized nature of the soils mapping. Further subdivision of the soils distribution could be achieved from image color relations; additional subdivision might be possible if well-defined type localities for soil mapping units could be identified as a basis for image classification.

F. Landsat MSS Image Interpretation

Figure 8-37 is a PC image of the June 12, 1977 scene covering Lisbon Valley and surrounding areas (Landsat scene 20872-16540). The color assignments are V1 = red, V2 = green, V3 = blue. The eigenvector loading diagram and covariance and correlation matrices for this rendition are given in Appendix C. With these assignments, heavily tree-covered areas appear red to magenta (South Mountain of the La Sal Mountains), grassy and/or shrub-covered terrain appears blue-green (East Coyote Wash), red beds appear blue (Cedar Mesa Member of Cutler Formation along Indian Creek, and Cutler Formation red beds along Big Indian Valley), and light-colored rocks appear green and dark green to black (outcrops of Navajo Sandstone along Hart's Point, exposures of the Navajo W–NW of Big Indian Valley, and Burro Canyon sediments on the south flank of Island Mesa).

By comparing this image with the geologic map of Figure 8-10, it is possible to distinguish the major lithologic units exposed in Lisbon Anticline, including the Hermosa, Cutler, Lower Chinle (Moss Back Member), Wingate, Kayenta, and Navajo. Because of the reduced resolution (~80 m), little of the detail present in the aircraft scanner data (Figures 8-21 and 8-30) can be discerned. However, bleached and unbleached facies of the Wingate can be separated, as well as variations in appearance of the Cutler sediments along Lisbon Valley.

In East Coyote Wash, the presence of a fold structure may be inferred from the symmetrical arrangement of the drainage pattern and by the symmetrical distribution of red and brown units about a NW-trending green strip occupying the axis of this structure. None of the detailed stratigraphic relations in the Burro Canyon and Dakota sections seen in the aircraft scanner data are apparent at this resolution.

Much of the lithologic variation present in this scene is masked by an extensive vegetation cover. Outcrops largely clear of grass and trees are found only along major canyons (such as Big Indian Wash) where extensive exposures of Cutler red beds are found. Except for areas of heavy tree cover (in red/magenta), the separation of vegetation variation from lithologic variation is difficult using these data alone.

The Lisbon Valley Fault may be located where it traverses the anticline by the linear NW-trending form of Lisbon Valley, and by the truncation of important sedimentary units on the southwest flank of the anticline.

Additional structural or stratigraphic features otherwise not identified in aerial photographs, in aircraft scanner data, or by previous geologic mapping have not been recovered from these data.

G. Fraunhofer Line Discriminator Observations at Lisbon Valley

1. General. Solar-induced luminescence from natural materials is extremely feeble compared to the intensity of ordinary reflected light. Special methods are needed to study luminescence behavior in rocks under ordinary daylight field conditions. Luminescence effects are totally inseparable from ordinary reflected light in image data. Here, areas of anomalous fluorescent behavior determined by aircraft observations were located on the images, and possible common (spectral) features among these areas were sought. The Fraunhofer line depth method is used to detect luminescence (fluorescence and phosphorescence) induced in surface material by solar radiation. Luminescence detection may be used in mineral prospecting in the same way that portable ultraviolet lamps are used to detect such minerals as fluorite (CaF_2), calcite ($CaCO_3$), and secondary uranium minerals. In the Fraunhofer line depth method, the filling of Fraunhofer lines in the solar absorption spectrum because of surface luminescence is observed. These observations are conducted during the daytime, using the sun as a luminescence source. The Fraunhofer Line Discriminator (FLD) is an airborne electro-optical device that is operated as a non-imaging radiometer and permits detection of solar-stimulated luminescence several orders of magnitude below the intensity detectable by the human eye.

The luminescence is characterized in terms of a parameter called the luminescent efficiency η, defined as the ratio of luminescent intensity to incident continuum intensity. The efficiency is determined independently of the surface reflectance by experimental measurement of four quantities a, b, c, and d representing, respectively, the downward-directed incident solar continuum, the downward-directed solar continuum at the Fraunhofer line position, the upward-directed reflected plus luminescent intensity at the Fraunhofer line position, and the

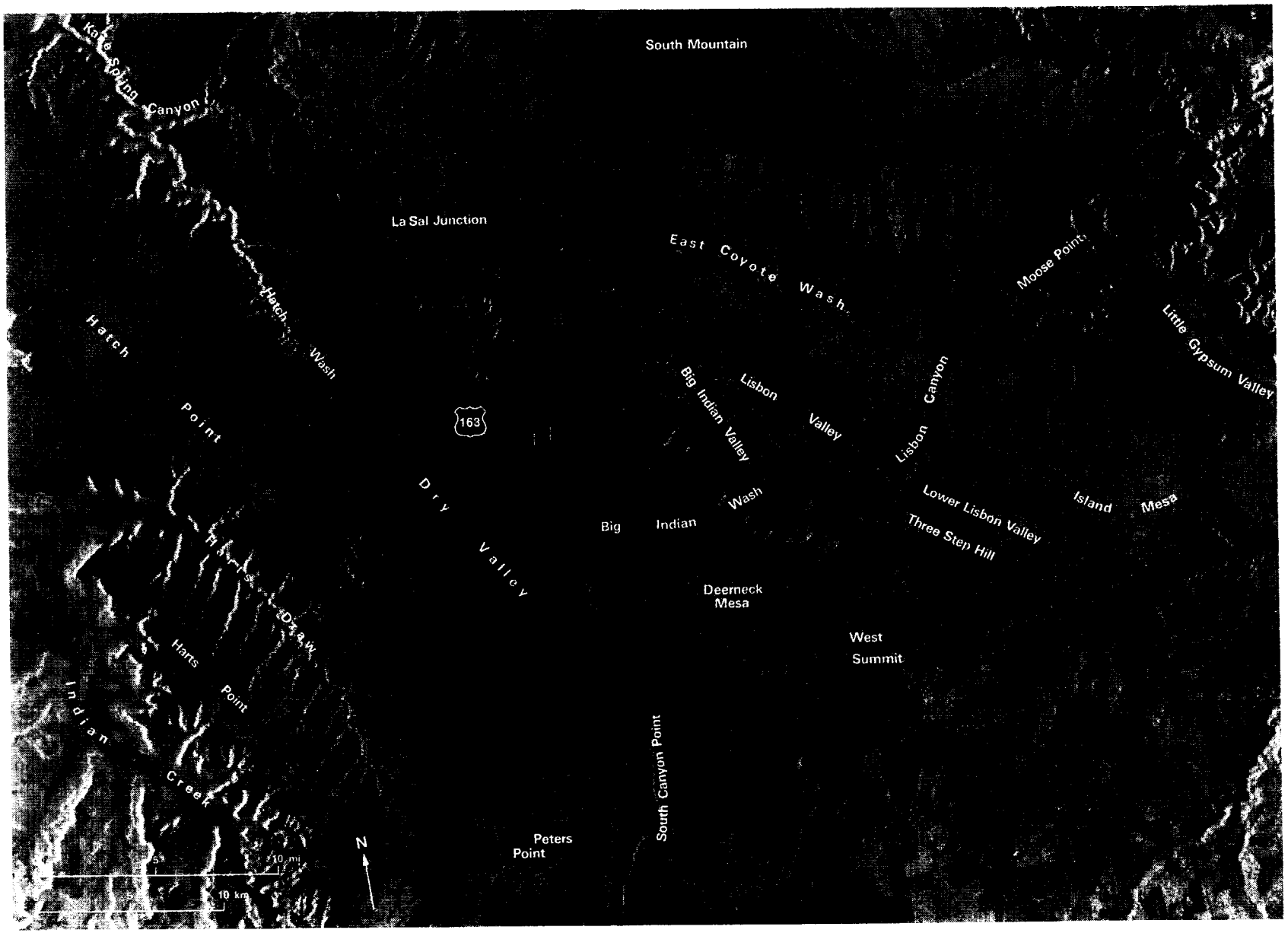

Figure 8-37. PC image of Landsat MSS scene 20872-16540, San Juan County, Utah (V1 = red, V2 = green, V3 = blue)

upward-directed reflected plus luminescent continuum intensity. These quantities are defined in Figure 8-38. The ratio η is given by

$$\eta = \frac{1}{a-b}\left(c - \frac{bd}{a}\right)$$

and independent of ρ, the surface reflectance (Watson and Hemphill, 1976).

Luminescence efficiency η is characterized by a scale given in terms of rhodamine WT dye equivalent luminescence. Slater's (1980) empirical relation between η and dye concentration in water is

$$\eta = 2.75 \times 10^{-3} C$$

where C is in ppb. Thus for C on the order of one ppb, the luminescence efficiency is three orders of magnitude less than the efficiency of ordinary surface reflectance.

Details of the FLD operation and data reduction problem are given in the Technical Appendix, Section 14. For additional material and reviews of earlier work, refer to papers by Hemphill and Settle (1981), Slater (1980), and Watson and Hemphill (1976).

2. Description of experiment. The U.S. Geological Survey used an advanced FLD system operating at two Fraunhofer wavelengths, 0.4861 and 0.5890 μm, at Lisbon Anticline (Big Indian Valley) to detect possible luminescence effects from uranium mineralization (Theisen and Watson, 1979). These observations were conducted as part of the Geosat uranium test case program and in conjunction with Atlas Minerals, the Geosat site-controlling company. The Big Indian area was overflown on June 12, 1978 at an altitude of 2382 m (7815 ft) and at a speed of 45 m/s (100 mi/h). Because of the experimental arrangement, observations at the two wavelengths were done in series. The system operated at 0.4861 μm during the first flight (9:15 A.M., MDT) and 0.5890 μm during the second flight (10:13 A.M., MDT). Additional features of the experimental arrangement are described below.

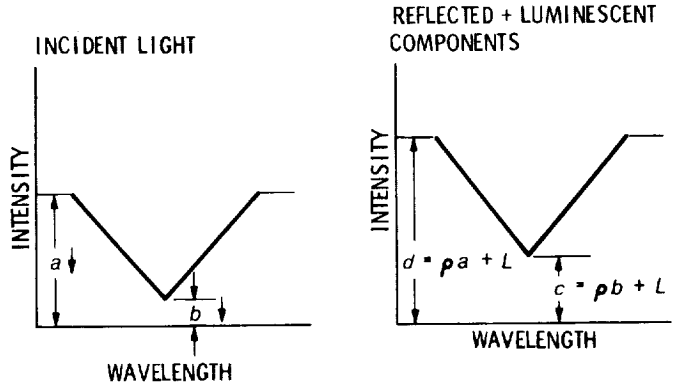

Figure 8-38. Definition of the quantities *a*, *b*, *c*, *d* measured in the FLD experiment. *L* is the intensity of luminescent energy and ρ is the surface reflectance.

Radiation from the surface is directed to the FLD optical head by an oscillating mirror that scans a 37° total angular field of view (FOV) centered about the nadir with an instantaneous circular field of view (IFOV) of 1°. The 37° angular field is covered in an observation period of 1s, representing an angular mirror motion of 0.65 rad/s. Observations of the energies *a*, *b*, *c*, and *d* are carried out sequentially, each for a duration of 6 ms. An additional 6 ms is required to return the mirror to its initial position for a new sweep. For the aircraft velocity and altitude quoted under perfectly collimated flight conditions, the FLD ground track provides complete areal coverage over the swath. Deviations from these flight conditions can produce gaps or overlap in the ground coverage. A detailed drawing of the footprint is shown in Figure 8-39. Here, for ease of calculation, the angular IFOV was taken to be 1° by 1° *square*. At the edge of the scan swath width, the footprint is approximately 46 m wide and narrows to 41 m beneath the aircraft. A 6-ms observation time smears the footprint of observation for the quantities *c* and *d* by 10.26 m at the edge and 9.1 m beneath the aircraft. For any complete sequence, the area of overlap common to *c* and *d* for one observation cycle is roughly 88 percent of the smeared observation footprint of either. The noncoincidence of footprints *c* and *d* may lead to anomalous values of the luminescence efficiency, especially in regions of complicated topography containing shadows or rapidly varying surface reflectance. Quantitative assessment of anomalous behavior of this type is not easily made with the observations at hand. A cursory examination of the data for Lisbon Valley in Theisen and Watson (1979) discloses no obvious correlation between topography and the distribution of anomalous FLD behavior. The magnitude of error from this source is probably less than 1.16 to 1.54 ppb rhodamine WT, which is typical of the maximum anomaly encountered in the rough terrain overflown at that site. To avoid these problems, the largest anomalies are considered here and those of a lesser magnitude are ignored.

3. Discussion of the image data base. Locations of spots in the Big Indian area showing anomalous luminescence greater than 1.93 ppb rhodomine WT dye equivalent are plotted as dots inside circles on an NS-001 PC image of this area (Figure 8-40). The PCs used were completed from an 8 by 8 covariance matrix formed from areal sampling of eight spectral channels

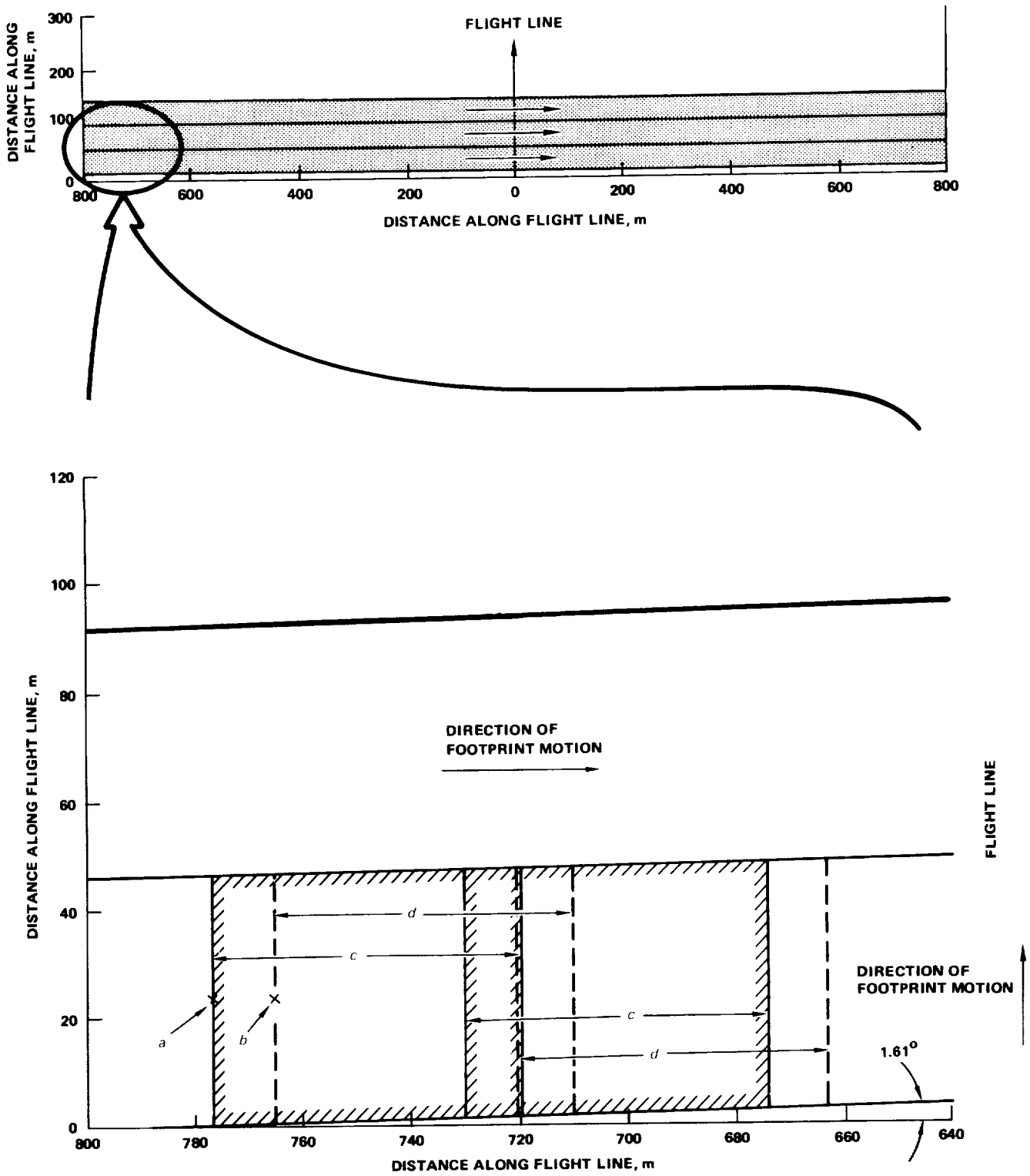

Figure 8-39. Ground track of the FLD for perfectly collimated aircraft track calculated for the following instrument and flight parameters: angular FOV = 1° by 1°; scan time for full mirror deflection = 1 s; sample time per channel = 6 ms; operating altitude = 2832 m; aircraft velocity = 45 m/s. Centers of the IFOVs at beginning of sampling time for each channel are *a* = center of IFOV during upward-looking continuum measurement, *b* = center of IFOV during upward-looking Fraunhofer line measurement, *c* = center of IFOV for downward line measurement, *d* = center of IFOV for downward continuum measurement. Smeared footprints for *c* and *d* only are shown.

(i.e., including the thermal channel) in line 5 of the August 1979 Lisbon Valley flight. The color assignments are V2 = green, V3 = blue, V4 = red. The eigenvalues and eigenvectors for the first four PCs are given in Table 8-12. Collectively, V2, V3, V4 account for 16 percent of the variance of the eight variates. The physical meaning of these components may be difficult to establish, but the color discrimination of rock units achieved is good. Geologic contacts shown illustrate some of the separations possible. From Table 8-12, the component V2 is heavily weighted on channel 8 and thus represents thermal radiance. In this image the Kayenta Formation (Jk) (consisting of tree-covered red, purple, and maroon sandstones), outcrops of Cutler Formation red beds (Pc) and grassy areas of alluvium, and material with Cutler red bed sources (Qeal) are all displayed in green. Component V3 is strongly weighted on channels 4 and 5, signifying a large contribution from vegetation. Some tree-covered areas and alluvial spots with green grass are represented in blue. For eigenvector components of significant magnitude, component V4 is positively weighted in channels 1 and 2, negatively weighted in 6 and 7, and positively weighted in 8. Empirically, bright outcrops of bleached Wingate Sandstone (Ꞧw), Navajo Sandstone (Jn), green Moss Back sandstone (Ꞧcl), and mine tailings are bright red in the image, signifying a dominance of component V4 in the representation of these cover types.

4. Registration of data to the image base and analysis of anomaly distributions. Accurate transfer of data points, representing anomalous behavior, to this image (Figure 8-40) had to be accomplished in two steps. Using the aerial photograph with the luminescence value overlay given in Theisen and Watson (1979), selected data points were first transferred to available CIR photographs of the area using a Zeiss Zoom Transfer Scope. This step reduced clutter and helped match scales between photographs and images. Next the data from this intermediate photographic base were transferred to the image. Repeated trials of the process were carried out to check the positions obtained. The locations shown are believed to lie within the circles indicated, which focus on the center point as the actual location of an anomaly. Even so, systematic differences appear to occur in some places between positions of anomalies reported by Theisen and Watson (1979) and the points obtained here. The best example of this is at Small Fry Mine, where these authors note (p. 7) that "... location C is a uranium ore stockpile from the Small Fry Mine which shows [η] values ranging from 2.70 to 3.08 ppb." The pattern of anomalous points found here has the elongate shape of this dump but is displaced 200 m south. No other anomaly in the Big Indian Wash area has a geometrically recognizable pattern that can be compared to geologic or cultural features. Location accuracies for these features are thus unknown. The anomalies are a few image pixels (one pixel $\simeq$ 15 $\times$ 15 m) in size. Locations of anomalous points to this accuracy are thus required before a detailed pixel-by-pixel analysis is worthwhile. It does not appear possible to transfer this accuracy from the data available.

The color relations for anomalies are dispersed among green, red, yellow, and blue image units. A similar examination using the 7-channel PC image of Figure 8-21 revealed an equally diverse array of color associations, but no systematic relationships.

5. Conclusion. The image data have not been useful in providing insights to the geologic meaning of the FLD anomalies, nor have the FLD results been useful in interpreting the image data. This situation might improve if the anomalies could be located with greater accuracy on the image data and if the mineralogical, botanical, or chemical origin of the anomalous behavior were better understood and correlated with rock or vegetation reflectance properties. A field procedure for observation of luminescent behavior (either active or passive) would be of great value in further geologic evaluation of the airborne FLD measurements.

Table 8-12. Eigenvalues and eigenvectors for PC transform of the NS-001 image, line 5, Lisbon Valley

Eigenvalue (%)	Eigenvector (color)	Channel							
		1	2	3	4	5	6	7	8
11,421 (84)	V1	0.27	0.30	0.31	0.32	0.35	0.39	0.40	0.40
1,165 (9)	V2 (G)	−0.30	0.29	0.21	0.22	−0.09	−0.01	0.01	0.85
644 (5)	V3 (B)	−0.30	−0.24	0.28	0.65	0.54	0.09	−0.24	−0.03
255 (2)	V4 (R)	0.51	0.40	0.13	0.16	−0.08	−0.37	−0.54	0.32

Davenport, W. B., Jr., and W. L. Root (1958). *An introduction to the theory of random signals and noise.* New York: McGraw–Hill, 96–99.

Davidson, E. S. (1967). Geology of the Circle Cliffs area, Garfield and Kane Counties, Utah. *U.S. Geol. Surv. Bull. 1229.*

Dixon, W. I. (Ed.) (1974). *Biomedical computer programs.* Los Angeles: University of California Press, UCLA, Health Sciences Facility, Department of Biological Mathematics, School of Medicine.

Donovan, T. J. (1974). Petroleum microseepage at Cement, Oklahoma: Evidence and mechanism. *AAPG Bull., 58*(3), 429–446.

Elston, D. P., and E. R. Landis (1960). Pre-Cutler unconformities and early growth of the Paradox Valley and Gypsum Valley salt anticlines, Colorado. *Short papers in the geological sciences, U.S. Geol. Surv. Prof. Pap. 400-B,* B261–B265.

Feiveson, A. H. (1979). Estimating crop proportions from remotely sensed data. *The LACIE Symposium, Proceedings of the Technical Sessions* (Vol. II). Houston: NASA–Johnson Space Center, 633–644.

Ferguson, J. D. (1979a). Subsurface alteration and mineralization of Permian red beds overlying several oil fields in southern Oklahoma, Part 1. *Shale Shaker Digest, J. Oklahoma City Geol. Soc., 29*(8), 172–178.

Ferguson, J. D. (1979b). Subsurface alteration and mineralization of Permian red beds overlying several oil fields in southern Oklahoma, Part 2. *Shale Shaker Digest, J. Oklahoma City Geol. Soc., 29*(9), 200–208.

Ferguson, J. D. (1981). Formation of diagenetic alteration zones by leaking reservoir hydrocarbons over three oil fields in Oklahoma. *AAPG Bull., 65*(34), 924. (Abstract)

Field, C. W., and M. L. Jensen (1960). Sulfur isotopes and the origin of sandstone type uranium deposits. *USAEC Biennial Rep., 1959–1960.*

Gabelman, J. W. (1970). Speculations on the uranium ore fluid. *Uranium exploration geology.* Vienna: International Atomic Energy Agency, 315–330. (Panel proceedings)

Gabelman, J. W., and W. H. Boyer (1958). Relation of uranium deposits to feeder structures, associated alteration and mineral zones. *Proceedings of the United Nations International Conference on the Peaceful Uses of Atomic Energy* (Vol. 2), 338–350.

Garrels, R. M., and C. L. Christ (1965). *Solutions, minerals, and equilibria.* New York: Harper & Row.

Gates, D. M., H. J. Keegan, J. C. Schleter, and V. R. Weidner (1965). Spectral properties of plants. *App. Optics, 4*(1), 11–20.

Gnanadesikan, R. (1977). *Methods for statistical data analysis of multivariate observations.* New York: John Wiley & Sons.

Gross, E. B. (1956). Mineralogy and paragenesis of the uranium ore, Mi Vida Mine, San Juan County, Utah. *Econ. Geol., 51,* 632–648.

Gruner, J. W. (1956). Concentration of uranium in sediments by multiple migration-accretion. *Econ. Geol., 51*(6), 495–520.

References

Adler, H. H. (1970). Interpretation of color relations in sandstone as a guide to uranium exploration and ore genesis. *Uranium Exploration Geology Proceedings* (Publication PL-391/13). International Atomic Energy Agency, 331–344.

Bender, M. L. (1972). Carbon isotope formation. In R. W. Fairbridge (Ed.), *The encyclopedia of geochemistry and environmental sciences* (Vol. IVa). Stroudsburg, Pennsylvania: Dowden, Hutchinson and Ross.

Bohn, R. T. (1977). A subsurface correlation of Permian–Triassic strata in Lisbon Valley, Utah. *Brigham Young Univ. Sci. Bull. Geol. Studies, 24*(2), 103–116.

Breger, I. A., and M. Deul (1959). Association of uranium with carbonaceous materials, with special reference to Temple Mountain region. *U.S. Geol. Surv. Prof. Pap. 320*, Pt. 12, 139–149.

Campbell, J. A. (1981). Uranium in Permian Cutler Formation, Lisbon Valley, San Juan County, Utah. *AAPG Bull., 65*(34), 556. (Abstract)

Carter, W. D. (1956). The Burro Canyon–Dakota contact in the Mt. Peale No. 1 quadrangle, western Colorado and eastern Utah. *Intermountain Assoc. Petrol. Geol. 7th Ann. Field Conf.*, 1956, 113–115.

Carter, W. D., and J. L. Gualtieri (1957a). Preliminary geologic map of the Mount Peale 1 SE quadrangle, Montrose County, Colorado, and San Juan County, Utah. *U.S. Geol. Surv. Min. Invest. Field Studies Map MF-123.*

Carter, W. D., and J. L. Gualtieri (1957b). Preliminary geologic map of the Mount Peale 1 SW quadrangle, San Juan County, Utah. *U.S. Geol. Surv. Min. Invest. Field Studies Map MF-124.*

Carter, W. D., and J. L. Gualtieri (1965). Geology and uranium–vanadium deposits of the La Sal quadrangle, San Juan County, Utah and Montrose County, Colorado. *U.S. Geol. Surv. Prof. Pap. 508.*

Collins, A. G. (1975). Geochemistry of oil field waters. *Developments in petroleum science* (Vol. 1). New York: Elsevier Scientific Publishing Company.

Conel, J. E., M. J. Abrams, and A. F. H. Goetz (1978). *A study of alteration associated with uranium occurrences in sandstone and its detection by remote sensing methods* (JPL Publication 78-66, Vol. I). Pasadena, California: Jet Propulsion Laboratory.

Craig, L. C., and D. D. Dickey (1956). Jurassic strata of southeastern Utah and southwestern Colorado. *Intermountain Assoc. Petrol. Geol., 7th Ann. Field Conf.*, 1956, 93–104.

Acknowledgments

The authors wish to thank Preston L. Niesen, Atlas Minerals, Division of Atlas Corporation, Moab, Utah, for his help during the investigation. He spent time in the field, and provided maps, specimens, and numerous hours of consultation. His support, encouragement, and geologic knowledge of the Lisbon Valley area were of great value.

Dr. John Gabelman, Utah International, Inc., suggested the Lisbon Valley area as one of the NASA/Geosat test sites for uranium. Many discussions of the geology of uranium and of the Lisbon Valley area have been of great value and are gratefully acknowledged.

The technical help and support of the following people at the Jet Propulsion Laboratory are greatly appreciated: Helen Paley, Richard Machida, Kathy Baird, Elsa Abbott, Daryl Madura, Mustafa Ukayli, Bob Dewar, Anne Kahle, Barry Rock, Alan Gillespie, and Alex Goetz.

James Soha and Cathy LeVine of the JPL Image Processing Laboratory devised the method of vegetation spectrum removal and image analysis presented in the text for the Bendix 24-channel data.

Brad Govreau and Dr. Jerry Smith of Union Oil Company supplied the samples of oil and gas used for isotope analyses. Their cooperation and the cooperation of Union Oil Company is gratefully acknowledged.

Cliff Franklin, Bureau of Land Management, Moab, Utah, provided preliminary vegetation maps used in these studies. His release of the data prior to formal publication is gratefully recognized. Any misinterpretation of these data, of course, is the responsibility of the present authors.

Dr. Mark Settle of NASA Headquarters, Terry Offield of the U.S. Geological Survey, Robert Scott of the Department of Natural Resources, state of Washington, and William Buckingham of Gulf Research and Development reviewed the manuscript and offered many important suggestions.

Duane Lammers of the Soil Conservation Service, Moab, Utah, also made available preliminary soil maps and soil unit descriptions for the site. His cooperation is acknowledged.

Finally, the senior author wishes to thank his wife, Cheryl, for her help during the course of this work.

to the extent that the linear relationship holds and is employed.

C. Problems for Future Research

The following topics need additional study:

(1) Field and scanner spectral measurements should be used to establish precisely the functional nature that may be expected for a scanner calibration relationship under prescribed observation conditions. This includes removal of atmospheric effects by empirical methods using image data alone as well as theoretical modeling of the actual corrections required.

(2) A method allowing geometric rectification of aircraft multispectral image data based on detailed variations in flight path needs to be developed. Accurate detailed image rectification would greatly facilitate comparison with existing topographic and geologic data largely by eliminating the need for manual correction. This methodology would most naturally incorporate continuous onboard aircraft position and attitude data and air speed to allow "instantaneous" determination of the correction factors needed.

(3) Methods for comparing the "information content" of the image data sets need to be developed beyond those that involve purely personal selectivity. This is a composite problem combining:

   (a) Statistical problems of discrimination and classification.

   (b) Methods of color display and separation.

   (c) Human physiology as a factor in the perception of color differences.

diagram. The tie lines in these diagrams represent proportions directly. Examples are presented in Appendix E of the use of these two diagrams for analysis of proportions in simple two-component mixing problems involving sandstone and tree cover.

3. FLD observations. U.S. Geological Survey FLD observations over the Big Indian District were analyzed and compared to image data. No correlation was found between anomalous FLD behavior and specific color units in image data. Analysis was complicated by uncertainties in location of the initial anomalies and by an uncertain noise level in the measurements related to the method of data sampling.

4. Landsat MSS images. Landsat data for the Lisbon Valley area were examined. At 80-m resolution, it was possible to determine the structure of the anticline and to discriminate the major formations present. Bleached and unbleached Wingate facies could be separated. No additional geologic features not otherwise reported were discovered from these images.

XI. Conclusions for Remote Sensing Analysis

A. Analysis of the Lisbon Valley Images and Photographs

The following conclusions were made from the investigations:

(1) High-resolution and stereoscopic coverage improved the geologic interpretation possible for all problems studied. The stereoscopic color aerial photographs were the best for resolving stratigraphic and structural problems in the area.

(2) Images at the resolution available provided a good synoptic view that could be adjusted by the color display to highlight important features. Availability of scanner data at a resolution comparable to aerial photographs (1 m) and in stereoscopic coverage would materially enhance utility of images for study of geologic problems.

(3) While the Bendix 24-channel and NS-001 scanners have comparable distributions of channels in wavelengths, the Bendix data were more valuable geologically because of the high spatial resolution (estimated at 7 m versus 15 m). Both scanner systems provided good separations of geologic units.

(4) The canonical transformation method produced a clearer separation of bleached and unbleached Wingate units than the principal components or raw band composites of the same data. In general, the information content may be expected to improve as the number of data channels increases. However, lacking quantitative rules to gauge the utility of one image product versus another, these comparisons remain qualitative.

B. Remote Sensing Radiance Measurements

The following conclusions were made from the remote sensing measurements:

(1) The (calibration) relationship between scanner DN and surface reflectance is approximately linear over the range of intrinsic brightness studied in these data.

(2) The relationship between scanner DN values and ground reflectance data is highly linear for most channels but quasi-linear to parabolic for some. The sources of these variations are not understood; the variations may result from scatter in the field data rather than from nonlinear instrument behavior or atmospheric interaction.

(3) The spectra obtained by analysis of the image data agree qualitatively with the field data. Since the scanner and the PFRS data provide samples of vastly different fields of view, precise agreement would not be expected. Both data sets contain significant variations in reflectance values from place to place. This uncertainty for scanner data results both from uncertainties in the calibration curve and from scene scatter. The scatter, which results from variations in surface orientation, vegetation cover, shadows, and inhomogeneous rock type, is inherent in the use of multispectral scanner data. For a specified field of view scanners limit the extent to which spectral detail can be recovered from the data regardless of the radiometric precision achieved.

(4) An advantage is not gained by calibrating scanner radiance before image display because the linear calibration transform is usually superseded by subsequent scaling and/or stretching transforms used for image display. The production of CRCs entails a nonlinear transformation for which application of a calibration step is actually inappropriate.

(5) A linear calibration relationship has the following useful consequences for PC or canonical transformation analysis of image data:

  (a) The estimated covariance matrix is independent of the offset term in the calibration equation.

  (b) The correlation matrix derived from the estimated covariance matrix is independent of both the gain and offset terms and may thus be thought of as representative of average (Lambertian) ground reflectance directly.

(6) The images based on use of the correlation matrix thus are independent of atmospheric and instrumental effects,

Oil and gas deposits in Lisbon Anticline are found in partially fault-bounded dome-shaped reservoirs in Mississippian dolomites beneath the Paradox salt member of the Hermosa Formation. The reservoirs are fault bounded and are separated by a graben into which salt flowage has occurred to produce the anticlinal structure. Faults bounding the graben do not extend to the surface. The graben does not contain major accumulations of gas or condensate, although productive horizons of the Paradox are known. Hermosa rocks above the salt interval are productive in Lisbon Canyon Anticline on the northeastern side of Lisbon Valley Fault.

The major uranium mineralization of the Big Indian District together with bleached Wingate strata are completely enclosed within the oil- and gas-producing limits of these deeper reservoirs or associated source rocks. The approximate coincidence of bleaching, uranium mineralization, and oil and gas production suggests that some causal relationship may exist among them. The significance of a coincidence for these limits is uncertain because earlier distributions of petroleum and gas in the subsurface were probably much more wide spread, having escaped with breaching of the anticline. The remaining sandstone alteration near the anticlinal crest coincides with uranium distribution and roughly with the distribution of deeper oil and gas accumulations. Similar relations between bleaching of red sandstones in anticlines over oil and gas reservoirs have been observed in anticlines in Oklahoma, but no uranium deposits have thus far been discovered in these structures.

5. Isotope studies. Carbon and sulfur isotope measurements were made on organic carbon, on calcite cement, on ore stage pyrite from Moss Back ore bodies, and on oil (condensate) and gas samples from all major producing oil and gas reservoirs and horizons in the anticline. $\delta^{13}C$ values for reservoir CO_2 and ore-body calcite are similar but also do not differ significantly from those for present atmospheric CO_2 or freshwater limestone. $\delta^{13}C$ values for condensate match those for organic carbon in the ore samples, but these latter values correspond closely with those for land plants. All of the $\delta^{34}S$ numbers obtained for ore samples in the present study and in previous investigations by Field and Jensen (1960), Miller and Kulp (1963), and Schmitt (1968) may be explained by simple mixing of indigenous isotopically light sulfur of local bacterial origin with isotopically heavier introduced sulfur of petroleum or petroleum gas origin. These measurements are consistent with a petroleum derivation of the carbon and sulfur in the ore bodies, but they do not establish that such mixing actually took place.

D. Other Remote Sensing Measurements and Analyses

1. Spectral reflectance. The NS-001 image data were calibrated from ground reflectance measurements and used to calculate image-derived spectra of multiple-pixel areas. There is an inherent uncertainty in any image spectrum that relates to the scatter of points in the calibration curve and to the scatter in the radiance values over the test areas. In general, scatter is least over flat, uniformly vegetated areas and greatest over rock or mixed vegetation and rock outcrops. From the calibrated image spectra, red and purple rocks show broad absorptions due to Fe^{+3} at 0.8 to 0.9 μm; in addition, the Fe^{+3} charge transfer band below 0.7 μm can be discriminated. From green rocks, a broad absorption probably due to Fe^{+2} near 1.0 μm is recovered. The presence of chlorophyll absorption introduces a sharp kink at 0.7 μm in the image reflectance curves, which is distinct from the absorption in that region arising from Fe^{+3}. Curiously, chlorophyll absorptions are not recovered from the image spectrum of dense piñon–juniper tree cover. This may perhaps arise from the presence of a large shadow component and indicate an actual small projected area of green material in this cover type. Dormant grasses or dead vegetation reduce the observed spectral reflectance at all wavelengths. Chlorophyll absorptions are not observed in areas where dead or dormant vegetation is thought to be present.

2. Vegetation signatures and unmixing models. The Lisbon Valley area contains a 10 to 70 percent cover of evergreens, shrubs, and grasses. The vegetation contribution has been analyzed two ways:

(1) A simple two-component photometric mixing model was used to estimate percent "green" cover directly. Training areas representing 100 percent piñon–juniper cover and 100 percent Wingate outcrop were used to obtain the end-member spectral signatures in the 0.65-μm chlorophyll band. Partly vegetated areas have intermediate reflectances, which are linearly related to the percent tree cover. An example is shown (Figure 8-33) of an image display giving percent tree cover over Wingate Sandstone outcrops.

(2) Analysis of the cover with more than two components can be carried out using a new type of diagram called the PC diagram or, an equivalent in terms of the canonical coordinates, the canonical scatter diagram. The PC representations of spectral groups can be thought of as analogous to tristimulus values in a chromaticity diagram. Thus, for simple mixtures with two end members, each member plots as a separate point in a three-space, representing three components. Mixtures fall on tie lines between the end members, with position dependent on fractional areal abundance. These arguments may be extended to higher dimensions and larger numbers of groups. The canonical scatter plot is obtained computationally with the BMD discriminant analysis program. These diagrams possess the same properties as the PC

NS-001 data (band-ratios 2/3, 2/4, 4/5) designed to separate rock outcrops from vegetation cover (Figure 8-23). Detailed image analysis allowed subdivision of the Cretaceous Burro Canyon Formation into three previously unmapped subunits. The structure of this fold is well defined in the images. The new image units are not easily mapped on aerial photographs. In general, they correspond to light-colored and red bed subunits of the upper Burro Canyon section.

3. Distribution of Wingate alteration. A canonical transform image of the Bendix 24-channel data was prepared from 10 spectral channels covering the wavelength interval 0.46 to 2.36 μm. The scanner provided an effective ground resolution of 7 m, more than twice that of the NS-001 images at 15 m. The canonical transform separates desired spectral groups (bleached versus unbleached) in an optimum statistical way. Five subunits of the Wingate can be mapped from rock color variations. A sixth image unit represents shadowed ground. No stratigraphic significance can be ascribed to these subdivisions on the basis of the image data alone, and different cosmetic stretches applied to the images change the distribution of units in detail.

To provide a basis for image interpretation, a new photogeologic analysis of the Wingate section was prepared from high-resolution (1-m) stereoscopic color aerial photographs. Six informal stratigraphic units were identified that subdivide the section into three major stratigraphic intervals. These crop out successively from north to south in the Big Indian District: (1) an upper unit consisting of predominantly bleached rock, feathering to the south and overlying (2) a middle unit of thinly interlayered bleached and pigmented strata called the laminated unit, and (3) a lower unit of massively bedded unaltered (red) sandstone. The thinly bedded laminated unit may persist unbroken throughout all exposures, merging in northern and southern parts with prevasively bleached rocks. Bleaching stratigraphically is confined principally to the Wingate section. An interfingering relationship with the overlying Kayenta Formation exists and makes placement of a well-defined boundary between these two formations uncertain.

The principal upper Wingate unit identified as bleached is identical in both image and photogeologic interpretations. Since there is less correspondence between the remaining units, the image units for the most part have no conventional stratigraphic significance. They may represent a composite of cover types (trees, shrubs, grass, soil, or outcrop), alteration effects unrecognized in the aerial photographic interpretations that transgress stratigraphic boundaries; or, they may be a special effect of the image processing.

Stereoscopic coverage in the aerial photographs was essential in understanding the geology and the image interpretations. The NS-001 image data at 15-m resolution are useful for highlighting the distribution of bleached and unbleached rocks, but the photographs with higher surface resolution were essential in providing an actual stratigraphic and structural analysis of this problem.

A composite interpretation from analysis of aerial photographs and images shows the northern and southern Wingate outcrops to be bleached and a middle interval approximately 5.5 mi long to be unaltered. A thin stratigraphic interval of partly bleached strata traverses the middle section in the upper part of the formation.

Bleached strata in the anticline occupy high outcrops 6200 to 6400 ft in elevation. Structurally, the bleached strata lie near the Lisbon Valley Fault and near the crest of Lisbon Valley Anticline. While much of the bleached rock has been removed by erosion, it appears likely that bleached sandstone occupied a cap-like distribution structurally high in the anticline. The bleached strata may have tilted slightly after the time of bleaching.

4. Distribution of uranium and of oil and gas with respect to bleached outcrops. In the Big Indian District, Moss Back uranium mineralization occupies linear trends along fluvial channels cut in the Cutler subcrop. Major Cutler Formation ore is confined to sugar-textured sandstone units in the formation adjacent to and beneath the Moss Back uranium ore. Moss Back ore bodies in the southern part of the anticline are distributed irregularly. Lekas and Dahl (1956) showed that all Moss Back uranium ore is confined between the 6200- to 6700-ft elevation contours drawn on the top of the Cutler Formation; however, the new Velvet (2) ore body lies at approximately 5500 ft. The stratigraphic position of this ore body is uncertain. Analysis of cross sections indicates that it may lie either in Moss Back, Cutler, or possibly Moenkopi rocks.

Uranium mineralization in plan view is always overlain by bleached or partly bleached Wingate strata. In the transition zone near Expectation and Mi Vida Canyons, the Standard, Louise, and Mi Vida ore bodies fall below the partly bleached laminated interval. From analysis of cross sections, bleached strata were removed by erosion in this interval. Thus, the spatial coincidence of outcropping totally bleached strata and uranium mineralization was probably more complete in the past than at present.

From analysis of cross sections, the mineralized Moss Back/Cutler intervals fall slightly above or below the boundary between bleached and unbleached strata in the anticline. The boundary of bleaching, however, is only approximate as determined by projection from the photogeologic data and is not geometrically constrained apart from the surface exposures.

for the flight times on the surface and at altitude are unknown. An analytical study shows that a simple linear relationship is approximately preserved by these empirical atmospheric corrections relating the adjusted scanner radiance and average reflectance properties of surface resolution elements. The gain and offset constants in this calibration equation combine together the atmospheric and instrumental parameters of the model. The calibration constants may be fixed by comparison with the field reflectance data (Appendix B). Thus, the scanner radiance may be transformed to a pixel-averaged nondirectional surface reflectance. The reflectance (a nondimensional parameter) is a proportionality constant between radiance incident at the scanner and encoded voltage. However, rescaling and cosmetic stretching transformations usually required for image display either as raw bands or ratios generally distort calibrated image data and do not impart any fundamental significance to the images so adjusted. Ratio transformations are in general nonlinear transformations.

The linear (or nearly so) relationship between gradient-corrected radiance and ground reflectance leads to the important result that the correlation matrix computed over the scene is independent of both the gain and offset factors. Thus, the relationship is computationally equivalent to the correlation matrix that would be obtained if it were computed from the average Lambertian surface reflectance directly.

PCs based on eigenvectors from the correlation matrix are independent of gain and offset factors. PC images based on the correlation matrix can be made independent of all atmospheric and instrumental effects utilizing the linear model. A comparison of results obtained using the covariance matrix shows that computationally the results based on the covariance and the correlation procedures are highly correlated and essentially equivalent, although the covariance formally contains products of gain factors as multiples to each matrix element. These multiplying factors rotate and expand or contract the ellipsoid describing the data swarm with respect to the original (radiance) axes. Coincidence of the covariance and correlation results shows that the cross products in gain factors are approximately equal element for element in the matrices.

PC images, constructed from three of the first four variables, separate adequately spectrally different cover types on an average basis. The PC method is a self-consistent linear reduction technique. The PCs themselves are uncorrelated and describe orientations of the principal directions of the scatter ellipse, ordered according to decreasing variance. Marginal enhancements (stretches) applied to separate components expand the data swarm and separate the points in radiance space. This expansion is the basis of the decorrelation enhancement process which also entails an inverse rotation to original axes. Here the actual PCs are used and the inverse transformation is ignored because the latter transformation does not help to separate the groups. The PC transformation (plus the usual marginal enhancements required for image display) provides an optimum method for image analysis. First, the linear reduction property of the transformation allows the data from all wavelengths to be included. Second, the components corrected for angular-dependent atmospheric effects are representative of average ground reflectance properties directly; field calibration is unnecessary for the transformations based on the correlation matrix. Third, marginal enhancements required for artistic image construction stretch the separation of spectral groups in radiance space and thus enhance these characteristics for display. A similar method based on the canonical transform provides for optimum separation of specified groups in the data swarm.

C. Geological, Geochemical, and Remote Sensing Results

The NS-001 and Bendix 24-channel aircraft data have been used for geologic mapping throughout the Lisbon Valley area and for mapping in greater detail bleached (altered) and unbleached (unaltered) facies of the Wingate Sandstone.

1. Lisbon Anticline. The distribution of rock types throughout the anticline was described from PC image mosaics constructed from the second, third, and fourth components (Figure 8-21). This transformation was computed from a covariance matrix estimate from sampling flight line 6 and is referred to as transform I (Appendix C). Transform I provides an excellent separation of the bleached and unbleached facies of the Wingate throughout the anticline and a good separation of all mapped formations on the southwestern flank. Subunits of several formations can also be identified. A major unconformity separating Paleozoic and Mesozoic strata is represented. The Lisbon Valley Fault is displayed by topographic alignments and by truncation of important rock units where such units intersect the fault. Major areas of cultural disturbance (removal of tree cover for land reclamation) can be identified and easily mapped.

To improve separation of the Wingate and its informally defined subfacies from other rock units present and from each other, PC transformations were prepared from subareas of the images encompassing mainly the Wingate outcrop (Figure C-1). Transform II (Appendix C) was prepared from sampling a subarea comprising approximately 20 percent of the Wingate outcrop. These images are presented for comparison, but are not analyzed in detail. The analysis (Appendix E) shows that actual separation of points in PC space remains invariant under these two transformations or under any orthogonal transformation like them.

2. East Coyote Wash. East Coyote Wash Syncline lies northeast of Lisbon Anticline. CRC images were prepared from

and Paradox sulfur alone can account for the sulfide sulfur in Moss Back pyrite, but not for the complete range in $\delta^{34}S$ for uranium (and copper) sulfides observed by Field and Jensen (1960) and by Schmitt (1968). On a simple mixing model, this range could be accommodated by varying degrees of incorporation of local light bacteriogenic sulfur together with either indigenous or outside sources of heavier sulfur. The case for possible outside sources of crude oil and associated gases is strengthened by reports of the presence of tar residues and asphaltic sands in some deposits (Loring, 1958; P. Niesen, personal communication, 1981).

For carbon the findings were:

(1) The isotopic composition of organic (i.e., noncarbonate) carbon in Moss Back ore samples has $\delta^{13}C$ values ranging between -20 and -28, well within the range of land plants, and organic C in sediments and petroleum. It is not possible to distinguish among such sources on the basis of these measurements alone.

(2) $\delta^{13}C$ in carbonate lies within the expected range of freshwater limestone, atmospheric CO_2, and the CO_2 values for Leadville reservoir CO_2. It is not possible to distinguish among these sources on the basis of isotopic measurements alone.

The sulfur and carbon isotopic measurements on ore samples reported are consistent with the presence of outside sources of carbon and sulfur from oil and gas reservoirs beneath, but do not establish that such admixing has actually taken place.

It is possible that post-faulting (Laramide) and hence post-ore deposition seepage of petroleum has occurred along fault-associated fractures. In this case, the petroleum might be a transporting agent for uranium (Breger and Deul, 1959) but would not have an effective role in the emplacement of Triassic-age Chinle/Cutler ore bodies. The association of crude oil with uranium would then be fortuitous or, at least, be relegated to a secondary role.

X. Summary

The Geosat uranium test site at Lisbon Valley represented a unique opportunity to apply remote sensing techniques to mapping problems in a major sandstone uranium district. The structural setting, lithologic diversity, presence of mappable alteration, and generally good rock exposures enhanced these investigations and provided excellent targets for application of the methods. Aircraft scanner images have been used to map for the first time the distribution of altered rocks in the area. These distributions have been related spatially to the distribution of uranium ore bodies and oil and gas accumulations or petroleum source rocks present in the subsurface. The geologic relationships are emphasized in the main body of the report. Developments in the remote sensing formalism that resulted from this work are included in Appendixes A–F. These appendixes, summarized below, cover data reduction methods, image calibration, vegetation/rock mixing models, and PC analysis.

A. Geologic Setting

Lisbon Anticline in southeastern Utah is a breached diapiric salt structure developed in Paleozoic and Mesozoic sediments. The anticline is the locus of major sandstone host uranium deposits in the Moss Back Member of the Triassic Chinle Formation and the Permian Cutler Formation. The host sediments crop out on the southwestern flank of the anticline, but the mineralized rocks themselves do not and are in general overlain by 20 to 300 ft of red beds of fluvial (upper Chinle) and eolian (Wingate) origin. The Wingate Sandstone is bleached of iron-oxide pigmentation (altered) over the mineralized areas, but the intervening section of upper Chinle sediments is unaltered. Deeper in the anticline are accumulations of oil and gas occupying four distinct Mississippian, Devonian, and Pennsylvanian reservoirs as well as a wide distribution of nonproducing but still petroliferous rocks. The reservoirs have probably been faulted and the nonproducing and petroliferous source zones fractured and deformed by salt flowage in the anticline. Many of these more extended sources may have leaked to higher stratigraphic intervals along fractures, possibly even to the surface.

Alteration (bleaching) of permeable red beds in the crest of the anticline has occurred. The areal extent of alteration is bounded approximately by the present oil and gas accumulations; the uranium mineralization coincides in projected area with the distribution of bleaching and deeper petroleum source rocks.

B. Correction and Analysis of Aircraft Scanner Data

Aircraft remote sensing data are corrected for geometrical distortions (mirror profile or panorama aspect ratio and a rubber-sheet distortion for compensation of aircraft motion) for approximate registration to a map base. Additional radiometric corrections to the radiance data themselves are essential to remove atmospheric and possibly directional surface scattering effects (Appendix A). Scattering typically introduces a strong brightness variation across the aircraft flight path. The correction functions are estimated empirically from line averages of the scanner radiance values and are introduced multiplicatively. The corrections accurately eliminate spurious angular atmospheric effects appearing in the raw image data. These atmospheric corrections would be cumbersome to model and remove mathematically because constraining atmospheric parameters

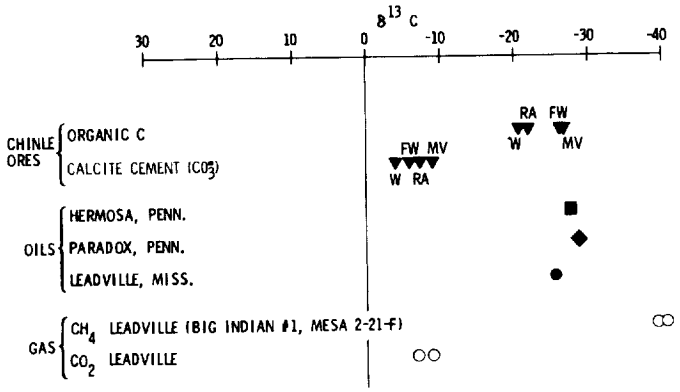

Figure 8-54. Distribution of $\delta^{13}C$ in petroleum (condensate), natural gas, and total organic carbon and carbonate from Moss Back uranium host sandstone. W = Wood, RA = Rio Algom, FW = Far West, MV = Mi Vida.

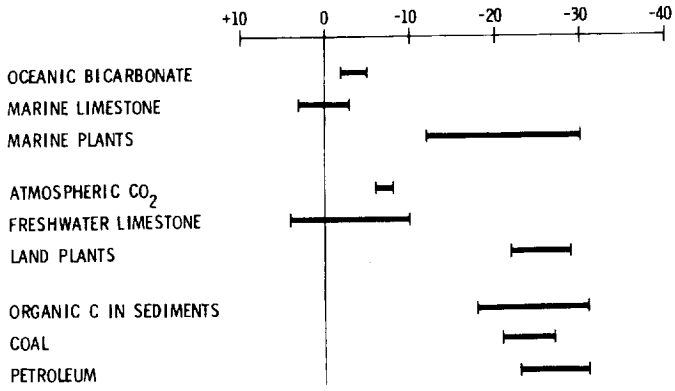

Figure 8-55. Variations in the isotopic carbon composition in some natural materials (data from Bender, 1972)

Table 8-19. Carbon isotope data

(a) Uranium ore samples, Moss Back Member, Chinle Formation

Mine Sample	Carbon		$CaCO_3$	
	% TOC	$\delta^{13}C$[a]	$CaCO_3$, %	$\delta^{13}C$[a]
Rio Algom	0.06	−22.06	23.3	−7.33 ±0.06[b]
Far West	0.07	−26.34	4.07	−5.90
Wood	2.56	−20.5	53.4	−4.51
Mi Vida (Steen)	0.07	−26.29	0.91	−8.95 ±0.05

(b) Crude oil samples

Oil Sample	Reservoir	$\delta^{13}C$ (Total C)[a]
Big Indian No. 4	Hermosa	−27.37 ±0.06[b]
Union B63 (Pure No. 2 USA "C")	Paradox	−29.04 ±0.03
Union B84 (Northwest Lisbon)	Leadville	−25.71 ±0.04
Lisbon Northwest	Leadville	−25.61

(c) Gas samples, Leadville reservoir

Gas Sample	$\delta^{13}C(CH_4)$	$\delta^{13}C(CO_2)$
Big Indian No. 1	−40.46	−6.70
Lisbon Northwest	−42.41 ±0.02	−7.07 ±0.03
Mesa Petroleum (No. 2-21-F)	−39.52	−8.87

[a]Standard isotope is Peedee Formation belemnite.
[b]Standard deviation is based on duplicate runs.

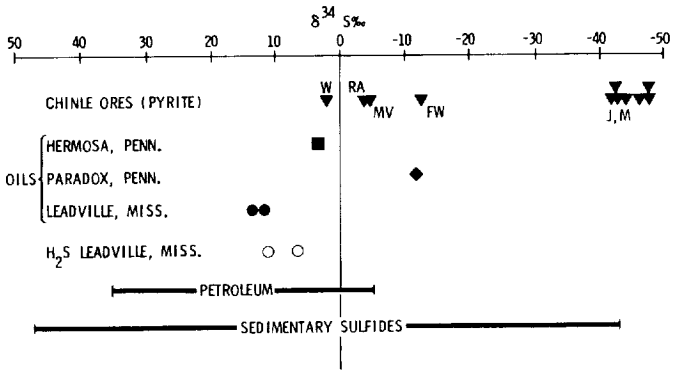

Figure 8-53. Distribution of sulfur isotopic values found for ore stage pyrite, H_2S, and petroleum (condensate) in Lisbon Anticline. Ranges of petroleum and sedimentary sulfide values are from Thode (1972). W = Wood Mine, RA = Rio Algom Mine, FW = Far West, MV = Mi Vida. J and M are sulfur values reported by Jensen (1958) and by Miller and Kulp (1963), respectively.

The carbon isotopic values for ore samples and for crude oils are virtually inseparable on a simple mixing model. The carbon isotopic composition of these ore sandstone samples could accordingly be pictured as arising from any admixture of land plant carbon and petroleum carbon. The isotopic values for CO_2 between reservoir gas and sandstone cement are also inseparable. Based on the limited sampling, the carbon isotopic results are consistent with petroleum sources of carbon in the ore sediments, but the results do not establish that these carbon sources have actually been admixed.

6. Summary. Sulfur and carbon isotopic measurements were made on ore stage pyrite and diagenetic stage calcite from Moss Back ore deposits and on Mississippian(?)/Pennsylvanian crude oil and methane, H_2S, and CO_2. The sampling involved examining a limited number of ore samples from throughout the mineralized belt and examining oil and gas samples from all of the major producing reservoirs and strata in Lisbon Anticline. For sulfides, the findings were:

(1) The Chinle ore stage pyrite values obtained are 40 per mil heavier than observed by Jensen (1958) and Miller and Kulp (1963), who advocated a predominantly bacterial source for the ore stage sulfur in sulfide. The heaviest values indicate (outside?) sources of heavier sulfur in addition to any indigenous bacterial sources present.

(2) δ-values for ^{34}S for crude oil and H_2S range from -12 per mil for Mississippian reservoirs to -11 per mil for a Paradox Formation condensate. The range for Hermosa

Table 8-18. Sulfur isotope data

(a) Pyrite in uranium ore samples, Moss Back Member, Chinle Formation

Mine Sample	S as Sulfide, %	$\delta^{34}S$ Pyrite[a]
Rio Algom	0.13	−3.70
Far West	0.06	−12.5
Wood	0.29	+2.0
Mi Vida	0.26	−4.28 ± 0.18[b]

(b) Crude oil samples

Oil Sample	Reservoir	Total S, %	$\delta^{34}S$ (Total S)[a]
Big Indian No. 4	Hermosa	0.01	+3.49
Union B63 (Pure No. 2 USA "C")	Paradox	0.04	−9.30
Union B84 (Northwest Lisbon)	Leadville	0.050	+13.19, +13.28
Lisbon Northwest	Leadville		+11.49

(c) Gas samples, Leadville reservoir

Gas Sample	$\delta^{34}S$ (H_2S)
Big Indian No. 1	Insufficient H_2S to measure
Lisbon Northwest	+6.54 ± 0.17[b]
Mesa Petroleum (No. 2-21-F)	+10.98

[a] Standard isotope is Canyon Diablo meteorite.
[b] Standard deviation is based on duplicate runs.

Table 8-15. Paragenetic mineral sequence at Mi Vida Mine[a]

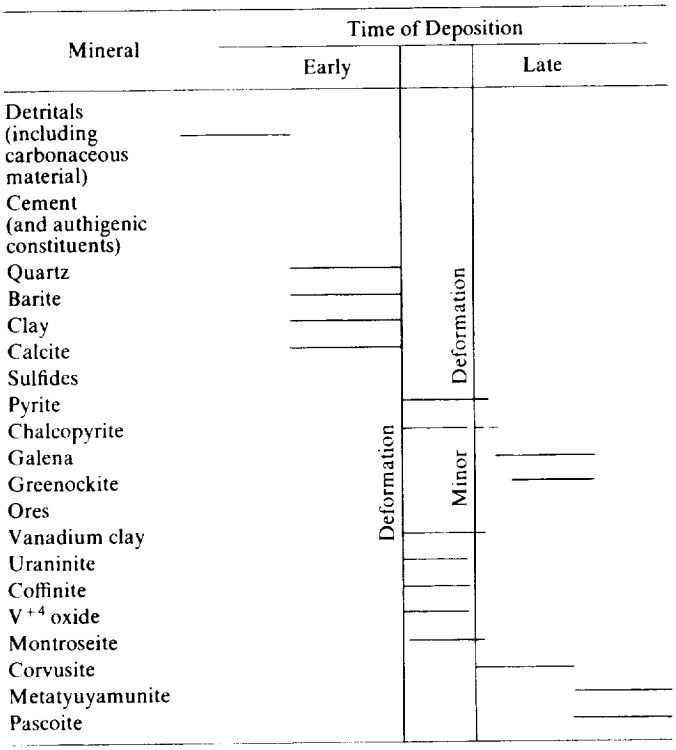

[a]From Gross (1956).

Table 8-17. Chemical analysis of samples from Lisbon Anticline oil and gas reservoirs[a]

Component	Mesa Petroleum (Fed 2-21-F), mol %	Big Indian Well No. 1, mol %
Oxygen	0	0
Nitrogen	9.75	0.51
Carbon dioxide	19.03	5.63
Hydrogen sulfide	0.97	0.17
Methane	62.16	6.30
Ethane	5.05	6.05
Propane	1.62	5.67
Iso-butane	0.39	3.07
N-butane	0.50	5.54
Iso-pentane	0.23	4.92
N-pentane	0.11	4.26
Hexanes	0.19	10.82
Heptanes and higher		47.06
Total	100	100
Specific gravity (60° F)	0.847	0.716

[a]Provided by B. Govrean, Union Oil Company (1981).

The distribution of carbon isotopic values found for Chinle ores, crude oil, and gases at Lisbon Valley is given in Figure 8-54. These data are tabulated in Table 8-19. The variation in isotopic carbon composition for some natural materials is given in Figure 8-55. Isotopic values for organic carbon in the Chinle ores range from $-20 > \delta^{13}C > -28$, while those for oil samples range from $-25 > \delta^{13}C > -30$. These values are in the range usually found for land plants or organic carbon in sediments and in petroleum, respectively. Methane from the Big Indian No. 1 and Mesa reservoirs is isotopically 12 per mil lighter than crude carbon from these reservoirs and, based on this difference, is most likely to be "thermogenic" as opposed to "biogenic" in origin (Hoefs, 1980, p. 134).

The $\delta^{13}C$ values for calcite cements in the ore samples studied span $-4 > \delta^{13}C > -9$ and from Figure 8-55 fall within the range found for freshwater limestones and atmospheric CO_2. Values of CO_2 reported are 32 per mil heavier than the associated methane and fall outside the range reported for marine limestones by 6 to 7 per mil. These differences are close to those expected from decarbonation for marine limestone by nonequilibrium reactions of +3 to +5 per mil (Hoefs, 1980, p. 164).

Table 8-16. Well locations and data on samples for isotope analysis from producing zones and oil and gas reservoirs, Lisbon Valley

Reservoir	Designation	Location	Formation	Production Depth or Interval, ft	Gravity
Oil	Big Indian No. 4	Sec. 14, T30S, R25E	Hermosa (Pennsylvanian)	4234–4681	47° API[d]
	Pure No. 2 USA "C"[a]	Sec. 3, T30S, R24E	Paradox (Pennsylvanian)	6050–6065	
	Lisbon field composite[b]	Sec. 4, T30S, R24E	Leadville (Mississippian)	8500–9000	52° API in oil ring[d]
	NW Lisbon field[c]	Sec. 4, T30S, R24E	Leadville	8500–9000	71° API in gas cap[d]
Gas	Big Indian No. 1	Sec. 33, T29S, R24E	Leadville	9886–10,500	
	Lisbon field composite	Sec. 4, T30S, R24E	Leadville	8500–9000	
	Mesa Petroleum 2-21-F	Sec. 21, T30S, R25E	Leadville	9220–9400	

[a]Union Well No. B63.
[b]Collected February 1981 by B. C. Govreau, Union Oil Company of California.
[c]Union Oil Company, Well No. 1384.
[d]Parker (1966).

Table 8-13. Location and description of uranium ore samples used in isotope studies, Moss Back Member, Chinle Formation, Lisbon Valley

Mine	Location	Hand Specimen Description
Rio Algom	SE 1/4, Sec. 21, T29S, R24E	Sandstone, dark brownish-gray color, medium grained, poorly sorted; bedding indistinct, defined by flattened black resinous carbonaceous blebs well indurated with abundant calcite cement.
Far West Incline	SW 1/4, NW 1/4, Sec. 28, T29S, R24E	Sandstone, dark-gray to black color, fine-grained, well sorted, grains rounded to subangular; bedding indistinct, marked by black bands and blebs. Medium-well indurated.
Wood	NE 1/4, Sec. 1, T31S, R25E NW 1/4, Sec. 6, T31S, R26E	Sandstone, light-gray color, coarse grained, poorly sorted, grains rounded to angular; bedding indistinct to absent; dark-gray to black resinous blebs. Brown and black dusting of pyrite in crude vein structure; well indurated with abundant calcite cement.
Mi Vida (Steen)	C, Sec. 11, T30S, R24E	Sandstone, dark-gray to black color, medium to coarsely grained, poorly sorted, grains rounded to subangular; bedding indistinct, marked by flattened dark blebs. Pyrite in dark colored patches.

Table 8-14. XRD analysis of uranium ore samples

Mineral		Location Name			
Name	Composition	Rio Algom	Far West	Wood	Mi Vida
Organic material	Amorphous		Present		
Quartz	SiO_2	Very major	Major	Minor	Very major
Barite	$BaSO_4$				
Clay (kaolinite)	$Al_2Si_2O_5(OH)_4$	Trace			
Calcite	$CaCO_3$	Major	Major	Major	
Pyrite	FeS_2	Very minor	Very minor	Trace	Very minor
Chalcopyrite	$CuFeS_2$				
Galena	PbS				
Greenockite	CdS				
Vanadium clay	?				
Uraninite	UO_{2+x}?				
Coffinite	$U(SiO_4)_{1-x}(OH)_{4x}$		Very minor	Minor	Trace
V^{+4} oxide	$V^{+4}O$?				
Montroseite	$(V^{+3}Fe^{+3})O(OH)$				
Corvusite	$V_2^{+4}V_{12}^{+5}O_{34}NH_2O$				
Metatyuyamunite	$Ca(UO_2)_2(VO_4)_2 3-5H_2O$	Very minor			
Pascoite	$Ca_3V_{10}O_{28.17}H_2O$				
Oligoclase	An 10-30	Very minor	Very minor		Very minor
K-feldspar	$KAlSi_3O_8$	Trace			Very minor
Roscoelite	$K(V,Al,Mg)_2$ $AlSi_3O_{10}(OH)$				
Glauconite	$(K,Na)(Fe^{+3},Al,Mg)_2$ $(Si,Al)_4O_{10}(OH)_2$	Minor	Minor	Very minor	Very minor
Corrensite	$(Mg,Fe,Al)_9(Si,Al)_8O_{20}(OH)_{10}\cdot\eta H_2O$ Al, Fe^{+2}, Fe^{+3} Li, Mg, Mn, Ni = Al, B, Si, Fe^{+3}		Very minor		Trace

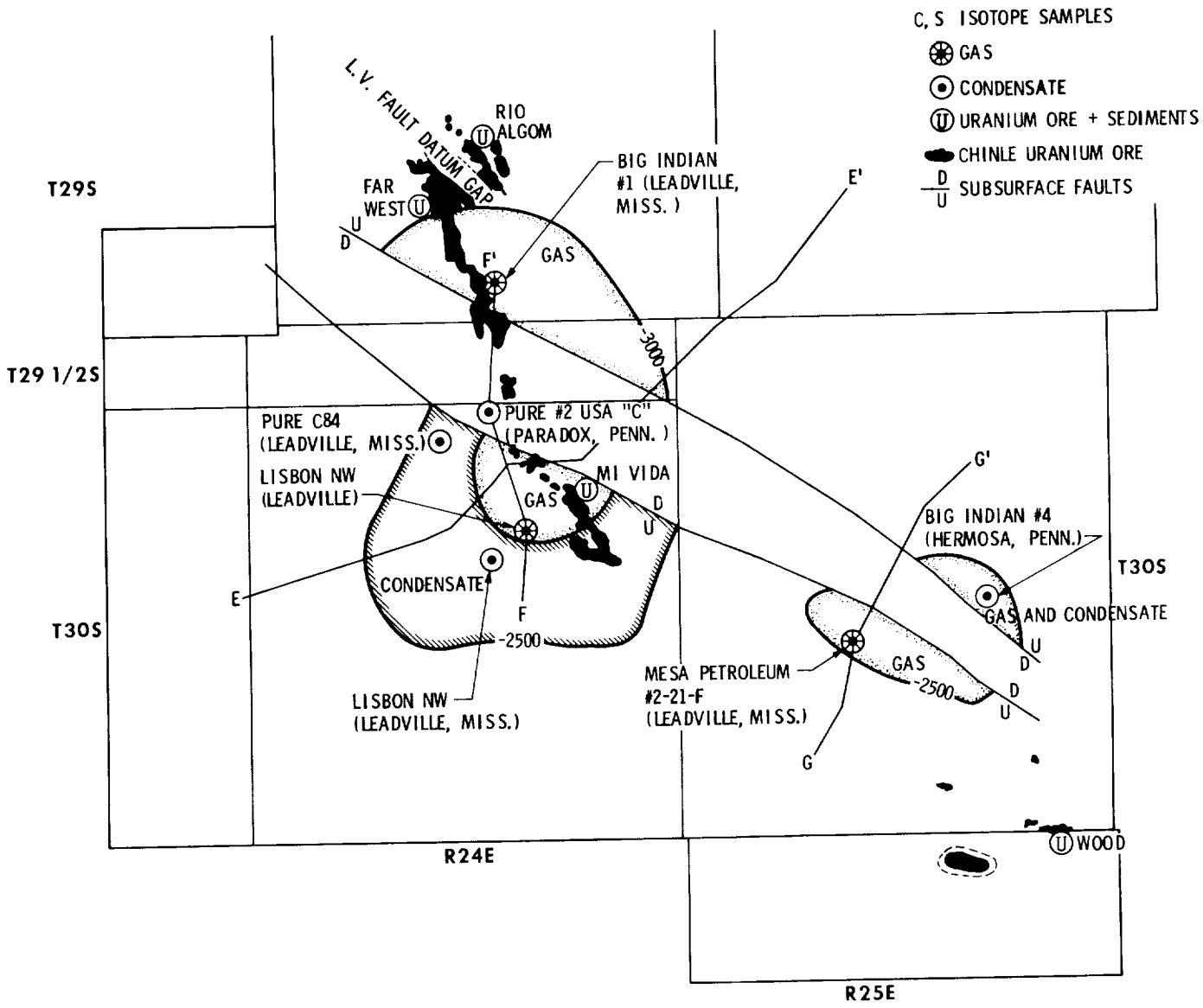

Figure 8-52. Isotope sample sites for oil and gas reservoirs and for uranium deposits in the anticlines. See Table 8-13 for detailed township and range locations of wells and mines. Big Indian Well No. 4 provided condensate.

value. The Big Indian No. 1 Mississippian reservoir gas sample does not contain enough H_2S for analysis.

The isotopic value for sulfur from ore stage pyrite in the uranium samples analyzed are all isotopically heavier than the extremes reported by Jensen (1958) and by Miller and Kulp (1963). This indicates that the isotopic history of sulfur in these deposits during the mineralization episode is, insofar as it is reflected by the sulfur value in pyrite, more complicated than a simple, uniform derivation of pyrite sulfur from local bacterial sources. On the basis of a simple sulfur mixing model, the range of sulfur isotopes observed for these ores could be accounted for by:

(1) Hydrothermal origin of the sulfur.

(2) Derivation of the sulfur from Hermosa and Paradox crude oil directly, with no contribution of local bacterially formed sulfur from sulfate.

(3) Derivation of the sulfur from Leadville crude and/or H_2S with mixing of local bacterially formed sulfur from sulfate.

(4) Derivation of sulfur from Hermosa and Leadville petroleum sources together with locally derived contributions of bacterially formed sulfur from sulfate.

The sulfur data alone cannot distinguish among these possibilities.

oil was combusted in a Parr bomb in 30 atm oxygen to produce sulfate in solution. $BaCl_2$ was used to precipitate the sulfate as $BaSO_4$, which was combusted in quartz powder to evolve SO_2. For sediments, samples were treated with phosphoric acid in closed tubes to dissolve dispersed carbonate cement and liberate CO_2 for subsequent analysis.

The procedures for rocks/sulfides were as follows: crushed rock was leached with dilute HCl to remove sulfide present, followed by aqua regia digestion. The sulfide present was thereby oxidized to SO_4^{-2} and subsequently precipitated as $BaSO_4$. The $BaSO_4$ was precombusted at 600° C to remove organics, then combusted with quartz powder to produce SO_2. To study the organic carbon, crushed rock was first treated with dilute HCl to remove carbonate. The remaining procedures were identical to those used for analyzing sulfur in oil.

Isotopic ratio measurements are reported as δ-values given in per mil by

$$\delta^{34}S = \frac{\left(\frac{^{34}S}{^{32}S}\right)_{Sample} - \left(\frac{^{34}S}{^{32}S}\right)_{Standard}}{\left(\frac{^{34}S}{^{32}S}\right)_{Standard}} \times 1000$$

$$\delta^{13}C = \frac{\left(\frac{^{13}C}{^{12}C}\right)_{Sample} - \left(\frac{^{13}C}{^{12}C}\right)_{Standard}}{\left(\frac{^{13}C}{^{12}C}\right)_{Standard}} \times 1000$$

3. Uranium ore samples. Sandstone samples containing uranium ore from four mines were provided by P. Niesen of Atlas Minerals Corporation. The locations of the ore bodies are given in Figure 8-52, and sample locations and descriptions are included in Table 8-13. These samples were analyzed by XRD methods for the major, minor, and trace mineral phases present; the results are listed in Table 8-14. For all samples, the only sulfide found is pyrite and the only carbonate, if detected, is calcite. Gross (1956) has studied the mineralogy and paragenesis of uranium ore at Mi Vida Mine. The paragenetic sequence determined is listed in Table 8-15. All of the detrital quartz, feldspar, micas, rock fragments and carbonaceous trash were cemented by authigenic silica, barite, calcite, or clay. Vanadium clay, coffinite, uraninite, montroseite, and V^{+4} oxide replaced carbon trash, calcite cement, detrital grains, and the pyrite found in mudstone pellets. Pyrite was introduced at the time of uraninite and V^{+4} oxide emplacement. Chalcopyrite was also early in the sequence, but its age relative to pyrite and uraninite could not be determined. The isotopic composition of sulfur in pyrite thus appears to provide the isotopic composition of sulfur present during mineralization.

Campbell (1981) notes that for Cutler ore the diagenetic sequence indicates uranium and vanadium were introduced late in the sequence, after oxidation had formed hematite and before calcite cement had formed. These ore bodies apparently formed without reductants, perhaps through sorption of uranyl by hematite.

4. Oil and gas samples. Oil and gas samples from five separate reservoirs or producing horizons throughout Lisbon Anticline were obtained courtesy of Union Oil Company of California. The locations of these samples are included in Figure 8-52. Precise well locations and producing intervals are listed in Table 8-16. The production intervals are shown in cross sections of Figure 8-47. Chemical composition of the samples from two wells is given in Table 8-17. For additional chemical data on gas and crude from Hermosa and Mississippian reservoirs, refer to Parker (1966). According to Parker (1966), the most significant chemical differences between Upper Hermosa and Mississippian gases are the higher percentages of nitrogen, CO_2, and helium in the Mississippian. The Upper Hermosa and Mississippian gases are not reported to contain H_2S, except for Mississippian well 2-21-F.

The Upper Hermosa sandstones are not productive at Lisbon field because the beds crop out and are buried only a few hundred feet beneath the surface. These sandstones do produce from Lisbon Canyon Anticline on the downthrown blocks of Lisbon Fault. The reservoir is now shut in; the sample in hand represents the only one available of Hermosa condensate.

5. Results. The distribution of sulfur isotopic values found for ore stage pyrite and for total sulfur in oil and H_2S is plotted in Figure 8-53 and listed in Table 8-18. In addition, the values for pyrite with organic trash from Mi Vida Mine were plotted (reported by Jensen, 1958, and Miller and Kulp, 1963) and represent extremes found for H_2S of supposed bacterial origin at this site. The sulfur isotopic values reported here for ore stage pyrite are $+2 > \delta^{34}S > -13$, considerably heavier than earlier numbers and among the heaviest reported by Field and Jensen (1960) for Big Indian Wash sulfides (Figure 8-51). The present numbers are approximately equal to those reported by Field and Jensen for "hydrothermal" pyrite from Miner's Basin. They are near the mid-range found for the spread of normal sedimentary sulfides given by Thode (1972).

For crude oil, the sulfur isotope values for Hermosa, Paradox, and Leadville samples are isotopically distinct from sulfur. The Hermosa and Leadville numbers fall within the range for crude oils reported by Thode (1972), whereas the Paradox value is substantially lighter.

The values of $\delta^{34}S$ for H_2S for Mississippian gas are isotopically lighter by a few per mil than the associated petroleum

leached during past or modern alteration episodes. All pyrite present has been altered to limonite or goethite. Petroleum residues are extremely sparse (coatings on a few grains in cores from Rio Algom Mine), and insufficient material was presently available for analysis.

Field and Jensen (1960) and Jensen (1958) made an isotopic study of sulfide minerals with sandstone-type uranium deposits of the Colorado Plateau and Wyoming. Specimens of pyrite with coalified wood at Mi Vida Mine have $\delta^{34}S$ values ranging between -42.8 and -47.7 per mil. Similar light values for sulfur have been found by Miller and Kulp (1963) for the Lisbon Valley deposits. These light δ-values were attributed to H_2S derived from anerobic bacteria in carbonaceous-rich zones acting on sulfates in ordinary groundwater. Schmitt (1968) studied uranium and copper mineralization in the Lisbon Valley Mining District and summarized all of the previous sulfur isotopic measurements for the area (Figure 8-51). He pointed out that the average values for the Lisbon Valley sulfides are nearly identical, suggesting ordinary sedimentary fractionation processes as the source of observed variation.

Alternatively Jacobs (1963), as reported by Schmitt (1968), suggested that these variations could result from multiple sources of sulfur, including hydrothermal solutions, evaporites, petroleum, and artesian waters, although no isotopic data were presented for such source materials for the area. Schmitt (1968) concluded that to account for the extreme sulfur isotopic lightness observed, bacterial fractionation must have affected much of the sulfur as sulfide in the deposits studied. Multiple episodes of bacterial fractionation may have been involved. Individual deposits were found to be isotopically distinct with respect to sulfur.

2. Chemical procedures. All carbon and sulfur isotopic measurements reported here were made by Global Geochemistry Corporation, Canoga Park, California. The following chemical procedures were used (1) for analyzing carbon and sulfur in gas and liquid petroleum phases, and (2) for analyzing carbonate cements, organic carbon, and pyrite in sediments.

CO_2 in gas phases was separated from methane in a gas chromatograph. H_2S was precipitated with silver nitrate. The silver sulfide precipitate was ground with cuprous oxide and burned in a vacuum line to evolve SO_2. For carbon, crude oil was mixed with cupric oxide, placed with silver foil (for removal of halogens and sulfur) in a closed combustion system, and fired at 850° C for 8 hours to evolve CO_2. For sulfur, crude

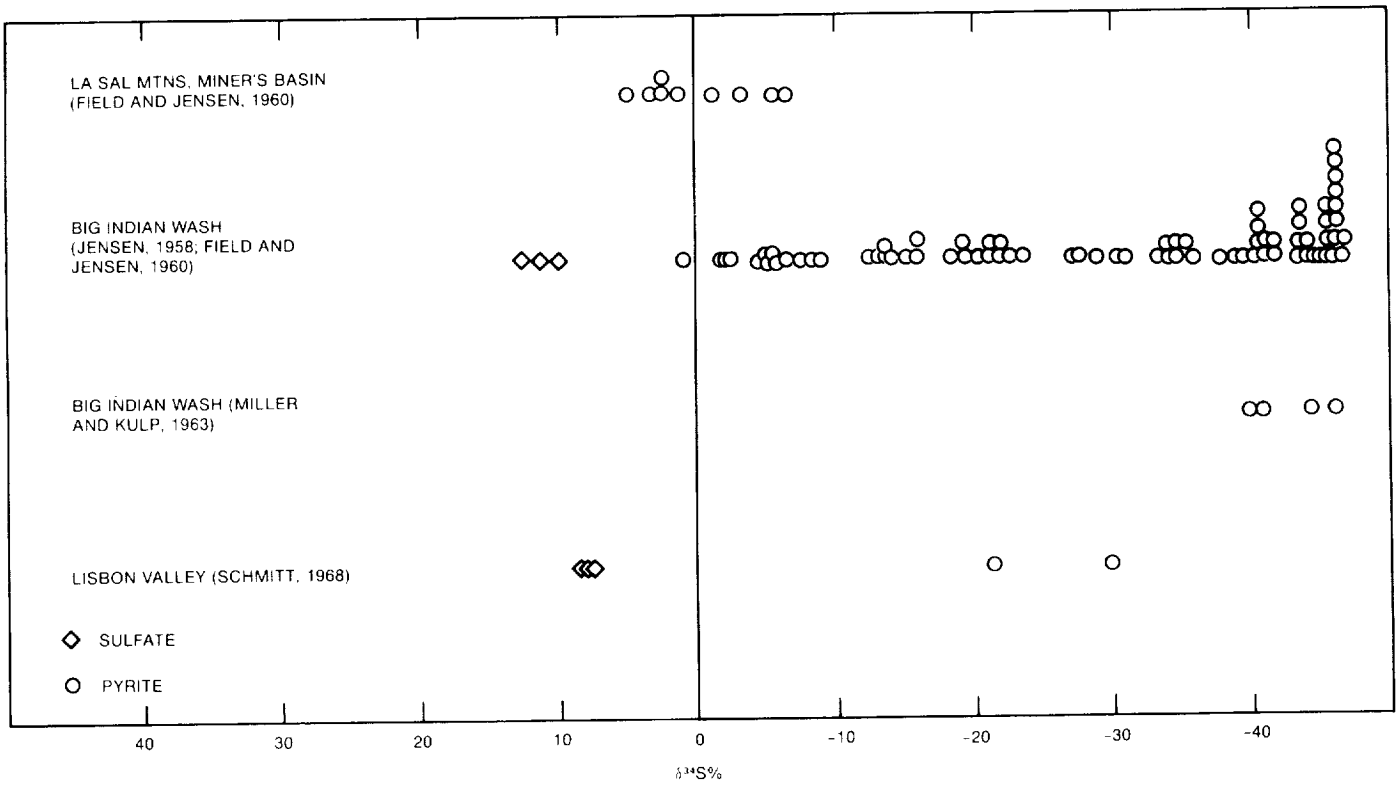

Figure 8-51. Distribution of δ-values for sulfur isotopes from hydrothermal uranium deposits (Miner's Basin, La Sal Mountains, Utah) and sedimentary uranium deposits (Big Indian Wash and Lisbon Valley) (from Schmitt, 1968)

(1974) and Ferguson (1979a, 1979b, 1981) discussed the relationship between the bleached Permian red sandstones in anticlines and the oil and gas accumulations in underlying Pennsylvanian formations for several oil fields in Oklahoma. Donovan (1974) described alteration in Cement Anticline of gypsum beds along the flanks to carbonate rocks in the crest. Associated red sandstones there are altered to pink, yellow, and white on the flanks, and to hard carbonate-cemented gray sandstone in the crest. Color changes in the sandstones were related to reduction and dissolution of ferric iron in the presence of hydrocarbons. Calcite found in rocks containing abundant petroleum residue was interpreted to result from hydrocarbon reaction with sulfate (gypsum) to form carbonate. The H_2S thereby liberated changed hematite to pyrite and aided in the bleaching of the rock. Calcitized gypsum has a light carbon isotopic composition over the oil productive zones, suggesting an influence of hydrocarbons on the isotopic compositions of these carbonate cements.

2. Velma, Eola, and Chickasha fields. Ferguson (1979a, 1979b, 1981) described the distribution of carbonate cement and pyrite with depth in anticlines in bleached Permian red sandstones over three Oklahoma oil fields (Velma, Eola, and Chickasha). The surface anticlines overlie complexly folded and faulted Pennsylvanian reservoir rocks. Permian sandstones are typically altered to white over anticlinal crests—a color change that results from alteration of clay, limonite, and hematite cement to calcite, dolomite, and pyrite. Bleaching is restricted to sandstones and probably resulted from reduction of iron oxides to pyrite. Pyrite cement occurs in zones overlying pre-Permian faults and oil-productive areas. The pyritiferous Permian zones have sharp vertical boundaries and are largely confined to regions above oil accumulations. Solid petroleum residues are common.

3. San Rafael Swell. Davidson (1967) has described the distribution of bleaching in red Moenkopi sandstone throughout the San Rafael Swell. The lower part of this sandstone unit is bleached. The upper boundary of bleaching is a nearly horizontal surface extending across the anticline. The degree of bleaching is correlated with the abundance of solid hydrocarbon residue present, with the most intense alteration accompanying the highest abundance of "dead oil."

4. Comparison to Lisbon Anticline. In Lisbon Anticline, alteration is largely confined to the Wingate Sandstone and to the thin sugar sandstones of the Cutler Formation; the sugar sandstones appear to control the distribution of Cutler and Moss Back uranium mineralization. The Wingate Sandstone has been removed by erosion from much of the axial region and is not exposed on the northeastern side of the fault. Consequently, the initial pattern of alteration throughout the structure is incompletely known. Geometry of the known outcrops suggests that altered rocks formed a cap in the structure and that the sandstone is largely unaltered on the flanks. Bleached rocks contain no carbonate cement, and petroleum residues are exceedingly rare or have not been recognized. Limonite and goethite pseudomorphous after pyrite have been reported from bleached Wingate (Loring, 1958), but pyrite is absent. The distribution of bleaching near Big Indian Valley is encompassed within oil- and gas-producing limits of reservoirs in Mississippian dolomites lower in the anticline. A large area of potential Mississippian reservoir rocks in a graben beneath the salt diapir does not contain oil or gas that may have leaked to the surface. The source rocks are problematical. Other formations including Paradox black shales and Upper Hermosa sandstones are also petroliferous and have a wide distribution in the anticline. Since these oils or condensates are all of amber color and high gravity, weathered residues at the surface might not easily be retained or identified. Identification of the bleaching agent with hydrocarbons or the related sour gases cannot be made with certainty, but the distribution of known production and the provable extent of other petroleum source beds make such liquids and gases good candidates.

E. Carbon and Sulfur Isotope Measurements on Oil, Gas, and Uranium Ore Samples

1. Background. The possible role of petroleum or H_2S as a reductant helping to fix uranium in these deposits cannot be settled by geometrical arguments alone. As an aid in sorting out the possible significance of petroleum or petroleum-related H_2S and CO_2 in the formation of the Lisbon Valley deposits, carbon and sulfur isotope measurements have been made on calcite and pyrite from four separate Moss Back ore bodies extending over the entire mineralized zone. In addition, oil and gas samples representing all of the major reservoir or producing horizons in the anticline have been obtained; carbon and sulfur isotope measurements were made of CH_4, CO_2, H_2S in gas phases and for total carbon and total sulfur in the petroleum liquids.

In addition to measuring sulfides, bleached Wingate was examined for evidence of the reductants or processes involved in that alteration. Donovan (1974), for example, described carbon and oxygen isotopic measurements on calcite cement over the Cement field, Oklahoma. Calcite is found in sandstones containing abundant petroleum residue and was interpreted to result from hydrocarbon reaction with gypsum. All of the carbonate cements examined were isotopically light ($\delta^{13}C = -25$ per mil) when compared to values expected if in equilibrium with atmospheric or oceanic sources of carbon or carbonate (-7 per mil). This suggested a hydrocarbon source for at least some of the carbonate carbon present. Calcite cement is absent from all bleached Wingate outcrops and hand specimens examined from Lisbon Anticline, evidently having been

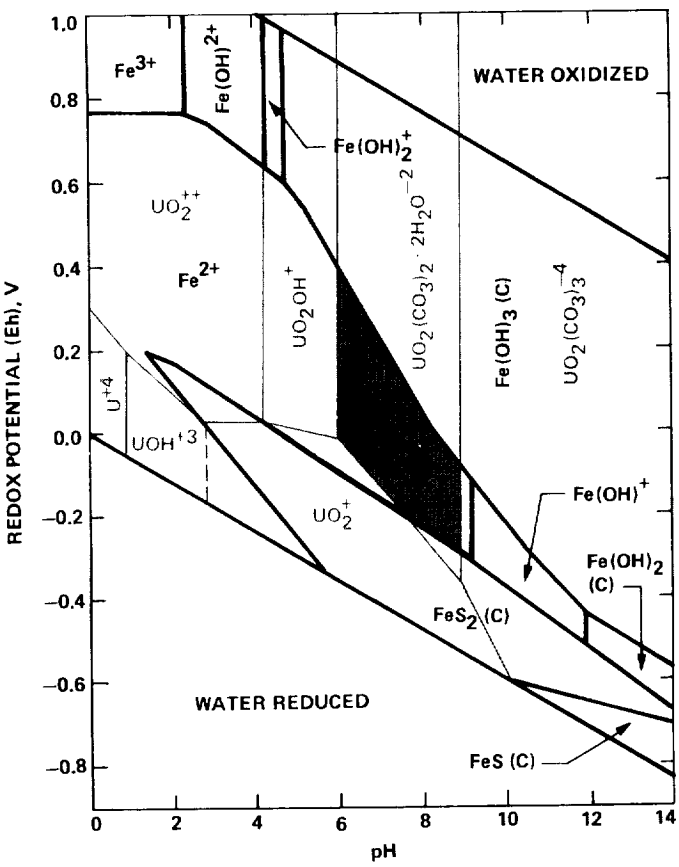

Figure 8-49. Stability fields from ferrous and ferric iron species in equilibrium with FeS_2 and iron hydroxide species superimposed on the stability field for uranyl carbonate and other species in the system $U-O_2-H_2O$. Blackened area represents Eh–pH field for simultaneous stability of soluble uranium species and soluble ferrous species in equilibrium with FeS_2. Heavy line diagram represents data from Adler (1970); light line diagram from Hostetler and Garrels (1962).

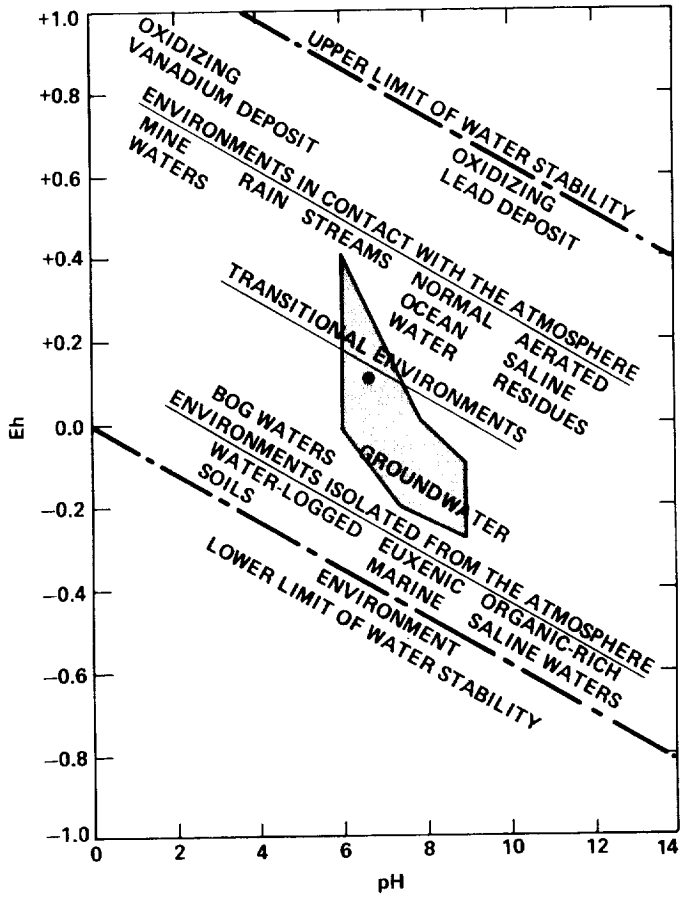

Figure 8-50. Eh–pH relations of natural environments with the field of simultaneous stability of uranyl dicarbonate and the Fe^{+2}(aq)–Fe-hydroxide system (Garrels and Christ, 1965). • is Eh–pH value of brine from Lisbon field.

Removal of the pigment together with redistribution as hydrated iron oxide (limonite) is thought to occur in a two-step process. Iron is cast into soluble ferrous and ferric species as follows:

(1) Pyrite is formed (Karstev et al., 1959):

$$2H_2S + Fe_2O_3 \rightarrow FeS_2 + FeO + 2H_2O$$

(2) Iron sulfides are put into solution in oxygenated water by the stochiometric reaction (Singer and Stumm, 1968):

$$FeS_2 + \frac{7}{2}O_2 + H_2O \rightarrow Fe^{+2} + 2SO_4^{-2} + 2H^+$$

and

$$Fe^{+2} + \frac{1}{4}O_2 + H^+ \rightarrow Fe^{+3} + \frac{1}{2}H_2O$$

The ferric species produced hydrate to form ferric hydroxide

$$Fe^{+3} + 3H_2O \rightarrow Fe(OH)_3 + 3H^+$$

or they may react with pyrite to give additional ferrous iron

$$FeS_2 + 14Fe^{+3} + 8H_2O \rightarrow 15Fe^{+2} + 2SO_4^{-2} + 16H^+$$

These relationships show that dissolution of pyrite leads to production of acidic waters, four equivalents of acidity being released for every unit of pyrite dissolved. The low resulting pH may account for the absence of calcite in bleached Wingate facies.

D. Relationship to Bleaching of Red Beds in Other Anticlines

1. Cement field, Oklahoma. Bleaching of red beds over petroleum accumulations has been noted elsewhere. Donovan

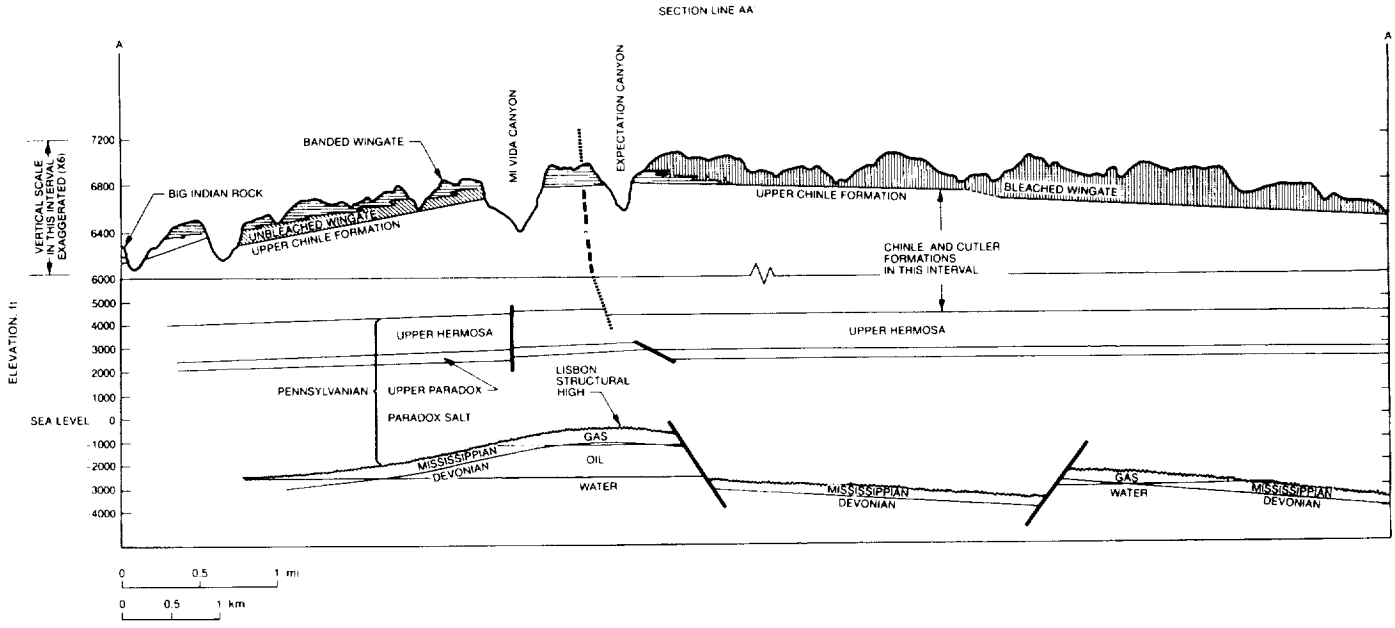

Figure 8-48. Cross section along the portion AA′ of profile AA‴ (Plate 8-4) showing the relation between doming in Lisbon reservoir and flexure of Wingate Sandstone at the surface. The high point of the topographic surface coincides with the crest of the reservoir dome. Note scale expansion of vertical dimension by a factor of six in the upper part of the section.

The possible geochemical compatibility of bleaching red beds and transporting uranium in solution needs to be mentioned. Such compatibility is suggested to exist if it is assumed that mineralizing and bleaching events are tied to the same fluid transport system and, thus, that the mineralization and bleaching are roughly coincident in time. For a time-coincident model, the uranium-bearing solutions are responsible for the solution and transport of iron in the sandstone. Where these solutions encounter extraordinary reducing conditions, uranium ore is accumulated. The entire motion of fluids is governed by detailed variations in permeability so that porous sandstones act as good fluid conduits, whereas tighter clay-rich mudstones such as the Upper Chinle are impermeable. This also means that ore emplacement and bleaching episodes follow periods of some anticlinal flexure of the host and superincumbent strata. The model also assumes that the Wingate Sandstone existed with either initial detrital or authigenic hematite pigment.

C. Stability Relations for Ferrous and Ferric Iron Species and the Transport of Uranium

Bleaching of the Wingate Sandstone corresponds to a reduction of the iron present from Fe^{+3} to Fe^{+2}, together with a decrease of the total iron present by a factor of five or so. Where bleached rocks are in contact with red Chinle mudstone, these latter rocks are altered from red to green in a band several inches wide near the contact. The altered band crosscuts bedding in the Chinle, thus establishing it as later than the time of sedimentation.

The solution chemistries for transport of Moss Back uranium as complexed carbonate ions in groundwater may be compatible with the solution redox potential (Eh) and pH required for bleaching of the Wingate. As an approximation, the stability field of Fe^{+2} in aqueous solution in the presence of PCO_2 was used as a rough measure of the conditions for Wingate alteration. According to a diagram given by Adler (1970) and by Garrels and Christ (1965), the stability field for Fe^{+2} in aqueous solution depends on the coexisting iron species present.

The simultaneous stability field of Fe^{+2} coexisting with pyrite and $Fe(OH)_3$ for the aqueous equilibrium UO_2–H_2O–CO_2 (Hostetler and Garrels, 1962) is shown in Figure 8-49. Fe^{+2} and hydrated uranyl carbonate, $UO_2(CO_3)_2 \cdot 2H_2O^{-2}$, coexist in a roughly trapezohedral region between Eh –0.25 and +0.4 V and pH 6 and 8.5. In natural waters (Figure 8-50), these conditions are found in transition environments and environments isolated from the atmosphere, possibly ones containing organic materials. These environments are not inconsistent with those imagined for groundwaters circulating in contact with buried organic matter or possibly containing petroleum components. Collins (1975) has, in fact, measured redox potentials ranging from −0.27 to −0.30 V in oil field effluents. The Eh–pH value for brines from Lisbon field is shown in Figure 8-50.

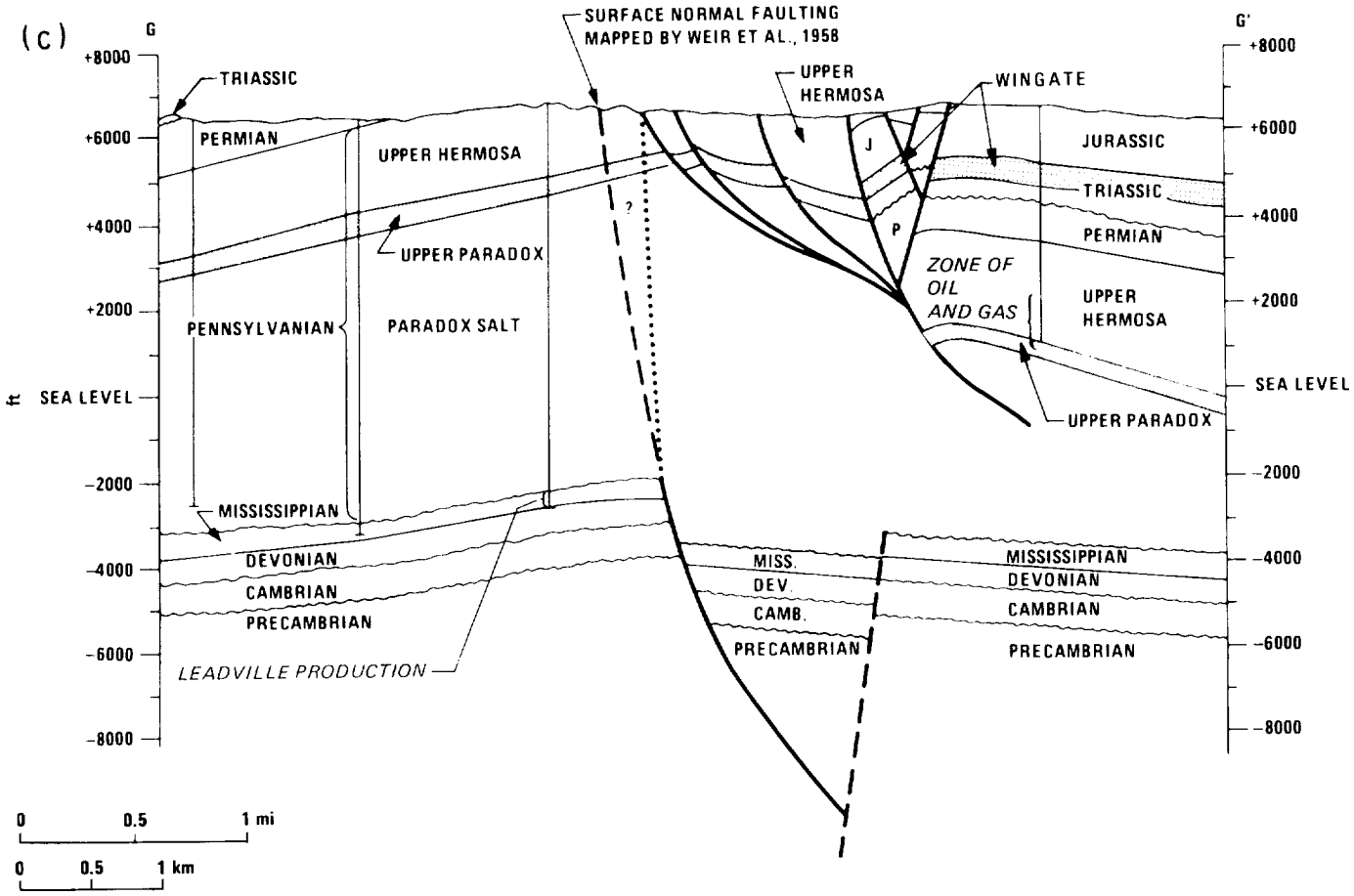

Figure 8-47. Reinterpretation of structure sections in Figure 8-46 according to a fault model of the Upper Paradox Formation structural surface (modified from Parker, 1966): (c) GG'

time because the Leadville Dolomite is thinned by 145 ft over the dome, and the Molas and Pinkerton Trail Formations do not thicken over this area. Some post-Pennsylvanian faulting is indicated if the structural interpretations presented here are correct. Probably the timing of these folding and faulting events account in part for the fact that there is no corresponding surface expression of the graben depicted in the Mississippian–Pennsylvanian section. The lack of surface expression of the downdropped block could represent reactivation of the Lisbon reservoir fault along with continued quiescence of the more northern structure bounding the graben.

4. Discussion. The arguments thus far are purely geometrical and show that faults may be introduced in the Upper Paradox dolomite and black shale sequence above the Lisbon reservoir. Introduction of these structures is consistent with available well data. These structures are required to traverse the entire section of Middle Paradox rocks, which consist predominantly of salt within beds of black shale, siltstone, and dolomite. Flowage of the Middle Paradox is responsible for the diapiric structure in the anticline. Consequently, the faulted rocks may have sealed themselves and the actual upward fluid flow along the structural channel envisaged may have been limited. Indeed, the presence of oil and gas accumulations suggests that such sealing has occurred around the reservoir rocks.

The existing reservoirs are not the only sources available, however. According to Parker (1966), black shales of the Paradox Formation are probably important petroleum source beds and the Paradox itself has productive intervals. In addition, sandy horizons in the lower part of the Upper Hermosa Formation are productive and may have had different source rocks. These sandstones do not act as reservoirs on the southwestern side of the Lisbon Valley Fault because the beds are exposed without closure in the core of Lisbon Valley Anticline. Taken together, these additional petroleum sources are widespread and occur within and stratigraphically above the Paradox salt barrier.

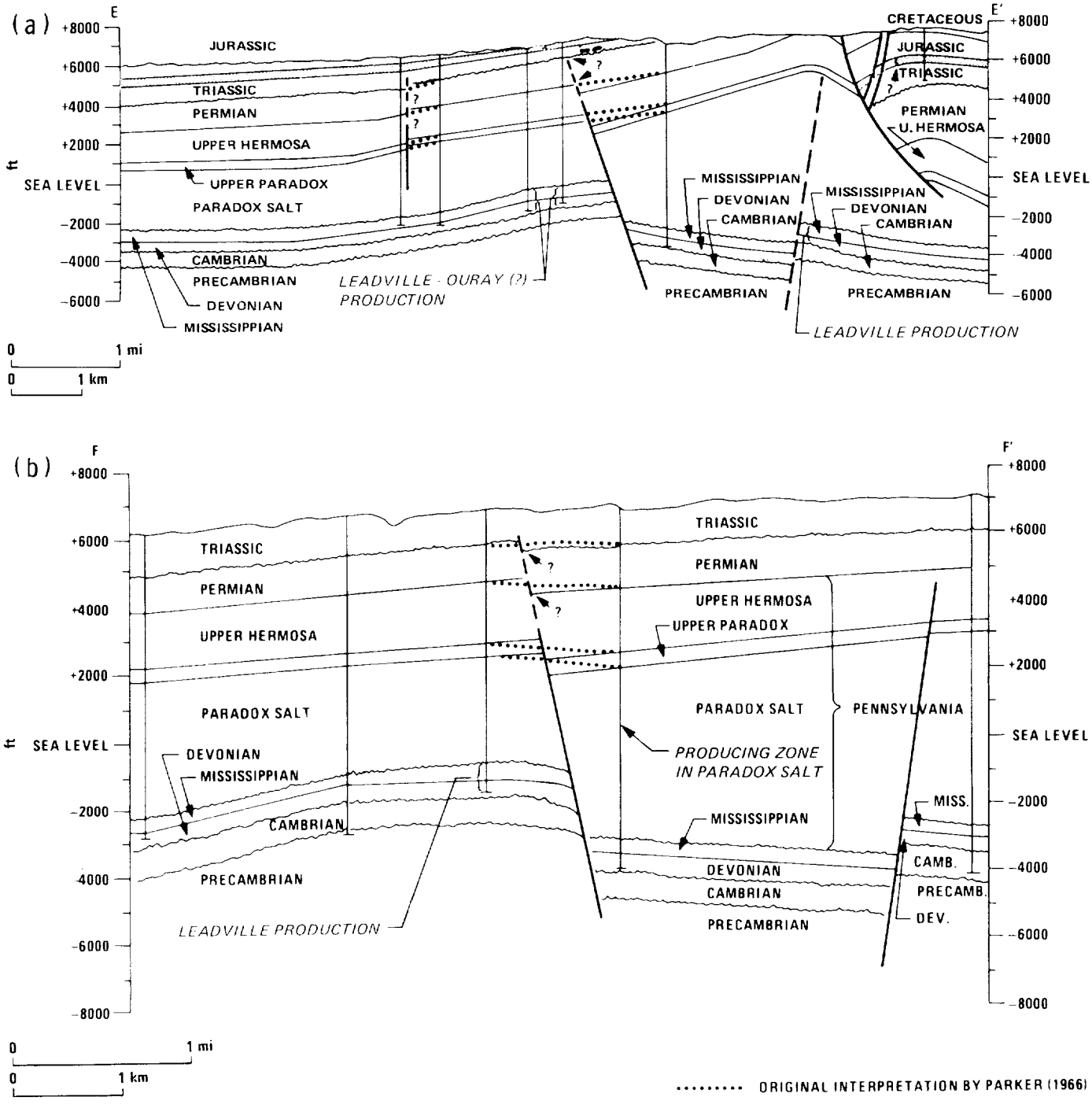

Figure 8-47. Reinterpretation of structure sections in Figure 8-46 according to a fault model of the Upper Paradox Formation structural surface (modified from Parker, 1966): (a) EE'; (b) FF'

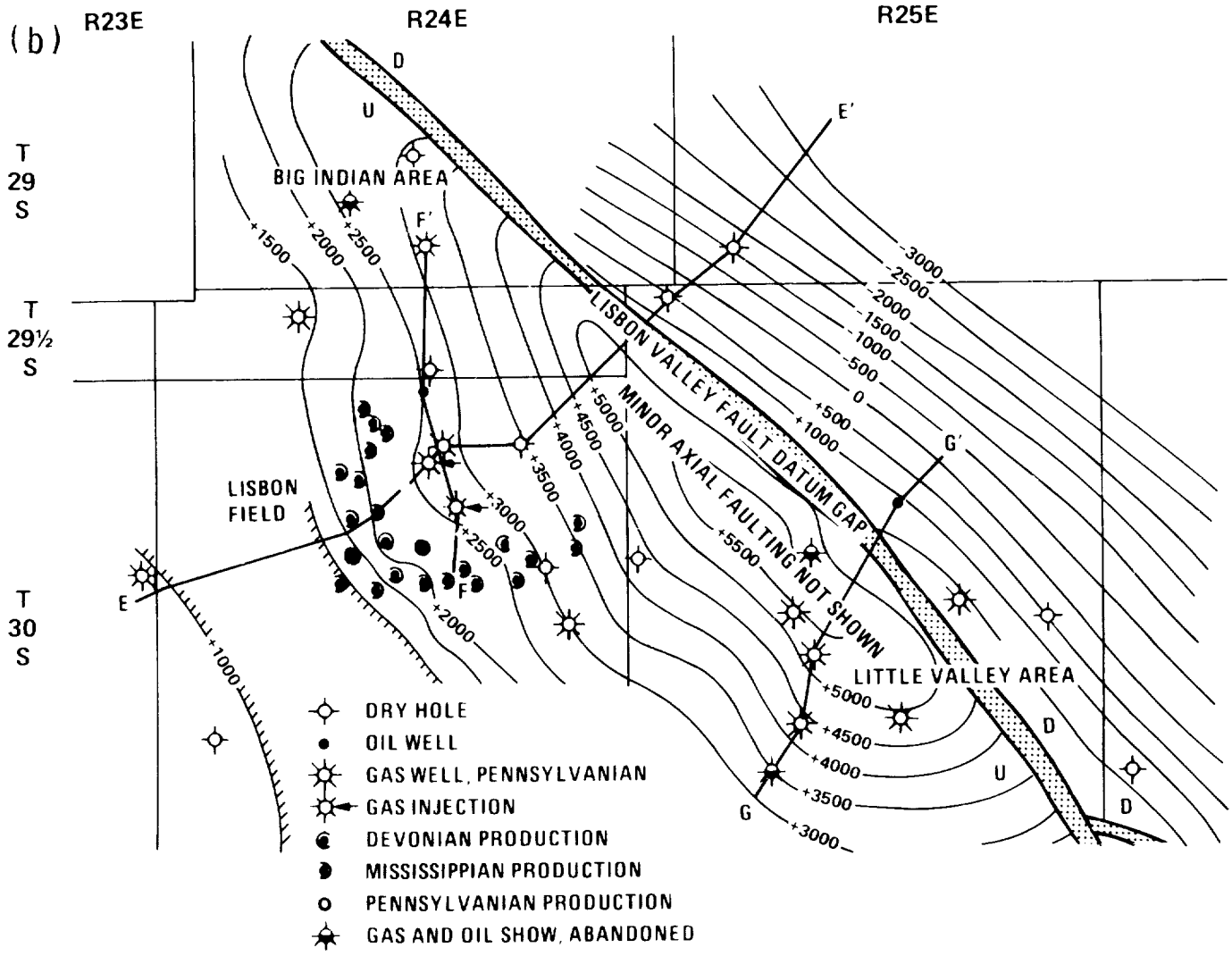

Figure 8-46. Pennsylvanian Paradox Formation (modified from Parker, 1966): (b) original contour data

2. Modification to cross sections. The required modifications in cross sections EE′, FF′, and GG′ (Figure 8-46), consistent with a fault interpretation of the upper reservoir surface, are depicted in Figure 8-47. In these cross sections, dotted lines represent the previous interpretation according to Parker (1966) and solid lines the new interpretation. The present interpretation permits a normal displacement of approximately 400 ft along the reservoir-bounding faults. Extension of the faults introduced past the Upper Paradox is of course not possible from data presently available. However, several possibilities exist for further extrapolation upward: (1) these faults propagate through to the surface and are not recognized except possibly where noted in section GG′, (2) the displacements are pre-Triassic in age and are confined to beds below the Moss Back–Cutler unconformity, or (3) these faults cut the unconformity, but displacements die out before reaching the surface.

3. Relationship of reservoir and surface structural configurations. A structural section through the Lisbon and Big Indian fields along the portion AA′ of section AA‴ (Plate 8-4) is shown in Figure 8-48. The vertical scale of the upper part of the section is exaggerated six times over the lower part. The dome of the Lisbon reservoir, here shown without faulting, lies directly beneath an arch in the surface profile between Mi Vida and Expectation Canyons. Closure on the reservoir rocks is about 2500 ft, whereas closure at the surface is estimated to be about 600 ft. Parker (1966) has pointed out that the Mississippian accumulation pictured in the Lisbon structural high is unique for the Rocky Mountain area because the folding and faulting that account for the trap are in part of pre-Pennsylvanian age and in part of Late Pennsylvanian–Permian age—not Laramide, which is common elsewhere. Most of the Lisbon structural feature was in place before Molas (Pennsylvanian)

B. A Reinterpretation of the Structure Above Lisbon Reservoir

The physical alignment of bleaching, uranium mineralization, and oil and gas accumulations in the Big Indian area suggests a genetic connection may exist among the three. Oil, gas, and H_2S are possible reductants for fixation of uranium and for alteration of iron oxides in red beds (Donovan, 1974; Ferguson, 1979a, 1979b). The simple idea examined here consists of extending the NE-dipping fault bounding the Lisbon reservoir on the northeast upward through the section to provide a direct structural connection for passage of such reductants from reservoirs or other source rocks at depth to permeable near-surface units. No obvious surface faulting of appropriate alignment has been observed, suggesting that the displacements either die out below the surface or are truncated at an unconformity. Alternatively, the faults may change in dip toward the surface and emerge elsewhere from positions determined by simple upward extrapolation. To proceed, structural contour data were reinterpreted for the Upper Paradox Formation, for which the well data have been compiled by Parker (1966).

1. Fault interpretation of Upper Paradox structural surface. In Figure 8-46(a), the Upper Paradox surface has been reconfigured to accommodate passage of the reservoir-bounding fault through that horizon. Additional NE-trending faults bounding a block with upward displacement, centered over the reservoir, have been introduced to complete the interpretation. Structural control data for the upper Mississippian in Figure 8-44 represent the upper surface of the Lisbon reservoir. These data can also be interpreted according to a fault model that includes an upwardly displaced block over the reservoir. (This interpretation will not be developed here.) According to available well-control data, several additional fracture systems may thus be in contact with the reservoir and can be extended through the overlying rock layers.

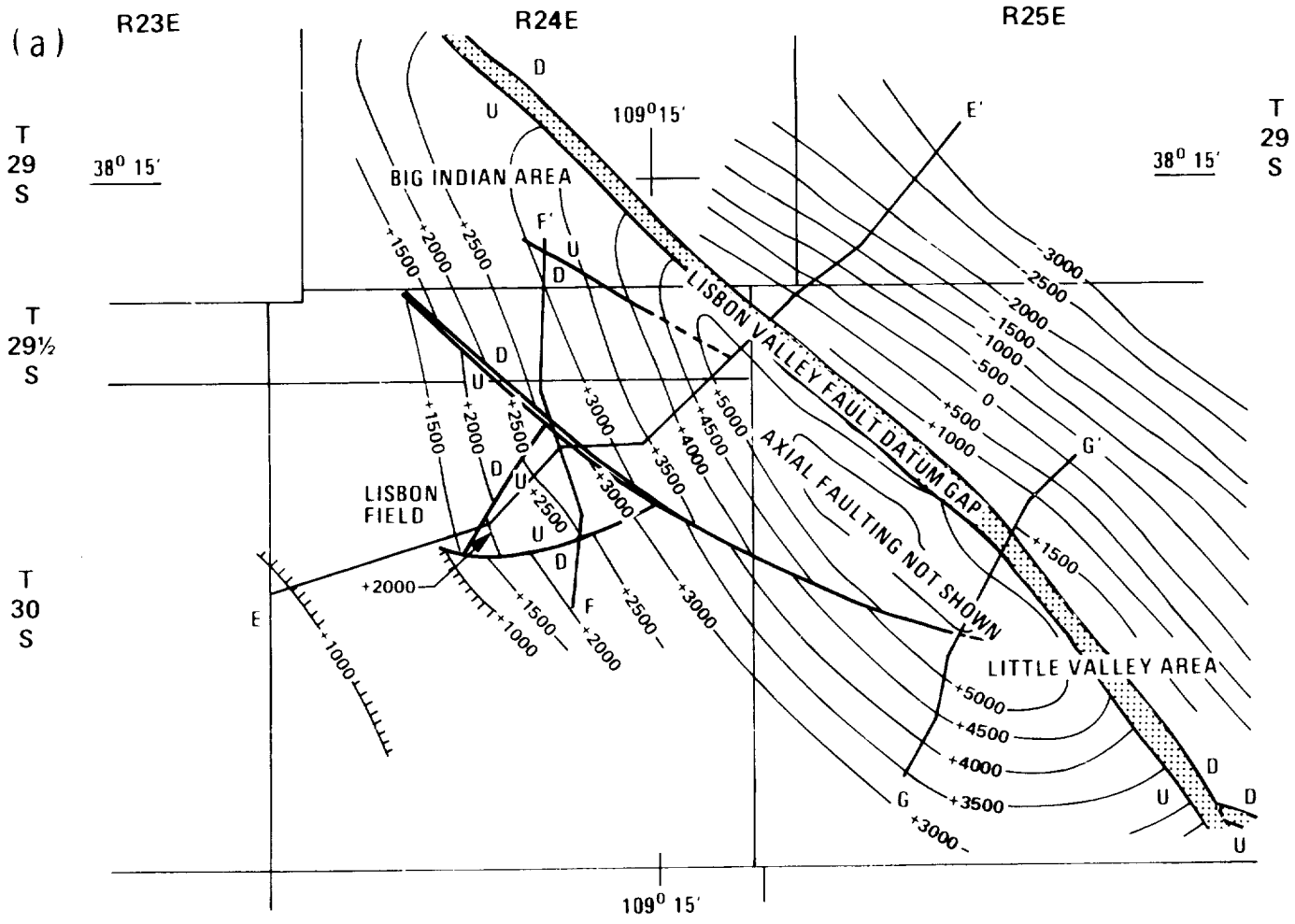

Figure 8-46. Pennsylvanian Paradox Formation (modified from Parker, 1966): (a) structure contours on the upper surface of the formation, interpreted on the basis of a fracture model

from the Lisbon Canyon Anticline on the northeastern side of Lisbon Valley Fault. On the southwestern side these rocks are exposed updip in the core of the anticline (Figure 8-10) and are not productive (Parker, 1966). Thus, the distribution of oil (i.e., condensate) and gas in the subsurface is more widespread and both higher and lower in the section than implied in Figure 8-44; the details of this distribution in formations other than the Mississippian are not known.

The relations among bleaching, uranium deposits, and oil and gas accumulations along section line EE′ of Figure 8-44 are shown in the cross section of Figure 8-45. The cross section is adapted from Parker (1966) and additions are made from the geologic maps of Weir and Dodson (1958a, 1958b, 1958c). The major oil and gas reservoir comprising the Lisbon field resides in a faulted anticlinal arch on the southwestern flank of the anticline 2.5 mi from the surface trace of the fold axis. The position of uranium deposits residing in the Lower Chinle section along EE′ is taken from the ore distribution map, Figure 8-41. The distribution of bleached Wingate rocks is more problematical. Here the transition between altered and unaltered sandstone is shown at 6200 to 6400 ft in elevation, corresponding to the lowest altered outcrops observed south of the section line. The position of this boundary, however, is inferred. Bleached Wingate rock is shown to be displaced by the Lisbon Valley normal fault. This is consistent with truncation of altered strata by the fault in both northern and southern parts of the anticline and by the presence of bleached strata in drill cores from Rio Algom Mine. However, the distribution of Wingate alteration on the downthrown side is not known, and the boundary shown is inferred.

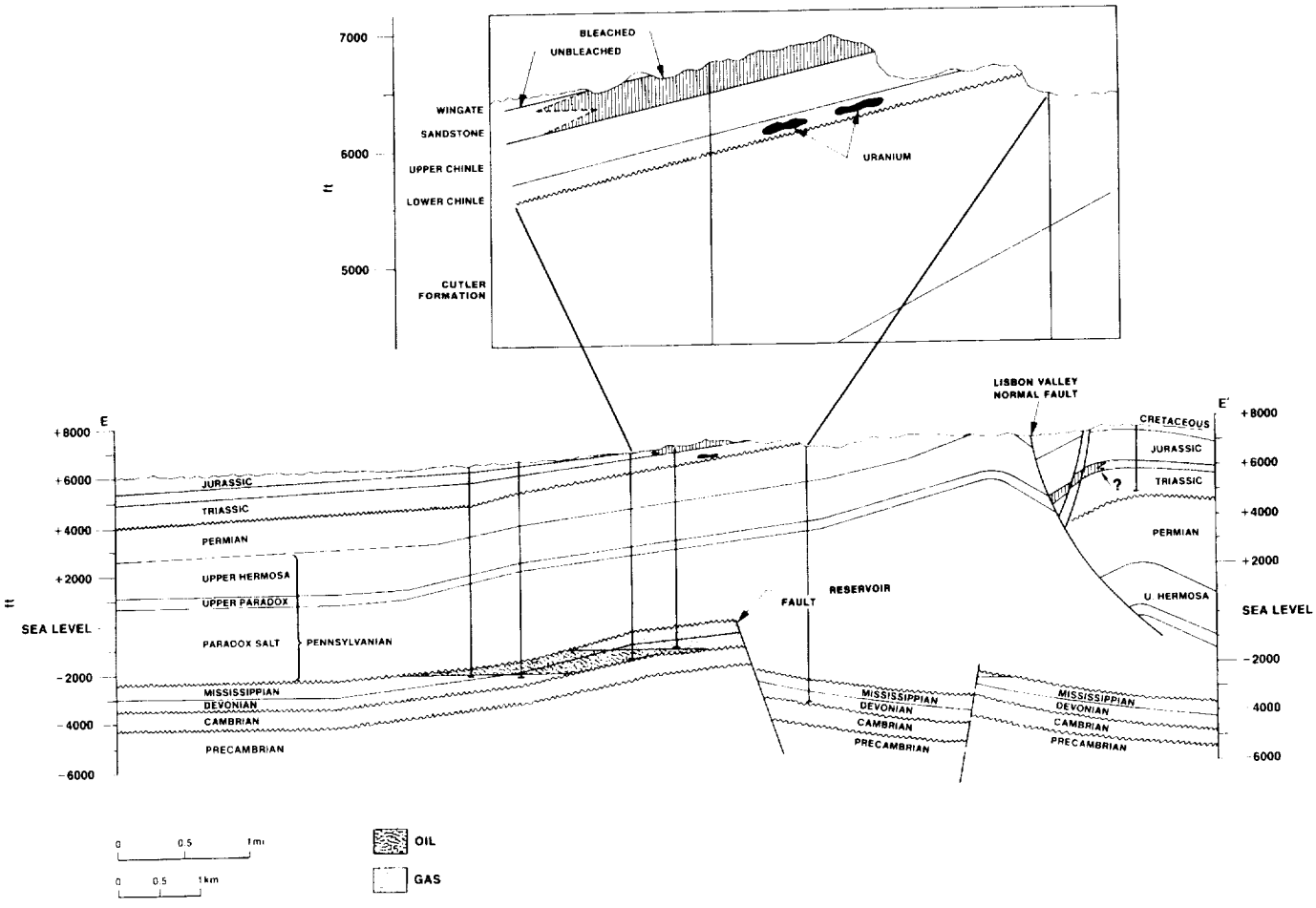

Figure 8-45. Cross section along line EE′ showing generalized distribution of Wingate bleaching and relations of bleaching to uranium mineralization and oil and gas accumulations. Principal section was modified from Parker (1966); enlarged portion from Weir and Dodson (1958a, 1958b, 1958c). Positions of uranium ore bodies were calculated approximately from ore distribution shown in Figure 8-41. Minor normal faulting northeast of Lisbon Valley Fault not shown in Figure 8-44.

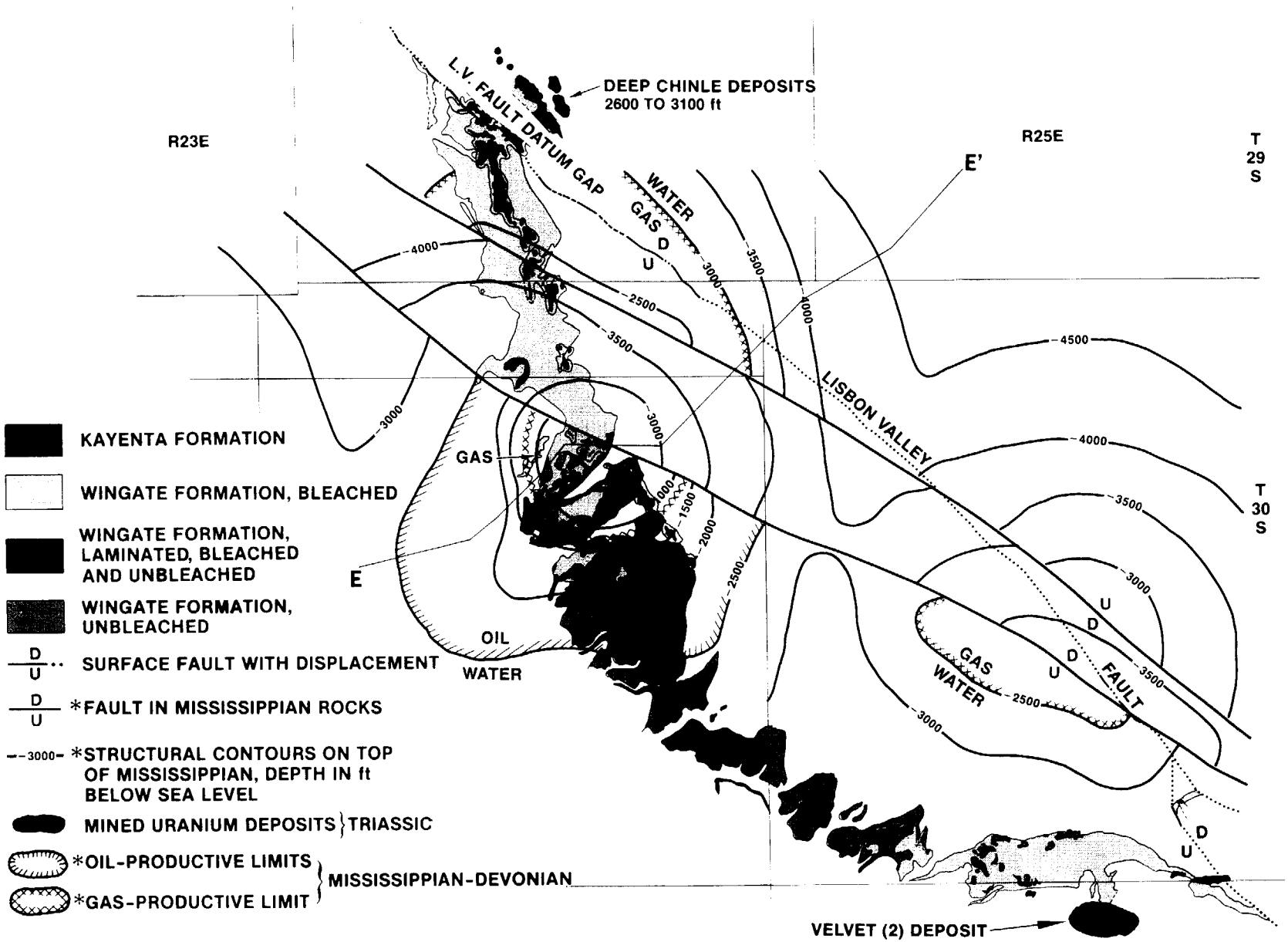

*DATA FROM PARKER (1966)

Figure 8-44. Structural contour map of Mississippian-age reservoir rocks (Leadville Dolomite) in Lisbon Anticline and the distribution of Wingate bleaching and Moss Back uranium mineralization. Northeast of Lisbon Valley Fault, the minor normal faults at the surface have been omitted.

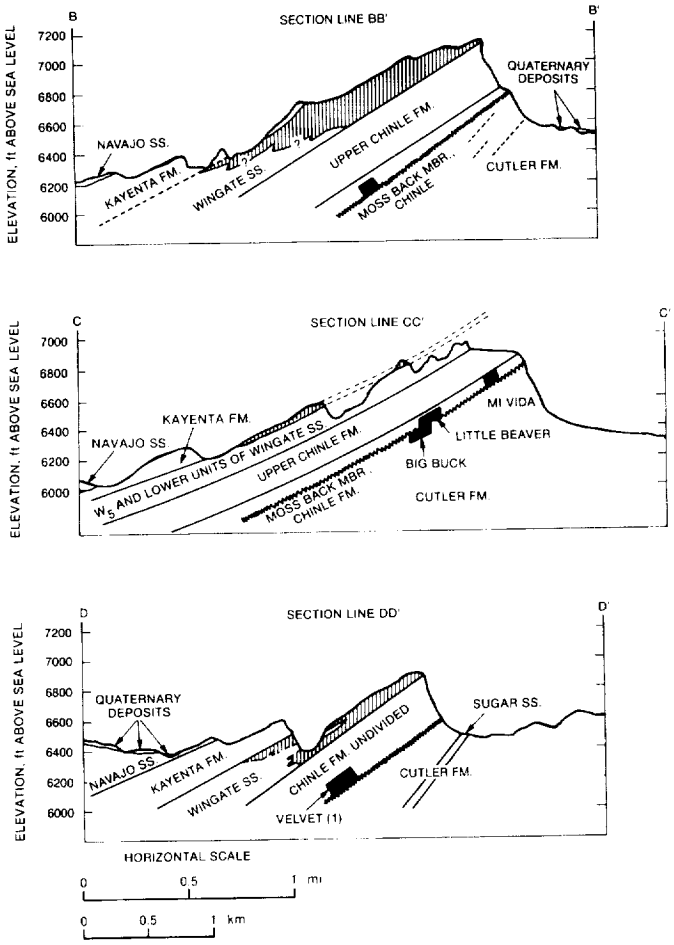

Figure 8-43. Transverse sections across bleached and mineralized intervals. Positions of sections are given in Plate 8-4. Hachured unit is designated as W_5 in Figure 8-27, and as a bleached facies of Wingate Sandstone in Plate 8-1.

These bleached intervals are separated by a middle interval of largely unbleached strata in the center portion of the structure. The unbleached section lies on the flank farthest from the crest and is at a lower elevation. The transition from the bleached to unbleached section is abrupt, but a laminated, partly bleached section can be traced along most of the Wingate exposure. This banded unit is difficult to recognize and map in some places to the south because the interval appears to thin, and the intensity of bleaching diminishes significantly. The banded unit is not discriminated in any of the scanner data studied. Erosion has modified the distribution of bleached strata. Uranium mineralization is always overlain by bleached or strongly banded partially bleached units (such as at Mi Vida Mine), and is absent beneath the unbleached section. This Lekas–Dahl interval of mineralization rises in elevation with the bleached section and is contained within the domain of bleached or partly bleached rocks.

The initial distribution of bleached sandstone throughout the anticline of course cannot be determined, but the high topographic position of remnant outcrops near the axis suggests that bleached rocks may have formed a cap in the structure. The lower boundary of bleaching crosscuts the Wingate interval in the transition zone. Here the stratigraphic details are partly worked out; additional field study is needed to characterize fully this boundary and to determine its present orientation in space. The presence of a hood-like distribution of bleaching in the anticline suggests the presence of a fluid or gaseous medium at some point in the history of anticlinal development that may have participated in the alteration process. The history of this can of course only be surmised. Some flexure of the beds prior to bleaching is implied, and some additional flexure may have occurred since cessation of the bleaching time interval.

The spatial relations between bleaching and uranium mineralization in Lisbon Anticline have been illustrated. The distribution of deposits and the distribution of bleaching correlate areally. Mineral deposits appear to lie both above and below but, in general, are adjacent in elevation to the bleached–unbleached interface since it is projected horizontally and down section toward the anticlinal axis. The possibility of further rotation of the beds since the time of mineralization and bleaching further confuses the geometry and obscures the precise significance of the Lekas–Dahl interval.

2. Distribution of petroleum with respect to uranium and bleached outcrops. The distribution of oil and gas in the Lisbon Anticline is known from exploration drilling and production. Parker (1966) and Preston (1961) have discussed the stratigraphic and structural configuration of the major producing reservoirs in detail. The data used here are taken from these papers. The structural contour map drawn on top of the Mississippian Leadville Dolomite defines the configuration of the major reservoir unit in this anticline. This map has been superimposed on the bleaching and ore deposit distribution maps in Figure 8-44. The major dome-shaped reservoirs in Mississippian rocks are fault-bounded against Paradox Formation salt and black shale beds in a NW-trending graben. Taken together, the oil- and gas-producing limits of the Big Indian and Lisbon fields almost completely enclose the distribution of uranium deposits and the distribution of bleaching. To the southeast, bleached outcrops are found 1.5 to 2 mi south of the Little Valley gas accumulation in Mississippian rocks, in the southern portion of T30S, R25E, Figure 8-44.

Mississippian rocks in the anticline are not the only horizons where oil and gas are found. Producing intervals occur in the McCracken Sandstone Member of the Devonian Elbert Formation, in the Pennsylvanian Paradox Formation of the Hermosa Group, and in sandy horizons of the lower part of the Hermosa Formation. The lower Hermosa rocks produce only

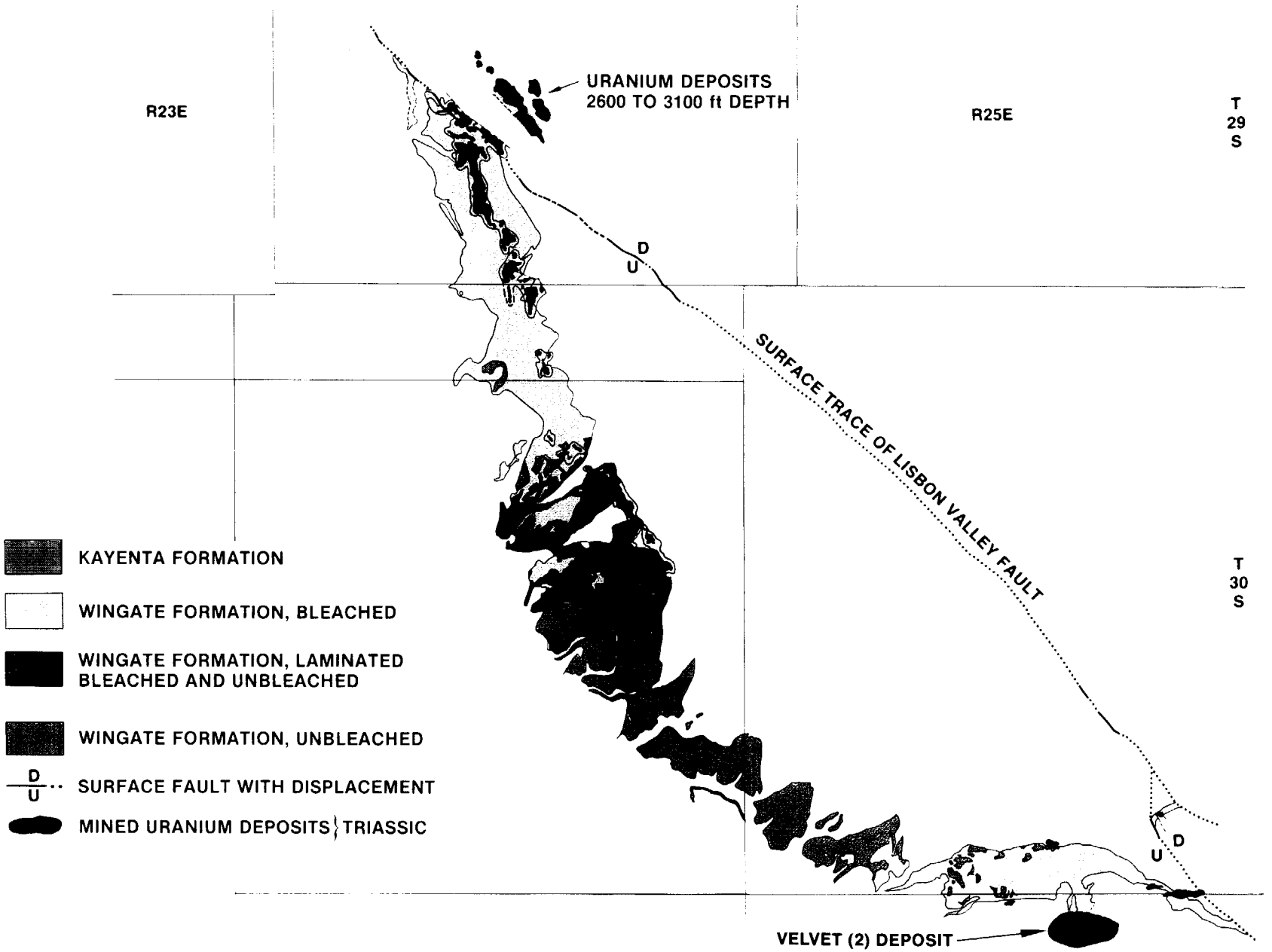

Figure 8-42. Distribution of uranium deposits with respect to bleached, unbleached, and laminated Wingate Sandstone in Lisbon Valley Anticline. Lines enclosing ore bodies represent probable commercial limits of these deposits (> 0.01% U_3O_8).

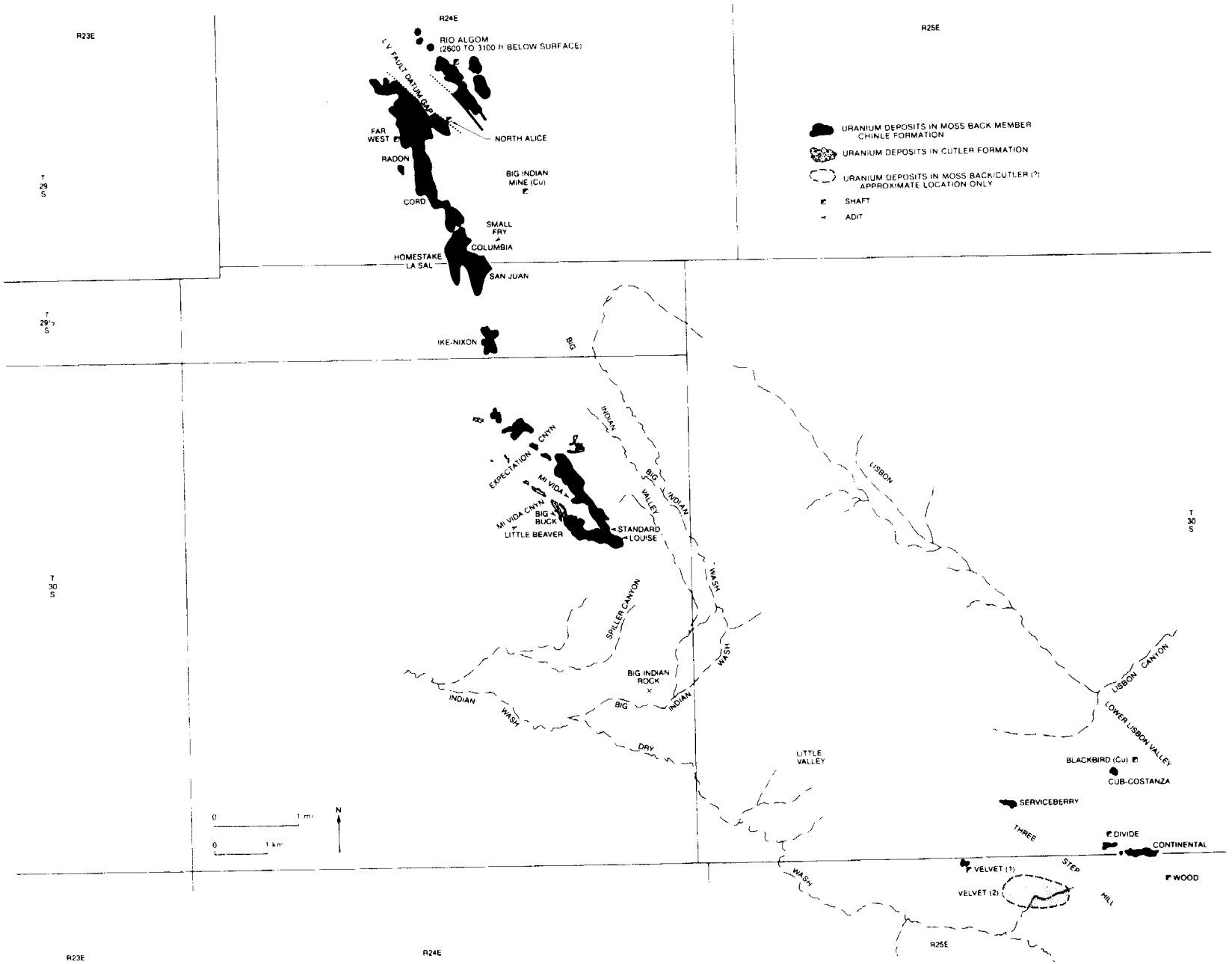

Figure 8-41. Distribution of Moss Back and Cutler massive ore deposits in the Big Indian District and in the southern part of Lisbon Anticline (data courtesy of Atlas Minerals, Division of Atlas Corporation, Moab, Utah)

IX. Structural and Geochemical Relationship Between Bleaching and the Uranium and Oil and Gas Deposits

A. Distribution of Uranium and Oil and Gas Deposits With Respect to Distribution of Bleached Wingate Sandstone

1. Uranium deposit distribution and bleached outcrops. The distribution of known uranium deposits in both the Moss Back and in the Cutler Formation is shown in Figure 8-41. The distribution maps for ore bodies in the Big Indian Valley area, together with approximate location of the Rio Algom deposits on the northeastern downthrown side of Lisbon Valley Fault, were provided by Atlas Minerals. Locations of ore bodies in the southern portion of Lisbon Valley Anticline were obtained from small-scale maps in Wood's (1968) paper. An approximate location of the Velvet (2) ore zone was obtained from patterns of exploration drill sites in August 1979 aerial photographs.

Ore bodies of the Big Indian area form a belt roughly paralleling the face of the escarpment formed by resistant Moss Back and Wingate sediments. Cutler ore bodies in this zone occur largely in a linear trend, some following a sugar sandstone horizon in the Cutler subcrop. Ore bodies in the southern area, on the other hand, are widely scattered as far as the distribution is presently known. The Moss Back and Cutler horizons are devoid of major mineral accumulations between the Standard–Louise ore bodies in the north and Velvet (1) in the south (a distance of 5.5 mi). Lekas and Dahl (1956) noted the discontinuous nature of the mineralized belt and how, where present, it paralleled the strike of enclosing beds. They further pointed out that mineralization on the southeastern flank of Lisbon Valley Anticline is confined almost entirely to a strip between the 6200- and 6700-ft contours drawn on the top of the Cutler Formation, although mineralization is not found continuously within this interval. Within the strip, the ore belt rises up the dip to the southeast. Note that the new Velvet (2) deposit appears to form an exception to the "magic interval" rule of Lekas and Dahl. From its areal position this deposit lies approximately between the 5700- and 5900-ft contours, assuming it falls within the usual Moss Back or upper Cutler stratigraphic interval.

The distribution of uranium deposits within bleached and partly bleached Wingate outcrops is given in Figure 8-42. Except near Expectation and Mi Vida Canyons, all of the ore bodies lie beneath or are closely adjacent to bleached outcrops, including deposits on the northeastern (downthrown) side of Lisbon Valley Fault.

In the Expectation–Mi Vida Canyon interval, the stratigraphic relations are characterized by a transition from predominantly bleached strata in the north to predominantly unbleached strata in the south. Layered sandstones in the upper Wingate consist of intercalated bleached and unbleached laminae with the fraction of altered or bleached strata decreasing gradually southward. Moss Back ore bodies in this interval of the Big Indian belt are all found beneath such mixed rocks. No sharp limits of bleaching, visible from above, appear to exist that may be compared with the comparatively well-defined limits of mineralization.

The three-dimensional relations between bleached rocks and uranium deposits are illustrated in the cross section AA ''' of Plate 8-4. Bleached sandstones are unit W_1. The magic interval for uranium deposits of Lekas and Dahl (1956) is projected onto the plane of the cross section. Mineralized intervals at specific places noted are obtained by projection from the map data of Figure 8-41. The elevation positions of the intervals shown are computed from the known planar positions of ore bodies, while approximate dips of the Moss Back strata are deduced from the geologic mapping of Weir and Dodson (1958a) and Weir et al. (1961). The apparent disagreements noted result because the actual relations were compressed into a single cross-section line. In general, the Lekas–Dahl interval rises and widens to the southeast, for the most part paralleling the rise in elevation of bleached strata in the profile.

Three profiles, transverse to the cross-section line AA''', are shown in Figure 8-43. In section BB', the position of the bleached boundary is fixed in elevation near 6400 ft by exposures of bleached sandstone in a window through the Kayenta Formation. Both shape and position of the lower boundary are not known. The approximate interval of Moss Back mineralization is between 6100 and 6350 ft. In section CC', the lowest exposures of bleached upper Wingate section (unit W_1) lie at an elevation of 6200 ft. Projection of this horizon updip indicates that much of it may have been removed by erosion over the mineralized interval beneath. The subsurface extension downdip of unit W_1 or the subjacent banded unit W_5 is not known. The mineralized Moss Back and Cutler intervals lie between 6300 and 6800 ft. In section DD', the lowest exposures of bleached rocks are at 6400 ft, which is the same elevation observed for the transition between bleached and unbleached sandstone along profile AA''' to the northwest. The mineralized Moss Back interval (Velvet (1) deposit) is estimated to be between 6100 and 6300 ft along the line of this section.

To summarize, the distribution of Wingate bleaching and Moss Back and Cutler uranium mineralization has been compared throughout the mineralized belt in Lisbon Anticline. Bleached sandstones occupy topographically high outcrops near the crest and at either end of Wingate exposures in the anticline.

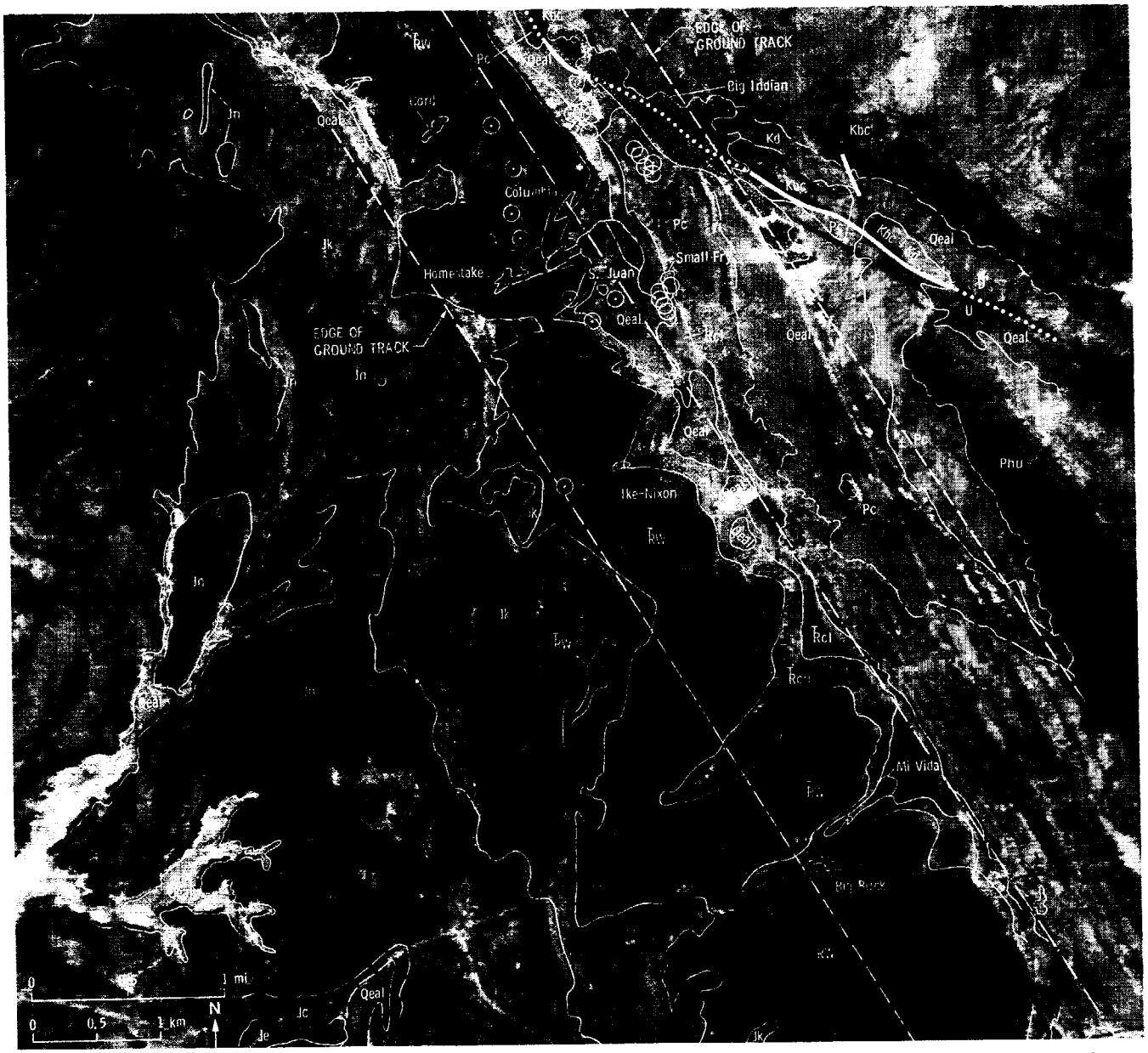

Qeal	QUATERNARY ALLUVIUM AND EOLIAN DEPOSITS
Kd	DAKOTA SANDSTONE (CRETACEOUS)
Kbc	BURRO CANYON FORMATION (CRETACEOUS)
Je	ENTRADA FORMATION (JURASSIC)
Jc	CARMEL FORMATION (JURASSIC)
Jn	NAVAJO SANDSTONE (JURASSIC)
Jk	KAYENTA FORMATION (JURASSIC)
TRW	WINGATE SANDSTONE (TRIASSIC)
TRcu	UPPER CHINLE FORMATION (TRIASSIC)
TRcl	MOSS BACK MEMBER OF CHINLE FORMATION (TRIASSIC)
Pc	CUTLER FORMATION (PERMIAN)
Phu	UPPER HERMOSA FORMATION (PENNSYLVANIAN)

Figure 8-40. Eight-channel PC image from NS-001 scanner for a portion of the Big Indian District. Circles denote locations of major anomalies (greater than 1.93 ppb rhodamine WT dye equivalent) as obtained by analysis of FLD data for the area by Theisen and Watson (1979). The major anomalies there are described as arising from mineralized outcrops of Permian-age Cutler sediments (Pc), copper ore tailings at Big Indian Copper Mine (stippled area), the dump at Small Fry Mine, beneath Moss Back (TRcl) outcrops, and other single-point sites scattered about. The spot size of resolution of the FLD aircraft system is approximately 45 m, whereas the scanner data have a ground resolution of 15 m. It is likely that the FLD data represent unresolved point sources on the ground which would be difficult to pinpoint. A PC rendition of the NS-001 data generally yields excellent separability of major rock units as seen from examination of the figure. No correspondence between prominent FLD anomalies and color patterns on the images has been recognized. Comparisons of other image renditions yield similar results.

Hemphill, W. R., and M. Settle (Eds.) (1981). *Workshop on applications of luminescence techniques to earth resource studies* (LPI Technical Report 81-83). Houston: Lunar and Planetary Institute.

Hite, R. J., and F. W. Cater (1972). Pennsylvanian rocks and salt anticlines, Paradox Basin, Utah and Colorado. In W. W. Mallory (Ed.), *Geologic atlas of the Rocky Mountain region.* Denver: Rocky Mountain Association of Geologists, 133–138.

Hoefs, J. (1980). *Stable isotope geochemistry.* New York: Springer-Verlag.

Horwitz, H. M., J. T. Lewis, and A. P. Pentland (1975). *Estimating proportions of objects from multispectral scanner data* (ERIM Report No. 109600-13-F). Ann Arbor: Environmental Research Institute of Michigan.

Horwitz, H. M., R. F. Nalepka, P. D. Hyde, and J. P. Morgenstern (1971). Estimating the proportions of objects within a single resolution element of a multispectral scanner. *Seventh International Symposium on Remote Sensing of Environment* (Report No. 10259-1-X). Willow Run Laboratories of the Institute of Science and Technology, the University of Michigan, Ann Arbor, 1307–1320.

Hostetler, P. B., and R. M. Garrels (1962). Transportation and precipitation of uranium and vanadium at low temperatures, with special reference to sandstone-type uranium deposits. *Econ. Geol., 57*(2), 137–167.

Huber, G. C. (1979). *Stratigraphy and uranium deposits of the Lisbon Valley District, San Juan County, Utah.* Unpublished doctoral dissertation, Colorado School of Mines, Golden.

Hunt, G. R., and J. W. Salisbury (1976). Visible and near-infrared spectra of minerals and rocks: XI. Sedimentary rocks. *Mod. Geol., 5,* 211–217.

Hunt, G. R., J. W. Salisbury, and C. J. Lenhoff (1971). Visible and near-infrared spectra of minerals and rocks: IV. Sulphides and sulphates. *Mod. Geol., 3,* 1–14.

Jacobs, J. A., and P. F. Kerr (1965). Hydrothermal alteration along the Lisbon Valley fault zone, San Juan County, Utah. *Geol. Soc. Am. Bull., 76,* 423–440.

Jacobs, M. B. (1963). *Alteration studies and uranium emplacement near Moab, Utah.* Doctoral dissertation, Columbia University, New York.

Jensen, M. L. (1958). Sulfur isotopes and the origin of sandstone-type uranium deposits. *Econ. Geol., 53,* 598–616.

Karstev, A. A., S. A. Tobasaranskii, M. I. Subbota, and G. A. Moglievskii (1959). *Geochemical methods of prospecting and exploration for petroleum and natural gas.* Berkeley: University of California Press.

Lekas, M. A., and H. M. Dahl (1956). The geology and uranium deposits of the Lisbon Valley Anticline, San Juan County, Utah. *Intermountain Assoc. Petrol. Geol. 7th Ann. Field Conf.,* 1956, 161–168.

Loring, W. B. (1958). *Geology and ore deposits of the northern part of the Big Indian District, San Juan County, Utah.* Unpublished doctoral dissertation, University of Arizona, Tucson.

Miller, D. S., and J. L. Kulp (1963). Isotopic evidence on the origin of the Colorado Plateau uranium ores. *Geol. Soc. Am. Bull., 74,* 609–630.

Miller, L. J. (1958). The chemical environment of pitchblende. *Econ. Geol., 53,* 521–545.

Morin, F. J. (1954). Electrical properties of α-Fe_2O_3. *Phys. Rev., 93*(6), 1195–1199.

Parker, J. M. (1966). Lisbon field area, San Juan County, Utah. *AAPG Mem. 9, 2,* 1371–1388.

Peterson, F., and G. N. Pipiringos (1979). Stratigraphic relations of the Navajo Sandstone to Middle Jurassic Formations, southern Utah and northern Arizona. *U.S. Geol. Surv. Prof. Pap. 1035-B.*

Peterson, J. A., and R. J. Hite (1969). Pennsylvanian evaporite cycles and their relation to petroleum occurrence, southern Rocky Mountains. *AAPG Bull., 53,* 884–908.

Preston, D. (Ed.) (1961). Lisbon field, San Juan County, Utah. *A Symposium of the Oil and Gas Fields of Utah.* Intermountain Association of Petroleum Geologists.

Schmitt, L. J. (1968). *Uranium and copper mineralization in the Big Indian Wash–Lisbon Valley Mining District, southeastern Utah.* Doctoral dissertation, Columbia University, New York.

Schneider, R. C., B. Tohill, and J. R. Taylor (1969). Petroleum potential of the Paradox Basin in future petroleum provinces of the United States–Their geology and potential. In I. H. Cram (Ed.), *AAPG Mem. 15,* 470–488.

Singer, P. C., and W. Stumm (1968). Kinetics of the oxidation of ferrous iron. *Second Symposium on Coal Mine Drainage Research.* Paper presented to the Mellon Institute, Pittsburgh, Pennsylvania, 12–34.

Slater, P. (1980). *Remote sensing: Optics and optical systems.* Reading, Massachusetts: Addison–Wesley Publishing Company.

Soha, J. M., and A. A. Schwartz (1978). Multispectral histogram normalization contrast enhancement. *Proceedings of the Fifth Canadian Symposium on Remote Sensing,* 86–93.

Stieff, L. R., T. W. Stern, and R. G. Milkey (1953). A preliminary determination of the age of some uranium ores of the Colorado Plateau by the uranium–lead method. *U.S. Geol. Surv. Circ. 271.*

Stokes, W. L. (1956). Nature and original of Paradox Basin salt structures. *Intermountain Assoc. Petrol. Geol. 7th Ann. Field Conf.,* 1956, 42–47.

Theisen, A. F., and R. D. Watson (1979). Interpretation of luminescence image of mineralized areas, Big Indian Valley, Utah. *U.S. Geol. Surv. Open File Rep. 79–574.*

Thode, H. G. (1972). Sulfur isotope fractionation in biological processes. In R. W. Fairbridge (Ed.), *The encyclopedia of geochemistry and environmental sciences* (Vol. IVa). Stroudsburg, Pennsylvania: Dowden, Hutchinson and Ross, 1152–1158.

Walker, T. R., E. E. Larson, and R. P. Hoblitt (1981). Nature and origin of hematite in the Moenkopi Formation (Triassic) Colorado Plateau: A contribution to the origin of magnetism in red beds. *J. Geophys. Res., 86*(B1), 317–333.

Watson, R. D., and W. R. Hemphill (1976). Use of an airborne Fraunhofer line discriminator for the detection of solar stimulated luminescence. *U.S. Geol. Surv. Open File Rep. 76202.*

Weir, G. W., W. D. Carter, W. P. Puffett, and J. L. Gualtieri (1960a). Preliminary geologic map and section of the Mount Peale 4 NE quadrangle San Juan County, Utah, and Montrose and San Miguel Counties, Colorado. *U.S. Geol. Surv. Min. Invest. Field Studies Map MF-150.*

Weir, G. W., and C. L. Dodson (1958a). Preliminary geologic map of the Mount Peale 3 NE quadrangle, San Juan County, Utah. *U.S. Geol. Surv. Invest. Field Studies Map MF-145.*

Weir, G. W., and C. L. Dodson (1958b). Preliminary geologic map of the Mount Peale 3 SE quadrangle, San Juan County, Utah. *U.S. Geol. Surv. Min. Invest. Field Studies Map MF-147.*

Weir, G. W., and C. L. Dodson (1958c). Preliminary geologic map of the Mount Peale 4 SW quadrangle, San Juan County, Utah. *U.S. Geol. Surv. Min. Invest. Field Studies Map MF-148.*

Weir, G. W., C. L. Dodson, and W. P. Puffett (1960b). Preliminary geologic map of the Mount Peale 2 SE quadrangle, San Juan County, Utah. *U.S. Geol. Surv. Min. Invest. Field Studies Map MF-143.*

Weir, G. W., and W. P. Puffett (1960). Preliminary geologic map of the Mount Peale 4 SE quadrangle, San Juan County, Utah and San Miguel County, Colorado. *U.S. Geol. Surv. Min. Invest. Field Studies Map MF-149.*

Weir, G. W., W. P. Puffett, and C. L. Dodson (1961). Preliminary geologic map and section of the Mount Peale 4 NW quadrangle, San Juan County, Utah. *U.S. Geol. Surv. Min. Invest. Field Studies Map MF-151.*

Wiersma, D. J., and D. A. Landgrebe (1980). Analytical design of multispectral sensors. *IEEE Trans. Geosci. Rem. Sens., GE-18*(2), 180–189.

Wood, H. B. (1968). Geology and exploitation of uranium deposits in the Lisbon Valley area, Utah. In J. D. Ridge (Ed.), *Ore deposits of the United States, 1933–1967* (Vol. 1). New York: American Institute of Mining, Metallurgical, and Petroleum Engineers, 770–789.

Appendix A
Relation of Scanner DN Values to Ground Reflectance

I. Basic Relations

Aircraft scanner image data are recorded on magnetic tape as digital number (DN) values representing a radiance level for each spectral channel within the scanner's instantaneous field of view (IFOV). Recorded radiance data contain contributions from atmospheric scattering and attenuation in addition to the sought-after information on bidirectional ground reflectance. The DN values also incorporate instrument electronic gain and offset factors. A correction must be applied to the image data to remove variations in brightness transverse to the flight path. The "brightness gradient," which is the object of this correction, originates from scattering effects in the atmosphere and to some extent from the surface. The angular distribution of anomalous brightness is not reproducible using a Rayleigh scattering atmosphere model and, thus, probably arises from aerosol or water vapor scattering from large particles. A glory effect is often conspicuous in aerial photographs taken simultaneously with the scanner data. This effect consists of a bright aureole in a direction opposite the sun, with the maximum intensity lying in the plane of solar incidence. It is often possible to see concentric oscillations in brightness about the maximum intensity that arises from Mie-type single particle diffraction (Deirmendjian, 1969, p. 51–55; Greenler, 1980). The image brightness gradient corrections are empirically estimated by examining the variations in radiance across the flight path, where possible, over areas of generally uniform surface properties. The measured radiance in each band is adjusted to a flat field across the image.

All of the instrumental factors and proposed corrections represent linear and nonlinear transformations on the actual surface reflectance values. The following heuristic arguments are intended to clarify the nature of these transformations and to provide a basis for estimating ground reflectance properties from the image radiance values, given a minimum of information about actual reflectance of the terrain.

Previous methods of accounting approximately for atmospheric effects from the images themselves include dark object subtraction (Goetz et al., 1975) or a variation of this method (Bolivar et al., 1981). The subtraction method uses deeply shadowed or poorly reflecting portions of the scene to estimate contributions of the atmosphere alone. Switzer et al. (1981) have developed a method using the covariance matrix and the reflectance from homogeneous areas. The alternative to such internal estimation schemes lies in the use of standard atmospheric models to provide atmospheric absorption and scattering directly. In general, information was not available on surface relative humidity, air temperature, water vapor, aerosol content, or the variation of these quantities at altitude for any of the sites studied. Thus, applications of the standard models are questionable, although they still have to be investigated and compared to the results obtained by the present method.

The radiative transfer model used to secure a functional form for the emergent radiance in terms of ground reflectance is adapted from Slater (1980). The model is equivalent to that describing solar radiance reflected from Earth, as measured by a satellite. Since aircraft are in fact immersed in the atmosphere, this approximation is equivalent to neglecting the atmosphere above the aircraft. Apart from alteration of various attenuating path lengths, the approximation (1) neglects diffuse illumination beneath the aircraft of both the atmosphere and the Earth's surface, as provided by the missing atmospheric slice, and (2) neglects diffuse downward reflection of upwelling radiation by the missing layer. Neither of these terms is expected to be important at the operational altitudes used.

At the ground, the radiance passing through the atmosphere is composed of directly transmitted and diffusely scattered contributions, represented as follows:

PRECEDING PAGE BLANK NOT FILMED

$$E(\lambda) = E_o(\lambda)\cos\theta_z \exp[-\tau(\lambda)\sec\theta_z]$$

$$+ \int_o^{2\pi}\int_o^{2/\pi} L_d(\lambda;\theta_z,\theta',\phi')\cos\theta'\sin\theta'\,d\theta'\,d\phi' \quad \text{(A-1)}$$

where

$E_o(\lambda)$ = solar spectral irradiance at wavelength λ

$L_d(\lambda;\theta_z,\theta',\phi')$ = downward spectral radiance from scattered solar flux

θ_z = incidence angle of the sun

θ',ϕ' = spherical polar coordinates of a scattered beam

$\tau(\lambda)$ = atmospheric optical depth at wavelength λ

Radiance at the sensor neglecting multiple reflections between the atmosphere and the ground is

$$L_S(\lambda) = \frac{1}{\pi}[E(\lambda)\rho(\lambda)\tau_u(\lambda)] + L_u(\lambda) \quad \text{(A-2)}$$

where

$\rho(\lambda)$ = surface bidirectional reflectance at wavelength λ, assumed here to be Lambertian, i.e., independent of angle

$\tau_u(\lambda)$ = atmospheric attenuation between the surface and the sensor at wavelength λ

$L_u(\lambda)$ = upward-directed diffusely scattered atmospheric radiation

The throughput radiance arriving at the detector is

$$L_i = G\int_{\Delta\lambda_i} L_S(\lambda)T_i(\lambda)\,d\lambda \quad \text{(A-3)}$$

where $T_i(\lambda)$ = instrument throughput for channel i, and G is a constant factor that depends on the optical characteristics of the system. The radiances represented by Eq. (A-3) are converted to voltage and recorded on tape as DN values dn_i. This instrument transformation for the Landsat 4 Thematic Mapper (TM) is linear. For the NS-001 the form is not known, but over the total range of the L_i is assumed to be linear, i.e.,

$$dn_i = \pi\alpha_i L_i + \beta_i \quad \text{(A-4)}$$

In the aircraft system, the constants α_i and β_i may be determined using the standard lamp pixel values obtained as engineering data. At the end of each image scan line, observations of a standard (bright) lamp and a standard (dark) blackbody serve to fix two points on the radiance scale of each detector. Thus, any inherent system nonlinearity is indeterminant from the scanner and ancillary engineering data.

Combining Eqs. (A-2, A-3, and A-4) gives

$$dn_i = \alpha_i G\int_{\Delta\lambda_i} E(\lambda)\rho(\lambda)\tau_u(\lambda)T_i(\lambda)\,d\lambda$$

$$+ \alpha_i G\int_{\Delta\lambda_i} L_u(\lambda)T_i(\lambda)\,d\lambda + \beta_i \quad \text{(A-5)}$$

Using the mean value theorem, the integral in the first term of Eq. (A-5) can be rewritten to remove $\rho(\lambda)$ from beneath the integral sign as

$$dn_i = \alpha_i G\bar{\rho}_i\int_{\Delta\lambda_i} E(\lambda)\tau_u(\lambda)T_i(\lambda)\,d\lambda$$

$$+ \pi\alpha_i G\int_{\Delta\lambda_i} L_u(\lambda)T_i(\lambda)\,d\lambda + \beta_i \quad \text{(A-6)}$$

where $\bar{\rho}_i$ represents a value within the limits of $0 < \rho(\lambda) < 1$.

Equation (A-6) may be simplified as

$$dn_i = \alpha_i G\bar{\rho}_i E_i + \alpha_i G_i A_i + \beta_i \quad \text{(A-7)}$$

where

$$E_i = \int_{\Delta\lambda_i} E(\lambda)\tau_u(\lambda)T_i(\lambda)\,d\lambda \quad \text{(A-7a)}$$

$$A_i = \pi\int_{\Delta\lambda_i} L_u(\lambda)T_i(\lambda)\,d\lambda \quad \text{(A-7b)}$$

The values dn_i vary over the scene in response to changes in ground reflectance and atmospheric conditions. Thus, the quantities $\bar{\rho}_i$, E_i, and A_i in Eq. (A-7) are functions of position. Let (x_k, y_k) represent the coordinates of a pixel with y_k measured along the flight line, and x_k defining the sample within line y_k. Eq. (A-7) modified to account for this is

$$dn_i(x_k,y_k) = \alpha_i G\bar{\rho}_i(x_k,y_k)E_i(x_k,y_k) + \alpha_i A_i(x_k,y_k) + \beta_i \quad \text{(A-8)}$$

One way to estimate atmospheric properties from the radiance data, themselves, is to find a portion of the scene where

the $\bar{\rho}_i$ is constant for a range of x_k,y_k. Call the value of Eq. (A-8) obtained for a specific line y_o and all x_k within the line the reference function. Thus,

$$dn_i(x_k,y_o) = \alpha_i[G\bar{\rho}_i(y_o)E_i(x_k,y_o) + A_i(x_k,y_o)] + \beta_i \quad \text{(A-9)}$$

in which the variations in dn_i are due to instrumental and angular atmospheric effects alone.

Two empirical methods are available to remove the angular-dependent atmospheric (and surface) contributions. These are called the additive and the multiplicative procedures because position-dependent empirical functions are either added to or multiplied into the position-dependent image radiance function to effect the desired corrections. Examples of each process are given below, but only the multiplicative procedure will be described in detail because this procedure has been used in practice.

To remove the atmospheric effects by the multiplicative procedure, define the function $dn_i(x_k,y_o)$ in terms of the reference function as

$$d\bar{n}_i(x_k,y_o) \cdot dn_i(x_k,y_o)^{-1} = k_i^{-1} \quad \text{(A-10)}$$

where k_i is an arbitrary constant. Then multiplying Eq. (A-9) by $d\bar{n}_i$ gives

$$DN_i = dn_i(x_k,y_o) \cdot d\bar{n}_i(x_k,y_o)$$

$$= \bar{k}_i \cdot \frac{\alpha_i G\bar{\rho}_i(x_k,y_k)E_i(x_k,y_k) + \alpha_i A_i(x_k,y_k) + \beta_i}{\alpha_i G\bar{\rho}_i(y_o)E_i(x_k,y_o) + \alpha_i A_i(x_k,y_o) + \beta_i}$$

$$+ \text{constant} \quad \text{(A-11)}$$

where the constant is added and k_i is adjusted to $\bar{k}_i$ to rescale the DN_i to fill the available dynamic range ($0 \leq DN_i \leq 255$). Equation (A-11) is in general a nonlinear transformation, but *a posteriori* can be verified by inspection that it, in fact, produces highly linear results. Let

$$X_i = \alpha_i G\bar{\rho}_i(x_k,y_k)E_i(x_k,y_k)$$

$$X_{io} = \alpha_i G\bar{\rho}_i(y_o)E_i(x_k,y_o)$$

$$\epsilon_i = \alpha_i A_i(x_k,y_k) + \beta_i$$

$$\epsilon_o = \alpha_i A_i(x_k,y_o) + \beta_i$$

Then Eq. (A-11) becomes

$$DN_i = \bar{k}_i \frac{X_i + \epsilon_i}{X_{io} + \epsilon_{io}} + \text{constant} \quad \text{(A-12)}$$

To simplify this fraction, atmospheric effects are assumed to be small relative to the principal terms, i.e., $\epsilon_i << X_i$, $\epsilon_o << X_{io}$. Thus,

$$DN_i \simeq \bar{k}_i \frac{1}{X_{io}}(X_i + \epsilon_i)\left[1 - \frac{\epsilon_{io}}{X_{io}} + R\left(\frac{\epsilon_{io}^2}{X_{io}^2}\right)\right] + \text{constant}$$

$$\simeq \left[\bar{k}_i\left(1 - \frac{\epsilon_{io}}{X_{io}}\right) + R\left(\frac{\epsilon_{io}^2}{X_{io}^2}\right)\right]\frac{X_i}{X_{io}} + \bar{k}_i\frac{\epsilon_i}{X_{io}}\left(1 - \frac{\epsilon_{io}}{X_{io}}\right)$$

$$+ R\left(\frac{\epsilon_{io}^2}{X_{io}^2}\right) + \text{constant} \quad \text{(A-13a)}$$

where $R(\cdot)$ represents quantities of second and higher order. The various terms in Eq. (A-13a) are

$$\frac{X_i}{X_{io}} \approx \frac{\alpha_i G\bar{\rho}_i(x_k,y_k)E_i(x_k,y_k)}{\alpha_i G\bar{\rho}_i(y_o)E_i(x_k,y_o)} \approx \frac{\bar{\rho}_i(x_k,y_k)}{\bar{\rho}_i(y_o)} \cdot \frac{E_i(x_k,y_k)}{E_i(x_k,y_o)} \quad \text{(A-13b)}$$

If the atmospheric term E_i remains stationary at x_k for all y_k, then $E_i(x_k,y_k) \approx E_i(x_k,y_o)$, as indicated by the uniformity of the gradient-corrected images along the flight line, discussed below. Thus,

$$\frac{X_i}{X_{io}} \simeq \frac{\bar{\rho}_i(x_k,y_k)}{\bar{\rho}_i(y_o)} \quad \text{(A-14a)}$$

The additional factors in Eq. (A-13) have

$$\frac{\epsilon_{io}}{X_{io}} = \frac{\alpha_i A_i(x_k,y_o) + \beta_i}{\alpha_i G\bar{\rho}_i(y_o)E_i(x_k,y_o)}$$

and (A-14b)

$$\frac{\epsilon_i}{X_{io}} = \frac{\alpha_i A_i(x_k,y_k) + \beta_i}{\alpha_i G\bar{\rho}_i(y_o)E_i(x_k,y_o)}$$

These terms contain any remaining dependence upon x_k (i.e., angular dependence) present in the gradient-corrected images. An exact functional form for the angular part cannot be specified unless a specific atmospheric model is assumed. Instead, the results of applying such corrections to images were inspected. The transformed images were seen to be free of gradient-related atmospheric effects in x_k everywhere, i.e., for all y_k. This implies that the quantities on the left-hand sides of Eqs. (A-14a) and (A-14b) are constants in x_k and y_k. A similar argument

applies to the y_k dependences of A_i in Eq. (A-14b) and for the statement $A_i(x_k,y_k) \approx A_i(x_o,y_o)$.

Figure A-1(a) is a three-color composite image of Bendix 24-channel scanner data for Lisbon Valley, Utah, depicting the transverse brightness gradient effect typically encountered in the aircraft scanner data of this and other areas. The aircraft and solar position parameters for the flight are given in Table 8-6.

Figure A-1(b) represents the results of applying an additive gradient removal transformation to these image data. The (linear) empirical transformation function was obtained by averaging data collected over uniform sage and grass-covered alluvial slopes comprising the northern-most part of the image. The transformation of the standard area is uniform in brightness, and the remaining area of the image is largely gradient-free also.

Figure A-1(c) represents the result of a multiplicative gradient removal transformation applied to this image. The result is similar to that shown in Figure A-1(b) (blue and red have been switched in this case).

The terms in Eq. (A-13a) containing R are of order ϵ_{io}^2/X_{io}^2 or higher. These terms are small but not necessarily negligible, and are probably of greater importance at shorter wavelengths where Rayleigh atmospheric scattering is important. They too are independent of x_k since they are a function of ϵ_{io}.

Eq. (A-13) resolves itself ultimately into the linear form

$$DN_i = k_i'\bar{\rho}_i(x_k,y_k) + k_i'' \qquad \text{(A-15)}$$

where the k_i' and k_i'' are constants, containing all the instrumental atmospheric and computer scaling parameters present in the model.

The determination of k_i' and k_i'' is in principle made by a two-point calibration using known values of ground reflectance $\bar{\rho}_i(x_1,y_1)$, $\bar{\rho}_i(x_2,y_2)$ corresponding to DN values $DN_i(x_1,y_1)$, $DN_i(x_2,y_2)$. Estimates of the $\bar{\rho}_i$ can be obtained from field reflectance (PFRS) data over sites that are spatially uniform at the multiple pixel level. In practice, better determinations of the constants can be made by least square fits to data points from multiple sites representing a range of $\bar{\rho}_i$ as a function of λ, thus more accurately assessing the subpixel size variability in $\bar{\rho}_i$ and grossly accounting for nonlinearities in the lumped instrument/atmospheric response.

II. Effects of the Constants k_i' and k_i'' on Ratio, Principle Component, and Canonical Transformation Image Data

A. Ratio Data

If accurate estimates of the constants k_i' and k_i'' are not obtainable from field and scanner observations, then these constants carry over into the image data as "distortions" of the chosen representation of reflectance information.

If the image data are to be presented as ratios, the resulting DN values before application of any stretching functions are of the form

$$\frac{DN_i + K_i}{DN_j + K_j} = \frac{k_i'\bar{\rho}_i(x_k,y_k) + k_i'' + K_i}{k_j'\bar{\rho}_j(x_k,y_k) + k_i'' + K_j}$$

$$= \left(\frac{k_i'\bar{\rho}_i}{k_j'\bar{\rho}_j} + \frac{k_i'' + K_i}{k_j'\bar{\rho}_j}\right)\left(1 - \frac{k_j'' + K_j}{k_j''\bar{\rho}_j} + \cdots\right) \qquad \text{(A-16)}$$

where the K_i are additional scaling constants entered for computer processing of the ratio data to ensure that the ratio is not close to zero.

The only case where it is easily possible to get an idea of how this nonlinear transformation affects the display of such ratio quantities is to suppose that

$$\frac{\bar{\rho}_i k_i'}{\bar{\rho}_j k_j'} >> \frac{k_i'' + K_i}{k_j'\bar{\rho}_j}$$

and

$$(k_i'' + K_i) << k_i'\bar{\rho}_j$$

which leads to a linear form in the ratio of reflectances

$$R_{ij} \equiv \frac{DN_i}{DN_j} \simeq \frac{k_i'\bar{\rho}_i}{k_j'\bar{\rho}_j} \qquad \text{(A-17)}$$

Here R_{ij} signifies the ratio of the ith to the jth band. Thus, in this circumstance the ratio quantities R_{ij} are proportional to the ratio of reflectances through the ratio of quantities k_i'/k_j'. The application of a new (say linear) scaling or stretching function to Eq. (A-17) determines the final quantity representative of the ratio as

$$\bar{R}_{ij} = A_m R_{ij} + B_m \qquad (m = 1,2,3) \qquad \text{(A-18)}$$

In this approximation, the ratio image data are proportional, but not equal, to the ratio of reflectance value. Thus, the representation of perfectly calibrated reflectance values as ratios,

Figure A-1. Bendix 24-channel color composite images: (a) uncorrected for atmospheric/surface effects; (b) additive gradient correction; (c) multiplicative gradient correction. Noise-free bands were 1 (0.34–0.40 μm), blue; 13 (2.10–2.36 μm), green; 14 (3.54–4.00 μm), red. Blue and red bands were switched in images (b) and (c).

if rescaled according to Eq. (A-18), does not represent true ratios of reflectance.

The approximations represented by Eq. (A-18) are atypical and probably extreme. Combinations of scaling and stretching transformations in the general case represented by Eq. (A-16) actually serve to distort in a nonlinear way any direct representation of reflectance ratios even for perfectly calibrated radiance measures. These transformations are required for pictorial (image) representation of the reflectance ratios so that numerically $0 < \overline{R}_{ij} < 255$. Although the outcome would be hard to predict, transformations such as Eq. (A-18) almost always provide significant advantages in separation of lithologic, vegetation, or soil units over arbitrarily scaled representations of the same data. The transformations are not, however, simple direct representations of the band ratios.

B. Principal Component and Canonical Transformations

The principal component (PC) transformation begins with a calculation of the elements u_{ij} of the scatter or the (covariance) matrix for the images in the form

$$u_{ij} = \sum_{\xi}^{N} (DN_{i\xi} - \overline{DN}_i)(DN_{j\xi} - \overline{DN}_j) \qquad \text{(A-19)}$$

where the i and j refer to spectral channels and the summation runs over N pixels ξ. The quantity DN_i represents average DN value in band i

$$\overline{DN}_i = \frac{1}{N}\sum_{\xi}^{N} DN_{i\xi} \qquad \text{(A-20)}$$

Using Eq. (A-15),

$$u_{ij} = k'_i k'_j \sum_{\xi}^{N} (\rho_{i\xi} - \overline{\rho}_i)(\rho_{j\xi} - \overline{\rho}_j) = k'_i k'_j u'_{ij} \qquad \text{(A-21)}$$

The problem is how to impart physical meaning to the eigenvalues and eigenvectors of matrices $\|u_{ij}\|$ and $\|u'_{ij}\|$ (related by Eq. A-21), which represent, respectively, the scatter matrix based on the unadjusted scanner radiance data alone, and the scatter matrix based on reflectance numbers alone. A simple representation of these differences for the general case does not seem possible; however, since the characteristics of the distribution change, the principal axes will be different in orientation and the principal values will be different in magnitude for each.

The only simple case assigns equal values k_o to all of the gain factors k'. The secular equation for $\|u_{ij}\|$ determining the eigenvalues $\lambda_{(n)}$ is

$$|u_{ij} - \lambda_{(n)}\delta_{ij}| = 0 \qquad (n = 1,2,\ldots,L) \qquad \text{(A-22)}$$

where δ_{ij} is the Kronecker delta. L represents the number of channels in the analysis. If, for example, $L = 2$, then

$$\begin{vmatrix} k_o^2 u'_{11} - \lambda & k_o^2 u'_{12} \\ k_o^2 u'_{12} & k_o^2 u'_{22} - \lambda \end{vmatrix} = 0 \qquad \text{(A-23)}$$

Expanding leads to

$$\lambda_{(n)} = k_o^2 \lambda'_{(n)} \qquad (n = 1,2) \qquad \text{(A-24)}$$

where the $\lambda'_{(n)}$ are characteristic values for the covariance matrix of reflectances. The components $X_i^{(n)}$ of the eigenvectors are given by

$$\sum_{j=1}^{2} u_{ij} X_j^{(n)} = \lambda_{(n)} X_i^{(n)} \qquad (n = 1,2) \qquad \text{(A-25)}$$

Using Eqs. (A-24) and (A-21)

$$\sum_{j=1}^{2} k_o^2 u'_{ij} X_j^{(n)} = k_o^2 \lambda'_{(n)} X_i^{(n)} \qquad \text{(A-26)}$$

and these components remain unchanged; that is, the principal axes of scatter for the observation in space remain the same. The scatter ellipsoid is changed in scale by the factor k_o^2. The values of DN_i given by Eq. (A-15) are

$$DN^{(n)} = \sum_{j=1}^{2} DN_j X_j^{(n)} \qquad \text{(A-27)}$$

so the PCs for an image transformed according to eigenvectors given by Eq. (A-21) are unaffected by this change in scale.

If the gain factors are changed by small quantities $k_o\epsilon_1$ and $k_o\epsilon_2$, then the secular Eq. (A-27) using Eq. (A-21) becomes

$$\begin{vmatrix} k_o^2(1+\epsilon_1)^2 u'_{11} - \lambda & k_o^2(1+\epsilon_1)(1+\epsilon_2)u'_{12} \\ k_o^2(1+\epsilon_1)(1+\epsilon_2)u'_{12} & k_o^2(1+\epsilon_2)^2 u'_{22} - \lambda \end{vmatrix} = 0 \qquad \text{(A-28)}$$

Multiplying this out and collecting terms, the equation for λ is

$$\lambda^2 - k_o^2(\theta + \theta')\lambda + k_o^4 \theta'_2 = 0 \qquad \text{(A-29)}$$

where

$$\left.\begin{aligned}
\theta &= u'_{11} + u'_{22} \\
\theta' &= (2\epsilon_1 + \epsilon_1^2)u'_{11} + (2\epsilon_2 + \epsilon_2^2)u'_{22} \\
\theta'_2 &= f(\epsilon)\theta_2 \\
\theta_2 &= u'_{11}u'_{22} - u'^2_{12} \\
f(\epsilon) &= (2\epsilon_1 + \epsilon_1^2) + (2\epsilon_2 + \epsilon_2^2) \\
&\quad + (2\epsilon_1 + \epsilon_1^2)(2\epsilon_2 + \epsilon_2^2)
\end{aligned}\right\} \quad \text{(A-30)}$$

Changes in the eigenvectors $\lambda_{(n)}$ arising from the addition factors θ' and θ'_2 may be investigated relatively easily if these quantities are small. Thus, from Eq. (A-29) with the unimportant constant k_o set equal to one,

$$d\lambda_{(n)} = \frac{\lambda'_{(n)}\theta' - \theta'_2}{2\lambda'_{(n)} - \theta} \quad \text{(A-31)}$$

which is the total differential of Eq. (A-29) with θ' and θ'_2 as the differential quantities $d\theta \equiv \theta'$ and $d\theta_2 \equiv \theta'_2$. (That is, $d\lambda = (\partial\lambda/\partial\theta)d\theta + (\partial\lambda/\partial\theta_2)d\theta_2$.) The new eigenvalues are

$$\lambda_{(n)} = \lambda'_{(n)} + d\lambda'_{(n)} \quad \text{(A-32)}$$

For computational purposes $\Sigma\lambda_{(k)} = (\lambda_1 - \lambda_2)^2\theta'(2\lambda_1\lambda_2)^{-1}$. The new eigenvectors are

$$(1 + \epsilon_1)^2 u'_{11}X_1^{(n)} + (1 + \epsilon_1)(1 + \epsilon_2)u'_{12}X_2^{(n)} = \lambda_{(n)}X_1^{(n)} \quad \text{(A-33)}$$

$$(1 + \epsilon_1)(1 + \epsilon_2)u'_{12}X_1^{(n)} + (1 + \epsilon_2)^2 u'_{22}X_2^{(n)} = \lambda_{(n)}X_2^{(n)} \quad \text{(A-34)}$$

To illustrate the effects produced by departure of the gain increments ϵ_i from zero, it is useful to deal with a numerical example. Again, two dimensions and small quantities are used, first taking $\epsilon_1 = 0.1$, $\epsilon_2 = 0$ and $k_0 = 1$. Take the matrix

$$\overline{\overline{U}} = \begin{vmatrix} 760.35 & 803.38 \\ 803.38 & 884.56 \end{vmatrix} \quad \text{(A-35)}$$

which is a submatrix consisting of the first two rows and first two columns of the 7 × 7 covariance matrix derived from the uncalibrated NS-001 data of line 6, Lisbon Valley (Table C-1). The principal values of Eq. (A-35) are

$$\overline{\overline{\Lambda}} = \begin{vmatrix} 1628.23 & 0 \\ 0 & 16.68 \end{vmatrix} \quad \text{(A-36)}$$

With the gain increments chosen above, Eq. (A-35) becomes

$$\overline{\overline{U}}' = \begin{vmatrix} 628.39 & 730.34 \\ 730.34 & 884.56 \end{vmatrix} \quad \text{(A-37)}$$

The principal values of Eq. (A-37) are

$$\overline{\overline{\Lambda}}' = \begin{vmatrix} 1497.96 & 0 \\ 0 & 14.99 \end{vmatrix} \quad \text{(A-38)}$$

The eigenvectors for Eq. (A-36) obtained by solving Eq. (A-33) or (A-34) are

$$\overline{\overline{X}}' = \begin{vmatrix} X_1^{(1)} & X_1^{(2)} \\ X_2^{(1)} & X_2^{(2)} \end{vmatrix} = \begin{vmatrix} 0.6794 & -0.7339 \\ 0.7339 & 0.6794 \end{vmatrix} \quad \text{(A-39)}$$

For Eq. (A-37),

$$\overline{\overline{X}}' = \begin{vmatrix} 0.6432 & -0.7657 \\ 0.7657 & 0.6432 \end{vmatrix} \quad \text{(A-40)}$$

The principal axes of the scatter ellipsoid representing reflectances (calibrated for gain factors) and radiance (not calibrated for gain factors) are obtained from Eqs. (A-37) and (A-40), and from (A-36) and (A-39), respectively. Some examples are plotted in Figure A-2. These ellipsoids differ in size and orientation. The differences reflect a (linear calibration) transformation connecting the two. A gain factor applied to the first radiance value ($\epsilon_1 > 0$, $\epsilon_2 = 0$) rotates the first principal axis of the scatter ellipsoid toward the first original axis and expands the scatter distribution from that obtained for reflectances alone. A similar rotation toward the second principal axis would arise with application of the second gain factor ($\epsilon_2 > 0$, $\epsilon_1 = 0$). If both ϵ_1 and ϵ_2 differ from zero, the scatter ellipsoid changes in shape and orientation accordingly. The case for $\epsilon_1 = \epsilon_2 = 0.1$ is plotted in Figure A-2. For equal gain factors, the principal axes remain unchanged from those for the reflectance scatter matrix, u'_{ij}; on the other hand, the eigenvalues and consequently the scatter ellipsoid expand by the factors $(1 + \epsilon_1)^2$, $(1 + \epsilon_2)^2$, or $(1 + \epsilon_1)(1 + \epsilon_2)$, which for this case are all equal to 1.21. The scatter matrix has the eigenvalues given by Eq. (A-36), and the corresponding ellipsoid is the same as that derived for the radiances in Eq. (A-35).

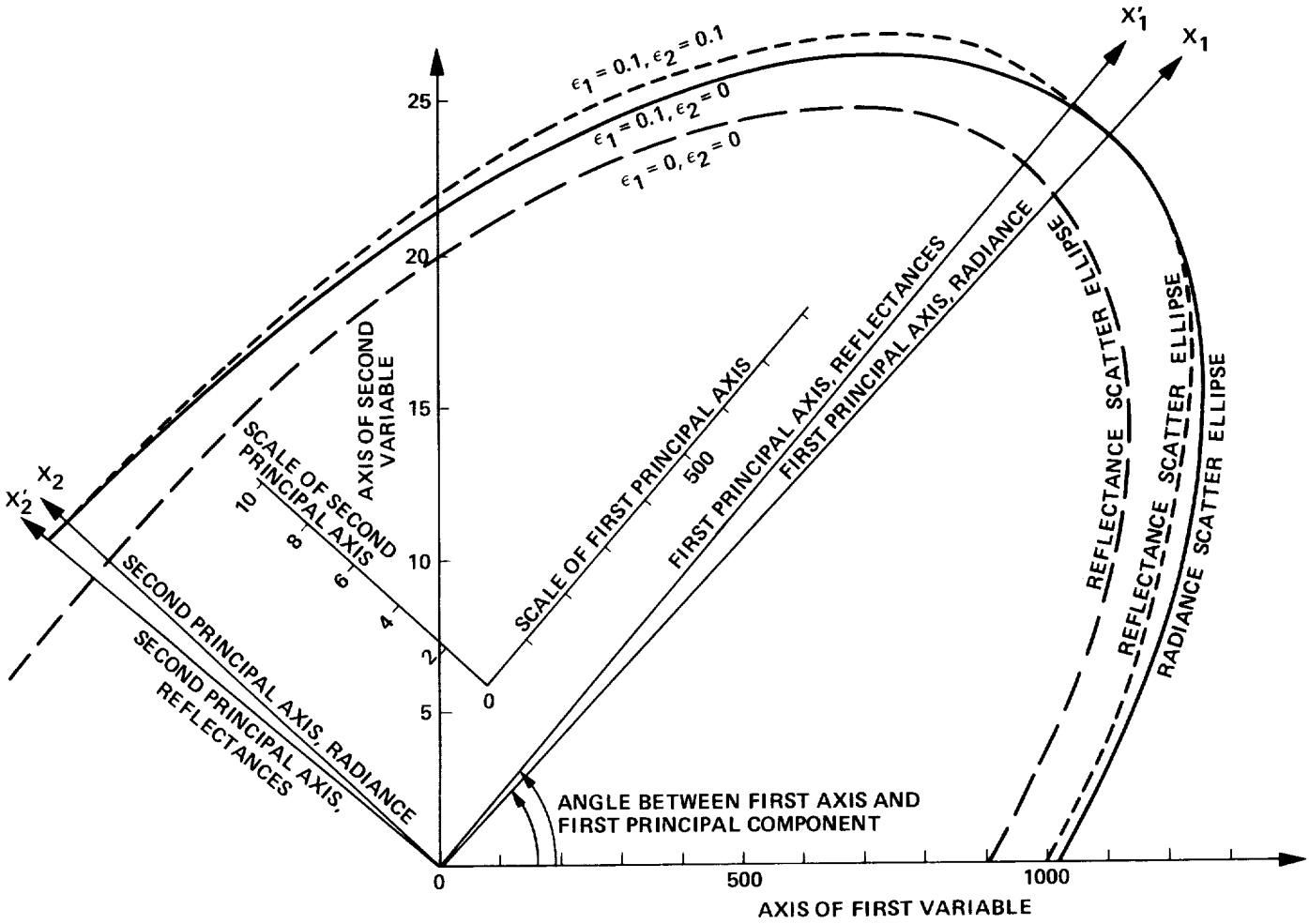

Figure A-2. Various transformations of the scatter ellipsoid resulting from application of gain factors ϵ_1 and ϵ_2 to radiance variables. Reflectance ellipsoid corresponds to scatter computed from the calibrated covariance matrix from the reflectances. Radiance ellipsoid corresponds to scatter computed from the uncalibrated covariance matrix from the radiances. The scale of the second variable axis is 10 times greater than the scale of the first variable.

Judgments on the quality of image products resulting from one transformation method or another are almost totally subjective because quantitative mathematical statements capable of providing an assessment of superior or inferior discriminability based on the images themselves do not exist. Thus, any preference for "calibrated" versus "uncalibrated" image data must be based on a criterion that selects between two descriptions of the same statistical data that differ only by a linear transformation. The PCs themselves may undergo an additional stretching transformation of the type in Eq. (A-18), thus further modifying any sought-after representation as raw reflectance values. In view of these alterations, which are often introduced as visual enhancements, the expected virtues of the calibrated data are probably nonexistent.

The canonical transform (Wilks, 1962, p. 574) is another linear transformation that seeks directions (lines) in sample space along which orthogonal projections of sample clusters provide the largest possible variation between these samples relative to the variation within the projected samples. For two samples from a k-dimensional distribution, the vector components C_k specifying this direction are given by

$$\sum_{j=1}^{k} \left(u_{ij}^{B} - \ell_1 u_{ij}^{W}\right) C_j = 0 \qquad (i = 1,2,\ldots,k) \qquad \text{(A-41)}$$

Where ℓ_1 is the largest nonzero root of the characteristic equation

$$\left| u_{ij}^{B} - \ell u_{ij}^{W} \right| = 0 \qquad \text{(A-42)}$$

The u_{ij}^{B} and u_{ij}^{W} are components of the between-sample and within-sample scatter matrices given by

$$u^B_{ij} = \sum_{\gamma=1}^{2} n_\gamma \left[\bar{x}_i^{(\gamma)} - \bar{x}_i\right]\left[\bar{x}_j^{(\gamma)} - \bar{x}_j\right] \qquad (i,j = 1,2,\ldots,k) \tag{A-43a}$$

and

$$u^W_{ij} = \sum_{\gamma=1}^{2} \sum_{\xi_\gamma=1}^{n_\gamma} n_\gamma \left[x_{i\xi_\gamma}^{(\gamma)} - \bar{x}_i^{(\gamma)}\right]\left[x_{j\xi_\gamma}^{(\gamma)} - \bar{x}_j^{(\gamma)}\right] \tag{A-43b}$$

In Eq. (A-43),

$$\bar{x}_i = \frac{1}{2}\sum_{\gamma=1}^{2} \bar{x}_i^{(\gamma)} \tag{A-44}$$

is the mean of the grand sample of $\Sigma\, n_\gamma$ and

$$\bar{x}_i^{(\gamma)} = \frac{1}{n_\gamma}\sum_{\xi_\gamma=1}^{n_\gamma} x_{i\xi_\gamma}^{(\gamma)} \tag{A-45}$$

is the mean value of group γ.

Applying Eq. (A-15) to Eqs. (A-43) through (A-45) leads to results for the matrix elements u^B_{ij} and u^W_{ij} like in Eq. (A-21). Thus, for example,

$$u^B_{ij} = k'_i k'_j \sum_{\gamma=1}^{2} n_\gamma \left[\bar{\rho}^{(\gamma)} - \bar{\rho}_i\right]\left[\bar{\rho}_j^{(\gamma)} - \bar{\rho}_j\right]$$

$$= k'_i k'_j\, u'^B_{ij} \tag{A-46}$$

and

$$u^W_{ij} = k'_i k'_j \sum_{\gamma=1}^{2} \sum_{\xi_\gamma=1}^{n_\gamma} n_\gamma \left[\rho_{i\xi_\gamma}^{(\gamma)} - \bar{\rho}_i^{(\gamma)}\right]\left[\rho_{j\xi_\gamma}^{(\gamma)} - \bar{\rho}_j^{(\gamma)}\right]$$

$$= k'_i k'_j u'^W_{ij} \tag{A-47}$$

Calculating changes in the eigenvalues ℓ from Eq. (A-42) due to the gain factor k'_i and due to change in the eigenvectors C_j from Eq. (A-41) may be approached in a fashion similar to that used to derive Eqs. (A-31) and (A-33). These results are complicated algebraically and provide little additional insight. In general, as before, the magnitude of the generalized eigenvector ℓ will change, and its orientation (C_1,C_2) defining the line along which the variation is greatest will also change in space with changes in the k'_i. These, in turn, alter the "canonical" variables $DN_c^{(n)}$, which are linearly related to the original DN values through

$$DN_c^{(n)} = \sum_{j=1}^{2} DN_j C_j^{(n)} \tag{A-48}$$

The canonical variates may also be rescaled by Eq. (A-18) to fill the available dynamic range. Any advantage gained by calibration of the raw image data, i.e., by determination of the k_i, may in principle be duplicated by appropriate assignment of the constants A_m and B_m in Eq. (A-18).

C. Use of Correlation Versus Convariance Matrix for Computation of PCs and Canonical Variates

To this point, only the covariance matrix and the relationship between such matrices calculated for calibrated and uncalibrated radiance data have been discussed. This emphasis results from the fact that routine processing of image data in terms of either PCs or canonical variables uses the covariance matrices for determining the required eigenvalues and eigenvectors. The PCs and canonical variables could equally well be calculated from the corresponding correlation matrices, although the eigenvalues and eigenvectors obtained would be different. The question of which transformation is better reduces to which can be considered a more reliable measure of equal differences, equal changes in the DN, or standard deviations. From a numerical standpoint, and as a rule of thumb, if the primary source of error (or noise) is additive, the covariance transformation is preferred. If the major source is multiplicative, the correlation transformation is preferred.

The correlation matrix possesses another distinct advantage, however, because it is independent of instrument and atmospheric factors. To see this, recall from Eq. (A-21) that the elements of u_{ij}, the scatter (covariance) matrix based on the uncalibrated radiances, are related to elements u'_{ij} of the corresponding scatter (covariance) matrix based on the reflectances by

$$u_{ij} = k'_i k'_j u'_{ij} \tag{A-49}$$

where the k'_i are gain factors that combine together atmospheric, instrumental, and other scaling transformations. Elements of the correlation matrix c_{ij} are calculated from the usual formula

$$c_{ij} = \frac{u_{ij}}{\sqrt{u_{ii}u_{jj}}}$$

Using Eq. (A-49), the c_{ij} are also given by

$$c_{ij} = \frac{u'_{ij}}{\sqrt{u'_{ii}u'_{jj}}}$$

Thus, the correlations in the linear reflectance model are functions solely of the surface reflectances. This important result

shows that PC (or canonical) transformations computed on the basis of the correlation matrix represent reflectance values directly and are independent of the need for calibration apart from the usual correction of the scanner data. The result is based on the derived linear nature of the relationship between DN and reflectance given by Eq. (A-15). Equation (A-15) is verified in practice by matching the image-derived reflectance curves with ground-measured reflectance data. Based on field results, the equation is valid for analysis of image data in the manner described.

Note that if the distribution of DN values is normalized to zero mean and unit variance, the covariance of the normalized variables is equal to the correlation of the *original* DN distribution. The process of gradient removal entails a rescaling designed to saturate a specific fraction of the data. If the original distribution of DN values is Gaussian (which for large samples is almost always true) this rescaling would have the effect of normalizing the data.

To demonstrate this effect, PC images were generated for line 5 at Lisbon Valley (NS-001 data), first using covariance statistics, then using correlation statistics. Images generated in these two ways would be expected to be very similar. Table A-1, which displays the correlation among the images generated, indicates that the two sets of images are quite similar, as predicted. All diagonal terms are nearly unity (in absolute value), indicating a very high correlation of each component generated by correlation statistics to its corresponding component generated from covariance statistics.

Table A-1. Correlation matrix between two sets of PC images, NS-001 data, line 5, Lisbon Valley

PCs Using Correlation Statistics	PCs Using Covariance Statistics			
	V1	V2	V3	V4
C1	0.992	−0.094	−0.177	0.034
C2	−0.310	0.955	0.105	0.310
C3	0.304	−0.165	−0.935	−0.005
C4	−0.069	0.402	0.006	0.992

Appendix A
References

Bolivar, S. L., S. H. Balog, K. Campbell, L. E. Fugelso, T. A. Weaver, and G. W. Wecksung (1981). *Multisource data set integration and characterization of uranium mineralization for the Montrose Quadrangle, Colorado* (LASL Informal Report LA-8807-MS). Los Alamos, New Mexico: Los Alamos Scientific Laboratory.

Deirmendjian, D. (1969). *Electromagnetic scattering on polydispersions*. New York: American Elsevier Publishing Company.

Goetz, A. F. H., F. C. Billingsley, A. R. Gillespie, M. J. Abrams, R. L. Squires, E. M. Shoemaker, I. Lucchitta, and D. P. Elston (1975). *Application of ERTS images and image processing to regional geologic problems and geologic mapping in northern Arizona* (JPL Technical Report 32-1597). Pasadena, California: Jet Propulsion Laboratory.

Greenler, R. (1980). *Rainbows, halos, and glories*. Cambridge, London: Cambridge University Press.

Slater, P. (1980). *Remote sensing: Optics and optical systems*. Reading, Massachusetts: Addison–Wesley Publishing Company.

Switzer, P., W. S. Kowalik, and R. J. P. Lyon (1981). Estimation of atmospheric path-radiance by the covariance matrix method. *Photogr. E.R.*, *47*(10), 1469–1476.

Wilks, S. S. (1962). *Mathematical statistics*. New York: John Wiley & Sons.

Appendix B
Calibration of the Scanner Data for Ground Reflectance and Estimation of Data Noise Level

I. Calibration

The aircraft scanners used record multispectral radiance from individual surface elements constituting the instantaneous fields of view (IFOVs) throughout the flight path. The radiance recorded is solar energy that was (1) attenuated once by the total atmospheric column, (2) reflected by the surface, (3) attenuated by the atmospheric column between surface and scanner, and (4) encoded by the scanner system. An approximate analysis of this problem was presented in Appendix A. It was shown *a posteriori* by examination of the corrected image data that empirical removal of the atmospheric and instrumental effects leads to a linear relation between scanner radiance and surface reflectance

$$DN_i = k_i'\bar{\rho}_i + k_i'' \qquad (i = 1,2,\ldots,L) \qquad \text{(B-1)}$$

In Eq. (B-1), the DN_i are the encoded radiance values in L channels, and the k_i' and k_i'' are empirical gain and offset parameters containing the model description of atmospheric and instrumental effects and reference area reflectances. The $\bar{\rho}_i$ are assumed Lambertian reflectance measures that specifically ignore possible angular dependences in these quantities. Note that the reflectance here acts as a proportionality constant between the magnitude of the incident energy (embodied in k_i' and k_i'') and voltage (encoded as a digital number, DN). Determination of the constants k_i' and k_i'' provides an interpretation of scanner DN values in terms of average spectral reflectance within the spectral interval of each channel and over each pixel. These measures are largely independent of the atmosphere for purposes of comparison with field data obtained with the Portable Field Reflectance Spectrometer (PFRS).

Calibration of image data is achieved by determining the disposable constants in Eq. (B-1). In practice, a method was used in which scanner radiance measurements were related to ground reflectance measurements for the same areas and over a range of surface brightness values. This method was proposed by Abrams (Conel et al., 1978). Ground measurements were obtained using the PFRS. The field spectral reflectance curves were averaged over the spectral interval of each scanner channel. Computer printouts of the DN values of the gradient-corrected scanner data were obtained for areas of interest, and mean values and standard deviations for each channel were computed from these data. The histogram showing distribution of DN values was also provided.

Figure B-1 shows three-point calibration curves for NS-001 data from Lisbon Valley and illustrates the generally linear nature of the relations obtained between instrumental DN and surface reflectance. The "uncertainty" bars on data points refer to $\pm 1\ \sigma$ limits in the scatter. Scatter physically is due to variability in cover types over the (supposed homogeneous) chosen calibration areas and does not arise from instrumental or atmospheric sources. Values obtained for the calibration constants are given in Table B-1.

From analysis of the scatter, the calibration curves of Figure B-1 also provide an estimate of the uncertainty in determination of surface reflectance using raw scanner data. Thus, if the standard deviation of the scanner values is σ, the uncertainty in reflectance ΔR_i is $\pm k_i'\sigma$. In addition to this source of uncertainty in ΔR_i, which arises strictly from scene variation measured by σ, there is the standard error in determination of the regression coefficients k_i' and k_i''. The standard error for k_i' is given as S_{k_i}' in Table B-1. A $100\,(1 - \alpha)$ percent confidence interval for the true slope k_i' is given by

$$k_i' \pm t_{\alpha/2,n}\ {}_2S_{k_i}'$$

where $t = k_i'/S_{k_i}'$. For example, 95 percent confidence interval on k_i' is $t_{0.025,1} \times S_{k_i}'$, which is equal to 12.7 S_{k_i}'. The determi-

PRECEDING PAGE BLANK NOT FILMED

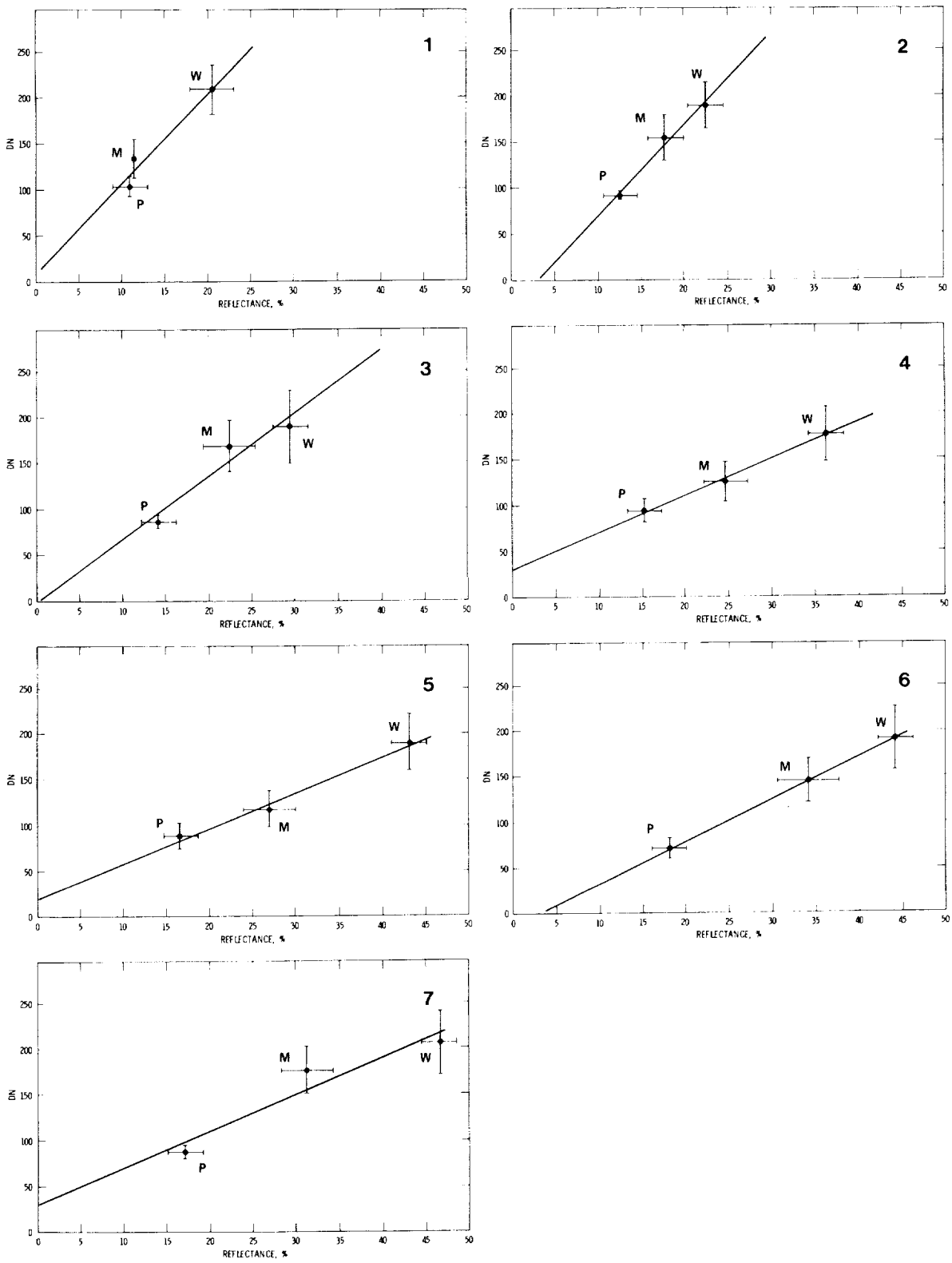

Figure B-1. Calibration curves for channels 1–7 of the NS-001, Lisbon Valley data (Mission 407, August 1979 flight). Note the approximately linear nature of these curves over the DN reflectance range investigated. W = Wingate Sandstone, average of 38 pixels, 4 field spectra; M = Moss Back Member, Chinle Formation, average of 30 pixels, 3 field spectra; P = pavement, average of 24 pixels, 4 field spectra.

Table B-1. Value for the constants k_i' and k_i'' in the calibration equation $DN_i = k_i'\bar{p}_i + k_i''$ obtained from three-point least square fits

Channel	k_i'	k_i''	r ①	S_{DN_i} ②	$S_{k_i''}$ ③	$S_{k_i'}$ ④
1	9.84	7.96	0.973	17.75	35.2	2.35
2	9.93	29.45	0.991	9.40	23.98	1.33
3	6.83	−2.02	0.961	21.3	45.1	1.97
4	3.97	30.46	0.997	4.52	8.23	0.30
5	3.96	18.1	0.994	8.57	14.06	0.456
6	4.69	−13.47	0.999	0.062	0.113	0.003
7	4.08	28.93	0.955	26.4	42.8	1.27

①Sample correlation coefficient.
②Scatter in DN direction of the observed points about the regression line.
③Standard error of the intercept.
④Standard error of the regression coefficient.

nation of absolute instead of differential reflectance from scanner data depends on the coefficient k_i''. The standard error in determination of k_i'' is given by S_0. A 100 $(1 - \alpha)$ percent confidence interval for k_i'' is

$$k_i'' \pm t_{\alpha/2,n-2} S_{k_i''}$$

and the 95 percent confidence interval on k_i'' is 12.7 $S_{k_i'}$.

The statistical sources of error entering determination of reflectance from scanner DN value can obviously be controlled by carefully constructing calibration curves. The production of an accurate calibration curve by matching ground and scanner reflectance values benefits from acquisition of data points over a wide range of ground reflectance values in each spectral channel.

A simple procedure may be used to guide the detailed selection of sample sites. For each channel over the scene, a density slice is made of the scanner radiance values; the distribution is color coded and displayed as an image. As an example, Figure B-2 shows an image of channel 2 (0.52–0.60 μm) of line 5 of the NS-001 for Lisbon Valley, where the histogram of DN values (Figure B-3) has been divided into six parts bounded by $\pm 2\ \sigma$ and $\pm 1\ \sigma$ about the mean value of the distribution. A calibration scale may be assigned to the DN distribution based on measurement of surface reflectance in areas corresponding to various portions of the range.

II. Estimate of Noise Levels in Scanner Data

Surface targets of high photometric uniformity can be used to estimate total system plus atmospheric noise levels by direct examination of scatter in radiance values over the sampled areas. Large natural targets with high uniformity are rare, but rough limits can be assigned to noise levels by measuring fields with good visual uniformity. For Lisbon Valley, highly vegetated sites provided the most uniform areas. Three examples are presented in Table B-2. From such data, the atmospheric and system noise contributions constitute, at the greatest, less than 10 percent of the total area observed. These are worst-case figures since the data still contain an unknown and indeterminate variability arising from natural variations in the surface cover itself.

Table B-2. NS-001 raw DN responses with standard deviations at vegetated sites, Lisbon Valley

Channel	Alluvial Flat[a]		Sage and Piñon–Juniper on Dakota Sandstone[b]		Grass on Navajo Sandstone[c]	
	Mean ± 1 σ	% of Mean in 1 σ	Mean ± 1 σ	% of Mean in 1 σ	Mean ± 1 σ	% of Mean in 1 σ
1	96 ± 4	4.17	69 ± 2	2.90	95 ± 3	3.16
2	103 ± 4	3.88	72 ± 2	2.78	107 ± 3	2.80
3	120 ± 6	5.00	90 ± 4	4.44	130 ± 4	3.08
4	140 ± 5	3.57	107 ± 3	2.80	141 ± 4	2.84
5	149 ± 5	3.36	125 ± 3	2.40	150 ± 3	2.00
6	136 ± 5	3.68	119 ± 4	3.36	146 ± 3	2.05
7	152 ± 8	5.26	120 ± 6	5.00	161 ± 5	3.11

[a]462 elements.
[b]80 elements.
[c]45 elements.

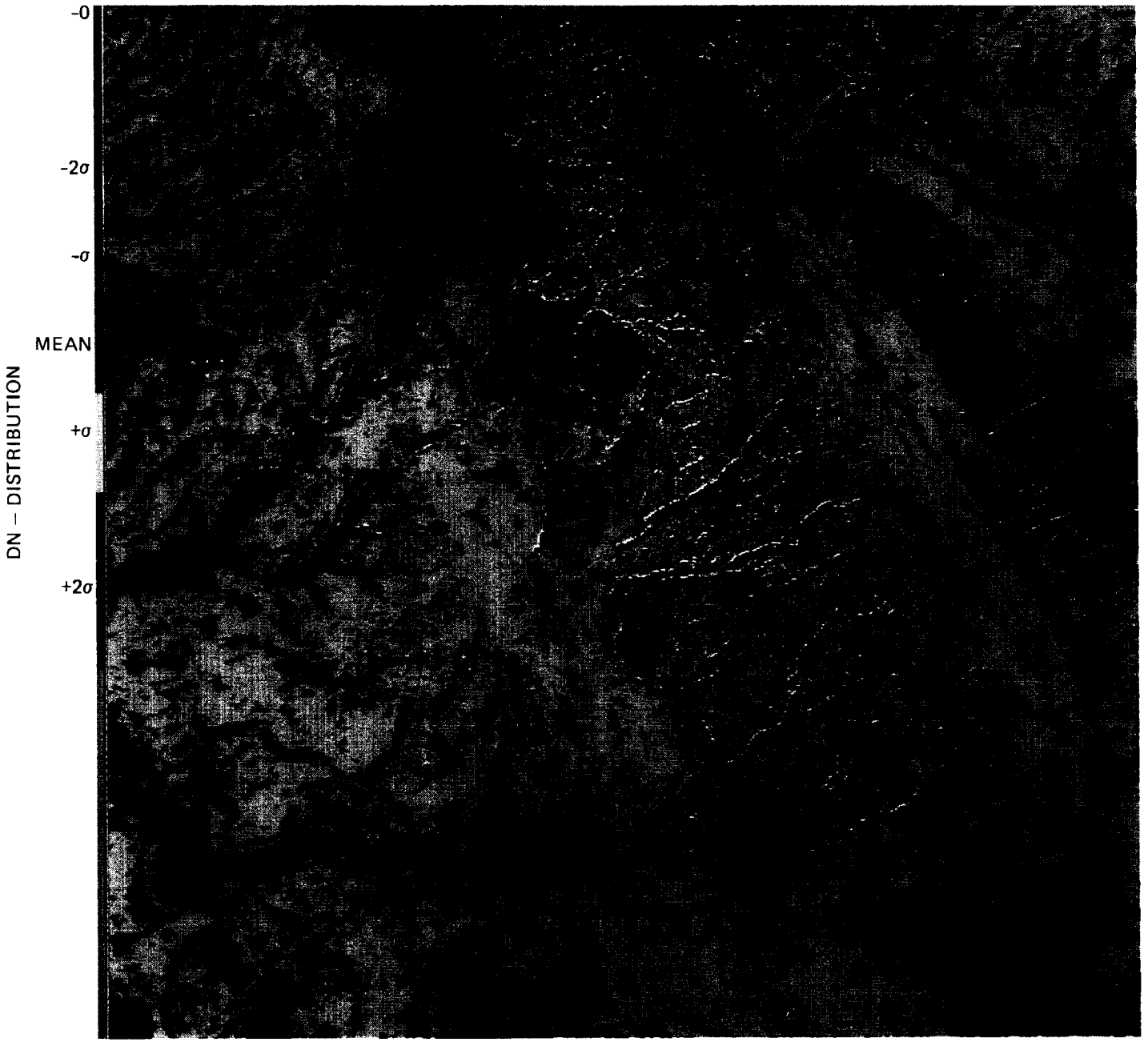

Figure B-2. An example of the areal distribution of DN values in channel 2, line 5, of NS-001 data, Lisbon Valley, for a slice of the range divided into six intervals corresponding to $\pm 1\,\sigma$, ± 1 to $\pm 2\,\sigma$, and $> \pm 2\,\sigma$ about the mean. The histogram of value is shown in Figure B-3.

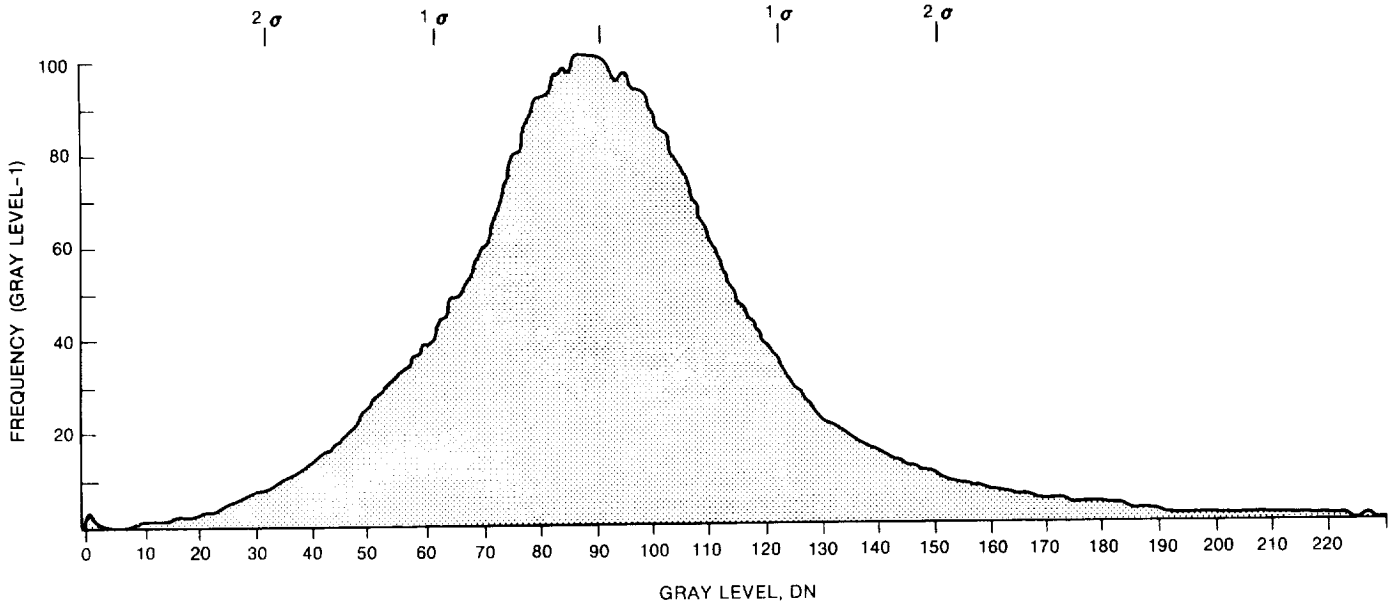

Figure B-3. Histogram of gray levels for the 2,426,400 elements in channel 2, line 5, of the NS-001 data, Lisbon Valley. Average gray level = 92.5, standard deviation = 29.2.

Appendix B
Reference

Conel, J. E., M. J. Abrams, and A. F. H. Goetz (1978). *A study of alteration associated with uranium occurrences in sandstone and its detection by remote sensing methods* (JPL Publication 78-66, Vol. I). Pasadena, California: Jet Propulsion Laboratory.

Appendix C
Principal Components for Lisbon Valley Images

I. General

Some of the NS-001 image data for Lisbon Valley are presented as principal component (PC) composites. Covariance matrices, eigenvalues and eigenvectors, correlation matrices, and histograms describing loadings of the eigenvectors for the PC representation of image data studied are discussed below.

The PCs for NS-001 data describe the geometry of the scatter swarm in seven-dimensional space with orthogonal axes arranged along the direction of decreasing scatter in the swarm. These directions may or may not be highly correlated with the original variables. Where the correlations are high, they may then possess a "physical" interpretation.

The first PC has a straightforward interpretation and represents an average of the radiances. This results from the fact that all of the variables used to produce the covariance matrix tend to be equicorrelated, in which case the first PC tends to be proportional to the mean of the original responses (Morrison, 1976, p. 289). The mean value is usually interpreted as albedo, although strictly speaking this term applies to an average value of the reflectance, not of the radiances.

For all applications described here, the principal axes are derived from analysis of the covariance matrix. The correlation matrix may be used as well, but the eigenvalues and eigenvectors obtained and their statistical distribution will be different. The advantages in use of the correlation matrix are described in Appendix D. Primarily, the correlation matrix is independent of linear scaling transforms and, thus, the derived PCs are representative of *surface reflectance* directly. The first PC of the correlation matrix should thus directly represent surface albedo or average reflectance.

The possible interpretative advantages of the correlation versus the covariance procedure were not realized until late in the study. Consequently, the covariance results have been used for most PC usages presented in the test case reports. An example comparing covariance and correlation images is presented in the Copper Mountain, Wyoming, Uranium Test Site Report, Section 9, where the results obtained from the two procedures are essentially the same.

II. PCs From Line 6 and From Subareas of Lines 5, 6, and 7

PCs have been generated from the NS-001 scanner image data by sampling several different areas within the Lisbon Valley test site. Areas of different sizes were sampled to investigate the possibility of increasing the apparent separation in display of geologic units. The mathematical basis of this separation is discussed in Appendix E. The covariance and correlation matrices and properties of the transformation are briefly discussed below for three such areal samplings. In addition, the effects of calibrating the scanner data (reducing the covariance matrix to a matrix based on reflectance) are also presented.

A. Transform I Based on Line 6 Data

The covariance matrix for transform I was prepared by sampling the 2,376,150 pixels, over seven channels (0.45–2.35 μm), comprising the total area of line 6 of the August 28, 1979 NS-001 flight. Formulas for computing the covariance elements are given in Appendix A. The area of line 6 is depicted in Figure C-1, and its geographic location is shown in Figure 8-2. PCs derived from sampling the total area were used to transform the image data in lines 5 and 7, and the data for these three lines were stretched individually to provide closely similar color renditions. The resulting mosaic, shown in Figure 8-21, clearly depicts the distribution of bleached and unbleached Wingate Sandstone, which was a major objective of the image analyses in this area.

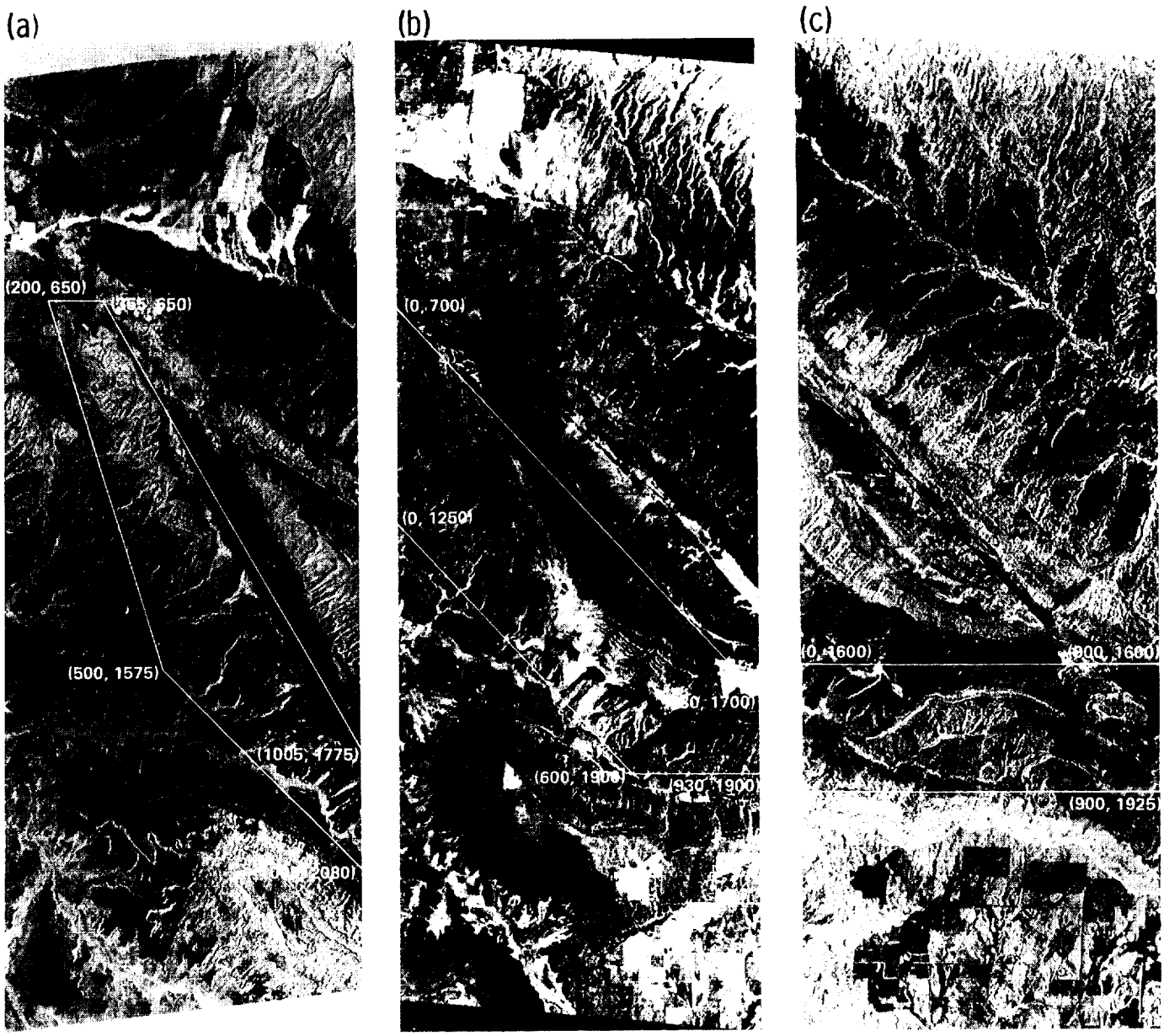

Figure C-1. Subareas of Lisbon Valley sampled to form PC transform II: (a) NS-001 line 5, 15 percent of total area; (b) NS-001 line 6, 19 percent; (c) NS-001 line 7, 9 percent. The average subarea is approximately 15 percent of the total area sampled. Vertices of polygons are marked by image coordinates, and the origin of the coordinates is in the upper left-hand corner of each image.

The covariance matrix of this sample population is given in Table C-1(a), and the corresponding correlation matrix in Table C-1(b). Elements c_{ij} of the correlation matrix are derived from elements u_{ij} of the covariance matrix by the formula

$$c_{ij} = \frac{u_{ij}}{\sqrt{u_{ii}u_{jj}}}$$

For analyses of the correlation matrix, it is impractical to depict the great diversity of spectral types represented in the scanner data, but some essential properties of the correlations may be understood by considering pure end members such as rocks and vegetation. Table C-1(b) discloses that elements c_{14}, c_{15}, c_{24}, c_{25}, c_{17}, c_{47}, and c_{57} are relatively small. Figure C-2 implies that these correlations represent places dominated by chlorophyll and Fe^{+3} (c_{14}, c_{15}, c_{24}, c_{25}) or H_2O (c_{47}, c_{57}) absorptions when compared to a portion of the spectrum (0.7–1.3 μm) not populated by saturated bands. Effects introduced in the correlation matrix by spectral contributions from green vegetation alone can be estimated by comparison with a result for the Lost River, West Virginia, test site, which is 94 percent tree covered (Section 12). The correlation matrices are appropriate for this comparison because they are independent of site-specific atmospheric and instrumental factors. The Lost River site is mainly deciduous forest, with minor coniferous contributions, whereas the Lisbon Valley site is mixed grass, shrubs, and piñon–juniper. (This comparison is, of course, approximate and should be made quantitatively on the basis of representative vegetation and rock samples from the same site. The disturbed, mixed, and highly variable vegetation cover at Lisbon Valley makes adequate sampling a difficult job. The present strategy was chosen to provide qualitative guidance for interpretation of these matrices.)

Effects of vegetation-free distribution can be estimated from the Silver Bell, Arizona, site where the Sonoran Desert community provides a vegetation cover of approximately 10 percent (Section 4).

Correlation matrices for data from the Lost River and Silver Bell sites are given in Tables C-2 and C-3, which reveal the variations introduced by the vegetative component. In Table C-4, the correlation matrix for the Lisbon Valley line 6 data discloses a strong influence of vegetation cover at that site.

The results of PC analysis can be appraised by plotting the vector quantities $\boldsymbol{W}_j$ versus wavelength. These quantities are related to the column eigenvectors by

$$\boldsymbol{W}_j = \sqrt{\lambda_j}\,\boldsymbol{u}_j$$

where λ_j is the jth eigenvalue and $\boldsymbol{u}_j$ is the jth eigenvector (Maxwell, 1977). Thus, the magnitude of each $\boldsymbol{W}_j$ is equal to the corresponding value of the latent root, since the quantity $\boldsymbol{u}_j \cdot \boldsymbol{u}_j$ is normalized to unity.

The resulting eigenvector correlation diagrams may be viewed as a graphical representation of the first four successive basis functions in a finite, i.e., seven-term orthogonal expansion (the

Table C-1. Covariance $||u_{ij}||$ and correlation $||c_{ij}||$ matrices from NS-001 data, line 6, Lisbon Valley[a]

(a) Covariance matrix

760.35						
803.38	884.56					
849.42	953.47	1183.22				
535.35	646.25	784.17	833.84			
603.60	731.01	922.55	888.59	1035.33		
810.93	929.94	1181.17	822.97	1044.24	1328.16	
775.94	881.96	1139.62	718.91	719.61	1241.27	1277.23

(b) Correlation matrix

1.000	0.980	0.896	0.672	0.680	0.807	0.787
	1.000	0.932	0.753	0.764	0.858	0.830
		1.000	0.790	0.834	0.942	0.927
			1.000	0.956	0.782	0.697
				1.000	0.891	0.798
					1.000	0.953
						1.000

[a]Transformation based on sampling of complete area.

Table C-2. Correlation matrix for the 7-band NS-001 data from Lost River, West Virginia, September 1979

1.000	0.97	0.90	0.55	0.53	0.75	0.75
	1.00	0.94	0.64	0.63	0.84	0.82
		1.00	0.60	0.60	0.86	0.87
			1.00	0.98	0.83	0.68
				1.00	0.87	0.69
					1.00	0.87
						1.00

Table C-3. Correlation matrix for the 7-band NS-001 data from Silver Bell, Arizona, October 1978

1.000	0.973	0.956	0.839	0.853	0.845	0.854
	1.000	0.983	0.904	0.883	0.868	0.870
		1.000	0.900	0.927	0.916	0.910
			1.000	0.890	0.842	0.815
				1.000	0.973	0.927
					1.000	0.952
						1.000

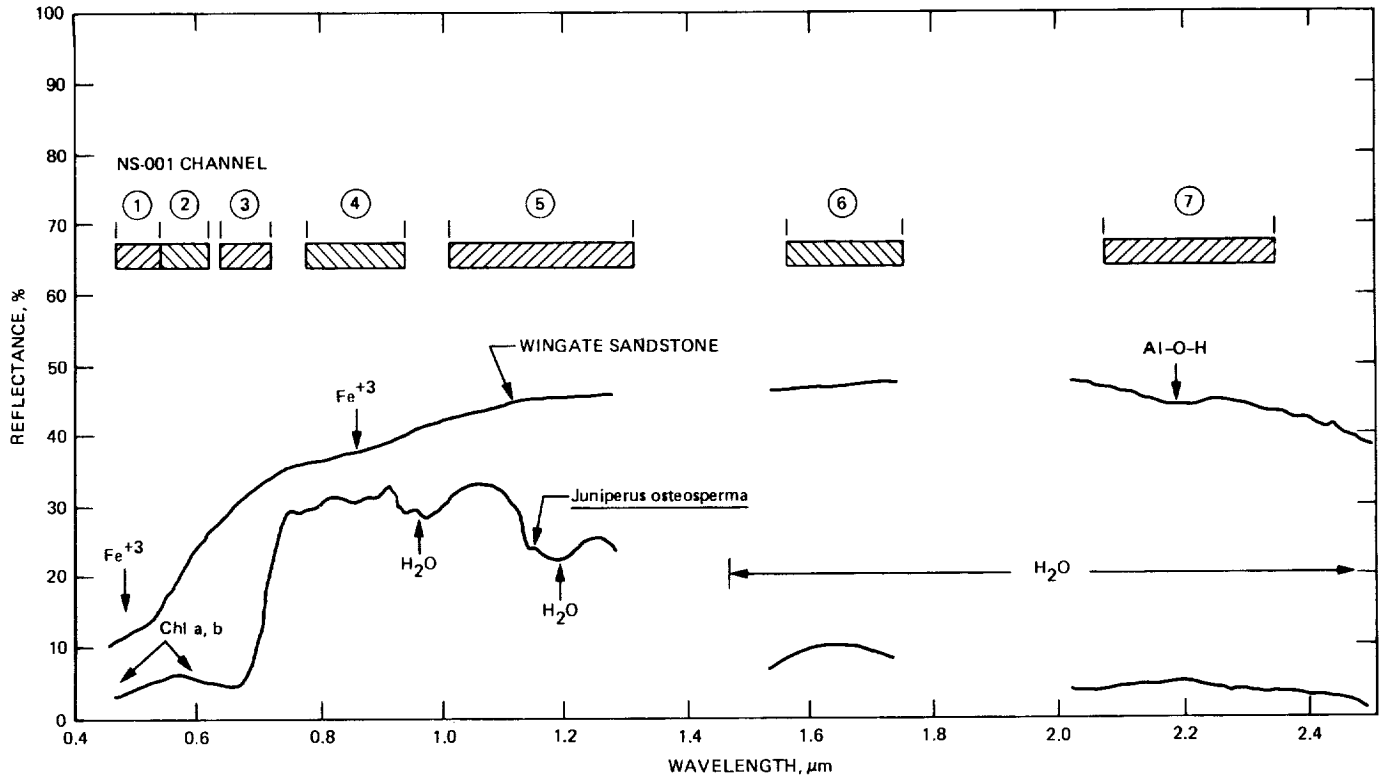

Figure C-2. Spectral reflectance of sandstone and juniper (*Juniperus osteosperma*) with important absorption bands due to Fe^{+3}, chlorophyll, Al–O–H, and water

Karhunen–Loeve expansion) of the average scanner spectrum represented by the covariance matrix. (Refer to Wiersma and Landgrebe, 1980, for a discussion of this expansion based on the covariance matrix.) These empirical basis functions often have a polynomial-like appearance with respect to wavelength.

Figure C-3 includes the first four eigenvectors scaled to W_j for transform I and the reflectance spectra for pigmented Wingate Sandstone and juniper (*Juniperus osteosperma*), representing end-member spectral classes. These plots illustrate the general difficulty of assigning clear physical significance to the PC (compare Lost River data, Figure C-4, to Silver Bell data, Figure C-5). A comparison between the Lisbon Valley and Lost River data shows the heavy influence of vegetation on the first three PCs for transform I of Lisbon Valley. The fourth PC compares favorably with the fourth PC of the Silver Bell transform, except for the disagreement at band 3 and a difference in sign.

Table C-4. Transform I: Eigenvalues and eigenvectors from NS-001 data, line 6, Lisbon Valley, total area

Band	Eigenvalue	%[a]	Eigenvector						
			1	2	3	4	5	6	7
1	6352.3	87.1	0.307	0.348	0.422	0.311	0.368	0.445	0.421
2	505.9	6.9	-0.406	0.297	-0.186	0.582	0.576	0.001	-0.206
3	326.7	4.5	-0.469	-0.438	0.010	-0.340	0.012	0.382	0.572
4	57.3	0.8	0.191	0.117	-0.462	0.377	0.288	0.604	0.383
5	42.8	0.6	0.219	0.168	0.730	0.134	0.066	-0.259	0.549
6	10.4	0.1	0.647	0.741	0.016	-0.148	0.071	0.076	0.002
7	7.3	0.1	0.138	-0.090	0.202	-0.517	0.664	-0.468	0.067

[a]Percent variance explained by successive PCs.

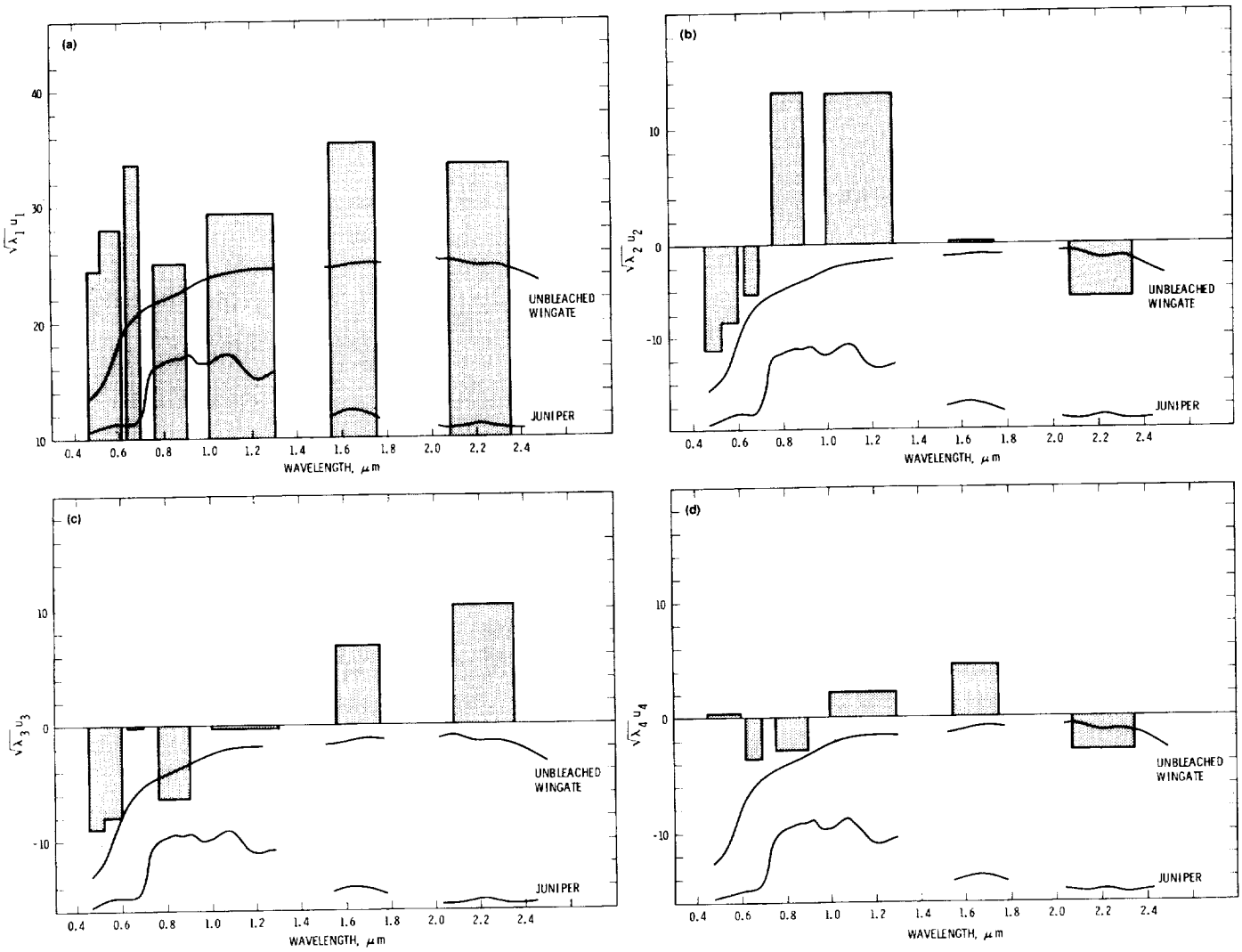

Figure C-3. First four PCs for transform I of NS-001 data, line 6, Lisbon Valley, Utah; principal values and directions from covariance matrix: (a) $\sqrt{\lambda_1}u_1$; (b) $\sqrt{\lambda_2}u_2$; (c) $\sqrt{\lambda_3}u_3$; (d) $\sqrt{\lambda_4}u_4$

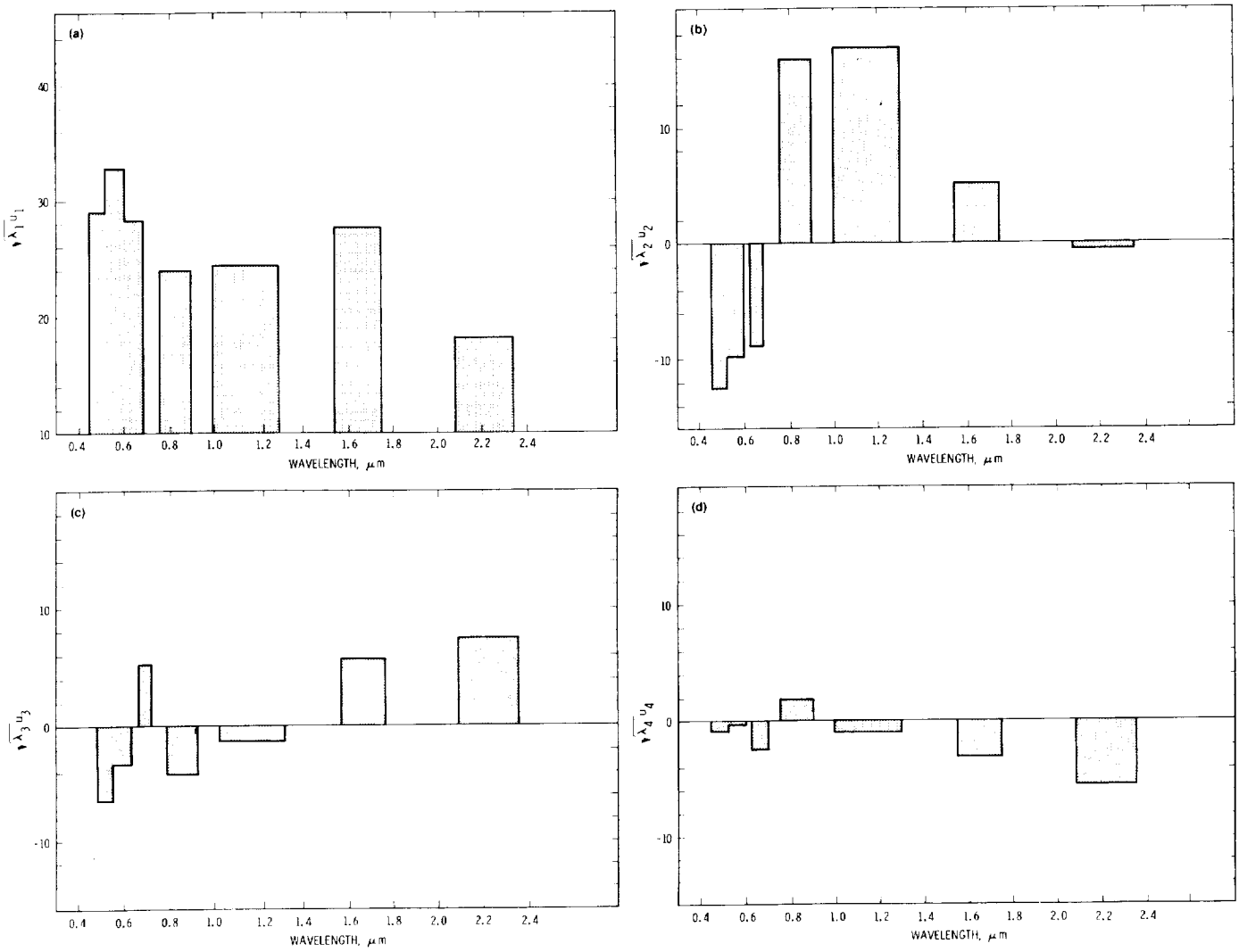

Figure C-4. First four PCs for NS-001 data from Lost River, West Virginia; principal values and directions from covariance matrix: (a) $\sqrt{\lambda_1}u_1$; (b) $\sqrt{\lambda_2}u_2$; (c) $\sqrt{\lambda_3}u_3$; (d) $\sqrt{\lambda_4}u_4$

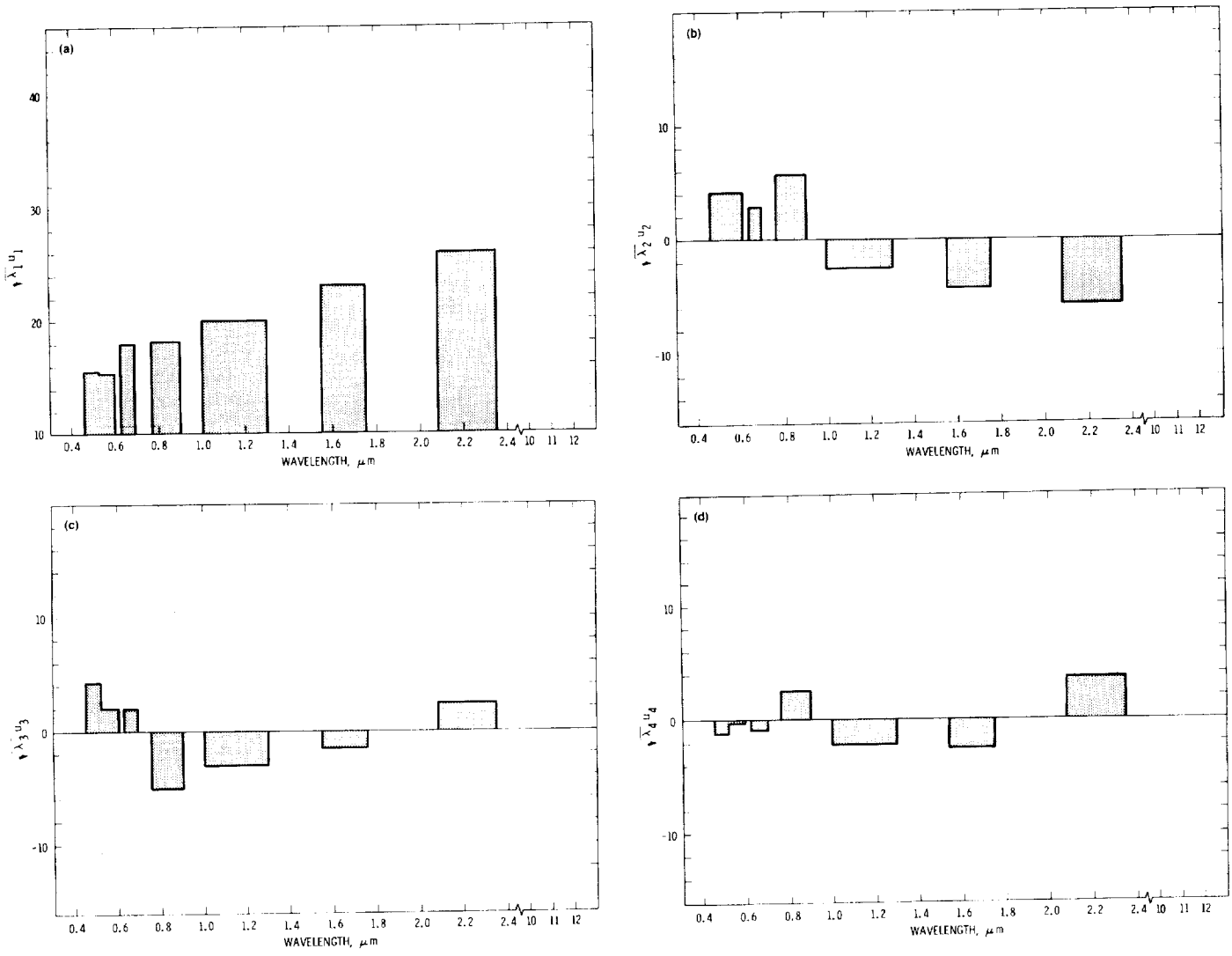

Figure C-5. First four PCs for NS-001 data from Silver Bell, Arizona; principal values and directions from covariance matrix: (a) $\sqrt{\lambda_1}u_1$; (b) $\sqrt{\lambda_2}u_2$; (c) $\sqrt{\lambda_3}u_3$; (d) $\sqrt{\lambda_4}u_4$

B. Transform II Based on Averages of Subareas for Lines 5, 6, and 7

The covariance matrix for transform II was prepared by sampling pixels over seven channels (0.45–2.35 μm) comprising the subareas of lines 5, 6, and 7 outlined in Figure C-1. These subareas are confined principally but not exclusively to outcrops of Triassic (Wingate) strata exposed in the flank of Lisbon Anticline. The subareas include a greater percentage of rock outcrop and exclude large areas covered dominantly by trees, shrubs, and grass both north and south of the anticline that are included in transform I. Discrimination of Wingate strata from neighboring units within the section was expected to be enhanced by reducing vegetation cover in the samples; in addition, distinction of facies within the formation (bleached versus unbleached rock) was expected to improve. The distribution of eigenvector weightings on the original spectral channels has certainly been changed by the subarea sampling, but the interpretation in terms of a simple two end-member model is not obvious. The restricted area (transform II) PCs were used to transform the image data for lines 5, 6, and 7. These images were used to study the distribution of rock units and were compared with renditions produced by transform I. A detailed analysis of the differences will not be given, but examples of the results are included in Appendix F for comparison with Figure 8-21. Qualitatively, little or no improvement in the separation of rock units can be recognized by these restricted sampling transforms. Improvements were achieved, however, in separation of Quaternary alluvium in modern stream channels, as shown in figures in Appendix F.

The covariance matrix for the transform II sample population and the corresponding correlation matrix are given in Table C-5. This information, when compared to the earlier result for transform I, discloses less vegetation-like structure. This is indicated by correlation values such as c_{14}, c_{15}, which are closer to unity. Eigenvalues and eigenvectors for this transformation are given in Table C-6. Plots of the weighted eigenvector PCs (Figure C-6) for transform II also disclose a strong correlation with vegetation, although the magnitudes of some components have changed and reversals in sign are common.

Table C-5. Transform II: Covariance $||u_{ij}||$ and correlation $||c_{ij}||$ matrices from NS-001 data, Lisbon Valley, restricted area

(a) Covariance matrix

1009.26						
1094.04	1232.37					
1083.16	1255.76	154.89				
901.46	1074.75	1293.20	1283.14			
918.11	1100.38	1358.46	1308.91	1410.51		
1047.04	1226.95	1499.78	1310.54	1438.13	1598.67	
949.80	1113.29	1389.20	1165.49	1265.65	1430.73	1382.69

(b) Correlation matrix

1.000	0.981	0.866	0.792	0.770	0.824	0.804
	1.000	0.909	0.855	0.835	0.874	0.853
		1.000	6.917	0.919	0.953	0.949
			1.000	0.973	0.915	0.875
				1.000	0.958	0.906
					1.000	0.962
						1.000

C. Transform III, Line 5 Sampling

Thus far, the PC transformation described has been restricted to bands 1 through 7 of the NS-001 data. Inclusion of the eighth band (10.4–12.5 μm), composed of radiance due to thermal radiation, produces a transformation with some useful rock discrimination properties. Transform III was prepared by sampling pixels over eight channels comprising the total area of line 5 of the August 28, 1979 Lisbon Valley flight. The area of line 5 is depicted in Figures C-1 and 8-2. The 8-band PC transformation is used for comparison with Fraunhofer Line Discriminator (FLD) data (Paragraph VIII.G.).

The covariance and correlation matrices for transform III are given in Table C-7. As expected, the thermal radiance data

Table C-6. Transform II: Eigenvalues and eigenvectors from NS-001 data, Lisbon Valley

Band	Eigenvalue	%[a]	Eigenvector						
			1	2	3	4	5	6	7
1	8637.2	91	0.305	0.354	0.415	0.367	0.388	0.421	0.383
2	464.7	5	0.647	0.546	0.009	0.248	-0.386	0.212	0.168
3	216.3	2	0.087	0.139	0.223	0.598	0.360	-0.259	-0.608
4	77.6	0.8	0.160	0.967	-0.739	0.276	0.287	0.510	0.003
5	44.5	0.5	0.015	0.103	-0.465	0.344	0.102	-0.450	0.665
6	13.8	0.1	-0.675	0.728	-0.017	0.056	0.077	0.061	-0.051
7	12.3	0.1	0.005	0.091	0.125	-0.499	0.687	0.495	0.102

[a]Percent variance explained by successive PCs.

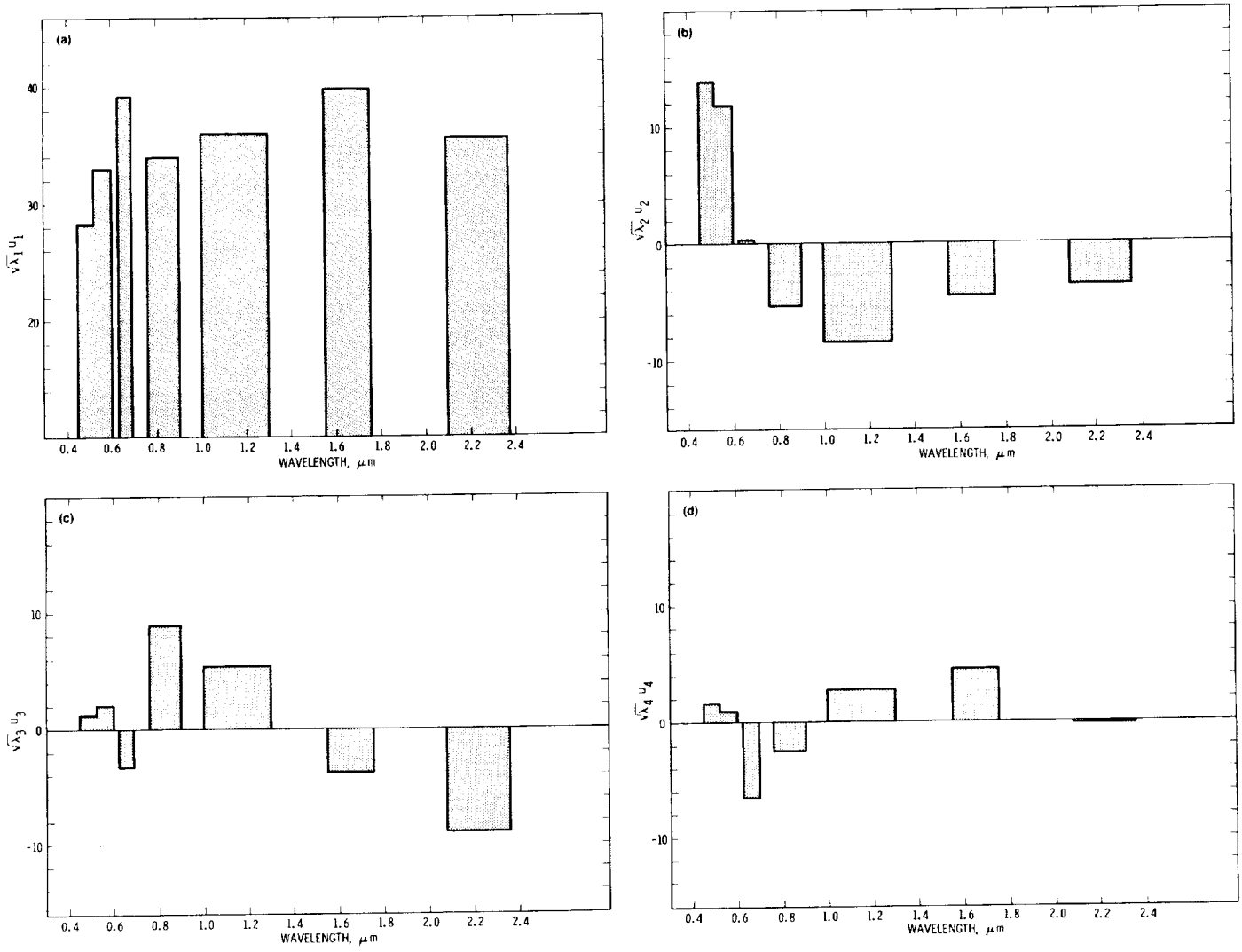

Figure C-6. First four PCs for transform II of NS-001 data, Lisbon Valley, restricted area; principal values and directions from covariance matrix: (a) $\sqrt{\lambda_1}u_1$; (b) $\sqrt{\lambda_2}u_2$; (c) $\sqrt{\lambda_3}u_3$; (d) $\sqrt{\lambda_4}u_4$

Table C-7. Transform III: Covariance $\|u_{ij}\|$ and correlation $\|c_{ij}\|$ matrices from the 8-channel (including thermal) NS-001 data, Lisbon Valley

(a) Covariance matrix

1060.24							
1105.09	1187.53						
1233.67	1346.98	1696.55					
959.97	1084.46	1297.82	1534.20				
1004.37	1134.77	1397.51	1529.69	1615.04			
1170.33	1297.13	1674.61	1366.13	1535.50	1763.37		
1230.64	1358.06	170.25	1374.16	1543.77	1822.69	1988.26	
990.16	1115.30	1493.05	1272.07	1515.48	1741.57	1836.85	2734.70

(b) Correlation matrix

1.000	0.985	0.920	0.753	0.768	0.856	0.848	0.582
	1.000	0.949	0.803	0.819	0.903	0.884	0.619
		1.000	0.804	0.844	0.953	0.948	0.693
			1.000	0.972	0.831	0.787	0.621
				1.000	0.857	0.862	0.721
					1.000	0.973	0.793
						1.000	0.788
							1.000

are relatively uncorrelated with the data for all visible and near-infrared channels.

Eigenvalues and eigenvectors for this transformation are given in Table C-8. The weightings of eigenvectors on the original axes are given in Figure C-7. The histogram for the first PC typically portrays a nearly equal weighting of all channels on the first component. The second PC is strongly dominated by the contribution from the eighth channel and thus represents the thermal radiation or loosely the "temperature." The distribution of weights for the third PC resembles that for the second PC of the Lost River data and may thus be correlated with vegetation. The fourth PC of the 8-channel transform (excluding channel 8) resembles the second PC of the Silver Bell 7-channel transform and may thus describe both a non-vegetative and a nonthermal component in the same radiance, i.e., rocks and soils.

III. Covariance Matrices and PCs for Calibrated Radiance Data

Thus far the covariance matrices and properties of the PCs derived from the raw or uncalibrated image radiance data have been described. Such data are linearly related to surface reflectance values. Consequently, a covariance matrix element u'_{ij} in terms of the reflectance ρ_j is related to a covariance matrix element computed from the raw values u_{ij} by

$$u_{ij} = k'_i k'_j u'_{ij}$$

where k'_i is the gain factor for channel i.

To determine the differences in information that may exist between these two descriptions, the data for transforms I and II were compared. Note that the correlation matrix is independent of both gain and offset parameters in the model described and no new information is introduced or deleted by obtaining calibrated matrix elements. The gain (plus offset) factors used are given in Table C-9.

Tables C-10 and C-11 include the covariance matrix and corresponding eigenvalues and eigenvectors for transform I. The histogram of eigenvector weightings for the first four PCs is given in Figure C-8, and the same data for transform II are presented in Tables C-12 and C-13 and in Figure C-9. Except for small changes in weightings of various components, the eigenvector histograms for these two cases are identical. In both cases, the first PC closely follows the reflectance curve that is characteristic of rock. The second PC is again weighted heavily on channels 4, 5, and 7—those associated with the representation of vegetation. The remaining PCs have more or less equal weight distribution.

Table C-8. Transform III: Eigenvalues and eigenvectors from NS-001 data (eight channels), Lisbon Valley

Band	Eigenvalue	%[a]	Eigenvector							
			1	2	3	4	5	6	7	8
1	11420.0	84.1	0.270	0.297	0.369	0.323	0.351	0.386	0.404	0.404
2	1164.9	8.6	0.296	0.290	-0.208	-0.218	0.087	0.012	0.009	0.854
3	643.6	4.7	0.300	0.237	0.282	0.650	0.536	0.088	0.238	0.032
4	225.3	1.7	0.512	0.400	0.128	0.163	0.082	0.373	0.538	0.316
5	57.9	0.4	0.313	0.125	0.809	0.215	0.225	0.201	0.298	0.078
6	48.2	0.3	0.018	0.009	0.085	0.329	0.262	0.645	0.631	0.023
7	11.4	0.08	0.591	0.722	0.184	0.125	0.239	0.150	0.010	0.005
8	7.5	0.06	0.199	0.273	0.173	-0.479	0.631	0.474	0.061	0.000

[a] Percent variance explained by successive PCs.

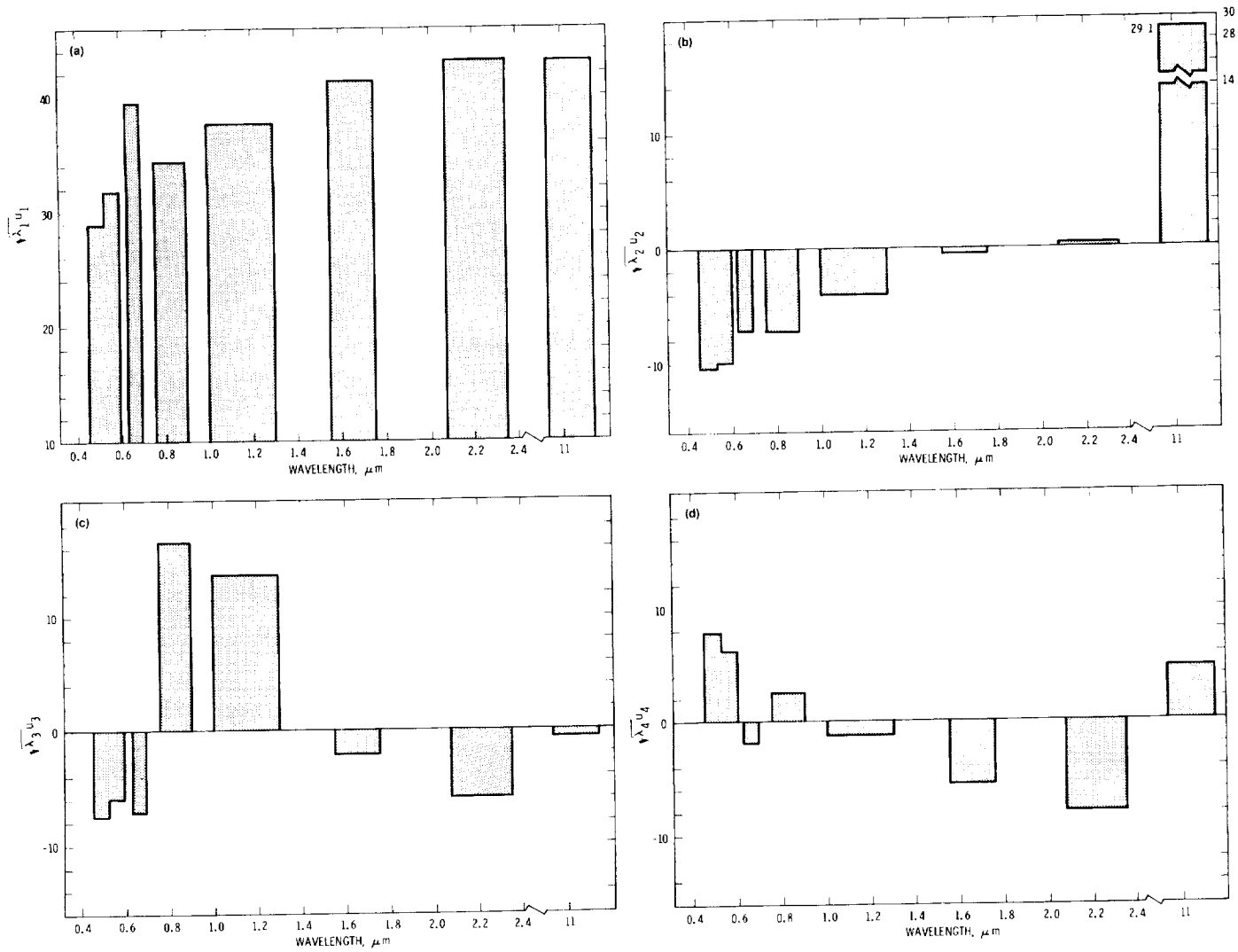

Figure C-7. First four PCs for transform III of NS-001 data, line 5, Lisbon Valley; principal values and directions from covariance matrix: (a) $\sqrt{\lambda_1}u_1$; (b) $\sqrt{\lambda_2}u_2$; (c) $\sqrt{\lambda_3}u_3$; (d) $\sqrt{\lambda_4}u_4$. PCs include the eighth (thermal) channel.

Table C-9. Constants used to calculate gain- and offset-corrected covariance matrices: $DN_i = k'_i\bar{o}_i + k''_i$, where k'_i is percent reflectance

i	k''_i	k'_i
1	7.96	9.84
2	29.45	9.93
3	−2.02	6.83
4	30.46	3.97
5	18.098	3.96
6	−13.47	4.69
7	28.93	4.08

Table C-10. Transform I: Covariance matrix of the reflectances obtained from element-by-element gain correction of the matrix $\|u'_{ij}\|$

7.85						
8.22	8.97					
12.64	14.06	25.36				
13.71	16.39	28.93	52.91			
15.49	18.59	34.11	56.53	66.03		
17.57	19.97	36.88	44.20	56.23	60.44	
19.33	21.77	40.89	44.38	56.78	64.85	76.71

Table C-11. Transform I: Eigenvalues and eigenvectors from the calibrated covariance matrix based on reflectances, NS-001 data, Lisbon Valley

Band	Eigenvalue	%[a]	Eigenvector						
			1	2	3	4	5	6	7
1	260.7	87.6	−0.142	−0.164	−0.297	−0.399	−0.478	−0.470	−0.507
2	27.2	9.1	0.097	0.066	0.153	−0.630	−0.443	0.230	0.563
3	6.5	2.2	−0.557	−0.504	−0.420	−0.213	0.355	0.167	0.243
4	2.3	0.8	0.132	0.094	−0.055	−0.326	0.133	0.721	−0.573
5	1.02	0.3	0.450	0.384	−0.649	−0.210	0.338	−0.206	0.168
6	0.04	0.01	−0.036	0.027	0.534	−0.498	0.562	−0.370	−0.107
7	0.01	0.003	0.662	−0.747	0.409	0.008	0.036	−0.018	0.007

[a]Percent variance explained by successive PCs.

In conclusion, with possible exceptions to PC 1, a linear transformation representing calibration does not change the distribution of weighting for any component on any band in a significant fashion. The correlation matrices are strictly unaffected.

Table C-12. Transform II: Covariance matrix of the reflectances obtained from element-by-element gain correction of the matrix $\|u_{ij}\|$

10.42						
11.20	12.50					
16.12	18.52	33.22				
23.08	27.26	47.70	81.42			
23.56	27.99	50.22	83.26	89.96		
22.69	26.35	46.82	70.38	77.45	73.70	
23.66	27.48	49.85	69.78	78.32	74.75	83.04

IV. Covariance Matrix and PCs for Landsat Image at Lisbon Valley

Table C-14 gives the covariance matrix for Landsat MSS scene 20872-16540 (June 1977) derived from sampling 90,000 pixels over the subarea shown in Figure 8-37. The corresponding eigenvalues and eigenvector matrix are given in Table C-15. The eigenvector loading diagram, plotted in the usual way and compared to the spectral reflectance of vegetation and rocks, is shown in Figure C-10.

Table C-13. Transform II: Eigenvalues and eigenvectors from the calibrated covariance matrix based on reflectances, NS-001 data, Lisbon Valley

Band	Eigenvalue	%[a]	Eigenvector						
			1	2	3	4	5	6	7
1	358.2	93.0	0.143	0.167	0.295	0.460	0.491	0.443	0.463
2	13.3	4.0	0.134	0.100	0.180	−0.585	−0.416	0.230	0.610
3	6.6	2.0	−0.618	−0.566	−0.263	0.193	−0.300	0.191	0.254
4	3.0	1.0	0.217	0.167	−0.195	−0.450	0.310	0.608	−0.467
5	1.4	0.4	0.266	−0.240	0.837	−0.058	−0.117	0.176	−0.351
6	0.7	0.2	0.112	0.085	0.270	0.449	0.621	0.560	0.086
7	0.1	0.0	0.670	0.741	−0.008	−0.038	−0.004	−0.002	−0.011

[a]Percent variance explained by successive PCs.

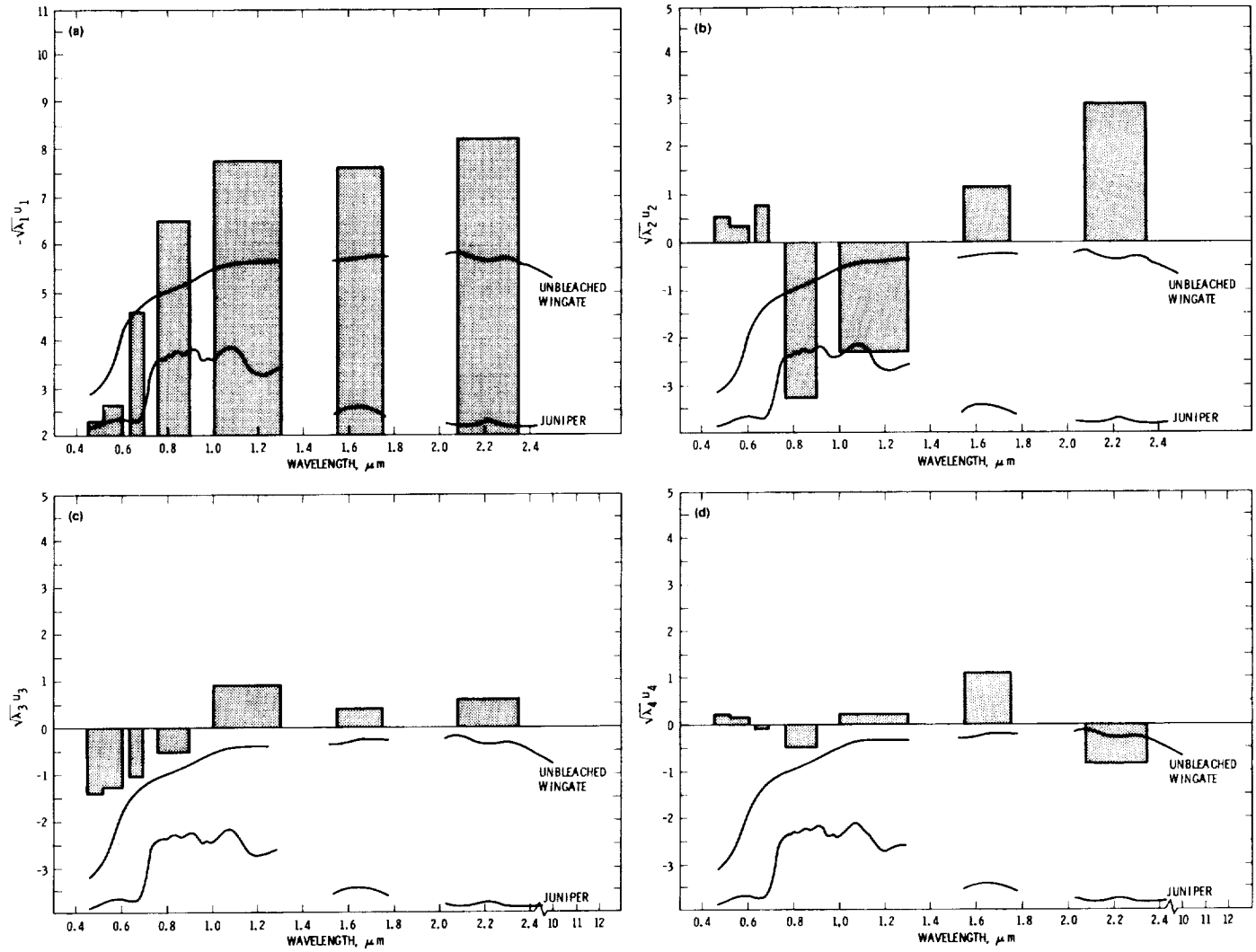

Figure C-8. First four PCs for transform I of NS-001 data, line 6, Lisbon Valley; principal values and directions from calibrated covariance matrix: (a)-$\sqrt{\lambda_1}u_1$; (b) $\sqrt{\lambda_2}u_2$; (c) $\sqrt{\lambda_3}u_3$; (d) $\sqrt{\lambda_4}u_4$

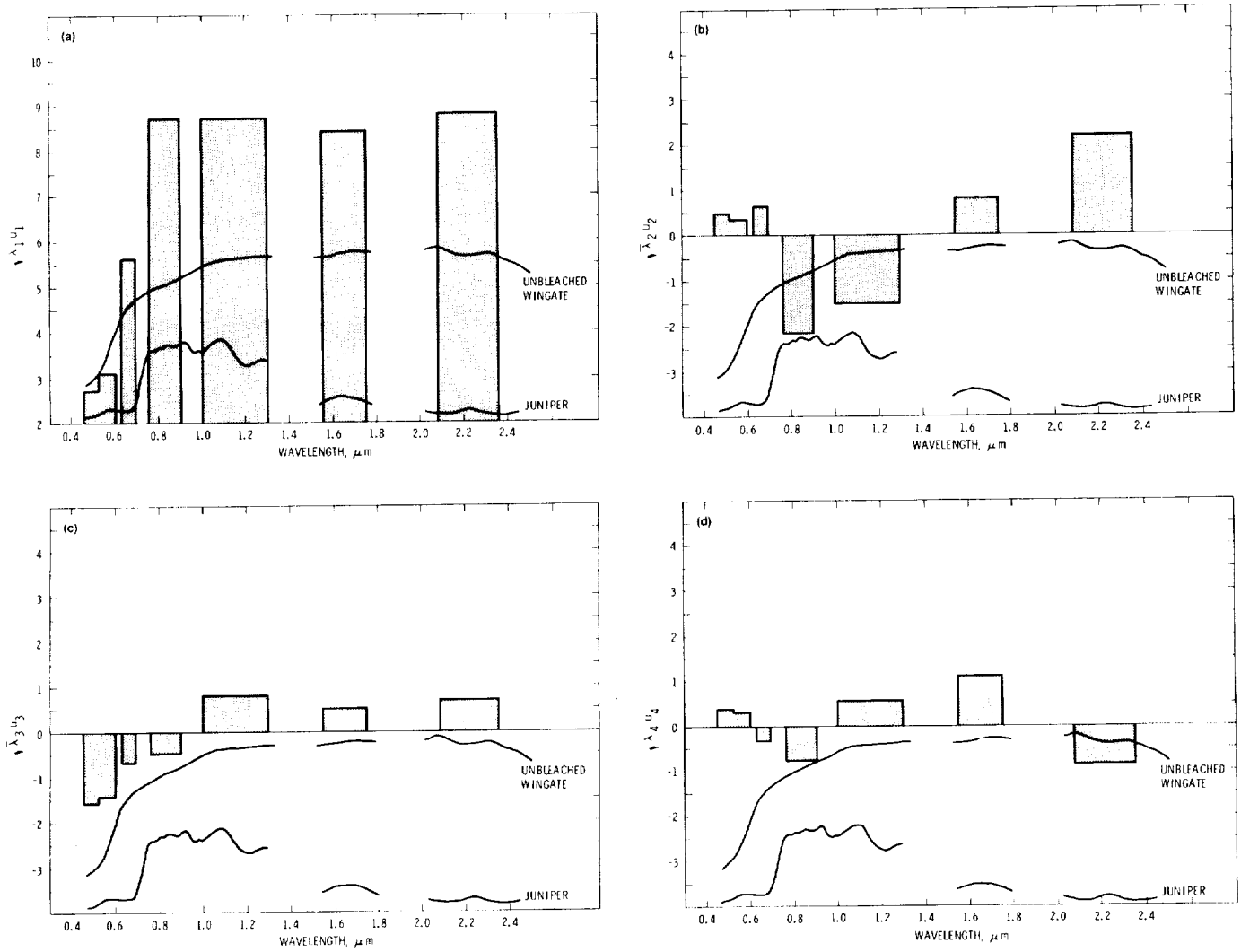

Figure C-9. First four PCs for transform II of NS-001 data, Lisbon Valley, restricted area; principal values and directions from calibrated covariance matrix: (a) $\sqrt{\lambda_1}u_1$; (b) $\sqrt{\lambda_2}u_2$; (c) $\sqrt{\lambda_3}u_3$; (d) $\sqrt{\lambda_4}u_4$

Table C-14. Covariance matrix for the area shown in the Landsat MSS image (Figure 8-37)

77.01			
129.93	307.63		
137.93	321.89	366.05	
123.04	281.50	312.95	284.34

Table C-15. Eigenvalues and eigenvectors from the covariance matrix in Table C-14

Band	Eigenvalue	%	Eigenvector			
			1	2	3	4
1	989.1	95.6	0.240	0.548	0.602	0.528
2	22.4	2.2	0.898	0.178	−0.354	0.190
3	14.4	1.4	−0.329	0.798	0.180	−0.473
4	9.2	0.9	−0.165	0.178	−0.693	0.679

[a]Percent variance explained by successive PCs.

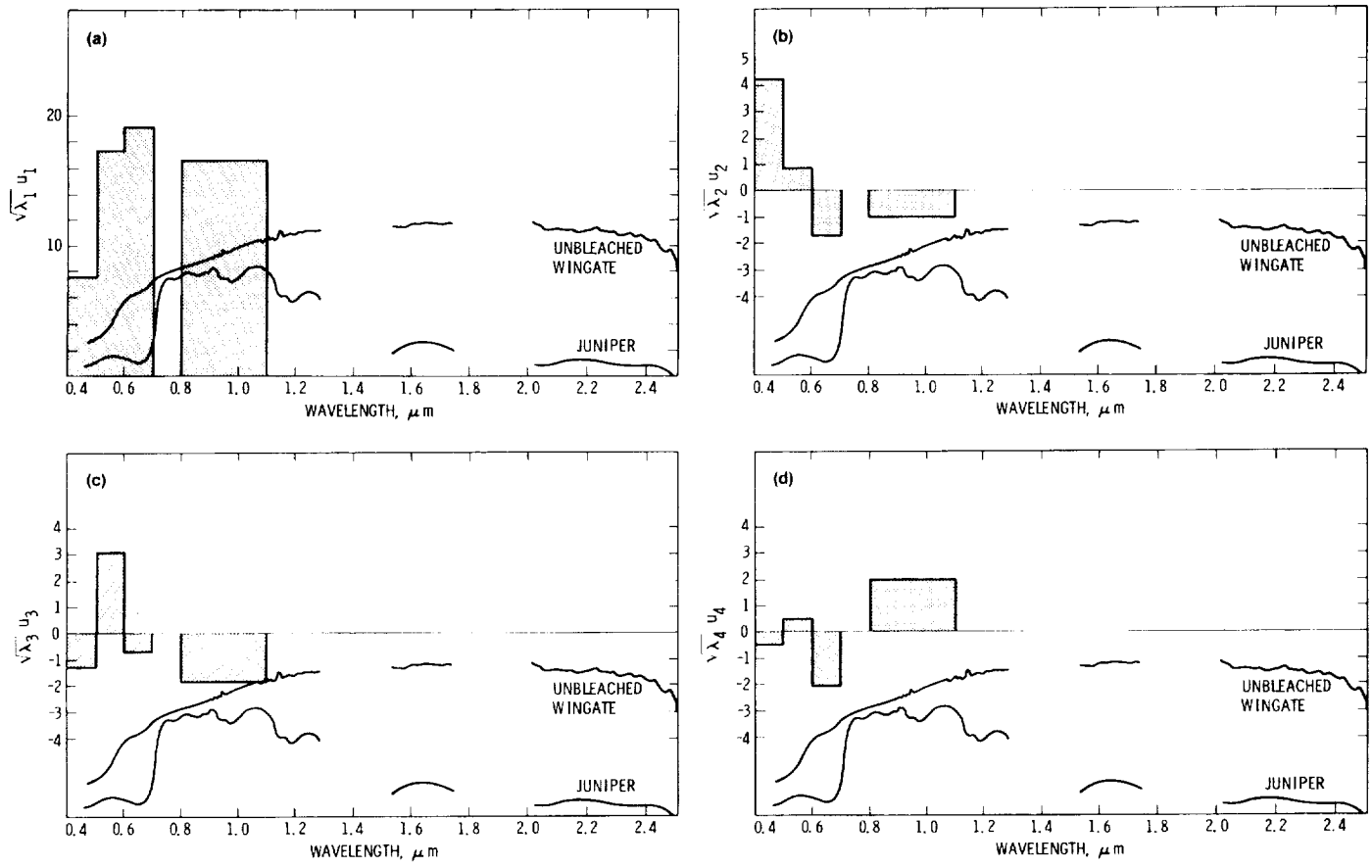

Figure C-10. Eigenvector diagram of the four PCs from the covariance matrix given in Table C-14: (a) $\sqrt{\lambda_1}u_1$; (b) $\sqrt{\lambda_2}u_2$; (c) $\sqrt{\lambda_3}u_3$; (d) $\sqrt{\lambda_4}u_4$

Appendix C
References

Maxwell, A. E. (1977). *Multivariate analysis in behavorial research*. London: Chapman and Hall.

Morrison, D. F. (1976). *Multivariate statistical methods* (2nd ed.). New York: McGraw–Hill.

Wiersma, D. J., and D. A. Landgrebe (1980). Analytical design of multispectral sensors. *IEEE Trans. Geosci. Rem. Sens.*, *GE-18*(2), 180–189.

Appendix D
Systematics of Correlation Matrices From Lisbon Valley NS-001 Scanner Data

I. Hierarchical Structure and Analysis With Factors

Previously, the covariance matrices of areas such as Lost River and Silver Bell were studied in order to assign physical meaning to the principal components (PCs). These two sites represent, respectively, heavily vegetated and largely unvegetated areas. Another way of understanding PCs is to study the correlation matrix itself. This matrix has the advantage (described in Appendix A) that its elements are independent of the linear scaling transformation associated with calibration and contrast stretching; therefore, PCs based on the correlation matrix will be independent of such transformations. The resulting image transformation can be thought of as calibrated. From a mathematical viewpoint, the statistical distribution function of the eigenvalues for a correlation matrix is more complicated than that of the corresponding covariance matrix (Morrison, 1967) and, therefore, analysis into PCs is not usually emphasized. Here the hierarchical and factor structures of the correlations are examined.

Table D-1 presents the correlation matrices for all sites previously described. Elements were rearranged so that variates correlating on the average most highly with the others are placed first, and so on. The arrangements obtained disclose interesting patterns. In Table D-1(a), the matrix for Lisbon Valley, line 6, has been rearranged. For any selected coefficient, all coefficients below it in the same column progressively decrease (with few exceptions), and all those to the right progressively increase (with few exceptions). For all sites except Silver Bell, the variates group themselves in similar hierarchical patterns. For 7-channel data, groupings in the first column are bands 1, 2, and 3 together, 6 and 7 together, and 4 and 5 together. In Table D-1(e), describing the 8-channel results, the thermal channel (variable 8) falls in a separate group; other groups previously noted are present as well. For Silver Bell,

Table D-1. Hierarchical arrangement of the correlation matrices for NS-001 data of Lisbon Valley and other test sites

(a) Lisbon Valley, line 6

Band	1	2	3	6	7	5	4
1	1.000						
2	0.980	1.000					
3	0.896	0.932	1.000				
6	0.807	0.858	0.942	1.000			
7	0.787	0.830	0.927	0.953	1.000		
5	0.680	0.764	0.834	0.891	0.798	1.000	
4	0.672	0.753	0.790	0.782	0.697	0.956	1.000

(b) Lisbon Valley, averaged subareas, lines 5, 6, and 7

Band	1	2	3	6	7	4	5
1	1.000						
2	0.981	1.000					
3	0.866	0.909	1.000				
6	0.821	0.874	0.953	1.000			
7	0.804	0.853	0.949	0.962	1.000		
4	0.792	0.855	0.917	0.915	0.875	1.000	
5	0.770	0.835	0.919	0.958	0.906	0.973	1.000

(c) Lost River, West Virginia

Band	1	2	3	6	7	4	5
1	1.00						
2	0.97	1.00					
3	0.90	0.94	1.00				
6	0.75	0.84	0.86	1.00			
7	0.75	0.82	0.87	0.87	1.00		
4	0.55	0.64	0.60	0.83	0.68	1.00	
5	0.53	0.63	0.60	0.87	0.69	0.98	1.00

Table D-1 (Continued)

(d) Silver Bell, Arizona

Band	1	2	3	7	5	6	4
1	1.000						
2	0.973	1.000					
3	0.956	0.983	1.000				
7	0.854	0.870	0.910	1.000			
5	0.853	0.883	0.927	0.927	1.000		
6	0.845	0.916	0.916	0.952	0.973	1.000	
4	0.839	0.904	0.900	0.815	0.890	0.842	1.000

(e) Lisbon Valley, line 5, 8-channel

Band	1	2	3	6	7	5	4	8
1	1.000							
2	0.985	1.000						
3	0.920	0.949	1.000					
6	0.856	0.903	0.953	1.000				
7	0.848	0.884	0.948	0.973	1.000			
5	0.768	0.819	0.844	0.857	0.862	1.000		
4	0.753	0.803	0.804	0.831	0.787	0.972	1.000	
8	0.582	0.619	0.693	0.793	0.788	0.721	0.621	1.000

two groups emerge: the first contains bands 1, 2, and 3; the second contains all remaining bands.

Systematic arrangements of variables suggest the presence of common factors that may account for the correlation structure observed. To check this, factor analyses were made of the covariance matrices (Table D-2) for Lisbon Valley, line 6, and Lisbon Valley averaged subarea data using a factor analysis program in the BMD07 computing package (Dixon, 1974). Expressed algebraically, the factor model is (Maxwell, 1977, p. 47)

$$Z_i = (\lambda_{i1} f_1 + \lambda_{i2} f_2 + \cdots + \lambda_{ik} f_k) + e_i \qquad (i = 1,2,\ldots,7)$$

in which the ith variate Z_i consists of a weighted sum of k factors f_k plus a residual term e_i specific to the ith variate itself. The λ_{ik} constitute factor loadings. Results for a three-factor model of the correlation matrix are presented.

The three clusterings of bands noted previously are clearly displayed by these results. For line 6, the first three variables are associated with the first factor, variables 4 and 5 with the second, and 6 and 7 with the third (a relatively heavy weighting of the third variable on the third factor is also present). Although similar groupings can be seen in the matrix for subarea data, separations here are not as clear. This corresponds to the generally higher correlations derived for the restricted area data collection.

Table D-2. Loading of seven variables in three factors for Lisbon Valley

Band	Factor		
	I	II	III
	Transform I, line 6		
1	24.22	7.50	−9.66
2	24.17	10.71	−12.04
3	22.55	13.69	−22.65
4	9.54	27.53	−7.33
5	8.21	25.38	−13.75
6	15.18	15.61	−25.94
7	16.03	12.18	−29.11
	Transform II, averaged subareas, lines 5, 6, and 7		
1	11.15	−27.62	10.32
2	15.55	−28.60	12.62
3	22.49	−21.95	22.04
4	28.63	−16.44	12.64
5	29.80	−14.81	16.90
6	24.72	−18.74	24.27
7	19.27	−16.77	26.46

These results are amenable to a straightforward physical interpretation in terms of bands present in the spectral reflectance of rocks and vegetation. In Figure C-2, bands 1, 2 and 3 correspond to a region of chlorophyll and Fe^{+3} charge transfer absorption; bands 6 and 7 span an interval dominated by absorption due to constitutive water and to overtone and combination bands from OH and from aluminum and hydroxyl. The intervening region of bands 4 and 5 is populated by weaker overtones and a combination of OH plus electronic bands, but this is not a region containing strong absorptions of either electronic or molecular origin. This interval accounts for the high-infrared reflectance of vegetation.

To summarize, the correlation matrices for the several Geosat test areas are composed of an aggregate of millions of data points. These data reveal groupings of the 7-channel scanner spectral bands associated with regions of distinctive spectral reflectance. The groupings are correlated with contributions from rock and dominantly from vegetation. Three clusterings are evident: (1) bands 1, 2, and 3 in the spectral interval 0.45 to 0.70 μm, (2) bands 4 and 5 in the interval 0.76 to 1.30 μm, and (3) bands 6 and 7 in the interval 1.55 to 2.35 μm. This factor structure discloses a high degree of dependence within the groups, suggesting a redundance of the spectral information contained within each. As an example, one correlation matrix is examined (restricted area statistics using transform II, line 6, Lisbon Valley). The rank of this matrix is certainly less than its order and is suspected to be close to three. This is consistent with the presence of three linearly independent factors that explain more than 97.5 percent of the total variance.

II. Use of Covariance Versus Correlation Matrices To Calculate PCs

Use of the correlation matrix is preferred in computation of PCs from the aircraft data sets because the correlation coefficients depend on ground reflectances alone and not on gain or offset parameters characterizing the atmospheric and rescaling transformations that appear in the calibration equations. Since the covariance matrix was used in all cases for production of image data at Lisbon Valley, the differences produced are important because the covariance matrix does contain products of gain factors in each element.

The eigenvalues and eigenvectors for transform II, based on the correlation matrix, are presented in Table D-3, and the histogram of weighted eigenvector component $\sqrt{\lambda_j}\, u_j$ is shown in Figure D-1. The first three of the seven eigenvalues encompass 98.5 percent of the variance and the determinant of the correlation matrix has the value 6.759×10^{-8}. This suggests that the determinant is singular, that the matrix has a rank (probably three) less than its order and, therefore, that considerable linear dependence exists among elements.

The histogram of eigenvector components resembles, except for magnitudes that may be rescaled and unimportant differences in sign, the corresponding covariance matrix of Figure C-6 and Table C-5. For this typical example, both approaches yield equivalent results.

Table D-3. Transform II: Eigenvalues and eigenvectors computed from the correlation matrix

Band	Eigenvalue	%[a]	Eigenvector						
			1	2	3	4	5	6	7
1	6.34	90.7	0.359	0.375	0.388	0.377	0.379	0.387	0.379
2	0.40	5.6	-0.666	0.494	0.039	0.276	0.386	0.217	0.198
3	0.16	2.3	-0.072	-0.118	0.225	-0.601	-0.335	0.258	0.625
4	0.05	0.7	-0.147	-0.059	0.726	0.288	0.334	0.508	0.015
5	0.03	0.5	0.009	0.102	-0.502	0.342	-0.130	-0.438	0.642
6	0.01	0.2	-0.633	0.764	-0.017	-0.090	-0.046	0.048	-0.054
7	0.01	0.1	0.028	0.055	0.132	0.461	0.681	0.539	0.110

[a] Percent variance explained by successive PCs.

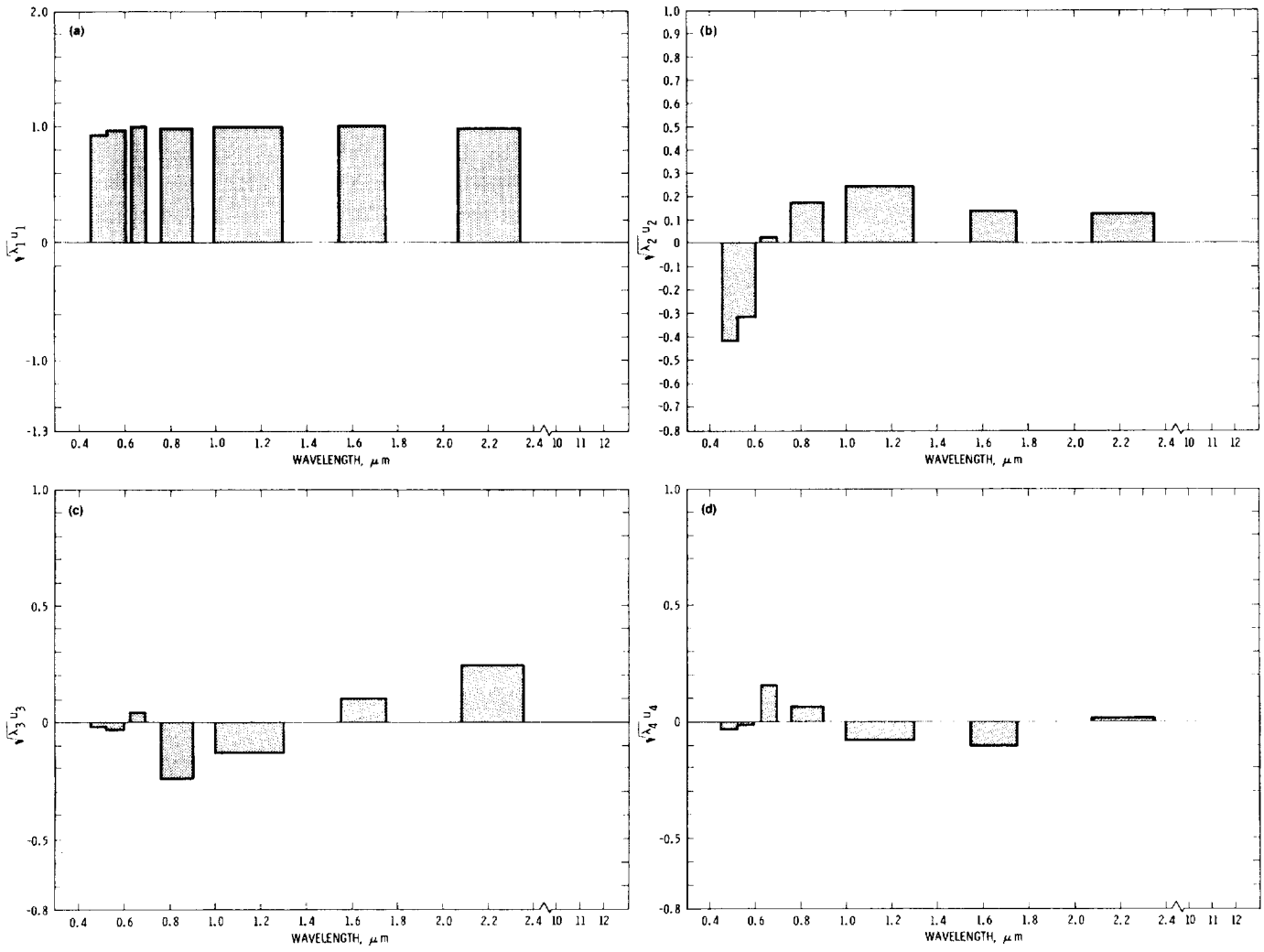

Figure D-1. First four PCs for transform II of NS-001 data, Lisbon Valley, restricted area; principal values and directions from correlation matrix: (a) $\sqrt{\lambda_1}u_1$; (b) $\sqrt{\lambda_2}u_2$; (c) $\sqrt{\lambda_3}u_3$; (d) $\sqrt{\lambda_4}u_4$. (See Table D-1a.)

Appendix D
References

Dixon, W. I. (Ed.) (1974). *Biomedical computer programs*. Los Angeles: University of California Press, UCLA, Health Sciences Facility, Department of Biological Mathematics, School of Medicine.

Maxwell, A. E. (1977). *Multivariate analysis in behavorial research*. London: Chapman and Hall.

Morrison, D. F. (1967). *Multivariate statistical methods*. New York: McGraw–Hill.

Appendix E
Principal Component and Canonical Scatter Diagrams: The Analysis of Mixed Spectral Collections

At the spatial resolution provided by NS-001 images at Lisbon Valley (~15 m), very few if any of the pixels are composed of rock outcrop alone; most contain a mixture of one or more components consisting of vegetation, soil, talus, alluvium, eolian deposits, and rock outcrop. The quantitative interpretation of image spectra and the images themselves, either in terms of rock composition or as vegetation diversity, requires methods for estimating and separating the components present. To study the estimation question, two methods, based on the uses of the principal component (PC) transformation and on the canonical transform, are presented here. Two diagrams are used: (1) a new diagram, called the PC diagram, that allows a simple graphical estimate of proportions in mixed systems, and (2) the familiar canonical scatter diagram, reinterpreting this latter diagram for purposes of proportion estimation.

To study the separation of units in images, a method accounting for the color discrimination properties of the eye is required. This method should permit an estimate of what established spectral groups are just separable from one another in our perception, given the image rendition and color assignments of the composite. The concept of the McAdam ellipse would appear to be fundamental here. The detailed working out of this second question is left for a subsequent study.

I. The PC Diagram

The PC diagram is constructed by analogy with the familiar chromaticity diagram used in colorimetric matching theory (refer to Wyszecki and Stiles, 1967, for a discussion of chromaticity diagrams). In the PC diagram, the primary colors of the chromaticity diagram are replaced by the PC representations (usually linearly transformed) of a spectrum or spectral collection. The PCs are statistically uncorrelated quantities, just as the primary colors are linearly independent colors. These PC components involve weighted contributions from all spectral channels and are often spoken of as providing a means of "data compression." These properties make the PCs desirable variables, although they are obviously not the only choices possible. For example, the raw reflectances (or digital number, DN, values) may be used to define points in a seven-dimensional space (NS-001 data) and to define the properties of the distribution by projections designed to reduce the number of dimensions and thereby ease the problem of visualization and analysis. Thus, the choice of projection may not be obvious.

The dimensionality is reduced in a statistically meaningful and parsimonious fashion by using the PCs since, typically, a large fraction of the variance (98 to 99 percent) is contained within the first three or four variables.

II. The Canonical Scatter Diagram

Another example of projection is the canonical scatter diagram. This diagram contains all of the convenient properties described above for the PC diagram. The canonical variates are quantities made up of linear combinations of original variables and may be thought of as a data compression scheme with the additional important property that the axes are chosen to optimize separation of chosen groups in the data swarm relative to scatter inherent within these groups. This transformation (here orthogonal) selects the plane of projection through seven-dimensional space that accomplishes the separation desired for two variables. Groups existing outside the plane may appear in slices perpendicular to the axis of the third (or other) canonical variate. The canonical scatter plots used here are produced as part of the BMD07 discriminant analysis computing package (Dixon, 1974).

PRECEDING PAGE BLANK NOT FILMED

III. Derivation of Coordinates in the PC Diagram

In terms of the scanner data, the radiance from a single pixel may be described by a point in a seven-dimensional space, the axes of which are measures of their energy in each channel. In terms of the radiances (DN values), the ith PC is defined as

$$V_i = \sum_{\alpha=1}^{7} \lambda_{i\alpha} DN_\alpha \qquad (i = 1,2,\ldots,7) \qquad \text{(E-1)}$$

where the $\lambda_{i\alpha}$ are direction cosines between the positive end of the ith principal axis and the position end of the αth original (radiance) axis. The DN_α are adjusted for atmospheric attenuation and instrument response in accordance with Eq. (A-15) to obtain quantities proportional to surface reflectance.

Since the PCs given by Eq. (E-1) may assume a wide range of values both positive and negative, these values must be rescaled to the 0 to 255 DN range before pictorial representation. The rescaling to positive values is in practice accomplished by applying a linear gain-plus-offset transformation. A second transformation, clipping the DN distribution at high and low ends and representing a stretching of these values for image display, is applied for each PC. These two transformations may be combined into a single linear transformation to yield variables U_i given by

$$U_i = A_i V_i + B_i \qquad (i = 1,2,\ldots,7) \qquad \text{(E-2)}$$

where A_i and B_i are constants. As a result of this (cosmetic) stretch transformation, a small percentage of DN values occupying extreme positions in the DN distribution may be set to saturation (0 to 255) values. For purposes of comparison with the image data, the transformation of Eq. (E-2) has been applied, using those constants employed in production of the images dealt with in practice. The transformation may, of course, be adjusted to achieve any range of values.

Take the coordinates of a point P in PC space (Figure E-1) to be (U_1,U_2,U_3) and the intersection of the vector **P**, with the unit plane (the PC diagram) to be Q (u_1,u_2,u_3). In colorimetry, the u_i are termed tristimulus values represented by primary colors U_1,U_2,U_3. The u_i are then the chromaticity coordinates in the unit plane, which is the plane of the chromaticity diagram. In terms of the principal coordinates (U_1,U_2,U_3), the unit plane is given by

$$U_1 + U_2 + U_3 = 1 \qquad \text{(E-3)}$$

while the plane passing through P' (U_1',U_2',U_3') parallel to the unit plane is

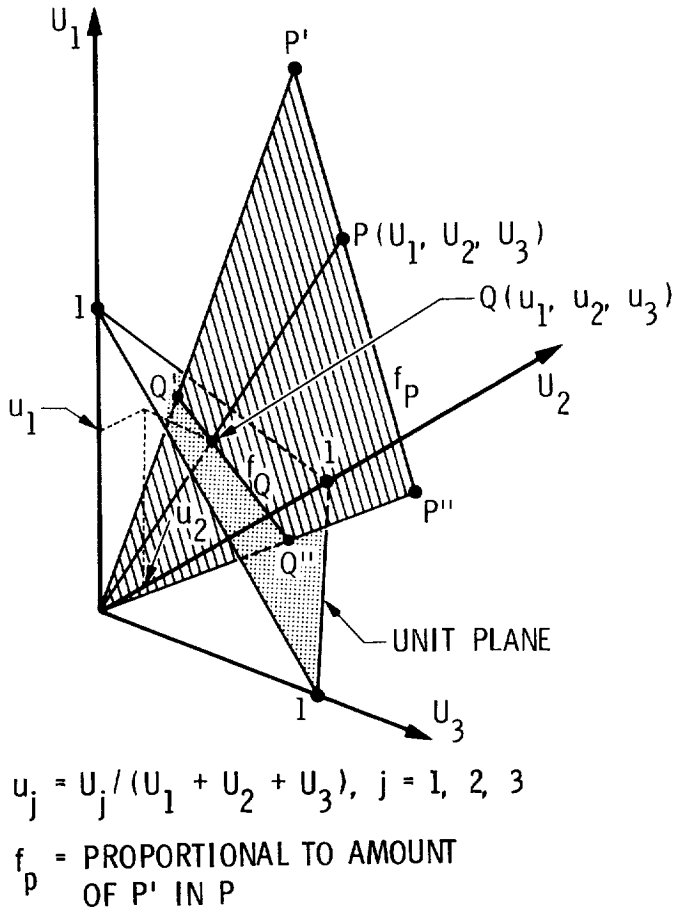

Figure E-1. Coordinate system of the PC diagram. Points P' and P'' represent end-member spectral groups in a space of the first three PCs. Point P represents a mixture with proportions f_P of P' and (1 − f_P) of P''. These points project to the unit plane as Q', Q'', and Q and a distorted proportion f_Q for the amount of Q' in Q.

$$U_1 + U_2 + U_3 = U_1' + U_2' + U_3' \qquad \text{(E-4)}$$

Without loss of generality, and to simplify discussion, consider a situation in two dimensions obtained by letting $U_3 = 0$ (Figure E-2). From this diagram, the coordinates of point Q' referred to the unit plane are

$$u_1' = \frac{U_1'}{U_1' + U_2'} \qquad \text{(E-5)}$$

$$u_2' = \frac{U_2'}{U_1' + U_2'} \qquad \text{(E-6)}$$

These formulas are identical to the chromaticity coordinates computed from the tristimulus values in the corresponding colorimetric problem.

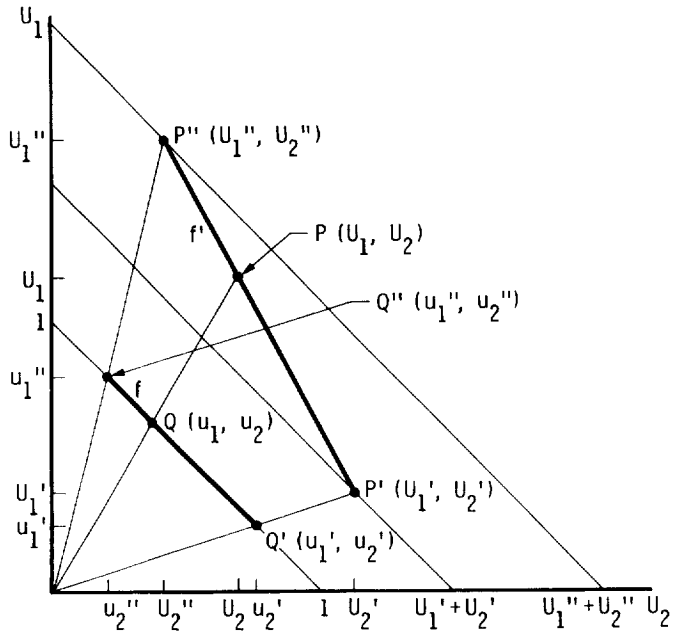

Figure E-2. Detailed relationships between the principal coordinates P, P', P" and principal coordinates reduced to the unit plane Q, Q', and Q"

Formulas applicable to mixtures of (supposedly) well-defined pure end members can be derived from simple photometric proportionality arguments. Consider a pixel to be of unit area and to contain two components. If an areal fraction f is made up of end-member A with reflectance in band i of R_{iA} and the fraction $(1-f)$ of end-member B with reflectance in i of R_{iB}, then the reflectance R_i of the total is obtained from the expression

$$f = \frac{R_i - R_{iB}}{R_{iA} - R_{iB}} \tag{E-7}$$

The reflectances are essentially linearly related to DN values, so Eq. (E-7) can be rewritten as

$$f = \frac{DN_i - DN_{iB}}{DN_{iA} - DN_{iB}} \tag{E-8}$$

Using Eq. (E-1) for the PCs

$$V_i = fV_{iA} + (1-f)V_{iB} \tag{E-9}$$

where

$$V_{iA,B} = \sum_{\alpha} \lambda_{i\alpha} R_{\alpha A,B}$$

Finally, since from Eq. (E-9)

$$f = \frac{V_i - V_{iB}}{V_{iA} - V_{iB}} \tag{E-10}$$

the application of Eq. (E-2) yields

$$f = \frac{U_i - U_{iB}}{U_{iA} - U_{iB}} \tag{E-11}$$

and the photometric proportionality expressed in Eq. (E-7) carries over when the variables are transformed to the system of the U_i.

Consider a system consisting of two pure end members represented by the points $P'(U_1', U_2')$ and $P''(U_1'', U_2'')$ (Figure E-2). If a mixed system consists of a proportion f of U_1' and a proportion of $1-f$ of U_2' and is represented by the points U_1 and U_2, then corresponding point $P(U_1, U_2)$ has coordinates related by

$$\frac{U_1'' - U_1}{U_1'' - U_1'} = \frac{U_2'' - U_2}{U_2'' - U_2'} = f \tag{E-12}$$

Equation (E-12) is the equation of the line through P' and P", with f the fractional distance of P from P', i.e., $f = \overline{PP'}/\overline{P'P''}$. The coordinates (u_1, u_2) of P, projected onto the unit plane, are given by

$$\begin{aligned} u_1 &= \frac{U_1}{U_1 + U_2} \\ u_2 &= \frac{U_2}{U_1 + U_2} \end{aligned} \tag{E-13}$$

The statement of these results in three dimensions follows from the vector nature of the quantity P' and P'' (see, for example, Wyszecki and Stiles, 1967, p. 231). In three dimensions, the principal coordinates reduced to the unit plane

$$\left.\begin{aligned} u_1 &= \frac{U_1}{U_1 + U_2 + U_3} \\ u_2 &= \frac{U_2}{U_1 + U_2 + U_3} \\ u_3 &= \frac{U_3}{U_1 + U_2 + U_3} \end{aligned}\right\} \tag{E-14}$$

Representations in the unit plane are a simple way of comparing the relative positions of important spectral groups in reduced dimensions. Furthermore, these representations may

tral groups, and (2) what linear transform optimizes the separation between groups present if the spectral band selection is fixed? The first question falls within the framework of discriminant analysis, to be discussed later. The second question is answered by the canonical transform if the separable groups are known. The PC transformation uses the (unsupervised) covariance matrix to provide average separation based on the scatter properties. Regardless of the transformation, it is possible to estimate group separation by a simple Euclidean distance measure in PC space.

To illustrate the method, the distance between two points (U_1,U_2,U_3) and (U_1',U_2',U_3') is computed. Further, to simplify, assume that the reflectance is zero except for a single band r_β where $\beta = 1, \ldots, 7$. Then in terms of reflectance, the U_i are

$$U_i = A_i\lambda_{i\beta}r_\beta + B_i \qquad (i = 1,2,\ldots,7) \qquad \text{(E-17)}$$

where the constants A_i, B_i lump all the atmospheric, instrumental, gain, offset, calibrations, and cosmetic stretching components present in the model. The Euclidean distance (squared) D_β^2 separating spectral classes in a three-dimensional subspace appropriate to PC on canonical variate diagram representation is

$$D_\beta^2 = (A_1^2\lambda_{1\beta}^2 + A_2^2\lambda_{2\beta}^2 + A_3^2\lambda_{3\beta}^2)(r_\beta - r_\beta')^2 \qquad \text{(E-18)}$$

Thus, any inherent separation between points due to differences in reflectance is *amplified* for display by the factor $\Sigma(A_i^2\lambda_{i\beta}^2)^{1/2}$. If it had been possible to work in terms of reflectance alone, the A_i could be taken equal, say to A, and Eq. (E-18) would be reduced to

$$D_\beta^2 = A^2(\lambda_{1\beta}^2 + \lambda_{2\beta}^2 + \lambda_{3\beta}^2)(r_\beta - r_\beta')^2 \qquad \text{(E-19)}$$

Equations (E-18) and (E-19) show that a given amplification factor may be achieved, changing either the constants A_i or the direction cosines $\lambda_{i\alpha}$. Image calibration is one possible transformation changing the A_i, but an equivalent result may be obtained formally by a stretching transformation unrelated to the calibration procedure. There is *a priori* no way to decide that calibration provides a "better" result since such linear transformations are clearly similar. Regarding the second factor in Eq. (E-19), different $\lambda_{i\alpha}$ may be obtained by using different starting covariance matrices. The covariance matrix depends on the sample area chosen.

To get a feeling for magnitudes of PC amplification factors, the quantities $\Sigma\lambda_{i\beta}^2$ are computed for four PC transformations derived from separate areal samplings of Lisbon Valley NS-001 image data. These results are shown in Table E-1.

An example of this procedure applied to image data of Lisbon Valley is given in Tables E-2 and E-3, where the separation distance D is computed for outcrops of bleached and unbleached Wingate Sandstone according to two different PC transformations. The covariance matrix for transform I was derived from sampling the total area covered in August 1979, NS-001

Table E-1. Calculated Euclidean distance amplification factors for various Lisbon Valley PC transformations

Unit Plane[a]	Band 1	2	3	4	5	6	7
				Line 5 (transform I)			
(1,2,3)	0.6957	0.6177	0.5011	0.7833	0.6492	0.5771	0.7174
(2,3,4)	0.6843	0.5368	0.7046	0.7820	0.6392	0.6192	0.5888
				Line 6 (transform I)			
(1,2,3)	0.6915	0.6332	0.4612	0.7420	0.6834	0.5857	0.7395
(2,3,4)	0.6487	0.5418	0.4981	0.7721	0.6440	0.7143	0.7183
				Line 7 (transform I)			
(1,2,3)	0.7001	0.6446	0.4202	0.7494	0.6583	0.5909	0.7570
(2,3,4)	0.6618	0.5419	0.5749	0.7327	0.6206	0.6980	0.7273
				Average of lines 5, 6, and 7 (transform II)			
(1,2,3)	0.7206	0.6651	0.4709	0.7438	0.6548	0.5375	0.7385
(2,3,4)	0.6720	0.5715	0.7718	0.7036	0.6007	0.6096	0.6313

[a] $(1,2,3) = (\lambda_{1\beta}^2 + \lambda_{2\beta}^2 + \lambda_{3\beta}^2)^{1/2}$
$(2,3,4) = (\lambda_{2\beta}^2 + \lambda_{3\beta}^2 + \lambda_{4\beta}^2)^{1/2}$

Table E-2. Comparison of Euclidean separation distances *D* under various PC transformations for bleached and unbleached Wingate facies, NS-001 data, Lisbon Valley

(a) Raw channel values after Gradrem (line 5)

Facies[a]	Channel						
	1	2	3	4	5	6	7
Bleached $\bar{R}w$ (9)[b]	207 ±25	190 ±26	180 ±27	158 ±29	148 ±29	152 ±28	170 ±23
Unbleached $\bar{R}w$ (15)[c]	155 ±11	179 ±15	232 ±19	211 ±17	224 ±18	228 ±18	237 ±13

(b) PC transforms I and II

Facies[a]	Principal Component			
	V1	V2	V3	V4
	Transform I: Line 6, total area, 7-channel			
Bleached $\bar{R}w$ (9)[b]	448 ±70	−32 ±48	−82 ±10	117 ±23
Unbleached $\bar{R}w$ (15)[c]	557 ±42	44 ±5	5 ±4	151 ±12
	Transform II: Average of three areas, 7-channel			
Bleached $\bar{R}w$ (9)[b]	450 ±70	82 ±2	9 ±6	−6 ±1
Unbleached $\bar{R}w$ (15)[c]	558 ±42	−27 ±2	−10 ±3	−8 ±1

(c) Euclidean distance *D* between bleached and unbleached $\bar{R}w$

Unit Plane[d]	Transform I	Transform II
(1,2,3)	154 ±115[e]	115 ±82
(2,3,4)	113 ±57	111 ±4

[a]Numbers in parentheses are sample sites.
[b]Average of 72 pixels, ± 1 σ.
[c]Average of 24 pixels, ± 1 σ.
[d](1,2,3) based on PCs 1, 2, and 3; (2,3,4) based on PCs 2, 3, and 4.
[e]See text for method of calculation.

data, line 6. The covariance matrix of transform II was computed from areas of reduced size in lines 5, 6, and 7, principally restricted to outcrops of Wingate Sandstone and stratigraphically adjacent rock units (see Figure C-1 for these areas). Comparison of the figures indicates that while the D distances for (1,2,3) space and (2,3,4) space for these two rock units remain the same regardless of the transformation, the uncertainties derived from scatter in pixel radiances have been reduced dramatically. The uncertainties given were computed as total differentials from the formula

$$\delta D = \frac{\Delta V1}{D}\delta V1 + \frac{\Delta V2}{D}\delta\Delta V2 + \frac{\Delta V3}{D}\delta V3, \qquad \text{etc.}$$

where

$$\Delta V1 = |V1\,(\text{bleached}) - V1\,(\text{unbleached})|, \qquad \text{etc.}$$

and

$$\delta V1 = |\delta V1\,(\text{bleached})| = |\delta V1\,(\text{unbleached})|, \qquad \text{etc.}$$

VI. Generalization of the Distance D^2 for Group Separability To Include a Spectrum of p Discrete Reflectances

It is not difficult to generalize the preceding analyses to a case of p spectral bands and provide insight into a means of maximizing the separation of points in PC space. Here points rather than clusters are discussed, with the understanding that these points may represent the mean direction of clusters. Let the spectrum be characterized by p reflectance values (r_α = 1,2, ..., p) and represented by a point in an orthogonal p-space, the jth axis representing the jth reflectance value in

Table E-3. Mean values of principal coordinates and separation distances for bleached and unbleached Wingate Sandstone

(a) Mean values and standard deviation for groups

Unit Plane[a]	Wingate Sandstone	
	Bleached	Unbleached
	Transform I	
(1,2,3)	457 ±74	559 ±42
(2,3,4)	146 ±34	157 ±12
	Transform II	
(1,2,3)	457 ±69	559 ±42
(2,3,4)	83 ±3	30 ±3

(b) Separation distances *D* with 95 percent confidence intervals

Unit Plane[a]	Transform I	Transform II
(1,2,3)	154 ±24	155 ±23
(2,3,4)	113 ±9	111 ±1

[a](1,2,3) based on PCs 1, 2, and 3; (2,3,4) based on PCs 2, 3, and 4.

the usual way. The coordinates U_j ($j = 1,2, \ldots, p$) give the combined effects of linear transformations representing (1) instrumental encoding, (2) orthogonal (PC or canonical) transformations, and (3) rescaling for color display (i.e., $0 \leq U_j \leq 255, j = 1,2, \ldots, p$). In subscript notation

$$U_j = a_j \sum_{\alpha=1}^{p} \lambda_{j\alpha} k'_\alpha r_\alpha + a_j \sum_{\alpha=1}^{p} \lambda_{j\alpha} k''_\alpha + b_j$$

$$(j = 1,2, \ldots, p) \qquad \text{(E-20)}$$

Equation (E-20) represents an affine transformation on the continuum of possible values in r, representing the scene, to values in U. A useful geometrical interpretation emerges using the languages of the infinitesimal theory of elasticity (Sokolnikoff, 1956, p. 6). Part of Eq. (E-20) represents rigid body motion (translation and rotation) of the r-values and part pure deformation. From the standpoint of the assumed criterion of separability—maximizing the separation distance (squared) D^2 between pairs of points for spectral classes—only the *dilitational* part of this deformation is needed (pure shear changes shape only), and it is sufficient to consider the changes in distance D^2 resulting from the transformation. In subscript notation

$$D^2 = \sum_{j=1}^{p} a_i^2 \left(\sum_{j=1}^{p} \lambda_{ij} k'_j \Delta r_j \right)^2 \qquad \text{(E-21)}$$

where Δr_j represents the difference in reflectance between two groups in band j. The only adjustable parameters in Eq. (E-21) are the p gain factors a_i since the λ_{ij} are fixed by the PC transformation and the k'_j are instrumental gain factors fixed for each flight. It is easy to see that D^2 increases directly as the square of the a_i. Adjustments of the a_i, consistent with rescaling of the U_i to the available dynamic range, are performed routinely and are called *marginal* contrast enhancements by Soha and Schwartz (1978). Their transformations are nonlinear (Gaussian), whereas the present analysis supposes linear operations only. The procedure is analogous to that of decorrelation enhancement, except that an inverse transformation to original axes has not been included here. This step is not essential to illustrate the geometrical consequences of the transformation since D^2 is unchanged by this additional pure rotation. The earlier example worked out here in detail (Eq. E-19) is a one-dimensional case, representing a simple extension (i.e., elongation) of the distance Δr_β. Decorrelation enhancement introduces this additional pure rotation to original axes to preserve color relations (Soha and Swartz, 1978). Such rotations, of course, leave the dilitational aspects of the affine transformation (Eq. E-20) unchanged.

Marginal enhancements amplify not only the distances between spectral groups but the inherent scatter about the mean as well. The effectiveness of such procedures must still rely on the interpreter's judgment to provide a measure of the usefulness of the results.

VII. Representation of a Spectrum With Discrete Uniform Reflectances in PC Diagrams

The general relations between the principal coordinate reduced to the unit plane (u_1,u_2,u_3) and an arbitrary spectral reflectance $(R_1,R_2, \ldots, R_7)$ are algebraically complicated, but important properties of the diagrams and insight into a physical interpretation of the PCs themselves are obtained by considering a simplified situation where the reflectance in all bands is equal to $\overline{R}$, for example. This simplified spectrum corresponds physically to the effects produced by deep shadowing (zero reflectance) where, for a diffuse, perfectly reflecting target, the quantity $1 - \overline{R}$ corresponds to the fractional area of shadows present.

Derivation of the principal coordinates in terms of the components of reflectance is straightforward, so the details are omitted. The ith coordinate u_i is given in terms of the parameter $\overline{R}$ by

$$u_i = \frac{A_i \overline{R} + B_i}{\sum_{j=1,2}^{3,4} A_j \overline{R} + \sum_{j=1,2}^{3,4} B_j} \qquad (i = 1,2,3,4) \qquad \text{(E-22)}$$

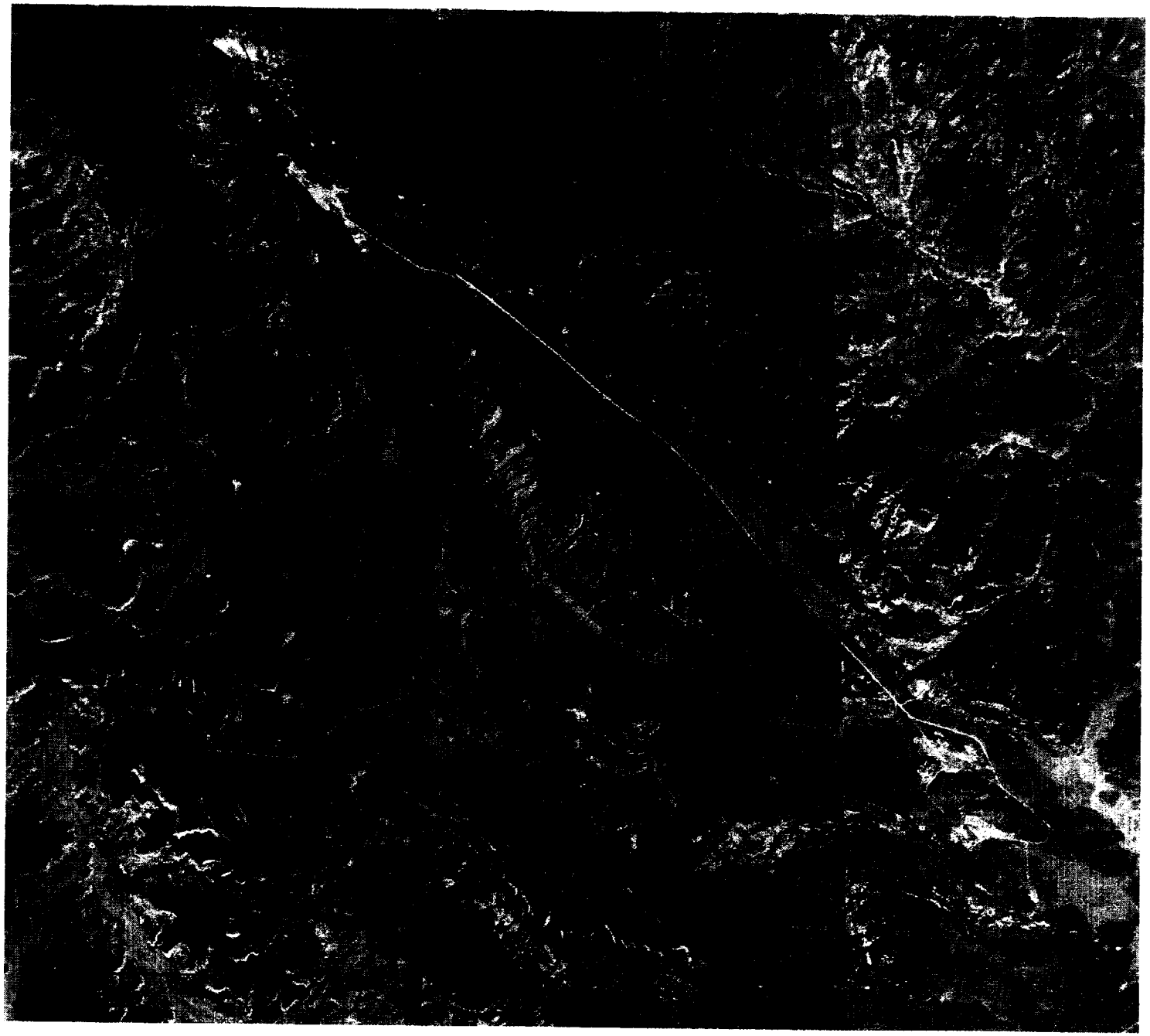

Figure F-1. PC image of the NS-001 data for the Lisbon Valley area prepared according to transform II (restricted area of Appendix C); V1 = red, V2 = green, V3 = blue

Equations (E-23) and (E-24) are independent of $\bar{R}$, i.e., the path depends upon the gain, offset, and transformation factors only.

These diagrams provide a graphical demonstration that the variable u_1 predominantly measures the albedo or average value of the reflectance since variation of reflectance with wavelength is specifically excluded from this calculation.

The distance between points in the u_1,u_2 plane between any two values of the reflectance $\bar{R}_1$ and $\bar{R}_2$ is given by computing

$$S_{\bar{R}_1,\bar{R}_2} = \int_{\bar{R}_1}^{\bar{R}_2} ds \qquad \text{(E-25)}$$

where $ds^2 = du_1^2 + du_2^2$. From this expression,

$$S_{\bar{R}_1,\bar{R}_2} = -B\sqrt{\left(\frac{A_1}{A} - \frac{B_1}{B}\right)^2 + \left(\frac{A_2}{A} - \frac{B_2}{B}\right)^2}$$
$$\left[\frac{1}{(A\bar{R}_1 + B)} - \frac{1}{(A\bar{R}_2 + B)}\right] \qquad \text{(E-26)}$$

For a point of reflectance R_p fractional distance f between the endpoints is

$$f = 1 - \frac{R_p}{S_{100,0}} \qquad \text{(E-27)}$$

$$f = \frac{\frac{1 - R_p}{100}}{1 + \left(\frac{A}{B}\right)R_p} \qquad \text{(E-28)}$$

VIII. A Note on Statistical Analysis and PC Diagrams

The discussion of PC diagrams given above centered on a largely geometrical representation of spectra in PC space, with no attempt to derive these results from any statistical basis. Horwitz et al. (1971, 1975) and Nalepka et al. (1972) presented a statistical method for proportion estimation based on a maximum likelihood principle. This method uses a photometric model equivalent to that represented by Eq. (E-9). In the model of Horwitz et al., the signature of an object class i (e.g., rocks, trees, dirt, weeds) is represented by an N-dimensional (N-spectral channel) Gaussian distribution with mean A_i and covariance matrix M_i. If the proportions of a mixture are λ^i, the signature of the mixture is a Gaussian distribution with mean $A_\lambda = \Sigma\lambda^i A_i$ and covariance

$$M = \Sigma\lambda^i M_i$$

If y denotes the N-dimensional data vector obtained from the scanner, the method of maximum likelihood leads to proportion λ that minimizes a function

$$G(\lambda) = \|y - A_\lambda\|$$

These results have simple geometrical interpretations and have in fact been drawn on in the construction of hypothetical scatter plots and the binary and ternary systems depicted above.

Since PCs are linear combinations of random variables (i.e., the reflectances) with distributions that are nearly Gaussian, the PCs themselves are Gaussian distributions. Thus, the statistical and geometrical formalism developed by Horwitz et al. (1971) applies to the problem in PC space, provided the A_λ is reinterpreted as mean values for the resultant PC vectors and M as the associated covariance matrix.

Appendix E
References

Dixon, W. I. (Ed.) (1974). *Biomedical computer programs*. Los Angeles: University of California Press, UCLA, Health Sciences Facility, Department of Biological Mathematics, School of Medicine.

Horwitz, H. M., J. T. Lewis, and A. P. Pentland (1975). *Estimating proportions of objects from multispectral scanner data* (ERIM Report No. 109600-13-F). Ann Arbor: Environmental Research Institute of Michigan.

Horwitz, H. M., R. F. Nalepka, P. D. Hyde, and J. P. Morgenstern (1971). Estimating the proportions of objects within a single resolution element of a multispectral scanner. *Seventh International Symposium on Remote Sensing of Environment* (Report No. 10259-1-X). Willow Run Laboratories of the Institute of Science and Technology, University of Michigan, Ann Arbor, 1307–1320.

Nalepka, R. F., H. M. Horwitz, and P. D. Hyde (1972). *Estimating proportions of objects from multispectral data* (NASA Report No. CR-WRL 31650-73-T). Willow Run Laboratories of the Institute of Science and Technology, University of Michigan, Ann Arbor.

Soha, J. M., and A. A. Schwartz (1978). Multispectral histogram normalization contrast enhancement. *Proceedings of the Fifth Canadian Symposium on Remote Sensing*, 86–93.

Sokolnikoff, I. S. (1956). *Mathematical theory of elasticity* (2nd ed.). New York: McGraw–Hill.

Wyszecki, G., and W. S. Stiles (1967). *Color science*. New York: John Wiley & Sons.

Appendix F
Additional Renditions of Principal Component Images From the Bendix 24-Channel and NS-001 Scanners, Lisbon Valley, Utah

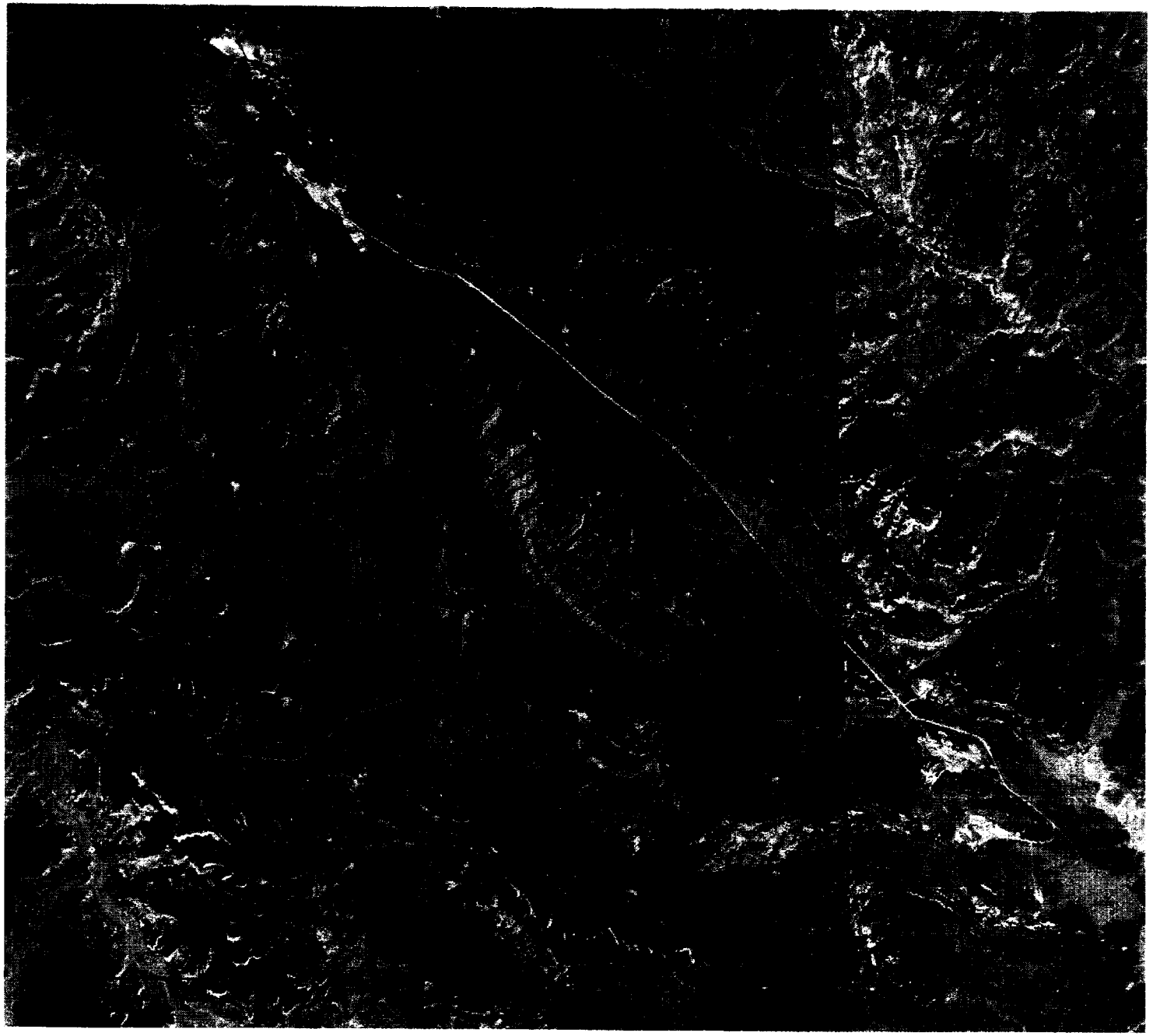

Figure F-1. PC image of the NS-001 data for the Lisbon Valley area prepared according to transform II (restricted area of Appendix C); V1 = red, V2 = green, V3 = blue

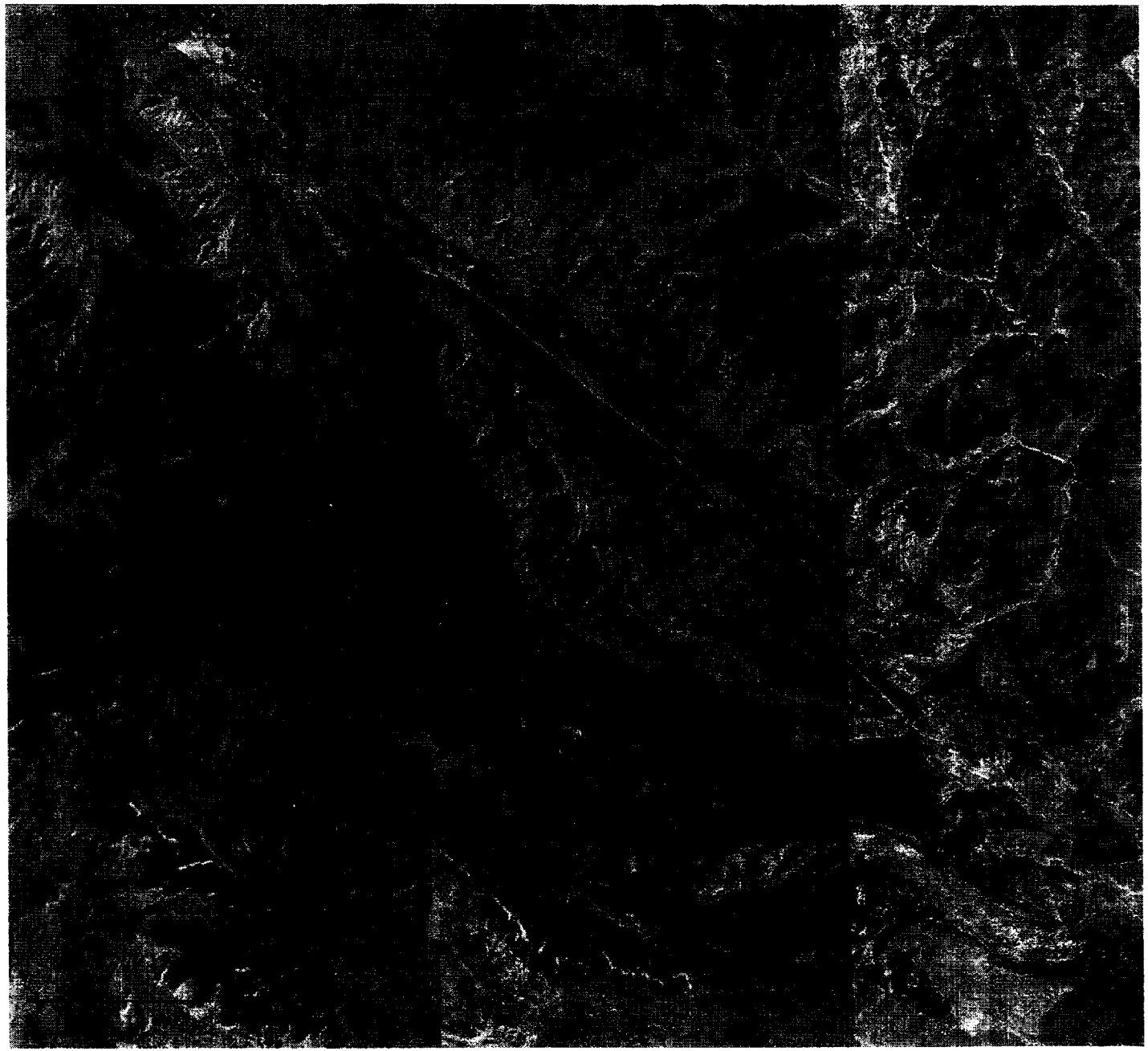

Figure F-2. Seven-band PC image of the NS-001 data for Lisbon Valley area prepared according to transform II (restricted area of Appendix C); V2 = blue, V3 = red, V4 = green

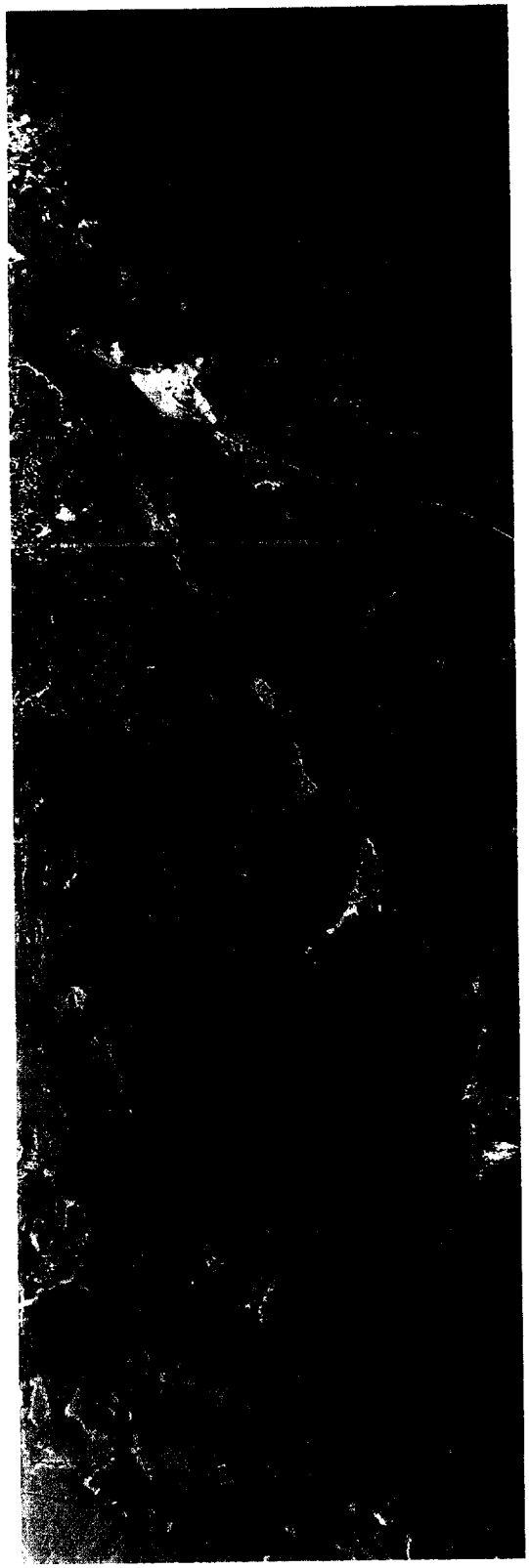

Figure F-3. Seven-band PC image of the Big Indian area prepared from 10 channels of the Bendix 24-channel scanner data; V1 = blue, V2 = green, V3 = red

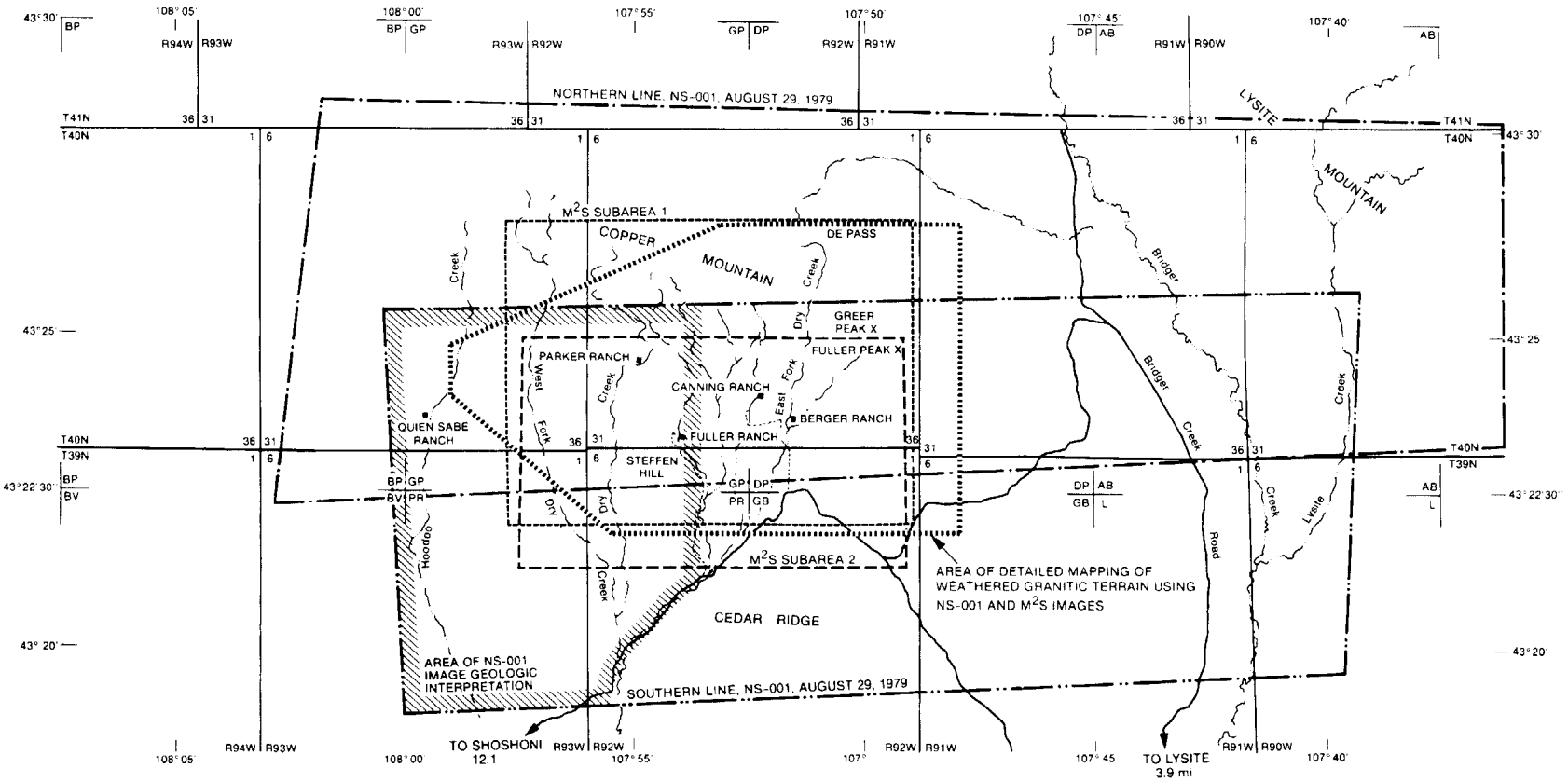

Figure 9-22. Index of geologic mapping, image interpretation, and approximate ground coverage of NS-001 and M²S scanners for the Copper Mountain area, Fremont and Hot Springs Counties. Geologic quadrangles are designated by symbols as follows: BP =Birdseye Pass (Thaden, 1980a), BV = Bonneville (Thaden, 1978), GP = Guffy Peak (Thaden, 1980d), PR = Picard Ranch (Thaden, 1980e), DP = De Pass (Thaden, 1980b), GB = Gates Butte (Thaden, 1980c), AB = Arapahoe Butte (Thaden, 1981), and L = Lysite (Thaden, 1979).

tree and shrub cover except in rocky portions and along stream courses.

c. Tertiary formations. The stratigraphically lowest Tertiary formation exposed in the map area is the Lower Eocene Wind River Formation. The Wind River consists of sandstone, siltstone, claystone, and coal beds, together with separately mapped chromolithofacies of conglomerate, siltstone, and sandstone. The chromolithofacies (Thaden, 1980e) characterize this formation. They are described as beds of characteristic color, grain-size distribution, physical character, and composition. The chromolithofacies are high-energy deposits of fluvial origin and are complexly interbedded with sandstones and siltstones, rocks that constitute the bulk of the formation. Basal units of the Wind River Formation are generally not exposed, except in the Guffy Peak Quadrangle along the eastern side of Steffen Hill, where the formation rests on Paleozoic and Precambrian rocks. The upper part of the formation has been eroded, leaving a maximum residual thickness of 2300 m in the southwestern part of the Picard Ranch Quadrangle. In the Guffy Peak Quadrangle, the Wind River is exposed mostly in complexly faulted horsts along the southern boundary, and is in part buried by younger formations. On aerial photographs the Wind River Formation is characterized by sparsely vegetated outcrops of buff, gray, tan, red, and dark-brown rocks; the bedding is indistinct. These relatively soft rocks weather to rounded slopes or form low cliffs where the units are resistant.

The Upper and Middle Eocene Wagon Bed Formation is deposited on top of the Wind River Formation on a surface that may have locally more than 100 m of erosional relief. The Wagon Bed consists of volcaniclastic claystone and sandstone composed of crystal and vitric tuff. These beds may incorporate locally derived detritus, particularly from the Wind River Formation beneath. The claystones are pale green to grayish-yellow and become orange, pink, maroon, and purple when sands from ferruginous sources are incorporated in them. Deposits of boulders made up of lower Paleozoic and Precambrian rocks fill paleovalleys on the flank of the mountain and contain basal Wagon Bed volcanic ash and sand in the interstices. Examples of such deposits in the paleodrainage may be found in Hoodoo Creek and the West Fork of Dry Creek in the map area. The Wagon Bed in general was deposited on an extremely rough paleotopographic surface. The formation possibly buried the mountains at one time. Much of the formation has been removed by erosion. The maximum remaining thickness is approximately 200 to 300 m. On aerial photographs the Wagon Bed Formation is typified by light-colored buff and gray interbedded outcrops that are mostly free of vegetation, except for a discontinuous cover of shrubs and grasses. The light-colored monotonous character of the Wagon Bed contrasts with the varicolored lithology of the underlying Wind River section.

d. Quaternary sediments. Quaternary sediments consist of older gravel deposits that cap pediment surfaces, alluvium that fills the bottoms of modern stream channels, and dune deposits (Thaden, 1980e).

Gravel deposits of Holocene and Pleistocene age occur as fan remnants and pediment caps flanking Hoodoo Creek and the West Fork of Dry Creek. Clasts in these deposits range in size from boulders to silt with mostly cobbles. Sources consist of detritus from the weathering of Precambrian metasediments in the quadrangle and include quartz–feldspar–mica schist, hornblende schist, uralitic hornblende schist, garnet–mica schist, quartzite, minor Precambrian granite, and rare Paleozoic sediments, including Flathead, Amsden, Park City, and Madison Formations. The clasts are mostly dark-colored, and consequently the deposits appear dark-brownish to black in aerial photographs. Most deposits are 2 to 5 m thick, but may reach 20 m. The deposits mapped exceed 1.5 m in thickness, although lag gravels a cobble or two in thickness have a wider distribution. Multiple fan gravels of probably distinct ages can be separated based upon differences in composition, elevation, and form. However, these deposits are undifferentiated in the geologic map of Figure 9-23.

Deposits of older alluvium from sheet wash occur as fans and bajadas on the low flanks of highland areas and fill paleovalleys that coincide approximately with contemporary drainages. These poorly sorted deposits consist of sand, silt, and clay, and their colors vary from gray to pale reddish-brown where oxidized ferruginous materials are present.

Younger alluvium corresponds to deposits found in arroyos and modern watercourses. These deposits consist mostly of sand, silt, and gravel derived from the reworking of older alluvium and weathering of Tertiary rocks. These deposits reflect a change from an aggradational cycle in which older alluvium was deposited, to an arroyo-cutting degradational cycle with deposition of alluvium.

Dune deposits of mappable thickness are limited to occurrences along the eastern side of the West Fork of Dry Creek south of Steffen Hill. The sand is principally very fine-grained quartz with a minor amount of accessories. Source beds include the Wind River and Wagon Bed Formations and alluvial deposits. Deposits of light-buff, windblown sand too thin to map cover terrace gravels and other rock outcrops about 3 km to the east of the main deposits shown.

analyses of the images, aerial photographs, and topographic maps.

B. Use of Aircraft Scanner Image Data for Geologic Mapping

1. Description of the geologic mapping. Geologic quadrangle mapping of the east end of the Owl Creek Mountains, covering the area of aircraft scanner images, was carried out in 1967 through 1974 by R. E. Thaden of the U.S. Geological Survey (USGS). An index map giving the locations of these published quadrangles and the ground coverage of the airborne scanner data is shown in Figure 9-22.

Figure 9-23 is a geologic map for a portion of the Guffy Peak (Thaden, 1980d) and Picard Ranch (Thaden, 1980e) Quadrangles, the geology of which is typical of that exposed along the range front. Tertiary sediments, including the Wind River and the Wagon Bed Formations, lap onto Precambrian granitic rocks and metasedimentary schists and gneisses that constitute the core of the East Owl Creek Mountains. Paleozoic sandstones and limestones are found unconformably overlying granite in Steffen Hill. Steffen Hill represents a structurally downdropped, intensely faulted block of sediments in the collapsed toe of the Owl Creek overthrust. This thrust fault, in Laramide time, carried Precambrian, Paleozoic, and Mesozoic rocks southward toward the Wind River Basin and over an upturned Mesozoic and Paleozoic section in the basin. The distribution, lithologic character, and structural relations of these formations pertinent to the remote sensing observations are described below.

a. Archean rocks. Dark-colored metasedimentary schists and gneisses of widely variable composition are found in the northern part of the map area. These trend in bands N 50° E to N 80° E, dipping steeply, mostly to the south. The metasediments have been divided into three groups (Hamil, 1971). All groups are similar and include biotite schists, hornblende schists, and garnet–biotite schists, all of variable mineralogy, and quartzite.

Granitic rocks range in composition from quartz–microcline to quartz–microcline–plagioclase–biotite–muscovite granite. Their color ranges from pale orangish-pink to bright, rusty orange in outcrops north of Steffen Hill, where the granite was probably buried beneath alkaline, saline lakes during part of the Tertiary and possible Quaternary time (Thaden, 1980d).

b. Paleozoic rocks. Paleozoic rocks in the map area in Figure 9-23 are confined to Steffen Hill, where Middle Cambrian through Upper Mississippian rocks are exposed. This section rests unconformably on granite.

The Middle Cambrian section is represented by the Flathead Sandstone, which is composed of poorly sorted, medium- to coarse-grained sandstone. It has a variety of pigmentations, and may appear dark yellow, brown, dark red, or purple in the field. The formation forms low cliffs where well indurated. The Flathead was deposited on a paleotopographic surface cut in granite and metamorphic rock with many meters of vertical relief. In Steffen Hill the thickness of this formation is on the order of 20 m. Extensive growths of juniper may be found beneath cliff-forming portions of the unit, marking the base of the unit.

The Middle Cambrian Gros Ventre Formation consists of siltstone, sandstone, and limestone. The siltstone is mostly sandy and includes some claystone. These rocks weather olive-gray to maroon. The formation forms gently concave slopes with thin ledges, prominently visible in aerial photographs above the smooth dip slopes of Flathead Sandstone.

The Upper Cambrian Gallatin Formation is composed of limestone and siltstone with a total thickness of about 130 m. Limestone in the upper part of the formation weathers to a maroon color and commonly forms cliff scarps. The middle section consists of limestone that weathers pale yellowish-brown. The basal limestone forms a cliff with flaggy bedding and weathers pale yellowish-orange to pale yellowish-brown. On aerial photographs the formation appears light grayish-brown and is distinguished by its contrast with the darker reddish-brown of rocks in the Gros Ventre beneath. The formation forms rounded slopes with resistant layers which are largely devoid of shrub and tree cover except along stream courses and on some dip slopes.

The Bighorn Dolomite is the only Ordovician formation represented in the Paleozoic section at the Copper Mountain test site. This thin unit is a light-gray dolomite weathering yellowish-gray. Its thickness ranges from 10 to 15 m throughout the area. The unit is a thin cliff-former, photogeologically nearly indistinguishable from the stratigraphically surrounding carbonate formations.

The Madison Limestone of Upper and Lower Mississippian age consists of dolomite, limestone, and sandstone. The dolomite and limestone beds weather yellowish-gray. The sandstones form lenticular, thin, discontinuous beds. The formation stands as a ledgy, gray-white, cliff-forming unit with smooth debris-covered dip slopes and talus-covered cliff slopes. These outcrops are largely devoid of

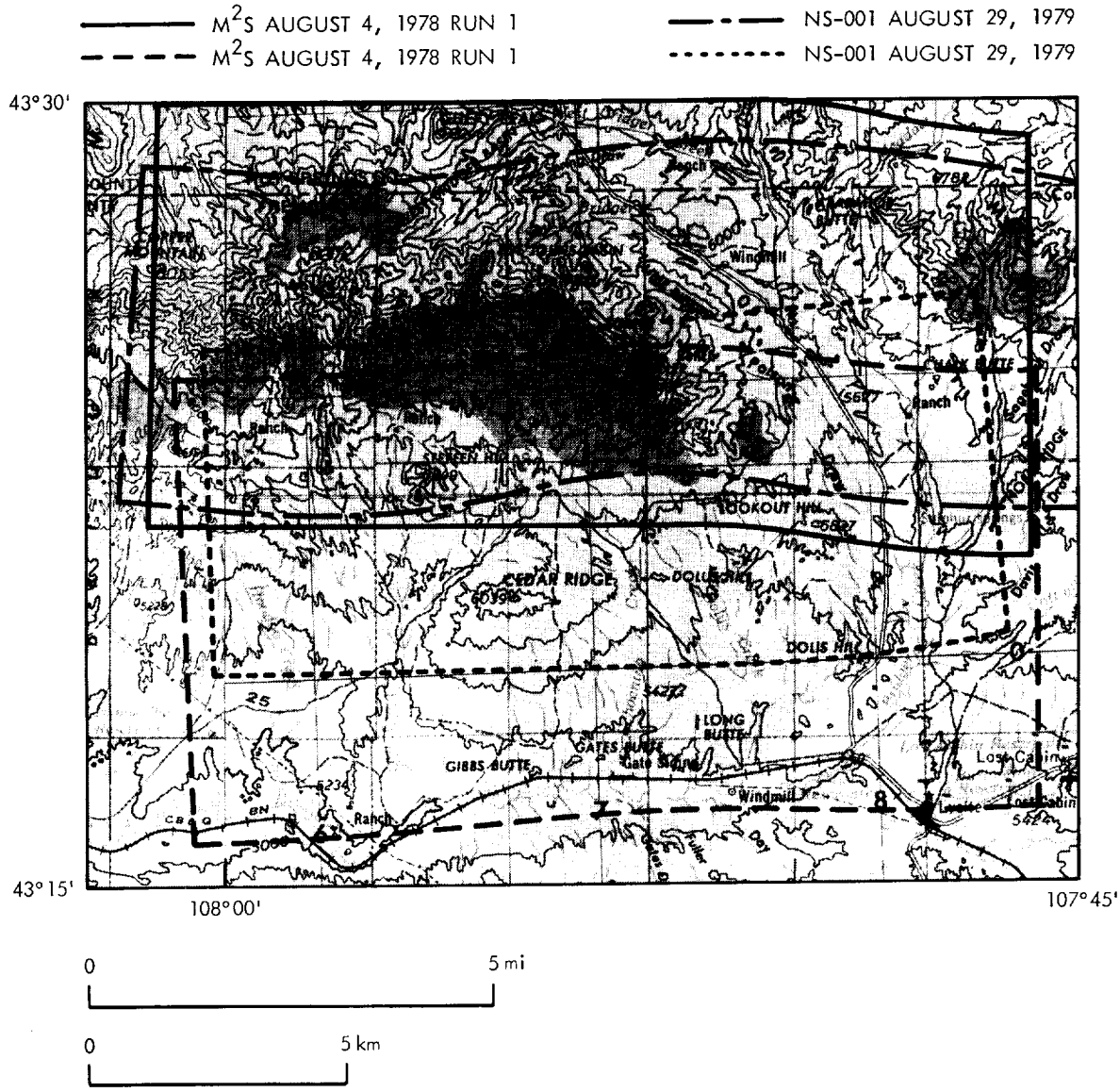

Figure 9-21. Index map showing approximate areas covered by the NS-001 and M²S scanner images at Copper Mountain

The plan of the remainder of Section 9 is as follows: First the application of the NS-001 scanner results to geologic mapping problems will be described by presenting a detailed comparison of published maps with interpretations based on the PC renditions for a selected area. Next, based on informal studies by Thaden (personal communication, 1980), comparisons of the NS-001 images with the geologic maps will be presented for 26 localities throughout the Copper Mountain area. These will highlight important statigraphic and structural problems encountered during the earlier mapping project (1967–1974) and demonstrate how the scanner results both support or allow elaboration of the published interpretations. Finally, the distribution of oxidation effects in the granitic rocks will be discussed, and these will be related to the uranium occurrences. Relations between the distribution of oxidation and Tertiary and Quaternary paleotopography are presented to the extent that they can be established through

maps. In other cases the images depicted units and boundaries not previously recognized. Fieldwork and examination of PFRS spectral reflectance data helped to explain these new units.

Several problems were addressed in this fashion. General geologic mapping capabilities of the remote sensing data were evaluated with the aid of detailed published maps. The distribution of oxidation effects was studied and mapped from the images, and related to distribution predicted by the genesis models. An attempt was also made to determine the distribution of hematitic staining in the granites. The geology of recent fans was studied using topographic information and image data. The relationship of oxidation to erosional surfaces was examined in an attempt to elucidate the history of mineralization, tectonics, and weathering. In all these studies, it was anticipated that the remote sensing data would provide additional information not depicted on published maps, and thus help clarify problems related to uranium mineralization and emplacement.

X. Interpretation of Multispectral Scanner Data

A. Introduction

The Bendix M²S (11-channel) and the NS-001 (8-channel) aircraft multispectral scanner data have been used to study the geology of the Copper Mountain area and to map the distribution of oxidized granitic rocks both over the pediments at the foot of the mountains and throughout the Canning Stock higher in the range. The areas covered by these image data are shown in Figure 9-21. The NS-001 image data have an approximate surface resolution of 12.5 m, while the M²S data have a resolution of 11 m. Eight geologic maps at a scale of 1:24,000 have recently been published (Thaden, 1978, 1979, 1980a–1980e, 1981). These maps afford a detailed basis for comparison of the aircraft images and the mapped distribution of rock types.

Oxidation of the granitic terrain may be genetically limited to the origin of secondary (Tertiary) uranium concentrations in the granites (Yellich et al., 1978). Patterns of oxidation and/or surface weathering have a complicated relationship to erosion surfaces in the granite and to exhumed pre-Middle Eocene (pre-Wagon Bed) paleotopography higher in the Canning Stock. The origin of oxidation is not completely understood and may have multiple (superimposed) causes. Both the NS-001 and M²S image data may provide representations of these oxidation effects that differ from the published distribution as given by Yellich et al. (1978). The scanner-derived distributions of oxidation will allow comparisons with geologic and physiographic data that may contribute to the understanding of these effects.

Image products used for interpretation consist of NS-001 principal component (PC), M²S color ratio composite (CRC), and M²S band-ratio density slice images. The raw scanner radiance data, corrected only for atmospheric gradient and some surface directional effects, have been used in the images presented here. Scanner radiance values have not been converted to equivalent ground reflectance. It is shown in the Lisbon Valley, Utah, Uranium Test Site Report, Section 8, Appendix A, and discussed by example below, that for PC images, conversion to ground reflectance is essentially unnecessary. PCs based on the covariance matrix for the raw scanner data are largely free of the modeled instrumental and atmospheric contributions. PC transformations based on the correlation matrix with a linear radiance-reflectance model are precisely free of these effects.

Band-ratioing is in general a nonlinear transformation that results from scaling the radiance data for presentation in image format (Section 8, Appendix A). Combined as CRCs, the ratio data are difficult to interpret quantitatively. On the other hand, single-ratio density slices may be interpreted quantitatively. The M²S single-ratio density slices have been calibrated approximately by reference to ground measurements to provide an index of iron absorption-band strength as a function of digital number (DN) or assigned color in a density-slice image.

The image data for both the NS-001 and M²S scanners are presented as separate flight lines rather than mosaicking the images together. These lines overlap by approximately 50 percent. Geometric control needed for careful image rectification throughout the overlap regions tends to be poor because of low surface relief. This has prevented accurate adjustment of the overlapping image area to a map base, and has complicated efforts to mosaic adjacent swaths. More importantly, differing solar illumination and scanner viewing conditions between flight lines give rise to strong directional photometric effects. These effects relate to shadowing at both macroscopic and microscopic scales, and possibly to variations in surface reflectance properties between north- and south-facing slopes. These latter variations arise from variations in lichen cover or vegetation density from one slope to another. The separate flight lines thus display important unique photometric directional characteristics of the surface and must be accounted for in any quantitative interpretation of the image data.

interval preceded deposition of the Eocene Wagon Bed Formation. After deposition of Wagon Bed sediments and possibly during removal of these sediments in the Late Miocene, additional lateral secretion of uranium from granitic and possibly Tertiary sedimentary source rocks occurred, leading to occurrences of mineralization that locally transect the Tertiary–Precambrian boundary. Episodes of mineralization thus predate and postdate the mid-Miocene surface-weathering event.

Hematite-rich fractures in fault zones sometimes extend to the surface and may locally contribute to the iron-oxide staining of surface rocks (Figure 9-10 shows a possible example of this). Optically opaque iron-oxidation coatings at the surface in the weathered zone tend to mask propylitic and argillic alteration effects which might otherwise represent remote sensing targets of direct genetic significance for uranium mineralization. Weathering appears to predate emplacement of mineralization. RME geologists infer a genetic history for the deposit which consists of four separate periods of mineralization but which, for the purposes of this study, includes two essential parts. The first episode occurs in pre-Middle Eocene time and corresponds to the time period during which major surface weathering was occurring. This episode accounts for about one-half the mineralization present through leaching of surface and subsurface rocks. The second period of mineralization occurs during the time when the Tertiary sediment cover was removed following renewed uplift in post-Middle Miocene time. Thus the surface-weathered zone in granites marks a portion of the source area for leached uranium comprising the resource. Surface-weathering effects in both granitic and sedimentary rocks are potential targets for mapping on scanner images.

C. Relationship of the Hydrothermal Model to the Remote Sensing Model

Mobilization and precipitation of uranium in the hydrothermal model of Shrier and Parry (1982) is accompanied by alteration of plagioclase to sericite (Stage I) and to Na-montmorillonite (Stage II). Oxidation of magnetite to hematite may accompany uraninite precipitation in fractured rock (Stage II). These mineral phases contain important diagnostic spectral absorption features that might serve as observable remote sensing parameters, and might therefore act as potential guides to mineralization of leached source rocks.

Granitic rocks adjacent to the deposits are oxidized (weathered) at the surface as described above. This oxidized horizon plays no role of genetic significance in the hydrothermal model. However, the presence of surface weathering serves to mask the hydrothermal effects described by production of clay phases (predominately kaolinite) from feldspars and pervasive hematite staining from the oxidation of magnetite, pyrite, and biotite.

Timing of the hydrothermal events described by Shrier and Parry (1982) is not made clear apart from the necessity that fracturing and brecciation provide permeability in the model. Hence the mineralizing events are constrained to a post-Laramide interval.

The hydrothermal model offers an alternate driving mechanism for the motion of the mineralizing fluids. Therefore a distinction between the gravity flow (supergene) model and the radioactive heat-driven (hydrothermal) model could presumably be made, provided the spatial distribution of alteration were known. Thus the supergene gravity flow mechanism would presumably be horizontally stratified with higher temperature assemblages occurring at greater depth. In the hydrothermal mechanism, which is driven by convection, the distribution of alteration products would conform to the flow pattern of mineralizing fluids under whatever temperature and permeability conditions existed at the time of movement. In this sense the alteration distribution might resemble that occurring with circulation models imagined for porphyry copper deposits (Norton, 1982).

On the other hand, the supergene mechanism offers little that allows its alteration products to be distinguished from those of the hydrothermal mechanism or from effects of ordinary surface weathering where the two alteration zones physically intersect.

D. Approach

The remote sensing image data form the basis for geological, lithological, structural, geomorphological, and spectral evaluations of the Copper Mountain test site. The genetic models provide a possible group of surface features that may be detectable from the images. In the remainder of this section the analyses of the remote sensing data *vis-à-vis* the problems and hypotheses presented by the models are described.

The image data were analyzed and interpreted by use of overlays. Color boundaries were traced from the images without reference to other data sources such as maps. These interpretations were then compared with the geologic maps, soils maps, etc., to identify the color units seen on the images. In some cases, one-to-one correlations could be made between the image interpretations and the

spectral resolution required to discriminate specific mineral assemblages that could be uniquely related to supergene enrichment, hydrothermal alteration, or surface weathering processes. The presence of surface weathering and lichen surface coatings are additional complications for detecting hydrothermal alteration mineral assemblages.

Detecting and mapping iron-oxidation effects this way should be very successful and be in many ways more effective than ground-based investigations. The spectral region available, the scanners' radiometric sensitivity, the possibility of digital manipulation of the data, and the complete areal coverage are advantages not available to a field mapper.

There is an empirical association between the pervasiveness of iron-oxidation effects and local uranium occurrences at Copper Mountain. Iron oxidation of Archean granite appears to be a necessary but not sufficient condition for ore occurrence in localized areas. This implies that the remote sensing tools may lead to errors of commission, but very few to errors of omission. This is an important capability that can greatly assist in devising a regional exploration strategy.

B. Relationship of the Supergene Model to the Remote Sensing Model

Figure 9-20 summarizes the geologic relations discussed previously. Uranium in the North Canning resource is found in fractured and crushed zones in the granites, in association with blocks and inclusions of metasedimentary rocks, such as biotite–hornblende schists and amphibolite. Rocks in crushed zones have been subjected to low-temperature propylitic and argillic alteration in which biotite and hornblende are altered to chlorite, and feldspars are altered to clay. Hematite is present on fracture surfaces, particularly in strongly crushed rock, and is produced by alteration of pyrite through the uranium deposition process. The mineralized zones are covered by Tertiary sediments and are not exposed as remote sensing targets. Surface outcrops of the granitic rocks are weathered and stained with hematite and limonite; these outcrops represent loci beneath which uranium enrichment may have existed at one time. The interval of surface weathering is associated with percolation of oxidizing meteoric waters into the subsurface. These waters were probably uranium-bearing, but may also have served to leach preexisting accumulations at depth. The weathering

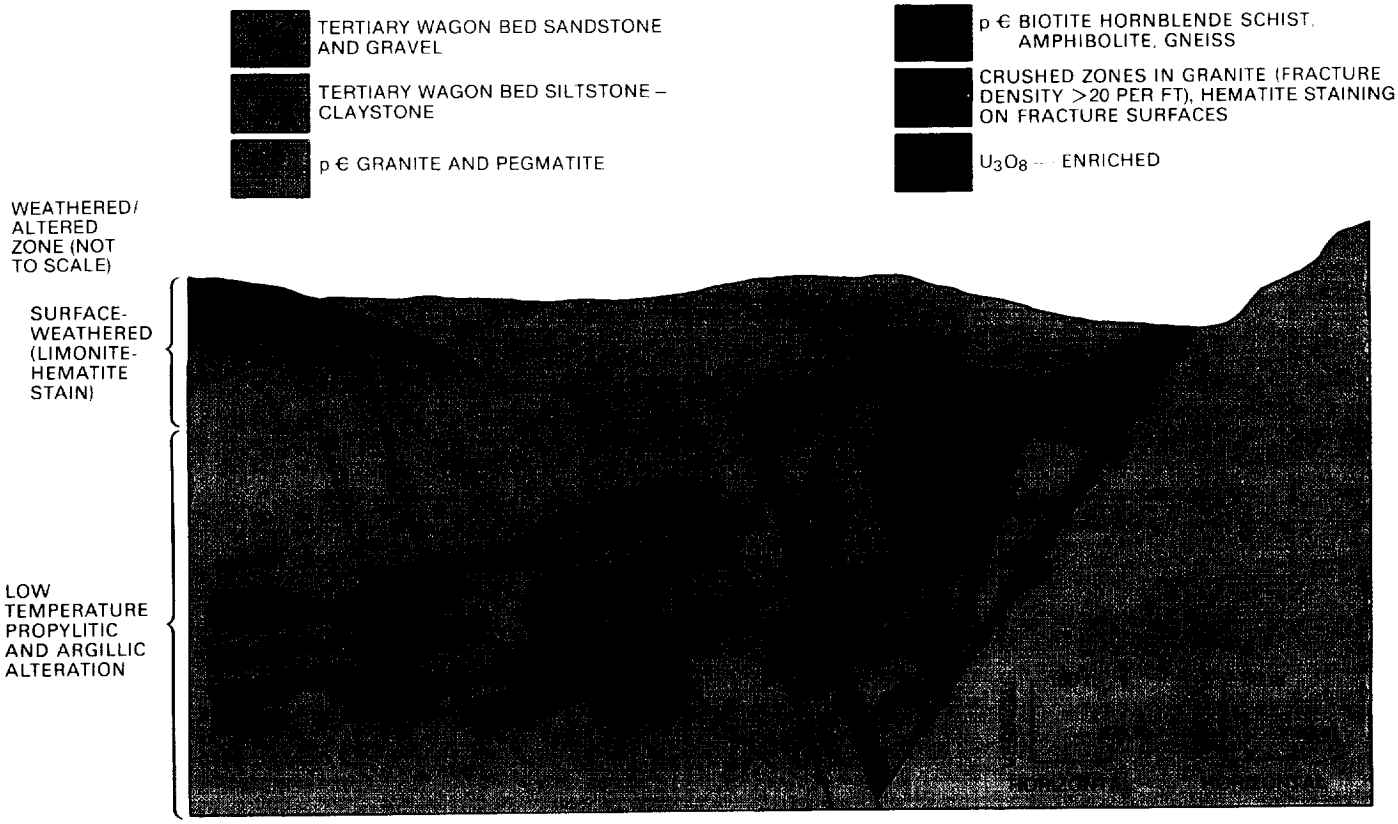

Figure 9-20. North Canning prospect hypothetical cross section through weathered–altered layer (modified from Yellich et al., 1978)

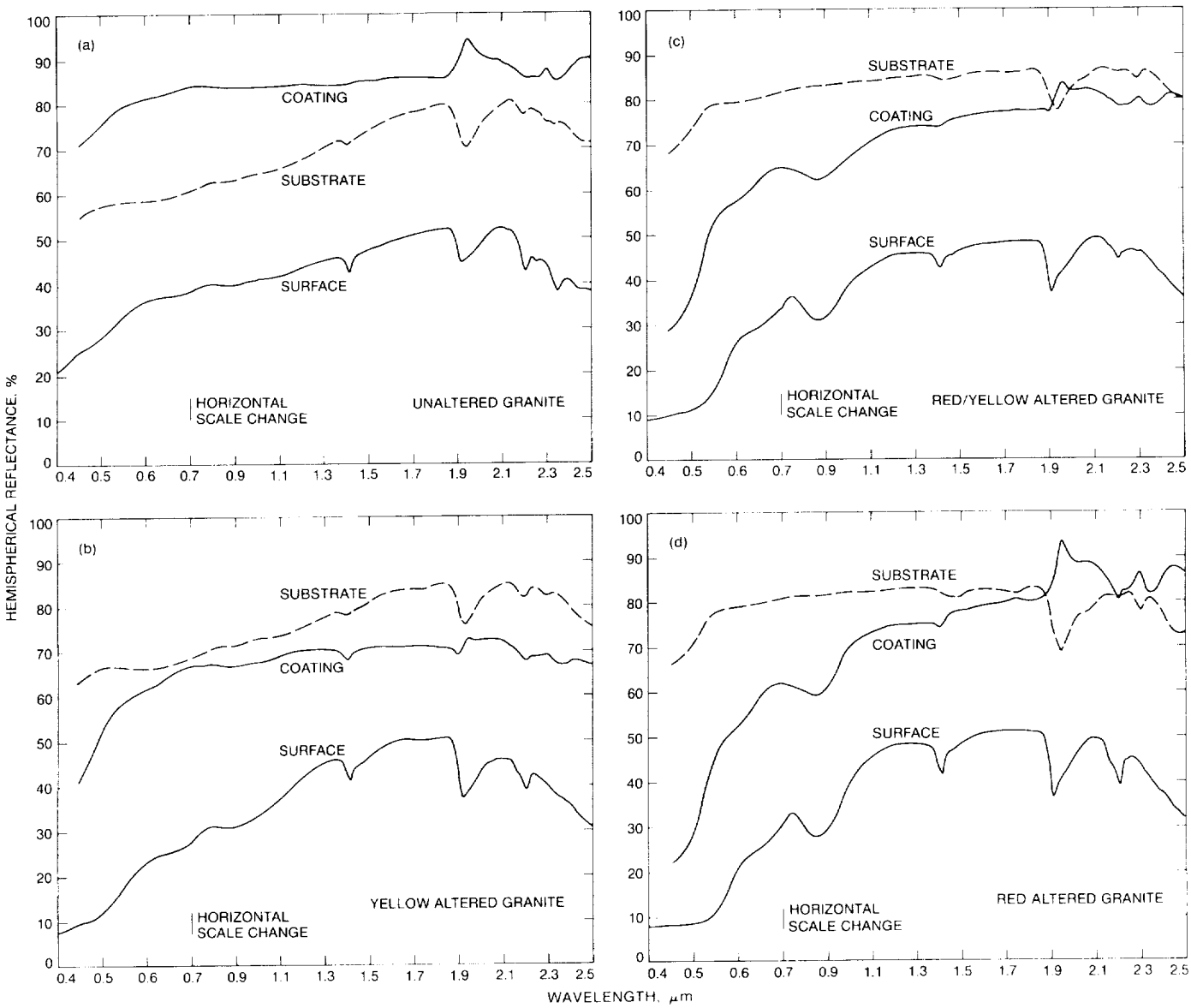

Figure 9-19. Analysis, using a differential spectrophotometric method, of the substrate and surface iron-oxide/hydroxide coatings of altered and unaltered granite at Copper Mountain. The curves marked "coating" are offset relative to the surface and substrate curves, and should be examined only for the shapes of spectral features.

these low-temperature hydrothermal suites have spectral features similar to those of ordinary rock-forming minerals. In the Copper Mountain area, these alteration suites have been discussed only for the granitic and metamorphic rocks at depth and have not been mapped at the surface. The apparent lack of identifiable surface exposure due to the presence of surface coatings is another strong limitation on the application of scanner methods to mapping of these alteration types. Emphasis in this study is therefore directed to the mapping of iron oxides and weathering/alteration distributions.

IX. Remote Sensing Objectives, Models, and Approach

A. Introduction

Remote sensing methods are used to map surface cover conditions and to relate these conditions to the geology and mineralization of the test site. The tools that are available can be used to detect variations in iron staining, clay abundance, geologic structure, and extent of green vegetation cover. The airborne scanners may not possess the

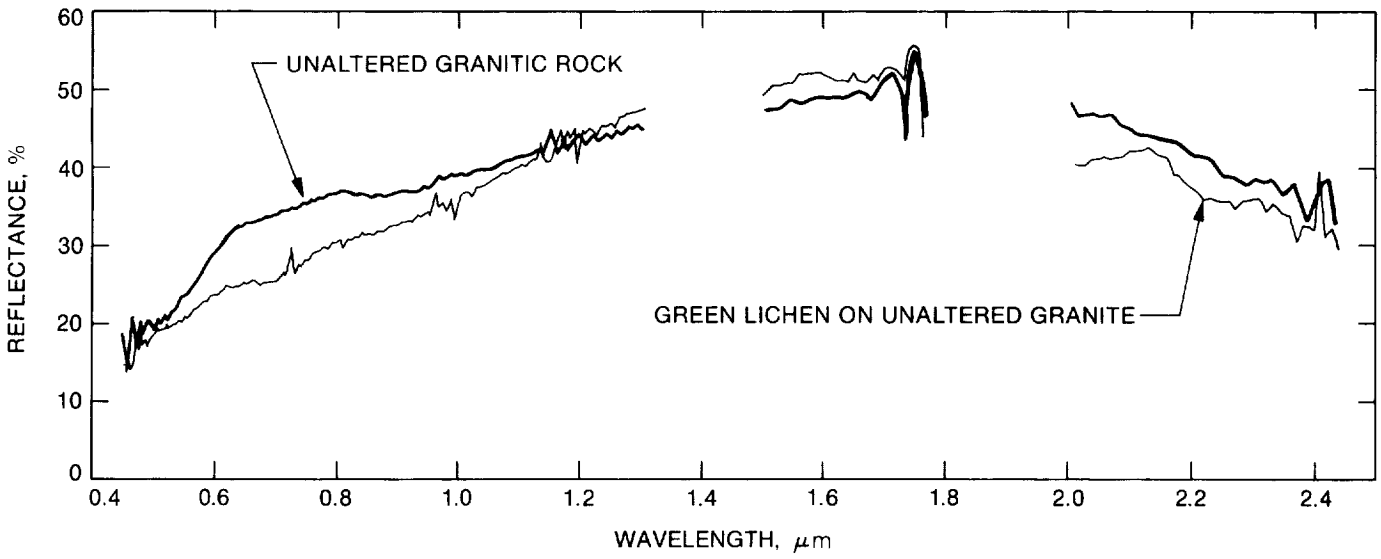

Figure 9-18. Effects of lichen cover on spectral reflectance of granite rocks

Table 9-8 shows that biotite, chlorite, and epidote contribute broad, intense absorption bands which possibly extend between 0.6 and 1.8 μm and are due to Fe^{+2}, and additional weak structures at 2.25 and 2.35 μm which are due to water or hydroxyl absorptions. Montmorillonite produces a well-defined band near 2.20 μm that is clearly resolved in the analyses. An additional structure, which is of uncertain origin, is also present at 2.30 μm. No distinct bands due exclusively to hematite or goethite can be identified.

b. Altered granite substrate. In Figure 9-19(b) the substrate spectrum below 1.9 μm is similar to that for unaltered granite (Figure 9-19a), with iron absorption bands probably resulting from the presence of mafic minerals. Two bands at 2.20 μm and 2.31 μm are resolved that may be contributed by montmorillonite and possibly a ferromagnesian (amphibole?) mineral.

The substrate reflection spectra of Figures 9-19(c) and 9-19(d) are fundamentally different from those shown in Figures 9-19(a) and 9-19(b) because they lack the prominent absorption bands near 1.0 μm attributed to ferrous iron in the ferromagnesian minerals. In addition, these spectra (Figures 9-19c and 9-19d) show prominent structures near 2.3 μm that are not present in the spectra of the surface samples. The interpretation of these absorptions is incomplete. Possibly they arise from the presence of an amphibole, a mineral type displaying strong absorptions at this and longer wavelengths (Hunt and Salisbury, 1970, p. 289–290). If so, the amphibole is iron-free or does not otherwise contribute absorptions at ~1.0 μm. In any event, the substrate spectra indicate an apparent intense alteration or removal of the dark minerals present in these samples, together with a masking effect for some absorption bands.

c. Surface coatings. The differential spectra of surface iron-oxide/hydroxide coatings shown in Figure 9-19 support, in general, interpretations that could be obtained by analysis of the surface sample reflectance directly. The sample with yellowish pigment (Figure 9-19b) has an absorption band at 0.9 μm, indicating the presence of limonite/goethite, while samples with reddish pigment (Figures 9-19c and 9-19d) display minima near 0.85 μm, indicating the presence predominantly of Fe_2O_3, but possibly small amounts of goethite/limonite as well (Figure 9-19c). The prominent HOH absorption at 1.9 μm routinely appears inverted in the surface coating spectra. The inversion occurs because the water band is deeper in the substrate (reference) spectrum than in the surface sample. This too indicates the unmasking of this spectral feature, which is possibly associated with clay, by the removal of surface pigments.

3. Summary. Iron-oxide pigments (hematite/goethite or limonite) mask the reflectance properties of altered rocks present at the surface. The observation of propylitic, argillic, or possibly potassic alteration using scanner data is hindered by the presence of such coatings. In addition,

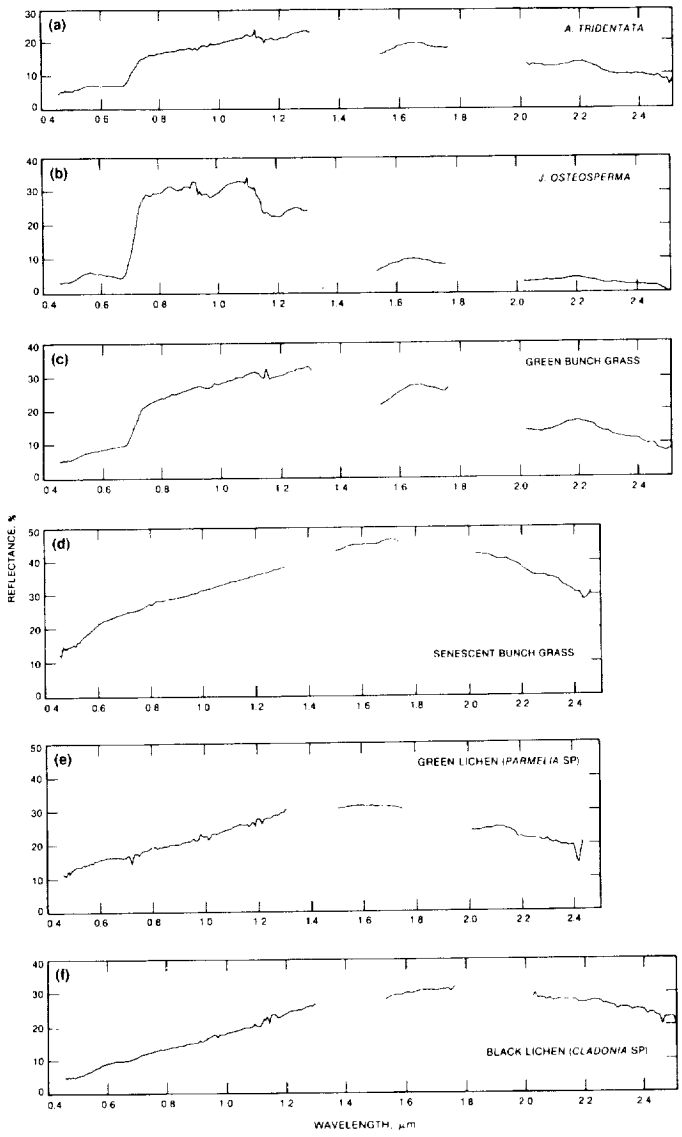

Figure 9-17. PFRS vegetation reflectance spectra for some plant types in the Copper Mountain area

Figures 9-17(e) and 9-17(f) show the field spectral reflectance of green and black lichen. These spectra resemble those of dead grass above, but with lower overall albedo. In particular the green lichen (*Parmelia* (?) sp.) does not show a well-defined chlorophyll band. Possibly this reflects a dormant state of the lichens during the time of field observation.

D. Masking Effects of Surface Coatings

Both plant cover and optically opaque iron-oxide pigments serve to mask the presence of underlying substrate materials. Studies of the distribution of hydrothermal alteration using the scanner data require measurements of the distribution of mineral species quite distinct from the distribution of iron oxidation. Iron-oxide leaching experiments were performed on the oxidized and unoxidized granitic rocks using the dithionite–citrate extraction method (Conel et al., 1978). The leached samples were used in the spectrophotometer to define the nature of the oxide pigments, to determine the spectral properties of the rock substrate, and to illustrate the masking effects of the colored pigments.

1. Effects of lichen cover. Lichens form optically thick (opaque) coverings of the surface that contribute their own diffuse components to the macroscopic reflectance. The spectral reflectance of a partially covered surface is made up of the reflectances of the components, each weighted according to areal abundance (Lisbon Valley, Utah, Uranium Test Site Report, Section 8, Appendix E). Figure 9-18 shows the field-acquired PFRS spectral reflectance curves of bare unaltered granite and a granite obtained with a partial covering of green lichens (35 percent estimated surface cover). In the region below 1.2 μm, the surface reflectance is decreased by the presence of a lichen cover, and the Fe^{+3} absorption band at $\sim$0.9 μm is decreased in prominence. Beyond 2.0 μm, the lichen cover decreases the reflectance over that obtained for the exposed surface and introduces an absorption feature near 2.2 μm, possibly from clay particles washed or wind blown into the lichen layer.

2. Effects of iron-oxide/hydroxide coatings. The dithionite–citrate extraction method was used to remove hematite and goethite/limonite coatings from granitic samples. Pigment-free samples were subsequently examined to study the spectral reflectance of the substrates and the coatings themselves. The reflectances of the uncoated substrate and the natural surfaces were obtained directly in the spectrophotometer. The reflectance spectrum of the coatings was obtained using a differential method in which the uncoated substrate replaces halon as the reflectance standard in the spectrophotometer (the natural surface spectrum divided by the uncoated substrate spectrum equals the coating spectrum). Figure 9-19 presents an analysis of this type for four specimens of the altered and unaltered granites at Copper Mountain.

a. Unaltered granite substrate. Spectra of the surface and substrate samples given in Figure 9-19(a) are quite similar, reflecting the sample's low degree of oxidation coating. The principal absorption features result from the presence of biotite (and possibly epidote or chlorite), a clay mineral (possibly kaolinite), and a residual iron oxide, perhaps resident in K-feldspar.

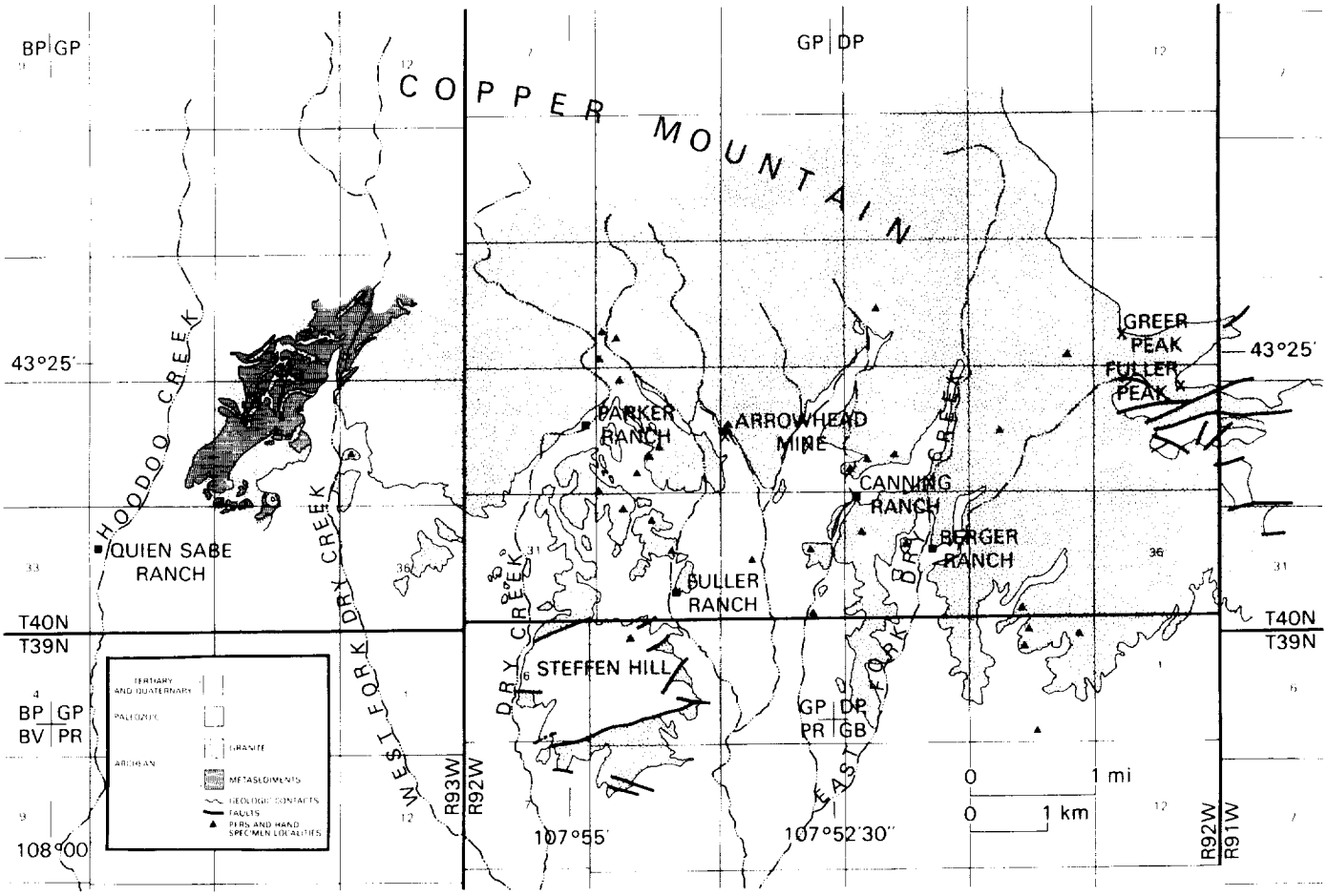

Figure 9-16. Index map with locations of PFRS measurements and hand specimen sites for the Copper Mountain area. Quadrangles are identified as follows: BP = Birdseye Pass, BV = Bonneville, GP = Guffy Peak, PR = Picard Ranch, DP = De Pass, and GB = Gates Butte. (Geologic base map modified from Thaden, 1980b–1980e.)

in reflectance below approximately 0.72 μm. Other, less intense absorption bands are due to structural and imbibed water in the plant mass. The general values of reflectance throughout the spectrum depend upon the spatial density of green material, the vigor of chlorophyll-producing parts, the water content, the leaf geometry and arrangement, shadows, the visibility of the stem or branch structure, and possibly the nature of the rock or soil substrate.

b. Senescent grass. Dead or senescent plant materials (Figure 9-17d) do not have chlorophyll absorption bands. The spectrum instead is characterized by a gradual rise through the chlorophyll absorption region, probably related to the presence of tannins or carotenoid pigments. In addition, the reflectance between 1.4 to 2.4 μm is increased because of a decrease in or absence of the water and OH absorption present in this region in green plants. Also, the open structure of the grass clumps may catch windblown or water-washed materials that contribute to the reflectance properties. Thus weak Fe^{+3} absorption features may be present below 0.6 μm in this spectrum. Clay absorption bands at 2.22 μm are present as well.

c. Lichens. Several genera of crustose and foliose lichens (*Parmelia* sp., *Cladonia* sp.) have been tentatively identified in the Copper Mountain area (B. Rock, personal communication, 1982). No systematic study of the taxonomy has been made, and it is possible other types are present as well. In the field these plants may form dense, multicolored mats on outcrops, completely dominating the surface reflectance properties. While lichens can appear strongly colored in the field, the spectral reflectance may not be demonstrative of this. Lichens freshly cultivated in water baths in the laboratory and in bloom possess, in addition to water, strong absorption bands from the chlorophyll and other pigments present.

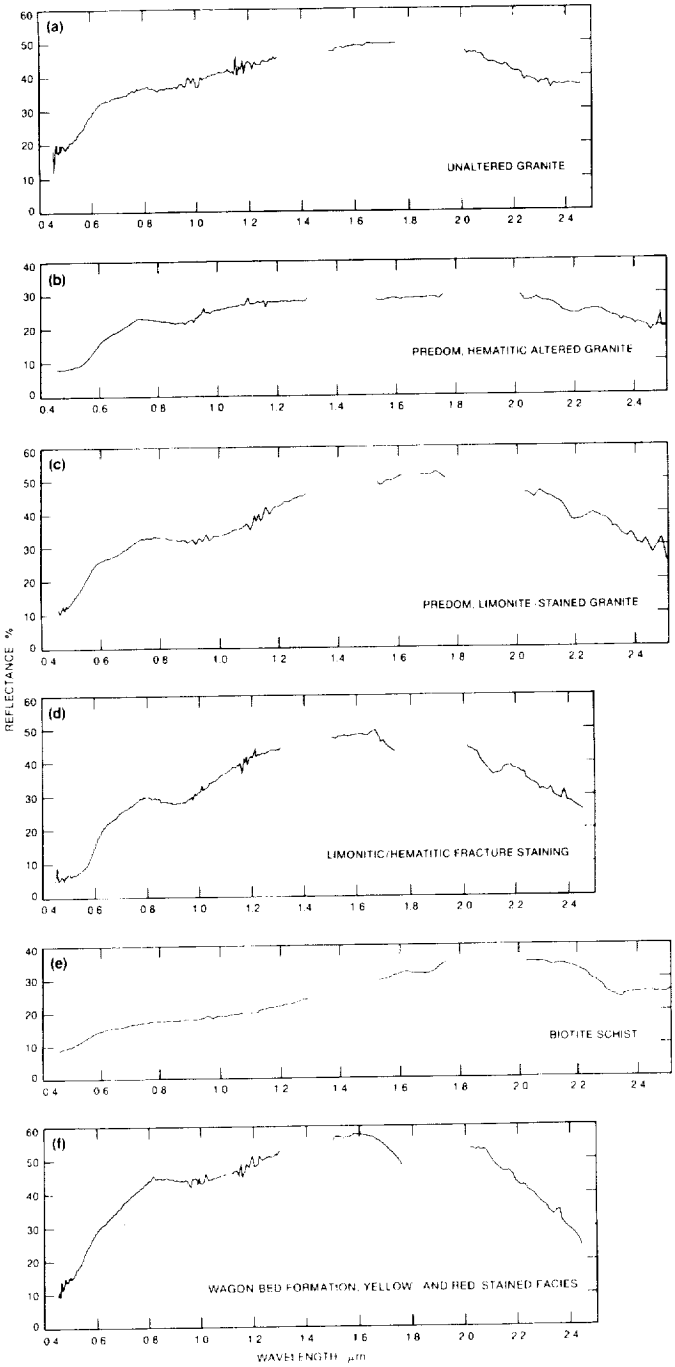

Figure 9-15. PFRS reflectance spectra of some granitic rocks, metasediments, and Tertiary sediments from the Copper Mountain area

present are due to this mineral. These include a broad absorption band between 0.8 and 1.8 μm due to Fe^{+2}, as well as a weaker, narrower band near 2.35 μm resulting from OH(?) or Mg-O-H(?) absorption (Table 9-8). An additional absorption band, not reported by Hunt and Salisbury (1970), can be seen at 1.70 μm. The precise origin of this structure is in question, but it may represent another OH absorption not obtained with laboratory samples, and arising because such samples have a strong preferred crystallographic orientation (Hunt and Salisbury, 1970, p. 291, discuss this problem).

d. Tertiary sediments. The Eocene Wagon Bed Formation is mostly composed of light-buff, clear, and pale-green tuffaceous mudstone, and isolated, thin, yellow and red silty mudstone beds. The reddish Wagon Bed strata may appear similar to altered granite rocks in some renditions of the multispectral scanner data, but in general the higher albedo of these Tertiary rocks, together with the geologic relations, should permit distinction of the two in scanner data, provided the spatial resolution is great enough. Figure 9-15(f) is an example of yellow-stained siltstone facies from the Wagon Bed Formation. The generally higher reflectance of this sample site compared to sites in the igneous and metasedimentary terrain is evident. The spectrum is characterized by strong Fe^{+3} absorption in the ultraviolet, visible, and near-infrared regions, i.e., below 0.8 μm, and by a shallow band centered near 1.0 μm but extending from 0.8 μm to perhaps 1.6 μm in the near infrared. Shallow bands in the 2.2-μm region indicate the presence of a small amount of clay in the surface layer.

2. Spectra of vegetation cover types. Figure 9-17 presents examples of the field spectral reflectance of important vegetation species in the Copper Mountain area. Evergreens, deciduous trees, shrubs, grasses, sedges, and annuals make up a diverse and highly variable vegetation cover throughout the area. In addition, lichens are a significant rock covering that may approach 100 percent locally, especially over north-facing rock outcrops. The amount of green leafy matter present in the vegetation cover is seasonally dependent. In addition, wildlife and cattle may graze on these plants. A complete spectral characterization of the vegetation cover is not feasible, but a few examples of reflectance spectra will serve to illustrate the nature of the spectral contributions introduced by photosynthetic and senescent plant cover in the macroscopic surface reflectance.

a. Green shrubs, trees, and grasses. Figures 9-17(a) through 9-17(c) give the reflectances of *Artemisia tridentata, Juniperus osteosperma,* and *Bouteloua gracilis* (?), which are three important plant cover types. A detailed interpretation of the absorption bands present in green plants has been given in the Lisbon Valley, Utah, Uranium Test Site Report, Section 8, and is summarized here. The green plants are all characterized by prominent chlorophyll absorption bands which contribute to the steep drop

Table 9-8. Important spectral reflectance features for propylitic alteration and rock-forming minerals for the Copper Mountain site

Mineral	Generalized Chemical Formula	Spectral Features[a]	
		Absorption Features	Band Assignments, μm (Band Strength)[b]
Kaolinite[c]	$Al_2Si_2O_5(OH)_4$	Fe^{+2}	0.97(w), 0.5(w)
		OH	1.4(vs), 1.9(w)
		OH(?)	2.325(w), 2.38(w)
		Al-O-OH	2.16(s), 2.21(vs)
Montmorillonite[c]	$(Al, Mg, Fe)_4(OH)_n$ $(Si, Al, Fe)_8O_{20-n}(OH)_n$ $6H_2O$	Fe^{+2}	~0.5(w)
		HOH	1.15(w), 1.41(vs), 1.90(vs)
		Al-O-H	2.20(s)
Epidote[d]	$Ca_2(Al, Fe)Al_2O$ $OH(Si_2O_7)(SiO_4)$	Fe^{+2}, Fe^{+3}	0.41(w), 0.47(w), 0.6(w), 1.0(ms)
		OH	1.4(vw), 1.54(w), 1.85(w), 1.9(vw)
		HOH, OH	2.14(w), 2.25(m), 2.34(vs)
Chlorite[c]	$(Mg, Fe)_5(Al, Fe^{+3})_2$ $Si_3O_{10}(OH)_8$	Fe^{+3}	<0.4(vs), 0.7(m), 0.9(m)
		Fe^{+2}	1.0–1.1(vs)
		OH	1.4(w), 2.0(m), 2.14(vw), 2.26(s), 2.355(s)
		HOH	1.9(w)
Muscovite (sericite)[d]	$KAl_3Si_3O_{10}(OH)_3$, $K_2Al_4(Si_6Al_2O_{20})$ $(OH, F)_4$	Fe^{+2}	0.44(w), 0.9(w)
		OH	1.15(w), 1.4(s), 1.9(vw), 2.18(vs), 2.32(vs), 2.42(vs)
		AL-O-H(?)	2.18(vs)
Biotite[c]	$K(Mg, Fe)_3AlSi_3O_{10}$ $(OH)_2$	Fe^{+2}, Fe^{+3}	0.6–1.8(vs)
		OH(?)	2.12(vw), 2.22(vw), 2.31(w), 2.37(vw)
Microcline[d]	$(K, Na)AlSi_3O_8$	Fe^{+3}	<0.55(vs), 0.9(m)
		OH	1.2(w), 1.45(w)
		HOH	1.95(s), 2.33(m)
Hematite[e,f]	Fe_2O_3	Fe^{+3}	0.85(s), 0.67(m), 0.5(vs)
		Ti^{+4}	1.6–1.7(ms)
Goethite/ Limonite[f]	FeO(OH)	Fe^{+3}	0.9(s)
		OH	1.4(s)
		HOH	1.9(s)

[a]Locations and strengths of absorption features obtained with Beckman 5240.
[b]Band assignments from references cited. Abbreviations used for band strength are: vw = very weak, w = weak, m = moderate, ms = moderately strong, s = strong, and vs = very strong.
[c]Identification of spectral features from Hunt and Salisbury (1970).
[d]Identification of spectral features from Hunt et al. (1973).
[e]Identification of spectral features from Conel et al. (1978).
[f]Identification of spectral features from Hunt et al. (1971).

result from alteration of pyrite and is thought to accompany uraninite deposition (Bramlett et al., 1980). The spectrum is characterized by an intense absorption band that is due to Fe^{+3} and is located at 0.9 μm, and by the usual strong ultraviolet and visible absorption bands that give rise to the reddish color. The position of the major electronic absorption at 0.9 μm indicates that a probable mixture of hematitic and limonitic/goethitic phases is present. The spectrum contains an additional, moderately strong absorption feature near 2.1 μm, which is possibly due to clay minerals present.

c. Metasediments. Figure 9-15(e) shows a typical reflectance spectrum for biotite schist, which is a major rock type comprising the belt of metasediments bounding the North Canning Stock to the northwest and to the north. The spectrum is typified by low overall reflectance. The rock is biotite-rich and all of the major absorption features

An examination of the lithologic sections for the NURE drill cores discloses that the oxidized granitic surface layer is absent beneath the covering Wagon Bed section (Twb in DH-1 and DH-5, Figure 9-14). This supports the view discussed elsewhere that the oxidation may have been removed by erosion or was never developed on rock surfaces along the pre-Eocene paleodrainages at these sites.

VIII. Spectral Reflectance of Cover Types

A. Introduction

The visible and near-infrared reflectance (0.45 to 2.5 μm) properties of rock and vegetation materials at the Copper Mountain test site are presented here. Surface reflectance properties have been studied in two ways:

(1) *Field spectral measurements* have been carried out using the JPL Portable Field Reflectance Spectrometer (PFRS), which operates throughout the spectral region of 0.45 to 2.5 μm. It measures bidirectional reflectance of a 200-cm^2 area of the surface, with a spectral resolution ($\lambda/\Delta\lambda$) on the order of 100. The spectral regions of 1.3 to 1.5 μm and 1.75 to 2.0 μm are excluded from the field spectral reflectance curves because of strong atmospheric water extinction. Reflectance spectra were obtained at surface locations throughout the Copper Mountain area during the summers of 1978 and 1979.

(2) *Laboratory spectral reflectance measurements* were made using the Beckman DK2A and Beckman 5240 Spectrophotometers on field-acquired samples from the PFRS measurement locations. Both of these instruments measure hemispherical reflectance and can cover the spectral region of 0.4 to 2.5 μm. The standard procedure is to measure reflectance of powdered samples (<0.49 mm particle size) rather than surfaces. The laboratory data are ordinarily used for more precise interpretation of absorption features observed in the field spectra, and no precise photometric comparisons are intended.

B. Spectral Properties of Alteration and Other Rock-Forming Minerals

Table 9-8 records the band positions and strengths of spectral reflectance absorption features for the important alteration and rock-forming minerals described in the discussion of models (Paragraph VII). The spectral data summarized in Table 9-8 were taken from reflectance spectra of standard laboratory samples. (Examples are presented below of the reflectance of some rock types at Copper Mountain.) Examples of the reflectance spectra for minerals of these types may be seen in the references cited in Table 9-8.

C. Field-Acquired Spectral Reflectance Measurements

1. Spectra of rocks. Figure 9-15 presents examples of the PFRS-acquired spectral reflectance data of altered (weathered), unaltered (fresh), and hydrothermally (?) altered igneous rocks, metasediments, and Tertiary sedimentary rocks from throughout the Copper Mountain site (Figure 9-16). These examples do not exhaust the variations present in the exposed rocks but do serve to illustrate many of the absorption features, the magnitude of the effects, and the (maximum) differences between groups. Below results are presented dealing specifically with the oxide coatings and their masking effects on the substrate igneous mineralogy as these may apply to the detection of propylitic (?) alteration in the area.

a. Unaltered granitic rock. Figure 9-15(a) shows the spectrum of unaltered granite. The spectrum is characterized by a relatively strong absorption band in the visible and toward the ultraviolet present below 0.6 μm, which is typical of Fe^{+3}. A broad, weak band centered near 0.9 μm and also due to Fe^{+3} is the only additional absorption band present. These features reflect the low degree of surface weathering, the small amount of iron-oxide pigment present in the surface skin, and the absence of identifiable (clay) alteration of the microcline feldspar in the substrate. A portion of the 0.9-μm feature may arise from Fe^{+3} in the K-feldspar.

b. Altered (weathered) granite rocks. Figures 9-15(b) through 9-15(d) are examples of the reflectance of oxidized rock. The principal features of Figure 9-15(b) between 0.4 and 1.2 μm are all due to Fe^{+3}, probably in a mixed limonite/hematite assemblage. The iron-oxide features include a very strong band below 0.6 μm, a weak, poorly defined absorption band near 0.65 μm, and a broad, moderately intense band with the center near 0.85 to 0.90 μm. At 2.20 μm a moderately intense band due to montmorillonite or kaolinite may be seen.

Figure 9-15(c) shows the reflectance spectrum of a heavily weathered, yellowish-stained rock typical of most outcrops throughout the pediment area. Between 0.4 and 1.2 μm the absorption features are due to Fe^{+3}. This spectrum, however, shows a very broad, intense absorption band spanning the interval between 0.8 and 1.2 μm, with the band center near 1.0 μm. A band at 2.20 μm of moderate intensity is also present and represents clay.

Figure 9-15(d) is an example of "hematite" red-staining found in association with fracturing in the granitic rock. This type of pigmentation in such structural settings may

Table 9-7. Copper Mountain core analysis for the NURE drill holes

Drill Hole	Sample Description	Depth, ft	X-Ray Diffraction Analysis
DH-1	Fresh gneissic monzonite. K-feldspars altering to clay. Gray, powdery zones of S, FeS_2, magnetite, pyrite.	350–360	Gray, powdery zones = pyrite, magnetite. Yellow halo = hematite. Clay = kaolinite.
DH-2	Fresh gneissic Ag, hematite-montmorillonite stains on	335–344	Red deposits = hematite.
DH-2	fracture surfaces. Near horizontal joints with dark-red iron-oxide alteration of secondary biotite plus green montmorillonite-chlorite alteration.	398–407	Green alteration on joint surfaces = montmorillonite.
DH-3	Highly altered, powdery, gray-green rock, serpentinized, plus a sample of fresh monzonite with biotite, microcline, and plagioclase.	231–241	Major thuringite (chlorite), microcline (intermediate), montmorillonite-chlorite (tosudite), and secondary albite (low). Minor quartz.
DH-3	Lightly altered monzonite with microcline and plagioclase and a mafic mineral. A trace of iron oxide occurs as small (0.25-in. diameter) aureoles.	275–288	Major albite and microcline. Minor quartz, thuringite (chlorite). Very minor tosudite, enstatite, and fayalite (olivine). Trace of hematite and chromite.
DH-3	Highly altered, gray monzonite with much microcline and several black quartz crystals weathering out of matrix.	460–468	Very major tosudite. Major thuringite and microcline. Very minor albite and antigorite. Trace of chromite.
DH-4	Ag. Lavender, white, orange, dark-red alterations. Albitization evident.	29–34	Lavender alteration = hematite, montmorillonite-chlorite mixture. White alteration = kaolinite. Red alteration = poorly crystallized hematite.
DH-4	Relatively fresh Ag plus limonite alteration. Red-oxide coating and schlieren of crushed, altered, black mineral on fracture surfaces.	64.5	Black mineral on fractures = serpentine, montmorillonite (trace).
DH-4	Highly altered, albitized Ag from fault zone. Fractures filled with thick (0.25-in.) layer of oxidized biotite (red) books. Limonitic stain on rock. Higher gamma counts (750 to 900 counts/s).	275	Clay alteration in rock = montmorillonite.
DH-5	Fractured Ag. Slickensides with montmorillonite on surfaces. Gneissic banding with pyrite crystals. Highly altered mafic dike section. Yellow halos (hematite) with magnetite centers and finely disseminated pyrite through the area.	494–503	Trace amounts of pyrite. Mafic dike = montmorillonite, biotite, hornblende, and calcite. Yellow halo = poorly crystallized hematite. Euhedral dark gray crystals = magnetite.
DH-5	Biotite-hornblende schist. Slickensides as above.	520–528	Biotite, hornblende, antigorite, and montmorillonite.

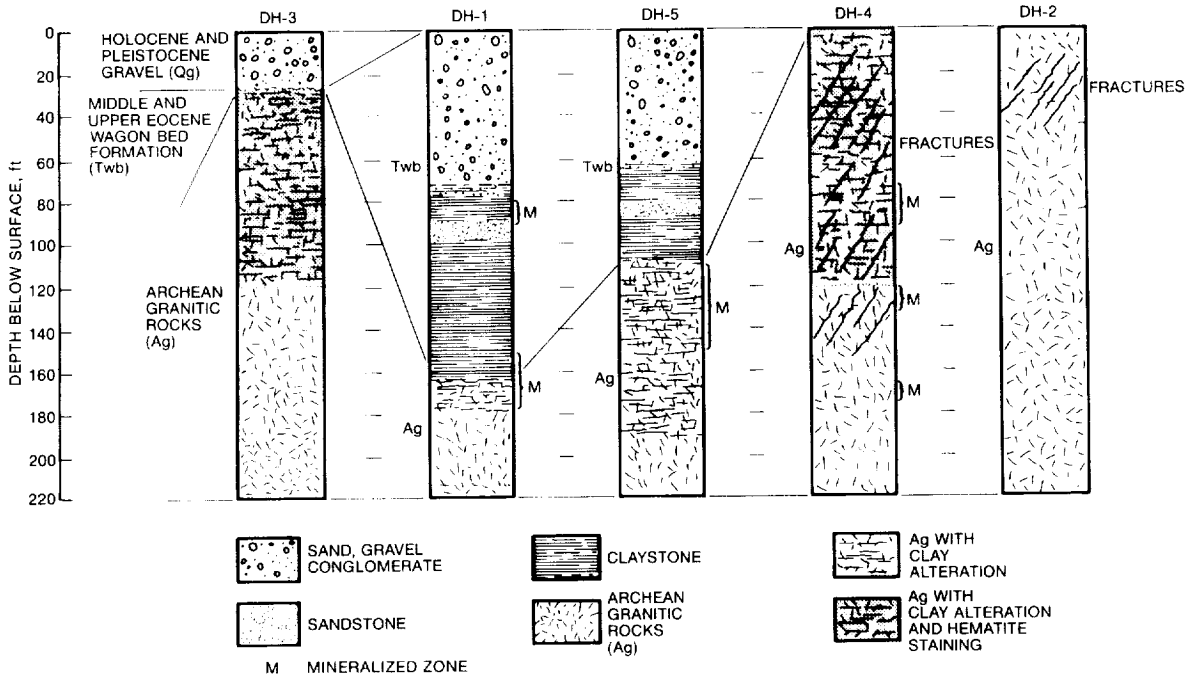

Figure 9-14. Lithologic sections for NURE drill holes DH-1 to DH-5

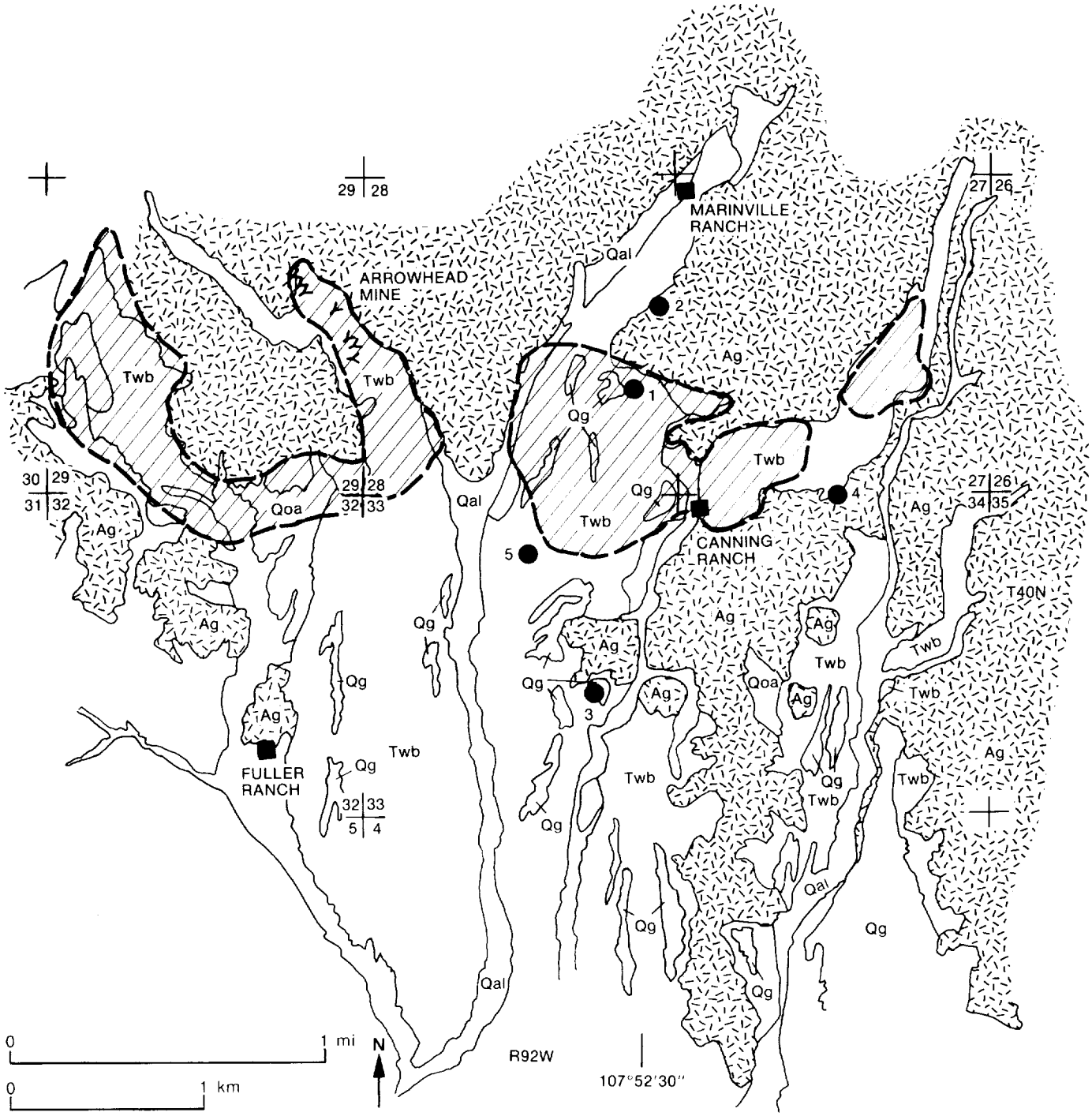

Figure 9-13. Geologic map of the Canning–Fuller area at Copper Mountain showing locations of NURE drill holes (solid circles). Numbers 1 to 5 correspond to drill holes DH-1 to DH-5 in Table 9-7. Hachured areas are approximate outlines of Fuller (left) and Canning (right) ore bodies as determined by RME exploration drilling. Geologic units are as follows: Ag = Archean granite, Twb = Wagon Bed Formation, Qg = gravel, Qoa = older alluvium, and Qal = alluvium. (Geologic boundaries from Thaden, 1980b, 1980d.)

the granite produced syngenetic enrichment in bentonitic mudstones and basal conglomerates of the Wagon Bed Formation (Bramlett et al., 1980). The present distribution of these zones of enrichment reflects the present distribution of impervious Tertiary cover at the surface.

B. Hydrothermal Ore-Genesis Model

An alternative hydrothermal mechanism of origin for the North Canning mineral body has been proposed by Shrier and Parry (1982). In this model, oxygenated meteoric waters reacted with overlying Paleozoic and Mesozoic sediments to develop a low pH environment. These fluids subsequently filtered into fractured granite, and concentrated uranium in solution by reaction with biotite, feldspar, and magnetite. Formational waters circulated convectively due to the heat generated through radioactive decay of potassium, uranium, and thorium. Reactions involved with wall-rock alteration are inferred to have produced conditions favoring uraninite precipitation and stability. The most important of these reactions reduced oxygen fugacity, inducing the precipitation of uranyl species as uraninite. Uranium mobilization was accompanied by a regional (Stage I) alteration event. Modification of the solutions by alteration reactions with wall-rock materials (Stage II) led to the precipitation of uranium. These stages of alteration differ in timing and mineralogy from those identified by Kendall et al. (1980) and by Bramlett et al. (1980) and are as follows:

Stage I: Wall-rock alteration of granitic rocks occurs with plagioclase being altered to sericite, plagioclase and biotite being replaced by epidote, and biotite being partially altered to chlorite. Magnetite is altered to hematite and hydrous iron-oxide phases along fractures, but is fresh elsewhere. Metasedimentary xenoliths and primary microcline remain unaltered. Secondary or alteration K-feldspar may occur in some samples, with K-feldspar replacing plagioclase. Healed fractures in quartz grains contain fluid inclusions; analyses of inclusions imply a filling temperature of 140°C. Identical alteration is described in other granites exposed throughout the range (Gliozzi, 1967), suggesting a regional event; but based on fluid inclusion homogenization the event is too low in temperature to represent fluid circulation at the time of magma crystallization as was suggested by Gliozzi (1967) and Nkomo et al. (1978).

Stage II: Uranium deposition in the resource is accompanied by the filling of fractures with white to green montmorillonite, and with local hematite staining and kaolinite development. Breccias are typically bleached of iron staining. The matrix, dominantly Na-montmorillonite, is also bleached of iron staining. Plagioclase is altered to K-feldspar, which floods the matrix in places.

The fracture and breccia alteration of Stage II postdates the Stage I event. Fragments of Stage I altered granite are found in breccias, and Stage II fractures displace healed quartz fractures of Stage I origin. Fractures with iron-oxide staining and iron-hydroxide filling are most commonly mineralized. Breccia mineralization is not accompanied by iron staining, and such staining therefore can have no relationship to mineralization in these zones. In fractures, pyrite is not found in association with iron oxides. In breccia, trace pyrite occurs intimately with uraninite.

Many reactions can be devised that lead to uraninite precipitation (Shrier and Parry, 1982). Among the possibilities is oxidation of magnetite according to the scheme:

$$2Fe_3O_4 + UO_2(CO_3)_2^{-2} + \tfrac{1}{2}O_2 \rightarrow UO_2 + 3Fe_2O_3 + 2CO_3^{-2}$$

which leads to association of uraninite and hematite. Sulfide solution species may have acted as reducing agents, precipitating uraninite and pyrite together according to:

$$Fe^{+2} + 2H_2S + UO_2(CO_3)_2^{-2} \rightarrow UO_2 + FeS_2 + 2H_2CO_3$$

thus accounting for the observed association of these two minerals.

C. Analysis of NURE Cores

As described above, the various forms of the supergene genetic models proposed by Yellich et al. (1978) and Bramlett et al. (1980) and the hydrothermal genetic model of Shrier and Parry (1982) produce distinctly different suites of minerals in both the source and host rock materials. Core samples from five drill holes, which were supplied by the Bendix Field Engineering Corporation and obtained in 1978 as part of the NURE program (Figure 9-13), have been analyzed as part of the present study. These analyses are presented in Table 9-7. The mineralogies observed generally are those described by Shrier and Parry (1982). The distribution of NURE drill tests is sparse, and there has not been an opportunity to examine cores obtained from other parts of the deposit by RME geologists. Evidently the purported alteration products are diverse throughout the mineralized and surrounding zones. Reconciliation of these differences and the sorting out of consequences for different models must await future studies.

(2) Deposits of sediment and volcanic ash (carrying 8 to 21 ppm uranium) were laid down, covering the entire mountain range between mid-Eocene and mid-Miocene time, burying the granites, and preventing further circulation of meteoric waters to mineralized zones at depth.

(3) Erosion following late Miocene uplift stripped away the Tertiary sedimentary cover and again exposed the granites. During this interval the bentonitic sediments, together with the granites, were again accessible for uranium leaching and redeposition in the deposit, providing a second important episode of uranium enrichment.

A key element of this model is the presence of corrosive formational fluids, including chloride brines, derived from Paleozoic and Mesozoic strata at depth. These fluids, free to migrate in brecciated zones of the granites, both leached uranium from and altered the rocks through which they circulated by chloritizing biotite and hornblende. They also liberated excess Fe^{+2} from both ferromagnesian minerals in granites and metamorphic rocks, and supplied H_2S from depth to form pyrite on fractures.

Leached uranium is probably transported in solution as uranyl dicarbonate (Garrels and Christ, 1965). Reduction and precipitation are thought to occur by reaction with pyrite according to the following scheme proposed by R. Honea (personal communication, 1973):

$$2FeS_2 + UO_2(CO_3)_2 \cdot H_2O + 18H_2O \rightarrow UO_2\downarrow + Fe_2O_3\downarrow + 4SO_4^{-2} + 2HCO_3^- + 36H^+ + 26e^-$$

Thus deposition of uranium is pictured to be accompanied by the destruction of pyrite and by the precipitation of hematite.

The mechanism involving mixing reducing waters from deep sources and surface-derived oxidizing waters to produce biotite alteration and uranium deposition operated widely and accompanied progradation of sediments over the range in post-Early Eocene time. Migration of surface-oxygenated waters into the granite was prevented by thick Tertiary sediment accumulation. At the same time deep formational waters were confined to granitic rocks beneath this impermeable sediment blanket. These fluids migrated along the Tertiary–Precambrian interface as a route of higher permeability. Only at the edge of the sediment cover were surface and subsurface waters mixed to produce supergene mineralization. This implies a distribution of uranium mineralization wider than there is at present, beneath a once considerably more extensive Tertiary sediment cover that has been removed by erosion since the Pliocene. Uranium subjected to this episode of regional erosion was remobilized by meteoric waters and deposited elsewhere. The present distribution of deposits reflects the protection of these areas from the infiltration of oxidizing water during post-Pliocene time by the Tertiary blanket of impervious sediments.

Quantitative estimates of the uranium potentially available from granitic and Tertiary sediment sources are based on delayed-fission neutron assays of uranium concentration (Bramlett et al., 1980). The average uranium content of unleached granite is 25 to 40 ppm, and in unleached Tertiary sediment sources, 11 to 33 ppm. Uranium content in leached granite is 11 to 21 ppm and in the Tertiary rocks, 8 to 25 ppm. The available leached uranium is thus 14 to 19 ppm from granite and 3 to 8 ppm from Tertiary sediment.

The role of the Tertiary cover as an actual source of uranium is speculative. Bramlett et al. (1980) depict the role of sediment cover to be predominantly that of impeding infiltration of oxidizing meteoric water. The low permeability of this clay-rich formation and its stratified nature suggests lateral rather than downward percolation of surface-derived water.

To summarize, formation of the North Canning deposit by supergene enrichment proceeded in as many as three important episodes:

(1) Post-Paleocene uplift provided structural preparation and exposure of granitic rocks to erosion and leaching. During this supergene enrichment period, the pre-Wagon Bed exposed granitic surface was weathered (oxidized), biotite was chloritically altered, and feldspar weathered to clay. Material balance calculations by RME geologists suggest that approximately one-half the total accumulation present at North Canning occurred during this episode (Reyher, personal communication, 1981). On the other hand, Bramlett et al. (1980) believe the major portion occurred in this interval.

(2) Burial of the granitic terrain by rocks of the Wagon Bed Formation occurred, covering the weathered surface and sealing the mineralized horizons from further remobilization.

(3) Renewed post-Middle Miocene removal of Tertiary cover reexposed the granite. Enhancement of the accumulation by leaching of the bentonitic sediment cover and granite occurred (Kendall et al., 1980). Lateral secretion of uranium from accumulations in

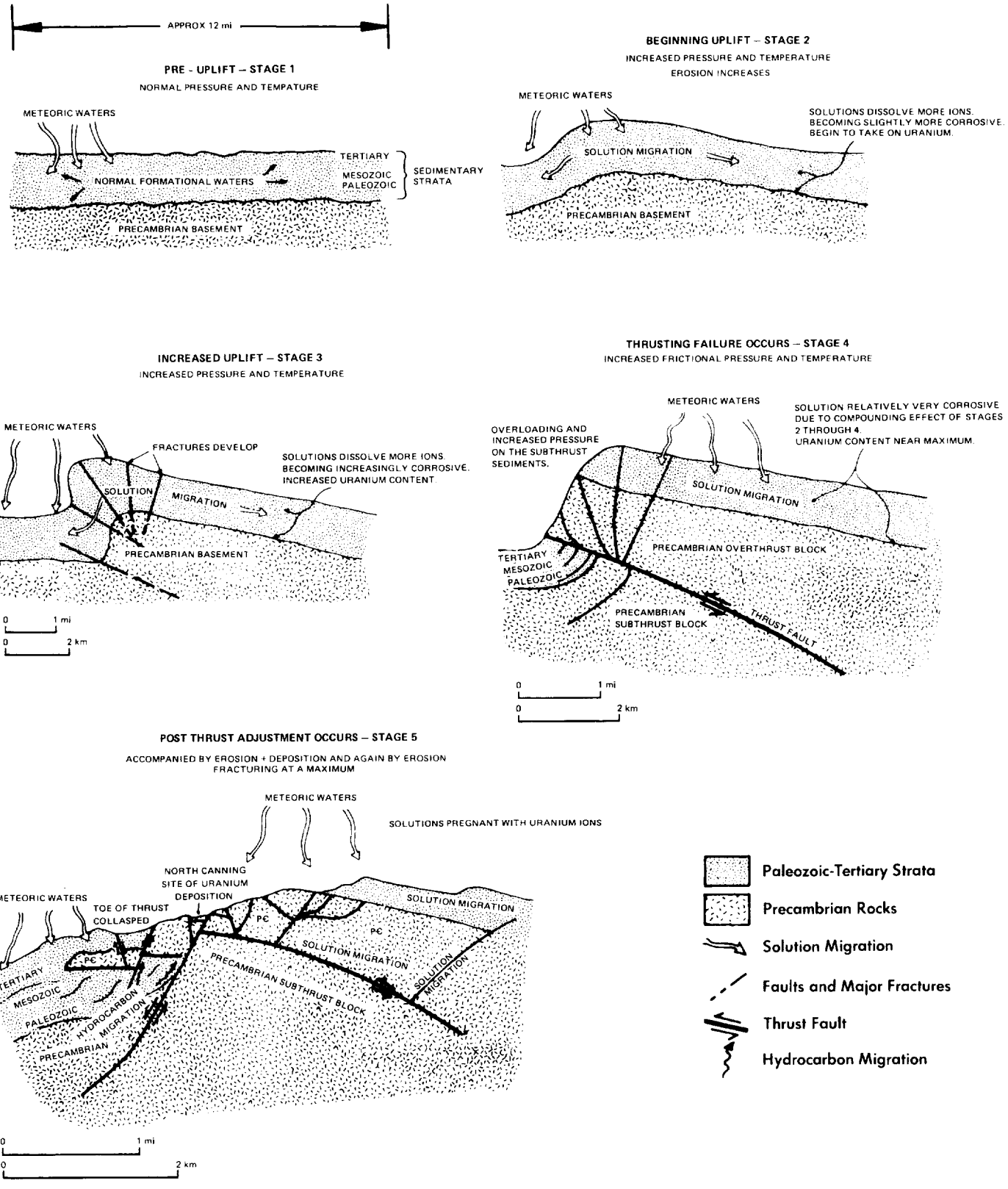

Figure 9-12. Owl Creek Mountains and North Canning structural and genetic model for uranium deposition (Yellich et al., 1978)

ORIGINAL PAGE
COLOR PHOTOGRAPH

Figure 9-9. Weathered, hematite-stained granitic outcrops, Copper Mountain site (SW 1/4, SE 1/4, Sec. 33, T40N, R92W)

Figure 9-10. Cut exposing weathered layer in granites (SW 1/4, Sec. 29, T40N, R92W). Note red hematitic staining along fractures.

Figure 9-11. Chip samples from an exploration drill hole penetrating the weathered horizon (SW 1/4, Sec. 29, T40N, R92W). Sample interval is 1.5 m (5 ft). Sample from the top of the hole is indicated. White materials are unoxidized granite at depth.

VII. Models of Ore Deposition

A. Supergene Ore-Genesis Model and Relationship to Surface Effects

Models of ore genesis for the North Canning uranium resource at Copper Mountain have been presented by Bramlett et al. (1980), Kendall et al. (1980), and Yellich et al. (1978). Bramlett et al. present the information that is contained in Kendall et al. as well. Similar ore-genesis models are thought to apply to both the Canning and adjacent Fuller accumulations (Reyher, personal communication, 1981).

The genetic model proposed by Yellich et al. (1978) that reflects the entire geologic history of the Owl Creek Uplift is represented schematically in Figure 9-12. Uplift and locally intense faulting and brecciation commenced in Paleocene time, accompanied by movement of corrosive meteoric and formational fluids that attacked accessible sedimentary and granitic rocks. Alteration was confined to regions of high fracture-density along which fluids could circulate. Corrosive meteoric waters acted to leach uranium from sediments and granitic rocks and to oxidize the granitic rocks at the surface. Uranium precipitation occurred in fractured ground at places where upward-migrating (reducing) solutions mixed with downward-migrating (oxidizing) waters from the surface.

Kendall et al. (1980) pieced together elements of the geologic history and identified important sources of uranium contributing to the deposit. Two source rocks, granites and bentonitic sediments, were recognized, together with several periods of mineralization:

(1) Precambrian granitic rocks carrying large quantities of primary uranium (25 to 40 ppm) were exposed in the mountains during early and mid-Eocene time, following post-Paleocene uplift and faulting. At this time, the granite was leached of uranium, and the uranium both carried basinward and deposited locally in breccia zones along faults. This interval corresponds to the major period of mineralization described by Yellich et al. (1978), and to the development of major pre-Eocene weathering surfaces along pediments at the base of the mountains.

(1) Regolith-type weathering is present in granitic rocks to a depth of several meters beneath the Paleozoic–Precambrian unconformity. On exposed surfaces the granites are iron stained and friable to crumbly. Pits dug beneath the surface-weathered cover show the granite to contain chalk-white, kaolinized feldspar and bright-green clay formed from chlorite.

(2) Silicification was observed along NE-trending shear zones and consists of cherty and milky quartz as shear fillings.

(3) Alteration, accompanying fracturing of the granite, consists of the formation of clay minerals after feldspar, and alteration of biotite to chlorite and locally to hematite and goethite. Alteration intensity is related to the degree of fracture. Oxidation of biotite to form chlorite is inferred to be a moderate- to low-temperature hydrothermal event (Bramlett et al., 1980) that accompanied leaching of predominantly intercrystalline uranium from fractured rock (Kendall et al., 1980). Such alteration is observed to have a large areal extent with sharp boundaries between altered and unaltered rocks.

In association with the uranium accumulations, Bramlett et al. (1980) recognized propylitic (?) and argillic (?) alteration in Precambrian rocks within the deposit. The propylitic alteration within granite consists of (1) chloritized biotite, (2) argillized albite, and (3) green montmorillonite on fractures and around chlorite. Argillic alteration consists of (1) nearly complete alteration of chlorite to montmorillonite, (2) moderate argillization of shattered ground, (3) green montmorillonite on fractures, and (4) pyrite on fracture surfaces. Metamorphic rocks show weak to moderate propylitization, and diabasic dikes are chloritized.

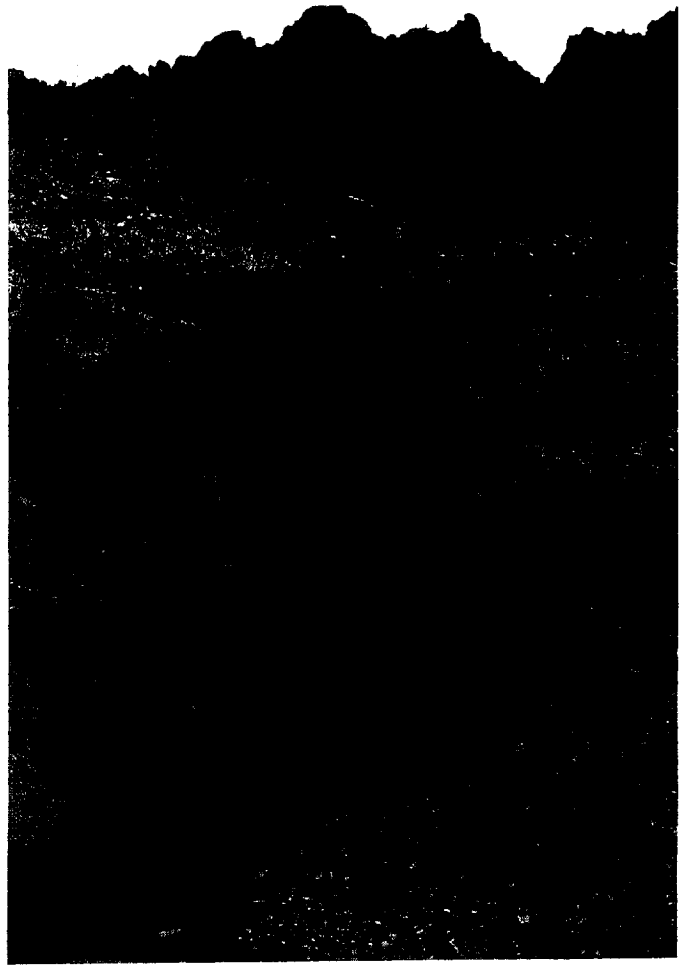

Figure 9-8. Gem prospect pit in SW 1/4, Sec. 34, T40N, R92W, south of Canning Ranch. Granitic rocks in the face beneath the weathered granitic (oxidized) surface are stained by limonite, predominantly on fracture surfaces. The cut is about 30 m in height. Green lichens are seen on north-facing slopes.

Granitic outcrops adjacent to the North Canning and Fuller deposits on the southern side of the Canning Fault are stained bright rusty orange by limonite and hematite (Figures 9-8 and 9-9), and, along fractures and faults, by hematite (Figure 9-10). In drill holes, nearly pervasive hematite staining predominates (over limonite) as fracture coatings, on cleavages in feldspars, and along grain boundaries. Hematite halos are seen surrounding pyrite; hematite also occurs pseudomorphously after magnetite (Kendall et al., 1980).

The oxidized terrain is represented by altered rocks beneath the surface (Figure 9-8). The principal manifestation of this is the formation of limonitic goethite. Examination of chip samples recovered from exploration drill holes (Figure 9-11) and drill cores showed that the surface-oxidized horizon was not found at a depth greater than 15 m beneath the surface. The thickness of the oxidized zone in granite correlates inversely with the amount of Tertiary cover above; e.g., where the Tertiary cover is thick, the oxidized layer is thin or missing, and vice versa. These observations suggest that the surface weathering or oxidation effect is at least in part pre-Wagon Bed in age and was removed by erosion along paleodrainages or prevented from forming before deposition of Wagon Bed rocks. Continued weathering might also be expected on granitic outcrops exhumed from beneath the cover. Thus the age of such weathering might actually span the interval from the Eocene to the present, excluding the period during which the granites were covered.

ORIGINAL PAGE
COLOR PHOTOGRAPH

tite ranging from 1 to 8 percent and muscovite 1 to 6 percent (Bramlett et al., 1980). Abundances of these minerals are generally higher where the granites are in contact with metasediments. The granites are fine- to coarse-grained with 1- to 3-cm microcline phenocrysts. Pegmatites and other late magmatic segregations rich in quartz and specularite are common in the granite (Thaden, 1980d). Pale-green dikes of feldspar-epidote-zoisite-olivine are also found. Pegmatites are also found in the adjacent metasedimentary terrain (Bramlett et al., 1980).

Fresh granitic rocks are pale gray, grayish-orange, pink, and moderately brownish-red and weather to resistant, bouldery outcrops (Figure 9-7). Red hematite forms a pervasive coating on quartz and feldspar grains to give weathered surfaces a reddish appearance. Outcrops may be extensively covered by lichens that are gray, black, yellow, red, or green in color. The lichen cover may be locally complete, especially on north-facing surfaces.

Granitic rocks containing mineralization in the North Canning deposit are not exposed at the surface, and mineralized rock is covered by up to 50 m of Wagon Bed bentonitic claystone, siltstone, sandstone, and gravel (Yellich et al., 1978). These rocks at depth (Bramlett et al., 1980) consist of microcline–albite granite enclosing blocks of biotite–hornblende schist, amphibolite, gneiss, and granite gneiss (Yellich et al., 1978). Pegmatites cut the granite and metamorphic rocks. Diabase dikes composed of augite and other pyroxenes and calcic plagioclase occur in places.

2. Alteration in the granitic rocks. Bramlett et al. (1980) have recognized three types of alteration present in the granitic rocks:

Figure 9-7. Fresh granitic outcrops northwest of the Arrowhead Mine (SW 1/4, Sec. 20, T40N, R92W)

Table 9-6. Mineralogical characteristics of hematitic and limonitic altered granite rocks of Copper Mountain[a]

Mineral	Samples			
	"Fresh" Rock	Red Altered Rock (red-oxidized area)	Yellow Altered Rock (yellow-oxidized area)	Yellow Sand (yellow-oxidized area)
Quartz	major	major	major	major
K-feldspar	major	major	minor	major
Plagioclase	minor	minor albite	very minor	minor
Mica	biotite	white, biotite	white	biotite
Calcite	trace	very minor	very minor	trace
Iron oxides		hematite	trace hematite	
Clay		kaolinite, montmorillonite	trace kaolinite	trace montmorillonite
Chlorite	trace	trace chlorite, montmorillonite	very minor	trace chlorite

[a]Analysis by X-ray diffraction.

e-7

Table 9-5 (Continued)

Age	Formation	Lithology	Thickness, m
	major hiatus		
Archean	Metasedimentary Rocks	Metasedimentary schists and gneisses. These rocks are of widely ranging composition and color. Three groups of metasedimentary schists recognized. Southern group: greenish-gray, olive-gray, and gray quartz-muscovite-biotite schist. Minor greenish-black hornblende schist. Middle group: quartzite, quartz-mica schist, dark grayish-red, garnet-biotite schist, andalusite-sericite schist, hornblende-quartz-plagioclase schist, cummingtonite schist, corderite schist, together with other pelitic, quartz-magnetite, and quartz specularite rocks. Northern group: black hornblende-plagioclase-quartz-schist, quartz-biotite-plagioclase schist, and cross-bedded quartzite. Uralitic amphibole dikes (generally < 15 m thick) transect strike of metasediments at acute angles. Next to large bodies of granite, metasediments are included as xenoliths altered to migmatitic gneiss with abundant quartz segregations and biotite. Mineral layering in these metasediments is parallel to bedding of iron-formation-quartzite or other identifiable original sedimentary units. Ages of 3100 to 3500 m.y.	

[a]Data summarized from description by Thaden (1978, 1979, 1980a 1980e, 1981).

overrode upturned Paleozoic and Mesozoic strata. Fanshawe (1939) has recorded 10 km of horizontal displacement resulting from these thrust movements.

Subsequent vertical normal faulting of the toe of the thrust has resulted in extensive development of crushed or highly fractured rock near normal faults along the range front and development of a structural inlier of Paleozoic rocks in Steffen Hill (Figure 9-6). Steffen Hill is bounded on the north and south (and cut in its interior) by steeply dipping normal and reverse faults that have displaced the block into Precambrian granite (Ferris, 1968). Keefer and Love (1963) give a combined vertical uplift of the Owl Creek Mountains and subsidence of the adjacent (north-central) Wind River Basin amounting to some 10,500 m.

According to Fanshawe (1939) the time of anticlinal arching and southward thrusting correlates with the unconformity at the top of the Paleocene Fort Union Formation. Uplift ceased prior to deposition of Wind River sediments in Lower Eocene time. In late Miocene time (Kendall et al., 1980) the Owl Creek Mountains and Wind River Basin underwent renewed uplift, and many normal faults in the toe of the thrust were reactivated. This initiated a period of erosion, with removal of the Tertiary cover beginning during the Pliocene and continuing to the present time.

Stearns et al. (1978) have performed model experiments in sandboxes dealing with the Owl Creek Mountains structure. The combination of shallow-dip reverse faulting and closely associated normal faulting appears when sawtooth-like displacement fields are applied to rigid lower basement boundaries in these model experiments, and when the horizontal-modeled lithostatic pressure is augmented by additional constant horizontal pressures of supposed tectonic origin. This vertical tectonic model contrasts with that of Berg (1962), who envisages the deformation to be thrusting, the result of predominantly horizontal compression.

VI. Geologic Relations of the Mineralization

A. Relations to Structure

The Canning deposit is fault-bounded (Kendall et al., 1980) and lies within pervasively shattered and crushed granitic rock. The accumulation lies beneath Tertiary sediments of the Wagon Bed Formation. Mineralized ground is in close proximity to the Tertiary–Precambrian contact and to Recent unconformities. The deposit is limited on all sides by faults and is transected in the interior by several such structures. With the exception of the Canning Fault (which forms the northern limit), none of these structures is exposed at the surface. The faults in part place definite geometric limits on the distribution of permeability from mechanical fracturing. Brecciation is more extensive along the Canning structure and the resultant permeability more extensive than along other structures of the system. Mineralization is confined to such zones of intensive brecciation.

B. Relations in the Granitic Rocks

1. Nature of the granitic rocks. The granitic rocks at the Copper Mountain test site have been described by Bramlett et al. (1980), Thaden (1980b, 1980d), and Yellich et al. (1978). Mineralogical characteristics of altered and unaltered material are given in Table 9-6.

The granitic rocks are generally leucocratic and include the following rock types: quartz monzonite, microcline–albite granite, syenite, quartz-microcline binary granite, and quartz-microcline-plagioclase-biotite microgranite. Biotite and muscovite are common varietal minerals, with bio-

Table 9-5 (Continued)

Age	Formation	Lithology	Thickness, m
	unconformity		
Middle Pennsylvanian	Tensleep Sandstone	Sandstone, clayey and dolomitic in basal part, pale gray to pale yellowish-gray, locally stained pink, red, purple; weathers yellowish-gray to pale yellowish-brown; very fine- to medium-grained, clear angular to subrounded quartz, poorly cemented with silica. Cherty in places but generally friable.	100
Middle to Lower Pennsylvanian and Upper Mississippian	Amsden Formation	Formation consists of three members: an upper dolomite member, a middle shale member, and a lower sandstone member. Sandstone is confined to the lower member and is the most abundant facies in the formation. The sandstone is silty, greyish-orange to reddish-brown (weathers dark brown), fine- to medium-grained, and well-sorted. Composed of angular to subangular quartz cemented in part by silica. Sandstone member is 65 m thick. The upper member is limestone or dolomitic limestone with white to pink quartzite beds in upper part. Dolomite is pale orange to grayish-orange-pink, medium crystalline to saccharoidal in upper part, finely crystalline in lower part, and porous. Contains gray to white chert nodules. The upper member grades into overlying Tensleep Sandstone. The middle shale member consists of grayish- to purplish-red, clayey siltstone, that weathers yellow and ocher. Unit poorly exposed, weathers to powdery surface; a few meters in thickness but possibly thinned by tectonic flowage.	100
	unconformity		
Upper and Lower Mississippian	Madison Limestone	Dolomite, limestone, and sandstone. Dolomite is limey and clayey, yellowish-gray to very pale orange or pale orangish-pink in color (weathers yellowish-gray), fine to medium crystalline, saccharoidal, and porous in very thin, even beds, but bedding is obscure. Comprises the major part of this formation. Limestone, with most beds clayey and dolomitic, is pale yellowish-gray (weathers yellowish-gray), predominantly sublithographic, and medium- to thick-bedded, but bedding indistinct. Sandstone, calcareous in most places, is distributed throughout formation in 0.1-m- to 10-m-thick beds, and is white to reddish-brown and in thicker beds in upper part. Formation makes ledgy cliffs.	130
Upper and Middle Ordovician	Bighorn Dolomite	Dolomite. Very light gray and light yellowish-gray, mottled light grayish-orange (weathers in places yellowish-gray), finely crystalline, saccharoidal, slightly porous, indistinctly thick-bedded to structureless, and deeply pitted on weathered surfaces, and contains scattered limonitic spots.	6–15
	unconformity		
Upper Cambrian	Gallatin Formation	Limestone and siltstone. Limestone cliff at top of formation is clayey, with some beds glauconitic, some beds dolomitic in upper part. Edgewise conglomerates common. Rocks are pale grayish-red, gray, pale orange, and mottled green and pinkish-orange; weather maroon, medium gray, and pale orange, with the distant appearance of a ribboned maroon cliff. Middle limestone forms slope, some beds of which are silty, glauconitic, and yellowish-gray to pale olive color (weathers pale yellowish-brown), medium to coarsely crystalline, dark-colored where conglomeratic, lithographic to sublithographic, and light-colored elsewhere. Pebble conglomerates near top. Basal limestone cliff clayey and silty, most beds slightly glauconitic; pale yellow, brown, grayish-orange, and yellowish-gray (weathers pale yellowish-brown), finely crystalline, with half of beds containing sublithographic limestone pellets or pebbles that form conglomerates. Thin, even beds, flaky to slabby splitting.	125–135
Middle Cambrian	Gros Ventre Formation	Siltstone, sandstone, and limestone. Siltstone is mostly sandy, clayey in places, with thin seams of silty claystone and claystone, micaceous in most places, glauconitic, calcareous; pale yellowish-gray, dusty yellow, and dusty yellowish-green (weathers olive-gray to maroon) with even-bedded to undulatory bedding in thin beds. Forms gently concave slope with thin ledges. Sandstone is silty, in part micaceous, with few thin maroon to brown glauconitic beds near base, fine-grained, pale orange, and cross-bedded to structureless lenticular beds in lower part. Basal 5 to 9 m is olive-gray (weathers yellowish-brown) and highly glauconitic; forms resistant cliff.	105–125
Middle Cambrian	Flathead Sandstone	Sandstone and siltstone. Sandstone in part silty, in part conglomeratic, especially near base. Dark yellowish-brown but contains highly ferruginous dark red and purple beds, and glauconitic, dark green beds, mostly in lower part; fine- to coarse-grained, poorly sorted, angular to subangular grain, arkosic, micaceous in places, and weakly to moderately cemented, as well as containing quartzitic irregular zones, especially near base. Conglomerate clasts include quartz, feldspar, and angular cobbles of granite and metasedimentary rock. Forms ledgy cliffs and slopes. Siltstone is dark red, greenish-gray, and pale orange; some glauconite, confined mostly to upper part of formation. Flathead Sandstone deposited on irregular surface cut on Precambrian rocks with 10 to 30 m of relief.	60–75
	major uplift and unconformity		
Precambrian X	Mafic dikes	Grayish and dark greenish-black, finely crystalline, tholeiitic dikes. Consist predominantly of augite and plagioclase, with minor amounts of magnetite, pyrite, olivine, and quartz. Chloritic alteration. Assigned a Precambrian X age (1600 to 2500 m.y.) based on petrographic comparisons with dated dikes cutting Precambrian units in the Bighorn, Beartooth, western Owl Creek, and Wind River Mountains. Dates of 1900 to 2100 m.y. are given by Condie et al. (1969).	
Archean	Granite	Pale gray and grayish-orange pink to moderate brownish-red; white, pale gray, and yellowish-gray where pegmatitic. The granite is bright rusty-orange along the base of the mountains where old, pre-Eocene (pediment) surface has been exhumed from beneath Tertiary sediment cover. The granite ranges in composition from quartz-microcline binary granite to quartz-microcline-plagioclase-biotite-muscovite granite with garnet, apatite, zircon, epidote, pyrite and magnetite as accessories. Composition varies widely from place to place. Average modal analysis 28% quartz, 34% microcline, 35% plagioclase (albite and oligoclase), and 3% biotite (Thaden, 1980a). Cataclastic texture near large faults; gneissic and ferromagnesian-rich (biotite) adjacent to bodies of metasedimentary rock. Ages reported range between 2640 to 2720 m.y.	

Table 9-5. Stratigraphy of the Copper Mountain area for formations and other map units mentioned in the text[a]

Age	Formation	Lithology	Thickness, m
Holocene	Alluvium	Sand and gravel. Sandy, silty, and slightly clayey, deposited in arroyos and contemporary streams. Gravels are sandy and composed of large clasts of granitic and metamorphic rocks. Sand fraction consists of quartz, feldspar, micas, amphiboles, garnet, and magnetite.	10–12
	unconformity		
Holocene	Old alluvium	Sand, very silty and clayey. Gray-brown to light brown to pale reddish-brown from oxidation of ferruginous grains. Poorly sorted. Composed of quartz, feldspar, mica, and variable amounts of volcanic ash. Contains chips and pebbles of unweathered bedrock. Deposited as fans and bahadas on low flanks of highland areas, and fills paleodrainages that are approximately coextensive with contemporary drainages.	15
	unconformity		
Holocene and Pleistocene	Gravel	Clasts, consisting mostly of granite, quartzites, amphibolite gneisses and schists, quartz, feldspar-mica schist, amphibolite, small quantites of quartzitic sandstone from the Flathead Sandstone and Amsden Formation, and limestones from the Gallatin, Madison, and Park City Formations. Deposited on gently sloping, dissected pediment surfaces at several levels. Clasts are silt- to boulder-size, but predominantly cobbles. Deposits unconsolidated but calichified, most extensively in the oldest deposits, which constitute the topographically highest units.	Up to 20. Average of 2–5
	unconformity		
Upper and Middle Eocene	Wagon Bed Formation	Volcaniclastic claystone and sandstone including vitric, crystal-vitric, and crystal tuff, and admixed and interbedded detritus of local origin. Claystones are pale green, grayish-yellow, and green where pure, grading to grayish-orange, orange, pink, maroon, and purple where abundant ferruginous detrital sand is incorporated. Contains glass shards. Deposited mostly as airfall material that is locally reworked by streams to form cross-bedded channel deposits and mudflows. Weathered surfaces form "popcorn" texture when wetted. Sandstones of the unit are yellowish-gray to pink and grayish-orange and are composed of milky quartz, feldspar, and minor amounts of dark minerals and muscovite, with interstitial, devitrified volcanic ash in varying amounts. These units are mostly even-bedded airfall material reworked by water into cross-bedded channel complexes. Tightly cemented silica zone within 5 m of base, not present everywhere. Boulder deposits up to 40 m thick fill paleovalleys on the flanks of the mountains. These valleys are filled with basal Wagon Bed volcanic ash and sand. Detrital sand layers intertongue and are interbedded with volcanic material. The Wagon Bed Formation was deposited on a paleoerosion surface of extreme relief, and possibly buried the mountains at one time. Erosional remnants now consist of resistant basal deposits of boulders and fine-grained material now protected in grabens. Equivalent to the Tepee Trail Formation used by RME geologists (Yellich et al., 1978) and originally described by Tourtelot (1953).	225
	major uplift and unconformity		
Lower Eocene	Wind River Formation	Sandstone and siltstone with separately mappable chromolithofacies of conglomerate and siltstone. Sandstone, silty and clayey, pale yellowish-gray and grayish-orange. Some beds stained brown and tightly cemented by iron oxides. Unit weathers pale greenish-yellow to pale blue. Very fine-grained to very coarse-grained, but moderately well-sorted in individual beds. Individual sandstone beds up to several meters thick. Siltstones are sandy and clayey olive-green weathering to pale blue. Extensive limonitic staining. Chromolithofacies (Thaden, 1980d, 1980e) are characterized by specific color, grain-size distribution, physical character, and composition. They typically constitute high-energy deposits of fluvial origin.	190
	major uplift and unconformity		
Upper and Middle Jurassic	Sundance Formation	Upper part—sandstone, limestone, and claystone. Sandstone is glauconitic, pale yellowish-gray, fine-grained, very poorly sorted, weakly cemented, and friable, with some beds ripple-laminated. Constitutes principal facies of upper part. Limestone is glauconitic, light olive-gray to moderate olive-brown (weathers olive-brown), medium-crystalline, thinly laminated, and thickly bedded. Contains abundant fossils, mostly pelecypods. Claystone is very silty to sandy, glauconitic, yellowish-gray to dark olive-gray, and thinly laminated. Formation is fossiliferous, mostly belemnites.	40
		Lower part—sandstone and claystone. Sandstone is calcareous clayey, silty, pale yellowish-gray to white, very fine-grained to fine-grained, poorly sorted, weakly cemented, and friable, with low-angle cross-beds; forms crumbly, rounded ledges, sandy slopes. Claystone is calcareous, silty, sandy, and dusty-yellow to light olive-gray; weathers grayish-yellow to powder surface.	50 or less
	unconformity		
Upper Triassic	Crow Mountain Sandstone	Sandstone, siltstone, and claystone. Sandstone is calcareous, yellowish-orange to reddish-orange, mostly fine-grained, moderately well-sorted, silica-cemented, cross-bedded with irregular bedding. Sandstones dominate lower 15 to 40 m of formation. Forms ledgy slope with sandy surface. Siltstone is calcareous, micaceous, and reddish-orange to reddish-brown. Moderately well-sorted arkosic siltstone make up upper half of formation. Forms weak ledges and powdery surfaces. Claystone is slightly calcareous, is yellowish-brown to reddish-brown and purplish-red, and occurs as thin seams throughout the formation except near base.	Probably greater than 85
Lower Triassic	Red Peak Formation	Siltstone and claystone. Siltstone is slightly micaceous, with most beds slightly dolomitic; is light reddish-brown; is well-sorted, mostly in thin, even beds; and weathers to powdery surface of gentle slopes except where protected from above; here the slopes are steeper, with chips. Claystone is dark reddish-brown in thin seams interbedded with siltstone beds at intervals of a few centimeters to many meters. Tabular gray-green bleached zones common along fractures and bedding planes. Upper part of formation is bleached pale greenish-yellow to thickness of 15 m beneath upper contact. Bleaching of base of formation to pale yellowish-orange in first few meters.	125–165
Permian	Park City Formation	Limestone and siltstone. Limestone is mostly dolomitic, pale yellowish-gray, gray, and pale gray (weathers yellowish-gray), mostly finely crystalline, porous to cavernous near base; mostly thin-bedded. Siltstone is limey, dolomitic, and clayey, grayish-yellow to reddish-orange, in thin, shaly, splitting beds interbedded with limestone near middle of formation only.	60–75

9-16 9-17
PRECEDING PAGE BLANK NOT FILMED

Common Plant Name	102	104	105	206	206f	231	237	242	270	271	2
Grasses											
Bluebunch wheatgrass		■	■	■	■	■	■	■	■		
Indian ricegrass	■	■	■	■	■		■	■	■	■	
Needle-and-thread grass		■		■	■	■	■	■			
Rhizomatous wheatgrass		■			■	■	■				
Western wheatgrass	■			■			■	■	■	■	
Inland saltgrass				■							
Green needlegrass			■						■		
Prairie junegrass								■			
Sandberg bluegrass			■		■		■		■		
Mutton bluegrass											
Basin wild rye				■							
Plains reedgrass											
Thickspike wheatgrass											
Canby bluegrass											
Mountain bromegrass											
Bluegrasses		■				■					
Columbia needlegrass											
Slender wheatgrass											
Idaho fescue	■										
Blue grama					■		■				
Spike fescue											
Annual weeds and grasses		■			■	■	■			■	
Sedges		■				■					
Perennial forbs		■									
Prickly pear cactus					■		■			■	
Shrubs											
Black sagebrush		■				■					
Bud sagebrush	■										
Big sagebrush	■						■		■		
Birdfoot sagewort							■			■	
Serviceberry											
Bottlebrush squirreltail	■			■			■	■		■	
Gardner saltbush				■			■	■		■	
Alkali sacaton				■							
Low rabbitbrush	■		■								
Greasewood							■			■	
Antelope bitterbrush											
Saneless horsebrush											
Trees											
Juniper											
Mountain mahogany											

Table 9-3 (Continued)

Rock Outcrops	Parent	Depth, in.		Color of Surface Unit				Slope, %	Comments
		Surface Unit	Total to Bedrock	Olive	Yellow	Brown	Gray		
	alluvium from schist, gneiss, granite	3	≥60					2–20	
		3	25			■	■	1–12	
	schist, granite	3	24			■	■	10–40	
	mixed alluvium from gneiss, granite	3	≥60			■		2–20	
	mixed alluvium	2	60		■	■		1–8	20–40% pebbles on surface
	mixed alluvium	4	60			■		1–25	30–60% pebbles on surface
	mixed alluvium	2	60		■	■		1–8	Gypsum in lower part
	colluvium from Flathead Sandstone	5	8–20			■		2–25	5–35% gravel, cobbles on surface
Flathead Sandstone						■			
	alluvium from limestone	5	31			■	■	2–20	Unit contains 15% of other loamy and cobbly or stony loam series
	mixed alluvium	3	≥60			■	■	2–15	
	alluvium from limestone	0	15			■	■	5–20	
	colluvium from limestone	7	10–20			■		1–45	
limestone									
	mixed alluvium	7	60			■		2–30	40–50% pebble cover on surface
	colluvium from shale and sandstone	2	10–20			■	■	10–40	

Table 9-4. Vegetation types occurring within the soil units at the Copper Mountain site according to SCS mapping

Soil Unit														
277	298	306	342	372	3109	4109	2a32	2a32s	2f72	2g11	2g72	2h71	2h72	2n11
■	■	■		■	■	■	■	■	■	■	■		■	■
■	■	■	■	■		■	■	■					■	
■		■	■	■	■		■	■		■			■	■
		■				■				■			■	
■		■	■	■			■	■	■	■				■
		■												
■	■			■										
		■	■											
	■	■		■	■		■	■	■	■				
				■										
		■												
				■										
				■										
■														
									■					
		■									■	■	■	
									■			■		
	■	■		■	■		■	■		■	■	■	■	■
										■			■	■
	■	■		■	■		■	■		■			■	■
		■								■				
												■	■	
														■
■	■	■				■	■	■	■	■	■	■		■
														■
■		■				■								■
	■					■					■	■		
		■												
				■	■				■					
				■										
					■				■					
											■	■		

Soil Unit	Major Series Comprising Unit	Areal Coverage, %	Locations	Chemistry		Texture					Sources		
				Alkaline	Calcareous	Stony (Channery)	Gravelly, Cobbly	Loam	Sand	Clay	Residual	Trans-ported	Eolian
2a32s	Lupinto Variant	55	irregular with rock outcrops		■			■				■	
	Bosler Variant	25	on valley fill and fans								■	■	
2f72	Pesmo	40	hill and ridge side-slopes			■[c]		■	■		■		
	Lupinto	30				■[f]		■				■	
	Rock outcrop	10	exhumed ridges and knobs										
2g11	Emblem	30						■	■			■	
	Clifterson	30	dissected alluvial fans and terraces				■	■	■	■		■	
	Rairdent	30						■				■	
2g72	Chittum	60	cuestas back slopes			■		■				■	
	Rock outcrop	20	ridges, escarpments										
2h71	Woolsey	40	hills					■			■		
	Decross	30	valley fill, north-facing toeslopes					■				■	
	Starman	15	hills				■	■			■	■	
2h72	Pensore	45						■				■	
	Rock outcrop	30	ridges, knobs, escarpments										
2n11	Clifterson	45	terraces, hills, ridges				■	■				■	
	Persayo	30	sides of hills and ridges					■				■	

[a]Data summarized from SCS descriptions (J. Iiams, personal communication, 1982).
[b]Strongly
[c]Trace
[d]Very
[e]Channery
[f]Stony

Soil Unit	Major Series Comprising Unit	Areal Coverage, %	Locations	Chemistry		Texture					Sources		
				Alkaline	Calcareous	Stony (Channery)	Gravelly, Cobbly	Loam	Sand	Clay	Residual	Transported	Eol
102	Rock outcrop	40			■								
	Persayo	25	gentle to steep slopes		■			■		■	■		
	Birdsley	15	slopes and saddles	■				■	■	■	■		■[a]
104	Rock outcrop	40	finely intermingled		■								
	Penrose	35			■		■	■	■		■		
105	Rock outcrop	55			■						■		
	Blazon	20	hills, ridges					■		■	■		
206	Youngston	35	flat, low					■		■		■	
	Lostwells	35	elevated					■	■	■		■	
	Binton	10	flat, level	■[b]				■		■		■	
206f	Youngston	30	finely intermingled					■				■	
	Apron	20						■	■			■	
	Lostwells	20						■				■	
231	Norte Variant	60	steep alluvial slopes				■	■				■	
	Pensare	15	cuestas, hills, ridges				■	■	■			■	
237	Uffens	30	terraces, fans					■				■	
	Muff	30	hill slopes					■	■			■	
	Fruita	10	terraces, fans					■				■	
242	Apron	35	slopes					■	■			■	
	Lostwells	30	gentle slopes					■	■	■		■	
	Apron, Alkaline phase	20	level floodplains	■[c]				■	■			■	
270	Blazon	50	hills and knobs		■			■		■	■		
	Patent	20	narrow valley fill					■			■		
271	Rock outcrop	15	hill, ridge tops										
	Persayo	60	hill slopes, escarpments					■		■		■	

Table 9-3 (Continued)

n	Rock Outcrops	Parent	Depth, in.		Color of Surface Unit				Slope, %	Comments
			Surface Unit	Total to Bedrock	Olive	Yellow	Brown	Gray		
		weathered from sandstone	4	10–20			■		6–45	
	shale, sandstone									
		weathered from shale	3	4–20		■	■		6–45	
		colluvium from sandstone	2	24			■		2–15	
		mixed alluvium sandstone	6	≥60			■	■	2–15	
		colluvium from shale	3	≥60			■		5–30	
		shale	2	19			■		3–45	
	shale									
		mixed alluvium	4	60			■		0–5	
		mixed alluvium	4	60			■		0–3	
		mixed alluvium	3	60			■		2–8	
		mixed alluvium	≥60	≥60					1–10	
		colluvium from sandstone	3	≥60		■	■		1–10	
		sandstone	3	34			■		2–15	
		clayey sandstone	2	12			■		6–50	
		sandstone	4	24			■		6–40	
		shale	2	19			■	■	6–45	
	schist, granite									
		schist, granite	3	14			■	■	5–130	
	schist, gneiss, granite									Contains up to 25% of other loamy and gravel loam series in intricate mixture.
		granite	3	10			■		1–12	15–45% pebbles and cobbles.
		alluvium from gneiss	3	≥60			■	■	2–20	
		schist, granite	3	25			■	■	1–12	

Soil Unit	Major Series Comprising Unit	Areal Coverage, %	Locations	Chemistry		Texture					Sources		
				Alkaline	Calcareous	Stony (Channery)	Gravelly, Cobbly	Loam	Sand	Clay	Residual	Trans-ported	Eoli
274	Oceanet	40	hill slopes					■	■			■	
	Rock outcrop	20	hilltops, ridges										
	Persayo	15	hill slopes, ridge sides					■		■		■	
277	Diamondville	45	fans, terraces					■				■	
	Forelle	25	fans, terraces					■				■	
	Patent	25	steep fans, backslopes					■				■	
298	Blazon	60	hills and ridges		■			■		■	■		
	Rock outcrop	15											
306	Youngston	35	floodplains and slopewash					■		■		■	
	Effington	25		■[b]				■	■			■	
	Fruita		slopewash, valley sides					■	■			■	
342	Apron	35	fans and valley fill					■	■			■	
	Wallson	30	fans and toeslopes					■	■			■	
	Worland	20	hills, sides of ridges					■	■		■		
372	Cragosen	40	ridges, hilltops				■	■		■			
	Carmody	25	hill and ridge slopes		■			■	■		■		
	Blazon	15	ridges, hillsides		■			■		■	■		
3109	Rock outcrop	40											
	Ashbon	35	irregular areas around exhumed ridges and knobs			■		■			■		
4109	Rock outcrop	40	exhumed knolls, ridges, and ledges										
	Mosroc	35	mountain ridges and hill slopes				■[d]	■	■		■		
2a32	Lupinto Variant	55	valley fill, fans				■	■				■	
	Bosler Variant	25	slopes, fans					■	■		■	■	

Table 9-3. Description of soil units for the Copper Mountain test site[a]

Rock Outcrops	Parent	Depth, in.		Color of Surface Unit				Slope, %	Comments
		Surface Unit	Total to Bedrock	Olive	Yellow	Brown	Gray		
	calcareous shale	3	16		■	■		6–45	
	alkaline shale	2	14	■				6–15	
limestone, sandstone	limestone	2	10–20			■		10–45	20–60% gravel surface cover
calcareous shale	calcareous shale	2	19			■	■	6–45	
	alluvium	4	≥60			■		1–6	
	alluvium	10	≥60			■	■	1–6	
	alluvium	3	≥60			■		1–6	
	mixed alluvium	6	60			■		0–3	
	mixed alluvium	4	60		■	■		0–3	
	mixed alluvium	2	60			■		0–3	
	alluvium from limestone	3	60			■		1–10	5–40% gravel, cobble surface
	weathered from limestone	2	10–20			■		6–20	20–60% gravel, cobble surface
	weathered from shale, sandstone	4	60		■	■		1–8	
	weathered from shale and sandstone	2	20–40	■		■		1–12	
shale, sandstone	mixed alluvium	3	60			■		1–5	High salt content locally
	mixed alluvium		60			■		1–10	
	alluvium	10	≥60			■	■	1–8	
	mixed alluvium	4	≥60					1–6	
	shale	2	≥19			■	■	6 40	
	shale/ alluvium	3	≥60			■		3–20	
shale									
	weathered from shale	3	20		■	■		3–45	

Section 9

Copper Mountain, Wyoming, Uranium Test Site Report

Contents

I. Introduction 9-1
- A. Purpose and Background of the Test Site Report 9-1
- B. Site Selection and Geologic Problems 9-1
- C. Remote Sensing Data Types and Methods of Study 9-2
- D. Plan of the Copper Mountain Report 9-2

II. General Description of the Test Site 9-2
- A. Location and Access 9-2
- B. Physiographic Description 9-4
- C. Climate 9-5
- D. History of Discovery and Development 9-5

III. Vegetation Cover 9-6

IV. Soil Types and Distribution 9-8
- A. Introduction 9-8
- B. SCS Soil Mapping 9-8

V. Regional Geology 9-9
- A. General Geology 9-9
- B. Stratigraphy 9-11
  - 1. Precambrian rocks 9-11
  - 2. Paleozoic rocks 9-11
  - 3. Mesozoic rocks 9-11
  - 4. Tertiary rocks 9-11
  - 5. Quaternary rocks 9-11
- C. Structure 9-11

VI. Geologic Relations of the Mineralization 9-20
- A. Relations to Structure 9-20
- B. Relations in the Granitic Rocks 9-20
  - 1. Nature of the granitic rocks 9-20
  - 2. Alteration in the granitic rocks 9-21

PRECEDING PAGE BLANK NOT FILMED

VII. Models of Ore Deposition 9-23
A. Supergene Ore-Genesis Model and Relationship to Surface Effects 9-23
B. Hydrothermal Ore-Genesis Model 9-26
C. Analysis of NURE Cores 9-26

VIII. Spectral Reflectance of Cover Types 9-29
A. Introduction 9-29
B. Spectral Properties of Alteration and Other Rock-Forming Minerals 9-29
C. Field-Acquired Spectral Reflectance Measurements 9-29
1. Spectra of rocks 9-29
2. Spectra of vegetation cover types 9-31
D. Masking Effects of Surface Coatings 9-33
1. Effects of lichen cover 9-33
2. Effects of iron-oxide/hydroxide coatings 9-33
3. Summary 9-34

IX. Remote Sensing Objectives, Models, and Approach 9-35
A. Introduction 9-35
B. Relationship of the Supergene Model to the Remote Sensing Model 9-36
C. Relationship of the Hydrothermal Model to the Remote Sensing Model 9-37
D. Approach 9-37

X. Interpretation of Multispectral Scanner Data 9-38
A. Introduction 9-38
B. Use of Aircraft Scanner Image Data for Geologic Mapping 9-40
1. Description of the geologic mapping 9-40
2. Detailed interpretation of the NS-001 image for the western portion of the southern line 9-44
3. Comparison of the NS-001 images with the geologic maps for specific areas 9-49
4. Subdivision of Quaternary gravel deposits using topographic and image data 9-54
5. Description of directional photometric effects in NS-001 images 9-61
C. Image Analysis and Interpretation of the Oxidized Granitic Terrain 9-64
1. Introduction 9-64
2. Analysis of M^{2}S image data 9-65
3. Analysis of NS-001 image data 9-72
4. Comparison of the M^{2}S and NS-001 data interpretations 9-74
5. Comparison of oxidation patterns with physiographic features 9-76
6. Comparison of oxidation patterns with the distribution of uranium-mineralization and Tertiary sediments 9-79
D. Soil and Vegetation Mapping Using Aircraft Data 9-87
1. Comparison of soil mapping with interpretation of NS-001 image data 9-87
2. Comparison of SCS soil map and M^{2}S CRC 9-87

3. Use of M²S 6/8 ratio density slice to obtain vegetation density estimates ... 9-87
E. Analysis of M²S Thermal Data ... 9-91
F. Interpretation of Landsat MSS Data ... 9-91
1. Introduction ... 9-91
2. False-color infrared composite ... 9-93
3. Color ratio composite ... 9-93
G. PC Images Based on Covariance and Correlation Matrices ... 9-96
1. Difference between covariance and correlation formulations ... 9-96
2. Comparison of images ... 9-96
3. Inferences about the calibration relationship ... 9-99

XI. Summary of Geology and Models ... 9-100
A. Geologic Setting of the Study Area ... 9-100
B. Uranium Mineralization and Relations to Oxidation ... 9-100

XII. Conclusions ... 9-101

Acknowledgments ... 9-103

References ... 9-104

Appendixes
A. Plant Species List for the Copper Mountain Test Site ... 9-107
B. Correspondence Between Soil Mapping and Geologic Mapping Units ... 9-109

Figures

Frontispiece. *Antilocapra americana* contemplating *Artemisia tridentata* atop Quaternary terrace gravels of Cambrian Flathead Sandstone and Archean granitic rock at Copper Mountain ... 9-x
9-1. Wyoming: (a) showing major basins, mountain ranges, and uplifts; (b) showing location of the Copper Mountain uranium test site ... 9-3
9-2. High-oblique aerial view looking north toward the East Owl Creek Mountains and the area surrounding the North Canning deposit ... 9-4
9-3. Temperature and precipitation data as a function of elevation for the Copper Mountain site ... 9-5
9-4. Distribution of vegetation community types for the Copper Mountain site ... 9-7
9-5. Soil map of the Copper Mountain site ... 9-9
9-6. Generalized lithologic map of the East Owl Creek Mountains ... 9-10
9-7. Fresh granitic outcrops northwest of the Arrowhead Mine (SW 1/4, Sec. 20, T40N, R92W) ... 9-21
9-8. Gem prospect pit in SW 1/4, Sec. 34, T40N, R92W, south of Canning Ranch ... 9-22
9-9. Weathered, hematite-stained granitic outcrops, Copper Mountain site (SW 1/4, SE 1/4, Sec. 33, T40N, R92W) ... 9-23
9-10. Cut exposing weathered layer in granites (SW 1/4, Sec. 29, T40N, R92W) ... 9-23

9-11. Chip samples from an exploration drill hole penetrating the weathered horizon (SW 1/4, Sec. 29, T40N, R92W) 9-23
9-12. Owl Creek Mountains and North Canning structural and genetic model for uranium deposition 9-24
9-13. Geologic map of the Canning–Fuller area at Copper Mountain showing locations of NURE drill holes 9-27
9-14. Lithologic sections for NURE drill holes DH-1 to DH-5 9-28
9-15. PFRS reflectance spectra of some granitic rocks, metasediments, and Tertiary sediments from the Copper Mountain area 9-31
9-16. Index map with locations of PFRS measurements and hand specimen sites for the Copper Mountain area 9-32
9-17. PFRS vegetation reflectance spectra for some plant types in the Copper Mountain area 9-33
9-18. Effects of lichen cover on spectral reflectance of granite rocks 9-34
9-19. Analysis, using a differential spectrophotometric method, of the substrate and surface iron-oxide/hydroxide coatings of altered and unaltered granite at Copper Mountain 9-35
9-20. North Canning prospect hypothetical cross section through weathered–altered layer 9-36
9-21. Index map showing approximate areas covered by the NS-001 and M²S scanner images at Copper Mountain 9-39
9-22. Index of geologic mapping, image interpretation, and approximate ground coverage of NS-001 and M²S scanners for the Copper Mountain area, Fremont and Hot Springs Counties 9-42
9-23. Geologic map of a portion of the Guffy Peak and Picard Ranch Quadrangles, Fremont County 9-43
9-24. NS-001 PC image covering western one-third of the southern flight line 9-45
9-25. Eigenvector correlation diagram for Copper Mountain NS-001 image, southern line, based on covariance matrix 9-46
9-26. NS-001 PC image of the southern flight line, Copper Mountain:
(a) western half 9-50
(b) eastern half 9-51
9-27. Interpretation of contact relations between the Wind River (Twr) and Wagon Bed (Twb) Formations at Location (E) as derived from the PC image of Figure 9-26(a) 9-55
9-28. NS-001 PC image of the northern flight line, Copper Mountain:
(a) western half 9-56
(b) eastern half 9-57
9-29. Subdivision of the Quaternary terrace gravel and alluvial deposits along the West Fork of Dry Creek 9-58
9-30. Profiles of gravel deposits Qgl to Qg5 projected into the cross section NS in Figure 9-29 9-59
9-31. Distribution of Qal, Qoa, and Qg deposits, from interpretation of the NS-001 PC image 9-60
9-32. DN values of the PCs V1, V2, V3, and V4 along the profiles A′B′ and AB in Figures 9-26(a) and 9-28(a) 9-62

9-33. Geometry of the scan and illumination directions: (a) along line AB; (b) along line A'B' 9-63
9-34. Green (Genus *Parmelia* (?)) and black (Genus *Cladonia* (?)) crustose and folios lichens covering north-facing sides of (a) weathered granitic outcrops (NW 1/4, Sec. 32, T40N, R92W); (b) a fresh granite boulder in Tertiary (?) fan gravel (NE 1/4, Sec. 27, T40N, R92W) 9-64
9-35. CRC of Landsat band equivalents of M^2S data for the Copper Mountain test site, subarea 1, northern line 9-67
9-36. CRC for subarea 2, southern line 9-68
9-37. Approximate viewing and illumination geometry for (a) subarea 1, M^2S, northern flight line; (b) subarea 2, M^2S, southern flight line 9-69
9-38. Representation of the degree of iron oxidation in subarea 1 by an eight equal-level density slice of the M^2S band-ratio 4/6 9-70
9-39. Relationship between reflectance ratio 0.56 μm/0.64 μm as determined from PFRS measurements and DN values for the eight equal-level density slice image (Figure 9-38) 9-71
9-40. Distribution of oxidized granitic outcrops from the M^2S CRC and ratio density slice images of Figures 9-35, 9-36, and 9-38 9-73
9-41. Distribution of oxidized granitic outcrops from the NS-001 PC images of Figures 9-26 and 9-28 9-75
9-42. Photomosaic view looking southeast from Tertiary Wagon Bed gravel terrace in the East Fork of Dry Creek (predominantly SW 1/4, Sec. 26, T40N, R92W) 9-76
9-43. Outline of the interpreted physiographic elements and mapped geologic units along the range front covering portions of the Guffy Peak, De Pass, Picard Ranch, and Gates Butte Quadrangles 9-78
9-44. High-oblique aerial view looking south southwest along the East Fork of Dry Creek 9-79
9-45. Outcrops of bouldery granite terrain displaying fractures surrounded by rounded (rotten granite) grus-mantled terrain 9-80
9-46. Outline of red–magenta–black areas of the M^2S density slice rectified to aerial photograph base 9-81
9-47. High-oblique aerial view looking north up the West Fork of Dry Creek 9-82
9-48. Distribution of mines, prospect pits, cuts, and uranium accumulations in the Canning and Fuller resources 9-83
9-49. Canning and Fuller resources (in granitic rocks) and minor uranium prospects (in granite and Tertiary sediments) plotted with respect to the distribution of Wagon Bed and Quaternary sediments and surface oxidation patterns, obtained from the M^2S image, in the granitic rocks 9-84
9-50. Canning and Fuller resources (in granitic rocks) and minor uranium prospects (in granite and Tertiary sediments) plotted with respect to the distribution of Wagon Bed and Quaternary sediments and surface oxidation patterns, obtained from the NS-001 image, in the granitic rocks 9-85

9-51. A portion of the soil map of Figure 9-5 superimposed on the M²S CRC of subarea 1 ... 9-88
9-52. Density slice of the M²S band-ratio 6/8 ... 9-89
9-53. Calibration line for the M²S band-ratio 6/8 ... 9-90
9-54. M²S thermal and albedo composite, Copper Mountain ... 9-92
9-55. Landsat MSS scene covering central Wyoming and Copper Mountain ... 9-94
9-56. Interpretations of area A from Figure 9-55 ... 9-95
9-57. CRC of Landsat MSS data for area B in Figure 9-55 ... 9-97
9-58. Comparison of PC images prepared from the correlation and covariance matrices for the southern line of NS-001 data at Copper Mountain ... 9-98

Tables

9-1. Spectral coverage of multispectral scanners ... 9-2
9-2. Dominant species for the vegetation communities as outlined in Figure 9-4 ... 9-8
9-3. Description of soil units for the Copper Mountain test site ... 9-11
9-4. Vegetation types occurring within the soil units at the Copper Mountain site according to SCS mapping ... 9-17
9-5. Stratigraphy of the Copper Mountain area for formations and other map units mentioned in the text ... 9-18
9-6. Mineralogical characteristics of hematitic and limonitic altered granite rocks of Copper Mountain ... 9-21
9-7. Copper Mountain core analysis for the NURE drill holes ... 9-28
9-8. Important spectral reflectance features for propylitic alteration and rock-forming minerals for the Copper Mountain site ... 9-30
9-9. Copper Mountain NS-001 northern line covariance matrix, August 1979 ... 9-46
9-10. Color key for PC image (Figure 9-24) ... 9-47
9-11. Contingency table used for analysis of independence of the gravel units Qgl to Qg5, based on the first four PCs, PC1 to PC4 ... 9-61
9-12. Confidence levels, %, of separation for class pairs from Table 9-11 ... 9-61
9-13. Overflight parameters for NS-001 mission at Copper Mountain, Mission 407, August 29, 1979 ... 9-64
9-14. Bandpasses of the Bendix 11-channel M²S scanner ... 9-65
9-15. Overflight parameters for Bendix 11-channel M²S mission at Copper Mountain, Mission 383, August 4, 1978 ... 9-66
9-16. Field site descriptions, PFRS ratio values, and M²S ratio (density slice) image colors for sites in Archean granitic rocks and sediments used in construction of calibration curve ... 9-72
9-17. Vegetation, density, and image data for 6/8 M²S density slice ... 9-90
9-18. Explanation of unit symbols in Figure 9-54 ... 9-91

9-19. Landsat MSS scenes 9-93
9-20. Descriptions of units in Landsat MSS interpretation (Figure 9-56) 9-96
9-21. Copper Mountain NS-001 southern line correlation matrix, August 1979 9-99
B-1. Examples of geologic and soil unit correspondences 9-109

Plate[1]

9-1. Copper Mountain, Wyoming: Correspondence between NS-001 image interpretation and soil unit mapping

[1]The plate is contained in Part 3 (envelope) of *The Joint NASA/Geosat Test Case Project.*

Frontispiece. *Antilocapra americana* contemplating *Artemisia tridentata* atop Quaternary terrace gravels of Cambrian Flathead Sandstone and Archean granitic rock at Copper Mountain (photograph by C. Conel)

Section 9

Copper Mountain, Wyoming, Uranium Test Site Report

I. Introduction

A. Purpose and Background of the Test Site Report

The Joint NASA/Geosat Test Case Project was undertaken to evaluate the utility of remote sensing methods for geologic mapping and resource assessment and exploration. A description of the Project's aims and history are given in the Project Description, Section 1. While the uranium test case program was in practice carried out by Jet Propulsion Laboratory (JPL) personnel, a key element of the program was the cooperation between NASA and the participating Geosat companies: NASA provided aircraft overflight data for the site and additional ground-based observations, while the Geosat companies were to provide geologic and subsurface data on the deposits and the privilege of access to the test site property.

This section describes remote sensing and field investigations carried out at Copper Mountain, Wyoming. The operating company at Copper Mountain is the Rocky Mountain Energy Company (RME), Denver, Colorado.

B. Site Selection and Geologic Problems

The Copper Mountain uranium test site was selected as a prototype district thought to represent a vein-stockwork type of deposit in granitic rocks. Significant concentrations of uranium were also present in a Tertiary-age regolith overlying the Precambrian granite terrane and in Tertiary sediments at various places in and above the Tertiary regolith. These uranium deposits were believed to have been derived from leaching of nearby granitic rocks and Tertiary sediments and were possibly the source of the more extensive mineralization in the granite at the 100-m depth.

Some of the criteria governing the site choice were:

(1) Both the gravels and fractured igneous host rocks are exposed at the surface throughout the area, thus offering the possibility of observing uranium-related alteration or other effects at the surface.

(2) The fractured granitic occurrences of uranium mineralization at depth were drilled extensively as part of a mineral development program by RME. Thus the geology of the resource, its controls, and its distribution were well known.

(3) A paper describing the geology of the occurrence had been published (Yellich et al., 1978). In addition, the geology of eight contiguous fifteen-minute quadrangles had been mapped (1:24,000 scale) and were either published or scheduled for publication shortly (Thaden, 1978, 1979, 1980a–1980e, 1981). These maps provided a basis for detailed geologic evaluation of the image data.

(4) The site had been the subject of an extensive grid-sampling (0.5 by 0.5 km) geochemical and geophysical study conducted as part of the National Uranium Resource Evaluation (NURE) Program by the Bendix Field Engineering Company (Bramlett et al., 1979a, 1979b). This program was intended to assess "halo" effects surrounding uranium ore bodies.

(5) The Copper Mountain test site was wholly controlled by RME, a Geosat member company. The problem of land access was thus simplified.

Two principal geologic and image interpretation problems were evaluated: (1) use of multispectral scanner data for geologic mapping throughout the test site, and (2)

detailed geologic and image analysis of oxidation effects in the granites as these might relate to the distribution of uranium mineralization.

C. Remote Sensing Data Types and Methods of Study

The remote sensing data available for study consist of aircraft multispectral scanner data, including data from the Bendix Modular Multispectral Scanner (M^2S) and the NS-001 Thematic Mapper Simulator, Landsat Multispectral Scanner (MSS) satellite data, and ground-based spectral reflectance measurements with the JPL Portable Field Reflectance Spectrometer (PFRS). In addition to these sources, stereoscopic color or color-infrared photographs were acquired for portions of each flight line covered by the scanners.

The predominant effort in this study was devoted to analysis of the aircraft-acquired multispectral scanner data. The 11-channel M^2S scanner covers the spectral range of 0.33 to 1.1 μm in 10 bands, and the NS-001 covers the spectral range of 0.45 to 2.35 μm in seven bands, as well as a broadband thermal channel at 10.4 to 12.5 μm (Table 9-1). The scanners measure reflected or emitted radiation from the Earth's surface. These measurements include atmospheric effects that should be eliminated from the data before they are displayed and analyzed.

Aircraft data from both the M^2S and NS-001 scanners cover an extended portion of Copper Mountain and the adjacent northern part of the Wind River Basin, roughly as depicted in Figure 9-1(b). The total area covered by these scanner data amounts to approximately 832 km^2 (320 mi^2). Figure 9-2 shows an aerial view of the test site and surrounding areas and gives the approximate location of the North Canning uranium resources.

Table 9-1. Spectral coverage of multispectral scanners

Band	Landsat MSS, μm	M^2S, μm	NS-001, μm
1		0.33–0.44	0.45–0.52
2		0.44–0.49	0.52–0.60
3		0.49–0.54	0.63–0.69
4	0.5–0.6	0.54–0.58	0.76–0.90
5	0.6–0.7	0.58–0.62	1.00–1.30
6	0.7–0.8	0.62–0.66	1.55–1.75
7	0.8–1.1	0.66–0.70	2.08–2.35
8		0.70–0.74	10.4–12.5
9		0.76–0.86	
10		0.97–1.065	
11		8.0 –13.5	
IFOV[a]	80 m	11 m	12.5 m

[a] Instantaneous field of view.

The scanner data can be evaluated qualitatively for their utility in solving geologic or other problems. This can be done by comparing the patterns of separable colors obtained in different image renditions with geologic or soils maps, or by using photogeologic interpretations prepared for special purposes. Stereoscopic color aerial photographs (resolution ~1 m) form the best basis for "resolving" detailed geologic or physiographic features when field checking is not possible.

The PFRS data were used in this study to define the nature of surface reflectance properties. In general the images were interpreted without resorting to a calibration transformation, in which PFRS data are used to establish a reflectance scale for the scanner radiances. Calibration is required if the scanner data are to be used to study surface reflectance directly.

D. Plan of the Copper Mountain Report

The main body of this report is concerned with geologic descriptions, image interpretation, and reflectance measurements. Included as appendixes to this section and to the Lisbon Valley, Utah, Uranium Test Site Report, Section 8, are ancillary field data and analyses of problems relating to the interpretation of remote sensing data as radiance data. Most of the appendix examples were originally developed for the Lisbon Valley test site. Repeated reference is made to these results in explanation of the procedures that were applied to the Copper Mountain multispectral surveys.

II. General Description of the Test Site

A. Location and Access

The Copper Mountain uranium test site is 55 km northeast of Bonneville and 40 km southeast of Thermopolis, in the northern part of Fremont County, Wyoming (Figure 9-1). The test area relating to uranium mineralization lies at the base of Copper Mountain on the northern perimeter of Wind River Basin and covers most of the southern half of T40N and R92W. The area examined during the course of this study includes portions of T40N, R91W, R92W, and R93W, and T39N, R91W, R92W, and R93W, as shown in Figure 9-1(b). Scanner images from various aircraft scanner systems are available over this enlarged area. These data are informative when compared to detailed geologic maps of the area (Thaden, 1978, 1979, 1980a–1980e, 1981) and are useful for assessment of the geologic mapping potential of NS-001 and M^2S scanner data.

The Copper Mountain study area is reached by light-duty, unpaved roads. From U.S. Highway 20 near Bonneville, the road follows Badwater Creek east for 3 mi, then

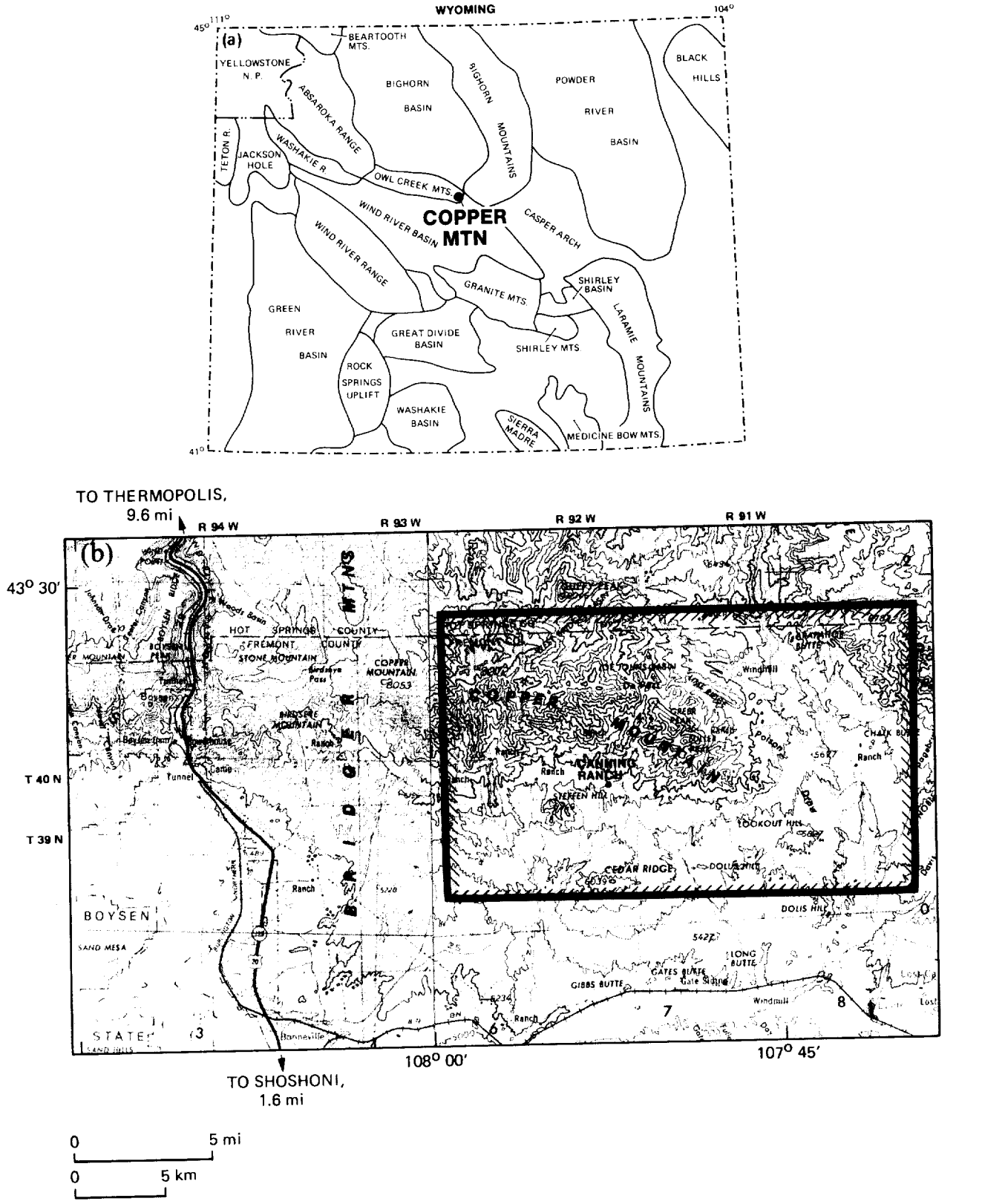

Figure 9-1. Wyoming: (a) showing major basins, mountain ranges, and uplifts; (b) showing location of the Copper Mountain uranium test site outlined by heavy hachured lines

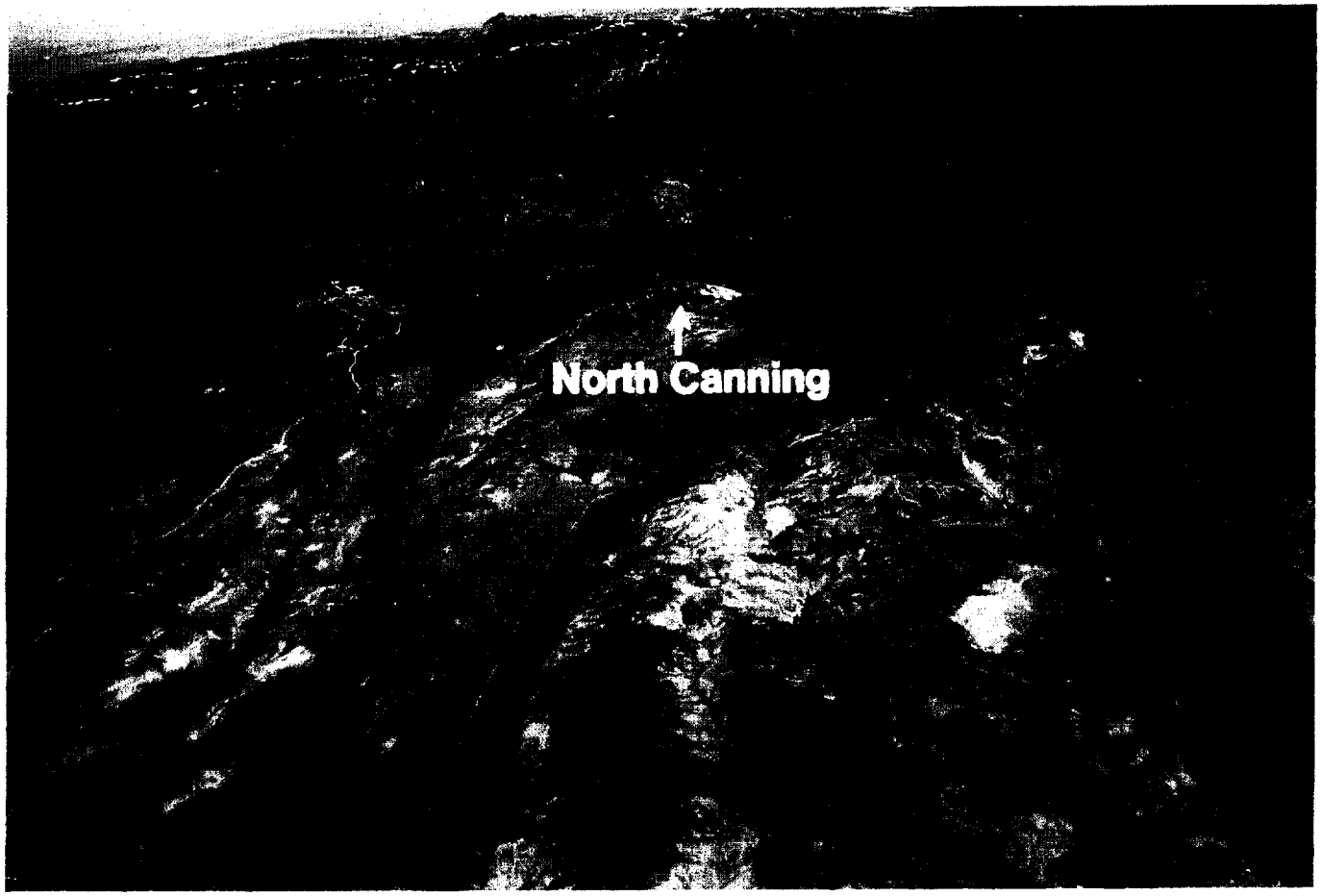

Figure 9-2. High-oblique aerial view looking north toward the East Owl Creek Mountains and the area surrounding the North Canning deposit. White area to the far left of the arrow is the Arrowhead Mine. (Photograph courtesy of RME.)

turns northeast, eventually following the East Fork of Dry Creek. Improved dirt roads leading to Fuller Ranch (SE 1/4, Sec. 32, T40N, R92W) and Canning Ranch (NE 1/4, Sec. 34, T40N, R92W) allow access to the test site. A few unpaved and unimproved dirt roads provide access to some parts of the study area. Some of these secondary roads are passable by automobile in dry weather.

B. Physiographic Description

The Owl Creek Mountains of central Wyoming lie in the northern Rocky Mountain physiographic province. The Wind River Basin to the south (Figure 9-1a) lies at the northern edge of the Wyoming Basin province, with the division between these two provinces passing along the range front.

East of Wind River Canyon the mountains are called the Bridger Mountains (or East Owl Creek Mountains), and the central, elevated ridge is named Copper Mountain. The Bridger Mountains form the northern boundary of the Wind River Basin and are divided from the Bighorn Mountains to the north and northeast by Bridger Creek. The Owl Creek tectonic uplift extends to Bridger Creek on the east and includes both the Owl Creek Mountains and the Bridger Mountains (Copper Mountain).

The Bridger and Owl Creek Mountains form an E - W-trending, asymmetrical anticline overturned to the south and broken on the southern flank by thrust and normal faulting. In the study area the anticline has been breached to expose a core of Precambrian igneous and metamorphic rocks. The range is flanked on the north and northeast by hogbacks of Paleozoic and Mesozoic strata. To the south, Tertiary sediments in the Wind River Basin lap onto the granites and Paleozoic strata. The axial crest of the range (Copper Mountain) lies at an elevation of 2300 m or

greater with accordant peaks reaching to 2500 m. A widespread, high-level erosion surface slopes gently outward from the axis before dropping off abruptly to the basin to the south, which lies at an elevation of 1700 to 1850 m. Remnants of intermediate erosion levels are preserved along the range front. Some of these remnants are capped by Tertiary sediments and by early Quaternary fan gravels. The sediments and fan deposits have been partially removed by erosion, and the mountain front is dissected by streams flowing south to the basin. Some, and perhaps all, of these major drainages in the range front (Dry, Hoodoo, and Tough Creeks, for example) follow paleodrainages established in a pre-Middle Eocene erosion cycle. The older channels may host additional Tertiary deposits not yet stripped by erosion.

In the Precambrian granitic terrane of the Owl Creek Mountains, minor drainages are exclusively controlled by conjugate fractures (or fault) systems; individual streams often follow zigzag courses across such terrain, abruptly changing direction by 90° or more, reorienting from one fracture set to another.

C. Climate

The climate of the Copper Mountain area is semiarid with cold winters and relatively hot summers: temperatures may fall to −55° F during January and February and climb to above 100° F during July and August. Figure 9-3 gives average temperature and precipitation data as a function of elevation.

D. History of Discovery and Development

Tertiary-age uranium mineralization occurs in crushed granitic rock along major normal faults bounding the eastern part of the Owl Creek Uplift on its southern side. Mineralized zones of possible economic interest, which have been outlined by an extensive RME drilling program, occupy portions of the southern halves of Secs. 27, 28, and 29 in T40N, R92W. The total area of potential mineral interest under study by RME included portions of adjacent granitic rock comprising the Canning Stock and portions of the Tertiary sediment cover bounding the granitic rocks to the south. The principal region for uranium interest lay between lat. 43°22′30″ N and 43°27′30″ N, and long. 107°48′45″ W and 107°55′ W, or an area of 25 mi^2 (65 km^2).

Yellich et al. (1978) have provided the following summary of exploration and development at Copper Mountain.

> In 1953, prospecting for uranium in the Copper Mountain area encountered shallow surface occurrences. Uranium minerals are associated with both the

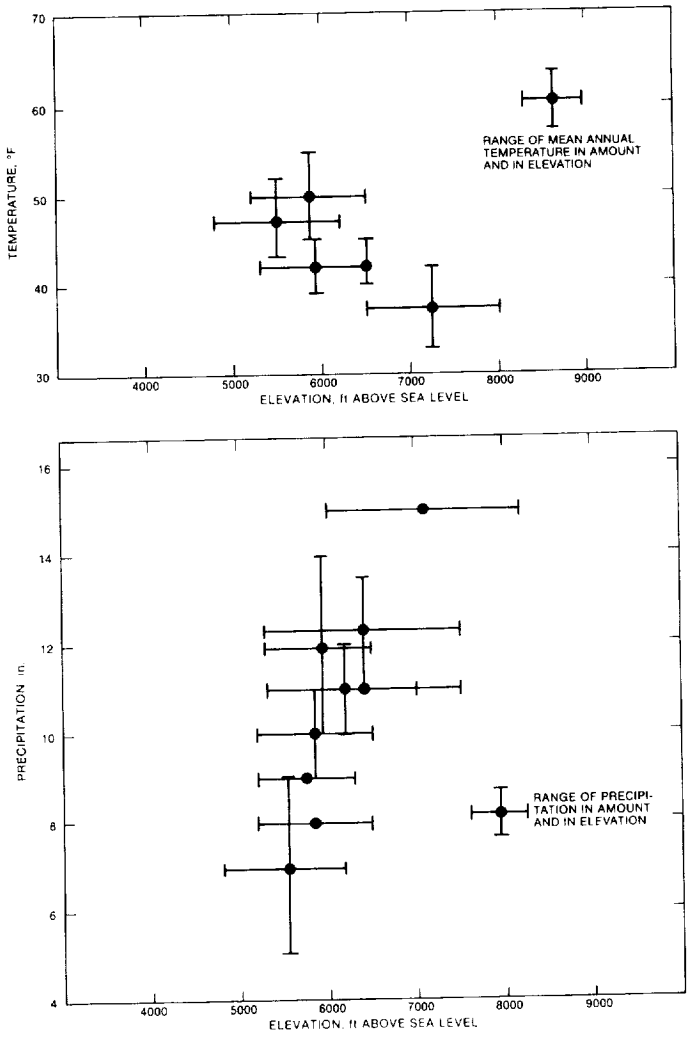

Figure 9-3. Temperature and precipitation data as a function of elevation for the Copper Mountain site (U.S. Department of Agriculture Soil Conservation Service, 1981)

> Eocene Tepee Trail [Wagon Bed] Formation and the Precambrian rocks. Identified uranium minerals are autunite, meta-autunite, coffinite, uraninite, sooty pitchblende and uranophane. Production began in 1955 (Osterwald et al., 1966) at the Little Mo–Arrowhead Mine and continued to 1964 when Susquehanna Western mined at an average grade of 0.15% U_3O_8. Western Nuclear continued production from 1968–1970. Uranium found within the Tepee Trail [Wagon Bed] Formation is associated with hematitic alteration 'halos' and abundant carbon trash. Asphaltic material is reported in the mining area.
>
> Oxidized and unoxidized uranium minerals within the sands and silts of the Tepee Trail [Wagon Bed] Formation were mined at the Bonanza Mine. A reported

resource of 30,000 tons of undetermined grade remains in the ground (Osterwald et al., 1966).

An occurrence of schroeckingerite is found associated with the Tepee Trail [Wagon Bed] Formation in proximity to the granite surface. Shallow prospect pits intercepted low-grade uranium minerals within coarse-grained arkosic sandstone. Exploration by dozer was done with no production (Osterwald et al., 1966).

Tertiary occurrences are also reported at the Day–Berger Prospect where dozer exploration found uranium minerals associated with bentonitic claystone and freshwater limestone. Limited production has been reported. Approximately two miles north of the Day–Berger occurrence, uranium minerals occur at the Hesitation Prospect within a claystone and sandstone matrix surrounding granitic, mafic and quartzite boulders. A shallow 15-foot shaft was sunk with subsequent exploration by dozer. The Tertiary debris has accumulated within a north–south fault valley with Precambrian granites on either side. No production is known (Osterwald et al., 1966).

The De Pass Mine was sporadically active between 1879 and 1918 with copper, gold, and silver concentrates being shipped. Geologically, the mine is within a brecciated fault zone of biotite and hornblende schists, granite and diorite intrusions with some diabase dikes. Copper minerals occur in quartz veins as carbonate (malachite and azurite) and sulfide (bornite, chalcopyrite and chalcocite) minerals. Uranium was reported from dump material in 1954 and was later mapped in the old workings. Uraninite was identified with uranium assay values of 1.03%, 0.70% and 0.41% U_3O_8 within a brecciated quartz carbonate rock. No uranium production is known (Grutt, 1954).

The Last Hope Prospect was initially evaluated by shallow drilling and a 468-foot prospect drift which allowed evaluation of the mineralized Eocene Tepee Trail [Wagon Bed] Formation and the Precambrian bedrock immediately beneath the sediments.

Uranium prospecting has continued throughout the southern flank of the Owl Creek Mountains from 1950 to the present with pits, shafts, drifts and adits being driven, as well as rotary drilling and coring. Production approached approximately 500,000 pounds of uranium from 1955–1970.

Rocky Mountain Energy began land acquisition in 1960 with veins as the exploration target. Detailed underground mapping of the Last Hope Prospect indicated the association of uranium with fractures in the mafic rocks. Asphaltic residue was reported dripping from the back of the drift with uranium confined to fractures in the mafic dikes, as well as dispersed in the granites and overlying Eocene Tepee Trail [Wagon Bed] Formation. Surface mapping of the area aided projection of the complex structural features and the variable rock types beneath the Tertiary cover (Voss, 1973). A truck-mounted radon gas analyzer was used to further outline target areas, but the initial results were inconclusive as a result of swampy ground conditions in the test area to the north of the Last Hope Prospect. A hole drilled near the Last Hope Prospect to investigate supergene enrichment in the faulted granite intercepted mineralized rock within the intensely altered, structurally prepared, granitic and metamorphic rocks of the North Canning area.

III. Vegetation Cover

The Copper Mountain test site lies within the southwestern temperate region of the northern Rocky Mountain physiographic province. The southwestern temperate region supports Sierra Madre flora (Benson, 1979), represented in the area by species typical of Northern Juniper–Piñon Woodlands (Great Basin Woodland) and sagebrush deserts.

Generalized maps of the vegetation community types present on and around the Copper Mountain area, together with detailed plant species lists, were compiled as part of an environmental impact assessment by RME. The general distribution of plant communities, obtained without regard to vegetation density, is given in Figure 9-4. The dominant species present in each of these vegetation communities are given in Table 9-2. The complete distribution of plant species present throughout the area is listed in Appendix A. Four plant communities, whose distributions are governed physiographically, are recognized:

(1) Sagebrush–grasslands. This community occupies alluvial fans, outcropping Tertiary sediments, and grus-covered granitic outcrops, mainly on pediments along the base of the mountains. It also occurs along sides of major drainages situated at higher elevations in areas of moderate to low soil development. Estimates of the plant cover for these areas were made during July 1981, using transects of 10-m length at sites I and II in Figure 9-4. At site I the average sage cover was found to be 26 percent with variations from 13 to 54 percent. Clump grasses provided an average cover of 5 percent with variations of 0 to 24 percent. Site II sustained an average clump grass cover of 27 percent with density of clumps as high as 53 percent. The areal density of sage and grass cover is quite heterogeneous in gen-

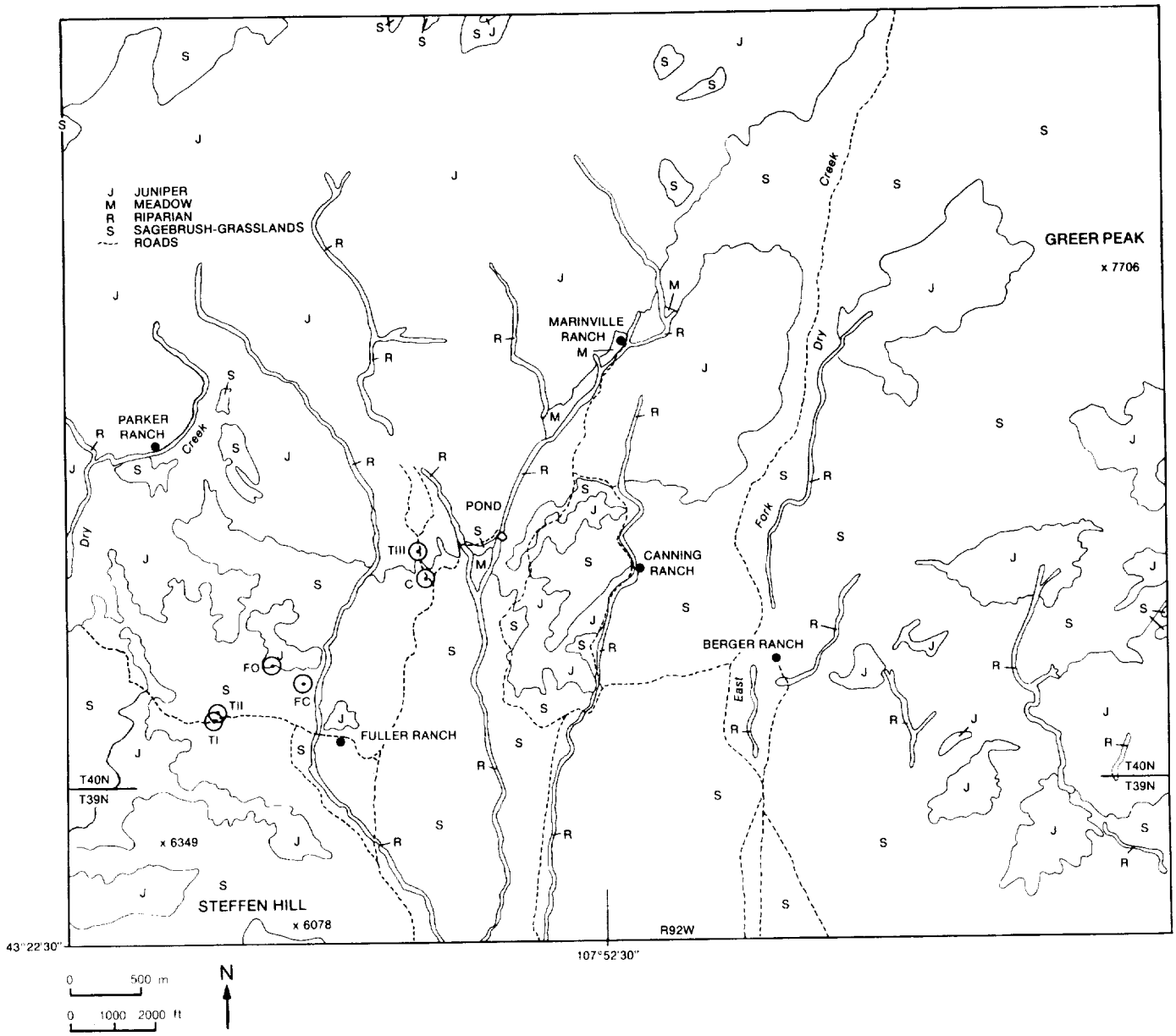

Figure 9-4. Distribution of vegetation community types for the Copper Mountain site (vegetation community map courtesy of RME)

eral. For example, ridge areas may have less than 1 percent sage cover, which increases to nearly 100 percent in proximity to intermittent stream courses.

(2) Juniper woodlands. This community occupies gravelly and bouldery alluvial slopes and moderate to steep rocky outcrops of limestone, sandstone, and granitic rocks; the tree cover is highly variable. Local dense stands of these trees are found along the unconformity between the Cambrian and Precambrian rocks, and in narrow stream drainages incised in high-standing remnant Quaternary gravel deposits. Transect measurements at a site of moderately dense cover of this type where the influences may be easily recognized in the multispectral scanner data (site III, Figure 9-4) showed a mixed assemblage predominantly of sagebrush and juniper (*Juniperus osteosperma*) cover to be composed of 14 percent sagebrush (range, 0 to 31 percent) and 26 percent juniper (range, 11 to 36 percent), with a total vegetation cover from these two types of 33 percent (range, 12 to 55 percent).

Table 9-2. Dominant species for the vegetation communities as outlined in Figure 9-4[a]

Vegetation Community	Dominant Species	Common Name
Sagebrush-Grasslands	*Artemisia pedatifida*	Birdfoot sagewort
	Artemisia tridentata	Big sagebrush
	Bouteloua gracilis	Blue grama
	Stipa comata	Needle-and-thread grass
Juniper	*Agropyron spicatum*	Bluebunch wheatgrass
	Artemisia tridentata	Big sagebrush
	Bouteloua gracilis	Blue grama
	Juniperus osteosperma	Utah juniper
Riparian	*Agrostis exarata*	Spike bentgrass
	Artemisia tridentata	Big sagebrush
	Populus augustifolia	Narrowleaf cottonwood
Meadow	*Agropyron smithii*	Western wheatgrass
	Agrostis exarata	Spike bentgrass
	Bromus inermis	Smooth brome

[a]Data courtesy of R. Arjal, RME, 1982.

(3) Riparian woodlands. This community occupies the bottom of modern watercourses. In these areas the cottonwood canopy cover may approach 60 to 70 percent. Dense growths of sagebrush are found adjacent to these streams and in more scattered distribution beneath the dense deciduous tree cover.

(4) Meadows. This community is found along alluviated stretches of modern waterways where surface drainage is slow or where there is ponding of groundwater. In these areas, which are generally small, the cover of grasses and sedges is essentially complete.

IV. Soil Types and Distribution

A. Introduction

The distribution of soil types throughout the Copper Mountain test site is related to the (1) parent rock material (substrate), (2) topography, (3) climatic factors, and (4) Quaternary and Tertiary history of the area. Each soil unit supports a characteristic vegetation assemblage. The factors governing soil development probably extend back to pre-Eocene time, especially over areas that have been recently (Holocene–Pleistocene (?)) exhumed by erosion from beneath Eocene (Wagon Bed) and Quaternary sediment cover. The present distribution of soils represents the superposition of Holocene climatic conditions upon an early Tertiary weathering and erosion history.

A grus-covered red surface extends over the pre-Eocene paleodrainage system, and it may be a manifestation of the exhumed (pre-Eocene) weathering profile and superimposed modern weathering processes. The distribution of soil units mapped by the Soil Conservation Service (SCS) follows the distribution of paleodrainages, and individual soil units locally correspond to older erosional surfaces. The distribution of these soil units differs from the distribution of Quaternary, Tertiary, and Precambrian rocks as determined by conventional geologic mapping.

The aircraft multispectral scanner data have been used to map the distribution of surface iron oxidation throughout the area. These oxidation patterns closely follow the distribution of erosion surfaces and mantled cover in the paleodrainages, and reflect in part the distribution of soil units that developed on erosion surfaces of the Precambrian granitic rocks.

Uranium accumulations in Precambrian rocks throughout the area are intimately related to the distribution of residual Tertiary sediment cover. The present distribution of Tertiary sediments is closely tied to the distribution of pre-Eocene topographic erosion surfaces. The distribution of soil units emphasizes the Quaternary and early Tertiary physiographic history of the East Owl Creek (Bridger) Mountains.

B. SCS Soil Mapping

In the summer of 1981, the Lander, Wyoming, office of the SCS completed a soil mapping project covering portions of the Wind River Basin, Fremont County, Wyoming. Mapping (1:24,000 scale) included the Arapahoe Butte, Lysite, De Pass, Gates Butte, Guffy Peak, Picard Ranch, Birdseye Pass, and Bonneville Quadrangles, and covered most of the area overflown by aircraft scanners. The Copper Mountain uranium test site covers portions of the De Pass, Gates Butte, Guffy Peak, and Picard Ranch Quadrangles.

Figure 9-5 shows the distribution of soil units compiled from the SCS photographic-based mapping over the Copper Mountain test site. Each of the 26 soil mapping units that have been recognized within the area consists of a complex of two or more soil series. Table 9-3 summarizes important descriptive properties of the SCS's composite mapping units. Vegetation types associated with the soil units are summarized in Table 9-4. Table B-1 (Appendix B) provides examples of correspondence between the soil and geologic mapping units. The geologic units are as given by Thaden (1978, 1979, 1980a-1980e, 1981).

Soil units in the test site represent complex assemblages genetically derived as residual deposits from the subjacent geologic units or as horizons developed on colluvial and alluvial materials. Soils on the colluvium usually represent

Figure 9-5. Soil map of the Copper Mountain site. Soil mapping units designated by number and number–letter combinations are described in Table 9-3. (Compiled from 1:24,000 aerial photograph mapping data by SCS.)

a limited range of source materials (e.g., the Uffens Series of unit 237, Table B-1), whereas soils on alluvium in streams or older terrace gravels represent weathering of mixed and diverse rock types (e.g., unit 2a32, Table 9-3). Soils with significant eolian components have not been mapped by the SCS.

The array of soil textures represented is diverse, ranging from stony and channery soils (such as unit 2g72) to clay loam (such as unit 105). Clay and fine-textured soils tend to develop from parent materials with large silt or clay size fractions (Wagon Bed claystone and sandstone), whereas those of coarse, stony texture are derived from gravel deposits or granitic bedrock. The thickest soils develop in alluvial deposits (unit 206), terrace gravel (units 231 and 2g11), or older alluvium (unit 237) with low slopes, while thin soils and weathering rinds (?) are found on rocky exposures (unit 3109) or on loosely consolidated materials with steep slopes (unit 372).

V. Regional Geology

A. General Geology

The geology of the Copper Mountain test site and surrounding areas has been mapped by Thaden (1978, 1979, 1980a–1980e, 1981) and summarized by Yellich et al. (1978). The regional geologic map of Figure 9-6, modified

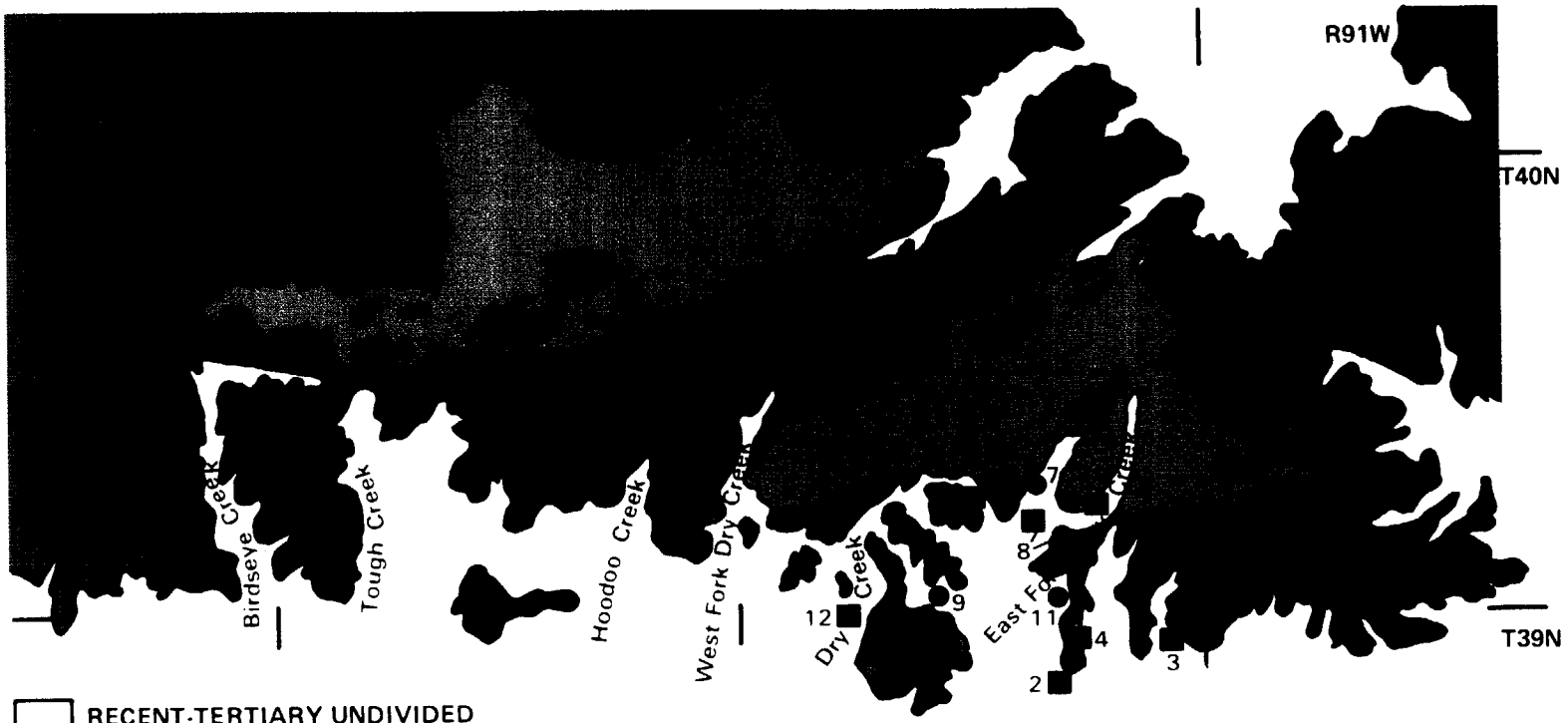

Figure 9-6. Generalized lithologic map of the East Owl Creek Mountains, showing the general distribution of rock types and the distribution of oxidized granitic facies as obtained from field mapping by RME geologists (map from Yellich et al., 1978)

from Yellich et al. (1978), depicts the general distribution of rock units and the occurrences of mineralized areas and important mines throughout the area. Characteristics of the formations discussed in the text are listed in Table 9-5.

B. Stratigraphy

1. Precambrian rocks. The Copper Mountain test site is underlain predominantly by the Canning Stock, a Precambrian crystalline intrusive consisting of quartz monzonite, microcline–albite granite, granite, syenite, and a two-mica granite (Bramlett et al., 1980). A 3-km-wide belt of older metasedimentary schists and gneisses of widely ranging composition strikes mostly N 50° E to N 80° E and dips primarily to the south across the northern part of the site. As mapped by Thaden, metasediments are only locally in fault contact with granitic rocks. Elsewhere the contacts are intrusive (sometimes cataclastic) with the intrusive rocks locally forming a rectangular megascopic box work in the metamorphic country rock. Metasediments are altered to migmatitic gneisses where they are next to large bodies of granitic rocks or where they are included in the granites as xenoliths.

Metasedimentary rocks (Table 9-5) are the oldest rocks in the area, with ages estimated at 3100 to 3500 m.y. The granitic intrusives have been dated at 2640 to 2720 m.y. The last Precambrian intrusive event recorded in the area consists of a N–NE-trending mafic dike swarm that has been dated at 1900 to 2100 m.y. (Condie, 1967).

The Precambrian metasediments and igneous rocks are overlain unconformably by the Middle Cambrian Flathead Sandstone, and above this formation by a succession of marine and nonmarine sediments of Paleozoic and Mesozoic age. Paleozoic sediments bound the exposures of igneous and metamorphic rocks along the eastern and northern limits of the study site.

2. Paleozoic rocks. The Paleozoic section above the basal Flathead Sandstone includes siltstone, sandstone, and limestone of the Middle Cambrian Gros Ventre Formation; limestone and siltstone of the Upper Cambrian Gallatin Formation; Bighorn Dolomite of the Upper and Middle Ordovician age; dolomite, limestone, and sandstone of the Mississippian Madison Limestone; and sandstone, siltstone, and limestone of the Middle and Lower Pennsylvanian and Upper Mississippian Amsden Formations. The uppermost Paleozoic formations present are represented by the Tensleep Sandstone of the Middle Pennsylvanian age, and the Permian Park City Formation composed of limestone and siltstone.

3. Mesozoic rocks. Mesozoic formations are exposed mostly in the Arapahoe Butte Quadrangle to the northeast of the main study area, and in the Birdseye Pass Quadrangle to the west. The Mesozoic rocks include siltstone of the Lower Triassic Dinwoody Formation; siltstone and claystone of the Lower Triassic Red Peak Formation; Alcova Limestone of the Triassic age; sandstone, siltstone, and claystone of the Upper Triassic Crow Mountain Sandstone; siltstone, claystone, limestone, and sandstone of the Middle Jurassic Gypsum Springs Formation; sandstone, limestone, and claystone of the Upper and Middle Jurassic Sundance Formation; and sandstone of the Upper Jurassic Morrison Formation.

4. Tertiary rocks. To the south, granitic rocks exposed on an erosion surface at the base of the mountain (and including Paleozoic sediments where they are exposed in Steffen Hill) are covered by an overlapping sequence of Lower Eocene sediments of the Wind River Formation, and by the overlying Upper and Middle Eocene rocks of the Wagon Bed (Tepee Trail) Formation. The Wind River Formation consists of siltstones, sandstones, and claystones with coal beds, with some claystones representing volcanic (bentonitic) material. The Wagon Bed Formation is predominantly volcaniclastic claystone and sandstone composed of vitric and crystal vitric tuffs with locally derived detritus; included in the basal part are boulders of Paleozoic and Precambrian rocks shed from the mountains along paleostream channels.

According to Thaden (1980d) the Wagon Bed was deposited on an extremely rough paleotopographic surface and possibly buried the mountains at one time. Most of the Wagon Bed has now been eroded away, leaving only the resistant basal boulder accumulations and other fine detrital deposits in large paleodrainages or in graben.

5. Quaternary rocks. Quaternary sedimentary rocks form elevated alluvial fan and remnant terrace deposits as well as deposits along major and minor contemporary drainages at the base of the mountains. The clast composition and size of these deposits are highly variable from place to place, reflecting variations in source material within the range as well as conditions of deposition.

C. Structure

Copper Mountain, with its core of Precambrian granitic and metamorphic rocks flanked on the north by Paleozoic sediments, is the result of southward thrusting of basement rocks during the Laramide orogeny. The toe of the thrust

Figure 9-23. Geologic map of a portion of the Guffy Peak and Picard Ranch Quadrangles, Fremont County. Letters and numbers are places referred to in the text.

e. Structure. Throughout the map area of Figure 9-23, Tertiary and Quaternary sediments onlapping the igneous and metamorphic rocks in the mountains to the north are broken by a series of NW- to nearly E–W-trending, steeply dipping normal and reverse faults. On the western side of the area the Wind River and Wagon Bed Formations are exposed in a series of horsts and graben bounded by such faults, with Wind River sediments occupying the horsts and Wagon Bed rocks filling the low areas; 750 to 1500 m west of the West Fork of Dry Creek (Sec. 2, T40N, R93W, and Sec. 11, T39N, R93W), the Wind River sediments are buried beneath the Wagon Bed cover. These boundary faults continue eastward through the Wagon Bed sediments and are covered by Quaternary terrace gravels or more recent alluvium along the West Fork of the Dry Creek.

The Cedar Ridge Fault (Figure 9-23) is a major north-dipping normal fault trending roughly northwest along the southern portion of the area. The measurable displacement is on the order of 200 m (Thaden, 1980c, 1980e). The Cedar Ridge Fault evidently produced high-standing terrain to the south throughout Wagon Bed time (Upper and Middle Eocene), permitting Wind River sediment to be reworked into the Wagon Bed section and contributing to a large thickness of these later rocks to the north of the fault.

Faulting has spanned the interval from the Lower Eocene to the present. Many of the structures are covered by gravel deposits. Some, however, cut the gravel caps (Secs. 10 and 11, T39N, R92W). Faulting has continued into the present, with offset of the asphalt pavement on the highway 2 km south of Lysite at least twice since 1969 (Thaden, personal communication, 1981).

2. Detailed interpretation of the NS-001 image for the western portion of the southern line

a. PC images. Various CRC and PC images of the Copper Mountain NS-001 data were prepared for geologic mapping studies and for analysis of uranium-related surface-oxidation problems. Visual inspection of these image products led to the selection of the PC images as presenting the greatest diversity of rock units and vegetation patterns. Two versions of PC images were subsequently analyzed, those based on computations from the covariance matrix for the northern line and those estimated from computations from the covariance matrix for the southern line (Figure 9-22). The northern-line rendition is used here because of the superior presentation of suspected uranium-related alteration effects in the granitic rocks. As pointed out in the Lisbon Valley, Utah, Uranium Test Site Report, Section 8, Appendix C, and as discussed below by example, the PC method has the advantages that: (1) it is an easily implemented linear reduction (data compression) technique, (2) it is largely independent of atmospheric and instrumental factors, (3) images are transformed (contrast-stretched) in such a way as to separate groups of points related to individual units as much as possible (i.e., the space is dilated by the contrast stretch), (4) the PC transformation is representative of the average scatter of points in character space without regard to specific knowledge of where major clusters reside, and (5) higher-order components (second, third, etc.) are mostly independent of simpler surface albedo effects.

Probably the greatest disadvantage of this method is that it tends to reduce surface resolution by introduction of noise into the image data. This noise component is largest for the higher PCs because the scatter in these principal directions approaches or falls below the inherent noise level of the scanner data themselves. The components may also be difficult to interpret in terms of ordinary spectral reflectance.

Figure 9-24 is a PC image covering the western one-third of the southern NS-001 flight line at Copper Mountain corresponding to the area shown on the geologic map (Figure 9-23). In this rendition the second (V2 = blue), third (V3 = red), and fourth (V4 = green) PCs have been employed. The covariance matrix used for the transformation, given in Table 9-9, has been estimated from a sampling of radiance data for the entire northern flight line, and then applied to the southern as well as northern image tracks.

An appraisal of the "physical" significance of these components can be made approximately by utilizing an eigenvector correlation diagram for the covariance matrix (Figure 9-25). The procedure is similar to that used for analysis of the PC images for the Lisbon Valley, Utah, Uranium Test Site Report, Section 8. The eigenvector correlations for the present data in fact show great similarity to those derived for transformation I of the Lisbon Valley NS-001 data given in Figure C-2, Section 8. Thus the second and third components reflect a substantial contribution of vegetation, while the fourth component appears to include a contribution predominantly from rocks exposed at the surface. The details of this analysis have been presented in Appendix C and will not be repeated here.

b. Color relations in the PC image. Direct interpretation of color PC composite image data in terms of average surface spectral reflectance is ordinarily not possible because the transformed scanner radiances are linear combinations

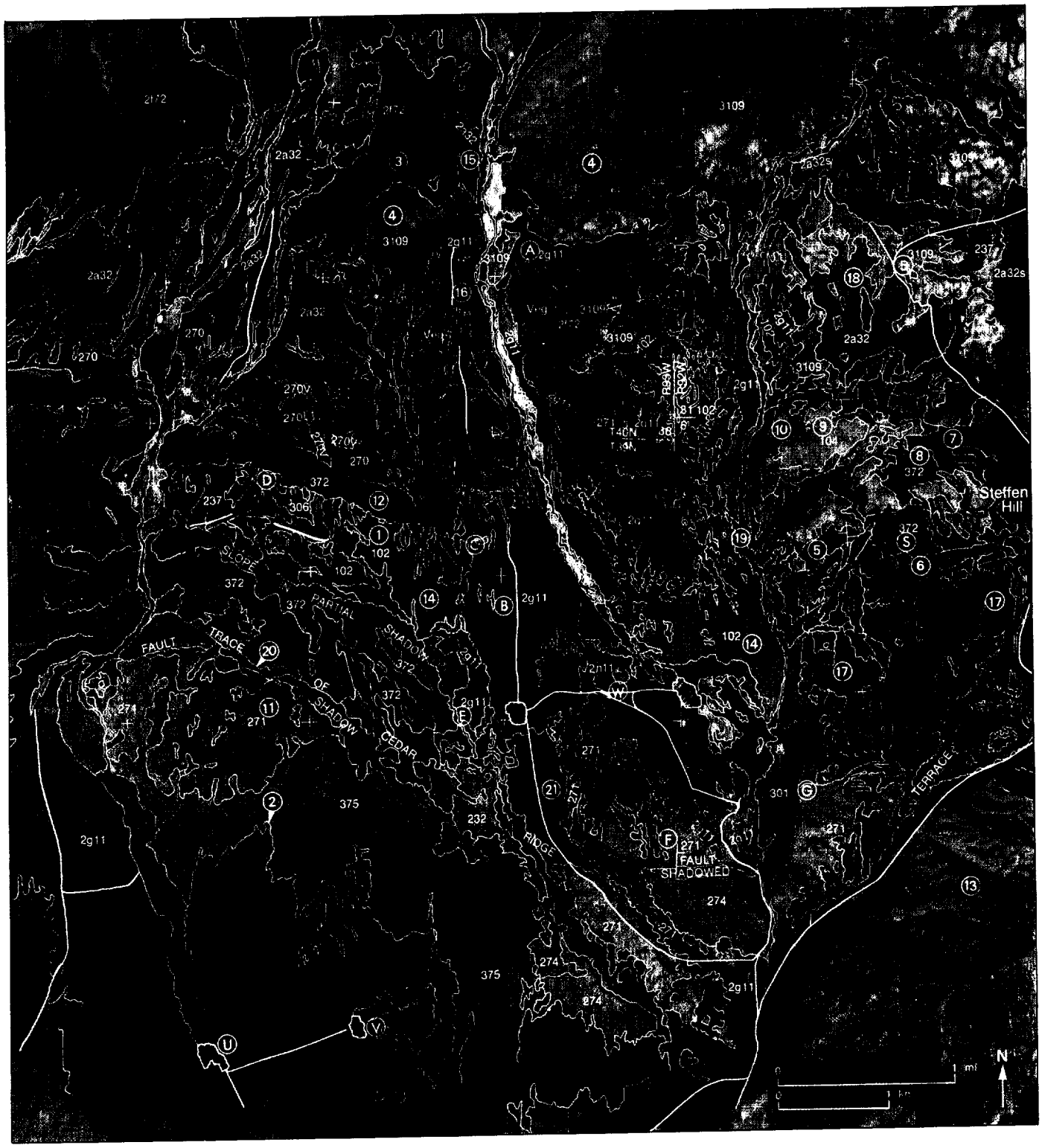

Figure 9-24. NS-001 PC image covering western one-third of the southern flight line (Mission 407, August 29, 1979). Image prepared using seven channels of data. PCs have the following color assignments: V2 = blue, V3 = red, and V4 = green. Numbers such as 274 and 2g11 refer to soil units given in Figure 9-5. Refer to index mapping and image interpretation (Figure 9-22) for location of area. Circled letters and numbers are places referred to in the text.

Table 9-9. Copper Mountain NS-001 northern line covariance matrix, August 1979 (2,255,400 samples)

1413.47						
1475.19	1579.02					
1479.70	1599.83	1750.18				
1202.41	1341.97	1440.72	1480.74			
1081.59	1199.35	1310.78	1349.41	1330.13		
1231.05	1327.23	1471.03	1243.22	1258.88	1455.61	
1343.89	1448.62	1603.88	1308.74	1276.05	1512.30	1751.60

of the original bands and are further rescaled by linear or nonlinear transformations for display as images. Thus the spectrum represented by a p-dimensional PC could only be recovered if all p-components were available. The data from such an image thus cannot ordinarily be inverted to the reflectance spectrum, even if numerical equivalents of the colors were provided. The strategy for spectral analysis of such images must involve the additional steps of reexamination of the image radiance data, and a calibration of these data in terms of ground reflectance. This additional step will not need to be made here, since the discrimination properties of the NS-001 data are of principal interest.

To aid interpretation of the PC images presented, a simple color key (Table 9-10) is given delineating the correspondence between geologic unit or cover type (principally vegetation) and image color. These are qualitative descriptions, but approximate numerical values for the PCs can be determined by reference to a three-component color additive chart (Figure 12-32, Lost River, West Virginia, Petroleum Test Site Report) if such numerical values are needed.

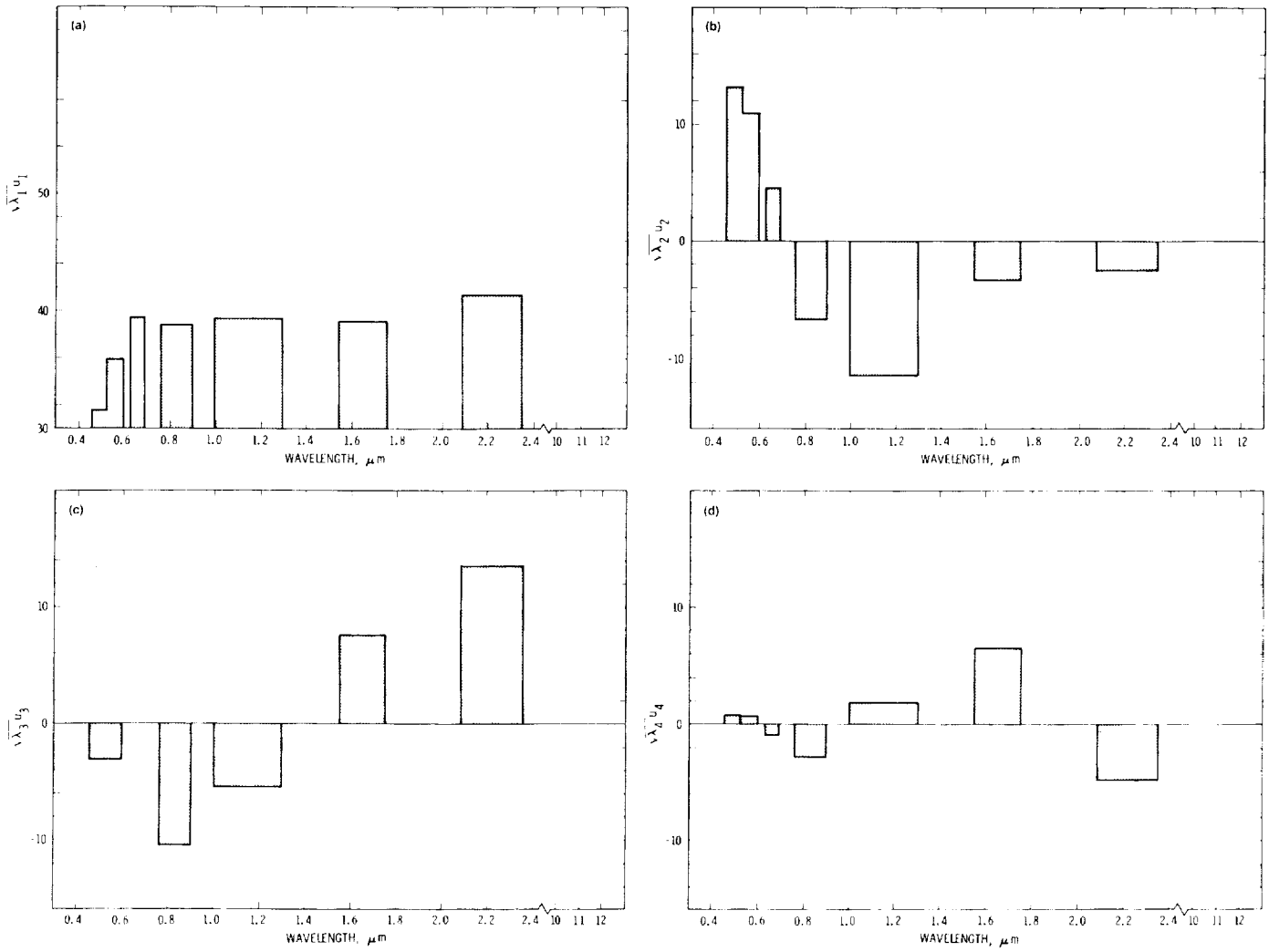

Figure 9-25. Eigenvector correlation diagram for Copper Mountain NS-001 image, southern line, based on covariance matrix

Table 9-10. Color key for PC image (Figure 9-24)[a]

Geologic Unit or Cover Type[b]	Colors on PC Image
Vegetation – Green grasses, shrubs, or deciduous trees with high leaf density and strong green pigmentation. Appear deep ruby-red or dark gray-green on false-color infrared photographs	Deep, moderate, or light blue colors correlate with deep to sparse red and dark gray-green on color-infrared photographs
Vegetation – Dense cover of juniper (*Juniperus osteosperma*) with interspersed sage and grass.	Blue to bluish-purple and bluish-black
Vegetation – Conifer (limber pine) and deciduous mixture with deep shadows in canyon bottoms.	Deep blue
Vegetation – Overbank areas of modern stream. No specific interpretation possible.	White (saturated)
Deep shadows.	Dark brownish-black
Highly reflecting buff, tan, or white outcrops (Twb, Twr).	Gray-green to olive-green
Dark gray-brown alluvial flats (Qg).	Red-brown, olive-brown, and brown
Dark gray and brown outcrops with tan and reddish chromolithofacies (Twr).	Red and red-orange, greenish-red-mottled where bedded tan or reddish units present
Dark gray and dark gray-brown outcrops (Ag).	Deep orange and deep reddish-orange mixed with brown, and saturated red
Bright orange and tan rocky outcrops (oxidized Ag).	Pink
Light tan and light brown rocky outcrops (unoxidized Ag).	Green, yellow-green, and yellow-gold
Medium and dark brown outcrops (Cf, Cgv, Cg).	Magenta, red, and orange-red
Light gray and buff gray outcrops (Mm).	Blue-green

[a]The color assignments for PCs are V2 = blue, V3 = red, and V4 = green.

[b] Qg Quaternary terrace gravel
Twb Wagon Bed Formation
Twr Wind River Formation
Mm Madison Limestone
Cg Gallatin Formation
Cgv Gros Ventre Formation
Cf Flathead Sandstone
Ag Archean granite

c. Plotting of interpretative boundaries. Interpretative boundaries presented on the overlay of Figure 9-24 for the most part are drawn surrounding areas of different color on the image. Many of these color differences are obvious, such as the red-green boundary at ① in Figure 9-24. Others are more subtle, such as at ②, requiring considerable study to establish. Not all interpreters would locate such boundaries in the same places, and the boundaries drawn could, in any case, differ in detail depending upon the precise cosmetic stretches and color assignments employed in constructing the images. Experience shows that differences in interpretation by more than one observer usually hinge on how image units are lumped together in the interpretations, not upon the ability to distinguish between the possibilities present.

d. Stratigraphic and lithologic problems. Comparison of the image interpretation (Figure 9-24) with the geologic map (Figure 9-23) discloses a substantial similarity between the two. Nearly all of the extensive Quaternary, Tertiary, Paleozoic, and Precambrian formations depicted on the geologic map can be mapped separately in the image data, and some formations may be further subdivided into distinct surface units. From examination of aerial photographs these additional subdivisions may represent unmapped intraformational beds, vegetation cover,

slope wash deposits, or partly shaded slopes. The actual stratigraphic significance of any of the image units so depicted must usually be worked out by field studies or examination of aerial photographs. However, lateral continuity is easily established for most of the formations mapped.

Precambrian rocks. Locally, Precambrian metasediments, (3), are easily distinguished from enclosing granites of the Canning Stock, (4), based on differences in image color. The granitic rocks themselves are divided into unoxidized green, (4), and oxidized (weathered) pink, (5), phases. This subdivision of the granitic terrain has been studied in relation to the uranium deposits and will be described in detail below.

Paleozoic outcrops. The only exposures of Paleozoic rocks present in the restricted image and map areas of Figures 9-24 and 9-23 occur in Steffen Hill. As examples, the Cambrian Flathead Sandstone, (6), and the Gros Ventre, (7), and Gallatin, (8), Formations are depicted in red and red-orange colors and the Mississippian Madison Limestone in green, (9). Talus deposits from topographically higher Madison outcrops, (10), obscure the subjacent Gallatin rocks.

Tertiary formations. Extensive exposures of Wind River Formation sediments are found south of the trace of the Cedar Ridge Fault. Two image units are depicted: a red and red-green mottled unit, (11), corresponding to dark-brown and gray interfingering outcrops, and a green unit, (13), that represents generally lighter-colored sandstone. Red and red-green mottled units at (11), (12), and (13) correspond to chromolithofacies as mapped by Thaden (1980e). While some general subdivisions of Wind River rocks have been made that correspond to these facies as mapped, the stratigraphic intermixing is in general at too fine a scale, and the color differences between units too subtle, to be depicted in these image renditions.

Sediments of the Wagon Bed Formation are nearly uniformly green, (14), throughout the image area except where the formation contains external boulder trains of metamorphic rock types derived from adjacent Archean metasedimentary outcrops, (15). Green units of Wagon Bed and green units of Wind River sediments may be difficult to separate. Compare, for example, areas (13) and (14). Some of this similarity results from reworking of Wind River sediments into the Wagon Bed.

Quaternary deposits. In general, Quaternary deposits, including pediment-capping terrace gravels, older alluvium, and modern stream deposits, are easily separable in the image data. Quaternary fan and terrace gravels, (16), along the West Fork of Dry Creek may be broken into units of differing age based on elevation differences and image color patterns. These subdivisions will be discussed below in greater detail. In general these deposits can be related to source rock type based on the image colors, especially where vegetation cover is not too great. As examples, predominantly dark metasedimentary clasts occur at (16) and Cambrian sandstone and siltstone gravels at (17). Colluvial or older alluvial deposits, (18), representing slope wash from granitic terrain, are easily separated from the adjacent source outcrops in this area covering green facies of the Wagon Bed Formation. Modern alluvial deposits along watercourses are often heavily vegetated, appearing deep blue in the image. Where unvegetated, these deposits may also reflect the source rock types, such as at (19), where oxidized granitic and Cambrian sandstone units contribute to the deposits.

Fault structures.[1] Fault structures can be recognized in the Precambrian, Paleozoic, and Tertiary rocks, and a few examples of these will be described here. Major faults bounding horsts and graben in the highly colored Tertiary section located in the west-central part of the image area (location (1) is such a boundary) are clearly depicted by color contrasts in the adjoining image units. Faults confined to the Wind River Formation, such as the Cedar Ridge Fault at (20), are less conspicuous, but are in part delineated by alignments of ridges and valleys cut in the soft Tertiary rocks.

Numerous normal fault structures divide the Paleozoic and Precambrian rocks in Steffen Hill into a series of lensoid and rectangular fault slices. Some of these structures may be traced in a broken fashion across the inlier by virtue of the strong color contrasts in rock units across them.

Faults or fractures confined to the granitic rocks are usually aligned with conspicuously straight stream courses; most such canyons are sharply V-notched in cross sections, are partly in shadow, and contain thick stands of conifers and deciduous trees. These conjugate alignments, marked by blue traces on the image, stand out against the usual green and yellow-gold colors of the background in unfractured granitic rock.

Recognition of faulting that may cut the Quaternary deposits is more problematical, because these sand and gravel units tend to appear homogeneous on the images.

[1]This term replaces "lineament" in the present report and describes features that almost always relate to fractures, whether or not displacement can be recognized in the bedrock.

Places can be found however (near (21)) where enhanced growths of vegetation (perhaps senescent grasses) are thought to occur throughout the Quaternary gravel outcrop. Vegetation produces dark (blue to black) hues in the image colors at these places. The darkened zones coincide broadly with steeply dipping normal faults of a few meters' displacement that are mapped cutting the Wagon Bed above. Thus the images suggest enhanced growths of vegetation in the thin covering of Quaternary gravels that coincide with fault patterns recognized in the older unit. These fault patterns follow the Cedar Ridge Fault or faults branching from it. The vegetation patterns easily outlined on the image probably mark the damming of groundwater along the fault.

3. Comparison of the NS-001 images with the geologic maps for specific areas[2]

a. Introduction. While geologic quadrangle mapping of the area covered by digital aircraft scanner data was accomplished during 1967 through 1974, the NS-001 data became available only in the spring of 1981, and have been used retrospectively in an attempt to confirm or to deny geologic interpretations found in earlier published maps. Mapped relations between surface units tend to be confirmed by the images.

Preliminary study of the images demonstrated immediately that the pixel size of about 12 m is a vast improvement over that of the Landsat MSS images, making it possible to compare the images with the geology at the relatively large scales ordinarily of most interest to geologists. More importantly, the images render rock facies in highly saturated, contrasting colors, which are not normally attained by any of the color reversal films (e.g., the Kodak 244x series or the GAF D/200 or D/500 films), however carefully filtered or sparse the vegetation cover.

Interpretation of the images must allow for certain inconsistencies in the colors due both to natural and to mechanical effects. Of greatest importance are:

(1) A color change of single stratigraphic units beyond any small area that may be due to electronic and/or photographic manipulation or drift, but that cannot be attributed to a change of facies.

(2) A darkening on north-facing slopes, as on the south walls of canyons, due to an extraordinarily oblique sun angle or to the presence in these places of exceptionally heavy vegetation.

(3) A darkening, even to black, caused by the presence of heavy vegetation at any place, but especially in stream valleys and other places where the water table is at or near the surface.

(4) Color changes due to differences in the type of vegetation growing on a single lithology, as between grassy areas and areas vegetated by the big sagebrush (*Artemisia tridentata*).

(5) Color changes in areas of Quaternary or Holocene surficial cover due to gradation over short distances from thick to thin deposits, or gradation from nearly pure deposits derived from the weathering of a single homogeneous stratigraphic unit to deposits that contain a blend of a laterally changing mixture of materials derived from heterogeneous sources.

(6) Color changes in the Quaternary deposits along the range front that signify differences in source material.

(7) Color changes that can be attributed to certain kinds of chemical changes in the rocks, such as the argillization of some rock units in an area by hydrothermal activity or by reaction with adjacent rock units of contrasting chemical nature; ferrugination by deposition of iron oxides, hydroxides, or sulfates from the presence of acid surface waters or groundwaters; or a valence change of iron in ferruginous minerals from the ferrous to the ferric state.

b. Comparisons

Various stratigraphic examples. Erosion and removal of soft Tertiary units which lap onto the Owl Creek Mountains in this area, and which likely buried the mountains at one time, have resulted in a well-developed pediment surface that subsequently was covered by a deposit of cobbly gravel. The gravel is derived from erosion of indurated older rock units in the mountains, composed mostly of granitic and metamorphic rocks. Continuing erosion dissected the pediment and resulted in a series of younger, lower, partially developed pediments, each of which is also capped with gravel. In Figure 9-26(a) (also Figures 9-23 and 9-24 where sites (A) through (G) are denoted), the deposit at (A) is a pediment gravel cap of metamorphic clasts on the highest pediment level, as are also the similarly olive- to brown-colored pediment caps to the west at (A1). Still other capping gravels occur at (A2), where they are too thin to be mapped. These deposits are more extensive on the image than on the geologic maps because geologic mappability was defined as a thickness of at least 1.5 m, whereas the image data depict distributions that are effectively of vanishing thickness.

[2]This section was prepared mostly by R. E. Thaden, 1981.

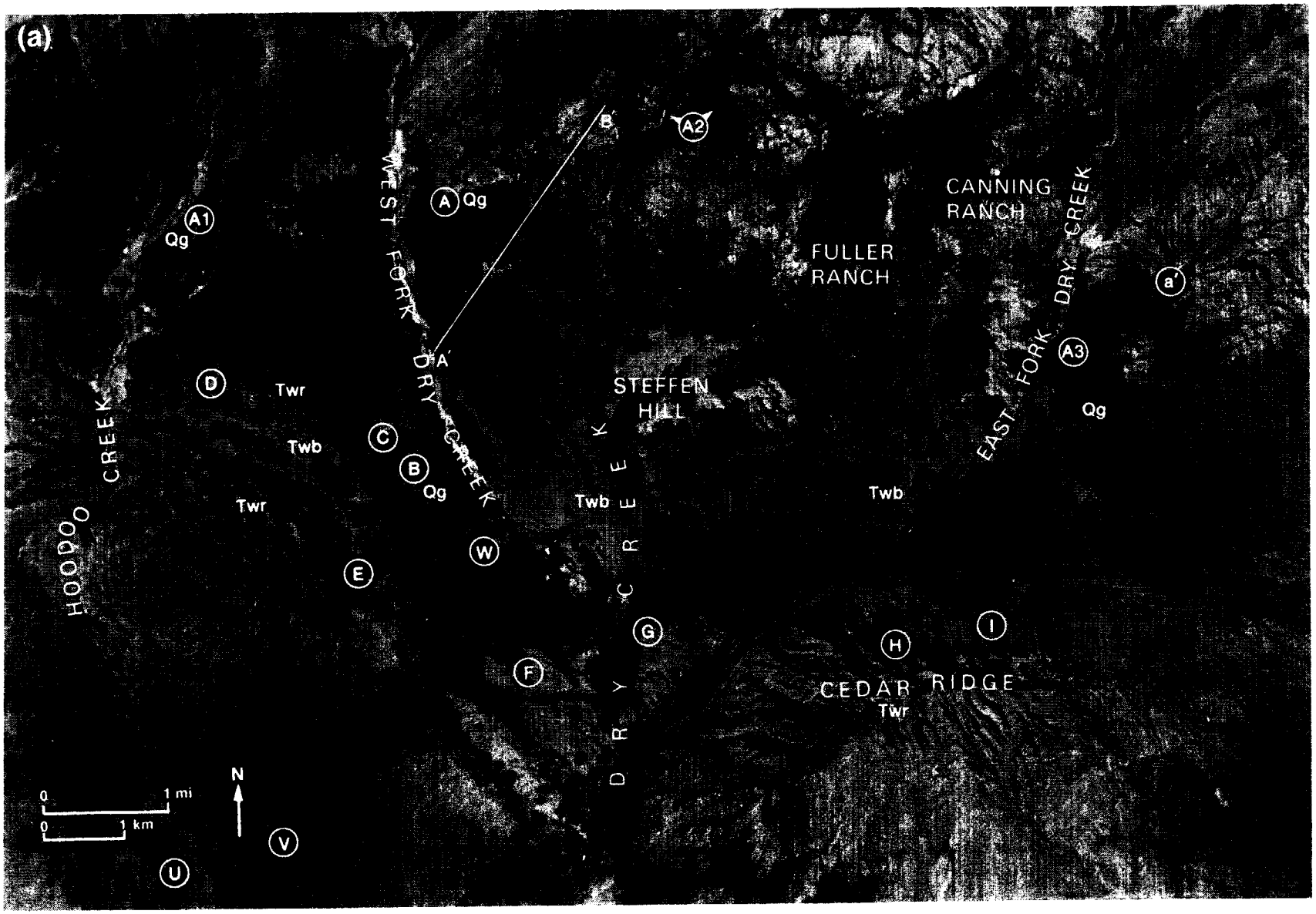

Figure 9-26. NS-001 PC image of the southern flight line, Copper Mountain: (a) western half. Image prepared using seven channels of data. PCs have the following color assignments: V2 = blue, V3 = red, and V4 = green. Letters refer to places discussed in the text.

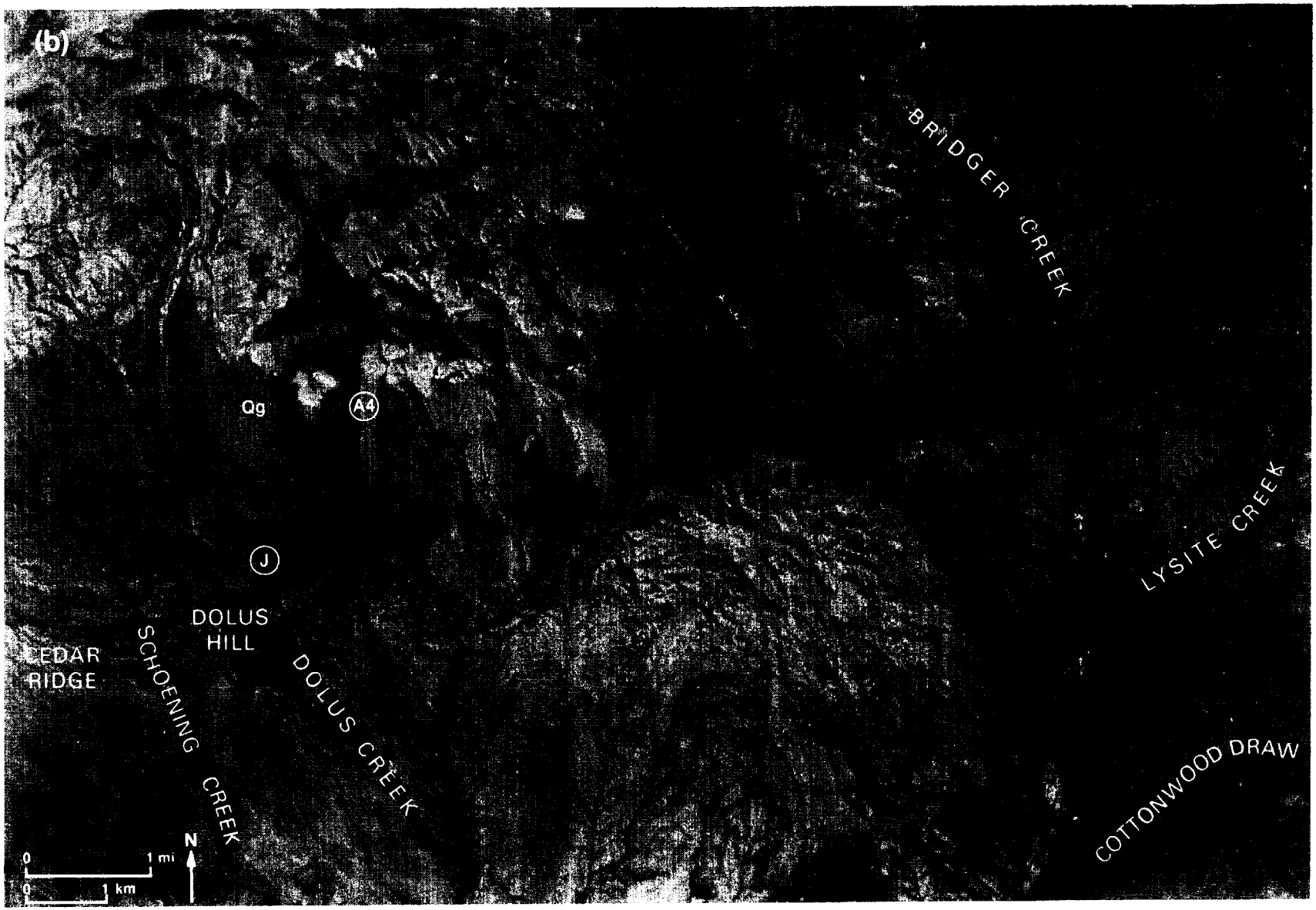

Figure 9-26. NS-001 PC image of the southern flight line, Copper Mountain: (b) eastern half. Image prepared using seven channels of data. PCs have the following color assignments: V2 = blue, V3 = red, and V4 = green. Letters refer to places discussed in the text.

Although a pediment cap of metamorphic clasts on a lower pediment at Ⓑ appears degraded in color relative to those at and west of Ⓐ, it too exceeds the definition for conventional geologic mapping. Only south of Ⓑ is it eroded to extreme thinness in many places, with only a thin or single layer of gravel remaining on the pediment surface. The color change is related to incorporation in the gravel of (1) large quantities of fine-grained material of nonmetamorphic origin, (2) fluvial detritus derived from the Wagon Bed Formation and exposed on the scarp at the southern edge of the higher pediment surface to the north, and (3) mostly windblown material carried in from the west through the topographic low of the West Dry Creek graben. These rather quartzose materials apparently add a yellow component to the olive-brown color of the metamorphics, a yellow similar to the yellow of nearby outcrops of such other quartzose units as the Wind River Formation and the granite. At sites Ⓐ3 (Figure 9-26a) and Ⓐ4 (Figure 9-26b), the contributions of different source materials change the color of the geologic unit represented. Thus at Ⓐ3 the gravel deposits are predominantly composed of granitic clasts, while at Ⓐ4 the gravels received contributions from (green) Paleozoic limestones higher in the range. The Quaternary gravel deposits may also be subdivided in the image data. These problems are discussed separately below.

West of Ⓑ is the West Dry Creek graben. The graben is filled with volcanic ash-fall materials of the Late Eocene Wagon Bed Formation (Twb). This formation is rendered mostly in green and medium olive-green throughout the images. The graben is bounded on the south by a highland of faulted Early Eocene Wind River Formation and on the north by a horst, Ⓒ, also of Wind River, which also stands topographically high. This unit is rendered mostly in rose-red and yellow-green, with purple on partially shadowed slopes. The faulting that produced these structures took place (or was reactivated) during deposition of the Wagon Bed Formation which, in this area, was deposited on top of the Wind River. Consequently the Wagon Bed contains in many places, and especially in places proximate to outcrops of the Wind River, large quantities of detritus derived from the Wind River by gravity and fluvial wash. The Wagon Bed also contains, here and elsewhere throughout its belt of outcrop, detrital materials derived from other pre-Wagon Bed units. Mostly this detritus was deposited as thin fan wedges of quartz-rich sand in the enclosing Wagon Bed ash beds.

What is of interest in the West Dry Creek graben area is the relative confirmation by the images of the contacts mapped by the geologist of these rock units that, because of the detritus included in the Wagon Bed, look very much alike in many places on the ground. North of Ⓒ the horst gradually is buried to the east under a cover of Wagon Bed and pediment deposits. The color change on the image indicates burial at a point virtually identical with that mapped in the field (Figure 9-23).

North of Ⓓ (Figure 9-26a), however, the images and mapping disagree (compare with the geologic map, Figure 9-23, at Ⓓ). This is an area where the Wagon Bed filled a valley in the preexisting rough topographic surface of the Wind River. The Wagon Bed includes detritus washed or fallen from topographically high areas of the Wind River and a thick, persistent, quartz-rich sandstone of unknown, but probably Wind River, origin. In addition, the Wagon Bed is covered by a thin and discontinuous layer of cobbles of metamorphic clasts that have washed down from topographically higher pediment gravel deposits. A drill hole just northwest of Ⓓ encountered Wind River at a depth of 21.8 m; however, the image does not identify Wagon Bed on the surface by appropriate colors. This may be an example of reworking of older into younger sedimentary units without perceptible image color change. One area of the sandstone bed just northeast of Ⓓ is saturated with interstitial, dead, inspissated petroleum residue that leaked up the nearby fault and gave the sandstone a brownish aspect. It also is possible that residues of petroliferous fluids, sensible to the scanner but unrecognized on the ground because the sandstone is not discolored, impregnate the sandstone in a large surrounding area.

Location Ⓔ (Figures 9-23 and 9-26a) is a place that worried the mapping geologist for several years. Both east and west of the stream to the north of Ⓔ is hilly ground similar to that which characterizes the Wind River. In addition, the beds east of the stream look decidedly like those west of the stream and both look like Wind River—thick beds of clasts derived from Paleozoic and Precambrian rock units, sandstone beds, and siltstone and claystone beds. Yet the cobbles west of the stream are mostly unweathered and ring when struck by a hammer, whereas those east of the stream have had all feldspars altered to clay and can be gouged with a finger. The similar appearance of the beds on either side of the stream had led earlier geologists to consider both outcrops as Wind River (Tourtelot, 1953). But careful observation of areas where the clasts are altered, together with recognition of the many other criteria that define the two formations, led to the mapping of a natural contact of Wagon Bed on a rather steeply eastward-sloping topographic surface cut on the Wind River west of the stream. The image very gratifyingly exhibits the green colors of the Wagon Bed in the places where the Wagon Bed was mapped, not only east of

the stream north of Ⓔ, but also south of Ⓔ, as shown on the geologic map.

An alternate interpretation by the senior author of the area at Ⓔ, using both aerial photographs and images, suggests a modified picture from that given on the published maps. In this interpretation (Figure 9-27) the ridge of sediments containing hills 5570 and 5571, and mapped as Wagon Bed, has sediments protruding as knolls at these high points that are indistinguishable from Wind River in the image data. The Wind River contains 60 m or more of erosional relief and is mantled by Wagon Bed sediments, possibly with intermixed Wind River debris weathering from its slopes. The lobe of Wagon Bed sediments mapped by Thaden (1980d) (center, Sec. 11, T39N, R92W) is indistinguishable from the Wind River section, according to the image data. The Wagon Bed can be divided into two stratigraphic units in the E 1/2 and NE 1/4 of Sec. 14; both units rest with a possible large initial southeast dip on an irregular, dissected Wind River surface. The Wagon Bed and Wind River sediments are both overlain to the east by deposits of Quaternary gravel.

The contact of the Wagon Bed with the Wind River is well shown by the images in other places, too. The Wagon Bed surrounding Ⓕ (Figure 9-26a) is choked with detritus from the Wind River that stands as a high fault scarp to the south. A well-displayed natural contact of the two formations extends east from Ⓖ (Figure 9-26a) and northwest from Ⓗ (Figure 9-26a). Wash of detritus from the Wind River is shown (yellow and yellow-green) covering the outcrop of Wagon Bed (green) in the area east and west of Ⓘ (Figure 9-26a).

Mesozoic rock units are not discriminated well by the images in many places. Most of the outcropping Mesozoics are easily eroded maroon siltstones and sandstones; consequently there are large areas where thick and extensive deposits of alluvium derived from these rocks are contiguous with the outcrops, and the two are not separable on the image. The alluvium surrounding Ⓚ (Figure 9-28b) and extending north into a terrain of exposed red beds is one such place. Where the bedrock is partially covered by a thin lag of cobbles in areas of formerly more extensive gravel deposits, the color on the images is mottled yellow and orange rather than the dark pink of the bedrock, as at Ⓛ (Figure 9-28b). Likewise, disaggregated red beds deposited as alluvial fans, the loose material of which has been partially redistributed by wind, also show as mottled yellow and orange on the image at Ⓜ (Figure 9-28b) and Ⓝ (Figure 9-28b).

On the other hand, there are other places where the images display Mesozoic lithologic units with great fidelity. The complex graben of Sundance rocks at Ⓞ (Figure 9-28b), mostly pale sandstones and calcareous claystones dropped into the underlying red bed sequence of the Crow Mountain Sandstone and Red Peak Formation, shows well on the image, as do also the two large outcrops of Sundance to the south. The limy beds tend to be green on the image. Outcrops of red beds protruding through the Wagon Bed in the area around Ⓟ (Figure 9-28b) nearly perfectly match the geology as mapped on the ground. Even very small outcrops of red beds protruding through the Wagon Bed, as above Ⓠ′, show on the image.

In general, outcrops of Paleozoic rocks appear to be only poorly to moderately well-discriminated by the images, perhaps because they tend to hold moisture better and to offer a better anchor against wind for the root structures of plants than do the younger rocks and to support, therefore, a denser floral cover. The distribution of the Madison Limestone, Ⓠ, in Figure 9-28(b), and the limestone of the Permian Park City Formation is shown fairly well by green color in the large area of Paleozoic rocks in the northeast corner of the image and along the eastern flank of the Owl Creek Mountains. The limits of the Cambrian and Ordovician rock units are difficult to discern, however.

Precambrian units. The Precambrian units in this area consist of granite enclosing three sequences (Hamil, 1971) of pelitic schists. The two rock types, which crop out in the western half of the image, are easily distinguished even, if one is careful, where massive quantities of granite and granitic pegmatites have been injected into the schists as at Ⓡ (Figure 9-28a) and eastward. On the ground schist units are nearly uniformly black except for some thin, silvery-gray, mica-rich units and a few narrow zones of thin quartzite lenses. Individual schist sequences are not clearly discriminated on the image. The middle unit, about 910 m wide centered on Ⓢ (Figure 9-28a), extends as a light-brown unit from the large granite outcrop (green) north of Ⓢ to the main stream junction south of Ⓢ. But the color difference between it and the bounding schist units does not persist either east or west along the belt of outcrop.

Two places in the granite show pink on the image, one north of Steffen Hill at Ⓣ (Figure 9-28a) and the other farther east—places that may represent areas of deuteric alteration. North of Steffen Hill the granite is cut by late magmatic granitic dikes and by specularite-rich quartz veins. Although specularite-bearing veins were not seen in the eastern pink area, that area is also rich in iron and "rusty" in many places. It includes a considerable volume of granite in which the feldspars are green and iron-rich. Complicating the picture, however, is the fact that the

whole drainage basin north and east of Steffen Hill was also an area drowned for a considerable length of time by ponding of the drainage north of the Cedar Ridge Fault 3 or 4 km to the south. What the chemical effect was of the intimate contact of the granite with the overlying Wagon Bed in a saturated environment for a long period is not known.

Faults. The Cedar Ridge Fault, poorly discernible both on the image and on the ground west-southwest from Ⓙ (Figure 9-26b), is nicely marked by ponding and the growth of vegetation in a series of drainages for a considerable distance east from Ⓙ. Beyond that, the fault can be traced to the east edge of the image by the color difference between the Wind River to the south and the Wagon Bed to the north, modified and confused in places by the presence of various kinds of surficial deposits.

Cultural features. Cultural features are well shown: Ⓤ and Ⓥ (Figure 9-26a) are oil wells; the two features east and west of Ⓦ along the road are recently occupied drilling pads; the black marks above Ⓧ and Ⓨ (Figure 9-28a) are tailings piles of unweathered metamorphic rock at the McGraw and Williams–Luman Mines, respectively; and Ⓩ (Figure 9-28b) is a ranch house with outbuildings and trees. The easily discernible airstrip east of the ranch house shows on the image by virtue of the removal of the sagebrush. The soil is nearly undisturbed.

4. Subdivision of Quaternary gravel deposits using topographic and image data

a. Introduction. The extensive deposits of Quaternary gravel found along the West Fork of Dry Creek form fans and other deposits capping the pediment surfaces. Examples of these deposits were pointed out previously on the image data. In the geologic mapping (Thaden, 1980d, 1980e) all such deposits have been lumped together into an undivided gravel unit (Qg), but they may be broken into a number of topographically distinct subdivisions. The gravel units and their dissection may thus provide a record of Holocene to Pleistocene tectonic uplift along the range front. For example, a rate of uplift could be computed if ages for terrace deposits were obtainable. The principal concern here is to provide a means of mapping and differentiating these deposits.

The distribution of these gravels, as shown by the image data, is much more extensive than outlined on the published maps. The gravel units are also not uniform in appearance. The reason for this is that geologic boundaries were placed where gravel units are 1.5 m or greater in thickness. The image data record the distribution of the talus or lag deposits that are sparse but largely continuous, perhaps only a few pebbles in thickness.

Inspection of the geologic map (Figure 9-23) and topographic relations for the (Qg) gravel deposits along the West Fork of Dry Creek discloses the presence of multiple Holocene to Pleistocene gravel units to either side of that drainage. These units have statistically distinct signatures (as represented by the PCs) in the scanner data, which may be used to map the gravel distributions without recourse to the topographic relations.

b. Topographic and geologic relations. The distribution of Quaternary alluvial and older gravel deposits along the West Fork are shown in Figure 9-23 (Ⓐ to Ⓑ to Ⓕ), as taken from the mapping of Thaden (1980d, 1980e). From analysis of the topographic relations alone, these alluvial deposits may be broken into six groups (Figure 9-29). To do this, simplified or generalized contour maps were prepared averaging the topography over the outcrop of each gravel or alluvial unit. Such contours represent approximately the original topographic surface before extensive dissection or stripping of the gravel had taken place. The deposits interpreted and mapped in this way, labeled Qgl through Qg5 in Figure 9-29, have surfaces reconstructed in such a manner that they are distinct from one another, are continuous for each unit, and are characterized by regularly spaced contours. An example of the type of complete idealized fan-shaped forms expected is provided by Qgl. The topographic elevation relations between all alluvial units mapped may be made clear by projecting each gravel or alluvial surface onto the line of the cross section NS (Figure 9-30). The topographically highest gravels representing the oldest deposits are designated Qgl. These gravels were once of greater extent, and probably covered the pediment surface whose nickline is shown at the top of the map. Successively younger (i.e., topographically lower) units, Qg2 through Qg5, are separated from each other by vertical intervals of 50 to 70 ft. When the profile for Qg4 and Qg5 is examined, it is clear that the lower of these two (Qg5) may be extrapolated upstream to connect unbroken with the upper example (Qg4). This suggests that the two deposits may be the same, with the lowest part of the Qg5 elevated and bowed upward by normal faulting on the eastern side of the modern stream course. No evidence of longitudinal faulting along the stream has been found. The youngest deposits, consisting of dunes, older alluvium, and modern alluvium, all essentially fall along the approximate projected modern stream profile, which is topographically up to 70 ft below the level of Qg5 and as much as 190 ft below the level of other units (Qg3). Unit Qoa lies on flat, alluviated floodplains 10 to 20 ft above Qal, but this small difference is not depicted in the cross section.

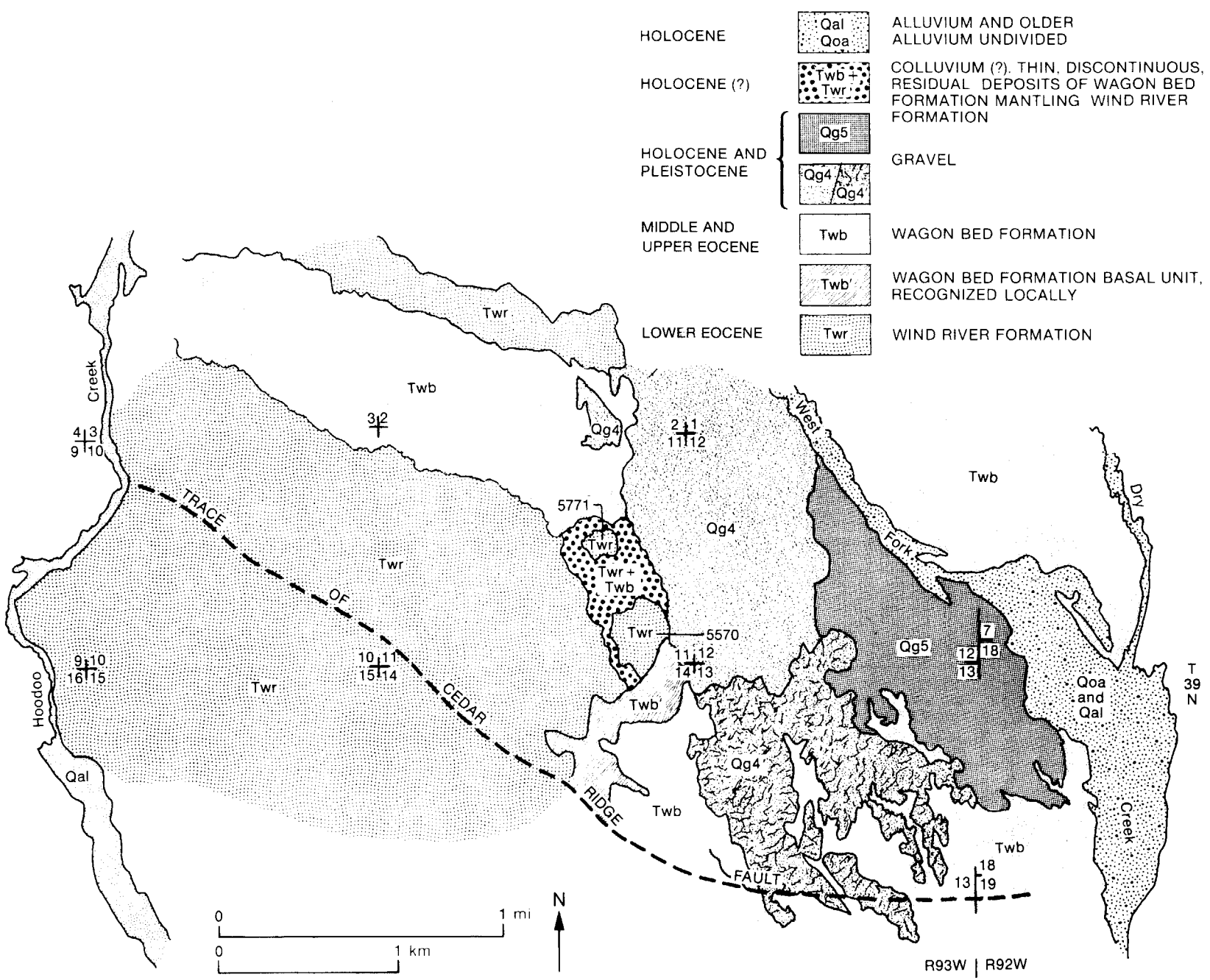

Figure 9-27. Interpretation of contact relations between the Wind River (Twr) and Wagon Bed (Twb) Formations at Location (E) as derived from the PC image of Figure 9-26(a)

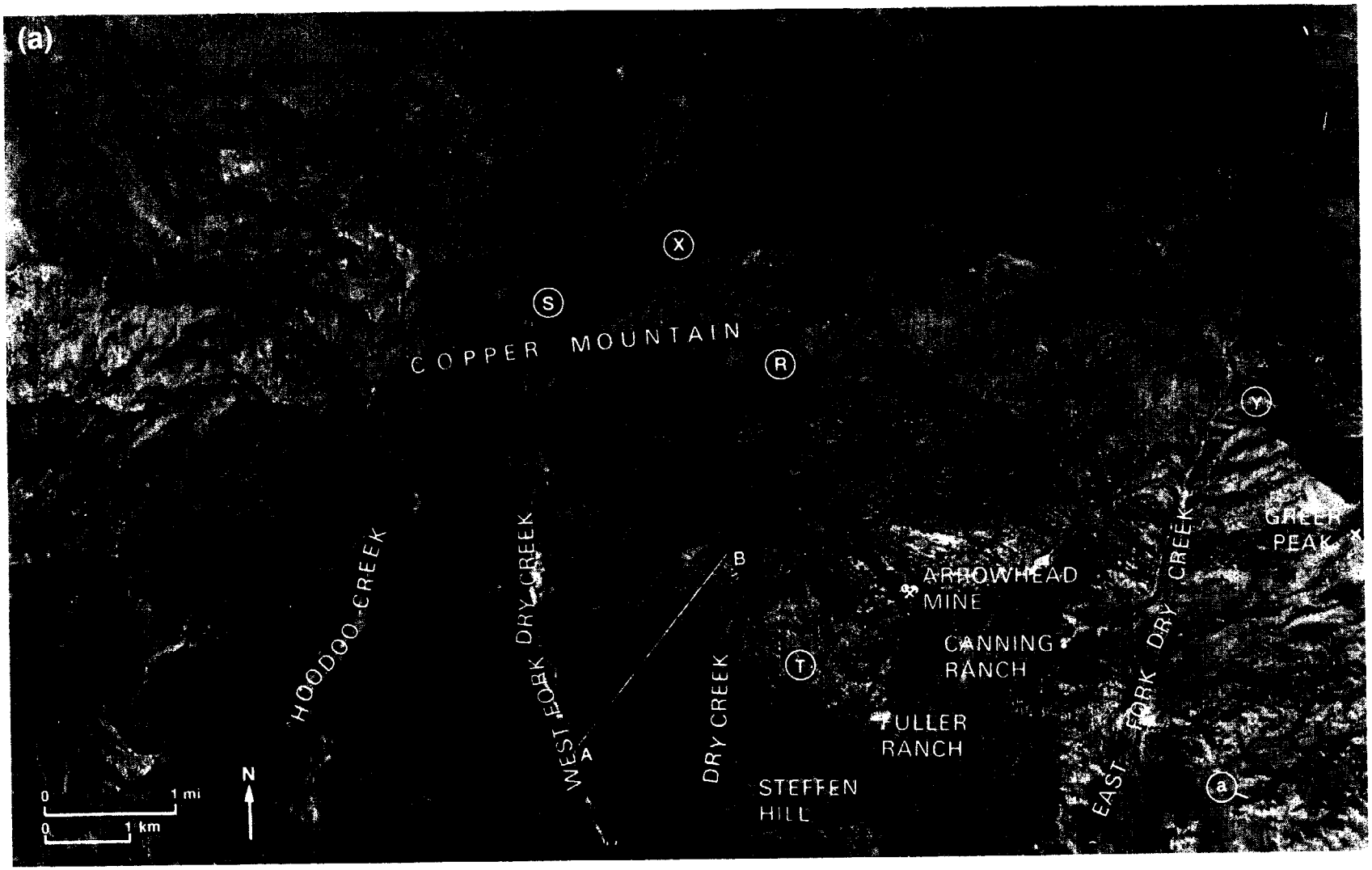

Figure 9-28. NS-001 PC image of the northern flight line, Copper Mountain: (a) western half. Image prepared using seven channels of data. PCs have the following color assignments: V2 = blue, V3 = red, and V4 = green. Letters refer to places discussed in the text.

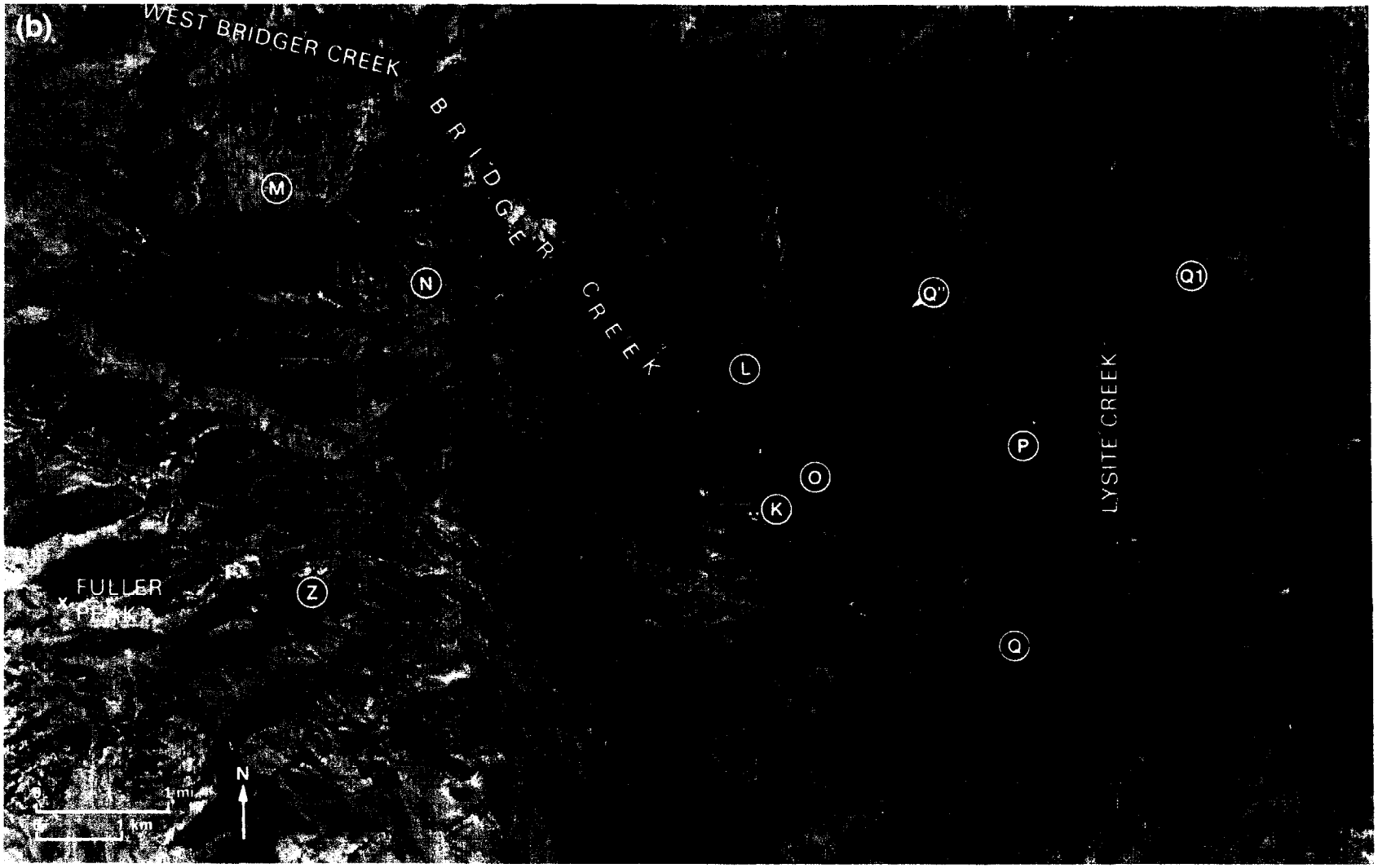

Figure 9-28. NS-001 PC image of the northern flight line, Copper Mountain: (b) eastern half. Image prepared using seven channels of data. PCs have the following color assignments: V2 = blue, V3 = red, and V4 = green. Letters refer to places discussed in the text.

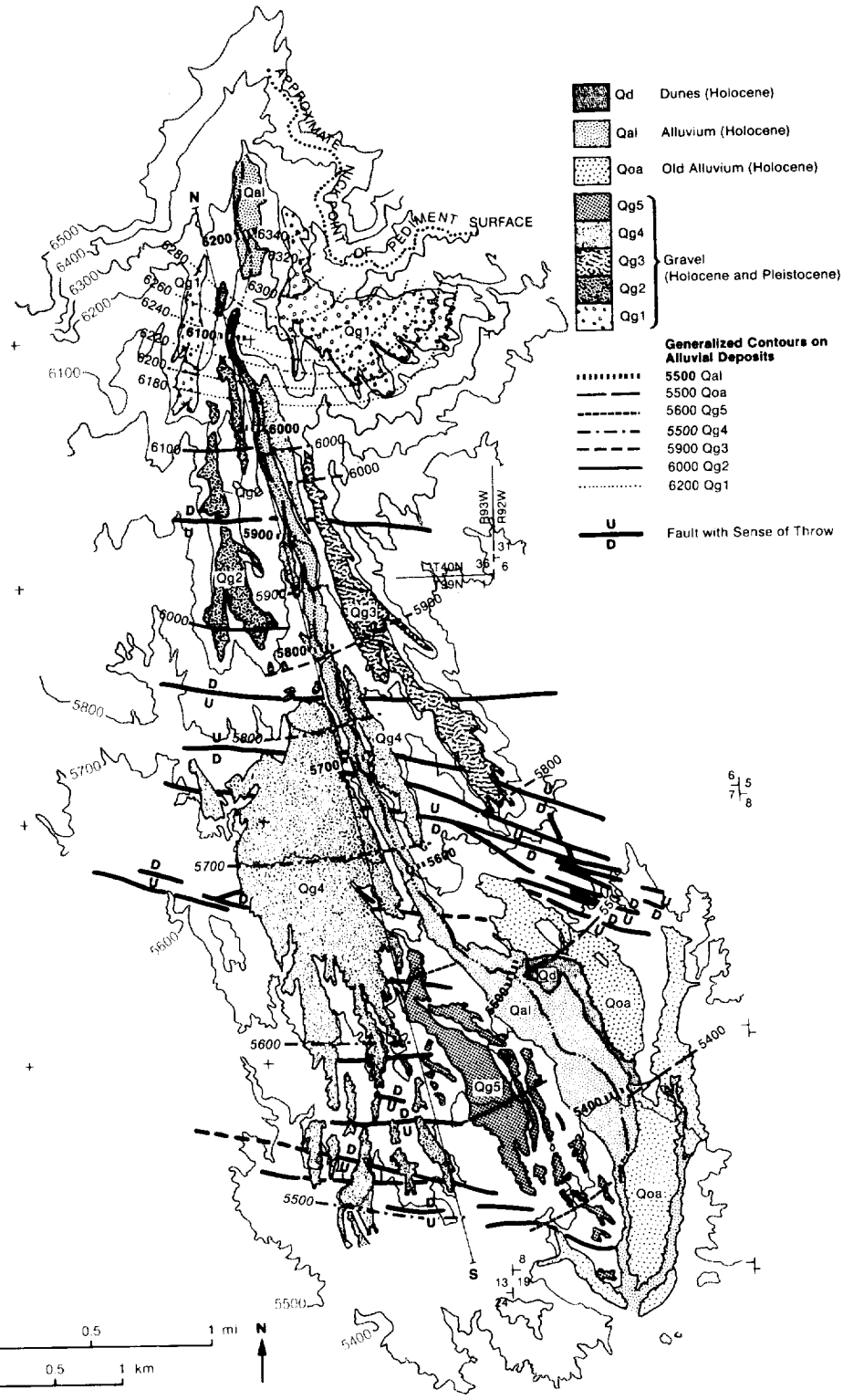

Figure 9-29. Subdivision of the Quaternary terrace gravel and alluvial deposits along the West Fork of Dry Creek. These gravels are undivided in the published map (Thaden, 1980d). Faults and geologic boundaries of alluvial deposits from mapping by Thaden (1980d, 1980e). Subdivision of Qg gravels, this study (1982).

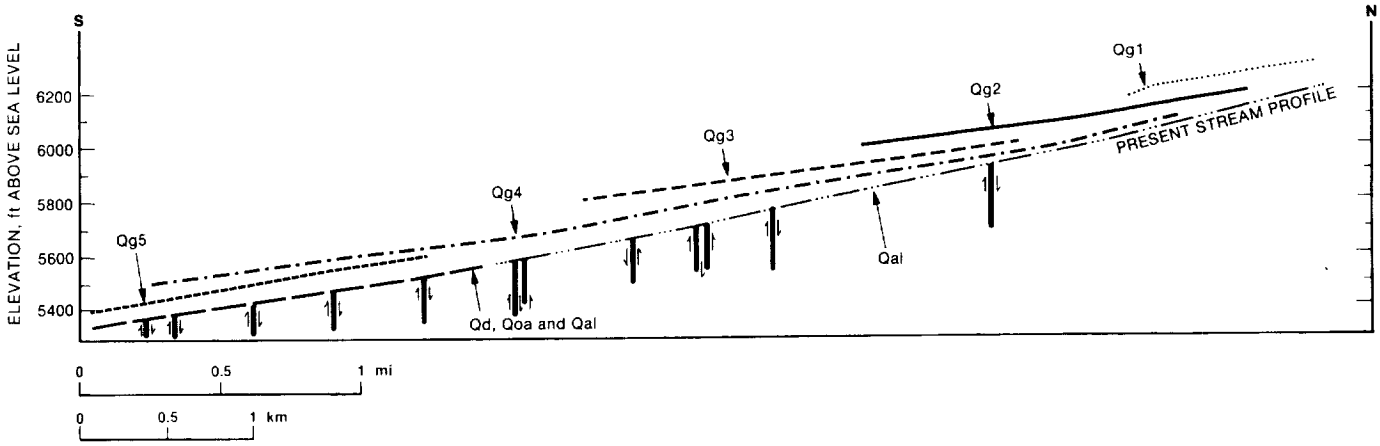

Figure 9-30. Profiles of gravel deposits Qg1 to Qg5 projected into the cross section NS in Figure 9-29, using the generalized contours for reconstruction of initial distributions. Note upward deflection of the profile for Qg4, a region of normal faulting in the Tertiary rocks. This establishes the time of faulting to be before deposition of Qg4 and cutting of the modern stream channel.

c. Distribution of deposits based on the NS-001 images. Figure 9-31 shows the distribution of gravel and alluvial deposits obtained from interpretation of the NS-001 PC images in Figures 9-24 and 9-26(a). The map of Figure 9-31 is a marginally simplified version of the detailed map (Figure 9-23), in which main units representing shadowed or vegetated terrain, and mixed units of sediments, vegetation, and gravels have been suppressed.

Comparison of the image distribution with that obtained by conventional field mapping (Figure 9-29) shows that the image-derived distributions are more extensive (have greater continuity).

The image units identified may be susceptible to other subdivisions; the most interesting of these is the separation of the fourth gravel unit (Qg4) into two parts. The additional unit, Qg4′, is easily distinguished on the images from the main body of Qg4 distribution by its dark-brown, red, or golden-brown color. The unit Qg4′ occupies about the southern one-half of outcrops for the entire unit and corresponds to an area of gravel outcrops on erosional remanent terraces. The Tertiary rocks beneath are cut by extensive normal faulting (Figures 9-29 and 9-30). The cross section of Figure 9-30 shows that the Qg4 level in its southern part has been deformed (bowed upward) over the interval described. In Figure 9-26, the image for the entire southern line, the dark Qg4′ deposits can be seen as a continuation of a linear trend of dark image outcrops corresponding to enhanced vegetation growth from damming of groundwater along the Cedar Ridge Fault to the east. The Qg4′ gravels are interpreted to be geologically equivalent to the main body of Qg4 deposits.

The units described differ in ease of separability on the images. Thus Qg4 is easily distinguished from the surrounding gravels, whereas Qg1 and Qg2 are very similar in their color relations. To illustrate and to help quantify some of these separations, statistical studies are presented below for all of these units except Qg4′. Deposits of dune sand, Quaternary alluvium, and older alluvium are all covered by growths of green vegetation and cannot be separated in the images with great confidence. The older alluvial deposits shown correspond to a slightly elevated plain in the present stream course. The boundaries drawn reflect a prejudice of the interpreter derived from the geologic mapping rather than a genuine basis for separation of the unit as depicted.

d. Statistical analysis of the PC data.[1] Pseudocolor images produced by PC transformations of the NS-001 multispectral data provide a high degree of separability with respect to lithologic classification. The gravel mapping problem is an excellent example of this. Since visual assessment involves a certain amount of subjective judgment, it is desirable to bolster the argument using statistical methods. These methods provide a quantitative basis from which to accept or reject the hypothesis that two selected areas in fact come from different populations.

The test chosen for this case is the two-way contingency table test for independence (Everitt, 1977; Goodman, 1978; Upton, 1978). For analysis, DN values for the gravel

[1]This section was prepared by Dr. J. Solomon, Image Processing Laboratory (IPL), JPL.

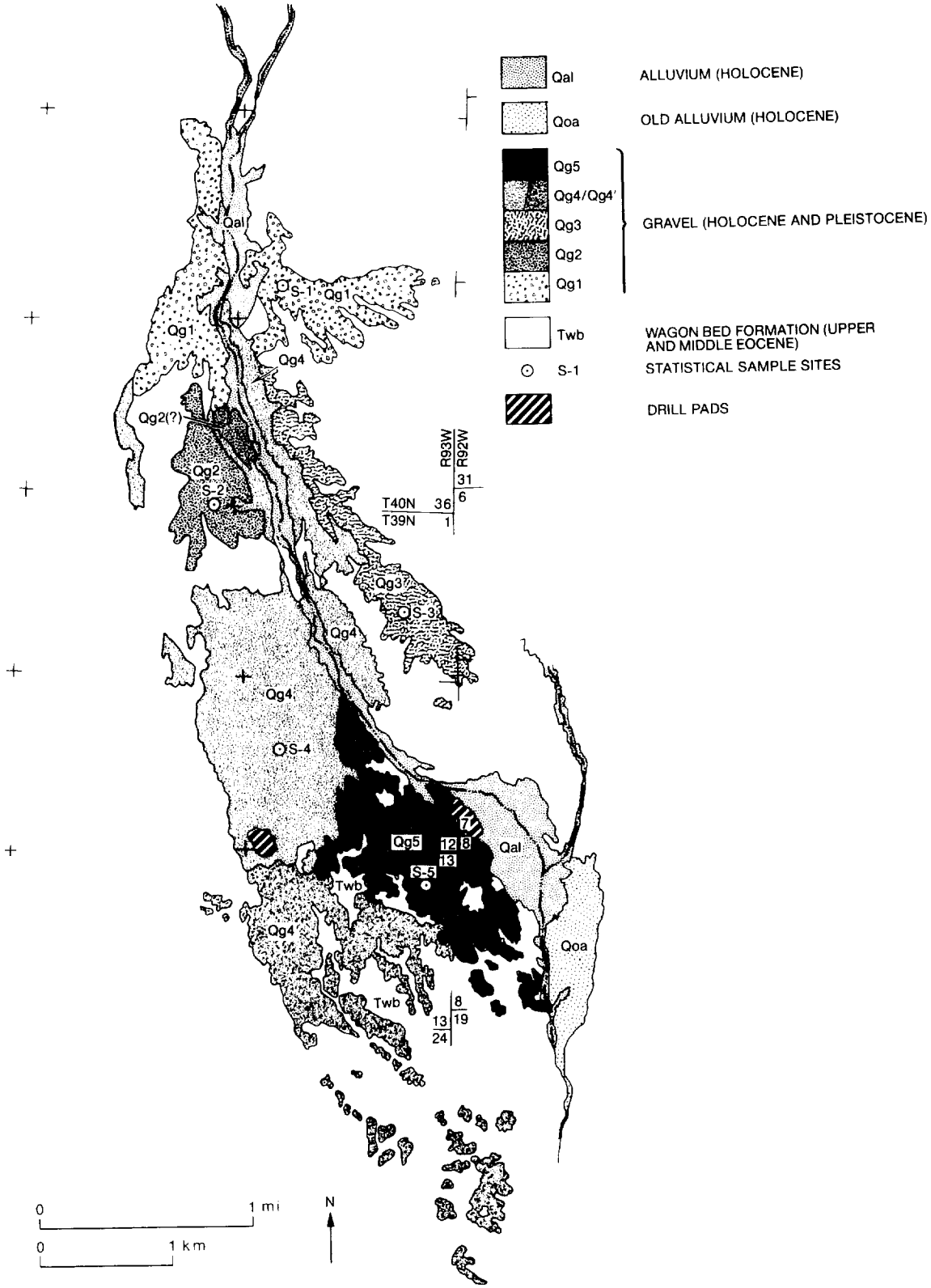

Figure 9-31. Distribution of Qal, Qoa, and Qg deposits, from interpretation of the NS-001 PC image. S-1, S-2, S-3, S-4, and S-5 are sample locations used in statistical studies of unit separability.

Table 9-11. Contingency table used for analysis of independence of the gravel units Qg1 to Qg5, based on the first four PCs, PC1 to PC4[a]

Gravel Unit	PC1	PC2	PC3	PC4
Qg1	95.1 (13)	210.0 (21)	102.2 (20)	149.4 (23)
Qg2	54.0 (20)	191.4 (33)	107.4 (25)	131.3 (23)
Qg3	104.9 (20)	201.5 (10)	116.2 (28)	81.7 (18)
Qg4	65.9 (11)	161.9 (16)	143.9 (17)	157.8 (21)
Qg5	89.5 (18)	180.7 (15)	162.0 (24)	109.8 (23)

[a]Table entries represent mean DN values of the four components obtained from the 20 x 20 pixel sample areas shown in Figure 9-31. Values in parentheses are measures of the standard deviation.

units extracted from the NS-001 PC images were laid out as shown in Table 9-11 The table was then analyzed in standard fashion by examining pairwise the available combinations of classes. For each class pair, the hypothesis was tested that the two classes came from different parent populations, and a confidence level was computed from chi-squared tables. The results of this analysis for the Quaternary gravel data are shown in Table 9-12. The results confirm the classifications made from visual assessment, and furthermore show good agreement in ranking of confidence levels with those made on a visual basis. For example, the contingency table tests show the least confidence (although still an acceptable level) in the separation between Qg1 and Qg2. This agrees with visual inspection of the pseudocolor images.

The analysis has also been repeated using PCs 2, 3, and 4 alone (not shown here). The confidence levels for separation of the groups are not significantly different.

5. Description of directional photometric effects in NS-001 images. Aircraft multispectral scanners used here have angular fields of view on the order of 100° (± 50° from nadir). The scanners are flown at sufficiently low altitudes so that strong directional photometric effects are observable in the resulting image data over surfaces that are not flat.

Observationally, the directionality takes the form of differences in the appearance of the image for the same area, as seen in separate flight lines. Both the representation of topographic forms and the colors of rock units may be affected. The directional effects can result from influences of topography, solar illumination, nonuniform or directional effects in the microscopic surface reflectance, and differences in vegetative cover between north- and south-facing or gentle- and steep-dipping slopes. Some effects might be introduced by transit of the sun in the sky during the times of observation, or by uncompensated motion of the observing aircraft platform, producing a variation in the surface field of view. These effects, however, are of second-order importance compared to those introduced by shadowing or vegetation. An unknown, possibly systematic component of the surface directional reflectance, related both to surface macroscopic and microscopic structures and to shadowing in vegetation, is probably removed by the correction for atmospheric effects (the GRADREM procedure). The directional effects discussed here persist over and above such reflectance components removed by the standard procedures.

The directional effects pose problems for image mosaicking, separate from the ordinary problems of image rectification and geometrical correction. This is because essentially different reflectance and photometric information is contained in each view.

The southern and northern NS-001 flight lines for Copper Mountain, given in Figures 9-26 and 9-28, respectively, overlap by roughly 50 percent. Within the overlap area, numerous examples can be found where the two images differ from each other in appearance and in colors displayed for the mappable units. Two such cases are at (a) in Figure 9-28(a) and (a') in Figure 9-26(a), and along line AB in Figure 9-28(a) and line A'B' in Figure 9-26(a). Areas (a) and (a') are located in oxidized granites adjacent to outcrops of Tertiary sediments, whereas the profile AB traverses oxidized granite, Tertiary sediments, and

Table 9-12. Confidence levels, %, of separation for class pairs from Table 9-11

Gravel Unit	Qg1	Qg2	Qg3	Qg4
Qg2	96.5			
Qg3	99.9	99.9		
Qg4	99.9	98.0	99.9	
Qg5	99.9	99.9	99.5	99.8

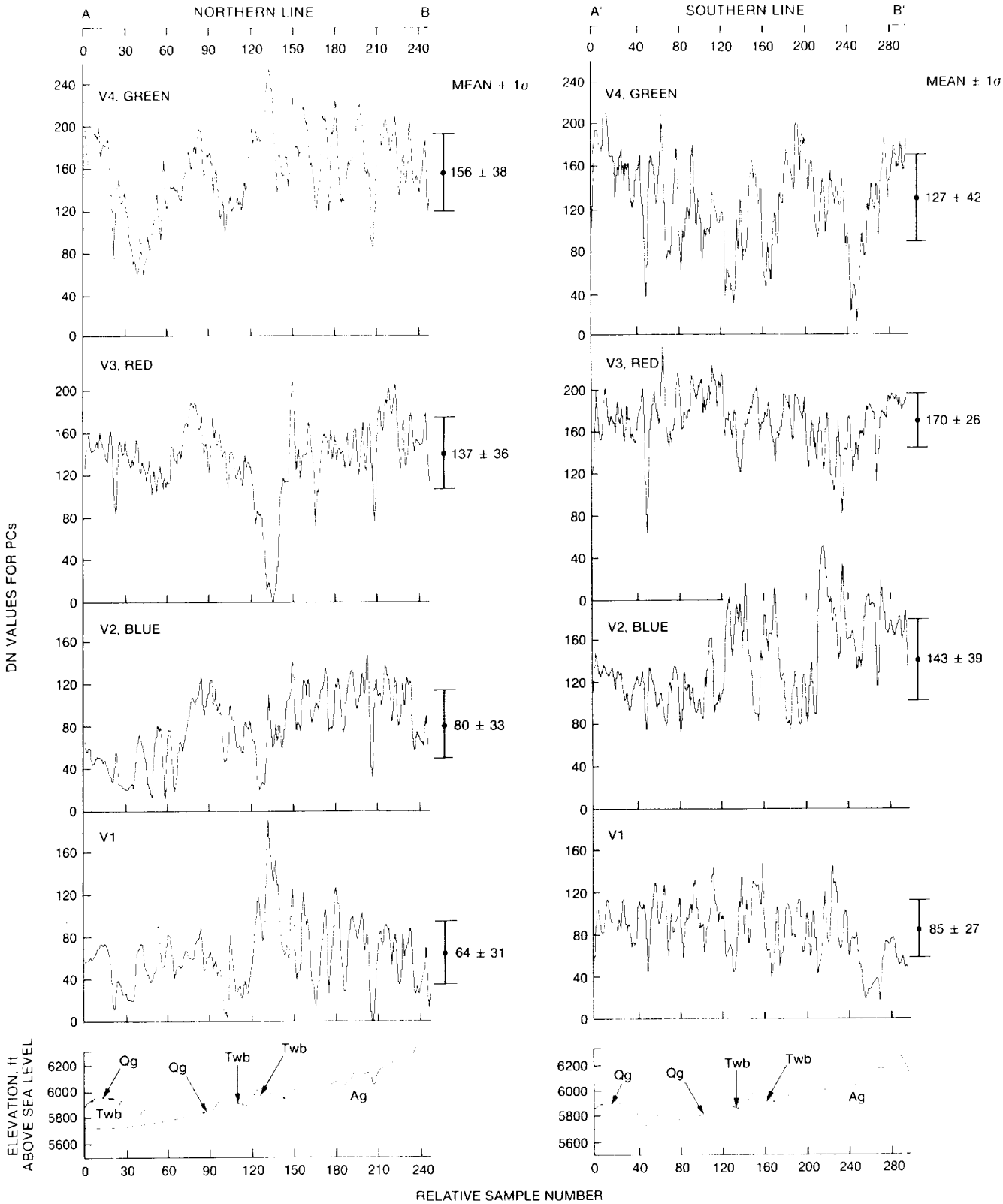

Figure 9-32. DN values of the PCs V1, V2, V3, and V4 along the profiles A′B′ and AB in Figures 9-26(a) and 9-28(a)

Quaternary gravel deposits. (An interpretation of oxidation in the granites based on image data will be presented below.) Based on field observation, outcrops with pink and magenta hues on the images are granitic rocks physically stained orange and yellow from surface oxidation or weathering, whereas outcrops colored green and yellow on the images are less oxidized or "fresh" granites. An interpreter examining the southern line alone would conclude that the rocks in area (a') were heavily oxidized. On the other hand, examination of area (a) in the northern line would result in a different qualitative (reduced) estimate of the oxidation effects present. Neither interpretation would provide an unambiguous picture of the surface reflectance properties encountered.

Similar conclusions would be reached by comparing the images along profiles AB and A'B'. The northern image line depicts the rocks to be essentially free of oxidation effects, whereas the southern line portrays the opposite.

In Figure 9-32 profiles of the actual DN values along the lines AB and A'B' are given for the first four PCs. The first component (V1), while not used in construction of the images, is useful in seeking correlations between the topographic profiles and geologic cross sections. In addition to the profile data, mean values and standard deviations for each PC are given. The profiles reveal extremely great variation both within each component and between AB and A'B'. While some PCs along either line AB or A'B' can be seen to correlate and to correspond to topographic features, no simple pattern emerges between the lines. Thus the profiles are photometrically distinct and cannot be derived one from the other by simple linear transformations such as constant stretching or rescaling.

The variation in photometric properties depicted must be sought in both the macroscopic and microscopic topographic properties of the surface, and in actual variations in surface reflectance. Some correlation can be seen between macroscopic topographic variations, as determined from the contour maps, and variations in the PCs. From the geometry of scan and illumination directions for the two flight lines, it can easily be seen how such variations arise. Figure 9-33 shows the situation for the two lines in the present case. These drawings are to scale (surface topography excepted) with the position of aircraft and solar zenith angles computed for the flight conditions summarized in Table 9-13. Thus for the northern line, topographic elements in profile AB are viewed from the north and illuminated directly from the south, whereas for the southern line, the profile A'B' is both viewed and illuminated from the south, that is, it is illuminated directly. In the first case the north-facing slopes are partly in shadow,

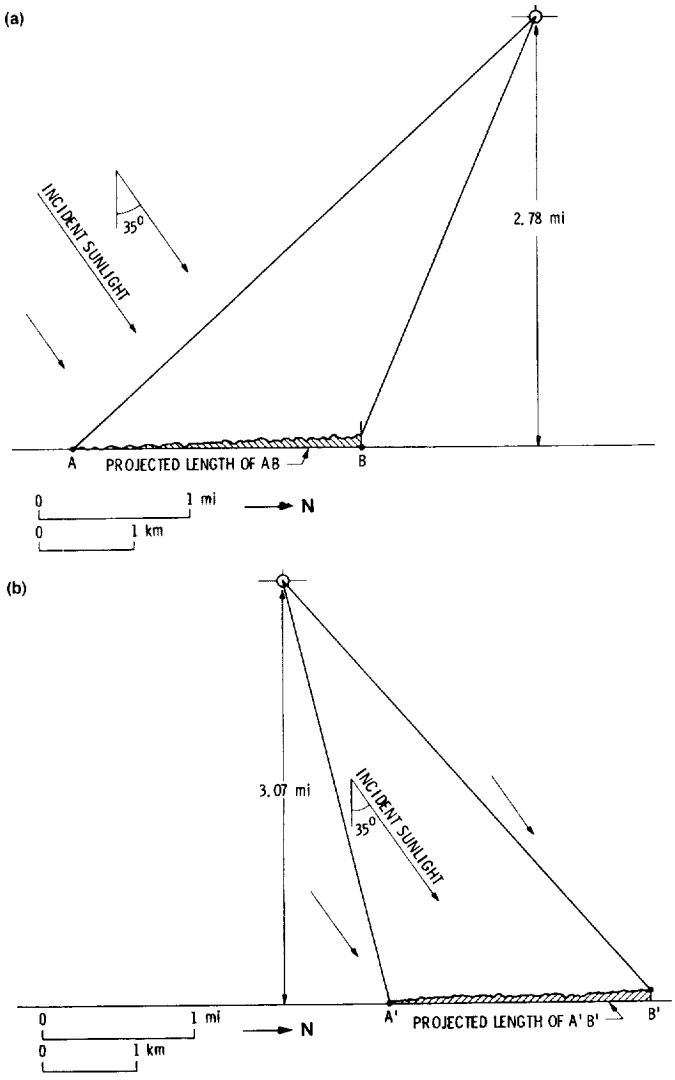

Figure 9-33. Geometry of the scan and illumination directions: (a) along line AB in the northern flight line (Figure 9-28); (b) along line A'B' in the southern flight line (Figure 9-26). Point A has been projected into the N–S direction containing the scan line and point B. Solar zenith angle is approximately 35°.

or illuminated at a low angle to surface elements, with resulting decrease in surface brightness. On the other hand, the south-facing surface elements tend to be free of topographic shadows and, together with possible surface backscatter, therefore appear brighter. Differences in the values of the first PC for the northern and southern lines support this idea.

A possible major contribution to directional effects on north- and south-facing facets is vegetation cover. It is well known that plants in semiarid environments favor north-facing slopes where water retention is greater; in consequence, north-facing rock surfaces support dense, often

Table 9-13. Overflight parameters for NS-001 mission at Copper Mountain, Mission 407, August 29, 1979

Line	Start GMT Stop GMT	Start Latitude Stop Latitude	Start Longitude Stop Longitude	Altitude X 10^3, ft	Apparent Solar Right Ascension (R.A.)	Apparent Solar Declination	Solar Zenith Angle[a]
Northern	$18^h\ 08^m\ 00^s$ $18^h\ 13^m\ 35^s$	43° 26.0′ 43° 25.9′	108° 03.9′ 107° 35.5′	14.7	$10^h\ 27^m\ 38^s$	9° 39′ 02″	34.87°
Southern	$18^h\ 17^m\ 20^s$ $18^h\ 23^m\ 10^s$	43° 20.2′ 43° 19.8′	107° 36.8′ 108° 06.2′	16.2	$10^h\ 27^m\ 38^s$	9° 39′ 02″	34.87°

[a] $\cos(z) = \sin\lambda \sin\delta + \cos\lambda \cos\delta \cos H$, where z = zenith angle.
λ = latitude, δ = apparent solar declination.
H = local time. H in radians is computed approximately from

$$\frac{2\pi}{24}\ (\text{Local Noon} - \text{GMT} + 7^h)\ \text{radians}$$

nearly complete, covers of lichens as well as trees and shrubs. Examples of lichen cover favoring the northern sides of boulders and outcrops almost to the exclusion of covering on the southern sides are shown in Figure 9-34 and can also be seen as green tints covering north-facing outcrops of granitic rock in Figure 9-8. The reflectance properties of lichens differ substantially from those of oxidized granite rocks and can thus contribute markedly to variations in the surface reflectance properties quite apart from shadowing.

C. Image Analysis and Interpretation of the Oxidized Granitic Terrain

1. Introduction. Yellich et al. (1978) thought the granites along the range front were oxidized by corrosive, descending meteoric waters that carried uranium ions in solution downward to be precipitated in the fractured granites at depth. They mapped these (oxidized) granites as occupying a continuous zone 4 km in width along the base of the mountains, extending from the West Fork of Dry Creek to approximately 13 km east, where the crystalline rocks disappear beneath the Paleozoic sediment cover. Thaden (1980b, 1980d) described these bright rusty-orange rocks in the Guffy Peak and De Pass Quadrangles but did not differentiate them in mapping the granites. He attributed the oxidation to weathering beneath saline alkaline lakes, where the granite lay shallowly buried during part of Tertiary as well as Quaternary time.

This current study used the Bendix 11-channel M^{2}S scanner images as well as the 7-channel NS-001 data to determine the surface distribution of oxidation/weathering effects in the crystalline rocks. For the M^{2}S data the degree of oxidation was measured by determining band ratios in the visible wing of the Fe^{+3} charge transfer band. For the NS-001 data the PC transformation, which utilized scatter properties of the data to effect the separations, was used.

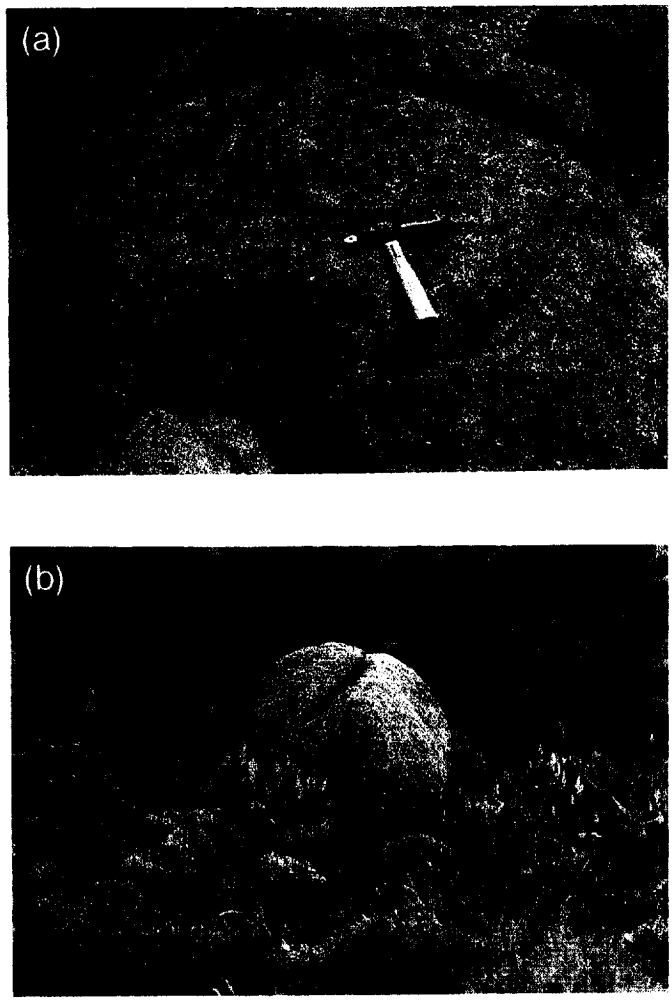

Figure 9-34. Green (Genus *Parmelia*(?)) and black (Genus *Cladonia*(?)) crustose and folios lichens covering north-facing sides of (a) weathered granitic outcrops (NW 1/4, Sec. 32, T40N, R92W) (north is to the left); (b) a fresh granite boulder in Tertiary (?) fan gravel (NE 1/4, Sec. 27, T40N, R92W) (north is to the right). Note additional lichen-mantled, north-facing fracture surfaces on outcrops in background of Figure 9-8.

The distributions of oxidized granites implied from the two data sets differ from one another and from the distribution as presented by Yellich et al. (1978). Since for the two instruments information at different wavelengths is being compared with the radiances combined in different ways and in different numbers (CRCs versus PCs), detailed disagreement between these two results is not surprising. The distributions obtained by the same scanner also differ between flight lines. These findings seemingly raise concern about the internal consistency of the image results. While it is not possible to reconcile all of the results, one interpretation is that they arise predominantly from directional "effects" in the surface reflectance due to shadowing, topography, and variable vegetation cover. Directional effects emerge because of strongly differing conditions of illumination and viewing between the flight lines. They are prominent in areas of high topographic relief, and are absent or greatly reduced on flat alluvial or other surfaces of low relief.

The patterns of surface oxidation obtained from each of the scanner systems were transferred piecemeal to a topographic base to facilitate detailed comparison with the topography and geology. Intense oxidation is found to correlate with old pediment surfaces, and with rotten granitic terrain that weathers to grus-mantled slopes and that follows old topographic drainages (paleodrainages) high in the range. The two terrains are continuations of one another, with pediments falling at low elevation along the range front, and the grus-mantled terrain along valleys and parts of ridges higher in the range.

A curious and complicating aspect of the oxidation/weathering skin is that the oxidation may develop progressively from unoxidized but weathered granite as these rocks are stripped of tuffaceous sedimentary cover in the pediments and exposed to subaerial weathering. This time dependence, together with the directional effects described above, can reconcile most differences between the scanner results and the results of the Yellich et al. (1978) geologic mapping. If the oxidation skin is relatively modern in origin, then it can have little bearing on the genesis of the uranium ores, which were emplaced intermittently and subsequently reorganized during Tertiary and Quaternary time.

An empirical correlation exists between the distribution of oxidized terrain and the occurrence of major uranium in the granite. Uranium occurs beneath Tertiary sediment cover in the granite or adjacent to the granite–sediment contacts in the sediments. In both cases the exposed granites are oxidized. The granites appear largely barren of uranium enrichment where oxidized at the surface or where fresh outcrops occur. Minor exceptions to this are found along weathered fracture zones in the granite topographically higher in the range. These occur without the accompanying sediment cover; none of these occurrences is of economic importance.

2. Analysis of M²S image data. The Bendix 11-channel M²S scanner is an aircraft-mounted instrument covering the spectral region of 0.33 to 1.1 μm. The spectral distribution of the scanner's 10 channels (excluding the thermal infrared) is given in Table 9-14. The angular field of view is 2.5 mrad. At Copper Mountain the scanner was flown at altitudes of 4800 and 5300 m above terrain, resulting in a surface spatial resolution of approximately 11 to 12 m. The M²S data were acquired over two E–W-oriented flight lines, as shown in Figures 9-21 and 9-22. The flight parameters are given in Table 9-15. The area of overlap corresponds to approximately 45 percent of each flight line. For this study two subareas of these data were examined in detail. These two areas are outlined on the index of mapping and interpretation of Figure 9-22.

a. CRCs. Rowan et al. (1974) successfully distinguished iron oxide and vegetation using the Landsat MSS bands 4, 5, 6, 7 and determined that ratios such as 4/5, 4/6, 5/6, and 6/7 were useful for this purpose. These methods basically use radiance ratios as measures of absorption band slope and hence band strength.

Ratio quantities tend to suppress effects due to brightness variation alone. To map the distribution of iron oxidation effects and vegetation at Copper Mountain using these techniques, first CRCs were formed from the Landsat-equivalent combinations of M²S bands. The bands so lumped are indicated in Table 9-14.

Table 9-14. Bandpasses of the Bendix 11-channel M²S scanner

Channel	Wavelength Interval, μm	Landsat MSS Equivalent Band[a]
1	0.33–0.44	
2	0.44–0.48	
3	0.49–0.54	
4	0.54–0.58	4
5	0.58–0.62	
6	0.62–0.66	
7	0.66–0.70	5
8	0.70–0.74	6
9	0.76–0.86	
10	0.97–1.065	7

[a]For purposes of computing ratios, radiance within the M²S band is taken to represent the radiance's approximate value in the corresponding Landsat band. Band 7 is taken as average of values in M²S bands 9 and 10.

Table 9-15. Overflight parameters for Bendix 11-channel M²S mission at Copper Mountain, Mission 383, August 4, 1978

Line	Start GMT Stop GMT	Start Latitude Stop Latitude	Start Longitude Stop Longitude	Altitude X 10^{-3}, ft	Apparent Solar Right Ascension (R.A.)	Apparent Solar Declination	Solar Zenith Angle[a]
Northern	$20^h\ 07^m\ 20^s$ $20^h\ 11^m\ 05^s$	43° 26.0′ 43° 26.0′	107° 38.4′ 108° 02.0′	15.5	$8^h\ 54^m\ 55.5^s$	17° 23′ 41″	29°
Southern	$20^h\ 14^m\ 15^s$ $18^h\ 23^m\ 10^s$	43° 19.7′ 43° 19.8′	108° 01.5′ 108° 06.2′	17.0	$8^h\ 54^m\ 55.5^s$	17° 23′ 41″	29°

[a]See formula in footnote to Table 9-13.

Figure 9-35 is the Landsat band equivalent CRC for subarea 1, which lies in the northern line. Figure 9-36 shows the same CRC for subarea 2, which lies in the southern line. Figures 9-37(a) and 9-37(b) show the illumination and viewing geometry for subarea 1 and subarea 2, respectively.

The CRC image renders areas of heavy vegetation cover (e.g., stream valleys and canyons) and shadows in blue, and areas of granitic rock with varying degrees of surface oxidation in shades of deep blackish-red (heavily oxidized) to light red and yellow (light oxidation). Areas of vegetation-free, light-tan and gray sediments are tan to cream-colored. Alluvial or colluvial slopes that contain grasses and shrubs appear deep tan to reddish-tan, depending on rocks, substrate, or source material. Areas with extensive juniper cover are light blue with red mottling.

Comparison of these two images reveals many detailed differences in presentation for areas common to both. For example, a number of the units in Steffen Hill, ①, are discriminated in the rendition of subarea 2, but are indistinct or less well-defined in the rendition of subarea 1. Also, most areas of red, oxidized granitic rocks differ in appearance between these two images (areas ②, ③, and ④). Areas ② and ④ have been previously discussed as examples of directional effects in the surface reflectance. It was previously indicated that back-reflecting slopes appeared to provide enhanced representation of the oxidation effects over those in which the illumination was observed in the specular (forward) direction. An example of a seemingly opposite effect can be found (area ⑤), where the surface observed in back-scattered light (subarea 2) appears less oxidized than in forward-scattered light (subarea 1). These are areas of gently rounded (grass-covered) slopes, as opposed to the angular faceted terrain characterizing most of the other areas described.

b. Density slice of M²S ratio image. To provide a definitive mapping of the distribution of oxidation effects together with a quantitative measure of the degree of oxidation as measured by absorption band slope (i.e., degree of saturation), a General Electric Image 100 image analyzer was used to examine the various ratios and density slices of the M²S image data from subareas 1 and 2.

Figure 9-38 is an eight equal-level density slice of the M²S band-ratio 4/6, giving the iron oxidation representation sought and giving an index of degree of oxidation. In the color scale, black indicates the lowest ratio values, followed by magenta, red, yellow, green, light blue, blue, and white for the highest ratio values. This color scale can be made quantitative in terms of the ratio values by use of field spectral reflectance measurements, as shown in Figure 9-39. Here the reflectance ratios measured for 32 field spectra from 27 sites throughout the oxidized and unoxidized granitic terrain are plotted as a function of DN ranges representing the colors used. Brief descriptions of some representative field sites are given in Table 9-16. Areas were selected on the image for each color at sites where PFRS data were available. Groupings (vertical stacks) of data appear above each color slice in Figure 9-39 because of the 8-level splitting of the DN range.

In addition to the distribution of iron oxidation and the intensity, the density-slice image of Figure 9-38 also shows approximately the distribution of green vegetation and partially vegetated outcrops. In the 4/6 density slice, ratios for green foliage are consistently high, whereas those for ordinary rocks and heavily oxidized rocks with strong Fe^{+3} ultraviolet absorption bands are consistently low. This is because the positions of the two principal chlorophyll absorption bands at 0.45 and 0.65 μm leave a residual maximum in plant reflectance near 0.55 μm. Thus the ratio 0.56 μm/0.64 μm in green plants tends to be greater than unity, whereas this same ratio for ordinary iron oxides (Fe^{+3}-charge transfer absorption) is always less than unity. A detailed comparison of the density-slice image of Figure 9-38 with aerial photographs shows that oxidized outcrops in the field are largely represented by the image colors red,

Figure 9-35. CRC of Landsat band equivalents of M^2S data for the Copper Mountain test site, subarea 1, northern line. Color assignments are as follows: 4/6 = blue, 4/8 = green, 8/(9 + 10) = red.

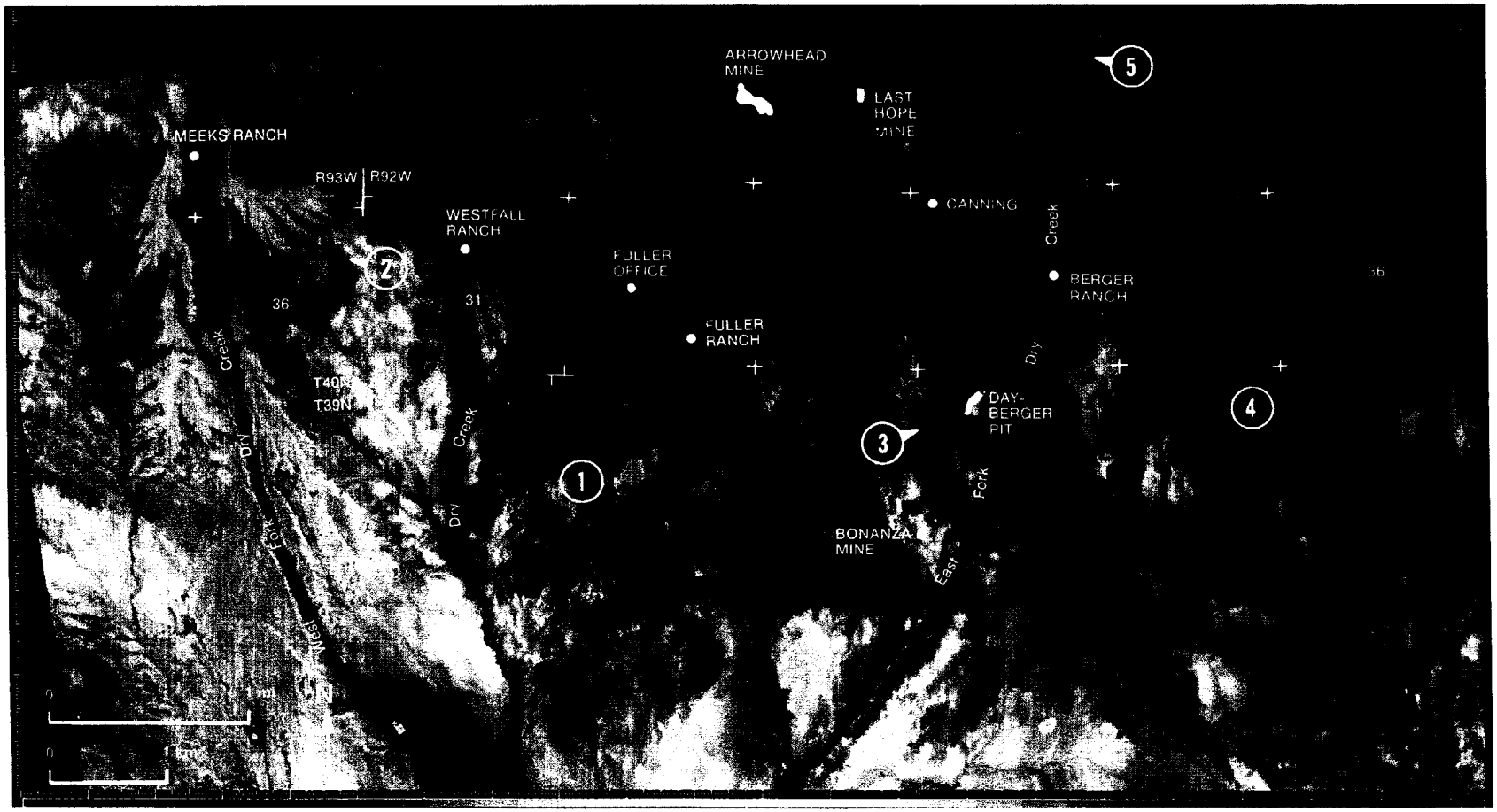

Figure 9-36. CRC for subarea 2, southern line. M^2S band-ratios are as follows: 4/6 = blue, 4/8 = green, 8/(9 + 10) = red.

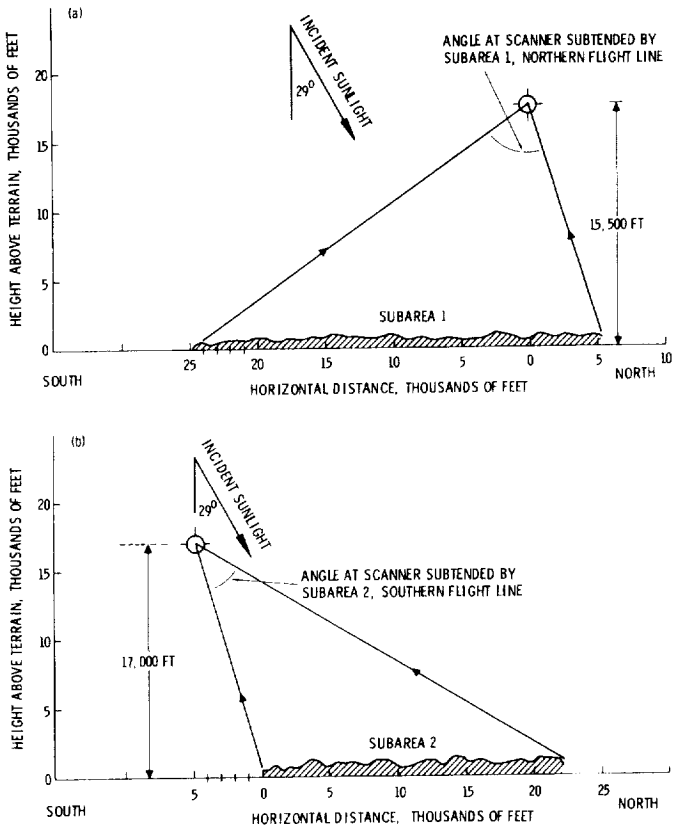

Figure 9-37. Approximate viewing and illumination geometry for (a) subarea 1, M²S, northern flight line; (b) subarea 2, M²S, southern flight line

magenta, and black. Hence restricting attention to these areas conveniently focuses on the oxidized granitic outcrops of interest to the exclusion of most other rock or cover types.

c. Composite map of oxidation effects from M²S CRC and density-slice images

Construction of map. To facilitate later correlation of surface oxidation patterns with topography, erosion surfaces, rock types, and geologic structure, and to facilitate comparison with the other distribution pattern obtained from NS-001 PC images (to be discussed subsequently), a composite interpretation (originally at the 1:24,000 scale of the geologic map) was compiled featuring all of the granitic outcrops shown to be oxidized from the M²S CRC and density slice images. The result is shown in Figure 9-40, together with the distribution of Tertiary and Quaternary sediments (undivided), Paleozoic rocks (undivided), and Precambrian metasedimentary, granitic, and dike rocks as taken from the geologic mapping by Thaden (1980b–1980d). Some discussion of this compositing procedure is required, since two different image products were used for the compilation.

(1) The density slice image (Figure 9-38) was used whenever possible to obtain the discontinuous and patchy distribution of oxidation indicated in the CRC image figure. The red-, pink-, and black-colored areas were chosen to represent the most intensely oxidized rocks. This is because it seemed preferable to transfer definite boundaries from the density slice image (i.e., red-pink-black versus the rest) rather than interpret indefinite ones from the CRC (i.e., one subtle shade of red versus another).

(2) Because image rectification to map coordinates is "good" on a scale of 1 km or more, but "poor" on a scale the order of 100 m or so, it proved necessary to transfer the data first to an aerial photograph base and then to the map base with constant adjustments of position in each case. Reasonably accurate but tedious mapping of the image pattern was thereby achieved wherever aerial photographs were available to allow this to be carried out. Where high densities of well-defined drainages or topographic forms were present it sometimes proved possible to map directly from the image to the topographic map base.

(3) Wherever aerial photographic coverage was not available or the images and photographs were too distorted or featureless to effect a transfer of the data, the CRCs were usually relied on and the distribution of oxidized outcrops were mapped directly from the images. This is generally the case for all granitic outcrops between Steffen Hill and the Arrowhead Mine in a N–S direction, and the West and East Forks of Dry Creek in an E–W direction. This has led to some approximation of the oxidation patterns so mapped. In particular the oxidized outcrops of granitic rocks are actually *smaller* than the distribution mapped in Figure 9-40 because individual outcrops are usually surrounded by deposits of sage-covered colluvium.

(4) Because of the "directionality" effects described earlier, which lead to different patterns of the oxidation between flight lines, both the major patterns of oxidation as presented in the two subareas of the M²S data and the patterns from the density slice representation were used. Qualitatively these two patterns are the same. In detail many boundaries differ. The alteration was mapped as long as it appeared on any of the images examined.

Figure 9-38. Representation of the degree of iron oxidation in subarea 1 by an eight equal-level density slice of the M²S band-ratio 4/6. This ratio provides a measure of the "strength" of the ultraviolet Fe^{+3} charge transfer band, by measurement of reflectance slope in the visible.

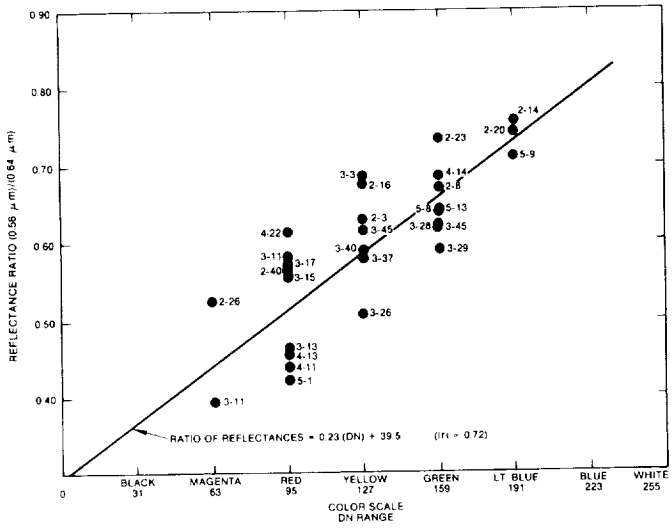

Figure 9-39. Relationship between reflectance ratio 0.56 μm/0.64 μm as determined from PFRS measurements and DN values for the eight equal-level density slice image (Figure 9-38). Equivalent color DN ranges are 0 to 31, black; 32 to 63, magenta; 64 to 95, red; 96 to 127, yellow; 128 to 159, green; 160 to 191, light blue; 192 to 223, blue; and 224 to 255, white. Numbers refer to site descriptions in Table 9-16.

The advantage gained by mapping the distributions described using image data is that, except for the obvious and mostly continuous oxidized outcrops, these patterns are not recoverable using ordinary field mapping procedures, nor are they necessarily obvious from aerial photographs. Thus the scanner data, particularly in the simple form of a density slice, provide a quick, photometrically accurate, and consistent method of mapping these effects. The tedious methods of data transfer employed here were only required because it was not feasible to rectify the image data at a sufficiently fine scale to a map base. Careful analysis of these oxidation effects and their relationships to geologic structure or uranium mineralization ultimately depends on such accurate mapping.

Description of the composite map. The M²S scanner images provide a uniformly consistent representation of the distribution of iron oxidation throughout the area of granite exposure in the North Canning Stock. The distribution in Figure 9-40 is mostly continuous along the base of the mountains east to the East Fork of Dry Creek and correlates with a pre-Eocene pediment surface. Between the East Fork and the Paleozoic boundary, patchy areas are shown to be oxidized, with most of the details being governed by topography. As may be verified by reference to the images, there is a distinct, apparent reduction in the extent of oxidation in the surface rocks adjacent to the finger of Tertiary sediments extending into the granite, and generally a lower degree and patchy distribution of this alteration over the entire area. The degree of surface alterations is relatively great, though discontinuous, along the East Fork drainage itself; this drainage, as discussed below, probably represents the pre-Eocene paleotopographic surface correlating with the pediment lower in elevation. Isolated patches, such as near De Pass, show heavy oxidation effects. Part of this intense pattern appears to lie over the Flathead Sandstone–Precambrian contact. The Flathead Sandstone and the Gros Ventre and Gallatin Formations all have a brown or red-brown oxidized appearance in the field. The M²S ratio data do not distinguish clearly between these brown units and the granitic oxidation effects. Similarily, numerous outcrops of reddish Tertiary sediments and Quaternary terrace gravels are depicted as oxidized in the CRC and density-slice images. Thaden's geologic maps were used to eliminate these areas from inclusion as oxidized granites. Had the maps not been available, geomorphic characteristics of the sediments could have been used to separate them from the granitic rocks, so little ambiguity would have resulted.

Elsewhere, throughout the North Canning Stock between Arrowhead Mine and the Precambrian metamorphic terrain to the north, the distribution of oxidation is spotty. Some of these patches are correlated with topography, such as north and east of the West Fork. In a few places, such as north of Arrowhead Mine, the distribution may be controlled by faulting in the granite. No obvious correlations exist with the mapped distribution of metasedimentary xenoliths or with Precambrian dikes that lie in the East Fork drainage.

d. Separation of hematitic outcrops using classified M²S data. Heavy hematite staining may be a uranium exploration guide because of the possible genetic significance of this mineral for uranium deposition in the North Canning uranium resource. In general, the more heavily oxidized outcrops are represented in black on the density-slice image (Figure 9-38). However, the separation of hematite-stained outcrops from those with mixed oxides and hydroxides was attempted using the M²S data and a Bayesian parallelepiped maximum likelihood classifier. This classifier is used in the JPL image processing fast-classification algorithm. To do this, training areas with known hematitic staining were picked, and the remainder of the image was classified utilizing these specialized signatures. The best-exposed and largest examples of such staining known were located at the Berger Pit (center, Sec. 34, T40N, R92W) and in outcrops at a prospect along an intermittent stream south of Canning Ranch (SW 1/4, SE 1/4, Sec. 33, T40N, R92W). These latter outcrops are shown in

Table 9-16. Field site descriptions, PFRS ratio values, and M^2S ratio (density slice) image colors for sites in Archean granitic rocks and sediments used in construction of calibration curve

Site ID	PFRS Ratio (0.56 μm/ 0.64 μm)	Image Color (Figure 9-38)	Description
2-3	72.73	Green	Unaltered red granitic outcrop
2-8	77.27	Green	Fresh K-feldspar-rich granite, black lichen
2-14	82.14	Blue	Fresh granite, yellow, green, and black lichen
2-16	77.78	Yellow	Pale tan-gray granite, black and gold lichen
2-20	84.85	Blue	Gray granite, some black lichen
2-23	84.00	Green	Altered granite, gold lichen
2-26	62.96	Pink	Pink microcline-syenite dike
2-40	66.67	Red	Altered ocher-colored granite, 50 percent gray lichen
3-3	78.51	Yellow	Flathead Sandstone
3-11	40.91	Red	Very red hematite-stained granitic outcrop
3-13	56.52	Red	Red granitic outcrop
3-15	66.67	Red	Pink, gray, and white gravel deposits from granitic outcrops
3-17	68.00	Red	Yellow boulder with gray lichen
3-26	60.71	Yellow	Yellow boulder
3-28	68.71	Green	Spheroidal-weathered granite, yellow, red, and gray boulder
3-29	69.29	Green	Gray-tan boulder
3-37	68.00	Yellow	Light red boulder
3-40	68.42	Yellow	Dark red-black-stained boulder
3-45	72.00	Green	Gray quartz-rich granite, yellow lichen
4-11	54.17	Red	Heavily oxidized granitic rock, Berger Pit
4-13	55.56	Red	Red granitic boulder
4-14	78.95	Green	White quartz-feldspar-rich boulder plus debris and chips
4-22	71.87	Red	Silty sand, red-orange on image
5-1	52.38	Red	Granitic rock
5-8	72.39	Green	Unoxidized granitic gneiss
5-9	81.48	Blue	Red stains in feldspar and quartz-rich granite
5-13	73.91	Green	Arrowhead Mine, red granite rock with green and black lichen

Figure 9-9. The results of these classification experiments were negative, almost certainly because of the small training sites available (a few pixels at most) and the difficulty of accurately locating the small outcrops in the image at the resolution of the scanner data.

Deep-red, thin beds of hematitic sandstone also occur in the basal Wagon Bed strata northwest of Canning Ranch (Sec. 27, T40N, R92W). These too are inseparable from the normal oxidized granitic terrain in both the CRC and density slice images.

3. Analysis of NS-001 image data

a. Introduction. The NS-001 PC images for the Copper Mountain area have been described previously, and the remarkable power of these scanner data in discriminating between rock, vegetation, and soil types present in the area has been pointed out. An example of the so-called directional surface reflectance effects involving the oxidized granite was also described. How these scanner results can be applied to the mapping of granite oxidation effects will now be described in greater detail.

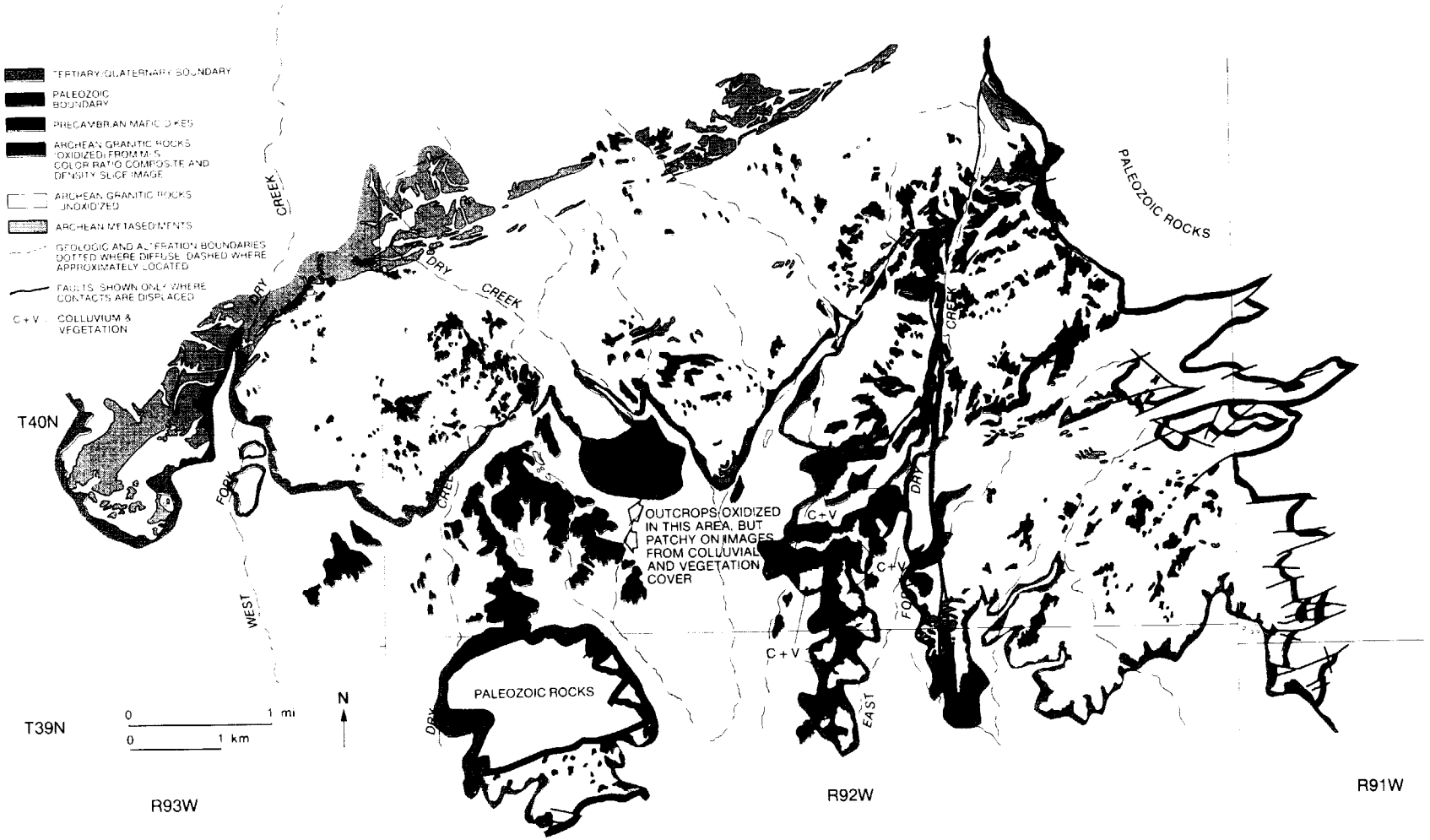

Figure 9-40. Distribution of oxidized granitic outcrops from the M²S CRC and ratio density slice images of Figures 9-35, 9-36, and 9-38 (geologic boundaries for the Archean, Paleozoic, and Tertiary/Quaternary sedimentary rocks from Thaden, 1980b–1980e)

b. Contrast of the PC and CRC methods. The PC method, based on the principal component transformation, differs fundamentally from the method based on ratios or CRCs. The band-ratio method depends on representing variations in the slopes of the reflectance curves. In contrast, the PC method is based upon fitting a set of orthogonal axes to the scatter of points in a p-dimensional (p-channel) data space, where p corresponds to the number of spectral channels analyzed. Each surface cover type or surface element with a distinctive spectral signature in this p-space forms a separate cluster or a point isolated from its neighbors. The PCs represent reductions in dimensionality of the original data space to a few (usually less than or equal to four) variables (the first few PCs). Higher-component principal axes point in directions of successively lower scatter in the original data swarm. Points in PC space are separated by distances dependent on differences in the spectral reflectance (Lisbon Valley, Utah, Uranium Test Site Report, Section 8, Appendix E). Furthermore, the cosmetic contrast stretches applied to the image act directly to separate further the points in this space; that is, they act as a dilational transformation on the data swarm. The relative positions of data points in the space do not change relative to one another under this orthogonal transformation. The PC method relies on separating spectral groups along the principal axes, based on differences in reflectivity for the entire scene observed by the scanner. The so-called canonical transformation is a special case of the PC transformation to direct the axes for maximum separation of specified groups. Thus the canonical transformation may achieve greater separation for specialized groups, but the PC transformation provides the best possible (untrained) separation for all spectral groups present in the image without regard to the actual distribution.

c. Map of oxidation effects from the NS-001 PC image. Outcrops of oxidized granite in the NS-001 images of Figures 9-26 and 9-28 appear pink to magenta in hue, and a careful examination of these images discloses that such weathered granite outcrops are the only ones depicted in this way. There is no confusion with other iron-bearing rocks such as the red beds. The outcrops of granite thus identified as oxidized were compiled onto the 1:24,000 topographic map base of the geologic map. Using procedures and criteria similar to those described earlier in construction of Figure 9-40, the distribution of oxidized granite outcrops so obtained is shown in Figure 9-41. For granite outcrops lying between Steffen Hill (labeled "Paleozoic Rocks") and Arrowhead Mine in a N–S direction and between the West and East Forks of Dry Creek, the surface oxidation depicted is essentially complete. The oxidation along the northern flight line occurs in a thin strip adjacent to the contact between granite and Tertiary–Quaternary sediment. East of the East Fork and south of Berger Ranch, and 3.5 km east to the Paleozoic section, the oxidation is patchy in the northern part and shown to occur mostly continuously along the southern boundary and up into the East Fork. A significant lack of oxidation is depicted surrounding the dogleg-shaped finger of Wagon Bed sediments extending northeast into the granite (Sec. 35, T40N, R92W) which is shown on the map of Figure 9-41 and which may be verified by study of the images in Figure 9-28.

To the north along the East Fork of Dry Creek and along the next valley to the west, oxidized pink outcrops occur along the canyon bottoms and valley sides. Some of these distributions coincide with trains of metasedimentary xenoliths in the granite. To the east stringers of oxidized rocks extend northeast toward Greer Peak, and follow belts of metamorphic inclusions to the southeast. Elsewhere throughout the North Canning Stock essentially no pink granite outcrops are depicted in the NS-001 PC results.

4. Comparison of the M²S and NS-001 data interpretations. While the M²S CRC and density slice data may have a quantitative interpretation in terms of Fe^{+3} absorption band strength according to the calibration curve of Figure 9-39, the NS-001 PC data possess no such clear-cut interpretation. Thus, while a quantitative comparison of these two distributions is not feasible, a broad similarity between the results emerges. Over the southern one-half of the map corresponding to heavily oxidized, continuous outcrops, the two sets of scanner results agree. East of the East Fork in the southern half, the pattern depicted on both is complicated by topography, but both show reduced oxidation effects in the pre-Wagon Bed drainage of Secs. 35 and 36, T40N, R92W, near the Tertiary sediments occupying part of that drainage. To the north, both scanners show similar distribution patterns along the East Fork of Dry Creek and an adjacent drainage to the west. Beyond these, few similarities in the patterns are found. Qualitatively it appears the two results depict different degrees of oxidation intensity, largely agreeing where the effects are intense, disagreeing where they are subtler.

Additional possible explanations for the disagreement are the difference in wavelength regions sensed by the M²S and NS-001 instruments and the variation in processing methods used. The M²S is restricted to wavelength regions short of 1 μm; the type of ratio processing used emphasizes only the intensity of the iron absorption band at 0.9 μm, regardless of what other mineral constituents are present. The NS-001 data sample spectral reflectance in various

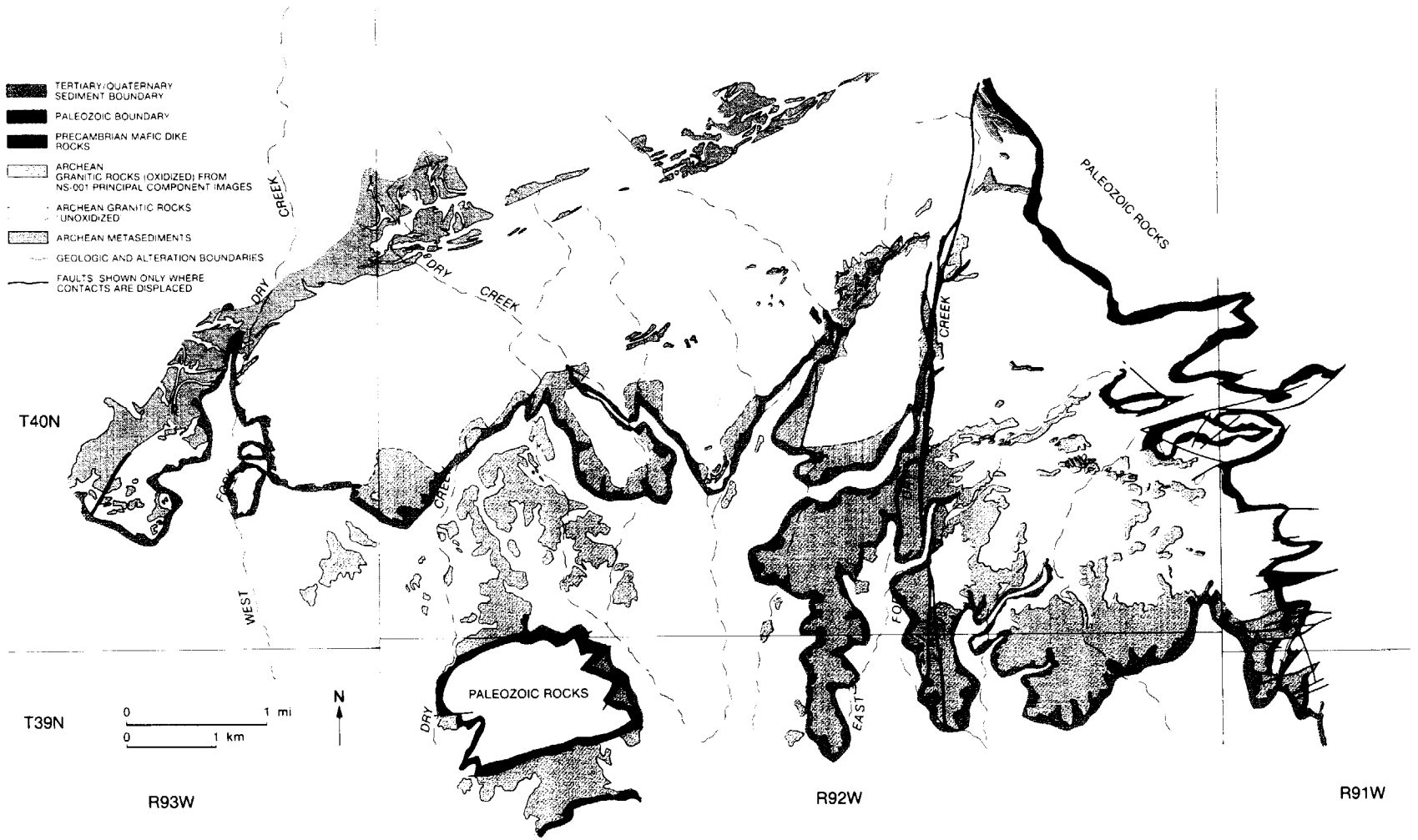

Figure 9-41. Distribution of oxidized granitic outcrops from the NS-001 PC images of Figures 9-26 and 9-28 (geologic boundaries for the Archean, Paleozoic, and Tertiary/Quaternary sedimentary rocks from Thaden, 1980b–1980e)

bands between 0.45 μm and 2.2 μm. The PC method separates groups based on spectral characteristics throughout this wavelength region; thus it is sensitive mainly to the presence of iron-oxide minerals, and to a lesser extent to hydrous minerals also. The combination of bands results in a delineation of the heavily oxidized granites versus other iron-rich rocks elsewhere in the scene, which the M²S data are unable to accomplish.

5. Comparison of oxidation patterns with physiographic features

a. Introduction. Based on the work of Blanchard (1968), Yellich et al. (1978) regarded the oxidized granite of the Copper Mountain area to be a result of alteration by corrosive meteoric (ore) fluids carrying the uranium. The oxidized layer might be pictured as analogous to the alteration tongue in a sandstone roll-front deposit. Observations in prospect pits show the oxidation along fractures to extend to a depth of at least 10 m (Figure 9-8). Presumably under these circumstances the oxidation could proceed while the granites were still buried beneath Tertiary sediments; indeed it is unclear from Yellich et al. (1978) whether they thought the oxidation to be subaerial, to have taken place at depth beneath the Tertiary cover, or both. As described above in the studies of the NURE drill cores, the oxidation is not everywhere present beneath the Tertiary adjacent to the ore bodies. The oxidation may have been removed by erosion or may never have existed in the old paleodrainages that were subsequently filled with tuffaceous Wagon Bed sediments. Bramlett et al. (1980) discussed derivation of uranium from the granite and concluded that uranium accumulated in the Canning resource was, from a material balance point of view, about that expected from leaching of the weathered layer above the accumulations. This suggests a circumstantial connection between the weathered layer and the uranium accumulation, but does not establish the weathered layer as the original uranium source.

Since the scanner data provide surface distribution of the oxidation effects that are not easily mapped on the ground, it might be expected that analysis of this distribution with respect to landforms, lithologies, or structures would yield further insight into the geologic significance of the alteration and its possible relationships to ore occurrences. Some observations on the physiographic relations of the oxidation distribution and the relations to Tertiary sediment cover are described below.

b. Erosion surfaces along the range front

Description of the surfaces. Two, and possibly more, major stages of pediment formation are represented in the Tertiary and granitic rocks along the range front at Copper Mountain. Here the predominantly Tertiary-age surfaces, as opposed to younger features produced during Quaternary time alone, are discussed. The youngest surface is cut in folded and faulted sediments of the Wagon Bed Formation. This surface is capped by Quaternary gravels (Holocene–Pleistocene), examples of which are found along the West Fork of Dry Creek. These relationships place the age of surface development between Middle to Upper Eocene and possibly as late as the Pleistocene. Examples of sharp truncation relations are found in the area south of Steffen Hill (Figure 9-23). The oldest surface identified is cut in the Precambrian granite along the range front and is interpreted to be overlain with Wagon Bed sediments and possibly Quaternary gravels throughout the study area. Mantling by the Wagon Bed would indicate the age of this surface to be older than Middle to Upper Eocene. Figure 9-42 is a photomosaic view showing part of

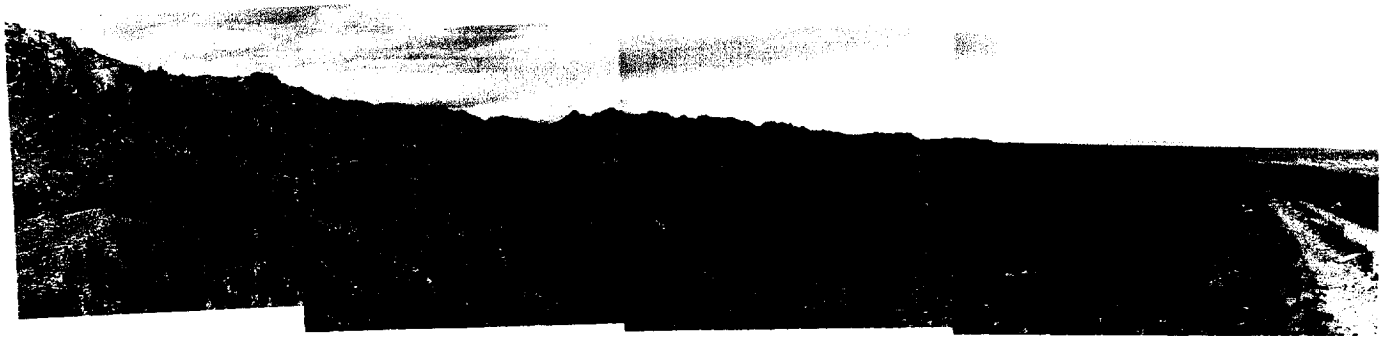

Figure 9-42. Photomosaic view looking southeast from Tertiary Wagon Bed gravel terrace in the East Fork of Dry Creek (predominantly SW 1/4, Sec. 26, T40N, R92W). Hummocky and grus-covered erosion surface cut in the Archean granite. Nickpoint is defined by an abrupt rise in slope on left side of picture. Canyon in foreground is the East Fork of Dry Creek. Limits of this pediment surface are defined by topographically similar nickpoints along the range front, the distribution of which is shown in Figure 9-43.

the upper portion of the granitic erosion surface exposed east of the East Fork of Dry Creek. Typically the surface is hummocky, rolling, and covered with grus derived from breakdown and disaggregation of the underlying granitic rocks.

Mapping the older erosion surface. The northern limit to planar parts of the older (pre-Middle or Upper Eocene) erosion surface cut in the granite is defined by a pronounced topographic inflection (nickline) separating the gently dipping (5° to 7°) lower surface from the steeper range front. The nickline for the small segment shown in Figure 9-42 follows along the left side of this photograph. Using this physiographic criterion, a nickline defining the northern limit may be traced almost continuously along the range front. This older pediment nickline is depicted throughout the study area in Figure 9-43. The nickline traced in this manner is generally identifiable between the 6200- and 6300-ft contours on the topographic map. The surface edge defined in this way rises in elevation to the east where it is found between 6300 and 6400 ft. In general, all outcrops of granitic rock south of the nickline depicted in Figure 9-43 may have been part of the subaerial pre-Middle Eocene physiography. Substantial topographic relief probably existed in the pre- to Middle Eocene granite surfaces, thus contributing to a rugged as opposed to a flat planar aspect for the whole.

Distribution of Tertiary–Quaternary sediments. The distribution of Tertiary and Quaternary sediments (undivided) as taken from the mapping of Thaden (1980b–1980e) is shown with respect to the older pre-Eocene surface in Figure 9-43. Tertiary rocks occupy the slopes along the range front with islands or elongated outcrops of granite rock (possibly representing buried ridge tops) protruding through the blanket. Long finger-like deposits of the Tertiary rock extend up the major drainages to elevations as great as 6800 ft (Hoodoo Creek, not shown). Apart from these extensions the preserved limits of the Tertiary deposits largely parallel the limits of the pre-Eocene granite erosion surface, with the Tertiary rocks probably having been eroded back in post-Middle or Upper Eocene time.

c. Grus-mantled terrain as possible extensions of the pre-Middle Eocene pediment physiography

Description of the terrain. Above the E–W-trending nickline that defines the older pediment surface, the mountains are characterized by steep slopes and rugged physiography. Two contrasting physiographic types occur: (1) those dominated by blocky, rugged forms, and (2) those dominated by rounded forms, characterized by smooth slopes and few apparent rocky outcrops. Both the metasedimentary terrain and the granite terrain display this rounded appearance; the granitic terrain alone will be discussed in the following paragraphs.

The best-developed example of rounded or mantled terrain occurs along the East Fork of Dry Creek in Secs. 14, 15, 22, and 23, T40N, R92W (Figure 9-43). This terrain is shown in the high-oblique aerial view of Figure 9-44, which looks south along the East Fork drainage toward Steffen Hill. This drainage and the one intersecting from the west display typical aspects of the rounded physiography defining the mantled appearance, which contrasts sharply with that of the blocky intervening ridge. In the field, the rounded physiography is characterized by grus-mantled slopes and ridges, and low immature soil development.

Distribution of the grus-mantled terrain. The general distribution of rocky and rounded terrain may be mapped fairly easily using stereoscopic aerial photographs. An interpretation of the distribution obtained from such mapping is shown in Figure 9-45. The distinctions are easily made because blocky terrain is characterized by extensive fracturing, whereas in mantled terrain fracturing is not present or is indistinct. Examples of the mappable, nearly vertical fracture system cutting the granitic outcrops are shown in the interpretation. Fractures (with no displacements discernible) or faults also cut the mantled terrain and bound some of the blocky units. In general these structures are subtle, and are marked by slight color changes or reduced physiographic alignments.

Although characterized by rounded surfaces, the mantled terrain is essentially continuous with the topographically lower, older erosion surface. This older surface itself displays numerous low, rounded ridges and hills, whose tops are concordant and constitute the pediment. Thus the physiographic character of these two terrain types is roughly similar.

Origin of mantled terrain. Mantled terrain coincides with the bottoms of drainages and the slopes along the sides of valleys. Its distribution in these places and continuity with obvious paleotopographic features suggest it originally formed during the pre-Middle Eocene erosion cycle that produced the pediments below. This terrain was probably once covered by Wagon Bed or younger sediment, perhaps to great depth, in keeping with the notion of a general mantling of the topography by Wagon Bed rocks (Thaden, 1980b).

The mantled outcrops have been characterized as residing in rotten granites that were at one time covered with

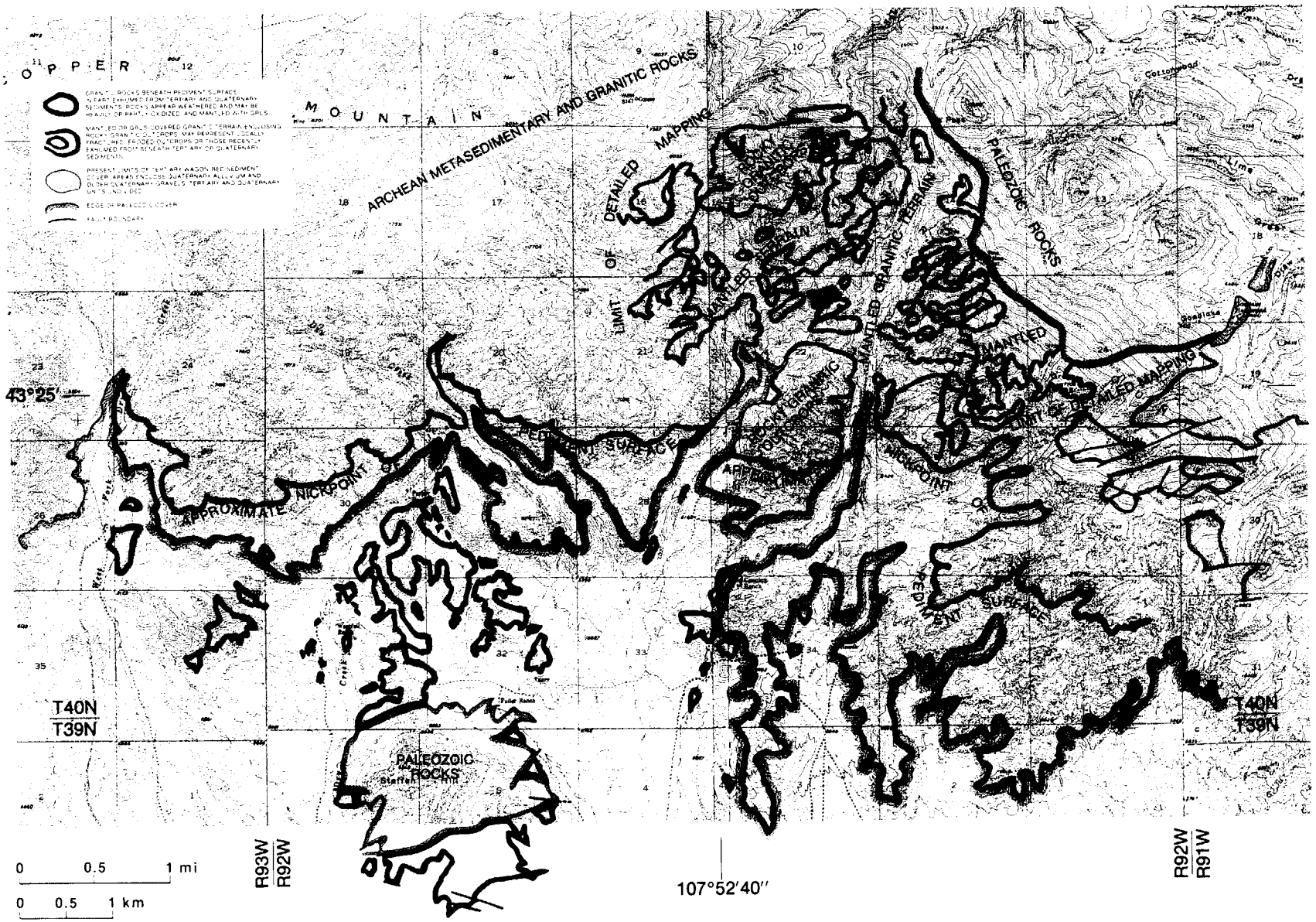

Figure 9-43. Outline of the interpreted physiographic elements and mapped geologic units along the range front covering portions of the Guffy Peak, De Pass, Picard Ranch, and Gates Butte Quadrangles. (Mapped geologic units from Thaden, 1980b–1980e.)

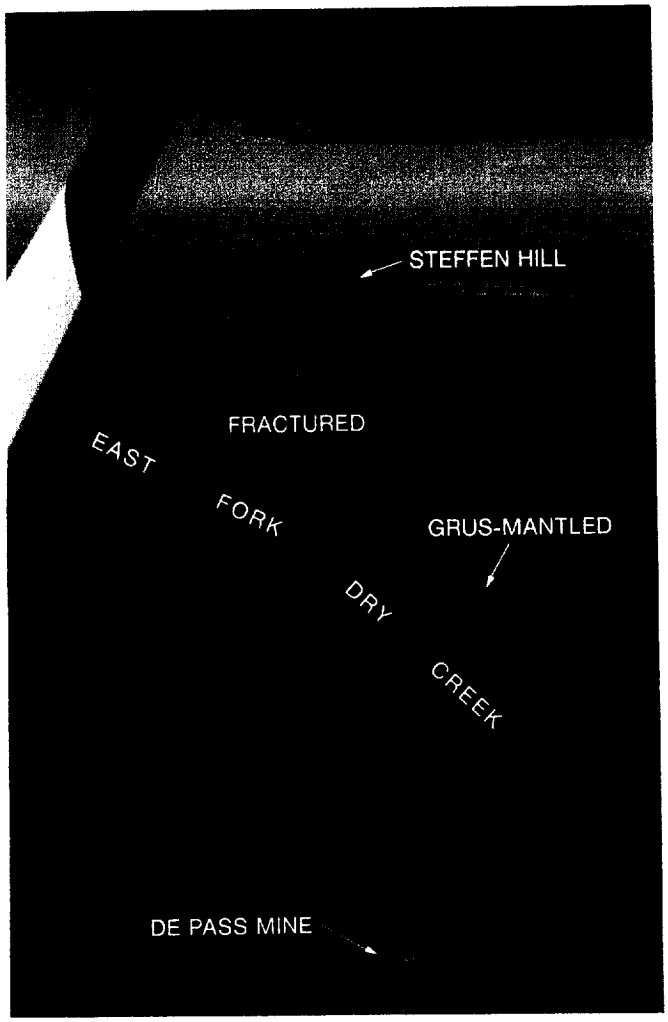

Figure 9-44. High-oblique aerial view looking south-southwest along the East Fork of Dry Creek. De Pass Mine is in foreground, and Steffen Hill is in the middle distance. Contrast in massive (fractured) and grus-mantled terrain may be seen in middle of photograph to the west (right) of Dry Creek.

sediments and submerged in a shallow lake dammed to the south by Cedar Ridge (Thaden, personal communication, 1981). Rocks saturated with oxygenated alkaline fluids would probably weather more rapidly than ones that were dry or unsaturated. Reemergence to subaerial conditions with erosion of the sediment might be expected to promote rapid decomposition of feldspars and alteration of iron-rich minerals to clays and iron-oxide compounds. The mantled terrain may also be the locus for (1) intense fracturing, (2) larger abundance of (unmapped) xenoliths, (3) changes in composition of the granite to include more ferromagnesian minerals, or (4) possibly a combination of these.

d. Relationship of the oxidation to physiography

Relationship to the older pediment surface. A comparison of the exhumed granitic portion of the older pediment contained between the nickline and the Tertiary–Precambrian sedimentary contact (Figure 9-43) and the distribution of oxidized rocks (Figures 9-40 and 9-41) shows that the pediment-surface rocks are to one extent or another oxidized. In places, the boundaries of image-depicted oxidation and the pediment nickline agree in detail with oxidized terrain contained within the surface. Elsewhere, the agreement is not as good (for example, the pediments east of the East Fork of Dry Creek).

Relationship of the mantled terrain and oxidation, upper East Fork of the Dry Creek drainage. To provide an example of the relationship between the image-derived distribution of oxidation and the aerial-photography-derived distribution of mantled terrain, the (red–magenta–black) image patterns of the two-channel ratio density slice (Figure 9-38) have been transferred to the aerial photographic base of Figure 9-45. The pattern of oxidation thus adjusted is shown in Figure 9-46. In the upper East Fork drainage, the correspondence between mantled and oxidized terrain is good. These relationships were difficult to establish from the color aerial photographs alone.

Possible time dependence of the granitic oxidation. The age of surface weathering in the granites is important for its possible relationship to uranium mineralization. Examination of Figure 9-47 suggests the possibility that red coloration may develop progressively after removal of the overlying sediment cover. The granitic spur along the center of this aerial view shows an apparent variation of surface oxidation from the foreground to middle distance. The spur has probably been progressively uncovered along its length from higher to lower elevation. The apparent orange coloration appears to deepen with increasing elevation and this effect may be caused by additional weathering in the subaerial environment or by removal of a residual light-colored sediment coating.

If the surface oxidation effects are more modern in origin (i.e., post-Miocene and extending into the present time), the relationship to uranium mineralization becomes more tenuous. The problem of the age of the surface weathering is then an important topic for additional study in the context of establishing a relationship between surface effect and deeper uranium mineralization.

6. Comparison of oxidation patterns with the distribution of uranium-mineralization and Tertiary sediments. The supergene ore deposition model proposed for the

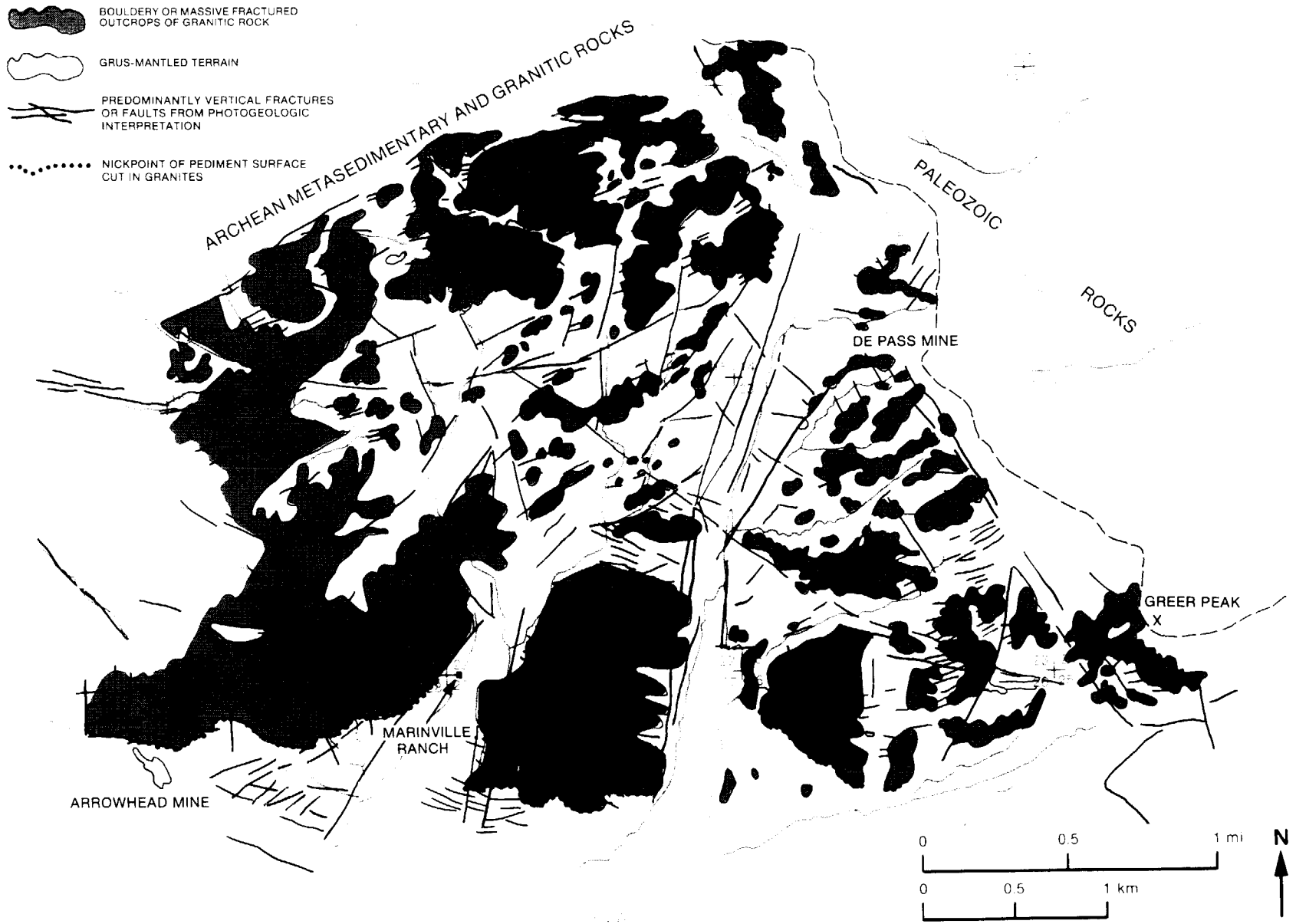

Figure 9-45. Outcrops of bouldery granite terrain displaying fractures surrounded by rounded (rotten granite) grus-mantled terrain. Fractures are well displayed in massive outcrops and seen as subtle fault lines in mantled areas. (Photogeologic interpretation from photo 88-007, NASA Johnson Space Center (JSC) Mission 383, August 1978.)

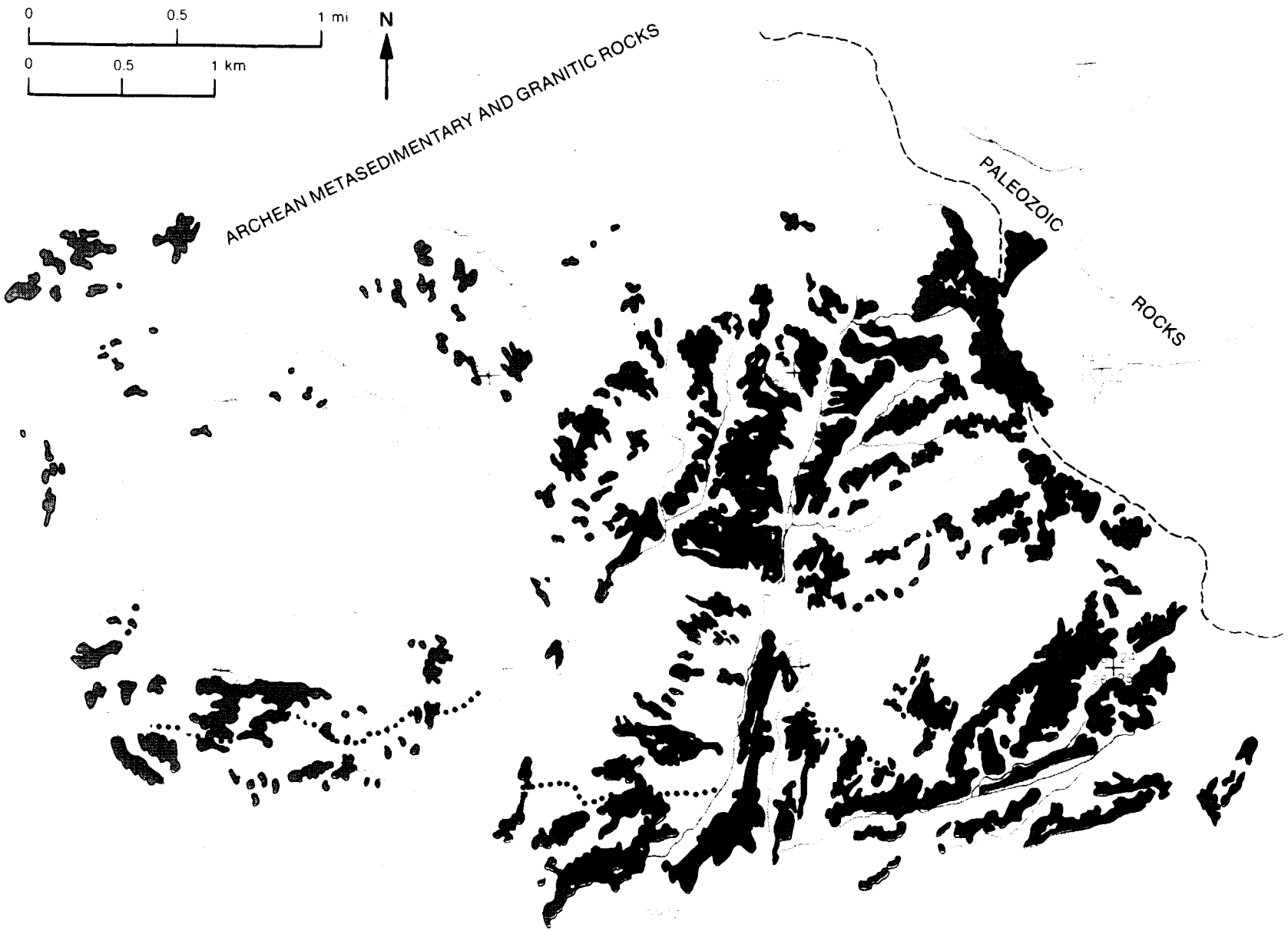

Figure 9-46. Outline of red–magenta–black areas of the M²S density slice rectified to aerial photograph base (photo 88-007, NASA JSC Mission 383, August 1978). Dotted line is nickline of pediment.

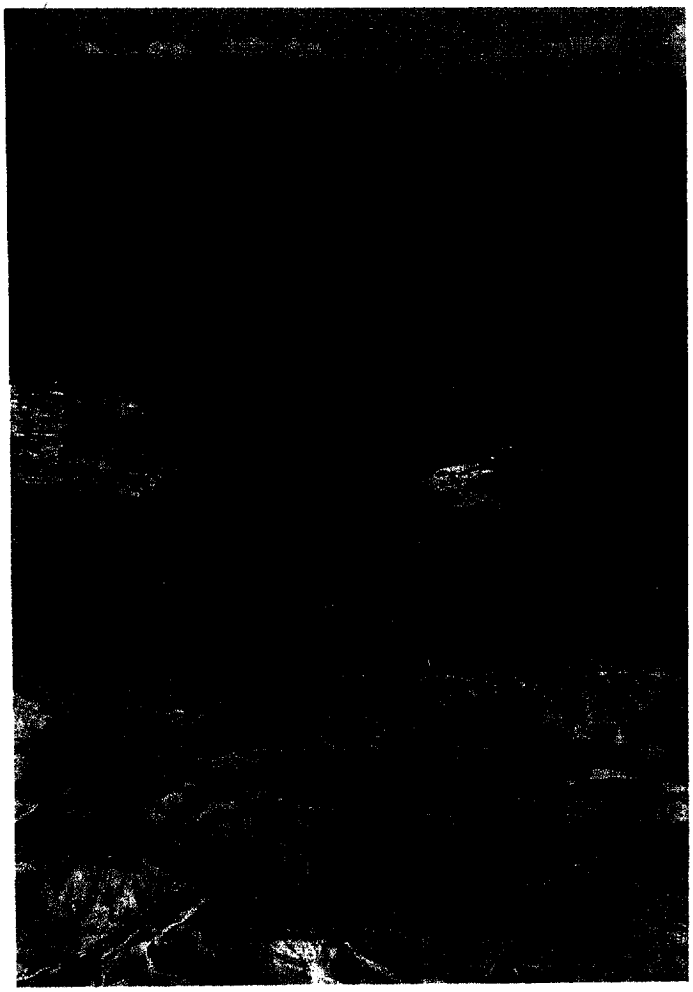

Figure 9-47. High-oblique aerial view looking north up the West Fork of Dry Creek. Granitic spur along center of picture shows apparent variation of surface oxidation from foreground to middle distance. If the spur has been uncovered with time along its length, the emergence of the red-orange coloration may be a time-dependent effect developing only or additionally after Wagon Bed sediments have been removed. Alternate view is that oxidation is pre-Wagon Bed with residual sediment coating newly exposed outcrops.

Copper Mountain uranium resource (Yellich et al., 1978) suggests that granitic rocks near the surface were leached of their uranium, and the dark minerals and pyrite were oxidized. Using the interpreted distribution of surface oxidation obtained from the aircraft scanner data, these relations, as well as the relationship of mineralization to the other geologic boundaries, can be studied.

a. Distribution of mineralization. Yellich et al. (1978) described the distribution of mineralization in the North Canning uranium prospect. The mineralization is locally controlled by fracture porosity arising from brecciation with faulting. Mapping of the North Canning resource from drill-hole data shows the enriched zone in plan view to be wholly within the outcrop pattern of the Wagon Bed Formation. Granitic rocks outside the limit of sedimentary cover are not found to be mineralized, a pattern followed by all of the other fracture-controlled granitic accumulations in the test site. These observations are interpreted to mean that the Tertiary sediments provide a protective cover preventing remobilization of the uranium and destruction of the accumulation by leaching.

Figure 9-48 shows the approximate distribution of uranium mineralization for the Fuller and Canning resources in the Copper Mountain test site, as well as the locations of earlier uranium mines, prospect pits, and open cuts.

The approximate subsurface limits of mineralization were obtained from the distribution of exploration drill holes throughout the study area. Two sources for this distribution were: (1) drill-hole location maps provided by RME, giving positions of all holes emplaced up to August 1978, and (2) NASA aerial photography of August 1979, giving all additional holes drilled to that time. These patterns of drill holes, of course, are likely to encompass the actual ore body (however it is defined by uranium abundance) and to extend beyond it. The actual detailed limits of mineralization are proprietary information, and in any event are not important. The hachured areas of Figure 9-48 represent the areas common to the pattern of drill holes and to the outcrops of Tertiary sediments. The Tertiary sediment outcrops were taken from the published maps of Thaden (1980b–1980e). The Wagon Bed may be capped by a thin veneer of Quaternary gravel deposits and be so represented on the image data. These hachured patterns of ore accumulation are likely to over estimate somewhat the actual distribution of residual mineralization, but they give an idea sufficiently accurate for the purposes intended here. The additional locations of mines, prospects, open cuts, shafts, adits, and prospect pits were obtained from the geologic maps of Thaden (1980b–1980d). The geology of some of the more important of these places of exploration interest was summarized earlier.

b. Comparison with patterns of oxidation and sedimentation. Figures 9-49 and 9-50 show the distribution of the major residual uranium accumulations in the granite, obtained in the manner just described, and in the Tertiary sediment; these are given with respect to the distribution of oxidized rocks, the Tertiary–Precambrian depositional contacts, and the border of the pre-Wagon Bed pediment surface.

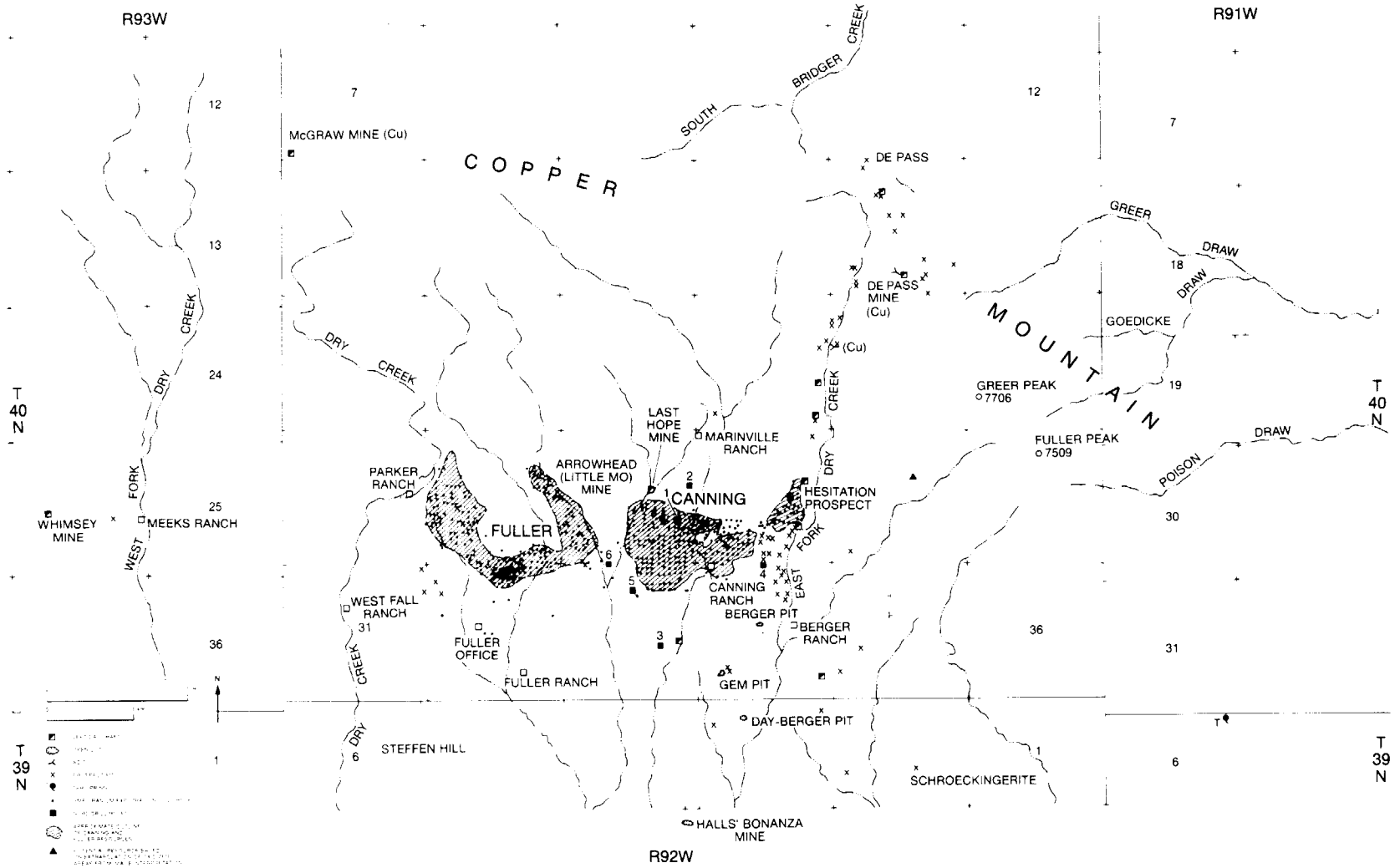

Figure 9-48. Distribution of mines, prospect pits, cuts, and uranium accumulations in the Canning and Fuller resources, given approximately by the area common to patterns of exploration drill holes and outcrops of overlying Tertiary sediments. Shafts, cuts, adits, pits, and tar spring from mapping by Thaden (1980b, 1980e) and Yellich et al. (1978). Drill-hole data to August 1978 courtesy of RME. Drill-hole data to August 1979 based on approximate locations from NASA JSC aerial photography, August 1979.

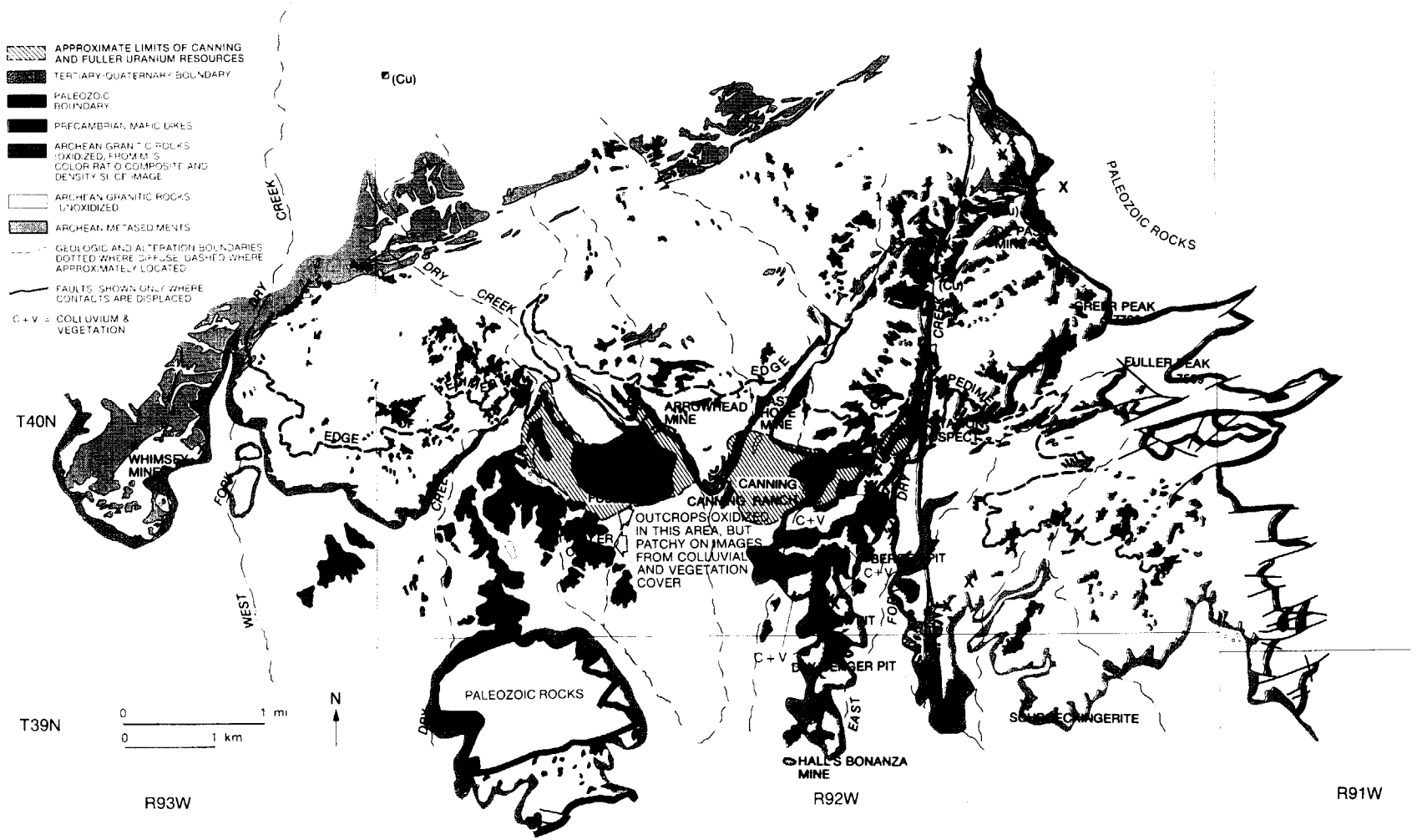

Figure 9-49. Canning and Fuller resources (in granitic rocks) and minor uranium prospects (in granite and Tertiary sediments) plotted with respect to the distribution of Wagon Bed and Quaternary sediments and surface oxidation patterns, obtained from the M²S image, in the granitic rocks. For color code, see Figure 9-40, and for mine and prospect symbols, see Figure 9-48. (Geologic boundaries for the Tertiary, Paleozoic, and Precambrian units from Thaden, 1980b–1980e.)

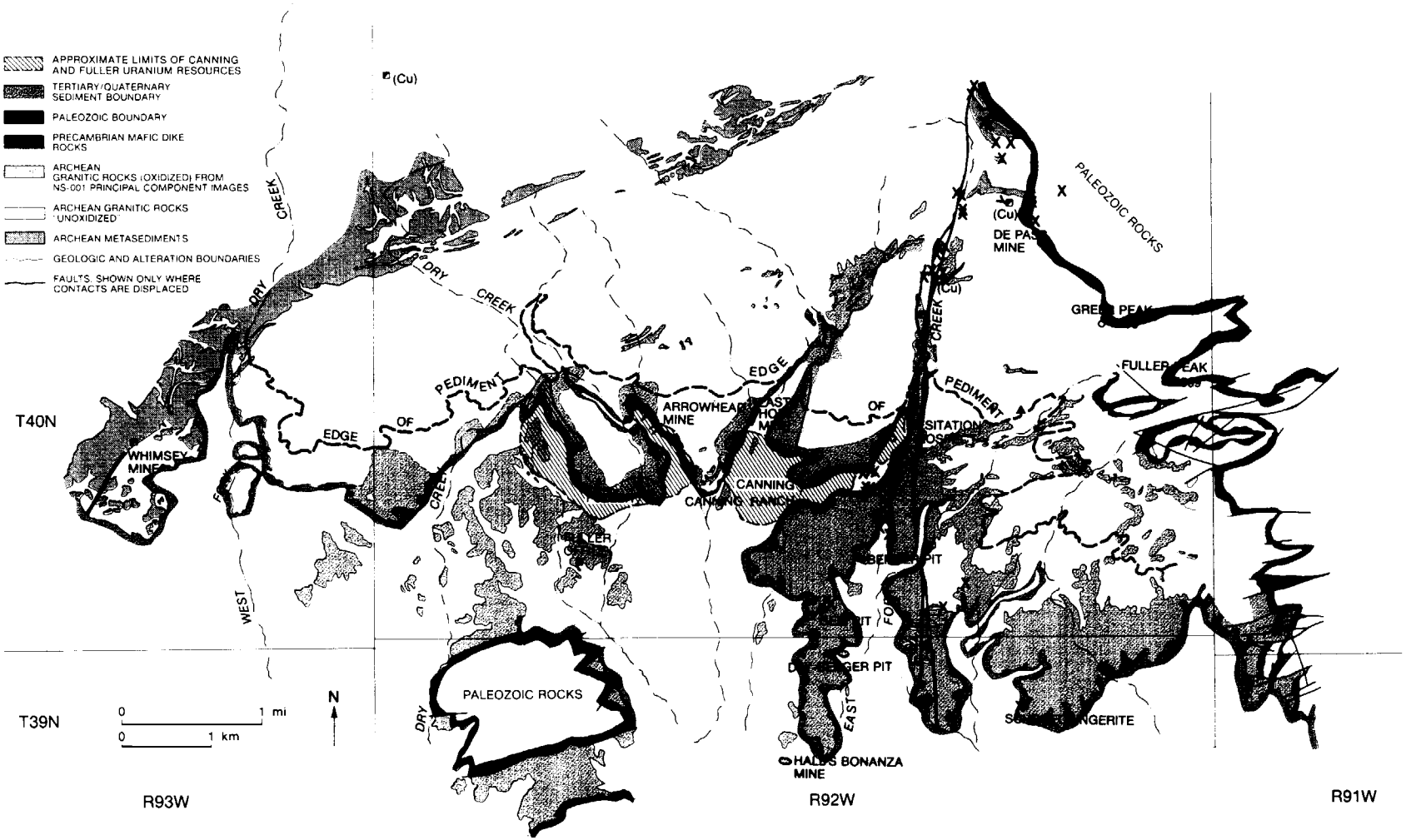

Figure 9-50. Canning and Fuller resources (in granitic rocks) and minor uranium prospects (in granite and Tertiary sediments) plotted with respect to the distribution of Wagon Bed and Quaternary sediments and surface oxidation patterns, obtained from the NS-001 image, in the granitic rocks. For color code, see Figure 9-41, and for mine and prospect symbols, see Figure 9-48. (Geologic boundaries for the Tertiary, Paleozoic, and Precambrian units from Thaden, 1980b–1980e.)

The Fuller and Canning accumulations fall near the pediment edge and therefore within the zone where the surface oxidation of outcrops is nearly complete. The distribution of ore also correlates with Wagon Bed sediment cover. The deposits appear to fall below embayments where the pediment surface, because of the gentle southward dip (5° to 7°), is seen to extend back into the mountains along the old paleodrainages. The surface is poorly defined at these points and cannot actually be mapped in the Last Hope and East Fork drainages where the canyons are partly filled with Wagon Bed sediments.

The distribution of other uranium accumulations in the granite and Tertiary sediment is interesting because, with the exception of the Arrowhead and Last Hope Mines, these fall largely along the drainage defining the East Fork of Dry Creek. None of these has been the site of major production. A number of examples fall close to the Tertiary–Precambrian depositional contact, sometimes within the granites (Gem Pit, for example), and sometimes within the Tertiary section (Day–Berger and Hall–Bonanza).

On an empirical basis then, uranium accumulations in the granites are found in association with oxidized granitic rock. Oxidized terrain exposed at the surface includes (1) smooth but "hard" granite outcrops on the pediments, and (2) grus-mantled outcrops in the paleodrainages. Large uranium accumulations are overlain by Tertiary sediments and bordered by areas of oxidized granite. Other minor prospects occur adjacent to oxidized rock in the Tertiary section. However, accumulations of Tertiary rocks are present adjacent to oxidized terrain where no uranium deposits in the granites are as yet known.

c. Extrapolation of the correlations. Early in this investigation the CRC images of the M^2S data were studied and the distribution of oxidation depicted by the remote sensing data was qualitatively compared with the distribution obtained from field mapping (Figure 9-6 and Yellich et al., 1978). Systematic differences were observed between the two interpretations. In particular, the images first suggested the granitic terrain between the East Fork of Dry Creek and Paleozoic cover (Secs. 35 and 36, T40N, R92W) to be less oxidized or of a different character than designated by the field mapping. Second, the images indicated new areas of oxidized terrain outside the previously mapped oxidized zones, which were occurring among "fresh" granitic rocks according to the field interpretations. These new areas corresponded to the mantled terrain of the upper East Fork of Dry Creek, as well as numerous outcrops between that drainage and Greer and Fuller Peaks. Subsequent RME field exploration disclosed the presence of anomalously radioactive outcrops along shear zones in the granites associated with the oxidized zones. This new anomalous mineralization in the surface rock is located at "▲" in Figures 9-48, 9-49, and 9-50. Thus far these outcrops have not proven to be of economic significance.

From the two types of observations given above, the interpretation of partially oxidized terrain of Secs. 35 and 36 might now be recognized to result from directional effects in the image data together with effects related to recent uncovering of the weathered pediment surface. In this latter instance the rocks may have a residuum of Wagon Bed sediment at the surface, or they might not yet have developed their fully oxidized appearance upon removal of the sediment cover.

d. Discussion of observations. On a causal basis it is difficult to present a convincing case that the surface granite oxidation is a useful guide to the distribution of mineralization. Some important points concerning the geologic history of the oxidation need to be clarified before such terrain can be considered to have anything other than a coincidental relationship to mineralization.

(1) The distribution of uranium mineralization is controlled in detail by fracture porosity at depth, but no useful surface guide to the fracture porosity has been worked out. Consequently, no correlation with oxidation effects present at the surface can yet be established.

(2) The distribution of mineralization is also apparently governed by the distribution of capping Tertiary sediments at the surface. No hint of the initial distribution of uranium is evident before its remobilization and removal. Thus the present distribution of mineralization may bear little resemblance to the original distribution or to the distribution of oxidized outcrops.

(3) Development of the oxidation surface layer may be a modern effect accompanying reexposure of the granitic pediment surface. This question could possibly be studied by examination of many drill cores to estimate a depth of weathering as a function of surface exposure age. A relatively modern (Pleistocene–Holocene) origin of the oxidation would eliminate a troublesome contradiction in apparent age of the weathered surface and the apparent time of mineralization.

An alternate scenario might be that the uranium accumulated independent of the development of these surface

effects. However, the reconciliation of these difficulties lies outside the arena where remote sensing observations can play a role.

D. Soil and Vegetation Mapping Using Aircraft Data

1. Comparison of soil mapping with interpretation of NS-001 image data. Soils cover the outer portion of the Earth's surface and result from chemical weathering and mechanical breakdown of the surface rocks. Different soils support different plant communities. The soil scientist classifies and maps the distribution of soil types on the basis of characteristics both at the surface and in subsurface horizons. His basis of mapping is substantially different from that of the mapping geologist. The scanner data pertain mostly to the soils or to the weathered near-surface. Thus any discussion of geologic interpretation based on scanner data must include a discussion of the soils and associated vegetation communities. Here some simple comparisons between image data and soil maps are presented. This study is not exhaustive in that there has been no attempt to reconcile all differences between soil and image unit boundaries. The utility of scanner data is, however, clearly demonstrated when applied to soil-mapping problems.

The NS-001 images provide a convenient basis for comparison of the SCS soil mapping and the image representations of surface units. Considering that the basis of soil classification is largely the subsurface B-horizon, plus the surface vegetation community, the agreement between these two sets of results is perhaps surprising. Examination of the soil-mapping data shows a good correlation of soil units with the surface albedo and topography. The albedo corresponds to the surface morphology and the net reflectance effects of lithology, weathering, and vegetative cover. The scanner data respond to surface reflectance and topography. The results suggest that the deeper chemical effects of soil development leave characteristic surface properties that may be studied by the ordinary aggregate reflectance properties of the surfaces.

The image interpretation given in Figure 9-24 is shown in Plate 9-1 with the addition of all identifiable soil units from the SCS mapping. As a general comment, these image data can be used to recover all soil boundaries depicted and provide additional subdivisions. All soil boundaries found in the field are represented together with additional subdivisions that correspond to slope wash deposits and vegetation cover. Thus the image data may be of considerable benefit in soil mapping to the extent that surface properties can be correlated with the defining subsurface-soil profile.

2. Comparison of SCS soil map and M²S CRC. Recognition of the red terrain in the East Fork of Dry Creek drainage is difficult from photographs, but SCS soil mappers made subdivisions of the soil units in this area. Figure 9-51 shows the soil map of Figure 9-5 superimposed on the CRC image of subarea 1. While many correlations between map colors and SCS soil units may be pointed out, probably none are more interesting because of their inherent subtlety in the field than those involving mantled and blocky terrain. Thus in the East Fork drainage, soil units 2f72 (Pesmo–Lupinto Variant) and 3109 (Rock outcrop–Ashbon complex) correspond to mantled rotten outcrops and blocky, weathering-resistant outcrops, respectively. Examination of the images shows how some soil boundaries could easily and quickly be made more accurate by reference to the image data.

3. Use of M²S 6/8 ratio density slice to obtain vegetation density estimates. The vegetation community map, given in Figure 9-4, shows the distribution of important plant communities throughout the Copper Mountain test site without presenting details of vegetation type or vegetation density. The distribution of major species is relatively insensitive to season, but the abundance of photosynthetic vegetative tissue at any place depends mainly upon season, rainfall, temperature, and possibly other factors. Plant survey data were not available for the periods of M²S or NS-001 overflights so a quantitative assessment of the plant cover characteristics from the images themselves is not possible. However, analysis of image data does provide insight into the effect of plant cover upon the mapping of alteration effects and lithologic units.

Field surveys of the shrub, grass, and juniper cover were made for selected areas in the test site during July 1981. The surveys consisted of simple 10-m transects to count plant types and to determine percent ground cover. The data from these sites (Table 9-17) were used to construct calibration curves for the image data used in the exercise.

Figure 9-52 is a density slice of the band-ratio 6/8 (i.e., Landsat 5/6) from the M²S data of the northern flight line (subarea 1). For neutral backgrounds in the absence of strong coloring effects in the rock or soil substrate due to Fe^{+3}, or in the absence of abundant dead vegetation, this ratio is relatively sensitive to the presence of chlorophyll pigmentation. The ratio indexes the "strength" of the chlorophyll absorption near 0.65 μm relative to the level of the adjacent continuum at 0.72 μm. For strongly varying backgrounds, the image can be expected to provide the most accurate results where density of green vegetation is high so that background effects are minimized. Wholesale interpretation of the image by itself in terms of a variation in plant cover alone is of course not warranted.

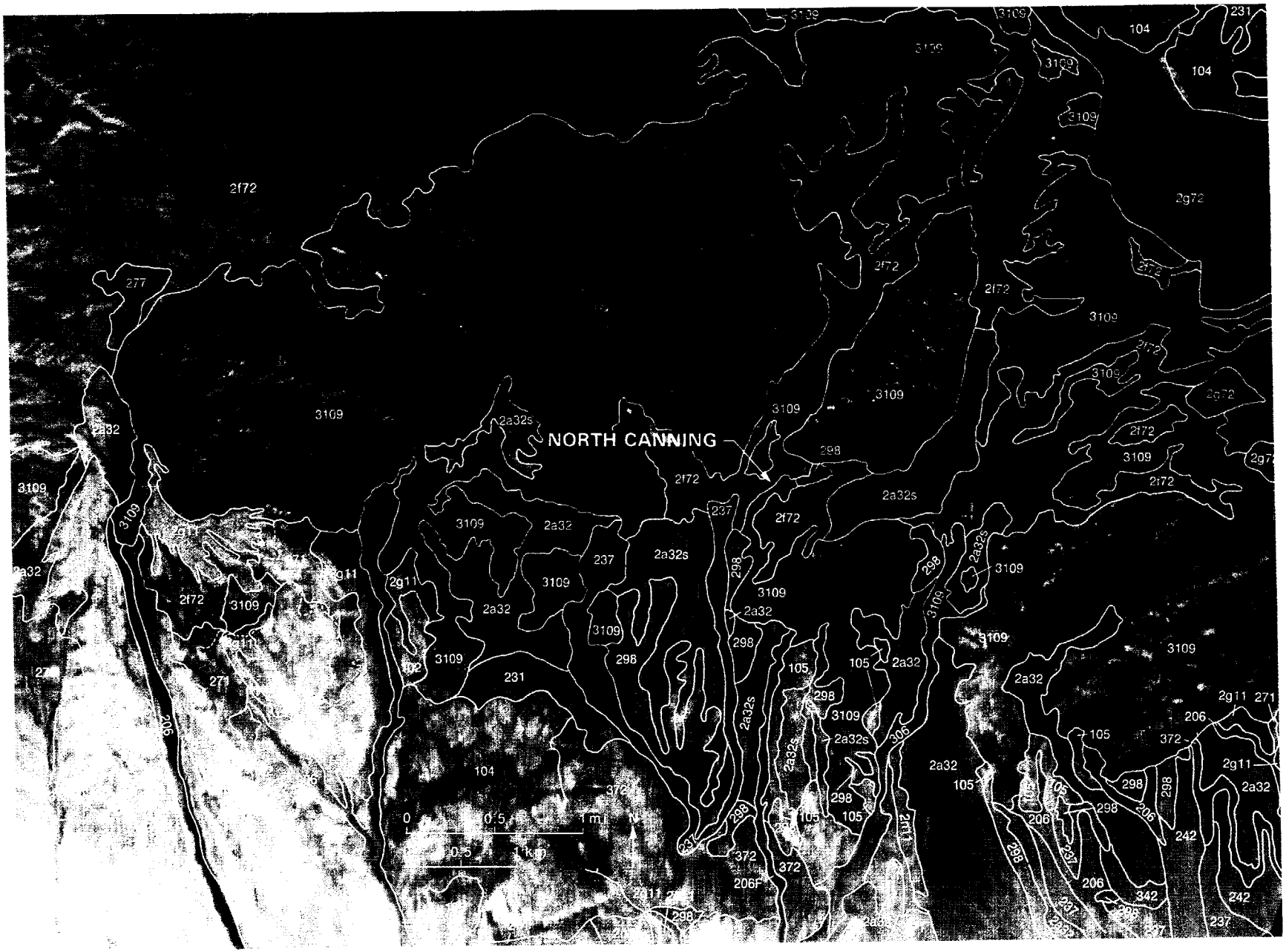

Figure 9-51. A portion of the soil map of Figure 9-5 superimposed on the M^2S CRC of subarea 1. Note that near East Fork of Dry Creek the soil mapping grossly distinguishes but inaccurately locates the boundaries of grus-mantled and blocky (massive) granitic physiographic units. The image colors are assigned as follows: 4/6 = blue, 4/8 = green, and 8/(9 + 10) = red.

Figure 9-52. Density slice of the M^2S band-ratio 6/8, equivalent to Landsat MSS band-ratio 5/6. Sites TI, TII, TIII, and CI represent control points for the calibration curve. Calibration of the color code as a function of macroscopic vegetation density is from Figure 9-53. Outlines of vegetation community distribution are from Figure 9-4.

Table 9-17. Vegetation, density, and image data for 6/8 M²S density slice (data collected July 1981)

Site[a]	Vegetation			Image Color[b]	Estimated DN Values	Average Total Cover, %	Range of Cover Estimate, %
	Type	Percent	Range				
CI	Sage	5	[c]	Light blue	140–166	17	[d]
	Grass	17	[c]	Light blue	140–166	17	[d]
	Juniper	1–5	[c]	Light blue	140–166	17	[d]
TI	Sage	26	15–54	Light blue	140–166	35	26–56
	Grass	Minor	Minor	Light blue	140–166	35	26–56
TII	Grass	27	[c]	Light blue	140–166	27	20–31
TIII	Juniper	26	11–36	Dark green	31–44	33	12–55
	Sage	14	0–31	Dark brown Dark red	31–44	33	12–55
"Fuller"	Cottonwood			Dark blue	0–13	60–70[e]	
Creek (FC)	Sage			Dark blue	0–13	60–70[e]	
Fuller Office (FO)	Bare			Red-orange	219–235	0[f]	

[a]Site locations given in Figure 9-52.
[b]From Figure 9-52.
[c]Range not available.
[d]Single traverse only.
[e]Visual estimate of canopy.
[f]Visual estimate of cover.

Approximate vegetation cover density may be obtained using the percent cover data of Table 9-17 together with the corresponding color code of DN equivalent. The calibration relationship obtained is shown in Figure 9-53. The larger error bars found for the measured points reflect much heterogeneity in the ground cover at the scale of the 10-m transects. These transects correspond approximately to the pixel size in this rendition.

When the vegetation community distribution is compared with the distribution of colors in the image rendition, it can be noticed that generally sagebrush–grasslands are areas of low vegetation density. Juniper-covered areas have intermediate densities, and the riparian and meadow sites have high densities. In a few places (for example between sites CI and TIII) sharp color boundaries on the image correspond to major changes in vegetation types. Using this key for the signature of juniper-dominated terrain (i.e., dark red and green mixed image colors near TIII), it can be inferred that extensive juniper cover can be found over portions of the old pediment surface near the Arrowhead Mine (which is anomalous for its locale) and both east and west of this point. This may explain in part the irregular distribution of oxidation effects mapped over pediments in this area in the M²S CRCs (Figure 9-35) and NS-001 PC images (Figure 9-28).

The image of Figure 9-52 may be used to refine and extend the distribution of riparian and meadow communi-

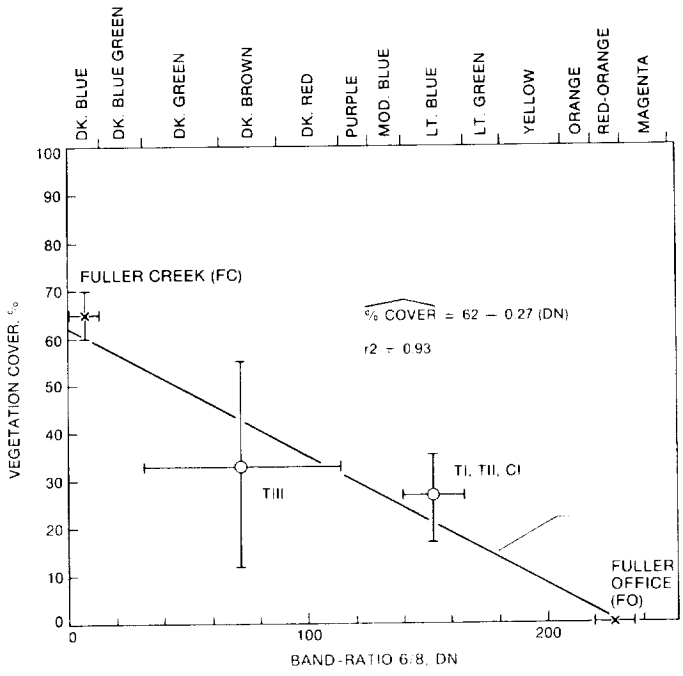

Figure 9-53. Calibration line for the M²S band-ratio 6/8, equivalent to the Landsat MSS band-ratio 5/6. The "X" near Fuller Creek represents a visual estimate of vegetation cover. Fuller Office is a cleared area. TIII and TI, TII, and CI are mean values of vegetation cover obtained from multiple field transects. Ranges of DN values were estimated from Figure 9-52, and the color scale is given in Figure 9-52.

ties and possibly the distribution of juniper elsewhere as well when compared to the generalized RME vegetation community map. This procedure would best be carried out with aerial photographs or other image data to secure separation of topographic and lithologic effects from those of the vegetation. The image could then form a useful guide to a quantitative assessment of plant cover variations.

E. Analysis of M²S Thermal Data

Thermal-infrared image data were acquired over the Copper Mountain test site with the M²S scanner operating in the 8.0 to 13.5 μm region. Two data flights occurred, one near noon, and the other predawn (night) on August 29, 1979. The data were processed in the standard fashion to reformat the bands (day data) and geometrically correct the panorama distortion. Further processing was done to register the nighttime data to the daytime data by identifying a large number of common tie points, then creating a "rubber sheet" stretch to force the geometry of the nighttime data to fit the daytime data.

The times of overflight were selected for different reasons. The daytime thermal data were acquired simultaneously with the 10 channels of visible and near-infrared reflectance data. The near-noon time was dictated by the desire to minimize shadow effects and maximize illumination. The nighttime data were acquired during predawn hours because of a combination of factors: (1) temperatures are relatively stable, (2) the effects of topography are greatly reduced or absent, and (3) large temperature differences occur for materials with varying emissivities (Kahle, 1980).

An effective, simple method of displaying the thermal and albedo information is to produce a color composite, assigning each of the three data types to either red, blue, or green (Kahle et al., 1981). Such a method was used to create the color image shown in Figure 9-54, which has an interpretive overlay superposed. The explanation of the unit symbols is given in Table 9-18.

The Precambrian granites appear red on the image: they have low albedo (green), low nighttime temperature (blue), and high daytime temperature (red). Limestones appear yellow to yellow-green, due to high albedo and moderate to high daytime/low nighttime temperatures. The Tensleep Sandstone is orange, implying lower albedo and higher daytime temperature than the limestone. This separation could not be made on the NS-001 PC images. The Wagon Bed Formation is green, blue-green, and yellow, depending on the lithology present. High-albedo consolidated materials are warmer in the daytime and tend more toward a yellow color than the green color of the high-albedo claystones. The bluer areas of Wagon Bed imply higher nighttime temperatures due to lower albedo (the areas absorb more energy). The Wind River Formation is not only the most extensive unit in the area, but also the most variable in color. Purple areas (labeled Ss) are sandstone facies, which have low albedo and high daytime and nighttime temperatures. The green areas are higher-albedo facies that do not heat up in the day and are cold at night. Yellow areas are conglomeratic or sandy facies, which have high albedos, but heat up in the daytime. Thin, blue areas are coal beds, which have low albedos and stay warm at night. Gravel outcrops have variable colors, depending on the source material and degree of consolidation.

Table 9-18. Explanation of unit symbols in Figure 9-54

Symbol	Corresponding Unit
Qal	Alluvium
Qoa	Older alluvium
Qg	Gravel
Twb	Wagon Bed Formation
Twr	Wind River Formation
C	Conglomerate
Ss	Sandstone
Silt	Siltstone
Mm	Madison Limestone
Ls	Limestone
Pt	Tensleep Sandstone
Pma	Amsden Formation
€gv	Gros Ventre Formation
€f	Flathead Sandstone
Ag	Granite
Am	Metasedimentary rocks

The amount of lithologic separation on this image is substantial. A fair amount can be attributed to albedo and the related temperature effects, though not everything. While there is only limited additional information compared to what the visible and near-infrared data can provide, thermal data can add to geologic mapping, particularly where density and thermal conductivity differences between rock units are important.

F. Interpretation of Landsat MSS Data

1. Introduction. Four Landsat MSS scenes covering Copper Mountain were obtained in digital form from the Earth Resources Observation Systems (EROS) Data Center (Table 9-19).

The March and December scenes were taken at times with excessive snow cover, and therefore were not used. The October and July scenes were further processed using

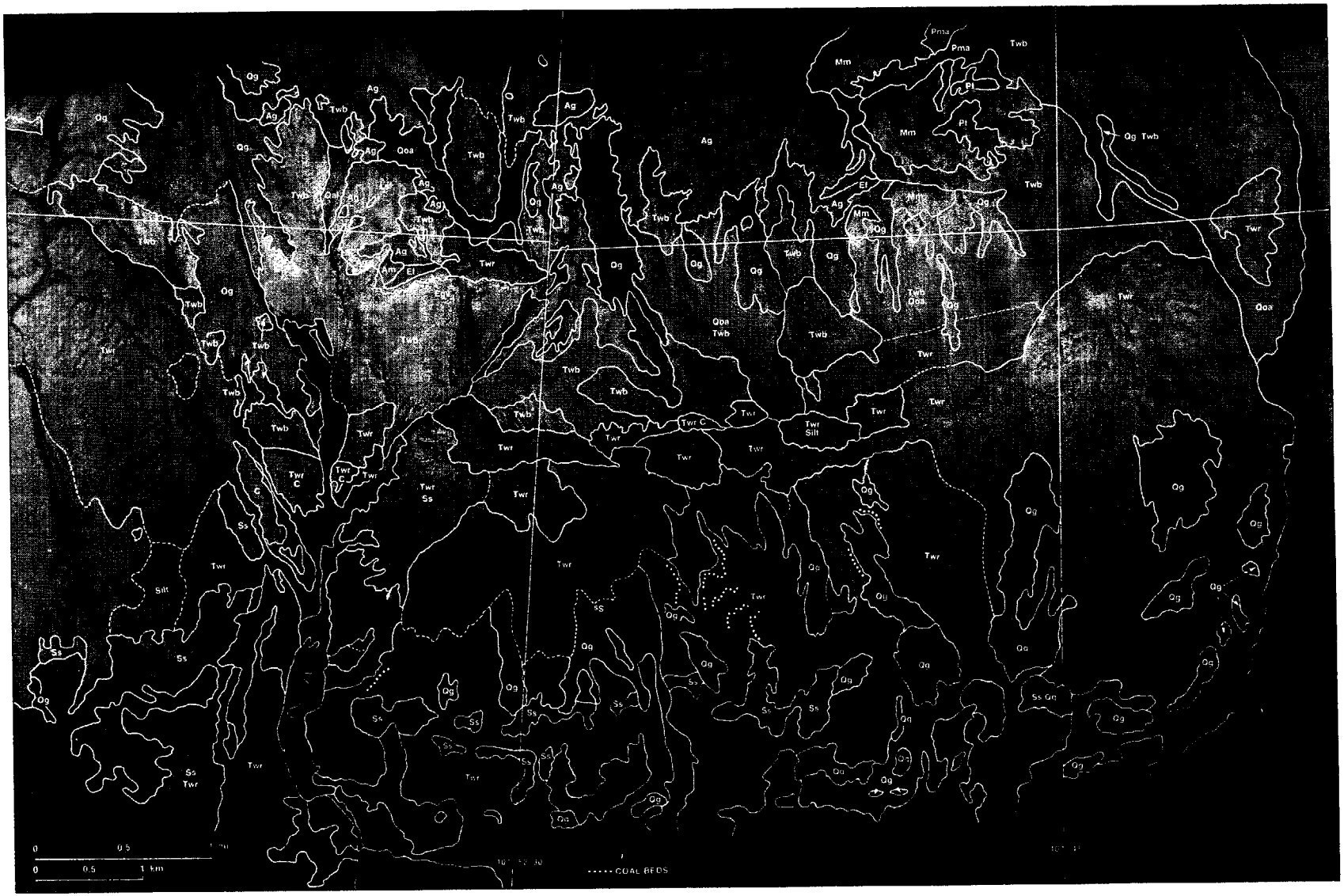

Figure 9-54. M^2S thermal and albedo composite, Copper Mountain. Night infrared, day infrared, and albedo data are displayed as red, blue, and green respectively. See Table 9-18 for explanation of symbols.

Table 9-19. Landsat MSS scenes

Date Acquired	Scene Number
March 26, 1973	10246-17251
July 5, 1976	20530-17060
December 14, 1976	20692-17003
October 16, 1977	20998-16453

contrast enhancements, PC analysis, and band ratioing. Examination of these products indicated that the decorrelation stretch and band ratioing of the October data were the most useful; these two products will be described in more detail below.

2. False-color infrared composite. The full-scene October Landsat image shown in Figure 9-55 is a composite of MSS bands 4, 5, and 7 displayed as blue, green, and red, respectively. The data were processed using decorrelation stretching techniques, which greatly exaggerate saturation and intensity variations, but preserve the hue information.

The most striking features in the scene are the yellow areas, which correspond to red beds. These are mostly Triassic sandstones and siltstones; some of the more diffuse areas are either alluvium derived from outcrops of these rocks or redder facies of the Tertiary section.

Red-colored areas have heavy vegetation cover and correspond to river valleys, cultivated fields, tree-covered mountainous areas, and grasslands. The red color is due to the relatively high reflectance of vegetation in MSS 7 (the red component), and relatively low reflectance in MSS 4 and MSS 5. Blue areas are spectrally flat, vegetation-free rocks and soils. The increased atmospheric scattering in the shorter wavelengths (predominantly band 4) contributes the relatively higher blue component. Water bodies are black due to very low reflectance in all wavelength bands.

The extensive mapping information contained in these data has been studied and reported for an adjoining area in Wyoming by Houston et al. (1977). They interpreted Landsat MSS data and compared their results with the published geologic map of Wyoming. More accurate portrayal of outcrop patterns and the subdivision of certain units were the major improvements reported.

A similar analysis (Figure 9-56) was done for this report of area A shown on Figure 9-55 along the eastern flank of the Bighorn Mountains. A tracing of the published geologic map (Love et al., 1955) covering this area is shown as Figure 9-56(a). The unit numbers are explained in Table 9-20.

The map shows several contacts as dashed lines, indicating only approximate locations. Contacts are smooth and without detail; no structures are shown. An interpretation map of the Landsat MSS data is shown for comparison in Figure 9-56(b). More detail can be seen in the shapes of the contacts between units. Individual units are discriminable based on color differences in the image related to the rock type. For example, unit 11, the Chugwater, Dinwoody, and Phosphoria Formations, is yellow in color on the image, indicating that the rocks are red. The gray to black shales appear dark on the image because they have low reflectance in the Landsat MSS bands. Grossly the geology is similar; in detail there is more information on the Landsat interpretation, indicating mapping inaccuracies on the state of Wyoming map.

A structural interpretation based on the interpreted outcrop patterns and bedding attitudes visible on the Landsat MSS image is shown in Figure 9-56(c). The synclines and anticlines reveal a pattern of intense folding in this area. The state map shows no structural information at all. It is clear from this example that Landsat data can provide a valuable basis for updating and upgrading regional geologic maps, even for areas which were thought to be fairly well mapped.

3. Color ratio composite (CRC). The process of band ratioing to highlight lithologic differences was first reported by Rowan et al. (1974). Ratioing subdues topographic effects and enhances subtle color differences by portraying spectral reflectance slopes rather than albedo information. A CRC of the Landsat MSS data for the area around Copper Mountain (area B in Figure 9-55) is shown in Figure 9-57. This image is a combination of band-ratios 4/5, 4/6, and 6/7 displayed as blue, green, and red, respectively. This particular combination depicts vegetation in blue (higher reflectance in the green when compared to the red part of the spectrum) and iron oxides in red (due to a ferric-iron absorption band near 1.0 μm). Most of the image is dominated by the presence of vegetation in the mountains. The oxidized granites at Copper Mountain appear as red patches on the image (areas marked A). However, similar-appearing red patches correspond to outcrops of Triassic red beds (areas marked B) and red beds in the Tertiary section (areas marked C and scattered areas in the southern third of the image). At the scale of this image (covering 28 by 35 km), Copper Mountain is still a very small area. It is doubtful whether the oxidized granites would have been found in a regional survey using an entire Landsat scene due to the small size of the area of interest.

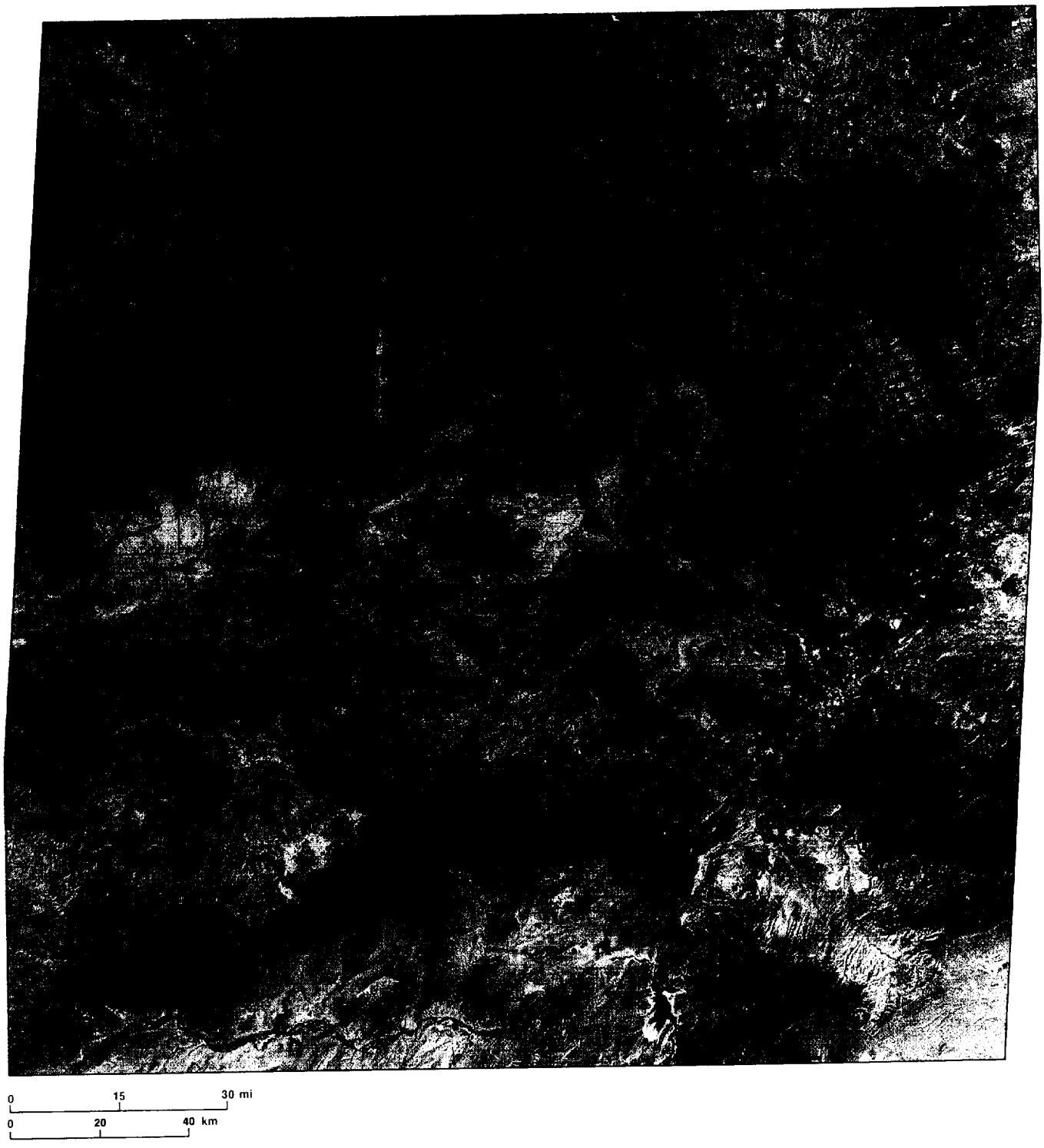

Figure 9-55. Landsat MSS scene covering central Wyoming and Copper Mountain (frame number 20998-16453, acquired October 16, 1977). Bands 4, 5, and 7 are displayed as blue, green, and red, respectively. Geologic interpretation of area A appears in Figure 9-56; CRC of area B appears in Figure 9-57.

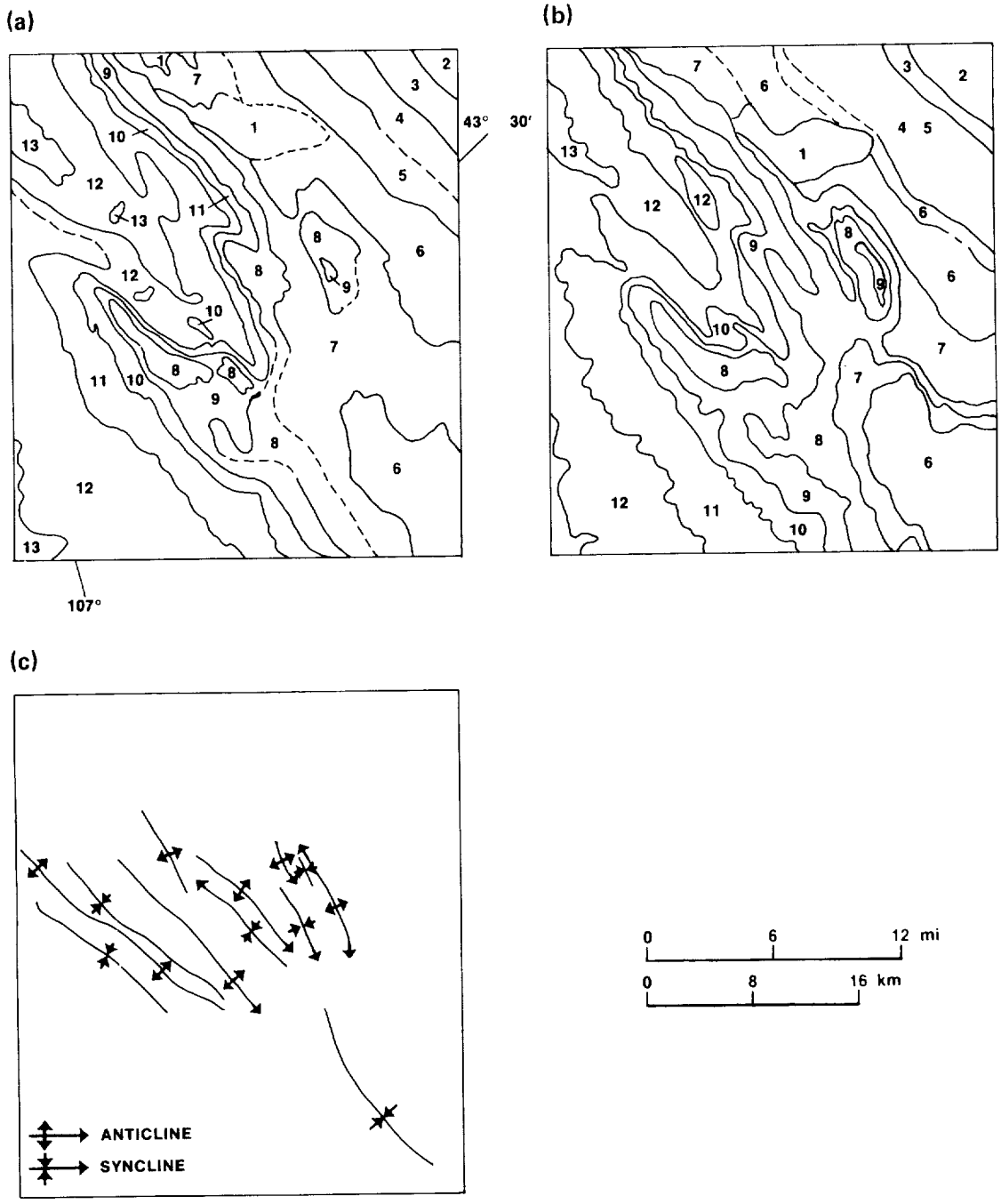

Figure 9-56. Interpretations of area A from Figure 9-55: (a) published geologic map (Love et al., 1955); (b) interpretation from Landsat image; (c) structures interpreted from Landsat image. See Table 9-20 for unit designations.

Table 9-20. Descriptions of units in Landsat MSS interpretation (Figure 9-56)

Unit	Age	Name	Description
1	Recent	Alluvium	
2	Tertiary	Wasatch Formation	Drab-colored sandstone, claystone, and shale
3	Tertiary	Fort Union Formation	Brown to gray sandstone, and black shale
4	Cretaceous	Lance Formation	Brown, gray, and tan sandstone
5	Cretaceous	Mesaverde Formation	Gray to tan sandstone and shale
6	Cretaceous	Cody Shale	Gray shale
7	Cretaceous	Frontier Formation	Gray shale and sandstone
8	Cretaceous	Mowry and Thermopolis Shales	Black and gray shale, and tan sandstone
9	Cretaceous-Jurassic	Cloverly and Morrison Formations	Light-gray sandstone, and variegated claystones
10	Jurassic	Sundance Formation	Greenish-gray and red sandstone and shale
11	Triassic-Permian	Chugwater, Dinwoody, and Phosphoria Formations	Red shale and sandstone, and cherty dolomite
12	Carboniferous	Tensleep Sandstone and Amsden Formation	Gray sandstone, and limestone
13	Carboniferous	Madison Limestone	Blue-gray limestone

G. PC Images Based on Covariance and Correlation Matrices

1. Difference between covariance and correlation formulations. In the Lisbon Valley, Utah, Uranium Test Site Report, Section 8, Appendix A, it was shown that if the relationship between encoded p-channel scanner radiance DN_i and nondirectional (Lambertian) surface reflectance ρ_i is of the form

$$DN_i = k_i' \rho_i + k_i'' \qquad (i = 1, \ldots, p) \tag{9-1}$$

where k_i' and k_i'' are constants, then the elements of the covariance matrix u_{ij} computed from the DN_i are related to the elements of the covariance matrix u_{ij}' computed from the ρ_i by the relationship

$$u_{ij} = k_i' k_j' u_{ij}' \tag{9-2}$$

and the covariance matrix is independent of the constant offset (additive terms k_i''). In addition, elements of the correlation matrix c_{ij} are related to elements of the covariance matrix by

$$c_{ij} = \frac{u_{ij}}{\sqrt{u_{ii} u_{jj}}} \tag{9-3}$$

Using the relationship (9-2) in Eq. (9-3) it is easily seen that the correlation matrix is independent of the constant gain factors k_i'. The factors k_i' and k_i'' incorporate instrumental and atmospheric parameters plus possible microscopic non-Lambertian reflectance properties of the surface. Thus the correlation matrix is seen to be independent of atmospheric and instrumental effects in the linear model, and has numerical values that would be obtained if it were computed from the surface reflectances directly.

PC images are usually calculated using eigenvectors derived from the scene covariance matrix, and thus contain atmospheric/instrumental effects in each component stemming from inclusion of the cross-channel gain factor products $k_i' k_j'$. It was shown in Section 8, Appendix A, that these gain factor products generate a dilation (or contraction) plus a rotation of the scatter ellipsoid between the so-called calibrated (gain factors removed) and uncalibrated (gain factors not removed) covariance matrices.

The color effects introduced in images by rotation and dilatation (i.e., noncalibration) of the radiance data swarm are not obvious from these calculations, but it is easy to eliminate effects introduced by the gain factors by calculating PCs using the correlation matrix. Examples of PC images derived from the correlation and from the covariance matrices for the southern line of NS-001 data at Copper Mountain are presented in the following paragraphs.

2. Comparison of images. The two PC images used in this comparison are shown in Figure 9-58. The processing for each is identical with the exception that the PCs for

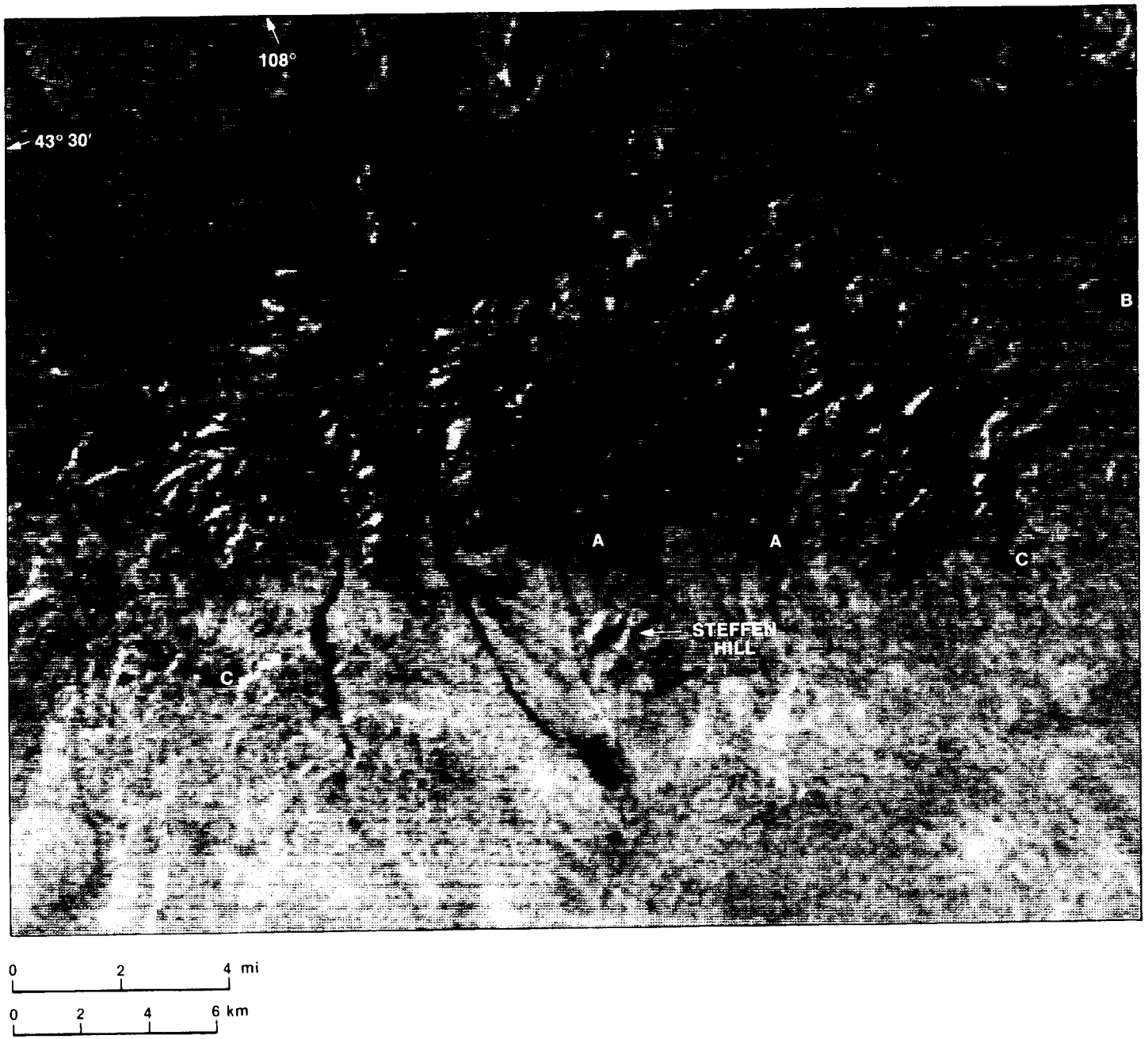

Figure 9-57. CRC of Landsat MSS data for area B in Figure 9-55. Band-ratios 4/5, 4/6, and 6/7 are displayed as blue, green, and red, respectively. See Paragraph X.F.3 for explanation of areas marked A, B, and C.

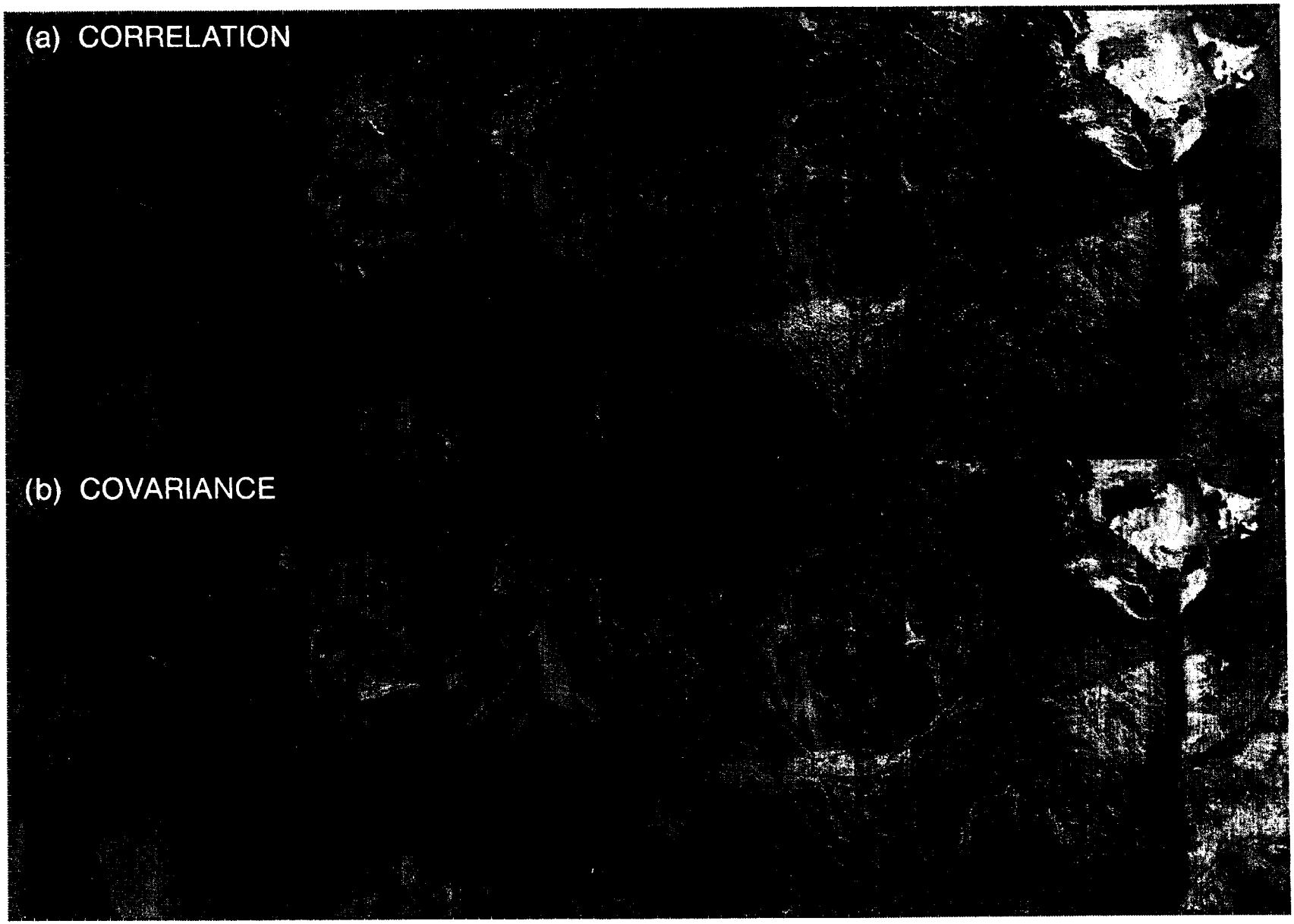

Figure 9-58. Comparison of PC images prepared from the correlation and covariance matrices for the southern line of NS-001 data at Copper Mountain: (a) eigenvectors for the PC transformation from the correlation matrix; (b) eigenvectors from the covariance matrix. PCs have the following color assignments: V2 = blue, V3 = red, and V4 = green.

Figure 9-58(a) were generated from eigenvectors of the correlation matrix, while those of Figure 9-58(b) were derived from the covariance matrix. The covariance and correlation matrices used for calculation of the PCs are given in Tables 9-9 and 9-21, respectively.

A PC transformation of byte data requires a rescaling after transformation. This was done automatically by choosing a linear scaling factor that saturated 0.5 percent of the data at 0 DN and 0.5 percent of the data at 255 DN. Since this rescaling method relies entirely on the outriding points of the distributions, the distribution functions for the bulk of the data do not necessarily match for the two images. Furthermore no attempt was made to force the two distribution functions to match in this example. Contrast stretches were made for one image and the same stretches applied to the other, i.e., an attempt was made to apply precisely the same contrast enhancement to each image product.

Comparison of the two images of Figure 9-58 shows the results to be nearly equivalent visually. Images that include the first PC rather than the fourth show even greater similarity. Closer correspondence could be achieved by matching one image to the other using appropriate but dissimilar contrast stretches.

These results suggest that computationally the covariance matrix based on the reflectances and the covariance matrix based on the DN are proportional element for element, and that the multiplicative factors connecting matrix elements in Eq. (9-2) are nearly equal. Therefore these factors may be removed (approximately) from the matrix formed from the right-hand side. The factor so removed becomes an additional constant multiplier that is inconsequential in determining the eigenvectors and merely scales the eigenvalues, all equally. Formation of the correlation matrix of course removes the influence of the cross-multiplied gain factors exactly, as indicated by Eq. (9-3).

Analysis of image data using the PC method based upon the correlation rather than the covariance matrix for the calculation of eigenvectors thus minimizes the influences of atmospheric and instrumental factors insofar as the transformant itself is concerned, *without* the need for laborious radiance calibration of the image data. This result exploits the linear relationships between encoded scanner radiance and surface reflectance found to hold widely for aircraft image data. For the data sets employed, the results using the covariance matrix eigenvectors are essentially equivalent.

Table 9-21. Copper Mountain NS-001 southern line correlation matrix, August 1979 (2,255,400 samples)

1.000						
0.933	1.000					
0.920	0.957	1.000				
0.823	0.875	0.914	1.000			
0.780	0.833	0.887	0.972	1.000		
0.833	0.880	0.934	0.872	0.917	1.000	
0.814	0.854	0.911	0.832	0.866	0.952	1.000

A closely related transformation, commonly referred to as the *canonical transform*, employs between- and within-group scatter matrices to find directions along which specified groups are separated as much as possible relative to scatter within the groups. It may be possible to employ equivalent between- and within-group *correlation* matrices for determination of their direction. In this case the canonical transform is also rendered independent of instrumental and atmospheric effects.

3. Inferences about the calibration relationship. The close similarity between PC images based upon the correlation matrix and the covariance matrix suggests that the relationship between scanner DN and surface reflectance is approximately linear, which is argued as follows.

The ith PC V_i is formed algebraically from the p-component eigenvector λ_{ij} by the relationship

$$V_i = \sum_{j=1}^{7} \lambda_{ij} DN_j$$

when the DN_js are scanner radiance values in channel j. Apart from scaling transformations, which in any event are the same for the two images of Figure 9-58, the PCs displayed are functions of the λ_{ij}. These are computed from the covariance and correlation matrix. The observation is that PCs for the two images are the same and therefore that the eigenvectors for the two images are nearly parallel. From Section 8, Appendix A, eigenvectors of the scatter ellipsoid are unchanged if gain factors in the calibration relationship are equal because they may be factored from the matrix. Computationally the variances for all channels, i.e., u'_{ii}, are observed to be nearly equal. Consequently all factors $1/\sqrt{u'_{ii}u'_{jj}}$ are similar, leading to the result that the covariance and correlation matrices are approximately proportional to each other and that their eigenvectors are thus nearly parallel. Linear transformation on the DN values, from which these matrices are computed, is the only transformation in which the "gain" factors alone appear as multiplication terms. This implies that the calibration relationship is approximately linear.

Since a quantitative means of comparing images is not available it can only be concluded that this relationship is approximate (i.e., any nonlinear terms are likely to be of second-order importance).

XI. Summary of Geology and Models

A. Geologic Setting of the Study Area

The eastern Owl Creek Mountains (Bridger Mountains) are located in central Wyoming and form the northern boundary of the Wind River Basin. Copper Mountain consists of a core of Precambrian metasedimentary and granitic rocks overlain with minimal unconformity by Paleozoic sandstones, shales, and limestones (Flathead, Gros Ventre, Gallatin, Bighorn, Madison) that form an arcuate dip slope on the northern side of the range dipping to the north and northeast.

In Laramide time the mountains were thrust southward over upturned Paleozoic and Mesozoic sediments deep in the basin. The "toe" of the thrust collapsed in a series of steeply dipping normal faults that mainly trend in an east–west direction. These faults with several thousand feet of displacement cut the Paleozoic rocks and the granites, and at the present time form boundaries of structural outliers of Paleozoic and granitic rock that are as much as several miles removed from the mountain front (Steffen Hill).

A series of soft fluvial and tuffaceous sedimentary rocks and gravels comprising the Lower Eocene Wind River Formation and the Middle and Upper Eocene Wagon Bed (Tepee Trail) Formation fill the basin to the south and lap onto the granitic (and locally the Paleozoic) rocks along the range front. The base of the Wind River Formation is generally not exposed, except in Steffen Hill where the formation rests on the Paleozoic section and Precambrian granitic rocks. The Wagon Bed Formation was deposited on a topographically rough surface cut in the deformed Wind River sediments and upon pediments cut in the granites. Locally the Wagon Bed is composed of sediments derived from scarps and hillsides in the underlying Wind River section. The Wagon Bed also contains boulder trains of granitic and metasedimentary rocks in high-energy depositional sites along canyons and near scarps in the Precambrian terrain. The bouldery Wagon Bed sediments were mostly deposited in paleovalleys cut in the mountains and, together with later formations, probably covered the mountain at one time. Since Miocene time, continued uplift and erosion has stripped this soft sedimentary cover from the range, exposing the mountain and portions of the granite pediment surface along the mountain front. Erosional new units of the bouldery Wagon Bed can be found at elevations as high as 7200 ft in Bridger Basin north of the crest and to elevations of 6800 ft in, for example, the West Fork of Dry Creek.

Following deposition of Wagon Bed sediments, the sediments were faulted and folded and a pediment surface cut in them along the range front. The Wagon Bed pediment (also possibly the older granitic pediment) was capped by gravels of Pleistocene and Holocene age that have themselves been uplifted and now exist as dissected fans and as terrace remnants.

B. Uranium Mineralization and Relations to Oxidation

Yellich et al. (1978) described uranium mineralization (Canning deposit) in fractured granites at Copper Mountain. A supergene origin was proposed in which uranium was leached from the granites and possibly the overlying sediments and deposited at depth by downward-migrating solutions in fractured, porous, and chemically reducing environments beneath. These same solutions were envisioned to be agents oxidizing the granites exposed at the surface. This process is analogous to the formation of a roll-type deposit in a sandstone environment; in the present case, however, oxidized rock at the surface represented a vertically oriented alteration tongue with ore fluids moving predominantly vertically as opposed to predominantly horizontally as in the case of a sandstone deposit. In the analogy the oxidized horizons would form ready guides to mineralization in the granite.

Examination of the origin and age relations of the oxidized surface layer itself suggests a more complicated picture. Several alternatives are possible:

(1) The oxidized horizon in the granites corresponds to a pre-Middle Eocene, pre-Wagon Bed Formation weathered surface developed on pediments locally exposed by erosion. Drill-core evidence indicates the weathering surface may have been incised and the oxidized layer removed locally or may have been prevented from developing along major paleostream channels cutting it in pre-Wagon Bed time. The leaching of uranium from the granites and its transport to the structurally prepared rocks beneath accompanied development of the weathered horizon in accordance with the supergene model. Material balance calculations by RME geologists tabulating the available leachable uranium in the granites versus the accumulated sooty pitchblende at depth indicate this episode of mineralization would account for no greater than one-half of the mineralization present in the deposit. Subsequently burial by sediments and uranium-rich tuffaceous rocks of the

mid-Eocene and later formations filled the stream channels and buried the pediment surface, and by mid-Miocene time covered the mountain range itself. During this period circulation of oxygen-rich surface waters through the granites beneath the sediments ceased, and uranium deposition terminated.

Uplift and erosion subsequent to mid-Miocene time partially stripped the Tertiary cover, reexposing the granites and at the same time reinitiated uranium leaching and redistribution into the granites and into the Tertiary sediments themselves. This second period of mineralization is visualized by RME geologists as contributing the remainder of the uranium now found in the Canning deposit. The present distribution of mineralization in the granites at depth closely reflects the present distribution of Tertiary cover, insofar as this clay-choked sedimentary blanket prevents effective circulation of oxygenated water that would act to remobilize uranium and destroy the deposit.

The distribution of weathering in the granite, where exposed beneath Tertiary cover, thus is pictured as representing approximately the first half of the total mineralization history of this resource. Surface oxidation of the granite in this picture represents a necessary but not a sufficient condition for the occurrence of mineralization. A sufficient condition includes the existence of structurally prepared, chemically reducing environments in the granites at depth. Determination of the distribution of such environments is outside the scope of remote sensing methods.

(2) A second alternative is that the surface-oxidation effects are of late origin and that they accompanied the reexposure of the granites to subaerial weathering conditions after extended "weathering" in saturated, aqueous, subsurface environments. This idea combines the notion of Thaden (1980b) with observations from the present study that the oxidation may be of late origin, possibly post-Pleistocene. In this case the surface-weathering effects are less important for uranium prospecting because the oxidation effects postdate most of the supposed mineralization episodes. The distribution of oxidation may conceivably be a secondary indicator of propylitic or other hydrothermal alteration.

(3) A third alternative for a mineralization model is that presented by Shrier and Parry (1982). They attempt to incorporate the observational data into a low-temperature hydrothermal model for the deposit. This involves radioactive heat driving the circulation of a closed water-rich system in the granite, where the uranium is dissolved and the rock altered by the transporting solutions. Observationally the alteration effects are dominated by Na-montmorillonite from K-feldspar, sericite replacing plagioclase and biotite, and chlorite sporadically replacing biotite.

This view of the applicable alteration mineralogy suggests many species with hydrous absorptions near 2.3 to 2.5 μm which might be of use in remote sensing studies. Laboratory studies indicate the important low-temperature propylitic alterations may be masked by more important (opaque) iron-oxidation products and the iron minerals may themselves be destroyed.

XII. Conclusions

(1) The relations between ore deposition and observable surface effects of the deposition process are not settled and need further study, i.e., the model is in question.

(2) The supergene and hydrothermal models make specific predictions, but the supergene model alone is subject to testing using remote sensing data. This results from the masking of the alteration effects (mainly hydrous silicates and epidote) in the hydrothermal model by iron oxides that result from surface weathering.

(3) The spectral reflectance characteristics of iron-oxide coatings and uncoated substrates were studied by using the dithionite–citrate extraction method to remove iron-oxide coatings. Subtle, masked, spectral absorption bands were revealed when the coatings were removed. However, these coatings effectively masked spectral features that are important for verification of the ore-deposition models.

(4) The NS-001 Thematic Mapper Simulator data were examined for geological information by comparison of PC composites with existing detailed geologic maps. The scanner data could be used to recover most of the lithologic boundaries appearing on the published maps. In addition, problems encountered during the field mapping could be resolved using the scanner data. This additional information, combined with a faithful representation of lithologic boundaries, indicates that the NS-001 wavelength bands and the 15-m spatial resolution of the aircraft scanner can be used to produce detailed, accurate geologic maps.

(5) The distribution and subdivision of six Quaternary gravel deposits were successfully accomplished using

the NS-001 data. These units were not separated on the published maps of the area. Separation was based on spectral differences of the different-aged units, morphological appearances, and inferred overlap relationships.

(6) The Bendix 11-channel M²S scanner data were used to map the distribution and intensity of iron-oxide-coated materials. A density slice of the band-ratio 4/6 was quantitatively related to the degree of oxidation by calibration with field-acquired reflectance measurements. The resulting image displayed the distribution of all iron-oxide-bearing rocks without regard to source. No separations were made between moderately oxidized granites and Paleozoic red beds. However, oxidized granites associated with uranium occurrences were found to be the most intensely oxidized areas in the M²S density slice image.

(7) The NS-001 PC images portray the oxidized granites in a color distinct from the display of other iron-oxide-bearing rocks. This indicates that spectral information from the wavelength region beyond 1.0 μm may contribute to separating different types of iron-bearing rocks. Analysis of field spectral measurements supports this conclusion: the association of hydrous minerals (clays) with the altered granites produces spectral absorption features near 2.2 μm which are being sensed by the NS-001 scanner bands. However, the iron absorptions dominate.

(8) Oxidation patterns in the granite were found to be related to old, exposed pediments and to old, exposed paleosurfaces in pre-Middle Eocene valleys in the range. These mantled areas probably reflect topography long covered and weathered in water-saturated environments and thus subject to more rapid subaerial weathering and oxidation.

(9) Good agreement is obtained in the comparison of published SCS soil maps and image data. The soil units are important because they represent the surface horizon actually measured in remote sensing studies. The study of soils and weathered layers should reflect the importance of the surface layer because remote sensing data of this type can greatly aid soil mapping projects.

(10) The relationship between uranium mineralization and surface oxidation of the granites remains unresolved. The distribution of mineral deposits probably reflects a relatively modern influence of uranium deposit removal by vertically circulating waters after the capping Tertiary sediments have been removed by erosion. This problem cannot be pursued further without access to additional detailed drill-core data and probably further drilling in the area at sites that would be scientifically beneficial but probably commercially unattractive.

(11) Directional effects in the scanner data arising at the surface are prominent. They are not removed by atmospheric correction procedures that assume homogeneous surface reflectance, and they pose problems for accurate mosaicking of image data when large angular fields of view are involved in areas with substantial topographic relief.

(12) PC images can be prepared in two ways: (1) using the correlation matrix, and (2) using the covariance matrix. The images that result are equivalent. Those of the correlation matrix eliminate *all* atmospheric and instrumental effects in the transformation based on a linear model of the relation between scanner radiance and surface reflectance.

After completion of the present report, a new study on the Copper Mountain Uranium District was reported by geologists of the Bendix Field Engineering Corporation working with the National Uranium Resource Evaluation (NURE) Program of the Department of Energy (Sayala et al., 1982). This report provides geological, geochemical, geophysical, and soil survey data on the occurrences of uranium, ages of ore deposition, detailed maps of mineralization distribution (not previously available), as well as additional thoughts on models of occurrence for the deposit. For further information about the site, refer to this extensive compendium.

Acknowledgments

The authors wish to thank J. Babcock, R. Cramer, J. Davis, R. Farewell, R. Honea, J. Kendall, S. Reyher, and J. Yellich of RME for their help and advice during the course of this work.

Dr. J. Gabelman, of Utah International, Inc., suggested the Copper Mountain area as one of the NASA/Geosat test sites for uranium. The authors' many discussions with him on the geology of uranium and on the Copper Mountain test site have been greatly appreciated. H. Horton, also of Utah International, Inc., provided assistance in the field.

The technical help and support of the following people at JPL are greatly appreciated: R. Machida, H. Paley, K. Baird, E. Abbott, B. Rock, A. Gillespie, D. Madura, A. Kahle, A. Goetz, and F. Palluconi.

J. Soha of JPL's IPL offered useful advice and insights into image processing and statistical problems. Dr. J. Solomon, also of IPL, produced, on very short notice, the statistical studies of PC data described in the text. He also has acted as a sounding board for many ideas during the last two years of the study.

Dr. R. Thaden of the U.S. Geological Survey provided an informal analysis of the NS-001 image data and comparisons with his geologic mapping of the area. His help with this study and his lengthy, detailed letters describing other unpublished findings of his fieldwork were invaluable.

J. Iiams of SCS provided the preliminary soil maps and soil unit descriptions used in this report. His cooperation is greatly appreciated. Any misrepresentation of the work is the responsibility of the present authors.

R. Arjal, with permission of RME, supplied the vegetation maps and plant species lists used in the report.

Dr. M. Settle of NASA Headquarters reviewed the document and offered helpful suggestions for improving this final report.

Finally, the senior author wishes to thank his wife, Cheryl, for her patience and help throughout the course of this study.

References

Benson, L. (1979). *Plant classification* (2nd ed.). Lexington, Massachusetts: D. C. Heath and Co., 753–815.

Berg, R. R. (1962). Mountain flank thrusting in the Rocky Mountain foreland, Wyoming and Colorado. *AAPG Bull., 46,* 2019–2032.

Blanchard, R. (1968). Interpretation of leached outcrops. *Nev. Bureau of Mines Bull. 66*

Bramlett, L. B., D. Emilia, J. Holden, R. Kerns, S. Moll, and R. Sadowski (1979a). *Uranium exploration systems case study, Copper Mountain, Wyoming.* Unpublished conference report, Bendix Field Engineering Corporation, Grand Junction, Colorado.

Bramlett, L. B., R. F. Czarnecki, D. A. Emilia, J. C. Pacer, R. M. Sadowski, and J. S. Schmidt (1979b). *Uranium geophysics, Copper Mountain, Wyoming* (Preprint 79-336). Paper presented at the Society of Mining Engineers of AIME, Fall Meeting, Tucson, Arizona, 1979.

Bramlett, L. B., S. L. Reyher, and G. G. Southard (1980). *Uranium geology and geochemistry, Copper Mountain, Wyoming* (Preprint 80-102). Paper presented at the Society of Mining Engineers of AIME, Annual Meeting, Las Vegas, 1980.

Condie, K. C. (1967). Petrologic reconnaissance of the Precambrian rocks in Wind River Canyon, central Owl Creek Mountains, Wyoming. *Wyo. Univ. Dep. Geol. Contrib. Geol., 6,* 123–129.

Condie, K. C., A. P. Leech, and H. Baadsguard (1969). Potassium–argon ages of mafic dikes from Wyoming. *Geol. Soc. Am. Bull., 80,* 899–906.

Conel, J. E., M. J. Abrams, and A. F. H. Goetz (1978). *A study of alteration associated with uranium occurrences in sandstone and its detection by remote sensing methods* (JPL Publication 78-66). Pasadena, California: Jet Propulsion Laboratory.

Everitt, B. S. (1977). *Analysis of contingency tables.* New York: John Wiley & Sons.

Fanshawe, J. R. (1939). Structural geology of Wind River Canyon area, Wyoming. *AAPG Bull., 23,* 1439–1492.

Ferris, C. S., Jr. (1968). Tertiary faults with reversed movements near Copper Mountain, central Wyoming. *Wyo. Univ. Dep. Geol. Contrib. Geol., 1,* 117–128.

Garrels, R. M., and C. L. Christ (1965). *Solutions, minerals and equilibria.* New York: Harper & Row.

Gliozzi, J. (1967). *Petrology and structure of the Precambrian rocks of the Copper Mountain District, Owl Creek Mountains, Fremont County, Wyoming.* Unpublished doctoral dissertation, University of Wyoming.

Goodman, L. A. (1978). *Analyzing qualitative/categorical data.* Cambridge, Massachusetts: Abt Books.

Grutt, E. W. (1954). Unpublished report, U.S. Atomic Energy Commission.

Hamil, M. M. (1971). *Metamorphic and structural environment of Copper Mountain, Wyoming.* Unpublished doctoral dissertation, University of Missouri.

Houston, R., R. Marrs, N. Short, and P. Lowman (1977). Earth observations from remote-sensing platform. In W. Smith (Ed.), *Remote sensing application for mineral exploration* (NASA SP 99-156).

Hunt, G. R., and J. W. Salisbury (1970). Visible and near-infrared spectra of minerals and rocks: I. Silicate minerals. *Mod. Geol., 1,* 283–300.

Hunt, G. R., J. W. Salisbury, and C. J. Lenhoff (1971). Visible and near-infrared spectra of minerals and rocks: III. Oxides and hydroxides. *Mod. Geol., 2,* 195–205.

Hunt, G. R., J. W. Salisbury, and C. J. Lenhoff (1973). Visible and near-infrared spectra of minerals and rocks: VI. Additional silicates. *Mod. Geol., 4,* 85–106.

Kahle, A. (1980). Surface thermal properties. In B. Siegal and A. R. Gillespie (Eds.), *Remote sensing in geology.* New York: Wiley and Jones, 257–274.

Kahle, A. B., J. P. Schieldge, M. J. Abrams, R. E. Alley, and C. J. LeVine (1981). *Geologic application of thermal inertia imaging using HCMM data* (JPL Publication 81-55). Pasadena, California: Jet Propulsion Laboratory.

Keefer, W. R., and J. D. Love (1963). Laramide vertical movements in central Wyoming. *Wyo. Univ. Dep. Geol. Contrib. Geol., 2,* 47–54.

Kendall, R. G., S. L. Reyher, D. Atherley, K. A. Taylor, and D. K. Morton (1980). *Geologic evaluation of the Copper Mountain development project, Fremont County, Wyoming.* Unpublished report, Rocky Mountain Energy Company, Denver, Colorado.

Love, J. D., J. L. Weitz, and R. K. Hose (1955). Geologic map of Wyoming. *U.S. Geol. Surv. Map MS-7.*

Nkomo, I. T., J. S. Stucklen, R. E. Thaden, and J. N. Rosholt (1978). Petrology and uranium mobility of a granite of early Precambrian age from the Owl Creek Mountains, Wyoming. In *Wyoming Geological Association Guidebook, 30th Annual Field Conference,* 335–348.

Norton, D. L. (1982). Fluid and heat transport phenomena typical of copper-bearing pluton environments. In S. R. Titley (Ed.), *Advances in geology of the porphyry copper deposits, southwestern North America.* Tucson: University of Arizona Press, 59–72.

Osterwald, F. W., D. B. Osterwald, J. S. Long, and W. H. Wilson (1966). Mineral resources of Wyoming. *Geol. Surv. Wyo. Bull. 50.*

Rowan, L. C., P. H. Wetlaufer, A. F. H. Goetz, F. C. Billingsley, and J. H. Stewart (1974). Discrimination of rock types and detection of hydrothermally altered areas in south-central Nevada by use of computer-enhanced ERTS images. *U.S. Geol. Surv. Prof. Pap. 883.*

Sayala, D., J. Lindgren, and L. Babcock (1982). *An exploration systems approach to the Copper Mountain area uranium deposits, central Wyoming* (GJBX-201(82)). Grand Junction, Colorado: Bendix Field Engineering Corporation. (NURE report prepared for the U.S. Department of Energy)

Shrier, T., and W. T. Parry (1982). A hydrothermal model for the North Canning uranium deposit, Owl Creek Mountains, Wyoming. *Econ. Geol., 77,* 632–645.

Stearns, D. W., G. Couples, and M. T. Stearns (1978). Deformation of non-layered materials that affect structures in layered rocks. In *Wyoming Geological Association Guidebook, 30th Annual Field Conference,* 213–225.

Thaden, R. E. (1978). Geologic map of the Bonneville Quadrangle, Fremont County, Wyoming. *U.S. Geol. Surv. Quadrangle Map GQ-1439.*

Thaden, R. E. (1979). Geologic map of the Lysite Quadrangle, Fremont County, Wyoming. *U.S. Geol. Surv. Quadrangle Map GQ-1511.*

Thaden, R. E. (1980a). Geologic map of the Birdseye Pass Quadrangle, Fremont and Hot Springs Counties, Wyoming. *U.S. Geol. Surv. Quadrangle Map GQ-1537.*

Thaden, R. E. (1980b). Geologic map of the De Pass Quadrangle, Fremont and Hot Springs Counties, Wyoming. *U.S. Geol. Surv. Quadrangle Map GQ-1526.*

Thaden, R. E. (1980c). Geologic map of the Gates Butte Quadrangle, Fremont County, Wyoming. *U.S. Geol. Surv. Quadrangle Map GQ-1538.*

Thaden, R. E. (1980d). Geologic map of the Guffy Peak Quadrangle, Fremont and Hot Springs Counties, Wyoming. *U.S. Geol. Surv. Quadrangle Map GQ-1527.*

Thaden, R. E. (1980e). Geologic map of the Picard Ranch Quadrangle, Fremont County, Wyoming. *U.S. Geol. Surv. Quadrangle Map GQ-1539.*

Thaden, R. E. (1981). Geologic map of the Arapahoe Butte Quadrangle, Fremont and Hot Springs Counties, Wyoming. *U.S. Geol. Surv. Quadrangle Map GQ-1558.*

Tourtelot, H. A. (1953). Geology of the Badwater area, central Wyoming. *U.S. Geol. Surv. Oil Gas Invest. Map OM-124.*

Upton, G. J. G. (1978). *Analysis of cross-tabulated data.* New York: John Wiley & Sons.

Voss, W. C. (1973). Unpublished report, Rocky Mountain Energy Company, Denver, Colorado.

Yellich, J. A., R. T. Cramer, and R. G. Kendall (1978). Copper Mountain, Wyoming, uranium deposit–rediscovered. In *Wyoming Geological Association Guidebook, 30th Annual Field Conference,* 311–327.

Appendix A
Plant Species List for the Copper Mountain Test Site

The following plant list, which covers the area depicted in Figure 9-4, was prepared and provided by RME botanists, October 1976.

Scientific Name	Common Name
Anacardiaceae	sumac family
Rhus trilobata	skunkbush sumac
Apiaceae	carrot family
Lomatium sp.	biscuitroot
Cymopterus sp.	cymopterus
Asteraceae	sunflower family
Achillea millefolium	common yarrow
Antennaria microphylla	littleleaf pussytoes
Antennaria rosea	rose pussytoes
Artemisia cana	silver sagebrush
Artemisia frigida	fringed sagewort
Artemisia pedatifida	birdfoot sagewort
Artemisia porteri	Porter sagewort
Artemisia tridentata	basin big sagebrush
Bahia nudicaulis	basin bahia
Centaurea repens	Russian centaurea
Chaenactis douglassii	Douglas dusty maiden
Chrysothamnus nauseosus	rubber rabbitbrush
Chrysothamnus viscidiflorus	Douglas rabbitbrush
Chichorium intybus	common chicory
Cirsium sp.	thistle
Erigeron pumilus	low fleabane
Grindelia spuarrosa	curlycup gumweed
Gutierrezia sarothrae	broom snakeweed
Haplopappus multicaulis	stemmy goldenweed
Haplopappus sp.	goldenweed
Haplopappus spinulosus	ironplant goldenweed
Helianthus rigidus	stiff sunflower
Heterotheca villosa	hairy goldenaster
Hymenopappus filifolius	fineleaf hymenopappus
Hymenoxys acaulis	stemless actinea
Iva axillaris	poverty sumpweed
Iva xanthifolia	rag sumpweed
Machaeranthera canescens	hoary tansyaster
Taraxacum officinale	common dandelion
Wyethia scabra	badlands wyethia
Betulaceae	birch family
Betula occidentalis	water birch
Boraginaceae	borage family
Cryptantha sp.	cryptantha
Brassicaceae	mustard family
Cardaria pubescens	hairy whitetop
Descurainia sophia	flixweed tansymustard
Lepidium virginicum	Virginia pepperweed
Sisymbrium linifolium	unnamed hedgemustard
Stanleya pinnata	desert princesplume
Thlaspi arvense	field pennycress
Cactaceae	cactus family
Opuntia polyacantha	plains pricklypear
Caprifoliaceae	honeysuckle family
Symphoricarpos sp.	snowberry
Caryophyllaceae	pink family
Arenaria (hookerii) sp.	sandwort
Cerastium arvense	starry cerastium
Chenopodiaceae	goosefoot family
Atriplex confertifolia	shadscale saltbush
Atriplex gordonii	Gordon saltbush
Atriplex sp.	saltbush
Atriplex wolfii	Wolf saltbush
Ceratoides lanata	winterfat
Chenopodium sp.	goosefoot
Halogeton glomeratus	halogeton
Kochia scoparia	fireweed summercypress
Sarcobatus vermiculatus	black greasewood
Cornaceae	dogwood family
Cornus stolonifera	redosier dogwood
Crassulaceae	stonecrop family
Sedum lanceolatum	wormleaf stonecrop
Cupressaceae	juniper family
Juniperus osteosperma	Utah juniper
Juniperus scopulorum	Rocky Mountain juniper
Cyperaceae	sedge family
Carex filifolia	threadleaf sedge
Carex sp.	sedge

Scientific Name	Common Name
Juncaceae	rush family
Juncus sp.	rush
Luzula sp.	woodrush
Lamiaceae	mint family
Mentha arvensis	field mint
Leguminosae	pea family
Astragalus bisulcatus	two-grooved milkvetch
Astragalus grayi	Gray milkvetch
Astragalus sp.	milkvetch
Glycyrrhiza lepidota	American licorice
Lupinus argenteus	silvery lupine
Lupinus lepidus	pacific lupine
Melilotus officinalis	yellow sweetclover
Oxytropis besseyi	Bessey locoweed
Psoralea lanceolata	lemon scurfpea
Trifolium sp.	clover
Vicia americana	American vetch
Liliaceae	lily family
Allium textile	prairie onion
Calochortus nuttallii	mariposa lily
Malvaceae	mallow family
Sphaeralcea coccinea	scarlet globemallow
Onagraceae	evening primrose family
Epilobium anagallidifolium	alpine willowherb
Oenothera caespitosa	tufted evening primrose
Orobanchaceae	broomrape family
Orobanche fasciculata	purple broomrape
Pinaceae	pine family
Pinus flexilis	limber pine
Plantaginaceae	plantain family
Plantago patagonica	woolly plantain
Poaceae	grass family
Agropyron dasystachyum	thickspike wheatgrass
Agropyron smithii	western wheatgrass
Agropyron sp.	wheatgrass
Agropyron spicatum	bluebunch wheatgrass
Agrostis exarata	spike bentgrass
Agrostis sp.	bentgrass
Aristida fendleriana	Fendler threeawn
Aristida longiseta	red threeawn
Bouteloua gracilis	blue grama
Bromus inermis	smooth brome
Bromus japonicus	Japanese brome
Bromus tectorum	cheatgrass brome
Distichlis stricta	inland saltgrass
Elymus canadensis	Canada wildrye
Elymus cinereus	basin wildrye
Hordeum jubatum	foxtail barley
Koeleria macrantha	prairie junegrass
Muhlenbergia filiformis	pullup muhly
Munroa squarrosa	false buffalograss
Oryzopsis hymenoides	Indian ricegrass
Poa pratensis	Kentucky bluegrass
Poa sandbergii	Sandberg bluegrass
Poa sp.	bluegrass
Polypogon sp.	beardgrass
Schizachyrium scoparium	little bluestem
Sitanion hystrix	bottlebrush squirreltail
Sporobolus airoides	alkali sacaton
Stipa comata	needle-and-thread grass
Vulpia octoflora	sixweeks fescue
Polemoniaceae	phlox family
Ipomopsis spicata	spike gilia
Leptodactylon caespitosum	mat pricklygilia
Phlox hoodii	Hood phlox
Polygonaceae	buckwheat family
Eriogonum brevicaule	shortstem wildbuckwheat
Eriogonum ovalifolium	cushion wildbuckwheat
Eriogonum sp.	wildbuckwheat
Portulacaceae	purslane family
Lewisia rediviva	bitterroot lewisia
Primulaceae	primrose family
Dodecatheon pulchellum	darkthroat shootingstar
Ranunculaceae	buttercup family
Delphinium sp.	larkspur
Rosaceae	rose family
Prunus virginiana	common chokecherry
Rosa sayi	prickly rose
Rosa sp.	rose
Salicaceae	willow family
Populus angustifolia	narrowleaf cottonwood
Populus deltoides	plains cottonwood
Populus tremuloides	quaking aspen
Salix exigua	coyote willow
Saxifragaceae	currant family
Ribes inerme	whitestem currant
Scrophulariaceae	figwort family
Castilleja chromosa	desert Indian paintbrush
Mimulus guttatus	common monkeyflower
Orthocarpos luteus	yellow owlclover
Penstemon angustifolius	narrowleaf penstemon
Penstemon eriantherus	fuzzytongue penstemon
Penstemon nitidus	waxleaf penstemon
Veronica americana	American speedwell
Tamaricaceae	tamarisk family
Tamarix chilensis	tamarisk

Appendix B
Correspondence Between Soil Mapping and Geologic Mapping Units

This appendix tabulates examples of the correspondence between soil mapping units and geologic mapping units. The soil mapping units and soil series data are from descriptions provided by J. Iiams, SCS, 1982. Where typical pedons fall within the area of geologic mapping, equivalent geologic units for soil series are also given.

Table B-1. Examples of geologic and soil unit correspondences[a]

Soil Unit	Geologic Unit and Location
102	Twb, near Dry Creek, Sec. 31, T40N, R92W
104	Paleozoic outcrop undivided, Steffen Hill, Secs. 5 and 6, T39N, R92W; €g, Ob, Mm
105	Twb, Secs. 2, 3, and 4, T39N, R92W, Sec. 13, T40N, R92W
206	Qa1, Dry Creek granitic, Twb sources, Sec. 31, T40N, R92W
206f	Qa1, Hoodoo Creek granitic, Mm, southern T40N, R93W
231	Twb, Qoa, Qg, Paleozoic sources undivided, Secs. 5 and 6, T39N, R91W
237	Twb, Sec. 3, T39N, R93W; Qoa, Sec. 32, T40N, R92W
242	Twb, Sec. 1, T39N, R92W
271	Twb, Qa1, Sec. 36, T40N, R93W; Sec. 1, T39N, R93W; Ag, NW 1/4, Sec. 31, T40N, R92W
274	Twb, Sec. 1, T39N, R92W
277	Am, SW 1/4, NW 1/4, Sec. 24, T40N, R93W
298	Twb, Secs. 32 and 33, T40N, R92W; Twb, Ag, SE 1/4, Sec. 2, T39N, R92W
306	Twb, SE 1/4, Sec. 93, T39N, R93W
342	Twb, NE 1/4, Sec. 11, T39N, R92W
372	Twb, Sec. 1, T39N, R92W
3109	Ag outcrops, Sec. 36, T40N, R92W, Sec. 20, T40N, R92W
2a32	Qoa mainly, SW 1/4, Sec. 32, T40N, R92W; Qg, Sec. 3, T39N, R92W; Sec. 25, T40N, R93W
2a32s	Twb in canyons of East Fork of Dry Creek, Sec. 27, T40N, R92W
2f72	Ag, mantled rock outcrop, NW 1/4, Sec. 23, T40N, R92W; Am, metamorphic (soil-covered) outcrops, Sec. 18, T40N, R92W; €f, Sec. 30, T40N, R91W
2g11	Qg, probable Paleozoic source, Sec. 6, T39N, R91W
2g72	€f and €gv, Sec. 24, T40N, R92W
2n11	Twb, Sec. 5, T39N, R91N

[a]Abbreviations used for geologic units are as follows (cf. Thaden, 1978, 1979, 1980a–1980e, 1981):
Quaternary (Holocene)–Qa1, alluvium; Qoa, older alluvium
Quaternary (Holocene and Pleistocene) –Qg, gravel
Upper and Middle Eocene–Twb, Wagon Bed Formation volcaniclastic claystone and sandstone
Upper and Lower Mississippian–Mm, Madison Limestone
Upper and Middle Ordovician–Ob, Bighorn Dolomite
Upper Cambrian–€g, Gallatin Formation
Middle Cambrian–€qv, Gros Ventre Formation siltstone, sandstone, limestone
Middle Cambrian–€f, Flathead Sandstone
Archean –Ag, granite
Archean–Am, metasedimentary rocks

Appendix B
References

Thaden, R. E. (1978). Geologic map of the Bonneville Quadrangle, Fremont County, Wyoming. *U.S. Geol. Surv. Quadrangle Map GQ-1439.*

Thaden, R. E. (1979). Geologic map of the Lysite Quadrangle, Fremont County, Wyoming. *U.S. Geol. Surv. Quadrangle Map GQ-1511.*

Thaden, R. E. (1980a). Geologic map of the Birdseye Pass Quadrangle, Fremont and Hot Springs Counties, Wyoming. *U.S. Geol. Surv. Quadrangle Map GQ-1537.*

Thaden, R. E. (1980b). Geologic map of the De Pass Quadrangle, Fremont and Hot Springs Counties, Wyoming. *U.S. Geol. Surv. Quadrangle Map GQ-1526.*

Thaden, R. E. (1980c). Geologic map of the Gates Butte Quadrangle, Fremont County, Wyoming. *U.S. Geol. Surv. Quadrangle Map GQ-1538.*

Thaden, R. E. (1980d). Geologic map of the Guffy Peak Quadrangle, Fremont and Hot Springs Counties, Wyoming. *U.S. Geol. Surv. Quadrangle Map GQ-1527.*

Thaden, R. E. (1980e). Geologic map of the Picard Ranch Quadrangle, Fremont County, Wyoming. *U.S. Geol. Surv. Quadrangle Map GQ-1539.*

Thaden, R. E. (1981). Geologic map of the Arapahoe Butte Quadrangle, Fremont and Hot Springs Counties, Wyoming. *U.S. Geol. Surv. Quadrangle Map GQ-1558.*

Section 9

Copper Mountain, Wyoming, Uranium Test Site Report

James E. Conel
Ronald E. Alley
Michael J. Abrams
Jet Propulsion Laboratory